

PROCEEDINGS OF THE SIXTH EUROPEAN CONFERENCE ON NUMERICAL
METHODS IN GEOTECHNICAL ENGINEERING, GRAZ, AUSTRIA, 6–8
SEPTEMBER 2006

Numerical Methods in Geotechnical Engineering

Edited by

Helmut F. Schweiger

Graz University of Technology, Austria



Taylor & Francis
Taylor & Francis Group

LONDON / LEIDEN / NEW YORK / PHILADELPHIA / SINGAPORE



Copyright © 2006 Taylor & Francis Group plc, London, UK

All rights reserved. No part of this publication or the information contained herein may be reproduced, stored in a retrieval system, or transmitted in any form or by any means, electronic, mechanical, by photocopying, recording or otherwise, without written prior permission from the publisher.

Although all care is taken to ensure the integrity and quality of this publication and the information herein, no responsibility is assumed by the publishers nor the author for any damage to property or persons as a result of operation or use of this publication and/or the information contained herein.

Published by: Taylor & Francis/Balkema
P.O. Box 447, 2300 AK Leiden, The Netherlands
e-mail: Pub.NL@tandf.co.uk
www.balkema.nl, www.tandf.co.uk, www.crcpress.com

ISBN10 Set: 0-415-40822-9
ISBN10 Book: 0-415-40477-0
ISBN10 CD: 0-415-40821-0

ISBN13 Set: 978-0-415-40822-6
ISBN13 Book: 978-0-415-40477-8
ISBN13 CD: 978-0-415-40821-9

Printed in Great-Britain

Table of Contents

Preface	XV
<i>ERTC7 benchmark exercise</i>	
Results from the ERTC7 benchmark exercise <i>H.F. Schweiger</i>	3
<i>Constitutive modeling and numerical implementation</i>	
Modeling the behavior of expansive clays <i>M. Sánchez, A. Gens, S. Olivella & L. do N. Guimarães</i>	11
A constitutive model for undrained anisotropic behaviour of clays <i>G. Grimstad, S. Nordal & C. Athanasiu</i>	19
Calculation of shear band thickness in sensitive clays <i>H.P. Jostad, L. Andresen & V. Thakur</i>	27
Response envelopes of the elasto-plastic S-CLAY1 model <i>R. Zentar, N.-E. Abriak, M. Karstunen & D. Rangeard</i>	33
Modelling small-strain stiffness with the multilaminate framework <i>F. Scharinger, H.F. Schweiger & G.N. Pande</i>	41
An evaluation of constitutive models to predict the behaviour of fine-grained soils with different degrees of overconsolidation <i>V. Hájek & D. Mašín</i>	49
An elasto-plastic constitutive model for clays considering microstructure <i>L.R. Kong, P.Y. Hicher, C.S. Chang, H.W. Huang & D.M. Zhang</i>	57
A multilaminate model with destructuration <i>V. Galavi & H.F. Schweiger</i>	63
Coupled analysis of an <i>in situ</i> experiment in a soft argillaceous rock using a new constitutive model <i>J. Vaunat, B. Garitte & A. Gens</i>	71
An elasto-plastic cap model for partially saturated soils <i>R. Kohler & G. Hofstetter</i>	79
Modelling of partly saturated weathered broken rock <i>E. Bauer, W. Cen, Y. Zhu, K. Kast & S.F. Tanton</i>	87
A Generalized Plasticity approach for describing the behaviour of silty soils forming the Venetian lagoon basin <i>L. Tonni, S. Cola & M. Pastor</i>	93
Hypoplastic description of the frictional behaviour of contacts <i>M. Arnold & I. Herle</i>	101

Micro-polar modelling of a reinforced soil structure under shearing <i>S.F. Tantonio & E. Bauer</i>	107
A stress-strain integration algorithm for unsaturated soil elastoplasticity with automatic error control <i>W.T. Sołowski & D. Gallipoli</i>	113
Implicit integration of a new hyperelastic mixed isotropic-kinematic hardening model for structured clays <i>A. Amorosi, V. Germano & D. Boldini</i>	121
Influence of the initial void ratio on the evolution of the passive earth pressure <i>J. Tejchman & E. Bauer</i>	127
The relevance of small-strain soil stiffness in numerical simulation of excavation and tunnelling projects <i>R.B.J. Brinkgreve, K.J. Bakker & P.G. Bonnier</i>	133
Numerical study of pressuremeter strain and stress holding test <i>D. Rangeard, R. Zentar & N.-E. Abriak</i>	141
Identification of soil parameters from pressuremeter tests <i>Z.Y. Yin, P.Y. Hicher & H.W. Huang</i>	147
Investigation on the mechanical resistance of reinforced sand samples <i>A. Cividini & U. Arosio</i>	153
Testing and modelling stabilised soft clay <i>P. Vepsäläinen, A. Aalto & M. Lojander</i>	157
Effect of testing conditions on the shear strength parameters – a numerical study <i>O. Ravaska</i>	161
Hydro-bio-mechanical modelling of landfilled waste: Decomposition, density and moisture retention <i>J.R. McDougall</i>	167
 <i>Dynamic problems</i>	
3-D FEM-BEM method for analysing the transmission vibrations of soil to a pile foundation <i>S. Messast, A. Boumekik & M. Mansouri</i>	175
Dynamic analysis of piles embedded in transversely isotropic soils using hybrid elements <i>Assadollah Noorzad, Ali Noorzad & K. Mohammadi</i>	183
Application of the Boundary Element method to analyze dynamic soil compaction control techniques <i>I. Paulmichl, C. Adam & D. Adam</i>	189
Finite element analyzes of dynamic compaction techniques and integrated control methods <i>P. Erdmann, D. Adam & F. Kopf</i>	197
Numerical approach of detection of foundations of buildings by propagation of a wave <i>P. Alfonsi & E. Bourgeois</i>	205
Effective stress analysis for the seismic response of shallow foundations on liquefiable sand <i>K.I. Andrianopoulos, G.D. Bouckovalas, D.K. Karamitros & A.G. Papadimitriou</i>	211

Vertical compliance function of adjacent surface rigid footings in heterogeneous soil layer <i>B. Sbartai & A. Boumekik</i>	217
Efficient numerical simulation of waste landfills' seismic response <i>V. Zania, Y. Tsompanakis & P.N. Psarropoulos</i>	223
Dynamic FE analysis of ground vibrations and mitigation measures for stationary and non-stationary transient source <i>L. Kellezi</i>	231
Three-dimensional analyses of transition zones at railway bridges <i>M.E. Smith, P.-E. Bengtsson & G. Holm</i>	237
Free field vibrations due to the passage of high-speed trains <i>S. Sica, F. Santucci de Magistris & A. Melazzo</i>	243
Application of pseudo-static limit analysis in geotechnical earthquake design <i>J. Shiau, A. Lyamin & S. Sloan</i>	249
BIEM for seismic wave propagation in fluid saturated multilayered media <i>P. Dineva, M. Datcheva & T. Schanz</i>	257
 <i>Discontinuum modelling</i>	
Numerical modeling of the soil structure interaction during sinkholes <i>M. Caudron, F. Emeriault, R. Kastner & M. Al Heib</i>	267
Smoothed particle hydrodynamics for soil mechanics <i>H.H. Bui, R. Fukagawa & K. Sako</i>	275
Research on the pre-process of three dimensional composite element method for discontinuous rock <i>S. Qiang, Y. Zhang, Y. Zhu & S. Chen</i>	283
 <i>Tunnels and caverns</i>	
The influence of the soil-structure interface on tunnel induced building deformation <i>J.N. Franzius & D.M. Potts</i>	291
Morphological effects on settlements induced by shallow tunnelling <i>D. Segato & G. Scarpelli</i>	299
Eurocode-based ultimate limit state design of NATM tunnels using nonlinear constitutive models for sprayed concrete and soil <i>H. Walter</i>	305
Numerical investigation of the failure of a shotcrete lining <i>R. Pöttler</i>	313
Three-dimensional modelling for the widening of existing tunnels <i>G. Altamura & S. Miliziano</i>	319
Squeezing effects in the excavation of deep tunnels <i>D. Sterpi</i>	325

Numerical modeling of tunnel lining at high temperature <i>M. Zaki Abd Elrehim & G. Swoboda</i>	333
A “multi-phase” model for finite element analysis of traction forces in bolts used in the reinforcement of tunnel walls <i>E. Bourgeois, C. Rospars, P. Humbert & P. de Buhan</i>	341
Abandonment of caverns in rock salt mass <i>K. Staudtmeister & D. Zander-Schiebenhöfer</i>	347
Long-term behavior of shield tunnel crossing the new-built embankment in soft soil <i>J.-Y. Yan, D.-M. Zhang & H.-W. Huang</i>	353
Excavation plan and preliminary support design of an underground control room using 3D analysis in soft and weathered rocks <i>F. Vahedi Fard, M. Talebi, F. Jafarzadeh & M. Dianat Nejad</i>	359
Socorridos pumping station – numerical modelling <i>A. Pedro, J.A. Sousa, A. Ambrósio & J.M. de Brito</i>	367
 <i>Deep excavations and retaining walls</i>	
Excavation-induced ground movements behind a single-propped wall <i>M.Z.E.B. Elshafie, R.J. Mair, K. Soga & C.K. Choy</i>	375
Elastic-plastic flexure of embedded retaining walls <i>P.J. Bourne-Webb, D.M. Potts, S. Godden & D. Rowbottom</i>	383
Large scale excavation model test on single strutted sheet pile wall and back calculation of soil parameters <i>T.H. Tefera, S. Nordal & R. Sandven</i>	391
Parametric FE study of loads and displacements of braced excavations in soft clay <i>L. Andresen</i>	399
Numerical modeling of propped retaining walls – influence of parameters <i>H. Popa, L. Thorel, C. Gaudin & J. Garnier</i>	405
Elastoplastic joint element for the finite element analysis of the Hochstetten sheet pile wall <i>F. Elmi, E. Bourgeois, A. Pouya & C. Rospars</i>	411
Numerical modelling of a diaphragm wall production process in Rotterdam compared to monitoring data <i>H.P. Neher & A. Lächler</i>	417
Back analysis on the deep excavation in Stockholm with finite element method <i>J.Q. Ma, B.S. Berggren, P.E. Bengtsson, H. Stille & S. Hintze</i>	423
Design of a deep building pit with numerical and limit equilibrium methods <i>V. Račanský, R. Thurner & C. Kummerer</i>	431
Numerical modelling of earth pressure loading of the vertical stem of L-shaped retaining walls <i>M. Achmus</i>	437

Embankments

The pre-failure deformation of an embankment predicted by two kinematic hardening models 447
A. Grammatikopoulou, L. Zdravkovic & D.M. Potts

Numerical modelling of Murro test embankment with S-CLAY1S 455
M. Koskinen & M. Karstunen

Numerical design, installation and monitoring of a load transfer platform (LTP) 463
for a railway embankment near Rotterdam
A.E.C. van der Stoel, J.M. Klaver, A.T. Balder & A.P. de Lange

Results of the settlement prediction exercise of an embankment founded on soil 471
improved by stone columns
Ph. Mestat, J.P. Magnan & A. Dhouib

Deformation analyses of land reclamation and a test construction with finite element method 477
M.M. Hassan, M. Lojander & J. Takala

Slopes and cuts

Factors of safety by limit equilibrium and strength reduction methods 485
Y.M. Cheng, W.B. Wei & T. Lämsivaara

Slope safety factor calculations with non-linear yield criterion using finite elements 491
J. Clausen & L. Damkilde

A study on interslice force function and line of thrust in slope stability analysis 497
K. Aryal, L. Grande & R. Sandven

Sensitivity analyses of global stability in sanitary landfills 501
I. Petrovic, D. Kovacic, T. Ivsic & F. Veric

Numerical analysis of the behaviour of a cut slope in stiff clays by finite difference method 507
P. Lollino, F. Santaloia, A. Amorosi & F. Cotecchia

Simulation of a large excavation using a Hoek-Brown model 513
T. Benz, R. Kauther & R. Schwab

Investigation of interaction of landslide soil with the piles of a double-row construction 519
with the help of the finite-element method
S. Matsiy, Ph. Derevenets & S. Shiyani

Numerical analysis of an open excavation close to an embankment on improved ground 525
J.A. Barco, J. Cañizal, J. Castro, A. da Costa & C. Sagasetta

Shallow foundations

Undrained bearing capacity and mechanisms of collapse of square footings under 533
vertical and moment loads
S. Gourvenec

Advanced FE versus classical settlement analyses 539
J. Hintner, P.A. Vermeer & C. Baun

Foundation analyses with unsaturated soil model for different suction profiles 547
A.A. Abed & P.A. Vermeer

Piles

Numerical modelling of laterally loaded short pile 557
S.W. Lee, A.R. Pickles & T.O. Henderson

Modelling piles under multi-directional loading conditions 563
N.H. Levy & I. Einav

Nonlinear analysis of laterally loaded piles by a pseudo three-dimensional FE model 569
Dj.A. Bouzid, B. Tiliouine & P.A. Vermeer

Numerical modelling of the combined axial and lateral loading of vertical piles 575
K. Abdel-Rahman & M. Achmus

Analysis of piled raft foundations with piles of different lengths subjected to horizontal and vertical loadings 583
H.S.W. Chow & J.C. Small

Prediction of pile group response using a simplified non-linear finite element model 589
B.A. McCabe & B.M. Lehane

Numerical investigation into stress and strain development around a displacement pile in sand 595
J. Dijkstra, W. Broere & A.F. van Tol

Axisymmetric and 3D analyses of pile test using FEM 601
V. De Gennaro, I. Said & R. Frank

Interpretation of pile load test failure using FEM simulation 607
S.A. Tan & T.Y. Bui

Different aspects of large deformation contact formulations applied to pile-soil FE-analysis 613
K.A. Fischer & D. Sheng

Numerical analyses of pile foundation in complex geological conditions 619
Y. El-Mossallamy

Reliability and probability analysis

Implementation and validation of a simple probabilistic tool for finite element codes 629
S. van Baars

Inverse analysis of an embankment using the Ensemble Kalman Filter including heterogeneity of the soft soil 635
A. Hommels & F. Molenkamp

System reliability assessment of friction drilled shafts in gravel soils 641
A.M. Harraz & M.M. El-Meligy

Artificial intelligence

A neural network equivalent of hardening soil model of PLAXIS 651
S.I. Drakos & G.N. Pande

Application of artificial neural networks in solving inversion problem of surface wave method <i>T. Akhlaghi</i>	657
Simulating the seismic response of an embankment using soft computing techniques <i>E.C. Georgopoulos, Y. Tsompanakis, N.D. Lagaros & P.N. Psarropoulos</i>	663
Hybrid neural network and genetic algorithm approach to the prediction of bearing capacity of driven piles <i>H.I. Park, J.W. Seok & D.J. Hwang</i>	671
Application of evolutionary programming techniques in geotechnical engineering <i>M. Rezanian & A.A. Javadi</i>	677
 <i>Miscellaneous</i>	
Some experiences developing software for seepage with phreatic surfaces <i>M. Mavroulidou, M.J. Gunn & R.I. Woods</i>	685
Flow-deformation due to two-phase flow: A loose coupling simulation <i>A. Chinkulkijniwat & S. Semprich</i>	693
Identification of characteristic coefficient of seepage in inhomogeneous and anisotropic rock masses <i>Y. Zhu, D. Sun, W. Cen & S. Semprich</i>	701
Numerical determination of soil deformations around a penetrating object in 2D and 3D models <i>S. Farhangi, D.J. Richards & C.R.I. Clayton</i>	707
CIP-based numerical simulation for large deformation problems considering the interaction between geomaterial and rigid body <i>K. Sawada, S. Moriguchi, A. Yashima, M. Goshima, S. Inoue & Y. Nishida</i>	713
Reservoir, dam and rock mass interaction modeling <i>D. Divac, D. Vuckovic, M. Zivkovic & S. Vulovic</i>	721
Study on rheological property of rockfill and its influence on deformation and stress in concrete face rockfill dams <i>W. Cen, Y. Zhu & G. Heigerth</i>	727
Sensitivity analysis to examine tree root effectiveness in soft ground stabilisation <i>B. Indraratna & B. Fatahi</i>	735
Parallel three dimensional finite element analysis of dinosaur trackway formation <i>L. Margetts, J.M. Leng, I.M. Smith & P.L. Manning</i>	743
Finite element analysis of buried flexible culverts subjected to rockfall loading <i>R. Ebeltoft, J. Gløpestad & S. Nordal</i>	751
Two and three-dimensional modeling of abutment-backfill system on soft ground <i>S. Dashdorj, S. Miura, S. Yokohama & K. Masumura</i>	759
 <i>Special session on numerical modelling of ground improvement</i>	
Stone columns – group behaviour and influence of footing flexibility <i>W.C.S. Wehr</i>	767

Exercise on calculation of stone columns – Priebe method and FEM <i>J. Wehr & I. Herle</i>	773
Modelling stone columns in soft clay <i>P. Andreou & V. Papadopoulos</i>	777
Bearing capacity of group of stone columns <i>M. Etezzad, A.M. Hanna & T. Ayadat</i>	781
Tracking the settlement of sand layers stabilized by stone piles using numerical modeling <i>M.F. Mishriki, J.D. Hussin, E.A. Eissa, S.I. Shalaby & A.K. Ashmawy</i>	787
Numerical modelling of deep mixing by volume averaging technique <i>U. Vogler, M. Karstunen & H. Krenn</i>	793
Equivalent-uniform soil model for the seismic response analysis of sites improved with inclusions <i>G.D. Bouckovalas, A.G. Papadimitriou, A. Kondis & G.J. Bakas</i>	801
Equivalence between 2D and 3D numerical simulations of the seismic response of improved sites <i>A.G. Papadimitriou, G.D. Bouckovalas, A.C. Vytiniotis & G.J. Bakas</i>	809
Three-dimensional modelling of an embankment over soft soil improved by rigid piles <i>O. Jenck, D. Dias & R. Kastner</i>	817
Influence of the soil nonlinearity and the interface on the seismic response of micropiles <i>H. Al Saleh & I. Shahrour</i>	823
Modeling various types of reinforced soil by the finite element method – application to piled raft foundations <i>M. Yazdchi, H.C. Yeow & B. Simpson</i>	829
Numerical modelling of vertical drains with advanced constitutive models <i>A. Yildiz, M. Karstunen & H. Krenn</i>	835
Coupling finite elements and discrete elements methods, application to reinforced embankment by piles and geosynthetics <i>B. Le Hello, P. Villard, A. Nancey & Ph. Delmas</i>	843
D.E.M. modeling in impact condition of geocomposite cells dedicated to rockfall protection barriers <i>D. Bertrand, Ph. Gotteland, S. Lambert & F. Nicot</i>	849
Experimental observations and theoretical interpretation of the mechanical behaviour of a grouted pyroclastic silty sand <i>A. Flora, S. Lirer, A. Amorosi & G. Elia</i>	857
Numerical method for sheet pile quay walls with sea-side ground improvement <i>M.R.A. Khan, K. Hayano & M. Kitazume</i>	865

Conference Chairman

Helmut F. Schweiger
Graz University of Technology, Austria

Conference Secretary

Florian Scharinger
Graz University of Technology, Austria

Scientific Committee (ERTC7)

Chairman

Cesar Sagaseta *Spain*

Core Members

P. Mestat *France*
M. Pastor *Spain*
D. Potts *UK*
H.F. Schweiger *Austria*
I.M. Smith *UK*

National Representatives

S. Aleynikow *Russia*
K. Bakker *The Netherlands*
I. Bojtár *Hungary*
A. Bolle *Belgium*
H. Burd *UK*
A. Cividini *Italy*
G. Dounias *Greece*
T. Edstam *Sweden*
P. Fritz *Switzerland*
M. Gryczmanski *Poland*
F. Haahr *Denmark*
I. Herle *Czech Republic*
J.C. Marques *Portugal*
S. Nordal *Norway*
O. Ravaska *Finland*
T. Schanz *Germany*
H. Walter *Austria*

Scientific Committee Special Session

Numerical Modelling in Ground Improvement
(TC17)

Chairman

Isam Shahrour and Jean Marc Debats *France*

Members

B. de Souza Bueno	<i>Brazil</i>
M. Bouassida	<i>Tunisia</i>
F. van Tol	<i>The Netherlands</i>
G.A. Munfakh	<i>United States</i>
I. Juran	<i>United States</i>
I.M. Pinto	<i>Portugal</i>
J. Maertens	<i>Belgium</i>
L. Korkiala-Tanttu	<i>Finland</i>
M.C. Alfaro	<i>Canada</i>
N. Consoli	<i>Brazil</i>
R. Bathurst	<i>Canada</i>

Preface

The 6th Conference on Numerical Methods in Geotechnical Engineering held in Graz, Austria, from September 6 to 8, 2006, is a continuation of a series of conferences organized by the European Regional Technical Committee ERTC7 (Numerical Methods in Geotechnical Engineering) under the auspices of the International Society for Soil Mechanics and Geotechnical Engineering (ISSMGE). Previous meetings were held in Stuttgart, Germany (1986), Santander, Spain (1990), Manchester, UK (1994), Udine, Italy (1998) and Paris, France (2002).

The meeting has been intended to provide a forum for exchange of ideas and discussion on important issues related to numerical analysis in geotechnical engineering. Special emphasis has been given to presentations of young researchers and it was attempted to provide a good balance between scientists and practitioners. The results of a benchmark exercise, namely the ULS-design of an embedded wall, are also presented at the conference.

A novel feature of this conference is the participation of the Technical Committee “Ground Improvement” (TC17) of the ISSMGE in form of organizing a special session on “Numerical Modelling in Ground Improvement” which provides a state-of-the-art coverage of this increasingly important topic.

The proceedings contain 125 papers, 16 of which belong to the special TC17 session. The remaining 109 papers have been organized in 12 sessions:

1. Constitutive modelling and numerical implementation
2. Dynamic problems
3. Discontinuum modelling
4. Tunnels and caverns
5. Deep excavations and retaining walls
6. Embankments
7. Slopes and cuts
8. Shallow foundations
9. Piles
10. Reliability and probability analysis
11. Artificial intelligence
12. Miscellaneous

I would like to thank all national representatives of ERTC7 for promoting the conference in their respective home countries and for reviewing papers. In particular I would like to thank the chairman of ERTC7, Cesar Sagaseta, for his support in the organization of this conference and for keeping the activities of the Technical Committee alive. Thanks also go to Isam Shahrour for taking care of the special session on ground improvement.

I wish to thank all authors for their efforts in preparing papers and highly appreciate their participation in the conference.

I am grateful to the members of the Institute for Soil Mechanics and Foundation Engineering at the Graz University of Technology who helped in getting the organizational details done. Special thanks however go to Florian Scharinger who cared for everything. Without him it would have been difficult to run this conference.

Helmut F. Schweiger

Results from the ERTC7 benchmark exercise

H.F. Schweiger

*Computational Geotechnics Group, Institute for Soil Mechanics and Foundation Engineering,
Graz University of Technology, Graz, Austria*

ABSTRACT: A benchmark example addressing ultimate limit state (ULS) design of an embedded retaining wall has been specified by the ERTC7 on the occasion of the 6th European Conference on Numerical Methods in Geotechnical Engineering. The main goal of the exercise was to highlight possibilities and limitations of numerical methods for ULS design with particular reference to Eurocode7 (EC7), where three design approaches (DA1, DA2 and DA3) have been specified. These design approaches differ in the way partial factors of safety are introduced in the analysis. However, the exercise was not restricted to the use of EC7 and thus a wide spectrum of results, which are summarized in this paper, could be expected. Some of the 13 submissions did not actually present design values as requested but provided parametric studies showing the influence of various design assumptions or did an analysis using characteristic values, some introduced factors without given explicit reference to a particular code or standard.

1 INTRODUCTION

Numerical methods have gained increasing importance in the geotechnical profession and are widely used for solving problems in practical engineering. Traditionally the main emphasis of numerical analysis has been on calculating displacements and stresses in the ground and internal forces in structural elements. However, more recently numerical methods are also employed to assess the ultimate limit state of a geotechnical structure. Although in principle possible there are a number of issues which have to be considered when performing an ULS-analysis with numerical methods such as the finite element method or the finite difference method. For example type of element used and discretisation are more important than in serviceability analysis (SLS) and of course the question arises how to introduce partial or global factors of safety in correspondence with existing codes of practice and relevant standards, the requirements of which have to be fulfilled in an approved design.

The latter is of particular importance in Europe when the EC7, which introduces the concept of partial factors of safety, will come into operation in the near future. In EC7 various design approaches have been identified. They differ in the way the partial factors of safety are applied to soil strength, resistance and different types of loads (actions). It seems that, although numerical methods are mentioned in EC7 as

a possible design tool, not all of the design approaches can be applied in a straightforward way within the framework of numerical modelling for all types of problems. Up to now the problem is not extensively discussed in the literature, exceptions are e.g. Bauduin, de Vos & Simpson (2000), Simpson (2000), Bauduin, de Vos & Frank (2003) and Schweiger (2005).

In addition to the problem of appropriate consideration of safety factors a number of modelling assumptions have to be made for a numerical analysis. Most of them are not explicitly specified in codes of practice or are based on experience made with limit equilibrium calculations which are not necessarily applicable in the same manner in a finite element analysis. A good example for this is wall friction, which is well defined in limit equilibrium analysis but the numerical results may be significantly influenced by the element type a particular code uses for modelling interfaces. Thus many modelling details are left to the user and therefore results obtained for the same problems may differ significantly depending on individual experience. This has been demonstrated in a number of benchmark exercises (see e.g. Schweiger 1998 and 2000). In this paper, first the design approaches as defined in EC7 will be briefly recalled. Then the results submitted for the benchmark problem will be discussed and finally additional analyses, addressing in particular the issue of determination of the required embedment depth by means of finite element analysis, are presented.

2 EC7 DESIGN APPROACHES

Eurocode7 allows for three different design approaches DA1, DA2 and DA3 which differ in the application of the partial factors of safety on actions, soil properties and resistances. EC7 states:

“It is to be verified that a limit state of rupture or excessive deformation will not occur with the sets of partial factors”.

The factors are given in Tables 1 and 2 for all three approaches. It is noted that 2 separate analyses are required for design approach 1. The problem which arises for numerical analyses is also immediately apparent because DA1/1 and DA2 require permanent unfavourable actions to be factored by a partial factor of safety, e.g. the earth pressure acting on retaining structures. This is not possible in a numerical analysis because the earth pressure is result and not input. However, there is a way around it because EC7 also states that instead of applying a partial factor on the action itself it may be applied to the “effects of the action”, e.g. the bending moment in a retaining wall.

3 SPECIFICATION OF ERTC7 BENCHMARK

The benchmark is a deep excavation problem supported by a single strut. The geometry is depicted in Figure 1. The significant difference to examples previously examined by various working groups around Europe (Orr 2005) is that it was the intention here to solve this problem, including determination of the required embedment depth (!), by means of numerical methods, although a check by simple limit equilibrium calculations was certainly recommended. As the

Table 1. Partial factors for actions according to EC7.

Design approach	Permanent unfavourable	Variable
DA1/1	1.35	1.50
DA1/2	1.00	1.30
DA2	1.35	1.50
DA3-Geot.	1.00	1.30
DA3-Struct.	1.35	1.50

Table 2. Partial factors for soil properties and passive resistance according to EC7.

Design approach	$\tan \phi'$	c'	c_{ui}	Passive resistance
DA1/1	1.00	1.00	1.00	1.00
DA1/2	1.25	1.25	1.40	1.00
DA2	1.00	1.00	1.00	1.40
DA3-Geot.	1.25	1.25	1.40	1.00

emphasis is on the ULS design and not on the serviceability limit state (SLS) only parameters required for simple elastic-perfectly plastic analysis have been provided (Table 3). These parameters have to be considered as characteristic values and not design values.

The following construction steps should be modelled in the numerical analysis:

- initial phase ($K_0 = 0.5$)
- activation of diaphragm wall (wished-in-place)
- activation of surcharge loads
- excavation step 1 to level -2.0 m
- activation of strut at level -1.50 m, excavation step 2 to level -4.0 m
- groundwater lowering inside excavation to level -6.0 m
- excavation step 3 to level -6.0 m.

The surcharge of 10 kPa is a permanent load, the surcharge of 50 kPa is a variable load. Bedrock was assumed at a depth of 20 m below ground surface. The axial stiffness of the strut was set to $EA = 1.5E6$ kN/m.

Results to be provided:

- Embedment depth of wall
- Design bending moment for the wall
- Design strut force.

On purpose it was not specified how the water draw-down inside the excavation should be taken into account because different codes and standards would allow different assumptions. The same argument holds for wall friction because individual national standards would have different requirements. The

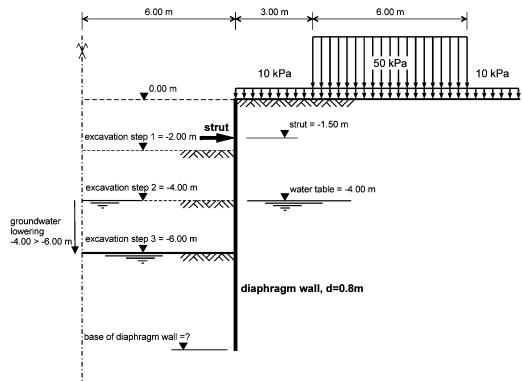


Figure 1. Geometry of benchmark example.

Table 3. Material properties for soil and wall.

	E (kN/m ²)	ν (-)	ϕ' (°)	c' (kN/m ²)	γ (kN/m ³)
Soil	30 000	0.3	27.5	10	20/19
Wall	3.0E7	0.18	–	–	24

choice of the dilatancy angle, rarely given in a conventional geotechnical report, is also left to the user in most cases and was therefore not given.

4 SUBMITTED RESULTS

4.1 Notes on individual submissions

13 results have been submitted, but as mentioned previously not all of them have provided the results in the form as specified. Because all entries are considered in the comparison presented in this paper a very brief summary of individual assumptions – as far as described by the authors – is given in the following. This should help explaining – at least to some extent – the differences observed in the results.

- No.1: gives no information at all on analysis.
- No.2: provides results for EC7 design approaches DA2 and DA3, uses different wall friction on active and passive side ($2/3\phi$ and $1/3\phi$). Partial factor of 1.4 on soil weight on active side (does not conform to EC7 > possibly national annex (Italy)).
- No.3: does not apply any safety factors, wall friction 0.9ϕ .
- No.4: provides finite element and limit equilibrium results, global safety factor applied, stiffness of strut/ per unit length of excavation obviously different from specification, wall friction 0.8ϕ .
- No.5: compares finite element and beam spring results, loads, soil weight and strength parameters factored (similar to DA3) but with different factors than in EC7, cohesion and friction angle have different partial factors, wall friction 0.3ϕ , refers to Russian code of practice.
- No.6: applies Dutch CUR-method, which has some similarity with design approaches in EC7 but with different partial factors, wall friction $2/3\phi$.
- No.7: load factors on service loads according to British (1.4) or Australian standards (1.5), partial factor on soil strength of 1.2, provides additional results with subgrade reaction method, wall friction $2/3\phi$.
- No.8: provides finite difference and subgrade reaction analyses under various assumptions (e.g. undrained conditions), wall friction $2/3\phi$ and $1/3\phi$, does not explicitly provide design results, no safety factor given or applied to actions or parameters.
- No.9: a second submission applying the Dutch CUR-method, wall friction $2/3\phi$.
- No.10: compares EC7 design approaches DA2 and DA3 with partial factors according to EC7 and EAB (German recommendation for deep excavations) respectively, wall friction 0.5ϕ , assumes stiffness increasing with depth.
- No.11: does not apply a particular code but determines embedment from finite element analysis employing the strength reduction technique on the basis of a

global factor of safety of 1.5, design bending moment obtained from calculated value at final excavation step multiplied by 1.5, wall friction 0.5ϕ .

No.12: does not apply a particular code but determines embedment from finite element analysis employing the strength reduction technique on the basis of a global factor of safety of 2.0, wall friction $2/3\phi$, Drucker-Prager failure criterion for soil.

No.13: assumes in an alternative calculation capillary cohesion above groundwater level (determined from seepage analysis), design approach DA3 according to EC7 and analysis with characteristic soil parameters, wall friction $2/3\phi$.

The lowering of the groundwater table was taken into account by means of phreatic levels by No.3, 5, 9, 10 and No.6, 7, 11 performed an additional interpolation in order to achieve continuous pore pressures at the base of the wall. No.4, 8, 12 and 13 performed a seepage analysis.

4.2 Results

Figure 2 shows the variation in embedment depth of all entries. As indicated in the previous section some submissions provided more than one solution (depending on assumptions made) and this is why there is more than one result plotted in these cases. It follows that the minimum embedment depth is 1.8 m and the maximum 5.5 m, but there is a tendency towards an embedment depth between 3.0 and 4.0 m.

The maximum embedment depth of No.4 (5.5 m) is obtained by conventional analysis applying a global factor of safety $\eta = 1.5$. The same embedment depth has been used in the numerical analysis. No.3 indicated a factor of safety of 1.76, No.2 factored the soil weight and No.12 obtained a factor of safety from strength reduction technique of 2.0. Thus these higher embedment depths can be explained by higher safety levels as compared to the other submissions. At the lower end

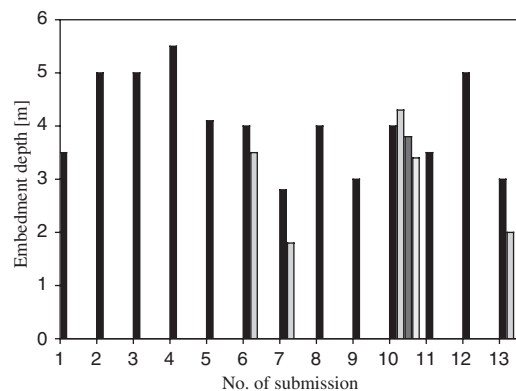


Figure 2. Embedment length – all entries.

(embedment depths around 2 m) it is found that these results are obtained from numerical analyses, either by means of a strength reduction technique or by factoring soil strength parameters. However, No.7 employed a factor of safety of $\eta = 1.2$ which is lower than in EC7. No.13 indicated that the low depth is possible only by modelling the groundwater lowering by means of a 2-phase flow formulation resulting in suction effects above groundwater. From comments provided it can be concluded these two authors would not have designed a wall for a real project with this low embedment depth.

Only 3 authors explicitly used EC7 for their analysis (DA2 and DA3), 3 authors used an approach similar to EC7 but with different partial factors of safety. It is somewhat encouraging to see that except for No.2 (where the soil weight was factored) the embedment depth is between 3.0 and 4.0 m despite differences in assumptions of partial factors and wall friction. No.10 investigated the difference between DA2 and DA3 and obtained a slightly shorter wall with DA3.

Figure 3 shows bending moments and there we find a difference of approx. 300% but this includes

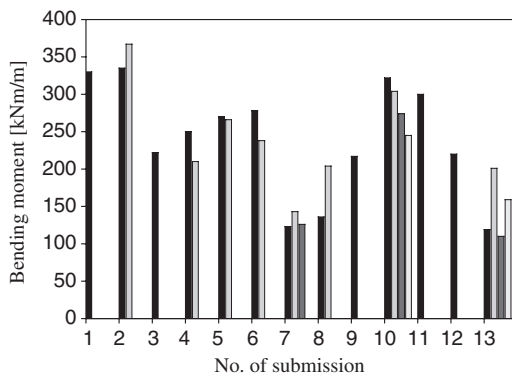


Figure 3. Bending moments – all entries.

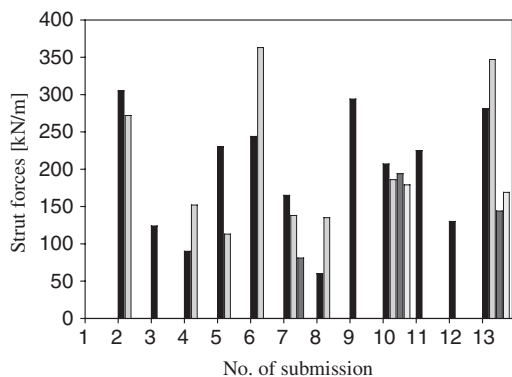


Figure 4. Strut forces – all entries.

values which are obviously not ULS-design values. This is however not surprising considering the different assumptions made in the various analyses. If we consider again the EC7 and related approaches (i.e. No. 5, 6, 9, 10 and 13) we see a range from 201 to 278 kNm/m for DA3. DA2 results in approximately 20% higher bending moments. If we multiply obvious SLS-bending moments by a partial factor of 1.35 we find that results also fall in this range.

A similar picture is obtained for strut forces (Figure 4). Considering all solutions submitted the range is from 60 to 363 kN/m (including values representing SLS) and in this case also the EC7 and related approaches show a significant difference with the minimum being 194 and the maximum force being 363 kN/m.

5 ADDITIONAL ANALYSES

5.1 Geometry and assumptions

In this section some additional results from analyses performed in order to elaborate on the differences observed in the benchmark exercise as well as on the EC7 design approaches are presented. The finite code Plaxis (Brinkgreve 2002) is used and the finite element mesh, consisting of 15-noded triangles, follows from Figure 5. The fine mesh was chosen in order to minimize the discretisation error when calculating the factor of safety by means of the strength reduction technique. The diaphragm wall is modelled by continuum elements and a soft beam has been added in the centreline for easy evaluation of bending moments. Wall friction has been assumed as $2/3\phi$ and the dilatancy angle ψ is 0. The groundwater lowering inside the excavation has been modelled by creating a phreatic surface just underneath the excavation and by interpolating the water pressure down to the bottom of the

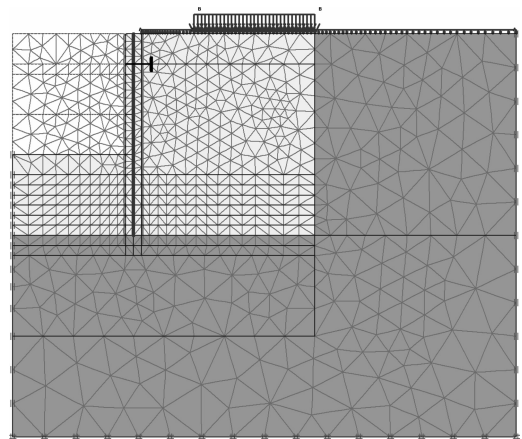


Figure 5. Finite element mesh (15-noded triangles).

wall so that there is no discontinuity of pore water pressure at the base of the wall.

Two EC7 design approaches have been investigated, namely DA2 and DA3. DA3 is straightforward because soil strength is factored by the partial factor given in Table 2 and the surface loads by the partial factors given in Table 1. For DA2 it is slightly more complicated because the earth pressure (permanent unfavourable load) cannot be factored and therefore the partial factors of safety are applied on the “effects of the action”, namely the resulting bending moment, strut force and passive earth pressure. An additional slight inconvenience arises due to the fact that different partial factors have to be applied on permanent and variable loads. This has been taken into account by multiplying the permanent surface load by 1.11 (1.5/1.35).

5.2 Results

In order to determine the embedment depth analyses were performed with different wall lengths. Starting with an embedment depth of 5 m the wall was shortened in 0.5 m intervals and for each wall length a new analysis was performed. Horizontal displacements of the base of the wall, bending moments, strut forces and the factor of safety, obtained by means of a strength reduction technique, were evaluated. Figure 6 shows the increase of horizontal deformation of the base of the wall when decreasing the length of the wall for DA2, DA3 and for an analysis with characteristic parameters. The characteristic analysis and DA2 is almost the same because the only difference is the factor of 1.11 for the variable load in DA2. Numerical convergence could not be achieved for an embedment depth of 1.5 m for DA2 and characteristic parameters and a depth of 3.0 m for DA3 respectively.

Figure 7 plots the safety factor obtained from a strength reduction technique, again for different embedment depths. Again values for DA2 and characteristic parameters do not vary much and values for DA3 are

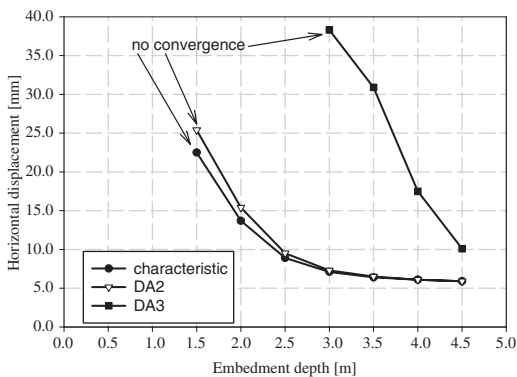


Figure 6. Horizontal wall displacement vs embedment depth.

much smaller because the soil strength is already factored at the beginning of the analysis. Figure 7 features an additional line, namely the value obtained for DA2 divided by the partial factor which has been put on the strength parameters in DA3. They compare well for embedment depths between 3.5 and 4.5 m but for factors around or below 1 they differ. To some extent this can be attributed to details of the iteration procedure and convergence settings which become more sensitive for states at or very near to failure. No attempt has been made to achieve a closer matching by tightening tolerance factors because this was not the main goal of this investigation.

Figure 8 plots bending moments vs embedment depths. It is interesting to see that the design bending moment of DA2 (which is the result of the DA2 analysis multiplied by the partial factor of 1.35) coincides with DA3 for an embedment depth of 4 m but is significantly different for 3.5 and 4.5 m. The same holds for the strut forces (Figure 9), with DA3 resulting in higher strut forces than DA2 where the resulting force is factored.

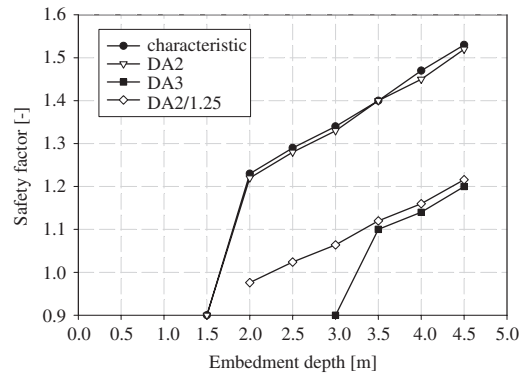


Figure 7. Factor of safety vs embedment depth.

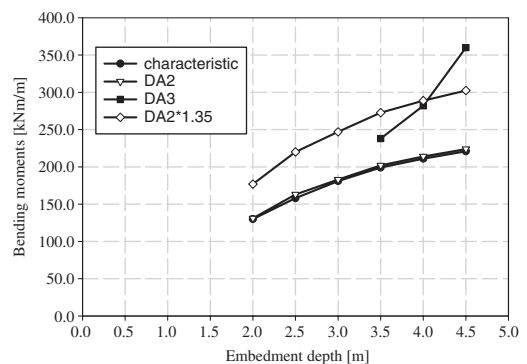


Figure 8. Bending moments vs embedment depth.

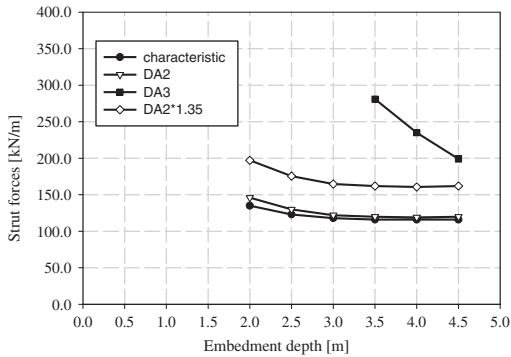


Figure 9. Strut forces vs embedment depth.

Table 4. Check of passive resistance depending on embedment depth (DA2).

Embedment depth	$E_{\text{passive design calc.}}/E_{\text{passive design allow.}}$
4.5	1.18
4.0	1.12
3.5	1.06
3.0	1.01
2.5	0.99
2.0	0.98

When applying DA2 an additional check has to be made with respect to the passive resistance for which a partial factor of 1.4 (see Table 2) has to be applied. One way of checking this is to compare the passive earth pressure obtained from the finite element analysis (multiplied by the partial factor of 1.35), denoted $E_{\text{passive design calc.}}$ in Table 4 to the maximum theoretical passive pressure divided by 1.4 ($E_{\text{passive design allow.}}$). This corresponds roughly to consider a mobilisation of 50% of the passive resistance which is sometimes assumed in practical design. Of course different theoretical solutions can be used to obtain the maximum passive resistance but here Coulomb's solution is employed for simplicity.

From Table 4 follows that the required embedment depth is around 3.0 m for DA2, which is less than for DA3 where a minimum embedment depth of approximately 3.5 m is required for a factor of safety >1.0 (Figure 7). However this result is considered to be quite acceptable given the various modelling assumptions involved in the two approaches. It is worth mentioning though that submission No.10 obtained slightly higher embedment depths with DA2 but this could be due to the fact that No.10 used a lower wall friction which might have a more pronounced influence in DA2 than in DA3.

6 CONCLUSION

The results from a benchmark exercise addressing the design of a diaphragm wall for a deep excavation problem have been presented. Unfortunately not all of the submissions provided their results in form of design values but discussed the influence of various modelling assumptions without a clear statement on what they would use for design.

However the results gave some valuable insight into the way design calculations are performed in different countries applying their respective codes of practice and standards and the differences in results are not surprising and not larger than in similar exercises which have been performed using conventional limit equilibrium analysis (Orr 2005). It can be considered encouraging that the calculated embedment depth based on numerical analysis applying EC7 design approaches are within reasonable limits. Differences in bending moments and strut forces are less encouraging and clearly show the need for recommendations of good practice in numerical modelling in geotechnical engineering.

Finally some additional studies have been presented comparing DA2 and DA3 in more detail.

REFERENCES

- Bauduin, C., de Vos, M. & Simpson, B. 2000. Some considerations on the use of finite element methods in ultimate limit state design. *Proc. Int. Workshop on Limit State Design in Geotechnical Engineering, Melbourne*.
- Bauduin, C., de Vos, M. & Frank, R. 2003. ULS and SLS design of embedded walls according to Eurocode 7. *Proc. XIII ECSMGE, Prague (Czech Republic)*, Vol. 2, 41–46.
- Brinkgreve, R.B.J. 2002. *Plaxis, Finite element code for soil and rock analyses, users manual*. Rotterdam: Balkema.
- Orr, T.L.L. 2005. Review of workshop on the evaluation of Eurocode 7. *Proc. Int. Workshop on the Evaluation of Eurocode 7, Dublin, 31.3.–1.4.2005*, 1–10.
- Schweiger, H.F. 2005. Application of FEM to ULS design (Eurocodes) in surface and near surface geotechnical structures. *Proc. 11th Int. Conference of IACMAG, Turin, Italy, 19–24 June 2005*. Bologna: Patron Editore. 419–430.
- Schweiger, H.F. 1998. Results from two geotechnical benchmark problems. *Proc. 4th European Conf. Numerical Methods in Geotechnical Engineering*, Cividini, A. (ed.), Springer, 645–654.
- Schweiger, H.F. 2002. Results from numerical benchmark exercises in geotechnics. *Proc. 5th European Conf. Numerical Methods in Geotechnical Engineering*, Mestat, P. (ed.) Presses Ponts et chaussees, Paris, 2002, 305–314.
- Simpson, B. 2000. Partial factors: where to apply them? *Proc. Int. Workshop on Limit State Design in Geotechnical Engineering, Melbourne*, 145–154.

Constitutive modeling and numerical implementation

Modeling the behavior of expansive clays

M. Sánchez

University of Strathclyde, Glasgow, UK

A. Gens & S. Olivella

Geotechnical Engineering Department, Technical University of Catalunya, Barcelona, Spain

L. do N. Guimarães

Federal University of Pernambuco, Recife, Brazil

ABSTRACT: The behavior of expansive clay is potentially very complex owing to the interaction between the volume change of aggregates made up of a highly expansive clay mineral (microstructural level) and the rearrangement of the granular-like skeleton formed by the aggregates (macrostructural level). A model that considers explicitly the two structural levels present in expansive clays is presented in this work. The inclusion of the microstructural level allows the consideration of the physico-chemical phenomena occurring at particle level. To formulate the model a framework for multidissipative materials has been adopted. A classical elastoplastic model (for the macrostructure), is combined with a generalized plasticity model that takes into account the interaction between the macrostructural and the microstructural level. The model has been formulated in the space of stresses, temperature and suction. Finally, the model has been applied to explain an actual case involving high suction and temperature changes.

1 INTRODUCTION

The study of expansive soils has been a subject of increasing interest in the last few years. A major aspect is the possible use of those materials as engineered barriers and seals in radioactive waste repositories (i.e. FEBEX Report, 2000; Sanchez & Gens, 2005). Many disposal concepts consider the barrier made up from highly expansive compacted clay, in an initially unsaturated state. During its lifetime the barrier will undergo processes of heating (induced by the heat-emitting waste) and hydration (due to the water coming from the host rock, which is generally in a saturated state). This scenario has led to a growing interest in the knowledge of the behavior of unsaturated expansive soils under a wide range of testing conditions; in particular the THM behavior has received special attention (i.e. Romero, 1999; Lloret et al., 2003). However, the interest on these materials is not limited to nuclear waste disposal applications, but they are present in other engineering problems such as shallow and deep foundations, slopes with stability problems, desiccation and formation of fissures in soils in arid regions, and clay based liners for waste isolation from the environment.

The swelling behavior of unsaturated expansive clays has often been reproduced through relatively simple and empirical laws, which relate the material response to suction changes and applied stresses. The weakness of this kind of ad-hoc laws is that it can be generally used only for the stress paths and conditions from which they are derived. However, the general approach proposed by Gens & Alonso (1992) attempts to integrate the main aspects of behavior in a unified framework. In that work, particular attention is placed on the clay fabric and how it can be integrated in the constitutive modeling. The fabric of expansive clays has been actively studied (i.e. Pusch, 1982; Romero, 1999; Lloret et al., 2003) observing a marked double structure. A clear bimodal pore distribution, with two dominant pore sizes, has been observed using mercury intrusion porosimeter tests.

The double structure model introduced in this work is based on the general framework proposed by Gens & Alonso (1992). A series of modifications and developments have been performed in order to enhance the constitutive law and also to formulate the model in a more suitable form for its implementation in a finite element code. One of the aims is to provide a more general mathematical framework in order to achieve a

more general interpretation of the phenomena that take place in expansive clays when they are subjected to complex THM paths. With this objective, concepts of generalized plasticity theory have been included in the formulation of the model. The governing small strain-stress equations have been derived in the framework introduced by Rizzi et al. (1996), which provides a consistent and formal mathematical structure when there are several sources of energy dissipation.

2 DOUBLE STRUCTURE MODEL

Expansive clays generally present a clear double structure, made up from clay aggregates and large macrostructural pores (i.e. Pusch, 1982). As an example, the mercury intrusion porosimetry tests performed to examine the pore size distribution of the statically compacted samples of FEBEX bentonite are presented in Figure 1. This figure shows the measured incremental pore volume for two samples compacted to very different values of dry density (ρ_d), 1.5 Mg/m³ and 1.8 Mg/m³. It can be observed that the pore size distribution is clearly bi-modal. The dominant values are 10 nm that would correspond to the pores inside clay aggregates and a larger pore size that depends on the compaction dry density and ranges from 10 μ m (for $\rho_d = 1.8$ Mg/m³) and 40 μ m (for $\rho_d = 1.5$ Mg/m³). These larger voids would correspond to the inter-aggregate pores. The boundary between the two pore size families can be seen to be around 0.13 μ m, as pores smaller than this size do not appear to be affected by the magnitude of the compaction load. The pore space inside the aggregates was constituted by voids of a much smaller size. These two dominant pores size could be associated with two basic structural levels (Figure 1):

- The macrostructure, related to the global arrangements of clay aggregates (the skeleton of the material), with macropores between them.
- The microstructure, which corresponds to the active clay minerals and their vicinity.

Only these two basic structural levels identified above are considered herein. The approach is open enough and it could be extended to include more structural levels in the analysis, if it deemed relevant.

The soil fabric plays a crucial role to understand and to reproduce the behavior of expansive clays. In this model, the inclusion of the clay fabric in the analysis is considered in the definition of laws for: (1) the macrostructural level, (2) the microstructural level, and (3) for the interaction between both structural levels.

2.1 Macrostructural model

The inclusion of this structural level in the analysis allows the consideration of phenomena that affect the

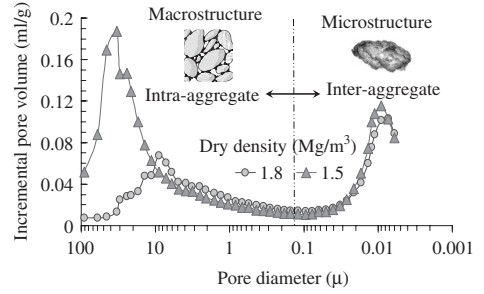


Figure 1. Distributions of incremental pore volume obtained using MIP technique (Lloret et al., 2003) and schematic representation of the two structural levels considered.

skeleton of the material, for instance deformations due to loading and collapse. The *BBM* (Barcelona Basic Model) has been adopted to describe the macrostructural behavior (Alonso et al., 1990). The *BBM* considers two independent stress variables to model the unsaturated behavior: the net stress (σ) computed as the excess of the total stresses over the gas pressure, and the matric suction (s), computed as the difference between gas pressure and liquid pressure ($p_g - p_l$). Figure 2a shows the *BBM* yield surface (F_{LC}), defined as:

$$F_{LC} = 3J^2 - \left[\frac{g(\theta)}{g(-30^\circ)} \right]^2 M^2 (p + p_s)(p_0 - p) = 0 \quad (1)$$

where M is the slope of the critical state, p_0 is the apparent unsaturated isotropic pre-consolidation pressure, $g(\theta)$ is a function of the lode angle and p_s considers the dependence of shear stress on suction and temperature. A basic point of the model is that the size of the yield surface increases with matric suction. The trace of the yield function on the isotropic p - s plane is called *LC* (Loading-Collapse) yield curve, because it represents the locus of activation of irreversible deformations due to loading increments or collapse. The position of the *LC* curve is given by the pre-consolidation yield stress of the saturated state, p_0^* (hardening variable), according to:

$$\dot{p}_0^* = \dot{p}_0^* \frac{(1+e)}{(\lambda_{(0)} - \kappa)} \dot{\varepsilon}_v^p \quad (2)$$

where e is the void index, $\dot{\varepsilon}_v^p$ is the volumetric plastic strain, κ is the elastic compression index for changes in p and $\lambda_{(0)}$ is the stiffness parameter for changes in p for virgin states of the soil in saturated conditions. Finally, it is considered that temperature increases reduce the size of the yield surface and the strength of

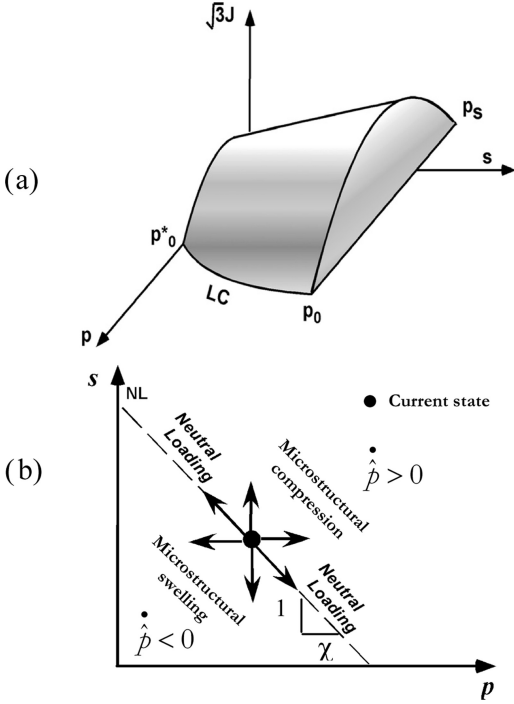


Figure 2. (a) *BBM* yield surface. (b) Microstructural load directions on the p - s plane.

the material (Gens, 1995). Appendix contains the main model equations.

2.2 Microstructural model

The microstructure is the seat of the basic physical-chemical phenomena occurring at clay particle level. The strains arising from microstructural phenomena are considered elastic and volumetric (Gens & Alonso, 1992). The increment of microstructural strains is expressed as:

$$\dot{\varepsilon}_{v,1} = \frac{\dot{\hat{p}}}{K_1} = \frac{\dot{p}}{K_1} + \chi \frac{\dot{s}}{K_1} \quad (3)$$

where \hat{p} ($=p + \chi s$) is the microstructural effective stress, the subscript 1 refers to the microstructural level, the subscript v refers to the volumetric component of the strains and K_1 is the microstructural bulk modulus.

It is assumed that the total suction is equal to the matric suction (s). χ is a constant. The Neutral Line (*NL*) (Figure 2b) corresponds to constant \hat{p} and no microstructural deformation occurs when the stress

path moves on the *NL* (Figure 2b). The *NL* divides the p - s plane into two parts, defining two main generalized stress paths, which are identified as: *MC* (microstructural contraction) and *MS* (microstructural swelling).

2.3 Interaction between macro and micro structure

In expansive soils there are other mechanisms in addition to the ones included in the *BBM* which induce plastic strains. This irreversible behavior is ascribed to the interaction between the macro and micro structures (Gens & Alonso, 1992). It is assumed that the microstructural mechanical behavior is not affected by the macrostructure but the opposite is not true. An assumption of model is that the irreversible deformations of the macrostructure are proportional to the microstructural strains according to interaction functions f . The plastic macrostructural strains are evaluated by the following expression:

$$\dot{\varepsilon}_{v,2}^p = \dot{\varepsilon}_{v,LC}^p + f \dot{\varepsilon}_{v,1} \quad (4)$$

where $\dot{\varepsilon}_{v,LC}^p$ is the plastic strains induced by the yielding of the macrostructure (*BBM*).

In fact the coupling is given by p_0^* , hardening variable of the macrostructure (Figure 2a), which depends on the total plastic volumetric strain (2). In this way is considered that microstructural effects can affect the global arrangements of aggregates. More details can be found in Sánchez et al. (2005).

The following section presents the stress-strain relations used to implement the model in the finite element program *CODE_BRIGHT* (Olivella et al., 1996).

3 ELASTO-PLASTIC STRESS-STRAIN RELATIONS

The behavior of the soil described by the double structure model can be regarded as the consequence of joint action of several mechanisms that can act simultaneously. A procedure similar to the proposed in Sánchez et al. (2005) has been followed hereafter. That is, the first step is the assumption of an additive decomposition of the strains into elastic and plastic components, indicated as follows:

$$\dot{\varepsilon} = \dot{\varepsilon}^e + \sum_{n=1}^{i=na} \dot{\varepsilon}_n^p \quad (5)$$

where na is the number of active plastic mechanisms that correspond to one subset of the total plastic possible mechanisms. The model has three inelastic

mechanisms: lc , due to yield of the BBM , and mc or ms when one of the two interaction mechanisms is active (two is the maximum number of simultaneous active plastic mechanisms, i.e. lc plus mc or ms).

In classical plasticity theory, it is assumed that the material behaves either as an elastic or a plastic solid. The yield surface defines the transition from elasticity to plasticity, stress states inside the yield surface are considered as elastic ($F < 0$). In generalized plasticity theory the state of the material is determined from the control variables: generalized stresses, strains and a finite number of internal variables. A process of loading is defined as elastic if the set of internal variables remains unchanged (Lubliner & Auricchio, 1996).

In the case of an elastic loading, the stress increment is related to the increment of strains, suction and temperature by the following relation:

$$\dot{\boldsymbol{\sigma}} = \mathbf{D}_e \cdot \dot{\boldsymbol{\varepsilon}}^e + \boldsymbol{\alpha}_s \dot{s} + \boldsymbol{\alpha}_T \dot{T} \quad (6)$$

where \mathbf{D}_e is the global elastic matrix which considers the elastic component of the two structural levels. $\boldsymbol{\alpha}_T$ and $\boldsymbol{\alpha}_s$ are the elastic vectors associated to temperature and suction respectively (Sánchez, 2004).

When a loading process is inelastic, the plastic strain rates are assumed to be governed by a flow rule. For the macrostructural model, the strain increment can be expressed as:

$$\dot{\boldsymbol{\varepsilon}}_{lc}^p = \dot{\lambda}_{lc} \frac{\partial G}{\partial \boldsymbol{\sigma}} = \dot{\lambda}_{lc} \mathbf{m}_{lc} \quad (7)$$

where $\dot{\lambda}_{lc}$ is the plastic multiplier associated to the lc plastic mechanism, G is the plastic potential and \mathbf{m}_{lc} is the flow rule direction. However, when the plastic mechanism related to the interaction between both structural levels is active, the plastic strain increment related to the stress increment can be expressed as:

$$\dot{\boldsymbol{\varepsilon}}_{\beta}^p = \dot{\lambda}_{\beta} \mathbf{m}_{\beta} \quad (8)$$

where $\dot{\lambda}_{\beta}$ is the plastic multiplier associated to the β plastic mechanism, and \mathbf{m}_{β} is the flow rule direction.

The material behavior is described by elasto-plastic mechanisms that can be activated during the loading process. The set of active plastic mechanisms is not known in advance. Therefore it is necessary to use an iterative procedure to find them (i.e. Simo & Hughes, 1988; Carol & Prat, 1999). A possibility is to assume that all the plastic mechanisms are initially active. Herein, it is assumed that both plastic mechanisms are initially active, that is: lc and β (i.e. mc or

ms). The system of equation for two active mechanisms is given by:

$$\begin{cases} \dot{\lambda}_{lc} \bar{H}_{lc} + \dot{\lambda}_{\beta} \bar{h}_{\beta} = \dot{e}_{lc} + \dot{s}_{lc} + \dot{t}_{lc} \\ \dot{\lambda}_{lc} \bar{h}_{lc} + \dot{\lambda}_{\beta} \bar{H}_{\beta} = \dot{e}_{\beta} + \dot{s}_{\beta} + \dot{t}_{\beta} \end{cases} \quad (9)$$

where $\dot{\lambda}_{lc}$ and $\dot{\lambda}_{\beta}$ are the unknowns. \bar{H}_{lc} , \bar{h}_{β} , \bar{h}_{lc} and \bar{H}_{β} are moduli related to the lc and β plastic mechanisms, while \dot{e}_{lc} , \dot{s}_{lc} , \dot{t}_{lc} , \dot{e}_{β} , \dot{s}_{β} and \dot{t}_{β} are variables linked to the increment of strains, suction and temperature. More details can be found in Sánchez (2004). System (9) can be expressed in a compact form, as:

$$\bar{\mathbf{H}} \cdot \dot{\boldsymbol{\lambda}} = \dot{\mathbf{e}} + \dot{\mathbf{s}} + \dot{\mathbf{t}} \quad (10)$$

The solution of the system (9) requires the inversion of the $\bar{\mathbf{H}}$ matrix, which would be a P -matrix (Rizzi et al., 1996; Sánchez et al., 2005). In this case, the unknowns are obtained as follows:

$$\dot{\boldsymbol{\lambda}} = \bar{\mathbf{H}}^{-1} \cdot \left(\dot{\mathbf{e}} + \dot{\mathbf{s}} + \dot{\mathbf{t}} \right) \quad (11)$$

The choice of the plastic mechanisms assumed initially active should be verified by checking that they are actually active (Carol & Prat, 1999). If one of them is not active, the problem becomes a single dissipative model. Finally, the net stress increment can be expressed as:

$$\dot{\boldsymbol{\sigma}} = \mathbf{D}_e \cdot \left(\dot{\boldsymbol{\varepsilon}} - \dot{\boldsymbol{\varepsilon}}_s^e - \dot{\boldsymbol{\varepsilon}}_T^e - \sum_{n=1}^{na} \dot{\boldsymbol{\varepsilon}}_n^p \right) \quad (12)$$

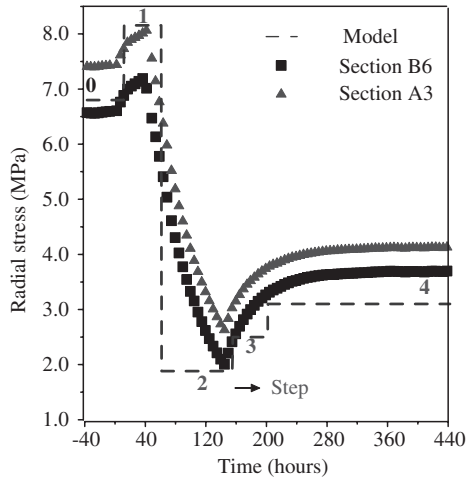
where $\dot{\boldsymbol{\varepsilon}}_s^e$ and $\dot{\boldsymbol{\varepsilon}}_T^e$ are the elastic strain increments due to suction and temperature changes. After some algebra (Sánchez, 2004) the following general form is obtained:

$$\dot{\boldsymbol{\sigma}} = \mathbf{D}_{ep} \cdot \dot{\boldsymbol{\varepsilon}} + \boldsymbol{\gamma}_s \dot{s} + \boldsymbol{\gamma}_T \dot{T} \quad (13)$$

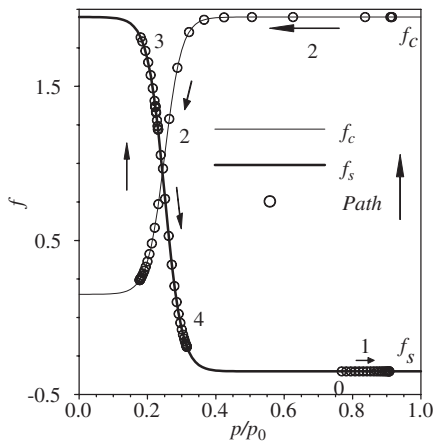
where \mathbf{D}_{ep} is the global elasto-plastic matrix, $\boldsymbol{\gamma}_T$ and $\boldsymbol{\gamma}_s$ are the elasto-plastic vectors associated to temperature and suction, respectively. In Sánchez (2004) the expressions of these matrices are presented in detail.

4 APPLICATION CASE

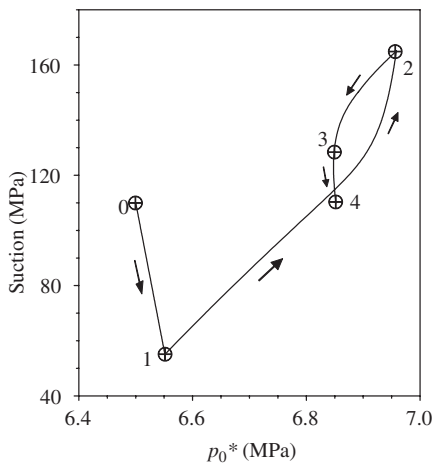
The application case focuses on the analysis of an accidental overheating that took place in the mockup test of the FEBEX project (FEBEX Report, 2000).



(a)



(b)



(c)

Figure 3. (a) Computed values of radial stress. (b) Evolution of the stress state on the interaction functions. (c) Evolution of the hardening parameter.

Table 1. Main loading stages considered in the analysis (average records).

Stage	s (MPa)	T ($^{\circ}\text{C}$)
0 Initial conditions	110	90
1 Vapor front passage	55	135
2 Maximum drying	165	200
3 Cooling down	155	45
4 Re-establishment of initial conditions	110	90

The main objective of this experiment is the validation of the numerical codes developed for the analysis of clay barriers. The phase of heating and hydration of the test (operational stage) has started in February 1997 and is ongoing nowadays. During this stage the barrier has been hydrated uniformly from all around the cylinder and, simultaneously, the barrier has been heated maintaining a constant temperature of 100°C at the contact between heaters and clay barrier. Comprehensive THM numerical analyses of the FEBEX tests have been performed (Sanchez & Gens, 2005).

On day 1391 of the experiment an accidental overheating occurred. Points close to the heater reached temperatures in excess of 200°C . Afterwards the heaters were switched off and (four days after) the prescribed thermal conditions of the test were re-established (i.e. a constant temperature of 100°C at the contact between heaters and clay). The aim of this section is to explain and reproduce the main features of the mechanical behavior observed during the overheating. In this respect, the more relevant aspect was the unexpected mechanical behavior of the FEBEX bentonite. As an illustration, Figure 3 presents (with symbols) the evolution of radial stress in two representative sections of the barrier (time zero corresponds to: 13:00 hrs. 11-26-2000). Just after overheating, there was a moderate increase of radial stress followed by a strong reduction down to around 2 MPa. The radial stress recovered somewhat subsequently but it remained very far from the initial values. So, there was a large irreversible net reduction of radial stress.

To check whether the mechanical model (introduced below) is consistent with the observations of irreversible phenomena observed during the overheating a synthetic generalized stress path was applied to the constitutive law, corresponding to the four major episodes observed during the overheating, indicated as follows: a wetting due to the passage of a vapor front, an intense drying associated with the increase of temperature, a subsequent cooling due to the switching off of the heaters and, finally, the re-establishment of the prescribed test conditions.

Table 1 summarizes the four main loading stages of the overheating episode (Sanchez & Gens, 2005). Table 2 presents the parameters adopted in this work.

Table 2. Mechanical constitutive law parameters.

<i>Parameters defining the BBM (macrostructure)</i>						
κ	κ_s	$\lambda_{(0)}$	r	ζ (MPa ⁻¹)	p_0^* (MPa)	α_0 (°C ⁻¹)
5 ⁻³	1 ⁻³	8 ⁻²	9 ⁻¹	1.	6.5	1. ⁻⁵
<i>Parameters defining microstructural behavior</i>						
α_m (MPa ⁻¹) = 2.1 e ⁻⁰² β_m (MPa ⁻¹) = 2.3 e ⁻⁰³						
<i>Interactions functions</i>						
$f_c = 1 + 0.9 \tanh(20(p_r/p_0) - 0.25)$			$f_s = 0.8 - 1.1 \tanh(20(p_r/p_0) - 0.25)$			

In Lloret et al. (2003) the validation of mechanical model is presented.

The following considerations should be pointed out: (i) only the constitutive law is checked so there are no time effects due to the transient phenomena occurring in the barrier, (ii) the information attributed to the constitutive law point corresponds in fact to a zone of the barrier of finite size, and (iii) the aim is not to reproduce the full behavior of the barrier but to check whether the main features of the observed mechanical behavior are a natural outcome of the constitutive model.

Figure 3 also shows the model results when the loading stages indicated in Table 1 were applied. The suction and temperature changes were applied under conditions of no volume change, mimicking the confined state of the test. Zero strain in all directions and an isotropic stress state was assumed. A reasonable correspondence between measured and calculated values of radial pressure is observed in Figure 3a. Figure 3b depicts the calculated evolution of the interaction functions and Figure 3c shows the evolution of the hardening parameter. In the first loading stage the elastic mechanisms associated with suction reduction and temperature increase tend to increase the swelling pressure because they are associated with soil expansion. In this path the interaction function f_s has negative values, which implies a hardening of the material. Heating continues in the second stage but now it is associated with a drying of the soil. This intense drying dominates and causes a tendency to contract and, consequently, a swelling pressure reduction occurs. During this stage (mc mechanism active) the interaction between the two structural levels produces a densification of the macrostructure. The third stage is characterized by a reduction of temperature and a wetting of the material; the latter dominates causing a tendency to expand and hence an increase of swelling pressure. At the final stage, the initial thermal and hydraulic variables are again prescribed, continuing the wetting of the material and increasing the temperature. These two factors lead to a tendency for expansion of the soil and hence an increase of swelling pressure. During the last two stages the ms mechanism is active. The interaction between the two

structures causes an expansion of the macrostructure and a reduction of p_0^* during the main part of this path.

According to the model, the intense drying affects strongly the behavior of the bentonite during this event, inducing changes in the clay structure that are not recovered when returning to the conditions before the overheating. The final outcome is that the constitutive model response to this complex THM generalized stress path is a significant reduction in swelling stress, the same behavior as that observed in the heating test.

Naturally, this analysis does not reproduce exactly the conditions of the test, as it involves instantaneous application of the thermal and hydraulic loading without considering the transient phenomena that actually occurred in the barrier. It is therefore not surprising that there is a certain time lag between test observations and constitutive model predictions. In any case, the main objective of proving the capability of the model to reproduce irreversible behavior when is submitted to complex THM loading paths has been largely achieved. Also a physical explanation has been suggested to explain the observed bentonite behavior.

5 CONCLUSIONS

A double structure model, based on the general framework for expansive materials proposed by Gens & Alonso (1990) has been presented. In order to be closer to the typical fabric of expansive materials, the existence of two pores structures has been explicitly included in the formulation. The distinction between the macrostructure and microstructure provides the opportunity to take into account the dominant phenomena that affect the behavior of each structure in a consistent way. The application case corresponds to the study of an overheating episode that took place in a large scale heating test. The performance of the constitutive mechanical model is also good in this problem. It has been shown that the model is able to reproduce the major features of the observed mechanical behavior in response to a complex history involving temperature and suction changes.

REFERENCES

- Alonso, E., Gens, A. & Josa, A. 1990. A constitutive model for partially saturated soils. *Geotechnique*, 40(3): 405–430.
- Carol, I. & Prat, P. 1999. A multicroack model based on the theory of multisurface plasticity and two fractures energies. *Proceedings IV Conference on Computational Plasticity, Barcelona*, 1583–1594.
- FEBEX Report 2000. Final project report. EUR 19612 EN, European Commission, Brussels.
- Gens, A. 1995. Constitutive Laws. In A. Gens, P. Jouanna & B. Schrefler. *Modern issues in non-saturated soils*: 129–158. Wien New York: Springer-Verlag.
- Gens, A. & Alonso, E.E. 1992. A framework for the behavior of unsaturated expansive clays. *Can. Geot. Jnl.*, 29: 1013–1032.
- Lloret, A., Villar, M.V., Sánchez, M., Gens, A., Pintado, X. & Alonso, E. 2003. Mechanical behaviour of heavily compacted bentonite under high suction changes. *Geotechnique*, 53(1): 27–40.
- Lublner, J. & Auricchio, F. 1996. Generalized plasticity and shape-memory alloys. *Int. J Solids Struct.*, 33(7): 991–1003.
- Olivella, S., Gens, A., Carrera, J. & Alonso, E.E. 1996. Numerical formulation for a simulator (CODE-BRIGHT) for the coupled analysis of saline media. *Engineer. Comp.*, 13(7): 87–112.
- Push, R. 1982. Mineral water-interaction and their influence on the physical behaviour of highly compacted Na bentonite. *Can. Geotech. Jnl.*, 19: 381–387.
- Rizzi, E., Giulio, M. & Willam, K. 1996. On failure indicators in multi-dissipative materials. *Int. J. Solids Structures*, 33 (20–22): 3187–3124.
- Romero, E. 1999. *Characterization and thermo-hydro-mechanical behavior of unsaturated Boom clay: an experimental study*. Ph.D. Thesis, Technical University of Catalonia, Spain.
- Sánchez, M. 2004. *Thermo-hydro-mechanical coupled analysis in low permeability media*. Ph.D. Thesis, Technical University of Catalonia, Barcelona.
- Sánchez, M., Gens, A., Guimaraes, L. & Olivella, S. 2005. A double structure generalized plasticity model for expansive materials. *Int. Jnl. Num. Anal. Meth. in Geom.*, 29: 751–787.
- Sánchez, M. & Gens, A. 2005. Final Report on THM modelling. FEBEX II. ENRESA Report: 70-UPC-L-5-015.
- Simo, J. & Hughes, T. 1998. *Computational Inelasticity*. New York: Springer-Verlag.

APPENDIX

The dependence of the tensile strength on suction and temperature is given by:

$$\hat{p}_s = k_s e^{-\rho \Delta T} \quad (A1)$$

where k and ρ are model parameters. The dependence of p_0 on suction is given by:

$$p_0 = p_c \left(\frac{\hat{p}_{0T}}{p_c} \right)^{\frac{\lambda_{(s)} - \kappa}{\lambda_{(s)} - \kappa}}; \hat{p}_{0T} = p_0^* + 2(\alpha_1 \Delta T + \alpha_3 \Delta T |\Delta T|) \quad (A2)$$

where p_c is a reference stress, α_1 and α_3 are models parameters, $\lambda_{(s)}$ is the compressibility parameter for changes in net mean stress for virgin states of the soil; which depends on suction according to:

$$\lambda_{(s)} = \lambda_{(0)} \left[r + (1-r) \exp(-\zeta s) \right] \quad (A3)$$

where r is a parameter which defines the minimum soil compressibility. ζ is a parameter that controls the rate of decrease of soil compressibility with suction. The macrostructural bulk modulus (K_1) is evaluated as follows:

$$K_1 = \frac{(1 + e_M)}{\kappa} p \quad (A4)$$

The microstructural bulk modulus (K_1) is evaluated as follows:

$$K_1 = \frac{e^{-\alpha_m \hat{p}}}{\beta_m} \quad (A5)$$

where α_m and β_m are model parameters. The macrostructural bulk modulus for changes in suction (s) is computed considering the following law:

$$K_s = \frac{(1 + e_2)(s + p_{atm})}{\kappa_s} \quad (A6)$$

where κ_s is the macrostructural elastic stiffness parameter for changes in s . The macrostructural bulk modulus for changes in T is computed as follows:

$$K_T = \frac{1}{(\alpha_0 + \alpha_2 \Delta T)} \quad (A7)$$

where α_0 and β_2 are parameters related to the elastic thermal strain. More details are given in Sánchez (2004).

A constitutive model for undrained anisotropic behaviour of clays

G. Grimstad & S. Nordal

Geotechnical Division, Norwegian University of Science and Technology, Trondheim, Norway

C. Athanasiu

Geotechnical Division, Norwegian University of Science and Technology/Multiconsult

ABSTRACT: This paper describes a material model for undrained behavior of normally consolidated clay, developed and implemented in the finite element program PLAXIS v. 8.2. The model is based on elastoplasticity for plane strain, undrained, total stress analyses. The main intention with the model is to account for anisotropy, both in strength and stiffness. The model is conceptually rather simple and only a few input parameters are used. These parameters may be obtained directly from conventional laboratory tests. The model is validated against biaxial and direct simple shear tests and applied in a finite element analysis of a supported excavation in soft clay. The results are compared to simulations with an isotropic soil model and discussed.

1 INTRODUCTION

Classical soil mechanics normally assumes isotropic soil behavior. Even in the advanced numerical methods we use today, most of the soil models applied are isotropic. Still, it is well known that soils often show anisotropic behavior both in strength and stiffness. This becomes especially important when modeling excavations in soft clay, where an anisotropic model is needed to obtain reliable results for all construction stages (Athanasiu 1999).

The anisotropic model presented in this paper, is formulated and implemented for undrained, plane strain calculations in PLAXIS v. 8.2, www.plaxis.nl. The total stress adopted approach simplifies soil behavior, but is found to be adequate in practice for short term conditions in clays. The authors do, however, strongly believe that an effective stress based soil model would be an advantage and work is initiated in this direction. Nevertheless, the present total stress based anisotropic model may be very useful in practice and is the subject of this paper.

The variation of undrained shear strength with the direction of loading was reported by Bjerrum (1973), for several Norwegian clays. Based on these results an anisotropic model is suggested and developed into constitutive equations by Athanasiu (1999). Andresen and Jostad (1999) have formulated and applied an anisotropic total stress based model which also may account for softening (Andresen 2002). An interpolation function for strength and stiffness as a function of the stress orientation is used. A similar procedure

is applied in the proposed model in this paper, as described by Grimstad (2005). In our model a different interpolation functions are assumed compared to Andresen (2002), and no inner elastic stress region exists. An elliptically shaped yield surface is adopted and loading from the initial state towards failure will produce different amount of plastic strains depending on both the size and the direction of loading. The input parameters are the active, direct and passive undrained strengths and the three corresponding failure shear strain levels. The strength will normally be given as a function of depth. In addition information on the initial stresses is needed.

2 FORMULATION AND INPUT PARAMETERS

The yield criterion is stated in equation (1a).

$$F = r - \kappa \cdot R_f = 0 \tag{1a}$$

Where r , κ and R_f are defined in equation (1b), (1d) and (3a). Compression is positive.

$$r = \sqrt{\chi^2 + \tau_{xy}^2} \tag{1b}$$

$$\chi = \frac{\sigma_y - \sigma_x}{2} - \tau_0 \tag{1c}$$

The y-axis is assumed vertical and the x-axis horizontal. The initial vertical stress is $\sigma_{y0} = \sigma_{v0}$. The scalar

hardening parameter, κ in equation (1d), follows equation proposed by Vermeer and de Borst (1984):

$$\kappa = \begin{cases} 2 \cdot \frac{\sqrt{\gamma_p^p / \gamma_p^p}}{1 + \gamma_p^p / \gamma_p^p} & \gamma_p^p \leq \gamma_p^p \\ 1 & \gamma_p^p > \gamma_p^p \end{cases} \quad (1d)$$

where γ_p^p , is the peak plastic shear strain which is a function of the stress rotation angle, $\hat{\theta}$, as defined in figure 1. The peak plastic shear strain is determined by interpolation between the three input values depending on the stress rotation angle, figure 2. The accumulated plastic shear strain, γ_p , is to be integrated along the strain path. Equation (2) expresses one infinitesimal increment in plastic shear strain.

$$d\gamma_p^p = \sqrt{(d\varepsilon_y^p - d\varepsilon_x^p)^2 + (d\gamma_{xy}^p)^2} \quad (2)$$

R_f is the distance from the initial shear stress, τ_0 , to the failure surface, figure 1. The equation for the

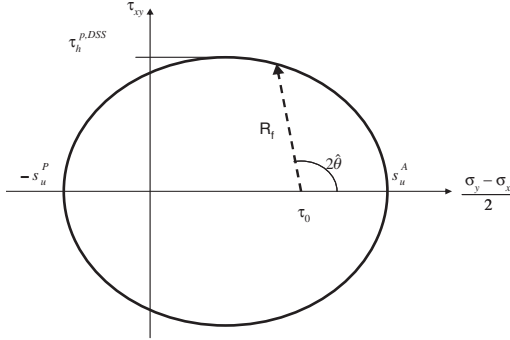


Figure 1. Elliptic failure criteria.

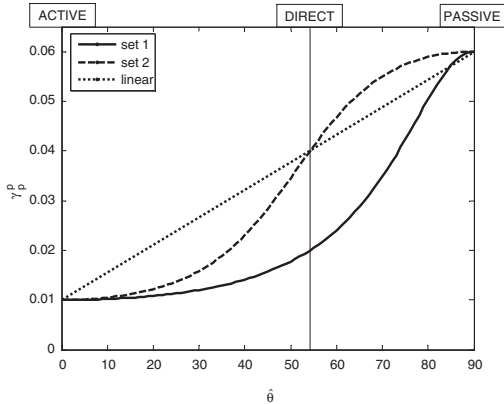


Figure 2. Interpolation of peak plastic shear strain with rotation.

elliptic failure surface is expressed as:

$$R_f = \frac{R_B \cdot R_D \cdot \sqrt{(R_D^2 - R_C^2) \cdot \left(\frac{\chi}{r}\right)^2 + R_C^2 - R_D^2 \cdot R_A \cdot \frac{\chi}{r}}}{R_B^2 - (R_B^2 - R_D^2) \cdot \left(\frac{\chi}{r}\right)^2} \quad (3a)$$

The parameters R_A , R_B , R_C^2 , and R_D are calculated from the input parameters.

$$R_A = \tau_0 - \frac{s_u^A - s_u^p}{2} \quad (3b)$$

$$R_B = \frac{s_u^A + s_u^p}{2} \quad (3c)$$

$$R_C^2 = (s_u^A - \tau_0) \cdot (s_u^p + \tau_0) \quad (3d)$$

$$R_D = \tau_h^{p,DSS} \quad (3e)$$

Figure 1 shows the relation between the input parameters and the elliptic failure criteria. The angle $\hat{\theta}$ is defined through equation (4).

$$\cos(2\hat{\theta}) = \frac{\chi}{r} \quad (4)$$

In figure 2 the interpolation of the peak plastic shear strains is presented for the input values in table 1. If the elliptic interpolation function is used one should be aware that the yield surface may become concave for inappropriate input parameter sets.

The constitutive relation is put together following conventional methods based on an associated flow rule using the following yield surface gradient:

$$\frac{\partial F}{\partial \boldsymbol{\sigma}} = \frac{1}{2 \cdot r} \cdot \begin{bmatrix} -(\chi + \mu \cdot \tau_{xy}) \\ \chi + \mu \cdot \tau_{xy} \\ 2 \cdot (\tau_{xy} - \mu \cdot \chi) \end{bmatrix} \quad (5a)$$

$$\mu = -\frac{\tau_{xy}}{r^2} \cdot \left(R_f \cdot \frac{\partial \kappa}{\partial \gamma_p^p} \cdot \frac{\partial \gamma_p^p}{\partial \cos 2\hat{\theta}} + \kappa \cdot \frac{\partial R_f}{\partial (\cos 2\hat{\theta})} \right) \quad (5b)$$

Table 1. Input parameters.

Set	Undrained strength			Shear strain at failure		
	s_u^A / σ_{v0}'	s_u^p / σ_{v0}'	$\tau_h^{p,DSS} / \sigma_{v0}'$	γ_{pA}^p	γ_{pP}^p	γ_{pDSS}^p
1	0.4	0.2	0.3	0.01	0.06	0.02
2	0.4	0.2	0.3	0.01	0.06	0.04

The initial maximum shear stress, τ_0 , may be determined from an initial at rest coefficient, K_0 . This gives $\tau_0 = \sigma_{v0}'(1 - K_0)/2$, which may grow unrealistically large at depth and conflict with $\tau_0 < s_u^A$. A more consistent alternative is to determine τ_0 from the initial degree of mobilization, f_0 , as $\tau_0 = f_0 \cdot s_u^A$. In the latter case the initial horizontal stress is assumed to be:

$$\sigma_{h0}' = \langle \sigma_{v0}' - 2f_0 \cdot s_u^A \rangle \quad (6)$$

where $\langle \cdot \rangle$ is the Macauley brackets making sure that we always have a positive horizontal stress, $\sigma_{h0}' > 0$.

3 SIMULATION OF BIAXIAL AND DIRECT SIMPLE SHEAR

3.1 Input parameters

The input parameters are given in the table 1. In addition the elastic shear modulus G is needed. In the numerical simulation of biaxial and direct simple shear, $G = 300 \cdot \sigma_{v0}'$ is used. The initial mobilization is assumed to be $f_0 = 0.5$.

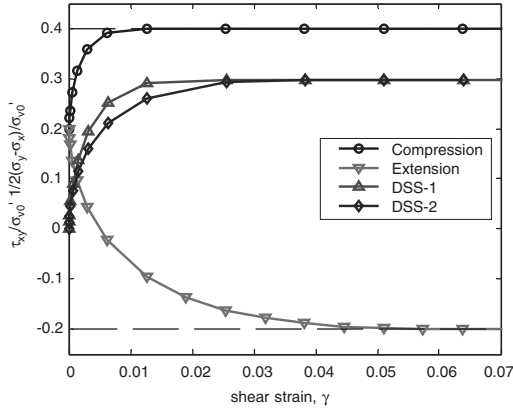


Figure 3. Normalized stress-strain curves from numerical simulations.

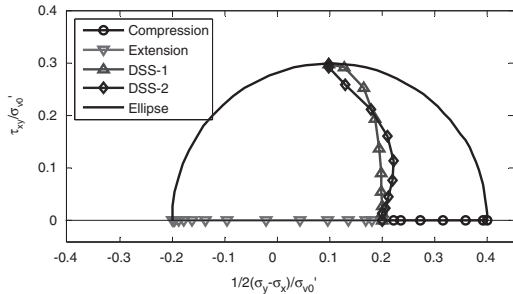


Figure 4. Normalized stress paths from numerical simulations.

3.2 Results

Stress strain plot for the compression and extension biaxial test is shown together with plots for two different direct simple shear tests in figure 3. The stress paths in the shear stress plane are shown in figure 4. It may be noticed that the principal stresses are rotated 35.8° at failure in the direct simple shear tests. The normalized stress paths for the two DSS test simulations show the effect of different peak plastic shear strain when subjected to horizontal shear. We may notice that although the failure criterion is the same, the yield surfaces will not coincide.

4 DISCUSSION OF THE MODEL

Undrained Biaxial or DSS tests on high quality samples cut and loaded at different angles to the vertical are needed to evaluate the quality and accuracy of the model. Here model predictions are compared to results from DSS test on soft Norwegian clays as reported by Bjerrum (1973) and Soedemir (1976). In order to compare the test results with the model, it is an advantage to rewrite the model equations as shown in the following, inspired by Athanasiu (1999).

The angle ω , defined in equation (7a), relates to the direction of pure plastic shear strain as given by the associated flow rule. The rotation of the failure plane from the initial horizontal stress is β . The rotation of the failure plane from the principal stresses is then α_f according to equation (7c). The angle θ is the rotation of the principal stresses. The critical shear stress on a potential failure plane, τ_{cr} , is given by equation (7d).

In figure 5 the critical shear stress in the model is plotted together with results from undrained direct simple shear tests presented by Bjerrum (1973). The present model reproduces the test results reasonably well, even though some discrepancy is observed. In Athanasiu (1978) results from plane strain tests and direct simple shear tests are presented. These results are reproduced in figure 6 together with the best fit ellipse. The direction of the plastic shear strain at failure in these tests is also indicated. Obviously the assumption of associated plastic flow may be questioned. Although the proposed total stress model is able to account for anisotropy in undrained calculations, the total stress approach to some extent limits the understanding of the underlying soil behavior. For instance the failure plane observed in laboratory tests is in general not in accordance with the planes obtained from the model. In real clay samples the strength and possible failure along certain planes appears to be of a more complex nature than we may possibly capture in a classical elastoplastic total stress approach.

In figure 7 the current elliptic interpolation is used on data found in Whittle (1993), together with his

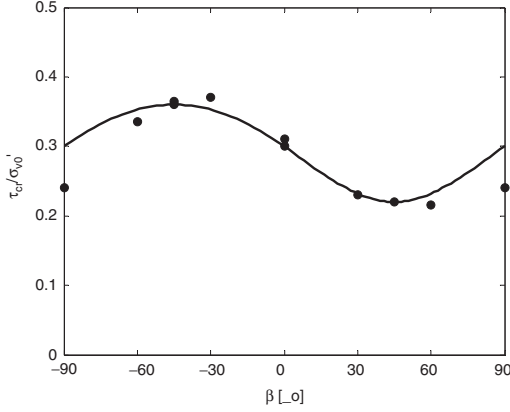


Figure 5. Results from simple shear test on Drammen plastic clay with samples of different rotation (Bjerrum 1973) plotted together fit from the proposed model.

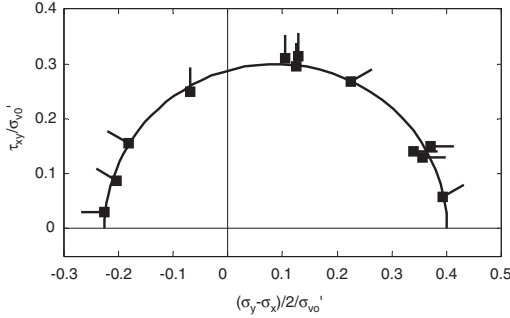


Figure 6. Shear strengths observed in simple shear test and plane strain device, presented by Athanasiu (1978).

predictions from the MIT-E3 model. We should notice that the MIT-E3 predictions are not obtained through a simple interpolation function as in our current model. Even though it appears like the total stress based model in this case fits the experimental data best, it is no doubt that an effective stress based model has a larger potential in consistently reproducing the anisotropic behavior of soil. Work on an effective stress based anisotropic model for soft clays is initiated.

$$\tan 2\omega = \frac{\{\tau_{xy}\}_f \cdot \left(\frac{s_u^A + s_u^p}{2}\right)^2}{\left(\left(\frac{\sigma_y - \sigma_x}{2}\right)_f - \frac{s_u^A - s_u^p}{2}\right) \cdot \tau_{h,DSS}^p} \quad (7a)$$

$$\beta = \pm 45^\circ + \omega \quad (7b)$$

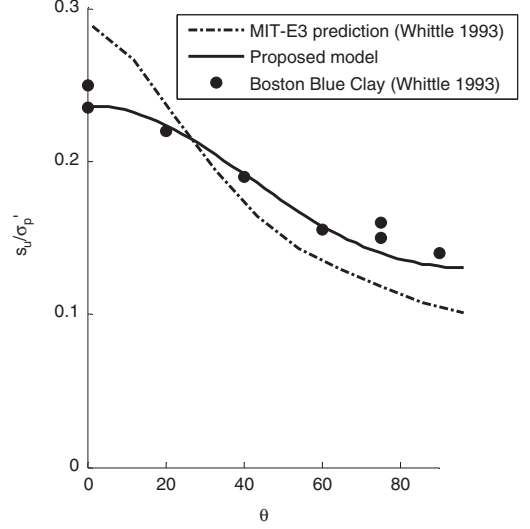


Figure 7. Comparison with data from tests on Boston Blue Clay in a directional shear cell (Whittle 1993), OCR \approx 4 in the test.

$$\alpha_f = 45^\circ - \theta + \omega \quad (7c)$$

$$\tau_{\sigma} = \left\{ \frac{\sigma_y - \sigma_x}{2} \right\}_f \cdot \cos 2\omega + \{\tau_{xy}\}_f \cdot \sin 2\omega \quad (7d)$$

5 NUMERICAL EXAMPLE

5.1 Case

In figure 8 a plane strain model for excavation in clay is shown. The Finite element program PLAXIS is used for the numerical calculation of the problem. The construction consists of two stages, stage one is installing sheet pile and excavating to level -1.5 m. Second stage is the installation of the anchor and further excavation to level -4.5 m. The soil parameters are given by table 2 and are typical for soft Scandinavian clays. Triangular elements with 15 nodes are used; the mesh is indicated in figure 8. The top layer of sand is assumed to act as a load only and has no strength. The anchor is not pre-stressed at installation and its capacity is restricted to 100 kN/m. The soil density is 20 kN/m³ for both layers.

5.2 Deformations in serviceability state

Horizontal wall displacement is shown in figure 9. We observe that assuming isotropic behavior using laboratory results from active biaxial tests only, will significantly underestimate the deformations. If we on the other hand assume isotropic behavior with average

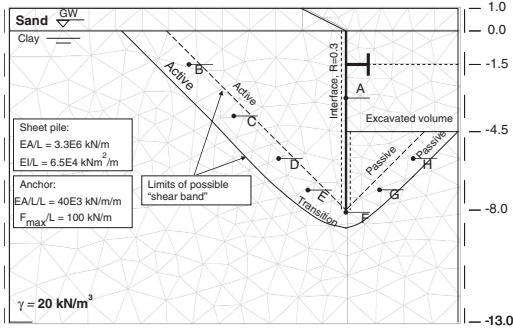


Figure 8. Plane strain model of sheet pile wall.

Table 2. Input parameters.

Parameter	Anisotropic	Isotropic(1)	Isotropic(2)
s_u^A	$0.4\sigma_{v0}' + 10 \text{ kPa}$	$0.3\sigma_{v0}' + 7.5 \text{ kPa}$	$0.4\sigma_{v0}' + 10 \text{ kPa}$
s_u^P	$0.2\sigma_{v0}' + 5 \text{ kPa}$	$0.3\sigma_{v0}' + 7.5 \text{ kPa}$	$0.4\sigma_{v0}' + 10 \text{ kPa}$
$\tau_{H}^P_{DSS}$	$0.3\sigma_{v0}' + 7.5 \text{ kPa}$	$0.3\sigma_{v0}' + 7.5 \text{ kPa}$	$0.4\sigma_{v0}' + 10 \text{ kPa}$
G	$300\sigma_{v0}' + 7.5E3 \text{ kPa}$	$300\sigma_{v0}' + 7.5E3 \text{ kPa}$	$300\sigma_{v0}' + 7.5E3 \text{ kPa}$
$\gamma_p^P_A$	0.01	0.03	0.01
$\gamma_{ap}^P_P$	0.06	0.03	0.01
$\gamma_p^P_{DSS}$	0.02	0.03	0.01
f_0	0.5	0.0	0.0
K_0	not constant	1.0	1.0

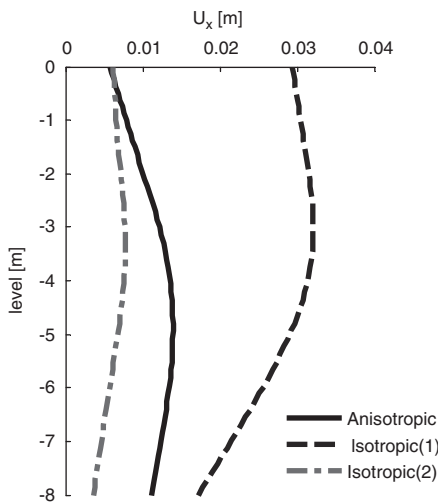


Figure 9. Horizontal displacement of sheet pile.

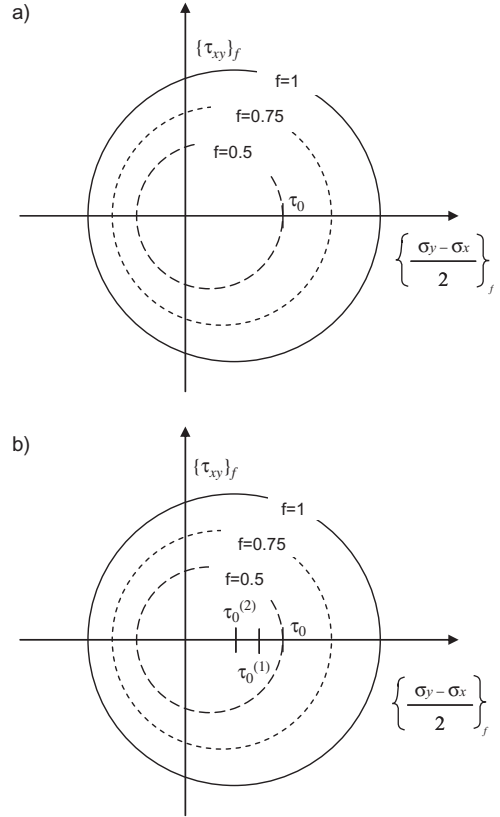


Figure 10. Two procedures for safety calculation.

undrained strength we will predict too large deformations. The anisotropic simulation falls in between the two isotropic cases and the differences between the simulations are significant. This shows the importance of taking anisotropy into account.

5.3 Calculation of factor of safety

The calculation of a factor of safety is based on incrementally reducing the strength of soil. When deformations become excessive a failure mechanism has developed. The corresponding strength reduction factor is taken as the factor of safety. For the anisotropic soil model two principally different methods may be used for calculating a factor of safety.

- (1) Reducing strength while keeping the initial maximum shear stress, i.e. τ_0 constant, figure 10a.
- (2) Reducing strength as well as the initial maximum shear stress, i.e. keeping f_0 constant, figure 10b.

The first one may appear most straightforward, but if the initial maximum shear stress is high, then the initial state limits the strength reduction, figure 10a.

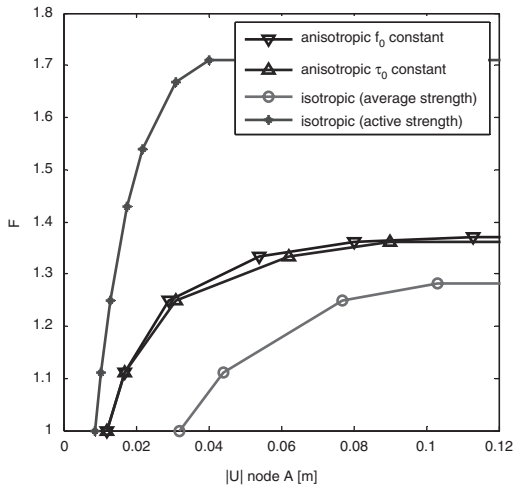


Figure 11. Calculation of factor of safety.

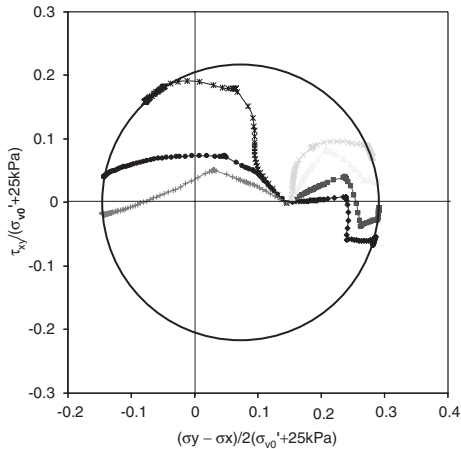


Figure 12. Normalized stress paths for the anisotropic model with reduced strength parameters.

Figure 11 gives results from calculation of safety factors. These curves are produced from manual decrease of input parameters until a limit state is reached. The node followed is located at the sheet pile at -3 m. As expected the isotropic soil model using active strength will dangerously over predict the safety giving $F \approx 1.7$. The isotropic simulation using average strengths gives a too low value of $F \approx 1.3$, while the anisotropic model provides a factor that is believed to be the most correct, $F \approx 1.4$. We may observe that in this example the ratio between the safety factors of the two isotropic cases (1) and (2) will be $\frac{3}{4}$, directly following the ratio between the corresponding input strength parameters. The stress-points B-H is monitored through the calculations. In figure 12 the stress paths for the different

points are followed until failure. The calculation is done with the anisotropic model and with an initial mobilization of 0.5 which is kept constant during the safety factor calculation. The sudden breaks in the stress paths are related to the two excavation stages and the plastification of the anchor. It may be noted that point F is on the passive side of the tip of the sheet pile.

6 CONCLUSION

Constitutive equations for a total stress based anisotropic soil model have been established. The soil model derived was implemented in PLAXIS using as a user defined soil model and applied to simulations of laboratory tests and a sheet pile wall. A limited amount of experimental data found in Bjerrum (1973), Athanasiu (1978) and Whittle (1993) is used to evaluate the proposed failure criterion. More experimental data is needed to conclude regarding the accuracy of the model, but the model significantly improves practical simulations compared to isotropic models.

The sheet pile wall problem was calculated using both the anisotropic soil model and an isotropic soil model. It is observed how an isotropic soil model using only results from undrained active biaxial tests significantly over predicts the safety factor and underestimates the deformations. On the other hand using average strength in an isotropic simulation shows too low factor of safety and too large deformations. The average is then the average of the active, direct and passive undrained shear strength. Using the anisotropic soil model the overall behavior is in agreement with expected results and much more realistic. It is believed that anisotropic soil models as developed herein represent a major improvement over isotropic models when it comes to simulating the undrained behavior of soft clays.

ACKNOWLEDGEMENTS

Acknowledgement is given to the International Centre for Geohazards (ICG) and to the 2005–2009 EC/Marie Curie Research Training Network “AMGISS” for their support to Geotechnical research at NTNU.

REFERENCES

- Andresen, L. and Jostad, H. P., 1999, Application of an Anisotropic Hardening Model for Undrained Response of Saturated Clay, Proc. Num. Mod. Geomech. – NUMOG VII, Graz, Austria, pp. 581–585
- Andresen, Lars, 2002, Capacity Analysis of Anisotropic and Strain-Softening Clay, Dissertation for the Degree Doctor Scientiarum, University of Oslo, Norway

- Athanasiu, Corneliu, 1978, Contributions to contact stress distribution between foundations and soil. PhD thesis, Bucuresti Romania
- Athanasiu, Corneliu, 1999, Proposal for an anisotropic, soft clay model to be incorporated in future development of PLAXIS, Beyond 2000 in Computational Geotechnics – 10 years of PLAXIS international, Balkema, pp. 271–280
- Bjerrum, Laurits, 1973, Problems of Soil Mechanics and Construction on Soft Clays, State of the Art Report to Session IV, 8th International Conference on Soil Mechanics and Foundation Engineering, Moscow, 1973, NGI report 100 (1974)
- Brinkgreve, Ronald Bastiaan Johan, 1994, Geomaterial Models and Numerical Analysis of Softening, PHD thesis
- Cook, R. D., Malkus, D. S., Plesha, M. E., Witt, R. J., 2002, Concepts and application of finite element analysis, Fourth edition, John Wiley & sons, inc.
- Grimstad, Gustav, 2005, A constitutive model for undrained anisotropic behavior of clays, Master thesis NTNU
- Nordal, Steinar, 1983, Elasto-plastic behaviour of soils analyzed by the finite element method, PhD. thesis NTH.
- Nordal, Steinar, 1998, EEU course in soil modelling, Lecture notes, NTNU
- PLAXIS, 2002, Manual V8, www.plaxis.nl
- Ottosen, Niels Saabye, 1987, Aspects of constitutive modeling, Report TVSM-3010, Division of structural mechanics Lund Institute of Technology, Sweden
- Soydemir C., 1976, Strength Anisotropy Observed Through Simple Shear Tests, Laurits Bjerrum Memorial Volume, NGI
- Søreide, Ole Kristian, 2003, Mixed hardening models for frictional soils, Ph.D. thesis, NTNU
- Vermeer, P. A. & de Borst R., 1984, Non-associated plasticity for soil, concrete and rock, HERON 29(3), pp. 1–64
- Whittle, A. J., 1993, Evaluation of a constitutive model for overconsolidated clays, Géotechnique 43 No. 2, 289–313.

Calculation of shear band thickness in sensitive clays

H.P. Jostad & L. Andresen

Norwegian Geotechnical Institute (NGI), Oslo, Norway

V. Thakur

Norwegian University of Science and Technology (NTNU), Trondheim, Norway

ABSTRACT: A key parameter in the calculation of capacity or peak load of sensitive clays is the shear band thickness which may develop due to the strain softening behavior of this material. The shear band thickness may govern the strain rate and thus also the rate of softening. In contrast to granular materials, where the shear band thickness depends on the grain size, the mechanisms that govern the shear band thickness in sensitive clays under undrained condition are not fully understood. The hypothesis considered in this paper is that the shear band thickness is governed by the deformation rate, where the time dependent mechanisms are local pore water flow and time induced shear deformations (creep). Finite Element Method is used to find conditions where the shear band thickness in sensitive clays becomes unique and not governed by the finite element discretisation.

1 INTRODUCTION

The shear stress-shear strain characteristics of sensitive clays may show a significant strain softening behavior under undrained deformation. After the peak shear stress is reached, the shear stress decreases with increasing shear strain toward a residual strength at large shear strain. This is illustrated in Figure 1 for an idealized direct simple shear (DSS) test.

A consequence of the strain softening behavior is that the continuing stress-strain curve at the peak stress is not unique. When the shear strength is reduced beyond the peak shear strength, the trivial response is that the material continues along the plastic loading branch

Trivial solution:

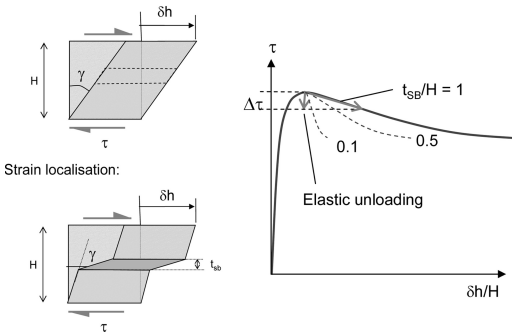


Figure 1. Bifurcation problem during direct simple shear of a strain softening material. Uniform trivial solution and strain localisation on a shear band with thickness t_{SB} .

with increasing plastic shear strain. However, material may, due to the reduced shear stress, also continue along the elastic unloading branch as illustrated in Figure 1.

While analyzing the capacity of a general boundary value problem this type of bifurcation problem can only be solved by using numerical methods such as the Finite Element Method. Stress equilibrium, material behavior and displacement compatibility of the soil mass are then satisfied throughout the loading phase. The uniqueness of the continuing solution curve at any load level may be checked by an eigenvalue analysis of the tangential stiffness matrix (de Borst, 1987 and Jostad & Nordal, 1995).

The loss of uniqueness may result in development of shear bands, i.e. thin zones with large plastic shear deformation and elastic unloading outside the shear band.

The thickness of the shear band governs the degree of softening and thus also the capacity or peak load of the boundary value problem (Jostad & Andresen, 2002). The degree of softening is in this case defined as the negative slope of the curve of shear stress versus differential tangential displacement across the shear band in the post peak shear stress branch (see Fig. 1).

Without a proper regularization technique the thickness of the shear band may theoretically be reduced to zero or limited by the finite element discretisation (de Borst et al. 1993).

However, in contrast to granular materials, where the shear band thickness is found to be governed by the grain size (e.g. Roscoe, 1970), the mechanisms that

govern the shear band thickness in sensitive clays under globally undrained condition are not fully understood.

In this paper the hypothesis that the shear band thickness is governed by the deformation rate is considered. The regularization mechanisms are time dependent local pore water flow and time dependent shear deformations (creep).

This hypothesis was also considered in Thakur et al. (2005) using a rate independent linear elastic perfectly plastic material model. However, in that case the local pore water flow was not able to regularize the solution.

2 FINITE ELEMENT PROCEDURE

The development of shear band in sensitive clay is studied by using a finite element code called BIFURC developed at NGL. For simplicity, a one dimensional idealization across a potential shear band is considered. The key ingredients in the Finite Element formulation used in these calculations are then:

- A two noded one dimensional consolidation element with normal displacement, lateral displacement and excess pore pressure degrees of freedom in each node.
- An implicit time stepping scheme with equilibrium iteration within each time step. The iteration is in this case performed with the elastic stiffness matrix of the soil skeleton, i.e. the initial stiffness method.
- A non-associated elasto-plastic model based on a plastic (permanent) strain dependent mobilized friction.
- A dilatancy angle controlled by input of an accumulated plastic shear strain induced excess pore pressure curve obtained from undrained shear tests.
- A time dependent plastic shear strain (creep).

The above ingredients are described in more details in the following.

2.1 1D Consolidation element

A 2-noded one dimensional consolidation element is used to model the effect of local pore water flow (drainage) during shear deformation.

The element describes both normal strain ε and shear strain γ :

$$\begin{bmatrix} \varepsilon \\ \gamma \end{bmatrix} = - \begin{bmatrix} \frac{\Delta u_n}{\Delta L} \\ \frac{\Delta u_t}{\Delta L} \end{bmatrix} \quad (1)$$

where u_n and u_t are the normal and the lateral displacements along the finite element length ΔL .

The element must also satisfy the continuity (mass balance) of the pore water, i.e.

$$\Delta v \cdot \Delta t = \Delta \varepsilon \cdot \Delta L \quad (2)$$

where Δv is the change in fluid flow velocity over the finite element length ΔL , and $\Delta \varepsilon$ is the change in normal strain (constant within the element) during the time increment Δt .

The pore water flow velocity v is given by Darcy's law:

$$v = - \frac{k}{\gamma_w} \cdot \frac{\Delta p}{\Delta L} \quad (3)$$

where k is the permeability, γ_w is the unit weight of the pore water, and Δp is the change in excess pore pressure over ΔL .

The element must also satisfy the equilibrium equations, where the internal forces due to the normal stress σ and shear stress τ are in equilibrium with the nodal point forces. In nodes without external forces, the stresses in the elements at both sides of the node must then be equal.

The normal stress σ is divided into effective stress σ' and excess pore pressure p (compressive stresses and pore pressure are taken as positive): $\sigma = \sigma' + p$. Effective stress change $\Delta \sigma'$ is given by the normal strain and the shear strain as described below.

2.2 Constitutive model

The stress-strain relationship of sensitive clays is described by an elasto-plastic model with a plastic shear strain dependent mobilized friction $\tan \rho$. The mobilized friction concept is for instance described in Janbu (1985). The yield criterion is then given as:

$$F = \frac{\tau}{\sigma} - \tan \rho = 0 \quad (4)$$

In this paper the relationship between the mobilized friction and the plastic shear strain is for simplicity described by a function proposed by Vermeer and de Borst (1984):

$$\tan \rho = \tan \rho_o + 2 \frac{\sqrt{\gamma_p / \gamma_{pf}}}{1 + \gamma_p / \gamma_{pf}} \cdot (\tan \phi - \tan \rho_o) \quad (5)$$

where γ_p is the plastic reference shear strain, ρ_o is the initial mobilized friction angle, ϕ is the peak friction angle and γ_{pf} is the plastic shear strain where the peak friction angle ϕ is reached under a constant (reference) shear strain rate.

The coupling between plastic normal strain and plastic shear strain is controlled by the dilatancy angle ψ , i.e.

$$\tan \psi = - \frac{\Delta \varepsilon_p}{\Delta \gamma_p} \quad (6)$$

Based on undrained DSS tests a relation between excess pore pressure p_γ and plastic shear strain may be found. In a standard DSS test the total normal stress is kept constant, which means that the measured pore pressure changes are shear induced. This relationship is in this paper, for simplicity described by a hyperbolic function:

$$p_\gamma = c_p \cdot \gamma_p + \frac{p_a}{1 + \gamma_p} \quad (7)$$

where c_p and p_a are parameters used to fit the measured shear induced pore pressure. The dilatancy angle is then calculated in order to give the shear induced pore pressure under perfectly undrained condition.

The time dependent plastic strain (creep) increment is calculated based on a modified formulation of Mitchell's equation (Mitchell et al. 1968):

$$\text{If } f > f_c: \Delta\gamma_{cp} = A \cdot (e^{\alpha \cdot f} - e^{\alpha \cdot f_c}) \cdot \ln\left(\frac{t_{eq} + \Delta t}{t_{ref}}\right) \quad (8)$$

$$\text{If } f \leq f_c \Delta\gamma_{cp} = 0 \quad (9)$$

where A and α are parameters used to control the strain rate, $f = \tan \rho / \tan \phi$ is the mobilized friction, f_c is a friction (threshold level) that must be exceeded before the creep strain becomes significant, t_{ref} is a reference time and t_{eq} is an equivalent time corresponding to the accumulated creep strain at the current mobilized friction.

The elastic strains are given by the elastic shear modulus G_0 and constrained modulus M_u . G_0 is derived from the initial part of the shear stress-shear strain curve obtained from a DSS test. G_0 is therefore not necessary taken equal to the small strain stiffness G_{max} . M_u is the secant constrained modulus obtained from an unloading phase during an oedometer test.

2.3 Material behavior

The constitutive behavior of saturated soft clay subjected to varying strain rates is in this paper, in lack of suitable DSS tests, taken from undrained triaxial compression tests on plastic Drammen clay (Berre, 1973). Some index data of the marine clay is given below:

- Water content, w (%) = 50%
- Plasticity index, I_p (%) = 25%
- Over-consolidation ratio, OCR = 1.25
- Clay content = 45–55%
- Sensitivity, S_t = 3–5

Specimens taken from approximately the same depth are deformed under three different nominal vertical

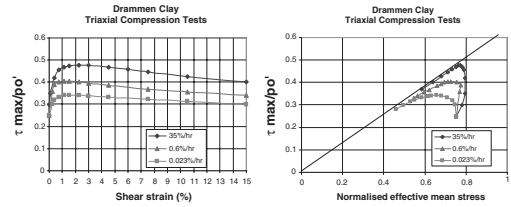


Figure 2. Results from undrained triaxial compression tests on plastic Drammen clay with different applied constant strain rate.

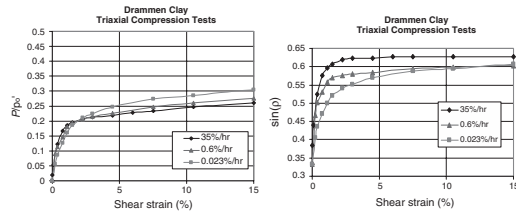


Figure 3. Interpreted normalized pore pressure p_γ/p_o' versus plastic shear strain and mobilized friction $\sin \rho$ versus plastic shear strain from undrained triaxial compression tests with different applied strain rates.

strain rates: 35%/hour (fast), 0.6%/hour (medium) and 0.023%/hour (slow).

Figure 2 (left) shows the shear strain $\gamma = \epsilon_v + \frac{1}{2} \epsilon_h$ versus the normalized maximum shear stress $\frac{1}{2} (\sigma_v - \sigma_h)/p_o'$ obtained from these tests, and Figure 2 (right) shows the corresponding effective stress paths, $\frac{1}{2} (\sigma_v - \sigma_h)/p_o'$ versus $\frac{1}{2} (\sigma_v + \sigma_h)/p_o'$. The specimens were initially consolidated to the initial in situ effective vertical stress $p_o' = 73 \text{ kPa}$ with an effective horizontal stress $\sigma_h' = 0.5 \cdot p_o'$.

From these tests it is found that the shear induced pore pressure p_γ is independent of the applied nominal strain rate as shown in Figure 3 (left), and that the nominal shear strain at a given mobilized friction $\sin \rho$ increases with reducing nominal strain rate (i.e. increasing time) as shown in Figure 3 (right).

The shear induced pore pressure is therefore in this paper described by Equation 7 where the plastic shear strain is the sum of a plastic reference strain (corresponding to the plastic strain obtained with a given strain rate) and an accumulated time dependent (creep) strain given by Equation 8 or by Equation 9 depending upon current mobilization level.

3 CALCULATIONS

The idealized problem analyzed in this paper is shown in Figure 4. It is a 1D column with the height H , which

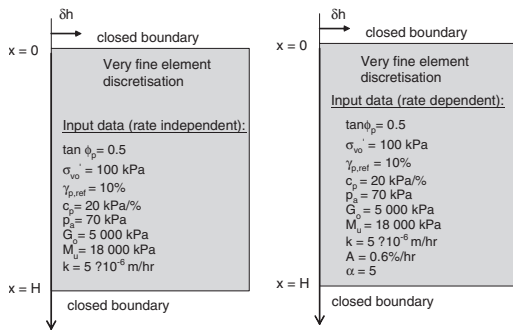


Figure 4. Example with input data.

may represent the soil on one side of a potential shear band. The 1D assumption is valid as long as the height H is small compared to the length of the potential shear band. However, the idealization is not valid close to the front of a propagating shear band where the mechanisms are more complex.

The shear stress is assumed to be constant over H , and H large enough to be globally undrained (i.e. the height is constant equal to H during the analysis). The differential lateral displacement rate over H is assumed to be constant during the analysis (e.g. as in a strain controlled DSS test). The lateral displacement δh is prescribed at the first node ($x = 0$) and the last node ($x = H$) is totally fixed. The shortest element length used is only 1 mm, which is short enough for the analyses presented herein.

The bifurcation problem, i.e. the possibility of switching to a non-uniform deformation mode, is checked by an iterative procedure as described below:

- The time dependent problem is solved by an implicit time stepping scheme.
- The lateral displacement δh is increased by $\dot{\gamma} \cdot H \cdot \Delta t$ (where $\dot{\gamma}$ is the applied nominal shear strain rate) in each time step. The time increment Δt is sufficient small to secure small strain changes during the time step.
- The iteration process is started by first assuming that the differential lateral displacement takes place only over the first element. This gives preference to develop the minimum possible shear band thickness for the actual mesh. The iteration process then continues until the equilibrium (same shear stress and total normal stress in all elements), and mass balance (no global volume change) for the actual excess pore pressure field are satisfied. The iteration is performed by using the elastic stiffness matrix which is most robust for this problem with the possibility of switching to elastic unloading outside the shear band.

The material properties used in the analyses are presented in Figure 4. In the first set of analyses the

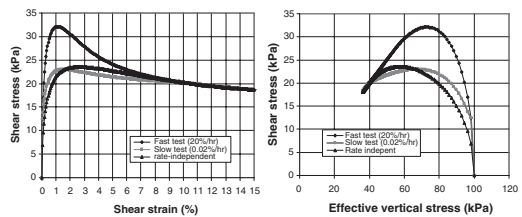


Figure 5. Normalized effective stress paths and shear strain versus normalized shear stress curves (homogeneous deformation).

effect of time induced shear strain (creep) is neglected. The stress-strain curves in these cases (referred as rate-independent) are shown in Figure 5.

These idealized curves agree rather well with results from DSS test on plastic Drammen clay subjected to a deformation rate of 1%/hour.

The second set of analyses are done by accounting for the rate effect. The input parameters for these cases are presented in Figure 4 (right) and the resulting stress-strain curves in Figure 5 for a fast and a slow test.

Figure 6 shows the calculated shear strain and pore pressure distributions at different nominal shear strains ($\delta h/H = 3\%$ to 4.3%) obtained with different applied nominal shear strain rates. The effect of time dependent strain is not taken into account. It is seen that the initial zone with localized shear strain (shear band) reduces with increasing applied nominal shear strain rate. Furthermore, the shear strain is largest in the centre of the shear band ($x = 0$) from where it reduces smoothly toward the strain outside the shear band.

From Figure 6 it is also seen that the shear band thickness is not constant but that it decreases with increasing strain. The reason for this is that the rate of pore pressure generation within the shear band is decreasing with increasing strain. When the rate of pore pressure generation becomes slow the effect of local pore water flow is not able to regularize the shear band thickness and the thickness becomes equal to the element size.

By performing analyses with different element lengths it is found that the solution (e.g. the post peak strain softening curve in Figure 7) is mesh independent, as long as the element length is sufficiently short compared to the resulting shear band thickness. This clearly demonstrates that the local pore water flow regularizes the solution.

Figure 8 shows the calculated initial shear band thickness (which due to assumed symmetry about the centre of the shear band is two times the length obtained in the analyses) as function of the applied nominal shear strain rate. It is seen that the initial shear band thickness becomes large at low nominal shear strain rates.

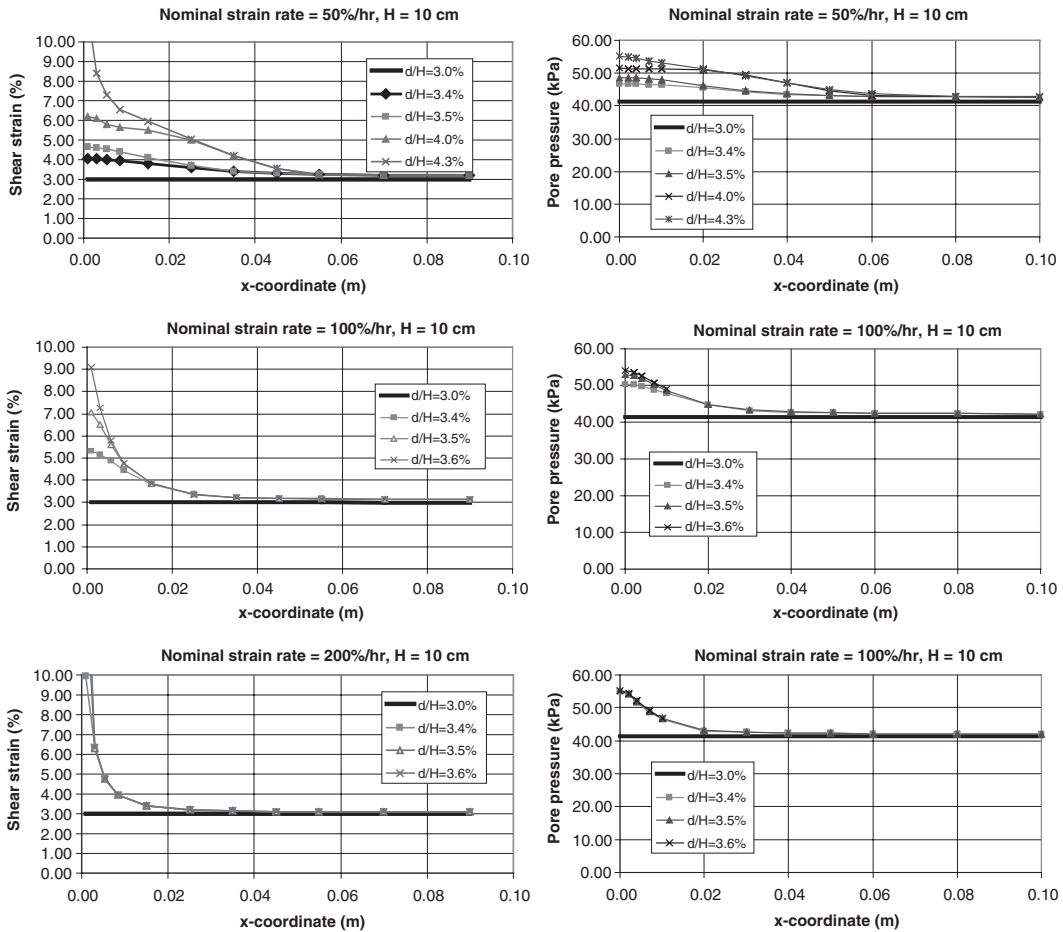


Figure 6. Calculated shear strain and excess pore pressure distribution at different global shear strain $\delta h/H$ and different applied nominal shear strain rates.

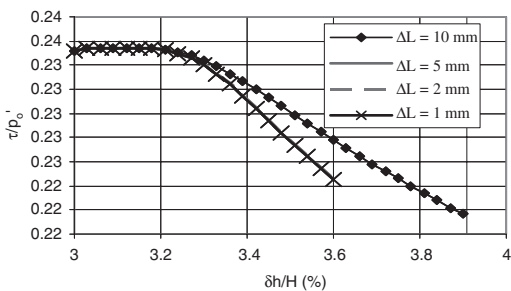


Figure 7. Calculated post peak load-displacement curves for an applied nominal shear strain rate of 100%/hour obtained with different minimum element lengths varying between 1 and 10 mm.

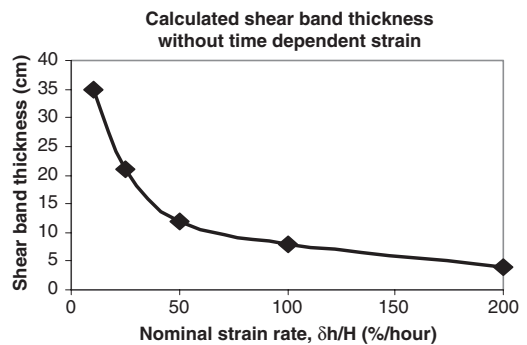


Figure 8. Calculated shear band thickness as function of applied shear strain rate.

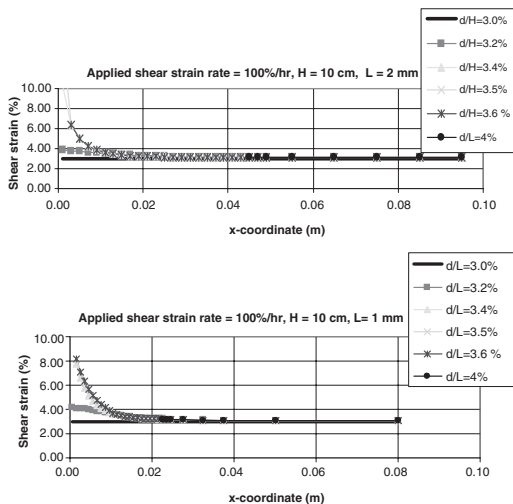


Figure 9. Influence of mesh discretization.

The effect of increasing strain rate and then reduced time dependent strain is not taken into account in Figure 8.

By taking into account the effect of time dependent shear strain it was found that strain localization was prevented before the peak friction was mobilized. This means a uniform deformation within a height of at least 20 cm in the post peak shear stress softening regime toward the peak friction. The reason is that strain localization will reduce the contribution from time dependent strain compared to a uniform strain field. This will also reduce the strain induced pore pressure and thus increase the shear strength. In these cases time dependent strain will therefore prevent the development of localized shear deformation.

4 CONCLUSIONS

The hypothesis that the shear band thickness in sensitive clays under rapid shear deformation is regularized by time dependent effects caused by local pore water flow, is demonstrated by 1D finite element analyses. However, it was necessary to use a constitutive model with a strain dependent mobilized friction where the mobilized friction increases with increasing pore pressure at the peak shear stress. The material close to the zone with localized shear strain is then prevented to elastically unload due to increased pore pressure from dissipation of pore water from the localized zone.

That a shear band may be prevented to develop due to the effect of time dependent shear strain (creep)

before the peak friction is mobilized is also demonstrated by using realistic properties for a plastic marine clay.

This study has however a limitation of proper rate dependent data for more sensitive clays. In order to extend the relationships between applied nominal shear strain rate and shear band thickness, it is necessary to achieve relevant properties for more sensitive clays.

It would also have been interesting to verify the results from the numerical analyses by measurements of the local strains during the test.

ACKNOWLEDGEMENTS

Financial support from the Research Council of Norway through the strategic institute project SIP 8 and from the International Centre for Geohazards (ICG) is gratefully acknowledged.

REFERENCES

- Andersen, K.H. Kleven, A. & Heien, D. 1988. Cyclic soil data for design of gravity structures. *Journal of Geotechnical Engineering, ASCE*; 114(GT5): 517.
- Andresen, L. & Jostad, H.P. 1998. Effect of strain softening in interpretation of laboratory compression test. *Proc. of 4th European Conf. On. Num. Meth. in Geotech. Eng.-NUMGE 98*.
- Berre T. 1973. Effect of rate of strain on the stress-strain relationship for undrained triaxial tests on plastic Drammen clay, NGI report number 50301-4.
- de Borst, R. 1993. Bifurcation in finite element models with a non-associated flow law. *Int. Journal for Numerical and Analytical Methods in Geomechanics*. 12: 99–116.
- de Borst, R. 1987. Computation of post bifurcation and post failure behaviour of strain softening solids. *Comp. & Stuct.*; 25(2): 211–224.
- de Borst, R., Sluys, L.J., Mühlhaus, H.-B. & Pamin, J. 1993. Fundamental issues in finite element analysis of localization of deformation. *Eng. Comp*; 10(2): 99–121.
- Janbu, N. 1985. The twenty fifth Renkin lecture of the British Geotechnical Society. *Geotechnique*; 35(3): 241–281.
- Jostad, H.P. & Andresen, L. 2002. Bearing capacity analysis of anisotropic and strain-softening clays. *NUMOG VIII, Rome, Italy*.
- Jostad, H.P. & Nordal, S. 1995. Bifurcation analysis of frictional materials. *NUMOG V*; Davos, Switzerland: 173–179.
- Mitchell, J.K., Campanella, R.G. & Singh, A. 1968. Soil creep as a rate process. *Journal of the soil mechanics and foundations division; ASCE*; 94: 231–253.
- Roscoe, K.H. 1970. The influence of strains in soil mechanics. *Geotechnique*; 20: 129–170.
- Thakur V, Nordal S., Jostad H.P. and Andresen L. 2005. Study on pore water pressure dissipation during shear banding in sensitive clays” 11th IACMAG, volume 4 page 289–296, Italy, Turino.
- Vermeer, P.A. & de Borst R. 1984. Non-associated plasticity for soil, concrete and rock. *HERON*; 29(3): 1–64.

Response envelopes of the elasto-plastic S-CLAY1 model

R. Zentar & N.-E. Abriak

Department of Civil and Environmental Engineering, Ecole des Mines de Douai, France

M. Karstunen

Department of Civil Engineering, University of Strathclyde, UK

D. Rangeard

Department of Civil Engineering, INSA de Rennes, France

ABSTRACT: In this paper, the features of S-CLAY1 model are explored through identification of the so-called response envelopes, which is very useful way of studying the incremental behaviour of a constitutive model. To highlights the effect of anisotropy induced by the S-CLAY1 model formulation a systematic comparison to the response of the well known isotropic Modified Cam-Clay model is performed.

1 INTRODUCTION

Due to construction activities, soils are subjected to a variety of loading paths involving not only increases in magnitudes of principal stresses, but also changes in the direction of stresses. The complexity of soil behaviour, combined with the wide variety of loading conditions in geotechnical problems, has resulted in development of a wide variety of advanced constitutive models. The performance of these models is investigated by modelling laboratory tests under few controlled stress or strains paths. Another way to assess and compare the performance of these models is to perform a stress or a strain probing to deduce so-called response envelope as proposed by Gudehus (1979) and Gudehus & Kolymbas (1979).

Description of soil behaviour as a function of loading direction is a key ingredient in the analysis of any geotechnical structure, where different zones of soil experience widely different stress-paths, both in size and direction.

The objective of this paper is to assess the performance of S-CLAY1 model, a recently developed elasto-plastic anisotropic model, compared to the well known isotropic Modified Cam-Clay model in terms of incremental behaviour for number of different stress paths all originating from a common initial state (stress probes). Due to the limitations of space, only a brief summary of the main features of the constitutive models employed is given below.

2 S-CLAY1 MODEL

In the simplified stress space of a triaxial test, when considering a cross-anisotropic sample, the yield curve of S-CLAY1 can be expressed in terms of p' (mean effective stress) and q (deviator stress) as:

$$f = (q - \alpha p')^2 - (M^2 - \alpha^2)(p'_m - p')p' = 0 \quad (1)$$

where M is the critical state value of the stress ratio η ($\eta = q/p'$) and p'_m and α define the size and the inclination of the yield curve (Fig. 1). For α equal to zero, Eq. (1) reduces to the yield curve of the Modified Cam Clay model (Roscoe & Burland 1968). The elastic behaviour is assumed to be isotropic as in the Modified Cam Clay model (MCC), and likewise, an associated flow rule is assumed.

The first hardening law describes changes in the size of the yield curve and is similar to that of MCC. The second hardening rule (Eq. 2) predicts the change in the inclination of the yield curve produced by plastic straining (Näätänen et al. 1999, Koskinen 2001, McGinty et al. 2001). In triaxial stress space, for a case where the main axes of anisotropy stay fixed, the rotational hardening law can be expressed as:

$$d\alpha = \mu \left(\left[\frac{3\eta}{4} - \alpha \right] \left\langle d\epsilon_v^p \right\rangle + \beta \left[\frac{\eta}{3} - \alpha \right] \left| d\epsilon_d^p \right| \right) \quad (2)$$

where $d\epsilon_d^p$ and $d\epsilon_v^p$ are the plastic shear strain increment and the plastic volumetric strain increment, respectively.

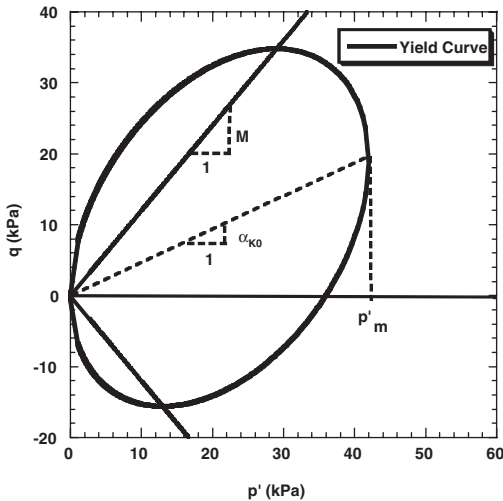


Figure 1. S-CLAY1 yield curve.

Constants μ and β control, respectively, the absolute rate at which α heads towards its current target value and the relative effectiveness of plastic shear strains and plastic volumetric strains in determining the current target value.

The model involves seven soil constants. Five conventional parameters are the same as in the MCC model and can be directly measured from standard laboratory tests. The initial state of the soil is defined by the stress state and the initial values of p'_m and α that define the initial size and inclination of the yield curve.

The two additional parameters (μ and β) relate to the rotational hardening law. Parameter β and the initial inclination of the yield curve α can be determined by simple procedures as proposed by Wheeler et al. (1999). There is no direct method for deriving the value of the parameter μ . In this paper; an attempt to highlight the effects of μ on the response envelope is investigated.

3 NUMERICAL PROGRAMME

3.1 Signs convention and numerical tool

In the following, the usual sign convention of soil mechanics (compression positive) is adopted throughout. In line with Terzaghi's principle of effective stress, all stresses are effective stresses. Also, the volumetric strains and shear strains are expressed in simplified strain space of a triaxial test and the main axis of anisotropy fixed.

For numerical simulation a single Gauss-Point program is used for all the presented results and

Table 1. Input parameters for S-CLAY1.

κ	ν'	λ	M	μ	β	α_{k0}	p'_m (kPa)
0.035	0.3	0.55	1.2	20	0.76	0.45	42.0

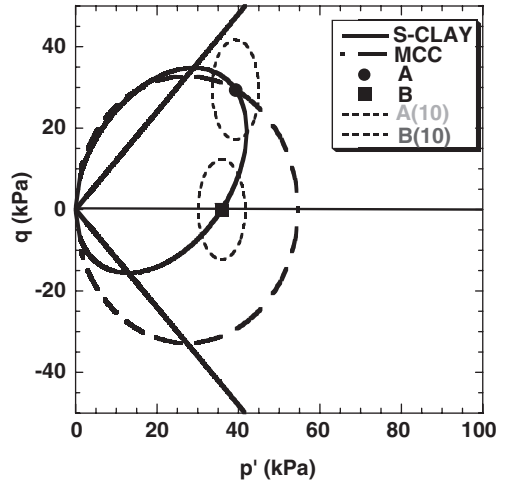


Figure 2. S-CLAY1 and MCC yield curves – initial state of stress explored.

calculations with MCC model are performed with the subroutine dedicated to S-CLAY1 by cancelling the effect of anisotropy by setting the initial value of α and parameter μ to zero.

3.2 Soil parameters

The soil parameters used in this study are typical of Scandinavian soft clays and have been derived based on a comprehensive experimental study, including drained and undrained triaxial tests and oedometer tests, done on samples of POKO clay taken near the town of Porvoo in southern Finland. The tests were carried out at Helsinki University of Technology and the full description can be found in Koskinen (2001).

For S-CLAY1 model, the input parameters are as shown on Table 1, where κ and λ are the slopes of swelling/recompression line and the normal compression line, respectively and ν' is Poisson's ratio. For Modified Cam-Clay model, the values for the standard soil parameters are the same as in Table 1. However, the parameter p'_0 defining the size of the initial yield curve for the MCC model is chosen so that the yield curve coincides with the S-CLAY1 yield curve for the stress path $\eta = \eta_{k0}$. Hence, the initial value of p'_0 is taken equal to 54.6 kPa (Fig. 2).

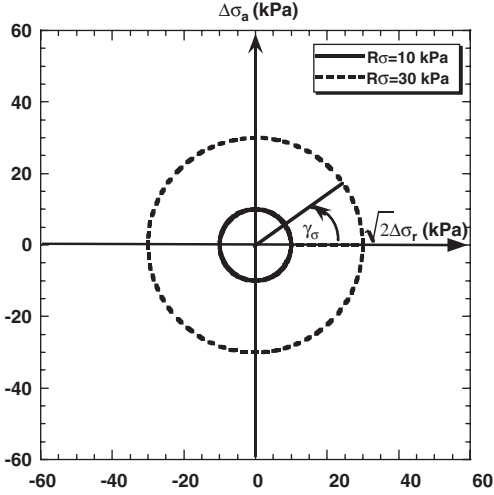


Figure 3. Stress probes performed.

3.3 Stress probing and initial state of stress

Each stress probe from an initial state $(\sigma_{a,0}, \sigma_{r,0})$ is described by the following parametric equations:

$$\begin{aligned} \Delta\sigma_a &= R_\sigma \sin(\gamma_\sigma) \\ \Delta\sigma_r &= \frac{1}{\sqrt{2}} R_\sigma \cos(\gamma_\sigma) \end{aligned} \quad (3)$$

where R_σ denotes the norm of the stress increment, and γ_σ represents its direction in the Rendulic plane of stress increments $(\Delta\sigma_a, \sqrt{2}\Delta\sigma_r)$; Fig. 3). For the presented simulations, two initial states of stress were adopted: anisotropic initial state of stress on the yield curve of both models for $\eta = \eta_{k0}$ (point A on Fig. 2) and an isotropic initial state of stress on the yield curve of S-CLAY1 model (point B on Fig. 2). The magnitudes of stress increments explored are 10 kPa for initial state of stress A and B (denoted A(10) and B(10), see Fig. 2) and 30 kPa for initial state of stress B (denoted B(30)).

4 NUMERICAL SIMULATIONS

4.1 Response envelopes of linear elastic model

The Gauss-Point program was first evaluated for a linear elastic material according to Hook's law for different values of Young's modulus with values of Poisson's ratio between 0.0 and 0.5. The response envelopes to a stress increment of 10 kPa in terms of axial strains versus radial strains and shear strains versus volumetric strains are shown respectively on

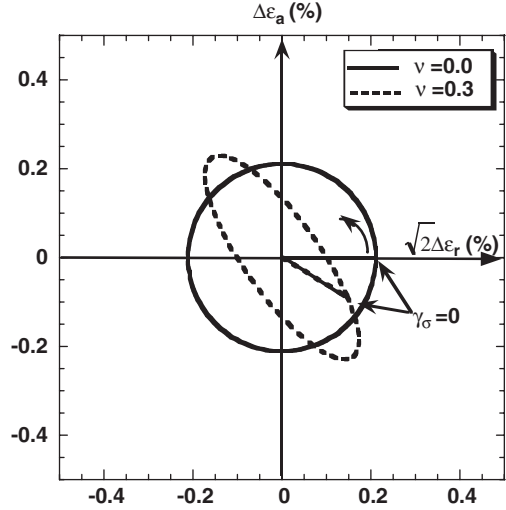


Figure 4. Response envelopes of linear elastic model (ϵ_a - ϵ_r).

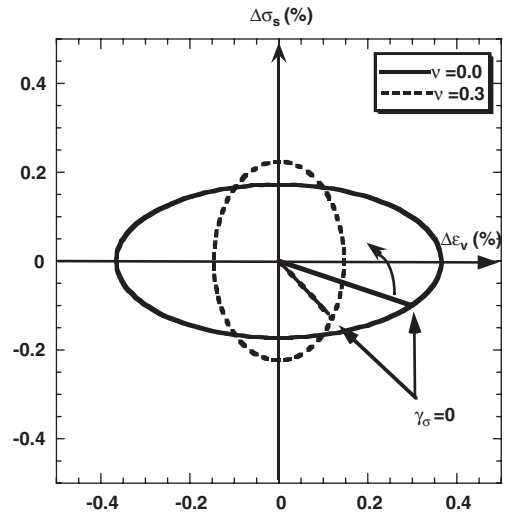


Figure 5. Response envelopes of linear elastic model (ϵ_s - ϵ_v).

Figure 4 and Figure 5 for ν' values of 0.0 and 0.3 and Young's modulus value of 4737 kPa.

As expected for $\nu' = 0$, a circle is obtained in the axial strains versus radial strains diagram and for increasing value of the Poisson's ratio inclined ellipse is obtained until it collapse to a straight line for $\nu' = 0.5$ (not represented on this Figure). The aspect ratio of the ellipse is controlled by the value of Poisson's ratio, whereas the size of the ellipse is controlled by R_σ/E and the Poisson's ratio.

The same stress-probes were performed using the elastic relationships in Modified Cam-Clay model

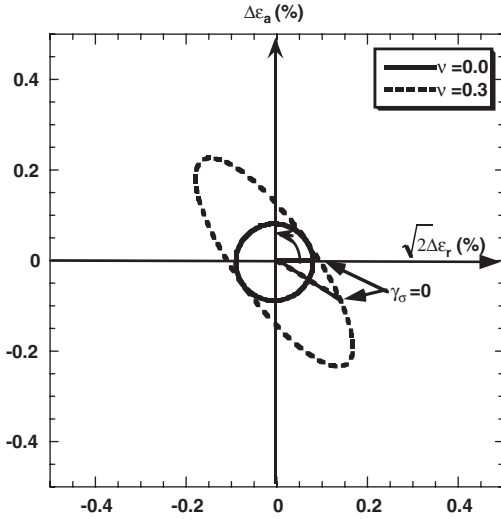


Figure 6. Response envelopes of elastic isotropic model (ϵ_a - ϵ_r).

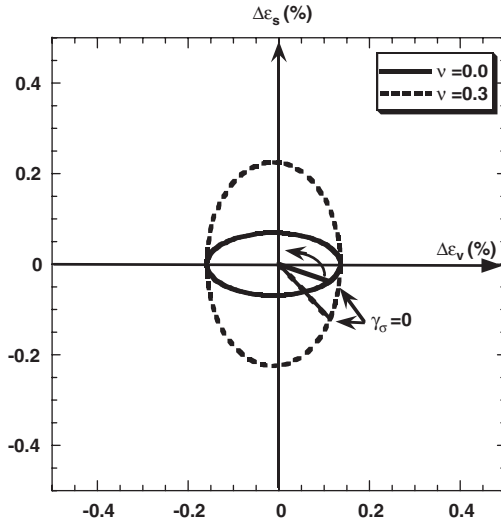


Figure 7. Response envelopes of elastic isotropic model (ϵ_s - ϵ_v).

assuming a constant Poisson's ratio. For illustration, the response envelopes for two different values of Poisson's ratio are shown on Figures 6 and 7 (for κ values as defined in Table 1). As the bulk modulus depends on the κ value, the void ratio and the mean effective stress, the response envelopes coincide for purely volumetric strain paths. The Poisson's ratio affects mainly the ratio of the response envelopes as shown in Figure 7.

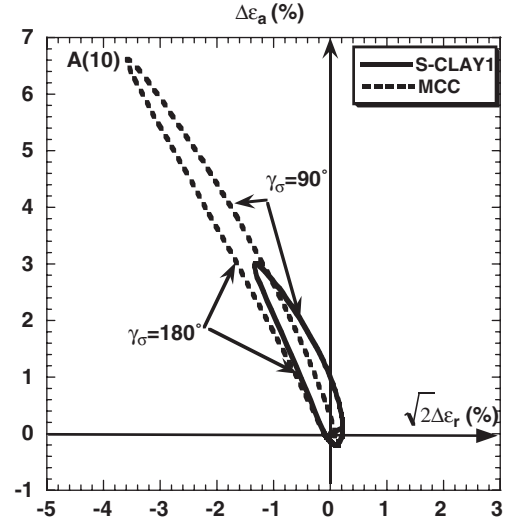


Figure 8. Response envelopes of MCC and S-CLAY1 - stress probe A(10) - (ϵ_a - ϵ_r).

4.2 Response envelopes of MCC and S-CLAY1

4.2.1 Stress probe A(10)

To investigate the differences in the incremental response of MCC and S-CLAY1, the stress probing for the initial state of stress and increment size denoted A(10) is performed. In terms of axial strains versus radial strains, similar qualitative results with both models are obtained (Fig. 8) where the softest response is associated to those paths which are characterised by a large deviatoric component. This predicted behaviour is in agreement with tests results performed on silty clay coming from southern France (Tamagnini et al. 2005).

Furthermore, the incremental response remains continuous as the stress increment rotates and convex except a minor irregularity observed in the envelopes for both models close to neutral loading in extension. The material response is softer when the probe points in the direction of continued loading, and stiffer upon unloading. In the purely elastic region, as expected, identical response is obtained. In terms of magnitude of strains, S-CLAY1 predicts higher axial strains than radial strains for γ_σ between 0° and about 135° and then this tendency is reversed until the elastic region is reached.

In terms of volumetric strains versus the shear strains (Fig. 9), for purely axial stress path MCC model predicts almost twice the shear strains predicted by S-CLAY1 model.

4.2.2 Stress probe B(10)

The predicted response envelopes for initial state of stress and stress increment denoted B(10) obtained

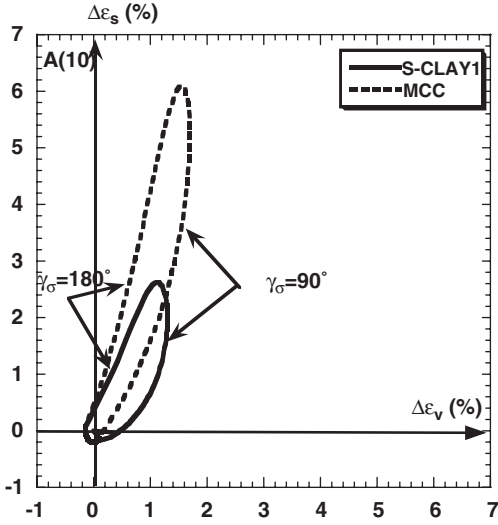


Figure 9. Response envelopes of MCC and S-CLAY1 – stress probe A(10) – (ϵ_s - ϵ_v).

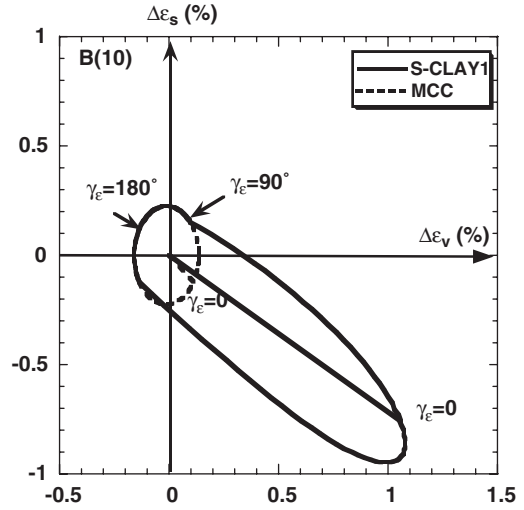


Figure 11. Response envelopes of MCC and S-CLAY1 – stress probe B(10) – (ϵ_s - ϵ_v).

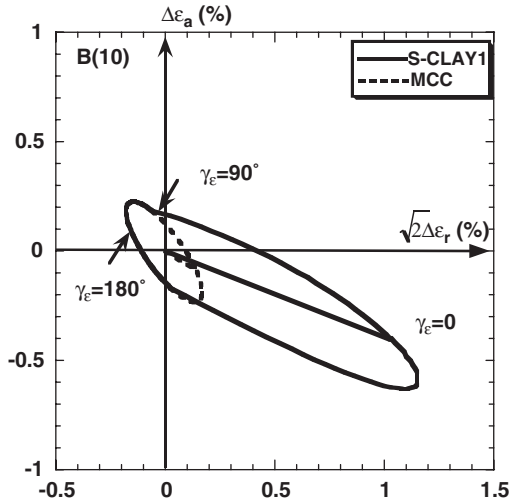


Figure 10. Response envelopes of MCC and S-CLAY1 – stress probe B(10) – (ϵ_a - ϵ_r).

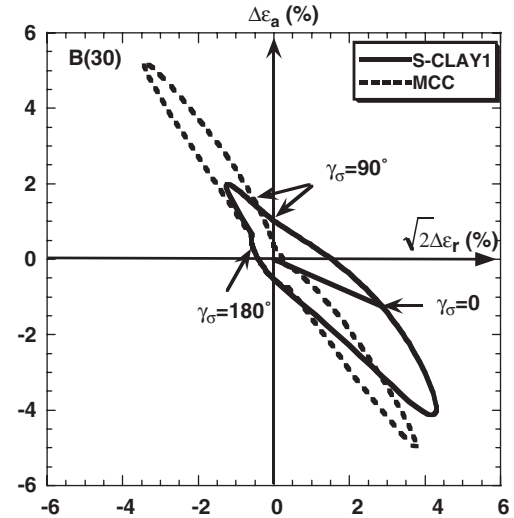


Figure 12. Response envelopes of MCC and S-CLAY1 – stress probe B(30) – (ϵ_a - ϵ_r).

using S-CLAY1 model and MCC model are shown on Figures 10 and 11. In terms of axial strains versus radial strains, as expected from Figure 2, MCC model response is basically elastic (no yielding occurs for stress increments $R_\gamma = 10$ kPa) and the form is similar to the results in Section 4.1.

The S-CLAY1 model predicts identical strain envelopes in the purely elastic region to the MCC model, but the results become different when yielding takes place. The elasto-plastic response of S-CLAY1

looks like an eccentric elongated ellipse. The incremental response remains continuous as the stress increment rotates.

4.2.3 Stress probe B(30)

To initiate yielding for MCC model, stress probing with initial state of stress and stress increment denoted B(30) is performed for both models. Strains envelopes obtained are shown in Figures 12 and 13, in terms of axial strains versus radial strains and shear

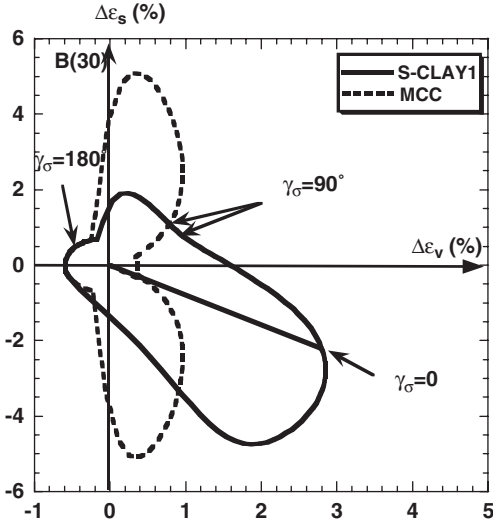


Figure 13. Response envelopes of MCC and S-CLAY1 – stress probe B(30) – (ϵ_s - ϵ_v).

strains versus volumetric strains, respectively. Due to the shape of Modified Cam-Clay model yield curve and the nature of stress probing (initiated from an isotropic stress state), the strains envelope obtained is symmetrical to the volumetric strains axis (Fig. 13).

For S-CLAY1 model, asymmetric strain envelope is obtained (Fig. 13). Again in the purely elastic region, both strains envelopes are identical.

4.3 The effect of μ value on the response envelopes of S-CLAY1 model

In order to investigate the effect of μ value on the response envelopes of S-CLAY1 model, numerical simulations for different values of μ parameter were performed for both initial states of stress A and B for $R_\sigma = 10$ kPa.

Results obtained in terms of strains envelopes for three values of μ parameter are reported on Figures 14 and 15, for initial state of stress A and initial state of stress B, respectively.

For initial state of stress A, the effect of μ value on the strain envelopes seems negligible. In the elastic region of the strain envelopes, as the inclination of the yield curve is not affected, the value of μ parameter has no influence. When plastic straining takes place, due to the small size of the stress increments, the inclination of the yield curves changes only a little.

For initial state of stress B, the initial yield curve is centred on the η_{k0} stress path. Therefore, stress probing with isotropic initial state of stress, plastic straining will induce substantial rotation of the yield curve

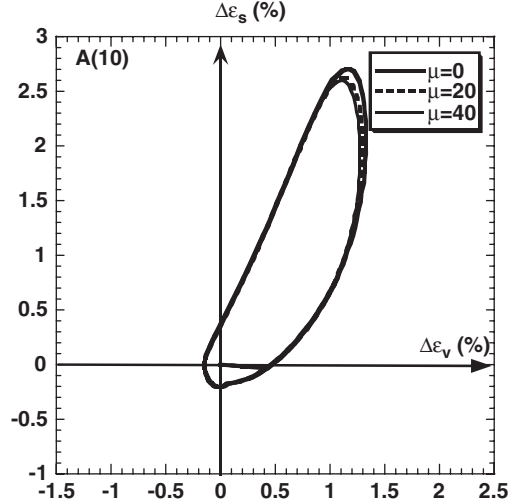


Figure 14. Effect of μ parameter on response envelopes of S-CLAY1 – stress probe A(10) – (ϵ_s - ϵ_v).

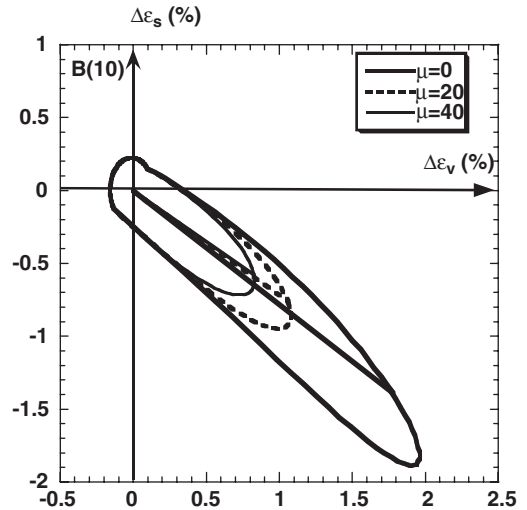


Figure 15. Effect of μ parameter on response envelopes of S-CLAY1 – stress probes B(10) – (ϵ_s - ϵ_v).

towards the isotropic axes. Therefore, a high value of μ will accelerate this rotation.

5 CONCLUSIONS

In this paper, the S-CLAY1 model, which takes into account both initial and plastic strain-induced anisotropy, was compared to isotropic elasto-plastic model MCC through investigating predicted response

envelopes. The main conclusions on the performance of the models can be drawn as follows:

- For stress probes A(10), the strain envelopes of both models are qualitatively similar. However, in terms of magnitude of strains, the MCC model predicts notably higher shear strains than S-CLAY1.
- For stress probes B(10) and B(30), which start on the isotropic axis, MCC model predicts a symmetric strain envelopes with respect to volumetric strain axis, whereas S-CLAY1 model predicts asymmetric strain response.
- In terms of the effect of μ value on the strain envelopes, the initial state of stress seems to have a major effect. The μ value has only a minor effect when the initial state of stress lies on a stress path that has the same target yield curve orientation as the initial yield curve (A(10) in Fig. 2). However, for stress probes from an isotropic initial state (B(10) in Fig. 2), the μ value has a major influence, as for any plastic straining significant yield curve occurs.

REFERENCES

- Gudehus, G. (1979). A comparison of some constitutive laws for soils under radially symmetric loading and unloading. In Wittke (ed.): *Proc. 3rd Int. Conf. Numerical Methods in Geomechanics*: Vol 4, 1309–1323. Aachen.
- Gudehus, G. & Kolymbas, D. (1979). A constitutive law of the rate type for soils. In Wittke (ed.): *Proc. 3rd Int. Conf. Numerical Methods in Geomechanics*: Vol 1, 319–329. Aachen.
- Koskinen, M. (2001). Anisotropy and destructuration of soft clays. *MSc thesis*, Helsinki University of Technology.
- McGinty, K., Karstunen, M. & Wheeler, S.J. (2001). Modelling the stress-strain behaviour of Bothkennar clay. *Proc. 3rd Int. Conf. Soft Soil Engineering, Hong Kong*, 263–268. A.A. Balkema.
- Näätänen, A., Wheeler, S.J., Karstunen, M. & Lojander, M. (1999). Experimental investigation of an anisotropic hardening model. *Proc. 2nd Int. Symposium on Pre-Failure Deformation Characteristics of Geomaterials*, Torino, 541–548. A.A. Balkema.
- Roscoe, K.H. & Burland, J.B. (1968). On the generalised stress-strain behaviour of ‘wet’ clay. *Engineering Plasticity*, 553–569. Cambridge University Press.
- Tamagnini, G., Masin, D., Costanzo, D. & Viggiani, G. (2005). An evaluation of different constitutive models to predict the directional response of a reconstituted fine grained soil. In *Proc. Int. workshop Modern trends in geomechanics, Vienna, Austria*.
- Wheeler, S.J., Näätänen, A. & Karstunen, M. (1999). Anisotropic hardening model for normally consolidated soft clay. *Proc. 7th Int. Symp. Numerical Models in Geomechanics (NUMOG)*, Graz, Austria, 33–44. A.A. Balkema.
- Wheeler, S.J., Näätänen, A., Karstunen, M. & Lojander, M. (2003). An anisotropic elasto-plastic model for soft clays. *Canadian Geotechnical Journal* 40, 403–418.

Modelling small-strain stiffness with the multilaminate framework

F. Scharinger & H.F. Schweiger

*Computational Geotechnics Group, Institute for Soil Mechanics and Foundation Engineering,
Graz University of Technology, Graz, Austria*

G.N. Pande

University of Wales Swansea, Swansea, UK

ABSTRACT: Based on the multilaminate framework, a first step towards modelling high elastic stiffness at small-strain level is presented. The basic feature of multilaminate models, namely the consideration of various integration planes to formulate the stress-strain relationship, is used in combination with a micromechanical approach for the determination of the elastic stiffness matrix. The employed extension of the model also includes the degradation of the elastic stiffness according to the material's strain history. In this paper only a non-linear elastic formulation for the micromechanical contact model is shown. The consequences and possibilities of improvement will be discussed on the basis of numerically simulated triaxial tests.

1 INTRODUCTION

The last decades have been characterised by a remarkable development in laboratory testing techniques on geomaterials. The use of more accurate sensors and local strain measurements allows a reliable and accurate investigation of the stress-strain behaviour in a wide range of strains, from very small ($<0.001\%$) to very large up to failure. But also the possibilities in soil modelling and the variety of different constitutive equations increased in the same time period and a number of sophisticated constitutive models have been developed to solve geotechnical problems.

Shear moduli of most soils decrease monotonically with the accumulation of strain. The maximum stiffness is observed at very small strains (e.g. strains $<10^{-6}$) which are associated with linear elastic material behaviour. It has been recognised that the stiffness at small strains should not be neglected in numerical calculations of boundary value problems.

2 MULTILAMINATE MODEL FOR SOIL

2.1 Framework

The Multilaminate Model for Soil (MMS), employed for this study was developed and implemented into the finite element code Plaxis (Brinkgreve, 2002) by Wiltafsky (2003) and extended by Scharinger & Schweiger (2005). The model offers the possibility to

incorporate shear and volumetric hardening on 21, 33 or 37 independently acting integration planes per hemisphere. It is one of the most important features of this model that the development of the yield surface on each sampling plane is based on the evolution of plastic strains on the respective plane. Only under hydrostatic loading the same preconsolidation pressures are obtained on each integration plane. When any deviatoric stress is applied, the state variables related to the state of the yield surface vary over the planes. An initially isotropic soil becomes anisotropic after loading when analysed within the multilaminate framework, thus it captures plastic flow induced anisotropy intrinsically (Pande & Sharma, 1982). In this paper however plastic deformation will not be addressed.

2.2 Local stress state on integration planes

In a constitutive model based on the multilaminate framework, all mathematical formulations are described for each integration plane explicitly and it is assumed that the same characterisation holds for all planes. According to the integration rule used, which defines the number of integration planes, the local components of the effective stress state σ'_i have to be computed from the global effective stress vector σ' .

$$\sigma'_i = \begin{bmatrix} \sigma'_n \\ \tau_1 \\ \tau_2 \end{bmatrix} = (T_i)^T \cdot \sigma' \quad (1)$$

T_i represents the transformation matrix for the respective integration plane i , which is a function of the direction cosines of the unit normal to the i -th integration plane.

3 DETERMINATION OF ELASTIC STIFFNESS AT SMALL STRAIN LEVEL

3.1 Concept

A micromechanics approach is implemented in the multilaminate model to describe the deformation behaviour at small strain levels. More precisely, the elastic stiffness of each plane is obtained from a micromechanics based contact model applied at each particle contact.

An assembly of equally sized spheres defined by the average radius r_{grain} of the grains, the shear modulus G_{grain} , Poisson's ratio ν_{grain} and internal friction angle φ_{grain} of the grain material is assumed to govern the contact behaviour of granular materials at small strains. In each contact between two spherical grains, the normal and the tangential component of the elastic stiffness are formulated with respect to above parameters and the contact forces. The number of contacts is dependent on the density and size of the particles. In a first step the non-linear elastic Hertz-Mindlin contact model is introduced to simulate the interaction between two spheres. For an assumed grain packing the compliance matrix for each integration plane can be related to the components of the stiffness at each particle contact (Pande, 1987). Employing the same integration rule as employed for the accumulation of plastic strains, the global elastic stiffness matrix can be obtained.

3.2 Number of contacts

According to Chang, Misra & Sundaram (1990) the number of contacts N per unit volume V for a packing of equal-sized spheres can be calculated from the void ratio e , the co-ordination number and the particle size as

$$\frac{N}{V} = \frac{3 \cdot C_n}{8 \cdot \pi \cdot r_{\text{grain}}^3 \cdot (1 + e)} \quad (2)$$

The co-ordination number C_n represents the average number of contact points per particle and r_{grain} denotes the radius of the spherical grains.

The relationship between the void ratio and the co-ordination number has been studied for different types of material by various authors. The interrelation of these two parameters was discussed by Graton & Fraser (1935) for different systematic assemblies of spheres. Table 1 summarises the results for various packings of grains with void ratio and co-ordination number.

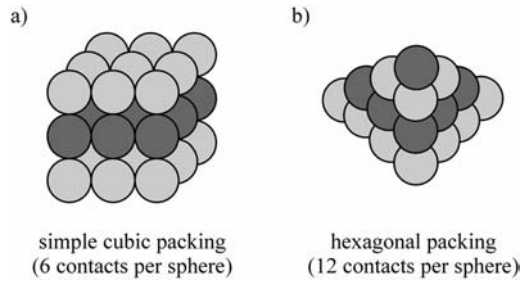


Figure 1. Different packings of regular assembled spherical grains.

Table 1. Systematic arrangements of equal sized spheres.

Type	Void ratio	Co-ordination number
Simple cubic	0.910	6
Ortho-rhombic	0.654	8
Tetragonal	0.433	10
Tricuboidal or hexagonal	0.350	12

Smith, Foote & Busang (1929) investigated different assemblies of lead shot and found a relationship between the porosity and the co-ordination number on the basis of the assumption that an irregular and disordered packing of spherical shots can be seen as a mixture of two systematic assemblies. Field (1963) studied random assemblies of rounded stones characterised by different grain sizes, different gradings and different void ratios and Oda (1977) made several investigations on various arrangements of glass balls. Very similar experiments with rock fill material were performed by Marsal (1973) to determine another relationship among grain size, density and contact points per particle. Yanagisawa (1983) also presented experimental data on glass balls and gravel with two kinds of particle shape.

For the application within the MMS one of the more recent approaches presented in literature was chosen. Chang et al. (1990) approximated the co-ordination number for the range of $0.38 \leq e \leq 0.87$ by

$$C_n = 13.28 - 8 \cdot e \quad (3)$$

Figure 2 shows the experimental results for different types of gravel, the results for the four systematic assemblies and the approximation characterised by Equation 3.

Substituting Equation 3 into Equation 2, the number of contacts per volume N/V can be written as a

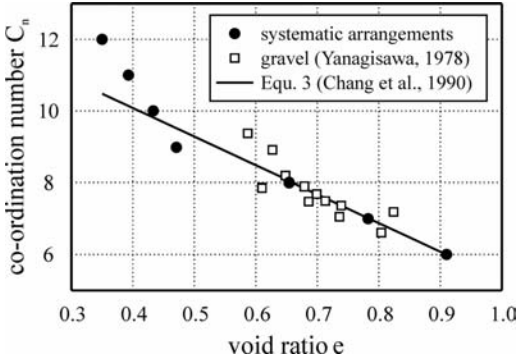


Figure 2. Implemented relationship between C_n and e compared with experimental results for gravel.

function of the average grain radius r_{grain} and the void ratio e .

$$\frac{N}{V} = \frac{4.98 - 3 \cdot e}{r_{\text{grain}}^3 \cdot \pi \cdot (1 + e)} \quad (4)$$

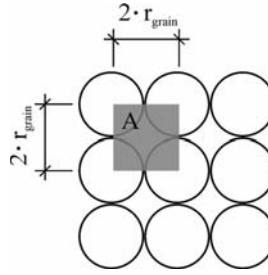
3.3 Contact force

As the elastic stiffness at small strain level is formulated as a function of the contact force in each single contact, the local stress state defined by σ_n and τ has to be converted to contact level for each integration plane. Yimsiri & Soga (2000) proposed Equation 5 to calculate the contact force between spherical grains from the grain radius r_{grain} , the number of contacts per volume N/V and the isotropic confining pressure σ_c . In their study the global stress state was directly transformed to contact level while multilaminar type of models involve the integration plane level as an intermediate step to derive the contact force. Therefore, the normal component of the stress on each integration plane can be directly substituted into Equation 5 to obtain a mathematical relationship for the normal contact force f_n between the grains and the normal stress σ_n calculated for each individual integration plane.

$$f_n = \frac{3 \cdot V}{2 \cdot r_{\text{grain}} \cdot N} \cdot \sigma_c \quad (5)$$

Together with Equation 4, the dependency of the normal contact force f_n on the grain radius r_{grain} , the void ratio e and the normal force σ_n can be formulated as following.

$$f_n = \frac{r_{\text{grain}}^2 \cdot \pi \cdot (1 + e)}{3.32 - 2 \cdot e} \cdot \sigma_n = \frac{4 \cdot r_{\text{grain}}^2}{\zeta_1} \cdot \sigma_n \quad (6)$$



$$\frac{N}{A} = \frac{1}{4 \cdot r_{\text{grain}}^2}$$

Figure 3. Number of contacts per unit area (N/A) for the least efficient close packing form, simple cubic packing.

To relate the contact force between the soil particles to the value obtained for the loosest close packing, a factor, ζ_1 , can be introduced as a ratio between the number of contacts for the actual grain assembly and the simple cubic arrangement with a co-ordination number of 6.

A comparison of the result from Equation 6 for the cubic packing and the analytical result gives exactly the same contact force (Equ. 7). The analytical solution is obtained from the maximal number of contacts per unit area, when the contacts in the presumed grain assembly are counted along one plane (Fig. 3).

$$f_n = \frac{r_{\text{grain}}^2 \cdot \pi \cdot (1 + 0.91)}{3.32 - 2 \cdot 0.91} \cdot \sigma_n = 4 \cdot r_{\text{grain}}^2 \cdot \sigma_n \quad (7)$$

The tangential contact force can now be written as:

$$f_t = \frac{r_{\text{grain}}^2 \cdot \pi \cdot (1 + e)}{3.32 - 2 \cdot e} \cdot \tau = \frac{4 \cdot r_{\text{grain}}^2}{\zeta_1} \cdot \tau \quad (8)$$

3.4 Local stiffness matrix

Using the inter-particle contact forces in the contact model described later, the components K_n and K_t of the local stiffness matrix K_i^e for each integration plane can be determined from the stiffness for each contact point and the number of contacts defined by the radius of the grains r_{grain} and factor ζ_1 .

$$K_i^e = \frac{f_i}{4 \cdot r_{\text{grain}}^2} \cdot \begin{bmatrix} K_n & 0 & 0 \\ 0 & K_t & 0 \\ 0 & 0 & K_t \end{bmatrix} \quad (9)$$

Before the transformation to global level, the compliance matrix for a set of planes with the same direction containing the normal and tangential compliance for each integration plane has to be formulated according

to Equation 10 by introducing the thickness of one layer of soil particles represented by the grain diameter (Pande, 1987).

$$C_i^e = \begin{bmatrix} C_n & 0 & 0 \\ 0 & C_t & 0 \\ 0 & 0 & C_t \end{bmatrix} = \frac{1}{2 \cdot r_{grain}} \cdot (K_i^e)^{-1} \quad (10)$$

3.5 Transformation of stiffness matrix

The transformation of the compliance matrix from integration plane level to global level can be performed by multiplication with the transformation matrix T_i and its transposed (Gerrard & Pande, 1985).

$$T_i = \begin{bmatrix} n_1^2 & n_1 \cdot s_1 & n_1 \cdot t_1 \\ n_2^2 & n_2 \cdot s_2 & n_2 \cdot t_2 \\ n_3^2 & n_3 \cdot s_3 & n_3 \cdot t_3 \\ 2 \cdot n_1 \cdot n_2 & n_1 \cdot s_2 + n_2 \cdot s_1 & n_2 \cdot t_1 + n_1 \cdot t_2 \\ 2 \cdot n_2 \cdot n_3 & n_3 \cdot s_2 + n_2 \cdot s_3 & n_2 \cdot t_3 + n_3 \cdot t_2 \\ 2 \cdot n_1 \cdot n_3 & n_3 \cdot s_1 + n_1 \cdot s_3 & n_3 \cdot t_1 + n_1 \cdot t_3 \end{bmatrix} \quad (11)$$

T_i can be formulated with respect to the direction cosines of the unit normal to the considered integration plane, where $n = \{n_1, n_2, n_3\}$ represents a unit vector in perpendicular direction and $s = \{s_1, s_2, s_3\}$ and $t = \{t_1, t_2, t_3\}$ denote unit vectors parallel to the integration plane.

$$D^e = (C^e)^{-1} = \left(\sum_{i=1}^{cp} T_i \cdot C_i^e \cdot T_i^T \cdot W_i \right)^{-1} \quad (12)$$

Finally, weighted summation over all integration planes, according to the employed integration rule, results in the complete elastic stiffness matrix of the investigated material.

3.6 Global stiffness matrix

The global stiffness matrix obtained from the equations presented before, accounts for stress induced anisotropy of the material. As the compliances on the integration planes depend on the local stress state σ_n and τ within the proposed contact model, only isotropic stress conditions result in an isotropic stiffness matrix on global level. When any deviatoric stress is applied, the local compliance matrices will vary over the different integration planes and the global result can be illustrated in terms of the generalised Hook's law depending on nine independent parameters.

$$C^e = \begin{bmatrix} \frac{1}{E_{xx}} & -\frac{\nu_{yx}}{E_{yy}} & -\frac{\nu_{zx}}{E_{zz}} & 0 & 0 & 0 \\ -\frac{\nu_{xy}}{E_{xx}} & \frac{1}{E_{yy}} & -\frac{\nu_{zy}}{E_{zz}} & 0 & 0 & 0 \\ -\frac{\nu_{xz}}{E_{xx}} & -\frac{\nu_{yz}}{E_{yy}} & \frac{1}{E_{zz}} & 0 & 0 & 0 \\ 0 & 0 & 0 & \frac{1}{G_{xy}} & 0 & 0 \\ 0 & 0 & 0 & 0 & \frac{1}{G_{yz}} & 0 \\ 0 & 0 & 0 & 0 & 0 & \frac{1}{G_{zx}} \end{bmatrix} \quad (13)$$

Here E_{xx} , E_{yy} and E_{zz} are Young's moduli in the directions of the x, y and z axes, G_{xy} , G_{yz} and G_{zx} are the shear moduli for planes parallel to the co-ordinate planes and ν_{xy} , ν_{xz} , ν_{yx} , ν_{yz} , ν_{zx} and ν_{zy} are Poisson's ratios. From the symmetry of the resulting compliance matrix, it follows that $\nu_{xy}/E_{xx} = \nu_{yx}/E_{yy}$, $\nu_{xz}/E_{xx} = \nu_{zx}/E_{zz}$ and $\nu_{yz}/E_{yy} = \nu_{zy}/E_{zz}$.

4 MICROMECHANICS BASED CONTACT MODEL

The non-linear elastic Hertz-Mindlin contact model can be employed to characterize the contact between elastic perfectly rounded and smooth-surface spheres. In such cases where the Hertzian theory is applicable, it predicts a plane, circular contact surface of radius a_0 .

$$a_0 = \left[\frac{3 \cdot (1 - \nu_{grain})}{8 \cdot G_{grain}} \cdot r_{grain} \cdot f_n \right]^{1/3} \quad (14)$$

Points outside the deformed zone move together by two times the distance w_0 (Equ. 15) during the deformation of two spheres, which can be expressed in terms of size and stiffness of the spherical particle and the applied force. Figure 4 shows the deformation w_0 and the radius of the contact zone a_0 of two grains due to the applied normal force f_n .

$$w_0 = 2 \cdot \left[\frac{3 \cdot f_n \cdot (1 - \nu_{grain})}{8 \cdot G_{grain} \cdot r_{grain}^{1/2}} \right]^{2/3} = \frac{2 \cdot a_0^2}{r_{grain}} \quad (15)$$

Hence the contact stiffness in perpendicular direction to the contact surface follows from Equation 15 and Equation 16 (Mindlin & Deresiewicz, 1953).

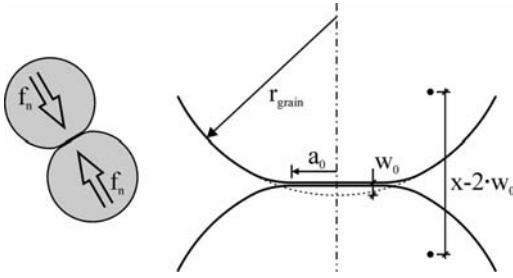


Figure 4. Deformation of two grains in contact according to the classical Hertzian contact theory.

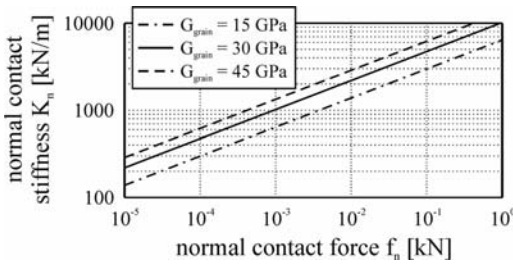


Figure 5. Normal stiffness K_n vs. normal force f_n in one contact.

Table 2. Input parameters for medium sand.

Parameter	Value	Unit
G_{grain}	15/30/45	[GPa]
ν_{grain}	0.2	[-]
r_{grain}	0.25	[mm]
φ_{grain}	35	[°]

$$K_n = \left(2 \frac{\partial w_0}{\partial f_n} \right)^{-1} = \left[\frac{3 \cdot r_{\text{grain}} \cdot G_{\text{grain}}^2}{(1 - \nu_{\text{grain}})^2} \cdot f_n \right]^{1/3} \quad (16)$$

The relationship between K_n and f_n (Equ. 16) is shown in Figure 5 for the set of parameters listed in Table 2 which correspond to average values of medium sand. Furthermore, the influence of the grain stiffness G_{grain} on the contact stiffness K_n is shown in Figure 5.

The tangential component of the contact stiffness formulated by Bowden & Tabor (1964) and Johnson (1985) is

$$K_t = \frac{2 \cdot (1 - \nu_{\text{grain}})}{(2 - \nu_{\text{grain}})} \cdot \left(1 - \frac{f_t}{f_n \cdot \tan \varphi_{\text{grain}}} \right)^{1/3} \cdot K_n \quad (17)$$

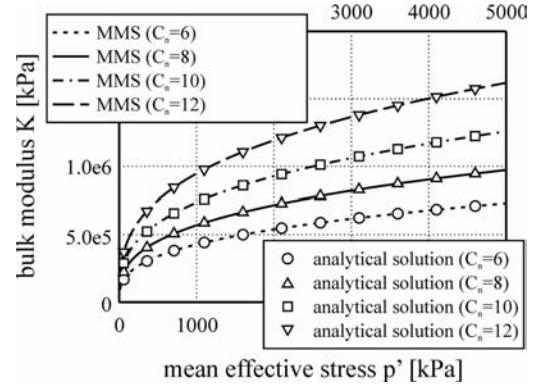


Figure 6. Bulk modulus K on global level vs. mean effective stress p' from isotropic compression.

In general, there is no explicit description for K_n and K_t obtained from the Hertz-Mindlin contact model since they are functions of f_n and f_t , which vary with the local stress state on each particular integration plane. On the basis of an isotropic fabric assembly under isotropic stress conditions on global level, a comparison of different results obtained with the Hertz-Mindlin contact model is presented in Figure 6. Independent of the employed approach an isotropic stress state on global level results in normal contact forces of the same magnitude and the tangential component equals to zero in all contacts between soil grains. The bulk modulus K plotted over the mean effective stress p' in Figure 6 is defined as the ratio between the hydrostatic pressure and the volumetric strain.

$$K = \frac{E}{3 \cdot (1 - 2 \cdot \nu)} = \frac{2 \cdot G \cdot (1 + \nu)}{3 \cdot (1 - 2 \cdot \nu)} \quad (18)$$

For the four isotropic compression tests on the same material with varying co-ordination number/void ratio (Fig. 6), the results from the multilaminar model and the closed-form solution (Equ. 19) proposed by Yimsiri & Soga (2000) show the same results.

$$G_{\text{max}} = \frac{10 \cdot r^2}{(10 - 7 \cdot \nu)} \cdot \left[\frac{4 \cdot G^2 \cdot (1 - \nu)}{3} \cdot \left(\frac{N}{V} \right)^2 \right]^{1/3} \cdot \sigma_c^{1/3} \quad (19)$$

In Equation 19, r , G and ν represent the radius, shear modulus and Poisson's ratio of the particles.

The exponent, which mainly influences the stress dependency of the stiffness, is a constant value of $1/3$ when the Hertz-Mindlin contact model is applied but variation with the grain size is observed in most experimental investigations. Except for this difference, the

described approach performs reasonably well. Reasons for this deviation are believed to be associated with the ideal contact conditions assumed for the Hertz-Mindlin contact model. Working with real soil materials, the requirement of perfectly rounded and smooth-surface particles will not be satisfied and therefore an extended contact model to account for the roughness of the sphere surface has to be introduced to obtain more realistic results.

5 DEGRADATION OF STIFFNESS

Numerous stiffness degradation curves from laboratory tests, describing the material behaviour at small-strain level during shearing can be found in literature. Plotting the shear modulus against the shear strains (logarithmic scale) results in a S-shaped curve, which can be simulated by various functions (Jardine 1986, Santos & Correia 2001). Soga, Nakagawa & Mitchell (1995) presented test results on different materials and gave an empirical expression (Equ. 20) to find a satisfactory stiffness degradation curve with a small number of additional parameters.

$$\frac{K_n}{K_{n,max}} = \frac{1}{1 + a_{deg} \cdot \gamma_i^{b_{deg}}} \quad (20)$$

a_{deg} and b_{deg} are material constants that control the shape of the normalised degradation curve. As a_{deg} decreases, the strain level at which the stiffness begins to degrade increases while the normalised degradation curve gets less steep when b_{deg} decreases.

Within the Multilaminate Model for Soil employing the Hertz-Mindlin contact model, the reduction of stiffness is governed by the change of the accumulated shear strain γ_i on each contact plane. Particularly, the contact stiffness K_n and K_t decay during shearing and influence the global stiffness degradation curve plotted in Figure 7.

$$\frac{K_n}{K_{n,max}} = \frac{1}{1 + a_{deg} \cdot \gamma_i^{b_{deg}}} \quad (21)$$

Hence, the two parameters, a_{deg} and b_{deg} , affect the stiffness degradation curve in the same way as proposed by Soga et al. (1995) but their magnitude changes if used on integration plane level.

6 NUMERICAL SIMULATIONS OF ELEMENT TESTS

In this section, numerical simulations of drained triaxial compression tests with isotropic initial conditions

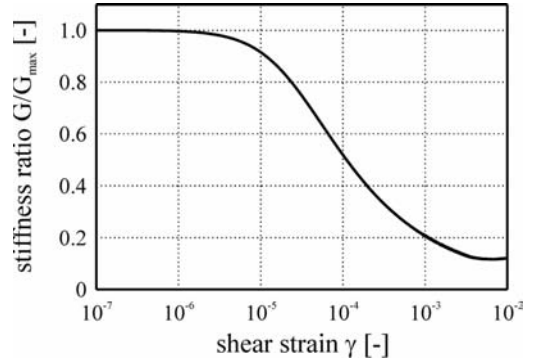


Figure 7. Typical plot of the global stiffness degradation at small-strain level.

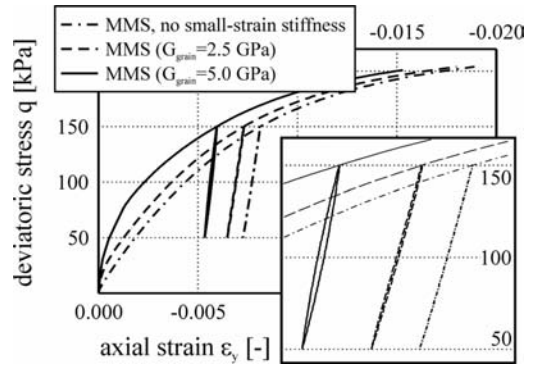


Figure 8. Stress-strain curves from triaxial compression tests.

are discussed. To analyse these element tests with different parameter combinations, the MMS with all its extensions was implemented into a simple integration-point program, whereas the programming structure of the model allows a direct combination with the finite element code Plaxis V8 via the user-defined soil model interface.

Figure 8 shows a comparison of results obtained from simulations with the Hertz-Mindlin contact model and different values for G_{grain} . Additionally, the result from an analysis with the basic version of the MMS, where no approach for the consideration of small-strain stiffness effects is implemented, is depicted in Figure 8. Due to the pronounced differences of the stiffness at small-strain level, the stress-strain curves in Figure 8 show distinct variations in this range. Particularly at the beginning of the loading phase and the unloading and reloading paths, areas where the stiffness is close to its maximum, the effects of the new approach can be clearly seen.

As the use of common values for all input parameters leads to an overestimation of the maximum stiffness obtained from the Hertz-Mindlin contact model, the calculations presented above, were performed with reduced values of the contact stiffness to attain more reliable results. Due to the assumptions made for the application of the used micromechanics model, the result represents an upper limit of the stiffness at small-strains. Only a modification of the contact model could improve the performance in this strain range.

7 CONCLUSION

As the required conditions for the application of the Hertz-Mindlin contact model will not apply for natural soil materials, the comparison of the numerical simulations with test results is limited. The stress dependency of the small-strain modulus observed in laboratory cannot be simulated with the presented contact model accurately and also the decay of the stiffness with accumulation of shear strains has to be described with a simplified approach. Nevertheless, the successful implementation of a micromechanics model into the multilaminate framework is presented in this study while the qualities of the contact model will be extended in future. The consideration of rough-surface grains will introduce various possibilities to improve the pressure dependency and degradation behaviour of the small-strain modulus obtained with the Multilaminate Model for Soil.

REFERENCES

- Bowden, F.P. & Tabor, D. 1964. *The friction and lubrication of solids*, Part II. Oxford: Clarendon Press.
- Brinkgreve, R.B.J. 2002. *Plaxis, Finite element code for soil and rock analyses, users manual*. Rotterdam: Balkema.
- Chang, C.S., Misra, A. & Sundaram, S.S. 1990. micromechanical modelling of cemented sands under low amplitude oscillations. *Geotechnique* 40(2): 251–263.
- Field, W.G. 1963. Towards the statistical definition of a granular mass. *Proc. 4th A. and N.Z. Conference on Soil Mech.*: 143–148.
- Gerrard, C.M. & Pande, G.N. 1985. Numerical modelling of reinforced jointed rock masses, I. Theory. *Computers and Geotechnics* 1: 293–318.
- Graton, L.C. & Fraser, H.J. 1935. Systematic packing of spheres with particular relation to porosity and permeability. *J. Geology* 43:785–909.
- Jardine, R.J., Potts, D.M., Furie, A.B. & Burland, J.B. 1986. Studies of the influence of non-linear stress-strain characteristics in soil-structure interaction. *Geotechnique* 36(3): 377–396.
- Johnson, K.L. 1985. *Contact Mechanics*. Cambridge University Press.
- Marsal, R.J. 1973. Mechanical properties of rockfill. In Hirschfeld, R.C. & Poulos, S.J. (eds), *Embankment-dam engineering, Casagrande Volume*: 109–200. New York: John Wiley & Sons.
- Mindlin, R.D. & Deresiewicz, H. 1953. Elastic spheres in contact under varying oblique forces. *Journal of Applied Mechanics* 20(3): 327–344.
- Oda, M. 1977. Co-ordination number and its relation to shear strength of granular material. *Soils and Foundations* 17(2): 29–42.
- Pande, G.N. 1987. Influence of grain shape and size on the behaviour of granular materials. In G.N. Pande & J. Middleton (eds), *Numerical Methods in Engineering: Theory and Applications, Proc. 2nd Int. Conference, Swansea, UK, 6–10 July 1987*: C26/1. Dordrecht: Martinus Nijhoff Publishers.
- Pande, G.N. & Sharma, K.G. 1983. Multilaminate model of clays – a numerical evaluation of the influence of rotation of principal stress axes. *Int. J. Numer. Anal. Meth. Geomech.* 7(4): 397–418.
- Santos, J.A. & Correia, A.G. 2001. Reference threshold shear strain of soil. Its application to obtain a unique strain-dependent shear modulus curve for soil. In Publications Committee of the XV ICSMGE (eds), *International Society of Soil Mechanics and Foundation Engineering, Proc. 15th Int. Conference, Istanbul, Turkey, 27–31 Aug. 2001*: 267–270. Lisse: Balkema.
- Scharinger, F. & Schweiger, H.F. 2005. Undrained response of a double hardening multilaminate model for soils. In G. Barla & M. Barla (eds), *International Association of Computer Methods and Advances in Geomechanics; Proc. 11th Int. Conference, Turin, Italy, 19–24 June 2005*: 505–512. Bologna: Patron Editore.
- Smith, W.O., Foote, P.D. & Busang, P.F. 1929. Packing of homogeneous spheres. *Physical Review* 34: 1271–1274.
- Wiltafsky, C. 2003. A Multilaminate model for normally consolidated clay. *Gruppe Geotechnik Graz*, Heft 18, Graz University of Technology.
- Yanagisawa, E. 1983. Influence of void ratio and stress condition on the dynamic shear modulus of granular media. In Mohsen Shahinpoor (ed.), *Advances in the mechanics and the flow of granular materials II*: 947–960. Houston: Gulf Publishing Company.
- Yimsiri, S. & Soga, K. 2000. Micromechanics-based stress-strain behaviour of soils at small strains. *Geotechnique* 50(5): 559–571.

An evaluation of constitutive models to predict the behaviour of fine-grained soils with different degrees of overconsolidation

V. Hájek & D. Mašín
Charles University, Prague

ABSTRACT: Incorporation of void ratio as a state variable into constitutive models allows, in principle, to use a single set of material parameters for soils with different degrees of overconsolidation. p constant experiments by Hattab and Hicher (2004) on soils with overconsolidation ratios (OCR) ranging from 1 to 50 are used for evaluation of three constitutive models of different complexity. It is demonstrated by means of a scalar error measure and stress-strain diagrams that at least two sets of parameters for different OCR intervals should be used. Further, advanced models perform significantly better than the Modified Cam clay model and a hypoplastic model for clays leads to better predictions than elasto-plastic three surface kinematic hardening model.

1 INTRODUCTION

It has been recognised since the development of critical state soil mechanics in 1960s that realistic constitutive models should consider void ratio e as a state variable. This approach, in theory, allows to use a single set of material parameters to predict the behaviour of soils with a broad range of overconsolidation ratios and thus simplifies practical application of constitutive models. As a matter of fact, however, qualitatively correct predictions of behaviour of soils with different OCR s based on a single set of material parameters do not necessarily imply satisfactory performance from the quantitative point of view. An engineer aiming to apply the constitutive model for solution of practical geotechnical problems should be aware of the range of OCR s for which a single set of material parameters may be used and design an experimental program accordingly.

In the present paper, performance of three constitutive models of different complexity is evaluated on the basis of triaxial tests by Hattab and Hicher (2004). Reconstituted kaolin clay was isotropically consolidated up to $p_{max} = 1000$ kPa and swelled to a mean effective stress $p = p_{max}/OCR$, with overconsolidation ratios ranging from 1 to 50. From this state a shear phase with constant mean stress p followed up to failure.

2 CONSTITUTIVE MODELS

Modified Cam clay model (CC) has been chosen as a reference for comparison with two advanced

constitutive models based on different mathematical backgrounds, namely the three surface kinematic hardening model (3SKH), and a hypoplastic model for clays (HC).

Modified Cam clay model (Roscoe and Burland 1968) is a basic critical state soil mechanics model. In this work a version which complies with Butterfield's (1979) compression law is used, thus the isotropic virgin compression line reads

$$\ln(1 + e) = N - \lambda^* \ln(p/p_r) \quad (1)$$

with parameters N and λ^* and a reference stress $p_r = 1$ kPa. Slope of the isotropic unloading line is controlled by the parameter κ^* , constant shear modulus G is assumed inside the yield surface and the critical state stress ratio is characterised by parameter M .

The 3SKH model (Stallebrass and Taylor 1997) is an advanced example of the kinematic hardening plasticity models for soils. The model, which may be seen as an evolution of the CC model, is characterised by two kinematic surfaces in the stress space (see Fig. 1), which determine the extent of the elastic behaviour (yield surface) and the influence of the recent stress history (history surface).

Parameters N , λ^* , κ^* and M have the same meaning as in the CC model, the shear modulus inside the elastic range G is calculated from

$$\frac{G}{p_r} = A \left(\frac{p}{p_r} \right)^n OCR^m \quad (2)$$

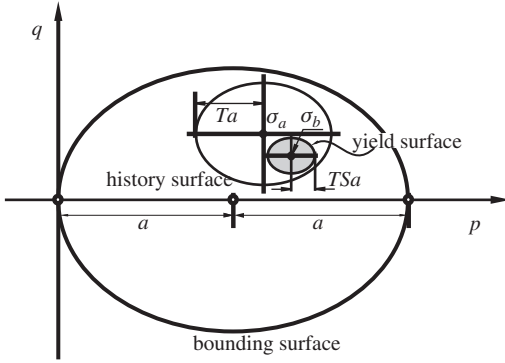


Figure 1. Characteristic surfaces of the 3SKH model, from Mašin et al. (2006).

with parameters A , n and m . Parameters T and S characterise relative sizes of kinematic surfaces (Fig. 1). The last parameter ψ controls the rate of decay of both bulk and shear moduli for states at the yield surface, inside bounding surface (Fig. 1).

A hypoplastic constitutive model for clays was proposed by Mašin (2005) and investigated further by Mašin and Herle (2005). It combines the mathematical formulation of hypoplastic models (e.g., Kolymbas 1991) with the basic principles of the CC model. The rate formulation is governed by a single nonlinear equation

$$\dot{\sigma} = f_s \mathcal{L} : \dot{\epsilon} + f_d \mathbf{N} \|\dot{\epsilon}\| \quad (3)$$

with constitutive tensors \mathbf{L} and \mathbf{N} and scalar factors f_s and f_d , no switch function is introduced to distinguish between loading and unloading and strains are not sub-divided into elastic and plastic parts as in elastoplasticity.

The model requires five parameters with a similar physical interpretation as parameters of the CC model. N and λ^* are coefficients in the Butterfield's (1979) compression law (1), κ^* controls the slope of the isotropic unloading line in the $\ln(1+e)$ vs. $\ln(p/p_r)$ space, φ_c is the critical state friction angle. The last parameter r determines the shear modulus. Due to non-linear character of Eq. (3), the parameter r is usually calibrated by means of a parametric study, similarly to the parameter ψ of the 3SKH model.

3 SCALAR ERROR MEASURE

A scalar error measure has been introduced in order to assess model performance in the pre-failure regime and in order to eliminate a high amount of subjectivity of model calibration.

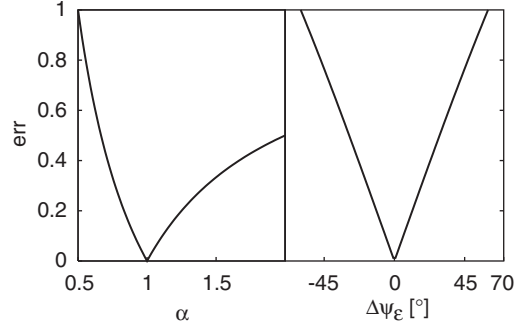


Figure 2. Numerical values of err for experiments and simulations that differ only in incremental stiffnesses (left) and strain path directions (right).

The suitable error measure should reflect differences in both predicted and observed stiffnesses and strain path directions. As experiments and simulations are characterised by identical stress paths, simulation error is measured in the strain space. Let the pre-failure part of the stress path be subdivided into L increments, of length $\Delta q = q_{max}/L$. Then, following Mašin et al. (2006), the simulation error can be defined as

$$err(OCR, q_{max}) = \frac{\sum_{k=1}^L \|\Delta \epsilon_{sim}^{(k)} - \Delta \epsilon_{exp}^{(k)}\|}{\sum_{k=1}^L \|\Delta \epsilon_{exp}^{(k)}\|} \quad (4)$$

where $\Delta \epsilon_{exp}^{(k)}$ and $\Delta \epsilon_{sim}^{(k)}$ are the measured and predicted strain increment tensors, respectively, corresponding to the k -th stress increment of size Δq .

In order to demonstrate the meaning of the numerical value of err , it is plotted for two special cases in Fig. 2. First, experiment and simulation with identical strain path directions and different incremental stiffnesses (measured by their ratio $\alpha = \|\Delta \epsilon_{exp}^{(k)}\| / \|\Delta \epsilon_{sim}^{(k)}\|$ from (4), i.e. $\alpha = G_{sim}/G_{exp} = K_{sim}/K_{exp}$, where G and K are shear and bulk moduli respectively) are considered. In the second case experiment and simulation are characterised by identical incremental stiffnesses ($\alpha = 1$), but different directions of the strain paths measured by the angle ψ_ϵ in the Rendulic plane of ϵ (ϵ_a vs. $\sqrt{2}\epsilon_r$, where ϵ_a and ϵ_r are axial and radial strains respectively). Investigation of (4) reveals that $err = |1 - 1/\alpha|$ for the first case and $err = |2 \sin(\Delta\psi_\epsilon/2)|$ for the second one (with $\Delta\psi_\epsilon = \psi_{\epsilon_{sim}} - \psi_{\epsilon_{exp}}$).

Calculation of err is complicated by the scatter in experimental data, in particular for low p (high OCR). For calculating of err the data were approximated by polynomial functions of the form

$$\epsilon_s = a_s q^{b_s} + c_s q^{d_s} + e_s q^{f_s} \dots \quad (5)$$

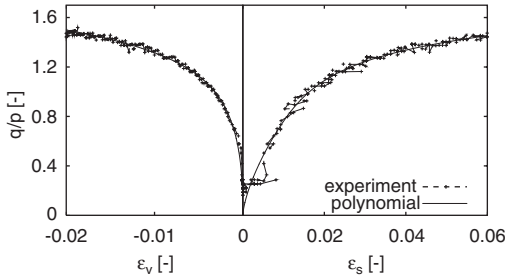


Figure 3. Approximation of experimental data for $OCR = 10$ by a polynomial function.

and

$$e_v = a_v q^{b_v} + c_v q^{d_v} + e_v q^{f_v} \dots \quad (6)$$

with coefficients $a_s, b_s, c_s, d_s, e_s, f_s \dots$ and $a_v, b_v, c_v, d_v, e_v, f_v \dots$. In this way a good fit of experimental data was achieved, as demonstrated in Fig. 3 for an experiment with $OCR = 10$.

In the present work, for all simulations q_{max} from (4) is chosen such that $q_{max} = 0.7q_{peak}$, where q_{peak} is the peak deviator stress achieved in the particular experiment. L in (4) is high enough so it does not influence calculated err (typically $L = 100$ was used).

4 CALIBRATION

The parameters of the studied constitutive models can be roughly split into two groups. In one group are parameters with a clear physical meaning, which are calibrated by standardized calibration procedures. On the other hand, parameters from the second group are less clearly defined and their calibration is more subjective. These parameters are usually found by means of parametric studies.

4.1 The first group of parameters

In the present work, parameters from the first group were calibrated only once and their values were kept constant for all simulations.

To this group belong parameters N, λ^* and κ^* , which were found by evaluation of an isotropic loading and unloading test, as demonstrated for the CC model in Fig. 4. Note that the numerical values of the parameter κ^* (Tab. 1) differ for the three constitutive models. In the 3SKH model κ^* specifies a bulk stiffness in the *small strain* range and it was calculated from an assumed Poisson ratio (accurate volumetric measurements in the small strain range were not available). In the HC model the slope of the isotropic unloading line is for higher $OCRs$ influenced also by the non-linear character of the hypoplastic equation.

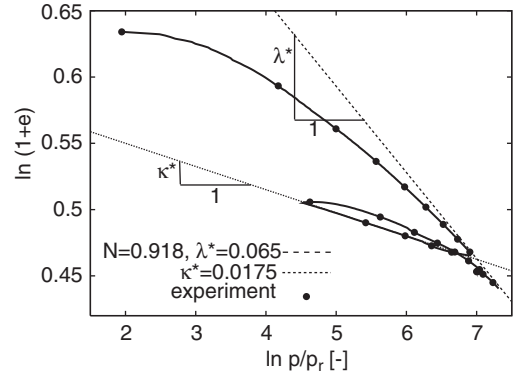


Figure 4. Calibration of parameters N, λ^* and κ^* of the CC model.

Table 1. Material parameters.

	M, φ_c	λ^*	κ^*	N
CC	1.1	0.065	0.0175	0.918
HC	27.5°	0.065	0.01	0.918
3SKH	1.1	0.065	0.0034	0.918

	A	N	M	T	S
3SKH	1964	0.65	0.2	0.25	0.08

	G, r, ψ (OCR1)		G, r, ψ (OCR10)	
CC	7330 kPa		2210 kPa	
HC	1.43		0.67	
3SKH	2.3		2.53	

For this reason κ^* of the HC model could be considered to belong to the second group of parameters. However, as it has only minor effect on predictions of constant p experiments (which are in scope of this study), its value was kept constant for all simulations. An approximate average value of the critical state friction angle from all shear experiments available was used to calculate the parameter M (φ_c).

The 3SKH model requires five further parameters that control the behaviour in the small strain range and the influence of the recent history (A, n, m, T and S). Data by Hattab and Hicher (2004) do not contain experiments required for their calibration. However, as similar soil (Speswhite kaolin) was used by Stallebrass and Taylor (1997), the additional parameters of the 3SKH model were taken over from their work.

4.2 The second group of parameters

These parameters, namely G (CC), r (HC) and ψ (3SKH), influence significantly results of constant p experiments in the pre-failure regime and their

calibration is to some extent subjective. In order to eliminate this subjectivity, these parameters were found by minimizing the scalar error measure err defined in Sec. 3. This procedure was applied on constant p experiments at $OCR = 1$ and $OCR = 10$, so two sets of material parameters (optimised for $OCR = 1$ and $OCR = 10$) were obtained (Tab. 1).

Calibration of parameters from the second group is in the following demonstrated by means of calibration of ψ using an experiment at $OCR = 10$.

Relation of err with respect to the value of ψ is shown in Fig. 5. The curve has a clear minimum that corresponds to $\psi = 2.53$. This optimised value of ψ , together with two different values, were used for simulation of the experiment at $OCR = 10$ (Fig. 6). In the pre-failure regime the value of ψ found by optimisation with respect to err corresponds quite well to the value that could have been chosen by means of a subjective trial-and-error calibration procedure.

Parameters r and G were found using the same procedure as outlined above, a clear minimum of err was obtained in all cases. The only difference was in the calibration of ψ for $OCR = 1$, as the stress state of the 3SKH model is on the bounding surface and therefore

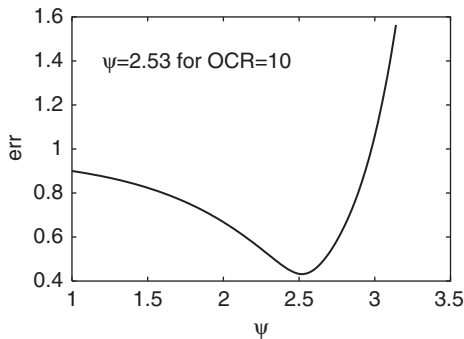


Figure 5. Calibration of ψ by means of minimalisation of err for experiment at $OCR = 10$.

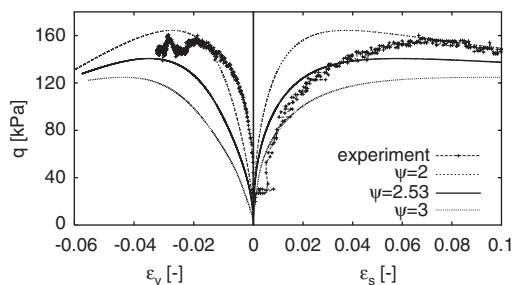


Figure 6. Predictions of the test $OCR = 10$ by the 3SKH model with err -optimised ($\psi = 2.53$) and two different values of ψ .

ψ does not influence model predictions. In this case ψ was found by trial-and-error by simulation of the isotropic unloading test from Fig. 4.

5 PERFORMANCE OF THE MODELS

The two sets of parameters found in Sec. 4 were used in simulating experiments at the whole range of OCR s. The initial states of p' , q and e measured in the experiments were used in the simulations. In addition, the 3SKH model requires to specify the initial positions of kinematic surfaces. These were aligned to reflect the stress history followed in the experiments (Sec. 1).

The obtained scalar error measure err is plotted with respect to OCR in Fig. 7. From this figure it appears that studied elasto-plastic and hypoplastic models have different ranges of validity of different sets of material parameters:

1. Hypoplastic (HC) model performs for higher OCR s less correctly than other two models when calibrated using data for $OCR = 1$. However, when calibrated at higher OCR , it produces the best predictions out of all tested models for the entire range of OCR s, with more-or-less constant value of err .

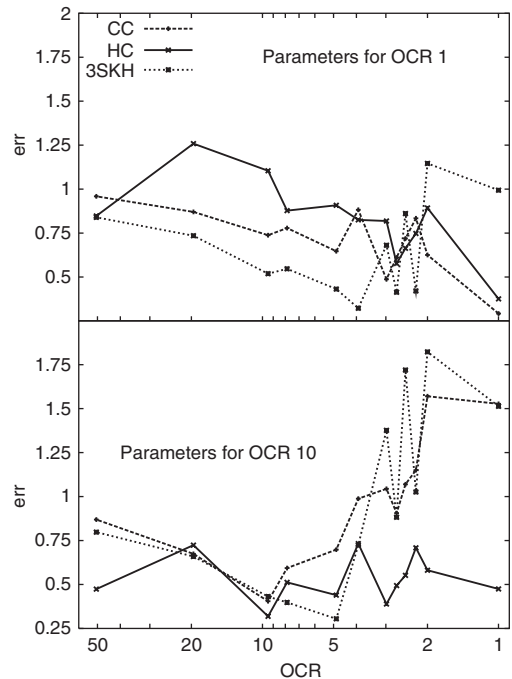


Figure 7. err for parameters optimised for $OCR = 1$ (top) and $OCR = 10$ (bottom).

2. Elasto-plastic (CC and 3SKH) models calibrated at $OCR = 10$ perform relatively correctly up to $OCR \approx 4$. For lower OCR s parameters for normally consolidated state lead to better predictions, but in the case of 3SKH still worst than predictions by hypoplasticity.

By definition, the value of err characterises model predictions in the pre-failure regime only. In order to evaluate predictions at failure, observed and predicted peak friction angles, φ_p were plotted with respect to OCR . The results were similar for both sets of parameters, Fig. 8 shows them for parameters optimised for $OCR = 10$. HC and 3SKH models predict peak friction angles relatively accurately (HC is more accurate for $OCR \leq 10$, 3SKH for $OCR \geq 20$). CC model overestimates significantly φ_p for all states with $OCR > 2$. This is a well-known shortcoming of the CC model, caused by the elliptical shape of the yield surface.

While err gives a convenient quantitative measure of the model performance, it does not specify the source of the prediction error. For qualitative comparison, the stress paths normalised by the Hvorslev equivalent pressure p_e^* are plotted for $OCR = 10$ optimised parameters in Fig. 9. Overprediction of φ_p by the CC model is clear, the shape of the normalised stress paths is predicted relatively correctly by both HC and 3SKH models. All models, however, overestimate dilation. Normalised stress paths of all models head towards a unique critical state point, which has not been reached in the experiments at higher OCR s (Fig. 9 top). A possible reason may be in localisation of deformation in shear bands at higher OCR s.

q vs. ϵ_s graphs for $OCR = 10$ optimised parameters are shown in Fig. 10. It is clear that higher errors for low OCR s of elasto-plastic models, reflected in Fig. 7, are caused by the underestimation of the shear stiffness in the case of CC and overestimation of the

shear stiffness in the case of 3SKH (with the exception of $OCR = 1$). Low prediction errors by the HC model (Fig. 7) are reflected also in qualitatively correct performance shown in Fig. 10. Volumetric changes shown in Fig. 11 reveal a general trend of overestimation of dilation for higher OCR s, as already discussed in the previous paragraph. The shape of ϵ_v vs. ϵ_s curves is best predicted by the HC model. For high OCR s the 3SKH model predicts dilatant behaviour immediately after the start of the shear phase, which has not been observed in the experiments. On the other hand, hypoplasticity overestimates the initial contraction for medium OCR s.

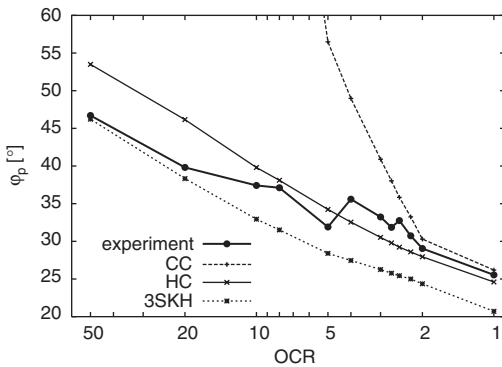


Figure 8. Peak friction angles φ_p predicted by the models with parameters optimised for $OCR = 10$.

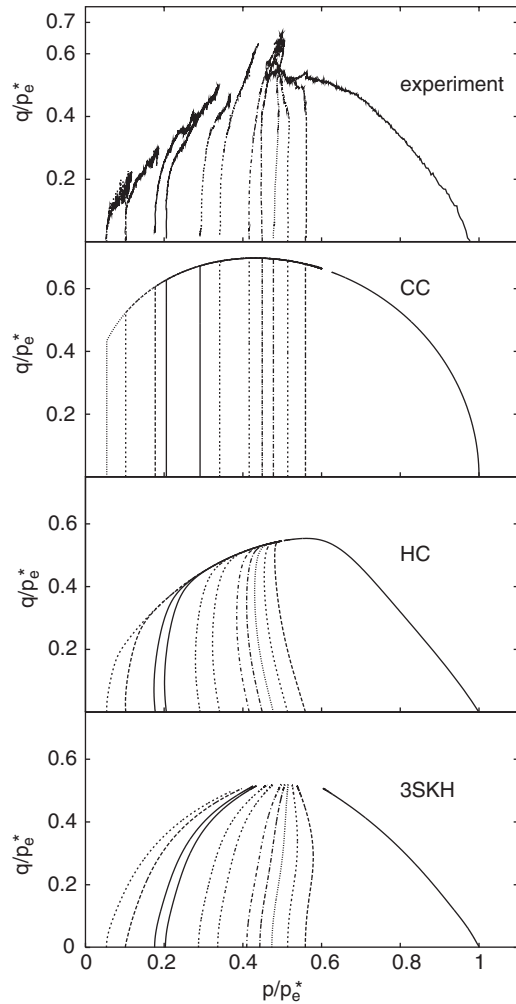


Figure 9. Stress paths normalised by p_e^* for $OCR = 10$ optimised parameters.

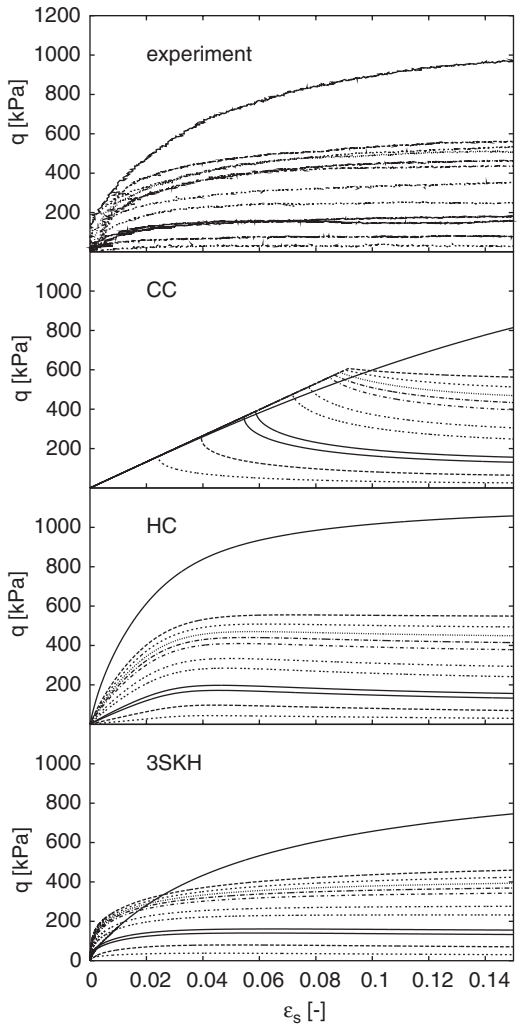


Figure 10. q vs. ϵ_s graphs for $OCR = 10$ optimised parameters.

6 CONCLUDING REMARKS

Results of this study must be seen as preliminary, as only one set of experimental data on one particular soil was investigated. Presented results however show that at least two sets of material parameters should be considered for both hypoplastic and elasto-plastic models. It appears that the HC model requires a different set of material parameters only for normally consolidated soil, a single set of parameters, which leads to accurate predictions for a broad range of $OCRs$, is sufficient for $OCR > 1$. Two sets of parameters should also be used for studied elasto-plastic models, with the approximate limiting $OCR \approx 4$.

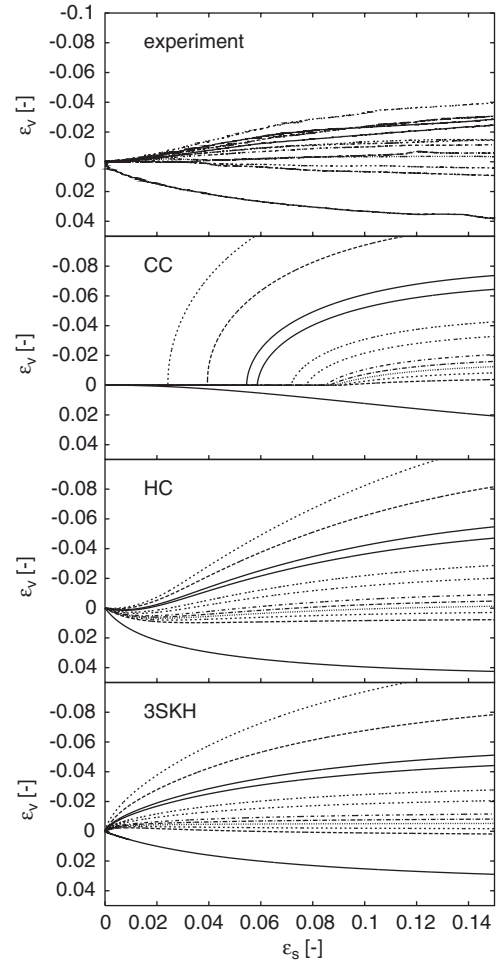


Figure 11. ϵ_v vs. ϵ_s graphs for $OCR = 10$ optimised parameters.

It is perhaps not surprising that the two advanced models performed significantly better than the CC model in predicting the non-linear behaviour in the pre-failure regime and correctly estimating the peak friction angles for high $OCRs$. For higher $OCRs$ the HC model leads to better predictions than the 3SKH, both from the point of view of the scalar error measure err and a qualitative performance expressed by the stress-strain diagrams. Also, the 3SKH model can not be effectively calibrated to predict correctly the behaviour of soils in normally consolidated state.

ACKNOWLEDGEMENT

Experimental data on kaolin clay were kindly provided by Prof. Mahdia Hattab. Financial support by

the research grant GAAV IAA200710605 is gratefully acknowledged.

REFERENCES

- Butterfield, R. (1979). A natural compression law for soils. *Géotechnique* 29(4), 469–480.
- Hattab, M. and P.-Y. Hicher (2004). Dilating behaviour of overconsolidated clay. *Soils and Foundations* 44(4), 27–40.
- Kolymbas, D. (1991). An outline of hypoplasticity. *Archive of Applied Mechanics* 61, 143–151.
- Mašin, D. (2005). A hypoplastic constitutive model for clays. *International Journal for Numerical and Analytical Methods in Geomechanics* 29(4), 311–336.
- Mašin, D. and I. Herle (2005). State boundary surface of a hypoplastic model for clays. *Computers and Geotechnics* 32(6), 400–410.
- Mašin, D., C. Tamagnini, G. Viggiani, and D. Costanzo (2006). Directional response of a reconstituted fine grained soil. Part II: Performance of different constitutive models. *International Journal for Numerical and Analytical Methods in Geomechanics* (reviewed).
- Roscoe, K. H. and J. B. Burland (1968). On the generalised stress-strain behaviour of wet clay. In J. Heyman and F. A. Leckie (Eds.), *Engineering Plasticity*, pp. 535–609. Cambridge: Cambridge University Press.
- Stallebrass, S. E. and R. N. Taylor (1997). Prediction of ground movements in overconsolidated clay. *Géotechnique* 47(2), 235–253.

An elasto-plastic constitutive model for clays considering microstructure

L.R. Kong^{1,2}, P.Y. Hicher², C.S. Chang³, H.W. Huang¹ & D.M. Zhang¹

¹ *Geotechnical Department of Tongji University, Shanghai, China*

² *Research Institute in Civil and Mechanical Engineering, Ecole Centrale de Nantes, Nantes, France*

³ *Department of Civil and mechanical Engineering, University of Massachusetts, Amherst, USA*

ABSTRACT: In this paper, we have extended the elasto-plastic model for granular materials with microstructural consideration (Chang and Hicher, 2004), to model the behavior of clays. The clay microstructure is assumed to be made of platelet aggregates which can't be destroyed during loading. The deformation is computed by integrating displacement at the particle contacts in all orientations. The behavior of aggregate contacts is assumed to follow an elastic-plastic law. A Hertz-mindlin's elastic law is used to the elastic behavior and two yield surfaces reflect the plastic behavior. The predictions of the constitutive model are compared with experimental results for normally and over consolidated clay under one-dimensional consolidation, drained and undrained triaxial test, which demonstrates that the model is able to reproduce the main features of clay behavior.

1 INTRODUCTION

Since the analysis of geotechnical problems requires constitutive models that can describe the deformation and strength of clay with reasonable accuracy, many different classes of constitutive models have been developed to capture clay behavior. Most of the models are based on macroscopic behavior, that is, they are often based on experimental data from clay specimen without considering their microstructure. However, these models can't clearly reflect the inherent micro properties of clays.

To obtain a constitutive model that can account for the inherent micro properties of clays, some micro constitutive models have been proposed. For example, Batdorf and Bodianski (1949) developed the slip theory of plasticity for polycrystalline materials based on Taylor's concept. Bazant et al. (1971, 1995) utilized the micro slip theory to clays and concretes respectively. For clay, Bazant assumed clay particles to be the soil skeleton model and founded the micro creep model of anisotropic clay by finite element method. The relationship between micro and macro is obtained by using the rate theory. Although such model can describe the behavior of clay, the choice of soil parameters is very difficult. Fleck (1995) founded particle contact model for metal powders through energy dissipation method and Houlsby (1999) developed Fleck's method for clays. In addition, some authors developed microstructural models for granular materials. For instance, Chang

and Hicher (2004) developed an elasto-plastic constitutive model for granular material considering the mean behavior of all contacts in each orientation and got satisfactory results.

In this paper, we develop a micro elasto-plastic constitutive model considering inter-particle forces and displacements for soft clays based on the model developed by Chang and Hicher. We consider two yield surfaces to capture the behavior of clay on a contact plane. The model is evaluated by comparing the predicted results with experimental data for the normally consolidated and over consolidated clay under one-dimensional consolidation, drained and undrained triaxial loading conditions test.

2 THEORY ANALYSIS

In this model, we extend the elasto-plastic model for granular materials with microstructural consideration (Chang and Hicher, 2004), to model the behavior of clays considering clay microstructure. In order to get a more reliable model, the following assumptions will be made. Assumption: 1. the microstructure is understood as aggregates which may include a large number of clay platelets; 2. the deformation consists in the contact interface of one aggregate over the adjacent aggregate; 3. the macroscopic stress-strain is equal to that expressed in terms of microscopic force and displacement through energy balance; 4. contact law between

two aggregates is assumed to follow a Hertz-Mindlin's elastic law and a plastic law based on a Mohr-Coulomb law.

2.1 Elastic part

The soil is considered as equal-sized aggregate, a contact plane between two aggregates is defined by the vector perpendicular to this plane. The elastic stiffness tensor is defined by:

$$f_i^a = k_{ij}^{ae} \mathcal{S}_j^{ae} \quad (1)$$

k_{ij}^{ae} can be related to normal stiffness k_n^a and shear stiffness k_t^a :

$$k_{ij}^{ae} = k_n^a n_i^a n_j^a + k_r^a (s_i^a s_j^a + t_i^a t_j^a) \quad (2)$$

where n , s , t are three orthogonal unit vectors that form the local coordinate system. The vector n is outward normal to the contact plane. Vectors s and t are on the contact plane.

The value of the stiffness for two elastic spheres can be estimated from Hertz-Mindlin's formulation (1969).

$$k_n = k_{n0} \left(\frac{f_n}{G_g l^2} \right)^n \quad (3)$$

$$k_t = k_{t0} \left(\frac{f_t}{G_g l^2} \right)^n \quad (4)$$

In equation (3) and (4), f_n is the contact force in normal direction. k_{n0} , k_{t0} and n are material constants. G_g is the elastic modulus of the clay aggregates. The branch length is equal to the aggregate size $l = d$, while we take $n = 0.5$ in the following simulations.

2.2 Plastic part

The elastic sliding behavior of two aggregates complies to a non-associated flow form, however the plastic sliding behavior often occurs along the tangential direction of the contact plane with an upward and downward

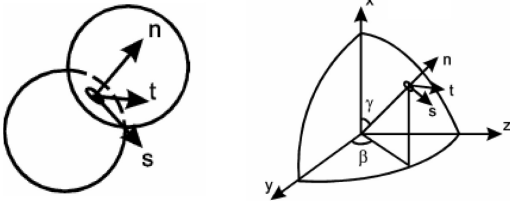


Figure 1. Local coordinate at inter-particle contact.

movement (associated flow form), then the shear dilation/contraction takes place. The dilation or contraction behavior can be described by

$$\frac{d\delta_n^p}{d\Delta^p} = \beta \left(\frac{T}{f_n} - \tan \phi_0 \right) \quad (5)$$

when $d\delta_n > 0$, it means contraction behavior of clay otherwise dilation behavior of clay. Here, we assumed that β is equal to 1, and ϕ_0 is a material constant which can be considered equal to the internal friction angle of clay ϕ_μ in most cases. The shear force T and the rate of plastic sliding $d\Delta^p$ can be defined as

$$T = \sqrt{f_s^2 + f_t^2} \quad (6)$$

$$d\Delta^p = \sqrt{(d\delta_s^p)^2 + (d\delta_t^p)^2} \quad (7)$$

2.3 Yielding function

Here two yield surfaces will reflect the clay behavior. one yield function is assumed to be of Mohr-Coulomb type:

$$F_1(f_i, k) = T - f_n \cdot k_1(\Delta^p) \quad (8)$$

$F_1 > 0$ means loading, while $F_1 < 0$ means unloading. $k_1(\Delta^p)$ is an isotropic hardening or softening parameter which can be defined as

$$k_1 = \frac{G_p \cdot \tan(\phi_p) \Delta^p}{|f_n| \tan(\phi_p) + G_p \cdot \Delta^p} \quad (9)$$

G_p represents the ratio between the elastic modulus and the plastic modulus.

The value of G_p is usually constant for a given soil and its value can be obtained by one-dimensional consolidation test. The peak friction angle ϕ_p can be defined as:

$$\tan \phi_p = \left(\frac{e_c}{e} \right)^m \tan \phi_u \quad (10)$$

ϕ_u means the internal friction angle which is constant for the given material. m is a material constant; the critical void ratio e_c is a function of the mean effective stress. The relationship can be written as follows:

$$e_c = e_{ref} - \lambda \log \left(\frac{p'}{p_{ref}} \right) \quad (11)$$

p' is the mean effective stress of the packing, (e_{ref} , p_{ref}) is a reference point on the critical state line.

In order to more accurately describe the behavior of the clay, another yield surface is added. The second yield function is assumed to be as follows:

$$F_2 = \sigma - k_2 \quad (12)$$

k_2 is another hardening parameter which can be written as:

$$k_2 = p_{ref} 10^{e^p / c_e} \quad (13)$$

Where c_e is the swelling coefficient in the e - $\log P'$ coordinate system.

2.4 Macro-micro relationship

Here we use the method developed in the elasto-plastic model for granular materials (Chang and Hicher, 2004) to obtain the relationship between microscopic and macroscopic level by energy balance method. The relationship between the macro strain and the inter-aggregate displacement can be written as:

$$u_{j,i} = A_{ik}^{-1} \sum_{a=1}^N \delta_j^a I_k^a \quad (14)$$

The relation between macro stress and mean force on the contact plane can be represented through energy balance as follows:

$$f_j^a = \sigma_{ij} A_{ik}^{-1} I_k^a V \quad (15)$$

The detailed explanations can be founded in Chang and Hicher (2004).

2.5 Summary of parameters

One can summarize the material parameters as:

- 1 Normalized contact number per unit volume: Nl^3/V , in the following analysis, we assume the value of Nl^3/V to be 34;
- 2 Mean aggregate size, d ;
- 3 Aggregate elastic constants: k_{n0} , k_{t0} and n ;
- 4 Aggregate friction angle: ϕ_u and m ;
- 5 Aggregate hardening rule: G_p and ϕ_p ;
- 6 Critical state for the packing: λ , c_e , e_{ref} and p_{ref} .

3 EVALUATION OF THE DERIVED MODEL

The capabilities of the proposed model are investigated by comparing its predictions with the results of a series of laboratory tests on clays under one-dimensional consolidation, drained or undrained triaxial test during loading conditions.

3.1 CID tests on normally consolidated clay

Two drained triaxial tests on normally consolidated clay had been reported and analyzed by Biarez and Hicher (1994). Both of the tests were performed at two isotropic compression 0.6 MPa and 0.8 MPa respectively. The model needs a number of input parameters, which include micro and macro parameters. The micro parameters contain mean aggregate size and aggregate stiffness. According to experience, we might assume that the mean aggregate size d is 0.1 mm, the initial aggregate stiffness k_{n0} is 50 N/mm, and the value of k_{t0}/k_{n0} is 0.35. The macro parameters, which can be determined from experimental curve or critical state in the e - $\log P'$ curve, are presented in Table 1.

As shown in Figure 2, both stress-strain relations and void ratio changes are in good agreement between experimental curves and predicted curves. When ε_j is reaching to 20%, the stress as well as the volume change becomes constant corresponding to the obtention of the critical state.

3.2 CID tests on over consolidated clay

Tests on overconsolidated Kaolinite clay had been undertaken by Zervoyannis and Bard, analyzed and reported by Biarez and Hicher (1994). The tests begin with an isotropic consolidation up to the preconsolidation pressure equal to 0.8 MPa, then unloading 0.4 MPa, 0.2 MPa and 0.1 MPa respectively. The corresponding over consolidation ratio P'_{ic}/P'_i (*O.C.R.*) is equal to 2, 4 and 8 respectively. We assume that the mean particle size d is 0.1 mm, the initial inter aggregate stiffness k_{n0} is 35 N/mm, and the value of k_{t0}/k_{n0} is 0.4. Other parameters are presented in Table 2.

Figure 3 shows the comparison between experiment data and predicted results with different over consolidation ratios. It can be seen that the model is able to predict satisfactorily the stress-strain behavior (Figure 3a). Based on Figure 3b, when the value of the overconsolidation ratio is small, the void ratio is decreasing, the material is contractive; while when the value of over consolidation ratio is higher than 2, the void ratio is first decreasing and then increasing, that is to say, the material is contractive and then dilatant. In this case, the void ratio has a peak value when ε_j is in the range 2% to 5%. The reason causing above phenomenon is that over consolidated sample is contractive as long as the mobilized friction angle is smaller than the internal friction angle ϕ_u and then dilatant up to failure.

Table 1. Model parameters for normally consolidated clay.

e_{ref}	P_{ref} (MPa)	λ	φ_{μ} (°)	φ_0 (°)	m	c_e	G_p
0.69	0.1	0.16	23	23	0.5	0.03	18

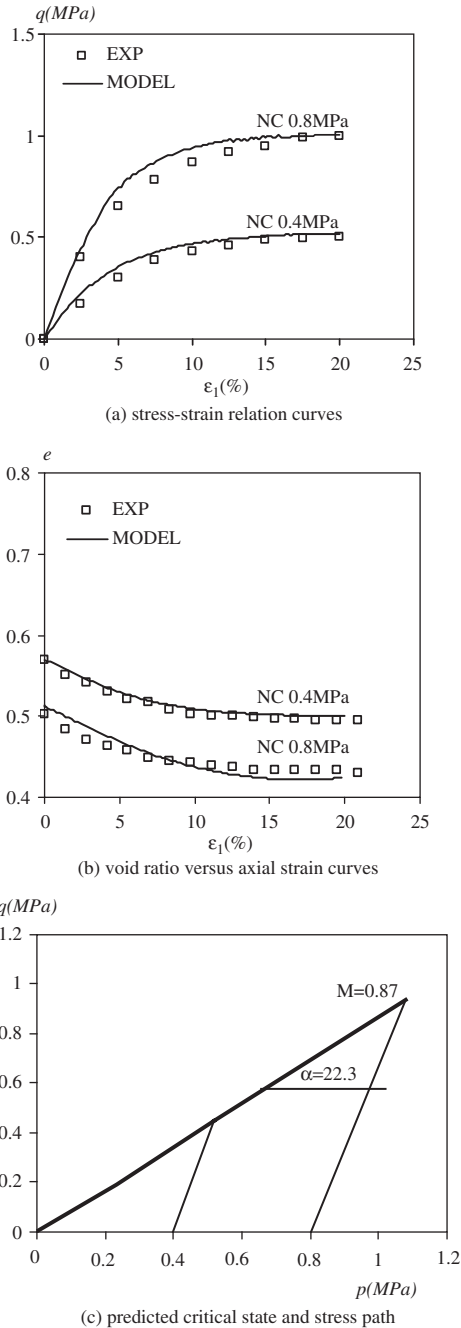


Figure 2. Comparison of predicted results and experimental results.

Table 2. Model parameters for over consolidated clay.

ϵ_{ref}	p_{ref} (MPa)	λ	φ_{μ} (°)	φ_0 (°)	m	c_e	G_p
1.39	0.1	0.53	20.7	20.7	2	0.03	16

3.3 CUD tests on over consolidated clay

Undrained triaxial tests on saturated clay samples were also computed. Experimented data were also reported by Biarez and Hicher(1994). Three samples were an isotropic compressed up to the preconsolidation 0.8 MPa, and then unload to 0.4 MPa and 0.067 MPa, so that the over consolidation ratio P'_{ic}/P'_i ($O.C.R.$) in the three samples was equal to 1, 2 and 12 respectively. We assume that the mean particle size d is 0.1 mm, the initial inter aggregate stiffness k_{n0} is 50 N/mm, and the ratio value of k_{t0}/k_{n0} is 0.35. Other parameters are presented in Table 3.

As shown in Figure 4a, the numerical curves and corresponding experiment curves are in good agreement. From Figure 4b, we can see that for normally consolidated sample ($O.C.R. = 1$), there is a contract decrease of the mean effective stress, which corresponds to a contracted behavior, while as the over consolidation ratio increases, clay will become dilatant leading to an increase of the mean effective stress.

3.4 One-dimensional consolidated test

One-dimensional consolidated test had been performed on Hangzhou clay (China). The experimental data had been presented by G. X. Wang (2003, PhD thesis). The depth of clay sample is about 13 m, while from $e-\log \sigma'_v$ curve, the value of the preconsolidation pressure is about 142 KPa, which indicates that Hangzhou clay is normally consolidated.

The one-dimensional consolidated test is simulated by applying a vertical strain increasing while keeping the horizontal strains equal to zero. We assume that the mean particle size d is 0.1 mm, the initial inter aggregate stiffness k_{n0} is 50 N/mm, and the ratio value of k_{t0}/k_{n0} is 0.432. Other parameters are presented in Table 4.

From Figure 5, we can see that the numerical curve is in good with the experimental data. As the intact Hangzhou clay, it represents obvious structure, and the new model can capture the character of clay.

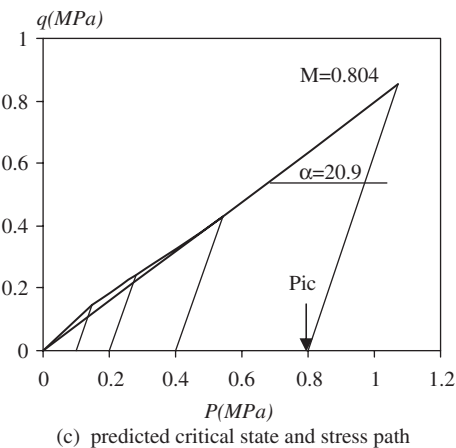
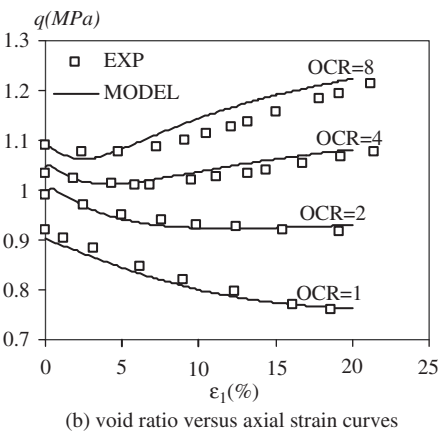
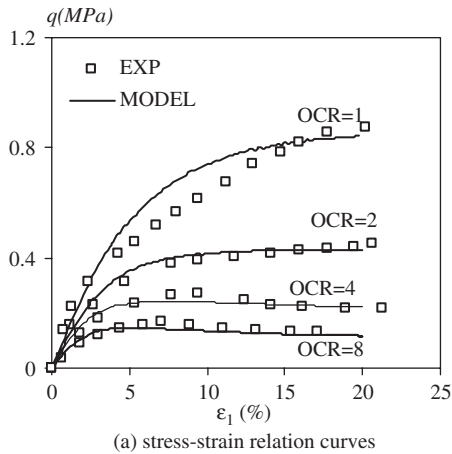


Figure 3. Comparison of predicted and experimental results.

Table 3. Model parameters for clay subjected to undrained triaxial test.

e_{ref}	p_{ref} (MPa)	λ	φ_{μ} (°)	φ_0 (°)	m	c_c	G_p
0.79	0.1	0.17	23	23	5	0.03	16

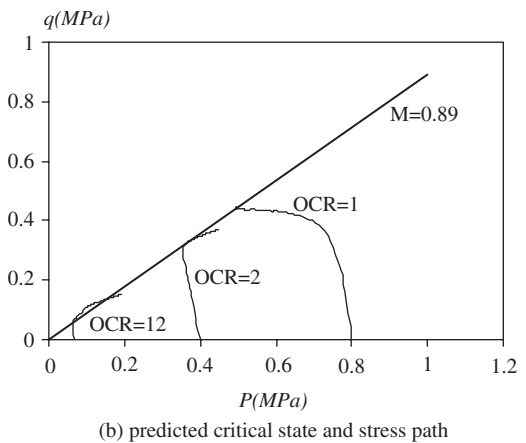
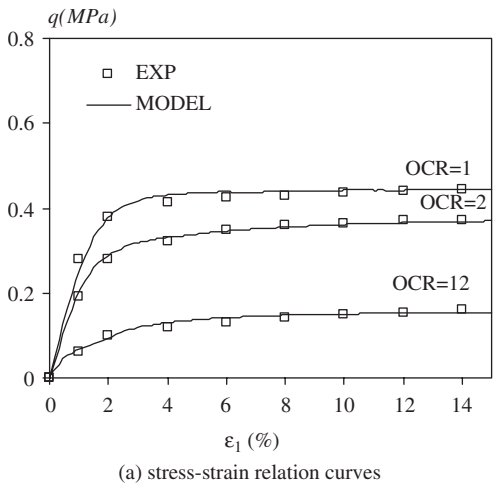


Figure 4. Comparison of predicted and experimental results.

Table 4. Model parameters for Hangzhou clay.

e_{ref}	p_{ref} (MPa)	λ	φ_{μ} ($^{\circ}$)	φ_0 ($^{\circ}$)	m	c_c	G_p
1.08	0.1	0.13	32.5	32.5	2	0.02	25

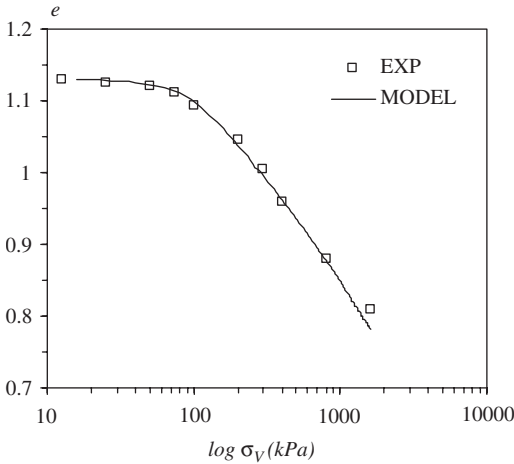


Figure 5. Comparison of predicted and experimental oedemeter test.

4 SUMMARY AND CONCLUSION

In the model, a simple elastio-plastic behavior is assumed on the contact plane. The elastic part is based on Hertz-Mindlin's contact formulation. As for the plastic part, we use two yield surfaces to reflect the clay behavior. One of the yield surfaces is based on the Mohr-Coulomb friction law with an isotropic hardening assumption and an associated flow rule; the other yield

mechanism is based on the description of the consolidation plastic strain. The ability of the model to reproduce the main features of the clay behavior is demonstrated. After comparing numerical simulations with experimental data, the following conclusions can be drawn:

- 1 The micromechanics model can correctly predict the behavior of normally consolidated and over consolidated clays under drained and undrained conditions. In addition, the model can also reflect the contractive or dilatant character of clays.
- 2 The model needs few material parameters that can be derived from one-dimensional consolidated test and conventional triaxial tests.

REFERENCES

- C. S. Chang, P. -Y. Hicher, 2004. An elastic-plastic model for granular materials with microstructural consideration. *International journal of solids and structures*. 42: 4258–4277
- J. Biarez, P. -Y. Hicher, 2002. Elementary mechanics of soil behaviour. *Balkema*. 19-21, 52, 59–60, 68–71
- Z. P. Bazant, I. K. Ozaydin, R. J. krizek, 1975. Micromechanics model for creep of anisotropic clay. *Journal of the engineering mechanics division*. EM1: 57–78
- G. T. Houlsby, R. S. Sharma, 1999. A conceptual model for the yielding and consolidation of clays. *Geotechnique*. 49(4): 491–501
- R. D. Mindlin, 1969. Microstructure in linear elasticity. *Archive for rational mechanisms and analysis*. 16: 51–78
- W. F. Chen, G. Y. Baladi, 1985. Soil plasticity, theory and implementation
- C. L. Chang, T. P. Young, D. Chang, C.S., 1997. Stress-strain relationship for granular materials bases on hypothesis of best fit. *International journal of solids and structures*. 34(31–32): 4087–4100
- Palisse Jérôme, 2005. Etude d'un modèle de comportement de l'argile. *Raport*.
- G. X. Wang, 2003. Study on structural property disturbed state model of soft soil. *PhD thesis*. 16–18

A multilaminate model with destructuration

V. Galavi & H.F. Schweiger

*Computational Geotechnics Group, Institute for Soil Mechanics and Foundation Engineering,
Graz University of Technology, Graz, Austria*

ABSTRACT: A constitutive model for structured soils, which is based on the multilaminate framework, is presented. The most important feature of the model is that since bonding, strength and preconsolidation pressure are defined independently on sampling planes, this model is able to consider bonding and preconsolidation induced anisotropy as well as strength anisotropy. It will be shown that in this model degradation of structure (bonding) and development of preconsolidation pressure are direction dependent. In this study only volumetric structure degradation is considered. To verify the capability of the model normal consolidation tests of two stiff clays, namely Pietrafitta and Pappadai clays, will be simulated and evaluated against experimental data.

1 INTRODUCTION

“Destructuration” is defined as degradation of structure by some mechanical, chemical or weathering effects, Leroueil et al. (1979). In this study only mechanical destructuration, namely degradation of structure with volumetric deformation is considered. The behaviour of natural soils depends on the initial structure of the soil in its natural state. The term “structure” is defined by Lambe & Whitman (1969), and Cotecchia & Chandler (1997) as the combination of “fabric”, the arrangement of the soil component particles, and “bonding”, those interparticle forces which are not of a purely frictional nature.

The effects of structure on the behaviour of soils have been reported for almost all weak rocks (e.g. Elliot & Brown, 1985) and soils, such as clays (soft, stiff or shales), granular soils, and deep-ocean sediments (e.g. Burland, 1990; Leroueil & Vaughan, 1990, Cotecchia & Chandler, 1997, 2000; Baudet & Ho, 2004).

The initial state of the structure of a soil is called “intact state”. In addition above definitions, Burland (1990) defined the “reconstituted state”. A reconstituted clay is defined as one that has been thoroughly mixed at a water content equal or greater than the liquid limit (between W_L and $1.5 W_L$). Burland (1990) designated the term “intrinsic” to describe the properties of reconstituted clays, because the properties are inherent to the material and independent of its natural state (Burland et al., 1996). In this study, following the suggestion of Burland (1990), the intrinsic properties are denoted by an asterisk (*) attached to the relevant symbol.

Burland (1990, 1996), Leroueil & Vaughan (1990), and Cotecchia & Chandler (1997, 2000) have studied compressibility and shear strength of some natural soils. It is seen from their work that structure of natural soils collapses during volumetric or shear deformations, thus the level of structure of a natural soil is decreased, and approaches the structure level of the reconstituted one. Changes of structure level depend on applied stress level (e.g. Amorosi & Rampello, 1998), thus in order to do a thorough study on a natural soil, this soil should be considered in a wide range of stress.

Some effects of structuring of natural soils can be summarized as follows:

1. The preconsolidation pressures of natural soils which are obtained from one-dimensional compression tests may be higher than the preconsolidation pressures of destructured soils (Burland, 1990, 1996; Leroueil & Vaughan, 1990).
2. The preconsolidation pressure and the limit state curve are affected by the stress history, distribution of contacts between particles, void ratio and strength of bonds between particles. The peak strength envelope of intact soil is above the envelope of destructured soil (Saihi et al., 2002, Burland, 1996).
3. The critical state of structured soils is inside the limit state curve while it coincides with limit state curves for non-structured soils (Saihi et al., 2002, Burland, 1996; Cotecchia & Chandler, 1997). The limit state shows strength of bonds while in the large deformation state (critical state) most of the bonds are broken.

Many constitutive models have been developed to describe the behaviour of soils, but most of the ones which are widely used in geotechnical engineering are not able to consider the behaviour of natural soils. In such models the effects of structure and bonding are neglected. However, some models have been developed recently to consider effects of destructuration (e.g. Rouainia & Muir Wood, 2000, Kavvasdas & Amorosi, 2000, Koskinen et al., 2002, Liu & Carter, 2002, Nova et al., 2003, Baudet & Stallebrass, 2004, Cudny & Vermeer, 2004, Liyanapathirana et al., 2005), but none of them consider both destructuration and strength anisotropy together. In this study it is tried to show how destructuration can be considered together with inherent anisotropy within the multilaminar framework.

Yield of structure is demonstrated by an irreversible post-yield change in the stiffness and strength of the material, Leroueil & Vaughan (1990). Leroueil & Vaughan (1990) defined three different kind of yielding in structure, namely yield in compression, in shear and in swelling. It should be noted that in this study only yielding in compression and in tension is considered.

2 MODEL FORMULATION

2.1 Multilaminar framework

In this section the formulation of the multilaminar model, which has been developed and implemented into PLAXIS (Brinkgreve, 2002) by Wiltafsky (2003) via the user-defined soil model option, is briefly summarized before the enhancements made to incorporate destructuration are discussed.

In this model in each stress point, 66 (2×33) planes, so-called sampling or contact planes, which are distributed on a sphere at various directions, are assumed. The yield surfaces are defined on each plane independently, thus, during loading, these yield surfaces are changed. Therefore this model is able to consider induced anisotropy intrinsically even for initially isotropic soils. Only plastic strains ϵ^p are calculated on sampling planes (micro-level), elastic strains ϵ^e are calculated on global (macro-level). In order to calculate the global deformation of a soil element, numerical integration over all contact planes is performed.

2.1.1 Yield surface and hardening law

The model developed by Wiltafsky (2003) includes both deviatoric and volumetric hardening. The yield surface of the model on each sampling plane consists of three parts f , f_c and f_t , where compressive stresses are assumed negative. The yield surface f (Eq. 1) is an extended Mohr-Coulomb criterion by introducing the mobilized friction angle ϕ'_m .

$$f = \tau + \sigma'_n \tan \phi'_m - \frac{c' \cdot \tan \phi'_m}{\tan \phi'} = 0 \quad (1a)$$

$$\tan \phi'_m = \tan \phi'_0 + \left(\tan \phi'_{mod} - \tan \phi'_0 \right) \frac{\epsilon_{\gamma, cone}^p}{A + \epsilon_{\gamma, cone}^p} \quad (1b)$$

ϕ'_0 , ϕ' and ϕ'_{mod} are initial, ultimate and modified effective friction angles respectively. $\tan(\phi'_{mod})$ is equal to $\tan(\phi')/R_f$ (failure ratio) and A is a parameter that governs the rate of deviatoric hardening. Mobilization of friction angle is controlled by plastic shear strains $\epsilon_{\gamma, cone}^p$. The second part of the yield surface is described by the function f_c (Eq. 2a), in which σ'_{nc} is the normal preconsolidation stress on the sampling plane calculated from Eq. 2b, and M_α governs the shape of the cap. The third part of the yield surface f_t is a tension cut-off criterion (Eq. 3). λ^* and κ^* are related to the compression and swelling index respectively.

$$f_c = \frac{\sigma_n'^2}{\sigma_{nc}'^2} + \frac{\tau^2}{(M_\alpha \cdot \sigma_{nc}')^2} - 1 = 0 \quad (2a)$$

$$\sigma_{nc}' = \sigma_{nc,i}' \cdot e^{-K \epsilon_{n, comp}^p}, \quad K = \frac{1+e}{\lambda^* - \kappa^*} \quad (2b)$$

$$f_t = \sigma'_n - \sigma'_i = 0 \quad (3)$$

2.1.2 Plastic flow

In this model, a non-associated flow rule is assumed for f and an associated flow rule for f_c and f_t . The plastic potential function of the deviatoric yield surface is defined by

$$g = \tau + \sigma'_n \cdot \tan \hat{\psi} - \frac{c' \cdot \tan \phi'_m}{\tan \phi'} = 0 \quad (4)$$

Where

$$\sin \hat{\psi} = \left(\frac{\sin \phi'_m - \sin \phi'_{cv}}{1 - \sin \phi'_m \cdot \sin \phi'_{cv}} \right) \left(\frac{\sin \phi'_m}{\sin \phi'} \right)^p \quad (5)$$

$$\sin \phi'_{cv} = \frac{\sin \phi' - \sin \psi}{1 - \sin \phi' \cdot \sin \psi}$$

This formulation corresponds to the stress dilatancy theory proposed by Rowe (1972) and modified by Søreide et al. (2002).

3 DEGRADATION OF STRUCTURE

In order to model degradation of structure, the yield surface (or bounding surface) is considered larger

than the yield surface (or bounding surface) of the corresponding reconstituted soil. This surface becomes smaller by increasing the plastic strain so that after a large plastic strain the two surfaces coincide.

From experimental tests it is evident that both volumetric and shear strains have influence on destructuration, because destructuration occurs in both compression and shearing. However, it is difficult to separate the influence of these two strains. In this study plastic volumetric and shear strains are assumed to contribute to destructuration and the relative contribution is defined by a parameter that will be introduced later. Similar assumptions have been made by Kavvas & Amorosi (2000), Koskinen et al. (2002), Gens & Nova (1993), and Rouainia & Muir Wood (2000). The damage strain ϵ_d on each sampling plane is defined as:

$$\epsilon_d = (1 - A_d)\epsilon_n^p + A_d\epsilon_\gamma^p \quad (6)$$

Where ϵ_n^p and ϵ_γ^p are the summation of absolute values of all plastic strains on each sampling plane as follows:

$$\epsilon_n^p = |\epsilon_{n,cap}^p| + |\epsilon_{n,cone}^p| + |\epsilon_{n,tens}^p| \quad (7)$$

$$\epsilon_\gamma^p = |\epsilon_{\gamma,cap}^p| + |\epsilon_{\gamma,cone}^p| + |\epsilon_{\gamma,tens}^p| \quad (8)$$

In equations 7 and 8 it is assumed that the plastic strains obtained from the cone, cap, and tension parts have the same influence on the degradation. A_d is a non-dimensional scaling parameter to control relative proportion of distortional and volumetric destructuration. It can be seen that for $A_d = 0$ the destructuration is entirely volumetric, whilst for $A_d = 1$ the destructuration is entirely distortional.

Normalized decrement of bonding with respect to initial bonding, which is assumed to be the bonding at gross yield (the point of starting destructuration, which is defined as a point where the stress-strain behaviour of the soil changes significantly), should be related to the increment of damage strain. The increase of the damage strain decreases the degree of structure. This can be expressed as follows:

$$\frac{db}{b} = -h.d\epsilon_d \quad (9)$$

where h is a non-dimensional parameter to control the rate of destructuration with damage strain, and b is the bonding parameter. By integrating Eq. 9, and consideration of stable and metastable structures, current bonding yields as:

$$b = b_{ult} + (b_i - b_{ult})\exp(h_0 - h_v\epsilon_d) \quad (10)$$

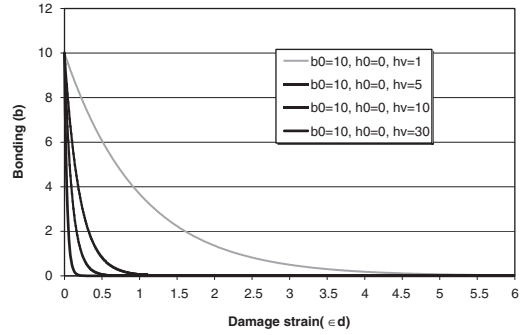


Figure 1. Representation of Eq. 10 with different rate of destructuration (h_v).

where b_i is the initial bonding on each sampling plane (at gross yield), and b_{ult} is the ultimate value of bonding (damage strain of infinity) on the representative sampling plane. h_0 and h_v are two parameters to determine the rate of decrease of bonding due to normal stresses. By increasing the damage strain the bonding is decreased because of exponential function that is used in the formula. Figure 1 plots equation 10 for a metastable structure ($b_{ult} = 0$) for different values of b_0 , h_0 and h_v . It should be noted that b_0 is defined as the mean value of initial bonding, and has the value of b_i in the case of isotropic soils.

4 DESTRUCTURATION LAW

The yield surface of the model on each sampling plane is depicted in Figure 2. In this figure σ'_{nc} and σ'^*_{nc} are the preconsolidation pressure of reconstituted and structured soil, respectively. As mentioned before, by increasing bonding or structure the preconsolidation pressure increases. Therefore the ratio of these two stresses is a function of bonding, thus:

$$\frac{\sigma'_{nc}}{\sigma'^*_{nc}} = f(b) \quad (11)$$

where $f(b)$ is a decreasing function with an ultimate value (at damage strain of infinity or when the amount of bonding is zero) of one (for metastable structure) or greater than one (for stable structure). Thus $f(b)$ may be defined as follows:

$$f(b) = 1 + b \quad (12)$$

where b is the amount of bonding that has been defined by equation 10. Now the relation between the preconsolidation stresses may be rewritten as:

$$\sigma'_{nc} = \sigma'^*_{nc} \cdot \{1 + b_{ult} + (b_i - b_{ult})\exp(h_0 - h_v\epsilon_d)\} \quad (13)$$

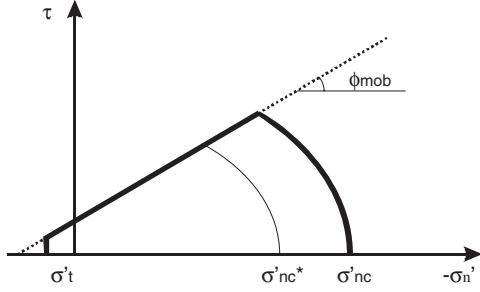


Figure 2. The yield surface of the model on each sampling plane.

By substituting the volumetric hardening rule of the model (Eq. 2b) into the above relation, it yields:

$$\sigma'_{nc} = \left\{ \sigma'^*_{nc,i} \exp(-K \varepsilon_{n,cap}^p) \right\} \cdot \left\{ 1 + b_{ult} + (b_i - b_{ult}) \exp(h_0 - h_v \varepsilon_d) \right\} \quad (14)$$

where $\sigma'^*_{nc,i}$ is the previous reconstituted preconsolidation stress on the respective plane.

In the same manner, the reduction of tensile strength, during degradation of structure can be modelled. The following relationship may be assumed, $\sigma_{t,max}$ is the maximum tensile strength and σ'_t the current tensile strength of natural soil.

$$\frac{\sigma'_t}{\sigma_{t,max}} = \alpha_t b_i \exp(-h_v \varepsilon_d) \quad (15)$$

α_t is a non-dimensional parameter to determine the rate of decrement of the tensile strength. The above expression indicates that the tensile strength tends to zero as the damage strain increases.

4.1 Effect of anisotropy on destructuration

In the previous section the parameter b_i was introduced, which defines the amount of bonding on a particular sampling plane. The value of the parameter is independent of the other planes. As the structure of soils causes a change of the yield surface (Leroueil & Vaughan, 1990) in different directions, thus it can be considered as one cause of inherent anisotropic response of natural soils. It may be assumed that in anisotropic soils, the amount of bonding is different in various directions. Therefore the parameter b_i should be a direction dependent parameter. Based on the work of Galavi & Schweiger (2006) and Pietruszczak & Mroz (2000) the spatial distribution of b_i may be defined as:

$$b_i = b_0 \left[1 - \frac{A_r - 1}{A_r + 2} \left(1 - 3(n_v)^2 \right) \right] \quad (16)$$

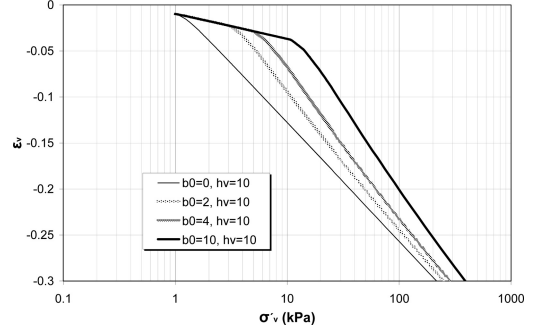


Figure 3. Effect of different amount of initial bonding on the normal compression line.

where b_0 and A_r are the mean value of the initial amount of bonding and anisotropy ratio, respectively, and n_v is the vertical component of the unit vector normal to the representative sampling plane.

As the bonding parameter is used in the definition of the preconsolidation normal stress and tensile stress, it follows that by defining the bonding parameter as a direction dependent parameter the above mentioned parameters are also direction dependent.

4.2 Model parameters

Five parameters are required to incorporate the structure to the model. The parameters are b_0 , b_{ult} , h_0 , h_v and α_t .

The parameter b_0 is related to the “yield stress ratio”, i.e. ratio between preconsolidation pressure on the normal consolidation line (NCL) of the natural soil to the corresponding preconsolidation pressure of the intrinsic soil. For soils with a metastable structure the value of h_0 is zero and the relation has the simple form as follows:

$$b_0 = \frac{\sigma'_{nc,i}}{\sigma'^*_{nc,i}} - 1 \quad (17)$$

Figure 3 shows the influence of the mean value of initial amount of bonding (b_0) on the resulting normal compression line. It should be noted that in this figure the value of the preconsolidation pressure of reconstituted soil is 1 kPa. The stress path of the test is shown in Figure 4 for two values of 4 and 10. It is obvious that the behaviour of soil up to gross yield is elastic. After this point the soil follows the K_0 stress path of the structured soil.

Figure 5 shows the normal compression line with different values for h_v . The value of A_d for all of these curves is zero. Therefore only volumetric plastic strains affect destructuration. In the case of other values for A_d , by changing h_v , the value of the gross yield stress will also change because plastic strains occur due to deviatoric yielding.

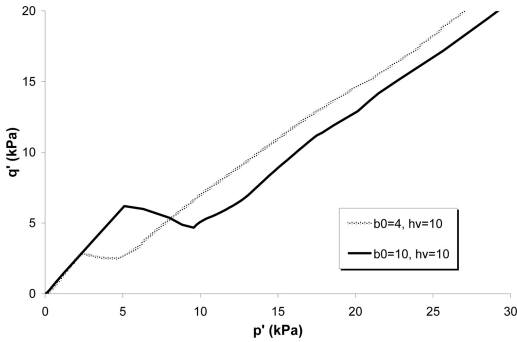


Figure 4. Stress path in oedometer test.

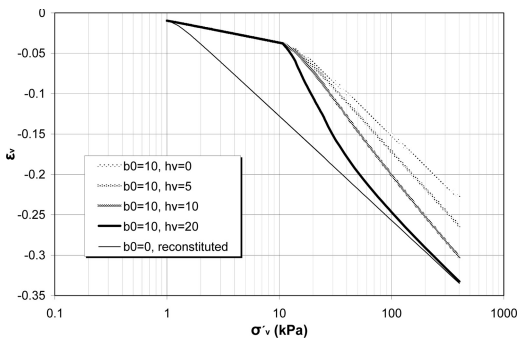


Figure 5. Effect of the rate of destructuration parameter (h_v) on compression line.

5 VERIFICATION

To verify the above-mentioned model, two stiff clays have been selected and the compression behaviour of them is modelled. The clays are:

- Pietrafitta clay; Burland et al. (1996).
- Pappadai clay; Cotecchia & Chandler (1997).

Both of them are modelled as isotropic soils ($A_r = 1$). Thus the amount of initial bonding (b_i) is the same for all sampling planes.

5.1.1 Pietrafitta clay

Experimental results of stiff clay Pietrafitta (Burland et al., 1996) are compared with simulations of the presented model. Burland et al. (1996) compared experimental data, shear strength and compressibility of four stiff clays in reconstituted and natural states. Therefore the experimental data of strength parameters and compressibility of the soil in intact state and reconstituted state can be obtained from their work and are given in Table 1.

The parameters for the model are based on Table 1 and given in Table 2. Some of the parameters can be

Table 1. Experimental data of Pietrafitta clay, Burland et al. (1996).

Parameter	Unit	Value
(C_c^*) conventional compression index	[-]	0.523
(C_s^*) conventional swelling index	[-]	0.118
(e_0) initial void ratio	[-]	1.14
(c') cohesion	[kPa]	0
(ϕ') friction angle	[°]	33.0
(σ'_{vy}^*) intrinsic vertical yield stress	[kPa]	490
(σ'_{vy}) intact vertical yield stress	[kPa]	1050

Table 2. Equivalent input data for the model for Pietrafitta clay.

Parameter	Unit	Value
(λ^*) compression index	[-]	0.2270
(κ^*) swelling index	[-]	0.0512
(ν') Poisson's ratio	[-]	0.20
(A) deviatoric hardening parameter	[-]	0.050
(M_α) shape parameter of cap	[-]	0.45tan ϕ
(e_0) initial void ratio	[-]	1.14
(c') cohesion	[kPa]	0
(ϕ') friction angle	[°]	33.0
(ψ') dilation angle	[°]	0
(b_0) initial bonding	[-]	1.14
(h_v) rate of damage	[-]	4.0
(σ'_{nc}^*) initial preconsolidation normal stress	[kPa]	490
(A_d) parameter of proportion of plastic strains	[-]	0.5

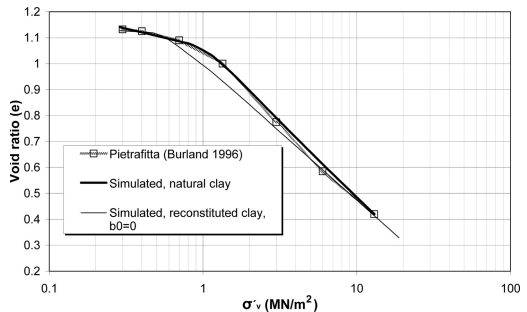


Figure 6. Comparison of simulation and experimental curves for Pietrafitta clay; Burland et al. (1996).

directly obtained but some have to be estimated such as ν' , A , ψ , A_d . Initial bonding is calculated from the “yield stress ratio” by means of equation 17, and the value of h_0 is assumed to be zero.

Comparison between the experimental normal compression curve and the simulated curve is shown in Figure 6. It is seen that the model has the capability of modelling of the compressibility of the soil with good accuracy.

Table 3. Model parameters for Pappadai clay, Cotecchia & Chandler (1997).

Parameter	Unit	Value
(λ^*) compression index	[-]	0.152
(κ^*) swelling index	[-]	0.0178
(ν') Poisson's ratio	[-]	0.20
(A) deviatoric hardening parameter	[-]	0.050
(M_α) shape parameter of cap	[-]	$0.67 \tan \phi$
(e_0) initial void ratio	[-]	0.98
(c') cohesion	[kPa]	0
(ϕ') friction angle	[°]	21.5
(ψ') dilation angle	[°]	0
(b_0) initial bonding	[-]	2.5
(h_v) rate of damage	[-]	11.0
(σ_{nc}^*) initial preconsolidation normal stress	[kPa]	750
(A_d) parameter of proportion of plastic strains	[-]	0.25

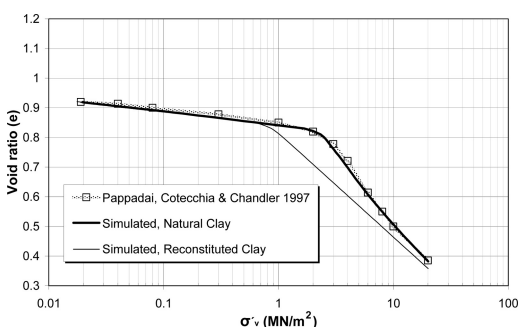


Figure 7. Comparison of simulation and experimental curves for Pappadai clay; Cotecchia & Chandler (1997).

5.1.2 Pappadai clay

Results of the experimental work on natural stiff Pappadai clay (Cotecchia & Chandler, 1997) are compared with the presented model. The soil samples were obtained from a block sample at a depth of 25.4 m from the Montemesola Basin, near Taranto, Italy.

This clay was deposited about 1.3 million years ago. There was subsequent erosion of some 120 m at the sampling location, resulting in the clay being overconsolidated.

Table 3 shows the values of model parameters used. A set of oedometer test on both natural and reconstituted Pappadai clay were used to determine parameters λ^* , κ^* and b_0 .

It can be seen again that the simulated curve matches quite accurately the experimental curve.

6 CONCLUSION

A constitutive model based on the multilaminar framework has been presented. It has been demonstrated

that the model is able to consider two important features of natural soils namely destructuration and anisotropy. The behaviour of two stiff clays was simulated with the model, and comparison with experimental data shows good agreement.

REFERENCES

- Amorosi, A., and Rampello, S. (1998). The influence of natural soil structure on the mechanical behaviour of a stiff clay. In Evangelista & Picarelli (eds), *The Geotechnics of Hard Soils-Soft Rocks; Naples, Italy, 12-14 October 1998*. Vol. 1, 395-401. Rotterdam: Balkema.
- Baudet, B., and Stallebrass, S. (2004). A constitutive model for structured clays. *Geotechnique* 54(4): 269-278.
- Baudet, B., and Ho, E.W.L. (2004). On the behaviour of deep-ocean sediments. *Geotechnique* 54(9): 571-580.
- Brinkgreve, R.B.J. (2002), *PLAXIS, Finite element code for soil and rock analyses, user manual*. Rotterdam: Balkema.
- Burland, J.B. (1990). On the compressibility and shear strength of natural clays. *Geotechnique* 40(3): 329-378.
- Burland, J.B., Rampello, S., Georgiannou, and Calabresi, G. (1996). A laboratory study of strength of four stiff clays. *Geotechnique* 46(3): 491-514.
- Cotecchia, F., and Chandler, R.J. (1997). The influence of structure on the pre-failure behaviour of a natural clay. *Geotechnique* 47(3): 523-544.
- Cotecchia, F., and Chandler, R.J. (2000). A general framework for the mechanical behaviour of clays. *Geotechnique* 50(4): 431-447.
- Cudny, M., and Vermeer, P.A. (2004). On the modelling of anisotropy and destructuration of soft clays within the multi-laminar framework. *Computers and Geotechnics* 31: 1-22.
- Elliott, G.M., and Brown, E.T. (1985). Yield of a soft, high porosity rock. *Geotechnique* 35(4): 413-423.
- Galavi, V., and Schweiger, H.F. (2006). The effect of strength anisotropy on slope stability analysis in soils. In J. Logar, A. Gaberc and B. Majes (eds), *Active Geotechnical Design in Infrastructure Development; Proc. 13th Danube-European Conference on Geotechnical Engineering, Ljubljana, Slovenia, 29-31 May 2006*. Vol. 2, 587-592. Ljubljana: Slovenian geotechnical society.
- Gens, A., and Nova, R. (1993). Conceptual base for a constitutive model for bonded soils and weak rocks. In Anagnostopoulos (eds), *Geotechnical Engineering of hard soils-soft rocks; Proc. intern. symp., Athens, 1993*. Vol. 1, 485-494. Rotterdam: Balkema.
- Kavvas, M., and Amorosi, A. (2000). A constitutive model for structured soils. *Geotechnique* 50(3): 263-273.
- Koskinen, M., Karstunen, M., and Wheeler, S.J. (2002). Modelling destructuration and anisotropy of a natural soft clay. In P. Mestat, (ed.), *Numerical Methods in Geotechnical Engineering; Proc., 5th European Conf, 2002*, 11-20. Presses de l'ENPC/LCPC, Paris.
- Lambe, T.W., and Whitman, R.V. (1969). *Soil Mechanics*. New York: Wiley.
- Leroueil, S., Tavenas, F., Brucy, F., La Rochelle, P., and Roy, J. (1979). Behaviour of destructured natural clays. *J. Soil Mech. Fdns Div. Am. Soc. Civ. Engrs* 105, GT6, 759-778.

- Leroueil, S., and Vaughan, P.R. (1990). The general and congruent effects of structure in natural soils and weak rocks. *Geotechnique* 40(3): 467–488.
- Liu, M.D., and Carter, J.P. (2002). A structured cam clay model. *Canadian Geotechnical Journal* 39(6): 1313–1332.
- Liyanapathirana, D.S., Carter, J.P. and Airey, D.W. (2005). Numerical Modeling of nonhomogeneous behavior of structure soils during triaxial test. *International Journal of Geomechanics, ASCE* 5(1): 10–23.
- Nova, R., Castellanza, R., and Tamagnini, C. (2003). A constitutive model for bonded geomaterials subject to mechanical and/or chemical degradation. *Int. J. Numer. Anal. Meth. Geomech* 27: 705–732.
- Pietruszczak, S., and Mroz, Z. (2000). Formulation of anisotropic failure criteria incorporating a microstructure tensor. *Computers and Geotechnics* 26: 105–112.
- Rampello, S., and Callisto, L. (1998). A study of the subsoil of the Tower of Pisa based on results from standard and high-quality samples. *Can. Geotech. J.* 35(6): 1074–1092.
- Rouainia, M., and Muir Wood, D. (2000). A kinematic hardening constitutive model for natural clays with loss of structure. *Geotechnique* 50(2): 153–164.
- Rowe, P.W. (1972). Theoretical meaning and observed values of deformation parameters for soil. In: Parry (Ed.), *Proc. Roscoe Memorial Symposium*, Cambridge, UK, 1971, 143–194. Cambridge: University Press.
- Saihi, F., Leroueil, S., La Rochelle, P., and French, I. (2002). Behaviour of the stiff and sensitive Saint-Jean-Vianney clay in intact, destructured, and remoulded conditions. *Can. Geotech. J.* 39: 1075–1087.
- Sørense, O.K., Nordal, S., and Bonnier, P.G. (2002). An impact friction hardening model for soil materials. In Mestat (ed.), *Numerical Methods in Geotechnical Engineering (NUMGE)*, Proc. Paris, France. 155–161, Paris: Presse de l'ENPC/LCPC.
- Wiltafsky, C. (2003). A multilaminate model for normally consolidated clay. Ph.D. Thesis, Graz University of Technology, Graz, Austria.

Coupled analysis of an *in situ* experiment in a soft argillaceous rock using a new constitutive model

J. Vaunat, B. Garitte & A. Gens

Department of Geotechnical Eng. and Geosciences, Universitat Politècnica de Catalunya, Barcelona, Spain

ABSTRACT: The paper addresses the issue of the description of the coupled thermo-hydro-mechanical behaviour of argillaceous rocks. A constitutive law, developed for this type of materials, is firstly described. It is based on an elastoplastic approach combined with damage concepts. Theoretical formulation and constitutive law are then used to analyze and interpret the observations gathered during the performance of an *in situ* heating test carried out in an underground laboratory. As a result of the analysis, a better understanding of the relationship between the various interacting phenomena is achieved.

1 INTRODUCTION

Argillaceous rocks (mudstones, claystones, marls, shales) result from mechanical, chemical and/or biological alteration of clay sediments during diagenesis. Their behaviour present challenging aspects related to their low porosity, significant bonding, marked anisotropy, stiffness reduction upon loading, brittle behaviour during shearing, crack opening during unloading, and mechanical degradation upon wetting.

In this paper a constitutive model for argillaceous rocks incorporating elasto-plastic and damage features is described. Formulation and constitutive model are then applied to the modelling of an *in situ* heating test performed on Opalinus clay in the Mont Terri laboratory. Neither chemical nor desaturation phenomena are considered in the work presented herein.

2 A CONSTITUTIVE MODEL FOR ARGILLACEOUS ROCK

2.1 General

The basis of the model consists in considering the presence of two different materials inside the medium: the argillaceous matrix and the bonds (Figure 1). When a load is externally applied to the medium, part of the stresses will be carried by the bonds and part by the matrix. The two materials will then experience different local values of stresses and strains. These values are constrained by the condition that local strains must be compatible with externally applied deformations, by

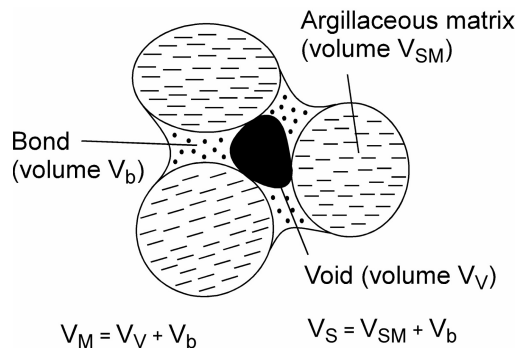


Figure 1. Schematic arrangement considered for a bonded argillaceous material.

the stress-strain relationships of the matrix and the bonds and by the fact that local stresses must be in equilibrium with the external load.

The model must therefore include a constitutive model for the matrix, a constitutive model for the bonds and a stress partitioning criterion to specify the way in which the applied stresses are shared. For simplicity, the equations are expressed in triaxial space.

2.2 Matrix

The model assumes that bonds are responsible of the main structuring effects. The argillaceous matrix has therefore the same local behaviour (expressed in terms of strains and stresses existing inside the matrix),

independently of the level of bonding. In this paper, a hardening elasto-plastic model based on the Hoek & Brown (1980) failure criterion has been adopted.

2.3 Bonding and stress/strain partitioning

The additional structuration caused by cement deposition is accounted for in the model through the introduction of second material component, called bond, endowed with a behaviour typical of quasi-brittle materials.

Let us suppose that bonding occurs at a given time during deposit history t_0 , characterized by in situ stress state (p_{b0}, q_{b0}) and strain $(\varepsilon_{v0}, \varepsilon_{q0})$. At that time, part of the void ratio will be occupied by the cementing material. Denoting $e = V_V/V_S$ the void ratio, $e_b = V_b/V_S$ the amount of volume occupied by bonds and $e_M = (V_b + V_V)/V_S$ the amount of volume not occupied by clay particles per unit volume of solid material, the following equality holds:

$$e_M = e + e_b \quad (1)$$

Changes in e , e_b and e_M are measured by the following volumetric strains: $d\varepsilon_v = -de/(1 + e)$, $d\varepsilon_{vb} = -de_b/(1 + e)$ and $d\varepsilon_{vM} = -de_M/(1 + e)$. $d\varepsilon_v$ is related to the change in porosity, $d\varepsilon_{vb}$ to the change in bond volume and $d\varepsilon_{vM}$ is the strain measured externally on a sample of cemented material.

From equation (1), it follows that the three strain increments are related by:

$$d\varepsilon_{vM} = d\varepsilon_v + d\varepsilon_{vb} \quad (2)$$

Equation (2) expresses the fact that change in porosity is not equal to the external volumetric strain because of bond deformability. It is extended to THE 3D strain increments by the expression:

$$d\varepsilon_{iM} = d\varepsilon_{ii} + d\varepsilon_{iib} \quad (3)$$

Integration of Equations (2) and (3) from time t_0 gives the following relationships between strains:

$$\varepsilon_{iM} - \varepsilon_{ij0} = (\varepsilon_{ij} - \varepsilon_{ij0}) + \varepsilon_{iib} \Leftrightarrow \varepsilon_{iM} = \varepsilon_{ij} + \varepsilon_{iib} \quad (4)$$

since $\varepsilon_{iM} = \varepsilon_{ij} = \varepsilon_{ij0}$ at t_0 .

Any load applied to an element of cemented material after the time of bond deposition will distribute itself between the soil matrix and the bonding according to a ratio that depends on the geometric arrangement of both components. Cordebois & Sidoroff (1982) proposed to use the energy equivalence principle that establishes the equality between the energy of the composite material and the sum of energies for all

components. For the case of a cemented material, this principle leads to:

$$(\sigma_{ij} - \sigma_{ijb0})(\varepsilon_{ij} - \varepsilon_{ij0}) = (\sigma_{ijM} - \sigma_{ijb0})(\varepsilon_{ijM} - \varepsilon_{ij0}) + \sigma_{iib}\varepsilon_{iib}, \quad \forall \varepsilon_{ij} = \varepsilon_{iM} - \varepsilon_{iib} \quad (5)$$

Defining $\chi_{ij} = \varepsilon_{iib}/(\varepsilon_{ij} - \varepsilon_{ij0})$, and using Equation (4), Equation (5) becomes:

$$\sigma_{ij} = \sigma_{ijM}(1 + \chi_{ij}) + \sigma_{iib}\varepsilon_{iib}, \quad \forall \varepsilon_{ij} = \varepsilon_{iM} - \varepsilon_{iib} \quad (6)$$

Equation (6) provides a relationship between the external stresses σ_{ij} , the stresses inside the bonds σ_{ijb} and "effective" stresses σ_{ijM} acting at the contact between clay particles. σ_{ijM} are related to ε_{ijM} by the constitutive law of the clay matrix described in section 3.1.

Relationship between σ_{ijb} and ε_{ijb} is provided by the constitutive law of the bonding. Damage elasticity is considered as the modelling framework for this material. More specifically, the damage model established by Carol et al. (2001) has been selected where a logarithmic damage measured is proposed:

$$L = \ln(1/(1 - D)) \quad (7)$$

Equations defining this law are:

$$\sigma_{iib} = (1 - D)K_{b0ijkl}\varepsilon_{bkl} = e^{-L}K_{b0ijkl}\varepsilon_{bkl} \quad (8)$$

D is a measure of damage or fissuring of the material and is equal to the ratio of bond fissures over the whole area of bonds. Fissures are assumed to have null stiffness while bond material between the fissures is considered as linear elastic with bulk and shear moduli K_{b0} and G_{b0} . When $D = 0$, the material is intact and bond stiffness is determined by K_{b0} and G_{b0} . As D increases, fissures develop and material stiffness decreases progressively. When $D = 1$, no more resisting area exists inside the bonding and bond stiffness is equal to 0. In that modelling framework, bond response is totally determined if K_{b0} , G_{b0} and evolution of D with load are known. Following Carol et al. (2001) proposal, change of D is linked to the energy increment input to the bonds du_b (equal to $\sigma_{ijb}d\varepsilon_{ijb}$ in triaxial conditions). The following expression has been used:

$$r(L) = r_0 e^{\eta L} = u_b \quad (9)$$

The current bond damage locus is defined in the stress space as a threshold of equal energy r , corresponding to the maximum energy input to the bond during its history. This condition draws an ellipse in the $p_b - q_b$ space. For a stress state moving inside the

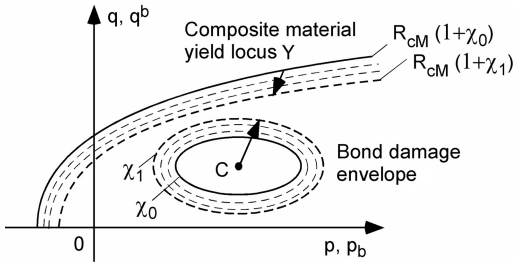


Figure 2. Schematic graphic description of the constitutive model.

ellipse, no further damage develops. When the ellipse is reached by the current stress state, damage occurs.

χ_{ij} define the part of load σ_{ij} carried respectively by bonds and matrix. Its evolution is defined by:

$$\chi_v = \chi_q = \chi = \sqrt{1 - D}\chi_0 \quad (10)$$

where χ_0 is a coefficient related to bonding intensity.

According to Equation (10), χ_{ij} evolve from χ_{ij0} to 0 during the process of bond damage. This mechanism is accompanied by a destructure of the material and a progressive transfer of load from bonds to clay matrix. Figure 2 shows a graphic summary of the model for triaxial conditions.

3 THE HE-D EXPERIMENT

The HE-D experiment has been carried out by ANDRA in the Mont Terri Underground Laboratory, excavated in Opalinus clay, a shale of Lower Aalenian age (Middle Jurassic). Opalinus clay may be described as a stiff overconsolidated clay with a strong bedding structure. The HE-D test is located in the shaly facies, that contains a higher proportion of clay minerals.

To perform the experiment, a niche was excavated from the main laboratory tunnel from which a 30 cm diameter borehole has been drilled with a total length of 14 m. In the section close to the end of the borehole, two heaters have been installed. The heaters are 2 m long and can be pressurized to ensure a good contact with the rock. The separation between heaters is 0.8 m. In addition, a number of auxiliary boreholes have been constructed to install a variety of instruments for the monitoring of the test. Figure 3 shows a schematic layout of the test.

Approximately one month after installation and pressurization, the heaters were switched on with a total power of 650 W (325 W per heater). The heaters were then left under constant power during 90 days. Afterwards the power was increased threefold, to 1950 W (975 W per heater) and maintained at that

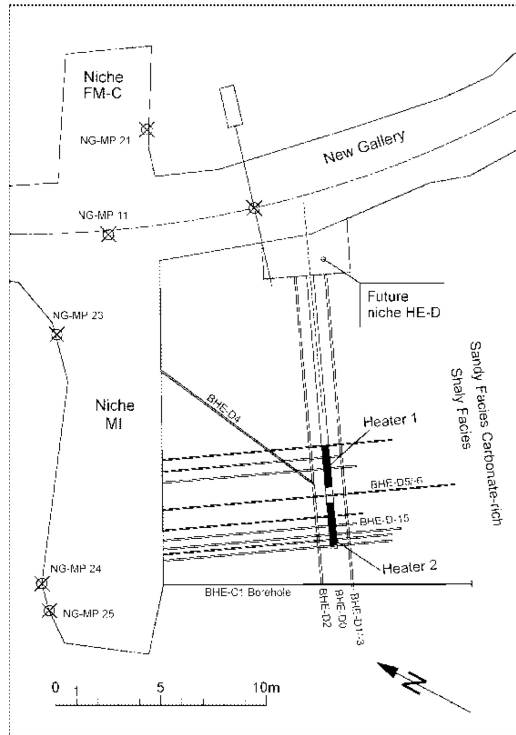


Figure 3. Layout of the HE-D experiment.

level for 248 days more. At the end of this second heating stage, the heaters were switched off and the rock allowed to cool. Temperatures, pore pressures and deformations were measured throughout.

4 FEATURES OF ANALYSIS

4.1 Type of analysis, discretization and computer code

The numerical analyses have been performed in 2-D axisymmetric conditions, with the axis of symmetry centred on the main borehole axis. This hypothesis obviously prevents the consideration of the anisotropy of material (mainly due to the presence of the bedding) and of the in situ stresses. Full 3D analyses are being carried out at present but are not presented here. In any case, the overall behaviour of the test is adequately represented by the axisymmetric model. The analyses have been performed using the computer programme CODE BRIGHT (Olivella et al., 2000) that incorporates a fully coupled thermo-hydro-mechanical formulation for multiphase flow in deformable porous media.

4.2 Boundary and initial conditions

The following stages are considered in the analysis: i) excavation of the borehole, ii) heater pressurization to 1 MPa, iii) application of the first stage of heater power (325 W/heater), iv) application of the second stage of heater power (975 W/heater), and v) switching off the heaters.

Initial stresses are assumed to be 4.28 MPa (an average value of the measurements made in the area). Initial pore pressures are set at 0.9 MPa in accordance with the observations made before the experiment. The initial temperature is 17°C and initial porosity is equal to 0.137 throughout the domain.

4.3 Material properties

The main material properties are summarized in Table 1. Most of the properties have been obtained from previously available information. However, the material stiffness value and the saturated hydraulic permeability have been determined from the evolution of pore pressures measured during the drilling of the main borehole. Also, thermal conductivity has been selected from a backanalysis based on 3D thermal modelling. As expected, thermal conductivity turned to be anisotropic with values of 2.8 and 1.6 W.m⁻¹.K⁻¹ parallel and perpendicular to the bedding planes, respectively. An average value of 2.2 W.m⁻¹.K⁻¹ has been used in the axisymmetric analyses.

Although there is a fair amount of scatter, laboratory tests on Opalinus clay show that there is a noticeable reduction of strength with temperature. This has been taken into account in the analysis by introducing a reduction of strength with temperature according to the expression (Laloui & Cekeravac, 2003):

$$R(T) = R(T_{ref}) \cdot \left(1 - s_T \cdot \log \left(\frac{T}{T_{ref}} \right) \right) \quad (11)$$

5 RESULTS AND DISCUSSION

5.1 Coupled phenomena

Test observations and results obtained from the coupled numerical analyses discussed below show a hierarchical arrangement of the various coupled phenomena identified. Relevant couplings are, by order of importance:

- a) Thermo-hydraulic coupling: thermal expansion of water and solid grain due to changes in temperature generate a build-up in water pressure. Because the increase in water pressure at one point of the massif depends basically on the increase in temperature, the development of thermal gradients is accompanied by the generation of hydraulic gradients.

Table 1. Material properties.

Material properties	Value
Mechanical	
Young modulus	$E = 7000 \text{ MPa}$
Poisson's ratio	$\nu = 0.23$
Biot's coefficient	$b = 0.6$
Uniaxial compression strength	$R_c = 10 \text{ MPa}$
Tensile strength	$P_t = 3.3 \text{ MPa}$
Strength reduction parameter	$s_T = 0.6$
Damage threshold	$r_o = 10^{-4} \text{ MPa}$
Damage evolution parameter	$r_l = 10^{-7} \text{ MPa}$
Hydraulic	
Saturated hydraulic conductivity	$K_w = 5.10^{-13} \text{ m/s}$
Thermal	
Linear thermal expansion of clay	$\alpha = 9 \cdot 10^{-6} \text{ K}^{-1}$
Thermal conductivity of clay	$\lambda_T = 2.2 \text{ W.m}^{-1}.\text{K}^{-1}$
Heat capacity of solid grain	$C^s = 840 \text{ J.kg}^{-1}.\text{K}^{-1}$

- b) Hydro-mechanical coupling: pore pressures generated by the thermo-hydraulic coupling dissipate with time. This process is often referred as thermo-consolidation and it causes further deformation of the medium.

The low porosity of Opalinus clay and the fact that it remains saturated during the test implies that neither pore pressure changes nor deformations cause noticeable changes in rock thermal properties; in particular the rock thermal conductivity remains almost constant. Thus, the temperature field is not affected by water pressures or displacements and, therefore, the coupling from hydro-mechanical to thermal is negligible. Consequently, the interpretation of the measurements will be made in the following order: i) temperatures and pore pressures and ii) deformations and other mechanical variables.

5.2 Temperatures and pore pressures

The evolutions of the observed and computed temperatures at one point adjacent to Heater 2 (see Figure 4 for point location) are presented in Figure 5. The two heating stages can be clearly seen. It can also be noted that the temperatures reached maximum values just above 100°C at the end of the second heating stages. There are some differences between the temperatures at the two points reflecting the thermal anisotropy of the Opalinus clay. About 200 days after switching off the heaters, the initial temperature is practically recovered and the experiment was terminated. The analysis reproduces well the observed variation of temperature throughout the test, although, naturally, an axisymmetric model can not account for any anisotropic effects.

Figures 6 to 11 present the evolution of temperatures and pore pressures for three points (D03, D14, D17), the locations of which are also shown in Figure 4.

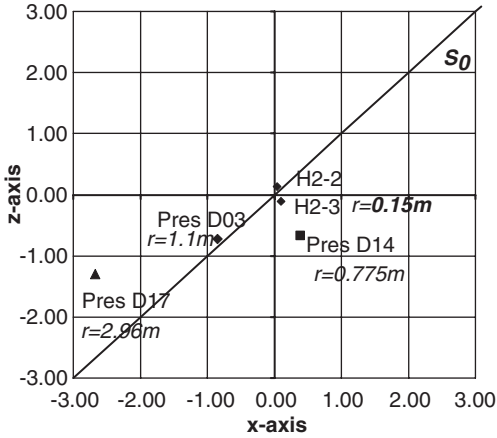


Figure 4. Observation points. Coordinate (0,0) corresponds to the main borehole axis. The line indicated by s_0 represents the bedding orientation.

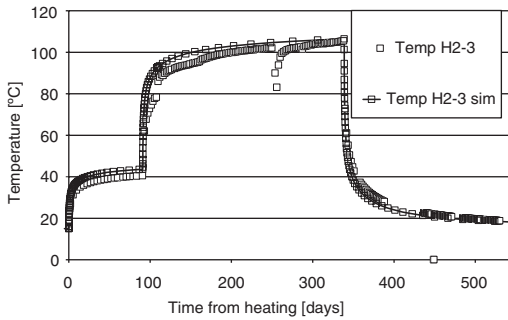


Figure 5. Evolution of temperature close to Heater 2.

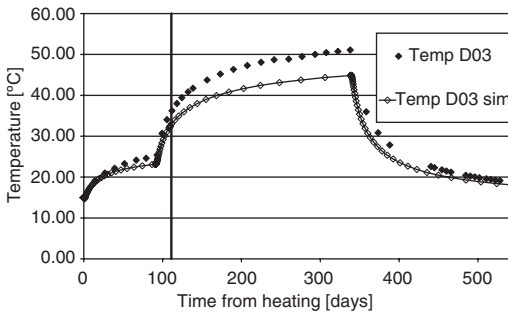


Figure 6. Evolution of temperatures at point D03. Observed and computed values.

Again, the two stages of heating and the cooling phase are clearly visible. Points D03 and D14 are located at different distances from the heater but they reach a similar temperature, about 50°C (Figures 6 and 8).

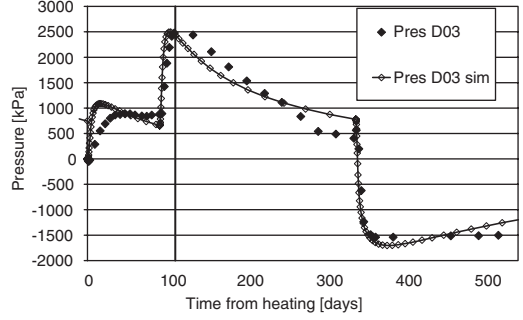


Figure 7. Evolution of pore pressures at point D03. Observed and computed values.

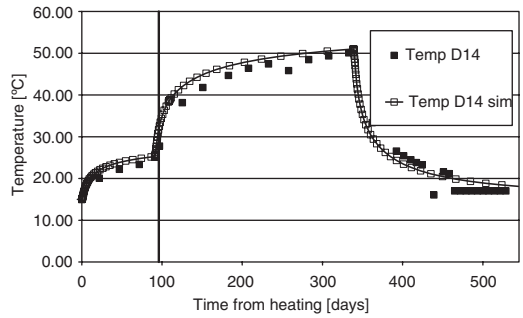


Figure 8. Evolution of temperatures at point D14. Observed and computed values.

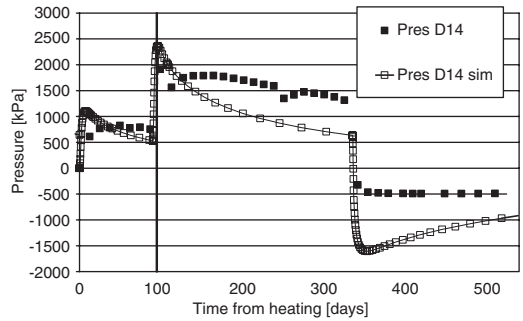


Figure 9. Evolution of pore pressures at point D14. Observed and computed values.

This again reflects the effect of thermal anisotropy. However, the reproduction of temperatures is globally quite satisfactory. Temperatures are of course lower at point D17, located further away from the heater (Figure 10).

Observations of pore pressures demonstrate quite clearly the connection between temperature variation

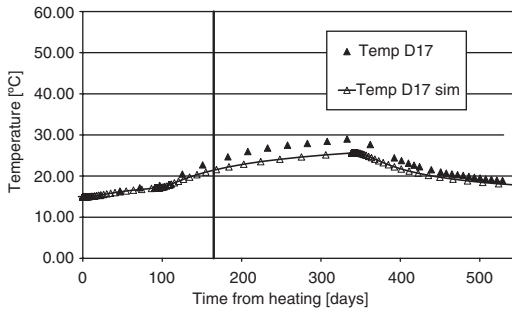


Figure 10. Evolution of temperatures at point D17. Observed and computed values.

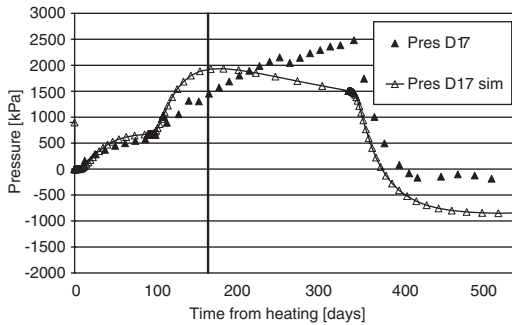


Figure 11. Evolution of pore pressures at point D17. Observed and computed values.

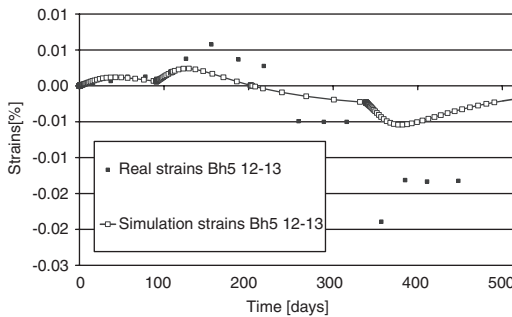


Figure 12. Evolution of deformation in section 12–13 in borehole BHE-D5. Observed and computed values.

and pore pressure response. An increase of temperature leads to an immediate increase of pore pressure. However, the relationship between the two variables is not straightforward. To illustrate this, the time at which the maximum of pore pressure is reached has been indicated in both the temperature and pore pressure plots. It can be clearly noted that the pore pressure

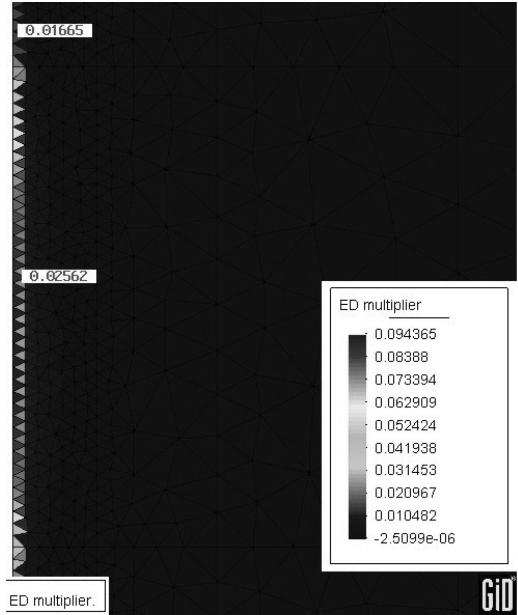


Figure 13. Damage parameter (L) contours at the end of the cooling phase.

peak corresponds to a first increase of temperature. However, as time passes and temperature keeps increasing, pore pressures in fact reduce because of hydraulic dissipation. Naturally, the degree and rate of dissipation depend strongly on rock permeability. The pore pressure response of point D17 (Figure 11), further away from the heater, is much less sharp, indeed it is even more gradual than analysis predicts.

5.3 Mechanical variables

Deformations have been measured along borehole BHE-D5. This observation borehole has been drilled perpendicular to the main borehole and it crosses the area between the two heaters. Deformations have been measured between a series of observation points along the borehole. Figure 12 shows the deformations measured in section 12–13 together with the analysis results. It can be noted that in the first stage of heating the computed results show a reasonable agreement with observations. However, this agreement breaks down from the start of the second stage of heating. Although the pattern of the evolution of deformations is quite similar, the observed magnitudes are much larger than the computed ones. The reason for the difference is not apparent and is being investigated; in particular the effect of the presence of steel and plastic tubing installed inside the borehole.

It is also interesting to check what is the extent of the EDZ predicted by the analysis. To that end contours of the damage parameter L have been plotted. Figure 13 shows the contours at the end of the cooling stage, when all effects due temperature have occurred. It can be observed that the predicted EDZ is remains small. Of course, the limited extent of the EDZ is very much related to the small diameter of the cavity considered in this case.

6 CONCLUSIONS

The development of a coupled formulation and an appropriate constitutive law provides a useful theoretical tool to examine rationally the response of argillaceous rocks to a variety of thermal, hydraulic and mechanical phenomena that interact with each other in a complex manner.

The approach has been applied to the analysis and interpretation of an intensively instrumented in situ heating test carried out on Opalinus clay in the Mont Terri underground laboratory. It can be stated that the model developed reproduces adequately the main phenomena observed in the experiment. Quantitative comparisons are largely satisfactory with the exception of deformations measured during the second heating stage. As a result of the study, a consistent set of parameters for Opalinus clay have been validated and can be used for the prediction of future works and experiments.

ACKNOWLEDGEMENTS

The Authors gratefully acknowledge the technical and financial contribution of ANDRA to this research.

The Authors want to acknowledge the support of the European Commission via Marie Curie Fellowship awarded to Benoit Garitte within the framework of the Mechanics of Unsaturated Soils for Engineering Research Training Network.

REFERENCES

- Carol, I., Rizzi, E. & Willam, K. 2002. On the formulation of anisotropic elastic degradation. I. Theory based on a pseudo-logarithmic damage tensor rate. *Int. J. Solids and Struct.* 38: 491–518.
- Cordebois, J.P. & Sidoroff, F. 1982. Endommagement anisotrope en élasticité et plasticité. *J. de Mécanique Théorique et Appliquée*, Numéro Spécial: 45–60.
- Gens, A. & Olivella, S. 2000. Non isothermal multiphase flow in deformable porous media. Coupled formulation and application to nuclear waste disposal. In D.W. Smith & J.P. Carter (eds.), *Developments on Theoretical Geomechanics – The John Booker Memorial Symposium, Sidney*, Rotterdam: Balkema: 619–640.
- Hoek, E. & Brown, E.T. 1980. Empirical strength criterion for rock masses. *Journal of the Geotechnical Engineering Division*, ASCE, 106: 1013–1035.
- Laloui, L. & Cekeravac, C. 2003. Thermo-plasticity of clays: an isotropic yield mechanism. *Computers and Geotechnics*, 30: 649–660.
- Olivella, S., Gens, A., Carrera, J. & Alonso, E.E. 1995. Numerical formulation for a simulator (CODE_BRIGHT) for the coupled analysis of saline media. *Engineering Computations*, 13: 87–112.
- Schnier H. 2005. LT experiment: Strength tests on cylindrical specimens, documentation and evaluation, (Phases 6 and 7), *Mont Terri Project: Technical Note, TN 2002-50*.

An elasto-plastic cap model for partially saturated soils

R. Kohler & G. Hofstetter

University of Innsbruck, Innsbruck, Austria

ABSTRACT: The present paper deals with the development and application of a numerical model for partially saturated soils. The mechanical behavior of the soil skeleton is described by a cap model, originally proposed for drained conditions. It is extended by introducing two stress state variables in order to account for partially saturated conditions. The theoretical background of the material model is briefly outlined and the implementation of the model into a finite element formulation is discussed. Finally the computational model is applied to the numerical simulation of a laboratory test on the behavior of a sand column subjected to cycles of dewatering and subsequent watering.

1 INTRODUCTION

In geotechnics the term “partially saturated” is employed for soils for which the void space is not fully saturated with water but also air is present in the pores. The presence of a second fluid phase in the pores affects the mechanical behavior of the soil skeleton such that material models based on the effective stress concept are not sufficient to describe the behavior of partially saturated soils. Due to the curved shape of the water-air interfaces and the presence of interfacial tension a difference in the pressures of the water phase and the air phase occurs, which is referred to as matric suction or capillary pressure (Fredlund & Rahardjo, 1993). Experimental evidence shows that an increase in matric suction in general results in an increase of the shear strength, the preconsolidation pressure and the elasto-plastic stiffness of the soil. Furthermore, a decrease in matric suction, i.e. an increase of the degree of water saturation, under high values of external stress can result in an irreversible decrease of the soil volume, denoted as collapse on wetting. As these features can only be taken into account using two stress state variables, a cap model, originally proposed for drained conditions, is extended in terms of the so called averaged soil skeleton stress and matric suction. By accounting for the evolution of the shear failure surface and the hardening law of the cap in terms of matric suction as well as including the third invariant of the deviatoric stress tensor in the formulation of the yield surfaces the material model is able to represent these features and provides good agreement with experimental results, see e.g. (Kohler & Hofstetter, 2006). The main focus of the present paper lies in the

implementation of this material model into a coupled three-phase FE-formulation. At first, the governing equations of the numerical model are outlined. Then the constitutive equations for the extended cap model are presented. Finally, the resulting computational model is applied to the numerical simulation of a laboratory test conducted by Klubertanz (1999) on a sand column which is subjected to cycles of dewatering and subsequent watering.

2 THREE-PHASE FORMULATION

The soil is treated as three-phase medium consisting of a deformable soil skeleton and the two fluid phases water and air. By applying averaging procedures a soil element can be considered as a mixture of these three phases, which continuously fill the entire domain according to their percentile share. The mixture is then treated with the methods of continuum mechanics and the governing equations are formulated in terms of the averaged quantities of the mixture. Following this approach the equilibrium equations are given as

$$-\operatorname{div} \boldsymbol{\sigma} + \bar{\rho} \mathbf{g} = \mathbf{0}, \quad (1)$$

where $\boldsymbol{\sigma}$ denotes the total stress tensor, \mathbf{g} is the vector of the gravitational acceleration and $\bar{\rho} = (1 - n)\rho^s + nS^w\rho^w + nS^a\rho^a$ is the averaged density with ρ^s , ρ^w and ρ^a representing the intrinsic densities of the soil grains, water and air (superscripts s , w and a); n is the porosity of the soil and S^f , $f = a, w$, denotes the degree of saturation of the respective fluid phase. Compressive stresses and pressures are defined as positive quantities throughout the present paper.

By considering an arbitrary domain of the three-phase medium, fixed in space, the mass balance equations for the two fluid phases are derived assuming incompressible soil grains and quasi-static conditions by making use of the law of conservation of mass as

$$-S^f \rho^f \dot{\varepsilon}^{vol} + n \rho^f \dot{S}^f + n S^f \dot{\rho}^f = -\text{div}(\rho^f \tilde{\mathbf{v}}^{fs}). \quad (2)$$

with $\tilde{\mathbf{v}}^{fs}$ denoting the artificial velocity.

Considering small displacements and small strains of the soil skeleton the relationship between the displacements \mathbf{u} and the strain tensor ε is given by the linearized kinematic equations.

The constitutive equations relate energy-conjugate expressions which can be derived from the conservation laws of the partially saturated porous medium, see e.g. Borja, 2004.

The constitutive equation relating the rate of the intrinsic density of a compressible barotropic fluid f to the rate of the fluid pressure is given as $\dot{\rho}^f/\rho^f = \dot{p}^f/K^f$ with K^f denoting the bulk modulus for the respective fluid phase.

For the approximation of the degree of water saturation under isothermal conditions in terms of the capillary pressure $p^c = p^a - p^w$ numerous empirical equations have been suggested in the literature. In the present model an approximation proposed in (Van Genuchten and Nielsen, 1985) is adopted

$$S^w = S_r^w + (S_s^w - S_r^w) \left[1 + \left(\frac{p^c}{p_b^c} \right)^n \right]^{-m}, \quad (3)$$

where S_s^w denotes the maximum degree of water saturation, S_r^w is the residual degree of water saturation and p_b^c denotes the air entry value. m and n are parameters to fit the empirical equation to experimental data. According to (Van Genuchten and Nielsen, 1985), the relation $n = 1/(1 - m)$ leads to adequate results for many soils.

For the transport of both fluid phases within the pores of the soil Darcys law is assumed to be valid. It can be derived from the equilibrium equation for a fluid phase as (Lewis and Schrefler, 1998)

$$\tilde{\mathbf{v}}^{fs} = \frac{k^f}{\gamma^f} (-\text{grad } p^f + \rho^f \mathbf{g}), \quad (4)$$

where γ^f denotes the unit weight and k^f the permeability of the soil with respect to the particular fluid f . For partially saturated soils the permeability coefficient k^f depends on the degree of saturation S^f and can be expressed as product of the permeability k^{of} for the fully saturated case ($S^f = 1$) and the relative permeability coefficient k^{rf} , accounting for the effect of

partial saturation, as

$$k^f = k^{of} k^{rf}(S^w) \quad \text{with } 0 \leq k^{rf}(S^w) \leq 1. \quad (5)$$

Various empirical equations relating the relative permeability coefficient to the degree of water saturation (3) are reported in the literature (Van Genuchten & Nielsen, 1985; Fredlund & Rahardjo, 1993).

The basis for the development of a constitutive model for the soil skeleton of partially saturated soils is the definition of the stress state variables in terms of which the mechanical behavior can be described. From the rate of work input per unit volume of a partially saturated soil possible definitions for stress state variables being work conjugate to the strains of the soil skeleton are derived, e.g. in Houlsby, 1997; Borja, 2004; Schrefler, 2002. In the present approach the so called average soil skeleton stress tensor

$$\boldsymbol{\sigma}^* = \boldsymbol{\sigma} - p^a \mathbf{I} + S^w (p^a - p^w) \mathbf{I} \quad (6)$$

is adopted. This choice is advantageous, because $\boldsymbol{\sigma}^*$ degenerates to the effective stress tensor for fully water saturated soils when S^w is equal to one. Thus, material models relying on $\boldsymbol{\sigma}^*$ allow a straightforward transition from partially saturated to fully water saturated conditions. As the formulation of the cap model in terms of $\boldsymbol{\sigma}^*$ as single stress state variable is not sufficient to fully describe the behavior of partially saturated soils matric suction p^c is considered as additional stress state variable. In order to be consistent with the thermodynamic considerations in (Houlsby, 1997; Borja, 2004; Schrefler, 2002) the latter is used as a stress-like plastic internal variable. Thus, the elastic strain tensor ε^e solely depends on the average soil skeleton stress and for the special case of linear elasticity the constitutive relations are given as

$$\boldsymbol{\sigma}^* = \mathbf{C} : \varepsilon^e = \mathbf{C} : (\varepsilon - \varepsilon^p), \quad (7)$$

where \mathbf{C} denotes the elasticity tensor. The determination of the plastic strain tensor ε^p requires a yield surface to indicate whether a certain stress state causes irreversible strains, a flow rule to determine the direction of the plastic strain rate and a suitable hardening law. The yield surface is chosen in accordance with the modified cap model proposed in (Hofstetter et al., 1993). The latter represents a reformulation of the original cap model (DiMaggio & Sandler, 1971) to make it suitable for the application of a closest point projection algorithm. In this multi-surface plasticity model the elastic regime is bounded by a convex yield surface, which consists of a shear failure surface $f_1(\boldsymbol{\sigma})$, a strain hardening cap $f_2(\boldsymbol{\sigma}, \kappa)$, where κ represents a hardening parameter, and a tension cutoff region $f_3(\boldsymbol{\sigma})$. The latter is not addressed in the present paper. In order to account for partially saturated conditions the

plasticity model is reformulated in terms of the average soil skeleton stress tensor σ^* and matric suction p^c is considered in the formulation of the yield surfaces. The functional form of the shear failure surface is reformulated as

$$f_1(\sigma^*, p^c) = L(\vartheta) \cdot \|\mathbf{s}\| - F_e(I_1^*) - F_s(p^c), \quad (8)$$

where

$$L(\vartheta) = \left(\frac{1 - \omega \cos 3\vartheta}{1 - \omega} \right)^{-\eta}, \quad F_e(I_1^*) = \alpha + \theta I_1^* \quad (9)$$

and

$$F_s(p^c) = k p^c \text{ or } F_s(p^c) = 3\theta \left[(S^w)^\zeta - S^w \right] p^c. \quad (10)$$

ω and η are parameters defining the shape of the yield surface within deviatoric planes with respect to the Lode angle ϑ . I_1^* denotes the first invariant of the average soil skeleton stress tensor and $\|\mathbf{s}\|$ is the norm of the deviatoric stress tensor, equal for the total stresses and the average soil skeleton stresses as p^a and p^w are only hydrostatic. The parameters α and θ define the shear failure envelope along the compressive meridian within planes of constant matric suction and the function $F_s(p^c)$ accounts for the increase of shear strength with matric suction. For the latter, two approaches are available in the present model. In the first one a linear increase of the shear failure surface with matric suction, controlled by the parameter k , is assumed (see (10₁)). Since the increase of shear strength with matric suction tends towards a maximum this approach may result in an overestimation of the shear strength for high values of matric suction. The second approach is obtained by linking the increase of shear strength with the degree of water saturation according to (Vanapalli et al., 1996) (see (10₂)). The fitting parameter ζ is a unique value for a certain soil which can be determined from the plasticity index I_p . For a non plastic soil with $I_p = 0$ the parameter $\zeta = 1$.

The proposed extension of the shear failure surface allows to predict the increasing shear strength of partially saturated soils with increasing matric suction as exemplarily depicted in Figure 1, where numerical results (solid lines) for triaxial compression tests at different values of matric suction are compared to experimental data (dotted lines) published in (Macari & Hoyos, 2001).

The functional form of the strain hardening cap of the original cap model is replaced by

$$f_2(\sigma^*, p^c, \kappa(p^c)) = F_c(\|\mathbf{s}\|, I_1^*, \kappa(p^c), \vartheta) - F_e(\kappa(p^c)) - F_s(p^c) \quad (11)$$

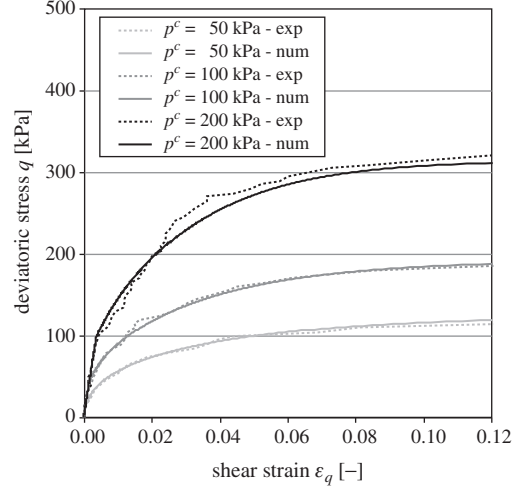


Figure 1. q - ε_q response for triaxial compression tests at different values of matric suction.

$$\text{for } \kappa(p^c) \leq I_1^* \leq X^*(\kappa(p^c)),$$

where

$$F_c(\|\mathbf{s}\|, I_1^*, \kappa(p^c), \vartheta) = \sqrt{L^2(\vartheta) \|\mathbf{s}\|^2 + \left(\frac{I_1^* - \kappa(p^c)}{R} \right)^2} \quad (12)$$

with R as a parameter defining the shape of the elliptic cap. The movement of the cap is governed by isotropic hardening. In contrast to the classical formulation both, the rate of the plastic volumetric strain $\dot{\varepsilon}_v^p$ and the hardening parameter κ , depend on matric suction. Due to numerical difficulties for the extension of the cap model in terms of two stress state variables using the original exponential hardening law the latter is replaced by a logarithmic one yielding the rate of the plastic volumetric strain as (Kohler, 2006)

$$\dot{\varepsilon}_v^p = \lambda(p^c) \frac{\dot{X}^*(\kappa(p^c)) - 3(\dot{S}^w p^c + S^w \dot{p}^c)}{X^*(\kappa(p^c)) - 3 S^w p^c}. \quad (13)$$

In (13) $X^*(\kappa(p^c))$ denotes the apex of the cap (Fig. 2) and $\lambda(p^c)$ is a scaling factor for the plastic volumetric strain rate. The latter is assumed to vary with matric suction according to an exponential law (Alonso et al., 1990)

$$\lambda(p^c) = \lambda(0) [(1 - r) \exp(-\beta p^c) + r] \quad (14)$$

with r and β as material parameters defining the increasing plastic stiffness under hydrostatic loading

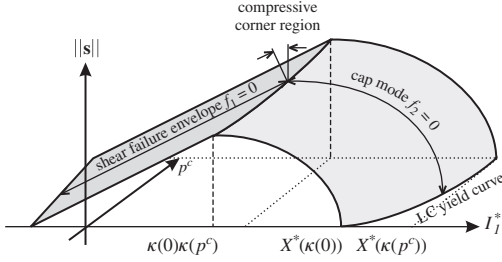


Figure 2. The yield surface of the extended cap model in terms of the averaged soil skeleton stress and matric suction.

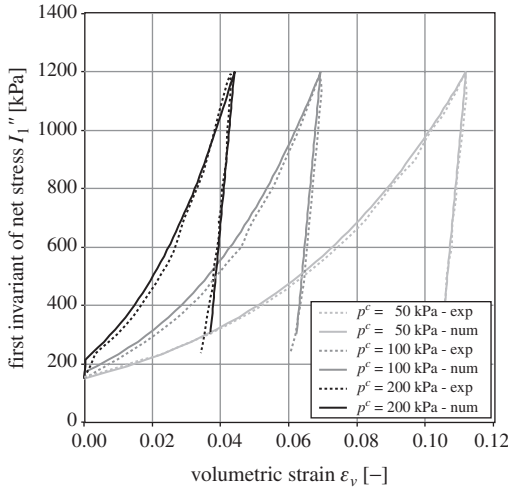


Figure 3. Comparison of the volumetric strain response for hydrostatic stress paths at constant matric suction predicted by the extended cap model with experimental data.

with matric suction, as shown in in Figure 3, which depicts the relations between the volumetric strain of the soil skeleton and the first invariant of the net stress tensor for hydrostatic tests at three different values of matric suction, $p^c = 50$ kPa (light grey curves), $p^c = 100$ kPa (dark grey curves) and $p^c = 200$ kPa (black curves). Solid lines refer to the numerical results and dotted lines to the experimental data redrawn from (Macari & Hoyos, 2001).

Making use of the fact that two points on the apex of the cap at two different values of matric suction are characterized by identical values of the plastic volumetric strain, the hardening parameter in terms of matric suction is finally obtained by integrating (13) as (Kohler, 2006)

$$\kappa(p^c) = \frac{X^c \left(\frac{\kappa(0) + R \cdot F_c(\kappa(0))}{X^c} \right)^{\frac{\lambda(0)}{\lambda(p^c)}} - R(\alpha + F_s(p^c))}{1 + R\theta} \quad (15)$$

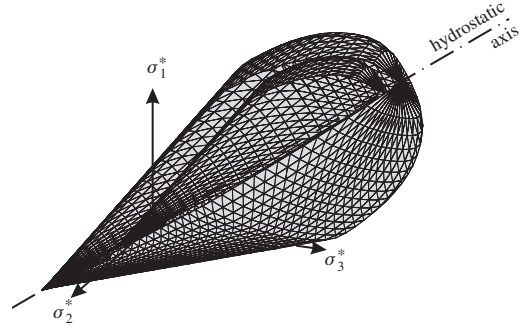


Figure 4. Sliced yield surfaces in the principal average soil skeleton stress space for two different values of matric suction.

The shape of the yield surface in the principal average soil skeleton stress space is depicted in Figure 4 for two different values of matric suction.

In contrast to a classical elasto-plastic material model in terms of a single stress state variable a second tensor of material tangent moduli is required for the implementation into the FE-formulation. The constitutive model for the soil skeleton, considering elasto-plastic behavior in terms of the average soil skeleton stress and matric suction, can be written in rate form as

$$\dot{\sigma}^* = \mathbf{C}_T \dot{\varepsilon} + \mathbf{C}_T^c \dot{p}^c = \mathbf{C}_T \dot{\varepsilon} + \mathbf{C}_T^c (\dot{p}^a - \dot{p}^w), \quad (16)$$

where $\mathbf{C}_T = \partial \sigma^* / \partial \varepsilon$ denotes the tensor of the material tangent moduli with respect to the total strains and $\mathbf{C}_T^c = \partial \sigma^* / \partial p^c$ contains the tangent moduli with respect to matric suction.

3 IMPLEMENTATION

The numerical solution of the problem within the framework of the finite element method relies on the weak formulations of the governing equations (1) and (2), the latter for both fluid phases, water and air. Dividing the (spatial) domain under consideration into a number of finite elements and interpolating the primary variables within a single finite element from the respective nodal values by suitable shape functions results in a coupled system of three nonlinear equations (Oettl, 2003):

$$\begin{aligned} -\mathbf{f}^{in}(\mathbf{U}, \mathbf{P}^w, \mathbf{P}^a) + \mathbf{C}^{sw} \mathbf{P}^w + \mathbf{C}^{sa} \mathbf{P}^a &= \mathbf{f}^{ex}, \\ -(\mathbf{C}^{sw})^T \dot{\mathbf{U}} + \mathbf{Q}^{ww} \dot{\mathbf{P}}^w + \mathbf{H}^{ww} \mathbf{P}^w + \mathbf{C}^{wa} \dot{\mathbf{P}}^a &= \dot{\mathbf{f}}^w, \\ -(\mathbf{C}^{sa})^T \dot{\mathbf{U}} + \mathbf{C}^{wa} \dot{\mathbf{P}}^w + \mathbf{Q}^{aa} \dot{\mathbf{P}}^a + \mathbf{H}^{aa} \mathbf{P}^a &= \dot{\mathbf{f}}^a. \end{aligned} \quad (17)$$

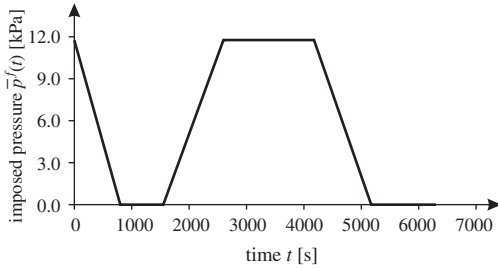


Figure 5. Imposed fluid pressure at the bottom of the sand column.

\mathbf{U} , \mathbf{P}^w and \mathbf{P}^a are the global vectors of the nodal values for the displacements and the fluid pressures, \mathbf{f}^{in} denotes the vector of the internal forces of the average soil skeleton stress tensor, the matrices \mathbf{C}^{sw} , \mathbf{C}^{sa} and \mathbf{C}^{wa} account for the coupling between the different phases, \mathbf{Q}^{ww} and \mathbf{Q}^{aa} contain the compressibility of the different phases and the constitutive relationship between the degree of water saturation and matric suction and \mathbf{H}^{ww} and \mathbf{H}^{aa} denote the permeability matrices. The external loads and the body forces are contained in the vector of the external forces \mathbf{f}^{ex} and the flow of the fluid phases through the surface of the domain under consideration is accounted for by the vectors \mathbf{f}^w and \mathbf{f}^a .

Applying the implicit Euler backward scheme for the approximation of the unknown solution of the primary variables at the discrete point of time t_{n+1} as well as substituting the constitutive law for the soil skeleton into the incremental vector of the internal forces finally yields a coupled set of equations for the incremental nodal values.

4 NUMERICAL EXAMPLE

4.1 Experiment

An experiment, dealing with the one-dimensional drainage of a soil column, conducted by (Klubertanz, 1999), is investigated numerically.

The experiment was conducted by means of a sand filled perspex column of 1.2 m height and a cross section of 0.25×0.25 m. Through holes in the bottom of this column water can be supplied or drained by applying specified pore water pressures. Initially, before the start of the experiment, the soil was fully water saturated and any outflow of water was prevented. Thus, hydrostatic conditions prevail within the soil column. In the course of the experiment, at $t \geq 0$, prescribed pore water pressures $p^w(t)$ are imposed at the bottom as depicted in Figure 5. The pore pressure of water is continuously measured during the experiment at 10

Table 1. Hydraulic parameters.

Parameter	Symbol	Value	Dimension
Permeability water	k^{ow}	$7.85 \cdot 10^{-6}$	m/s
Permeability air	k^{oa}	$4.36 \cdot 10^{-7}$	m/s
Bulk modulus water	K^w	$1 \cdot 10^3$	kPa
Bulk modulus air	K^a	$1 \cdot 10^2$	kPa
Residual saturation	S_r^w	0.1	–
Maximum saturation	S_s^w	1.0	–
Air entry value	p_b^c	8.9	kPa
Empirical parameter	m	0.79	–

Table 2. Mechanical parameters.

Parameter	Symbol	Value	Dimension
Young's modulus	E	$43 \cdot 10^3$	kPa
Poisson's ratio	ν	0.46	–
Porosity	n	0.44	–
Density soil grains	ρ^s	2.65	t/m ³
Material parameter	θ	0.51	–
Material parameter	α	3.8	kPa
Material parameter	$\lambda(0)$	0.0025	–
Shape factor	R	2.5	–
Material parameter	ζ	1.0	–
Material parameter	β	0.018	1/kPa
Material parameter	r	0.2	–

locations and the vertical displacements at the top of the soil column are recorded using two electronic sensors, one at the center and one at the edge.

4.2 Numerical simulation

The numerical simulation is carried out using a FE-mesh consisting of 24 equally-sized, plane strain isoparametric finite elements with a biquadratic interpolation for the displacements and bilinear interpolation for the fluid pressures. The displacements of the soil skeleton are horizontally constrained at the side-walls of the column and fully constrained at the bottom. The vertical boundaries are assumed to be impermeable for both fluid phases. Atmospheric conditions ($p^a = 0$) are imposed for the air pressure at the upper boundary whereas the pore pressures of both fluids at the lower boundary vary according to the evolution prescribed during the experiment.

All hydraulic parameters adopted for the analysis were measured by (Klubertanz, 1999) in independent experiments and are listed in Tab. 1.

The material parameters for the soil skeleton employed in the present simulation are found in Tab. 2. The parameters in the upper part are either adopted from (Klubertanz, 1999) or derived from a triaxial compression test and a oedometer test at fully saturated (drained) conditions conducted on the sand used for

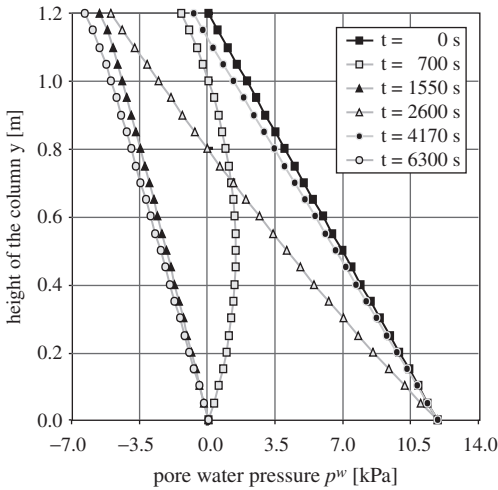


Figure 6. Pore water pressure vs. height.

the drainage test. The parameter ζ , accounting for the increase of shear strength with matric suction, can be assumed as 1.0 for sandy soils according to (Fredlund, 1995). Due to the lack of experimental data at $p^c > 0$ the material parameters defining the evolution of the cap with matric suction are estimated by adopting the respective values derived by the numerical simulation of a series of suction controlled tests published in (Macari and Hoyos, 2001).

4.3 Numerical results

Figure 6 depicts the pore water pressure vs. the height of the sand column for different instants of time. Before the start of the experiment hydrostatic conditions prevail in the water phase. The change of the water pressure with time at the bottom progresses with a delay of time along the height of the column leading to a curved distribution of the hydrostatic water pressures at early times.

Figure 7 depicts the evolution of the pore water pressure with time at different distances from the bottom of the soil column for both the experimental data (dotted lines) and numerical results (solid lines). As can be seen the results of the numerical simulation agree very well with the respective experimental data.

Figure 8 reveals that the numerically obtained surface settlements differ quite substantially from the experimental ones at the beginning of the test. The overestimation of the vertical displacements at the surface may result from friction effects between the soil and the perspex column in the experiment due to the instrumentation with pressure transducers, which are reported in (Klubertanz, 1999). They explain the difference

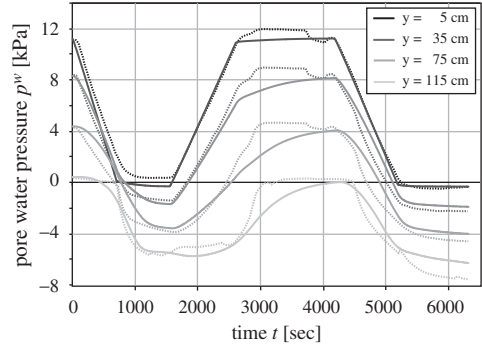


Figure 7. Pore water pressure vs. time.

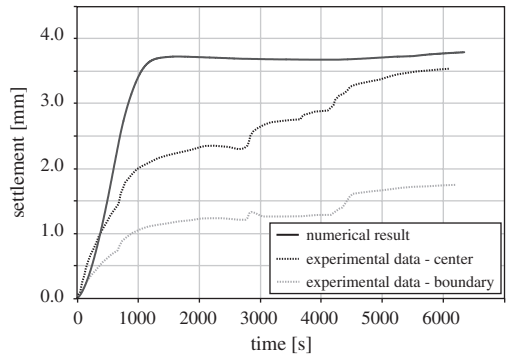


Figure 8. Settlement vs. time.

between the settlements measured at the boundary and at the center of the soil column. However, they are not considered in the numerical simulation. Since these discrepancies decay in the course of time, at the end of the test the experimentally obtained surface settlement is well predicted by the numerical simulation.

5 CONCLUSIONS

The implementation of an extended cap model for partially saturated soils in terms of the average soil skeleton stress and matric suction into a coupled three-phase soil model has been addressed in the present paper. After a brief presentation of the governing equations, the constitutive equations and the numerical implementation into a FE-code, the computational model was checked by applying the FE-formulation to a laboratory test subjected to cycles of watering and dewatering. The experimentally observed behavior is quite well predicted by the numerical simulation.

REFERENCES

- Alonso, E.E., Gens, A. & Josa, A. 1990. A constitutive model for partially saturated soils. *Géotechnique* 40(3): 405–430.
- Bishop, A.W. 1959. The principle of effective stress. *Teknisk Ukeblad* 106(39): 859–863.
- Borja, R.I. 2004. Cam-clay plasticity. part V: A mathematical framework for three-phase deformation and strain localization analyses of partially saturated porous media. *Comput. Methods Appl. Mech. Engrg.* 193: 5301–5338.
- DiMaggio, F.L. & Sandler, I.S. 1971. Material Models for Granular Soils. *Journal of the Engineering Mechanics Division ASCE*: 935–950.
- Fredlund, D.G. 1995. The scope of unsaturated soil mechanics. *Proc. 1st Int. conf. unsaturated soils, Paris* 3: 1155–1178.
- Fredlund, D.G. & Rahardjo, H. 1993. *Soil mechanics for unsaturated soils*. New York: John Wiley & Sons.
- Hofstetter, G., Simo, J.C. & Taylor, R.L. 1993. A modified cap model: closest point solution algorithms. *Computers & Structures* 46(2): 203–214.
- Houlsby, G.T. 1997. The work input to an unsaturated granular material. *Géotechnique* 47(1): 193–196.
- Klubertanz, G. 1999. *Zur hydromechanischen Kopplung in dreiphasigen porösen Medien*. Ph.D. thesis, École Polytechnique Fédérale de Lausanne, Switzerland.
- Kohler, R. & Hofstetter, G. 2006. Validation of an extended cap model for partially saturated soils. *3rd European Conference on Computational Mechanics*, Lisbon, Portugal.
- Kohler, R. 2006 *Numerical modelling of partially saturated soils in the context of a multi-phase-FE-formulation*. Ph.D. Thesis, University of Innsbruck, in prep.
- Lewis, R.W. & Schrefler, B.A. 1998. *The Finite Element Method in the Static and Dynamic Deformation and Consolidation of Porous Media*. Chichester: John Wiley & Sons, 2nd edition.
- Macari, E.J. & Hoyos, L.R. 2001. Mechanical behavior of an unsaturated soil under multi-axial stress states. *Geotechnical Testing Journal* 24(1): 14–22.
- Oettl, G. 2003. *A three-phase FE-model for dewatering of soils*. Ph.D. thesis, University of Innsbruck.
- Schrefler, B.A. 2002. Mechanics and thermodynamics of saturated/unsaturated porous materials and quantitative solutions. *Applied mechanics reviews* 55(4): 351–387.
- Van Genuchten, M. Th. & Nielsen, D.R. 1985. On describing and predicting the hydraulic properties of unsaturated soils. *Annales Geophysicae* 3(5): 615–628.
- Vanapalli, S.K., Fredlund, D.G., Pufahl, D.E. & Clifton A.W. 1996. Model for the prediction of shear strength with respect to soil suction. *Canadian geotechnical journal* 33: 379–392.

Modelling of partly saturated weathered broken rock

E. Bauer

Institute of Applied Mechanics, Graz University of Technology, Graz, Austria

W. Cen & Y. Zhu

Institute of Hydrostructure Engineering, Hohai University, Nanjing, P.R. China

K. Kast

Consulting Geotechnical Engineering ICOLD, Germany

S.F. Tantonio

Institute of Applied Mechanics, Graz University of Technology, Graz, Austria

ABSTRACT: The focus of the present paper is on modelling the essential mechanical properties of weathered and partly saturated broken rock using a hypoplastic continuum approach. In particular an increase of the compressibility and a decrease of the limit void ratios with an increase of the moisture content of the solid material is modeled in a simplified manner using only a moisture dependent granular hardness. The constitutive equation for the evolution of the stress is based on nonlinear tensor-valued functions depending on the current void ratio, the stress, a moisture dependent granular hardness and the rate of deformation. It is shown that the results obtained from numerical simulations of element tests are in a good agreement with laboratory experiments.

1 INTRODUCTION

The mechanical behaviour of broken rock is mainly determined by the grain hardness, the grain shape, the grain size distribution, the packing density, the orientation of contact planes, the stress state and the loading history. Stiffness and shear strength are influenced by the pressure level, the packing density and the rate of deformation and are therefore not material constants. The mechanical behaviour of broken rock is different for unweathered or weathered grains. The degree of geological disintegration, e.g. by chemical weathering or by the intensity and the orientation of micro-cracks, has a significant influence on the granular hardness and, as a consequence, on the evolution of grain abrasion and grain breakage. Depending on the state of weathering the propagation of micro-cracks due to water-induced stress corrosion can be strongly influenced by the moisture content of the grains. Under higher stress levels the disintegration of grains can be accelerated by moisture, which leads to a reduction of the resistance to compaction and shearing.

The focus of the present paper is on modelling the mechanical behaviour of broken rock materials using a hypoplastic continuum approach. In hypoplasticity the evolution equation for the stress is formulated with

a nonlinear isotropic tensor-valued function depending on the current state quantities and the rate of deformation. In contrast to the classical concept of elastoplasticity no decomposition of the deformation into elastic and plastic parts is needed (Darve 1991, Kolymbas 1991). In order to model an elastic material properties the rate of deformation tensor is incorporated in the constitutive equation in a nonlinear formulation. With a pressure dependent density factor the influence of pressure and density on the incremental stiffness, the peak friction angle and the dilatancy can be modeled for an initially loose or dense state using a single set of constants (e.g. Wu & Bauer 1993, Wu et al. 1996, Herle & Gudehus 1999). Limit states or so-called critical states are included in the constitutive equation for a simultaneous vanishing of the stress rate and volume strain rate (Bauer 1995). Originally, hypoplastic material models were developed and calibrated for dry and cohesionless granular materials like sand. While in the hypoplastic model by Gudehus (1996) and Bauer (1996) for granular materials with unweathered grains the so-called granular hardness is assumed to be constant, an extension of this version with a granular hardness depending on the moisture content is discussed for applications to weathered broken rock materials in the present paper. Herein the

granular hardness is related to the grain assembly in the sense of a continuum description and does not mean the hardness of an individual grain. The model is calibrated for a weathered broken granite and the results obtained from the numerical simulation of element tests are compared with experiments.

2 THE GRANULAR HARDNESS OF WEATHERED BROKEN ROCK

It is experimentally evident that for weathered rockfill materials the compressibility is higher for a wet than for a dry material as illustrated in Figure 1. For a pre-compressed material under dry conditions (path A-B) a following wetting leads to an additional settlement along path B-C. For a continuing loading the load-displacement curve (path C-D) follows the curve A-D obtained for an initially wet material, i.e. the memory of the material of the pre-compaction under dry conditions is swept out if the load-displacement curve obtained for the wet material (path A-D) starts from the same initial density. In this context it is important to note that for different initial densities the compression curves are different for both dry and wet states of the material (Kast 1992).

In the following the compression behaviour is first discussed for a dry granular material and modeled using a relation between the void ratio e and the mean pressure $p = -(\sigma_{11} + \sigma_{22} + \sigma_{33})/3$. The evaluation of numerous tests has shown that the compression behaviour of various cohesionless granular materials can be approximated with the following exponential function (Bauer 1995):

$$e = e_0 \exp[-(3p/h_s)^n]. \quad (1)$$

Herein the constant e_0 denotes the void ratio for $p \approx 0$, h_s has the dimension of stress and n is a dimensionless

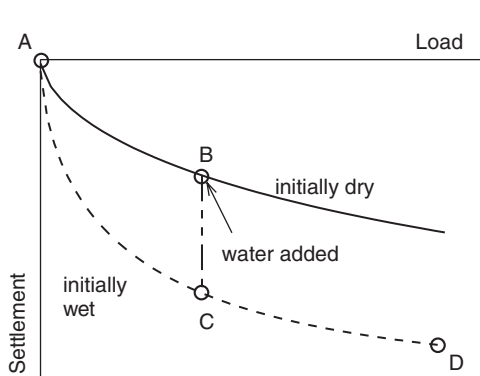


Figure 1. Compression behaviour of weathered broken rock in dry and wet states.

constant. The quantity h_s is called granular hardness (Gudehus 1996), which is related to the grain aggregate under isotropic compression and different from the hardness of an individual grain. Experimental investigations show that the quantity h_s reflects the isotropic pressure where grain crushing becomes dominant. More precisely, h_s represents the isotropic pressure $3p$ at which the compression curve in a semi-logarithmic representation shows the point of inflection while the exponent n is related to the inclination of the corresponding tangent (Figure 2). For high pressures the void ratio in Eq.(1) tends to zero, which can be explained by grain plastification and grain crushing.

In order to model the influence of the disintegration of stressed rockfill due to by a reaction with water, a degradation of the granular hardness with an increase of the moisture content of the solid material is assumed in the following. To this end the constant granular hardness h_s in Eq.(1) is replaced by the moisture dependent quantity h_s^* , i.e. (Bauer & Zhu 2004)

$$h_s^* = h_{s0} \psi(w). \quad (2)$$

Herein h_{s0} is the value of the granular hardness obtained for the dry material, i.e. h_{s0} is related to $\psi = 1$, and $\psi(w) \leq 1$ denotes the disintegration factor depending on the moisture content w of the grain material. A higher moisture content means a lower value of $\psi(w)$ and of h_s^* and consequently a higher compressibility of the material as illustrated in Figure 3. A time dependent behaviour of the degradation of the granular hardness can be accounted for in a simple manner by extending relation (2), which, however, is not considered in the present paper.

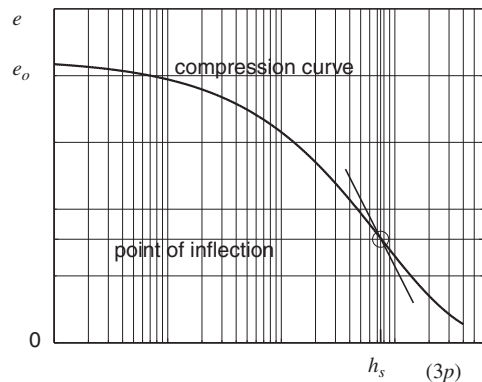


Figure 2. Isotropic compression relation (1) in a semilogarithmic representation.

3 THE PRESSURE DEPENDENCE OF THE LIMIT VOID RATIOS

It is experimentally evident that under the same pressure cohesionless granular materials can show different packing densities of the grain assembly so that the void ratio can range between a maximum void ratio e_i and a minimum void ratio e_d . In order to represent the range of possible void ratios for a given granular material it is convenient to consider the so-called phase diagram of grain skeletons (Gudehus 1997) as sketched in Figure 4. Herein the limit void ratios e_i and e_d are pressure dependent and they decrease with an increase of the mean pressure p . The upper bound, e_i , can be related to an isotropic compression starting from the loosest possible skeleton with grain contacts, i.e. there exists no homogeneous deformation which goes beyond $e = e_i$. Values of e_d will be achieved by cyclic

shearing with very low amplitudes and nearly fixed mean pressure.

By contrast, large monotonic shearing leads to a stationary state, which is characterized by a constant stress and constant void ratio. The void ratio in such a limit state, which is called critical void ratio, e_c , is again a pressure dependent quantity. Gudehus (1996) suggested postulating that the maximum void ratio e_i , the minimum void ratio e_d and the critical void ratio e_c decrease with the mean pressure according to

$$\frac{e_i}{e_{io}} = \frac{e_d}{e_{do}} = \frac{e_c}{e_{co}} = \exp \left[- \left(\frac{3p}{h_s^*} \right)^n \right], \quad (3)$$

where e_{io} , e_{do} and e_{co} are the corresponding values for $p \approx 0$ as shown in Figure 4. It is obvious that with a degradation of the granular hardness the pressure dependent limit void ratios and the critical void ratio are lower for $\psi(w) < 1$ as illustrated by the dashed curves in Figure 4.

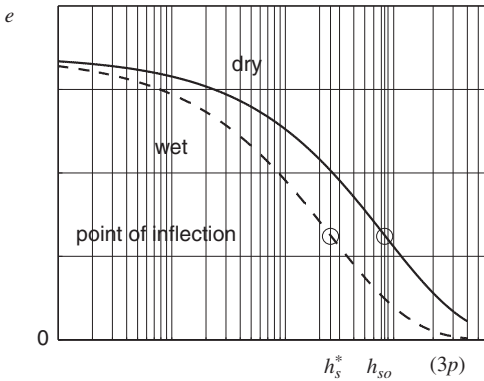


Figure 3. Influence of the moisture content on compression behaviour (solid curve: dry state, dashed curve: wet state).

4 THE HYPOPLASTIC MODEL

In order to model the dependence of the incremental stiffness of weathered broken rock on the current void ratio e , the stress state σ_{ij} , the rate of deformation $\dot{\epsilon}_{ij}$ and the moisture dependent granular hardness h_s^* the hypoplastic constitutive model by Gudehus (1996) and Bauer (1996) is extended using the moisture content w as an additional state quantity. The proposed constitutive equations for modelling non-linear and an elastic behaviour read:

$$\dot{\sigma}_{ij} = f_s \left[\hat{a}^2 \dot{\epsilon}_{ij} + (\hat{\sigma}_{kl} \dot{\epsilon}_{kl}) \hat{\sigma}_{ij} \right] + f_d \hat{a} (\hat{\sigma}_{ij} + \hat{\sigma}_{ij}^*) \nu \quad (4)$$

$$\dot{e} = (1 + e) \dot{\epsilon}_v, \quad (5)$$

with the normalised quantities: $\hat{\sigma}_{ij} = \sigma_{ij}/(-3p)$, $\hat{\sigma}_{ij}^* = \hat{\sigma}_{ij} - \delta_{ij}/3$, the Kronecker delta δ_{ij} and the volume strain rate $\dot{\epsilon}_v = \dot{\epsilon}_{11} + \dot{\epsilon}_{22} + \dot{\epsilon}_{33}$. Function \hat{a} in Eq.(4) is related to critical stress states which can be reached asymptotically under large shearing. With respect to the limit condition by Matsuoka & Nakai (1977) function \hat{a} can be represented as (Bauer 2000):

$$\hat{a} = \frac{\sin \varphi_c}{3 + \sin \varphi_c} \left[\sqrt{b} + \sqrt{\hat{\sigma}_{kl}^* \hat{\sigma}_{kl}^*} \right] \quad (6)$$

with

$$b = \frac{8/3 - 3(\hat{\sigma}_{kl}^* \hat{\sigma}_{kl}^*) + g \sqrt{3/2} (\hat{\sigma}_{kl}^* \hat{\sigma}_{kl}^*)^{3/2}}{1 + g \sqrt{3/2} (\hat{\sigma}_{kl}^* \hat{\sigma}_{kl}^*)^{1/2}},$$

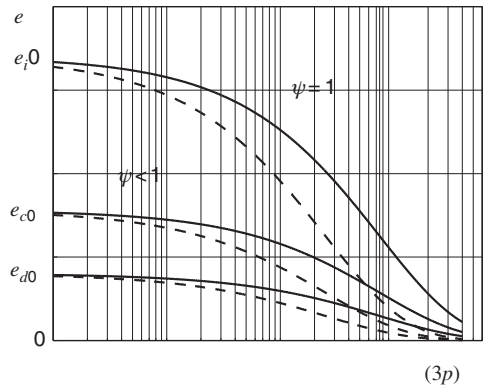


Figure 4. Influence of the moisture content on limit void ratios (solid curves: dry state, dashed curves: wet state).

and

$$g = -\sqrt{6} \hat{\sigma}_{kl}^* \hat{\sigma}_{lm}^* \hat{\sigma}_{mk}^* / (\hat{\sigma}_{kl}^* \hat{\sigma}_{kl}^*)^{3/2}.$$

Herein φ_c denotes the friction angle defined for the critical state under triaxial compression. The influence of the mean pressure and the current void ratio on the response of the constitutive equation (4) is taken into account with the stiffness factor f_s and the density factor f_d . The dilatancy behaviour, the peak stress ratio and strain softening depends on the density factor f_d , which represents a relation between the current void ratio e , the critical void ratio e_c and the minimum void ratio e_d , i.e.

$$f_d = \left(\frac{e - e_d}{e_c - e_d} \right)^\alpha, \quad (7)$$

where $\alpha < 0.5$ is a constitutive constant. The stiffness factor f_s is proportional to the moisture dependent granular hardness h_s^* and depends on mean stress p , i.e.

$$f_s = \left(\frac{e_i}{e} \right)^\beta \frac{h_s^* (1 + e_i)}{n h_i (\hat{\sigma}_{kl} \hat{\sigma}_{kl}) e_i} \left(\frac{3p}{h_s^*} \right)^{1-n}, \quad (8)$$

with

$$h_i = \frac{8 \sin^2 \varphi}{(3 + \sin \varphi)^2} + 1 - \frac{2\sqrt{2} \sin \varphi}{3 + \sin \varphi} \left(\frac{e_{io} - e_{do}}{e_{co} - e_{do}} \right)^\alpha,$$

and

$$h_s^* = h_{so} \psi(w).$$

Herein $\beta > 1$ is a constitutive constant. In (7) and (8) the current void ratio e is related to the pressure and moisture dependent maximum void ratio e_i , the minimum void ratio e_d and the critical void ratio e_c according to relation (3). A specific representation of the scalar function $\psi(w)$ can be obtained by curve fitting experimental data. Due to the lack of experimental data, only a distinction between the granular hardness in the dry and the water saturated state will be considered in the present paper.

The proposed hypoplastic model for weathered broken rock materials includes 9 constants which can be determined from simple index and element tests (Bauer 1996, Herle & Gudehus 1999). In the present paper the calibration of the constants is based on the experiments carried out by Kast (1992) with weathered broken granite. The following values were obtained:

$$\begin{aligned} \varphi_c &= 42^\circ, & h_{so} &= 75 \text{ MPa}, & n &= 0.6, \\ e_{io} &= 0.85, & e_{co} &= 0.39, & e_{do} &= 0.2, \\ \alpha &= 0.125, & \beta &= 1.05, & & \end{aligned}$$

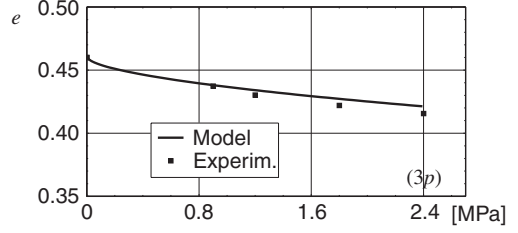


Figure 5. Isotropic compression of the specimen in the dry state ($e_0 = 0.46$, $\psi = 1$).

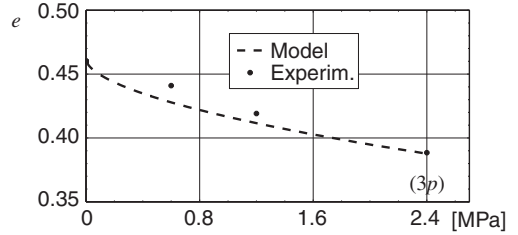


Figure 6. Isotropic compression of the specimen in the saturated state ($e_0 = 0.46$, $\psi = 0.34$).

for dry states of the solid material: $\psi = 1$,
for the water saturated state: $\psi = 0.34$.

It should be noted that in the present model the critical friction angle φ_c is assumed to be a constant because the experiments used for the present calibration did not show a clear influence of the moisture content on the critical friction angle.

4.1 Comparison of numerical simulations with experiments

The results obtained from the numerical simulation of homogeneous element tests are compared with experiments carried out by Kast (1992) for isotropic compression (Figure 5 and Figure 6) and triaxial compression (Figure 6–Figure 10).

Under isotropic compression starting from an initial void ratio of $e_0 = 0.46$ the densification is significantly higher for the water saturated state of the solid material (Figure 6) than for the dry state (Figure 5). For the isotropic pressure of $p = 0.8$ MPa the corresponding void ratios are $e = 0.418$ for the dry material and $e = 0.387$ for the saturated solid material. These are the initial states for the triaxial compression under a constant mean pressure of $p = 0.8$ MPa as shown in Figure 7 and Figure 8. As the initial void ratio is higher than the corresponding pressure dependent critical one, i.e. for $p = 0.8$ MPa $\rightarrow e_c = 0.34$

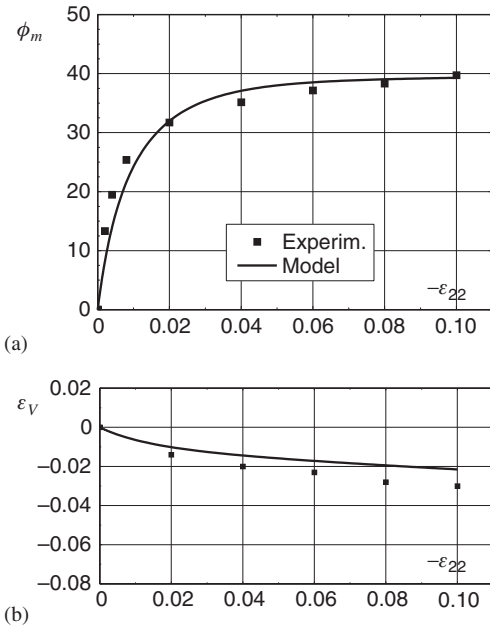


Figure 7. Triaxial compression of the specimen in the dry state ($e_0 = 0.418$, $\psi = 1$): (a) mobilized friction angle ϕ_m vs. axial strain ϵ_{22} , (b) volume strain ϵ_V vs. axial strain ϵ_{22} .

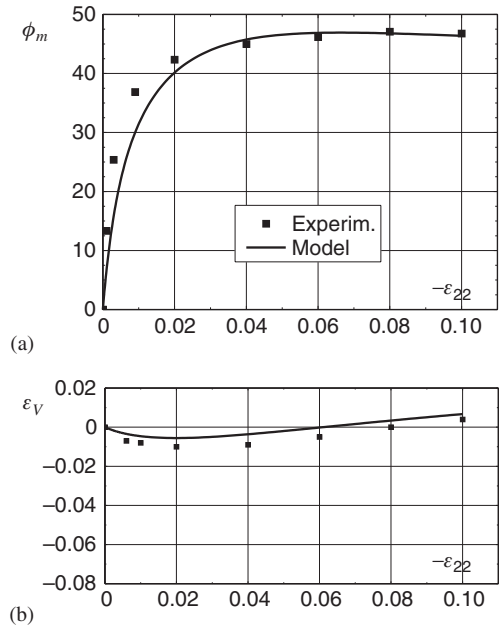


Figure 9. Triaxial compression of the specimen in the dry state ($e_0 = 0.29$, $\psi = 1$): (a) mobilized friction angle ϕ_m vs. axial strain ϵ_{22} , (b) volume strain ϵ_V vs. axial strain ϵ_{22} .

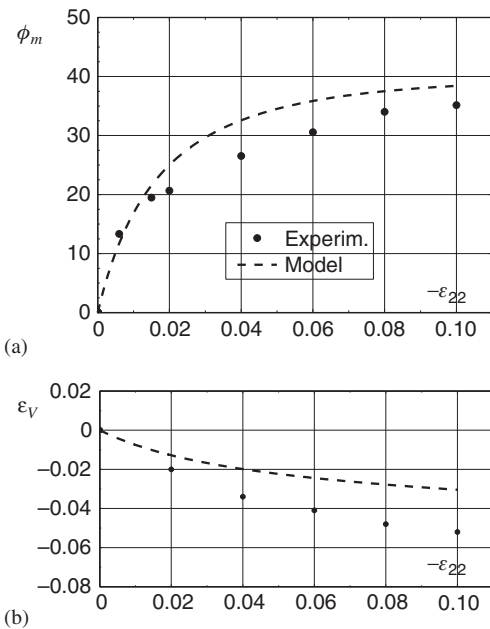


Figure 8. Triaxial compression of the specimen in the saturated state ($e_0 = 0.387$, $\psi = 0.34$): (a) mobilized friction angle ϕ_m vs. axial strain ϵ_{22} , (b) volume strain ϵ_V vs. axial strain ϵ_{22} .

for the dry material and $e_c = 0.31$ for the saturated material, the triaxial compression leads to a further densification for both the dry material and the saturated material. The increase of the mobilized friction angle ϕ_m with the vertical strain ϵ_{22} is more pronounced for the dry material (Figure 7) than for the saturated one (Figure 8), which is also in agreement with the experiments. In order to study the influence of an initially dense material the experiments for triaxial compression under a constant mean pressure of $p = 0.8$ MPa starting from $e = 0.29$ for the dry material and $e = 0.285$ for the saturated solid material are compared with the prediction of the hypoplastic model in Figure 9 and Figure 10. A comparison of Figure 7 with Figure 9 shows that the volume-strain behaviour is strongly influenced by the initial density and it differs for the dry and saturated states of the solid material. The additional densification is less pronounced and the maximum mobilized friction angle is higher for the initially dense material. A clear peak state for ϕ_m can only be detected for the dry and initially dense material (Figure 9). After the peak the value of ϕ_m slightly decreases with advanced vertical compression and it is accompanied by dilatancy. For the saturated and initially dense state of the material the dilatancy is less pronounced.

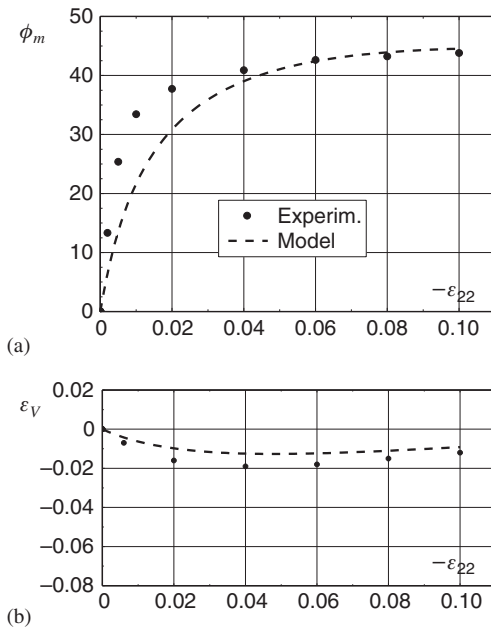


Figure 10: Triaxial compression of the specimen in the saturated state ($e_0 = 0.285$, $\psi = 0.34$): (a) mobilized friction angle ϕ_m vs. axial strain ϵ_{22} , (b) volume strain ϵ_v vs. axial strain ϵ_{22} .

5 CONCLUSIONS

A hypoplastic continuum model is presented to describe the essential properties of weathered broken rock materials. In particular an increase of the compressibility and a decrease of the limit void ratios with an increase of the moisture content of the solid material is modelled in a simplified manner using only a moisture dependent granular hardness. The constitutive equation for the evolution of the stress is based on nonlinear tensor-valued functions depending on the current void ratio, the stress, a moisture dependent granular hardness and the rate of deformation. As the hypoplastic concept does not need to distinguish between elastic and plastic deformation the calibration of the constitutive constants is rather easy. The calibration is carried out based on experiments for a weathered broken granite. It is demonstrated in this paper that the mechanical behaviour of an initially loose and dense material can be captured with a single set of constants. The comparison of the numerical simulations of isotropic compression and triaxial compression with experiments shows that the model captures the essential properties of weathered rockfill materials for both dry and water saturated grains.

ACKNOWLEDGEMENTS

Support from the Ministry for Science and Technology in China and the Federal Ministry of Education, Science and Culture in Austria for the bilateral scientific-technological co-operation between Hohai University in Nanjing and Graz University of Technology is greatly acknowledged.

REFERENCES

- Bauer, E. 1995. Constitutive Modelling of Critical States in Hypoplasticity. In Pande and Pietruszczak (eds.), *Proceedings of the Fifth International Symposium on Numerical Models in Geomechanics*: 3–10. Balkema press.
- Bauer, E. 1996. Calibration of a comprehensive hypoplastic model for granular materials. *Soils and Foundations* 36(1): 13–26.
- Bauer, E. 2000. Conditions for embedding Casagrande's critical states into hypoplasticity. *Mechanics of Cohesive-Frictional Materials* 5: 125–148.
- Bauer, E. & Zhu, Y. 2004. Constitutive modelling of the influence of pressure, density and moisture content on the mechanical behaviour of rockfill materials. In Wieland, Rena & Tan (eds.), *Proc. of the 4th Int. Conference on Dam Engineering*: 129–146. Nanjing: Balkema Publisher.
- Darve, F. 1991. Incrementally non-linear constitutive relationships. In Darve (ed.), *Geomaterials: Constitutive Equations and Modelling*: 213–237. Elsevier press.
- Gudehus, G. 1996. A comprehensive constitutive equation for granular materials. *Soils and Foundations* 36(1): 1–12.
- Gudehus, G. 1997. Attractors, percolation thresholds and phase limits of granular soils. In Behringer & Jenkins (eds.), *Powders and grains*: 169–183. Balkema.
- Herle, I. & Gudehus, G. 1999. Determination of parameters of a hypoplastic constitutive model from properties of grain assemblies. *Mechanics of Cohesive-Frictional Materials* 4: 461–486.
- Kast, K. 1992. Mechanisches Verhalten von Granitschüttungen. In *Veröffentlichungen des Institutes für Bodenmechanik und Felsmechanik der Universität Fridericiana in Karlsruhe*, Heft 125.
- Kolymbas, D. 1991. An outline of hypoplasticity. *Archive of Applied Mechanics* 3: 143–151.
- Matsuoka, H. and Nakai, T. 1977. Stress-strain relationship of soil based on the 'SMP'. In *Proc. of Speciality Session 9, IX Int. Conf. Soil Mech. Found. Eng.*: 153–162. Tokyo.
- Wu, W. & Bauer, E. 1993. A hypoplastic model for barotropy and pyknotropy of granular soils. In Kolymbas (ed.), *Proc. of the Int. Workshop on Modern Approaches to Plasticity*: 225–245. Elsevier.
- Wu, W., Bauer, E. & Kolymbas, D. 1996. Hypoplastic constitutive model with critical state for granular materials. *Mechanics of Materials* 23: 45–69.

A Generalized Plasticity approach for describing the behaviour of silty soils forming the Venetian lagoon basin

L. Tonni

Dpt. Distart, University of Bologna, Italy

S. Cola

Dpt. Image, University of Padova, Italy

M. Pastor

Centro de Estudios y Experimentación de Obras Públicas, Cedex, Madrid, Spain

ABSTRACT: In this paper, the mechanical response of silty sediments forming the upper profile of the Venice lagoon basin is modelled within a theoretical framework known as Generalized Plasticity. Starting from an existing formulation developed for the analysis of sand behaviour, some modifications are introduced in the original model in order to better simulate the stress-strain response of such non-active natural soils over a wide range of stresses and densities. A state dependent dilatancy is included in the constitutive equations. Moreover, according to recent developments on the isotropic compression of granular soils and on the modelling of softening in dense sands, adjustments to the plastic modulus expression are introduced. The approach is validated by comparing the model predictions with experimental results of drained triaxial compression tests on natural and reconstituted samples of soils, having different fine contents.

1 INTRODUCTION

Due to a very complex depositional history, the upper 100 m of the Venetian basin appear as a chaotic alternation of fine sediments, ranging from fine silty sands to silty clays.

High heterogeneity of such soils makes rather difficult any modelling within a unified theoretical framework.

In recent years attempts (Tonni *et al.*, 2003; Cola & Tonni, 2006) have been made to tackle this issue from the perspective of a rather versatile theoretical formulation known as Generalized Plasticity, with particular reference to a specific model for granular soils (*PZ* model) developed by Pastor *et al.* (1990). The preliminary application of the model to the analysis of Venetian soils resulted in rather acceptable predictions of the experimental behaviour but also suggested few corrections to be introduced within the constitutive equations in order to improve its predictive capability over a wide range of densities and stress levels.

In this paper we illustrate a simple development of the original *PZ* model, which allows to account for the internal-state dependence of granular soil behaviour without altering the general framework of the model itself.

Results of calibration studies on Venetian soils are discussed, with particular reference to such material parameters appearing in the modified relationships of dilatancy and plastic modulus.

2 BASIC FEATURES OF THE *PZ* MODEL

The *PZ* model was developed by Pastor, Zienkiewicz and Chan (Pastor *et al.*, 1990) as a particular type of Generalized Plasticity model, with the aim of predicting the granular soil behaviour under both monotonic and cyclic loading.

According to Generalized Plasticity premises, the model allows for plastic deformations at any stress level, irrespective of the stress increment direction, i.e. both in loading and unloading conditions. Moreover, no yield nor plastic potential surfaces are explicitly defined, but the gradients to the functions themselves.

A Generalized Plasticity model is fully determined by specifying the tangent elastic stiffness tensor \mathbf{D}_t^e , the loading direction \mathbf{n} , the plastic flow direction $\mathbf{m}_{L/U}$ and the plastic modulus $H_{L/U}$. Different expressions for the plastic modulus H and the plastic flow direction \mathbf{m} can be adopted, whether loading (L) or unloading (U) is occurring.

Therefore, the tangent elasto-plastic stiffness tensor \mathbf{D}_t can be expressed as follows:

$$(\mathbf{D}_{t,L/U})^{-1} = (\mathbf{D}_t^e)^{-1} + \frac{1}{H_{L/U}} [\mathbf{m}_{L/U} \otimes \mathbf{n}] \quad (1)$$

Since in this work the validation of the constitutive equations was restricted to drained triaxial tests in monotonic loading, the following brief outline of the PZ model is merely focused on the q - p' formulation under loading conditions (L).

In this case, the plastic flow direction $\mathbf{m}_L^T = (m_v, m_s)$ is given by:

$$m_v = \frac{d_g}{\sqrt{1+d_g^2}} \quad m_s = \frac{1}{\sqrt{1+d_g^2}} \quad (2a,b)$$

with the soil dilatancy d_g expressed as a linear function of the stress ratio η :

$$d_g = (1 - \alpha_g) \cdot (M_g - \eta) \quad (3)$$

M_g being the critical state line slope in the q - p' plane and α_g a material parameter.

The model assumes a non-associated flow rule, thus the loading direction \mathbf{n} is different from \mathbf{m} , but with similar expressions for its components n_v and n_s . These ones can indeed be still expressed by eqs. (2a,b), in which d_g must be replaced by d_f :

$$d_f = (1 - \alpha_f) \cdot (M_f - \eta) \quad (4)$$

M_f and α_f being material parameters.

For monotonic loading conditions the plastic modulus H_L can be expressed as follows:

$$H_L = H_0 \cdot p' \cdot H_f \cdot \{H_v + H_s\} \quad (5)$$

together with

$$H_f = \left(1 - \frac{\eta}{M_f} \cdot \frac{\alpha_f}{1 + \alpha_f} \right)^4 \quad (6a)$$

$$H_v = 1 - \eta / M_g \quad H_s = \beta_0 \beta_1 \exp(-\beta_0 \xi) \quad (6b,c)$$

Constants H_0 , β_0 and β_1 are constitutive parameters, while ξ is the accumulated deviatoric plastic strain.

Finally, the model assumes a non-linear elastic response of the soils, according to the following relationships:

$$dp' = K_o \cdot \frac{p'}{p'_0} \cdot d\varepsilon_v^e \quad dq = 3G_o \cdot \frac{p'}{p'_0} \cdot d\varepsilon_s^e \quad (7a,b)$$

in which K_0 and G_0 are the tangent bulk and shear moduli at the reference mean pressure p'_0 .

3 BASIC FEATURES OF VENETIAN SOILS

The 95% of sediments forming the upper 100 m of a typical Venetian soil profile can be grouped into 3 classes, i.e medium-fine sands with sub-angular grains (SP-SM), silts (ML) and very silty clays (CL). The remaining 5% is clay or peat.

Coarse sediments are predominantly composed of silicates and carbonates, while silts and silty clays, originated from mechanical degradation of sands, have a clayey mineral content never exceeding 20% in weight.

On the basis of a large amount of experimental data, Cola & Simonini (2002) observed that the stress-strain behaviour of such soils is mainly controlled by inter-particle friction. Moreover, since geotechnical parameters gradually vary as the grain size distribution changes from SP-SM to CL (except for organic samples), it seemed reasonable to relate a number of intrinsic soil parameters to a grain size index I_{GS} , defined as the ratio between the non-uniformity coefficient U and the mean particle diameter D_{50} . As regards the material constants defining the CSL, Cola & Simonini found that the dependence on I_{GS} can be expressed as follows:

$$\phi'_c = 38.0 + 1.55 \cdot \log I_{GS} \quad (8)$$

$$\lambda_c = 0.066 - 0.016 \cdot \log I_{GS} \quad (9)$$

$$e_{ref} = 1.13 + 0.10 \cdot \log I_{GS} \quad (10)$$

where e_{ref} is the critical void ratio at the reference mean pressure $p'_{ref} = 100$ kPa.

Another property related to I_{GS} is the maximum shear stiffness G_{max} , according to the following relationship:

$$\frac{G_{max}}{p'_{ref}} = D \cdot \frac{(2.97 - e)^2}{(1 + e)} \cdot \left(\frac{p'}{p'_{ref}} \right)^n \quad (11)$$

in which the exponent n can be assumed equal to 0.6 for all Venetian soil class, while D can be related to the grain size index by:

$$D = 470 + 60,4 \cdot \log I_{GS} \quad (12)$$

More recently Biscontin *et al.* (2006) applied the Pestana & Whittle approach (1995) to the analysis of the 1D compression behaviour of Venetian soils. Oedometric tests performed on the three different soil classes up to 30 MPa, showed that at very high pressures the 1D compression curves move towards the Limiting Compression Curve (LCC), whose equation is linear in the $\log e - \log \sigma'_v$ plane. The slope ρ_c of such line, intrinsically related to soil mineralogy, can be assumed as constant for almost all the Venetian soils, while its position – i.e. the void ratio e_1 at the reference pressure $\sigma'_v = 100$ kPa – depends on the fine content FF, that is the amount of particles smaller than $5 \mu\text{m}$.

4 EXPERIMENTAL DATABASE

The preliminary application (Tonni *et al.*, 2003) of the *PZ* formulation to the modelling of Venetian soil behaviour was carried out using a few drained triaxial tests on samples having different fine contents. Such tests provided experimental evidence that sandy and silty samples tended to form shear bands as soon as the maximum deviatoric stress was exceeded, thus making it difficult to detect the critical state condition.

In order to dispose of a more reliable set of experimental data for the current study, four $70 \text{ mm} \times 140 \text{ mm}$ cylindrical samples were tested in drained conditions, using an advanced triaxial cell provided with local displacement transducers and outfitted with lubricated heads for delaying as much as possible localization phenomena. Two further tests (SP-LD300 and SP-HD300), performed on 100 mm-diameter reconstituted samples of a medium-fine uniform sand,

prepared at different relative densities, were considered. Unlike the first group of tests, this latter was carried out using a standard triaxial equipment. The main characteristics of the samples are listed in Table 1.

Experimental results are plotted in Figure 1. It can be noted that although lubricated heads were used, localization was only delayed but not completely avoided.

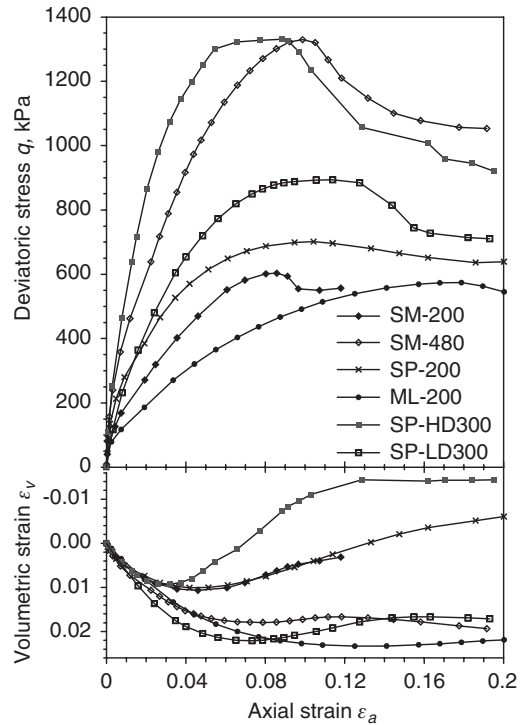


Figure 1. Deviatoric stress and volumetric strain vs. axial strain of all examined tests.

Table 1. Basic characteristics of the samples.

Test	SP-200	SM-200	SM-480	ML-200	SP-HD300	SP-LD300
Soil type	Fine sand	Sandy silt		Silt	Uniform fine sand	
Type of sample	Natural	Natural	Natural	Natural	Reconst.	Reconst.
Depth ⁽¹⁾ (m below MSL)	40.5	33.1	33.1	18.5	40.8	40.8
D_{50} (mm)	0.170	0.045	0.045	0.034	0.170	0.170
$U = D_{60}/D_{10}$	1.98	2.68	2.68	7.08	1.64	1.64
I_{GS}	0.086	0.017	0.017	0.0043	0.104	0.104
LL, IP	–	–	–	29.9	–	–
Fine fraction, FF ($d < 5 \mu\text{m}$) (%)	0.0	6.0	6.0	10.5	0.0	0.0
Cell pressure, σ_c (kPa)	200	200	480	200	300	300
Void ratio at consolidation, e_c	0.676	0.787	0.748	0.726	0.712	0.820

⁽¹⁾ All the samples were collected from MSgM2 bore, located at Malamocco at a point with bottom sea at 10,2m from MSL.

Except for ML-200, having a little fine content, all the other samples show a dilatant behaviour, thus confirming what observed by Cola & Simonini, i.e. that dilatancy of sandy and silty soils disappears at mean stress levels higher than 1 MPa or when the clay content is not negligible.

5 MODIFICATION OF THE PZ MODEL

5.1 A state dependent relationship for dilatancy

According to many contributions on sand modelling, the *PZ* model assumes that dilatancy d_g is a unique function of the stress ratio η , irrespective of the material internal state. One of the major shortcomings of such hypothesis is that different sets of constitutive parameters are needed for a single sand at different initial conditions.

In recent years attempts (i.e. Wan & Guo, 1998; Gajo & Muir Wood, 1999) have been made to treat dilatancy as a state-dependent quantity, with the concept of critical state as basis.

Following such developments on this issue, in the present work a modified expression of the plastic flow rule was introduced in the *PZ* constitutive equations, in order to address the limitations of the model in capturing the evolution of sand behaviour due to pressure and density changes.

In a previous study on Venetian soil behaviour, Cola & Tonni (2006) compared the predictive capability of two different flow rules, recently proposed by Li & Dafalias (2000) and Gajo & Muir Wood (1999) respectively, both expressing dilatancy as a function of the state parameter Ψ (Been & Jefferies, 1985). The authors observed that such relationships were able to successfully reproduce the experimental data, as well as giving similar responses.

In this work we considered the Li-Dafalias formulation and replaced the original dilatancy equation with

the following one:

$$d_g = D_0 \cdot [M_g \exp(m_d \psi) - \eta] \quad (13)$$

D_0 and m_d being material parameters.

Calibration of parameters appearing in eq.(13) can be easily performed by fitting the experimental ε_v - ε_a curve, taking into account that at the phase transformation point dilatancy becomes equal to zero. In order to avoid as much as possible multiple sets of parameters, after a preliminary estimation of D_0 and m_d based on every single test, a unique mean value was adopted for samples having the same I_{GS} . Final values of such parameters are listed in Table 2, together with all the other model parameters.

In Figure 2 the prediction of eq. (13) is compared with experimental data referring to SM-200 test, confirming the reliability of such approach.

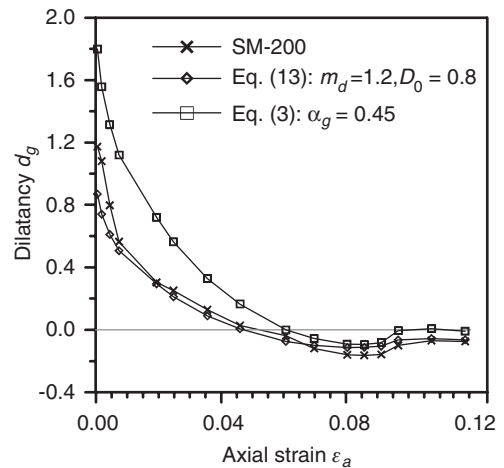


Figure 2. Experimental and predicted dilatancy for SM-200 test.

Table 2. Model parameters from calibration.

Test	SP-200	SM-200	SM-480	ML-200	SP-HD300	SP-LD300
ϕ'_c (°)	36.3	35.3	35.3	34.3	36.5	36.5
λ_c	0.083	0.095	0.095	0.104	0.082	0.082
e_{ref}	1.023	0.953	0.953	0.893	1.032	1.032
M_g	1.48	1.43	1.43	1.39	1.48	1.48
M_f	1.10	0.81	0.81	0.79	1.10	0.88
K_0 (kPa)	84575	64300	115160	63360	103550	88310
G_0 (kPa)	77221	58710	105150	57850	94540	80630
α_f	0.45	0.45	0.45	0.45	0.45	0.45
m_d	0.05	1.2	1.2	0.2	0.05	0.05
D_0	0.75	0.8	0.8	0.5	1	1
n	0.4	1	1	1	1.05	0.35
C	0.16	0.5	0.5	0.2	0.3	0.35

5.2 Plastic modulus at constant stress ratio compression

A large number of constitutive models for granular soils assume that under confining pressures not causing crushing of sand particles, constant stress ratio loadings do not induce any plastic deformation. Such an assumption implies that in isotropic compression the plastic modulus is infinite as long as the material remains within a “cap” limiting the elastic behaviour. This limitation is overcome in the *PZ* model, being the volumetric plastic strain inversely proportional to the material parameter H_0 , as evident from eqs. (6a–c) when $\eta = 0$.

In Tonni *et al.* (2003) the calibration of H_0 , performed by fitting the q - ε_a curves of three drained triaxial tests, gave values equal to 800, 1000 and 2800 for CL, ML and SP-SM samples respectively. Although such estimations were within the range of values proposed by Pastor *et al.* in their examples, the procedure did not appear sufficiently reliable.

Therefore in a recent work, Cola & Tonni (2006) examined alternative formulations on the isotropic compression of sands: attention was particularly focused on the studies of Pestana & Whittle (1995) and Jefferies & Been (2000), both expressing the plastic volumetric strain as a function of the distance between the current state and the crushing regime.

The application of such methods to the estimate of the initial value of H_0 for our six triaxial tests resulted in predictions which were almost equal or within the same order of magnitude, thus confirming the reliability of both formulations.

In this work, only the Jefferies-Been approach was considered because it relates the plastic modulus in isotropic compression H_0 to the same state parameter Ψ previously adopted in the dilatancy equation, thus allowing a unified modelling within the state parameter framework.

On the basis of several isotropic compression tests on Erksak sand, Jefferies & Been found that the plastic modulus K_p can be conveniently expressed in the form:

$$K_p = 0,3 \cdot \exp(-6,5\Psi) \cdot \left(1 + 1,3 \cdot \frac{p'}{\sigma_\chi} \right) \cdot K^e \quad (14)$$

where σ_χ is the apparent grain crushing pressure in shear, corresponding to a discontinuity of the CSL slope in the e - $\ln p'$ plane (Verdugo, 1992). According to experimental evidence, the apparent grain crushing pressure for Venetian soils was assumed equal to 1.2 MPa (see Cola & Tonni for further details).

As K_p coincides with H_L of eq.(5), it follows that H_0 can be determined as K_p/p' .

It must now be observed that eq.(14) was obtained by fitting experimental tests on Erksak sand samples,

hence a more sensitive calibration work would be necessary in order to properly apply such method to other granular soils. Nevertheless, as the Jefferies-Been formulation seemed to be in good agreement with the Pestana-Whittle approach (whose applicability to Venetian soils was verified by Biscontin *et al.*), we omitted any further calibration study.

5.3 General expression of the plastic modulus

The plastic modulus components proposed in the original *PZ* model and defined by eqs.(6a–c) account for the stiffness decrease as the shear plastic deformation increases and the critical state is drawing on. Such components are intended to reproduce some peculiar features of granular soil behaviour, i.e. failure at the critical state, softening of dense sands, the lack of dilatant response for loose sands.

In this work a simplified expression of the plastic modulus in monotonic loading is proposed. The modified formulation can be expressed as follows:

$$H_L = H_0 \cdot p' \cdot H_f^* \cdot H_s^* \quad (15)$$

in which H_0 is calculated according to the method illustrated in section 5.2, while components H_f^* and H_s^* are defined respectively as:

$$H_f^* = \left(1 - \frac{\eta}{M_g \cdot e^{-n\Psi}} \right) \quad H_s^* = \frac{C}{(C + \xi)^2} \quad (16a,b)$$

n and C being material constants.

The “failure” component H_f^* , replacing H_f , includes the idea that during the distortional process the sand is striving to attain the current peak stress ratio $\eta_p = M_g \cdot e^{-n\Psi}$. According to eq.(16a), η_p changes with Ψ in a way that results in $\eta_p > M_g$ for dense states and $\eta_p < M_g$ for loose states.

The concept of a virtual failure stress ratio depending on the material internal state was first introduced by Muir Wood *et al.* (1994) and later followed by other authors, as Manzari & Dafalias (1997) who adopted a linear function of the state parameter Ψ or Wang *et al.* (2002) who expressed such dependence in terms of the so called *state pressure index* I_p .

In this study the mobilized peak stress ratio was related to the state parameter Ψ through the exponential function defined in eq.(16a), as also recently proposed by Li & Dafalias (2000). The calibration of n can be easily performed at the drained peak stress state, at which eq.(16a) becomes equal to zero. Therefore it follows:

$$n = \frac{1}{\Psi_p} \cdot \ln \left(\frac{M_g}{\eta_p} \right) \quad (17)$$

where η_p and Ψ_p are the value of η and Ψ at the peak stress state, measured from experimental data.

As in the original *PZ* model, H_L is assumed to be dependent also on the accumulated deviatoric plastic strain ξ through the H_s^* component, which has the role of making the plastic stiffness degradation more smooth or more sharp.

The calibration of parameter C can be performed by fitting the q - ε_a curve. Estimations of n and C , referring to the six benchmark tests are listed in Table 2.

6 CALIBRATION AND FINAL REMARKS

In monotonic loading conditions the modified version of the *PZ* model requires the definition of 9 parameters. Table 2 summarizes the parameter values obtained through the calibration work here presented.

In this study, a number of parameters were rather easily estimated by using their dependence on the grain size index I_{GS} , through the relationships illustrated in section 2. Therefore, the quantities related to critical state conditions such as M_g or the internal state parameter Ψ were estimated from eqs.(8)–(10).

The elastic modulus G_0 was determined from eq.(11), reducing the value of G_{max} by a factor of 2.5,

as also suggested in Gajo & Muir Wood. The bulk modulus K_0 was consequently calculated through the well known relationship:

$$K_0 = \frac{2 \cdot (1 + \nu)}{3 \cdot (1 - 2\nu)} \cdot G_0 \quad (18)$$

with the Poisson ratio ν equal to 0.15.

The calibration procedure of dilatancy parameters m_d and D_0 has been already described in § 5.1: it's worth remarking here that different values of m_d and D_0 had to be considered for different soil samples. Nevertheless, a unique set of dilatancy parameters was adopted for soils having the same grain size index I_{GS} . Moreover, the small number of available tests did not allow to explain the m_d oscillations: difficulties in determining a reliable value of such parameter are maybe related to its dependence on the state parameter Ψ , which is in turn calculated from an empirical relationship having some degree of uncertainty.

In the absence of any particular test for determining α_f and M_f a constant value equal to 0.45 was adopted for the first parameter, while the latter was preliminary estimated according to suggestions of Zienkiewicz *et al.* (1999).

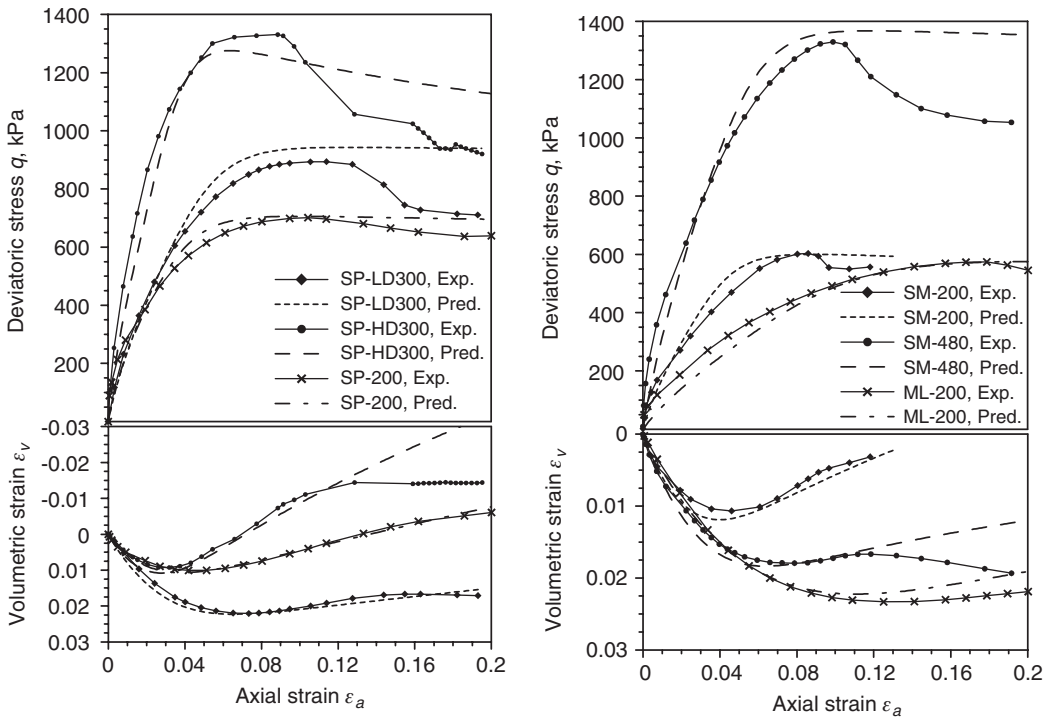


Figure 3. Experimental and predicted curves for the benchmark tests.

In Figure 3 the model predictions, plotted in terms of deviatoric stress and volumetric strain vs. axial strain, are compared with experimental data. Such predictions match fairly well the experimental plots for pre-peak deformations, while in the post-peak regime they show a lower rate of softening. However, due to localization phenomena, the steepness of the post-peak load-displacement curve can be significantly overestimated in laboratory tests and the softening, as experimentally observed, cannot be regarded as a material property. Therefore the calibration was performed so as to achieve the best fit of test data before reaching the post-peak regime, although numerical analyses were in general pushed up to an axial strain of around 20%. It's obvious that the comparison is no longer meaningful.

In conclusion, in this study we observed that the use of a state dependent dilatancy resulted in reliable predictions of the volumetric response through a unique set of constitutive parameters over a wide range of pressures.

On the other hand, the new expression of the plastic modulus has the advantage of embedding within a Generalized Plasticity approach recent developments on the isotropic compression behaviour of sands as well as on the internal state dependence of shear strength. The proposed formulation, although rather simple and susceptible of further improvements, allows capturing fairly well the peak strength conditions as well as the overall behaviour of Venetian soils.

Further improvements should be introduced in order to get a completely unified modelling of such natural soils over a full range of densities and stress levels.

REFERENCES

- Been, K. & Jefferies, M.G. 1985. A state parameter for sands. *Geotechnique*, 35(2): 99–112.
- Biscontin, G., Cola, S., Pestana, J.M. & Simonini, P. 2006. A unified compression model for the Venice lagoon natural silts. In printing.
- Cola, S. & Simonini, P. 2002. Mechanical behaviour of silty soils of the Venice lagoon as a function of their grading characteristics. *Canadian Geotechnical J.*, 39: 879–893.
- Cola, S. & Tonni, L. 2006. Adapting a Generalized Plasticity model to reproduce the stress-strain response of silty soils forming the Venice lagoon basin. *Geotechnical Symposium in Roma*, March 16 & 17, 2006. In printing.
- Gajo, A. & Muir Wood, D. 1999. Severn-Trent sand: a kinematic-hardening constitutive model: the q - p formulation. *Geotechnique* 49(5): 595–614.
- Jefferies, M. & Been, K. 2000. Implications for critical state theory from isotropic compression of sand. *Geotechnique* 50(4): 419–429.
- Li, X.S. & Dafalias, Y.F. 2000. Dilatancy for cohesionless soils. *Geotechnique*, 50(4): 449–460.
- Manzari, M.T. & Dafalias, Y.F. 1997. A two-surface critical plasticity model for sand. *Geotechnique* 47(2): 255–272.
- Muir Wood, D., Belkheir, K. & Liu, D.F. 1994. Strain softening and state parameter for sand modeling. *Geotechnique* 44(2): 335–339.
- Pastor, M., Zienkiewicz, O.C. & Chan, A.H.C. 1990. Generalized plasticity and the modelling of soil behaviour. *Int. J. Numer. and Anal. Methods in Geomechanics*, 14: 151–190.
- Pestana, J.M. & Whittle, A.J. 1995. Compression model for cohesionless soils. *Geotechnique*, 45(4): 611–632.
- Tonni, L., Gottardi, G., Cola, S., Simonini, P., Pastor, M. & Mira, P. 2003. Use of Generalized Plasticity to describe the behaviour of a wide class of non-active natural soils. *IS Lyon 2003*: 1145–1153, Di Benedetto *et al.* (eds), Swets & Zeitlinger: Lisse.
- Verdugo, R. 1992. The critical state of sands (discussion). *Geotechnique* 42(4): 655–663.
- Wan, R.G. & Guo, P.J. 1998. A simple constitutive model for granular soils: modified stress-dilatancy approach. *Computers and Geotechnics*, 22(2): 109–133.
- Wang, Z.L., Dafalias, Y.F., Li, X.S. & Makdisi, F.I. 2002. State pressure index for modelling sand behaviour. *J. Geotech. Geoenviron. Eng.*, 128(6): 511–519.
- Zienkiewicz, O.C., Chan, A.H.C., Pastor, M., Schrefler, B.A. & Shiomi, T. 1999. *Computational Geomechanics*. Wiley.

Hypoplastic description of the frictional behaviour of contacts

M. Arnold & I. Herle

Institute of Geotechnical Engineering, TU Dresden

ABSTRACT: Hypoplasticity is often used for analysing soil-structure interactions via the finite element method. A hypoplastic description of the frictional contact between soil and structures of different roughness is needed in order to provide a consistent modelling of the interface behaviour. Following this requirement, a new contact model based on hypoplasticity is presented. It takes into account not only the pressure and density effects, but also the roughness of the structure surface. Furthermore, it enables the modelling of line contacts in 2D as well as surface contacts in 3D. In addition to the hypoplastic parameters, the proposed formulation includes the relative surface roughness and the thickness of the shear zone as additional model constants. The results of simple shear tests are compared with calculations using the new contact formulation. An example for the application in a boundary value problem is also presented.

1 INTRODUCTION

Hypoplastic constitutive models have been proved to be well suited for the description of the mechanical behaviour of soils. Numerical predictions of several field problems demonstrated a good coincidence between the calculated and measured behaviour.

Many geotechnical boundary value problems deal with an interaction between the soil and the structure. Numerical approaches for the modelling of this interaction mostly include virtual contact surfaces requiring their own constitutive model. Usually, an elastoplastic Mohr-Coulomb model is used which yields the maximum tangential friction stress proportional to the applied normal stress (see Fig. 1a). However, this may be considered as an oversimplification of the contact behaviour. Whereas the hypoplastic model of the surrounding soil takes into account variations in stiffness and strength due to changes of the stress level and density, the Mohr-Coulomb description of the contact disregards these effects. There is an inconsistency between the modelling of the soil and the modelling of the contact behaviour, the latter neglecting also the experimental evidence (see Fig. 1b).

This unsatisfactory situation initiated a development of a new contact model based on and being consistent with the hypoplastic constitutive model. The first approach was presented by Herle and Nübel (1999) for plain-strain conditions (line contacts) and further extended by Gutjahr (2001, 2003). Nevertheless, such a model has been missing for general stress and strain conditions (surface contacts).

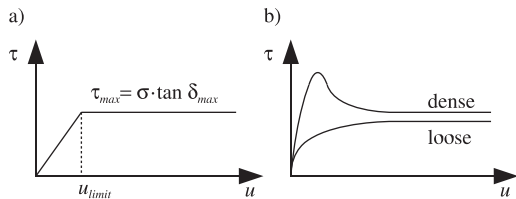


Figure 1. Mobilisation of the tangential contact stress.
 a) Mohr-Coulomb contact model b) test.

2 SOIL-STRUCTURE INTERACTIONS WITH CONTACT SURFACES

The classical approach for the modelling of interaction phenomena with the finite element method deals with contact elements. However, a common restriction on small strains implies inaccurate results for finite relative movements.

An application of contact surfaces is a more general approach. The authors used this approach within the finite element code ABAQUS and implemented the contact model via a master-slave concept. In this case, the surfaces consist of node sets. Two surfaces are assigned to each other as a master-slave contact pair.

In each time increment the contact condition of the penetration of a slave node into any part of the master surface is tested. In case of contact the normal stress is calculated based on the penetration depth. Using the finite-sliding formulation the master surface as well as the slave surface may be deformed. The normal vector of the contact is determined as the perpendicular

from the slave node on the master surface. For soil-structure interactions it is recommended to define the surface of the structure as a master surface and the soil surface as a slave surface.

Based on these preconditions the normal contact stress σ , the vector of the relative tangential displacements of a slave node to the master surface $[u_x, u_y]$ and the rates of these variables are known. To calculate the rates of the tangential contact stresses $[\dot{\tau}_x, \dot{\tau}_y]$ a further development of the model by Herle and Nübel (1999) has been undertaken.

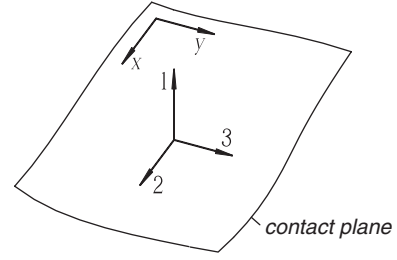


Figure 2. Global and contact coordinate systems.

3 HYPOPLASTIC CONTACT DESCRIPTION

3.1 Used constitutive formulation

The contact description is derived from the hypoplastic constitutive equations for continuum. It uses the hypoplastic version by von Wolffersdorff (1996), which performs well in particular for coarse-grained soils at monotonic stress paths. In tensor notation it reads:

$$\overset{\circ}{\mathbf{T}} = f_b f_e \frac{1}{\text{tr}(\hat{\mathbf{T}} \cdot \hat{\mathbf{T}})} [F^2 \mathbf{D} + a^2 \hat{\mathbf{T}} \text{tr}(\hat{\mathbf{T}} \cdot \mathbf{D}) + f_d a F (\hat{\mathbf{T}} + \hat{\mathbf{T}}^*) \|\mathbf{D}\|] \quad (1)$$

with

$$\hat{\mathbf{T}} = \frac{\mathbf{T}}{\text{tr} \mathbf{T}}, \quad \hat{\mathbf{T}}^* = \hat{\mathbf{T}} - \frac{1}{3} \mathbf{1} \quad \text{and} \quad a = \frac{\sqrt{3}(3 - \sin \varphi_c)}{2\sqrt{2} \sin \varphi_c}.$$

Considering the Matsuoka-Nakai failure condition, the stress coefficient F is given by

$$F = \sqrt{\frac{1}{8} \tan^2 \psi + \frac{2 - \tan^2 \psi}{2 + \sqrt{2} \tan \psi \cos 3\vartheta}} - \frac{1}{2\sqrt{2}} \tan \psi$$

with

$$\cos 3\vartheta = -6 \frac{\text{tr}(\hat{\mathbf{T}}^* \cdot \hat{\mathbf{T}}^* \cdot \hat{\mathbf{T}}^*)}{[\text{tr}(\hat{\mathbf{T}}^* \cdot \hat{\mathbf{T}}^*)]^{\frac{3}{2}}} \quad \text{and} \quad \tan \psi = \sqrt{3} \|\hat{\mathbf{T}}^*\|.$$

Pressure and density dependency are considered by the coefficients

$$f_e = \left(\frac{e_c}{e}\right)^\beta, \quad f_d = \left(\frac{e - e_d}{e_c - e_d}\right)^\alpha \quad (2)$$

and

$$f_b = \frac{h_s}{n} \left(\frac{e_{i0}}{e_{c0}}\right)^\beta \frac{1 + e_i}{e_i} \left(\frac{-\text{tr} \mathbf{T}}{h_s}\right)^{1-n} \cdot \left[3 + a^2 - a\sqrt{3} \left(\frac{e_{i0} - e_{d0}}{e_{c0} - e_{d0}}\right)^\alpha\right]^{-1} \quad (3)$$

The pressure dependent void ratios are described by

$$\frac{e_i}{e_{i0}} = \frac{e_c}{e_{c0}} = \frac{e_d}{e_{d0}} = \exp \left[- \left(\frac{-\text{tr} \mathbf{T}}{h_s} \right)^n \right] \quad (4)$$

3.2 Derivation of the contact formulation

A contact plane is given by the contact coordinate system (x, y) and is put into the global coordinate system $(1, 2, 3)$ of the continuum, having $x \parallel 2$ and $y \parallel 3$ (see Fig. 2)

This leads for the stress tensor \mathbf{T} to the stresses $\sigma_{11} = \sigma$, $\sigma_{12} = \tau_x$ and $\sigma_{13} = \tau_y$, in which σ is the normal contact stress (compression negative) and τ_x as well as τ_y are the shear stresses in the 2D contact plane. The other two normal stresses are assumed $\sigma_{22} = \sigma_{33} = \sigma$ and the out-of-plane shear stress is assumed $\sigma_{23} = 0$. Thus, the stress tensor reads

$$\mathbf{T} = \begin{bmatrix} \sigma_{11} & \sigma_{12} & \sigma_{13} \\ \sigma_{12} & \sigma_{22} & \sigma_{23} \\ \sigma_{13} & \sigma_{23} & \sigma_{33} \end{bmatrix} \stackrel{\text{def}}{=} \begin{bmatrix} \sigma & \tau_x & \tau_y \\ \tau_x & \sigma & 0 \\ \tau_y & 0 & \sigma \end{bmatrix} \quad (5)$$

The strain rate tensor is described analogously. The strain rates $\dot{\varepsilon}_i$ with $i \in \{1, 2, 3\}$ are set to be equal to the strain rate $\dot{\varepsilon}$ perpendicular to the contact. The shear strain rates $\dot{\varepsilon}_{12}$ und $\dot{\varepsilon}_{13}$ are obtained from $\dot{\gamma}_x/2$ and $\dot{\gamma}_y/2$. Because of Equation 5 $\dot{\varepsilon}_{23} = 0$ is required. This leads to the strain rate tensor

$$\mathbf{D} = \begin{bmatrix} \dot{\varepsilon}_{11} & \dot{\varepsilon}_{12} & \dot{\varepsilon}_{13} \\ \dot{\varepsilon}_{12} & \dot{\varepsilon}_{22} & \dot{\varepsilon}_{23} \\ \dot{\varepsilon}_{13} & \dot{\varepsilon}_{23} & \dot{\varepsilon}_{33} \end{bmatrix} \stackrel{\text{def}}{=} \begin{bmatrix} \dot{\varepsilon} & \frac{\dot{\gamma}_x}{2} & \frac{\dot{\gamma}_y}{2} \\ \frac{\dot{\gamma}_x}{2} & \dot{\varepsilon} & 0 \\ \frac{\dot{\gamma}_y}{2} & 0 & \dot{\varepsilon} \end{bmatrix} \quad (6)$$

he tensors of the relative stress $\hat{\mathbf{T}}$ are obtained with $\bar{\tau}_x \stackrel{\text{def}}{=} \tau_x/3\sigma$ and $\bar{\tau}_y \stackrel{\text{def}}{=} \tau_y/3\sigma$ as

$$\hat{\mathbf{T}} = \frac{\hat{\mathbf{T}}}{\text{tr}(\mathbf{T})} = \begin{bmatrix} \frac{1}{3} & \bar{\tau}_x & \bar{\tau}_y \\ \bar{\tau}_x & \frac{1}{3} & 0 \\ \bar{\tau}_y & 0 & \frac{1}{3} \end{bmatrix} \quad (7)$$

The coefficient F incorporating the Matsuoka/Nakai limit condition is derived to

$$F = \sqrt{1 - \frac{9}{4}(\bar{\tau}_x^2 + \bar{\tau}_y^2)} - \frac{\sqrt{3}}{2} \sqrt{\bar{\tau}_x^2 + \bar{\tau}_y^2} \quad (8)$$

The coefficients describing pressure and density effects f_b, f_e and f_d can be determined using $\text{tr}\mathbf{T} = 3\sigma$.

The coefficient a follows from the critical state behaviour (Herle & Nübel 1999) with critical void ratio $e = e_c$, i.e. $f_d = 1$. The constant volume condition during shearing in the critical state corresponds to $\dot{\varepsilon}_v = 3\dot{\varepsilon} = 0$. The stresses remain constant, thus stress rates vanish: $\dot{\sigma} = \dot{\tau}_x = \dot{\tau}_y = 0$.

Considering Equations 5–8, the critical state can be described by Equation 1 as

$$\mathbf{0} = \frac{f_b f_e}{\frac{1}{3} + 2\bar{\tau}_x^2 + 2\bar{\tau}_y^2} \left\{ F^2 \begin{bmatrix} 0 & \frac{\dot{\gamma}_x}{2} & \frac{\dot{\gamma}_y}{2} \\ \frac{\dot{\gamma}_x}{2} & 0 & 0 \\ \frac{\dot{\gamma}_y}{2} & 0 & 0 \end{bmatrix} + a^2 \begin{bmatrix} \frac{1}{3} & \bar{\tau}_x & \bar{\tau}_y \\ \bar{\tau}_x & \frac{1}{3} & 0 \\ \bar{\tau}_y & 0 & \frac{1}{3} \end{bmatrix} (\bar{\tau}_x \dot{\gamma}_x + \bar{\tau}_y \dot{\gamma}_y) + \frac{aF}{\sqrt{2}} \begin{bmatrix} \frac{1}{3} & 2\bar{\tau}_x & 2\bar{\tau}_y \\ 2\bar{\tau}_x & \frac{1}{3} & 0 \\ 2\bar{\tau}_y & 0 & \frac{1}{3} \end{bmatrix} \sqrt{\dot{\gamma}_x^2 + \dot{\gamma}_y^2} \right\}. \quad (9)$$

The identical equations from the main diagonal read

$$0 = \frac{a^2}{3} (\bar{\tau}_x \dot{\gamma}_x + \bar{\tau}_y \dot{\gamma}_y) + \frac{aF}{3\sqrt{2}} \sqrt{\dot{\gamma}_x^2 + \dot{\gamma}_y^2}.$$

In case of uniaxial shearing in direction x with $\bar{\tau}_y = \dot{\gamma}_y = 0$ the parameter a comes out as

$$a = -\frac{F}{\sqrt{2}\bar{\tau}_x} = \sqrt{\frac{1}{2\bar{\tau}_x^2} - \frac{9}{8}} - \frac{\sqrt{3}}{2\sqrt{2}}. \quad (10)$$

At the critical state for perfectly rough surfaces – like shear zones in sand – the ratio of shear stress and normal stress is limited by

$$\left| \frac{\tau_x}{\sigma} \right| = \tan \varphi_c = 3|\bar{\tau}_x|. \quad (11)$$

Putting this into Equation 10 one obtains

$$a = 3\sqrt{\frac{1}{2 \tan^2(\varphi_c)} - \frac{1}{8}} - \frac{\sqrt{3}}{2\sqrt{2}}. \quad (12)$$

In case of less rough surfaces the frictional coefficient is $\mu \leq \tan \varphi$. It is usual to define the ratio between the maximum of interface shear stress and the angle of internal friction (here named κ)

$$\kappa = \frac{\delta_{max}}{\varphi} \quad (13)$$

with $0 < \kappa \leq 1$. In analogy to the procedure of Gutjahr (2001) this ratio is assumed to be valid at the critical state, too:

$$\left| \frac{\tau_x}{\sigma} \right| = \tan(\kappa\varphi_c) = 3|\bar{\tau}_x|. \quad (14)$$

Instead of Equation 12 one obtains

$$a = 3\sqrt{\frac{1}{2 \tan^2(\kappa\varphi_c)} - \frac{1}{8}} - \frac{\sqrt{3}}{2\sqrt{2}}. \quad (15)$$

Equation 15 with $\kappa \leq 1$ makes the contact behaviour more soft. To adjust the mobilisation of the shear stresses to the results of contact shear tests, e.g. Kishida & Uesugi (1987) and Tejchmann (1989), the additional coefficient

$$f_c = \frac{1}{\kappa} \quad (16)$$

has been introduced.

A summary of all three equations for the description of the contact behaviour reads in vectorial notation

$$\begin{bmatrix} \dot{\sigma} \\ \dot{\tau}_x \\ \dot{\tau}_y \end{bmatrix} = \frac{f_b f_e f_c}{\frac{1}{3} + 2\bar{\tau}_x^2 + 2\bar{\tau}_y^2} \left\{ F^2 \begin{bmatrix} \dot{\varepsilon} \\ \frac{\dot{\gamma}_x}{2} \\ \frac{\dot{\gamma}_y}{2} \end{bmatrix} + a^2 \begin{bmatrix} \frac{1}{3} \\ \bar{\tau}_x \\ \bar{\tau}_y \end{bmatrix} (\dot{\varepsilon} + \bar{\tau}_x \dot{\gamma}_x + \bar{\tau}_y \dot{\gamma}_y) + f_d a F \begin{bmatrix} \frac{1}{3} \\ 2\bar{\tau}_x \\ 2\bar{\tau}_y \end{bmatrix} \sqrt{3\dot{\varepsilon}^2 + \frac{\dot{\gamma}_x^2}{2} + \frac{\dot{\gamma}_y^2}{2}} \right\}. \quad (17)$$

3.3 Shear strains and relative shear displacements

Due to its origin in continuum mechanics, Equation 17 contains the shear strains γ_i with $i \in \{x, y\}$. These strains are linked with relative displacements u_i between soil and surface of the structure via the thickness of the shear zone d_s (Fig. 3). In the modeling approach with contact surfaces this thickness is only virtual. For shear strain one can write

$$\tan \gamma_i = \frac{u_i}{d_s}. \quad (18)$$

The thickness of the shear zone depends on the roughness of the surface as well as on the average particle size d_{50} and has been found to be $2 \cdot d_{50} \dots 6 \cdot d_{50}$ for sand-steel contacts and $7 \cdot d_{50} \dots 20 \cdot d_{50}$

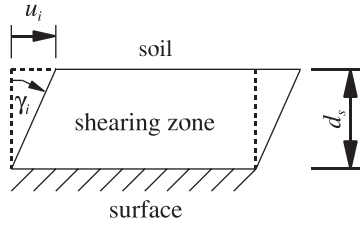


Figure 3. Relation between shear strains and relative shear displacements.

for shear zones in coarse grained soils (Maier 2002; Teichmann 1989).

Thus, additionally to eight hypoplastic material parameters, the contact description requires to define the coefficient of relative contact friction κ as well as the (virtual) thickness of the contact shear zone d_s .

3.4 Remarks on the implementation

Using the user subroutine `umat.f` of Nübel (1999), the contact description has been implemented into the user subroutine `fric.f` for ABAQUS using the programming language FORTRAN.

In each time increment the subroutine receives as input parameters among others the contact stress rates $\dot{\sigma}$ and the rates of displacements \dot{u}_i from the main ABAQUS code. Hence, Equation 17 is a mixed problem – besides of the shear stress rates $\dot{\tau}_x$ and $\dot{\tau}_y$, also the strain rate $\dot{\epsilon}$ perpendicular to the contact has to be determined (Niemunis 2004). Further remarks on the implementation can be found in Arnold (2005).

4 COMPARISON WITH RESULTS OF CONTACT SHEAR TESTS

The contact shear behaviour has been tested in the laboratory using standard experimental devices like direct shear, ring torsion and simple shear apparatus. Sometimes these devices have been adapted to the special problem. E.g. Kishida and Uesugi (1987) have used a special simple shear apparatus with a cross-sectional area of the sample of 100×400 mm. This apparatus has been capable to separate shear deformations of the tested sand from relative displacements between soil and solid surface.

In their tests Toyura sand has been used. The limit void ratios e_{max} and e_{min} have been 0.98 and 0.60, respectively. The average particle size d_{50} has been 0.19 mm. The initial state density index I_D corresponded approximately to 0.9 at a normal stress of 78 kPa. The used steel plates have had relative surface roughnesses R_{max} of 2.4, 20.5 and 46 μm over a length of 2.5 mm.

The calculations with the hypoplastic contact model use the hypoplastic parameters of the Toyura sand described by Herle and Gudehus (1999). The thickness

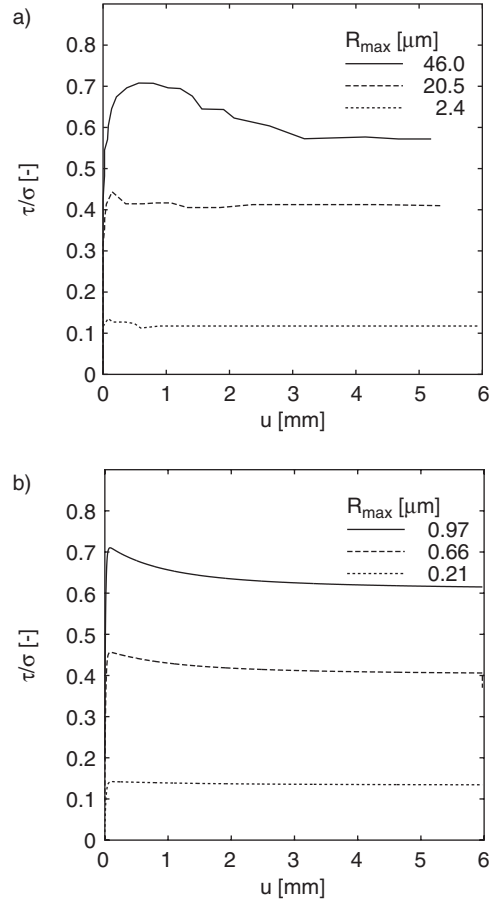


Figure 4. Mobilisation of the shear stress ratio. a) Test results of Kishida & Uesugi (1987) b) Simulation.

of the shear zone has been assumed to $10 \cdot d_{50}$, which corresponds to the upper range of the values given in Section 3.3. The parameter κ is obtained from Equation 13. The angle of contact friction δ_{max} follows from the maximum shear/normal stress ratio in the experiments. The angle of peak friction φ is determined from the hypoplastic simulations with $\kappa = 1$.

The observed frictional behaviour of contacts – independently of the surface roughness – is characterized by a very fast mobilisation of the peak shear stress, see Figure 4a. This is followed by a fast transition into the residual state. The peak value as well as the residual value of the shear resistance depend on the roughness of the surface.

Figure 4b well demonstrates a good reproduction of the test results by the hypoplastic simulation. This includes not only the peak shear stresses but also the transition to the residual stresses for large relative displacements, which typically occur at frictional contacts.

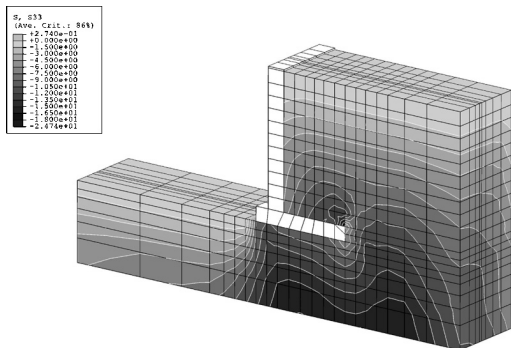


Figure 5. Vertical stresses in the soil, model test EWS15, in kN/m^2 .

5 APPLICATION TO A BOUNDARY VALUE PROBLEM

The presented hypoplastic contact model has been applied to a boundary value problem of the earth pressure acting on a cantilever retaining wall. Several model tests have been performed prior to the numerical simulations. The model tests have been described in detail by Arnold (2004).

The numerical simulations have had two aims. First, to study various boundary effects during the model tests. Second, to check the suitability of the finite element model for further plain strain calculations.

5.1 Modelling

In order to get a realistic reproduction of the model tests, it has been necessary to take into account important boundary effects of the experimental setup, including spatial effects. Thus, a 3D model has been necessary (Figure 5).

Beside hypoplastic soil behaviour, the numerical model has included hypoplastic modelling of the contacts between soil and the wall and between soil and the testing box, respectively. The special wall structure consisting of two non-instrumented side parts and one middle part covered with load cells and the layer-by-layer backfilling procedure have been considered, too. Arnold (2004) contains a detailed description of this model.

5.2 Stresses in the soil

In the sequel, some selected results of the final stage are presented in order to demonstrate the influence of the contact friction.

To illustrate the stress conditions in the soil, Figure 5 shows a typical distribution of vertical stresses σ_z . In this figure, the front view shows the symmetry plane of the model test. The other vertical surfaces of the soil continuum are the side walls of the testing box.

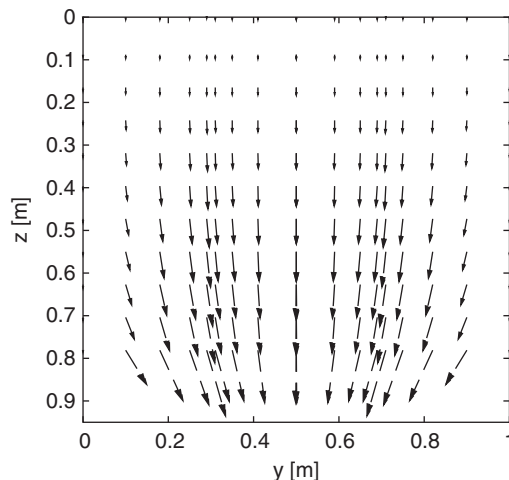


Figure 6. Distribution of the contact shear stress (tangential earth pressure) at the wall stem.

The formation of stress concentrations at the end of the wall heel and below the wall toe are well visible. Both concentrations result from the wall rotation away from the backfill.

In a homogenous half-space, vertical stress increases linearly with depth due to the overburden load. In a perfectly smooth testing box this should be observed at the continuum boundary, too. However, in reality a pronounced decrease of the vertical stress at the soil boundary appears, which is known as a silo effect. This can be well observed at the external right boundary. It is caused by the friction at the side walls of the testing box. Due to the increasing overburden, soil settles during backfilling. Relative movements occur between soil and walls which mobilise shear stresses at the non-smooth walls.

A similar behaviour can be observed between soil and the retaining wall. Also in this plane shear stresses increase and become to tangential components of the earth pressure on the retaining wall. Consequently, the vertical stress at the edge between the wall stem and the wall heel is reduced.

5.3 Distribution of the contact shear stress

Figure 6 shows the distribution of the contact shear stress (tangential earth pressure) at the wall stem. Vertical relative movements are caused by the backfilling process. These movements induce vertically oriented contact shear stresses, which increase with the overburden load. Due to the low earth pressure at the edge between the wall stem and the side wall ($y \rightarrow 0$ m and $y \rightarrow 1$ m), the contact shear stress becomes small as well.

One can also observe that the deformation of the load cells in the middle part causes horizontal deformations

with corresponding horizontal contact shear stresses. They are oriented towards the middle part.

The inclination of the earth pressure can be calculated from the contact shear stress (tangential earth pressure) and the normal part of the earth pressure.

$$\tan \delta' = \frac{\sqrt{e_{ty}^2 + e_{tz}^2}}{e_n} \quad (19)$$

and is shown in Figure 7. The earth pressure inclination varies between 0° at the bottom of the wall stem to approximately 45° in some parts of the wall head. The low inclination at the bottom is caused by the small relative displacements in this area. The high values at the top can be explained by the low stress level, and thus by the high peak frictional angle, of the soil at the surface of the backfill.

The earth pressure inclination is obviously not constant and depends on the stress level and the relative displacements. Nevertheless, the inclination in the middle part of the wall varies only a little bit around 30° .

6 CONCLUSIONS

The presented hypoplastic contact model enables a consistent modelling of contacts between soil and surfaces of various roughnesses. The general stress formulation takes into the account many important effects of the soil behaviour. In particular, the presented model has the ability to describe the pressure and density effects of coarse grained soils on solid surfaces with only one set of parameters. In addition to the standard hypoplastic parameters, the model formulation includes the relative surface roughness and the thickness of the shear

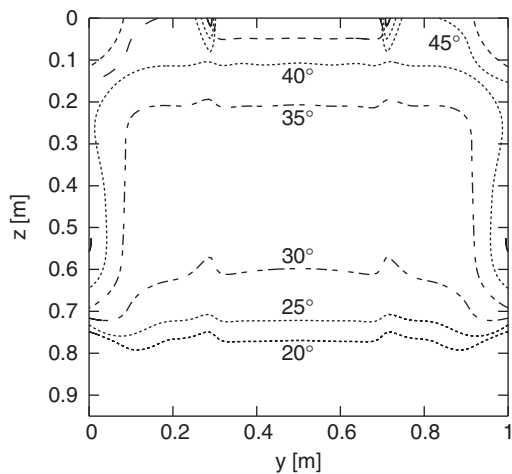


Figure 7. Distribution of the earth pressure inclination δ' at the wall stem.

zone as additional constants. Both constants are easy to estimate from published experimental results on the contact behaviour.

The contact constitutive model has been successfully validated in simulations of direct shear tests. Subsequently, it has been applied in a boundary value problem of the earth pressure acting on a cantilever retaining wall. The comparison between the results of the model tests with the results of 3D finite element analyses confirms a good capability of the model to capture all important phenomena of the contact behaviour.

REFERENCES

- Arnold, M. 2004. Zum Erd- und Auflastdruck auf Winkelstützwände im Gebrauchszustand. Dissertation. Heft 13, Mitteilungen des Instituts für Geotechnik der TU Dresden.
- Arnold, M. 2005. Hypoplastische Beschreibung zweidimensionaler Reibungskontakte. In I. Herle (ed.), *OHDE-Kolloquium 2005*: 67–86. Institut für Geotechnik der TU Dresden, Heft 15.
- Gutjahr, S. 2001. Ein hypoplastisches Reibungsgesetz zur Modellierung von Kontaktflächen zwischen Boden und Bauwerk. In D. Franke (ed.), *OHDE-Kolloquium 2001*: 49–64. Institut für Geotechnik der TU Dresden, Heft 9.
- Gutjahr, S. 2003. Optimierte Berechnung von nicht gestützten Baugrubenwänden in Sand. Dissertation. Heft 25, Schriftenreihe des Lehrstuhls Baugrund-Grundbau der Universität Dortmund.
- Herle, I. & Gudehus, G. 1999. Determination of parameters of a hypoplastic constitutive model from properties of grain assemblies. *Mechanics of Cohesive-Frictional Materials* 4(5): 461–486.
- Herle, I. & Nübel, K. 1999. Hypoplastic description of the interface behaviour. In G. Pande, S. Pietruszczak & H. Schweiger (eds.), *Int. Symp. Numerical Models in Geomechanics, NUMOG VII, Graz*: 53–58. A.A. Balkema.
- Kishida, H. & Uesugi, M. 1987. Tests of the interface between sand and steel in the simple shear apparatus. *Géotechnique* 37(1): 45–52.
- Maier, T. 2002. Numerische Modellierung der Entfestigung im Rahmen der Hypoplastizität. Dissertation. Heft 24, Schriftenreihe des Lehrstuhls Baugrund-Grundbau der Universität Dortmund.
- Niemunis, A. 2004. Extended hypoplastic models for soils. Dissertation. Heft 34, Schriftenreihe des Instituts für Grundbau und Bodenmechanik der Ruhr-Universität Bochum.
- Nübel, K. & A. Niemunis 1999. Hypoplastic subroutine umatib.f. URL: <http://www.rz.uni-karlsruhe.de/~gn25/ibf/lbg/forschung/hypoplasticity/umatibf.zip>.
- Teichmann, J. 1989. Scherzonenbildung und Verspannungseffekte in Granulaten unter Berücksichtigung von Korndrehungen. Dissertation. Heft 117, Veröffentlichungen des Institutes für Bodenmechanik und Felsmechanik der Universität Fridericiana in Karlsruhe.
- von Wolffersdorff, P.-A. 1996. A hypoplastic relation for granular materials with a predefined limit state surface. *Mechanics of Cohesive-Frictional Materials* 1(4): 251–271.

Micro-polar modelling of a reinforced soil structure under shearing

S.F. Tanton & E. Bauer

Institute of Applied Mechanics, Graz University of Technology, Graz, Austria

ABSTRACT: In this paper the behaviour of a reinforced soil element is numerically investigated for shearing parallel to the rigid geogrid reinforcement using a continuum approach. A micro-polar hypoplastic model is employed to model the essential mechanical properties of granular soil taking into account stress and couple stress, pressure dependent limit void ratios and the mean grain size as the characteristic length. Particular attention is paid to the influence of the grain size, the initial density and the fluctuation of the rotation resistance along the interface on the evolution of strain localization within the soil layer. The results of finite element calculations show that the interaction between the granular soil and the reinforcement has a strong influence on the deformation of the soil around the reinforcement.

1 INTRODUCTION

It is experimentally evident that the interaction mechanism between backfill soil and reinforcement is crucial for the overall bearing capacity of the reinforced soil structure. The interaction between the geogrid and the soil is dominated by the interlocking of grain particles within the geogrid cells, as shown in Figure 1. Under shearing parallel to the geogrid, the displacement of particles captured by geogrid cells is mainly dictated by the displacement of the geogrid. If the strength of the reinforcement is sufficiently high, the shear resistance arises from the skin friction along the reinforcement and the resistance of the soil to the bearing members of the geogrid (e.g. Ingold 1983, William & Houlihan 1987, Uesugi et al. 1988, Farrag et al. 1993, Bergado et al. 1996, Zettler 2000, Konietzky 2004). For large shear displacements failure of the reinforced structure occurs in the surroundings of the reinforcement where the deformation of the soil localizes in narrow zones called shear bands. Experiments with sand specimens show that the thickness of shear bands is not a material constant and mainly depends on the grain size, the grain shape and the surface roughness, the initial density, the stress state and the interaction with the chosen reinforcement. Within shear bands very sharp strain gradients, pronounced volume changes, strain softening and grain rotations can be observed (e.g. Oda et al. 1982, Mühlhaus & Vardoulakis 1987, Desrues et al. 1996, Gudehus 1997, Oda & Kazama 1998).

In this paper the interaction between the geogrid and the backfill soil during shearing is numerically

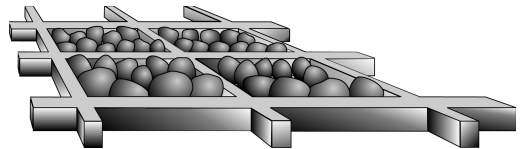


Figure 1. Sketch of the interlocking of soil particles within geogrid cells.

investigated with a continuum approach and the finite element method. Particular attention is paid to the influence of the initial density of the soil, the grain size and the rotation resistance of particles along the interface layer on the evolution of the shear resistance and strain localization. For a realistic prediction of the shear band thickness in the soil layer which is independent of the assumed size of the finite elements a continuum model is needed which takes into account a characteristic length. To this end a micro-polar continuum or so-called Cosserat continuum is proposed which includes displacement degrees of freedom and rotational degrees of freedom. It was shown by Pasternak & Mühlhaus (2001) that the additional rotational degree of freedom of a micro-polar continuum arises naturally from the mathematical homogenisation of an originally discrete system of spherical particles with contact forces and contact moments. As the thickness of the shear band is mainly related to the grain size, another benefit of using a micro-polar continuum is the possibility to relate the characteristic length directly to the mean grain diameter.

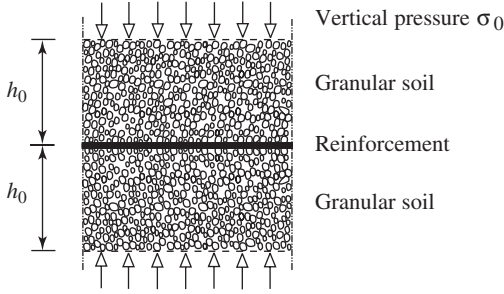


Figure 2. Section of a reinforced soil element.

The focus of the present paper is on studying the influence of the initial density of the soil, the grain size and the rotation resistance on the evolution of shear localization during the shearing of a geogrid reinforcement against the soil. For the numerical investigation a reinforced granular soil strip under a constant vertical pressure is considered where the reinforcement is assumed to be rigid and located in the middle of the lateral infinite extended plane strip (Figure 2). The mechanical behaviour of the cohesionless granular soil material is described with a micro-polar hypoplastic model (Huang & Bauer 2003). The model takes into account anelastic material properties and the influence of pressure, void ratio, grain size, grain hardness and grain roughness on the incremental stiffness and volume change behaviour. By including the concept of critical states and with a pressure dependent density factor the model describes the essential properties of initially dense and initially loose granular soils for a wide range of pressures and densities with a single set of constitutive constants. The rotation resistance of particles along the reinforcement is modelled with the micro-polar boundary conditions in a natural manner. This is demonstrated for a homogeneous distribution and a certain fluctuation of the micro-polar boundary conditions along the interface between the granular soil and the reinforcement.

2 THE MICRO-POLAR HYPOPLASTIC MODEL

The kinematics of a micro-polar continuum is defined by the macro-displacement field u_i and micro-rotations ω_i^c ($i = 1, 2, 3$). The rate of deformation and the rate of curvature are defined as $\dot{\epsilon}_{ij} = \partial \dot{u}_i / \partial x_j + \epsilon_{kij} \dot{\omega}_k^c$ and $\dot{\kappa}_{ij} = \partial \dot{\omega}_i^c / \partial x_j$, respectively, where ϵ_{ijk} denotes the permutation tensor. The proposed micro-polar hypoplastic model includes three state variables, i.e. the non-symmetric Cauchy stress tensor σ , the couple stress tensor μ and the void ratio e . The evolution of the state variables are described by

the following objective rate type equations (Huang & Bauer 2003):

$$\dot{\sigma}_{ij} = f_s \left[\hat{a}^2 \dot{\epsilon}_{ij} + (\hat{\sigma}_{kl} \dot{\epsilon}_{kl} + \hat{\mu}_{kl} \dot{\kappa}_{kl}) \hat{\sigma}_{ij} + f_d \hat{a} (\hat{\sigma}_{ij} + \hat{\sigma}_{ij}^*) \sqrt{\dot{\epsilon}_{kl} \dot{\epsilon}_{kl} + \dot{\kappa}_{kl} \dot{\kappa}_{kl}} \right], \quad (1)$$

$$\dot{\mu}_{ij} = f_s d_{50} \left[a_c^2 \dot{\kappa}_{ij} + \hat{\mu}_{ij} (\hat{\sigma}_{kl} \dot{\epsilon}_{kl} + \hat{\mu}_{kl} \dot{\kappa}_{kl} + 2 f_d a_c \sqrt{\dot{\epsilon}_{kl} \dot{\epsilon}_{kl} + \dot{\kappa}_{kl} \dot{\kappa}_{kl}}) \right], \quad (2)$$

$$\dot{e} = (1 + e) \dot{\epsilon}_{kk}, \quad (3)$$

with the normalised quantities: $\hat{\sigma}_{ij} = \sigma_{ij} / \sigma_{kk}$, $\hat{\sigma}_{ij}^* = \hat{\sigma}_{ij} - \delta_{ij} / 3$, $\hat{\mu}_{ij} = \mu_{ij} / (d_{50} \sigma_{kk})$, $\hat{\kappa}_{ij} = d_{50} \kappa_{ij}$. Herein δ_{ij} is the Kronecker delta and d_{50} denotes the mean grain diameter, which enters the constitutive model as the characteristic length. Function \hat{a} in Eq.(1) and factor a_c in Eq.(2) are related to the limit stress and limit couple stress at critical states which can be reached asymptotically under large shearing. Factor a_c is assumed to be a constant and \hat{a} depends on the intergranular friction angle φ_c , i.e. (Bauer 2000).

$$\hat{a} = \frac{\sin \varphi_c}{3 + \sin \varphi_c} \left[\sqrt{b} + \sqrt{\hat{\sigma}_{kl}^{**s} \hat{\sigma}_{kl}^{**s}} \right] \quad (4)$$

with

$$b = \frac{8/3 - 3(\hat{\sigma}_{kl}^{**s} \hat{\sigma}_{kl}^{**s}) + g \sqrt{3/2} (\hat{\sigma}_{kl}^{**s} \hat{\sigma}_{kl}^{**s})^{3/2}}{1 + g \sqrt{3/2} (\hat{\sigma}_{kl}^{**s} \hat{\sigma}_{kl}^{**s})^{1/2}},$$

and

$$g = -\sqrt{6} \frac{\hat{\sigma}_{kl}^{**s} \hat{\sigma}_{lm}^{**s} \hat{\sigma}_{mk}^{**s}}{(\hat{\sigma}_{kl}^{**s} \hat{\sigma}_{kl}^{**s})^{3/2}}.$$

Herein $\hat{\sigma}_{kl}^{**s}$ denotes the symmetric part of the normalized stress deviator, i.e. $\hat{\sigma}_{kl}^{**s} = (\hat{\sigma}_{kl}^* + \hat{\sigma}_{lk}^*) / 2$. The influence of the mean pressure and the current void ratio on the response of the constitutive equations (1) and (2) is taken into account with the stiffness factor f_s and the density factor f_d . The dilatancy behaviour, the peak stress ratio and strain softening depends on the density factor f_d , which represents a relation between the current void ratio e , the critical void ratio e_c and the minimum void ratio e_d , i.e.

$$f_d = \left(\frac{e - e_d}{e_c - e_d} \right)^\alpha, \quad (5)$$

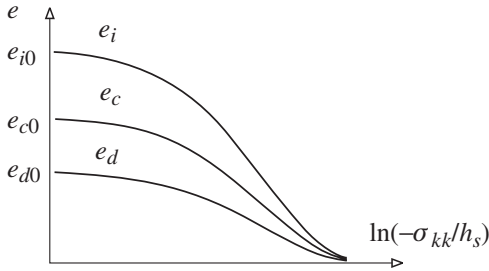


Figure 3. Decrease of the maximum void ratio e_i , the minimum void ratio e_d and the critical void ratio e_c with the normalized mean pressure σ_{kk}/h_s .

where $\alpha < 0.5$ is a constitutive constant. The stiffness factor f_s is proportional to the granular hardness h_s and depends on the stress level σ_{kk} , i.e.

$$f_s = \left(\frac{e_i}{e}\right)^\beta \frac{h_s(1+e_i)}{n h_i (\hat{\sigma}_{kl} \hat{\sigma}_{kl}) e_i} \left(-\frac{\sigma_{kk}}{h_s}\right)^{1-n}, \quad (6)$$

with

$$h_i = \frac{8 \sin^2 \varphi}{(3 + \sin \varphi)^2} + 1 - \frac{2\sqrt{2} \sin \varphi}{3 + \sin \varphi} \left(\frac{e_{i0} - e_{d0}}{e_{c0} - e_{d0}}\right)^\alpha.$$

Herein $\beta > 1$ is a constitutive constant. In Eq. (5) and Eq. (6) the current void ratio e is related to the maximum void ratio e_i , the minimum void ratio e_d and the critical void ratio e_c . These limit void ratios decrease with an increase of the mean pressure σ_{kk} , i.e.

$$\frac{e_i}{e_{i0}} = \frac{e_d}{e_{d0}} = \frac{e_c}{e_{c0}} = \exp\left[-\left(-\frac{\sigma_{kk}}{h_s}\right)^n\right],$$

where e_{i0} , e_{d0} , e_{c0} are the corresponding values for $\sigma_{kk} \approx 0$ (Figure 3).

The micro-polar hypoplastic model was implemented in the finite element code ABAQUS and for plane strain conditions a four-node linear element was used to describe the displacements and Cosserat rotations within the element (Huang 2000). For the present numerical investigations the following material constants for a medium sand are used (Huang & Bauer 2003):

$$\begin{aligned} e_{i0} &= 1.2, \quad e_{d0} = 0.51, \quad e_{c0} = 0.82, \quad \varphi = 30^\circ, \\ h_s &= 190 \text{ MPa}, \quad \alpha = 0.11, \quad \beta = 1.05, \quad n = 0.4, \\ a_c &= 1.0, \quad d_{50} = 0.5 \text{ mm (or 1.0 mm)}. \end{aligned}$$

3 NUMERICAL INVESTIGATIONS

Due to the horizontal and vertical symmetry of the reinforced granular soil layer (Figure 2) it is sufficient

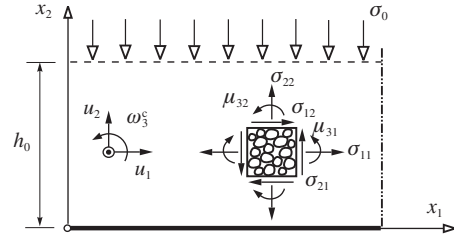


Figure 4: Modelling a reinforced plane granular layer with a micro-polar continuum.

to model a small section of the infinite layer (Figure 4). With respect to the rectangular coordinate system in Figure (4) and for plane strain conditions the relevant kinematic quantities are the displacements u_1 , u_2 and the micro-rotation ω_3^c . The non-zero static quantities are the stress components σ_{11} , σ_{22} , σ_{12} , σ_{21} , and the couple stress components μ_{31} and μ_{32} .

In all calculations a section of the granular layer with an initial height of $h_0 = 4$ cm and a width of $b = 10$ cm is discretized using four node linear elements with a height of 1.25 mm. The condition of a lateral infinite layer is modelled by applying constraint conditions to the side nodes of the finite element mesh, i.e. each node on the left boundary is controlled to have the same displacements and Cosserat rotation as the corresponding node with the same vertical coordinate on the right boundary (Bauer & Huang 1999). At the top of the layer, i.e. for $x_2 = h$, the boundary conditions are: $u_1 = 0$, $\omega_3^c = 0$ and $\sigma_{22} = \sigma_o = -100$ kPa. For the interaction between the granular soil and the reinforcement it is assumed that the grains are captured by the cell openings of the rigid geogrid so that at the boundary $x_2 = 0$ no relative displacements take place, i.e. $u_2 = 0$ and the prescribed shear displacement u_{1R} of the reinforcement is independent of the co-ordinate x_1 . This assumption also implies that the possibility of relative displacements along the surface of the geogrid as a result of a lower skin friction is not taken into account. Concerning the rotation resistance of particles in contact with the reinforcement a homogeneous distribution and a certain periodic fluctuation of the micro-polar boundary conditions are investigated as discussed in the following.

3.1 Homogeneous distribution of the micropolar boundary condition along the interface

For the case that the rotation resistance can be neglected along the interface the couples stresses are assumed to be zero at $x_2 = 0$. In Figure 5 the deformation localized in the soil close to the reinforcement is shown for an initially homogeneous void ratio of $e_0 = 0.6$ and after a horizontal reinforcement



Figure 5. Contour plot of the void ratio within a reinforced granular layer after a horizontal reinforcement displacement of $u_{1R}/h_0 = 1.4$ ($d_{50} = 1$ mm).

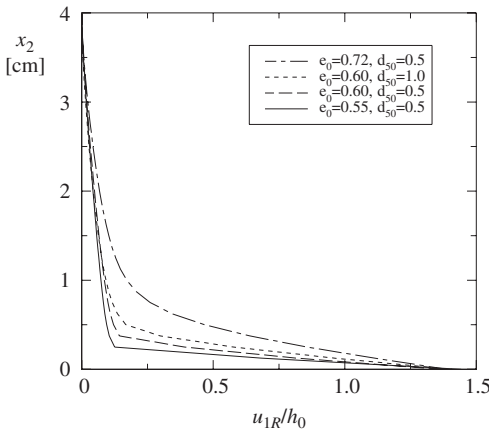


Figure 6. Influence of the initial void ratio e_0 and the mean grain diameter d_{50} on the distribution of horizontal displacement u_{1R} .

displacement of $u_{1R}/h_0 = 1.4$. The lighter strip indicates a higher void ratio, which reflects a strong dilatancy within the localized zone. The predicted thickness of the shear band is about $7 * d_{50}$.

In order to investigate the influence of the initial void ratio e_0 and the mean grain diameter d_{50} the following four calculations are performed:

e_0	0.6	0.6	0.55	0.72
d_{50}	0.5	1.0	0.5	0.5

A comparison of the calculated horizontal displacements u_1 across the height of the layer is shown in Figure 6. It is obvious that the thickness of the localized zone is higher for a higher initial void ratio and a large mean grain diameter. The micro-polar rotation are extremal at the interface, where the amount is larger for a lower initial void ratio and a lower mean grain diameter as shown in Figure 7.

At the beginning of shearing the mobilized interface friction angle $\phi_m = \arctan(\sigma_{12}/\sigma_{22})$ increases and reaches a peak state which is higher for an initially denser material (Figure 8). It can be observed that the peak friction angle is not influenced by the mean grain diameter. After the peak the interface friction

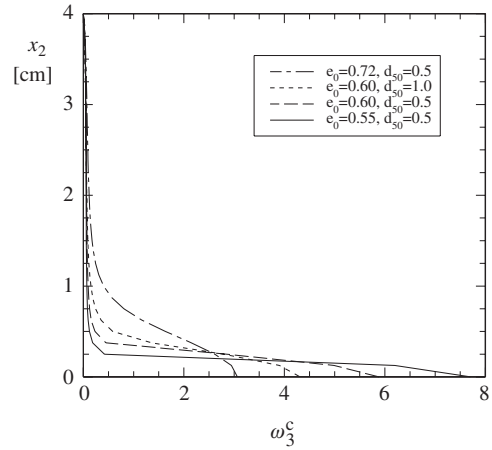


Figure 7. Influence of the initial void ratio e_0 and the mean grain diameter d_{50} on the distribution of micropolar rotation ω_3^c .

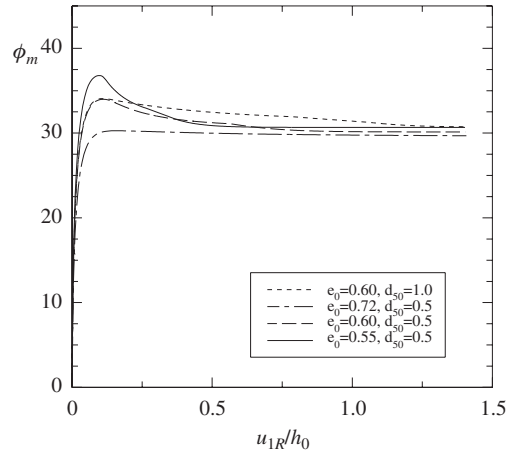


Figure 8. Influence of the initial void ratio e_0 and the mean grain diameter d_{50} on the distribution of the mobilized interface friction angle ϕ_m .

angle decreases and for large displacement of the reinforcement it tends towards a stationary value which is equal to the intergranular friction angle.

3.2 Periodic fluctuation of the rotation resistance

In order to model a bit-by-bit locking of particle rotation a periodic fluctuation of the micro-polar boundary conditions is assumed, i.e. along the interface $x_2 = 0$ the micro-polar rotation ω_3^c is zero within a distance of 5 mm followed by zero couple stress within a distance of 20 mm. For an initial void ratio of $e_0 = 0.6$, a mean grain diameter of $d_{50} = 1$ mm and a

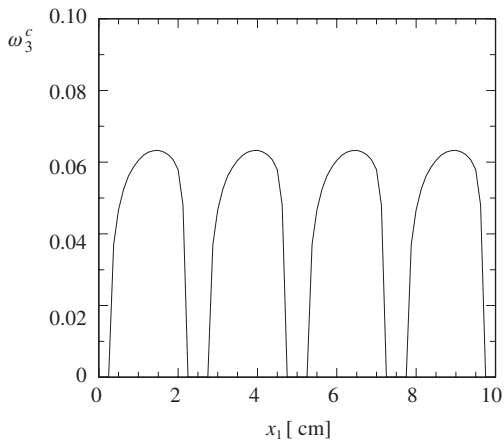


Figure 9. Fluctuation of the micro-polar rotation ω_3^c along the interface.

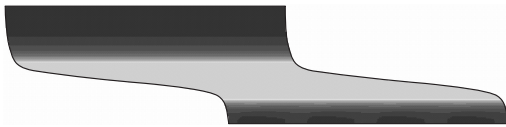


Figure 10. Part of a reinforced granular layer after a horizontal reinforcement displacement of $u_{1R}/h_0 = 2$ (homogeneous initial void ratio $e_0 = 0.6$, $d_{50} = 1$ mm, fluctuation of the micro-polar interface boundary conditions).

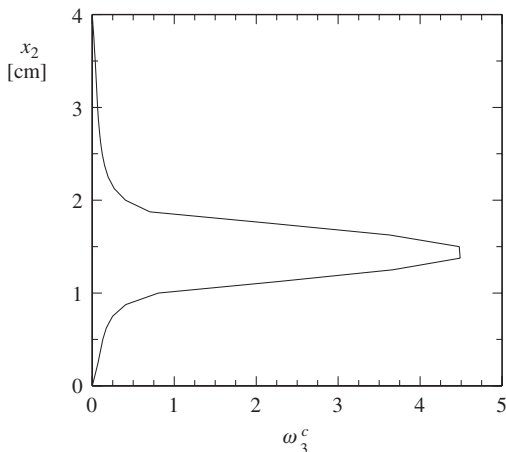


Figure 11. Distribution of micro-polar rotation ω_3^c across the height of the reinforced granular layer.

prescribed shear displacement of the reinforcement of $u_{1R}/h_0 = 2$ the results are shown in Figures 9–12. In particular, Figure 9 shows the calculated distribution of the micro-polar rotation for an interface section of

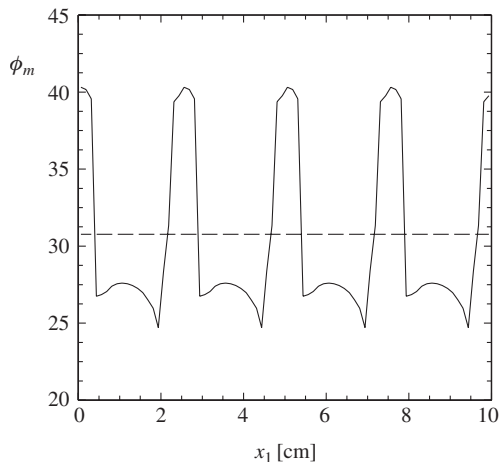


Figure 12. Fluctuation of mobilized interface friction angle ϕ_m (solid curve) and average value (dashed curve) for reinforced granular layer.

10 cm. A comparison of the contour plot in Figure 10 with the one in Figure 5 indicates that the location and thickness of the shear band strongly depends on the micro-polar boundary conditions at the interface. In contrast to the results in Section 3.1, the maximum micro-polar rotation (Figure 11) and shear strain localization is no longer located at the interface.

The thickness of the localized zone is about $10 * d_{50}$ and therefore larger than in the case of a constant zero couple stress along the interface. Furthermore, a fluctuation of the micro-rotation resistance leads to a fluctuation of the mobilized interface friction angle (Figure 12). However, in the steady state the average value is equal to the intergranular friction angle of the soil material.

Further numerical investigations with the assumption of a smoother surface of the geogrid have shown that the average value of the residual friction angle decreases while the micro-polar rotation increases.

4 CONCLUSION

The deformation of a cohesionless granular soil structure resulting from shearing a geogrid reinforcement has been studied based on a micro-polar hypoplastic continuum approach. The constitutive model takes into account stress and couple stress, pressure dependent limit void ratio and the mean grain size as the characteristic length. It is demonstrated that the initial density, the grain size and the rotation resistance of particles in contact with the reinforcement may have a strong influence on the location and thickness of shear bands when strain localization takes place. In particular the

predicted thickness of the shear band is higher for a looser material, a large mean grain size and a higher rotation resistance of particles along the interface. For a lower rotation resistance within the interface the shear localization is located closer to the reinforcement. The maximum mobilized shear resistance is higher for an initially dense granular soil but after the peak the shear resistance decreases with advanced shear displacements of the reinforcement and it tends towards a stationary value which is independent of the initial state of the granular soil. In a steady state or so-called critical state the predicted interface friction angle is equal to the intergranular friction angle of the soil material provided that no relative displacements between the geogrid reinforcement and the bounding soil particles occur. For a fluctuation of the rotation resistance of the particles along the interface the mobilized friction angle varies, however its average value is again equal to the intergranular friction angle. Only in cases where a lower skin friction of the geogrid surface is taken into account, is the average value of the residual interface friction angle smaller than the intergranular friction angle of the soil material.

ACKNOWLEDGEMENTS

This work is sponsored by Polyfelt Ges.m.b.H and the Austrian Exchange Service. The support is greatly appreciated.

REFERENCES

- Bauer, E. 2000. Conditions for embedding Casagrande's critical states into hypoplasticity. *Mechanics of Cohesive-Frictional Materials* 5: 125–148.
- Bauer, E. & Huang, W. 1999. Numerical study of polar effects in shear zones. In Pande, G.N., Pietruszczak, S. & Schweiger, H.F. (eds.) *Proc. of the 7th Int. Symposium on Numerical Models in Geomechanics*, Balkema Press, 133–138.
- Bergado, D.T., Anderson L.R., Miura, N. & Balasubramaniam, A.S. 1996. *Soft Ground Improvement*. ASCE. ISBN 0-7844-0151-9. 305–422.
- Desrués, J., Chambon, R., Mokni, M. & Mazerolle, F. 1996. Void ratio evolution inside shear bands in triaxial sand specimens studied by computed tomography. *Géotechnique* 46: 529–546.
- Farrag, K., Acar, Y.B. & Juran, I. 1993. Pullout resistance of geogrid reinforcement. *Geotextiles & Geomembranes* 12: 133–159.
- Gudehus, G. 1997. Shear localization in simple grain skeleton with polar effect. In Adachi, Oka & Yashima (eds.) *Proc. of the 4th Int. Workshop on Localization and Bifurcation Theory for Soils and Rocks*, 1998, Balkema Press, 3–10.
- Huang, W. 2000. Hypoplastic Modelling of Shear Localisation in Granular materials. *Doctoral thesis*, Graz University of Technology, Austria.
- Huang, W. & Bauer, E. 2003. Numerical investigations of shear localization in a micro-polar hypoplastic material. *Int. J. for Numer. Anal. Meth. Geomech.* 27: 325–352.
- Ingold, T.S. 1983. Laboratory pullout testing of grid reinforcement in sand. *Geotech. Testing Journal* 6(3): 101–111.
- Konietzky, H., te Kamp, L., Groeger, T. & Janner, C. 2004. Use of DEM to model the interlocking effect of geogrids under static and cyclic loading. In Shimizu, Hart & Cundall (eds.) *Numerical modelling in micromechanics via particle methods*, Kyoto, Japan, 3–11.
- Mühlhaus, H.B. & Vardoulakis, I. 1987. The thickness of shear bands in granular materials. *Géotechnique* 37: 271–283.
- Oda, M., Konish, J. & Nemat-Nasser, S. 1982. Experimental micromechanical evaluation of strength of granular materials: effect of particle rolling. *Mech. Mater.* 1: 269–283.
- Oda, M. & Kazama, H. 1998. Microstructure of shear bands and its relation to the mechanics of dilatancy and failure of dense granular soils. *Géotechnique* 48: 465–481.
- Pasternak, E. & Mühlhaus, H.B. 2001. Cosserat continuum modelling of granulate materials. In Valliappan S. & Khalili, N. (eds.) *Computational Mechanics – New Frontiers for New Millennium*: 1189–1194. Elsevier Science.
- Uesugi, M., Kishida, H. & Tsubakihara, Y. 1988. Behaviour of sand particles in sand-steel friction. *Soils and Foundations* 28(1): 107–118.
- Williams, N.D. & Houlihan, M.F. 1987. Evaluation of interface friction properties between geosynthetics and soils. In *Proc. of Geosynthetics '87 Conference*, New Orleans, USA, 2: 616–627.
- Zettler, T., Kasturi, G., Bhatia, S.K., Abdel-Rehman, A.H. & Bakeer, R. 1998. Influence of grid configuration on interface shear strength soil/geogrid system. In *Proc. of the 6th Int. Conference on Geosynthetics*, Atlanta, USA, 1: 733–738.

A stress-strain integration algorithm for unsaturated soil elastoplasticity with automatic error control

W.T. Sołowski & D. Gallipoli

Durham University, Durham, United Kingdom

ABSTRACT: Stress-strain integration algorithms are a very important component in the development of finite element codes. The use of accurate, robust and fast stress-strain integration algorithms accounts for a significant part of the performance of a finite element code, especially when complex elasto-plastic constitutive models are used. This paper presents the formulation of an algorithm for the stress-strain integration of the Barcelona Basic Model, an elasto-plastic volumetric hardening constitutive model for unsaturated soils. The proposed algorithm is based on some earlier ideas of substepping explicit integration with automatic error control. Stress-strain integration in the plastic domain is performed by using an explicit algorithm which accuracy is improved by dividing the initial strain increment in a number of substeps. The number of substeps depends on an estimation of the integration error that is obtained by using a modified Euler procedure. The performance of the stress-strain algorithm is presented for different types of stress paths to assess its dependency on factors such as, for example, the initial size of the strain increment, the error tolerance and the initial stress state. A drift correction algorithm is also proposed and its influence on the results is evaluated.

1 INTRODUCTION

Elasto-plastic models for soils are often presented in the form of non-linear differential relationships between stress and strains that need to be integrated numerically for use within finite element codes. The robustness and efficiency of such numerical algorithms affects the overall performance of the code. Integration algorithms are divided into two broad groups: a) explicit algorithms where the integrated stress is obtained using the stiffness at the start of each integration step and b) implicit algorithms, where the stress increment is calculated using the stiffness at the end of the integration step (this requires an iterative approach as the values at the end of the step are initially unknown). Both methods are used in practice and have some advantages.

A general description of implicit algorithms may be found in Simo & Hughes (1998) where also an extensive list of references is available. Implicit algorithms for the integration of elasto-plastic models for saturated soils were developed, among others, by Borja & Lee (1990) and Borja (1991); recently new ideas were presented by Wang et al. (2004) and Foster et al. (2005). With reference to unsaturated soils, Vaunat et al. (2000) proposed an implicit integration algorithm including a return mapping scheme for the Barcelona Basic Model (BBM) of Alonso et al. (1990). Further implicit

algorithms for unsaturated soil were proposed by Zhang et al. (2001) and Borja (2004).

Explicit algorithms have been often considered less efficient than implicit algorithms, although they are regarded as simpler to code and more generally applicable. A new class of explicit algorithms including error control based on a substepping method was proposed by Sloan (1987). Explicit algorithms with error control via substepping are now widely used and, especially for complicated elasto-plastic constitutive models, they are more robust and use less computational resources than implicit algorithms (see Potts & Zdravkovic 1999). Explicit algorithms using substepping have been constantly refined during past years and, recently, they have been applied to elasto-plastic models for unsaturated soils (e.g. Sheng et al. 2003a, b).

This paper presents an algorithm for the integration of BBM, however the concepts presented in the paper may be applied to any elasto-plastic model for unsaturated soils using two independent constitutive variables, such as net stress and suction. The integration of the stress-strain relationship is achieved explicitly via a substepping procedure to enforce error control.

For the sake of brevity the description of the purely elastic calculations is not presented in this paper and will be discussed in a future publication by the authors.

2 INTEGRATION OF ELASTO-PLASTIC STRAIN

2.1 General remarks

The stress-strain integration algorithm for unsaturated soils presented in this paper is similar to that proposed by Sheng et al (2003a). One important difference, however, is that, in the present work, the net stress and suction are treated as two separate constitutive variables (as in BBM) whereas Sheng et al. (2003a) use a single constitutive stress variable, which is defined as:

$$\boldsymbol{\sigma}' = \boldsymbol{\sigma}_{\text{tot}} - m\varphi(u_w)u_w = \boldsymbol{\sigma}_{\text{tot}} - \mathbf{m}\varphi(S_r)u_w \quad (1)$$

where $\boldsymbol{\sigma}'$ is the constitutive stress vector, $\boldsymbol{\sigma}_{\text{tot}}$ is the total stress vector, $\mathbf{m}^T = \{1, 1, 1, 0, 0, 0\}$, $\varphi(S_r)$ is a constitutive stress parameter depending upon the degree of saturation S_r and u_w is the pore water pressure. The algorithm presented in this paper is instead used for integration of constitutive models for unsaturated soils depending on the net stress vector $\boldsymbol{\sigma}$, defined as $\boldsymbol{\sigma} = \boldsymbol{\sigma}_{\text{tot}} - \mathbf{m} \cdot u_a$ (where $\boldsymbol{\sigma}_{\text{tot}}$ is the total stress and u_a is the air pressure), as well as suction s , defined as $s = u_a - u_w$ (where u_a is the pore air pressure). These are also the standard constitutive variables used in various unsaturated soil models such as BBM.

The algorithm described here is explicit and uses a substepping procedure to achieve automatic error control during numerical integration according to the concepts first introduced by Sloan (1987). The algorithm integrates over an "extended" strain step $\{\Delta\boldsymbol{\varepsilon}_{\text{tot}}, \Delta s_{\text{tot}}\}$ incorporating the conventional strain increment vector $\Delta\boldsymbol{\varepsilon}_{\text{tot}}$ as well as the increment of suction Δs_{tot} . These increments are automatically divided into a number of substeps, small enough to ensure the desired integration accuracy. It is also assumed that the change of suction in each substep Δs is proportional to the change of strain $\Delta\boldsymbol{\varepsilon}$, i.e. $\Delta s/\Delta s_{\text{tot}} = \Delta\varepsilon_{ij}/\Delta\varepsilon_{ij,\text{tot}}$. The integration error in each substep is estimated as the difference between the two stress increments calculated by using the elasto-plastic stiffness matrix corresponding to the stress states at the beginning and the end of the substep respectively. Based on such estimate of the error, the size of the next substep is calculated.

2.2 Integration of elasto-plastic substep

In each substep involving elasto-plastic deformation, the net stress increment $\Delta\boldsymbol{\sigma}$ is calculated from the strain substep $\Delta\boldsymbol{\varepsilon} = \Delta T^* \Delta\boldsymbol{\varepsilon}_{\text{tot}}$ and the suction substep $\Delta s = \Delta T^* \Delta s_{\text{tot}}$ (ΔT^* is a scalar). The yield function F and plastic potential G are defined in terms of the net stress $\boldsymbol{\sigma}$, suction s and hardening parameter p_0^* :

$$F = F(\boldsymbol{\sigma}, s, p_0^*) = 0 \quad (2)$$

$$G = G(\boldsymbol{\sigma}, s, p_0^*) = 0 \quad (3)$$

The plastic strain increment is given by:

$$d\boldsymbol{\varepsilon}^{\text{pl}} = \lambda \frac{\partial G(\boldsymbol{\sigma}, s, p_0^*)}{\partial \boldsymbol{\sigma}} \quad (4)$$

where λ is the plastic multiplier. The volumetric plastic strain increment $d\varepsilon_v^{\text{pl}} = d\varepsilon_{11}^{\text{pl}} + d\varepsilon_{22}^{\text{pl}} + d\varepsilon_{33}^{\text{pl}}$ is related to a change of the hardening parameter p_0^* according to the following equation:

$$dp_0^* = \frac{\partial p_0^*}{\partial \varepsilon_v^{\text{pl}}} d\varepsilon_v^{\text{pl}} \quad (5)$$

The consistency condition to be satisfied by all incremental quantities is:

$$dF = \left(\frac{\partial F}{\partial \boldsymbol{\sigma}}\right)^T d\boldsymbol{\sigma} + \left(\frac{\partial F}{\partial s}\right)^T ds + \left(\frac{\partial F}{\partial p_0^*}\right)^T dp_0^* = 0 \quad (6)$$

The differential form of the stress-strain relationship for BBM, is given by:

$$d\boldsymbol{\sigma} = \mathbf{D}^{\text{el}} d\boldsymbol{\varepsilon}^{\text{el}} = \mathbf{D}^{\text{el}} (d\boldsymbol{\varepsilon} - d\boldsymbol{\varepsilon}^{\text{pl}} - \frac{1}{3} \mathbf{m} \frac{\kappa_s ds}{p_{\text{at}} + s}) \quad (7)$$

where \mathbf{D}^{el} is the elastic tangent matrix calculated at the beginning of the increment, $d\boldsymbol{\varepsilon}$ is the strain increment, $d\boldsymbol{\varepsilon}^{\text{pl}}$ is the plastic component of the strain increment, κ_s is the swelling index associated to suction change and p_{at} is atmospheric pressure. Introducing (4) into (7) gives:

$$d\boldsymbol{\sigma} = \mathbf{D}^{\text{el}} d\boldsymbol{\varepsilon} - \lambda \mathbf{D}^{\text{el}} \frac{\partial G(\boldsymbol{\sigma}, s, p_0^*)}{\partial \boldsymbol{\sigma}} - \frac{1}{3} \mathbf{D}^{\text{el}} \mathbf{m} \frac{\kappa_s ds}{p_{\text{at}} + s} \quad (8)$$

After introducing (8) into (6) and noting that transposition of a scalar variable coincides with the scalar variable itself, the following relationship is obtained:

$$\left(\mathbf{D}_{\text{el}} d\boldsymbol{\varepsilon} - \mathbf{D}_{\text{el}} \frac{\partial G(\boldsymbol{\sigma}, s, p_0^*)}{\partial \boldsymbol{\sigma}} \lambda - \frac{1}{3} \mathbf{D}_{\text{el}} \mathbf{m} \frac{\kappa_s ds}{p_{\text{at}} + s} \right) \cdot \left(\frac{\partial F}{\partial \boldsymbol{\sigma}} \right)^T + \frac{\partial F}{\partial s} ds + \frac{\partial F}{\partial p_0^*} dp_0^* = 0 \quad (9)$$

As dp_0^* is a function of the plastic volumetric strain increment as indicated in (5), then:

$$\left(\frac{\partial F}{\partial p_0^*} \right) dp_0^* = \left(\frac{\partial F}{\partial p_0^*} \right) \left(\frac{\partial p_0^*}{\partial \varepsilon_v^{\text{pl}}} \right) d\varepsilon_v^{\text{pl}} \quad (10)$$

and, after expressing $d\varepsilon_v^{pl}$ as:

$$d\varepsilon_v^{pl} = \sum_{i=1}^3 d\varepsilon_{ii}^{pl} = \lambda \mathbf{m}^T \left(\frac{\partial G(\boldsymbol{\sigma}, s, p_0^*)}{\partial \boldsymbol{\sigma}} \right) \quad (11)$$

the following result is obtained:

$$\left(\frac{\partial F}{\partial p_0^*} \right) dp_0^* = \lambda \left(\frac{\partial F}{\partial p_0^*} \right) \left(\frac{\partial p_0^*}{\partial \varepsilon_v^{pl}} \right) \mathbf{m}^T \left(\frac{\partial G(\boldsymbol{\sigma}, s, p_0^*)}{\partial \boldsymbol{\sigma}} \right) \quad (12)$$

Introducing (12) into (9), λ can be expressed as:

$$\lambda = \frac{\mathbf{a}^T \mathbf{D}^{el} d\varepsilon + [c - \mathbf{a}^T \mathbf{D}^{el} \mathbf{b}] ds}{\mathbf{a}^T \mathbf{D}^{el} \mathbf{g} - d} \quad (13)$$

where:

$$\frac{\partial F}{\partial \boldsymbol{\sigma}} = \mathbf{a}, \quad \frac{1}{3} \frac{\kappa_s}{p_{at} + s} = \mathbf{b}, \quad \frac{\partial F}{\partial s} = c,$$

$$\frac{\partial F}{\partial p_0^*} \frac{\partial p_0^*}{\partial \varepsilon_v^{pl}} \mathbf{m}^T \frac{\partial G}{\partial \boldsymbol{\sigma}} = d, \quad \frac{\partial G}{\partial \boldsymbol{\sigma}} = \mathbf{g}$$

In the integration algorithm the infinitesimal increments in the above equations (denoted by “d”) are approximated with finite increments (denoted by “ Δ ”). Please note that equation (13) is different from the corresponding equation given in Sheng et al. (2003a) due to different assumptions made about the constitutive variables, as previously discussed.

Having computed the plastic multiplier λ , the stress increment is calculated from (8), the volumetric plastic strain increment is calculated from (11) and the hardening parameter increment is obtained from (5).

2.3 Evaluation of integration error

In each substep the algorithm calculates: a) two values of the stress increment, $\Delta \boldsymbol{\sigma}_1$ and $\Delta \boldsymbol{\sigma}_2$, b) two values of volumetric plastic strain increment $\Delta \varepsilon_v^{pl_1}$ and $\Delta \varepsilon_v^{pl_2}$ and c) two values of the hardening parameter increment Δp_{01}^* and Δp_{02}^* .

The increments with subscript equal to 1 are calculated according to the equations given in the previous section and using values of the stress and hardening parameter at the start of the increment:

$$\Delta \boldsymbol{\sigma}_1 = \Delta \boldsymbol{\sigma}_2 (\Delta \boldsymbol{\varepsilon}, \Delta s, \boldsymbol{\sigma}_0, p_0^*)$$

$$\Delta p_{0,1}^* = \Delta p_{0,1}^* (\Delta \boldsymbol{\varepsilon}, \Delta s, \boldsymbol{\sigma}_0, p_0^*) \quad (14)$$

The increments with subscript equal to “2” are calculated according to the same equations but using values

of the stress and hardening parameter at the end of the increment. Note that the values at the end of the increment are calculated by using the increments from equation (14):

$$\Delta \boldsymbol{\sigma}_2 = \Delta \boldsymbol{\sigma}_2 (\Delta \boldsymbol{\varepsilon}, \Delta s, \boldsymbol{\sigma}_0 + \Delta \boldsymbol{\sigma}_1, p_0^* + \Delta p_{0,1}^*)$$

$$\Delta p_{0,2}^* = \Delta p_{0,2}^* (\Delta \boldsymbol{\varepsilon}, \Delta s, \boldsymbol{\sigma}_0 + \Delta \boldsymbol{\sigma}_1, p_0^* + \Delta p_{0,1}^*) \quad (15)$$

Equations (14) and (15) define an interval of values containing the exact integration of these increments. The best estimates of the stress increment $\Delta \boldsymbol{\sigma}$ and the hardening parameter increment Δp_0^* are taken as the average of the corresponding two values defined above:

$$\Delta \boldsymbol{\sigma} = \frac{\Delta \boldsymbol{\sigma}_1 + \Delta \boldsymbol{\sigma}_2}{2} \quad (16)$$

$$\Delta p_0^* = \frac{\Delta p_{0,1}^* + \Delta p_{0,2}^*}{2} \quad (17)$$

The maximum integration error for the stress increment is therefore calculated from the previous expressions for each of the stress components as:

$$E_{ij} = 0.5 \left| \Delta \sigma_{ij,2} - \Delta \sigma_{ij,1} \right| \quad i, j = 1, 2, 3 \quad (18)$$

The relative error R_{ij} is defined as:

$$R_{ij} = \frac{E_{ij}}{\left| \Delta \sigma_{ij} \right|} \quad i, j = 1, 2, 3 \quad (19)$$

This is not sufficient to ensure that the relative error in shear stress q , crucial for soil behaviour, is limited. This is why also E_q and R_q is defined:

$$E_q = \max(|q_1 - q_{mid}|, |q_2 - q_{mid}|), \quad R_q = \frac{E_q}{q_{mid} - q_0} \quad (20)$$

In the formula above q_0 is the initial shear stress corresponding to the stress state $\boldsymbol{\sigma}_0$ and q_1, q_2, q_{mid} are shear stresses calculated for corresponding stress states $\boldsymbol{\sigma}_0 + \Delta \boldsymbol{\sigma}_1$, $\boldsymbol{\sigma}_0 + \Delta \boldsymbol{\sigma}_2$, and $\boldsymbol{\sigma}_0 + 0.5(\Delta \boldsymbol{\sigma}_1 + \Delta \boldsymbol{\sigma}_2)$. In the calculations the highest value of R is used:

$$R = \max(R_{11}, R_{22}, R_{33}, R_{12}, R_{13}, R_{23}, R_q) \quad (21)$$

Equations (18) and (19) provide an estimate of the maximum potential error occurring during integration; however the actual error is usually significantly smaller than these values.

Control of the integration error is enforced by imposing that R in equation (19) is equal or smaller

than a user defined substep tolerance SSTOL. If $R > \text{SSTOL}$, the current substep is rejected. Regardless of whether the current substep is accepted or rejected, a new substep size is calculated by the algorithm with the coefficient ΔT_{new} given by:

$$\Delta T_{\text{new}} = \beta \Delta T \quad (22)$$

where ΔT defines the current size of the substep and β is a coefficient; β is smaller than 1, if the step is rejected, or equal/greater than 1, if the step is accepted. In this way the substep size is continuously adapted to enforce a magnitude of the maximum possible relative error R close to SSTOL.

The error estimate associated with the new substep size can be approximated as:

$$E_{\text{new}} = \beta^2 E \quad (23)$$

Substituting equation (19) into equation (23) and imposing that the maximum relative error in the next substep is equal to the tolerance SSTOL, it is possible to calculate an approximated value of β as:

$$\beta \approx \sqrt{\frac{\text{SSTOL}}{R}} \quad (24)$$

Equation (24) relies on the approximation $\Delta \boldsymbol{\sigma} = \Delta \boldsymbol{\sigma}_{\text{new}}$. Because of this approximation, β is usually further reduced by a user defined scalar factor ξ as:

$$\beta = \xi \sqrt{\frac{\text{SSTOL}}{R}} \quad (25)$$

In the subsequent examples a value $\xi = 0.9$ is used.

2.4 Drift correction

Because of the approximation involved in the use of explicit integration, the stress state at the end of each substep does not lie on the yield locus. This phenomenon is known as yield surface drift and it requires a numerical correction to enforce consistency. Drift correction tends to become less of an issue as the tolerance used for the control of the integration error becomes stricter. The drift correction technique used in this work is similar to that advocated by Potts & Zdravkovic (1999) for saturated soil models.

The drift correction procedure is used when, after a successful substep (i.e. a substep where the integration error R is smaller or equal than the tolerance SSTOL), the stress state does not lie on the yield locus within a set tolerance. In the present algorithm a normalized yield function is used for BBM, similarly to the

normalized function proposed by Sheng et al. (2000) for the Cam-clay model. Employing a normalized yield locus ensures that the set tolerance is independent of the magnitude of the stress state.

Before integration, the initial stress state $\boldsymbol{\sigma}_A$ lies on the yield locus at point A in the stress space and therefore $F(\boldsymbol{\sigma}_A, s_A, p_{0A}^*) = 0$. After calculating the stress increase $\Delta \boldsymbol{\sigma}$, as explained in the previous section, the stress state changes to $\boldsymbol{\sigma}_B = \boldsymbol{\sigma}_A + \Delta \boldsymbol{\sigma}$ moving to point B of the stress space. and is not any longer on the yield locus, i.e. $F(\boldsymbol{\sigma}_B, s_B, p_{0B}^*) \neq 0$. The drift correction algorithm imposes a change of the elastic strain $\Delta \boldsymbol{\epsilon}^e$ (by maintaining unchanged the strain $\Delta \boldsymbol{\epsilon}$, i.e. $\Delta \boldsymbol{\epsilon}^e = -\Delta \boldsymbol{\epsilon}^{pl}$), which results in the correction of the stress state to point C lying on the yield locus. The yield locus equation after correction will therefore be:

$$F(\boldsymbol{\sigma}_C, s, p_{0C}^*) = F(\boldsymbol{\sigma}_B + \Delta \boldsymbol{\sigma}, s, p_{0B}^* + \Delta p_0^*) = 0 \quad (26)$$

where $\Delta \boldsymbol{\sigma}$ and Δp_0^* are the corrections to the stress state and hardening parameter respectively and no correction to suction is applied as explained below.

After expanding (24) in Taylor series we obtain:

$$F(\boldsymbol{\sigma}_C, s, p_{0C}^*) = F(\boldsymbol{\sigma}_B, s, p_{0B}^*) + \left(\frac{\partial F}{\partial \boldsymbol{\sigma}} \right)^T \Delta \boldsymbol{\sigma} + \frac{\partial F}{\partial s} \Delta s + \frac{\partial F}{\partial p_0^*} \Delta p_0^* + \dots \quad (27)$$

where the stress change $\Delta \boldsymbol{\sigma}$ is:

$$\Delta \boldsymbol{\sigma} = \Delta \boldsymbol{\sigma}(\Delta \boldsymbol{\epsilon}^{el}) = \mathbf{D}^{el} \Delta \boldsymbol{\epsilon}^{el} = -\mathbf{D}^{el} \Delta \boldsymbol{\epsilon}^{pl} = -\mathbf{D}^{el} \lambda \frac{\partial G}{\partial \boldsymbol{\sigma}} \quad (28)$$

After substituting (28) and (13) into (26), neglecting second order terms and above and noticing that the change of suction Δs is equal to zero (as suction change is proportional to the variation of strain $\Delta \boldsymbol{\epsilon}$ which remains unchanged) the following expression for λ is obtained:

$$\lambda = \frac{F(\boldsymbol{\sigma}_B, s, p_{0B}^*)}{\left(\frac{\partial F}{\partial \boldsymbol{\sigma}} \right)^T \mathbf{D}^{el} \frac{\partial G}{\partial \boldsymbol{\sigma}} - \frac{\partial F}{\partial p_0^*} \frac{\partial p_0^*}{\partial \boldsymbol{\epsilon}^{pl}} \mathbf{m}^T \frac{\partial G(\boldsymbol{\sigma}, s, p_0^*)}{\partial \boldsymbol{\sigma}}} \quad (29)$$

The stress state in point C is then equal to:

$$\boldsymbol{\sigma}_C = \boldsymbol{\sigma}_B - \lambda \mathbf{D}^{el} \frac{\partial G}{\partial \boldsymbol{\sigma}} \quad (30)$$

In the unlikely situation when, after the first correction, the stress state still lies outside the yield locus, the above algorithm is performed again until the

stress state is mapped back onto the yield locus within the set tolerance. The derivatives and stiffness matrix appearing in the above equations may be calculated either at point A or at point B. The effect of calculating those quantities at different points of the stress path during each substep is discussed later in the paper.

3 VALIDATION OF PROPOSED INTEGRATION ALGORITHM

3.1 Overview

To validate the algorithm results from number of simple cases with existing theoretical solution were compared to the solutions given by the algorithm. In all the cases a Barcelona Basic Model (BBM) developed by Alonso et al. (1990) was used. Although the theoretical solution (see equation 14) allows for a non-associated flow rule, as originally proposed by Alonso et al. (1990), in validation of the code and in all examples an associated flow rule was used. The parameters of the model in each case were the same: Shear Modulus (constant) $G = 20 \text{ MPa}$, elastic stiffness parameter for changes in net mean stress $\kappa = 0.02$, elastic stiffness parameter for changes in suction $\kappa_s = 0.008$, atmospheric pressure $p_{\text{atm}} = 100,000 \text{ Pa}$, parameter describing the increase in cohesion with suction $k = 0.6$, stiffness parameter for changes in net mean stress for virgin states of the soil (with suction $s = 0$) $\lambda(0) = 0.2$, parameter defining the maximum increase of soil stiffness with suction $\beta = 0.00001$, reference stress $p_c = 10,000 \text{ Pa}$, starting specific volume at means stress $p = p^c$ and suction $s = 0$ $N(0) = 1.9$, critical state line slope $M = 0.5$. The initial preconsolidation stress for saturated condition p_0^* was set to $200,000 \text{ Pa}$ and initial suction s used was equal to $100,000 \text{ Pa}$.

3.2 Test case 1 – isotropic loading of a sample subjected to drying

The test simulates isotropic loading of a preconsolidated and partially unloaded sample. The sample was initially in isotropic stress state with the mean stress $p = 350,000 \text{ Pa}$. The sample was subjected to strain change $\Delta \epsilon = \{0.05, 0.05, 0.05, 0, 0, 0\}$ and suction increase $\Delta s = 100,000 \text{ Pa}$. Created algorithm showed good convergence to the theoretical solution. (please refer to Fig. 1 & Table 1)

3.3 Test case 2 – oedometric test at variable suction

The test simulates oedometric test with drying of a sample during a test. The sample was in isotropic stress state at the beginning of the test with mean

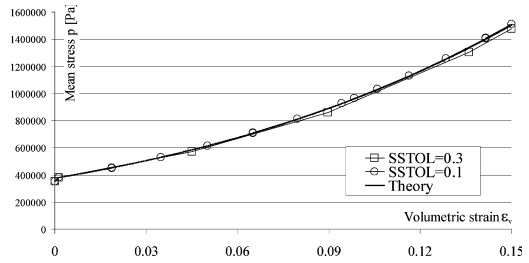


Figure 1. Comparison of the algorithm solutions obtained for different values of substep accuracy SSTOL with the theoretical solution (no drift correction).

Table 1. Comparison of drift correction algorithms.

Test case	Integration at:	SSTOL value [%]	Number of steps	Number of drift corrections	Relative Error (comparing to the theory), for mean stress p and shear stress q [%]
1	A	30	4	36	0.252*
1	B	30	28	177	1.006*
1	-	30	4	-	2.59*
1	A	10	10	109	0.669*
1	B	10	10	175	0.724*
1	-	10	10	-	0.490*
1	A	1	104	1040	0.0920*
1	B	1	104	1137	0.0929*
1	-	1	104	-	0.0274*
1	A	0.1	1043	6543	0.009229*
1	B	0.1	1043	6598	0.009238*
1	-	0.1	1043	-	0.002744*
2	A	30	30	161	0.0581/1.152
2	B	30	30	180	0.0451/1.059
2	-	30	26	-	0.570/0.555
2	A	10	59	286	0.0124/0.472
2	B	10	59	309	0.0105/0.465
2	-	10	56	-	0.292/0.0922
2	A	1	423	1306	4.22E-04/0.0585
2	B	1	423	1338	4.88E-04/0.0585
2	-	1	419	-	0.0414/0.00187
2	A	0.1	4026	4432	2.4E-05/0.00647
2	B	0.1	4026	4436	2.5E-05/0.00647
2	-	0.1	4022	-	0.00499/6.0E-04

*for test case 1 only error in p is given as q = 0.

stress $p = 350,000 \text{ Pa}$. Sample then was subjected to strain change $\Delta \epsilon = \{0.05, 0, 0, 0, 0, 0\}$ and suction increase $\Delta s = 100,000 \text{ Pa}$. Again a very good agreement of the data from the algorithm with the theoretical solution was found (see Fig. 2 and Table 1)

4 INFLUENCE OF DRIFT CORRECTION ALGORITHM

The choice of the drift correction algorithm influences the accuracy of the result. As mentioned in

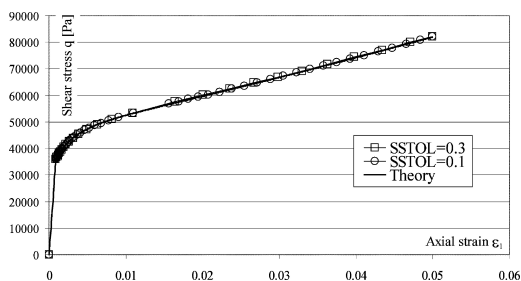


Figure 2. Comparison of the theoretical ε - q path with the solutions from the algorithm for different values of substep tolerance SSTOL (no drift correction).

point 2.4 two implementation of the algorithm are possible. In one case the derivatives and the elastic matrix are calculated at the beginning of the substep (point A), in the other in forbidden space at point B (neither solution is rigorous). To check the influence of the drift correction algorithm, both cases were implemented. Results show little difference, but in extreme cases when, because of crude accuracy, very few steps accompanied by multiple iterations of drift correction algorithm were computed (see Table 1). In such case calculating all the derivatives at point A was often advantageous and resulted in more accurate results and/or in less iteration needed to converge to the yield locus. Such uncommon amounts of iterations of drift correction algorithm were performed because of artificially set very strict tolerance for a stress state to be considered as being on the yield locus. These results are in a good agreement with data presented by Potts & Zdravkovic (1999). In table 1 are also included the values obtained without the drift correction algorithm (indicated with “-”). As the correction of the stress state in the algorithm proposed is artificial and not rigorous, although in result the stress state is returned back to the yield surface, in some cases the overall accuracy may be decreased.

5 CONCLUSIONS

The paper presents an algorithm for the numerical integration of the differential stress-strain relationship in BBM. The algorithm uses explicit integration and incorporates a substepping procedure for controlling the integration error. The methodology outlined in the present paper can also be applied to other unsaturated elasto-plastic models expressed in terms of two different constitutive variables, e.g. net stress and suction.

The difficulties in estimating the numerical integration error have been highlighted. It has been shown that the bound (maximum) error, as in equation (19),

significantly overestimates the actual error and therefore the level of accuracy is considerably greater (see also Gear 1971) than the tolerance SSTOL. This implies that the algorithm uses a larger number of substeps than what is required to achieve accuracy equal to SSTOL.

Different implementations of the drift correction algorithms have also been presented and discussed. It might seem somewhat surprising that in some cases (see Table 1) the use of the drift correction algorithm reduces the integration accuracy with respect to similar cases when no drift correction is applied. However, in most examples (including some not presented in this paper) the drift correction procedure proved to be useful and helped to improve integration accuracy. The examples presented here are rather basic which may explain why the algorithm without the drift correction works equally well. Results also show that similar levels of accuracy are obtained regardless whether the stiffness and the derivatives in the drift correction algorithm are calculated at the end or at the beginning of the substep.

The main advantage of the proposed algorithm lies in controlling the numerical integration error for BBM below a given tolerance set by the user. The algorithm also appears to be robust and yields accurate results for different types of stress paths (some not presented in this paper). Current research at Durham University is focusing on the application of the algorithm to advanced constitutive models proposed recently to link the mechanical behaviour to the retention properties of the soil, e.g. Gallipoli et al. (2003).

ACKNOWLEDGMENTS

Authors gratefully acknowledge funding by the European Commission through the MUSE Research Training Network, contract: MRTN-CT-2004-506861

REFERENCES

- Alonso, E.E., Gens, A. & Josa, A. 1990. A constitutive model for partially saturated soils. *Géotechnique* 40(3): 405–430.
- Borja, R.I. & Lee, S.R. 1990. Cam-Clay plasticity. Part I: Implicit integration of elastoplastic constitutive relations. *Comput. Methods Appl. Mech. Engg.* 78(1): 49–72.
- Borja, R.I. 1991. Cam-Clay plasticity, Part II: Implicit integration of constitutive equation based on a nonlinear elastic stress predictor. *Comput. Methods Appl. Mech. Engg.* 88(2): 225–240.
- Borja, R.I. 2004. Cam-Clay plasticity. Part V: A mathematical framework for three-phase deformation and strain localization analyses of partially saturated porous media. *Comput. Methods Appl. Mech. Engg.* 193(48–51): 5301–5338.
- Foster, C.D., Regueiro, R.A., Fossum, A.F. & Borja, R.I. 2005. Implicit numerical integration of a three-invariant,

- isotropic/kinematic hardening cap plasticity model for geomaterials. *Comput. Methods Appl. Mech. Engrg.* 194: 5109–5138.
- Gallipoli, D., Gens, A., Sharma, R. & Vaunat, J. 2003. An elastoplastic model for unsaturated soil incorporating the effects of suction and degree of saturation on mechanical behaviour. *Géotechnique* 53(1):123–135.
- Gear, W.G. (1971). *Numerical initial value problems in ordinary differential equations*. Englewood Cliffs, New Jersey USA: Prentice Hall Inc.
- Potts, D.M. & Zdravkovic, L. 1999. *Finite element analysis in geotechnical engineering. Theory*. London: Thomas Telford Publishing.
- Sheng, D., Sloan, S.W., Gens, A. & Smith, D.W. 2003a. Finite element formulation and algorithms for unsaturated soils. Part I: Theory. *Int. J. Numer. Anal. Meth. Geomech.* 27: 745–765.
- Sheng, D., Sloan, S.W., Gens, A. & Smith, D.W. 2003b. Finite element formulation and algorithms for unsaturated soils. Part II: Verification and application. *Int. J. Numer. Anal. Meth. Geomech.* 27: 767–790.
- Sheng, D., Sloan, S.W. & Yu, H.S. 2000. Aspects of finite element implementation of critical state models. *Computational Mechanics* 26: 185–196.
- Simo, J.C. & Hughes, T.J.R. 1998. *Computational inelasticity*. New York: Springer.
- Sloan, S.W. 1987. Substepping schemes for the numerical integration of elastoplastic stress-strain relations. *Int. J. Numer. Methods Eng.* 24: 893–911.
- Sloan, S.W., Abbo, A. J. & Sheng, D. 2001. Refined explicit integration of elastoplastic models with automatic error control. *Engineering Computations* 18(1/2): 121–154.
- Vaunat, J., Cante, J.C., Ledesma, A. & Gens, A. 2000. A stress point algorithm for an elastoplastic model in unsaturated soils. *International Journal of Plasticity*, 16: 121–141.
- Wang, X., Wang, L.B. & Xu, L.M. 2004. Formulation of the return mapping algorithm for elastoplastic soil models, *Computers and Geotechnics* 31: 315–338.
- Zhang, H.W., Heeres, O.M., de Borst, R. & Schrefler, B.A. 2001. Implicit integration of a generalized plasticity constitutive model for partially saturated soil. *Engineering Computations*, Vol. 18(1/2): 314–336.

Implicit integration of a new hyperelastic mixed isotropic-kinematic hardening model for structured clays

A. Amorosi & V. Germano
Politecnico di Bari, Bari, Italy

D. Boldini
University of Bologna, Bologna, Italy

ABSTRACT: The paper presents the implicit numerical integration by a Generalised Backward Euler algorithm of a mixed isotropic-kinematic hardening model for structured clays. In the first part the main characteristics of the model are presented. This is followed by the description of the return mapping algorithm which allows the model to be implemented in finite element codes, ensuring numerical accuracy and stability requirements to be satisfied. In the final part of the paper, numerical simulation of single element tests are illustrated.

1 INTRODUCTION

The mechanical response of natural clays is characterised by highly non-linear behaviour, memory of the past strain-history, evolving anisotropy, non-coaxiality and, when cemented, mechanically induced bond degradation phenomena. In recent years a number of constitutive models have been proposed to mathematically describe these features, often being characterised by complex formulations leading to non-trivial problems in their numerical integration. On the other hand, accuracy and stability are recognised as crucial requirements in the development of any integration algorithm for realistic material models, in order to ensure the necessary computational correctness and efficiency in their use within Finite Element codes.

The paper describes a fully implicit stress-point algorithm for the numerical integration of a single surface mixed isotropic-kinematic hardening plasticity model for initially bonded clays. The model is characterised by an ellipsoid-shaped yield function, inside which a stress dependent reversible stiffness is accounted for by a recently proposed non-linear hyperelastic formulation. The isotropic part of the hardening law extends the standard *Cam-Clay* one to include plastic strain-driven softening due to bond degradation, while the kinematic hardening part controls the evolution of the position of the yield surface in the stress space. This latter hardening term is formulated in such a way that along radial stress paths the centre of the yield

surface initially moves to then achieve a stabilised position, corresponding to the imposed direction of the path.

A Generalised Backward Euler algorithm is proposed for the numerical integration of the constitutive model. The return mapping algorithm is formulated in the space of elastic strain and internal variables, leading to a system of 14 unknowns and corresponding non-linear equations. The solution is achieved iteratively by means of the Newton's method. The proposed algorithm allows the consistent linearization of the constitutive equations guaranteeing the quadratic rate of asymptotic convergence in the global level Newton-Raphson iterative procedure. The accuracy and the convergence properties of the proposed algorithm are evaluated by numerical simulations of single element tests and represented by iso-error map.

In the following the soil mechanics sign convention is assumed and all stresses are effective stresses. Bold-face letters are used to represent tensor quantities of any order. The symbol $\mathbf{1}$ is used for the second-order identity tensor: $(\mathbf{1})_{ij} = \delta_{ij}$. Stress and strain states will also be represented using invariant quantities as: $p = (\boldsymbol{\sigma}:\mathbf{1})/3$ and $q = \sqrt{3}/2 \|\mathbf{s}\|$ to respectively indicate mean stress and deviatoric stress, $\varepsilon_v = \boldsymbol{\varepsilon}:\mathbf{1}$ and $\varepsilon_s = \sqrt{2}/3 \|\mathbf{e}\|$ to respectively indicate volumetric and deviatoric strain. The deviatoric part of the stress and strain tensors are represented by $\mathbf{s} = \boldsymbol{\sigma} - p\mathbf{1}$ and $\mathbf{e} = \boldsymbol{\varepsilon} - (\varepsilon_v/3)\mathbf{1}$. The symbol $\|\cdot\|$ indicate the L_2 -norm.

2 CONSTITUTIVE MODEL

2.1 Elastic behaviour

The reversible behaviour is described by a hyperelastic formulation recently proposed by Houlsby *et al.* (2005). The adopted free energy potential and the corresponding complementary energy have the following expressions:

$$F(\varepsilon_v, \varepsilon_s) = \frac{p_a}{2-n} k^{2-2n} (1-n)^{\frac{2-n}{1-n}} \times \left[k\varepsilon_v^2 + \frac{3g}{1-n} \varepsilon_s^2 \right]^{\frac{2-n}{2-2n}} \quad (1)$$

$$E(p, q) = \frac{1}{p_a^{(1-n)} k (1-n) (2-n)} \times \left(p^2 + \frac{k(1-n)}{3g} q^2 \right)^{\frac{2-n}{2}} \quad (2)$$

where p_a is a reference stress corresponding to the atmospheric pressure, while n , k and g are dimensionless experimentally determined parameters. The first and second derivative of (1) with respect to elastic strain ($\boldsymbol{\varepsilon}^e$) provide the corresponding stress state ($\boldsymbol{\sigma}$) and elastic stiffness (\mathbf{C}^e), respectively.

2.2 Elastoplastic behaviour

The elastic domain is defined by the convex set $\mathbf{E}_\sigma = \{(\boldsymbol{\sigma}, \mathbf{q}) | f(\boldsymbol{\sigma}, \mathbf{q}) \leq 0\}$, where the internal variables set $\mathbf{q} = \mathbf{q}(\alpha, \boldsymbol{\sigma}_K)$ define the dimension and the position of the yield function f :

$$f(\boldsymbol{\sigma}, \alpha, \boldsymbol{\sigma}_K) = \frac{1}{c^2} (\mathbf{s} - \mathbf{s}_K) : (\mathbf{s} - \mathbf{s}_K) + (p - p_K)^2 - \alpha^2 \quad (3)$$

The geometrical representation of the yield surface in the stress space $\boldsymbol{\sigma} \equiv (p, \mathbf{s})$ is an ellipsoid centred at point K with co-ordinates $\boldsymbol{\sigma}_K = p_K \mathbf{1} + \mathbf{s}_K$.

The isotropic hardening rule controls the size of the yield surface while the kinematic hardening governs the motion of the yield surface in the stress space. The former is a modified version of that originally proposed by Kavvasdas & Amorosi (2000) in their Model for Structured Soils:

$$\dot{\alpha} = \alpha \left[\frac{1}{\tilde{\lambda} - \tilde{\kappa}} \dot{\varepsilon}_v^p - \xi_v \exp(-\eta_v \varepsilon_v^d) \dot{\varepsilon}_v^d - \xi_s \exp(-\eta_s \varepsilon_s^p) \dot{\varepsilon}_s^p \right] = \dot{\gamma} h \quad (4)$$

It is composed by two volumetric terms and a deviatoric one. The first volumetric term is similar to the standard Modified Cam-Clay hardening law, while the following terms account for the volumetric and

deviatoric strain induced structure degradation (debonding) by means of two separate exponential damage-type form. The volumetric strain induced destructuring is controlled by $\dot{\varepsilon}_v^d = |\dot{\varepsilon}_v^d|$.

During plastic deformation the centre K of the yield surface moves as follows:

$$\dot{\boldsymbol{\sigma}}_K = \frac{\dot{\alpha}}{\alpha} \boldsymbol{\sigma}_K + \psi \frac{\dot{\alpha}}{\alpha} \left(\mathbf{s} - \chi \frac{p}{p_K} \mathbf{s}_K \right) \quad (5)$$

where χ and ψ are parameters. It is formulated in such a way that along radial stress paths the centre of the yield surface initially moves to then achieve a stabilised position, corresponding to the imposed direction of the path. Finally, the loading/unloading criterion is expressed by the Kuhn-Tucker complementary conditions $\dot{\gamma} \geq 0$, $f(\boldsymbol{\sigma}, \alpha, \boldsymbol{\sigma}_K) \leq 0$, $\dot{\gamma} f(\boldsymbol{\sigma}, \alpha, \boldsymbol{\sigma}_K) = 0$, leading to the standard consistency condition for the plastic multiplier $\dot{\gamma}$ as expressed by $\dot{\gamma} f(\boldsymbol{\sigma}, \alpha, \boldsymbol{\sigma}_K) = 0$.

3 IMPLICIT NUMERICAL INTEGRATION

A Generalized Backward Euler algorithm is adopted to integrate the constitutive model (e.g., Simo & Hughes, 1997) according to previously published works (Amorosi & Boldini, 2003; Germano, 2005). It is formulated in the space of the elastic strain and internal variables for a general time step Δt between $[t_n, t_{n+1}]$ over which an increment of total strain $\Delta \boldsymbol{\varepsilon}_{n+1} = \nabla^s(\Delta \mathbf{u}_{n+1})$ is assigned. Firstly, the elastic predictor problem is solved by freezing the plastic flow:

$$\begin{aligned} \boldsymbol{\varepsilon}_{n+1}^{e,trial} &= \boldsymbol{\varepsilon}_n^e + \Delta \boldsymbol{\varepsilon}_{n+1} \\ \boldsymbol{\varepsilon}_{n+1}^{p,trial} &= \boldsymbol{\varepsilon}_n^p \\ \alpha_{n+1}^{trial} &= \alpha_n \\ \boldsymbol{\sigma}_{K,n+1}^{trial} &= \boldsymbol{\sigma}_{K,n} \\ \boldsymbol{\sigma}_{n+1}^{trial} &= \frac{\partial F(\boldsymbol{\varepsilon}_{n+1}^{e,trial})}{\partial \boldsymbol{\varepsilon}^e} \end{aligned} \quad (6)$$

If the consistency condition is satisfied $f_{n+1}(\boldsymbol{\sigma}_{n+1}^{trial}, \alpha_{n+1}^{trial}, \boldsymbol{\sigma}_{K,n+1}^{trial} + 1) \leq 0$, the process is declared elastic, otherwise a plastic correction is required. In this case a system of 14 non-linear equations:

$$\begin{aligned} \boldsymbol{\varepsilon}_{n+1}^e &= \boldsymbol{\varepsilon}_{n+1}^{e,trial} - \Delta \gamma_{n+1} \hat{\partial}_\sigma f_{n+1} \\ f_{n+1} &:= f_{n+1}(\boldsymbol{\sigma}_{n+1}, \alpha_{n+1}, \boldsymbol{\sigma}_{K,n+1}) = 0 \\ \alpha_{n+1} &= \alpha_{n+1}^{trial} + \Delta \gamma_{n+1} h_{n+1} \\ \boldsymbol{\sigma}_{K,n+1} &= \left[\boldsymbol{\sigma}_{K,n+1}^{trial} + \psi \frac{\alpha_{n+1} - \alpha_n}{\alpha_{n+1}} \right. \\ &\quad \left. \times \left(\mathbf{s}_{n+1} - \chi \frac{p_{n+1}}{p_{K,n+1}} \mathbf{s}_{K,n+1} \right) \right] \left(1 - \frac{\alpha_{n+1} - \alpha_n}{\alpha_{n+1}} \right)^{-1} \end{aligned} \quad (27)$$

in the 14 unknowns $(\boldsymbol{\epsilon}_{n+1}^e, \alpha_{n+1}, \boldsymbol{\sigma}_{K,n+1}^T, \Delta\gamma_{n+1})$ is solved iteratively by means of Newton's method.

In order to maintain the quadratic rate of asymptotic convergence that characterises the application of the iterative Newton's method at the global level in a FE code, the consistent elasto-plastic tangent modulus has to be defined accordingly to the local integration algorithmic scheme. The described integration algorithm allows the consistent tangent operator to be computed in closed form. The following expressions is obtained in the elastic strain space:

$$\mathbf{C}_{n+1} := \frac{\partial \boldsymbol{\sigma}_{n+1}}{\partial \boldsymbol{\epsilon}_{n+1}} = \frac{\partial \boldsymbol{\sigma}_{n+1}}{\partial \boldsymbol{\epsilon}_{n+1}^{e,trial}} = \mathbf{C}_{n+1}^e \frac{d\boldsymbol{\epsilon}_{n+1}^e}{d\boldsymbol{\epsilon}_{n+1}^{e,trial}} \quad (8)$$

4 NUMERICAL EXAMPLES

The accuracy, stability and convergence properties of the proposed algorithm are evaluated by numerical simulations on one 3D-cubic FE element. The following material parameters have been adopted in all the numerical analyses: $c = 0.816$, $\tilde{\lambda} = 0.097$, $\tilde{k} = 0.01$, $n = 0.5$, $p = 1 \text{ kPa}$, $k = 500$, and $g = 375$. The global and the local tolerance (i.e., the tolerance for the convergence at the integration point level) are both set equal to 10^{-10} .

Figure 1 shows the response in terms of stress (Fig. 1b) to a closed strain cycle (Fig. 1a), applied in elastic region: the adopted hyperelastic formulation ensures that no energy is dissipated, i.e. a conservative response is obtained.

Figure 2 shows the influence of the time step dimension on the results of a radial path test from an initial isotropic state of stress given by $p = 75 \text{ kPa}$, $q = 0 \text{ kPa}$ and $\alpha = 150 \text{ kPa}$ and the yield locus centered on the isotropic axis. After two p -constant steps necessary to bring the state of stress on the radial path characterized by a stress ratio $\eta = 0.4$ ($p = 75 \text{ kPa}$, $q = 30 \text{ kPa}$), a total increment of $\Delta p = 900 \text{ kPa}$ and $\Delta q = 360 \text{ kPa}$ is applied in 120, 60, 30 and 15 steps, respectively. During this stage the kinematic hardening is activated ($\psi = 1.0$, $\chi = 4.0$) while the destructuration process is switched off. The results, given in terms of stress path (p - q curve) (Fig. 2a), location of the yield locus center (p_K - q_K curve) (Fig. 2a) and compression curve (e - $\log p$ curve) (Fig. 2b), demonstrate the high accuracy of the proposed algorithm even for large step sizes.

Starting from the final state of the radial stress path, a isochoric axisymmetric test is performed by applying a total deviatoric strain of 15% in 1000, 100, 20 and 10 steps, respectively (Fig. 3).

In these analyses the kinematic hardening is set off and the destructuration process is activated for values of the deviatoric degradation parameters equal to $\xi_s = 5$ and $\eta_s = 10$, with the volumetric degradation

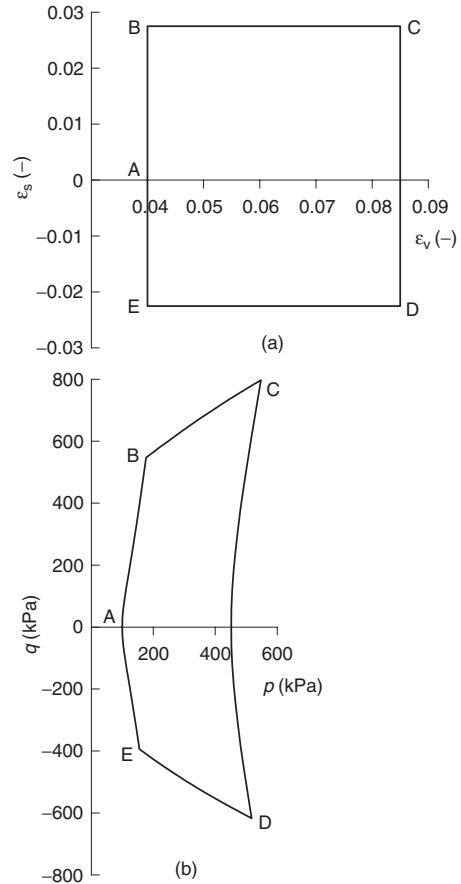
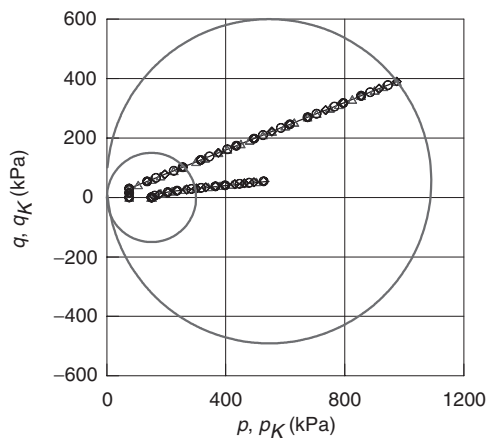


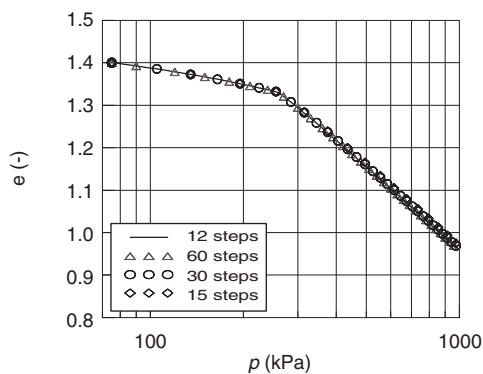
Figure 1. Closed stress and strain cycles in the elastic region.

parameters set equal to zero ($\xi_v = \eta_v = 0$). The plastic strains are initialized back to zero at the begin of the tests. The stress path (Fig. 3a) and the stress-strain curve (Fig. 3b) are characterized by a slight strain-softening before reaching the critical state: this is due to the activation of the destructuring process. Even in this case the error introduced by increasing the dimension of the step size is remarkable low. The local quadratic convergence profiles for the isochoric axisymmetric test performed in ten steps, are plotted in Figure 4.

The convergence profiles of the global Newton iterations for three selected steps of the radial stress path test performed in 15 steps (Fig. 2) are reported in Figure 5. The convergence is evaluated with reference to the largest residual norm of the equilibrium iteration normalized with respect to its initial value. The results clearly provide evidence of the asymptotic quadratic rate of convergence of the algorithm at the global level.



(a)



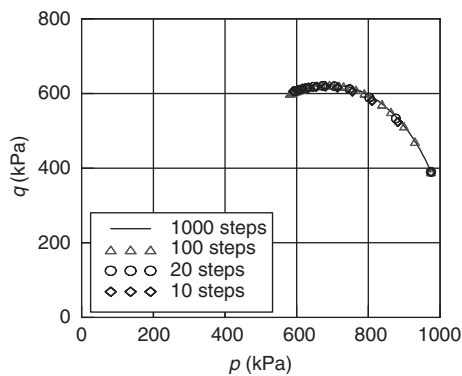
(b)

Figure 2. Radial test with $\eta = 0.4$: influence of time step dimension.

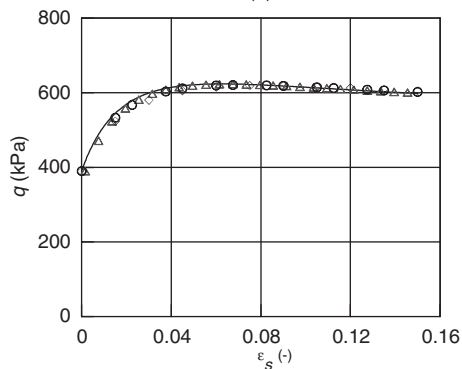
The satisfactory performance of the algorithm is confirmed by the iso-error map shown in Figure 6, obtained by applying linear combinations of volumetric and deviatoric strain increments starting from the following initial conditions: $p = 138$ kPa, $q = 92$ kPa, $\alpha = 100$ kPa and the yield locus centred on the isotropic axis. In the analysis all the material parameters are activated ($\xi_v = 10$, $\eta_v = 15$, $\xi_s = 5$, $\eta_s = 10$, $\psi = 1.0$, $\chi = 4.0$). The iso-error map confirms that the error is remarkably low.

5 CONCLUSIONS

In conclusion, this paper outlines the development of a new constitutive model for natural clays and its implicit numerical integration. The work has been aimed at obtaining a balanced compromise between



(a)



(b)

Figure 3. Isochoric axisymmetric test: influence of time step dimension.

a sufficiently accurate description of the mechanics of natural clays and a robust numerical algorithm to be adopted in the solution of Boundary Value Problems.

It is finally worth remarking that the proposed model, differently from other recently published ones (e.g., Tamagnini *et al.*, 2002; Foster *et al.*, 2005), is developed in the general stress/strain space, to account for the directional properties that might develop in anisotropically compressed clayey materials. As such, both the model and the related implicit algorithm here described are characterised by an enhanced level of complexity as compared to those based on invariant formulation.

REFERENCES

- Amorosi, A. & Boldini, D. 2003. Single surface hardening plasticity model for soft clays: mathematical formulation and implicit numerical integration. In Vermeer, Schweiger, Karstunen & Cundy (eds), *Geotechnics of Soft Soils – Theory and Practice*; Proc. intern. Work. Noordwijkerhout.

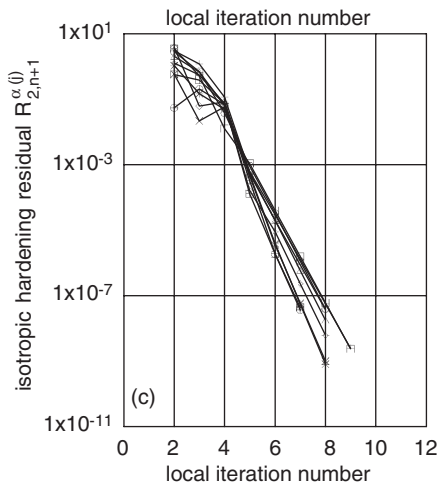
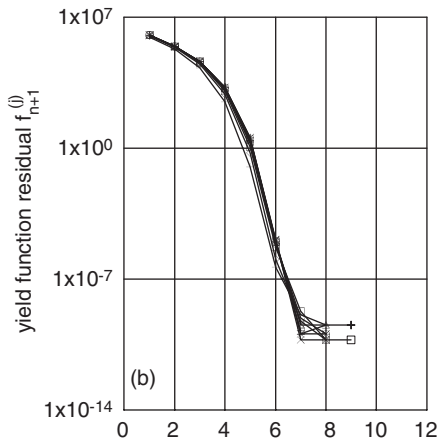
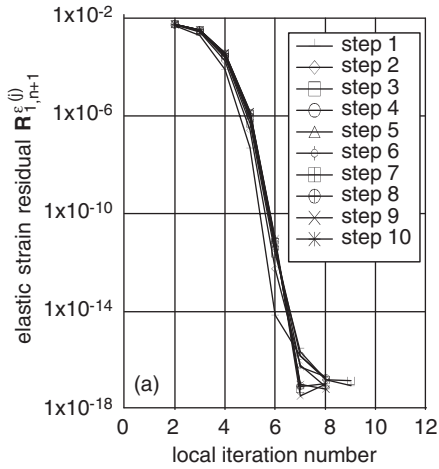


Figure 4. Local convergence profiles from isochoric axisymmetric compression test.

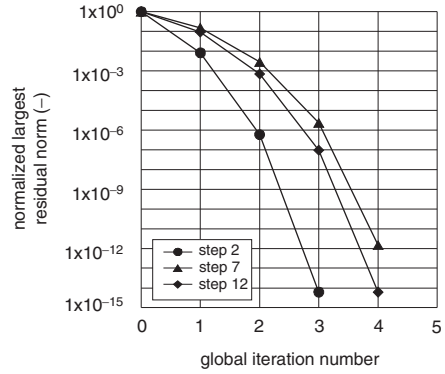


Figure 5. Convergence profiles for the global iterations for 3 selected steps.

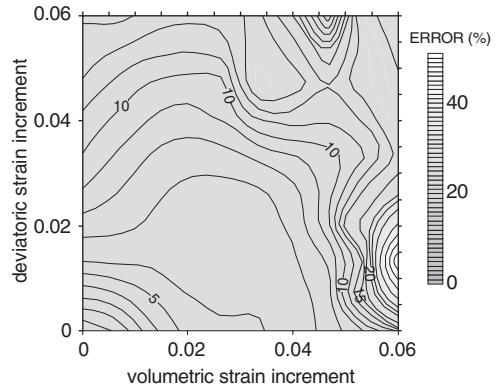


Figure 6. Iso-error map.

Foster, C.D., Regueiro, R.A., Fossum, A.F. & Borja, R.I. 2005. Implicit numerical integration of a three-invariant, isotropic/kinematic hardening cap plasticity model for geomaterials. *Computer Methods in Applied Mechanics and Engineering*, (194), 50–52: 5109–5138.

Germano, V. 2005. Integrazione implicita di un modello costitutivo per terreni naturali. Doctoral Thesis, Technical University of Bari, Italy.

Houlsby, G.T., Amorosi, A. & Rojas, E. 2005. Elastic Moduli of soils dependent on pressure: a hyperelastic formulation. *Géotechnique* 55 (5): 383–392.

Kavvas, M. & Amorosi, A. 2000. A constitutive model for structured soils. *Géotechnique* 50 (3): 263–273.

Simo, J.C. & Hughes, T.J.R. 1997. *Computational Inelasticity*. New York: Springer.

Tamagnini, C., Castellanza, R. & Nova, R. 2002. A Generalized Backward Euler algorithm for the numerical integration of an isotropic hardening elastoplastic model for mechanical and chemical degradation of bonded geomaterials. *Int. J. Numer. Anal. Meth. Geomech.* 26: 963–1004.

Influence of the initial void ratio on the evolution of the passive earth pressure

J. Tejchman

Civil Engineering Department, Gdansk University of Technology, Gdansk, Poland

E. Bauer

Institute of Applied Mechanics, Graz University of Technology, Graz, Austria

ABSTRACT: This paper focuses on the influence of the initial void ratio on the evolution of the passive earth pressure and the formation of shear zones in a dry sand body behind a retaining wall. For the numerical simulation a rigid and very rough retaining wall undergoing a horizontal translation against the backfill is considered. The essential mechanical properties of granular soil is described with a micro-polar hypoplastic model which takes into account stresses and couple stresses, pressure dependent limit void ratios and the mean grain size as the characteristic length. Numerical investigations are carried out with an initially medium dense and an initially loose sand in which a certain random distribution of the initial void ratio is assumed. The geometry of calculated shear zones is discussed and compared with a corresponding laboratory model test.

1 INTRODUCTION

The earth pressure on retaining walls belongs to a classical problem of soil mechanics. In spite of intense theoretical and experimental research on this problem over more than 200 years, there are still large discrepancies between theoretical solutions and experimental results due to the complexity of the deformation field in granular bodies near the wall caused by the localization of deformations. Realistic earth pressures can only be calculated with continuum models which are able to describe the formation of shear zones with a certain thickness, i.e. the constitutive model has to be endowed with a characteristic length of the micro-structure. Otherwise, finite element results are completely controlled by the size and orientation of the mesh and thus produce unreliable results, i.e. element size becomes the characteristic length, the shear zones become narrower upon mesh refinement and computed force-displacement curves change considerably depending on the thickness of the calculated shear zone. The experimental results show that the thickness of shear zones in granular materials depends on many different factors such as: pressure level, void ratio, mean grain diameter, grain roughness, grain hardness, surface roughness and the stiffness of the surrounding structure in contact with a granular body. In the localized shear zones, grain rotations, couple stresses, large strain gradients and volume changes and void ratio fluctuations occur (e.g. Oda et al.

1982, Mühlhaus & Vardoulakis 1987, Desrues et al. 1996, Gudehus 1997, and Oda & Kazama 1998).

In this paper the formation of the pattern of shear localization in a cohesionless soil behind a vertical retaining wall undergoing a horizontal translation against the backfill is numerically simulated with the finite element method. In order to model strain localization in the soil a micro-polar continuum or so-called Cosserat continuum is used which takes into account two linked levels of deformation: micro-rotation at the particle level and macro-deformation at the structural level. A characteristic length occurs which can be directly related to the mean grain diameter. When shearing takes place, the Cauchy stress tensor becomes non-symmetric. Pasternak & Mühlhaus (2001) demonstrated that the additional rotational degree of freedom of a Cosserat continuum arises naturally by the mathematical homogenisation of an originally discrete system of spherical grains with contact forces and contact moments. Ehlers et al. (2003) showed that a particle ensemble has the character of a micro-polar Cosserat continuum: the couple stresses naturally result only from the eccentricities of the normal contact forces. For the investigation in the present paper a micro-polar continuum model based on the framework of hypoplasticity is used which is apt to model anelastic material properties and the influence of pressure, void ratio, grain size, grain hardness and grain roughness on the incremental stiffness and volume change behaviour

(e.g. Bauer & Tejchman 1998, Huang & Bauer 2003, Tejchman & Bauer 2005a, 2005b, Tejchman 2001, 2002, 2004a, 2004b, 2006). The emphasis of the present investigation is on the influence of the initial void ratio on the evolution of shear zones and the development of the resulting passive earth pressure behind the retaining wall under a plane strain condition. For the initial state, a random (spatially non-correlated) distribution of the void ratio is assumed to take into account the void ratio fluctuation as an inherent property of nature soil skeletons. The calculated geometry of shear localization is compared with the experimental results of a model test. The computed earth pressure coefficients are compared with formulas based on slip surface mechanisms.

2 MICRO-POLAR HYPOPLASTIC MODEL

For the continuum modeling of granular materials hypoplasticity represents an alternative to elasto-plastic formulations (e.g. Kolymbas 1991, Wu & Kolymbas 2000, Bauer & Herle 2000). In contrast to elasto-plastic models, the decomposition of deformation components into elastic and plastic parts, yield surface, plastic potential, flow rule and hardening rule are not needed. Hypoplastic models are apt to take into account effects of barotropy (dependence on pressure level), pycnotropy (dependence on density), dilatancy, contractancy and material softening (e.g. Wu & Bauer 1993, Wu et al. 1996). Critical states are also included, i.e. states in which the granular body can be deformed continuously at a constant stress and a constant volume under a certain rate of deformation (Bauer 2000). A feature of the model is a simple formulation and procedure for the determination of material parameters with standard laboratory experiments. The parameters are related to granulometric properties encompassing the grain size distribution curve, shape, angularity and hardness of the grain ensemble (e.g. Bauer 1996, Herle & Gudehus 1999). Thus one set of material parameters is sufficient to reproduce the essential behaviour of granular materials within a large range of pressures and densities. For the present investigations of strain localization a hypoplastic model based on a micro-polar continuum is used. In a micro-polar continuum each material point has translational degrees of freedom and rotational degrees of freedom. The gradients of the rotation are connected to curvatures which are associated with couple stresses. The occurrence of couple stresses leads to a non-symmetry of the stress tensor and the presence of a characteristic length. In the present model the characteristic length is directly related to the mean grain diameter of the granular material. In the following it is assumed that the state of the granular material is determined by the stress tensor σ , the couple stress tensor μ and the void ratio e . Within the framework of micro-polar hypoplasticity the evolution of these state

quantities is described by the following objective rate type equations (e.g. Tejchman & Gudehus 2001, Tejchman & Bauer 1996, 2004):

$$\begin{aligned} \dot{\sigma}_{ij} = & f_s \left[a^2 \dot{\epsilon}_{ij} + (\dot{\sigma}_{kl} \dot{\epsilon}_{kl} + \dot{\mu}_{kl} \dot{\bar{k}}_{kl}) \dot{\sigma}_{ij} + \right. \\ & \left. + f_d a (\dot{\sigma}_{ij} + \dot{\sigma}_{ij}^*) \sqrt{\dot{\epsilon}_{kl} \dot{\epsilon}_{kl} + \dot{\bar{k}}_{kl} \dot{\bar{k}}_{kl}} \right], \end{aligned} \quad (1)$$

$$\begin{aligned} \dot{\mu}_{ij} = & f_s d_{50} a^2 \left[\dot{\bar{k}}_{ij} + \dot{\mu}_{ij} (\dot{\sigma}_{kl} \dot{\epsilon}_{kl} + \right. \\ & \left. + \dot{\mu}_{kl} \dot{\bar{k}}_{kl} + f_d a_c \sqrt{\dot{\epsilon}_{kl} \dot{\epsilon}_{kl} + \dot{\bar{k}}_{kl} \dot{\bar{k}}_{kl}} \right], \end{aligned} \quad (2)$$

$$\dot{e} = (1 + e) \dot{\epsilon}_{kk}, \quad (3)$$

where $\dot{\sigma}_{ij}$ is the Jaumann stress rate, $\dot{\mu}_{ij}$ the Jaumann couple stress rate, \dot{e} the rate of the void ratio, d_{50} the mean grain diameter, $\dot{\sigma}_{ij} = \sigma_{ij}/\sigma_{kk}$ the normalized stress, $\dot{\sigma}_{ij}^* = \dot{\sigma}_{ij} - \delta_{ij}/3$ the deviatoric part of the normalized stress, δ_{ij} is the Kronecker delta, $\dot{\mu}_{kl} = \mu_{kl}/(d_{50} \sigma_{kk})$, the normalized couple stress and $\dot{\bar{k}}_{ij} = d_{50} \dot{k}_{ij}$ the scaled rate of curvature. Function a in Eq. (1) and Eq. (2) is related to the intergranular friction angle φ_c , i.e.

$$a^{-1} = c_1 + c_2 \sqrt{\dot{\sigma}_{kl}^* \dot{\sigma}_{kl}^*} \left[1 - \frac{\sqrt{6} \dot{\sigma}_{kl}^* \dot{\sigma}_{lm}^* \dot{\sigma}_{mk}^*}{(\dot{\sigma}_{kl}^* \dot{\sigma}_{kl}^*)^{3/2}} \right] \quad (4)$$

with

$$c_1 = \sqrt{\frac{3}{8}} \frac{(3 - \sin \varphi_c)}{\sin \varphi_c}$$

and

$$c_2 = \frac{3}{8} \frac{(3 + \sin \varphi_c)}{\sin \varphi_c}.$$

The dilatancy behaviour, the peak stress ratio and strain softening depends on the density factor f_d , which represents a relation between the current void ratio e , the critical void ratio e_d and the minimum void ratio e_d , i.e.

$$f_d = \left(\frac{e - e_d}{e_c - e_d} \right)^\alpha. \quad (5)$$

The stiffness factor f_s is proportional to the granular hardness h_s , i.e.

$$f_s = \frac{h_s}{n h_i} \frac{(1 + e_i)}{e} \left(-\frac{\sigma_{kk}}{h_s} \right)^{1-n} \quad (6)$$

with

$$h_i = \frac{1}{c_1^2} + \frac{1}{3} - \frac{1}{c_1 \sqrt{3}} \left(\frac{e_{io} - e_{do}}{e_{co} - e_{do}} \right)^\alpha.$$

In (5) and (6) the current void ratio e is related to the pressure dependent maximum void ratio e_i , minimum void ratio e_d and critical void ratio e_c , i.e.

$$\frac{e_i}{e_{i0}} = \frac{e_d}{e_{d0}} = \frac{e_c}{e_{c0}} = \exp \left[- \left(- \frac{\sigma_{kk}}{h_s} \right)^n \right].$$

The constitutive model requires the following nine material constants: h_s , n , e_{i0} , e_{d0} , e_{c0} , φ_c , α , d_{50} and a_c . The parameters h_s and n are estimated from a single isotropic compression test with an initially loose specimen. The internal friction angle at the residual state φ_c is determined from the angle of repose or measured in a triaxial test with a loose specimen. The void ratios e_{i0} , e_{d0} and e_{c0} are related to the maximum, minimum and critical values at zero mean pressure. The constant α can be calibrated from the peak friction angle obtained in a triaxial or biaxial test with a dense specimen. The micro-polar constant a_c can be found with comparative numerical studies of shearing of an infinite narrow layer (Tejchman & Gudehus 2001). For the present investigations the following material constants for a fine quartz sand are used: $h_s = 190$ MPa, $n = 0.5$, $e_{i0} = 1.3$, $e_{d0} = 0.51$, $e_{c0} = 0.82$, $\varphi_c = 30^\circ$, $a_c = a^{-1}$, $\alpha = 0.3$ and $d_{50} = 0.5$ mm.

3 NUMERICAL INVESTIGATIONS

For the numerical investigations the same size of the sand body is used as for the laboratory test performed at Karlsruhe University by Gudehus & Schwing (1986), i.e. an initially height of $H = 200$ mm and a length of $L = 400$ mm. In the case of plane strain each point in a micropolar continuum has three degrees of freedom, namely two displacement degrees of freedom and one rotational degree of freedom (Figure 1). Quadrilateral finite elements composed of four diagonally crossed triangles are applied to avoid volumetric locking due to dilatancy effects (Groen 1997). Linear shape functions for displacements and the micro-rotation are used. The height of the retaining wall located on the right side of the sand body is assumed to be $h = 170$ mm. The calculations are carried out with large deformations and curvatures using the updated Lagrange formulation. The initial stresses are generated for a K_o -state without polar quantities. The top of the sand specimen is traction and moment free. The vertical retaining wall and the bottom of the sand specimen are assumed to be stiff and very rough, i.e. there are no relative displacements and micro-rotations along the vertical and horizontal surfaces. A uniform horizontal translation u of the wall against the backfill is prescribed. In order to investigate the influence of the initial density calculations with an initially medium dense sand and an initially loose sand are carried out. For the initial state a random distribution of the initial void ratio is

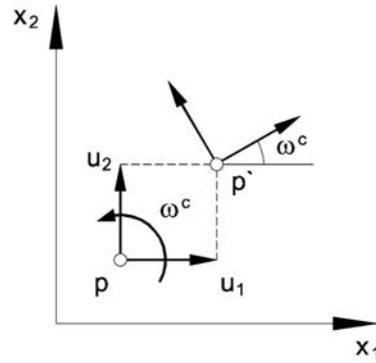


Figure 1. Degrees of freedom in the plane strain micropolar continuum: u_1 , u_2 displacement degrees of freedom and ω^c rotational degree of freedom.

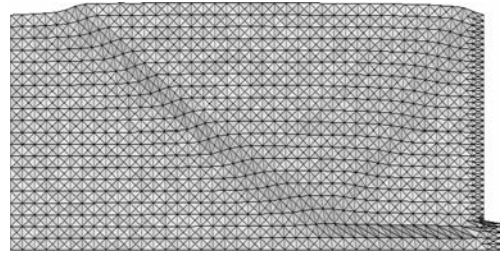


Figure 2. Deformed FE-mesh with distribution of void ratio for an initially dense sand after a wall translation of $u/h = 0.07$ (light and dark areas correspond to a small and a large void ratio, respectively).

assumed to enhance and promote the whole process of the shear zone formation. The fluctuation of the initial void ratio is an inherent property of natural soil skeletons and it is usually more marked for loose than for dense skeletons (Nübel & Huang 2004).

For the initially medium dense state ($\gamma_o = 16.58$ kN/m³, $e_o = 0.65$) the mean initial void ratio is distributed according to $\bar{e}_o = 0.60 + 0.1 r$, where r is a random number within the range of ($0 \leq r \leq 1$). The results obtained from the finite element calculation are shown in Figures 2–6. In particular Figure 2 shows the deformed mesh with the distribution of the void ratio after a wall translation of $u/h = 0.07$. The darker region indicates a higher void ratio, which is related to a significant dilatancy of the material in zones where shear localization takes place. Zones of shear localization are also indicated by the appearance of micro-rotations. The evolution of the micro-rotation in three different states of the wall displacement is shown in Figures 3–5, where the micro-rotation is marked by circles with a diameter corresponding to the magnitude of the rotation in the given state. The material starts to generate micro-rotations and to

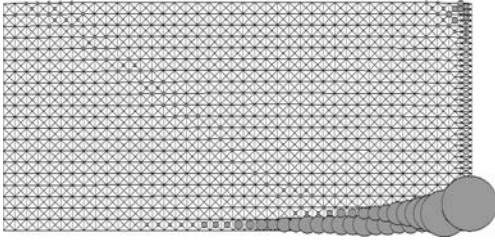


Figure 3. Deformed FE-mesh with distribution of micro-rotation for an initially dense sand after a wall translation of $u/h = 0.01$.

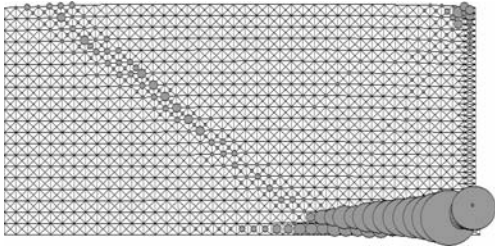


Figure 4. Deformed FE-mesh with distribution of micro-rotation for an initially dense sand after a wall translation of $u/h = 0.02$.

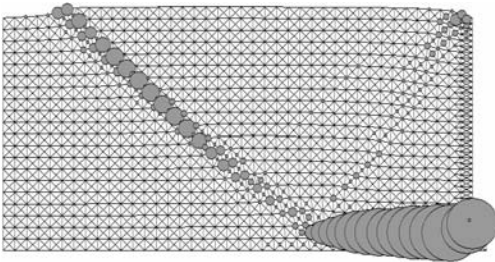


Figure 5. Deformed FE-mesh with distribution of micro-rotation for an initially dense sand after a wall translation of $u/h = 0.07$.

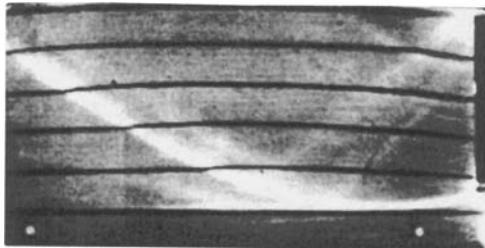


Figure 6. Shear zones in a sand specimen observed in experiments by radiographs (Gudehus and Schwing 1986).

dilate at three different locations: at the wall base, the wall top and the free surface boundary on the left side. For a small wall translation a pronounced shear localization can only be detected at the bottom (Figure 3). The onset of this horizontal shear zone is forced by the base of the wall. Strong dilatancy and high particle rotations occur from the beginning of the wall translation. The following inclined shear zone goes upwards, becomes straight and reaches the free surface boundary. It becomes dominant in the course of deformation (Figures 4–5). For larger wall displacements two additional radial shear zones appear. One starts from the wall top and the other one from the transition area between the horizontal shear zone to the inclined one (Figure 5) but both are not fully developed at $u/h = 0.07$. The dominant shear zone starts from the base and it has an inclination of about 40° . A comparison of Figure 2 with Figure 6 shows that the calculated geometry of shear zones is in agreement with experimental observations at Karlsruhe University by Gudehus & Schwing (1986).

In order to investigate the behaviour for an initially loose state of the sand material ($\gamma_o = 14.22 \text{ kN/m}^3$, $e_0 = 0.90$) the mean initial void ratio is distributed according to $\bar{e}_0 = 0.85 + 0.1 r$, where r is a random number within the range of ($0 \leq r \leq 1$). The results obtained from the finite element calculation are shown in Figures 7–8. In contrast to the initially dense sand the

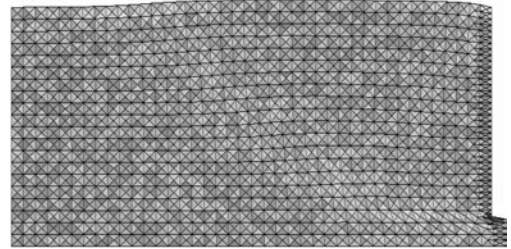


Figure 7. Deformed FE-mesh with distribution of void ratio for an initially loose sand after a wall translation of $u/h = 0.07$ (light and dark areas correspond to a small and a large void ratio, respectively).

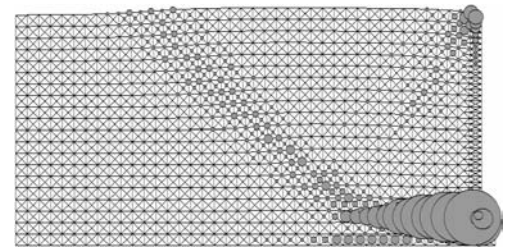


Figure 8. Deformed FE-mesh with distribution of micro-rotation for an initially loose sand after a wall translation of $u/h = 0.07$.

material shows compaction but the void ratio distribution does not indicate a clear shear band after a wall translation of $u/h = 0.07$ (Figure 7). However, a closer inspection of the distribution of the micro-rotation shows the appearance of at least three shear zones: a horizontal shear zone starting from the wall base, followed by a slightly curved and inclined zone spreading between the bottom of the wall and the free boundary, and one radially oriented diffuse shear zone starting at the top of the wall. A comparison of Figure 5 with Figure 8 shows that for the same horizontal wall translation the magnitude of the micro-rotation in the inclined shear zone is smaller for the initially loose state than for the dense one. In turn the thickness of the localized zone is larger for the initially loose state.

Figure 9 presents the evolution of the normalized horizontal earth pressure force versus the normalized horizontal wall displacement for both the initially dense and the initially loose state of the material. The force E_h is calculated as the integral of the mean horizontal normal stresses from quadrilateral elements along the retaining wall. For the initially loose state of the material (Figure 9.a) the horizontal force acting on the wall increases continuously. The maximum earth pressure coefficient is $K_p = 2E_h/(\gamma_o h^2) = 6.9$ at $u/h = 0.07$.

Based on slip line mechanisms and for the assumption of a rough wall the passive earth pressure coefficient is: $K_p = 10.1$ for the single slip line and $K_p = 7.6$ for the passive log-sandwich mechanism (Chen 1975) at $\delta = \varphi_c = 30^\circ$ with respect to the wall friction angle δ and the internal friction angle φ_c in the critical state. For the initially dense state (Figure 9.b) the horizontal earth pressure increases, reaches a maximum at about $u/h = 1\%$ and after the peak it shows softening. The high maximum earth pressure coefficient of $K_p = 15.8$ is caused by the high peak friction angle of the dense

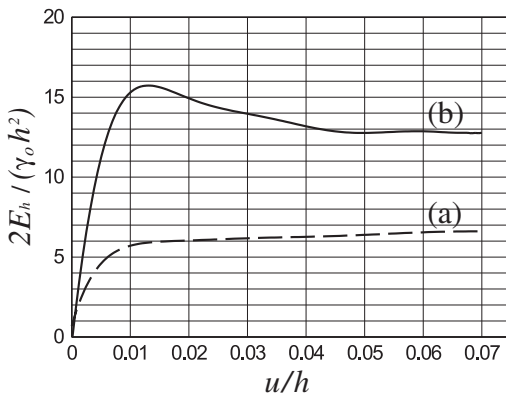


Figure 9. Resultant normalized earth pressure force $2E_h/(\gamma_o h^2)$ versus normalized wall displacement u/h for : (a) initially loose state, (b) initially dense state.

material. With respect to the pressure dependent density factor in Equation 5 the constitutive model predicts a peak friction angle which is higher for a denser material and a lower stress level. Considering the small height of the sand body the mean pressure obtained from the gravity load is very small, which for the initially dense sand leads to a friction angle of about $\varphi_p = 40^\circ - 43^\circ$. The maximum earth pressure obtained in the present calculation is much lower compared to the predictions based on slip line mechanisms. In particular for the internal peak friction angle of $\varphi_p = 42^\circ$ and the assumption of a wall friction angle of $\delta = 30^\circ$ the earth pressure coefficient is $K_p = 31$ for a single slip line mechanism and $K_p = 20$ for the passive log-sandwich mechanism. The earth pressure coefficient is high due to the assumption of a very rough wall. In turn for $\delta = (2/3)\varphi = 28^\circ$ one obtains: $K_p = 25$ for a single slip line and $K_p = 19.2$ for the passive log-sandwich mechanism. In this context it should be noted that the actual peak friction angles in the shear zones are not known in advance as they strongly depend on the initial and boundary conditions of the entire system. The different friction angles also occur along the same shear zone. Furthermore the numerical calculations also show that different friction angles are mobilized in the various shear zones at the same time. Therefore, it is difficult to obtain realistic earth pressures with a conventional earth pressure theory.

4 CONCLUSIONS

The evolution of shear localization, dilatancy, micro-rotation and earth pressure behind a very rough and rigid retaining wall undergoing a horizontal translation against the backfill under plane strain condition is numerically investigated with the finite element method and a micro-polar hypoplastic continuum model. The following conclusions can be drawn:

The proposed micro-polar hypoplastic approach is capable of capturing the complex patterning of shear zones in the granular body behind the retaining wall. The predicted geometry of shear zones are qualitatively in agreement with the experimental results of a model test. Shear zones are clearly indicated by micro-rotations for both initially dense and initially loose states of the material. The thickness of the localized zone is higher for the initially loose material. For the initially dense material strong dilatancy develops during passive wall translation within the localized zones. Herein dilatancy is accompanied with a reduction of the resulting earth pressure. In turn compaction of the material is observed in the case of the initially loose material. The earth pressures significantly change with the wall displacement. Conventional earth pressure mechanisms with slip surfaces are roughly reproduced. Realistic earth pressure coefficients can be

obtained with the actual values of internal friction angles. The maximum passive earth pressure strongly depends on the initial density and the pressure level. The peak friction angle for an initially dense material and a low pressure level can be very high, which leads to a high maximum earth pressure. After the peak the earth pressure is reduced with continuous passive wall translation. For the initially loose material the earth pressure increases during passive wall translation and shear localization takes place without a reduction of the resulting earth pressure. Thus, the global material softening is not always necessary to obtain shear localizations whose formation mainly depends on the boundary conditions of the entire system.

REFERENCES

- Bauer, E. 1996. Calibration of a comprehensive hypoplastic model for granular materials. *Soils and Foundations* 36(1): 13–26.
- Bauer, E. 2000. Conditions for embedding Casagrande's critical states into hypoplasticity. *Mechanics of Cohesive-Frictional Materials* 5: 125–148.
- Bauer, E. & Herle, I. 2000. Stationary states in hypoplasticity. In Kolymbas (ed.), *Constitutive Modelling of Granular Materials*: 57–105. Springer press.
- Bauer, E. & Tejchman, J. (1998). Influence of density, pressure and mean grain diameter on shear band localization in granular materials. In *Proc. of the 3th Int. Conf. on Mechanics of Jointed and Faulted Rock*, Wien, Austria, 6–9 April 1998: 151–156. Balkema press.
- Chen, W.F. 1975. Limit analysis and soil plasticity. *Development in geotechnical engineering* 7. The Netherlands: Elsevier.
- Desrues, J., Chambon, R., Mokni, M. & Mazerolle, F. 1996. Void ratio evolution inside shear bands in triaxial sand specimens studied by computed tomography. *Géotechnique* 46: 529–546.
- Ehlers, W., Ramm, E., Diebels, S. & D'Addetta, G. A. 2003. From particle ensembles to Cosserat continua: homogenization of contact forces towards stresses and couple stresses. *Int. J. Solids and Structures* 40: 6681–6702.
- Groen, A.E. 1997. Three-dimensional elasto-plastic analysis of soil. *PhD Thesis*, Delft University, The Netherlands.
- Gudehus, G. 1997. Shear localization in simple grain skeleton with polar effect. In Adachi, Oka & Yashima (eds.), *Proc. of the 4th Int. Workshop on Localization and Bifurcation Theory for Soils and Rocks*: 3–10. Balkema.
- Gudehus, G. & Schwing, E. 1986. Standsicherheit historischer Stützwände. *Internal Report of the Institute of Soil and Rock Mechanics, University Karlsruhe*.
- Herle, I. & Gudehus, G. 1999. Determination of parameters of a hypoplastic constitutive model from properties of grain assemblies. *Mechanics of Cohesive-Frictional Materials* 4(5): 461–486.
- Huang, W. & Bauer, E. 2003. Numerical investigations of shear localization in a micro-polar hypoplastic material. *Int. J. for Numer. Anal. Meth. Geomech.* 27: 325–352.
- Kolymbas, D. 1991. An outline of hypoplasticity. *Archive of Applied Mechanics* 3: 143–151.
- Mühlhaus, H.B. & Vardoulakis, I. 1987. The thickness of shear bands in granular materials. *Geotechnique* 37: 271–283.
- Nübel, K. & Huang, W. 2004. A study of localized deformation pattern in granular media. *Comp. Method Appl. M.* 193: 2719–2743.
- Oda, M. & Kazama, H. 1998. Microstructure of shear bands and its relation to the mechanics of dilatancy and failure of dense granular soils. *Géotechnique* 48: 465–481.
- Oda, M., Konish, J. & Nemat-Nasser, S. 1982. Experimental micromechanical evaluation of strength of granular materials: effect of particle rolling. *Mech. Mater.* 1: 269–283.
- Pasternak, E. & Mühlhaus, H.B. 2001. Cosserat continuum modelling of granulate materials. In Valliappan S. & Khalili, N. (eds.), *Computational Mechanics – New Frontiers for New Millennium*: 1189–1194. Elsevier Science.
- Tejchman, J. 2001. Shearing of an infinite narrow granular layer between two boundaries. In Mühlhaus, H.B., Dyskin, A. & Pasternak, E. (eds.), *Bifurcation and Localisation Theory in Geomechanics*: 95–102. Swets & Zeitlinger, Lisse.
- Tejchman, J. 2002. Patterns of shear zones in a granular materials within a polar hypoplastic continuum. *Acta Mechanica* 155(1–2): 71–95.
- Tejchman, J. 2004a. Influence of a characteristic length on shear zone formation in hypoplasticity with different enhancements. *Computers and Geotechnics* 31(8): 595–611.
- Tejchman, J. 2004b. FE-analysis of patterning of shear zones in granular bodies for earth pressure problems of a retaining wall. *Archives of Hydro-Engineering and Environmental Mechanics, Polish Academy of Sciences* 51(4): 317–348.
- Tejchman, J. 2006. FE-analysis of shear localization in 2-D random granular bodies. In Proc. Conf. ICCS “Advancing Science through Computation”, University of Reading, Great Britain, 28–31 May 2006.
- Tejchman, J. & Bauer, E. 1996. Numerical simulation of shear band formation with a polar hypoplastic constitutive model. *Computers and Geotechnics* 19(3): 221–244.
- Tejchman, J. & Bauer, E. 2004. Effect of cyclic shearing on shearing localization in granular bodies. *Granular Matter* 5: 201–212.
- Tejchman, J. & Bauer, E. 2005a. Fe-simulation of a direct and true simple shear test within a polar hypoplasticity. *Computers and Geotechnics* 32: 1–16.
- Tejchman, J. & Bauer, E. 2005b. Modelling of a cyclic plane strain compression-extension test in granular bodies within a polar hypoplasticity. *Granular Matter* 7: 227–242.
- Tejchman, J. & Gudehus, G. 2001. Shearing of a narrow granular layer with polar quantities. *Int. J. Num. Anal. Meth. Geomech.* 25: 1–28.
- Wu, W. & Bauer, E. 1993. A hypoplastic model for barotropy and pyknotropy of granular soils. In Kolymbas, D. (ed.), *Modern Approaches to Plasticity*: 225–245. Elsevier.
- Wu, W., Bauer, E. & Kolymbas, D. 1996. Hypoplastic constitutive model with critical state for granular materials. *Mechanics of Materials* 23: 45–69.
- Wu, W. & Kolymbas, D. 2000. Hypoplasticity then and now. In Kolymbas (ed.), *Constitutive Modelling of Granular Materials*: 57–105. Springer press.

The relevance of small-strain soil stiffness in numerical simulation of excavation and tunnelling projects

R.B.J. Brinkgreve

Delft University of Technology, Delft, The Netherlands

K.J. Bakker

Plaxis bv & Delft University of Technology, Delft, The Netherlands

P.G. Bonnier

Plaxis bv, Delft, The Netherlands

ABSTRACT: The Finite Element Method (FEM) has become quite popular among geotechnical engineers as a numerical tool to analyse embankments, foundations, excavations and tunnelling projects. It is realised that the accuracy of the computational results depend on the kind of soil model being used and the selection of the corresponding model parameters. Gradually, the use of more advanced models that are capable of describing more features of soil behaviour increases. However, a feature that has been neglected in most practical applications thus far is the high stiffness at small strain levels ($<10^{-5}$). Even in applications that are dominated by ‘engineering strain levels’ ($>10^{-3}$) small-strain stiffness can play an important role. It may be considered common knowledge that conventional models usually over-predict the width and under-predict the gradient of the settlement trough behind excavations and above tunnels. Small-strain models can improve this. In a recent study on this topic it was evaluated if the introduction of small-strain stiffness would improve the applicability of the FEM in this respect for excavations and tunnelling analysis. The small-strain model itself was developed and validated in another study (Benz, 2006). The results as presented here show that small-strain stiffness is not only relevant to the aforementioned issues, but it also makes finite element solutions less sensitive with respect to the dimensions of the numerical model.

1 INTRODUCTION

The accuracy of deformations predicted by geotechnical finite element calculations depends in particular on the type of soil model being used and the selection of the corresponding model parameters. Over the years, much research has been performed on development, improvement and implementation of constitutive models for soil. As a result, advanced soil models have become available in finite element computer programs, taking into account more and more aspects of soil behaviour.

Most finite element users nowadays recognize the advantages of soil models like the Plaxis Hardening Soil (HS) model with its stress(path)-dependent stiffness behaviour. Despite the larger number of stiffness parameters that have to be entered, the parameter selection is easier than for simplified models, because of the clear meaning of the individual stiffness parameters in the HS model.

One feature of soil behaviour that was still missing in the HS model is the high stiffness at small strain levels ($<10^{-5}$). Even in applications that are dominated by ‘engineering strain levels’ ($>10^{-3}$) small-strain stiffness can play an important role. It is generally known that conventional models over-predict heave in excavation problems. These models also generally over-predict the width and under-predict the gradient of the settlement trough behind excavations and above tunnels when compared to empirical data as published by Peck (1967) and Mair & Taylor (1997). Small-strain stiffness can improve this. Moreover, small-strain stiffness can reduce the influence of the particular choice (position) of the finite element model boundaries, which makes the results of FEM calculations more objective and (presumably) more reliable.

In this contribution some results are presented that demonstrate the advantages of the use of small-strain stiffness in a constitutive relationship for soils.

2 SMALL-STRAIN STIFFNESS MODEL

Recently, the Plaxis HS model (Schanz, 1998) was extended with small-strain stiffness. The small-strain stiffness formulation is based on research by T. Benz at the Federal Waterways Engineering and Research Institute (BAW) in Karlsruhe, and supervised by the Institut für Geotechnik of the University of Stuttgart (Benz, 2006; Benz et al., 2006). The extended HS model, named HSsmall, has been implemented in a special Plaxis version 8.3. The extra information that is needed for the small-strain stiffness formulation comes from S-shaped curves where the shear modulus, G , is plotted as a (logarithmic) function of the shear strain, γ , ranging from very small strain levels (vibrations) up to large strain levels. The S-curve is characterised by the small-strain shear modulus, G_0 , and the shear strain at which the shear modulus has reduced to 0.7 times G_0 ($\gamma_{0.7}$); Figure 1. These two parameters are the only extra parameters compared to the original HS model. In fact, it has been demonstrated by comparing S-curves of several different types of soil that the particular shape of the S-curves does not change much and that $\gamma_{0.7}$ is generally around 10^{-4} . G_0 generally ranges from around 10 times G_{ur} for soft soils, down to 2.5 times G_{ur} for harder types of soil, where $G_{ur} = E_{ur}/(2(1 + \nu_{ur}))$.

The decay of the shear stiffness depends on the amount of shear strain as depicted in Figure 1. A good approximation is given by Equation 1.

$$G = \frac{G_0}{1 + a \gamma / \gamma_{0.7}} \geq G_{ur} \quad (1)$$

The constant a is set to 0.385 to arrive at the best fit (central line Figure 1). It should be noted that the curve shows the secant shear modulus, not the tangent shear modulus. Another fact is that the curve reaches

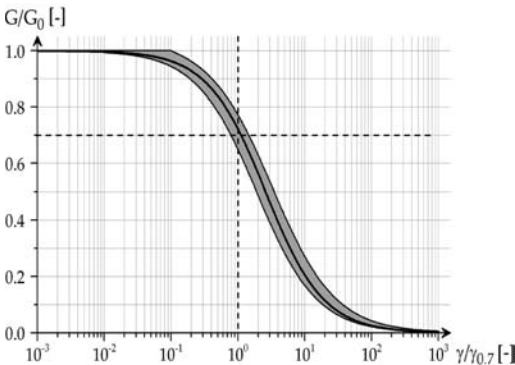


Figure 1. S-curve for reduction of shear modulus with shear strain.

far into the plastic domain. As the HSsmall model is an overlay model, the shear modulus is bounded by a lower limit, G_{ur} , of the original HS model. When combined with the HS model, the apparent secant modulus will reduce further due to plasticity. As for the original HS model, plasticity occurs due to an isotropic shear hardening surface and an isotropic cap hardening surface.

The model is primarily meant for shear stiffness reduction. The bulk modulus is calculated from the shear modulus using a fixed elastic Poisson's ratio.

$$K = \frac{2(1 + \nu)}{3(1 - 2\nu)} G \quad (2)$$

So far, only continuous loading was considered but in practice the stiffness increases when the loading direction changes. For a full '180 degrees' load reversal, the stiffness is supposed to restart at its maximum. For a new strain path that is in between a continuation in the same direction and a full load reversal, an intermediate (interpolated) stiffness is assumed. Therefore, the small-strain stiffness model memorizes the 'deviatoric' strain history and uses a generalised shear strain parameter to evaluate to what extent the loading direction deviates from the strain history. On the basis of this information it is determined which stiffness should be used. More details about the precise formulation of this generalised small-strain stiffness concept can be found in Benz (2006).

3 EXCAVATION PROJECT

To analyse the influence of small-strain stiffness, the HSsmall model was used in a characteristic excavation project. The soil and project data are based on a benchmark problem as defined by Schweiger (2005). Further results of this benchmark are also considered elsewhere in this conference (Schweiger, 2006).

An excavation to a total depth of 6 m in lightly overconsolidated clay is performed in three stages of 2 m each. A diaphragm wall is installed to retain the soil beside the excavation. After the first excavation stage a strut with an axial stiffness $EA = 1.5 \cdot 10^6$ kN/m is installed at a depth of 1.5 m below ground surface. The water table is 4 m below ground surface. In between the second and third excavation stage, the water table in the excavation is lowered to 6 m below ground surface.

The length of the diaphragm wall is not defined in the original benchmark, but is assumed here 10 m. The wall has an axial stiffness $EA = 2.4 \cdot 10^7$ kN/m, a flexural rigidity $EI = 1.28 \cdot 10^6$ kNm²/m and a Poisson's ratio $\nu = 0.18$. Interface elements are used to model the wall-soil interaction.

The soil was modelled using the simple Mohr-Coulomb (MC) model, the more advanced Hardening Soil (HS) model and the small-strain stiffness model (HSsmall), respectively. The corresponding model parameters are listed in Table 1.

Figure 2 shows the finite element mesh composed of 15-node cubic strain elements. Only one half of the excavation is modelled. The mesh clearly shows the excavation stages and the retaining wall. The other 'horizontal' and 'vertical' mesh lines are used with appropriate 'boundary' conditions to analyse the influence of various positions of the model boundaries. The initial stress field was generated using a K_0 -value of 0.5 and an OCR -value of 1.0.

Table 1. Soil model parameters.

Parameter	MC	HS	HSsmall	Unit
Unsaturated weight	19.0	19.0	19.0	kN/m ³
Saturated weight	20.0	20.0	20.0	kN/m ³
Poisson's ratio ν	0.3	0.2	0.2	–
Young's modulus E	30000			kN/m ²
E_{oed}^{ref}		20000	20000	kN/m ²
E_{50}^{ref}		20000	20000	kN/m ²
E_{ur}^{ref}		60000	60000	kN/m ²
G_0^{ref}			75000	kN/m ²
$\gamma_{0.7}$			$1 \cdot 10^{-4}$	–
Power	0.5	0.5	0.5	–
Ref. pressure	100.0	100.0	100.0	kN/m ²
Cohesion c	10.0	10.0	10.0	kN/m ²
Friction angle φ	27.5	27.5	27.5	°
Dilatancy angle ψ	0.0	0.0	0.0	°
Interface strength factor	0.7	0.7	0.7	–

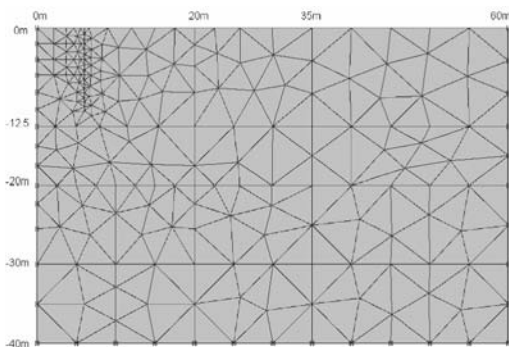


Figure 2. Finite element mesh of the excavation project.

Figure 3 shows the results after full excavation using the HSsmall model with boundaries at $x = 35$ m and $y = -20$ m. According to Peck (1969), the width of the settlement trough behind a retaining wall in relatively stiff soils extends to a maximum of two times the excavation depth (here 12 m). This corresponds well with the results of the HSsmall model. Calculations with the other models show a significant over-prediction of the width of the settlement trough (see Figure 4). The standard HS model gives more settlement (about 7 mm) than the HSsmall model (about 5 mm). This is because the average stiffness in the HS model is lower since this model does not take the high small-strain stiffness into account. The calculation with the MC model shows a little heave of the wall and a very wide settlement trough, which is quite unrealistic.

Variations with the position of the bottom boundary show significantly different deformations when using the MC model and (to a lesser extend) when using the HS model. The HSsmall model is rather insensitive for the position of the bottom boundary, as can be seen from Figure 5. Obviously, the largest settlement is obtained for the shallowest model, since this will give the least heave.

Variations with the position of the right-hand boundary show relatively little influence for all three models, although it may be argued that the boundary at $x = 20$ m is too close to obtain reliable results.

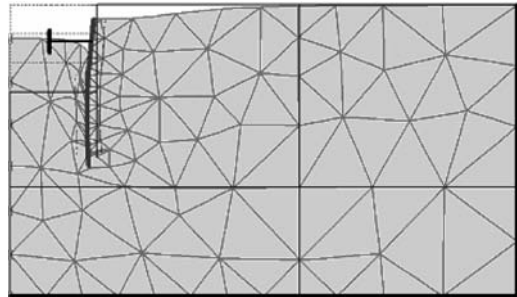


Figure 3. Deformed mesh (scale factor 200) using the HSsmall model with boundaries at $x = 35$ m and $y = -20$ m.

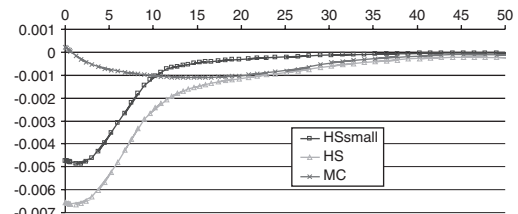


Figure 4. Settlement [m] as a function of the distance behind the wall [m]. Comparison for different models.

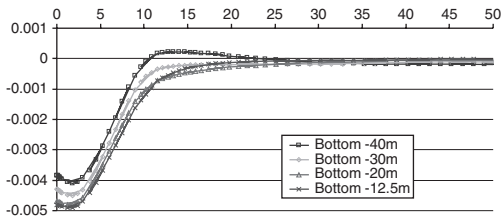


Figure 5. Comparison of settlement trough for different model depths using the HSsmall model.

4 TUNNELLING PROJECT

The second application that was used to analyse the influence of small-strain stiffness is a characteristic shield tunnelling project in lightly overconsolidated clay. The same soil models and parameters are considered as in the excavation project (see Table 1). The water table is 4 m below ground surface. Figure 6 shows the finite element mesh with a circular tunnel ($D = 8$ m) at a mean depth $z_0 = 16$ m below ground surface ($z_0/D = 2$). Again, mesh lines with appropriate ‘boundary’ conditions are used to analyse the influence of various positions of the model boundaries.

The excavation of the tunnel is simulated in three calculation phases according to the ‘grout pressure modelling’ procedure (Van Jaarsveld et al., 1999). In the first phase, the tunnel shield is installed and the soil inside the tunnel is excavated. In the second phase the shield is deactivated and a grout pressure is applied around the tunnel contour. The grout pressure 200 kN/m^2 at the top of the tunnel and 280 kN/m^2 at the bottom (gradient $10 \text{ kN/m}^2/\text{m}$). In the third phase the tunnel lining is installed and the pressure around the tunnel contour is removed.

Both the tunnel shield and tunnel lining have stiffnesses $EA = 1 \cdot 10^7 \text{ kN/m}$ and $EI = 1 \cdot 10^5 \text{ kNm}^2/\text{m}$, which is equivalent to a continuous concrete lining of 0.35 m thickness.

Figure 7 shows the results at the end of the calculation process using the HSsmall model with boundaries at $x = 35 \text{ m}$ and $y = -30 \text{ m}$. According to Mair & Taylor (1997) the point of inflection of the settlement trough (where 60% of the maximum settlement is found) should be about equal to the tunnel diameter D or half the mean depth z_0 (both 8 m). The MC model shows relatively low settlements with a point of inflection around $x = 5 \text{ m}$ (Figure 8), which is in contrast with what is usually found. This can be explained by the large amount of heave, which is quite unrealistic in this case. The HS model gives a relatively large settlements with a point of inflection near $x = 10 \text{ m}$. In this case the settlements are considered to be over-predicted. The HSsmall model gives a realistic settlement trough with a point of inflection just over $x = 8 \text{ m}$. Variations with the position

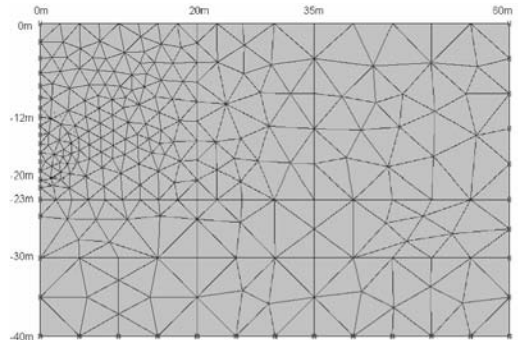


Figure 6. Finite element mesh of the tunnelling project.

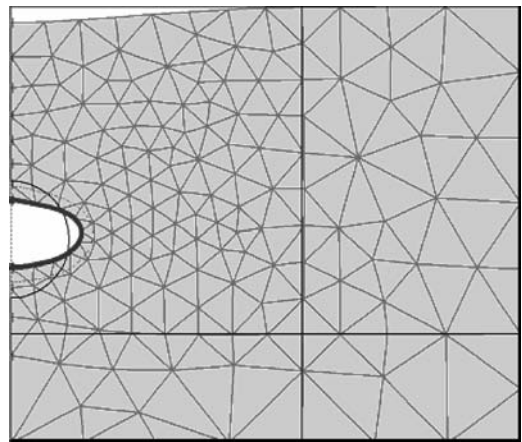


Figure 7. Deformed mesh (scale factor 200) using the HSsmall model with boundaries at $x = 35 \text{ m}$ and $y = -30 \text{ m}$.

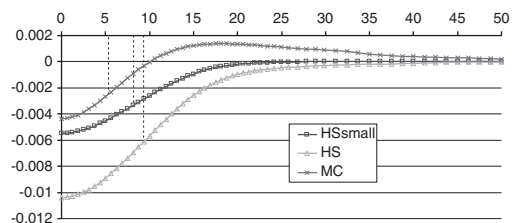


Figure 8. Settlement [m] as a function of the distance from the tunnel axis [m]. Comparison for different models.

of the bottom boundary show that the HSsmall model is again rather insensitive for the position of the boundary (Figure 9). Variations with the position of the right-hand boundary show relatively little influence for all three models, although it may be argued that the boundary at $x = 20 \text{ m}$ is again too close to obtain reliable results.

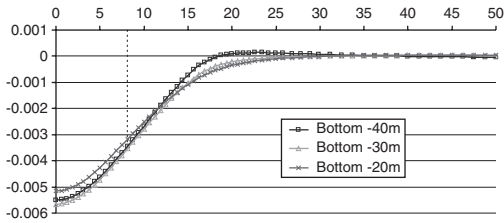


Figure 9. Comparison of settlement trough for different model depths using the HSsmall model.

5 CASE: THE 2ND HEINENOORD TUNNEL

The 2nd Heinenoord tunnel was the first large diameter bored tunnel in the Netherlands. For that reason, parallel to the tunnel construction a research and monitoring project was undertaken that left us with a lot of data that can be used for validation; e.g. see Bakker (1999).

During construction on both banks of the river Oude Maas, measurements were taken of surface settlement in a number of cross sections; for this study those at the north Bank were taken as characteristic.

On the North Bank of the oude Maas, the geology mainly consisted of a number of more or less loose sand and clay layers. During passage of the TBM, up to a distance of about 7 m, i.e. about one diameter of the TBM ahead of the machine, negligible settlements were observed. During passage of the TBM the settlements rapidly increased up to its maximum that was reached at about 30 m behind the face of the TBM. For a characteristic curve see Figure 10. The cross-sectional distribution of the settlements is given in Figure 11.

During the first passage of the field the maximum settlement varied between 22 and 37 mm, whereas during the second passage a maximum settlement between 7 and 17 mm was observed.

The contribution of front effects to the settlement was considered very limited, also during passage of the more clayey and peaty monitoring field at the South side. The settlements given in Figures 10 and 11 are more or less characteristic for the settlements observed during the project.

After evaluating both predictions and measurements there was some disappointment about the FEM predictions, though the agreement with the empirical models by Peck (1969) was reasonable. The FEM analyses with Mohr-Coulomb predicted a much too wide and shallow settlement trough, discounting for the volume loss of about 0.8 to 1.0 % that was back calculated from the cross-sectional volume of the settlement trough at soil surface; see Figure 11.

In the years thereafter, soil models improved, the HS model was introduced and in addition to that within the

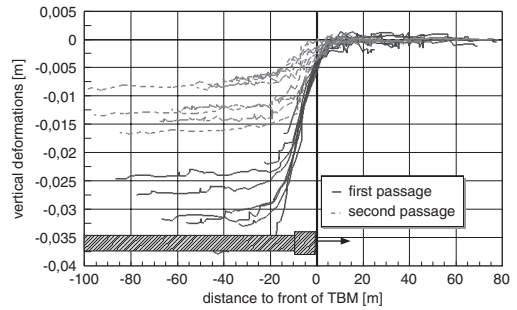


Figure 10. Development of green field settlements above tunnel axis at Northern monitoring area (after Van Jaarsveld et al. 1999).

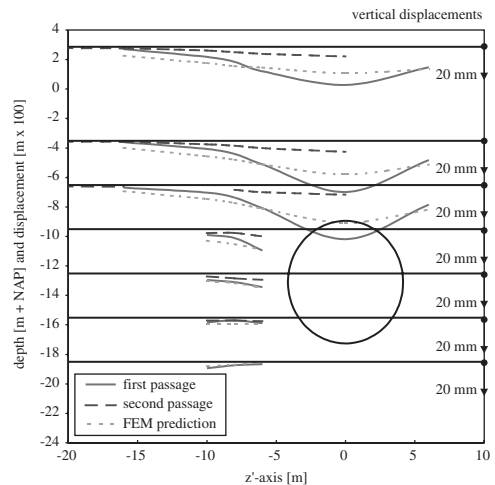


Figure 11. Soil deformations at measuring field North at the Second Heinenoord tunnel, Measurements and predictions with Mohr Coulomb model.

context of the design for the North-South Metroline in Amsterdam it was found that the boundary conditions applied to model the volume loss have a major influence on the width of the settlement trough.

Changing the contraction type of boundary condition by grout pressures that corresponded to the measurement at various different shield tunnel projects in the Netherlands gave a large improvement for the prediction of the width of the settlement trough; see Van Dijk & Kaalberg (1998) and Van Jaarsveld et al. (1999). Further browsing through the literature in the period between 1995 and 2005, the over-prediction of the width of the settlement trough by finite element analysis was observed more generally, and a number of possible causes for the difference between calculated and measured width of the settlement trough are named, see Mair (1997).

1. A higher K_0 -value such as due to over-consolidation may lead to a wider settlement trough, whereas normal consolidation would narrow the trough.
2. Anisotropy; The effect of a lower horizontal stress in comparison with the vertical stress, may also result into a lower horizontal Young's modulus. This effect is named as a feasible cause for narrowing of the settlement trough.
3. Small-strain stiffness; the use of an averaged Young's modulus in most of the numerical models might lead to an under-estimation of the soil stiffness in areas further away from the tunnel. Different studies indicate that a higher stiffness and an earlier development of plastic straining might also lead to narrowing of the settlement trough.

In this study we have compared different models: HS with contraction, HS grout pressure and HSsmall in combination with the the grout pressure model. For the comparison we have taken the same geology of the 2nd Heinenoord tunnel as was taken and published by Bakker (2000). The mesh used is indicated in Figure 12. In Figure 13, the results of different calculations are given, indicating that the best fit was derived with a combination of the HSsmall model and the grout pressure modelling. The grout pressure assumed here is

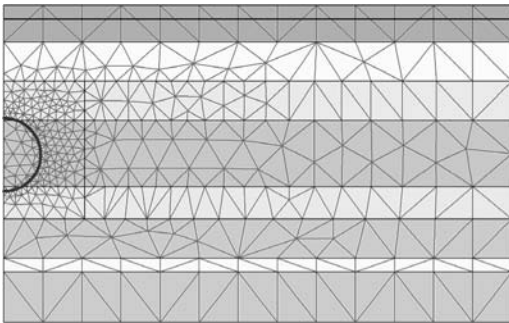


Figure 12. 2nd Heinenoord tunnel mesh used for back analysis.

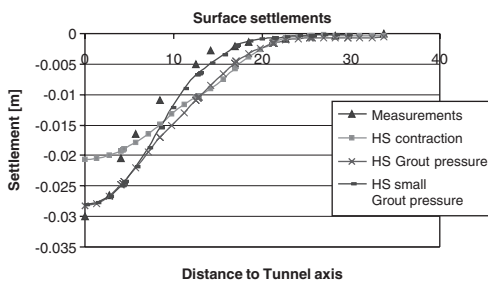


Figure 13. Comparison of measured and calculated surface settlements for various modelling alternatives.

142 kN/m² at the crest of the tunnel and increasing 8 kN/m²/m in depth, corresponding the measurements; see also Van Jaarsveld et al. (1999).

In Figure 14, the overall deformation distribution is given, indicating the localisation of the deformations above the tunnel.

6 CONCLUSIONS

This paper demonstrates the advantages of the use of small-strain stiffness in a non-linear constitutive relationship for soils on the basis of finite element calculations of a characteristic excavation project and a shield tunnel project. Both projects were calculated with three different models (including the small-strain stiffness model HSsmall). Emphasis was put on the (width of the) settlement trough behind the excavation and above the tunnel. Moreover, the influence of the position of the model boundaries was analysed using model boundaries at different depths and distances from the excavation and tunnel. On the basis of the computational results, the following conclusions can be made:

1. The HSsmall model gives realistic settlement troughs behind retaining walls of excavations and above shield tunnels, due to the small-strain stiffness effect. In shield tunnelling projects it is essential to perform calculations according to the grout pressure modelling procedure.
2. Small-strain stiffness also gives a more realistic (= reduced) heave of the tunnel and excavation bottom. Neglecting small-strain stiffness results in unrealistically large heave.
3. When using the HSsmall model, results are relatively insensitive with respect to the position of the model boundaries. This is also tributed to the small-strain stiffness effect. Nevertheless, a reasonable minimum distance from the problem considered needs to be taken into account.

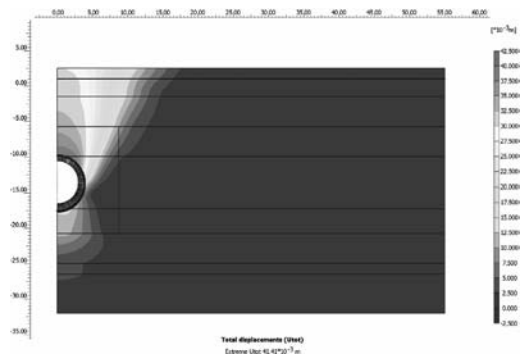


Figure 14. Deformation contour lines due to tunnelling.

Further, the results of the measurements at the 2nd Heinenoord tunnel were taken as input for a number of comparative calculations that indicate that the use of small-strain stiffness, i.c. the HSsmall model, further improves the agreement between measurements and numerical calculation.

REFERENCES

- Bakker, K.J., de Boer, F., Admiraal, J.B.M. and van Jaarsveld, E.P. 1999. Monitoring the 2nd Heinenoord tunnel and the Botlek Rail tunnel, Tunnelling and Underground Space Technology, Vol. 14, No. 2.
- Bakker, K.J. 2000. *Soil Retaining Structures, development of models for Structural analysis*, Balkema, Rotterdam.
- Benz, T. 2006. *Small-strain stiffness of soils and its numerical consequences*. Ph.D. Thesis. Institut für Geotechnik, Universität Stuttgart.
- Benz, T., Schwab, R. and Vermeer, P.A. 2006. *A small strain overlay model I: model formulation*. Int. J. Numer. Anal. Meth. Geomech., in progress.
- Mair, R.J. and Taylor R.N. 1997. Theme lecture: Bored tunnelling in the urban environment. 14th ICSMFE, Hamburg. Rotterdam, Balkema, 2353–2385.
- Peck, R.B. 1969. *Deep excavations and tunneling in soft ground*. State of the Art Report. 7th ICSMFE, Mexico City. 225–290.
- Schanz, T. 1998. *Zur Modellierung des Mechanischen Verhaltens von Reibungsmaterialien*. Habilitation. Stuttgart University.
- Schweiger, H.F. 2005. ERTC7-Benchmark: ULS-design of embedded wall. In: Plaxis Bulletin No. 18 (October 2005), Plaxis bv, Netherlands.
- Schweiger, H.F. 2006. Results from the ERTC7 benchmark exercise. This proceedings.
- Van Dijk, B.F.J. and Kaalberg, F.J. 1998. 3D Geotechnical Model for the North/Southlin in Amsterdam, Proc. European Conference on Numerical Methods in Geotechnical Engineering, Udine, Italy.
- Van Jaarsveld, E.P., Plekkenpol, J.W. and Messemackers van de Graaf 1999. Ground deformations due to the boring of the Second Heinenoord tunnel, Proc. XII ECSMGE, Amsterdam, Balkema, vol 1, 153–159.

Numerical study of pressuremeter strain and stress holding test

D. Rängeard

Laboratoire de Génie Civil et Génie Mécanique, Institut National des Sciences Appliquées, Rennes, France

R. Zentar & N.-E. Abriak

Department of Civil Engineering, Ecole des Mines, Douai, France

ABSTRACT: This paper focus on numerical analysis of strain and stress holding stage realized during a pressuremeter test. The aim of this study is to highlight the effect of the viscous behavior of soft clay on the response of the soil during this kind of tests. In this way different simulations are performed using to model implemented in the finite element code Plaxis: the soft soil model, which is an elastoplastic model, and the soft soil creep model which is an extension of the soft soil model that take into account creep behavior of the soil. The effects of consolidation and creep on the tests results are pointed out.

1 INTRODUCTION

The pressuremeter is widely used in foundation engineering to derived parameters of soil behavior. Concerning soft clay, the behavior is time dependant. Several reserchears are studied in the past the effects of time of shearing on the undrained characteristics of soil (Skempton and Bishop 1954, Bjerrum 1972, Vaid and Campanella 1977, Sheahan et al., 1996).

The pressuremeter test (cavity expansion test) generates a non homogeneous stress field in the soil near the probe. Hence, depending on the rate of loading and on the permeability of the soil, partial drainage can occur and induces changes of the mechanical properties of the material. Previous studies have identified the drainage conditions reached in the soil during this kind of test (Fukagawa et al., 1990, Rängeard et al., 2003). This time dependent behavior depends on two phenomena: the viscous part of the soil behavior, and the consolidation of the soil around the probe.

In this paper, our aim is to study the effect of consolidation and creep on the response of the soil during strain and stress holding test stage realized during a pressuremeter test.

In a first part, experimental result of strain and stress holding test realized on a natural soft clay are presented.

In a second part, the models behavior used in this study are briefly presented. The first one take into account only consolidation, and the second one take into account both consolidation and creep behavior. Finally, numerical simulations of strain and stress holding are performed using the two models. The effects of consolidation and creep are pointer out.

2 OBSERVED BEHAVIOR OF CLAY DURING PRESSUREMETER TEST

The pressuremeter behavior of a natural clay, the Saint Herblain clay, was investigated in laboratory using special equipment named “pressio-triax” (zentar et al., 2001). This equipment allow simulating self boring pressuremeter test in a triaxial cell. The pressio-triax offer the possibility of measuring the pore water pressure evolution near the probe during the test.

The mechanical characteristics and the permeability of the clay, derived from triaxial and one dimensional consolidation tests, are listed in Table 1.

Several pressio-triax tests with strain holding test stage and stress holding test stage were preformed on Saint Herblain clay. In figure 1, the results of a strain holding test stage was presented in term of excess

Table 1. Characteristics of Saint Herblain clay.

e_0	w (%)	γ_h (kN/m ³)	γ_d (kN/m ³)	k (m/s)	c_c	c_s	c_{ae}	σ'_p/σ'_{v0}	c' (kPa)	ϕ'
2,3	88	14,8	8,2	10^{-9}	1.85	0.03	0.03	1,1	0	30

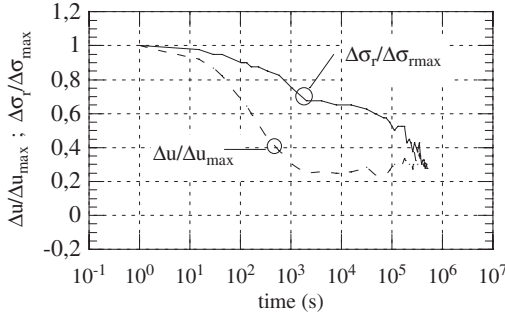


Figure 1. Normalized excess pore pressure dissipation curve and normalized stress evolution during experimental strain holding test stage.

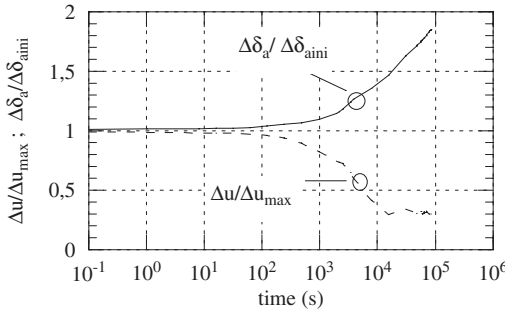


Figure 2. Normalized excess pore pressure dissipation curve and normalized cavity strain evolution during experimental stress holding test stage.

pore water dissipation and total radial stress at the cavity wall $\Delta\sigma_r$ evolution with time. In figure 2, the result of a stress holding test is presented. The evolution of the cavity strain δ_a is normalized by the value of the cavity strain at the start of the stress holding test (in this case, $\delta_{aini} = 5\%$).

Regarding to this typical result, different conclusions on the soft clay behavior during strain and stress holding test could be drawn:

- There is an important dissipation of the excess pore pressure generated during the loading stage of the test. This dissipation begin quickly after the beginning of the strain holding test
- The pore pressure seem to reach a stabilized value higher than the initial pore pressure
- During the strain holding stage, an important relaxation of the total stress at the cavity wall occur
- During the stress holding stage, the cavity strain increases at a constant rate with the logarithm of the time.

3 NUMERICAL SIMULATION OF PRESSUREMETER TEST

3.1 Constitutive models and parameters

In this paper, numerical simulations are performed using the finite element code: PLAXIS BV. To highlight the creep effects as the consolidation effects on pressuremeter tests, two constitutive models, implemented in PLAXIS, were assumed to predict realistically the behavior of natural soft clay. The first model is an elastoplastic model, called the Soft Soil Model (SSM) and the second one, called the Soft Soil Creep model (SSC), is an extension of SSM model which includes time and strain rate effects. SSC model compared to SSM model introduces only one additional input parameter.

The Soft Soil Model is inspired in it's major parts from Modified Cam-Clay model as described by Burland (1971). In the Soft Soil Model, the volumetric strain ε_v is used to describe the soil behavior instead of the void ratio e as in the Modified Cam-Clay model. For virgin isotropic compression and swelling line, the SSM model yields to:

$$\varepsilon_v - \varepsilon_{v0} = \lambda^* \ln \frac{p'}{p'_0} \quad (1)$$

$$\varepsilon_v^c - \varepsilon_{v0}^c = \kappa^* \ln \frac{p'}{p'_0}$$

The relationship between SSM model parameters λ^* and κ^* and corresponding parameters in Modified Cam-Clay model λ and κ is expressed as:

$$\lambda^* = \frac{\lambda}{1+e} \quad (2)$$

$$\kappa^* = \frac{\kappa}{1+e}$$

The yield function is an ellipse in the (p' - q) plane, and the failure is described by the Mohr Coulomb criterion, and so by the parameters c' and ϕ' .

The Soft Soil Creep model implemented in PLAXIS, is an extension of the SSM model that take into account the creep effects.

The creep effects are introduced by the modified creep parameter μ^* which can be related to creep index C_{ae} by:

$$\mu^* = \frac{C_{ae}}{\ln(10) \cdot (1+e)} \quad (3)$$

The total volumetric strain ε_v due to an increase in mean effective stress from p'_0 to p' in a time period $t_c + t'$ is expressed as the sum of an elastic part ε_v^e , an a visco-plastic part ε_v^{vp} . The visco-plastic component is separated into a part during consolidation $\varepsilon_v^{vp_c}$ and a

Table 2. SSM and SSCM parameters used in this study.

λ^*	κ	μ^*	c' (kPa)	ϕ'	M	OCR
0.244	0.014	0.011	0.	30°	1.2	1

part after consolidation $\varepsilon_{v\ ac}^{vp}$. The expressions of the different volumetric strain are expressed as follow:

$$\varepsilon_v = \varepsilon_v^e + \varepsilon_{v\ c}^{vp} + \varepsilon_{v\ ac}^{vp}$$

$$\varepsilon_v^e = \kappa^* \ln\left(\frac{p'}{p'_0}\right) \quad \varepsilon_{v\ c}^{vp} = (\lambda^* - \kappa^*) \ln\left(\frac{p'_{pc}}{p'_0}\right) \quad (4)$$

$$\varepsilon_{v\ ac}^{vp} = \mu^* \ln\left(\frac{\tau_c + t'}{\tau_c}\right)$$

Complete description of this two models can be found in Brinkgreve and et al. (1998).

In Table 2, parameters values used to simulate pressuremeter tests are summarized. Those values of the parameters are derived from laboratory tests performed on the Saint Herblain soft clay.

3.2 Geometry and boundary conditions

Regarding to the pressuremeter geometry, the test is modeled as an axy-symmetric problem. In this case, previous studies have shown that, for a probe with a L/D ratio higher than 6 (where L is the length of the probe and D the diameter) the test results are similar to those obtain considering plane strain conditions (Houlsby & Carter, 1993). For pressuremeter test simulations in soft soil with typical characteristics of Saint Herblain clay, a typical value of the ratio b/a about 30 (where b is the outer radii, a the initial probe radii) is sufficient to model the condition of infinite medium (Zentar et al., 1998).

Considering plane strain conditions, a unit height of soil are modeled. In terms of boundary conditions, the vertical displacements of the horizontal boundaries (sides A and B) are prevented whereas horizontal displacement could develop freely. A constant pressure corresponding to the horizontal stress in the ground is applied on the outer vertical boundary (side C, figure 3). The pressuremeter loading is modeled by applying incremental displacement of the cavity wall (inner boundary, side D). By the way, a pressuremeter test realized at constant strain rate is simulated.

3.3 Simulation of the cavity expansion test

The simulation of the expansion test was done previously using the two models SSM and SSC model (Rangear et al., 2004). In this study, the authors investigated the effect of strain rate on the pressuremeter curve. Firstly, the authors showed that the creep

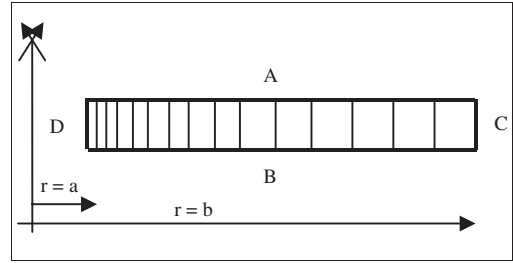


Figure 3. Finite element geometry.

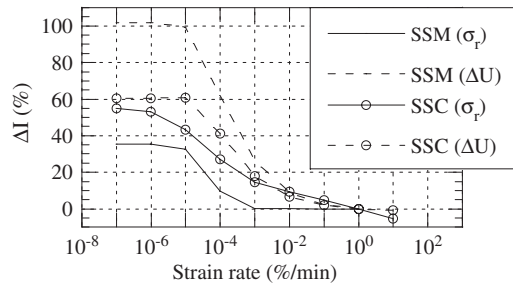


Figure 4. Strain rate effect on pressuremeter and pore pressure curve using SSM and SSC model.

parameter μ^* of the soft soil creep model influenced the total stress response, but had no effect on the generated excess pore pressure.

Then, it was shown that, using the soft soil model, the strain rate had an influence only in a limited range of strain rate values and, using the SSC model, the strain rate had an effect for all the range of investigated values of the strain rate. The main results are summarized in figure 4. In this figure, ΔI is the difference between a reference calculation (realized with a reference strain rate of 1%/min) and a calculation at a different strain rate. For the soft soil model, using the parameters presented in Table 2, the strain rate has no effect for values higher than $10^{-3}\%/min$ and lower than $10^{-5}\%/min$. Assuming the SSC model, the strain rate has an effect for all the range of investigated values (from $10^{-7}\%/min$ to 1%/min). Using the SSM only the consolidation effect is modeled. So, we can clearly see that the consolidation phenomena is predominant for strain rate values from $10^{-5}\%/min$ to $10^{-1}\%/min$. The SSC modeled both consolidation and viscous behavior. Using this model, the pressuremeter curve is affected by the strain rate for all the investigated values. That's mean that, for strain rate higher than $10^{-1}\%/min$ and lower than $10^{-5}\%/min$ the creep effect is predominant.

This results highlight the predominant effect of creep for small strain rate values (or small permeability of soil) and for high strain rate values (or high permeability of soil).

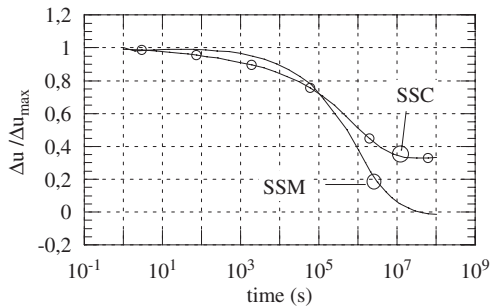


Figure 5. Normalized excess pore pressure dissipation during strain holding test simulated using soft soil model and soft soil creep model.

4 STRAIN AND STRESS HOLDING STAGE SIMULATION

In this part, numerical simulation of strain holding test stage and stress holding stress stage are performed using the soft soil model and the soft soil creep model. The strain (stress) holding stages are realized after an expansion cavity test from the initial radii to a cavity strain of 5%, and using the parameters values indicated in Table 2.

4.1 Strain holding test simulation

Fiovarante et al. (1994) have show that using an elasto-plastic model, the pore pressure dissipation during a strain holding test can be reproduced, but the relaxation of the total stress can't be totally achieve.

Figure 5 shows the evolution of the normalized excess pore pressure $\Delta u/\Delta u_{max}$ (where Δu is the excess pore pressure, and Δu_{max} is the excess pore pressure at the beginning of the strain holding test stage) with time during the strain holding test simulated using the two models.

We can see that, using SSM, the dissipation of the generated excess pore pressure begin for a time about 10^3 s. After relaxation time of $5 \cdot 10^7$ s, the generated excess pore pressure is totally dissipated. In this case, the consolidation occur between 10^3 s and $5 \cdot 10^7$ s from the start of the strain holding stage.

Using the SSC model (modeling both consolidation and creep behavior), the dissipation of the excess pore pressure start "immediately" after the beginning of the strain holding test stage. After a relaxation time of $5 \cdot 10^7$ s (corresponding to the end of the consolidation process as show using the SSM), the excess pore pressure isn't totally dissipated. The value of the pore pressure reach for this time is higher than the initial pore pressure value. The soft soil creep model modeled more accurately the pore pressure dissipation

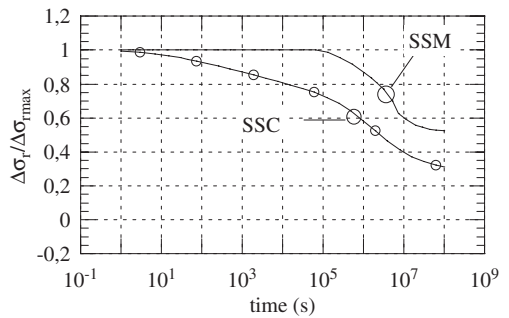


Figure 6. Normalized total stress evolution during strain holding test simulated using soft soil model and soft soil creep model.

observed experimentally during strain holding test realized on natural soft clay (Figure 1).

Figure 6 shows the evolution of the normalized total stress at the cavity wall $\Delta\sigma_r/\Delta\sigma_{rmax}$ (where $\Delta\sigma_r$ is the added total stress at the cavity wall, and $\Delta\sigma_{rmax}$ the value of $\Delta\sigma_r$ at the beginning of the strain holding test stage) with time during the strain holding test obtain using the two models.

Using the SSM, the total stress value change only for time between 10^5 s and $5 \cdot 10^7$ s (corresponding to the end of consolidation process, Figure 5). Using the SSC model, $\Delta\sigma_r$ value change during the entire test.

Using the SSM, the total stress reaches after the end of consolidation process is 50% of the initial value. ($\Delta\sigma_r/\Delta\sigma_{rmax}$ change from 1 to 0,5). Taking into account both consolidation and creep (SSC model), the stress relaxation is more pronounced ($\Delta\sigma_r/\Delta\sigma_{rmax}$ change from 1 to 0,3). The total stress relaxation observed experimentally on strain holding test realized on soft clay is highly affected by both consolidation and creep phenomena's.

Only the SSC model is able to reproduce the continuum evolution of stress during strain holding test stage.

4.2 Stress holding test simulation

Figures 7 and 8 present the results of the simulation of a stress holding test realized during a pressure-meter test.

In figure 7, the evolution of the normalized excess pore pressure $\Delta u/\Delta u_{max}$ with time during the stress holding test simulated using the two models is presented.

From this figure, we can note that the consolidation process takes place until a time of $2 \cdot 10^3$ s since the beginning of the stress holding stage (SSM). Assuming the SSC model, the pore pressure is not stabilized after a time of $2 \cdot 10^3$ s. Using this model, the pore pressure reach a value higher than the initial pore

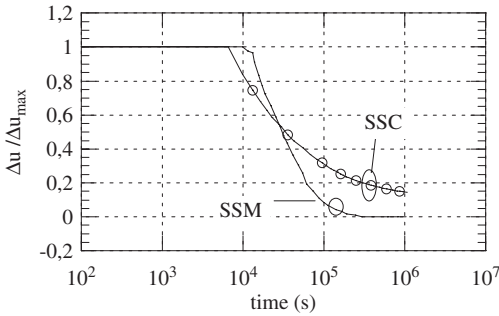


Figure 7. Normalized excess pore pressure dissipation during stress holding test simulated using soft soil model and soft soil creep model.

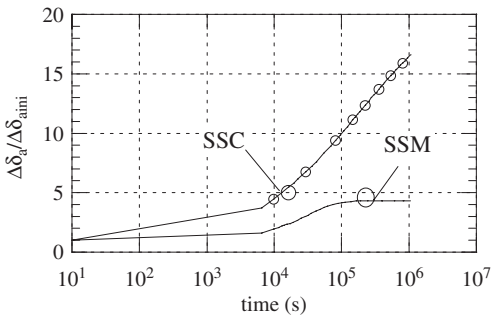


Figure 8. Normalized cavity strain evolution during stress holding test simulated using soft soil model and soft soil creep model.

pressure value ($\Delta u/\Delta u_{\max} > 0$). In this case, it's seems that the soft soil creep model modeled more accurately the pore pressure evolution observed experimentally during stress holding test realized on natural soft clay (Figure 2).

Figure 8 shows the evolution of the normalized cavity strain at the cavity wall $\Delta\delta_c/\Delta\delta_{aini}$ (where $\Delta\delta_c$ is the cavity strain at a time "t", and $\Delta\delta_{aini}$ the value of $\Delta\delta_c$ at the beginning of the stress holding test stage) with time during the stress holding test obtain using the two models.

Using the SSM, the cavity strain value changes only for time lower than 2.10^5 s, corresponding to the end of the consolidation process (Figure 5). For higher time, the cavity strain keeps constant. This model isn't able to reproduce the evolution of the cavity strain observed experimentally (Figure 2).

When using the SSC model, the cavity strain evolves continuously with time. This model reproduces more accurately the soil behavior observed experimentally during a stress holding test

5 CONCLUSIONS

In this paper, numerical simulation of strain holding test and stress holding test realized during a cavity expansion test are performed. In order to analyses the effect of consolidation and creep on the soil response, two models were used: an elastoplastic model (SSM) and a elasto viscoplastic model (SSC model). The simulation results obtained using the two models are compared.

The numerical simulations of strain holding stage realized during pressuremeter test show that:

- the pore pressure dissipation can be reproduced by both elastoplastic and elastoviscoplastic model; consolidation effect is predominant on pore pressure dissipation. However, better reliability with experimental test is obtain by tacking into account both consolidation and creep behavior.
- the stress relaxation is highly affected by viscous behavior of soil. The stress relaxation observed experimentally could be reproduced only using the elastoviscoplastic model.

The numerical simulations of stress holding stage realized during pressuremeter test show that:

- as for the strain holding test stage, the pore pressure dissipation can be reproduced by both elastoplastic and elastoviscoplastic model. However, better reliability with experimental test is obtain by tacking into account both consolidation and creep behavior.
- the increase of the cavity strain during the test is influenced by both consolidation and creep. However, after the end of the consolidation process, the cavity strain is not stabilized. Only the soft soil creep model is able to reproduced the experimental behavior.

Regarding to these results, it appears that a correct exploitation of the stress relaxation curve during a strain holding test and of the cavity strain evolution during a stress holding test needs to take into account the viscous behavior of the soil.

REFERENCES

- Bjerrum, L. 1972. Embankments on soft ground. *Proc. ASCE Speciality conf. On perle of earth and earth supported structure.*, Purdue Univ. West Lafayette, Ind. 2: 1–54.
- Fioravante, V., Jamiolkowski, M. & Lancellotta R. 1994. An analysis of pressuremeter holding tests. *Géotechnique* 25(3): 113–126.
- Fukagawa, R., Fahey, M. & Otha, H. 1990. Effect of partial drainage on pressuremeter test in clay. *Soils and Foundations*, 30(4):134–146.

- Rangeard, D., Hicher, P-Y., Zentar, R. & Moulin, G. 2003. Determining soil permeability from pressuremeter tests, *Int. J. Numer. Anal. Meth. Geomech.*, 27:1–24.
- Rangeard, D., Zentar, R. & Abriak, N-E. 2004. Influence of soil model on the analysis of pressuremeter test. *In proceedings of Int. Conf. on Numer. Models in Geomech., NUMOG IX*, 699–705.
- Sheahan, T.C., Ladd, C.C. & Germaine, J.T. 1996. Rate-dependent undrained shear behavior of saturated clay. *J. Geotech. Engrg., ASCE* 122 (2): 99–108.
- Skempton, A. W. Bishop, A. W. & 1954. Soils Building materials *North Holland Publishing Co.*: 417–482.
- Vaid, Y.P. & Campanella, R.G. 1977. Time dependent behavior of undisturbed clay. *J. Geotech. Engrg., ASCE* 103(7): 693–709.
- Zentar, R., Hicher, P-Y. & Moulin, G. 2001. Identification of soil parameters by inverse analysis. *Computers and Geotechnics*, 28(2): 129–144.

Identification of soil parameters from pressuremeter tests

Z.Y. Yin & P.Y. Hicher

Research Institute in Civil and Mechanical Engineering, Ecole Centrale de Nantes, France

H.W. Huang

Department of Geotechnical Engineering, Tongji University, Shanghai, China

ABSTRACT: The purpose of this paper is to present a methodology for identifying soil parameters from pressuremeter tests. A viscoplastic model coupled with consolidation theory was employed. At first, a numerical analysis of parameters effects on constant strain rate tests was carried out. Then the results were used to develop a method for identifying soil parameters. The drainage conditions during the pressuremeter tests were also analyzed to explain the strain rate effect on the evolution of pore pressure and total pressure. The results showed that the model can satisfactorily describe the time-dependent behavior of soils during pressuremeter tests, and the method allowed us to determine efficiently soil mechanical, including viscous and hydraulic parameters from constant strain rate pressuremeter tests.

1 INTRODUCTION

The identification of soil mechanical parameters from pressuremeter tests has been studied in the literature (for example, Anderson et al. 1987, Pye 1995, Hicher & Michali 1996, Zentar et al. 2001, Rangeard et al. 2003). But few of them were concerned by the delayed behaviour of fine soils.

In this paper, three objectives are presented in studying the identification of soil parameters from pressuremeter tests and the time-dependent pressuremeter behavior of soft clay: (i) to study the parameters sensibility on the constant strain rate pressuremeter test, using a viscoplastic model, taking into account geometry and boundary conditions in numerical simulation; (ii) to propose a back analysis method for identifying parameters from constant strain rate tests, and validate the approach by means of pressuremeter relaxation and creep tests; (iii) to analyze the drainage conditions during the pressuremeter tests as a function of the strain rate and the permeability.

2 NUMERICAL STUDY OF PRESSUREMETER TESTS

2.1 Constitutive model EVP-MCC

The constitutive model used in this study to model the time-dependent behavior of soil is the elasto-viscoplastic model EVP-MCC, based on the framework

of Perzyna's overstress theory and Modified Cam-Clay elastoplastic model, and developed by Yin et al. (2006). The model was implemented in a finite element program CESAR_LCPC, which allows us to simulate pressuremeter tests employing the EVP-MCC model coupled with Biot's consolidation theory. The constitutive equations are as follows:

$$\partial p_c^s = p_c^s \cdot \frac{1+e_0}{\lambda - \kappa} \cdot \partial \varepsilon_v^{vp} = p_c^s \cdot \frac{1}{\beta^*} \cdot \partial \varepsilon_v^i \quad (1)$$

$$f_d = \frac{q^2}{M^2} + p' \cdot (p' - p_c^d) = 0 \quad (2)$$

$$\mu \cdot \phi(F) = \mu \cdot \left(\exp \left[N \cdot \left(\frac{p_c^d}{p_c^s} - 1 \right) \right] - 1 \right) \quad (3)$$

$$\dot{\varepsilon}_{ij}^{vp} = \mu \langle \phi(F) \rangle \frac{\partial f_d}{\partial \sigma'_{ij}} \quad (4)$$

where p_c^s = static consolidation pressure; p_c^d = dynamic consolidation pressure; ε_v^{vp} = inelastic volumetric strain; β^* = compressibility index; M = slope of the critical state line; N = viscosity index; μ = viscosity coefficient; p' = effective mean stress; q = deviatoric stress; σ'_{ij} = effective stress tensor; $\dot{\varepsilon}_{ij}^{vp}$ = inelastic strain rate tensor; $\langle \rangle$ = function of MacCauley.

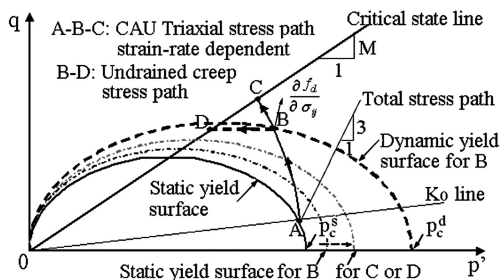


Figure 1. Schematic behavior of the EVP-MCC model during CAU triaxial compression and triaxial creep tests.

The principle of the viscoplastic model is presented in Figure 1. Taking into account the elastic stress-strain relations, constitutive equations of this viscoplastic model for normally consolidated clays are derived as follows:

$$\varepsilon_{ij} = \frac{s'_{ij}}{2G} + \frac{p'}{3K} + \mu(\phi(F)) \left(\frac{3s'_{ij}}{M^2} + (2p' - p_c^d) \frac{\delta_{ij}}{3} \right) \quad (5)$$

where G = shear modulus; K = bulk modulus; s'_{ij} = effective deviatoric stress tensor; δ_{ij} = Kronecker's delta.

2.2 Finite element analysis of pressuremeter tests

The numerical simulation was performed by considering a plane strain condition in the vertical direction, and an axisymmetric condition in horizontal direction as $a = 6.5$ mm, $b = 35$ mm corresponding to a special pressuremeter apparatus called pressio-triax which consists in reproducing the pressuremeter test conditions in a triaxial cell (Anderson et al. 1987, Bahar et al. 1995, Zentar et al. 2001, Rangeard et al. 2003). The mesh was composed of 24 elements with 123 nodes. The elements are isoparametric with 8 integration points.

For boundary conditions, all vertical displacement was prevented, whereas horizontal displacements could develop freely. The displacement was applied in the mini-pressuremeter probe on the side AD, and cell pressure was maintained on the side BC. No fluid flow was allowed to pass through the four faces for the undrained boundary conditions, as presented in Figure 2.

The soil was assumed to be saturated and isotropic.

2.3 Parameter effects on pressuremeter curves

The parameters sensibility study was carried out for a pressuremeter test at a strain rate of 6×10^{-5} /s with initial total stress $\sigma_1 = 85$ kPa, $\sigma_2 = \sigma_3 = 68$ kPa, and initial pore pressure $u = 56.5$ kPa. The parameters effects on the radial total stress and on the pore pressure at the cavity wall are presented in Figure 3, where A represents the value of the radial total stress or the pore pressure at a strain of 8% and Ar, the value corresponding to the reference value of the studied

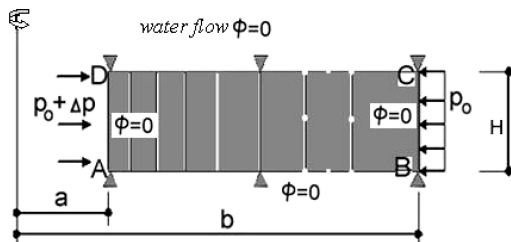


Figure 2. Finite element geometry (Rangeard et al., 2003).

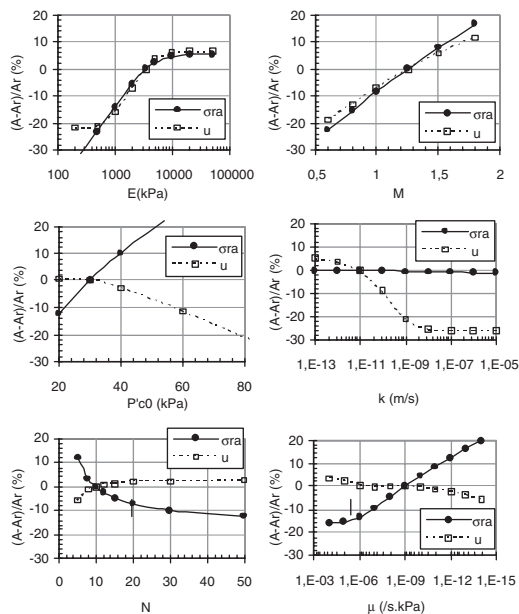


Figure 3. Parameters effects on the radial stress and pore pressure responses.

parameter, given in Table 1 within a range of reasonable values. We can point out:

- E , M , p'_{c0} have a significant effect on the radial stress as well as on the pore pressure;
- N and μ have an important effect on the radial stress, and a slight effect on the pore pressure;
- k has a very slight effect on the radial stress, but a significant effect on the pore pressure for values between 10^{-8} and 10^{-12} m/s, and a very slight effect for other values of k which represent either perfectly drained or undrained conditions during the pressuremeter test;
- ν and β^* have a very slight effect on both the radial stress and the pore pressure;
- only E can change the initial slope of the radial stress curve.

A special attention was given to the influence of the viscous parameters. For obtaining the same total

Table 1. Values of EVP model and hydraulic parameters

	E (kPa)	M	p'_{c0} (kPa)	N	μ (1/s · kPa)	k (m/s)
Ref	3500	1.25	30	10	1×10^{-9}	1×10^{-11}
Down	200	0.60	20	5	1×10^{-14}	1×10^{-13}
Up	50000	1.80	200	50	1×10^{-4}	1×10^{-6}

Remarks: Reference values of $\nu = 0.3$ and $\beta^* = 0.16$.

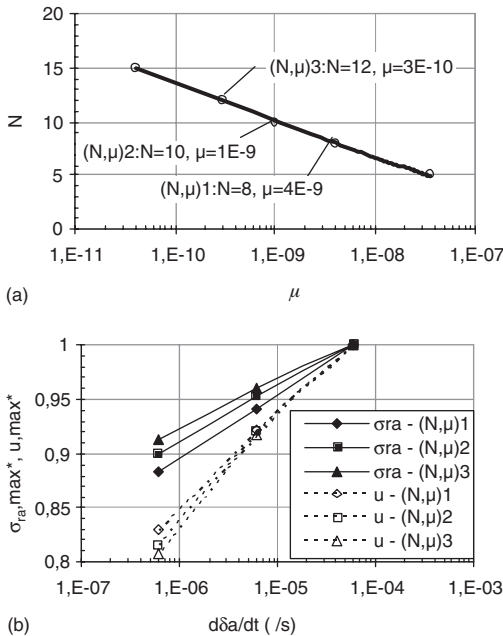


Figure 4. (a) Relationship between N and μ for the same total stress curve at a strain rate; (b) normalized total stress and pore pressure as a function of strain rate.

stress curve of a given constant strain rate test, there is a linear relationship between N and $\log(\mu)$ as shown in Figure 4a. For other strain rates, the selected values of (N, μ) bring much more changes on the total stress curve, whereas inverse but slighter effect on the pore pressure, as presented in Figure 4b. It allows us to determine the values of (N, μ) from pressuremeter tests with more than two different strain rates.

The effect of (N, μ) on a strain holding stage (stress relaxation test) at a strain of 8% and on a stress holding stage (creep test) at a stress increment of 41 kPa after a constant strain rate stage was also studied, as presented in Figure 5. The results show the influence of (N, μ) on the evolution of the radial stress during a strain holding stage or the radial strain during a creep. It is therefore possible to determine the values of (N, μ) from either a relaxation test or a creep test.

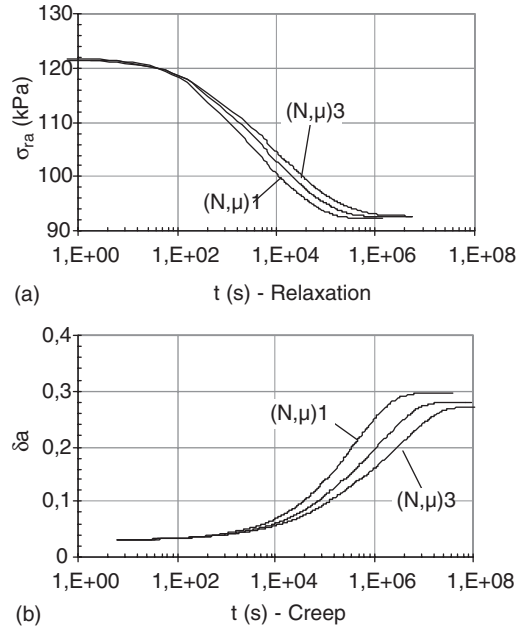


Figure 5. (a) Comparison of stress relaxation for different (N, μ) during strain holding stage; (b) comparison of strain evolution for different (N, μ) during stress holding stage.

3 PARAMETER IDENTIFICATION

3.1 Experimental results

As described by Rangeard et al. (2003), the pressuremeter tests were performed by an apparatus called pressio-triax on the Saint-Herblain clay, situated in the Loire Paleolithic period and made of modern river clayey alluvial deposits, characterized by a high plasticity index ($I_p = 42$) and slightly or moderately organic. The initial stress state of the samples at a depth of 5.5–6.5 m were $\sigma_1 = 85$ kPa, $\sigma_2 = \sigma_3 = 68$ kPa, $u = 56.5$ kPa, and $\sigma_1 = 110$ kPa, $\sigma_2 = \sigma_3 = 90$ kPa, $u = 68$ kPa for the samples at a depth of 6.5–7.5 m. The physical and mechanical characteristics for each test are summarized in Table 2, which include the strain rate values of the performed pressio-triax tests.

An oedometer test at a constant strain rate of 3.3×10^{-6} /s was carried out on a sample of the Saint-Herblain clay at a depth of 6.9–6.95 m using a modified oedometer apparatus (Rangeard, 2002). Lateral stress could also be measured during the test. The parameters deduced from the one-dimensional consolidation curves are presented in Table 3. The soil is slightly overconsolidated ($OCR = 1.73$) and $K'_0 = 0.5$.

Table 2. Physical and mechanical characteristics of Saint-Herblain clay samples.

Specimen	Depth (m)	w (%)	e_i	γ (KN/m ³)	Vitesse (/s)
Pre1A (CR)	6.5–7.5	113	2.69	14.91	3×10^{-5}
Pre3A (SR)	5.5–6.5	97	2.23	13.96	3×10^{-5}
Pre3B (SR)	5.5–6.5	96	2.48	14.21	6×10^{-7}
Pre3D (SR)	5.5–6.5	85	2.16	14.22	1.5×10^{-4}
Pre3F (SR)	5.5–6.5	90	2.51	14.41	6×10^{-6}
Pre3H (RE)	5.5–6.5	93	2.29	14.35	6×10^{-5}

Remarks: CR – creep test; SR – strain rate test; RE – relaxation test.

Table 3. Parameters deduced from oedometer test.

λ	κ	e_0	$\sigma'_{ra,0}$ (kPa)	$\sigma'_{v,0}$ (kPa)
0.43	0.02	2.1	26	52

Remarks: $\sigma'_{ra,0}$ – radial preconsolidation pressure; $\sigma'_{v,0}$ – vertical preconsolidation pressure.

3.2 Identification procedure

Based on the previous parametric study, we firstly determined several parameters as follows:

- Poisson’s ratio was taken equal to 0.3, which is a common value for clay.
- Young’s modulus was determined by the initial slope of the radial stress curve: $E = 3500$ kPa.
- Compressibility index was determined by oedometer test: $\beta^* = (\lambda - \kappa)/(1 + e_0) = (0.43 - 0.02)/(1 + 2.1) = 0.13$.

As the other parameters, they can be determined by using three levels of strain rate tests in addition to a very low strain rate test as follows:

- By using a low strain rate test in which the influence of hydraulic and viscous parameters is very slight, we can establish a relationship between M and p'_{c0} by curve fitting.
- For each $(M, p'_{c0})_i$, N et μ can be determined by the other three levels of strain rate tests.
- For each $(M, p'_{c0}, N, \mu)_i$, we can determine k by the pore pressure curve obtained with the test performed at the highest strain rate.
- By fitting the other pore pressure curves, there is only one series of parameters which can be adopted.

The values of the parameters determined by the proposed procedure were shown in Table 4. The value of M corresponds to a friction angle equal 31° and agrees the results of triaxial tests performed on the same sample. The value of p'_{c0} is located between the initial stress and the preconsolidation pressure determined by the oedometer test. The comparison between

Table 4. Values of EVP model and hydraulic parameters of Saint-Herblain clay.

E (kPa)	ν	M	β^*	p'_{c0} (kPa)	N	μ (1/s.kPa)	k (m/s)
3500	0.3	1.25	0.16	30	10	1×10^{-9}	1×10^{-11}

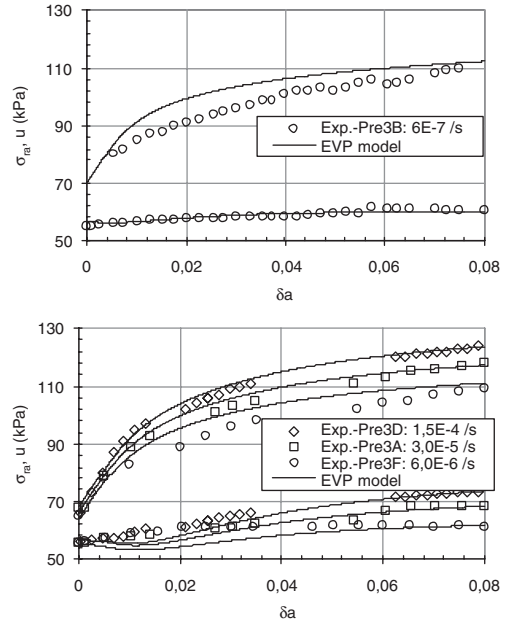


Figure 6. Comparison between experiment and simulation of strain rate tests.

calculated and experimental results is shown in Figure 6.

3.3 Verification of identification procedure

For verifying the methodology of this identification procedure, a constant strain rate pressuremeter test with a relaxation stage (Pre3H) was simulated using the determined parameter values. The time for dissipating the excess pore water pressure is identical for the numerical and experimental results during the relaxation stage, despite the fact that the final pore pressure is lower on the simulation. The comparison between predicted and measured results, presented in Figure 7, showed that the EVP-MCC is able to describe the time-dependent behaviour in pressuremeter tests, and that the proposed method can be applied for identifying the parameters.

Furthermore, the determined parameter values were taken for simulating a pressuremeter creep test (Pre1A), except for the value of the preconsolidation pressure (35 kPa) due to a different initial consolidation for a

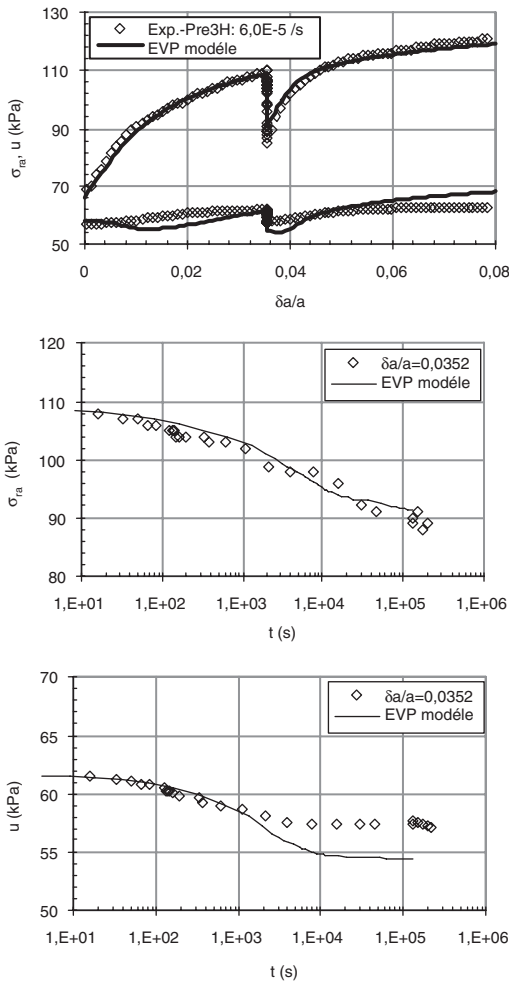


Figure 7. Comparison between experiment and simulation of a pressuremeter strain rate test with a relaxation stage (Pre3H).

1 meter deeper sample. Good agreement between predicted and measured results was achieved, as presented in Figure 8. The two cases show the ability of the proposed procedure to correctly identify the clay parameters by constant strain rate pressuremeter tests.

4 ANALYSIS OF DRAINAGE CONDITIONS IN CONSTANT STRAIN RATE TESTS

The phenomenon of local consolidation can take place during pressuremeter tests. It depends on the strain or stress rate at the cavity wall as well as on the soil permeability. Based on numerical tests at constant strain rates varying from 6×10^{-2} to 6×10^{-7} /s, the evolution of the total stress ($\sigma_{ra} - u_0$) and the effective stress ($\sigma_{ra} - u$) at a strain of 8% as a function

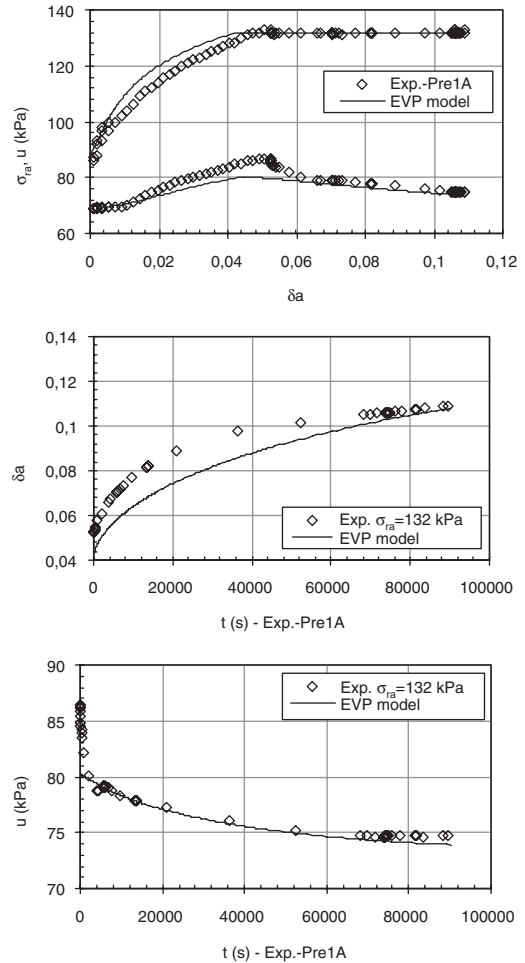


Figure 8. Comparison between experiment and simulation of a pressuremeter creep test (Pre1A).

of $(d\delta_a/dt)/k$ was carried out using the EVP-MCC parameters determined in Table 4. Four different types of behaviour during the pressuremeter test as described by Rangeard et al. (2003) were generally shown in Figure 9 with normalized pressures:

- Fully drained. There is no excess pore pressure during the pressuremeter test.
- Partially drained type A. The total pressure and the pore pressure are influenced by the drainage condition.
- Partially drained type B. the pore pressure is influenced by the drainage condition but not the total pressure.
- Fully undrained. The pore pressure and the total pressure remain the same values changing strain rate or permeability.

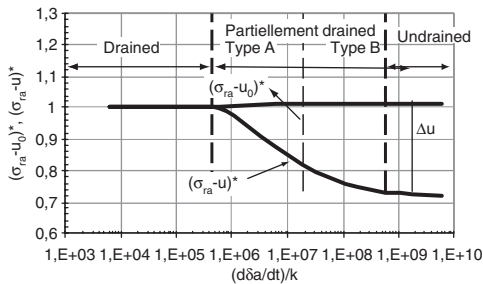


Figure 9. Evolution of $(\sigma_{ra} - u_0)$ and $(\sigma_{ra} - u)$ as a function of $(d\delta_d/dt)/k$.

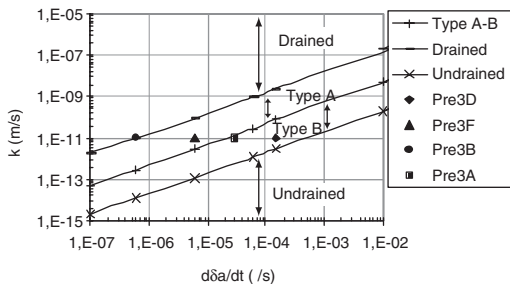


Figure 10. Drainage conditions as a function of the strain rate and the permeability.

To interpret the drainage conditions for given values of permeability and strain rate, we can transform Figure 9 into the one presented in Figure 10, as described by Rangeard (2003). The points representing each test allow us to determine their drainage conditions.

From Figure 10, we can note that the test Pre3B, with the lowest strain rate, is close to fully drained condition. The test Pre3F, with a lower strain rate, is in the partially drained type A condition. For the tests Pre3A and 3D, both in the partially drained type B condition, the difference in total pressure for different strain rates is due to the viscous behaviour of the soil skeleton.

We can also note that the different pore pressure curves in Figure 6 are generated by the viscous properties of the soil (as shown in Figure 4b) as well as by the different drainage conditions.

5 CONCLUSIONS

The parametric study made on constant strain rate pressuremeter test was carried out for highlighting the parameters effects on the pore pressure and total pressure at the cavity wall, using the EVP-MCC model. Based on this, a back analysis method for

identifying soil parameters from constant strain rate pressuremeter tests was proposed.

This method of identification was employed to determining the EVP-MCC model parameters of Saint-Herblain clay as well as its permeability. The procedure was then verified by simulating a pressuremeter test with a relaxation stage and a pressuremeter test with a creep stage. The values of parameters agreed with those obtained from triaxial tests on the same soil sample.

A drainage conditions analysis was then performed by looking the evolution of the total pressure and the effective pressure at the cavity wall as a function of the strain rate and the permeability. Four different types of drainage condition were defined by the ratio between strain rate and permeability. The drainage conditions of the pressuremeter tests on Saint-Herblain clay were then determined. They are in agreement with the different pore pressure curves obtained for the different strain rates.

REFERENCES

- Adachi, T. & Oka, F. 1982. Constitutive equations for normally consolidated clay based on elasto-viscoplasticity. *Soils and Foundations*, 22(4), Dec., p 57–70.
- Anderson, W.F. & Pyrah, I.C. & Ali, F.H. 1987. Rate effects in pressuremeter tests in clays. *Journal of Geotechnical Engineering*, v 113, n 11, Nov., p 1344–1358.
- Hicher, P.Y. & Michali, A. 1996. Identifying soil parameters by means of laboratory and in situ testing. *Computers and Geotechnics*, v 19, n 2, p 153–170.
- Perzyna, P. 1966. Fundamental problems in viscoplasticity. *Advances in Applied Mechanics*, volume 9, 243–377 Academic Press.
- Pye, C.N. 1995. Influence of constitutive models on self-boring pressuremeter interpretation in clay. *Canadian Geotechnical Journal*, v 32, n 3, June, p 420–427.
- Rangeard, D. 2002. *Identification des caractéristiques hydro-mécaniques d'une argile par analyse inverse des essais pressiométriques*. Thèse de l'Ecole Centrale de Nantes et l'Université de Nantes.
- Rangeard, D. & Hicher, P.Y. & Zentar, R. 2003. Determining soil permeability from pressuremeter tests. *International Journal for Numerical and Analytical Methods in Geomechanics*, v 27, n 1, p 1–24.
- Roscoe, K.H. & Burland, J.B. 1968. On the Generalized Stress-Strain Behavior of Wet Clay. *Engineering Plasticity*, p 535–609.
- Yin, Z.Y. & Hicher, P.Y. & Riou, Y. & Huang H.W. 2006. An elasto-viscoplastic model for soft clay. *ASCE Soil and Rock behaviour and modelling special publication*, Shanghai.
- Zentar, R. & Hicher, P.Y. & Moulin, G. 2001. Identification of soil parameters by inverse analysis. *Computers and Geotechnics*, v 28, n 2, p 129–144.

Investigation on the mechanical resistance of reinforced sand samples

A. Cividini & U. Arosio

Department of Structural Engineering, Politecnico di Milano, Milano, Italy

ABSTRACT: The results of an experimental and numerical study are summarized here concerning the mechanical behavior of reinforced sands. The experimental part of the investigation was carried out using both standard triaxial and plane strain equipments. In the latter case the specimens contained either horizontal reinforcements, or reinforcements inclined with respect to the vertical loading direction. A constitutive model and then two simple schemes were adopted for the preliminary interpretation of the test results. The comparison between experimental and numerical results led to some conclusions on the influence of the mechanical properties of the geotextiles, and of their inclination, on the overall resistance of the reinforced samples.

1 INTRODUCTION

A preliminary and comparative evaluation of two finite element schemes for the analysis of a vertical, reinforced earth wall (Cividini et al., 1997) showed that the available experimental information was not sufficient for a proper mechanical characterization of plane strain earth structures containing inclined reinforcements with respect to the principal stress directions. More recently another numerical study (Molenkamp, 2001) confirmed that for testing non isotropic materials, like reinforced soils, the use of a plane strain apparatus (Drescher et al., 1990; Cividini, 2002b) is preferable to that of standard triaxial and direct shear devices.

On that basis a laboratory investigation, consisting of standard triaxial and plane strain compression tests, was carried out on sand samples containing geotextiles reinforcements with various inclinations with respect to the vertical loading direction. A particular procedure, whose details can be found in (Cividini, 2001), was developed for preparing prismatic sand samples containing geotextiles reinforcements with various inclinations with respect to the vertical loading direction. The procedure is based on the moist tamping technique and on the subsequent freezing of the samples to allow their setting into the plane strain device.

The samples have dimensions of 4 cm × 8 cm × 14 cm and are reinforced with geotextile layers, 2 cm or 3 cm apart from each other. Some of them were reinforced with a thin and extensible reinforcement (non-woven polypropylene geotextile). The remaining tests concern specimens reinforced with non-woven polypropylene-polyethylene geotextile. The two geotextiles have comparable tensile strengths, but differ in thickness and in stiffness.

The experimental program carried out so far consists of about 50 plane strain tests on both natural sand and reinforced samples and the investigation leads to a quantitative assessment of the influence of the reinforcement orientation on the overall shear strength and stiffness of the samples.

In the following, first some of the experimental results are considered for modelling the evolution of the shear resistance at the interface between sand and reinforcements at the interface. Then the measured variation in peak shear resistance is interpolated using two different schemes. The comparisons between experimental and numerical results lead to some conclusions on the use of plane strain testing devices for the calibration of constitutive laws for reinforced samples.

2 MAIN CONCLUSIONS FROM THE EXPERIMENTAL INVESTIGATION

The experimental results indicate that the overall behaviour of a reinforced soil depends on various mechanical and geometrical parameters that characterise both its basic components (soil and geotextile) and their assemblage.

The axial stress-strain curves show that reinforced samples have different load carrying capacity, however in both cases a decrease of the overall stiffness and shear resistance is observed with increasing the reinforcement orientation β . The shear resistance is lower than that of the natural sand when β exceeds 30° and this implies that reinforced earth structures may give substantially different responses to external load increments, depending on the angle existing between the reinforcements and the compressive principal stress.

The main conclusions derived from the experimental results can be summarised as follows:

- The stress-strain (axisymmetric or plane-strain) regime during loading has a marked influence on the observed behaviour of natural sand samples. The triaxial results do not show the marked strain softening effect observed under plane strain conditions.
- The strain softening behaviour that characterises the natural sand samples under plane strain conditions is not shown by samples with horizontal reinforcements. In fact, they present an overall ductile or hardening behaviour, which is likely to depend on the stiffness of the adopted geotextiles.
- The influence of the surface roughness of the geotextiles on the load carrying capacity of the samples is barely significant in the case of horizontal reinforcements, but becomes more pronounced in the case of inclined reinforcements.
- An increase of the slope of the reinforcements leads to a decrease of the overall shear resistance (and stiffness) and to a transition from hardening to softening behaviour.
- The overall peak strength of the reinforced sand samples can be expressed in terms of a constant friction angle, coinciding with that of the natural sand, and of an apparent cohesion intercept that depends on spacing and inclination of the reinforcements.

The observed overall resistance is likely to depend on the frictional resistance between the reinforcement and the sand. In particular, the structure of one of the geotextile, quite deformable along its thickness, leads to a relatively high degree of interlocking with sand grains, thus increasing the surface frictional resistance of the reinforcements. Such interlocking, however, is less pronounced for the second one, characterized by smoother surfaces and low compressibility along its thickness (Cividini, 2002b). Consequently it appears that the results of the plane strain tests could permit deriving some further conclusions on the frictional characteristics of the sand/geotextile interface.

3 MODELLING OF THE SHEAR RESISTANCE AT THE SAND-GEOTEXTILE INTERFACE

In general terms, the numerical simulation of the tests can be based on two finite element schemes, referred to as “inhomogeneous” and “homogeneous” approaches (e.g. Cividini et al., 1997). When the first one is adopted the sample is discretized introducing separately the reinforcements and the soil layers between them. For sake of brevity, this aspect is not discussed here and additional comments are presented in (Cividini & Sterpi, 2000; Cividini, 2002a).

In the second case the inhomogeneous medium is made equivalent to a continuous homogeneous nonlinear and nonisotropic material characterised by a suitable constitutive law (Cividini, 2005). For modelling of the shear resistance at the sand-geotextile interface the stress state along the reinforcement direction is evaluated considering the specimen as a “homogeneous” element. Due to the anisotropy of the reinforced samples the evolution of the stress state depends on the angle β between geotextile layers and the horizontal direction. This effect is clearly shown by the diagram in Figure 1 since the lines, representing the variation of the normal and shear stresses σ_{ri} , τ_{ri} for the different reinforcement orientations, are not bounded by a circle.

For completeness, the figure shows also the peak and ultimate resistance envelopes for the sand-geotextile interface, obtained from direct shear box tests. From the experimental viewpoint, it can be observed that when the reinforcement orientation is equal to 45° and to 75° the stress state is in practice bounded by the ultimate (or residual) resistance curve characterising the sand-geotextile interface, while for the intermediate value of 60° the peak resistance is almost attained.

For the numerical representation of the stress state reached on the reinforcement at the overall peak and at the end-of-test conditions, the basic form of the Hierarchical Single Surface (HiSS) (Desai, 2001) constitutive law was chosen among the various isotropic hardening constitutive laws presented in the literature. Written in terms of the stress components σ_{ri} and τ_{ri} along the geotextile, the HiSS yield surface allows an approximation of both sets of experimental data (cf. solid and dashed interpolation curves in Figure 1) and the HiSS ultimate curves, obtained for the asymptotic stress state condition, almost coincide with the peak and ultimate lines obtained on the basis of the direct shear test results.

It is important to note that the HiSS model parameters were calibrated by curve fitting of the σ_{ri} , τ_{ri}

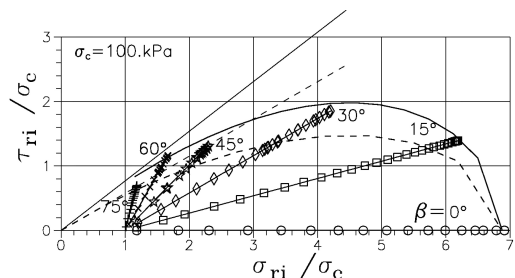


Figure 1. Influence of the reinforcement inclination β on the stress state at the geotextile/sand interface: stress path from plane strain tests on reinforced sand and numerical interpolation of the peak (continuous line) and of the end-of-test (dashed line) data (σ_{in} , τ_{in} normal and shear stress along the reinforcement orientation, σ_c cell pressure).

experimental data and that only subsequently the two HiSS ultimate lines, associated to the obtained interpolation curves, were drawn.

The above observations indicate that the shear resistance at the interface between reinforcement and sand can be evaluated on the basis of the results from plane strain tests, without making recourse to direct shear tests (e.g. Seo et al., 2004).

4 SIMPLE SCHEMES FOR MODELLING THE OVERALL SHEAR RESISTANCE

For the interpolation of overall shear resistance measured in plane strain tests on reinforced sand, two different schemes were adopted (Arosio, 2005). The first one (referred in the following as 'scheme I') considers the specimen as homogeneous apart for a plane of weakness, while the second one ('scheme II') accounts for the presence of the different reinforcement layers. In a broad sense the two schemes represent an application of the conventional schemes usually adopted in the design of reinforced earth structures.

With reference to the first scheme it is worthwhile to recall that the increase in strength observed in conventional triaxial tests on cylindrical samples can be regarded as the consequence of the increase in confining stress associated to the presence of the horizontal layers of geotextile (e.g. Ingold, 1982).

This observation suggests to adopt the same criterion in the case under examination, accounting for both the geotextile inclination and the presence of a plane of weakness, with a limiting shear resistance, as indicated in Figure 2b.

The interpolation curve obtained for the vertical stress σ_v is shown in Figure 3 and the comparison with the experimental data indicates that scheme I does not provide an adequate approximation of the observed

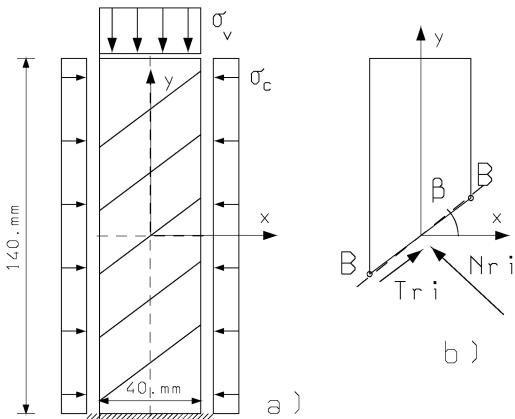


Figure 2. Plane strain sample (a) and block sliding along the reinforcement, considered in scheme I (b).

shear resistance variation. In particular the vertical stress at failure is overestimated for the lower inclinations of the geotextile reinforcements. An attempt to reduce this discrepancy led to the use of a decay function $d = \cos^5 \beta$ that does not appear meaningful in the case under examination.

In the framework of the second scheme, each reinforcement layer was made equivalent to a set of external loads F_r , as indicated in Figure 4a and for sake of simplicity the reinforcement forces were assigned the same value. This first version of scheme II led to an interpolation curve characterized by discontinuities. This drawback was easily removed, substituting the external forces with the corresponding boundary tractions, so that a smooth variation is obtained of the shear resistance with the reinforcement orientation.

Finally, Figure 5 shows the variation of the vertical stress measured in the laboratory tests and the interpolation curve obtained applying scheme II. It is worthwhile noting that the back-analyzed value of the F_r load

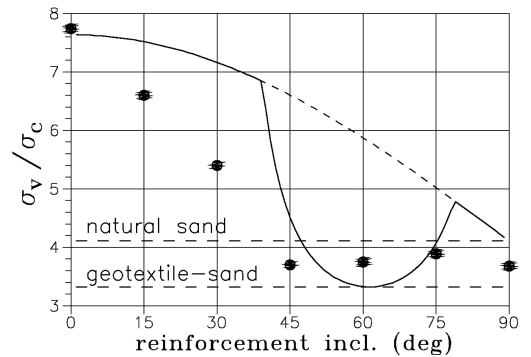


Figure 3. Variaton of the peak stress with the angle of the reinforcement inclination: measured values (dots) and interpolation curve according to scheme I.

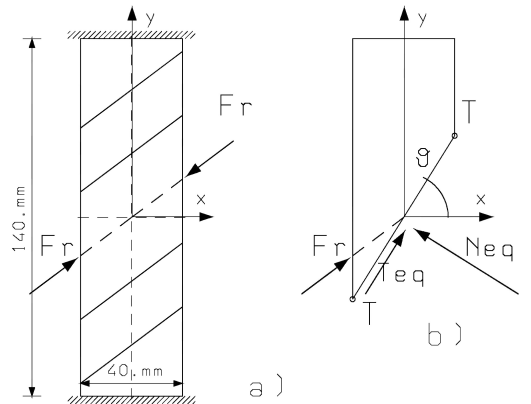


Figure 4. Plane strain test on reinforced sand: scheme II used for deriving the interpolation curve of the experimental data.

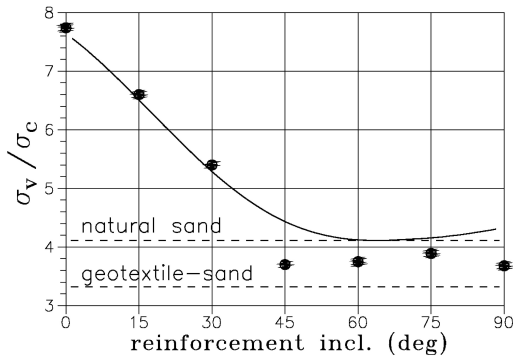


Figure 5. Variaton of the peak stress with the reinforcement inclination: measured values (dots) and interpolation curve obtained according to scheme II.

is lower than the tensile resistance of the “active” geotextile layers.

The second scheme provides a proper representation of the evolution of the peak resistance observed in sand specimens containing geotextile reinforcements with various inclination with respect to the vertical loading direction. Even if the results here presented concern a limited amount of data, obtained at constant confining pressure, they show that the interface resistance has a relevant effect on the overall mechanical resistance of the sample. This suggests broadening the experimental and numerical study carried so far.

5 CONCLUSIONS

The experimental results here discussed concern an ongoing research on the mechanical behaviour of reinforced sands, containing geotextile reinforcements with various inclinations with respect to the vertical loading direction.

First the results of a series of plane strain compression tests have been summarized. They indicate the marked influence of the reinforcement slope on the overall stiffness and shear resistance of the “composite” material. Subsequently, the experimental results have been compared with interpolation curves obtained adopting the HiSS constitutive model and two simple schemes similar to those frequently proposed in the design of reinforced earth structures.

The comparison indicates that the HiSS model provides an acceptable approximation of the experimental data, since the model can properly take into account of the shear resistance that develops at the interface between soil and geotextile.

Subsequently it is shown that the variation of the peak stress with the reinforcement orientation can be approximated considering an unreinforced block subjected to boundary tractions equivalent to the reinforcements.

On these bases it can be concluded that the described experimental investigation and its numerical modelling represent two necessary and interlaced steps towards a deeper understanding of the mechanical behaviour of reinforced sands and towards the stress analysis of actual engineering problems.

ACKNOWLEDGEMENTS

The tests were carried out at the Geotechnical Laboratory of the Department of Structural Engineering of the Politecnico di Milano. The assistance of Enzo Iscandri is gratefully acknowledged.

REFERENCES

- Arosio, U. 2005. Reinforced earth and influence of the reinforcement inclination: experimental and numerical investigation (in Italian). MS Thesis, DIS Politecnico di Milano.
- Cividini, A. 2002a. Reinforced sand parameters from plane strain compression tests. Proc. 5th Europ. Conf. Numerical Methods in Geotechnical Engineering, Paris, 45–50.
- Cividini, A. 2002b. A laboratory investigation on the behaviour of reinforced sand samples under plane strain and triaxial conditions. *Soils and Foundations*, 42(6):23–39.
- Cividini, A. 2005. Numerical analysis in the interpretation of plane strain compression tests (Key Note Lecture). Proc. 11th International Conference of the Association for Computer Methods and Advances in Geomechanics, Turin (Italy), 4:309–322.
- Cividini, A. & Gioda, G. 1992. A finite element analysis of direct shear tests on stiff clays. *International Journal for Numerical and Analytical Methods in Geomechanics*, 16:869–886.
- Cividini, A., Gioda, G. & Sterpi, D. 1997. An experimental and numerical study of the behaviour of reinforced sands (Invited paper). Proceedings of the 9th International Conference of the Association for Computer Methods and Advances in Geomechanics, Wuhan, P.R. China, 1:15–30, Rotterdam: Balkema.
- Cividini, A. & Sterpi, D. 2000. Plane strain tests on reinforced sand and their numerical modelling. Proceedings of the 2nd European Conference on Geotextiles, EUROGEO2000, Bologna.
- Desai, C.S. 2001. *Mechanics of materials and interfaces: the Disturbed State Concept*. Boca Raton (FL), USA: CRC Press.
- Drescher, A., Vardoulakis, I.G. & Han, C. 1990. A biaxial apparatus for testing soils. *Geotechnical Testing Journal*, 13:226–234.
- Ingold, T.S. 1982. *Mechanics and concept. Reinforced earth*. London: Thomas Telford.
- Molenkamp, F. 2001. Evaluation of axial shear test using plane strain simulation. *Geotechnique*, 51: 37–49.
- Seo, M.W., Park, I.J. & Park, J.B. 2004. Development of displacement-softening model for interface shear behaviour between geosynthetics. *Soils and Foundations*, 44(6): 27–38.

Testing and modelling stabilised soft clay

P. Vepsäläinen, A. Aalto & M. Lojander
Helsinki University of Technology, Espoo, Finland

ABSTRACT: Some features of the stress-strain behaviour in stabilised clay according to triaxial test results have been presented. Based on the observed test results, some principles for an elastoplastic hardening and softening material model for stabilised clay has been developed. Special attention has been paid to functional hardening and softening formulation. The behaviour of the model is studied in the boundary conditions of an idealised drained triaxial compression test.

1 INTRODUCTION

Deep stabilisation (deep soil mixing) is a modern soil improvement method of soft clays used especially in Scandinavia and in Japan but also in Central Europe, in North America and in the Far East. Although the deep stabilisation technique is nowadays quite well known, the mechanics of stabilised clay is not so well understood. This has led to oversimplified constitutive models for stabilised soil and crude and conservative design methods for deep stabilised columns.

2 STRESS-STRAIN BEHAVIOUR OF STABILISED CLAY

Results of triaxial compression tests on stabilised soft clay are presented in Figures 1 and 2. The binder agent was lime and cement in both cases. It is found that the stress-strain curves have a hardening and softening character at low cell pressures both in

undrained and in drained test, whereas at high cell pressures there seems to be only hardening and after that the strength is almost constant.

3 A MODEL FOR STRESS-STRAIN BEHAVIOUR OF STABILISED CLAY

The basic concept is illustrated by Figure 3 (deviatoric stress q /hydrostatic stress p') and Figure 4 (deviatoric stress q /axial strain ε_1 /volumetric strain ε_v), Cuihak (2002). In this case the time is fixed so that the possible material strengthening with time is not taken into account. Furthermore it is supposed that the deviatoric hardening is the most essential in practical hydrostatic stress levels.

Drained triaxial compression tests with a minimum of three different cell pressures are needed. In the first case the cell pressure is zero (as in the unconfined compression test). The highest cell pressure has to be somewhat larger than the in situ earth pressure at rest.

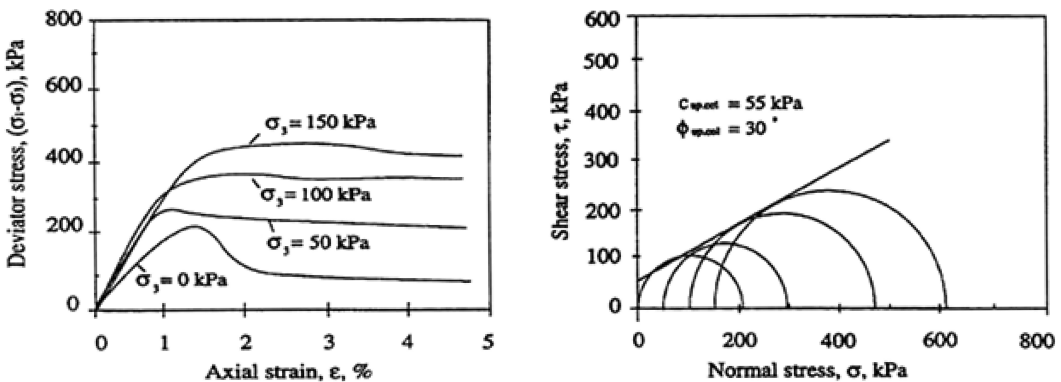


Figure 1. Examples of results of undrained triaxial compression test on lime-cement treated clay, laboratory manufactured samples (Kivelö 1998).

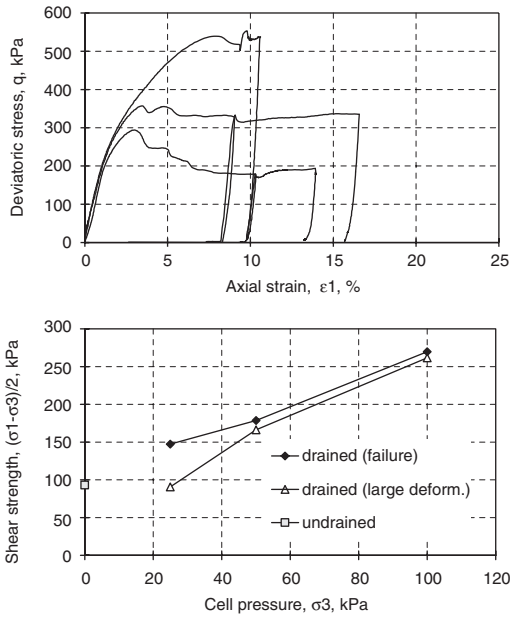


Figure 2. Examples of results of drained triaxial compression test on lime-cement treated clay, laboratory manufactured samples (Aalto 2001).

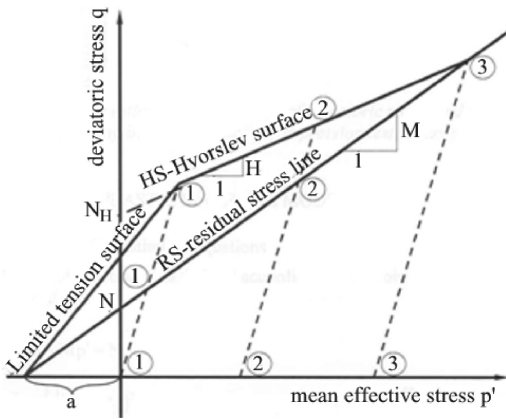


Figure 3. Yield surfaces of hardening and softening stabilised soil model in p' - q plane, drained triaxial compression test.

Both maximum and residual (critical state) values of deviatoric stress are measured. Then points 1, 2 and 3 in Hvorslev's line and residual stress line in Figure 3 and parameters for Hvorslev's line and residual stress line can be defined.

Hvorslev's line:

$$q = H p' + N_H \quad (1)$$

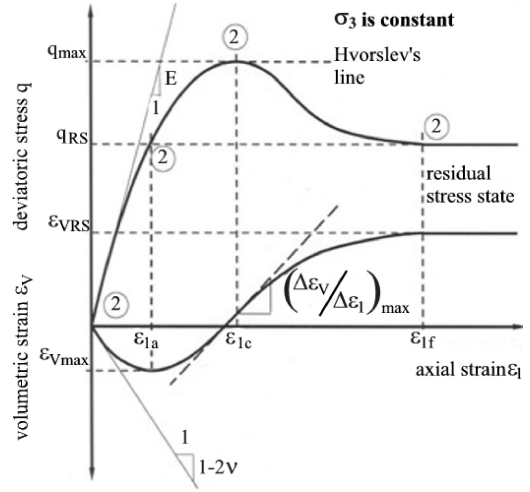


Figure 4. Estimated development of deviatoric stress and volumetric strain in primary loading in a drained triaxial compression test. Stress path 2-2 in Figure 3.

$$H = \frac{6 \sin \phi_H}{3 - \sin \phi_H} \quad (2)$$

$$N_H = \frac{6 c_H \cos \phi_H}{3 - \sin \phi_H} \quad (3)$$

Residual stress line:

$$q = M p' + N \quad (4)$$

$$M = \frac{6 \sin \phi_{RS}}{3 - \sin \phi_{RS}} \quad (5)$$

$$N = \frac{6 c_{RS} \cos \phi_{RS}}{3 - \sin \phi_{RS}} \quad (6)$$

ϕ_{RS} is the friction angle in residual stress state, c_{RS} is the cohesion in residual stress state, ϕ_H is the friction angle in Hvorslev's line and c_H is the cohesion in Hvorslev's line.

4 FORMULATION OF THE MODEL

4.1 General constitutive equations

The yield function F is defined according to the Mohr-Coulomb criterion (pressure is positive):

$$F = q - M p' - N \quad (7)$$

$$M = \frac{3 \sin \varphi^*}{\sqrt{3} \cos \theta - \sin \theta \sin \varphi^*} \quad (8)$$

$$N = \frac{3 c^* \cos \varphi^*}{\sqrt{3} \cos \theta - \sin \theta \sin \varphi^*} \quad (9)$$

p' is effective hydrostatic stress, q is the deviatoric stress, c^* is mobilised cohesion, φ^* is mobilised friction angle and θ is Lode's angle.

The plastic potential function Q is formally similar to the yield function F except that mobilised angle of dilation Ψ^* is used.

Stress and strain increments $d\sigma'$ and $d\varepsilon$:

$$\{d\sigma'\} = [D_{ep}] \{d\varepsilon\} \quad (10)$$

$$[D_{ep}] = [D_e] - \frac{[D_e] \{a_Q\} \{a_F\}^T [D_e]}{A + \{a_F\}^T [D_e] \{a_Q\}} \quad (11)$$

$$\{a_F\} = \frac{dF}{d\{\sigma'\}} \quad (12)$$

$$\{a_Q\} = \frac{dQ}{d\{\sigma'\}} \quad (13)$$

$$A = -\frac{dF}{dh} f(a_Q) \quad (14)$$

D_e is the elastic stiffness matrix, D_{ep} is the elasto-plastic stiffness matrix, A is hardening modulus and h is the measure of the yield (the generalised plastic strain or effective plastic strain). For deviatoric hardening/softening:

$$f(a_Q) = \sqrt{\frac{2}{3} \{a_Q\}^T \{a_Q\}} \quad (15)$$

$$\frac{dF}{dh} = \frac{dF}{dc^*} \frac{dc^*}{dh} + \frac{dF}{d\varphi^*} \frac{d\varphi^*}{dh} \quad (16)$$

4.2 Hardening and softening formulation

The hardening and softening formulation is based on the results of drained triaxial compression tests in stabilised clay samples. The basic idea is presented in Figures 3 and 4. The stress-strain behaviour below the residual stress line RS is hardening whereas the behaviour between the residual stress line and the Hvorslev surface is at first hardening and then softening. The hardening and softening behaviour is described by the mobilised friction angle φ^* and by the mobilised cohesion c^* .

The hardening part of the mobilised friction angle φ^* is solved either by ellipse or arcsine functions. Ellipse function:

$$\varphi^* = \frac{\varphi_{\max}}{\varepsilon_f} \sqrt{2\varepsilon_f h - h^2} \quad (17)$$

Arcsine function, Vermeer & de Borst (1984):

$$\varphi^* = \arcsin \left(\frac{2\sqrt{\varepsilon_f h}}{\varepsilon_f + h} \sin \varphi_{\max} \right) \quad (18)$$

ε_f is the effective plastic strain at the maximum mobilised friction angle φ_{\max} . The softening part of the mobilised friction angle is solved by the exponential function:

$$\varphi^* = \varphi_{RS} + (\varphi_{\max} - \varphi_{RS}) e^{-\left(\frac{h-\varepsilon_f}{\varepsilon_f}\right)^2} \quad (19)$$

φ_{RS} is the mobilised friction angle at the critical state or at the residual stress state. The mobilised angle of dilation Ψ^* is solved by using the dilation theory of Rowe (1972):

$$\Psi^* = \arcsin \left(\frac{\sin \phi^* - \sin \phi_{RS}}{1 - \sin \phi^* \sin \phi_{RS}} \right) \quad (20)$$

Two types of cohesion mobilisation has been studied. Firstly, mobilised cohesion c^* is kept constant and it represents cohesion at a residual stress state c_{RS} . Secondly, the attraction a in Figure 3 is kept constant, and in the later examples the effect of only this type of cohesion mobilisation has presented. The mobilised cohesion c^* is then:

$$c^* = a \tan \varphi^* \quad (21)$$

$$a = \frac{c_{RS}}{\tan \varphi_{RS}} \quad (22)$$

4.3 Calculated behaviour of stabilised clay sample in the standard drained triaxial compression test

In a drained triaxial compression test the relationships between deviatoric stress increments dq and axial strain increments $d\varepsilon_1$ and between volumetric strain increments $d\varepsilon_v$ and axial strain increments $d\varepsilon_1$ can be defined according to the formulae (23)–(26):

$$dq = D_{ep} d\varepsilon_1 \quad (23)$$

$$d\varepsilon_v = C_{ep} d\varepsilon_1 \quad (24)$$

$$D_{ep} = \frac{E}{1 + \frac{E}{A}(1 - \sin \varphi^*)(1 - \sin \psi^*)} \quad (25)$$

$$C_{ep} = \frac{(1 - 2\nu) - 2\frac{E}{A}(1 - \sin \varphi^*)\sin \psi^*}{1 + \frac{E}{A}(1 - \sin \varphi^*)(1 - \sin \psi^*)} \quad (26)$$

D_{ep} is here elastoplastic stress-strain modulus and C_{ep} is elastoplastic connection between volumetric and axial strain increments, E is modulus of elasticity and ν is Poisson's ratio. For a drained triaxial compression the hardening modulus A is:

$$A = -\frac{dF}{dh} f(a_Q) \quad (16bis)$$

$$f(a_Q) = \sqrt{\frac{4}{3}(1 + \sin \psi^* \sin \varphi^*)} \quad (27)$$

The partial derivatives for the formula (16) are not presented here. The strain hardening starts when axial strains begin to develop. But when the axial strain is very low near the origin in the Figure 4, the generalised plastic strain h is very small and it means that the hardening modulus A is very large. According to formulae (25) and (26) the limits for D_{ep} and C_{ep} are at the origin exactly the same as calculated by the theory of elasticity and presented in the Figure 4: $D_{ep} = E$ and $C_{ep} = 1 - 2\nu$.

Examples of the development of deviatoric stress q and volumetric strain ε_v with axial strain ε_1 are presented in Figure 5. The cell pressure $\sigma_3 = 20$ kPa, modulus of elasticity $E = 30\,000$ kN/m², Poisson's ratio $\nu = 0.3$, $\varphi_{max} = 35^\circ$, $\varphi_{RS} = 30^\circ$, $c_{RS} = 20$ kPa and $\varepsilon_f = 0.02$.

5 CONCLUSION

An elastoplastic deviatoric hardening and softening constitutive model for deep-stabilised clay has been developed. The behaviour of the model has been studied within the boundary conditions of idealised drained triaxial compression test. The calculated results show that the essential observed features of hardening, softening and dilating could be considered with the developed model. The dilating phenomenon may be important especially when the amount of stabilising agent is small and the shear strength of stabilised soft clay is under 100 kPa.

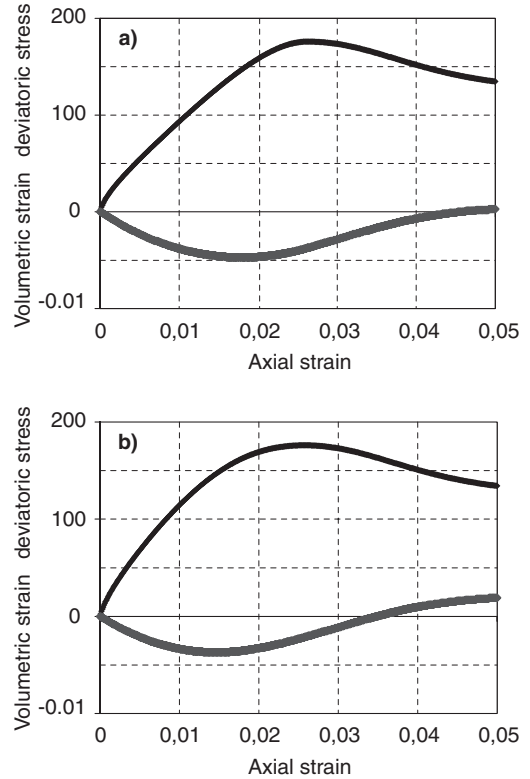


Figure 5. An example of hardening and softening in a drained triaxial test by the model. Development of deviatoric stress and volumetric strain. (a) The ellipse hardening function, (b) the sine hardening function.

REFERENCES

- Aalto, A. 2001. *Deep stabilisation research. Summary report, parts I-II*. Espoo: Helsinki University of Technology, Laboratory of Soil Mechanics and Foundation Engineering. (in Finnish).
- Ciuhak, K. 2002. Stress-strain behaviour of stabilised soil. *Soft Clay Modelling for Engineering Practice, Workshop 3, Helsinki, Finland 26–28 August 2002*. Espoo: Helsinki University of Technology, Laboratory of Soil Mechanics and Foundation Engineering.
- Kivelö, M. 1998. *Stabilization of embankments on soft soil with lime/cement columns. Doctoral Thesis 1023*. Stockholm: Royal Institute of Technology, Division of Soil and Rock Mechanics, Department of Civil and Environmental Engineering.
- Rowe, P.W. 1971. Theoretical meaning and observed values of deformation parameters for soil. *Proc. Roscoe Memorial Symp. On Stress-Strain Behaviour of Soils*. 143–194. Foulis, Henley-on-Thames, 1972.
- Vermeer, P.A. & Borst, R. 1984. Non-associated plasticity for soils, concrete and rock. *HERON* vol. 29, no. 3.

Effect of testing conditions on the shear strength parameters – a numerical study

O. Ravaska

Helsinki University of Technology, Finland

ABSTRACT: Factors affecting the results of laboratory triaxial tests are among other things the height/diameter ratio of the specimen, the specimen end restraint and stiffness of the rubber membrane. Their influence is very difficult or impossible to investigate under real circumstances, but theoretical and experimental studies on their effects are found in the literature. Numerical methods give, however, a possibility to have at least an estimate of their effect. This paper discusses the influence of these factors studied with Plaxis using a very fine element distribution. The present calculation results both agree and disagree with the results obtained previously.

1 INTRODUCTION

Geotechnical parameters obtained in the laboratory with small samples are supposed to represent the same in the soil layers. In addition to the specimen size or disturbance there are many other factors affecting the parameters obtained, for instance those related to the testing conditions. Such factors are the height/diameter ratio of the specimen (H/D), the specimen end restraint, stiffness of the rubber membrane, drainage conditions, piston friction and prevailing atmospheric pressure.

The effects of many of the factors listed above cannot be removed. For instance the membrane around the specimen is necessary in triaxial tests and end restraint due to friction on the end platens is very difficult or impossible to be fully eliminated particularly when frictional porous stones at the specimen ends are needed.

According to Lee (1978) Taylor concluded in the 1940s that reliable results could be obtained with soil specimens having regular ends provided their H/D was in the range 1.5–3.0. After that many experimental and analytical studies of the effect of end restraint, rubber membrane etc. have been carried out by e.g. Henkel & Gilbert (1952), Bishop & Green (1965), Duncan & Seed (1967), Duncan & Dunlop (1968), Lee (1978) and Kohonen (1987a, 1987b). The results of these studies are partly contradictory, but as a summary it can be stated that those factors can significantly affect the strength parameters. For example Lee (1978) concluded that the end friction had little influence on the undrained shear strength of sand, but just slight effects on the drained strength and on the internal friction angle. The undrained strength of dense sand

tested with lubricated ends was about 20% greater than that with regular ends.

Duncan & Seed (1967) concluded that the effect of the filter paper, membrane and piston friction together increased the axial stress by 20% or more for the San Francisco Bay Mud (a soft, normally consolidated silty marine clay). They did not pay attention to the specimen end restraint but for example to the effect of a rubber membrane, which was studied using the equations published by Henkel & Gilbert (1952). The equations give corrections to the observed triaxial test principal stresses assuming that the membrane forms an elastic shell around the specimen and that the specimen behaves like a cylinder without bulging. Based on these equations and CIUC triaxial tests for San Francisco Bay Mud the studies of Duncan & Seed (1967) resulted in the increase of axial stresses at failure by 4–7 kPa depending on the cell pressure of 100–400 kPa respectively.

The effects of some of these factors were also studied for soft clays in the Laboratory of SMFE of Helsinki University of Technology in the 1980s (Kohonen, 1987a, 1987b). The results indicated that the rubber membrane in CAUC tests increased cohesion by 0.5 kPa and increased the friction angle by 1.2°. The effect of end restraint was studied analytically by assuming that the specimen will get a shape of a barrel with parabolic walls. The effect of end restraint handled in this way was very small and considered to be insignificant.

These problems have also been studied numerically. E.g. Airey (1991) studied different end and drainage conditions in triaxial tests using the CRISP program concentrating to non-uniformities caused by drainage and end restraint, but not to the strength parameters of

which he concluded that in undrained shear they do not appear to be much affected by the end and drainage conditions, at least for the small stress range considered in his studies. Scheng & et al. (1997) studied the non-uniformities in a triaxial specimen caused by end restraint and drainage using the program ABACUS and the modified Cam Clay model. Liyanapathirana & et al. (2005) studied the same for structured soil using the structured Cam Clay model and the FEM program AFENA. Both of them used the element model with 100 eight-noded axi-symmetric elements and concentrated rather to the behaviour of the soil inside the specimen during loading than to the strength parameters.

Schanz & Gussman (1994) used a 3D linearly elastic and perfectly plastic model for studying the effect of end restraint and H/D ratio on the strength parameters. The results showed a considerable increase in the friction angle with increasing end friction. The geometry was varied from H/D = 1/1 to 4/1, but no significant effect on the strength was found.

2 PLAXIS MODEL

In this study a specimen with a height of 100 mm and a diameter of 50 mm (excluding the H/D calculations) was modelled axi-symmetrically with Plaxis 8.2. The specimen end restraint was modelled by full fixation at both ends. The rubber membrane around the specimen was modelled by a geogrid, Figure 1. The mesh

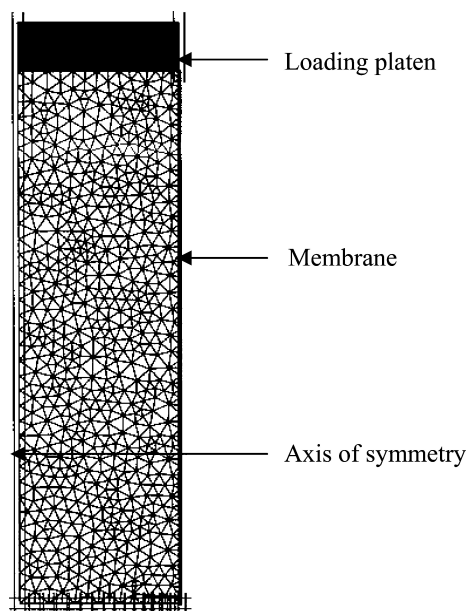


Figure 1. Axi-symmetric FEM model.

was as fine as possible in order that failure loads could be determined accurately. The number of 15-noded elements in the axi-symmetric section varied from 1182 to 1408. Because attention was directed to the strength parameters in a failure state, only the Mohr-Coulomb model was used.

3 RESULTS

3.1 Calculations

Materials, test types and parameters for studying the phenomena discussed above are presented in Table 1. The effect of the H/D ratio was studied by modelling unconfined compression tests on clay specimens and triaxial tests on sand specimens. The effect of end restraint was studied in unconfined compression tests using specimens with different cohesion and Young's modulus values. UC, DC and DE triaxial tests on clay, sand and till specimens were used to model the effects of end restraint and the rubber membrane.

3.2 Effect of specimen dimensions

The effect of the specimen dimensions together with end restraint on undrained shear strength s_u of clay was studied using specimens with a diameter of 50 mm and height/diameter ratios of H/D = 0.5, 1, 2 and 4. Given parameters for clay were $c = 20$ kPa and $E = 1$ MPa. The results are presented in Figure 2, which clearly shows that the shear strength decreases as the height of the specimen increases even though end restraint is not taken into account. The undrained shear strength of a normal (H/D = 2) specimen was 19,5 kPa, which was close to the given cohesion. The effect of end restraint is negligible for the H/D values greater than 1.

The corresponding results for sand in a drained triaxial test are presented in Figure 3. The specimen H/D ratio with no end restraint seems not to have the same effect on the friction angle as it had to cohesion

Table 1. Material and test data.

Soil	Test	c kPa	ϕ °	E MPa
Clay	UC*	10, 20, 40	0	0.5, 1, 2
	UC	7	20	0.5
	UC	10	20	1
	DC	10	20	1
Sand	DC	1	35	50
	DE	1	35	50
Till	DC	20	35	100
	DE	20	35	100

U = undrained, D = drained, C = compression, E = extension, * = unconfined.

in Figure 2. The friction angle is almost constant regardless of the specimen height. The effect of end restraint is, however, considerable with H/D values less than 1.5.

In Figure 4 the same effect as in Figures 2 and 3 separately for cohesion and friction is seen for soil having both cohesion and friction. For $H/D \geq 1$ the friction angle is constant regardless of the specimen height while cohesion tends to decrease with increasing specimen height.

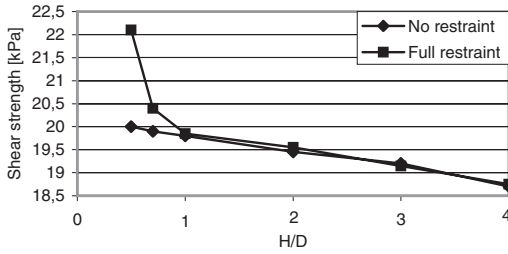


Figure 2. The effect of H/D ratio and end restraint on s_u of clay in unconfined compression tests. Given cohesion = 20 kPa.

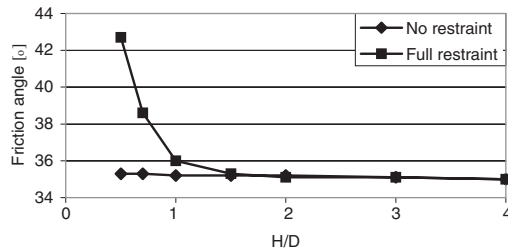


Figure 3. The effect of H/D ratio and end restraint on the friction angle in a drained triaxial test on a sand specimen. Given values: $\phi = 35^\circ$, $c = 1$ kPa, $E = 50$ MPa and $\sigma_3 = 50$ kPa.

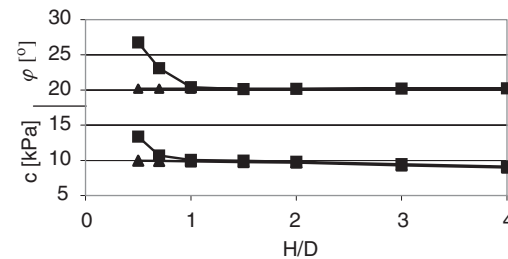


Figure 4. The effect of H/D ratio and end restraint on c and ϕ in a drained triaxial test on a clay specimen. Given values: $\phi = 20^\circ$, $c = 10$ kPa, $E = 1$ MPa.

3.3 Effect of end restraint

The effect of end restraint was involved in the previous considerations, but only the specimens with $H/D = 2$ are discussed here. In compression end restraint causes the specimen to get a shape of a barrel and in extension an hourglass. This causes problems in the determination of the specimen volume and cross-sectional area in the laboratory. Figure 5 presents horizontal displacements at failure in three vertical sections of a specimen perimeter with no end restraint and full end restraint calculated by Plaxis for specimens with $H/D = 2$.

3.3.1 Clay

The effect of end restraint on undrained shear strength of clay in unconfined compression tests is presented in Table 2.

The table shows that the effect is clear for soft clay, but decreases with increasing stiffness. For soft clay with $c = 10$ kPa the effect of end restraint on undrained shear strength is thus about 0.5 kPa, which can be regarded to be small.

The effect of end restraint in a triaxial test for clay was studied by modelling UC tests for soft clay with

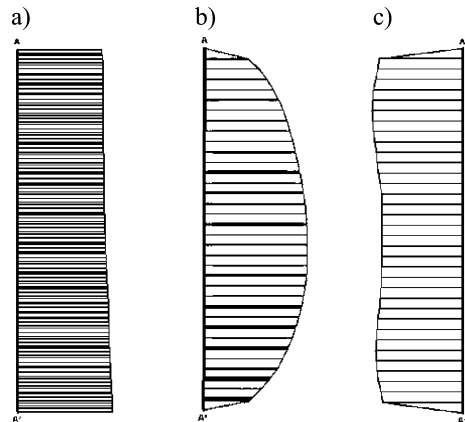


Figure 5. Horizontal displacements of a specimen perimeter at failure. (a) No end restraint, compression. (b) Full end restraint, compression. (c) Full end restraint, extension.

Table 2. Effect of end restraint on undrained shear strength s_u for different clays.

c^* kPa	E^* kPa	No restraint s_u kPa	Full restraint s_u kPa
10	0.5	9.5	10.0
20	1.0	19.4	19.6
40	2.0	39.6	39.6

* Given value.

Table 3. Results of triaxial tests for sand. Compression.

Cell pressure kPa	No restraint		Full restraint	
	σ_{1max} kPa	ϕ °	σ_{1max} kPa	ϕ °
50	190	35.2	189	35.1
100	377	35.3	376	35.1
200	753	35.5	748	35.2
400	1504	35.4	1495	35.2

Table 4. Results of triaxial tests for sand. Extension.

Vertical load σ_1 kPa	No restraint		Full restraint	
	σ_{3max} kPa	ϕ °	σ_{3max} kPa	ϕ °
50	193	35.6	181	34.1
100	382	35.6	356	33.9
200	758	35.5	707	33.9
400	1511	35.4	1413	33.9

cell pressures of 12.5–200 kPa. End restraint increased the axial load in failure only slightly and no clear correlation with the cell pressure was found.

3.3.2 Sand

The effect of end restraint in sand specimens were studied by modelling a drained triaxial test at the cell pressures of 50, 100, 200 and 400 kPa. The tests were modelled in compression and extension. The results of the compression tests are listed in Table 3. The friction angles were calculated from failure loads using Mohr-Coulomb's failure criterion.

As the results in Table 3 show, end restraint has practically no effect on the friction angles. Only a small decrease in the failure loads and accordingly in the friction angles can be found.

The corresponding results of the extension tests are presented in Table 4. The results show that end restraint clearly decreases the lateral pressure in failure. Correspondingly the angles of friction decreased by 1.7° as a maximum.

3.3.3 Till

The effect of end restraint for till corresponds to that for sand. Calculating the strength parameters c and ϕ based on Mohr-Coulomb's failure criterion for $\sigma_3 = 50$ kPa and 400 kPa gives the values presented in Table 5.

The results show that in the compression tests the effect of end restraint is very small, but in extension tests the effect is greater. In both tests the effect is the same: end restraint slightly increases cohesion, but decreases the friction angle.

Table 5. Results of triaxial test for till. Strength parameters in compression and extension. Given parameters: $c = 20$ kPa, $\phi = 35^\circ$.

Test type	No restraint		Full restraint	
	c kPa	ϕ °	c kPa	ϕ °
Compression	19.6	35.2	19.9	35.1
Extension	14.1	35.8	18.6	33.8

3.4 Effect of the membrane

In triaxial tests a rubber membrane is used around the specimen in order that a cell pressure by water can be applied. The membrane is normally made of thin flexible rubber in order to have as small influence on the test results as possible.

In their paper Duncan and Seed (1967) (see Chapter 1) do not give parameters for the rubber membrane, but in the present calculations the same parameters as measured by Kohonen (1987b) according to Head (1982) were used. They were: $E = 2000$ kPa and a thickness of 0.33 mm for 50 mm diameter specimens.

It is clear that the effect of the membrane in the simulations becomes apparent in the specimens with small Young's moduli. Therefore two soft clays and test types (end restraint included) were selected for this purpose:

- UC test, $c = 7$ kPa, $\phi = 20^\circ$, $E = 500$ kPa
- DC test, $c = 10$ kPa, $\phi = 20^\circ$, $E = 1000$ kPa

With this input data the Plaxis calculations resulted in a smaller effect than that in the analytical calculations carried out before. The rubber membrane increased the axial load in failure only by about 1–2 kPa independently of the cell pressure. It caused a small decrease in the friction angle and increase in cohesion. These changes were so small that they can be regarded to be insignificant, particularly because Plaxis could not define the failure load exactly as the membrane was included in the model. The analytical calculations had been performed with an assumption of cylindrical deformation, while in the Plaxis calculations also end restraint was present. This cannot, however, explain the difference in the results.

4 CONCLUSIONS

The influence of the specimen height/diameter ratio, end restraint and the rubber membrane on the unconfined compression test and triaxial test results were studied using Plaxis with a very fine element mesh. In general, the influence was smaller than in the

comparable experimental and analytical studies carried out before. The results can be summarized as follows:

- Unconfined compression strength of clay decreased with increasing H/D ratio. For the normal (H/D = 2) specimen it was 19,5 kPa, i.e. close to the given cohesion 20 kPa. The effect of end restraint was significant only for specimens with H/D \leq 1.
- Friction angle of sand in drained tests was independent of H/D ratio. The effect of end restraint was significant only for specimens with H/D \leq 1.5.

For normal (H/D = 2) specimens:

- End restraint increased undrained shear strength the more the softer the clay was. In triaxial UC tests for clay the effect of end restraint on the axial load in failure was small.
- End restraint had a negligible effect on the sand strength parameters in compression, only a small decrease in the friction angle was found. In extension tests the effect was clear. End restraint decreased the friction angle by 1.7° as a maximum.
- For till the effect of end restraint was negligible in compression, only a small increase in cohesion and decrease in the friction angle was found. In the extension tests the effect was considerable. Cohesion increased by 4.5 kPa and the friction angle decreased by 2°.
- The effect of the rubber membrane was tested only for soft clay. The membrane increased the axial load only slightly. This was far from results of the analytical studies carried out before.

REFERENCES

Airey, D.W. 1991. Finite element analyses of triaxial tests with different end and drainage conditions. *Proc. of 7th*

- Int. Conf. of Computer Methods and Advances in Geomechanics*. Beer, Booker & Carter (eds.), Vol. I: 225–230. Rotterdam: Balkema.
- Bishop, A.W. & Green, G.E. 1965. The influence of End Restraint on the compression strength of a cohesionless soil. *Geotechnique*. Vol. 15: 243–266.
- Duncan, J.M. & Dunlop, P. 1968. The significance of cap and base end restraint. *Journal of the Soil Mechanics and Foundation Division*, ASCE, Vol. 94, No. SM1: 271–290.
- Duncan, J.M. & Seed, H.B. 1967. Corrections for strength test data. *Journal of the Soil Mechanics and Foundation Division*, ASCE, Vol. 93, No. SM5: 121–137.
- Head, K.H. 1982. *Manual of Soil Laboratory Testing*. Volume 2: Permeability, Shear Strength and Compressibility Tests. London: Robert Harnold Ltd.
- Henkel, D.J. & Gilbert, G.C. 1952. Effect of the Rubber Membranes on the measured Triaxial Compression Strength of Clay Samples. *Geotechnique*, Vol. 3: 20–29.
- Kohonen, E. 1987a. *Koetekniikan vaikutus saven ja hiekan mekaanisiin parametreihin*. Diploma Thesis. Helsinki University of Technology. (in Finnish)
- Kohonen, E. 1987b. *Saven kolmiakselikooiden virhetarkastelu*. Special assignment. Helsinki University of Technology. (in Finnish)
- Lee, K.L., 1978. End restraint effects on undrained static triaxial strength of sand. *Journal of Geotechnical Engineering Division*, ASCE, No. 104: 687–703.
- Liyanapathirana, D.S., Carter, J.P. & Airey, D.W. 2005. Numerical Modeling of Nonhomogeneous Behavior of Structured Soils during Triaxial Tests. *International Journal of Geomechanics*, ASCE, March 2005: 10–23.
- Schanz, T. & Gussman, P. 1994. The influence of geometry and end restraint on the strength in triaxial compression in numerical simulations. *Proc. of the 3rd Eur. Conf. on Numerical Methods in Geotechnical Engineering, Manchester, 7–9 September 199: 129–133*. Rotterdam: Balkema.
- Sheng, D., Westerberg, B., Mattsson, H. & Axelsson, K. 1997. Effects of End Restraint and Strain Rate in Triaxial Tests. *Computers and Geotechnics*, Vol. 21, No. 3: 163–182.

Hydro-bio-mechanical modelling of landfilled waste: Decomposition, density and moisture retention

J.R. McDougall

Napier University, Edinburgh, Scotland, UK

ABSTRACT: The hydro-bio-mechanical model in question couples individual constitutive descriptions of hydraulic, biodegradation and mechanical phenomena into a single framework to provide a more fundamental treatment of the mechanical consequences of moisture-controlled decomposition. The aim is to explore the impact of decomposition (biodegradation) on unit weight profiles, phase composition and associated moisture retention during the filling of a landfill cell. It would appear that simply updating phase composition data in conjunction with invariant water retention parameters results in an overstatement of moisture retention and decomposition, particularly at low suctions. Rather, van Genuchten parameters controlling air entry and the rate of desorption must be related to changes in phase composition.

1 INTRODUCTION

Moisture (or leachate) retention in landfilled waste is a function of the interaction of hydraulic, biodegradation and mechanical phenomena. In rigid inert soils, moisture retention is dependent on suction in the liquid phase and pore structure, the latter being assumed fixed in both space and time. However, in landfilled waste, significant changes in pore structure/phase composition occur due to:

- Self weight filling – rearrangement of solid phase particles and reduction of void phase.
- Creep – rearrangement of solid phase particles and reduction of void phase under constant load
- Biodegradation – loss of solid phase and induced change in void phase volume.

In this paper, we explore the influence of self-weight, creep and biodegradation on the changing phase composition and leachate retention properties of landfilled waste. The analysis is performed using a hydro-bio-mechanical (HBM) model and considers the filling of a landfill cell with waste of a fixed initial moisture content.

2 CONCEPTUAL FRAMEWORK: HBM MODEL

The HBM framework is a three-part model developed specifically for the analysis of landfill settlement. It comprises coupled hydraulic, biodegradation and mechanical system modules. The algorithm passes

sequentially from module to module, through link routines, as shown in [Figure 1](#). System variables are used within link routines to update the conditions within which each module operates. In this way, a more representative condition at each stage of the simulation is obtained.

The model is implemented using the finite element method with each module sharing a common mesh. Finite elements enable various material property and operational features, such as waste heterogeneity, anisotropic hydraulic conductivity and simulation of the filling phase to be handled. Operation of the model, i.e. preparation of simulation input data and interrogation of output data, is done with a graphical user interface.

2.1 Hydraulic module

The hydraulic model is an unsaturated flow model that specifies the retention and flow properties of the waste using van Genuchten (1980) functions. Initial dry density and a simple solid phase classification system, in conjunction with phase specific gravities enable void volume and saturated moisture contents to be determined. Residual moisture contents are calculated as a function (gravimetric moisture content) of the solid mass.

Saturated moisture contents are continually updated for changes in void volume; residual volumetric moisture contents are updated for changes in solid mass. Absorptive capacity and associated discharge or retention throughout the cell are then automatically determined.

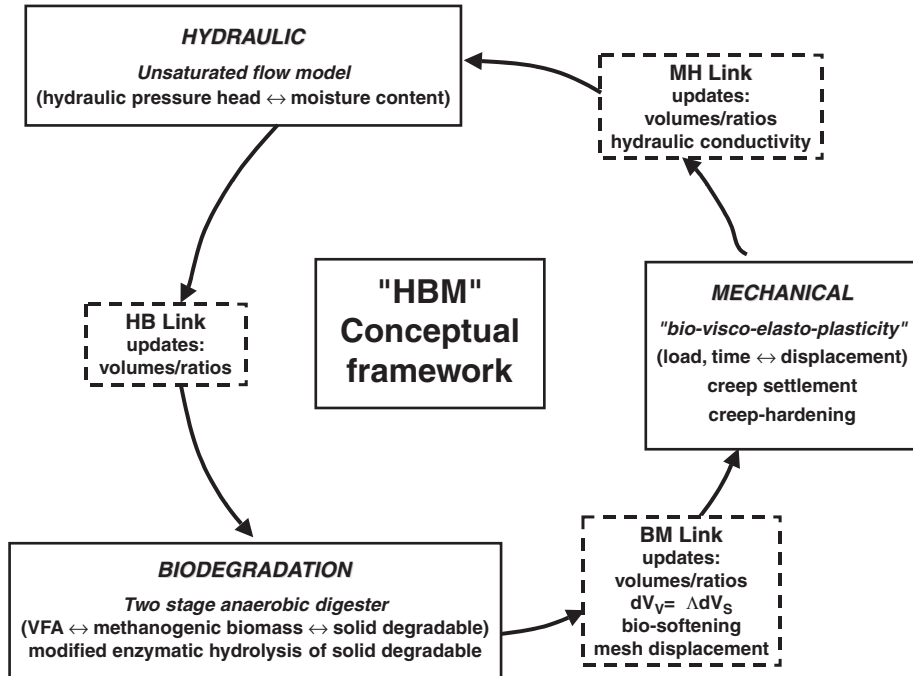


Figure 1. Schematic diagram showing HBM model components and link routines, together with their form and function.

2.2 Biodegradation module

The biodegradation model is a simple two-stage anaerobic digestion model in which indicative volatile fatty acid and methanogenic biomass concentrations control the mineralisation of organic matter. Spatial and temporal distributions of all field variables and related properties are available. Some key modifications have been made to reflect more realistically the enzymatic hydrolysis of solid organic matter including sensitivity to moisture content, product inhibition and the changing digestibility of the decomposable fraction. These modifications are described in detail in McDougall & Pyrah (2001). A number of natural phenomena and operational treatments can then be simulated, e.g. souring due to acid accumulation, addition of methanogenic inoculum, clean water flushing or leachate recirculation.

2.3 Mechanical model

The mechanical model combines identifiable load-, creep- and biodegradation-induced effects to analyse and predict landfill settlement. It is the distinction between time-dependent creep and rate-limited biodegradation effects that differentiates the HBM model from earlier landfill settlement models.

Load-induced settlement is treated as an elastoplastic process with volumetric hardening. Creep strain is

also an elastoplastic process using an equivalent time method (Yin & Graham, 1993), which also gives rise to volumetric hardening.

Biodegradation-induced effects are not treated as a simple time-dependent process but rate-limited. This means decomposition is constrained by a maximum rate but under the influence of acid accumulation or moisture/nutrient addition may slow down, accelerate, or stop completely.

A key component of this more fundamental analysis of landfill settlement is the interpretation of the mechanical consequences of decomposition, i.e. the impact of solid phase loss on void phase. Here a constitutive relation between two volumetric state variables, the void phase volume (V_V) and solid phase volume (V_S), accounts for the impact of decomposition on the mechanical state. This relation is given by,

$$dV_V = \Lambda dV_S \quad (1)$$

where Λ is a decomposition-induced void change parameter. A range of responses, summarised in Figure 2, can be accommodated from which it can be deduced that either hardening or softening (more likely) with decomposition can result. For example, when $\Lambda = -1$, loss of solids results in a direct and equal increase in void volume, i.e. there is no change in overall volume although the solid skeleton is likely

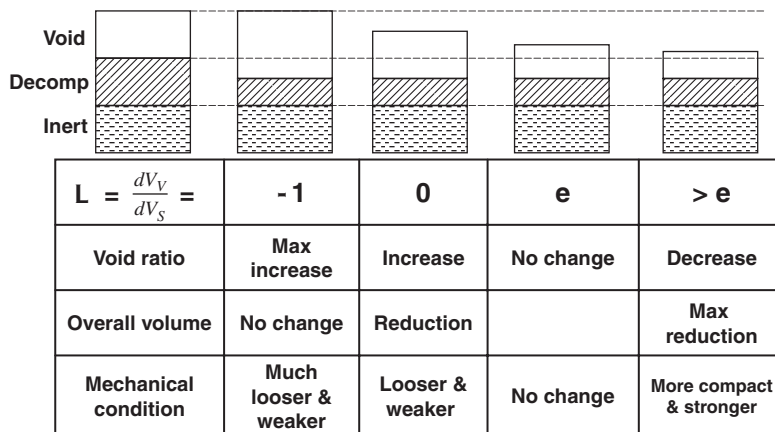


Figure 2. Reference values for decomposition induced void change parameter Λ and associated volumetric and mechanical conditions.

to be much weaker. At the other extreme, where $\Lambda > e$, loss of solid matter leads to a more compact particle rearrangement. In this case significant settlement would occur since both solid and void phase volumes reduce. A full derivation and explanation of Λ can be found in McDougall & Pyrah (2004).

3 SIMULATION OF CELL FILLING

3.1 Problem description, initial conditions & material properties

The simulations explore the relationship between phase composition, moisture and biodegradation during the filling of a landfill cell with waste of fixed initial volumetric moisture content (0.257). The problem is idealised as a vertical columnar section comprising forty elements of 0.5 m high. Each element is disclosed according to a set filling rate, in this case a rising fill rate of 0.02 m per day. The disclosure of each element causes an immediate elasto-plastic compression of underlying waste. On disclosure mechanical creep and decomposition are initiated. The base of the column is treated as a sump, which means any moisture accumulating in the form of a positive leachate head at the base of the column is removed from the system.

The simulations require a number of hydraulic, biodegradation and mechanical parameters and their initial conditions, a summary of which is given in Table 1 together with adopted values. Of particular importance is the decomposition-induced void change parameter, Λ . Fuller explanations of other parameters and their default values can be found in McDougall & Pyrah (2001) and McDougall & Philp (2001).

Table 1. Simulation input parameters and values.

Input parameter	Dimensions	Values
<i>Hydraulic</i>		
van Genuchten α		1.4
van Genuchten n		1.6
Residual m.c. (w/w)		0.25
Sat'd hydr. conductivity.	$m.s^{-1}$	5×10^{-5}
Ratio: v to h cond.		1
<i>Biodegradation</i>		
Max hydrolysis rate	$g.m^{-3}(aq).d^{-1}$	2000
Product inhibition	$m^3.g^{-1}$	2×10^{-4}
Digestibility		0.7
Half rate	$g.m^{-3}$	4000
Methanogen growth	day^{-1}	0.018
Methanogen death	day^{-1}	0.002
Yield coefficient		0.08
Diffusion coefficient	$m^2.day^{-1}$	0.05
Init. degradable fraction.		0.4
Initial VFA concentration.	$g.m^{-3}$	300
Init. methanogen. biomass	$g.m^{-3}$	250
<i>Mechanical</i>		
Elastic stiffness		0.10
Elastoplastic stiffness		0.38
Poisson's ratio		0.4
Initial yield stress	kPa	20
Creep viscosity		0.0015
Decomp-induced void chg		-0.6
Decomposition hardening	kPa	2
Dry unit wt (as-placed)	$kN.m^{-3}$	5
Inert phase particle wt.	$kN.m^{-3}$	17
Degrad. phase particle wt.	$kN.m^{-3}$	7.3

3.2 Simulation 1: Overburden and creep effects only

Simulation 1 is run with biodegradation effects switched off in order to identify load and creep effects.

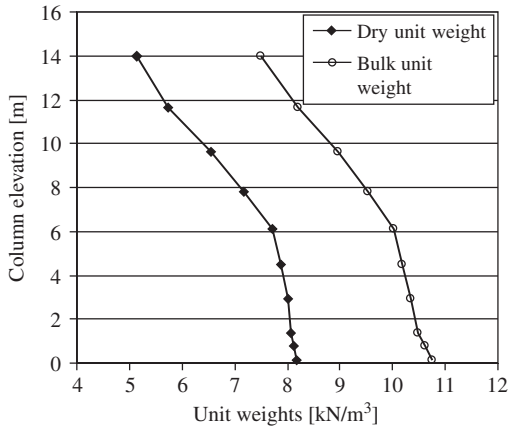


Figure 3. Simulation 1: load and creep only. Bulk and dry unit weights at 800 days.

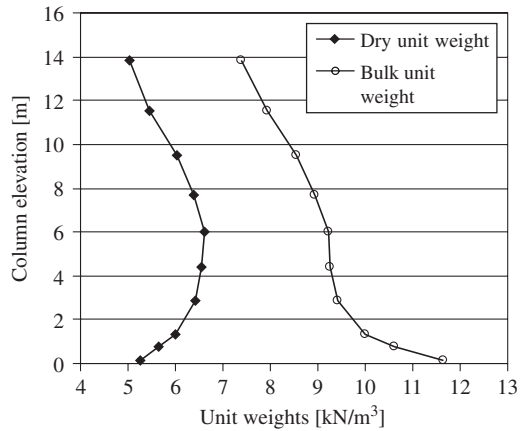


Figure 5. Simulation 2: load, creep and biodegradation. Bulk and dry unit weights at 800 days.

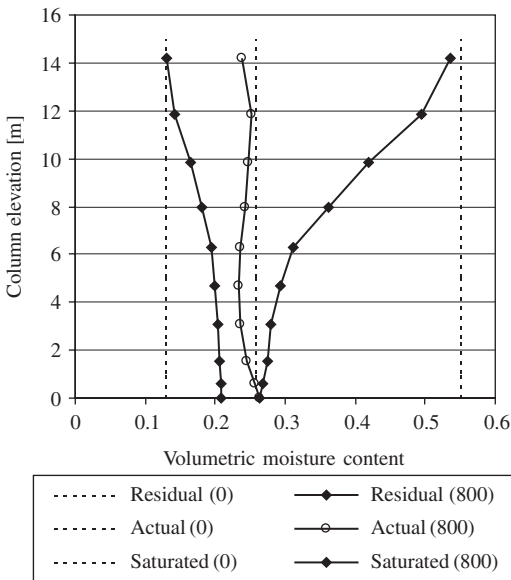


Figure 4. Residual (left), actual (middle) and saturated moisture profiles at 800 days.

Figure 3 shows dry and bulk unit weight profiles for the waste column after filling (800 days). Although the initial (as-placed) unit weight of 5 kN/m^3 is evident in the uppermost element, the effect of overburden compression and stress-dependent stiffness can clearly be seen in the column.

Figure 4 shows the residual, actual and saturated volumetric moisture contents, together with the as-placed conditions (broken lines). In accordance

with the unit weight profiles, there is a marked reduction in porosity and hence in saturated moisture content towards the base of the column. Moreover, the actual moisture content profile differs from that expected in the rigid soil case. There is no monotonic reduction in moisture with elevation, indeed the small increase occurring between 6 m and 12 m cannot be captured by a simple moisture retention curve function. Nevertheless, the profile is consistent with the indicated phase composition on which the van Genuchten moisture retention function is based.

3.3 Simulation 2: Overburden, creep and biodegradation

With biodegradation effects switched on, the bulk and dry unit weights shown in Figure 5 are seen to differ significantly from the previous simulation. Further signs of the changes in phase composition can be gained from the residual, actual and saturated moisture contents shown Figure 6.

Solid matter has clearly been removed and led to void enlargement throughout the system. This is to be expected where the decomposition-induced void change parameter, Λ is equal to -0.6 , thereby forcing a loosening or opening up of the waste skeleton. Note, however, that the degree of decomposition is greater at lower elevations. This is in part due to the fact that the lower waste is older and therefore has had longer to degrade. It is also due to the apparent increase in moisture content at lower elevations but care needs to be exercised in the interpretation of this phenomena. The increase in moisture may be consistent with a van Genuchten moisture retention function and the predicted phase compositions but it is unlikely to be the case in reality. Indeed, we would expect a more skeletal

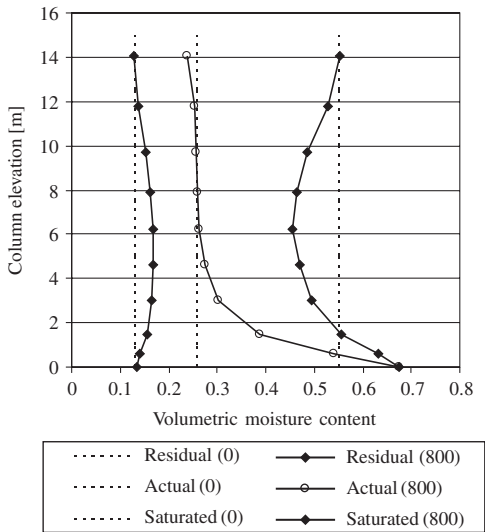


Figure 6. Residual (left), actual (middle) and saturated moisture profiles at 800 days.

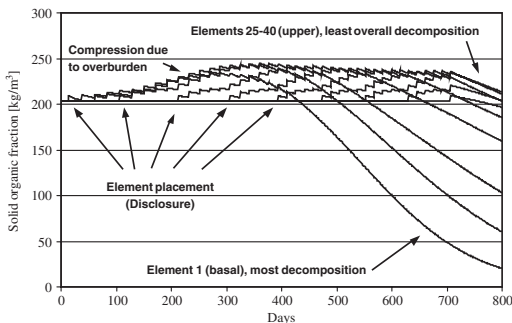


Figure 7. Solid organic fraction per unit total volume [kg/m^3] for selected elements over time.

waste structure, lacking in organic matter, to have a lower moisture holding capacity. It is therefore necessary to review the use of invariant van Genuchten retention parameters α & n and consider a dependence upon decomposition and the evolving phase composition.

The influence of biodegradation is restated in the solid organic depletion curves for the selection of elements shown in Fig. 7, where element 1 is at the base of the column and element 40 is at upper surface. Figure 7 also reveals the disclosure of each element during the filling phase. The effect of overburden loading on each element is evident from an increase in organic matter per unit volume. At the same time decomposition commences. Depletion curves confirm that decomposition is greatest, i.e. fastest (due to higher

moisture contents) and most advanced (due to early disclosure), in the basal elements.

4 CONCLUSIONS

The extent to which the foregoing simulations depict real behaviour in landfilled waste is uncertain. In the case of leachate retention, field data relating to crude waste is complicated by the existence of preferential drainage paths. However, in the future, a more homogeneous waste due to mechanical and biological treatment will generate better conditions for the type of numerical analysis of leachate hydraulics presented here. What has been demonstrated here is the synthesis of recognised hydraulic, biodegradation and mechanical phenomena within a constitutive framework. The simulations probe the changes in unit weight and phase composition due to filling in a highly compressible and degradable material. The indicated increase in moisture content at low suctions is not consistent with a more skeletal solid structure, hence it would appear that updated phase composition data in conjunction with invariant van Genuchten retention curve parameters cannot interpret correctly moisture retention in a decomposing soil and that some form of dependency on the evolving phase composition is required.

ACKNOWLEDGEMENTS

The work described herein has in part been made possible by Scottish and Northern Ireland Forum For Environmental Research (SNIFFER), under Research Contract UKW05.

REFERENCES

- McDougall, J.R. & Philp, J.C. (2001) Parametric study of landfill biodegradation modelling: methanogenesis and initial conditions. Sardinia 2001, 8th Intl Waste Man. & Landfill Symp, S.Margherita di Pula, eds. Christensen, Cossu & Stegmann, CISA Cagliari, Vol. 1, pp 79–88.
- McDougall, J.R. & Pyrah, I.C. (2001) Modelling biodegradation in landfill: a parametric study of enzymatic hydrolysis. 3rd B.G.A. Geoenvironmental Engineering Conference, Edinburgh, 2001, eds Thomas & Yong, Thos Telford.
- McDougall, J.R. & Pyrah, I.C. (2004). Phase relations for decomposable soils. *Geotechnique*, Vol. 54, No 7, pp 487–494.
- van Genuchten, M.T. (1980) A closed form equation for predicting the hydraulic conductivity of unsaturated soils. *Soil Science Society of America Journal*, Vol. 44, pp 892–898.
- Yin, J.H. & Graham, J. (1989) Viscous-elastic-plastic modelling of one-dimensional time-dependent behaviour of clays. *Canadian Geot. J.*, Vol. 25, pp. 199–209.

Dynamic problems

3-D FEM-BEM method for analysing the transmission vibrations of soil to a pile foundation

S. Messast

Departement of Civil Engineering, laboratory LARMACS, University of Skikda, Algeria

A. Boumekik

Departement of Civil Engineering, University of Constantine, Algeria

M. Mansouri

Departement of Civil Engineering, University of Setif, Algeria

ABSTRACT: In this communication a combined method Finite Elements Method – Boundary Elements Method is presented, which makes it possible to determine the displacements of a pile due to a harmonic load applied on the free surface of the adjacent soil. This method is based on the technique of decomposition of the soil-pile system used by Rajapakse that permits to separate the impact of soil and the pile on the response of the system, while imposing the condition of compatibility of the displacements at the end. The pile is discretized in beam's elements, its matrix of rigidity gets can be obtained by the superposition of the matrix characterizing the rigidity of the fictional pile and the one representing the contribution of the soil in the response of the system. This last and the matrix of flexibility of the adjacent soil are given by using the technique of the Boundary Elements combined with the thin layers method.

1 INTRODUCTION

Piles are frequently adopted as foundations for important structures, such as high buildings, nuclear power plants, bridges, offshore structures or machine foundations, etc. The study of dynamic response of these foundations, constitutes a very important element in their conception and in the security of structures they support. During the last decades, dynamic response of piles was the topic of several investigations. Although considerable efforts have been conducted to develop adequate analytical methods, conceptual and computational difficulties still remain essentially due to the three-dimensional nature and semi infinity of soil, as well as the embedding of the pile foundation.

Many researchers proposed approximate solutions using the concept of Winkler foundation, which consists in replacing soil around the pile by a set of springs and dashpots, where spring constants are obtained from analytical considerations or from experimental data. Such analysis have been proposed by (Pen-zien et al. 1964, Matlock 1979 & Novak 1974, 1978) and others.

Finite Elements method was also used widely to evaluate pile response (Kuhlmeyer 1979, Krishnanand et al. 1983 & Guoxi Wu et al. 1997). The advantage of

Finite Elements method resides in its easy adaptation to problems of complex geometry and strong heterogeneities, but to take in account the infinite nature of soil, appropriate boundaries may be used to eliminate waves reflections toward the inside of the model.

More lately a formulation in Boundary Elements has been used by (Kynia et Kausel 1982, Sen et al. 1985 & Mandoça et al. 2000), who obtained solutions in displacements of a ring of loads inside a multilayered soil. This method is better adapted to problems of dynamic soil-structure interaction because it is based on analytical solutions satisfying the conditions of radiation at the infinity. However it is hardly adaptable to the non-linear, strong heterogeneities and complex geometry problems.

Rajapakse et al. (1989) proposed a different modeling that consists to the decomposition of the soil-pile system into continuous soil without excavation and a fictional pile for which Young modulus and mass density result from the differences between those of the real pile and those of soil.

An alternative approach has been developed which consists in the combination of the last two methods in order to be able to take profit of their advantages and to eliminate their individual inconveniences

(Messast et al. 2005, Mendonça et al. 2003, Matos Filho et al. 2005, Sami Benjama et al. 2000, Mansouri 1998 & Caro et al. 2005).

In this article, a combined formulation Finite Elements-Boundary Elements is presented to analyze the soil-pile interaction under different dynamic load combinations (harmonic vibrations). In this formulation, the principle of decomposition of Rajapakse (1988) is used. The system can be decomposed into two fictional elements, a fictional pile that will be modeled by Finite Elements Method as one-dimensional element discretized in beam elements. The soil is modeled by the Boundary Elements Method (BEM) combined with Thin Layers Method as an elastic, continuous, linear, isotropic and homogeneous medium. The flexibility matrix of soil is formulated according to the formalism proposed by Kausal (1982). The conditions of compatibility are imposed any where in the volume of the soil (beam of soil) relative to the pile.

2 ANALYSIS METHOD

Figure 1 represents a pile foundation embedded in a viscoelastic soil and subjected to vertically load. The total system is composed of two different mediums: pile

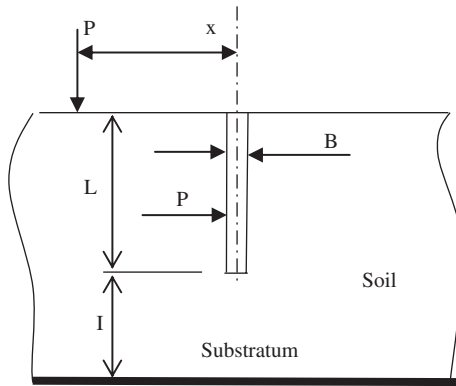


Figure 1. Pile-soil system.

and soil. The pile is considered as a one-dimensional element of length L and square section of side B with $L \gg B$. Pile's material is considered linear elastic characterized by Young modulus E_p , density ρ_p , and Poisson's ratio ν_p . The pile is embedded in a homogeneous viscoelastic soil limited in depth by a deep enough substratum in such a way that the soil well be considered as a semi infinite medium. The soil is modeled as an ideal continuous medium characterized by density ρ_s , Poisson ratio ν_s , shear modulus $G_s = E_s / 2(1 + \nu_s)$, and damping ratio β . To take into account the effect of material damping, shear modulus of soil is replaced by its complex modulus $G = G_0 e^{i\omega t}$. The harmonic load will be also expressed in complex form ($P = P_0 e^{i\omega t}$) with $i = \sqrt{-1}$ and ω is the vibration frequency. In the follows the factor $e^{i\omega t}$ will be omitted in order to simplify the writings.

The equilibrium equation of the pile can be expressed in general form as:

$$\{U\} = [F]\{p_s\} \quad (1)$$

Where U is the displacement vector of the pile, F is the flexibility matrix of the pile which take account the contribution of soil in the response of pile, and P is the exterior load vector applied at distance x from the pile.

In the first hand, we start by determining the response of a single pile under direct load applied to it. The total system soil-pile can be decomposed into two fictional mediums (Figure 2), where the total response can be expressed as the superposition of their responses. The first represents soil equivalent to the pile, it is modeled as a beam of soil. The second is a fictional pile for which $E = E_p - E_s$ and $\rho = \rho_p - \rho_s$. Each of the fictional elements equilibrates a fictional load, which represents a part of the applied outside load.

3 EQUILIBRIUM EQUATION OF SOIL BEAM

The soil-beam is divided in the vertical direction into N sections (interfaces), what corresponds to the same discretization of a beam by Finite Elements Method.

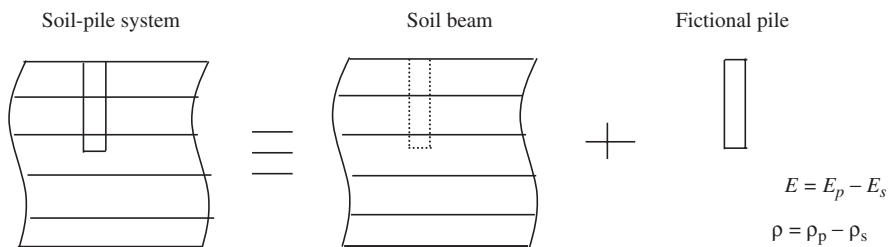


Figure 2. Decomposition of the system soil-pile.

Every interface is discretized into N_s square boundary elements that will be replaced thereafter by equivalent disks. Therefore the total number of the elements of the model is: $N_t = N_s \cdot N$. In the following U_i and P_i designate respectively displacements and loads vectors at interfaces nodes, while u_i and p_i refer respectively to displacements and loads vectors at disks nodes constituting the soil-beam.

The equilibrium equation of soil-beam can be written as:

$$u_i = F_i \cdot p_i \quad (2)$$

F_i refer to the flexibility matrix of soil.

Obtaining the flexibility matrix of soil implies the determination of soil's response. The soil is divided in the vertical direction into underlayers of thickness $h_i \leq \lambda_i/4$ (Sen et al., 1985), where λ_i is the length of shear wave of the underlayer i (Fig. 4), which permits to obtain an algebraic form of the problem, with considering the variation of displacement as a linear function of the displacements at the interfaces of the underlayer. To this effect, the massif of soil will be divided into N interfaces and every interface will be discretized into square elements which can be replaced by disks, of equivalent surfaces, for which the calculation of Green's functions is less laborious (Mansouri 1989, Kausel 1982).

Developing Loads and displacements in Fourier series according to the angular coordinate, leads to express the behavior of the soil massif by a system of three equations of partial derivatives, depending on the order of development in Fourier series (μ). Using variables separation technique the solutions of this system of equations can be written in term of Bessel functions, what leads to a system of three ordinary differential equations which are dependent of development order and wavenumber in which two coupled and one independent.

This last formulation shows that the problem will be governed by two equations coupled characterizing the movement in the vertical plan (wave of Rayleigh), and an equation uncoupled characterizing the perpendicular displacement on a vertical level (wave of Love).

The total stiffness matrix of soil massif can be obtained by assembly those of underlayers which are detailed by Kausel and Peek (1982). As the cited stiffness matrix is quadratic in wavenumber, theoretically exist $6N$ eigenvalues and $6N$ eigenvectors, but physically there are only $3N$ solutions, because the other $3N$ modes of vibration correspond to vibrations that their amplitudes decrease when going from the infinity toward the origin. As the loads are expressed in the spaces domain and Green's functions in the wavenumber domain, loads can be express in the wave number domain through Hankel transform, and displacements can be calculated in the same domain. Using the inverse

of the Hankel transform, displacements can be obtained in the spaces – frequency domain.

The rigid body condition imposed anywhere to the soil beam may be expressed as (figure 3):

$$U_d^i = R_d^i U_s^n \quad \text{where: } R_d^i = \begin{bmatrix} 1 & 0 & 0 \\ 0 & 1 & -x_i \end{bmatrix} \quad (3)$$

$U_s^n = \{U \ W \ \Phi_y\}^t$ where U , W and Φ_y are the three degrees of freedom of sections of the soil beam.

$U_d^i = \{u \ w\}^t$ where u and w are the two degrees of freedom of a disk.

After assembling of matrices, it can be written that:

$$u_t = R U_1 \quad \text{and} \quad P_1 = R^t p_t \quad (4)$$

The total equilibrium equation for the soil beam can be written as:

$$u_t = F_t p_t \quad (5)$$

From equations (4) and (5) it can be written:

$$R^t F_t^{-1} R U_1 = P_1 \quad (6)$$

If: $K_1 = F_t^{-1} R^t R$ equation (6) becomes:

$$K_1 U_1 = P_1 \quad (7)$$

4 EQUATION OF FICTIONAL PILE

The fictional pile is modeled by Finite Elements Method and divided into elements beam which have the same number of underlayers., its vibrations are considered to be in a vertical plan. The movement equation of the fictitious pile can be expressed as:

$$K_2 U_2 - \omega^2 M_2 U_2 = P_2 \quad (8)$$

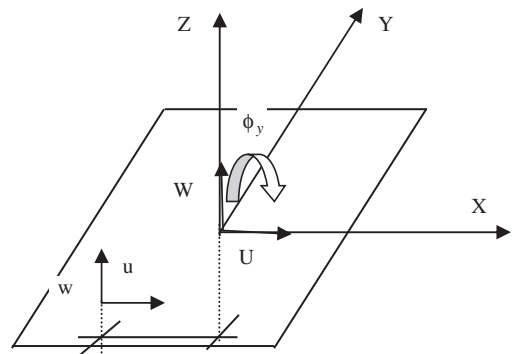


Figure 3. Rigid body displacements.

Where K_2 and M_2 are respectively the stiffness and masses matrix of the fictional pile, obtained using standard procedures of the structural analysis. P_2 is the part of the external load supported by the fictional pile. U_2 is the displacement of the fictional pile and ω is the circular frequency.

5 COUPLING OF FEM-BEM METHODS

The coupling of the FEM and BEM methods can be achieved through imposing the compatibility condition between the soil beam and the fictional pile. This condition can be expressed as:

$$U=U_1=U_2 \text{ and } P=P_1+P_2 \quad (9)$$

Let's pose $M = M_2$ and $K = K_1 + K_2$ where K is the stiffness matrix of the real pile.

From equations (7) and (8) it can be written:

$$(K-\omega^2 M)U=P \quad (10)$$

Where P and U are respectively external load vector and displacement vector of pile.

If $K_{tot} = K - \omega^2 M \Rightarrow K_{tot}U = P$, the displacement vector can be given by the following equation:

$$U=K_{tot}^{-1}P \quad (11)$$

The load under which the pile response will be calculated, results from the transmission of the effect from the soil to the pile. This task will be achieved by calculate the component of the exterior load which will be applied to the pile.

The interaction in terms of reaction of disks can be expressed as $F_{sp}P$ with F_{sp} is the flexibility matrix of interaction between the soil and the pile. The disk's reactions will be transformed to the section's reaction through the condition of rigid body deformation. From equation (4) it can be written:

$$P = R^T F^{-1} F_{sp} P_s \quad (12)$$

From equations (11) and (12) the pile's displacements can be expressed as:

$$U = K_{tot}^{-1} P = K_{tot}^{-1} R^T F^{-1} F_{sp} P_s \quad (13)$$

$$\text{In which } F = K_{tot}^{-1} R^T F^{-1} F_{sp}$$

6 NUMERICAL RESULTS

To permit the comparison between this study in which the pile have a square shape and others works cited in the literature with circular piles, it is necessary to

establish the dimensional equivalence between those two shapes. The side of a square cross section equivalent to the radius of a circle, is given by the following express [19,23].

$$\text{For translator modes: } B = (\sqrt{\pi})r_0$$

$$\text{For rocking modes: } B = (\sqrt[3]{3\pi})r_0$$

Where r_0 refer to the radius of the circular pile, and B the side of square cross section.

The correspondent non dimensional parameters are:

Non dimensional frequency: $a = \omega r_0 / c_s$.

Relative length: $l_r = L / r_0$

The others parameters remain unaltered.

Relative stiffness: $e_r = E_p / E_s$, relative mass:

$m_r = \rho_s / \rho_s$, relative depth: $h_r = D / B$.

Let's define respectively the vertical and the horizontal discretization ratio as: $n_s = h_i / B$ and $n_d = 2r / B$, where h_i refers to the thickness of an underlayer i and r is the radius of equivalent disks. The optimal discretization ratios can be given by the following express (Mansouri 1989):

Horizontal modes: $n_s = 1.5$, $n_d = 0.5$

Vertical modes: $n_s = 1.5$, $n_d = 0.333$

Table 1 present a comparison of the vertical impedance normalized by its static correspondent given by the present approach with those given by (Rajapakse et al. 1989 & Kuhlmeier 1979), for no dimensional frequencies $a = 0.1, 0.2, 0.3$, with $a = \omega B / c_s$, where ω is the circular frequency of the excitation, c_s is the propagation speed of the shearing waves in soil.

Table 1 shows a good agreement between the present method and those given in literature

For the coupled mode of translation and rocking, the results will be compared to those given by (Kuhlmeier 1979, Rajapakse and al 12 & Novak 1974). The comparison will be in terms of compliance functions normalized by those equivalent static compliance. The compliance function C_{ij} is the inverse of the impedance, it represents the harmonic displacement resulting in the i direction under the effect of a unit harmonic load applied in the j direction. Tables 2, 3 and 4 shows that

Table 1. Comparison of the vertical impedance normalized by its static correspondent.

	$\frac{E_p}{E_s}=100, \frac{\rho_p}{\rho_s}=1, \frac{L}{B}=30, \nu_s=0.25, \beta=0.0$					
	Real part			Imaginary part		
a	0.1	0.2	0.3	0.1	0.2	0.3
Present method	1.11	1.22	1.25	0.41	0.61	0.81
Rajapakse	1.13	1.26	1.36	0.51	0.59	0.8
Kuhlmeier	1.07	1.19	1.15	0.41	0.58	0.81

Table 2. Comparison of the normalized horizontal compliances $l_r = 35$, $m_r = 1.43$, $\nu_s = 0.4$, $e_r = 567$, $\beta = 0.0$.

Frequency	a = 0.1		a = 0.2		a = 0.3	
	Re(\bar{C}_{xx})	Im(\bar{C}_{xx})	Re(\bar{C}_{xx})	Im(\bar{C}_{xx})	Re(\bar{C}_{xx})	Im(\bar{C}_{xx})
Present method	1.00	-0.15	0.97	-0.34	0.87	-0.51
Rajapakse & Shah	1.00	-0.15	0.96	-0.33	0.82	-0.45
Kuhlmeyer	1.02	-0.16	0.90	-0.38	0.84	-0.50
Novak	-	-	-	-	0.86	-0.59

Table 3. Comparison of the normalised coupled compliances. $l_r = 35$, $m_r = 1.43$, $\nu_s = 0.4$, $e_r = 567$, $\beta = 0.0$.

Frequency	a = 0.1		a = 0.2		a = 0.3	
	Re($\bar{C}_{\varphi\varphi}$)	Im($\bar{C}_{\varphi\varphi}$)	Re($\bar{C}_{\varphi\varphi}$)	Im($\bar{C}_{\varphi\varphi}$)	Re($\bar{C}_{\varphi\varphi}$)	Im($\bar{C}_{\varphi\varphi}$)
Present method	1.04	-0.03	1.11	-0.15	1.11	-0.31
Rajapakse & Shah	1.04	-0.02	1.13	-0.15	1.07	-0.28
Kuhlmeyer	1.00	-0.03	1.02	-0.15	1.03	-0.30
Novak	-	-	-	-	1.15	-0.50

Table 4. Comparison of the normalised compliances of rocking $l_r = 35$, $m_r = 1.43$, $\nu_s = 0.4$, $e_r = 567$, $\beta = 0.0$.

Frequency	a = 0.1		a = 0.2		a = 0.3	
	Re($\bar{C}_{\varphi\varphi}$)	Im($\bar{C}_{\varphi\varphi}$)	Re($\bar{C}_{\varphi\varphi}$)	Im($\bar{C}_{\varphi\varphi}$)	Re($\bar{C}_{\varphi\varphi}$)	Im($\bar{C}_{\varphi\varphi}$)
Present method	1.00	-0.15	0.97	-0.34	0.87	-0.51
Rajapakse & Shah	1.00	-0.15	0.96	-0.33	0.82	-0.45
Kuhlmeyer	1.02	-0.16	0.90	-0.38	0.84	-0.50
Novak	-	-	-	-	0.86	-0.59

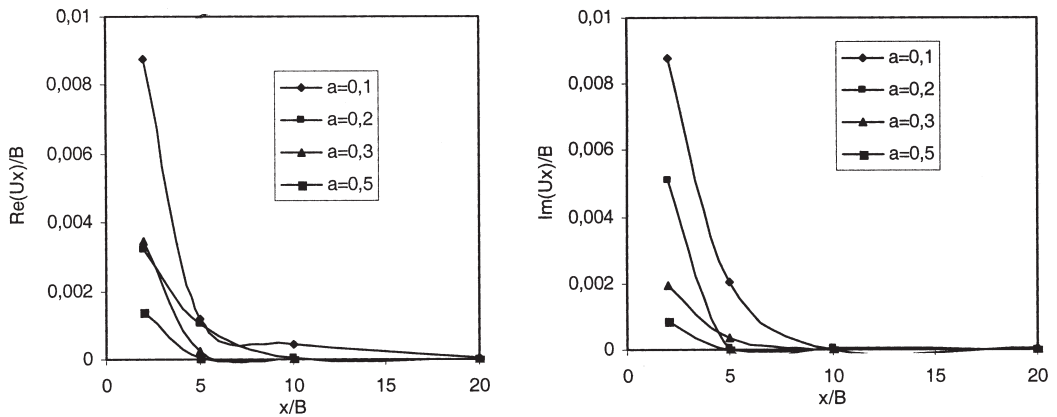


Figure 4. The relative horizontal displacement of the head of the pile versus the relative distance of the load.

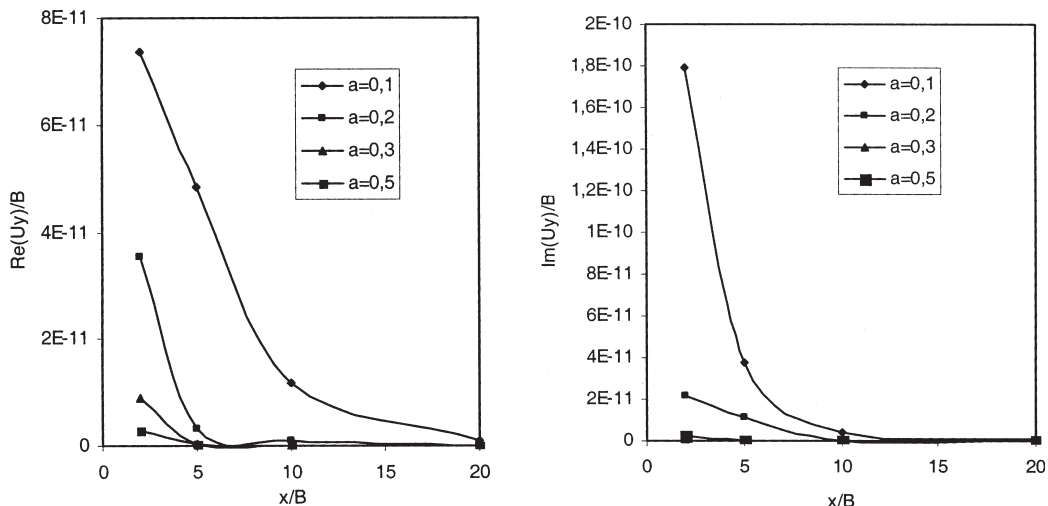


Figure 5. The relative vertical displacement of the head of the pile versus the relative distance of the load.

the results obtained with this method are in a good agreement with those cited in literature.

The presented method has been applied to determine the response of a single square pile embedded in a homogenous viscoelastic soil. The vertical exterior harmonic load is applied at the free surface of soil at x distance from the pile.

The problem will be treated with non dimensioned parameters than:

$$E_p/E_s = 1000, L/B = 20, \nu_s = 0,3, \beta = 0,05$$

Different vertical harmonic vibrations have been applied $a = 0.1, 0.2, 0.3$ and 0.5 at the relative distances $x/B = 2, 5, 10, 20$.

Horizontal and vertical relative displacements versus relative distances for different frequencies are represented in the Figures 4 and 5.

The amplitude of the horizontal displacement of the head of the pile is more important than the vertical displacement. We can also remark that the perturbation resulting in the head of the pile is more significant in the case of the small frequencies.

The amplitudes of the displacements are inverse proportionally to the distance between the pile and the loaded point.

7 CONCLUSION

In this article, a method combined FEM-BEM has been presented for the numerical analysis of pile-soil interaction. This approach permits to take in account

the infinite aspect of the soil massif and therefore to avoid the limitation of the geometric model that would impose to choose adequate boundaries to the limits of the model, and would not exclude any parasitic reflections. The pile-soil system is decomposed in two fictional mediums. A soil beam representing soil equivalent to the pile, and a fictional pile whose mechanical features result from the difference between those of the real pile and those of soil. The flexibility matrix of soil is determined according to the formalism presented in the work of E. Kausel (1982). The pile is modeled by one-dimensional elements in elements beams. The response of the real pile is given after coupling of the equilibrium equations of the fictional pile and the soil beam.

Several cases of the numerical simulations have been included, which confirm, by the agreement of results with those expected, the formulation and treatment proposed in this work are adequate for these types of problem.

This method has been used to obtain the response of single pile under the effect of transmitting of vibrations from a loaded at a distance (x) from the pile. It can be concluded that the small frequencies applied very near to the pile lead to a strong effect at the pile.

REFERENCES

- Boumekik Ahmed, 1985. Fonctions impédances d'une fondation vibrante en surface ou partiellement encastree dans un sol multicouche, Thèse de doctorat en sciences appliquées, Université Libre de Bruxelles, Belgique.

- Cairo R, Conte E, Dente G. 2005. Analysis of pile groups under vertical harmonic vibration, *Computers and geotechnics*, 32:545–554.
- Kausel E. and Peek R. 1982. Dynamic loads in the interior of a layered stratum: an explicit solution, *Bulletin of the Seismological Society of America*, 72, 5:1459–1480.
- Kausel, E. and Roesset, J. M. 1981. Stiffness matrices for layered soils, *Bulletin of the Seismological Society of America*, 71(6):1743–1761.
- Kaynia A. M. Kausel E. 1982. Dynamic behavior of pile groups, 2nd Int conf on num methods in offshore pilling. Austin, TX.
- Krishnan R, Gazetas G, Velez A. 1983. Static and dynamic lateral deflexion of piles in non-homogenous soil stratum, *Geotechnique*, 33(3):307–326.
- Kuhlmeyer R. L. 1979. Static and dynamic laterally loaded floating piles. *J Geotech Eng Division ASCE* 105(GT2):289–304.
- Kulhmayr R. L. 1979. Vertical vibration of piles, *Journal of the Geotechnical Engineering Division. ASCE*, Vol.105, N° GT2, Proc., Paper 14394, p. 273–287.
- Penzien J, Scheffley C. F, Parmelee F. A. 1964. Seismic analysis of bridges on long piles. *J. Eng Mech Division ASCE*; EM3:961–973.
- Matlock H, Foo S. H. C. 1979. Axial analysis of piles using hysteretic and degrading soil model. Proc. In: Symposium on numerical methods in offshore piling. London.
- Novak M. 1974. Dynamic stiffness and damping of piles. *Canadian Geotechnical Journal*, 11:574–278.
- Novak M, Abbou-Ella F. 1978. Impedance functions of piles in layered media. *J Eng Mech division ASCE*, 104, (EM1). Proc Paper 13847, p. 643–661.
- Guoxi Wu, W. D. Liam Finn W. D. 1997. Dynamic elastic analysis of pile foundations using finite element method in the frequency domain, *Canadian Geotechnical Journal*, 34:34–43.
- Mansouri M, 1999. Calcul des fonctions impédances d'un pieu dans un sol Multicouche par une méthode combinée Eléments Finis – Eléments Frontières, Thèse de Magistère, Université de Annaba, Algérie.
- Matos Filho R, Mendoça A. V, Paiva J. B. 2005. Static boundary element analysis of piles submitted to horizontal and vertical loads, *Engineering Analysis with Boundary Elements*, 29:195–203.
- Mendoça A. V, Paiva J. B. 2000. A boundary element method for static analysis of raft foundation on piles, *Engineering Analysis with Boundary Elements*, 24: 237–247.
- Mendoça A. V, Paiva J. B. 2003. An elastostatic FEM/BEM analysis of vertically loaded raft and piled raft fondation, *Engineering Analysis with Boundary Elements*, 27:919–933.
- Messast S, Boumékik A, 2005. Transmission of the harmonic vibrations around a pile foundation, Proc international conference on problematic soils, Eastern Mediterranean University, Famagusta, N. Cyprus, Vol. 3, p. 1260–1270.
- Rajapakse R. K. N. D, Shah A.H, 1989. Impedance curves for elastic pile, *Soil Dynamic and Earthquake Engineering*, 8(3):145–152.
- Rajapakse R. K. N. D, Dynamics of piles: 1988. A critical evaluation of continuum solution models, The Canadian Society of Civil Engineering, Annual Conference. Calgary.
- Rajapakse R. K. N. D, Shah A.H. 1987. On the longitudinal harmonic motion of an elastic bar embedded in an elastic half-space, *International Journal of Solids and Structures*, 23:287–303.
- Sami Ben Jamaa, Hiroo Shiojiri, 2000. A method for three dimensional interaction analysis of pile-soil system in time domain, *Transactions of JSCEs*, Paper N° 20000013.
- Sen R, Kausel E, P. K. Banerjee P. K. 1985. Dynamic analysis of piles and pile Groups Embedded in no-homogeneous soils, *Internatioual Journal for Numerical and Analytical Methods in Geomechanics*, Vol. 9, p. 507–524.
- Vallabhan C. V .G, Sivakumar J. 1986. Coupling of BEM and FEM for 3D problems in geotechnical engineering. In: Brebbia C. A, Connor J. J et al, editors. *BETECH 86*. Southampton: CML Publ.; p. 675–686.
- Whitaker T, Cooke R. W. 1966. An investigation of the shaft and base resistance of large bored piles in london clay. *Proc Symp Large Bored Piles*, 7–49.

Dynamic analysis of piles embedded in transversely isotropic soils using hybrid elements

Assadollah Noorzad

Civil Engineering Department, School of Engineering, Tehran University, Tehran, Iran

Ali Noorzad

Faculty of Water Engineering, Power and Water University of Technology, Tehran, Iran

Kami Mohammadi

Civil Engineering Department, Chamran University, Tehran, Iran

ABSTRACT: The soil-structure interaction analysis is of major interest in some situations. Especially, an important category of these problems is the behavior of piles as machine foundations subjected to strong earthquake motions and wind loads. Most of the previous studies are concerned on soil with isotropic behavior. But it is well known that many soil deposits possess a certain degree of anisotropy from the geological point of view. The assessment of the dynamic response of piles should be carried out by numerical methods except for some simplified cases. The paper deals with a development of a new method to compute the dynamic stiffness of piles. Numerical simulations demonstrate the influence of soil anisotropy and the applicability of the proposed model.

1 INTRODUCTION

The common use of piles as the foundation of structures constructed on soft soils dates back to many years (Poulos & Davis 1980). During the past decade considerable efforts have been undertaken to describe the interaction of soil-pile-structure. Penzien (1970) introduced soil surrounding pile as a spring with bilinear behavior capable modeling the hysteretic response. Berrones & Whitman (1982) used Winkler spring to study the soil-pile interaction. Tajimi et al. (1965) were the first to investigate the soil-pile interaction using continuum mechanics for the plane strain cases. Novak & Aboul-Ella (1978) generalized the Winkler model to two-dimensional dynamics solutions for the dynamic behavior of pile located in layered soils. Kaynia & Kausel (1982) performed the problem analytically by the Green's function, introducing the three dimensional analysis of soil-pile groups interaction. Although this method is improved for a better accuracy, however it is not applicable for the engineering purposes because of its complexity for computation. Maluis & Gazetas (1992) analyzed the soil-pile interaction by one-dimensional wave propagation method analytically. Nogami et al. (1992) formulated the nonlinear soil-pile interaction by two dimensional wave propagation theory considering the nonlinear dynamic behavior of Winkler spring which is used to model the sliding at the soil-pile interface.

Most of these pile studies assumed soil isotropy. In recent years, some researchers have investigated dynamic behavior of piles on transversely isotropic media. Among them, Liu & Novak (1994) used the finite element method to model the pile by beam column elements while the unbounded soil medium is modeled by a soil stiffness matrix derived from dynamic Green's function of the soil. More recently, Noorzad et al. (2005) proposed a method for the dynamic response of soil-pile system representing pile as beam element combined with radiation elements. The approach doesn't impose complexity in computation while maintaining accuracy and simple to analyzing the problem.

In this paper an attempt is made to generalize the previous work employing the effect of soil anisotropy on pile behavior. Predictions using the isotropic model appear to differ considering from predictions utilizing the anisotropic model which significantly affect the results.

2 STATEMENT OF THE PROBLEM

In this model, it is assumed that the wave propagation from pile to the unbounded semi-infinite medium occurs only from some finite nodes representing rigid massless circular disks, namely radiation elements as shown in [Figure 1](#).

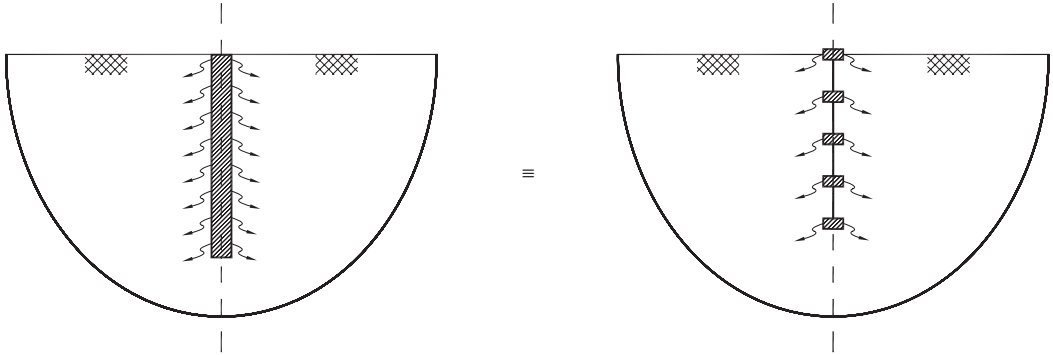


Figure 1. Radiation elements.

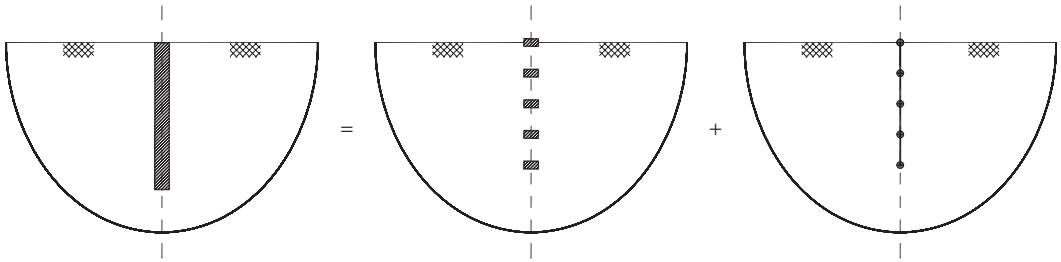


Figure 2. Model for pile foundation.

Figure 2 shows the interacting of pile-soil system which the pile is modeled by radiation elements demonstrating wave propagation through soil, combined with a set of finite elements expressing the pile vibration.

3 FORMULATION

In accordance to finite element formulation, the pile stiffness in frequency domain is used to compute the dynamic stiffness matrix which can be written as

$$\begin{Bmatrix} F_1 \\ F_2 \end{Bmatrix} = [K_p] \begin{Bmatrix} u_1 \\ u_2 \end{Bmatrix} \quad (1)$$

$$[K_p] = \frac{EA\gamma}{\sin(\gamma L)} \begin{bmatrix} \cos \gamma L & -1 \\ -1 & \cos \gamma L \end{bmatrix}$$

where F = force; u = displacement; E = modulus of elasticity; K_p = dynamic stiffness; A = area; L = length; and γ = bulk density.

The stiffness of radiation element is calculated utilizing the analytical solution of a disk resting on a transversely isotropic half-space as follows. The governing equations of a transversely isotropic media are given by

$$\begin{aligned} & A_{11} \left(\frac{\partial^2 u}{\partial r^2} + \frac{1}{r} \frac{\partial u}{\partial r} - \frac{u}{r^2} \right) - 2A_{11} \frac{1}{r^2} \frac{\partial v}{\partial \theta} + \\ & \left(\frac{A_{11} + A_{12}}{2} \right) \left(\frac{1}{r} \frac{\partial^2 v}{\partial r \partial \theta} + \frac{1}{r^2} \frac{\partial v}{\partial \theta} \right) + \left(\frac{A_{11} - A_{12}}{2} \right) \frac{1}{r^2} \frac{\partial^2 u}{\partial \theta^2} + \\ & A_{44} \frac{\partial^2 u}{\partial z^2} + (A_{13} + A_{44}) \frac{\partial^2 w}{\partial r \partial z} = \rho \frac{\partial^2 u}{\partial t^2} \\ & A_{11} \frac{1}{r^2} \frac{\partial^2 v}{\partial \theta^2} + 2A_{11} \frac{1}{r^2} \frac{\partial u}{\partial \theta} + \left(\frac{A_{11} + A_{12}}{2} \right) \left(\frac{\partial^2 u}{\partial r \partial \theta} - \frac{1}{r^2} \frac{\partial u}{\partial \theta} \right) + \\ & \left(\frac{A_{11} - A_{12}}{2} \right) \left(\frac{\partial^2 v}{\partial r^2} + \frac{1}{r} \frac{\partial v}{\partial r} - \frac{v}{r^2} \right) + A_{44} \frac{\partial^2 v}{\partial z^2} + \\ & (A_{13} + A_{44}) \frac{\partial^2 w}{\partial r \partial z} = \rho \frac{\partial^2 v}{\partial t^2} \\ & A_{44} \left(\frac{\partial^2 w}{\partial r^2} + \frac{1}{r} \frac{\partial w}{\partial r} + \frac{1}{r^2} \frac{\partial^2 w}{\partial \theta^2} \right) + A_{33} \frac{\partial^2 w}{\partial z^2} + \\ & (A_{13} + A_{44}) \left(\frac{\partial^2 u}{\partial r \partial z} + \frac{1}{r} \frac{\partial u}{\partial z} + \frac{1}{r} \frac{\partial^2 v}{\partial \theta \partial z} \right) = \rho \frac{\partial^2 w}{\partial t^2} \end{aligned} \quad (2)$$

In the above equations, u , v and w are displacement components along r , θ and z axes, respectively; A_{ij} = the elastic constants; and ρ = density of soil.

The elastic constants can be obtained as

$$\begin{aligned}
 A_{11} &= \frac{a_{11}a_{33} - a_{13}^2}{(a_{11} - a_{12})m}; & A_{33} &= \frac{a_{11} + a_{12}}{m}; \\
 A_{12} &= \frac{a_{13}^2 - a_{12}a_{33}}{(a_{11} - a_{12})m}; & A_{44} &= \frac{1}{a_{44}}; \\
 A_{13} &= \frac{-a_{13}}{m}; & A_{66} &= \frac{1}{a_{66}}; \\
 m &= (a_{11} + a_{12})a_{33} - 2a_{13}^2
 \end{aligned}
 \tag{3}$$

in which a_{ij} are related to elastic modulus (E_{ij}); shear modulus (G_{ij}); and Poisson's ratio.

$$\begin{aligned}
 a_{11} &= \frac{1}{E_{rr}}; a_{33} = \frac{1}{E_{zz}} \\
 a_{12} &= \frac{-\nu_{r\theta}}{E_{rr}} = \frac{-\nu_{\theta r}}{E_{\theta\theta}}; a_{44} = \frac{1}{G_{rz}} = \frac{1}{G_{\theta z}} \\
 a_{13} &= \frac{-\nu_{rz}}{E_{rr}} = \frac{-\nu_{zr}}{E_{zz}} = \frac{-\nu_{\theta z}}{E_{\theta\theta}} = \frac{-\nu_{z\theta}}{E_{zz}}; a_{66} = 2(a_{11} - a_{12})
 \end{aligned}
 \tag{4}$$

Let the general solution of Equation 2 is considered by the following set of equations in the frequency domain:

$$\begin{aligned}
 u(r, \theta, z, t) &= u(r, \theta, z)e^{i\omega t} \\
 v(r, \theta, z, t) &= v(r, \theta, z)e^{i\omega t} \\
 w(r, \theta, z, t) &= w(r, \theta, z)e^{i\omega t}
 \end{aligned}
 \tag{5}$$

Utilizing the potential functions X and ψ (Noorzad et al. 2003), the displacements are therefore taken the form

$$\begin{aligned}
 u &= -\alpha_3 \frac{\partial^2 \Psi}{\partial r \partial z} - \frac{1}{r} \frac{\partial X}{\partial \theta} \\
 v &= -\alpha_3 \frac{1}{r} \frac{\partial^2 \Psi}{\partial \theta \partial z} - \frac{\partial X}{\partial r} \\
 w &= (1 + \alpha_1)(\nabla_{r\theta}^2 + \beta \frac{\partial^2}{\partial z^2} + \frac{\rho_0}{1 + \alpha} \omega^2) \Psi
 \end{aligned}
 \tag{6}$$

where

$$\begin{aligned}
 \nabla_{r\theta}^2 &= \frac{\partial^2}{\partial r^2} + \frac{1}{r} \frac{\partial}{\partial r} + \frac{1}{r^2} \frac{\partial^2}{\partial \theta^2}; \alpha_1 = \frac{A_{66} + A_{12}}{A_{66}} \\
 \alpha_2 &= \frac{A_{44}}{A_{66}}; \alpha_3 = \frac{A_{13} + A_{44}}{A_{66}} \\
 \rho_0 &= \frac{\rho}{A_{66}}; \beta = \frac{\alpha_2}{1 + \alpha_1}
 \end{aligned}$$

Potential functions X and Ψ should satisfy the following wave equations, i.e.

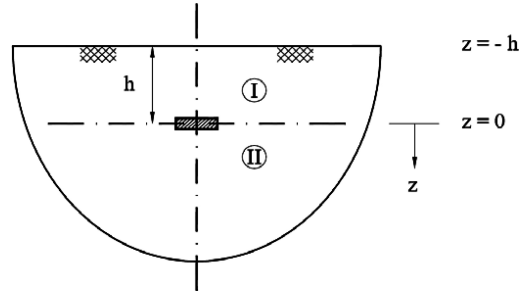


Figure 3. Schematic view of finite and semi-finite medium at above and below of the disk.

$$\begin{aligned}
 \nabla_0^2 X &= 0 \\
 \nabla_1^2 \nabla_2^2 \Psi &= 0
 \end{aligned}
 \tag{7}$$

in which

$$\begin{aligned}
 \nabla_0^2 &= \nabla_{r\theta}^2 + \frac{1}{S_0^2} \frac{\partial^2}{\partial z^2} + \rho_0 \omega^2 \\
 \nabla_i^2 &= \nabla_{r\theta}^2 + \frac{1}{S_i^2} \frac{\partial^2}{\partial z^2} + \frac{1}{\mu_i} \rho_0 \omega^2; (i=1,2) \\
 S_0^2 &= \frac{1}{\alpha_2} = \frac{A_{66}}{A_{44}} \\
 \mu_1 &= \alpha_2 = \frac{A_{44}}{A_{66}}; \mu_2 = 1 + \alpha_1 = \frac{A_{11}}{A_{66}}
 \end{aligned}$$

Using Fourier series expansion in θ direction and Hankel integral transform in r direction, the differential equation with partial derivatives will change to ordinary differential equations which can be solved analytically. The boundary conditions can be satisfied by determining the displacement vector and stress tensor in terms of potential functions (Figure 3). The dynamic stiffness of soil-pile system can be determined by calculating the dynamic stiffness of radiation elements and assembling with pile element.

4 VERIFICATION AND NUMERICAL STUDIES

Based on convergency study to control the number of radiation elements, the numerical results achieved by the proposed formulation is quite acceptable and compare favorably with those obtained by Liu & Novak (1994). As illustrated in Figure 4, there is also a good agreement of the present solution with those of other results achieved by boundary element method.

If the soil anisotropy is defined by Young's modulus ratio ($n = E_H/E_V$) and the dimensionless frequency is expressed as $a_0 = \omega r/v_s$, where ω = loading

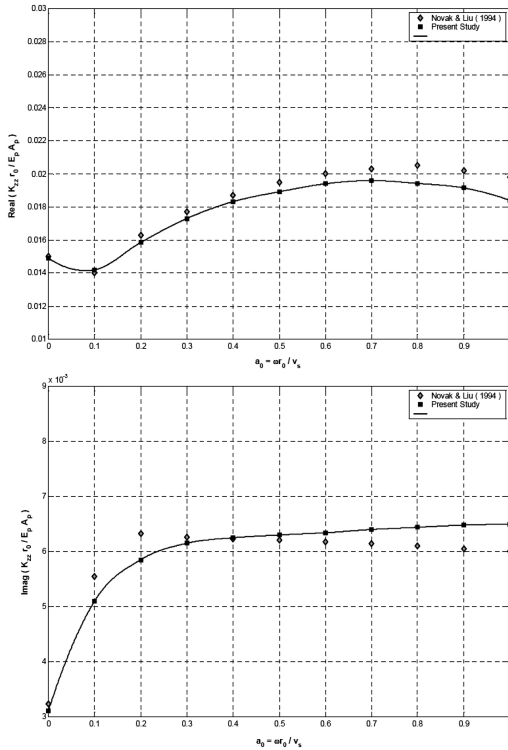


Figure 4. Comparison of the Liu & Novak results with the present study to compute the impedance function.

frequency; r = pile radius; and v_s = shear wave velocity, then the dynamic stiffness function for clayey soil can be exhibited in Figure 5 in terms of dimensionless frequency and soil anisotropy.

As the soil anisotropy increases, the stiffness decreases and damping ratio increases. Parametric studies are conducted for different materials as the parameters used to produce Figure 6 are listed in Table 1.

Figure 6 presents the real and imaginary parts of impedance variations for isotropic and anisotropic materials. It is evident that the soil anisotropy has great influence on the pile behavior and must be considered in computation.

5 CONCLUSION

The paper proposes an improvement to the soil-pile interaction problems under dynamic loading that takes into account the soil anisotropy. A series of simulations concerning different types of materials are conducted to explore the effect of soil anisotropy on the pile dynamic behavior. The validity and accuracy of the current formulation is demonstrated well in comparison with the

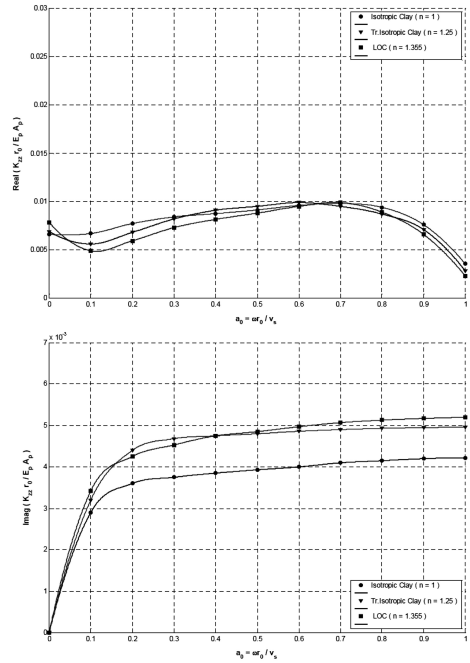


Figure 5. Impedance variation for isotropic and transversely isotropic clay.

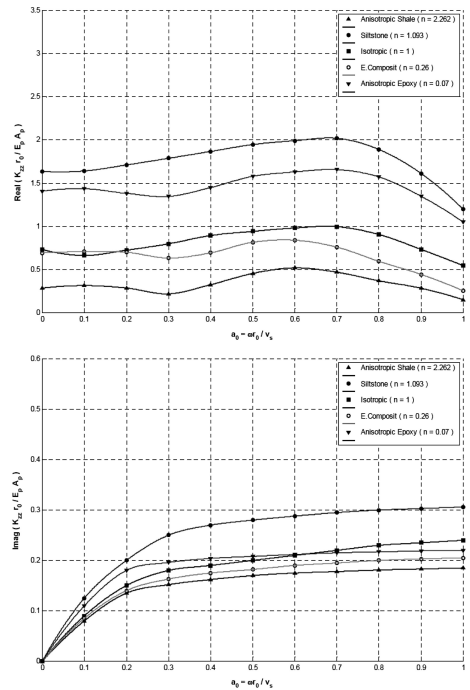


Figure 6. Impedance variation for different isotropic and transversely isotropic materials.

Table 1. Material constants.

Type of material	ν_{VH}	n
Anisotropic shale	0.25	2.262
Siltstone	0.24	1.093
Isotropic material	0.25	1.0
E-composite	0.24	0.26
Anisotropic epoxy	0.27	0.07

published results. To conclude, the following remarks should be mentioned:

- The trend of variation of the stiffness of isotropic and anisotropic materials depends on the anisotropy index.
- The stiffness of anisotropic material with a high and low anisotropy index is lower and higher than the stiffness of isotropic material, respectively.
- The damping ratio for anisotropic material with a high or low anisotropy index is higher than the stiffness of isotropic material.
- With the increase of pile stiffness relative to the soil in the vertical plane, the amount of stiffness and damping ratio also increase.

REFERENCES

- Berrones, R. & Whitman, R.V. 1982. Seismic response of end bearing piles. *Journal of Geotechnical Engineering*. ASCE. 108 (GT4): 554–569.
- Kaynia, A.M. & Kausel, E. 1982. Dynamic stiffness and seismic response of pile groups. *Report No. R82-03*. Massachusetts Institute of Technology, Cambridge.
- Liu, W. & Novak, M. 1994. Dynamic response of single piles embedded in transversely isotropic layered media. *Earthquake Engineering and Structural Dynamics*. 23: 1239–1257.
- Maluis, N. & Gazetas, G. 1992. Dynamic pile-soil-pile interaction. Part II: Lateral and seismic response. *Earthquake Engineering and Structural Dynamics*. 21: 145–162.
- Nogami, T., Konagai, K., Otani, J. & Chen, H.L. 1992. Nonlinear soil-pile interaction model for dynamic lateral motion. *Journal of Geotechnical Engineering*. ASCE. 118 (1): 106–116.
- Noorzad, A., Ghadi, M. & Konagai, K. 2003. Fundamental steady state solution for the transversely isotropic half space. *Iranian Journal of Engineering*. 16(2): 105–122.
- Noorzad, A., Noorzad, A. & Massoumi, H.R. 2005. Dynamic response of a single pile embedded in semi-infinite saturated poroelastic medium using hybrid elements. *Proceedings of the 16th International Conference on Soil Mechanics and Geotechnical Engineering, Osaka, Japan: 2027–2030*.
- Novak, M. & Aboul-Ella, F. 1978. Impedance functions of piles in layered media. *Journal of Geotechnical Engineering*. ASCE. 104(6): 643–661.
- Penzien, J. 1970. Soil-pile foundation interaction. In Wiegel R.L. (ed.), *Earthquake Engineering*: Chapter 14. New York: Prentice Hall.
- Polous, H.G. & Davis, E.H. 1980. *Pile foundation analysis and design*. New York: John Wiley and Sons.
- Tajimi, T., Terada, S. & Mochizuki, T. 1965. Vibrational property and earthquake response of tall building supported with caisson or pile. *Proceedings of the Third World Conference on Earthquake Engineering, Auckland*. 1: 173–179.

Application of the Boundary Element method to analyze dynamic soil compaction control techniques

I. Paulmichl, C. Adam & D. Adam

Vienna University of Technology, Vienna, Austria

ABSTRACT: In the present paper the static load plate test and dynamic load plate test with the Light Falling Weight Device (LFWD), and heavy tamping are evaluated by means of extensive numerical studies utilizing the Boundary Element Method. The compacted soil medium is modeled either as a horizontal semi-infinite layer with constant thickness and an underlying halfspace (in the case of the load plate tests) or as a homogeneous halfspace (in the case of heavy tamping). The dynamic load plate test is simulated by means of the substructure technique (substructure 1: falling weight and spring-damper element, substructure 2: load plate and elastic soil medium) separately and then coupling them iteratively. The static load plate test is evaluated using substructure 2, while for the simulation of heavy tamping the model is modified in order to consider a variable penetration depth of the falling weight. The results of the presented study cover a wide range of soil characteristics considering various material properties and layer thicknesses and/or penetration depths.

1 INTRODUCTION

The quality of layered earth structures depends on the built-in material and in particular on the construction work. The layers have to be compacted properly in order to prevent future damage of the structure connected to the earth structure. Therefore, compaction control is of particular importance. In the present paper selected indirect compaction control methods are evaluated by means of extensive numerical studies in order to analyze the reliability and quality of the test results of these methods.

2 STATIC LOAD PLATE TEST

2.1 Numerical model

The compacted soil medium is modeled as a horizontal semi-infinite layer with constant thickness, which is perfectly bonded to a halfspace with different stiffness. Both the layer and the underlying halfspace are assumed to be composed of a homogeneous, isotropic and linear elastic material. The circular load plate made of steel with a radius r of 150 mm rests on the surface of the layered subsoil (sliding interface, i.e. only normal stresses can be transferred between the plate and the soil).

The boundaries of the layered halfspace and the load plate are discretized by means of the Boundary Element Method (BEM) utilizing the rotational symmetry of

this substructure. For all computations the commercial software GPBEST is employed, Banerjee (2001). At the free surface of the soil semi-infinite elements are employed, and the circular plate is loaded by a uniformly distributed vertical load $Q = 200 \text{ kN/m}^2$.

The material parameters of the layer and the halfspace and the thickness of the layer d can be changed automatically for parametric studies: The Young's modulus E_o of the layer is kept constant and equal to 32 MN/m^2 while the Young's modulus of the halfspace E_u is swept from 4 to 256 MN/m^2 in such a way that layered subgrades with moduli ratios from 1/8 ("soft-stiff") up to 8/1 ("stiff-soft") can be simulated. In an automated simulation process for each soil medium with a certain moduli ratio E_o/E_u the thickness d of the layer is varied incrementally.

For selected nodes at the surface and for sampling points in the domain of the underground the deformations and stresses are determined. Note, the sampling points are arranged along a net composed of hyperbolic and elliptic functions (Fig. 1). The displacement of the load plate s_{\max} is of particular importance, because it is needed to determine the deformation modulus E_v according to Eq. (1).

$$E_v [MN / m^2] = \frac{45}{s_{\max} [mm]} \quad (1)$$

Eq. (1) can be determined with the halfspace theory for a Poisson's ratio ν of 0.212.

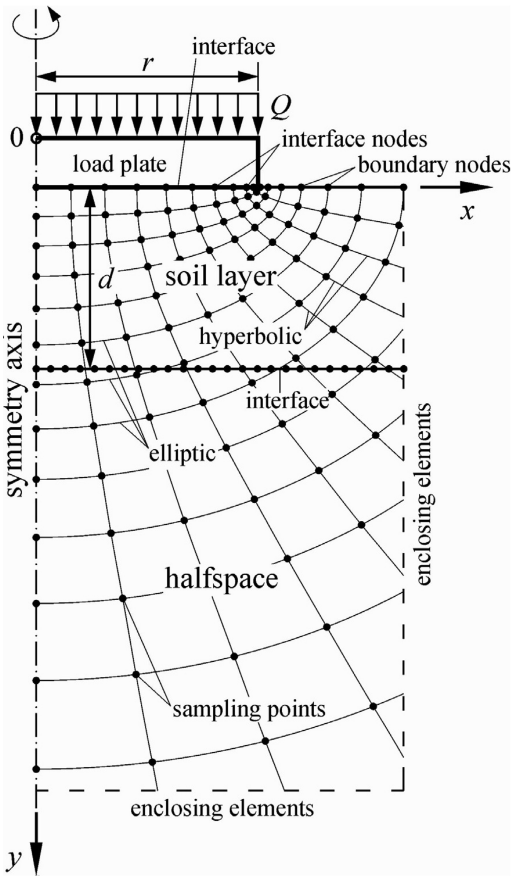


Figure 1. Rotationally symmetric model of the load plate and subsoil for BEM analyses.

2.2 Evaluation of the measuring depth

The measuring depth of the static load plate is the depth up to which inhomogeneities in the subsoil are reflected in the test results. This depth is of importance for detecting defects in earth structures, and for the investigation of soil packages composed of various layers with different material properties.

Figure 2 shows the deformation modulus E_v as a function of the layer thickness d for different ratios E_o/E_u . It can be observed that with increasing d the dynamic deformation modulus of a layered halfspace converges to the outcome of the homogeneous halfspace with material properties of the layer ($E_o/E_u = 1$, i.e. a horizontal straight line). According to the figure the difference of E_v isn't negligible for a layer thickness less than one meter. This outcome differs from experimental results, where a measuring depth of about 0.45 to 0.50 m has been verified (Kopf et al., 2005a). The difference between the numerical and

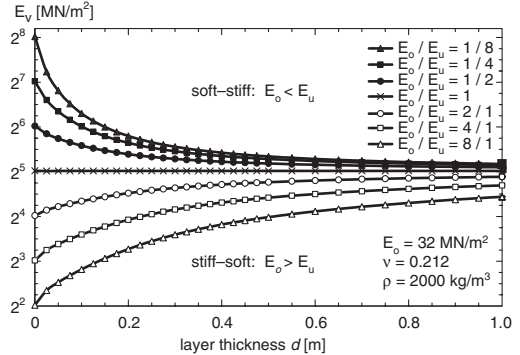


Figure 2. Semi-logarithmic representation of the deformation modulus E_v for different subsoil stratifications as function of the soil layer thickness d .

experimental results can be explained with the discrepancy between the conditions on site (measurement of relative plate displacements, load application, influence of local plasticity, etc.) and the ideal theoretical assumptions. The influence of selected factors on the test result is presented in the following.

2.3 Influence of error sources on the test result

From several objective and subjective influencing factors both, the measurement of the deformation and the load application, are singled out and analyzed. When during the test the load is applied to the plate by means of a counter weight a static equivalent force relieves the layered halfspace in the area of the footprint of the abutment. This loading results in a smaller vertical deformation of the soil. The measurement equipment used in the field detects only a part of this deformation, because also the measuring instrument is influenced by the deformation of the layered halfspace. Subsequently, the reference level for the deformation measurement is displaced and may also be rotated.

When the device with three gauges is used in the practice to measure the load plate displacements, only the relative vertical displacement between measuring bridge and load plate can be recorded. The displacements s_{III} measured with the three gauges device can be simulated in the numerical procedure by subtraction of the device displacements Δs_i due parallel translation from the absolute displacement s of the load plate (Paulmichl, 2004).

The parallel device translation Δs_i depends apart from the subsoil parameters on the distance R between the contact points of the device with the subsoil and the load: Δs_i is increasing with decreasing R . In the numerical simulations the distance is varied between 1.20 and 1.50 m in order to examine the overestimation of the stiffness of the tested subsoil in the

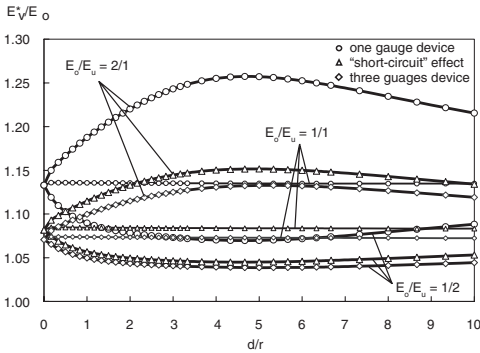


Figure 3. Normalized deformation modulus E_v^*/E_o for three sources of error (one gauge device, three gauges device and “short-circuit” effect) and three different subsoil stratifications as function of the non dimensional soil layer thickness d/r .

practice ($E_{vIII} > E_v$) for commonly used devices (Paulmichl, 2004). With the reduced absolute plate displacement s_{III} the corresponding deformation modulus E_{vIII} is determined utilizing Eq. (1).

The measuring bridge of the device with one gauge is subjected in addition to the mentioned parallel translation also to a rotation (Paulmichl, 2004). In order to simulate the displacements s_l measured with the one gauge device, the part Δs , due to the device rotation has to be subtracted in addition to the translational part Δs_l from the absolute plate displacement s . When using the one gauge device, the subsoil stiffness is further overestimated ($E_{vI} > E_{vIII}$).

During the static load plate test the subsoil can not be loaded by a global load because due to the loading of the plate the counterweight is unloaded in the same extent. Thus, only a more or less local load redistribution can be conducted what is called “short-circuit” effect.

The geometry of the different counterweights (roller, truck, excavator, etc.) used in the practice varies in a great range. In order to simulate the “short-circuit” effect using the rotationally symmetrical model, the counterweight is modeled as annulus with representative dimensions. The layered halfspace is loaded by the plate and unloaded in the same extension by the surrounding annulus load (static equivalent tension stress). The reduced plate displacements from this load case result in a deformation modulus denoted with E_v^{**} . Thus, the subsoil stiffness is overestimated and the measuring depth reduced.

Figure 3 shows the normalized deformation modulus E_v^*/E_o for three different soil stratifications ($E_o/E_u = 2/1$: “stiff to soft”, $E_o/E_u = 1$: homogeneous halfspace, $E_o/E_u = 1/2$: “soft to stiff”) as a function of the non dimensional layer thickness d/r . The notation “ E_v^* ” denotes the deformation modulus determined when

simulating a typical one gauge device ($E_v^* = E_{vI}$), a typical three gauges device ($E_v^* = E_{vIII}$) and the “short-circuit” effect ($E_v^* = E_v^{**}$) respectively. It can be observed that all lines are above the horizontal line with $E_v^*/E_o = 1$ representing the “effective” test result due to the calculated absolute plate displacements. The overestimation of the subsoil stiffness is increasing from the three gauges device over the “short-circuit” effect to the one gauge device whereas the simulated error is much greater in the case of “stiff-soft”: The curves for $E_o/E_u = 2/1$ start from the value determined for a homogeneous halfspace with $E = 32 \text{ MN/m}^2$ (1.07, 1.08, 1.13), reach a maximum at a certain ratio d/r (1.13, 1.15, 1.26) of and converge to the horizontal line representing the solution of the homogeneous condition. The curves for $E_o/E_u = 1/2$ however reach a minimum at a certain ratio d/r (1.04, 1.05, 1.07) before converging to the horizontal line representing the solution of the homogeneous condition.

Note, the presented overestimations are simulated separately. However, on site the error due to the measuring device and the load application occur simultaneously. This means that the errors simulated theoretically have to superimposed as to interfere with each other. Thus, the evaluated errors that are not of systematic nature are not negligible. In conclusion it has to be mentioned that the stiffness of the tested subsoil is overestimated and the measuring depth is reduced at the same time (Paulmichl, 2004).

3 DYNAMIC LOAD PLATE TEST WITH THE LIGHT FALLING WEIGHT DEVICE

3.1 Substructure technique

The computational procedure is based on the concept of partitioning the complete soil-device system in two substructures (Fig. 4): one substructure contains the falling weight and the spring-damper element of the LFWD, the second substructure includes the load plate and the elastic soil medium. The basic dynamic equilibrium equations of each subsystem are solved separately, and in the final step of the analysis, in an iterative procedure the results are combined by satisfying equilibrium and compatibility conditions at the interface nodes to provide the complete solution.

The falling weight and the spring-damper element of the LFWD (substructure 1) can be represented as a point mass and a Kelvin-Voigt body, respectively (Fig. 4). The connection of the spring-damper element to the load plate constitutes the interface to the second substructure. The equation of motion of this part of the interaction system is formulated in the time domain.

After release the point mass m_F drops from the height h_0 onto the spring-damper element of the load device. The subsequent motion of this subsystem

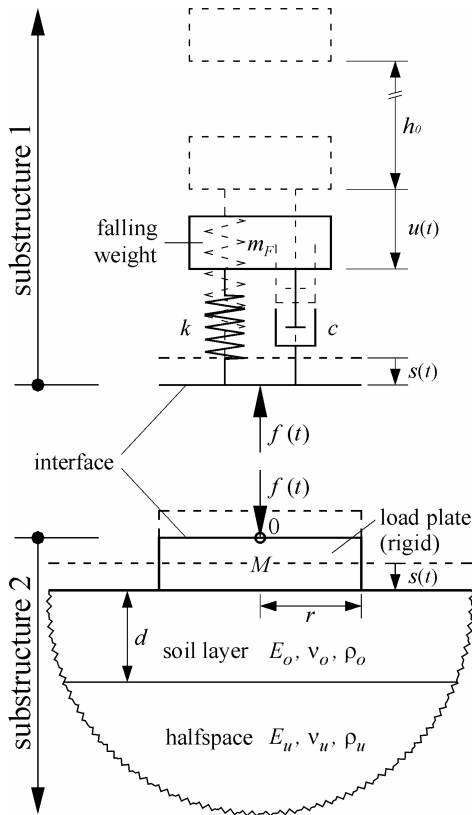


Figure 4. Mechanical model of the Light Falling Weight Device (LFWD) and the layered subsoil, separated in two substructures.

(vertical coordinate u), where the point mass m_F moves along with the spring-damper element, can be expressed according to a single-degree-of-freedom (SDOF) oscillator as

$$m_F \ddot{u} + c \dot{u} + k u = m_F g + c \dot{s} + k s \quad (2)$$

Thereby, c and k represent the damping coefficient and the stiffness, respectively, of the Kelvin-Voigt body, and g denotes the acceleration of gravity. The coupling terms to the soil/load plate substructure, i.e. the displacement s and velocity \dot{s} of the load plate, are assumed to be known parameters, and thus, written on the right hand side of Eq. (2).

In this contact phase of motion the load plate is stressed by the interface force $f(t)$ (Eq. (3)). For the coupling of both substructures it is assumed that the interface force $f(t)$ is a resultant force of a uniformly distributed load $q(t)$, which acts upon the load plate, i.e.

$$q = \frac{f}{r^2 \pi} = \frac{m_F (g - \ddot{u})}{r^2 \pi} \quad (3)$$

When the acceleration of \ddot{u} exceeds the acceleration of gravity g the point mass lifts up and moves separately from the load plate. During this phase the interface force f (and q) is zero.

The computational model of the static load plate test (Fig. 1) is used to formulate substructure 2 in the frequency domain loading the circular plate by a uniformly distributed harmonic vertical unit load. For selected nodes at the surface and for sampling points (characterized with j) in the domain of the underground the complex transfer function $H(i\bar{\nu})$ is determined by sweeping the frequency $\bar{\nu}$ of the harmonic unit interface load applied to the load plate. The transfer function $H_q(i\bar{\nu})$ in the center of the load plate (denoted by "0" in Fig. 4) is of particular importance, because the compatibility at the interface to substructure 1 must be satisfied in a subsequent step of calculation by iteration. $H_q(i\bar{\nu})$ is determined by application of uniformly distributed harmonic loads $Q(i\bar{\nu})$ to the load plate with an amplitude of 100 kN/m^2 .

The coupled system of LFWD and layered subsoil is analyzed by iteration (Paulmichl et al., 2005). When the iterative procedure is completed, stresses and displacements in the subsoil at certain nodes and sampling points are determined by multiplying the corresponding dynamic transfer function with the final value of $Q_q(i\bar{\nu})$. Application of the inverse FFT algorithm yields the time history of the corresponding variable \bar{v} .

At the end of each iteration also the time history of the soil contact stress $p(t)$ is determined by

$$p = \frac{m_F (g - \ddot{u}) - M \ddot{s}}{r^2 \pi} \quad (4)$$

where M denotes the mass of load plate and guide rod. Eq. (4) is derived by application of conservation of momentum to the free-body diagram of the load plate under the assumption that the soil contact stress is uniformly distributed (compressive stress is positive). Thus, $p(t)$ represents the mean of the actual soil contact stress distribution.

3.2 Numerical study

In all subsequent computations the following device parameters are utilized: mass of the falling weight $m_F = 10 \text{ kg}$, falling height $h_0 = 0.70 \text{ m}$, mass of load plate and guide rod $M = 20 \text{ kg}$, stiffness of the device spring $k = 337000 \text{ N/m}$, viscous damping parameter of the damping element $c = 130 \text{ N/(m/s)}$.

It can be proved that the time history of the soil contact stress is almost not affected from the subsoil conditions (Paulmichl et al., 2005). Thus, the standard test evaluation procedure, where a constant soil contact stress p_{\max} of 100 kN/m^2 is assumed to hold true for a wide range of soil deposits composed of different layers with different thickness and stiffness.

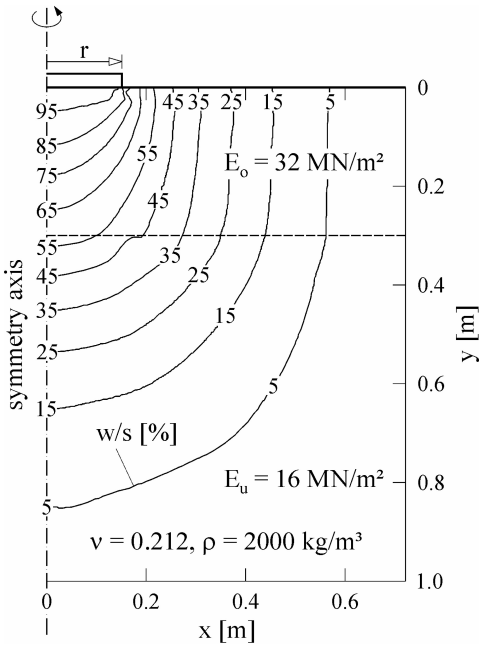


Figure 5. Distribution of the vertical displacement component w in a layered soil medium at time $t = 0.011$ s in percent of the load plate displacement s .

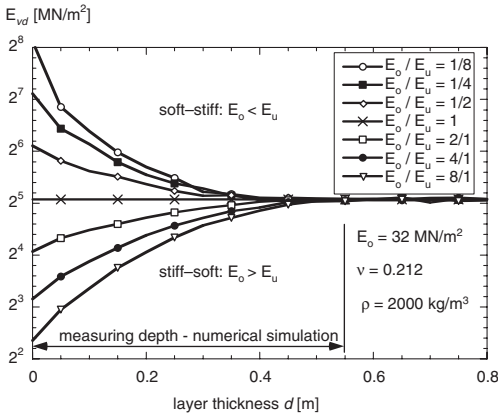


Figure 6. Semi-logarithmic representation of the dynamic deformation modulus E_{vd} for different subsoil stratifications as function of the soil layer thickness d .

In Figure 5 the distribution of the vertical soil displacement component for the layered soil medium (case 1) at time $t = 0.011$ s is presented in form of a contour plot. The contours correspond to a sequence of equal values of displacements (in percent), which

are normalized with respect to the load plate displacement s . Note, at $t = 0.011$ s the load plate displacement s is a maximum.

The plot of the corresponding distribution of the normal stress component σ_{yy} (tensile stresses are positive) shows a stress concentration below the edge of the load plate and close to the interface to the underlying halfspace (Paulmichl et al., 2005). It can be seen that the soil contact stress p according to definition of Eq. (4) is the mean of the actual stress distribution σ_{yy} at the interface to the load plate.

Figure 6 presents E_{vd} as a function of the layer thickness d . It can be observed that with increasing d the dynamic deformation modulus of a layered halfspace converges to the outcome of the homogeneous halfspace with material properties of the layer ($E_o/E_u = 1$, i.e. a horizontal straight line). For all considered soil stratifications the difference of E_{vd} becomes negligible if d exceeds 0.55 m. This outcome is in accordance with experimental results, where a measuring depth of 0.60 m has been verified (Brandl et al., 2003).

4 HEAVY TAMPING

During the compaction process of heavy tamping the soil is loaded below the original level with increasing numbers of impacts. The heavy pounder penetrates deeper and deeper into the ground. This changes the dynamic conditions of the system depending on several parameters. In order to quantify the specific effects extensive parameter studies were performed utilizing the Boundary Element Method.

The assumption of linear-elastic soil behavior is suitable for the present problem as the decay of the vibration after the compacting impact behaves as an elastic problem with sufficient accuracy.

The pounder-halfspace system was simulated in the frequency domain using the rotationally symmetric model (Fig. 1) in a modified form. The falling weight (pounder) with the mass m_F and radius r can penetrate into the soil whereas the changed geometry due to the varying penetration depth T can be modified in an automatic procedure. The transfer function in the center of the falling weight is determined by application of uniformly distributed harmonic loads to the pounder with an amplitude of 100 kN/m^2 . Material damping was neglected. For parametric studies the soil parameters (E , ν) and the penetration depth T were varied. The determined complex transfer functions were evaluated with the SDOF-analogy (Paulmichl, 2004).

Figure 7 shows the undamped natural frequency of the halfspace (corresponding to the undamped frequency $\omega/2\pi$ of the SDOF-system) depending on the Young's modulus E and the Poisson's ratio ν . The simulation was performed for a falling weight used for

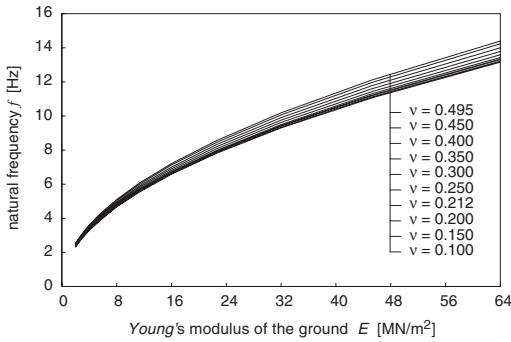


Figure 7. Natural frequency of the halfspace versus Young's modulus E . Poisson's ratio ν as parameter. Curves for a pounder of 1.8 m diameter and 16.5 tons. Penetration depth $T = 0$, no damping.

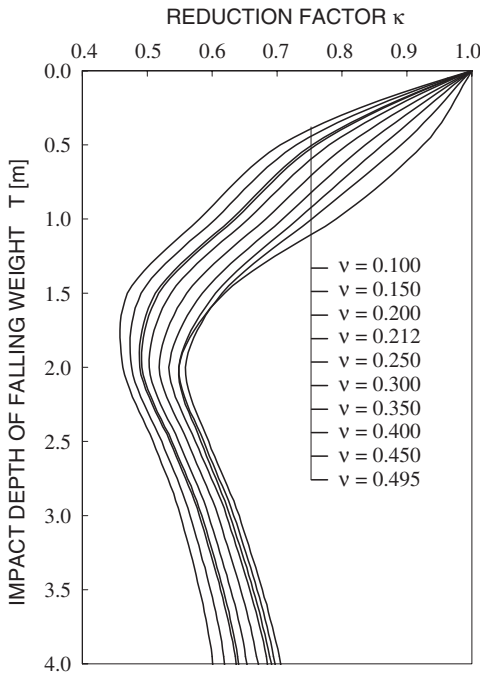


Figure 8. Reduction factor κ versus penetration depth T of the pounder into the soil. Poisson's ratio ν as parameter. Curves for a pounder of 1.8 m diameter and 16.5 tons. Soil parameters: Young's modulus $E = 16 \text{ MN/m}^2$, density $\rho = 2.0 \text{ t/m}^3$, no damping.

in-situ measurements. The correlation describes – in a first theoretical step – the idealized state of the falling weight situated on the surface of the halfspace, hence $T = 0$. Figure 7 reveals that the natural frequency of

the halfspace is widely proportional to \sqrt{E} and increases with Poisson's ratio ν .

Numerical calculations revealed that Lehr's damping coefficient ζ derived from the SDOF-analogy depends only on Poisson's ratio and is practically independent of the E -modulus of the halfspace (Kopf & Paulmichl, 2005). This phenomenon could be found for all penetration depths T of the falling weight (pounder), whereby ζ varies with depth (Kopf & Paulmichl, 2005).

The influence of the penetration depth of the pounder (i.e. the crater depth of the compaction point) can be described by a reduction factor κ , depending on Poisson's ratio (Fig. 8). The curves include the pounder parameters (diameter, mass) and the soil parameters (density, Young's modulus).

This theory and in-situ measurements allow to create a correlation between measured vibration parameters ($\omega/2\pi$ and ζ) and soil parameters (E , ν) of an idealized linear-elastic halfspace: The site-specific, known parameters T and ζ provide Poisson's ratio ν from the damping coefficient – penetration depth relationship. Taking into consideration ν and the natural frequency $\omega/2\pi$ the Young's modulus can be obtained from Figure 7 for the special case $T = 0$. Actually, the pounder penetrates into the ground, and this can be considered by multiplying the Young's modulus for $T = 0$ by the reduction factor κ for $T > 0$ (from Fig. 8). This theoretical approximation is valid because it could be proven that the lines of equal frequency (isolines) represent the axial-affine reproduction of only one mathematical function (Kopf & Paulmichl, 2005).

The discussed theoretical considerations provide the basis for a method to determine the soil parameters from free vibrations of the pounder measured immediately after the respective impact. Hence, a practical approach to control the optimum tamping process and to check the actual parameters after each impact can be developed (Kopf et al., 2006).

5 CONCLUSIONS

Numerical simulations of the static load plate test show that the overestimation of the subsoil stiffness due to selected influencing factors (measurement of the deformation, load application) are not of systematic nature and thus not negligible.

Theoretical evaluations of the dynamic load plate test demonstrate that a LFWD with well-defined parameters leads to unambiguous test results, because the dynamic parameters remain unaffected by the test procedure.

The outcomes of the simulations of heavy tamping provide the basis for the development of a compaction control by means of dynamic measurements.

REFERENCES

- Adam, D., Kopf, F. & Adam, C. 2004. The dynamic load plate test with the Light Falling Weight Device – Theoretical and experimental investigations (in German), *Der Bauingenieur*, Vol. 79 (No. 1): 32–41.
- Adam, D., Kopf, F. & Paulmichl, I. 2005a. Quality control for land reclamation. In: *Proc. of the X Baltic Geotechnics 2005*, October 12–14, 2005, Riga.
- Adam, D., Brandl, H., Kopf, F. & Paulmichl, I. 2005b. Heavy tamping integrated dynamic compaction control. In: *Proc. of the 6th International Conference on Ground Improvement Techniques*, July 18–19, 2005, University of Coimbra, Portugal.
- Brandl, H., Adam, D., Kopf, F. & Niederbrucker, R. 2003. *The dynamic load plate test with the Light Falling Weight Device* (in German). Vienna: Bundesministerium fuer Verkehr, Innovation und Technologie, Strassenforschung 528.
- Kopf, F. & Paulmichl, I. 2005. Deep dynamic compaction – compaction control by means of dynamic measurements (in German), *Österreich. Ingenieur-u. Architekten-Zeitschrift (ÖIAZ)*, Vol. 150 (No. 4–5), pp. 149–159, Vienna.
- Kopf, F., Adam, C. & Paulmichl, I. 2005a. Investigation of the static load plate test by means of the Boundary Element Method (in German), *Österreich. Ingenieur-u. Architekten-Zeitschrift (ÖIAZ)*, Vol. 150 (No. 4–5), pp. 102–111, Vienna.
- Kopf, F., Adam, D. & Paulmichl, I. 2005b. Investigation of the dynamic load plate test with the Light Falling Weight Device by means of the Boundary Element Method (in German), *Österreich. Ingenieur-u. Architekten-Zeitschrift (ÖIAZ)*, Vol. 150 (No. 4–5), pp. 116–125, Vienna.
- Kopf, F., Adam, D. & Paulmichl, I. 2006. Near-surface dynamic soil improvement and its control by means of dynamic measurements – new developments (in German). In: *Proc. of the 21st Christian Veder Kolloquium*, April 20–21, 2006, Graz.
- Paulmichl, I. 2004. *Numerical simulation of static and dynamic compaction control methods on layered half-spaces by means of the Boundary Element Method* (in German). Master's Thesis, Vienna University of Technology.
- Paulmichl, I., Kopf, F. & Adam, C. 2005. Numerical simulation of the dynamic load plate test with the Light Falling Weight Device by means of the Boundary Element Method. In: *Proc. of the 6th International Conference on Structural Dynamics*, September 4–7, 2005, Paris, pp. 1285–1290, Millpress, Rotterdam.

Finite element analyzes of dynamic compaction techniques and integrated control methods

P. Erdmann

BOMAG Boppard, Germany

D. Adam & F. Kopf

Vienna University of Technology, Austria

ABSTRACT: The bearing capacity of layered soil constructions can be measured by continuous compaction control systems (CCC) during the soil compaction process by means of dynamically excited rollers. Roller drums make use of various shapes (cylindrical, polygonal, pad foot, etc.) and the dynamic compaction effect is achieved by different kinds of dynamic excitation systems (vibratory, oscillatory, directed excitation). The finite element method has been applied for dynamic analyzes using elastic models and an inelastic hypoplastic material law. Thus, it has been enabled to simulate the dynamic compaction process and the change of the soil properties during compaction. Soil compaction with dynamic excited reversible plates has also been investigated by finite element calculations. The sophisticated motion behaviour of all compaction devices could be excellently described.

1 DYNAMIC COMPACTION TECHNIQUES

Dynamic rollers make use of a vibrating or oscillating mechanism, which consists of one or more rotating eccentric weights. During dynamic compaction a combination of dynamic and static loads occurs. The dynamically excited drum delivers a rapid succession of impacts to the underlying surface from where the compressive and shear waves are transmitted through the material to set the particles in motion. This eliminates periodically the internal friction and facilitates the rearrangement of the particles into positions in combination with the static load that result in a low void ratio and a high density.

1.1 Vibratory rollers

The drum of a vibratory roller is excited by a rotating eccentric mass, which is attached to a shaft on the drum axis (Fig. 1). The rotating mass sets the drum in a circular translatory motion, i.e. the direction of the resulting force is corresponding with the position of the eccentric weight. Compaction is achieved mainly by transmitted compression waves in combination with the effective static drum load. Thus, the maximum resulting compaction force is intended to be almost vertical and in fact it is only a little inclined.

Subject to the soil response the vibration of the roller drum changes the amplitude and shape. Numerous studies have revealed that the drum of a vibratory roller

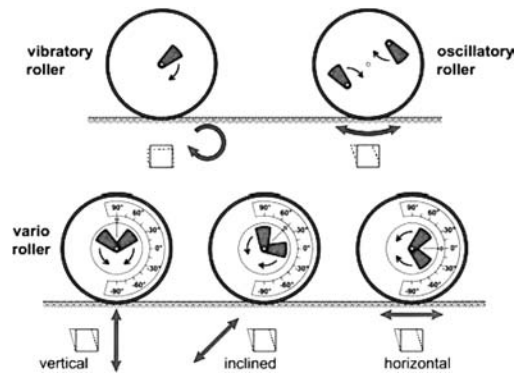


Figure 1. Description of different exciter systems.

operates in different conditions depending on roller and soil parameters. Five operating conditions specified in Figure 2 can occur; defining criteria is the contact condition between drum and soil and the drum motion cycle as a multiple of the excitation cycle (Adam 1996).

Continuous contact only occurs when the soil stiffness is very low, i.e. in case of low compacted or soft layers, or the drum amplitude is very small. Partial uplift and double jump are the most frequent operating conditions. The difference between these two operating conditions consists of the number of excitation cycles;

drum motion	interaction drum-soil	operating condition	soil contact force	application of CCC	soil stiffness	roller speed
periodic	continuous contact	CONT. CONTACT		yes	low ↓ high	fast ↑ slow
		PARTIAL UPLIFT		yes		
	DOUBLE JUMP		yes			
	ROCKING MOTION		no			
chaotic	non-periodic loss of contact	CHAOTIC MOTION		no		

Figure 2. Operating conditions of a drum of a vibratory roller.

consequently, the motion behavior of the drum repeats itself. With further increasing soil stiffness the vertical translation of drum axis is heterodyned with a rotation and the drum starts the so-called rocking. Very high soil stiffness in combination with disadvantageous roller parameters can cause chaotic motion of the drum. In this operating mode the roller cannot be controlled.

1.2 VARIO-roller

In a so-called VARIO roller two counter-rotating exciter masses, which are concentrically attached to shafts in the axis of the drum, produce a directed vibration. The direction of excitation can be adjusted by turning the complete exciter unit (Fig. 1). If the exciter direction is (almost) vertical or inclined, the compaction effect of a VARIO roller can be compared with that of a vibratory roller. However, if the exciter direction is horizontal, VARIO rollers operates like an oscillatory roller, although the motion behavior of the drum is different. The shear deformation of soil is caused by a horizontally translatory motion, whereas the drum of an oscillatory roller operates torsionally. Thus, a VARIO roller can be used both for dynamic compression compaction (like a vibratory roller), for dynamic shear compaction (like an oscillatory roller), and a combination.

1.3 VARIO CONTROL-roller and ACE-roller

Based on the findings related to the ways of operating of different dynamic rollers (Figure 2), the company BOMAG produced the first automatically controlled so-called VARIO CONTROL roller. The Swiss company AMMANN developed the auto-controlled roller ACE in connection with a roller-integrated control system providing dynamic compaction values independent from roller parameters. Exemplary, the direction of excitation (vibrations can be directed infinitely from the vertical to the horizontal direction) is controlled automatically in VARIO CONTROL

rollers by using defined control criteria, which allow an optimized compaction process. Following control criteria can be used:

- Operating criterion: definition that drum never operates in double jump mode.
- Force criterion: definition of a maximum force.

2 INTEGRATED CONTROL METHODS (CCC)

The roller-integrated continuous compaction control (CCC) represents a significant improvement and is based on the measurement of the dynamic interaction between dynamic rollers and soil (Adam 1996). The motion behavior of different dynamically excited roller drums changes in dependence of the soil response. This fact is used to determine the stiffness of the ground. Accordingly, the drum of the dynamic roller is used as a measuring tool; its motion behavior is recorded, analyzed in a processor unit, where a dynamic compaction value is calculated, and visualized on a display unit. Furthermore, an auxiliary sensor determines the location of the roller or the localization is GPS-based. Control data are already available during the compaction process and all over the compacted area (Fig. 3).

Four recording systems are available for vibratory rollers, VARIO rollers and ACE rollers with vertical or any inclined excitation direction (except horizontal direction). All systems consist of a sensor containing one or two accelerometers attached to the bearing of the roller drum. The sensor continuously records the acceleration of the drum. The time history of the acceleration signal is analyzed to determine dynamic compaction values.

Figure 4 gives a review of the recording systems of CCC. All defined CCC-values have proven suitable for roller-integrated checking of the actual compaction state. Nevertheless, it is essential to take into consideration the operating condition of the roller drum (see Table 1). Figure 5 shows the progress of CCC-values depending on soil stiffness and operation mode of the drum.

3 FEA SIMULATION OF DYNAMIC PROCESSES

3.1 FEA modeling

3.1.1 General aspects

Finite element models provide numerical calculations of dynamic soil compaction performed by vibratory rollers. For the simulation of soil compaction the FEA code must be capable to solve a so-called contact problem so that it is possible to calculate mechanical effects as impacts, deformations of interfaces, stick and slip, friction and the separation of the independent bodies (soil and compaction tool).

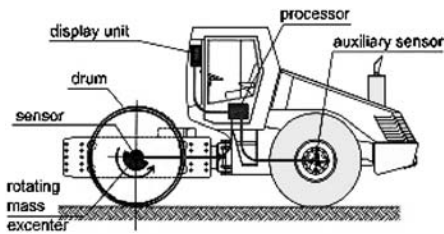


Figure 3. Vibratory roller with integrated CCC system.

CCC-system	CCC-value	definition of CCC-value
Compactometer	CMV []	acceleration amplitude ratio (first harmonic div. by excitation frequency amplitude) – frequency domain
Terrameter	OMEGA [Nm]	energy transferred to soil (considering soil contact force displacement relationship of 2 excitation cycles) – time domain
Terrameter	E_{ub} [MN/m ²]	dynamic elasticity modulus of soil beneath drum (inclination of soil contact force displacement relationship during loading) – time domain
ACE	k_{a} [N/m]	spring stiffness of soil beneath drum (derived from soil contact force displacement relationship at maximum drum deflection) – time domain

Figure 4. Existing CCC systems.

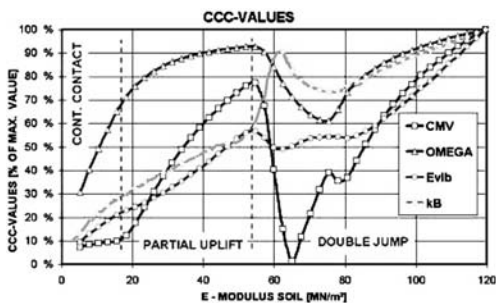


Figure 5. CCC values versus soil E-Modulus.

The FEA package MSC.MARC is one of the existing program codes including contact options (Fig. 6). Using MSC.MARC the contact between two bodies can be defined by two different methods: the contact between a rigid body, defined by geometric elements and a deformable body consisting of FEA elements or the contact between two deformable bodies. The first possibility is advantageous with respect to the size of the model and for parameter studies. The dynamic behavior of the rigid body must be calculated in a user subroutine. Defining the contact bodies as deformable

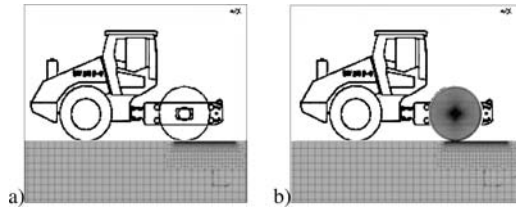


Figure 6. Models in MSC.MARC; a) with rigid drum, b) with deformable drum.

bodies using elements the dynamic behavior of the bodies is calculated automatically by the code. Model size and solution time increase.

The FEA model presented in this chapter uses an elastic material model. The choice of appropriate material parameters allows a realistic reproduction of the dynamic performance of the soil section.

The compaction process is a three-dimensional problem, which is reduced to a two-dimensional calculation model (planar modeling) in the presented examples.

3.1.2 Operation modes of the compaction tool

In Figures 7 and 8 results of numerical calculations of the compaction process using MSC.MARC are presented for a drum with a circular exciter. The MSC.MARC results are compared with measurements of a BOMAG single drum roller BW 213 D (Kröber 1988). The diagrams show sufficiently accurate results. The different declinations are the result of the use of different coordinate systems.

The MSC.MARC results show the status of permanent contact between drum and soil during the compaction process. The results differ due to unequal machine parameters (static load, dynamic mass, exciter force) and due to the diverse soil stiffness. The shapes of the measured and calculated accelerations and displacements are very similar.

The vertical excitation of a drum is modeled by applying a vertical sinusoidal force in the center, comparable to a directed exciter in vertical direction. Figure 9 shows the load-displacement diagram (soil contact force related to the static load versus the oscillation amplitude) for an increasing stiffness of the subgrade, reproducing an increasing compaction status of the soil during the compaction process.

The diagrams in Figure 9 show that the different operation modes of the drum (continuous contact, partial uplift, begin of jumping and double jump) can be calculated using FEA. Irrespective of the definition of the contact bodies (rigid or deformable drum) the results of the FEA simulation calculations are very close to the results of Adam (1996) regarding the quality and the quantity of the curves of the different operation modes of the compaction tool.

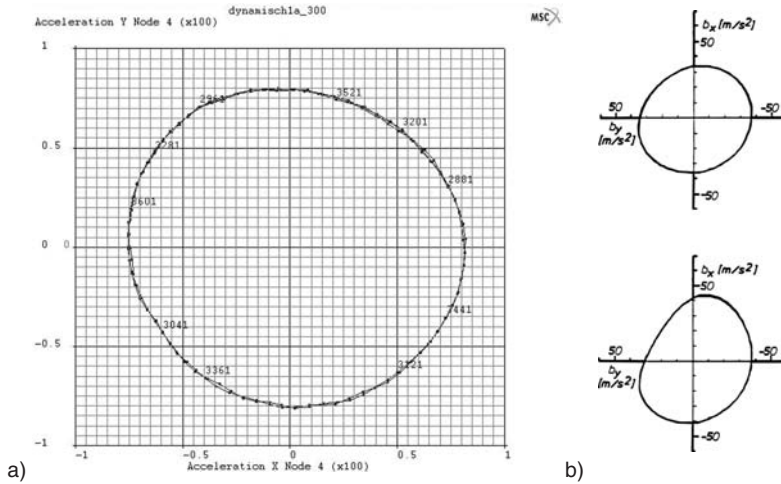


Figure 7. Vertical versus horizontal acceleration of the MSC.MARC calculations for a BOMAG single drum roller BW 213 D-3 with circular exciter system with high amplitude (on the left) in comparison to the measured data of a BW 213 D (Kröber 1988) (on the right).

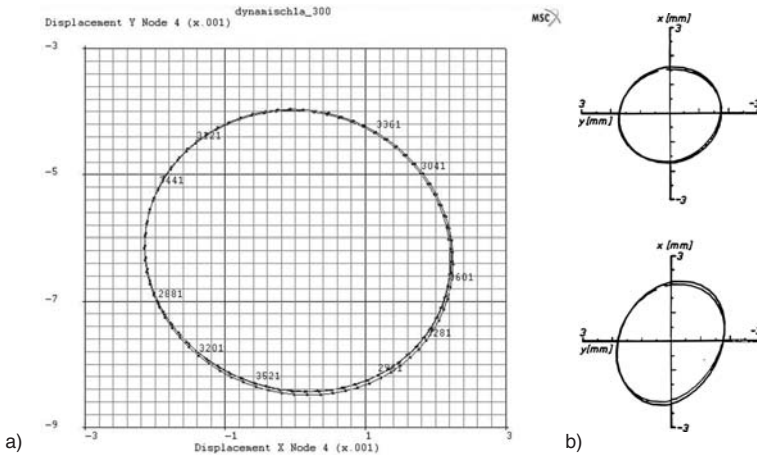


Figure 8. Vertical versus horizontal displacement of the MSC.MARC calculations for a BOMAG single drum roller BW 213 D-3 with circular exciter system with high amplitude (on the left) in comparison to the measured data of a BW 213 D (Kröber 1988) (on the right).

3.1.3 Soil behavior during dynamic compaction

The presented simulation model is not able to reproduce the increase of density and stiffness of soil during compaction due to the applied elastic material model, which does not take into account plastic deformation. Nevertheless, the variation of the soil stiffness enables the simulation of the different modes of the drum, which occur during the compaction process. Regarding the deformations and the stresses of the soil it is possible

to get sufficiently accurate estimations concerning compaction effects and compaction depths.

The main advantage of the FEA model for the system drum-soil in comparison to other present models is the description of the effects inside the subgrade. The stresses in the soil, which are linked to the soil deformations, can be used to predict the depth effect of the compaction tool. In Figure 10 the results of the stresses in the soil versus the corresponding (elastic)

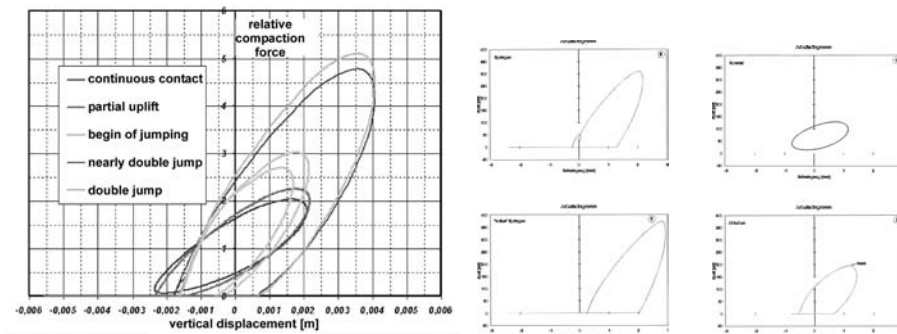


Figure 9. Load-displacement diagram for an increasing compaction with a BOMAG single drum roller BW 213 D-3 (left) compared with semi-analytical calculations (Adam 1996, right).

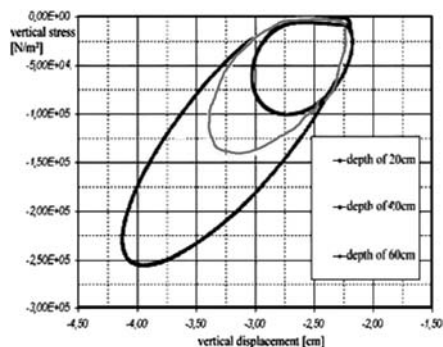


Figure 10. Vertical stresses versus vertical deformation in soil in various depths (20, 40, 60 cm), mode of partial uplift for a BOMAG single drum roller BW 213 D-3 (Erdmann 2002).

deformations in different depths underneath the drum are presented.

3.1.4 Optimization of the shape of a roller drum

A further advantage of the FEA code for simulating compaction processes is the possibility to model the influence of the shape of a compaction tool, e.g. the polygonal drum (Fig. 11). Results of experimental investigations (Markiewicz 2001, Saal 2002) show that compaction by a shaped drum provides a better compaction result in greater depths in comparison to a cylindrical drum as presented in Figure 12 (left) indicating the final densities after compaction with both drums. FEA modeling with MSC.MARC reveals the effectiveness of the polygonal drum and the better compaction result. The contour graphs in Figure 12 show the maximum propagation of the vertical pressure waves in the soil due to the compaction by polygonal and cylindrical drum (25 tons roller).



Figure 11. Polygonal drum and in a single drum roller BOMAG BW 226 DI with polygonal drum.

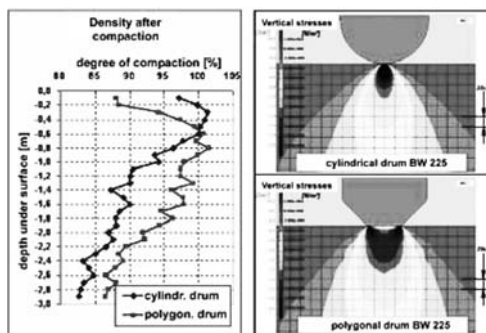


Figure 12. Results of density measurements and calculation results of the polygonal and cylindrical drum BW 225DH-3BVC.

3.1.5 Optimization for compaction performance of vibratory plates

A further example for the significant benefit of FEA analyzes is the simulation of vibratory plates. Thus, it is possible to optimize the running behavior and the compaction performance of the plate so that the number of necessary practical tests during the design process could be significantly reduced.

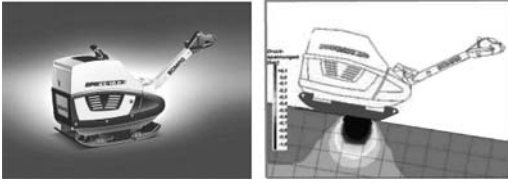


Figure 13. Reversible vibratory plate BPR 65/70 and results of FEA calculations on a slope and stiff soil.

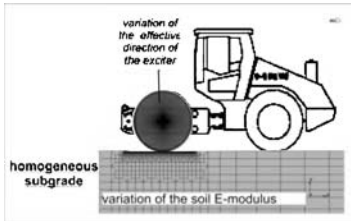


Figure 14. Model for CCC simulation on homogenous soil.

Table 1. Vertical drum amplitudes of a BOMAG BW213 DH-3 BVC.

Vario step	Vertical drum amplitude [mm]	Vertical drum exciter force [kN]	Vario factor
1	0,65	95	0.26
2	1.06	155	0.43
3	1.50	220	0.60
4	2.05	300	0.82
5	2.49	365	1.00

3.2 FEA simulation of CCC

Different compaction states of the subgrade can be modeled by varying the Young's modulus of soil. The calculations for CCC parametric studies have been based on the BOMAG single drum roller BW 213 DH-4 BVC with a directed exciter system and variable direction. Besides the variation of the soil stiffness it is necessary to modify the effective direction of the exciter system (see Figure 14). All necessary data of the variation of the exciter are listed in Table 1.

The graphs in Figures 15 and 16 show the results of the different CCC systems for the variation of the soil stiffness of the homogenous subgrade and of the effective direction of the exciter system. In Figure 15 the FEA results and in Figure 16 the results of the semi-analytical model are presented. The Young's modulus in these figures is based on different definitions in the two different models. The influence of the operation mode of the drum on the CCC value is shown. The values of the four different CCC systems are presented in Chapter 1.

The contour plots in each figure provide an objective comparison between the four different CCC

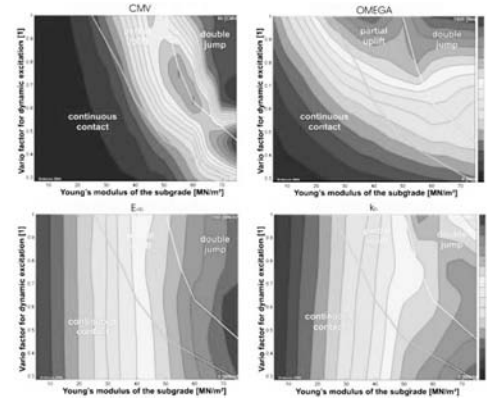


Figure 15. Results with FEA for the compaction of a homogenous subgrade; CCC value dependency on amplitude of drum and on soil stiffness and operation mode of drum.

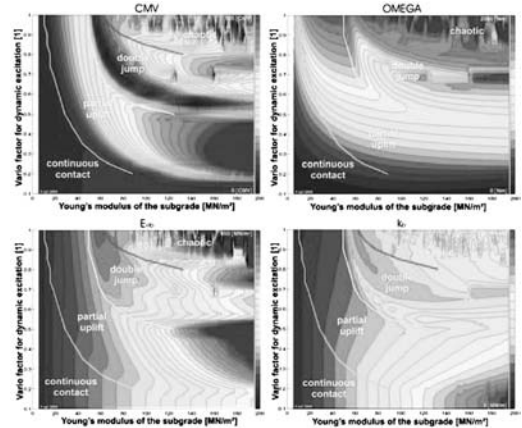


Figure 16. Results with the semi-analytical model for the compaction of a homogenous subgrade; compare Fig. 15.

values. None of them is independent from the dynamic excitation but the dependency of the CCC values E_{vib} and the k_B is minor.

These two values have been developed for rollers with variable and automatically controlled rollers. The regulations for the use of a CCC system demand constant parameters of the roller (amplitude and frequency of the drum) due to the necessity of constant measurement depth. Thus, the values Omega and CMV can be used for compaction control although they exhibit a higher dependency on the machine parameters.

Considering the CMV value in Figure 15 at a vario factor of 0,8, where the value is nearly constant for a Young's modulus between 5 and 35°MN/m² the operation mode changes from continuous contact to partial uplift. CMV value increases up to a Young's modulus of 55 MN/m² from where it decreases rapidly due to the

change to the operation mode double jump. The diagrams help to evaluate the strengths and weaknesses of the different CCC values, their sensibility regarding the variation of the soil stiffness, the operation mode of the drum, exciter force and drum amplitude (vario factor).

4 FEA SIMULATION OF COMPACTION PROCESS BY HYPOPLASTICITY

4.1 General aspects

Hypoplasticity is a material model for granular materials developed at the University of Karlsruhe in the 1970s (Kolymbas 1978). Since the first approaches the hypoplastic law was improved for a more realistic reproduction of the reality (Herle 1997, Niemunis 2002). The implementation in a FEA model was realized for the code ABAQUS by the material user subroutine UMAT. The hypoplastic law with intergranular strain (Herle & Niemunis 1997) enables the calculation of dynamic cyclic problems such as vibratory roller compaction (Kelm, 2004) taking into account the elastic deformations between the grains. The latest extension was done by Niemunis (2002) at the University of Bochum for cohesive materials, which is of interest for soil compaction calculations.

Hypoplasticity is a constitutive law of a rate type, a relation which associates strain rate to stress rate. The nonlinear behavior of the hypoplastic law is modeled by the stress dependence of the stiffness.

$$\overset{\circ}{\mathbf{T}} = \mathbf{h}(\mathbf{T}, \mathbf{D}, e)$$

- with: $\overset{\circ}{\mathbf{T}}$: objective stress rate
- h: tensor function
- D: strain rate
- e: void ratio

4.2 Element tests with MSC.MARC

Before starting complicated and extensive soil compaction calculations with FEA including the hypoplastic material law it is necessary to calibrate and validate the hypoplastic law integrated in MSC.MARC. In the literature (Kelm 2004) results of simulations with hypoplasticity of the so-called element tests are presented in comparison to practical tests. Figure 17 shows results of the static cyclic tri-axial test calculated with ABAQUS in comparison to the MSC.MARC providing similar results.

4.3 Compaction calculations with hypoplasticity

MSC.MARC enables the integration of the hypoplastic material law for soil so that compaction calculations can be executed with a reasonable plastic material model. The simulations are very complex due to the

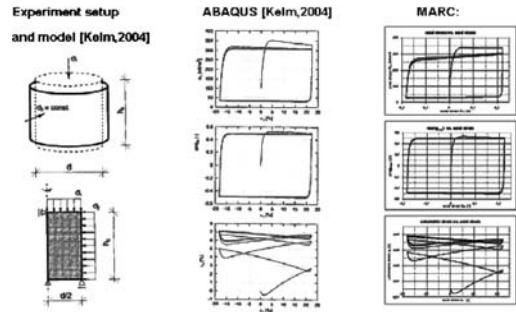


Figure 17. Static cyclic triaxial test.

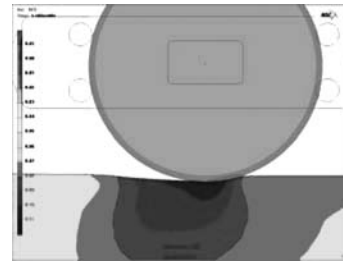


Figure 18. Compaction simulation calculation with MSC.MARC using the hypoplastic material law for the soil; void ratio in the soil during and after the pass with the roller.

non-linearity caused by the contact problem and the hypoplastic material law. An example of recent results of calculation with MSC.MARC is presented in the color contour plot of Figure 18, where the void ratio of the soil is shown during a compaction pass with a single drum roller.

5 CONCLUSION

The FEA model with elastic material properties describes excellently the dynamic performance of a compaction tool. It is very helpful for interpretations of compaction phenomena in the soil. Existing CCC systems have been simulated with the MSC.MARC model providing accordance to practical experiments and to the results of semi-analytical models.

For compaction simulation an appropriate material law including plastic deformations and dynamic cyclic loads is necessary. The hypoplastic law for soil simulates the phenomena in the soil during a compaction process with sufficient accuracy.

REFERENCES

Adam, D. 1996. Flächendeckende Dynamische Verdichtungskontrolle (FDVK) mit Vibrationswalzen. Dissertation. Technische Universität Wien.

- Erdmann, P. 2002. Einsatz von MSC.MARC zur Simulation von Problemstellungen in der Bodenverdichtung. *Beitrag zum MSC.MARC-Technologietag*. München.
- Herle, I. 1997. Hypoplastizität und Granulometrie einfacher Korngerüste. Dissertation. Universität Karlsruhe.
- Herle, I. und Niemunis, A. 1997. A hypoplastic model for cohesionless soils with elastic strain range. *Mechanics of cohesive-frictional materials Vol.2: 279–229*.
- Kelm, M. 2004.: Numerische Simulation der Verdichtung rolliger Böden mittels Vibrationswalzen. Dissertation. TU Hamburg-Harburg.
- Kolymbas, D. 1978. Ein nichtlineares viskoplastisches Stoffgesetz für Böden. Dissertation. Universität Karlsruhe.
- Kopf, F. 1999. Flächendeckende Dynamische Verdichtungskontrolle (FDVK) bei der Verdichtung von Böden durch dynamische Walzen mit unterschiedlichen Anregungsarten. Dissertation. Technische Universität Wien.
- Kröber, W. 1988. Untersuchung der dynamischen Vorgänge bei der Vibrationsverdichtung von Böden. Dissertation. Technischen Universität München.
- Markiewicz, R. 2001. Untersuchungen zur Arbeitsweise und Tiefenwirkung der "Polygonbandage" auf nichtbindigem Boden. Diplomarbeit. Technische Universität Wien.
- Niemunis, A. 2002. Extended hypoplastic models for soils. Habilitation. Universität Bochum.
- Saal, S. 2002. Verdichtungsuntersuchung mit einem BOMAG-Walzenzug mit Polygonbandage. Diplomarbeit; Universität Leipzig.

Numerical approach of detection of foundations of buildings by propagation of a wave

P. Alfonsi & E. Bourgeois

Laboratoire central des Ponts et Chaussées, Paris, France

ABSTRACT: Civil engineering works in urban areas induce strains and displacements in the structures at the ground surface, which can create a wide range of damage (from cracks in the walls to loss of stability). Several factors make it difficult to check that the planned works are likely or not to induce such damages: one of them is the fact that the exact location, depth and design of the foundations of structures built several decades (or more) ago are not always known with a good accuracy. This paper presents a preliminary numerical simulation aimed at discussing the possibility of detecting the position and size of foundations in the ground by emitting a wave and recording the reflected signal.

1 INTRODUCTION

Many underground works take place in urban areas, where the proximity of existing and more or less recent buildings becomes a major concern, since the available data on the geometry and design of their foundations is often inaccurate and incomplete: it is therefore difficult to assess whether or not the strains induced by the construction works are likely to damage the existing structures. It follows that it would be useful to develop innovative methods and equipment making it possible to get a complete knowledge of geotechnical conditions: this objective is referred to as “transparent ground” in the terms of the European Construction Technology Platform (ECTP, 2005).

Many studies have been carried out in order to discuss the feasibility and the performance of the detection of underground cavities by wave propagation. Geophysical techniques are cheaper and much simpler to use than the traditional techniques of geotechnical survey, which resort to borings and/or samplings; and experience has shown that anomalies such as cavities in relatively homogeneous grounds can be detected with an acceptable precision.

In what follows, we present some finite element numerical analyses of wave propagation in an heterogeneous medium, undertaken with the aim of increasing the information that can be gained from the results of geophysical surveys, and of discussing the feasibility of the detection of foundations by wave propagation techniques.

All computations presented hereafter were carried out with the code CESAR-LCPC (Finite Element Method).

2 FRAME OF THE ANALYSIS

The model is made up of the subsoil of a building and of the surrounding ground. An impact is emitted in a well dug vertically near the building. The foundations of the building are modeled by one to three “piles” with mechanical properties higher than those of the ground (fig.1). Note that the numerical model is built under plane strain assumptions, which implies that the simulation accounts for walls rather than piles.

First, we performed a preliminary calculation with mechanical characteristics homogeneous throughout the mesh (which means that there is no piles in the ground). Then, a second calculation was carried out with a greater stiffness for the left pile, nearest to the well.

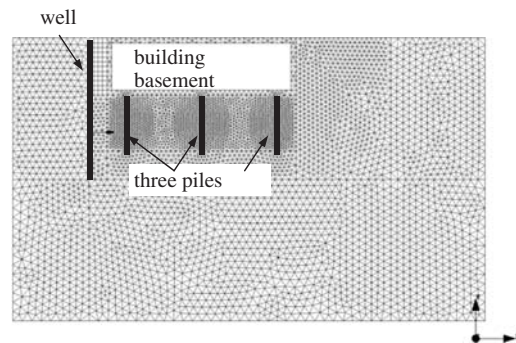


Figure 1. Numerical model with one well, the basement of a building, and three piles; mesh generated with CESAR-LCPC.

The analysis of results is focused on the horizontal displacements of points located in the well, near the building, at a depth greater than that of the basement floor. We also examined the possibility to detect the presence of the piles on the basis of a signal measured at the ground surface on the right of the building, but results are not presented hereafter.

A test in 3D will supplement the results but the difficulty in the modeling of dynamic phenomena lies in the size of the elements: avoiding numerical dispersion in a 3D model requires large numbers of nodes.

3 2D NUMERICAL MODEL

3.1 Main features of wave propagation simulation

The finite element simulation of wave propagation raises several difficulties:

- in the first place, special attention must be paid to numerical dispersion, which may lead to poor results if the mesh is too coarse (Semblat & Brioiat, 2000). The dispersion results from inconsistent choices between the discretizations in time and space (Bamberger & al., 1980). It can be reduced by adapting the average size of the elements to the wavelength;
- this strong requirement regarding the size of the elements implies that the mesh dimensions are limited, because the software can handle only a limited number of nodes (and because computation times increase steadily as the number of nodes increases);
- in isotropic and homogeneous solids, waves can propagate in the bulk of the material, with displacements parallel or orthogonal to the propagation direction (for P and S waves respectively). If there is a free surface, surface waves such as Rayleigh waves can be generated. In the simulation undertaken here, wave propagation takes place in a heterogeneous material: the presence of interfaces between materials creates perturbations in the wave propagation. One should also take into account the attenuation associated with the wave front expansion. In what follows, we limit the scope of the numerical simulations to the displacements in the vicinity of the emission well, so that the influence of the heterogeneities and of the free surface remain moderate. In this restricted framework, it has been shown that wave propagation can be modelled accurately by means of the finite element method (Eiselt, 1993);
- in the last place, it must be recalled that in a 2D approach, the piles are replaced by walls of infinite length in the direction perpendicular to the plane of the mesh. It is therefore very likely that their influence on the wave propagation is very different from that of the real piles because the latter are

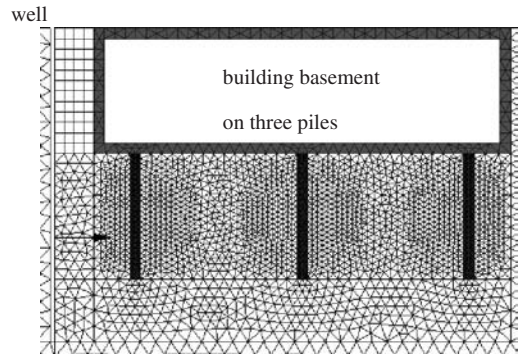


Figure 2. Close-up view of the central part of the mesh: well, basement, piles (mesh generated with CESAR-LCPC).

discontinuous: this truly three-dimensional feature of the real problem makes it necessary to make at least one 3-D simulation in order to check the validity of a 2-D approach, even if the mesh used for the three-dimensional computation is much coarser than that used for plane strain analyses.

3.2 Principle of the 2D simulation

The principle of the simulation consists in computing the response of the ground to a blow in the well at a depth of 7.5 m below the ground surface. The well diameter is 0.20 m and its depth is 15 m. The distance between the well and the basement wall is 2 m. The width of the basement is equal to 20 m. The building itself (above the ground surface) is not taken into account in the simulations. The walls are 0.50 m thick and the basement floor is 5 m below the surface. The pile length is 6 m and the distance between two rows of piles is 7.50 m.

The numerical model includes 21490 nodes and 10491 elements. The emission of the signal is located at a depth of 10 m (shown by the black arrow on fig.2).

It is recalled that the wave velocity is given by:

– for P-waves:

$$V_P = \left(\frac{E(1-\nu)}{\rho(1+\nu)(1-2\nu)} \right)^{1/2} \quad (1)$$

– for S-waves:

$$V_S = \left(\frac{E}{2\rho(1+\nu)} \right)^{1/2} \quad (2)$$

The elements associated with the basement, the ground and the piles are attributed different elastic properties, given in table 1. The corresponding velocities are given by table 2.

Table 1. Material properties.

	E (GPa)	ν	ρ (t/m ³)
Ground	10 ³	0.25	2.5
Basement walls and floor	10 ²	0.30	3.5
Piles	10 ³	0.29	3.8

Table 2. Wave velocities in the different materials.

	V _P (m/s)	V _S (m/s)
Ground	693	400
Basement walls	6202	3315
Piles	18570	10100

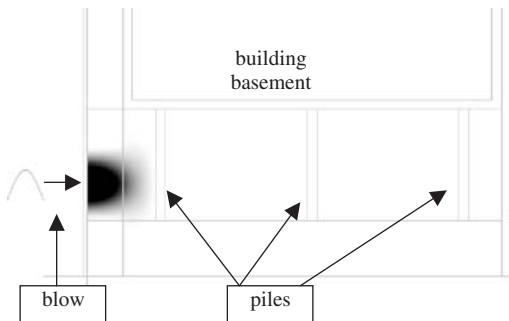


Figure 3. Principle of the simulation: emission of the signal.

It can be noted that there are significant differences between the velocities of P and S waves in the materials involved in the simulation (table 2). Given the contrast between the wave velocities in the ground and in the piles, one can expect to observe large differences between the displacements computed in the well in the computations carried out with and without piles.

3.3 Simulation with one row of piles (on the left)

The emitted signal is a half-sinusoid, with a frequency of 80 Hz (fig.3). The maximum applied force is $F = 1000$ N.

It must be emphasized that geophones provide velocities, but in a first approach, the analysis of the results will be based on the horizontal displacements in the well at depths of 8, 9, 10, 11 and 12 m (10 m being the depth of the blow).

In spite of the value of the force taken into account in the computations, the displacements are very small (fig.4) but compatible with the sensibility of standard geophones.

It can be observed that the amplitude of the signal decreases steeply as the distance to the blow increases,

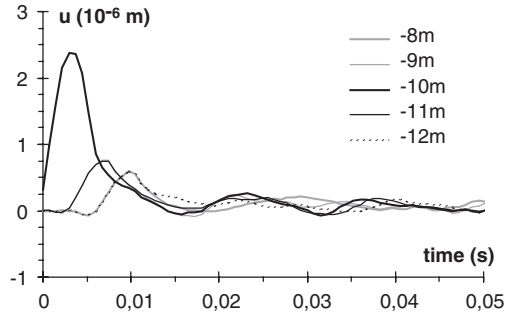


Figure 4. Horizontal displacements in the well.

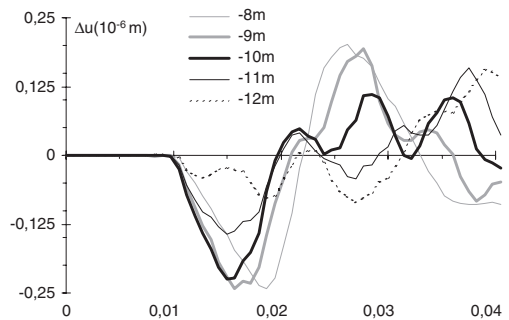


Figure 5. Differences between horizontal displacements computed in the well according to the properties of the pile (different or equal to those of the ground).

and that there is a difference in the signal computed above and below the source, due to the basement, the ground surface and the piles height.

3.4 Comparison of the displacements with and without pile

We now discuss the possibility to detect the presence of a pile on the basis of the displacements of the well: we compare the signal obtained in the previous computation with the signal obtained if the same material properties are associated with all the elements outside the basement. Figure 5 shows the difference between the horizontal displacements with one row of pile (on the left of the basement) and with a model in which the «pile» has the same properties as the surrounding ground.

The return of the wave occurs after roughly 0.01 s, which provides a confirmation of the presence of a material much stiffer than the soil (fig.5). The displacements are larger for points above the depth of the emission than below.

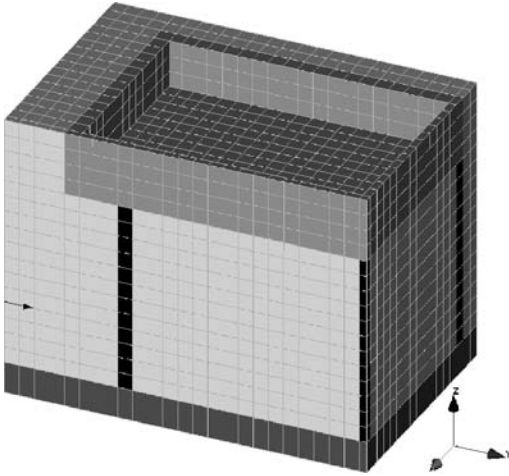


Figure 6. 3D mesh with a basement level and 4 piles. The position of the signal emission is shown by the black arrow. (mesh generated with CESAR-LCPC).

The conclusion of this preliminary plane strain analysis is that it seems that the reflected signal makes it possible to detect the presence of a foundation, or more generally of heterogeneities with much higher velocities than that of the ground. It must be pointed out that these heterogeneities can be of different natures, so that the method makes no difference between rock blocks, rubble, etc. If wave analysis shows the presence of heterogeneities in the ground, it remains necessary to check that they are foundations. Besides, the main shortcoming of the numerical approach lies in the fact that it is carried out under plane strain assumptions, the piles being implicitly replaced by infinitely long walls.

4 3D NUMERICAL MODEL

4.1 First approach

Given the limits of the numerical tools, a three-dimensional mesh has been designed to deal with a problem similar to the one discussed in the previous section. The three-dimensional mesh includes 29754 nodes and 6484 elements (fig.6). To keep the number of nodes and the computations times within acceptable limits, the dimensions of the mesh around the basement had to be significantly reduced.

The length of the piles is 6 m, the cross section is a 0.5×0.5 m square. The part of the building basement taken into account in the mesh is $8 \text{ m} \times 10 \text{ m}$ and the depth is 2 m. The impact is located at a depth $i = 10 \text{ m}$, on the left corner of the mesh.

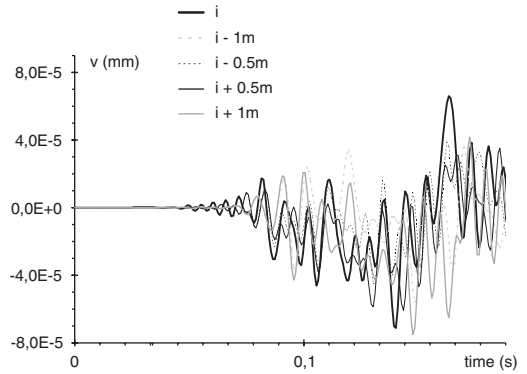


Figure 7. Horizontal displacements in the well (3D model).

The numerical solution requires high computational capacities: computations times are closer to one week than to one day.

The horizontal displacements computed in the well, at depths of $i \pm 1 \text{ m}$ and $i \pm 0.5 \text{ m}$ are plotted on figure 6 and compared to the displacements at the depth i of the impact. The values obtained are below what can be measured by standard geophones.

This analysis illustrates the difficulties of a 3D approach: computation times are prohibitive, and the results tend to show that, for realistic values of the geometrical and material parameters, the method does not make it possible to locate the foundations or even to detect their presence.

Two parameters have probably a significant influence on the numerical results: the minimal dimensions of the foundations, and the distance between the well and the piles.

4.2 Parametric analysis

For this parametric study, we had to simplify the geometry, in order to reduce the mesh to approximately 19000 nodes and 4000 elements (fig.8). The computation lasts approximately 5 hours on a NEC computer of the TX-7 series running under Red Hat Linux.

The basement is represented by a continuous slab (10 m long, 4 m wide and 0.5 m thick). The left pile is placed at a distance of 1 m from the corner of the slab, and the other one is placed on the opposite side of the mesh. Both piles have rectangular cross-sections with a width of 1.5 m along the y axis (see fig. 8).

The isolevel surfaces of the horizontal displacement along the direction of the wave propagation (y -axis) show that the perturbation created by the pile (fig. 9). The results correspond to a time step for which the wave tends to pass round the pile and a reflected wave appears. Besides, it can be noted that

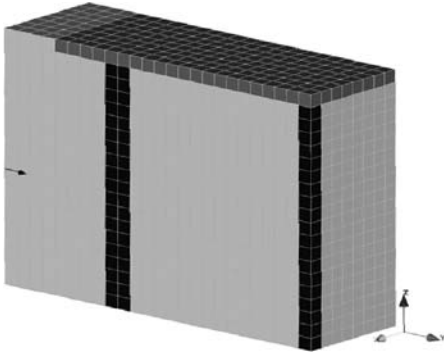


Figure 8. 3D numerical model with two piles and a slab. The black arrow is the position of the signal emission.

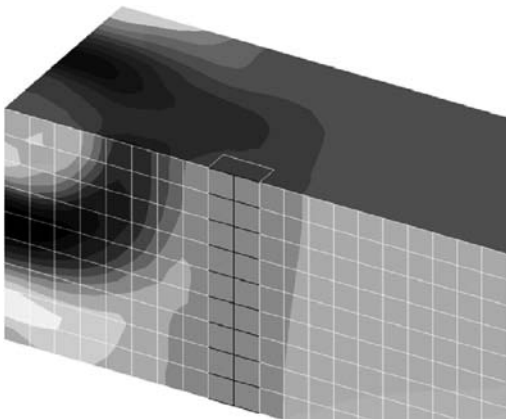


Figure 9. Horizontal displacements computed in the well for the 3D model ; the mesh is splitted by a horizontal plane at the depth of the signal emission.

the wave propagates very quickly throughout the entire pile, since the velocity of the wave is 20 times greater in the pile than in the ground.

The values of the horizontal displacements show a clean signal for small values of the time elapsed after the emission, and the amplitude seems to be large enough to be recorded by geophones (fig. 10). This result makes it possible to discuss, on the basis of numerical simulations, under what conditions (size of the pile and distance to the well) the presence of a material with higher mechanical characteristics can be detected by wave propagation.

4.3 Influence of the distance between the emission and the piles and of the pile diameter

The first 3D model included piles with small diameters, thus hardly detectable. In order to assess the

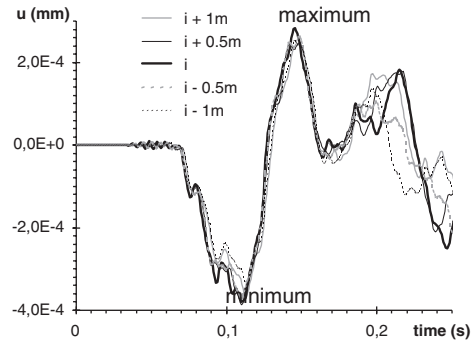


Figure 10. Horizontal displacements computed in the well for the 3D model.

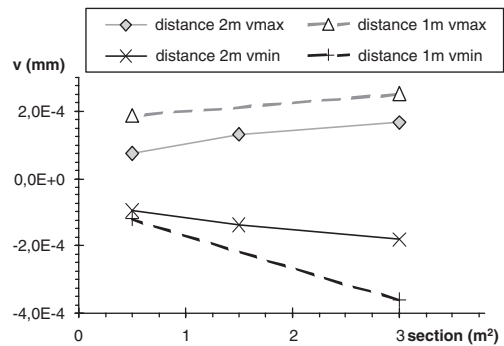


Figure 11. Maximum and minimal values of the horizontal displacement for various pile cross-sections, and for two values of the distance between the pile and the emission well.

validity of the method, we have undertaken additional simulations with different pile cross-sections, and different piles locations (1 or 2 m from the corner of the basement).

The comparison is based on the difference between the horizontal displacement with and without piles, averaged over five points above and below the emission depth. The time interval is limited to 0.2 s so that only the first reflection is taken into account.

It can be observed, on the one hand, that the amplitudes are greater for smaller values between the well and the piles, and, on the other hand, that the amplitude is greater for larger piles (fig.11).

5 CONCLUSION

The results of the preliminary numerical analysis presented here tend to confirm the feasibility of the

detection of foundations of buildings by wave propagation, at least if the foundations are large enough (such as foundation barrettes for instance).

It can be noted that the method discussed here is similar to phonic inspection methods, the main difference being that in the case of inspection the exact position of the foundation to be examined is known, whereas the detection deals with foundations whose presence and location are uncertain. The main difficulty lies in the fact that the emission well must be very close to the pile to get a clear signal and to limit the influence of damping and of multiple reflections (on rock blocks, basement walls, ...). The results thus remain to be confirmed by a wave propagation experiment on a real structure.

Computations show that a 2D analysis may give elements to locate an heterogeneity on the wave path, but only three-dimensional analyses can provide information about its size. Unfortunately, it is still

necessary to use very simplified models in order to keep computations times acceptable.

REFERENCES

- Bamberger Y., Chavent G., Lailly P. (1980). Etude de schémas numériques pour les équations de l'élastodynamique linéaire. Rapport de recherches 41, INRIA ed., France.
- ECTP (2005). FA-UndergroundConstructions_SRA-VISION 2030-23Nov05, www.ectp.org/, documentation.
- Eiselt F. (1993). Etude de la propagation d'ondes sismiques de hautes fréquences: application à la reconnaissance des cavités de proche sous-sol. Thèse de doctorat. Ecole Centrale de Lille.
- Semblat J.F., Brioist J.J. (2000). Efficiency of higher order finite elements for the analysis of seismic wave propagation *Journal of Sound and Vibrations*, vol. 231, no. 2, 460–467.

Effective stress analysis for the seismic response of shallow foundations on liquefiable sand

K.I. Andrianopoulos, G.D. Bouckovalas, D.K. Karamitros & A.G. Papadimitriou

School of Civil Engineering, Geotechnical Division, National Technical University of Athens, Greece

ABSTRACT: The seismic response of shallow foundations on liquefiable sand is studied herein through fully coupled effective stress analyses. The numerical methodology that is used, is based on a bounding surface model for non-cohesive soils implemented into the Finite Difference code FLAC2D. Model constants are calibrated against element laboratory tests on Nevada sand, while the simulation of centrifuge model tests of the VELACS project validates the User-Defined Model's performance on boundary value problems. Using this well established methodology, parametric analyses are performed, for the common case of a thin clay cap overlying a liquefiable sand layer, in order to provide insight to the mode of failure and the mechanism of settlement accumulation. It is shown that groundwater flow during and immediately after shaking affects the response, while there is a "critical thickness" of the clay cap beyond which sand liquefaction does not lead to bearing capacity degradation is also evaluated.

1 INTRODUCTION

Estimation of the seismic response of shallow foundations during a strong earthquake has been proven a difficult task throughout the years. The main cause of this difficulty arises from the fact that soil behaves in a highly non-linear manner when subjected to large cyclic strains. It can deform substantially and, when saturated, can develop high pore pressures and finally liquefy. Liquefaction consequently leads to severe loss of bearing capacity, which damages seriously the superstructure. Extensive damage to shallow foundations due to liquefaction has been reported in numerous cases in the past, from Niigata (1964) earthquake to the more recent 1999 M 7.4 Kocaeli earthquake.

Despite the severity of damages, relatively little has been achieved towards the development of a consistent methodology for the design of foundations systems under these circumstances. Usually, the presence of superstructure is neglected and calculations are performed for free-field conditions. The onset of liquefaction is evaluated and empirical correlations for settlements, developed for free-field conditions, are used. However, the presence of superstructure differentiates significantly the response from that under free-field conditions, so that such methods prove too approximate.

The complicated response of soil-structure system is studied herein through a fully coupled effective stress analysis. Using a recently developed numerical methodology, the common case of a non-liquefiable

clay cap overlying a liquefiable sand layer is investigated through parametric analysis.

The research focuses upon three crucial questions for the development of a design methodology:

- The shape of the failure surface, when the sand layer liquefies.
- The critical thickness of the clay cap beyond which sand liquefaction does not affect foundation system.
- The role of sand permeability and groundwater flow.

Findings of this research are compared with those of an analytical methodology, originally proposed by Cascone & Bouckovalas (1998) and extended by Bouckovalas et al. (2005), for the pseudo-static evaluation of seismic bearing capacity of footings on liquefiable soil.

2 NUMERICAL METHODOLOGY

The cornerstone of the numerical methodology used herein is a recently developed bounding surface model for non-cohesive soils which is implemented to FLAC (Itasca 2005) using its UDM (User-Defined Model) capability (Andrianopoulos et al. 2006). This new UDM is a bounding surface model with a vanished elastic region that incorporates Critical State Theory.

It is based on a recently proposed model (Papadimitriou et al. 2001, Papadimitriou & Bouckovalas 2002), and has been developed with the ambition to simulate the cyclic behavior of non-cohesive soils under various (small-medium-large)

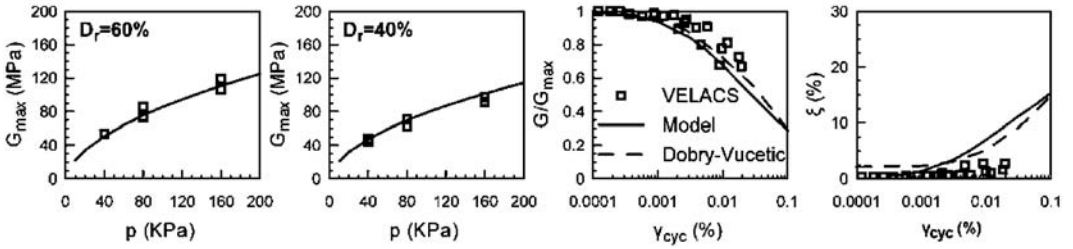


Figure 1. Summary comparisons of simulations versus laboratory data for cyclic shearing in terms of G_{max} , G/G_{max} - γ_{cyc} and ξ - γ_{cyc} .

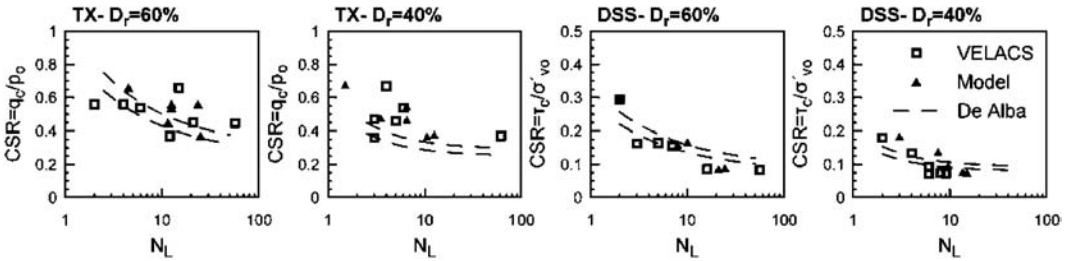


Figure 2. Summary comparisons of laboratory data versus simulations for cyclic shearing in terms of DSS- the number of cycles N_L to initiate liquefaction.

cyclic strain amplitudes, initial stress and density conditions, using a single set of parameters.

In its current form, the model incorporates three open cone-type surfaces with apex at the origin of stress space: (i) the critical surface, (ii) the bounding surface and (iii) the dilatancy surface. Its basic feature is the direct association of shear behavior to the state parameter ψ (Been & Jefferies 1985), which is defined with respect to a unique critical state line (CSL) or steady state line. The non-linear soil response under small to medium cyclic strain amplitudes is simulated mainly by introducing a Ramberg-Osgood type hysteretic formulation.

The aforementioned constitutive model was incorporated to the commercial code FLAC, using the UDM option. To ensure numerical stability, the sub-stepping technique with automatic error control (Sloan et al. 2001) was adopted, which belongs to the family of effective explicit algorithms.

The model was calibrated against data from element laboratory tests performed on fine Nevada sand at relative densities of $D_r = 40\%$ and 60% and initial effective stresses between 40 and 160 kPa (Arulmoli et al. 1992). In particular, the data originate from resonant column tests as well as undrained cyclic direct simple shear and triaxial tests. Thus, they offer a quantitative description of various aspects of non-cohesive soil response under cyclic loading, such as shear-modulus degradation and damping increase with cyclic shear strain, liquefaction resistance and cyclic

mobility. Results from this calibration are presented in Figures 1 and 2.

The numerical methodology has been consequently validated against results from the well known VELACS experimental project (Arulmoli et al. 1992). In that effect, results from centrifuge tests No. 1 and No. 2 were originally used, simulating the one-dimensional (1-D) response of a liquefiable soil under level and mildly sloping sites respectively.

Furthermore, centrifuge test No. 12 was used, which simulates the more complex response of shallow foundations on liquefiable sand layer, underlain a non-liquefiable crust. The results from the latter validation are presented in Figures 3 and 4. The comparisons are made in terms of excess pore pressures, accelerations and displacement time histories, at the vicinity of the structure as well as at the free-field. Further details from this comparison can be found at Andrianopoulos et al. (2006). As it is observed, the numerical methodology predicts reasonably well the measured response.

3 PARAMETRIC ANALYSES

3.1 Problem description

The common case of a strip foundation resting on a non-liquefiable clay crust, overlaying a liquefiable sand layer, is examined parametrically. The clay cap corresponds to an overconsolidated clay with undrained shear strength $c_u = 40$ kPa, while the sand layer refers

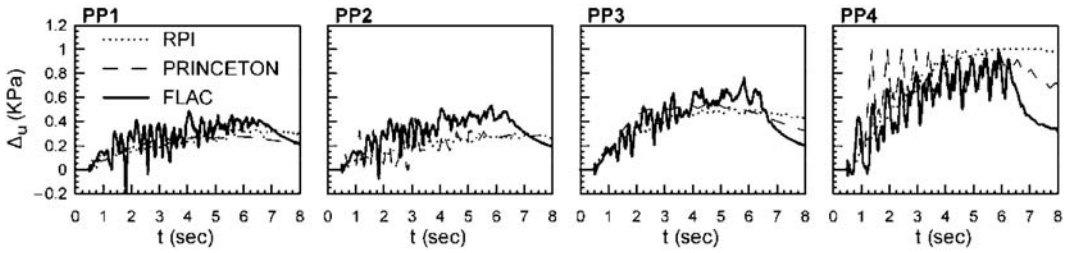


Figure 3. Excess pore pressure ratio time histories.

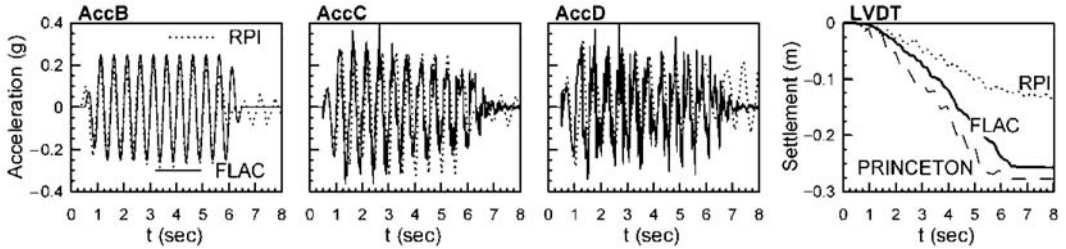


Figure 4. Acceleration and settlement time histories.

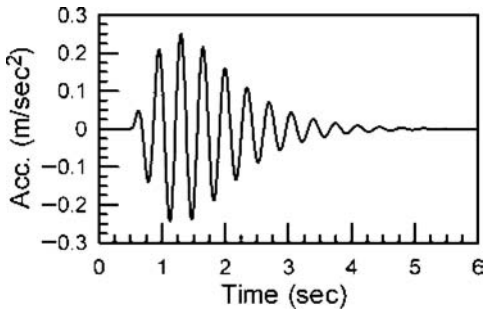


Figure 5. Input motion.

to a liquefiable fine-grained sand of relative density $D_r = 50\%$. The permeability of the sand layer is assumed equal to 2.1×10^{-3} cm/sec, while the clay cap is assumed practically impermeable, i.e. with permeability equal to 1×10^{-7} cm/sec.

The width of the foundation is taken as $B = 4$ m, while the thickness of the clay cap H is variable. The foundation system corresponds to a rigid foundation. Inertia effects are neglected. Furthermore, the model is subjected to a dynamic excitation, applied on the base of the sand layer. The input motion consists of a Chang's signal with peak acceleration equal to 0.25 g, and shaking time approximately 3 sec (Figure 5).

The numerical results presented herein, are commented in connection with a simple pseudo-static approach presented earlier by Cascone and Bouckovalas (1998) and refined by Bouckovalas et al. (2005), for the design of shallow foundations at

liquefiable regimes. Based on analytical solutions for shallow footings on a two layered soil, proposed by Meyerhof and Hanna (1978), this methodology computes the post-seismic static bearing capacity, taking into account the average excess pore pressure ratio that is expected to develop under the footing at the end of shaking. The correction coefficients are computed as a function of initial soil properties, geometry of the footing and soil profile. Also, the minimum required thickness of the clay cap is estimated, so that liquefaction does not affect the bearing capacity.

3.2 Simulation details

The width of the mesh used for the analyses, was 60 m ($=15B$), while the total simulated depth equals 20 m. The elements used varied from (width \times thickness) 1 m \times 1 m under the footing to 2 m \times 1 m at the free field.

The bottom nodes were fixed in both horizontal and vertical direction. "Tied-node" boundary conditions were considered for the lateral boundaries, by restraining the horizontal displacements of the corresponding nodes on the left and right boundary to have the same value. All boundaries were considered impermeable, apart from the top boundary where inflow and outflow were allowed.

The sand layer was modeled using the previously described UDM, while the inbuilt Mohr-Coulomb model ($c_u = 40$ kPa, $\phi = 0$) was used for the non-liquefiable clay crust. Three different clay cap thicknesses were examined, namely $H = B$, $2B$ and $3B$

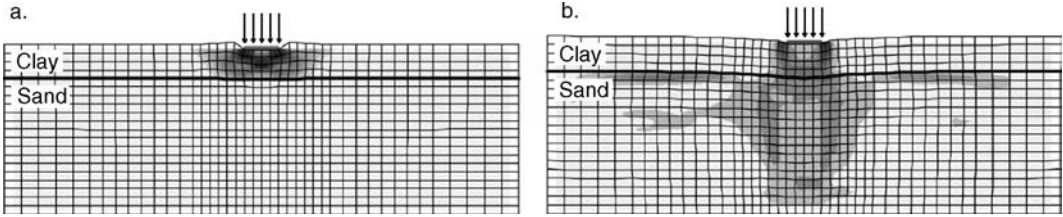


Figure 6. Deformed mesh, shear strain increment contours and displacement vectors indicating the mode of (a) static and (b) dynamic failure.

(i.e. 4 m, 8 m and 12 m, respectively). In all cases, water level was assumed to be located 1 m above the soil surface, in order to ensure saturated conditions.

The foundation was considered rigid and totally bonded to the soil. The analyses were performed in two (2) stages.

- The foundation was first loaded statically, with a uniform surcharge load (130 kPa). This value corresponds to a static factor of safety equals to 2, for the case of clay cap thickness $H = B$ ($q_{ult,cs}^{H=B} = 260$ kPa).
- Then, the model was subjected to dynamic excitation. During the dynamic analyses, groundwater flow was coupled to mechanical behavior.

3.3 Mode of failure

Figure 6 compares the deformed mesh and the contours of shear strain increments for two different modes of failure, namely failure for static loading equal to the ultimate bearing capacity and failure at the end of shaking, considering an initial static safety factor of 2.

Focusing in Figure 6a, failure due to static loading is shown to occur inside the clay cap. On the other hand, Figure 6b shows that the mechanism of failure after liquefaction of subsoil, is quite different. A punch-through type of failure is observed within the clay cap and the underlying sand, where the shear strain rate contours indicate the formation of an orthogonal prism underneath. Liquefaction of the surrounding soil seems to reduce this block's lateral support and result in the accumulation of large vertical strains. In fact, for the case of $H = B = 4$ m, liquefaction of the sand layer resulted in the development of settlements equal to 15.6 cm.

The above failure mechanism due to liquefaction, resembles the one assumed by the analytical method of Bouckovalas et al. (2005), where the bearing capacity of the sand layer degrades gradually as a function of pore pressures development. Furthermore, this type of failure has been observed in numerous earthquakes, and is typical of relatively low height over width ratio buildings, which settle almost vertically with little deviation from verticality.

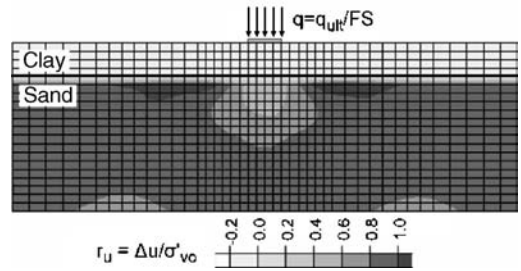


Figure 7. Excess pore pressure ratio contours at $t = 5.0$ sec.

Proceeding further to the investigation of the failure mechanism, Figure 7 provides insight to the evolution of excess pore pressures during shaking. Namely, contours of excess pressure ratio $r_u = \Delta u / \sigma'_{vo}$ are presented at the end of shaking ($t = 5$ sec). Note that excess pore pressure ratio r_u is an index of proximity to liquefaction, normalizing excess pore pressures Δu developed during shaking to the initial effective vertical stress σ'_{vo} . Values of r_u close to 1 indicate liquefaction of the subsoil.

It is clearly shown that the presence of the foundation, and the resulting increase of soil stresses underneath it, significantly differentiates the response from the free-field conditions.

Developed excess pore pressures inside the sand layer, immediately below the foundation, are not able to reduce the effective stresses to zero, and hence no liquefaction is observed. Also, at the perimeter of the superstructure, the increase of initial shear stresses, without an equivalent increase of the mean effective stresses, brings the subsoil closer to failure, and hence closer to liquefaction. This observation, accompanied with migration of water from the axis of foundation to free-field, potentially explains the presence of liquefied soil at the perimeter of foundations, that has been observed in numerous earthquakes. These effects of the superstructure are usually neglected in current practise.

Figure 8 compares the excess pore pressure ratio time histories developing at several depths underneath the footing and at the free field, as well as the recorded settlements. Even though the values of r_u

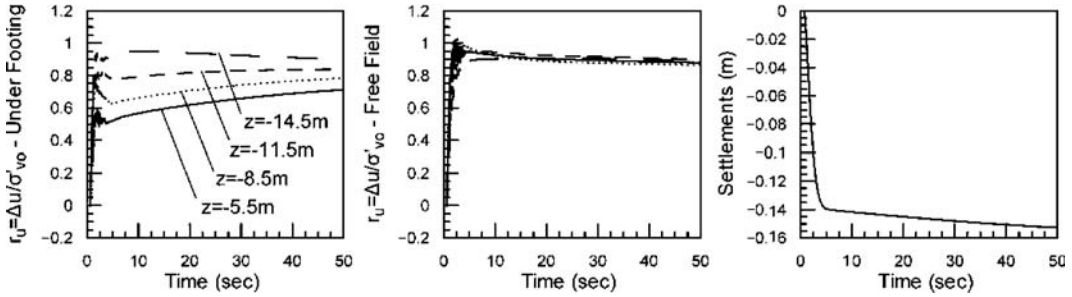


Figure 8. Long-term evolution of excess pore water pressures (at various depths underneath the footing and in the free field) and foundation settlements.

remain close to 1 at the free field, at the axis of foundation and 1.5 m below the clay cap (5.5 m below the soil surface) the excess pore pressure ratio remains lower than 0.6 during shaking. Moving to larger depths, normal and shear stresses applied from the footing are reduced, and excess pore pressure ratios tend to become equal to the ones developing in the free field.

This variation of pore pressures with depth initiates vertical upward flow, resulting to a long term increase of the excess pore pressure ratio under the footing, as clearly shown in Figure 8. On the other hand, excess pore pressures in the free field remain high, because of the existence of the relatively impermeable clay cap. It is noticed, though, that footing settlements continue to increase at a slow rate during the consolidation process. This is attributed to the redistribution of excess pore water pressures underneath the foundation. However, the long term settlements (1.6 cm) are generally smaller compared to the ones developing during shaking (14 cm).

3.4 Evaluation of “critical depth”

From a practical point of view, a crucial question to answer is whether a critical thickness of non-liquefiable layer exists, beyond which liquefaction of the underlying layer does not affect the superstructure. On that purpose, two more analyses were performed, considering different clay cap thicknesses, i.e. $H = 8$ & 12 m. Results from these analyses are presented at Figure 9, where the estimated foundation settlement is correlated with the ratio of cap thickness to the width of foundation H/B . Settlements due to excess pore pressure buildup are greatly reduced, with the increasing cap thickness. This finding is in agreement with the “critical depth”, obtained by the pseudo-static approach of Cascone & Bouckovalas (1998) and Bouckovalas et al. (2005). Note that the analytical solution predicts $(H/B)_{cr} = 2.00 \div 2.50$ when mean r_u ranges from 0.7 to 1.0, as in the case of Figure 7.

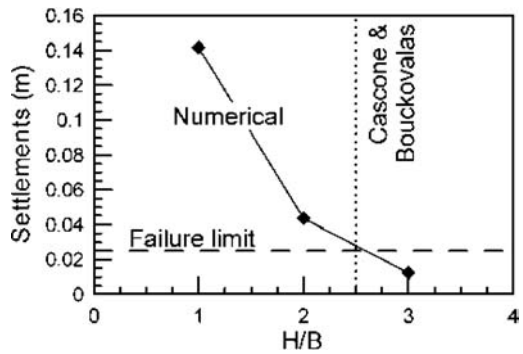


Figure 9. Comparison of the evolution of dynamic settlements for different clay cap thicknesses and variation of the final settlements with H/B .

3.5 Effect of groundwater flow and permeability

Figure 10 presents results for two different values of sand permeability, i.e. 2.1×10^{-4} m/sec and 2.1×10^{-5} m/sec (basic run). Both analyses predict similar response during shaking, indicating that, for these permeability values, flow is not significant during shaking and does not affect practically the results.

However, immediately after shaking, water flow from deeper to shallower layers affects greatly the computed response. Namely, an increase of excess pore pressure ratios is observed that leads to a further increase of foundation settlements. This is most prominent for the case of $k = 2.1 \times 10^{-4}$ m/sec, where flow occurs at faster rate. In the case of a less permeable sand layer (i.e. $k = 2.1 \times 10^{-5}$ m/sec), the change of pore pressures and settlements due to water flow, takes place at a slower rate.

Note also that, although the total value of displacement remains practically the same for both cases (15.6 cm at $t = 50$ sec), post-shaking settlements become greater part of the total displacements as soil permeability decreases, i.e. 10% for $k = 2.1 \times 10^{-5}$ m/sec compared to 6% for $k = 2.1 \times 10^{-4}$ m/sec. This phenomenon has also been observed in centrifuge

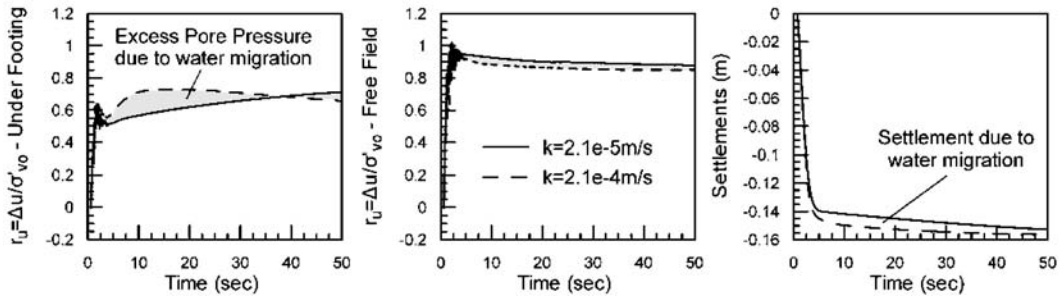


Figure 10. Comparison of dynamic analysis with different permeabilities, in terms of excess pore pressure ratio under the footing and in the free field and foundation settlements.

studies (Liu & Dobry 1997) and explains partly the delayed failure of foundation systems, observed in earthquakes where fine-grained soils have been liquefied (e.g. Adapazari 1999).

4 CONCLUDING REMARKS

The seismic response of shallow foundations on liquefiable sand is studied herein through fully coupled effective stress analysis. The common case of a non-liquefiable clay cap overlying a liquefiable sand layer is explored. On that purpose, a recently developed numerical methodology is used, that consists of a bounding surface model for non-cohesive soils, implemented in FLAC. The findings of this research are compared with those of a pseudo-static approach for the design of foundations where liquefaction occurs. As concluded from the parametric runs presented:

- Effective stress analysis can be used to analyze and explore significant aspects of dynamic soil-structure interaction and liquefaction phenomena
- The presence of superstructure affects greatly the response of the subsoil, differentiating it from the free-field response.
- A “critical depth” of clay cap exists, beyond which, liquefaction of the subsoil does not damage the foundation.
- Groundwater flow, immediately after the end of shaking, redistributes pore pressures, leading to a delayed increase of foundation settlements.
- For commonly used static factors of safety (e.g. 2), foundation settlements due to liquefaction can be excessive.

ACKNOWLEDGMENTS

The work presented herein has been financially supported by the General Secretariat for Research and Technology (Γ.Γ.Ε.Τ.) of Greece, through research

project EΠIAN – ΔΠ23 (“X-SOILS”). This contribution is gratefully acknowledged.

REFERENCES

- Andrianopoulos K.I., Papadimitriou A.G. & Bouckovalas G.D. (2006), “Implementation of bounding surface model for seismic response of sands”, 4th International FLAC Symposium, Proceedings (to appear)
- Arulmoli K., Muraleetharan K.K., Hossain M.M. & Fruth L.S. (1992), “VELACS: verification of liquefaction analyses by centrifuge studies; Laboratory Testing Program – Soil Data Report”, Research Report, The Earth. Technology Corporation
- Been K. & Jefferies M.G. (1985), “A state parameter for sands”, *Geotechnique*, 35 (2), pp. 99–112
- Bouckovalas G.D., Valsamis A.I. & Andrianopoulos K.I. (2005), “Pseudo static vs performance based seismic bearing capacity of footings on liquefiable soil”, Proceedings of the TC4 Satellite Confer., 16th ICSMGE, Osaka, pp. 22–29
- Cascione E. & Bouckovalas G. (1998), “Seismic bearing capacity of soils”, Proceedings 11th European Conference in Earthquake Engineering, Paris, September
- Liu L. & Dobry R. (1997), “Seismic response of shallow foundation on liquefiable sand”, *Journal of Geotech. & Geoenviron. Engrg., ASCE*, Vol. 123 (6), pp. 557–567
- Papadimitriou A.G., Bouckovalas G.D. & Dafalias Y.F. (2001), “Plasticity model for sand under small and large cyclic strains”, *J. Geotech. Geoenviron. Engrg., ASCE*, Vol. 127 (11), pp. 973–983
- Papadimitriou A.G. & Bouckovalas G.D. (2002), “Plasticity model for sand under small and large cyclic strains: a multi-axial formulation”, *Soil Dynamics and Earthquake Engineering*, Vol. 22, pp. 191–204
- Sloan S.W., Abbo A.J. & Sheng D. (2001), “Refined explicit integration of elastoplastic models with automatic error control”, *Engineering Computations*, Vol. 18(1/2), pp. 121–154
- Itasca (2005), “Fast Lagrangian Analysis of Continua”, Version 5
- Meyerhoff G.G. & Hanna A.M. (1978), “Ultimate bearing capacity of foundations on layered soils under inclined load”, *Canadian Geotechnical Journal*, Vol. 15 (4), pp. 565–572

Vertical compliance function of adjacent surface rigid footings in heterogeneous soil layer

B. Sbartai

University of Skikda, Dept of Civil Engineering, Skikda, Algeria

A. Boumekik

University of Constantine, Dept of Civil Engineering, Constantine, Algeria

ABSTRACT: This article studies the dynamic interaction between surface rigid foundations in a heterogeneous viscoelastic soil limited by a substratum. The vibrations come from rigid foundation placed in soil layer and subjected to vertical harmonic load. Required dynamic response of rigid surface foundations constitute the solution of the waves equations obtained by taking account of the conditions of interaction structure-soil-structure. The solution is formulated in frequency domain Boundary Element Method in conjunction with the Kausel-Peek Green's function for a layered stratum and quadrilateral constant element. This approach allowed establishing a mathematical model enabling us to determine the compliance function of adjacent foundations according to their different separations, the dynamic properties of the soil and the frequency of excitation.

1 INTRODUCTION

The dynamic foundation-soil-foundation interaction phenomena has long been recognized as an important factor in the seismic and machine vibration response of critical facilities and other closely spaced structures or portions of a structure. Rotative machines foundation constitutes a source of vibrations which are transmitted to the surrounding soil. Depending on the energy communicated to the medium, this disturbance may affect greatly either the soil or the adjacent structure. Rational analysis of the phenomenon requires taking into account the dynamic nature of the interaction between the soil and the foundation. This is essentially a wave propagation problem with mixed boundary condition (i.e. rigid body displacement under the foundation and none traction elsewhere). Although, a solution of a foundation-soil-foundation interaction problem in most cases involves a straightforward application of any of the well established soil-structure interaction methods, a relatively small number of 3-D investigations have appeared in the related literature. This is probably due to the substantial computational effort required by the Finite Element Method and the usual straightforward Boundary Element method formulations. Further more, there is a noticeable absence of simplified discrete models which is due, perhaps, to the general lack of rigorous results which would be used for the verification and calibration of such models. The complicated geometries,

loadings and soil conditions, have discouraged, in general, the development of analytical solutions. (Luco 1976) determined the impedance functions for a rigid circular disk on layered elastic and viscoelastic medium using an integral equation approach. (Apsel & Luco 1987) using the integral equation approach based on the green's functions for layered soil media reported in (Apsel 1979) for the determination of the impedance functions of embedded foundations. Using this approach (Wong & Luco 1986) studied the dynamic interaction between rigid foundations in a layered half-space. Using a semi-analytical formulation (Gazetas & Roesset 1979) analysed the 2-D problem of strip foundations on a layered half-space, (Boumekik et al. 1986) studied the 3-D problem of embedded foundations on a layered substratum, on the other hand (Sbartai & Boumekik, 2002, 2003) analysed the transmission of the wave in the soil layer caused by machine foundation. The Finite Element Method has also been applied by (Gonzalez 1974), (Kausel et al. 1976), (Kausel & Roesset 1981) and (Lin et al. 1987) in determining the behaviour of rigid foundations resting on or embedded in a stratum over bedrock. A frequency domain Boundary Element Method formulation has been developed to treat wave propagation problems, soil-structure problems and structure-soil-structure problems, which limit the discretization at the soil foundations interface. In this approach the field displacement is formulated as an integral equation in terms of Green's functions (Beskos

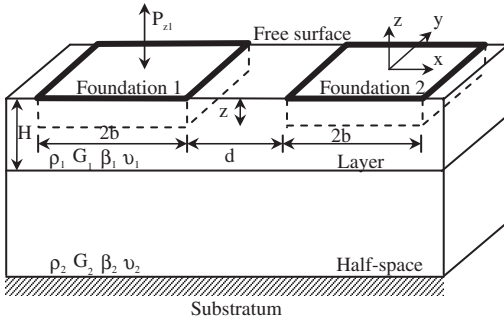


Figure 1. Model of calcul.

1987), (Abascal & Dominguez 1989), (Qian & Beskos 1996), (Qian et al. 1989), (Karabalis & Mohammadi 1998), (Mohammadi 1992) and (Sbartai & Boumekik 2005). In this work, the solution is formulated in frequency domain Boundary Integral Equation Method. Only the foundation-soil-foundation interface and a free surface between adjacent foundations are discretized. Within the discretized medium, the Green's functions (displacement of the i th element due to harmonic unit force applied on the j th element) are calculated using the Thin Layers Method, (Kausel & Peeck 1982). Using this approach allowed to establish a mathematical model enabling us to determine the vertical compliance functions of adjacent surface footings resting on heterogeneous soil layer.

2 BASIC EQUATIONS

2.1 Model of calculation

The model of calculation is represented on the figure.1. The two foundations considered are supposed to be rigid, massless, of form square placed at the surface in homogeneous soil limited by a substratum. The soil at height H , is supposed to be viscoelastic linear characterized by its mass density ρ , its shear modulus G , its damping coefficient β and Poisson's ratio ν . The footing (1) are subjected to vertical harmonic external force P_z . It is assumed that the time dependence of the excitation is of the type $e^{i\omega t}$ in which ω denotes the frequency. For brevity, this time factor will be omitted in the sequel. The goal being to obtain the compliance functions of two footings. The Displacements in an unspecified point " α " of the soil may be obtained from the resolution of the wave equation:

$$((C_p^2 - C_s^2)u_{,jik} + C_s^2 u_{,k,ji} + C_p^2 \omega^2 u_k) \quad (1)$$

where C_s , C_p are the celebrities of the waves of shearing and compression, ω the angular frequency of excitation and ρ the mass density of the soil. The

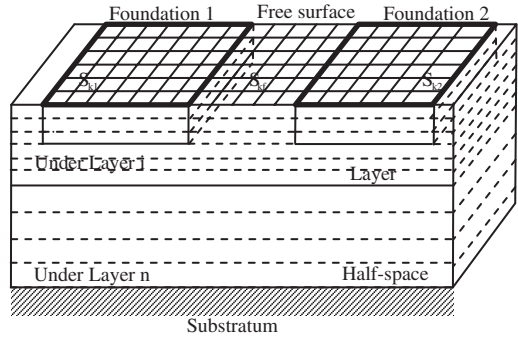


Figure 2. Horizontal and vertical discretization.

solution of equation (1) can be formulated by following boundary integral equation:

$$u_\alpha = \int_S U_{\alpha\beta} \cdot t_\beta \cdot dS_\beta \quad (2)$$

with $U_{\alpha\beta}$ are the Green's functions which represent displacements in a point α had with a load harmonic unit (vertical and horizontal) applied in another point β of soil and t_β represent a harmonic load distributed on a surface of soil dS_β . As long as the medium is continuous, this last relation remains very difficult to evaluate. However, if the solid mass of the soil is discretized in an adapted way, this relation can be made algebraic and displacement can then be calculated.

2.2 Discretization of the model

In this approach, the principle of the discretization of the solid mass of soil is represented on the figure.2. It is based on two types of horizontal discretization one and the other vertical. The horizontal discretization consists in subdividing any horizontal section of the solid mass of the soil in square elements of S_k sections. The average displacement of the element is replaced by displacement of its center and on which the distribution of the constraints is supposed to be uniform. For reasons of simplicity of integration and saving in calculation the square elements are replaced by disks. The vertical discretization consists in subdividing the solid mass of the soil in under layers (Infinite Elements in the horizontal direction) rather low thickness compared to the wavelength of Rayleigh ($\lambda/10$) to be able to linearize the displacement of under layer to the other. This discretization being characterized by the depth of embedding of the foundation and the depth of the substratum figure 2.

$$d_\alpha = \sum_{\beta=1}^{NRT} \int_S U_{\alpha\beta} \cdot t_\beta \cdot dS_\beta \quad (3)$$

where NRT represents the total number of elements discretizing the soil between two foundations and the interface soil-foundations.

2.3 Displacement matrix of discretized soil

The total matrix displacement of the soil is obtained by successive application of the loads units distributed on the constituent elements of the solid mass of the discretized soil. This matrix includes the terms of flexibilities of the soil which will be occupied by the first foundation (medium 1), the soil which will be occupied by the second foundation (medium 2) and those of the coupling between the two mediums which can be written as follows:

$$[F_1] = \begin{bmatrix} F_1 & F_{12} \\ F_{21} & F_2 \end{bmatrix} \quad (4)$$

where F_1 , $(3N_1 \times 3N_1)$ is the flexibility matrix of medium 1. F_2 , $(3N_2 \times 3N_2)$ is the flexibility matrix of medium 2. F_{12} , $(3N_1 \times 3N_2)$ is the flexibility matrix of coupling of medium 1 on the medium 2. F_{21} , $(3N_2 \times 3N_1)$ is the flexibility matrix of coupling of medium 2 on the medium 1. N_1 and N_2 are respectively the number of elements discretizing medium 1 and medium 2.

The Displacements in the two mediums are expressed then by:

$$\{d_1\} = [F_1] \{t_1\} + [F_{12}] \{t_2\} \quad (5)$$

$$\{d_2\} = [F_2] \{t_2\} + [F_{21}] \{t_1\} \quad (6)$$

where

$\{t_1\} = \{t_{11}, t_{12}, \dots, t_{1k}, \dots, t_{1N_1}\}^t$ represent the vector charges of the medium 1 in which $\{t_{1k}\} = \{h, t, n\}_k^t$ is the under-vector charges applied to the disk k, where h, t and n are the harmonic loads distributed according to respective directions x, y and z.

$\{t_2\} = \{t_{21}, t_{22}, \dots, t_{2k}, \dots, t_{2N_2}\}^t$ represent the vector charges of the medium 2 in which $\{t_{2j}\} = \{h, t, n\}_j^t$ is the under-vector charges applied to the disk j, where h, t and n are the harmonic loads distributed according to respective directions x, y and z.

$\{d_1\} = \{d_{11}, d_{12}, \dots, d_{1k}, \dots, d_{1N_1}\}^t$ represent the vector displacements of the medium 1 in which $\{d_{1k}\} = \{u, v, w\}_k^t$ is the under-vector displacements applied to the disk k.

$\{d_2\} = \{d_{21}, d_{22}, \dots, d_{2k}, \dots, d_{2N_2}\}^t$ represent the vector displacements of the medium 2 representing the same characteristics as the vector $\{d_1\}$.

2.4 Condition of compatibility and equilibrium

When the two foundations are in place, they impose their displacements on the various sections which will

be constrained to move like a rigid body. For all the elements of the model, one can write the following relations:

$$\{d_1\} = [R_1] \{D_1\} \quad (7)$$

$$\{d_2\} = [R_2] \{D_2\} \quad (8)$$

with

$\{D_1\} = \{\Delta x, \Delta y, \Delta z, \phi_x, \phi_y, \phi_z\}_1^t$ the vector displacement of the first foundation for the 6 degrees of freedom considered; $\{D_2\} = \{\Delta x, \Delta y, \Delta z, \phi_x, \phi_y, \phi_z\}_2^t$ the vector displacement of the second foundation (6 degrees of freedom) considered and $[R_1] = [R_1, R_{2,\Lambda}, R_{k,\Lambda}, R_{N_1}]^t$ is a matrix of transformation of dimension $(3N_1 \times 6)$, depending only on the geometrical characteristics of the discretized volume of the soil of the first foundation where under matrix is given by:

$$[R_1]_k = \begin{bmatrix} 1 & 0 & 0 & 0 & z & -y \\ 0 & 1 & 0 & -z & 0 & x \\ 0 & 0 & 1 & y & -x & 0 \end{bmatrix}_k \quad (9)$$

in which x_k , y_k and z_k are the co-ordinates of the element k compared to the center of the foundation; $[R_2] = [R_1, R_{2,\Lambda}, R_{k,\Lambda}, R_{N_2}]^t$ is also a matrix of transformation of dimension $(3N_2 \times 6)$, depending only on the geometrical characteristics of the discretized volume of the soil of the second foundation where under matrix $[R_2]_j$ is similar to that of the relation (9) in which x_j , y_j and z_j are the co-ordinates of the element j compared to the center of the second foundation. If one notes P_{i1} and M_{i1} the components of the vector charges applied to the first foundation, the equilibrium between the latter and the forces distributed on the elements discretizing the volume of the foundation are expressed for the loads of translations and rotations by:

$$P_{i1} = \sum_{k=1}^{N_1} t_k = \sum_{k=1}^{N_1} \begin{pmatrix} h \\ t \\ n \end{pmatrix}_k \quad (i = x, y, z) \quad (10)$$

$$M_{i1} = \sum_{k=1}^{N_1} \begin{pmatrix} y \cdot n - z \cdot t \\ z \cdot h - x \cdot n \\ x \cdot t - y \cdot h \end{pmatrix}_k \quad (i = x, y, z) \quad (11)$$

These two last expressions can be put in the following matrix form:

$$\{P\} = [R] \cdot \{t\} \quad (12)$$

Same manner, one can write the same thing for the second foundation one has then:

$$P_{i2} = \sum_{j=1}^{N_2} t_j = \sum_{j=1}^{N_2} \begin{pmatrix} h \\ t \\ n \end{pmatrix}_j \quad (i = x, y, z) \quad (13)$$

$$M_{i2} = \sum_{j=1}^{N_2} \begin{pmatrix} y \cdot n - z \cdot t \\ z \cdot h - x \cdot n \\ x \cdot t - y \cdot h \end{pmatrix}_j \quad (i = x, y, z) \quad (14)$$

These two last expressions can be put in the following matrix form:

$$\{P_2\} = [R_2] \cdot \{t_2\} \quad (15)$$

2.5 Response of the model

The relation binding the vector directly charges external $\{P_1\}$ applied to the centre of gravity of the footing with the vectors displacements $\{D_1\}$ and $\{D_2\}$ can be expressed starting from the relations (5), (6), (7), (8) and (12) by:

$$\{P\} = [K_1] \cdot \{D_1\} + [K_{12}] \cdot \{D_2\} \quad (16)$$

The relation binding the vector charges external applied to the centre of gravity of the second footing to the vectors displacements starting from the relations (5), (6), (7), (8) and (15) by:

$$\{P_2\} = [K_2] \cdot \{D_2\} + [K_{21}] \cdot \{D_1\} \quad (17)$$

If the second foundation is unloaded ($P_2 = 0$), the Eqs. (16) and (17) becomes:

$$\{P_1\} = [K_1] \cdot \{D_1\} + [K_{12}] \cdot \{D_2\} \quad (18)$$

$$\{0\} = [K_2] \cdot \{D_2\} + [K_{21}] \cdot \{D_1\} \quad (19)$$

From there system one can write:

$$[C_{11}] = \left[[K_1] - [K_{12}] [K_2]^{-1} [K_{21}] \right]^{-1} \quad (20)$$

is the compliance matrix of the loaded foundation and

$$[C_{12}] = -[K_2]^{-1} [K_{21}] [C_{11}] \quad (21)$$

is the coupling compliance matrix of the unloaded foundation.
where

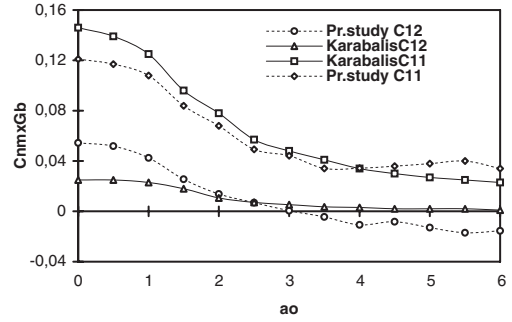


Figure 3. Validation of the model.

K_1 is the dynamic stiffness matrix of the loaded footing (1).

K_2 is the dynamic stiffness matrix of the unloaded footing (2).

K_{12} is the coupling matrix of the loaded footing on the unloaded footing.

In the following, these two last relations are used to analyse the dynamic interaction between two surface square rigid footings placed on homogenous soil where only one foundation is loaded.

3 VALIDATION FOR ADJACENT FOUNDATIONS

The results of this work will be validated while comparing results then obtained by the present study at those obtained by the 3-D frequency domain BEM formulation of Karabalis et al [20]. The comparison relates to the case of a square foundations placed at the surface of a viscoelastic and isotropic semi-infinite soil having the following characteristics: $\rho = 1$; $G = 1$; $C_s = 1$; $\nu = 0.333$; $\beta = 0.05$, $H/b = 16$ (to approach the semi-infinite one) with $b = 1/2$ is the half wide of the foundations. Only the first footing is loaded with the unit vertical force $P_z = 1$, however the second footing is unloaded. The dimensionless vertical compliance C_v is defined as:

$$C_v = Gb \cdot K_v^{-1} \quad (22)$$

The soil is discretized horizontally in 9 quadrilateral constant elements on the soil-footings interfaces and 9 quadrilateral constant elements on the free surfaces between the footings. For the vertical discretization the depth of the substratum will be subdivided in 10 under layers. The compliances are calculated at relative distance $d/b = 2$ between two footings versus different dimensionless frequency a_0 . The results thus presented on (fig.3) are practically comparable and the maximum errors are observed only in static case.

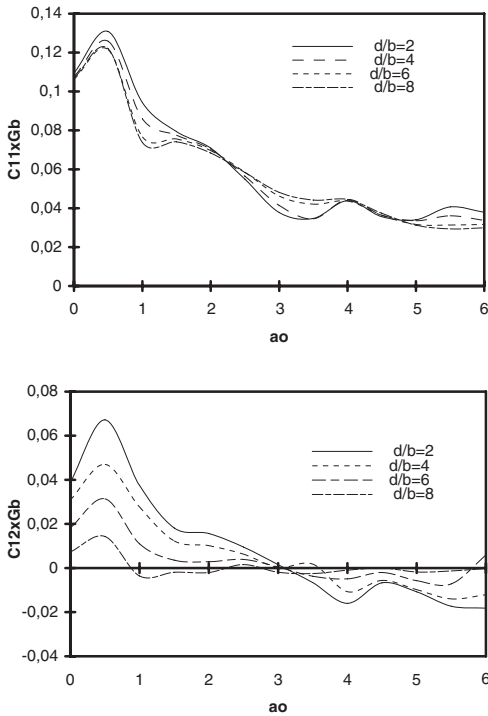


Figure 4. Homogeneous case: Vertical compliance C_{11} and C_{12} .

4 PARAMETRIC ANALYSES

In the case of one layer resting on rigid substratum (G_1/G_2 extending to zero), two square footings are considered but only first footing is subjected to unit vertical force $P_z = 1$. The soil is discretized in 9 quadrilateral constant elements to the interface soil-foundations and in 9 quadrilateral constant elements to the free surface and is characterised by $\rho = 1$, $G = 1$, $\nu = 0.333$, $\beta = 0.05$, $H/b = 8$. For this, the dimensionless vertical compliance $C_{11} \times Gb$ for loaded foundation and vertical coupling compliance of the unloaded foundation $C_{12} \times Gb$ have been studied for different cases of distance between two foundations ($d/b = 2, 6, 10, 14$).

In (fig. 4), the influence of the distance between foundations versus frequency $a_0 = \omega b/2C_s$ is examined. It is noticed that the variation magnitude of the compliance of the charged footing is appreciably affected in the vicinity of the maximum values with a reduction magnitudes as the distance between the two footings increases. Concerning coupling compliance of the no charged footing, we noted the same remark but with magnitude much less important. So, we noted that the coupling compliance is more affected by interaction phenomena that the charged footing.

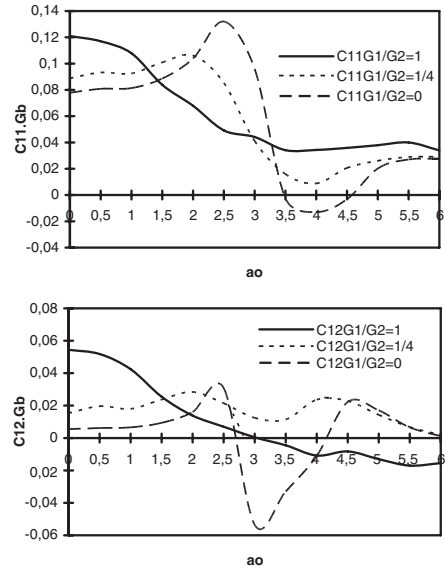


Figure 5. Heterogeneous case: Vertical compliance C_{11} and C_{12} .

The case of the layer on half-space medium is also examined (heterogeneous soil: type Gibson). The footings soil comprises a layer thickness ratio $H/b = 2$ resting on half-space medium. Each of the two media are viscoelastique, homogeneous and isotropic. Let the characteristics of the upper layer be designated by index 1 and the characteristics of the half-space by index 2. The case of the layer resting on half space is an intermediary one between that on the half-space ($G_1 = G_2$) and that of the layer resting on rigid substratum (G_1/G_2 extending to infinity). In this work, the ratio G_1/G_2 takes the values following (0, 1/4, 1). In (fig. 5), the influence of the shear modulus ratio versus frequency is examined while the foundations are massless, the distance ration between foundations $d/b = 2$, and the damping level is kept constant at $\beta = 0.05$ for the two media. While varying the shear modulus ratio according to the frequency we noted:

- The static response increase when the shear modulus ratio increases.
- A remarkable shift in the resonant frequencies.
- A variation in the peaks of resonance.
- An important variation in the magnitude on the level of the resonant frequencies with the smaller shear modulus ratio.

The behaviour of the unloaded foundation is similar to that described above for the loaded foundation, the

only difference being that the magnitude of the resonant peak decrease with the shear modulus ratio increase.

5 CONCLUSIONS

In this paper, the dynamic interaction between two surface rigid footings resting on heterogeneous viscoelastic soil subjected to vertical harmonic external force excitation has been developed and fully tested. The solution is formulated in frequency domain Boundary Element Method in conjunction with the Kausel-Peek Green's function for a layered stratum and quadrilateral constant element to study the dynamic interaction between adjacent footings with which the parameters of interaction structure-soil-structure in a soil layer profile will be numerically given. The advantage of the method used lies in limited the enough number of elements used in the discretization of the model on the one hand and the taking into account of the heterogeneity of the soil on the other hand. This study shows well us the great importance of the interaction foundation-soil-foundation which proves to be different from the interaction soil-foundation (single foundation). To this end, we recommend to take into account this phenomenon in account for the study of any structure.

REFERENCES

- Absacal, R & Dominguez, J. 1989. Vibrations of footings on zoned viscoelastic soils. *Journal of Engineering Mechanics*. 115: 913–934.
- Apsel, R.J & Luco, J.E. 1987. Impedance functions for foundations embedded in layered medium: an integral equation approach. *Earthquake Engineering and Structural Dynamics*. 15: 213–231.
- Apsel, R.J. 1979. Dynamic Green's functions for layered media and applications to boundary value problems. Ph.D. Thesis, University of California, San Diego.
- Beskos, D.E. 1987. Boundary Element methods in dynamic analysis. *Appl. Mech. Rev.* 40(1): 1–23.
- Boumekik, A, Nuyens, J & Canstantopoulos, I.C. Soil-Structure interaction effect on non circular structure embedded in multilayered soil . *Proc. Intern. Conf., on soil mechanics and foundations engineering*. San Francisco. 1986.
- Gonzalez, J.J. 1974. Dynamic interaction between adjacent structures. Research report. R77–30, MIT.
- Gazetas, G & Roesset, J.M.1979. Vertical vibration of machine foundations. *Journal of the Geotechnical Engineering Division, ASCE*. 105(12): 1435–1454.
- Karabalis, D.L & Mohammadi, M. 1998. 3-D dynamic foundation-soil-foundation interaction on layered soil. *Soil dynamics and Earthquake Engineering*. 17: 139–152.
- Kausel, E, Roesset , J.M & Waas, G. 1975. Dynamic analysis of footings on layered media. *Journal of Engineering Mechanics*. 101: 679–693.
- Kausel, E & Roesset, J.M. 1981. Stiffness matrix for layered soils. *Bull. Seismol. Soc. Am.* 72: 1459–1481.
- Kausel, E & Peek, R. 1982. Dynamic loads in the interior of layered stratum: an explicit solution. *Bull. Seism. Soc. Am.* 72(5): 1459–1481.
- Lin, T, Roesset, J.M & Tassoulas, J.L. 1987. Dynamic interaction between adjacent foundations. *Earthquake Engineering and Structural Dynamics*. 15: 323–343.
- Luco, J. 1976. Vibrations of a rigid disc on a layered viscoelastic medium. *Nuclear Engineering and Design*. 36: 325–340.
- Mohammadi, M. 1992. 3-D dynamic foundation-soil-foundation interaction by BEM. Ph.D. Thesis, University of South Carolina, Columbia.
- Qian, J & Beskos, D.E. 1996. Harmonic wave response of two 3-D rigid surface foundations. *Soil dynamics and Earthquake Engineering*. 15: 95–110.
- Qian, J, Tham, L.G & Cheung, Y.K. 1998. Dynamic analysis of rigid surface footings by boundary element method. *Journal of sound and vibration*. 214(4): 747–759.
- Sbartai, B & Boumekik, B. 2002. Propagation d'ondes dans un sol homogène générés par une machine vibrante, in E.M.Croitoro (ed), *Nonlinear mechanics, Proc. intern. conf., Vancouver, British columbia, e-Printit, Kingston, 2: 533–542.*
- Sbartai B. 2002. Transmission of wave in the soil layer. In J.L Auriault et al (eds), *Poromechanics: 789–793*. Rotterdam, Balkema.
- Sbartai, B & Boumekik, A. 2003. Propagation d'ondes dans un sol multicouche générées par une machine vibrante. In Sahli et al (eds), *13^{ème} Conference Régional Africain de la géotechnique, Proc. conf., Marrakech, I: 119–126.*
- Sbartai, B & Boumekik A. 2005. Dynamic interaction between two surface rigid foundations in soil layer in special issue Al-Azhar University Engineering Journal, 8(1): 356–364. *Proc. intern. conf., Al-Azhar Engineering, Cairo, 2004.*
- Wong, J.E & Luco, J. 1986. Dynamic interaction between rigid foundations in a layered half- space. *Soil dynamics and Earthquake Engineering*. 5(3): 149–158.

Efficient numerical simulation of waste landfills' seismic response

V. Zania & Y. Tsompanakis

Technical University of Crete, Greece

P.N. Psarropoulos

National Technical University of Athens, Greece

ABSTRACT: A major concern related to the seismic design of a geo-structure, such as a municipal solid waste landfill, is to avoid a potential instability of its slopes under seismic loading, a phenomenon directly related to the developed acceleration levels and the dynamic interaction of the geo-structure with the underlying soil. The aim of this study is to examine the seismic response and the stability of a typical above-ground landfill founded either on rock or on an intermediate soil layer. Extensive numerical analyses have been performed in order to achieve a realistic assessment of the dynamic behaviour of the landfill, while simplified procedures have been utilized to estimate the effects of earthquake excitation on its slope stability by quantifying the induced displacements.

1 INTRODUCTION

Municipal solid waste (MSW) landfills are geo-structures of extremely high engineering interest due to the environmental risk related to a potential failure. In regions with higher seismicity the aforementioned risk is more intense, as recent experience has shown. The performance of MSW landfills during the past earthquakes, such as Loma Prieta and Northridge, has provided significant information for failure mechanisms and seismic design. The critical failure modes that have been reported by Matasovic et al. (1998) include transverse and longitudinal cracks of cover soils, damage to gas system header pipes, local tears in geomembrane liners, landfill settlement, cracking of landfill slopes, cracks about the contact between refuse landfill and canyon bedrock, as well as cracks due to liquefaction induced lateral spreading of foundation soil.

In order to study the seismic response, as well as the related seismic stability issues of landfills it is important to determine the effect of the seismic excitation to the geo-structure. Earthquake induces time dependent deformations to the geo-structure, which are related to its dynamic response, i.e. the developed inertial accelerations. On the other hand, post-earthquake permanent deformations are related to potential liquefaction or fault movement effects on the geo-structure. The dynamic performance of landfills due to liquefaction or fault movement is a complicated problem and not a part of the current study.

Seismic design of MSW landfills can be evaluated according to current methods used in embankment/dam

seismic stability analysis. In relation to current seismic codes (e.g. Eurocode 8 1994), seismic stability analysis is usually performed via the pseudostatic method, which is conducted using a value of seismic coefficient equal to half of the design peak ground acceleration (PGA). In this way the dynamic response of the structure is not taken into account, resulting to incapability of predicting the true response and stability of the geo-structure during a moderate or severe seismic event.

Recent practice in seismic slope stability analysis is based on three categories of methods, namely: *stress-deformation analysis*, *pseudo-static analysis*, and *permanent deformation analysis*. Stress-deformation analyses are performed utilizing finite-element method with the application of sophisticated constitutive models to describe material nonlinearity. As the parameters required for the implementation of the models are not easily or accurately quantified in the laboratory or in situ (especially for waste material), this type of stability analysis is not part of the current study. A crude estimation of seismic slope stability is obtained through pseudostatic analysis. The results are provided in terms of minimum *factor of safety* (FS), based on limit equilibrium methods of static slope stability analysis, including horizontal and vertical inertia forces. The basic limitation of the method acquires the selection of the value of seismic coefficient (k_h). Permanent deformation analyses are based on the calculation of seismic deformations through a method proposed by Newmark (1965), known as sliding block analysis. Makdisi & Seed (1978) extended the aforementioned method by applying it to weighted

average values of seismic coefficient. The application of the aforementioned methods requires accurate estimation of inertial accelerations.

On the other hand, analytical methods have been also developed for the dynamic response of dams. One of the earliest approaches of this kind is the shear-beam approach (Gazetas 1987), which has been applied to landfills by Gunturi & Elgamal (1998). Nevertheless, a more realistic approach for the dynamic response of geo-structures is through dynamic nonlinear finite-element analysis. Finite-element analyses are capable of modelling actual deformations of a dam, both vertical and horizontal, in contrast to the analytical shear-beam approach that predicts only the horizontal component.

In the present study efficient two-dimensional (2D) finite-element models have been developed, and linear or equivalent linear dynamic ground response analyses have been conducted in order to: (a) examine in more detail the aggravation of horizontal acceleration due to local site conditions, (b) investigate the relationship between this aggravation, and (c) the potential nonlinear behaviour of soil and to examine the nonlinear dynamic interaction between a typical landfill and an underlying soil layer. Application of the aforementioned methods reveals the incapability of accurate evaluation of landfill's stability by current seismic codes.

2 SEISMIC RESPONSE OF LANDFILLS

2.1 Two-dimensional modelling

Dynamic response of landfills is examined through 2D finite-element modelling of two typical geometries. The first model (Model A) is an above-ground landfill founded on stiff rock (bedrock), while the second one (Model B) is founded on a soil layer (Fig. 1).

The finite-element analyses were conducted utilizing QUAD4M (Hudson et al. 1994), which evaluates the seismic response of 2D plane-strain models. Material

nonlinearity is taken into account using an iterative procedure according to which shear modulus and damping are consistent to the level of maximum shear strain. The models were discretized using three-noded triangular elements, the size of which was tailored to the wavelengths of interest resulting to a finer mesh from rock to soil.

Landfill material properties depend on the composition of municipal waste, the age of the waste, the soil content and the compaction during waste disposal. Due to the inherent uncertainties related to the determination of the aforementioned factors, it is extremely difficult to evaluate waste properties with great accuracy. The properties used for the analyses of this study correspond to two common cases: (a) a recently deposited waste, and (b) an old deposited waste. The recently deposited waste was considered to be characterized by a material that has no cohesion and an angle of friction equal to 30° , while the old deposited waste has cohesive strength

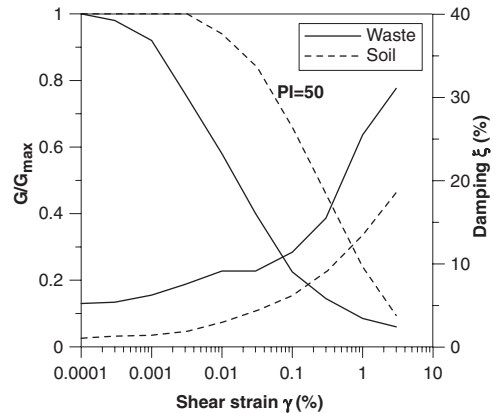


Figure 2. Shear-modulus reduction and damping-variation curves for waste material and clay (from Singh & Murphy 1990 and Idriss & Sun 1992 respectively).

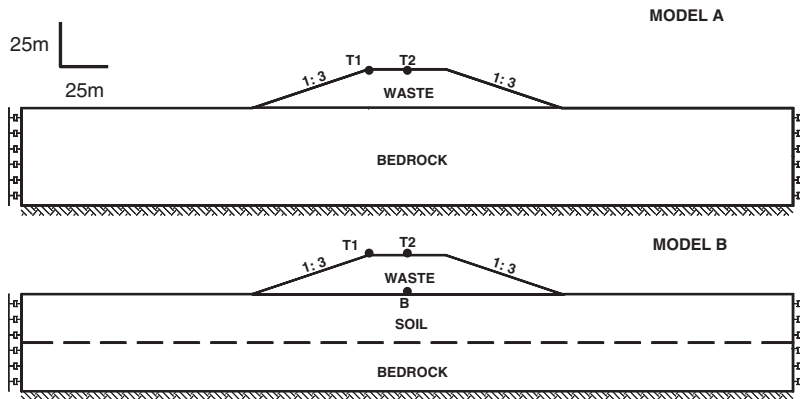


Figure 1. Models of the landfills examined. T1, T2 and B are the points of interest.

equal to 20 kPa. The unit weight of the waste material was set equal to 10 kN/m³. For recently deposited waste the shear wave velocity was assumed to be 160 m/sec, while for the old waste was 400 m/sec.

As shown in Figure 1, in Model B the landfill is founded on a relatively soft clay layer of 25 m. The clay is characterized by shear-wave velocity, V_s^s , equal to 310 m/sec, unit weight 18 kN/m³, and plasticity index, PI , 50. In Figure 2 the shear-modulus reduction curve (G/G_{max} , γ) and the damping-variation curve (ξ , γ) are given for waste material (Singh & Murphy 1990) and clay (Idriss & Sun 1992).

The excitation used in the present investigation is a simple Ricker pulse with central frequency $f_0 = 2$ Hz. Despite the simplicity of its waveform, Ricker pulse covers a broad range of frequencies up to $3f_0$ (see Fig. 3). Additionally, recent studies reveal that simple pulses like Ricker are capable of approaching near-fault excitations. Many researchers report that near-fault ground motions are characterized by a relatively simple long period pulse of strong motion that has a relatively small duration (Mylonakis & Reinhorn 2001).

In order to evaluate the linear and nonlinear behaviour of materials, two levels of PGA were examined: 0.01 g and 0.36 g, respectively. According to the aforementioned analytical method based on the shear-beam approach (Gazetas 1987) the first eigenperiod T_D of a trapezoidal dam is provided by:

$$T_D \cong 2.5 \frac{H_D}{V_s^D} \quad (1)$$

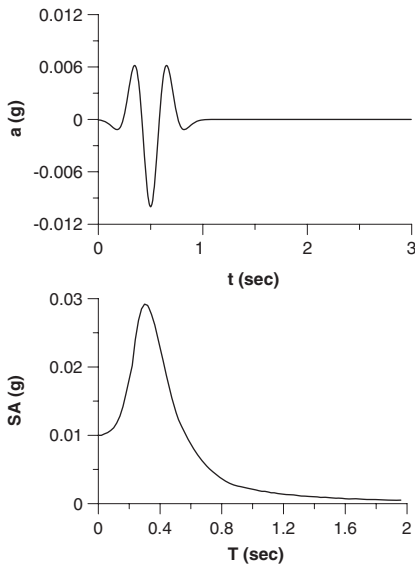


Figure 3. Ricker pulse $f_0 = 2$ Hz: acceleration time history and response spectra.

where H_D is the height of the landfill, and V_s^D is the shear-wave velocity of the embankment's material. Also, the first eigenperiod of a linear elastic soil layer overlying rigid bedrock is given by:

$$T_s = 4 \frac{H_s}{V_s^s} \quad (2)$$

where H_s is the height of the soil layer, and V_s^s is the shear-wave velocity of soil.

The fundamental period of the Ricker pulse is approximately 0.32 sec (Fig. 3). According to Equation 1 the first eigenperiod of Model A for a recently deposited waste is equal to the fundamental period of the Ricker pulse, while for the old deposited waste the first eigenperiod of the landfill is equal to 0.13 sec.

2.2 One-dimensional modelling

In order to investigate the capability of 1D response analyses to capture landfill's response, 1D response analyses were also conducted with SHAKE91 (Idriss & Sun 1992). The program computes the response of a horizontally layered soil deposit subjected to vertically propagating shear waves. An iterative procedure is also used to account for the nonlinear behaviour of the soil. A comparison between 1D and 2D response has been performed.

3 NUMERICAL RESULTS

3.1 Landfill on stiff rock

In this case the eigenperiod of the Ricker excitation and the landfill model for recently deposited waste coincide. Thus, the dynamic response of the landfill is expected to be indicative of potential resonance phenomena, as long as the landfill behaves linearly and its damping is low. Indeed, observing Figure 4, it can be seen that base motion is strongly amplified at both points T1 and T2 when the shear-strain level is small. For higher levels of imposed acceleration the resulting stiffness degradation and greater damping value lead to a higher eigenperiod of the geo-structure and therefore to a slight amplification, or even to a de-amplification of the base acceleration (Psarropoulos et al. 2006). On the contrary, when waste material consists of old waste (stiffer material) the amplification for the linear case is smaller, while on the nonlinear case the corresponding increase of landfill's eigenperiod affects significantly its response. As it is depicted in Table 1 the amplification of PGA for this case is even higher than in the case of soft-waste landfill's linear behaviour.

In addition, considering the 1D results for the seismic response of the landfill, the effect of the 2D geometry in dynamic response of the geo-structure becomes obvious.

Results presented in Table 1 shows that 1D analysis approximates to certain extent the 2D dynamic response of the landfill for linear behaviour of stiff waste material and for nonlinear behaviour of soft waste material. Nevertheless, 1D simulation of geo-structure leads to inaccurate prediction of the elastic response of the soft-waste landfill, as accelerations at the top of the landfill are amplified due to the effect of 2D geometry. Similar are the conclusions for the nonlinear response of stiff waste material, indicating that high amplification levels are associated not only with the nonlinear behaviour of the material, but with the geometric characteristics of the landfill as well.

Another important issue, which justifies the need for 2D analyses, is that although the base acceleration is applied on the horizontal direction, generation of

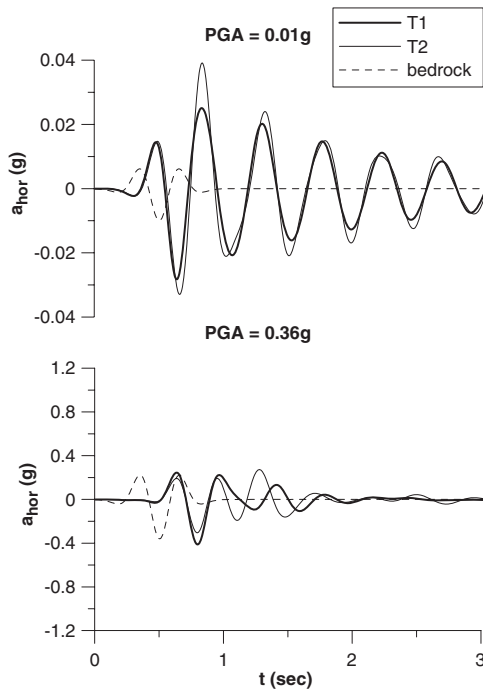


Figure 4. Horizontal acceleration response of Model A on receiver points T1, T2 compared to base acceleration for PGA = 0.01 g and PGA = 0.36 g.

vertical parasitic acceleration is observed on the top of the landfill. As it was observed, this phenomenon is more intense for the nonlinear case (Fig. 5). This is consistent with recent studies related to topography effects on ground motions (Gazetas et al. 2002, Bouckovalas & Papadimitriou 2004).

The initiation of parasitic vertical acceleration is attributed to the generation of surface waves resulting from wave reflections at slope surface. Note that 1D response analyses are incapable of capturing this phenomenon.

3.2 Foundation of landfill on soil layer

The seismic response of a landfill founded on soil layer (Model B) is examined for the case of soft waste material only. Equations (1) and (2) indicate that double resonance effects can be expected, as both landfill and soil layer have first eigenperiod coincident to the fundamental period of the Ricker pulse. However, the system responds in a more complicated manner than Model A due to the presence of the intermediate soil layer. As shown in Figure 6, for rather small levels of developed shear strains the base acceleration is amplified due to soil layer response. This results to higher levels of acceleration at the top of the landfill and especially at the inner point T2.

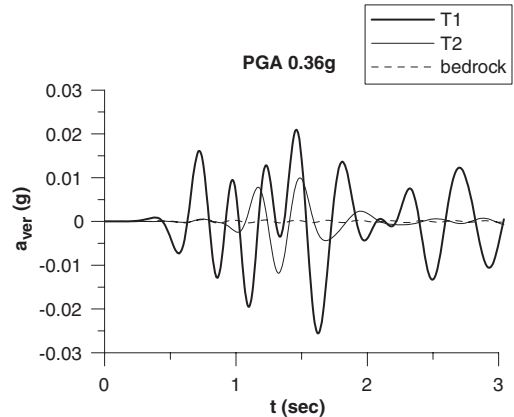


Figure 5. Vertical acceleration response of Model A on receiver points T1, T2 compared to base acceleration of PGA = 0.01 g and PGA = 0.36 g.

Table 1. Amplification factors for Model A in terms of PGA.

	2D Analyses				1D Analyses			
	PGA = 0.01 g		PGA = 0.36 g		PGA = 0.01 g		PGA = 0.36 g	
	Soft	Stiff	Soft	Stiff	Soft	Stiff	Soft	Stiff
T1	2.83	1.96	1.14	3.02	2.04	2.27	0.91	1.90
T2	3.91	2.04	0.85	3.32	2.04	2.27	0.91	1.90

In addition, it can be observed (Fig. 6) that for the nonlinear case high amplification of the base acceleration occurs till the interface between soil layer and landfill and de-amplification of the seismic motion through the landfill. Strong nonlinear waste material

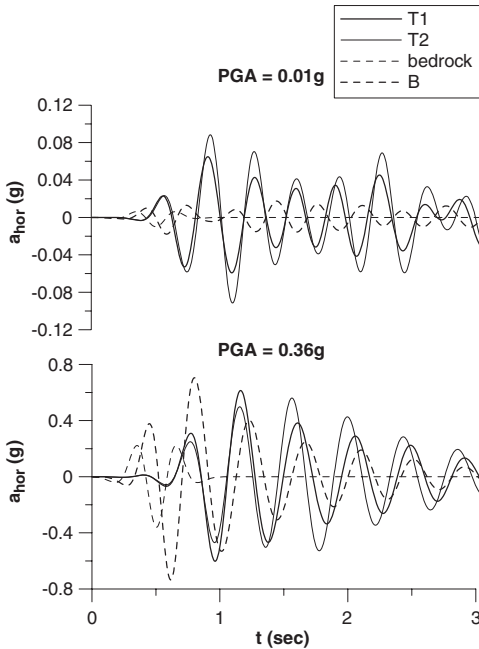


Figure 6. Horizontal acceleration response of Model B on receiver points T1, T2 and B compared to base acceleration for PGA = 0.01 g and PGA = 0.36 g.

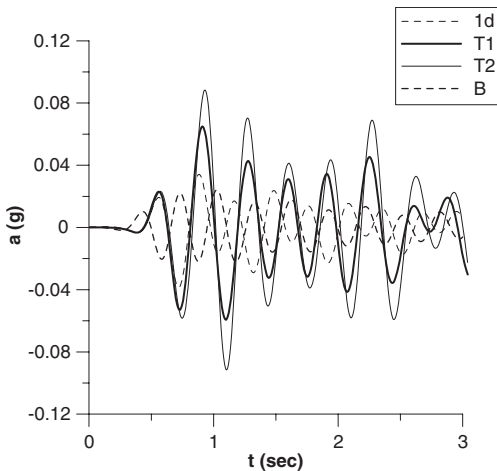


Figure 7. Horizontal acceleration response of Model B on receiver points T1, T2 and B compared to 1D response for PGA = 0.01 g.

behaviour, which corresponds to great reduction of stiffness and increase of its damping, reduces the amplified (by the soil layer) base acceleration. This trend becomes more evident when 1D cross-section responses of upper middle point and the interface middle point are compared to the corresponding 2D results. One-dimensional analysis simulates quite sufficiently landfill's response, due to highly nonlinear material behaviour which dominates the response. On the other hand, this is not the case for elastic material behaviour (Fig. 7), where 1D response predicts lower values of acceleration than 2D. In the latter case higher acceleration levels can be attributed to resonance of the geo-structure.

Furthermore, the generated parasitic vertical acceleration at the crest of the landfill presents relatively high values, comparable to horizontal acceleration levels for the elastic behaviour of the landfill. In conclusion, dynamic response of landfills is a complex problem, in which significant factors seem to be the excitation's characteristics, the waste material properties and the local soil conditions.

4 STABILITY ANALYSIS

4.1 Pseudostatic method

The simplest of the approaches used for seismic slope stability is pseudostatic analysis. The factor of safety (FS), obtained from a pseudostatic analysis depends on the selected value of seismic coefficient. Due to the dynamic response of the potential failure mass the induced inertial force varies with time and within the failure mass. Consequently, seismic coefficients that are proposed by seismic codes generally correspond to acceleration values that underestimate the predicted PGA.

Model A was analyzed pseudo-statically for both cases of soft and stiff waste using Bishop's simplified method of slices (Bishop 1954). A dynamic FS was obtained for the acceleration time history of the Ricker pulse for both acceleration levels of 0.01 g and 0.36 g. These analyses provide an estimation of the potential failure surface and are indicative of the time variation of FS.

In order to determine the seismic coefficients corresponding to each of the aforementioned critical failure surfaces finite-element analyses were conducted utilizing QUAD4M (Fig. 8). The program estimates the seismic coefficient as the force induced by the earthquake over the weight of the sliding surface. The forces acting on the surface are computed by multiplying shear and normal stresses acting on an element with the width of that element. Average stress is calculated between elements on either side of the interface. The summation of forces acting on the surface is computed as a function of time. Subsequently, the critical

surfaces were analyzed using the pseudostatic method, with the application of both horizontal and vertical seismic coefficients (k_h , k_v) obtained from the finite-element analyses. It is clear that variation of acceleration within the mass has affected the critical FS in most cases. Due to the dynamic response of the landfill the maximum k_h for the critical failure surfaces receive values even greater than PGA (see Table 2).

4.2 Permanent deformation method

Though pseudostatic analysis is a simple and straightforward procedure it is governed by the accuracy with which the simple pseudostatic inertial forces represent the complex dynamic inertia forces that actually exist in an earthquake (Kramer 1996). Methods based on evaluation of permanent slope deformation are being used increasingly as pseudostatic factors of safety provide none information on potential slope deformations. Newmark (1965) developed a simple procedure of estimating permanent seismic slope deformations using the analogous of a sliding block on an inclined plane.

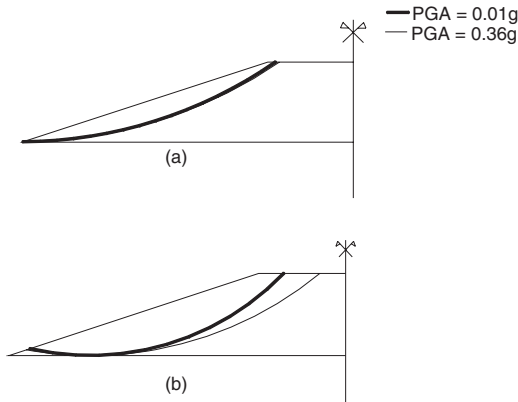


Figure 8. Critical failure surfaces of Model B for soft waste material (a), and stiff waste material (b) for both levels of acceleration $PGA = 0.01\text{ g}$ and $PGA = 0.36\text{ g}$.

Permanent deformations induced by the earthquake along the failure surface of the landfill were evaluated using the rigid sliding block model (Newmark method). The method was applied to the stiff waste material landfill, where critical safety factor reached a value less than one. The angle of inclined plane, along which the movement occurs theoretically, was determined through a method proposed by Sharma (1975). The direction of the vector of sum of shear forces along the failure surface gives the angle of the inclined plane. Seismic coefficient time histories were used for the analysis, taking into account both directions of motion initiated within the failure mass. The relative displacement from this type of analysis reached a maximum value of 0.12 m. Note that by not taking into account the parasitic k_v the magnitude of displacements is underestimated by 34% (Fig. 9).

The procedure used here to compute permanent deformations that are produced at the sliding interface is a decoupled one. The limitation of the method is that it is based on the assumption that dynamic response of the failure mass is not influenced by permanent displacements that occur on the failure surface.

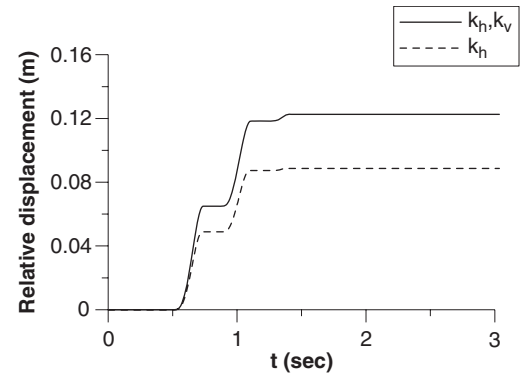


Figure 9. Relative displacement evaluated for the critical surface of stiff waste material landfill and $PGA = 0.36\text{ g}$.

Table 2. Factors of safety and corresponding values of acceleration obtained from pseudostatic analysis of Model A applying Ricker and seismic coefficient time history for both soft and stiff waste material.

	Ricker				Seismic coefficient			
	$PGA = 0.01\text{ g}$		$PGA = 0.36\text{ g}$		$PGA = 0.01\text{ g}$		$PGA = 0.36\text{ g}$	
	Soft	Stiff	Soft	Stiff	Soft	Stiff	Soft	Stiff
FS	1.94	3.10	0.86	1.38	1.86	3.00	1.65	0.71
k_h	0.01	0.01	0.36	0.36	0.022	0.02	0.10	0.70

5 CONCLUSIONS

Dynamic response analysis of rather simple MSW landfills has shown the complicated nature of the problem. Current seismic codes are incapable to cover fully the seismic design of landfills, or similar geostuctures, as they rather underestimate local site effects on ground shaking and slope stability. Therefore, proper seismic design of such structures should be performed on a case-by-case basis in order to take into consideration, apart from the seismological conditions, the specific local site conditions and the individual characteristics of each structure.

REFERENCES

- Bishop, A.W. 1954. The use of the slip circle in the stability analysis of slopes. *Geotechnique* 5(1): 7–17.
- Bouckovalas, G.D. & Papadimitriou, A.G. 2005. Numerical evaluation of slope topography effects on seismic ground motion. *Soil Dyn. & Earthquake Engng* 25: 547–558.
- Eurocode 8. 1994. *Design of structures for earthquake resistance, Part 5: Foundations, retaining structures and geotechnical aspects*. CEN-ENV, European Committee for Standardization, Brussels.
- Gazetas, G. 1987. Seismic response of earth dams: some recent developments. *Soil Dyn. & Earthquake Engng* 1(6): 3–47.
- Gazetas, G., Kallou, P.V., & Psarropoulos, P.N. 2002. Topography and soil effects in the MS 5.9 Parnitha (Athens) earthquake: the case of Adames. *Natural Hazards* 27: 133–169.
- Gunturi, V.R. & Elgamal, A.M. 1998. A class of inhomogeneous shear models for seismic analysis of landfills. *Soil Dyn. & Earthquake Engng* 17: 197–209.
- Hudson, M., Idriss, I.M., & Beikae, M. 1994. *User's Manual for QUAD4M*. Center for Geotechnical Modeling, Department of Civil and Environmental Engineering, University of California, Davis, CA, USA.
- Idriss, I.M. & Sun, J.L. 1992. *User's manual for SHAKE91*. Center for Geotechnical Modeling, Department of Civil and Environmental Engineering, University of California, Davis, USA.
- Kramer, S.L. 1996. *Geotechnical earthquake engineering*. Prentice Hall, New Jersey.
- Makdisi, F.I. & Seed, H.B. 1978. Simplified procedure for estimating dam and embankment earthquake induced deformations. *ASCE J. of Geotech. Engng Div.* 104: 849–867.
- Matasovic, N., Kavazanjian, E.Jr., & Anderson, R. 1998. Performance of solid waste landfills in earthquakes. *Earthquake Spectra* 14(2): 319–334.
- Mylonakis, G. & Reinhorn, A.M. 2001. Yielding oscillator under triangular ground acceleration pulse. *J. of Earthquake Engng* 5(2): 225–251.
- Newmark, N.M. 1965. Effect of earthquakes on dams and embankments. *Geotechnique* 15(2): 139–160.
- Psarropoulos, P.N., Tsompanakis, Y. & Karabatsos, Y. 2006. Effects of local site conditions on the seismic response of municipal solid waste landfills. *Soil Dyn & Earthquake Engng* (in press).
- Sarma, S.K. 1975. Seismic stability of earth dams and embankments. *Geotechnique* 25(4): 743–761.
- Singh, S. & Murphy, B. 1990. Evaluation of the Stability of Sanitary Landfills. In A. Landya & G.D. Knowles (eds), *Geotechnics of Waste Fills – Theory and Practice*: 240–258. Philadelphia: American Society for Testing and Materials.

Dynamic FE analysis of ground vibrations and mitigation measures for stationary and non-stationary transient source

Lindita Kellezi

GEO – Danish Geotechnical Institute, Lyngby, Denmark

ABSTRACT: For building constructions located on soft soil conditions and near heavy traffic or industrial areas ground vibrations are becoming more and more a great concern. In this paper a three-dimensional (3D) finite element (FE) model formulation and its application for simulating ground vibration and design of mitigation measures is presented. The effectiveness of wave barriers such as concrete walls and a row of concrete piles in reducing those vibrations is investigated. The analyses consider stationary and non-stationary dynamic, transient sources intending to simulate industrial foundation vibrations and traffic-induced vibrations respectively. For non-stationary source subsonic conditions are considered. The far field is simulated by absorbing boundaries constructed based on the radiation criterion and strength of materials theory and considered as doubly asymptotic approximations. Numerical examples are presented which highlight the efficiency of the method in deriving useful engineering solutions assessing that a concrete wall might give up to 70% vibration reduction and a row of concrete pile up to 50% reduction.

1 GENERAL INTRODUCTION

New infrastructure developments around the world are associated with an increased awareness regarding vibrations in buildings being an essential element in annoying people. Air borne noise is to an increasing extent being efficiently reduced by sound barriers, and the vibrations are remaining the dominant problem.

In different countries in Europe and elsewhere, official regulations have recently started focusing on limiting vibrations, setting up legal limits for acceptable levels.

Under these circumstances there is an increasing demand for better prediction methods regarding ground vibration, particularly for critical soil conditions involving soft soil layers at different depths. In addition, better tools for designing mitigation measures, which can reduce the through ground vibrations, are also required.

The predominant range of frequencies of such type of vibrations may be (5–50) Hz. The waves propagating at low frequency can interact with the modes of vibration of the nearby buildings, sometimes approaching resonance conditions, increasing the disturbance as schematized in Figure 1.

For heavy machineries operating in the industry or other similar situations the vibration source is considered fixed or stationary.

With the expansion of heavy traffic in the urban areas and railway network, concern has been raised about the

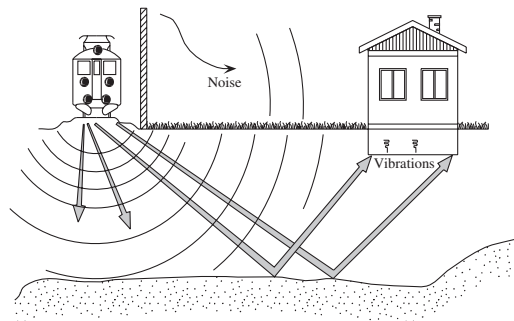


Figure 1. Noise and ground vibration transmission.

effect of non-stationary load on wave propagation and vibrations in the nearby buildings.

Different vibration mitigation measures are proposed and applied in the past and recently. Open or in-filled trenches, concrete or sheet pile walls and wave impeding barriers have been previously investigated analytically and numerically by Ahmad et al. (1996), Al-Hussaini & Ahmad (1996), Hawwa (1998), Lee & Its (1995), Fuyuki & Matsumoto (1980), Takemiya & Kellezi (1998), Kellezi & Nielsen (2000) etc.

Aviles & Sanchez-Sesma (1988) investigated analytically a row of circular piles as ground vibration barrier. A general analytical solution was presented also from

Boroomand & Kaynia (1991) considering dynamic pile-soil-pile-interaction. Kellezi & Foged (2001) investigated numerically different kinds of such barriers.

3D FE modeling of the ground vibrations and mitigation measures, with special attention on concrete walls and row of concrete piles, which are possibly cheaper engineering solutions in practice, are presented in this paper. The analyses are carried out for stationary and non-stationary load assumptions.

The description of the numerical method formulated, developed and applied in the analyses is given in the next section.

2 DEVELOPMENT OF 3D FE METHOD

2.1 Stationary transient source

When σ_{ij} and u_i denote the stress and displacement components respectively, ρ soil density and $p(t)$ the applied time function stress, the elasto-dynamic equations of motion are given as,

$$\frac{\partial \sigma_{ij}}{\partial x_j} - \rho \frac{\partial^2 u_i}{\partial t^2} + p(t) = 0 \quad (1)$$

When Equation 1 are multiplied by a weight function in the form of a virtual displacement field u_i followed by integration over the volume and reformulation using the divergence theorem, Equation 2 is derived.

$$\int_{\Gamma} \bar{u}_i (\sigma_{ij} n_j) d\Gamma - \int_{\Omega} (\bar{\epsilon}_{ij} \sigma_{ij} + \rho \bar{u} \ddot{u} - \bar{u} p) d\Omega = 0 \quad (2)$$

The stress σ_{ij} at the boundary integral in Equation 2 represent the stiffness of the far field and geometrical damping given in vector form in Equation 3.

$$\{\sigma\} = [D_K] \{u\} + [D_C] \{u_{,t}\} \quad (3)$$

The integral identity, Equation 2, reduces to a set of linear equations when the spatial variation of the actual and virtual displacement fields is represented by shape functions and Equation 3 is substituted. As a result the following equations of motions in matrix form derives,

$$[M] \{u_{,tt}\} + ([C] + [C]_{\infty}) \{u_{,t}\} + ([K] + [K]_{\infty}) \{u\} = \{P(t)\} \quad (4)$$

$\{u\}$, $\{u_{,t}\}$ and $\{u_{,tt}\}$ are the system vectors for displacement, velocity and acceleration respectively. $[M]$ is the mass matrix. The system stiffness consists of the volume contribution $[K]$ and the stiffness arising from the integral over absorbing boundary $[K]_{\infty}$. The FE consistent stiffness at the boundary surface is derived as,

$$[k]_{\infty} = \int_{\Gamma} [\bar{N}]^T [D_K] [\bar{N}] d\Gamma \quad (5)$$

The damping of the system consists of $[C]$ which models material damping for the near and the far field and the boundary integral, which models radiation damping $[C]_{\infty}$. Material damping matrix is constructed based on Raleigh damping. The FE consistent damping at the boundary surface derives as,

$$[c]_{\infty} = \int_{\Gamma} [\bar{N}]^T [D_C] [\bar{N}] d\Gamma \quad (6)$$

The load vector $\{P(t)\}$ is the usual weighted integral of the surface traction. The matrices in Equations 5 and 6 are formulated in terms of the element shape function matrix, constitutive matrix for the far field stiffness $[D_K]$ and constitutive matrix for the far field geometrical or radiation damping $[D_C]$.

The formulation of the absorbing boundaries consist of how the constitutive matrices $[D_K]$ and $[D_C]$ are derived.

When an impulse is acting on an elastic half space medium in the 3D analysis, the surface at infinity for body waves is a large hemisphere with radius $r \rightarrow \infty$. For R-waves the surface at infinity is a flat cylinder with radius r and height approximately one R-wave length λ_R .

From the one-dimensional wave theory hemispherical P- or S wave fronts traveling in the positive z-direction could be closely approximated by,

$$u_i(z, t) = \frac{1}{z} f(z - c_{P(S)} t) \quad (7)$$

For the conical horn, the differential equation of motion for a P or S wave reduces to,

$$\frac{1}{c_{P(S)}} u_{i,tt} - \frac{2}{z} u_{i,z} - u_{i,zz} = 0 \quad (8)$$

Considering only outgoing waves given as in Equation 7 the boundary differential equation reduces to,

$$\left[\frac{\partial}{\partial t} + \frac{c_{P(S)}}{z} + c_{P(S)} \frac{\partial}{\partial z} \right] u_i = 0 \quad (9)$$

The boundary stress at location z derives as,

$$\sigma_i(x, t) = - \left[\frac{\rho c_{P(S)}^2}{z} u_i(z, t) + \rho c_{P(S)} u_{i,t}(z, t) \right] \quad (10)$$

The cones from the boundary location z to infinity are modeled by a mechanical system, which contains a spring and a damper with frequency independent coefficients.

From this investigation cone models are used as absorbing boundary for body waves in 3D FE dynamic analysis. They are applied for all degrees of freedoms (DOF's) at the boundary defining the distance r of each Gauss integration point from the energy source, and knowing the coordinates of wave direction vectors \mathbf{r} and vectors \mathbf{n} normal to the boundary. Matrices $[D_K]$ and $[D_C]$ in Equations 3, 5 and 6 derive as,

$$[D_K] = \frac{\rho}{r} (\mathbf{n} * \mathbf{r}) \{c_p^2 [N] + c_s^2 ([I] - [N])\} \quad (11)$$

$$[D_C] = \rho (\mathbf{n} * \mathbf{r}) \{c_p [N] + c_s ([I] - [N])\} \quad (12)$$

Using Cartesian coordinates, $[I]$ is the identity matrix and $[N]$ is a 3×3 matrix. Its elements are products of coordinates of vectors \mathbf{n} (n_x, n_y, n_z).

So body waves in the 3D FE analysis are absorbed in the far field by a combination of cones simulated from springs and dashpots attached to the boundary nodes and connected to a rigid base. Apexes of the cones derive from the geometry of the model and source location.

Regarding surface waves, in the context of 1D wave theory a cylindrical wave traveling in the positive x -direction is approximated by,

$$u_i(x, t) = \frac{1}{\sqrt{x}} f(x - ct) \quad (13)$$

For soil half space model $c = c_R$ for example for the horizontal component of the in-plane motion. From the strength of materials theory the differential equation satisfied from a cylindrical wave front could be,

$$\frac{1}{c} u_{i,tt} - \frac{1}{x} u_{i,x} - u_{i,xx} = 0 \quad (14)$$

This is the equation of motion of a cone with linear area variation. Considering only outgoing waves the boundary differential equations equals,

$$\left[\frac{\partial}{\partial t} + \frac{c}{2x} + c \frac{\partial}{\partial x} \right] u_i = 0 \quad (15)$$

The boundary stress derives as,

$$\sigma_i(x, t) = - \left[\frac{\rho c^2}{2x} u_i(x, t) + \rho c u_{i,t}(x, t) \right] \quad (16)$$

The linear cones from the boundary location x to infinity are modeled also by a mechanical system, which contains a spring and a damper with frequency independent coefficients.

These models are used as absorbing boundary for surface waves in similar way as for the body waves with constitutive stiffness matrices $[D_K]$ and $[D_C]$ derived as,

$$[D_K] = \frac{\rho}{r} (\mathbf{n} * \mathbf{r}) \left\{ \frac{1}{2} (s c_R^2 n_x^2 + c_R^2 (1 - n_z^2)) + c_s^2 n_y^2 \right\} \quad (17)$$

$$[D_C] = \rho (\mathbf{n} * \mathbf{r}) \{s c_R n_x^2 + c_R (1 - n_z^2) + c_s n_y^2\} \quad (18)$$

In Equations 17 and 18, s is the ratio of P- to S wave velocities.

Development of the above method in two-dimensional (2D), plane strain, and axisymmetric conditions is presented in Kellezi (2000). Some verifications for 3D conditions are given in Kellezi & Takemiya (2001).

2.2 Non-stationary transient source

Several studies have been carried out on the linear dynamic response of continuous pavements subjected to non-stationary loads, Hardy & Cebon (1993), Kim & Roesset (1998), etc.

Alternatively, the problem was formulated for 2D FE applications, plane strain, by (Krenk et al, 1999) for transient source of vibrations directly in the time domain. That formulation is further developed and applied for the 3D case implementing modified absorbing boundary conditions.

The convected equations of motion are given from Equation 19,

$$\frac{\partial \sigma_{ij}}{\partial x_j} - \rho \frac{\partial^2 u_i}{\partial t^2} + 2V_y \frac{\partial u_i}{\partial x_j \partial t} - V_y^2 \frac{\partial^2 u_i}{\partial x_j \partial x_k} = p(t) \quad (19)$$

V_y denotes the velocity of the non-stationary load. The load is supposed to move in the y -direction.

In matrix form the equations of motion derive as in Equation 20 after multiplied by a weight function in the form of a virtual displacement field followed by integration over the volume and using the divergence theorem.

$$[M] \{u_{,tt}\} + ([C] + [C_V] + [C]_{\infty} + [C_V]_{\infty}) \{u_{,t}\} + ([K] + [K_V] + [K]_{\infty} + [K_V]_{\infty}) \{u\} = \{P(t)\} \quad (20)$$

The effect of convection is a nonsymmetrical term, containing mixed time and spatial derivatives, which for the element is given by Equation 21, and a symmetrical term, containing the second spatial derivatives, which for the element is given by Equation 22.

$$[c_V] = -2 \int_{\Omega} \left[\bar{N} \right]^T \rho V_y \left[\bar{N}_{,y} \right] d\Omega \quad (21)$$

$$[k_V] = - \int_{\Omega} \left[\bar{N}_{, y} \right]^T \rho V_y^2 \left[\bar{N}_{, y} \right] d\Omega \quad (22)$$

Equations 23 and 24 gives the change in the radiation damping and far field stiffness at the lateral boundary perpendicular to the moving direction, because of the non-stationary load effect,

$$[c_V]_{\infty} = - \int_{\Gamma} \left[\bar{N} \right]^T n \rho V_y \left[\bar{N} \right] d\Gamma \quad (23)$$

$$[k_V]_{\infty} = - \int_{\Gamma} \left[\bar{N} \right]^T n \rho V_y^2 \left[\bar{N}_{, y} \right] d\Gamma \quad (24)$$

These velocity dependant damping and stiffness will have negative values for $y > 0$ and positive values for $y < 0$.

A second order correction is implemented in the convected equations of motions, as the problem is not self-adjoint and Galerkin discretization is approximate. This is based on an alternative version of the Taylor-Galerkin approach for the spatial discretization, (Krenk et al, 1999).

The rest of the matrices in Equation 20 are as given in section 2.1

2.3 3D FE Method implementation and application

All the matrices given in sections 2.1 and 2.2 are implemented in the FE method building a program applicable for elasto-dynamic FE analyses. Direct time integration was applied to handle transient loads.

For stationary source, by using symmetry conditions only a quarter of the model was investigated. However, for non-stationary source moving in the y -direction, half of the FE model was considered using the symmetry conditions along the y -direction.

The transient load, simulating a heavy vehicle or moving train, is simulated by a hammer impulse function with period $T = 0.1$ s, generating frequencies (0–20) Hz. This load, which applies at point (0,0,0), is supposed to move with velocity $V_y = (70-90)$ km/h considering heavy traffic or existing slow-running trains going through areas with soft soil profiles.

Homogeneous half space soil conditions are considered with shear wave velocity $c_s = 120$ m/s, density $\rho = 1800$ kg/m³, Poisson ratio $\nu = 0.4$ and material damping coefficient $\gamma = 5\%$.

The 3D FE Model in Cartesian coordinates covers a sufficient area in the x - and y -direction. It goes deeply into the half space as well. 8-node isoparametric cubic FE is employed with dimensions $dx = dy = dz = \lambda_s / 6 = 2$ m. Absorbing boundaries are

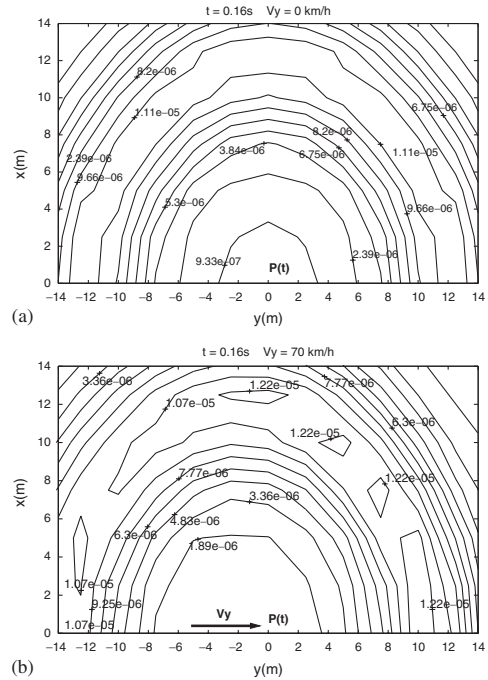


Figure 2. Vertical Displacement at $z = 0$. (a) Stationary load. (b) Non-stationary load.

implemented at the bottom and the sides of the model at a distance less than two λ_s from the source.

To see the non-stationary load effect compared to a stationary load, the vertical displacement component at the soil surface, $z = 0$, is given in Figure 2. The load with amplitude $P = 40$ kN is applied.

The change in the system behavior when the load is non-stationary in comparison when it is stationary can be noticed by comparing Figure 2a with 2b.

For moving load the ground vibration amplitudes are different in the front and on the back of the load. The velocity of wave propagation in the soil will decrease in the moving direction and increase in the opposite direction.

3 GROUND VIBRATION MITIGATION MEASURES

Among other types of ground vibration mitigation measures, attention is given to the concrete walls and a row of concrete piles applied for stationary and non-stationary transient load conditions.

3.1 Stationary load

In Figure 3, parameters like R – the distance of the barrier from the source, L – half of the barrier length L_b ,

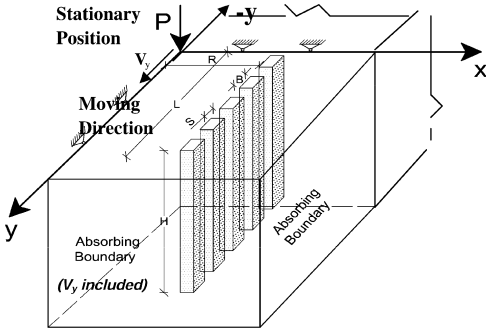
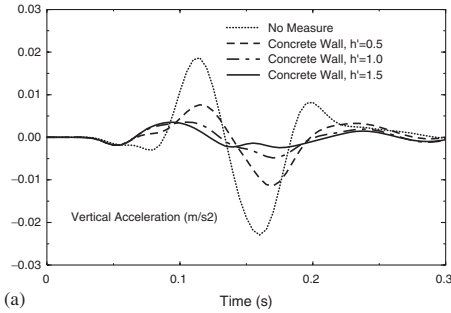
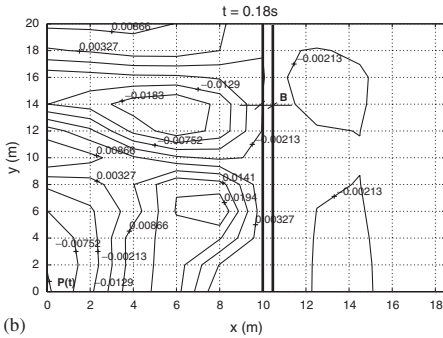


Figure 3. Solid wave barrier, row of concrete piles.



(a)



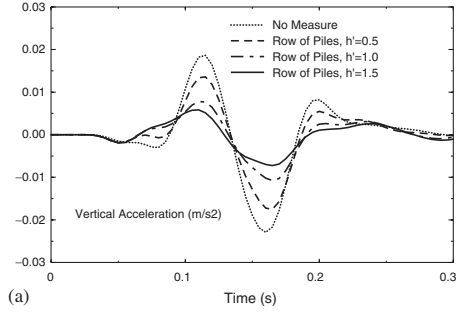
(b)

Figure 4. Concrete wall, vertical acceleration (a) After the measure, at $x = 12.5$ m, $R = 0.83\lambda_S$, $B = 0.04\lambda_S$, $L = 1.65\lambda_S$, (b) At the soil surface, $R = 0.83\lambda_S$, $B = 0.04\lambda_S$, $L = 1.65\lambda_S$, $h' = 1$.

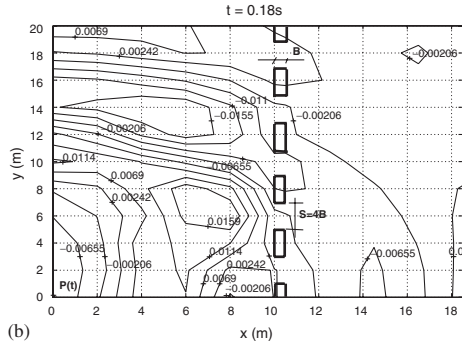
H – barrier depth and B – barrier width are noted. S – the net spacing between the piles for the row of piles is an important parameter as well.

$B = (0.03 \pm 0.04)\lambda_S$ is chosen considering the type of piles expected to be applied in Denmark.

For stationary load, $V_y = 0$ there is symmetry in the x - and y -direction. So a quarter of the model is considered. Computations given in Figures 4 and 5 are carried out varying the depth $h' = H/\lambda_S$ of the concrete wall and row of piles of cross section $B \times 4B$ and net spacing $S = 4B$.



(a)



(b)

Figure 5. Row of concrete piles, vertical acceleration (a) After the measure, at $x = 12.5$ m, $R = 0.83\lambda_S$, $B = 0.04\lambda_S$, $L = 1.65\lambda_S$, (b) At the soil surface, $R = 0.83\lambda_S$, $B = 0.04\lambda_S$, $L = 1.65\lambda_S$, $h' = 1$.

From Figures 4 and 5 we see that a concrete wall and a row of concrete sheet piles embedded in homogeneous soil conditions and designed as above, reduce the amplitude of ground vibrations at an amount (50–70)% and (30–50)% respectively for $h' = 0.5$ and $h' = 1.5$. This means that an amplitude reduction factor $A = (0.3–0.5)$ and $A = (0.5–0.7)$ or an isolation effectiveness $F = 1 - A = (0.5–0.7)$, and $F = (0.3–0.5)$ is achieved respectively at that location.

For the concrete wall as larger the width, larger the reduction capacity. When the wall is replaced with a row of concrete piles or sheet piles designed as in Figure 5 the reduction capacity drops, however considering the fact that construction work can be reduced and excavation work can be avoided, the profit is larger. On the other hand a row of piles can be constructed for areas below water table levels, which is not the case for a concrete wall.

The width B of the solid measures is an important parameter. Increasing B and decreasing the size of the net spacing S will increase the reduction capacity of the row of piles.

3.2 Non-stationary load

As the intention is to use concrete ground vibration mitigation measures in the heavy traffic or running

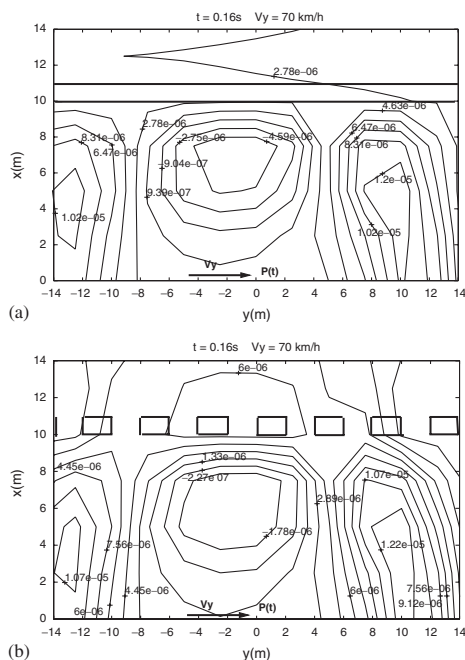


Figure 6. Vertical displacement at the soil surface (a) Concrete wall barrier, (b) Row of Piles of 1m×2m. $R = 0.83\lambda_S$, $h' = 1.5$, $L = 1.5\lambda_S$, $B = 0.08\lambda_S$, $S = 0.17\lambda_S$.

trains, it is interesting to see their effect in case of non-stationary vibration source. The parameters indicated in Figure 3 are still applicable but the moving load velocity is V_y .

In Figure 6a vertical displacement component is given when a concrete wall of width $B = 1\text{m}$ is constructed and embedded in the ground. In Figure 6b the concrete wall is replaced by a row of concrete piles of dimensions 1m×2m placed at a distance $S = 2B = 2\text{m}$ from each other. The soil parameters are the same as for calculation carried out in section 2.3.

4 CONCLUSIONS

3D FE analyses of ground vibrations and mitigation measures with emphasis on concrete walls and row of concrete piles were carried out in this paper. A 3D FEM program was formulated in Cartesian coordinates for stationary and non-stationary transient load.

To simulate unbounded soil domain, absorbing BC's were formulated and implemented at the boundaries of the FE model. For the frequency interval and soil stiffness considered a concrete wall as wave barrier will give maximum (50–70)% ground vibration reduction and a dashed wall or a pile row with $S = 2B$ or $S = B$ will give (30–50)% reduction. The

width of the barriers will determine the amount of reduction in the given intervals.

The method applies for the velocity of the non-stationary source smaller than the shear wave velocity of the ground, called subsonic conditions.

REFERENCES

- Ahmad, S.T.M., Al-Hussaini & K.L. Fishman, 1996. Investigation on Active Isolation of Machine Foundations by Open Trenches, *Journal of Geotechn. Eng.* 122(6), 454–461.
- Al-Hussaini, T.M. & Ahmad, S. 1996. Active Isolation of Machine Foundations by In-filled Trenches Barriers, *Journal of Geotech. Engrg.* Vol. 122(4), 288–294.
- Aviles, J. & Sanchez-Sesma, F.J. 1988. Foundation Isolation from Vibration Using Piles as Barriers. *Journal of Engrg. Mechanics*, Vol. 114(11), 1854–1870.
- Boroomand, B. & Kaynia, A.M. 1991. Vibration Isolation by an Array of Piles, *Soil Dyn. and Earthq. Engrg.* Ed IBF, Comp. Mech. Publicat. Elsevier Appl. Sc. 683–691.
- Fuyuki, M. & Matsumoto, Y. 1980. Finite Difference Analysis of Rayleigh Wave Scattering at a Trench, *Bulletin of Seism. Society of America*, Vol. 70(6), 2051–2069.
- Hardy, M.S.A. & Cebon, D. 1993. Response of Continuous Pavements to Moving Dynamic Loads, *Journal of Engrg. Mech.* Vol. 119, 1762–1780.
- Hawwa, A. Muhammad, 1998. Vibration Isolation of Machine Foundations by Periodic Trenches. *Journal of Engrg. Mech.* Vol. 124(4), 422–427.
- Lee, S.L. & Its, E.N. 1995. Surface Waves of Oblique Incidence Across Deep In-filled Trenches, *Journal of Engrg. Mech.* Vol. 12(3), 482–486.
- Kellezi, L. 2000. Transmitting Boundaries for Transient Elastic Analysis. *Journal of Soil Dynamics and Earthquake Engineering*. Vol. 19, No. 7, 533–547.
- Kellezi, L. & Nielsen, L.O. 2000. Dynamic Behaviour of a Soil Stratum and Vibration Reduction, *13th Nordic Geotech. Conf.* Helsinki, Proc. N99.
- Kellezi, L. & Takemiya, H. 2001. An Effective Local Absorbing Boundary for 3D FEM Time Domain Analyses, *4th Intern. Conf. on Recent Adv. on Geot. Earthq. Engrg. and Soil Dyn.* San Diego, Paper No. 3.42.
- Kellezi, L. & Faged, N. 2001. 3D FEM Analysis of Ground Vibration Measures for Moving and Stationary Transient Source, *4th International Conf. on Recent Advances on Soil Dynamics and Earthquake Eng.* March, San Diego, Paper No. 6.49.
- Kim, S.M., & Roesset, J.M. 1998. Moving Loads on a Plate on Elastic Foundation. *Journal of Eng. Mechanics*. Vol. 124, 1010–1017.
- Krenk, S., Kellezi, L., Nielsen, S.R.K., & Kirkegaard, P.H. 1999. Finite Elements and Transmitting Boundary Conditions for Moving Loads, *4th European Conf. on Structural Dynamics, Eurodyn'99*, Prague, Proc. Vol. 1, 447–452.
- Takemiya, H. & Kellezi, L. 1998. Parasismic Behaviour of Wave Impeding Block (WIB) Measured for Ground Vibration Reduction, *10th Japan Earthquake Eng. Symposium*, Yokohama, E3-13, 1879–1884.

Three-dimensional analyses of transition zones at railway bridges

M.E. Smith, P.-E. Bengtsson & G. Holm
Swedish Geotechnical Institute, Linköping, Sweden

ABSTRACT: Numerical analyses were performed to evaluate the behaviour of a railway bridge transition zone under the passing of trains. A numerical parametric study was performed to study the effects of the train velocity and the stiffness of the embankment materials. The parameter study was performed using the dynamic mode of FLAC3D. Results are expressed in terms of the maximum net horizontal stresses on the back of the abutment, and maximum vertical deflections behind the abutment for the case in which the train is directly above the back of the first bridge abutment. This paper provides a description of the methods used in the numerical parametric analyses, and results of the parameter study, including a discussion of the trends disclosed by the analyses.

1 INTRODUCTION

Railway lines in Europe are 60 to 100 years old, and are not designed in accordance with modern railway traffic. Due to faster and heavier modern trains, existing railway bridges are experiencing problems, such as deterioration and/or loss of ballast material, and the increase of differential settlements within the bridge transition zone. These issues have an adverse effect on the safety, reliability, and economy of the railway line, and therefore, many existing bridge systems require upgrading. Engineers are faced with the task of assessing the performance of existing bridges, and, if necessary, designing the strengthening or repair systems.

As part of the work performed for the EU project “Sustainable Bridges,” the authors have evaluated the stress distribution and deflections within the transition zone due to the passing of high speed trains. The analyses were performed using the finite difference computer code FLAC3D; train loads were applied using the dynamic mode. A bridge geometry representative of concrete bridges in Europe was considered. A numerical parametric study was performed to study the effects of the (1) train velocity, (2) stiffness of the ballast and subballast material, and (3) stiffness of the backfill/embankment fill.

This paper provides a description of the methods used in the numerical parametric analyses, and results of the parameter study, including a discussion of the trends disclosed by the analyses.

2 DESCRIPTION OF NUMERICAL ANALYSES

2.1 *Previous studies by others*

Olofsson & Hakami (2000) performed three-dimensional analyses using FLAC3D to evaluate the interaction between the train track, bridge abutment, and backfill at the transition zone. These analyses included structural beam elements to represent the rail and sleepers, and structural shell elements to represent the bridge abutments. The train load was applied statically by advancing a force along the structural nodes of the beam elements. Adolfsson et al. (1999) present the results of FLAC3D analyses performed to evaluate the critical train speed vibration effects at a soft site in Ledsgård, Sweden. These analyses considered a railway on a simplified soft soil section with no bridge. No structural elements were used in the analyses, and the train load was applied using the dynamic mode in FLAC3D. The analyses described by Olofsson & Hakami (2000) and Adolfsson et al. (1999) were made available to the authors and were a valuable source of information.

2.2 *Numerical analyses*

Numerical analyses of a simplified bridge geometry were performed using the finite different FLAC3D (Fast Lagrangian Analysis of Continua in 3 Dimensions) computer program (Itasca 2002). The

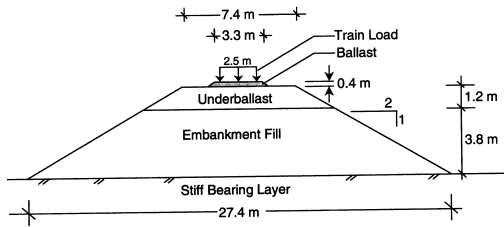


Figure 1. Cross-section of numerical model.

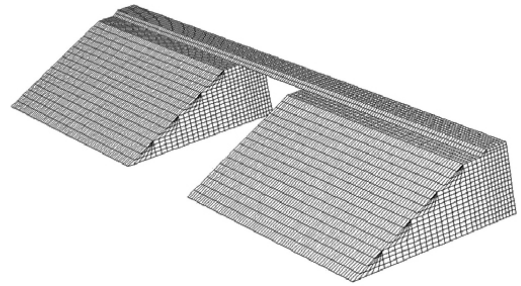


Figure 2. Mesh geometry of numerical model.

Table 1. Base case material property values used in the numerical analyses.

	Ballast	Subballast	Fill
Dry density (kg/m ³)	1900	1900	1700
Elastic modulus (MPa)	193	160	47.9
Poisson's ratio	0.30	0.30	0.31
Bulk modulus (MPa)	161	133	42
Shear modulus (MPa)	74	42	18.3
Friction angle (deg)	40	37	31
Dilation angle (deg)	4	3	2

base case geometry was chosen based upon a typical bridge geometry provided by the Swedish Railroad Administration, Banverket, and is representative of many concrete bridge systems. The bridge embankment profile is shown in Figure 1, where it can be seen that the profile consists of an upper ballast layer 0.4 m thick, which is underlain by a layer of subballast 1.2 m thick, which in turn is underlain by embankment backfill. A stiff, non-yielding, bearing layer is assumed to exist beneath the embankment fill. As can be seen in Figure 1, the geometry is symmetrical about its centre-line.

The material property values used in the numerical analyses are listed in Table 1. A linear-elastic perfectly plastic model with a Mohr-Coulomb failure criterion was used to represent the ballast, subballast, and embankment fill. No material damping was used.

The mesh geometry used in the numerical analyses is shown in Figure 2. The total length of the model is 56 m. The length of the bridge is 10 m. Zone sizes are on average $0.36 \times 0.31 \times 0.28$ m, and a total of 63,376 zones were used. In FLAC3D, the spatial element size should be smaller than approximately one-tenth to one-eighth of the wavelength associated with the highest frequency component of the input wave (Itasca 2002). For the analyses presented herein, the wavelength of the input wave is equal to 7.25 m, which corresponds to the length of the simplified load associated with one bogie.

No structural elements were used to model the bridge abutments, or the rail and sleepers. It was desired to model the train dynamically, and since the

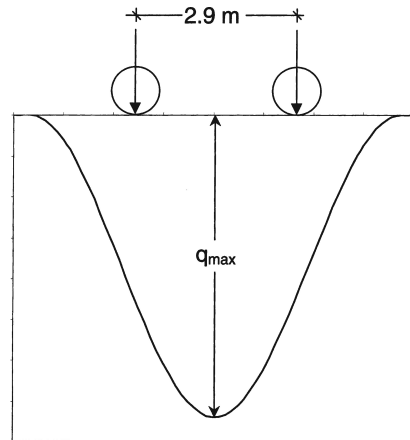


Figure 3. Approximation of the load from one bogie.

timestep in the dynamic mode is determined by the largest material stiffness, using structural elements would require unrealistically long model run times, and may cause numerical problems. Therefore, the bridge structure was represented by fixed gridpoints at the bridge-soil interface.

For these analyses, a hypothetical train load was used. The embankment system is relatively stiff and in order to obtain observable behavioural patterns, a relatively high train load was used. The applied train load was calculated based upon an axle load of 250 kN. For the base cases analyses, the maximum applied train load, q_{max} , is approximately 72 kPa.

The train load was applied dynamically along the top of the model over a width of 1.25 m from the centre-line. To gain a clear understanding of the behaviour of the system under a dynamic load, only one bogie of the train was considered. The approximated load representing one bogie is schematically shown in Figure 3. The shape of the load in Figure 3 is a simplified approximation of the load beneath two wheels of one bogie. This load was input as a cosine-wave, with a maximum magnitude of 72 kPa. The cosine-wave

Table 2. Variable material property values.

	E (MPa)	Poisson's ratio
Ballast	160	0.30
	193	0.30
	300	0.30
Subballast	47.9	0.31
	160	0.30
	300	0.30
Embankment fill	20	0.31
	47.9	0.31
	70	0.30

Bold values are base case values.

was applied successively over each zone. One load variable was created for each successive zone. Each load variable is a function of time, and has a duration that is equal to the length of one bogie (7.25 m) divided by the velocity of the train.

The first step in the numerical analyses was to initialize the vertical and horizontal stresses so that they satisfy both equilibrium and the gravitational gradient. To avoid shear stresses from developing in the soil at the bridge abutments during the initialisation process: (1) the model profile was built up in incremental layers for a total of four layers, with each layer being equilibrated prior to adding the subsequent layer, and (2) the gridpoints at the bridge abutments were fixed in the horizontal directions only, and not in the vertical direction. Once the model was brought to initial equilibrium, all gridpoints at the bridge abutments were fixed all directions prior to applying the train load.

3 PARAMETER STUDY

A parametric study was performed to study the effects of (1) the train velocity, (2) the stiffness of the ballast and subballast material, and (3) the stiffness of the embankment fill. The approach adopted for the numerical parameter studies relies on a base case analysis, with systematic variation of parameter values from the base case.

The train velocity was varied over a range of 50 to 350 km/hr. The stiffness of the ballast, subballast, and embankment fill were varied systematically according to the values listed in Table 2.

Results and conclusions presented in this section pertain to the behaviour of the system at the first bridge abutment when the train is directly above the back of the abutment. Results are expressed in terms of net horizontal stress, which represents the additional horizontal stress applied to the back of the structure due to the train load, and maximum vertical deflections behind the abutment.

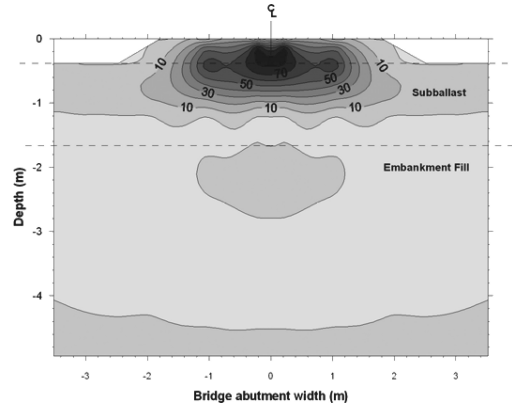


Figure 4. Distribution of net horizontal stresses behind first bridge abutment ($v = 350$ km/hr). (Contours given in kPa.)

A cross-section of the net horizontal stresses at the first bridge abutment is shown in Figure 4 for the case in which base case material properties were used and the train velocity was equal to 350 km/hr. A few general observations can be made based on the results shown in Figure 4. First, below a depth of 1.2 m, the net horizontal stresses in the fill are relatively small. This stress distribution pattern is not the same, however, for the case in which a soft embankment fill is used, as discussed below. Second, the maximum net horizontal stress for this case is on the order of 80 kPa, and occurs over a depth of 0.2 to 0.45 m. For all the analyses in this study, the net maximum horizontal stresses were observed in the ballast layer or at the ballast-subballast layer interface.

The variation in the maximum net horizontal stresses, net $\sigma_{h,max}$, with train velocity and material property values is given in Table 3. In all cases, the maximum net horizontal stresses were observed beneath the centre of the train load. The values presented in Table 3 are for the case in which the train is directly above the back of the first abutment. The variation of net horizontal stresses with train velocity and material property values is discussed in the following sections.

A cross-section of the vertical deflections 1 m behind the first bridge abutment are shown in Figure 5 for the case in which base case material properties were used and the train velocity was equal to 350 km/hr. The deflections in Figure 5 are the vertical deflections calculated when the train is directly above the back of the first abutment. When the train is at this location, the maximum vertical deflections occur approximately 1 m behind the train (unless noted otherwise). For the base case analysis, the maximum vertical deflection behind the first bridge abutment is 2.87 mm (Figure 5).

Table 3. Maximum net horizontal stresses at the first abutment.

Case	Net $\sigma_{h,max}$ (kPa)	Depth (m)	% Change from base case
$v = 50$ km/hr	36.6	0.2	
$v = 150$ km/hr	38.5	0.2	
$v = 250$ km/hr	52.1	0.2	
$v = 350$ km/hr	79.4	0.2–0.4	
Ballast (E = 160 MPa)	87.3	0.4	+10
Ballast (E = 300 MPa)	79.2	0.2	neg.
Subballast (E = 47.9 MPa)	107.4	0.2	+35
Subballast (E = 300 MPa)	42.6	0.4	-46
Fill (E = 20 MPa)	78.5	0.2	neg.
Fill (E = 70 MPa)	49.2	0.2	-38

Bold value is base case value.

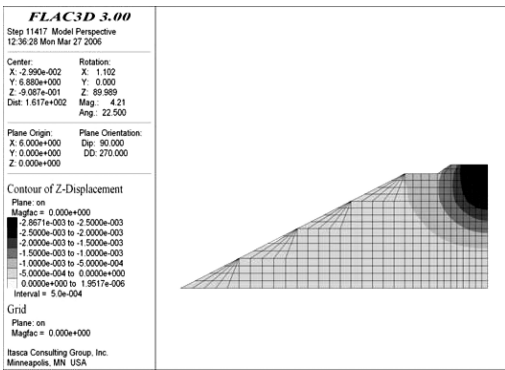


Figure 5. Distribution of vertical deflections 1 m behind first bridge abutment ($v = 350$ km/hr).

Table 4. Maximum vertical deflections, $\delta_{v,max}$, behind the first abutment as a function of train velocity.

Velocity (km/hr)	$\delta_{v,max}$ (mm)
50	1.45
150	1.49
250	1.93
350	2.87

A few general observations can be made based on the results shown in Figure 5. First, most of the vertical deflections occur in the ballast and subballast layers. Second, as would be expected, the maximum vertical deflections are concentrated beneath the width of the train.

The variation in the maximum vertical deflections, $\delta_{v,max}$, with train velocity and material stiffness values are given in Tables 4 and 5, respectively, and are discussed in the following paragraphs.

Table 5. Maximum vertical deflections, $\delta_{v,max}$, behind the first abutment as a function of material stiffness ($v = 350$ km/hr).

	E (MPa)	$\delta_{v,max}$ (mm)	% Change
Ballast	160	3.03	+5.6
	193	2.87	
	300	2.71	-5.6
Subballast	47.9	5.46	+90.2
	160	2.87	
	300	1.83	-36.2
Embankment fill	20	9.10	+217*
	47.9	2.87	
	70	1.43	-50.1

*Observed 3 m behind train.

3.1 Train velocity

The train velocity was varied over a range of 50 to 350 km/hr. The base case material property values, listed in Table 1, were not varied. In general, as the train velocity increases, the net horizontal stresses in the ballast and subballast layer increase, as can be seen in Table 3. However, the relationship between train velocity and maximum net horizontal stress on the back of the abutment is not linear. The largest incremental increase in the maximum net horizontal stresses at the first bridge abutment occurs when the train velocity increases from 250 to 350 km/hr.

As can be seen in Table 4, as the train velocity increases, the maximum vertical deflection behind the train increases. The largest increase in maximum vertical deflections occurs for the case in which the train velocity increases from 250 to 350 km/hr.

The goal of the ‘‘Sustainable Bridges’’ project is to evaluate the behaviour of bridge systems under high speed trains, which may have velocities up to 350 km/hr in the future. The remainder of the parametric analyses were performed using a train velocity of 350 km/hr.

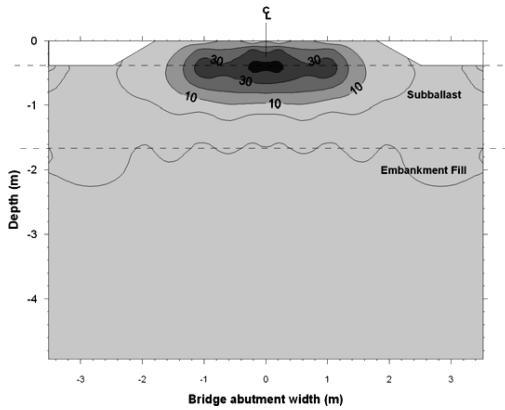


Figure 6. Net horizontal stresses behind first bridge abutment ($v = 350$ km/hr) for stiff subballast case. (Contours given in kPa.)

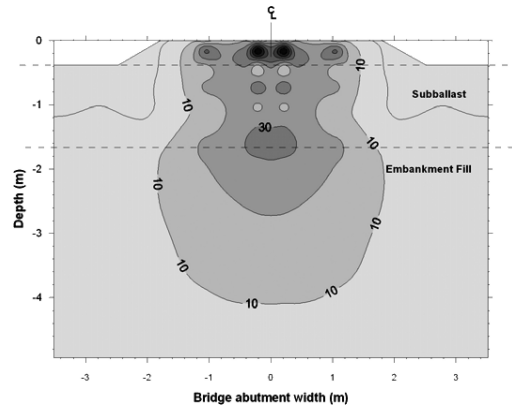


Figure 7. Net horizontal stresses behind first bridge abutment ($v = 350$ km/hr) for soft fill case. (Contours given in kPa.)

3.2 Ballast stiffness

The elastic modulus of the ballast was varied over a range of 160 to 300 MPa. Changing the stiffness of ballast material has only a small effect on the net horizontal stresses and the calculated vertical deflections behind the first bridge abutment (see Tables 3 and 5, respectively). This is likely due to the fact that the thickness of the ballast is relatively thin compared to the thicknesses of the subballast and embankment fill materials.

3.3 Subballast stiffness

The elastic modulus of the subballast was varied over a range of 47.9 to 300 MPa. When the stiffness of the subballast layer is equal to 47.9 MPa, it is equal to the stiffness of the embankment fill, and for this case, it is as if there is no subballast layer and the embankment fill extends to the bottom of the ballast layer. When the stiffness of the subballast layer is equal to 300 MPa, the subballast is 1.6 times stiffer than the ballast layer.

The stiffness of the subballast layer greatly affects the calculated maximum net horizontal stresses, which occur at the ballast-subballast interface. Of all the parameters evaluated, the greatest decrease in maximum net horizontal stress occurs for the case in which the stiffness of the subballast is greater than that of the ballast layer. This decrease in maximum net horizontal stresses is greater than the decrease that corresponds to the decrease in train velocity from 350 to 250 km/hr.

A cross-section of the net horizontal stresses at the first bridge abutment are shown in Figure 6 for the case in which the stiffest ($E = 300$ MPa) subballast layer was used and the train velocity was equal to

350 km/hr. As can be seen in Figure 6, the maximum net horizontal stresses are on the order of 40 kPa and occur at a depth of about 0.4 m. The net horizontal stresses below a depth of 1 m are relatively small.

In general, as the stiffness of the subballast layer increases, vertical deflections behind the first abutment decrease.

3.4 Embankment fill

The elastic modulus of the embankment fill was varied over a range of 20 to 70 MPa. An increase in the stiffness of the fill corresponds to an decrease in the net horizontal stresses in the ballast and subballast layers.

A cross-section of the net horizontal stresses at the first bridge abutment are shown in Figure 7 for the case in which the softest fill layer was used and the train velocity was equal to 350 km/hr. A decrease in stiffness of the embankment fill has little effect on the calculated magnitude of maximum net horizontal stress. As can be seen in Figure 7, the maximum net horizontal stress occurs at about a depth of 0.2 m and is approximately 79 kPa. However, net horizontal stresses on the order of 30 kPa occur at the subballast-fill interface, and net horizontal stresses on the order of 20 kPa are observed to a depth of approximately 2.7 m. This behaviour is different than that indicated in Figure 4, in which the net horizontal stresses below a depth of 1.2 m are relatively small.

The greatest vertical deflection behind the first bridge abutment was calculated for the case in which the soft embankment fill was used. This high value of calculated deflection occurs approximately 3 m behind the train.

4 LIMITATIONS

The results discussed in this paper are only for the conditions investigated. One limitation of the current analyses is that structural elements were not used to represent the rail and sleepers. As a result, the true distribution of the train load through the rail and sleepers was not taken into account. Future analyses will include structural elements to represent the rail and sleepers and/or the bridge, with a statically applied train load. Another limitation of the current analyses is that a stiff bearing layer was assumed to exist beneath the embankment fill. It is expected that a soft bearing layer beneath the embankment fill would have an effect on the distribution of stresses and deflections in the system.

The analyses presented in this paper constitute only a small portion of the analyses being performed for the Sustainable Bridges project. Analyses are currently underway to evaluate the effects of combinations of various realistic train loads and velocities, and multiple train passes. Future analyses will also be performed using a typical masonry arch bridge geometry.

5 SUMMARY AND CONCLUSIONS

Numerical analyses were performed to evaluate the behaviour of a bridge system under the passing of trains. A numerical parametric study was performed to study the effects of (1) the train velocity, (2) the stiffness of the ballast and subballast material, and (3) the stiffness of the backfill/embankment fill. The parameter study was performed using three-dimensional, dynamic analyses using the computer program FLAC3D.

Results were expressed in terms of the maximum net horizontal stresses on the back of the abutment, and maximum vertical deflections behind the abutment for the case in which the train is directly above the back of the first bridge abutment. The train velocity was varied initially, and then, for the remainder of the parameter study analyses, a train velocity of 350 km/hr was used.

For the analyses performed, it was observed that the maximum net horizontal stresses occur in the ballast or at the ballast-subballast interface. The magnitude of the maximum net horizontal stresses is affected the most by the stiffness of the subballast layer. However, the vertical deflections measured behind the train at the first abutment are affected the most by the stiffness of the embankment fill. Other key findings from the analyses include:

- As the train velocity increases, the net horizontal stresses in the ballast and subballast increase.

- There is a substantial increase in the maximum net horizontal stresses when the train velocity increases from 250 to 350 km/hr.
- Net horizontal stresses in the embankment fill are relatively small, except for the case in which a soft fill is used.
- When the train is located directly above the back of the first bridge abutment, the maximum vertical deflections are observed to occur approximately 1 m behind the train, except for the case in which a soft fill is used.
- Changing the stiffness of ballast material has little effect on the net horizontal stresses and the calculated vertical deflections behind the first bridge abutment.
- As the stiffness of the subballast layer increases, vertical deflections behind the first abutment decrease.
- An increase in the stiffness of the fill corresponds to a decrease in the net horizontal stresses in the ballast and subballast layers.
- When a soft embankment fill is used, the magnitude of the maximum net horizontal stress is not affected; however, greater net horizontal stresses are observed at greater depths.
- When a soft embankment fill is used, vertical deflections increase substantially. These deflections are observed to occur 3 m behind the train.

ACKNOWLEDGEMENTS

The authors acknowledge the important contributions of Alexander Smekal, Bo Andréasson and Olof Olofsson. The analyses described in this paper were performed within the EU Sixth Framework Programme; the project title is "Sustainable Bridges – Assessment for Future Traffic Demands and Longer Lives," TIP3-CT-2003-001653.

REFERENCES

- Adolfsson, K., Andréasson, B., Bengtsson, P.-E., Bodare, A., Madshus, C., Massarsch, R., Wallmark, G., & Zackrisson, P. 1999. *Evaluation and Analyses of Measurements from the West Coast Line*. Report.
- Itasca Consulting Group 2002. *FLAC3D Fast Lagrangian Analysis of Continua in 3 Dimensions*, Itasca Consulting Group, Minnesota, Minn., USA.
- Olofsson, S.s-O. & Hakami, E. 2000. *Interaction Spår-Bro-Grund-Jord, Sättningar i övergång mellan bro och till fartsbank för lanserade broar*. Itasca Geomekanik, Borlänge.

Free field vibrations due to the passage of high-speed trains

S. Sica

Dept. of Engineering, University of Sannio, Benevento, Italy

F. Santucci de Magistris

University of Molise, Termoli, Italy

A. Melazzo

Dept. of Geotechnical Engineering, University of Naples Federico II, Napoli, Italy

ABSTRACT: Soil vibrations induced by high-speed trains may often cause malfunctioning of sensitive equipments and discomfort to population in proximity to train lines. In this paper the propagation of ground-borne vibrations caused by high-speed trains have been numerically analyzed. Validation of the model has been carried out by simulating a real case-history represented by the train testing passages on a Belgium railway track. The effectiveness of different isolating systems, such as open trenches and concrete barriers, has been later investigated to provide countermeasure to high-speed train induced vibrations.

1 INTRODUCTION

In recent years, the increasing construction of railway lines for high-speed trains (HST) all over the world made the ground-borne vibrations a quite annoying environmental problem: malfunctioning of sensitive equipments and discomfort to people have been often denounced nearby to HST tracks. Major problems have been observed close to lines crossing very soft soils (peat, organic clays, loose sands), which are, in general, particularly sensitive to mechanical vibrations. It has been found both theoretically and experimentally (Wolfert et al., 1997) that when the train speed approaches the Rayleigh wave velocity in the soil deposit, ground vibration amplitude maximizes. In these circumstances further problems might occur in addition to the environmental ones, including, for instance, degradation of the tracks and superstructures or failure of the rails due to fatigue.

In recent years, several studies have been addressed to find predictive tools to (1) reliably assess the level of train-induced ground vibrations; and, (2) design effective isolating systems to reduce the vibration level to admissible values. The latter depend on receipt features. In general ground-borne vibration is almost never annoying people who are outdoors. A vibration is annoying population if its peak ground velocity (PGV) exceeds 2.5 mm/s; the threshold value for structural damage is 50 mm/s while lower values might interest historical buildings and monuments.

In this paper the propagation of high-speed train vibrations has been investigated by f.e.m. analyses, solved in time domain using the ABAQUS/Explicit code. Validation of the model has been achieved by simulating the propagation of ground vibrations induced by the passage of a HST on a Belgium railway track (Degrande & Schillemans, 2001).

In the second part of the paper, the effectiveness of various isolating systems to reduce the train vibrations has been investigated. Open trenches and barriers were taken into account. In accordance with previous parametric studies (Woods, 1968; Ahamad et al., 1996; Sica et al., 1999; Hung, 2004) it emerged that the frequency content of the input signal is a key parameter, since it strongly regulates the design and the performance of this type of isolating systems.

2 DESCRIPTION OF THE CASE-HISTORY

The case-history analyzed in this study refers to the passages of a high-speed train on a Belgium railway track. The test program was developed at Ath, about 55 km south of Bruxelles. The train is a “Thalys HST” type whose traveling speed was varied between 223 km/h and 314 km/h during the tests.

As schematically shown in [Figure 1](#), the ground vibrations were measured in different locations of the track (points from 1 to 4) and of the ground surface (points from 5 to 14) by means of piezoelectric

accelerometers. Details on the experimental test may be found in Degrande & Schillemans, 2001. In such a context it is worth pointing out that the experimental recordings relative to 9 passages of the Tallys high speed train were kindly provided by Prof. Degrande and his co-workers to support validation of numerical procedures.

From the interpretation of the vibration recordings in terms of velocity, the following observations may be drawn:

- (1) the signals recorded near the track (points 1, 2, 3 and 4 in Figure 1) show a dominant frequency almost equal to the frequency of the bogie passage (given by the ratio between the train speed and the distance L_b between train bogies); for the train speed adopted in the test and the geometrical features of the Tallys train this frequency is in between 3.31 and 4.66 Hz;

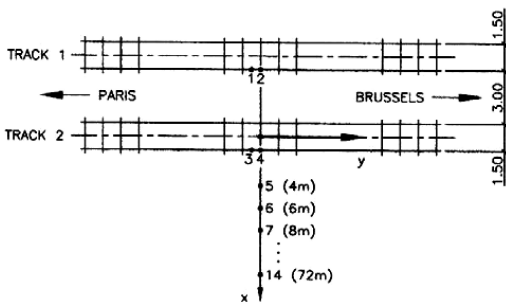


Figure 1. Experimental field set up at Ath (from Degrande & Schillemans, 2001).

- (2) the signals recorded along the ground surface in the direction normal to the railway axis (points from 5 to 14 in Figure 1) show a great modification in frequency content and amplitude as can be observed from Figure 2 in correspondence to three points located at different distances from the rail track (12, 32 and 72 m);
- (3) at each location on the ground surface, the peak particle velocity PPV is almost independent on the train speed.

At the test site the subsoil is essentially made of fine grained soils (sandy silt and clay).

By an in situ SASW test it was defined a subsoil model made of 3-layers having different shear wave velocity. In particular, a first layer having a thickness of 1.4 m is characterized by a shear wave velocity V_s of 80 m/s; a second layer with a thickness of about 2 m has a V_s of 133 m/s, and a third layer with V_s equal to 226 m/s. In the investigated depths (up to 15 m below the g.l.), the SASW investigation did not detect any bedrock. However, from a CPT test performed at the same site (data kindly provided directly by Prof. Degrande), a stiffer layer may be hypothesized at a depth of about 15 m below the g.l., even though its presence is not confirmed by the results of the SASW test and, hence, it was disregarded in the set up numerical model.

3 NUMERICAL MODELLING AND RESULTS

The case history above described was analyzed in time domain assuming a 2-D geometry and plain

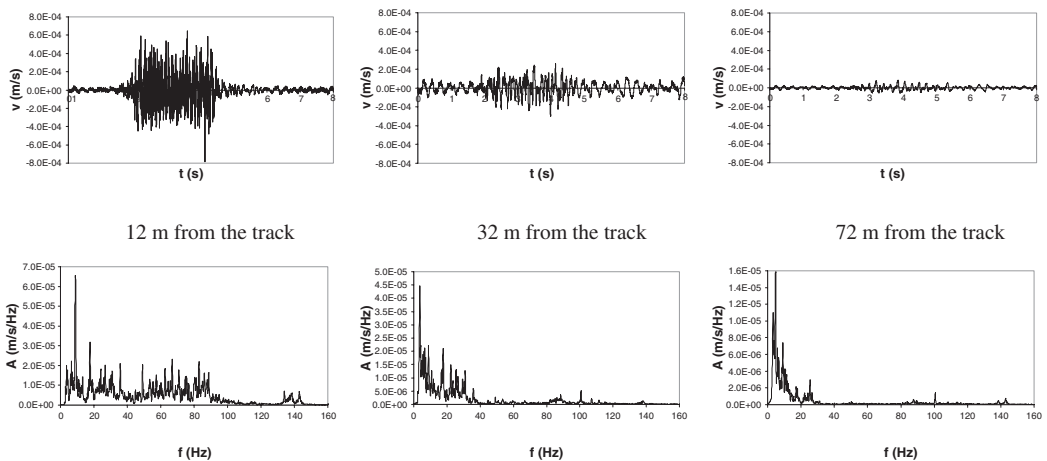


Figure 2. Time histories (up) and Fourier spectra (down) of the particle velocity measured on the ground surface at 12, 32 and 72 meters from the railway.

strain conditions. The analyses have been carried out with the finite element code ABAQUS/Explicit. The plain strain hypothesis, even if very simplified, may be justified assuming that the waves reaching a point of the ground surface from the direction normal to the railway track carry the most vibratory energy, while the waves reaching the same point from oblique directions (not possible to represent in a 2-D scheme) compensate each other and, hence, their contribute to the ground vibration in that point can be assumed null (Castellani & Valente, 2000).

To avoid simulating the whole vibration source mechanism, that requires an accurate modeling of the train and railway superstructure components (track and sleepers), further simplifying assumptions have been made. Particularly, the velocity time history recorded on the ground surface at the point closest to the track was assumed as input signal for studying the vibration propagation phenomenon within the model. Furthermore, the railway was supposed on the axis of symmetry (left boundary) of the model (Figure 3).

The modeled domain is 200 m long and 80 m deep and has been discretized in 69151 quadrilateral 4-node elements. Element heights are 0.25 m in the first layer characterized by lower shear wave velocity with the SASW test ($V_s = 80$ m/s), and not higher than 0.70 m in the remaining part of the domain. Coarser meshes were disregarded since they had the effect to artificially damp out the higher frequencies of the signal.

To avoid wave reflections in correspondence to the model boundaries, infinite elements were inserted along the bottom of the model and along the lateral boundary on the right (Figure 3). The infinite elements not only allow to model the unbounded domain required for the analysis of static problems, but they also provide the condition of energy transmission out of a finite region in dynamic problems, in an equivalent way as the viscous dampers suggested by Lysmer & Kuhlemeyer (1969).

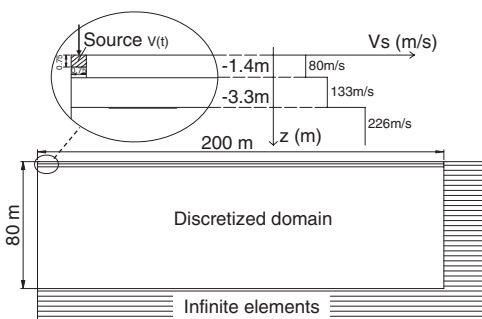


Figure 3. Domain modeled in the analysis.

Due to the reduced strain level induced in the subsoil by the train passages, soil behaviour was assumed to be linear elastic with stiffness values derived from the shear wave velocities measured by the SASW test. Soil damping has been included in the model in the form of Rayleigh damping, i.e. assuming that the damping matrix $[C]$ is a linear combination of the mass $[M]$ and stiffness matrix $[K]$ according to the following equation:

$$[C] = \alpha[M] + \beta[K] \quad (1)$$

where the coefficient α and β are function of the soil critical damping ratio D and of the frequency range that characterizes the problem in hand. In this study, due to the high uncertainties on subsoil features for depths greater than those investigated by the site tests (SASW and CPT) and on soil critical damping ratio D , the coefficient α and β were deduced from an iterative procedure trying to fit the experimental peak particle velocity, PPV, measured at different distances from the railway track (Figure 4). The couple $\alpha = 6.0$ and $\beta = 0.0004$ assures the best fitting between measured and computed PPV versus distance.

In Figure 5 the dependence of the damping ratio on frequency, that is typical of the Rayleigh formulation, has been plotted for different Rayleigh coefficients α and β . For the assumed couple of Rayleigh coefficients ($\alpha = 6.0$, $\beta = 0.0004$), the soil damping ratio is around 5% and it is almost constant in the frequency range between 10 and 30 Hz. It should worth pointing out that the damping ratio numerically estimated results a bit higher than that ($D = 3\%$) estimated by Degrande & Schillemans (2001) by interpreting analytically the transient signals of the SASW test.

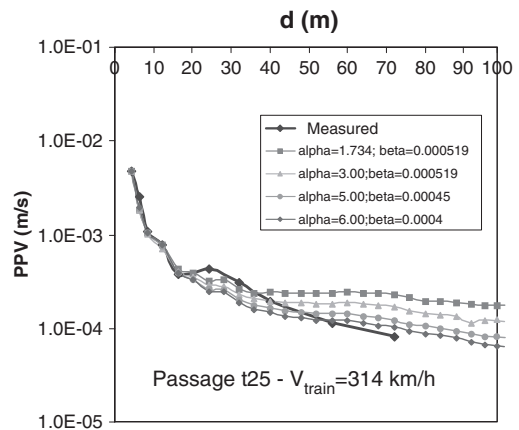
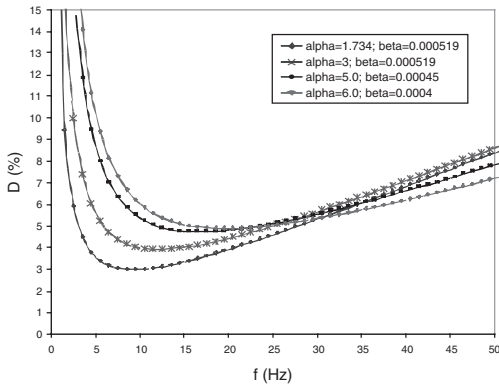


Figure 4. Measured versus computed PPV for increasing distances d from the track.



A higher value of soil damping may occur if a small amount of non linearity is induced in the foundation soils during the train passages.

The comparison between the response spectra of recorded and computed velocity (Figure 6) shows that the numerical model, even simplified, is able to reproduce the frequency content of the measured train-induced ground vibrations both in terms of PPV versus the distance from the track (Figure 4) and the shape of the response spectrum (Figure 6) at different distances from the rail track. Some discrepancies appear in some locations, such as point 9 and 12.

The actual complexity of the train-track-soil dynamic interaction and the simplifications of the adopted model should obviously be taken into account

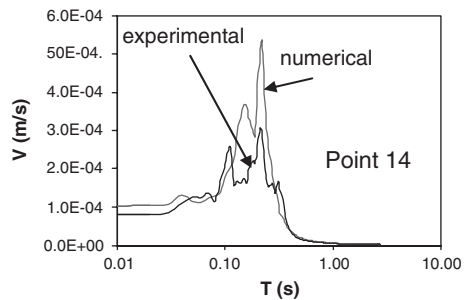
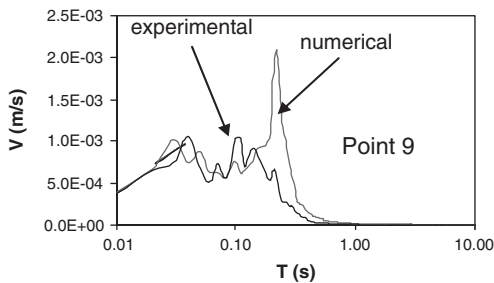
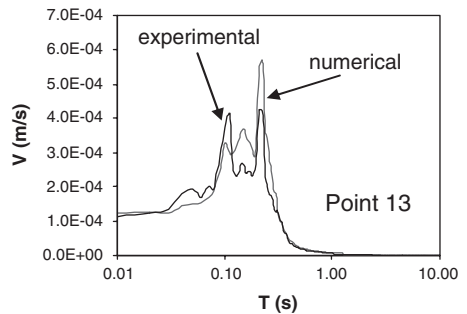
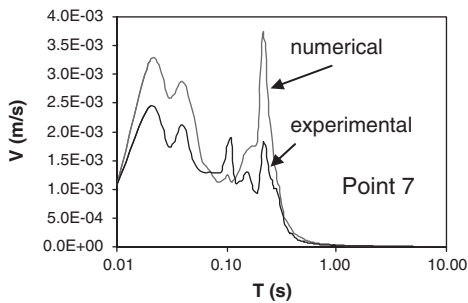
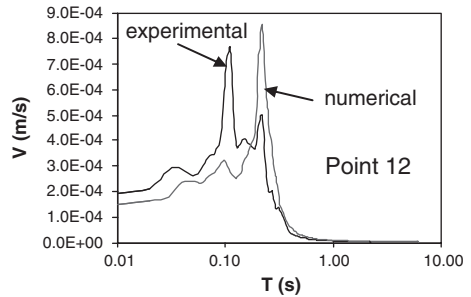
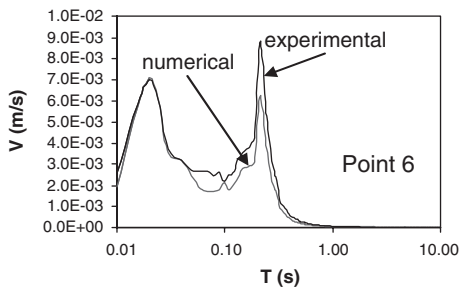


Figure 6. Response spectra (5% structural damping) of recorded and computed ground velocities at different distances from the train track (passage t25 - $V_{train} = 314$ m/s).

in interpreting these results. However, the adopted model, even if quite simplified if compared to more refined mathematical and numerical models proposed in literature (Kaynia et al., 2000, Hung et al., 2004) could be judged enough reliable, since it was able to predict qualitatively well the ground vibration propagation phenomenon; most of the times predictions result satisfactorily also quantitatively.

4 VIBRATION MITIGATION

When train-induced ground vibrations exceed acceptable limits which, as underlined before, depend on receipt features, countermeasures are required to mitigate them. Since ground vibration troubles generally come out when the HST line starts to operate, railway companies prefer countermeasures that do not prevent line functioning. Isolating systems such as open or in-filled trenches and barriers may hence be taken into account as possible vibration countermeasures.

In the past, such types of isolating systems were mainly adopted to face the problem of ground vibrations induced by machine foundations (Woods, 1968; Beskos et al., 1986; Ahmad et al., 1996; Sica et al., 1999). In these cases, being the input signal characterized by a few dominant frequencies, good isolating systems were assured by simply choosing a suitable trench depth (of an order comparable to that of the surface wavelength) or suitable dimensions of the barrier cross section.

However, few literature studies focus on performance of trenches and barriers in reducing ground-borne vibrations caused by high-speed trains.

In this study, the mitigation of HST vibrations by open trenches and concrete barriers has been investigated assuming as vibration source the same input motion adopted to simulate the case-history of Degrande & Scillemans (2001).

The discontinuity (trench or barrier) was supposed 1 m wide and located at 7 m from the vibration source. Its effectiveness was described by the ‘vibration reduction ratio’:

$$A_r = \frac{V_{isol}}{V_{ff}} \quad (2)$$

where V_{isol} and V_{ff} are the vibration amplitudes in terms of vertical velocity with and without (free-field) the screen, respectively.

In Figure 7 and 8 the vibration reduction ratio of open trenches and concrete barriers is plotted as function of the distance from the railway track. As expected, open trenches behave better than concrete barriers. To reach an average vibration reduction ratio

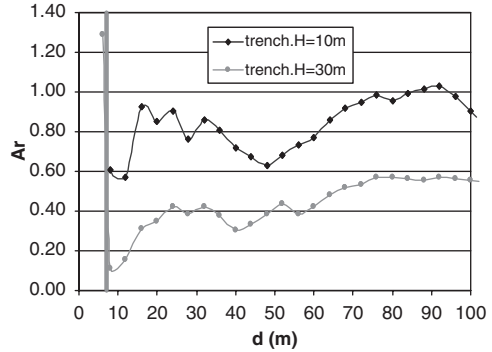


Figure 7. HST vibration isolation by open trenches.

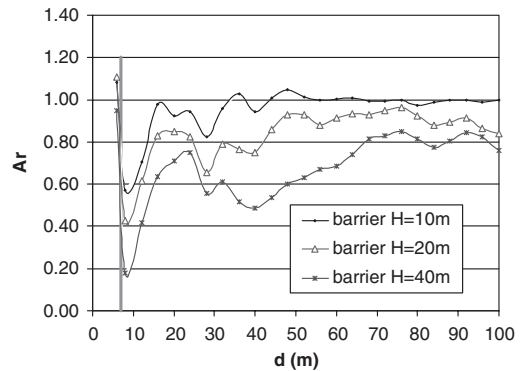


Figure 8. HST vibration isolation by concrete barriers.

of about 40% behind the trench, a depth of about 30 m should be provided, which is rather impracticable due to technological problems during both construction and exercise stage. As concrete barriers concern, it can be observed from Figure 8 that concrete barriers should be even deeper to guarantee a performance comparable to that of open trenches.

These results highlight that for ground vibrations induced by high speed trains, trenches and barriers perform not very well due to the wide range of frequencies characterizing the ground vibrations and the presence of very low frequencies (<5 Hz) which require very deep discontinuity to assure a satisfying level of vibration mitigation.

This aspect should address the railway companies to solve the HST ground vibration problems during the design stage of the railway (for example reducing the vibration level at the source, working on the track and its basement) and not by *a posteriori* countermeasures when the railway embankment and the superstructure have been already built and the line starts to work.

5 CONCLUSIONS

The propagation of ground vibrations caused by high speed trains traveling on superficial lines has been numerically analyzed by a 2-D model solved in time domain and by the finite element technique. Validation of the model has been carried out by simulating a real case-history represented by the HST passages on a Belgium railway track (Degrande & Schillemans, 2001). Albeit the simplifications in the vibration source simulation, the adopted model provided a satisfying prediction of the decay of the PPV versus the distance from the rail track and, in some cases, predictions were able to match well also the frequency content of the recorded signals.

Open trenches and concrete barriers have been investigated as possible countermeasures to mitigate HST vibrations. Even though these isolating systems have been successfully adopted to reduce vibrations induced by machine foundations, the wider frequency range characterizing the HST vibrations makes them less performable for the particular problem in hand. In particular, the presence of very low frequencies (<5 Hz) in the HST ground vibrations penalizes the design of this type of isolating system since too deep (and too expensive) screens are required to assure a satisfying level of vibration mitigation. This statement should address railway companies to solve ground vibration problems *a priori* during the railway design stage.

ACKNOWLEDGEMENTS

The authors wish to thank Prof. Geert Degrande and his co-workers for allowing them to use a precious set

of experimental recordings, supporting in this way numerical model validation.

REFERENCES

- Ahmad S., Al-Hussaini T.M., K.L. Fishman (1996) Investigation of active isolation by open and filled trenches. *Journal of Geotechnical Engrg*, ASCE, 122.
- Castellani A., Valente M. (2000) Vibrazioni trasmesse da veicoli su rotaia all'ambiente. *Ingegneria sismica*, 171 (1), pp. 40–49.
- Degrande G., Schillemans L. (2001) Free field vibration measurements during the passage of a Thalys high speed train, *Journal of Sound and Vibration*, 247(1), pp. 131–144.
- Hung H. H., Yang Y. B., ASCE F., Chang D. W. (2004). Wave barriers for reduction of train-induced vibrations in soils. *Journal of Geotechnical and Geoenvironmental Engineering*, ASCE, vol. 130 n. 12, pp. 1283–1291.
- Kaynia A.M., Madshus FC, Zackrisson P., Ground vibration from high speed trains: prediction and countermeasure (2000) *Journal of Geotechnical and Geoenvironmental Engineering*, ASCE, vol. 126 n. 6, pp. 531–537.
- Lysmer & R.L. Kuhlemeyer (1969). Finite dynamic model for infinite media, *Proc. ASCE EM4*.
- Sica S., Silvestri F., Vinale F. (1999) Effectiveness of trenches filled with geomaterials in the reduction of surface vibration amplitudes. In *Proc. Pre-failure Deformation Characteristics of geomaterials*, Balkema, pp. 759–766.
- Wolfert A.R.M., Dieterman H.A., Metrikine A.V. (1997) Passing through the 'elastic wave barrier' by a load moving along a wave guide. *Journal of Sound and Vibration*, 203(4), pp. 597–606.
- Woods R.D. 1968. Screening of surface waves in soils. *Jnl. Soil Mech. and Found. Div. ASCE* 94.

Application of pseudo-static limit analysis in geotechnical earthquake design

Jim Shiau

Faculty of Engineering and Surveying, University of Southern Queensland, Toowoomba, QLD, Australia

Andrei Lyamin and Scott Sloan

School of Engineering, The University of Newcastle, Newcastle, NSW, Australia

ABSTRACT: Based on the classical limit theorems of upper and lower bounds, the numerical procedures developed at Newcastle utilise finite elements and non-linear programming and has proven to be both effective and efficient in solving many geotechnical stability problems. The bounding techniques have yet to be applied to the seismic stability of geotechnical structures. In this paper, both seismic bearing capacity of footings located near slopes and seismic earth pressures on retaining walls will be examined.

1 INTRODUCTION

The effect of earthquake-induced horizontal force has the potential to cause failure of slopes, retaining walls, and many other types of geo-structures. Such a ground motion can induce significant inertia forces both in a soil stratum and in the structure. Therefore, the resulting “dynamic” normal and shear stresses along the potential failure surfaces need to be taken into account in a geotechnical earthquake design.

Past and most of the current practice in the seismic design of earth structures involves a pseudo-static analysis and the classical limit equilibrium method is usually employed (Kramer 1996). In this method, the effects of earthquake shaking are represented by horizontal and vertical inertia forces, $k_h W$ and $k_v W$, which act through the centroid of the assumed failure mass. Note that W is the weight of the failure mass and k_h and k_v are known as horizontal and vertical pseudo-static coefficients and are defined by $a_h = k_h g$ and $a_v = k_v g$, where a_h and a_v are horizontal and vertical accelerations. In practice, the values of k_h and k_v to be used may be found in earthquake design codes or selected on the basis of past experience. The limitation of the pseudo-static approach is clear as the complex, transient, dynamic effects of earthquake shaking are replaced by static horizontal and/or vertical forces. Nevertheless, the approach has continued to be used by geotechnical earthquake engineers mainly because it is easier to apply in design practice.

The pseudo-static limit equilibrium method presupposes collapse is triggered by large relative movements

along a predefined failure surface and that, simultaneously, the stresses on this surface reach limiting values which are governed by soil strength parameters. The solution is then found by invoking equilibrium and then optimizing the geometry of the failure surface, either analytically or numerically, to give the lowest load. An inherent limitation of the pseudo-static limit equilibrium method is the need to define the general shape of the failure surface in advance, as this may affect the accuracy of the solution obtained (Chen 1975).

Much research effort has been spent on the development of analytical upper bound limit analysis techniques for static and pseudo-static seismic loadings (Chen 1975; Michalowski 1995). Although it is a useful technique in its own right, using upper bound limit analysis alone yields unconservative estimates of the limit load. A more attractive approach for analysing the stability of geotechnical structures is to use the finite element upper and lower bound techniques, such as those developed at the University of Newcastle (Lyamin and Sloan 2002a,b). These techniques can be used to bracket the exact ultimate load from above and below, and therefore provide reliable values for use by design engineers.

The bounding techniques developed at Newcastle have yet to be applied to the seismic stability of geotechnical structures. It is thus the main objective of this paper to incorporate the pseudo-static approach into the current codes so that the effect of earthquake loadings can be considered in the analysis. A few examples will be presented in this paper.

2 SEISMIC STABILITY OF A FOOTING RESTING NEAR SLOPES

2.1 Statement of the problem

The first example presented in this paper consists of the seismic bearing capacity problem of a rigid foundation resting near slopes, as illustrated in Figure 1. A strip footing of width B is placed on a homogeneous soil with the slope angle b , the slope height H and the distance L from the edge of the slope to the footing edge. The soil is assumed to follow the Mohr-Coulomb yield criterion with the shear strength properties c and f . The coefficients of horizontal acceleration and vertical acceleration due to an earthquake are denoted by k_h and k_v , respectively. The limit behaviour under the pseudo-static seismic condition is expected to be influenced by the earthquake inertia of the soil, the structural foundation, and the applied surcharge. It would also be expected to be affected by the problem geometry such as the slope angle b , the slope height H , the footing width B and the distance L . The ultimate bearing capacity solution to the seismic stability problem can then be stated as

$$\frac{p}{\gamma B} = f\left(\beta, \frac{L}{B}, \frac{c}{\gamma B}, \frac{q}{\gamma B}, \phi, \tan \theta\right) \quad (1)$$

where p is the average limit pressure under the footing, q is the surcharge load, γ is the soil unit weight and $\tan \theta = k_h/(1 - k_v)$. The problem reduces to the static one when $\tan \theta = 0$. All results of the computations are presented in the dimensionless form as in equation (1) and are functions of β , L/B , $c/\gamma B$, $q/\gamma B$, ϕ and $\tan \theta$.

Except those mentioned in the paper, the earthquake acceleration for the soil, the structure, and the surcharge is assumed to be the same. The earthquake load on the structural foundation is represented by the shear load acting at the foundation level which leads to a problem similar to the bearing capacity solution under inclined loading. The overturning moment induced by the earthquake force on the structural foundation is not

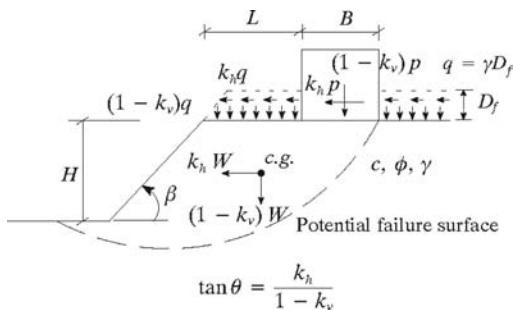


Figure 1. Problem notation for seismic bearing capacity of footings on slopes.

considered in this study. The shear strength of the soil is assumed to be unaffected by the earthquake loading and the effect of pore water pressure is not included.

2.2 Results and discussion

A comparison of the lower and upper bound limit analysis results against the limit equilibrium results by Bishop (1950) and Narita and Yamaguchi (1990) and the upper bound results by Kusakabe et al. (1981) is shown in Figure 2. It is found that results from the limit equilibrium method of Bishop (1950) are close to our numerical upper bounds while those analytical upper bound results of Kusakabe et al. (1981) are close to the averaged values of our upper and lower bound results. However, results from the limit equilibrium method of Narita and Yamaguchi (1990) using log-spiral sliding surfaces tend to be non-conservative. As can be seen in this Figure, a built-in error check on the accuracy of the limit solution is automatically provided by using the present lower and upper methods. By using either the limit equilibrium method or the conventional upper bound method alone, the range of true solutions can not be justified. This matter is especially important for complicated geotechnical problems where the true solution is unknown.

To investigate how the bearing capacity $p/\gamma B$ is affected by earthquake inertia forces ($\tan \theta$), numerical lower and upper bound estimates are presented graphically in Figure 3 for a 60 degree slope with $L/B = 0$. It indicates that the existence of earthquake forces tend to decrease the bearing capacity of foundations. As the value of $\tan \theta$ increases, the bearing capacity decreases for all friction angles. Numerical results

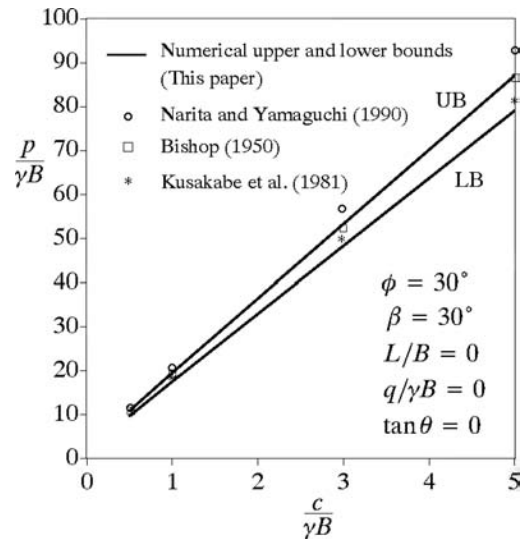


Figure 2. Comparisons of numerical bounds with other results under a static condition.

that are bounded by the lower and the upper solutions represent the range where the true limit loads are. It is interesting to see that the range of true solutions can always be closely bracketed and that the accuracy of bounding solutions increase as the value of $\tan \theta$ increases. The upper bound velocity diagrams for $\tan \theta = 0$ and $\tan \theta = 0.4$ are shown in Figure 4. Owing to a horizontal inertia force, the proportion of the velocity fields tends to decrease as $\tan \theta$ increases indicating a reduction in $p/\gamma B$.

The existence of surcharge on the slope surface could either decrease, increase or has no effect on the seismic bearing capacity of the footing, depending on parameters such as β° , L/B and $q/\gamma B$. As shown in Figure 5 for the case with $L/B = 0$ and $\tan \theta = 0.3$, the increase in $q/\gamma B$ has very little effect on $p/\gamma B$. But a slight decrease in $p/\gamma B$ is observed for a vertical slope. This is because for a vertical slope, the surcharge

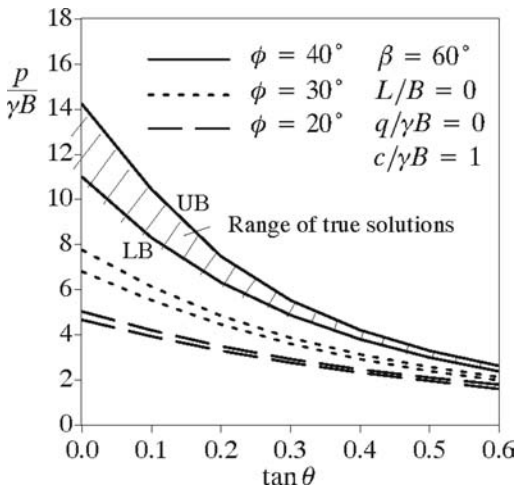


Figure 3. Effect of $\tan \theta$ on $p/\gamma B$ for various ϕ ($\beta = 60^\circ$).

on the slope surface contributes a driving force to the slope failure causing a reduction in the footing bearing capacity. As seen from the upper bound velocity diagrams in Figure 6, the proportion of deformed area is increased due to the existence of surcharge for a vertical slope with footing location $L/B = 0$. However, for cases with low slope angle, the contribution to failure of the footing-slope system due to a surcharge is very little and thus the value of $p/\gamma B$ remains constant as $q/\gamma B$ increases.

To ascertain the effect of soil inertia k_h on the bearing capacity of footings near slopes, the results in Figure 7 show the variation of $p/\gamma B$ with k_h for cases with and without $k_h W$. A comparison of these results for various slope angles indicates that by ignoring the effect of earthquake inertia of the soil slope, an unsafe estimate of the ultimate bearing capacity can be obtained. This is true irrespective of any soil slope angle.

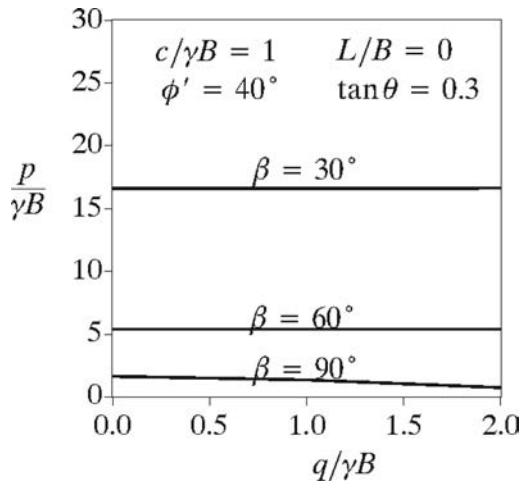


Figure 5. Effect of $q/\gamma B$ on $p/\gamma B$ for various β ($\tan \theta = 0.3$).

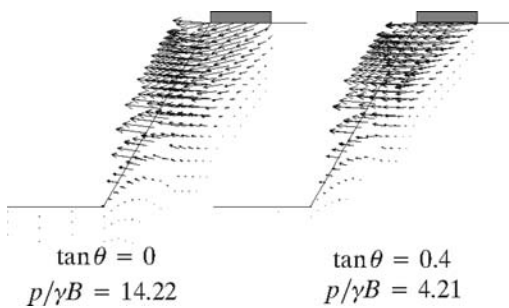


Figure 4. Upper bound velocity diagrams for $\tan \theta = 0$ and $\tan \theta = 0.4$.

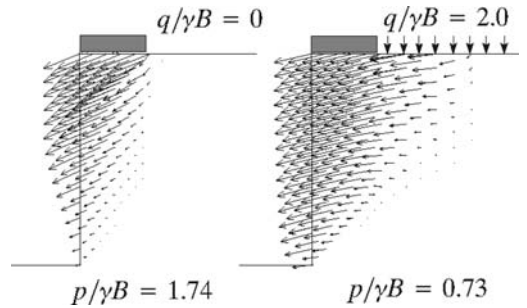


Figure 6. A comparison of upper bound velocity diagrams for the surcharge effects of a vertical cut.

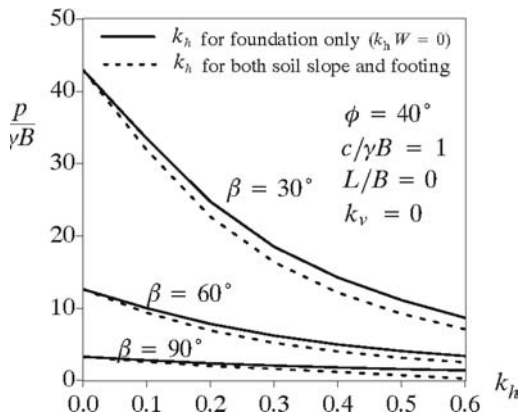


Figure 7. Effect of soil inertia k_h on $p/\gamma B$.

3 SEISMIC EARTH PRESSURE PROBLEMS

3.1 Statement of the problem

The seismic lateral earth pressure problem considered in this paper is illustrated in Figure 8. The back of the wall has an angle α to the horizontal and the surface of the backfill has a slope of β to the horizontal and a uniform surcharge q . In determining the passive earth resistance, a rigid retaining wall of height H is pushed horizontally into the soil. To induce active failure, the wall is allowed to move away from the backfill. The soil is taken to be $c - \phi$ Mohr-Coulomb material with a unit weight γ .

It is convenient to use soil-wall friction angle δ and adhesion c_a for representing the wall roughness. For a $c - \phi$ backfill, $\delta = 0$ and $c_a = 0$ indicates a perfectly smooth wall while a perfectly rough wall can be modelled by adopting $\delta = \phi$ and $c_a = c$. In a similar manner to the bearing capacity equation of Terzaghi, the total active and passive thrust acting on the wall, P_a and P_p , are defined in terms of earth pressure coefficients K_a , K_c and K_q according to

$$P_a = \frac{1}{2} \gamma H^2 K_{a\gamma} - cHK_{ac} + qHK_{aq} \quad (2)$$

$$P_p = \frac{1}{2} \gamma H^2 K_{p\gamma} - cHK_{pc} + qHK_{pq} \quad (3)$$

Equations (2) and (3) are governed by the geometric parameters α and β , the soil-wall friction angle δ and adhesion c_a , the surcharge q , and the backfill frictional angle ϕ . Note that the line of action of P_a and P_p is inclined at δ to the normal from the wall back. To consider the seismic effects, the coefficients of horizontal acceleration and vertical acceleration due to an earthquake are denoted by k_h and k_v , respectively and a new factor $\tan \theta = k_h/(1 - k_v)$ is defined.

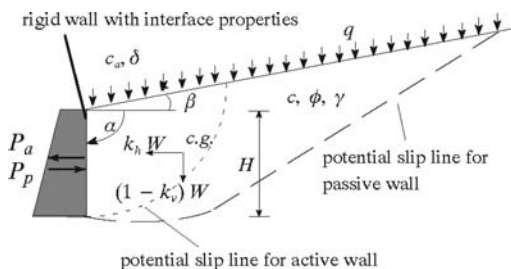


Figure 8. Problem notation for seismic earth pressures.

Table 1. Values of $K_{a\gamma}$ for various $\tan \theta$ and δ/ϕ .

		$(\phi = 35^\circ)$				
		0	1/3	1/2	2/3	1
tan $\theta = 0$	UB	0.266	0.245	0.241	0.242	0.247
	LB	0.272	0.268	0.260	0.257	0.261
tan $\theta = 0.1$	UB	0.323	0.306	0.302	0.301	0.315
	LB	0.329	0.325	0.319	0.316	0.325
tan $\theta = 0.2$	UB	0.386	0.376	0.377	0.381	0.403
	LB	0.399	0.396	0.392	0.393	0.412
tan $\theta = 0.3$	UB	0.469	0.464	0.471	0.482	0.525
	LB	0.487	0.485	0.486	0.494	0.532
tan $\theta = 0.4$	UB	0.573	0.581	0.596	0.617	0.691
	LB	0.597	0.602	0.611	0.629	0.699

Note: UB and LB are upper and lower bound results.

Given the above parameters, the total active and passive thrusts are computed from the finite element upper and lower bound analyses. Accordingly, the coefficients of earth pressure can be determined from equations (2) and (3).

3.2 Results and discussion

Results shown in Table 1 are calculated by putting $c = 0$ and $q = 0$ in equation (2). For a $\phi = 35^\circ$ backfill soil, we studied the effect of $\tan \theta$ on the active earth pressure coefficient $K_{a\gamma}$ for five values of soil-wall friction (δ/ϕ). As previously discussed, the line of action of P_a is normal to the vertical wall back for a smooth wall ($\delta = 0$) and, for rough walls, P_a is assumed to act at an angle of δ to the normal from the wall back. Accordingly, $K_{a\gamma}$ values shown in Table 1 are calculated from

$$K_{a\gamma} = K_{a\gamma,h} / \cos \delta = 2P_{a,h} / \gamma H^2 \cos \delta \quad (4)$$

where $P_{a,h}$ and $K_{a\gamma,h}$ are the horizontal active thrust and the coefficient of horizontal active earth pressure respectively.

It is clear that the introduction of seismic factor $\tan \theta$ is to increase the active earth pressure. Note that

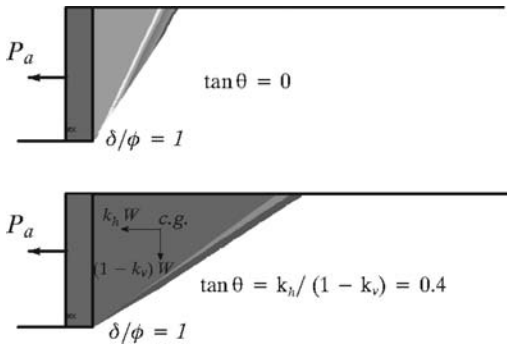


Figure 9. A comparison of velocity plots for different $\tan \theta$ ($\delta/\phi = 1$).

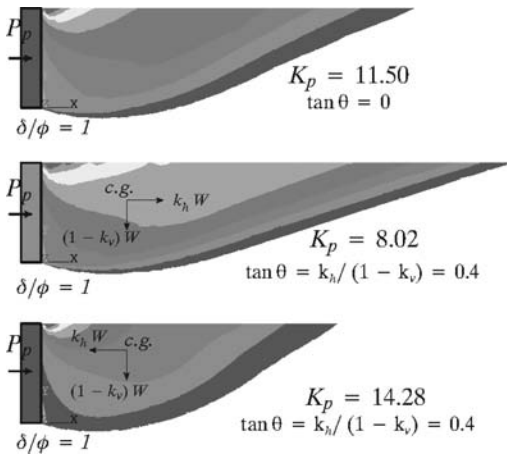


Figure 10. A comparison of velocity plots for the effect of $\tan \theta$ on passive earth pressures.

the increase is approximately 2.5–3 times for a value of $\tan \theta$ from 0 to 0.4. For higher values of $\tan \theta$ (for example $\tan \theta = 0.4$), the increase in δ/ϕ results in an increase of $K_{a\gamma}$. This trend is not observed for lower values of $\tan \theta$ in which the $K_{a\gamma}$ value may firstly decrease and then increase. The velocity diagrams shown in Figure 9 indicate that the failure plane is linear for all values of $\tan \theta$.

For passive cases, on the other hand, we present a simple upper bound study to demonstrate the effect of $\tan \theta$ (Figure 10). For a static condition ($\tan \theta = 0$), the analysis gives a value of $K_{p\gamma} = 11.50$. This value is decreased to $K_{p\gamma} = 8.02$ by introducing a “positive” $\tan \theta = 0.4$ (acting to the right of the soil mass). As expected, the passive pressure can be increased by applying a “negative” (acting to the left of the soil mass) $\tan \theta$. Also shown in Figure 10 is a comparison of velocity contour plots for the three cases. Note that the right hand edge of the mesh needs to be checked

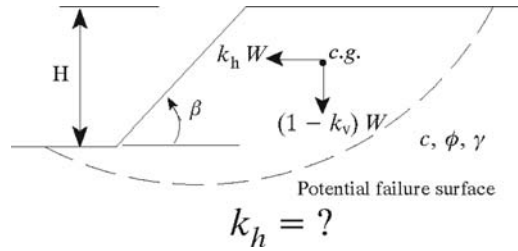


Figure 11. Problem notation for seismic stability analysis.

carefully to ensure that the failure mechanism is contained within – a case especially for “positive” values of $\tan \theta$.

4 YIELD ACCELERATION OF SEISMIC SLOPE STABILITY

In the fifth Rankine Lecture, Newmark (1965) proposed a sliding block theory for the design of seismic slope based on the evaluation of permanent displacement due to earthquake excitation. In the sliding block method, the earthquake inertia force is represented by a horizontal seismic coefficient using conventional pseudo-static approach in which the yield or critical acceleration for the soil slope at the limit state is determined. If the earthquake acceleration exceeds this critical value, slide occurs. The permanent displacements are then obtained by double integrating the difference between the design accelerogram and the computed yield acceleration. As pointed out by Seed (1966), the evaluation of permanent displacement depends on the accurate solution of yield acceleration. Most of the solutions currently available for estimating the yield acceleration of seismic slope stability are based on the limit equilibrium approach with the assumption of potential failure surface due to earthquake inertia forces. Very few rigorous analyses have been proposed to determine the seismic yield acceleration.

4.1 Statement of the problem

Yield acceleration is defined in this paper as the critical horizontal acceleration at which it produces a limit state of the slope stability under the pseudo-static earthquake forces. As illustrated in Figure 11, the seismic force is assumed to be proportional to the weight of the potential sliding mass W and the horizontal seismic coefficient k_h . The slope stability problems can then be evaluated under the combined effects of the weight W and the seismic force $k_h W$. To consider the effect of vertical earthquake inertia force, the weight W can be simply replaced by $(1 - k_v) W$ in which k_v is the vertical seismic coefficient and has positive value when it acts upward.

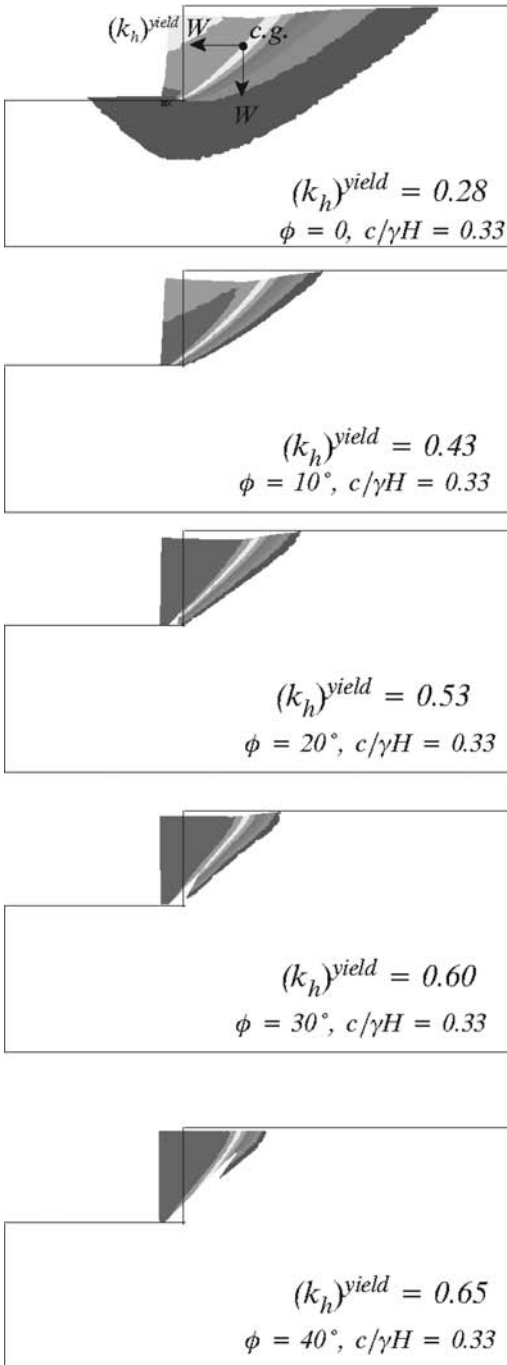


Figure 12. Deformed shapes and velocity diagrams showing slope failures under critical yield accelerations.

For a given slope of height H and inclination angle β , there exists a critical value $(k_h)^{yield}$ which will cause slope failure under the Mohr-Coulomb yield criterion with the strength parameters c and ϕ . The limit solution to the seismic coefficient $(k_h)^{yield}$ of the proposed problem can then be stated as

$$(k_h)^{yield} = f(\beta, \phi, c/\gamma H, k_v) \quad (5)$$

where γ is the soil unit weight and $c/\gamma H$ is termed as the stability number. In all the analyses, the shear strength of the soil is assumed to be unaffected by the earthquake loading and the effect of pore water pressure is not included.

4.2 Results and discussion

Numerical studies for the yield acceleration are for a vertical slope with stability factor $c/\gamma H = 0.33$ and $k_v = 0$. Shown in Figure 12 are velocity diagrams for various soil friction angles ($\phi = 0-40^\circ$). As expected, the $(k_h)^{yield}$ value increases with increasing soil friction angle. The soil gains more strength and therefore the proportion of failure mechanism becomes smaller as ϕ increases.

5 CONCLUSIONS

Three numerical models have been created for geo technical seismic stability problems using numerical limit analysis techniques developed at Newcastle. They are for seismic footing on slope, seismic earth pressures, and seismic yield acceleration for slopes. Numerical upper and lower bounds have been reported in most cases and they typically bracket the true solution within $\pm 10\%$ or better. Based on the associated flow rule, it is expected that solutions based on any available method should yield results that are located between our upper and lower bounds. More bounding results for a wide range of parameters should be reported in the near future to facilitate the design practice of geotechnical earthquake problems.

REFERENCES

- Bishop, A. W. (1955). "The use of the slip circle in the stability analysis of slopes." *Geotechnique*, 5, 7-17.
- Chen, W. F. (1975). *Limit analysis and soil plasticity*, Elsevier, Amsterdam.
- Kramer, S. L. (1996). *Geotechnical Earthquake Engineering*, Prentice-Hall, Inc.
- Kusakabe, O., Kimura T. and Yamaguchi, H. (1981). "Bearing capacity of slopes under strip loads on the top surface." *Soils and Foundations*, 21(4), 29-40.
- Lyamin, A. V. and Sloan, S. W. (2002a). "Lower bound limit analysis using nonlinear programming." *International*

- Journal for Numerical Methods in Engineering*, 55, 573–611.
- Lyamin, A. V. and Sloan, S. W. (2002b). "Upper bound limit analysis using linear finite elements and nonlinear programming." *International Journal for Numerical and Analytical Methods in Geomechanics*, 26, 181–216.
- Michalowski, R. L. and Shi, L. (1995). "Bearing capacity of footings over two-layer foundation soils." *Journal of Geotechnical Eng.*, ASCE, 121(5), 421–428.
- Narita, K. and Yamaguchi, H. (1990). "Bearing capacity analysis of foundations on slopes by use of log-spiral sliding surfaces." *Soils and Foundations*, 30(3), 144–152.
- Shiau, J. S., Lyamin, A. V. and Sloan, S. W. (2003). "Bearing capacity of a sand layer on clay by finite element limit analysis" *Canadian Geotechnical Journal*, 40, 900–915.
- Shiau, J. S., Lyamin, A. V. and Sloan, S. W. (2004). "Rigorous Solutions of Classical Lateral Earth Pressures" *Proceedings of the 6th Australia-New Zealand Young Geotechnical Professionals Conference*, 162–167.
- Shiau, J. S., Augarde, C. E., Lyamin, A. V. and Sloan, S. W. (2006). "Passive earth resistance in cohesionless soil." *Canadian Geotechnical Journal*. (Accepted)
- Shiau, J. S., Merifield, R. S., Lyamin, A. V. and Sloan, S. W. (2006). "Undrained stability of footings on slopes." *Journal of Geotechnical and Geoenvironmental Engineering*, ASCE. (Accepted)
- Sloan, S. W. (1989). "Upper bound limit analysis using finite elements and linear programming." *International Journal for Numerical and Analytical Methods in Geomechanics*, 13, 263–282.
- Sloan, S. W. and Kleeman, P. W. (1995). "Upper bound limit analysis using discontinuous velocity fields." *Computer Methods in Applied Mechanics and Engineering*, 127, 293–314.

BIEM for seismic wave propagation in fluid saturated multilayered media

Petia Dineva

Institute of Mechanics – Bulgarian Academy of Sciences, Sofia, Bulgaria

Maria Datcheva* & Tom Schanz

Laboratory of Soil Mechanics, Bauhaus-Universität Weimar, Germany

ABSTRACT: An efficient methodology is developed for solution of two-dimensional frequency dependent elasto-dynamic problems, related to seismic wave propagation in fluid saturated multilayered geological regions with accounting for complex geometry such as non-parallel layering and relief peculiarities. The proposed approach is based on the combined usage of both: (i) viscoelastic isomorphism to the Biot's dynamic poroelasticity and (ii) boundary integral equation method (BIEM) in frequency domain. Validation of the viscoelastic isomorphism and verification of the proposed BIEM are done by solution of benchmark examples. The example applications reveal that the developed method is able to depict the sensitivity of the obtained seismic signals to the existence of both fluid saturated material layers and surface topography. It is concluded finally, that the viscoelastic isomorphism implemented in an efficient BIEM software provides a straightforward tool for solving seismic wave propagation problems in multilayered fluid filled geological regions with complex geometry.

1 INTRODUCTION

Since Biot's (Biot 1956) contribution to dynamic poroelasticity, the problem of wave propagation in poroelastic materials has been extensively studied. There is a number of authors presenting results revealing the effect of boundaries and the influence of saturation on seismic wave propagation in homogeneous domains, see e.g. (Deresiewicz and Wolf 1964; Yang and Sato 2001; Lin et al. 2005). A review of methods applied to investigate the 2D site effects within elastodynamics is given in (Alvarez-Rubio et al. 2004). The usage of Biot's wave equations for seismic wave propagation in multilayered regions with complex geometry is still limited due to the complexity of the boundary value problem (BVP) which has to be solved. In most of the cases which have practical importance only numerical solution can be obtained. Among different numerical methods the BIEM is well proved in solving dynamic problems in infinite geological media. Although its well known advantages (Beskos 1991), the BIEM application in seismic wave problems for fluid saturated materials is still limited. The reason is the lack of fundamental solution in a simple form, which is easy to implement in a

BIEM code. The fundamental solutions have complex mathematical form due to the multiphase nature of the poroelastic models (Schanz and Pryl 2004). The poroelastic and viscoelastic materials have similar dynamic response (Simon et al. 1984) that hints at the possibility to use one phase model with special properties instead of multiphase one. An linear Kelvin-Voigt viscoelastic material which has equivalent to the Biot low frequency poroelastic dynamic response is proposed in (Bardet 1992).

The main purpose of this work is to develop an efficient and accurate BIEM for solution of 2D seismic wave propagation problems in multilayered fluid saturated geological region based on the viscoelastic isomorphism (Bardet 1992). The main advantage of the proposed technique is that it combines efficiently the simplicity of the viscoelastic monophasic formulation to describe the poroelastic dynamic response and all the benefits provided by the BIEM in solving wave propagation problems. BIEM advantages are: (i) reduction of the problem dimensionality; (ii) implicit satisfaction of the radiation condition in infinity; (iii) semi-analytical character of the method and (iv) discretization only on the boundaries of the considered domain.

The presented results are not aimed to reveal the physics of the phenomena but to demonstrate the

* on leave from the IMech-BAS

validity of the proposed methodology for solving wave propagation problems accounting for 2D site effects.

2 CONCEPTUAL MODEL AND PROBLEM FORMULATION

2.1 Governing equations in frequency domain

It is well known that due to the correspondence principle (Christensen 1971) no difference is made between elastic and viscoelastic media when dynamic time-harmonic problems are treated. In the following, the dynamic problem is analyzed in two dimensions and therefore plane strain condition is considered. The governing equations in the frequency domain for a time harmonic excitation of type $e^{i\omega t}$ are:

$$\begin{aligned} \left(\frac{k_s^2}{k_p^2} - 1\right) (U_{y,xy} + U_{x,xx}) + U_{x,xx} + U_{x,yy} &= -k_p^2 U_x \\ \left(\frac{k_s^2}{k_p^2} - 1\right) (U_{x,xy} + U_{y,yy}) + U_{y,xx} + U_{y,yy} &= -k_s^2 U_y \end{aligned} \quad (1)$$

where $u_x = U_x e^{-i\omega t}$, $u_y = U_y e^{-i\omega t}$ (u_x, u_y are the displacement components). Hereafter we consider that attenuations ξ_p and ξ_s and angular frequency ω are such that $\omega\xi_p \ll 1$ and $\omega\xi_s \ll 1$. In this case the approximated expressions for the wave numbers k_s and k_p read:

$$k_p \approx \frac{\omega}{C_p} \left(1 + \frac{i}{2}\omega\xi_p\right); \quad k_s \approx \frac{\omega}{C_s} \left(1 + \frac{i}{2}\omega\xi_s\right) \quad (2)$$

where C_p and C_s are the P- and SV-waves velocities. Bardet (Bardet 1992) stated a poroelastic-viscoelastic similarity by equating the wave numbers in (2) with wave numbers in Biot's poroelastic model. It results an equivalent to the poroelastic material linear Kelvin-Voigt viscoelastic material with velocities and attenuations of longitudinal and shear waves related to the poroelastic parameters as:

$$C_p = \sqrt{\frac{P + 2Q + R}{\tilde{\rho}}}, \quad C_s = \sqrt{\frac{N}{\tilde{\rho}}} \quad (3)$$

$$\xi_p = \frac{\tilde{\rho}}{b} \left(\frac{Q + R}{P + 2Q + R} \frac{n\rho_f}{\tilde{\rho}}\right)^2, \quad \xi_s = \frac{\tilde{\rho}}{b} \left(\frac{n\rho_f}{\tilde{\rho}}\right)^2 \quad (4)$$

Here $\tilde{\rho} = (1 - n)\rho_g + n\rho_f$, n is the solid skeleton porosity, ρ_f and ρ_g are the fluid and the solid grain

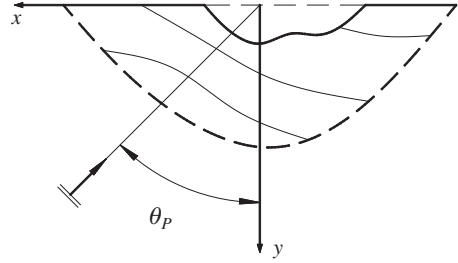


Figure 1. 2D geometry of the BVP.

densities, $b = n^2 g \rho_f / \hat{k}$ is the dissipation constant, \hat{k} is the fluid conductivity, $g = 9.81 \text{ m/s}^2$ is the gravitational constant. The Biot constants P , Q , N and R are related to the dry bulk moduli of the skeleton K_{dry} , soil grain K_g and fluid (water) K_f , porosity n and the Poisson's ratio ν by the following expressions:

$$\begin{aligned} P &= \frac{3(1 - \nu)}{1 + \nu} K_{dry} + \frac{Q^2}{R} \\ Q &= \frac{n(1 - n - K_{dry}/K_g) K_g}{1 - n - K_{dry}/K_g + nK_g/K_f} \\ R &= \frac{n^2 K_g}{1 - n - K_{dry}/K_g + nK_g/K_f} \\ N &= \frac{3}{2} \frac{1 - 2\nu}{1 + \nu} K_{dry} \end{aligned}$$

It has to be emphasized that the relations (3) and (4) hold only in case $\omega\tilde{\rho}/b \ll 1$, which is usually satisfied for the range of angular frequency and fluid conductivity encountered in earthquake engineering problems. Thus the two phase poroelastic dynamic behaviour is approximated by the dynamic response of one phase viscoelastic material. Following this approach it is not possible to account for boundary conditions for the pore fluid pressure. The proposed viscoelastic isomorphism is applicable for solving drained problems and it is verified in section 3.

2.2 Boundary conditions

The BVP comprises a finite, multilayered fluid saturated geological region with nonparallel boundaries and with topographic irregularities. A sketch is shown in Figure 1. The different material layers and the half-plane where the soil/rock deposit is situated may have different properties. The incident time-harmonic seismic wave with angular frequency ω is a plane longitudinal P-wave and it impinges under arbitrary angle θ_p according to the upward vertical direction.

The BVP consists of the governing equations (1) with wave numbers (2), velocities (3) and attenuation

coefficients (4). Traction t_i , $i = x, y$ at a given point of the surface element with normal n_i is defined as:

$$t_i = \sigma_{ij} n_j \quad i, j = x, y$$

where

$$\sigma_{ij} = \tilde{\rho} \left[\delta_{ij} \left(\tilde{C}_p^2 - 2\tilde{C}_s^2 \right) U_{k,k} + \tilde{C}_s^2 (U_{i,j} + U_{j,i}) \right],$$

$$\tilde{C}_p = C_p / (1 + i\omega\xi_p/2), \quad \tilde{C}_s = C_s / (1 + i\omega\xi_s/2)$$

The following boundary conditions are to be satisfied: (a) on the free surface of the half-space tractions are zero; (b) at infinity Sommerfeld radiation condition holds; (c) on the boundary between two soil/rock layers displacement continuity and traction equilibrium are satisfied; (d) on the boundary between the finite layered region and the rest of the half-space the displacement continuity is satisfied:

$$U_i = U_i^{free-field} \quad (5)$$

where $U_i^{free-field}$ are the free field displacement components.

2.3 BIEM solution

The formulated BVP is solved by the BIEM. The governing boundary integral equations (BIEs) in frequency domain for each of the N layers Ω_m ($m = 1, 2, \dots, N$) are:

$$C_{ij} U_j(x, y) = \int_{\Gamma_{\Omega_m}} U_{ij}^*(x, y, x_0, y_0) t_j(x_0, y_0) d\Gamma - \int_{\Gamma_{\Omega_m}} T_{ij}^*(x, y, x_0, y_0) U_j(x_0, y_0) d\Gamma \quad (6)$$

C_{ij} are constants depending on the geometry at the collocation point; $\{x, y\}$ and $\{x_0, y_0\}$ are the position vectors of the field and the source points respectively; Γ_{Ω_m} is the boundary of the m -th layer, U_{ij}^* is the fundamental solution of equations (1) and T_{ij}^* are the corresponding tractions. The system of integral equations (6) has to be solved with respect to unknown displacements U_i and tractions t_i .

The numerical solution of the problem follows the standard BIEM procedure. The boundary is described into quadratic boundary elements using piecewise polynomial approximations of the boundary geometry, displacements and tractions. After overcoming weak and strong singularities in the obtained integrals and satisfying the prescribed boundary conditions, an algebraic system according to the unknown displacements and tractions in the Fourier domain is obtained and numerically solved.

3 VALIDATION AND VERIFICATION

The aim of this section is: (a) to evaluate the applicability of the described in section 2 viscoelastic isomorphism for solution of seismic wave propagation in fluid saturated soil/rock regions (test example 1); (b) to study the accuracy of the proposed solution strategy and BIEM procedure (test examples 2 and 3).

3.1 Test example 1

Two analytical solutions for seismic wave propagation in half-space are compared. The first is the analytical solution given in (Lin et al. 2005), where the poroelastic dynamic problem is solved for drained boundary conditions in case the filling fluid is inviscid, thus the dissipation constant b is zero. The second solution is obtained solving the same problem as in (Lin et al. 2005) but for the viscoelastic material which is isomorphic to the poroelastic one. To find this solution we use (a) the analytical solution for free-field motion in elastic half-space subjected to incident P-wave, (Achenbach 1973) and (b) the correspondence principle between elastic and viscoelastic models.

The material is sandstone and the material properties are taken from (Lin et al. 2005): $K_g = 36000$ MPa; $\rho_g = 2650$ kg/m³; $\rho_f = 1000$ kg/m³; $K_f = 2000$ MPa. The porosity is $n = 0.3$ and $K_{dry} = 6167$ MPa. Four different values are taken for the Poisson's ratio, namely 0.1, 0.2, 0.3 and 0.4. The frequency is $f = 4$ Hz ($\omega = 8\pi$ s⁻¹).

Figure 2 shows the horizontal and the vertical components of the displacement at the free-surface versus the incident angle θ_p for different Poisson's ratios. The displacements are normalized by k_p , which is the displacement intensity of the incident P-wave. Figure 2 demonstrates that both models have very close and almost identical solutions. This means that the simpler equivalent viscoelastic model can be used successfully as an approximation to the solution of complex poroelastic dynamic problems.

3.2 Test example 2

The geological structure model given in Figure 3 is used for the second test example. The local geological region $T_1L_1R_1P_1$ is placed in a half-space. This test example verifies the method of superposition of the analytical solution for the infinite homogeneous half-space and the BIEM numerical solution for the embedded finite region. The mechanical properties of the local geological region are the same as the properties of the half-space. In this case there are no re-reflections and refractions on the boundary $T_1L_1R_1P_1$ and as a matter of fact the problem for fluid-saturated porous half-space subjected to incident P-wave is solved. The

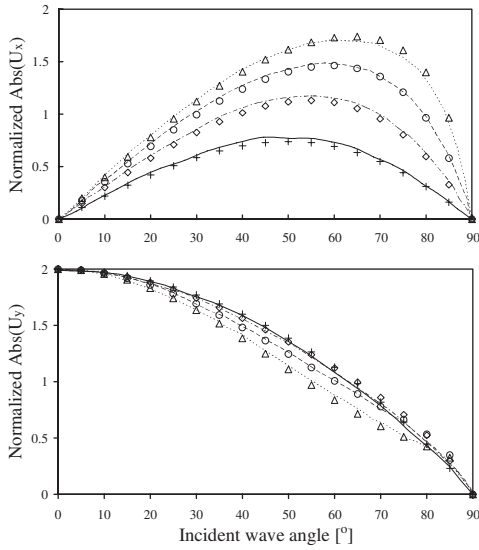


Figure 2. Test example 1 – poroelastic (lines) and viscoelastic (markers) analytical solutions: — + $\nu = 0.4$; - - - $\diamond \nu = 0.3$; - - $\circ \nu = 0.2$; ... $\Delta \nu = 0.1$.

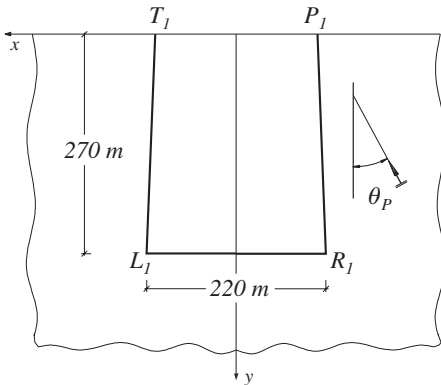


Figure 3. Geological structure model 1.

coordinates of the corner points (in meters) are: $T_1(100, 0)$, $P_1(-100, 0)$, $L_1(110, 270)$, $R_1(-110, 270)$. The Poisson's ratio equals to 0.3 and the other constants are the same as those in test example 1. In fact the same problem as in 3.1 is solved but this time applying the BIEM. In Figure 5 a comparison is done between the obtained BIEM results and the given in (Lin et al. 2005) analytical solution. The two solutions are very close and this reveals both the applicability of the viscoelastic isomorphism in such type of dynamic problems and also the accuracy and convergence of the applied numerical method.

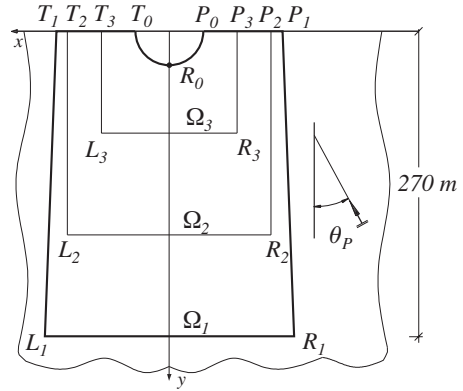


Figure 4. Geological structure model 2.

3.3 Test example 3

As a third example the geological structure model given in Figure 4 is considered. This example gives verification of the BIEM procedure for solution of seismic wave propagation in finite multilayered domains. The geological region consists of four layers. The coordinates (in meters) of the points indicating the geometrical boundaries of the layers are: $T_0(30, 0)$, $T_3(60, 0)$, $T_2(90, 0)$, $T_1(100, 0)$, $P_0(-30, 0)$, $P_3(-60, 0)$, $P_2(-90, 0)$, $P_1(-100, 0)$, $L_1(110, 270)$, $L_2(90, 180)$, $L_3(60, 90)$, $R_1(-110, 270)$, $R_2(-90, 180)$, $R_3(-60, 90)$.

The soil/rock layers and the rest of the half-space have the same mechanical properties equal to those used in 3.2. This simulates free field motion in fluid saturated porous half-space subjected to incident P-wave.

Figure 5 shows the displacements on the free surface versus the incident wave angle θ_P . Three types of solutions are compared: (a) analytical solution of Biot's wave equations for saturated poroelastic half-space from (Lin et al. 2005); (b) numerical BIEM solution of the same problem but using the viscoelastic isomorphism for the geological structure model in Figure 3; (c) numerical BIEM solution of the same problem using the viscoelastic isomorphism for the geological structure model in Figure 4. The three solutions are very close and this fact proves that it is reasonable to use the discussed viscoelastic isomorphism for synthesis of theoretical seismograms at the free-surface of geological region with complex morphology and geometry. The obtained BIEM solutions almost cover the analytical one, which demonstrates the good accuracy of the numerical method.

4 EXAMPLE APPLICATIONS

4.1 Example 1

This example aims to show the effect of fluid saturation on the free-field motion of a homogeneous halfspace.

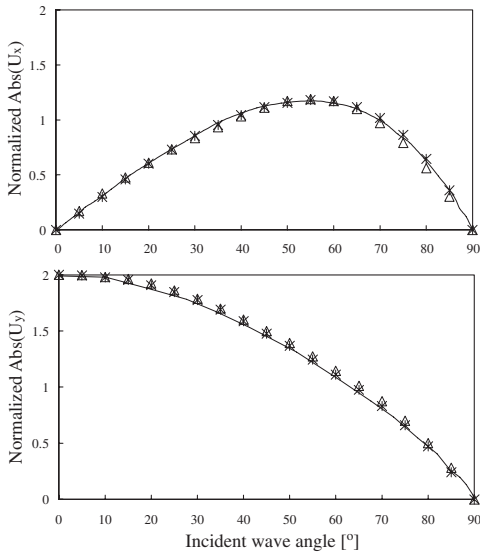


Figure 5. Test examples 2–3: lines – analytical solution; Δ – BIEM solution (test example 2); * – BIEM solution (test example 3).

The amplitudes of the displacement components u_x and u_y versus incident wave angle θ_p for elastic and porous materials are compared. The dynamic response of the saturated porous media is obtained employing the viscoelastic isomorphism. For comparison, the problem is solved for elastic media and it results the elastodynamic solution. In this case dry material properties are used. Figure 6 shows the results for materials with equal Poisson's ratio ($\nu = 0.2$) and four different porosities, namely 0.1, 0.2, 0.3 and 0.33. Figure 7 depicts results for materials with the same porosity $n = 0.3$, but having different Poisson's ratios. Dry bulk moduli are calculated using the expression given in (Lin et al. 2005) and stated there to be valid for sandstone:

$$K_{dry} = K_{cr} + (1 - n/n_{cr})(K_g - K_{cr}) \quad (7)$$

where $K_{cr} = 200$ MPa is the bulk modulus at critical porosity $n_{cr} = 0.36$. All the other material parameters are the same as in 3.1.

Figures 6 and 7 reveal the following effects: (a) in case Poisson's ratio is constant, the amplitudes of u_x decrease with increasing the porosity and for viscoelastic materials they are smaller than for the elastic ones; (b) the sensitivity of u_y to the presence of fluid is very little, but there is a tendency to increase with porosity increase; (c) in case Poisson's ratio does not change, the elastic dynamic response is not sensitive to the change of porosity, as it is expected for the range of angular frequencies used here; (d) the amplitudes of u_y for elastic

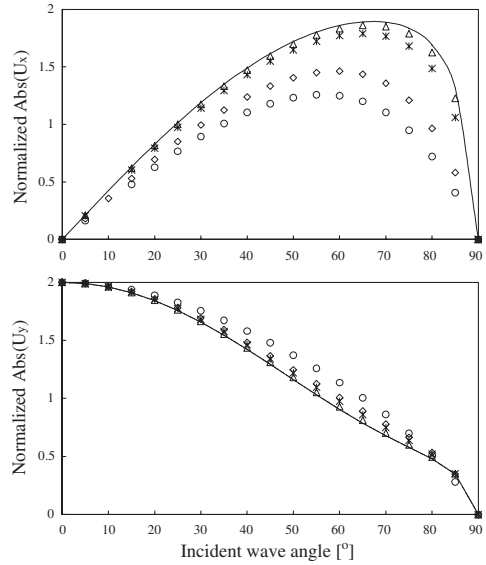


Figure 6. Comparison of elastic (line) and poroelastic (markers) dynamic response: $\nu = 0.2$; Δ for $n = 0.1$; * for $n = 0.2$; \diamond for $n = 0.3$; \circ for $n = 0.33$.

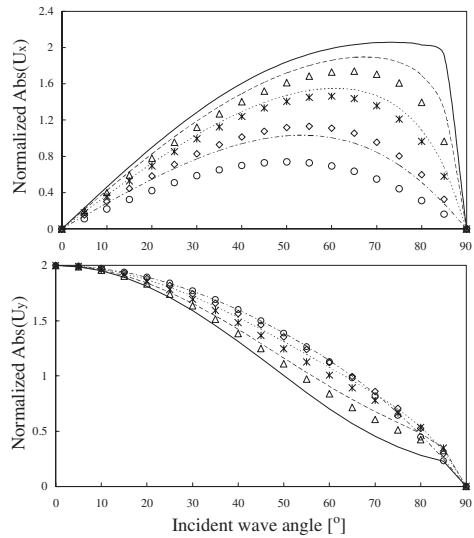


Figure 7. Comparison of elastic (lines) and poroelastic ($n = 0.3$, markers) dynamic response: – , Δ for $\nu = 0.1$; – – , * for $\nu = 0.2$; ... , \diamond for $\nu = 0.3$; – · – , \circ for $\nu = 0.4$.

and poroelastic materials at higher values of Poisson's ratio are almost the same; (e) in case the porosity is the same, the difference in amplitudes for both elastic and poroelastic cases is greater for low Poisson's ratios.

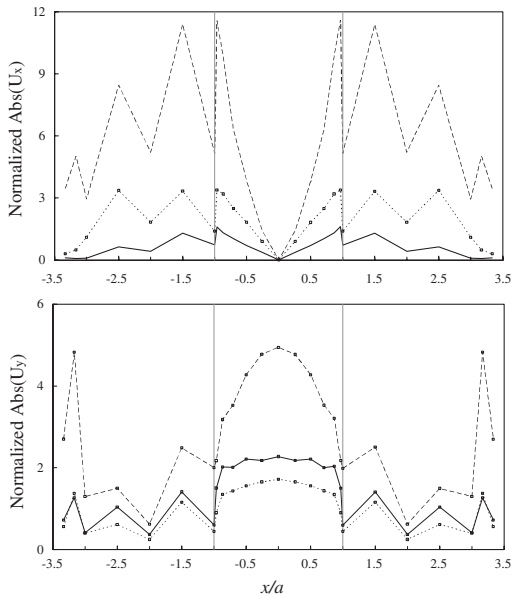


Figure 8. Comparison of the displacement amplitudes on the free surface of the embedded geological region: — case 1 (all layers with $n = 0.1$); - - case 2 (all layers with $n = 0.32$); ... case 3 (multilayered).

4.2 Example 2

For the purpose of this example the geological structure model in Figure 4 is used. The local geological region is with three non-parallel layers and its free surface holds a semi-circular gorge with a radius $a = 30$ m (contour $T_0R_0P_0$). Poisson's ratio equals to 0.2 for all the materials, used for this example. Three different cases are investigated and compared. In case 1 all three layers have the same porosity $n = 0.1$ and in case 2 the porosity of the layers is 0.32. In case 3 layer 1 (Ω_1) and layer 3 (Ω_3) have porosity 0.1, while the porosity of layer 2 (Ω_2) is 0.32. The bed rock has in all three cases porosity 0.2. Dry bulk moduli are calculated regarding (7). All the other properties of the materials are the same as in test example 3.1.

Figure 8 presents the surface displacement amplitudes versus x/a for normal incident plane time-harmonic P-wave with $\omega = 61 \text{ s}^{-1}$. These results clearly demonstrate both the site effects and the influence of porosity of the layers composing the finite geological region on the dynamic response. The components of the scattered displacement depict very exactly the gorge existence and its size. The important role of gorge's and layers' edges in the created diffraction wave field is also evident. The amplitudes of the surface displacements are different in the three cases. Numerical results show that there is an amplification

of the seismic signal on the free-surface of the multi-layered strata and in our case this is due to the existence of layers with different porosities and specially due to the layer with higher porosity, respectively lower wave velocity, than the bed rock. Results of this application example qualitatively and quantitatively evince the importance of considering in detail the 2D site properties.

5 CONCLUSIONS

Based on the viscoelastic isomorphism a BIE methodology is presented for solving seismic wave propagation problems in finite multilayered fluid saturated medium embedded in infinite half-space. The proposed technique benefits from combining efficiently: (A) the advantages of the viscoelastic isomorphism that are: (*) reduction of the complex two phase poroelastic model to simpler viscoelastic one that can assess the changes of stiffness and damping due to fluid flow; (**) the simpler mathematical form of the fundamental solution for viscoelasticity in comparison to poroelastic one, which contributes in efficiency and accuracy of the BIEM; (B) BIEM's facilities for solution of wave propagation problems in finite multilayered geological regions embedded in infinite domains.

The parametric study reveals that the developed method is able to depict the sensitivity of the wave field to both the existence of fluid saturated layers and free surface peculiarity. The proposed numerical BIEM tool can be extended further for: (a) synthesis of theoretical seismograms for finite multilayered fluid saturated geological regions; (b) modeling the dynamic behavior of soil-structure system with accounting for the poroelastic properties of the soil. It can be also used for verification of numerical codes based on the Biot's porodynamics.

ACKNOWLEDGMENT

The authors acknowledge the support of the NATO Program Security through Science (grant CLG982064). The second author has been supported by the HWP-Thüringen, Germany.

REFERENCES

- Achenbach, J. (1973). *Wave propagation in elastic solids*. Elsevier.
- Alvarez-Rubio, S., F. Sanchez-Sesma, J. Benito, and E. Alacon (2004). The direct boundary element method: 2D site effects assessment on laterally varying layered media (methodology). *Soil Dyn. and Earthquake Engng.* 24, 167–180.

- Bardet, J. (1992). A viscoelastic model for the dynamic behaviour of saturated poroelastic soils. *Trans. of the ASME* 59, 128–135.
- Beskos, D. (Ed.) (1991). *BEM in Mechanics*, Volume 3 of *Computational Methods in Mechanics*. Elsevier.
- Biot, M. (1956). Theory of propagation of elastic waves in a fluid-saturated porous solid. *J. of Acoustical Soc. Am.* 28(4), 168–191.
- Christensen, R. (1971). *Theory of Viscoelasticity: An Introduction*. New York: Academic Press.
- Deresiewicz, H. and B. Wolf (1964). The effect of boundaries on wave propagation in a liquid-filled porous solid: VIII. Reflection of plane waves at an irregular boundary. *Bull. Seismol. Soc. Am.* 54(5), 1537–1561.
- Lin, C., V. Lee, and M. Trifunac (2005). The reflection of plane waves in a poroelastic half-space saturated with inviscid fluid. *Soil Dyn. and Earthquake Engng.* 25, 205–223.
- Schanz, M. and D. Pryl (2004). Dynamic fundamental solutions for compressible and incompressible modelled poroelastic continua. *Int. J. of Solids and Structures* 41, 4047–4073.
- Simon, B., O. Zienkiewicz, and D. Paul (1984). An analytical solution for the transient response of saturated porous elastic solids. *Int. J. Num. Anal. Meth. Geomech.* 8, 381–398.
- Yang, J. and T. Sato (2001). Analytical study of saturation effects on seismic vertical amplification of a soil layer. *Géotechnique* 51(2), 161–165.

Discontinuum modelling

Numerical modeling of the soil structure interaction during sinkholes

M. Caudron, F. Emeriault & R. Kastner
URGC Géotechnique, INSA de Lyon, Villeurbanne, France

M. Al Heib
INERIS – LAEGO, Nancy, France

ABSTRACT: This article focuses on the simulation of soil-structure interactions during a sinkhole by the use of a coupled numerical approach. The 2D model uses a Finite Difference computer code coupled with a Distinct Elements code (FLAC^{2D} and PFC^{2D} from Itasca Consulting Group) to optimize the performances of both softwares.

1 INTRODUCTION

Sinkholes are caused by natural or man-made cavities. The very sudden nature of this phenomenon may be damaging for the buildings and endangers the life of the population. The soil-structure interactions occurring during this phenomenon are not well understood. The commonly employed approach (in which the soil movements obtained in greenfield condition are applied to a structure) is not satisfying.

The main purpose of this paper is the presentation and the validation of a numerical model allowing a satisfying modeling of the soil-structure interactions during this phenomenon (Figure 1). Two codes are used jointly: FLAC^{2D} uses the Finite Differences Method whilst PFC^{2D} is based on the Distinct Element Method. The results obtained in greenfield condition will be compared with those taking into account a building on the

ground surface. Moreover a relevant comparison can be made between this numerical simulation and the results of an experimental campaign carried out on a small-scale model, illustrated by Figure 1 (For more details on this experimentation, the reader can refer to Caudron et al. 2006).

2 THE CASE STUDY

The experimental small-scale model uses a geometric scale of 1/40 to model a 10 m wide and 2 m high gallery with a 8 m thick cover. It corresponds to the usual dimensions of the Parisian quarries that are responsible for several disorders each year. The soil mass modeled is 30 m wide and 20 m high.

The ground cover is composed of several different layers that can be roughly considered as two homogenous layers from a mechanical point of view: a 6 m thick cohesionless material overlies a 2 m thick cohesive layer. Their mechanical characteristics are presented in Table 1. In the small scale physical model, the cohesion of the material is reproduced by the addition of an



Figure 1. Laboratory small-scale model.

Table 1. Soil properties of the documented case study.

	Granular soil	Cohesive soil
E (MPa)	50–100	50–100
ν	0.30	0.30
ρ (kg/m ³)	2200	2200
φ (°)	~26	~26
c (kPa)	0	~100

Table 2. Characteristics of the building.

Beam length	3.2 m
Foundation width	1.65 m
Story height	2.7 m
Crawl space	1.2 m
Element section (m ² /m)	0.051 m ²
Element inertia (m ⁴ /m)	60.4 10 ⁻⁴ m ⁴
Number of spans	3

aqueous solution of glue to cohesionless metallic Schneebeli rods – Caudron et al. 2006.

The structure corresponds, with a 1/40 scaling factor, to a dwelling with three spans and two stories. Its total width is 10 m, each story is 2.7 m high and it comprises a crawl space of 1.2 m in height (more details are given in Table 2). The left foundation is located directly above the center of the cavity. The structure is made of standard steel beams and columns and the applied payloads are determined in order to induce stresses on the foundations corresponding to the Serviceability Limit State.

The creation of the cavity follows a simple procedure and five steps are necessary to obtain the 10 m total opening. The first step implies the creation of a small cavity: 2 m in width with the nominal 2 m height. Then, for each of the four following steps, one meter of cavity is opened on each side of the cavity until the final width is reached.

3 THE COUPLED NUMERICAL MODEL

The use of a coupled numerical approach based on two different numerical schemes (in the present case DEM and FDM) presents two main advantages:

On one hand, it is possible to refine the description of the behaviour of a soil mass in certain locations where large strains, displacement or shear stresses will develop (in the present case, the whole soil mass located above the cavity and in the vicinity of the structure).

On the other hand, it can reduce computation times by using a faster numerical resolution algorithm (such as the Finite Difference Method) in the rest of the soil where only small deformations will appear and for the modeling of the building and structural elements such as beams.

Figure 2 shows a schematic view of the coupled model that uses FLAC^{2D} and PFC^{2D} (both softwares have been developed and are commercialized by Itasca Consulting Group – 2005).

FLAC^{2D} uses a Finite Difference formulation applied to a continuum, whereas PFC^{2D} is based on the Distinct Elements Method. They can exchange informations with one another through a socket connection, in particular the data required to satisfy at any step of the calculation the interface conditions between the FD mesh and the particle assembly. The simple coupling

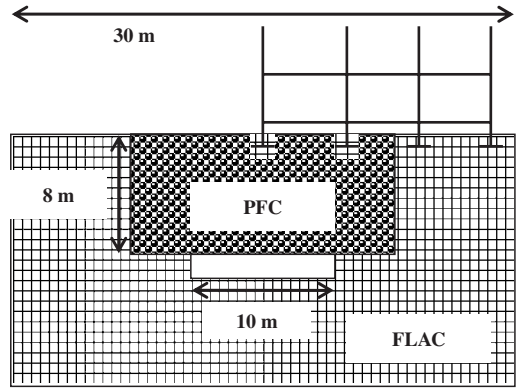


Figure 2. Schematic view of the coupled model.

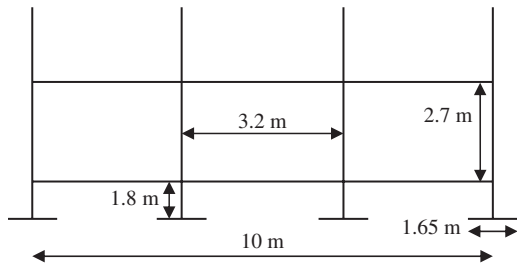


Figure 3. Dimensions of the considered building.

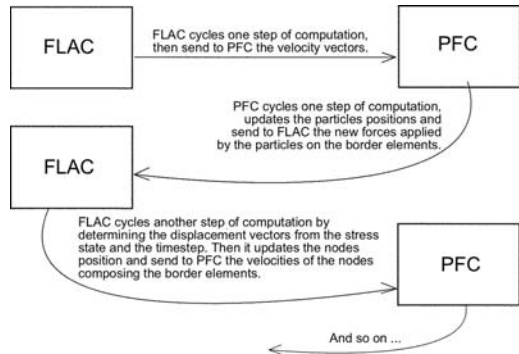


Figure 4. Basis for the FLAC-PFC coupling scheme.

procedure illustrated on Figure 4 can be strictly followed in a “simple” case, i.e. when no loss or creation of contact can occur between the particles and the border elements.

Nevertheless, in the present case, it is necessary to be able to take into account major modifications in the geometry of the border elements (when the cavity is gradually created by deleting FLAC^{2D} grid elements)

and also losses or creations of contacts of the border elements with moving particles.

Therefore, a specific scheme has been developed. This scheme includes the basic one (presented in Figure 4) and determines automatically when it is necessary to update the list of slave particles (PFC^{2D} particles linked to FLAC^{2D} border elements).

Step 1: The user specifies a total number X of calculation cycles to compute.

Step 2: A specific Fish function determines the maximum value of the particle velocities in the assembly, V_{max} . Given the smallest particle radius in the assembly, the program then determines the number of cycles x that can be safely achieved:

$$x = R_{min} / V_{max} \quad (1)$$

In Equation 1, it is assumed that in x cycles the displacement of the fastest particle can not exceed a maximum value arbitrarily taken equal to the smallest particle radius in the assembly, otherwise the list of slave particles has to be updated.

Step 3: y calculation cycles are computed using the coupling scheme detailed above where y is the minimum of x and X .

Step 4: PFC^{2D} frees the slave particles, get the new border elements list from FLAC^{2D} and defines the new list of slaves particles.

Step 5: The procedure goes back to Step 2 after replacing X by $X-y$. The loop is followed until the total number of calculation cycles X introduced in Step 1 is achieved.

When the FLAC^{2D} grid has to be modified during calculations, the same scheme is used: the required modifications of the border elements and their geometry are performed between Steps 4 and 5.

Between two stages of the creation of the cavity, stabilization of the soil is ensured: the maximum particle velocity in the assembly should be smaller than 10^{-11} m/calculation cycle.

Finally, Figure 2 shows that the structure represented by FLAC^{2D} beam elements is not directly in contact with PFC^{2D} particles but via small FLAC^{2D} grids. This modeling enables to cope with the limitation of the coupling scheme to the exchange of data between PFC^{2D} particles and FLAC^{2D} grid elements.

4 INTERPARTICLE CONTACT PARAMETERS (PFC2D)

The determination of the interparticle contact parameters required by the DEM and PFC^{2D} is based on the results of biaxial tests ($q - \varepsilon_1$ and $\varepsilon_v - \varepsilon_1$ curves) performed on the cohesionless and cohesive materials

Table 3. PFC parameters.

Parameters	Granular material	Cohesive material
k_n (MN/m)	16.0	16.0
k_s (MN/m)	8.0	8.0
Fric	0.50	0.45
Density	7.85	7.85
c_n & c_s (N)	0	1000

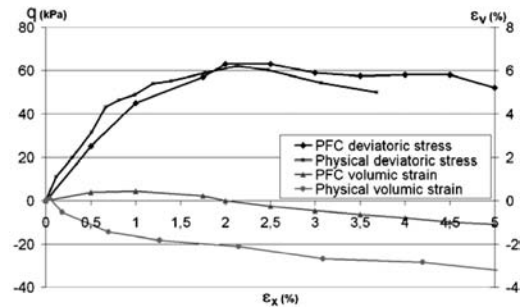


Figure 5. Deviatoric stress and volumetric strain for the cohesive soil (biaxial test performed with 50 kPa confining stress).

(Caudron et al. 2006). The main parameters describing the behaviour of the particles are:

- k_n and k_s , the normal and tangent stiffness of the contact between two particles,
- $fric$, the intergranular coefficient of friction,
- c_n and c_s , the normal and tangent strength of the contact bonds used to represent the overall soil cohesion (Potyondy & Cundall 2004).

For the sake of simplicity, two assumptions are made reducing to 3 the number of independent parameters: the ratio k_n/k_s is supposed to be equal to 2 and the ratio c_n/c_s to 1.

Two sets of parameters are determined (Table 3), respectively for the granular soil (standard metallic Schneebeli rods assembly) and for the cohesive material (Schneebeli rods soaked in an aqueous glue solution). Figure 5 gives an example of the results obtained for the cohesive soil.

The evolution of the deviatoric stress during biaxial compression is generally accurately reproduced, in particular the initial modulus and the deviatoric strength (as shown in Figure 5). The comparison of the experimental and computed volumetric strains presents more discrepancies. The DEM and its implementation in PFC^{2D} lead to an initial contractancy of the sample under shear stress whereas in the experiments dilatancy is observed even in the early stages of the loading. Nevertheless, after 1 or 2 % of axial strain, the same dilatancy angle is observed.

5 SIMULATIONS AND RESULTS

Two subsidence tests have been performed:

- one corresponds to greenfield conditions, i.e. without any structure, and will be considered as a reference,
- in the second one, the small scale model of building is positioned at ground level, with its left foundation located directly above the center of the cavity, in order to observe soil-structure interaction effects.

Deck (2002) showed that several main parameters are representative of the potential damage to a building induced by the soil movements induced by sink-holes. They include the maximum subsidence or vertical displacement, the shape of the settlement trough, the differential horizontal displacements and the slope of the ground surface in the vicinity of the building (or where it should be positioned if one explicitly takes soil-structure interaction).

5.1 The greenfield case

The cavity is created in five steps, it remains stable as it is observed in experimental test. The cohesive layer is then locally weakened in order to cause failure. Weakening is induced in the middle of the cavity roof by simultaneously applying a reduction factor to c_n and c_s the normal and tangential strength limits of the contact bonds in this area. When the crack development reaches a critical state, collapse appears in a very brutal manner and total failure of the cavity is observed.

Figure 6 illustrates the stress distribution at the end of the creation of the cavity when a stable state is obtained. The stress concentration on the vertical walls of the cavity is obvious, as the presence of tensile stress in the central lower part of the stiff bench and in its upper part above the side walls of the cavity.

Figure 7 shows the final state, i.e. after failure, and the induced ground surface deformation. The corresponding subsidence or settlement trough is presented

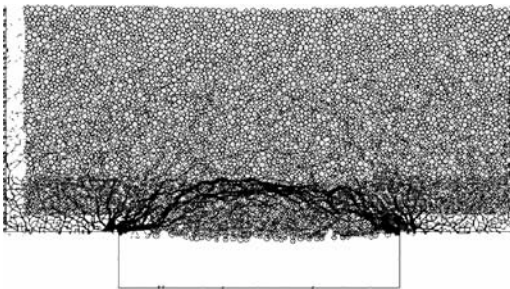


Figure 6. Stress distribution in the soil mass.

on Figure 8 and compared with the results of the experimental test and with a semi-empirical approach.

The latter is a modified version of Peck's semi-empirical approach proposed by Caudron et al. 2004 for rectangular shaped cavities. The total volume of the settlement trough is computed from the volume of the cavity multiplied by a factor depending on the expansion coefficient K ($K \approx 0.5$ in this particular case study):

$$V_{trough} = \frac{1}{1+K} V_{cavity} \quad (2)$$

An equivalent cavity radius R_{eq} is also calculated from the trough volume. Caudron et al. 2004 have shown that this enables the computation of i , the distance from the center of the settlement trough to the point of inflexion using Oteo & Sagaseta's empirical expression (1982).

$$i = 0.42R_{eq} + 0.525H \quad (3)$$

and S_{max} the maximum subsidence above the center of the cavity by:

$$S_{max} = \frac{V_{trough}}{2.51 \times i} \quad (4)$$

where H is the cavity cover.

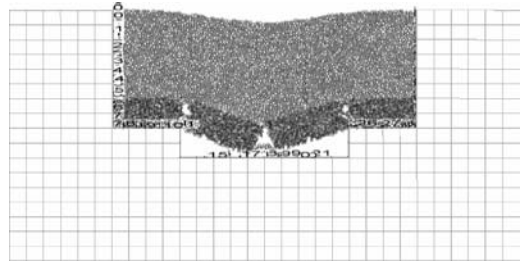


Figure 7. Final state after failure for the greenfield test.

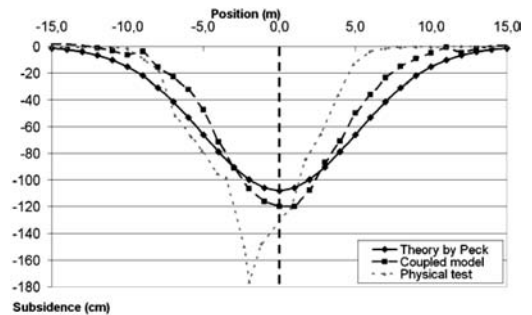


Figure 8. Subsidence troughs for the FLAC-PFC model, the physical test and the Peck approach.

Table 4 summarizes the main parameters of the settlement troughs resulting from the experimental, semi-empirical and coupled numerical approaches. It appears that:

- the numerical simulation gives a better description of the overall volume of the settlement trough,
- the width of the predicted trough is smaller than that resulting from the semi-empirical approach and closer to the observed experimental value,
- therefore the maximum settlement and the maximum slope observed on the trough are in closer agreement with the experiments.

However, it must be noted that the failure mechanism observed in the physical test (shown on Figure 9) is different from that considered in the numerical and semi-empirical approaches (leading to symmetric settlement trough). Only the left part of the cohesive layer felt into the cavity, the right part remained overhanging.

5.2 Soil-structure interaction

The coupled model that explicitly considers the presence of a building at ground surface uses the same

Table 4. Geometric characteristics for the troughs in greenfield condition.

Characteristic	Physical test	Semi-empirical approach	FLAC-PFC model
S_{max}	176 cm	108 cm	120 cm
I	~3.5 m	~5 m	~4 m
% of V_{cavity}	60%	66%	58%
Maximum slope	39%	13%	24%

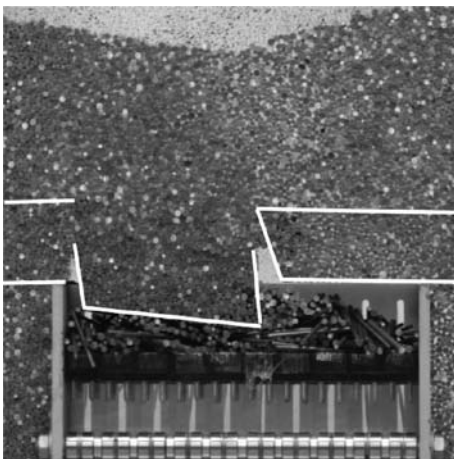


Figure 9. Partial failure during the small-scale physical test in greenfield condition.

procedure for the cavity creation and the weakening of the cohesive layer. The final state reached is illustrated on Figure 10. The failure is quite similar to the one observed in greenfield conditions.

It appears that the left foundation is not completely resting on the particles. A void is clearly visible under this foundation as well as in the upper part of the rigid bench directly above the cavity sidewalls.

The subsidence trough is plotted on Figure 11 with the position of the three foundations laying in the particles assembly. The results of the physical test with the structure on the ground surface are compared with the outcome of the coupled numerical simulations a) in greenfield condition and b) with the building. The main differences are located on the right part of the curves where the building model is situated. Table 5 summarizes the main characteristics of the observed and computed settlement troughs.

The computed trough volumes are smaller than the average value obtained from the physical tests. The values of S_{max} , i and the maximum slope predicted by the numerical model with structure are closer to the experimental results than the greenfield simulation. Both numerical models predict a maximum differential settlement between foundation 2 and 3, i.e. in the

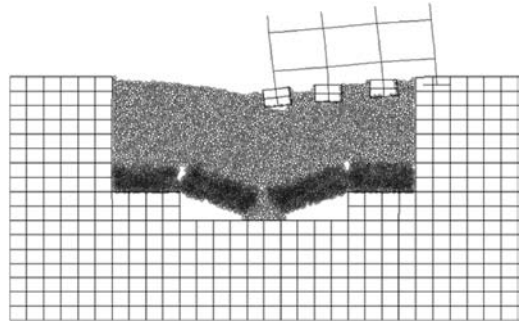


Figure 10. Final state for the model with the building.

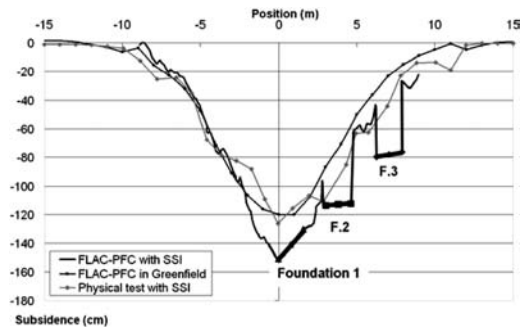


Figure 11. Subsidence trough for the computation with the soil-structure interaction.

Table 5. Quantitative results for the models with the building.

Characteristic	Physical test with SSI	FLAC-PFC in greenfield	FLAC-PFC with SSI
S_{max}	127 cm	120 cm	151 cm
i	~4.5 m	~4 m	~4 m
% of V_{cavity}	64%	58%	54%
Maximum slope	35%	24%	34%
Maximum slope on the building	~18%	~15.3%	~11%
Situation (span)	F_2-F_3	F_2-F_3	F_2-F_3

central span. However, in the case with structure, the predicted maximum slope is smaller than that observed value in the greenfield case and also smaller than the experimental value. This can be partly explained by the stiffness of the link between the right foundation (foundation 4) with the FLAC^{2D} grid (Figure 10).

Figure 12 illustrates the impact of the structure on the distribution of the horizontal displacements: the numerical simulation roughly reproduces the reduction in horizontal displacements in the vicinity of the structure and the dissymmetry of the distribution. On the left part of the trough, the experimental and numerical results almost coincide with the greenfield semi-empirical approach.

The induced stresses and efforts in the structure may be analyzed from a qualitative point of view. It appears that the two left columns concentrate the maximum efforts and more particularly their lower part (between the foundation and the first floor): an increase of bending moments of about 13 kN.m is observed. Moreover, the opposite signs of the moments indicate that the left span is subjected to horizontal compression during the test. This is confirmed by comparing the horizontal displacement vectors on Figure 12.

For the horizontal elements of structure, the coupled numerical approach predicts that the maximum induced bending moment is localized in the central span of the lower floor (more exactly near the junction with the third column). Similar results have been obtained in the physical test: it appeared that the maximum stress (measured by strain gauges) is located in the column 1 and 2 and in the span F_1-F_2 of the lower beam.

Finally, during the simulation, the total force acting on the sidewalls and away from the cavity can be computed. Figure 13 clearly shows that each step of the creation of the cavity leads to an increase of this vertical force and that the effect of the stress redistribution is limited a 2 to 3 m thick zone from the sidewalls. The computed values presented in Figure 13 are relevant with the conclusions of the small-scale test (Caudron et al. 2006).

Nevertheless, it should be mentioned that in both numerical and physical tests, the walls of the cavity

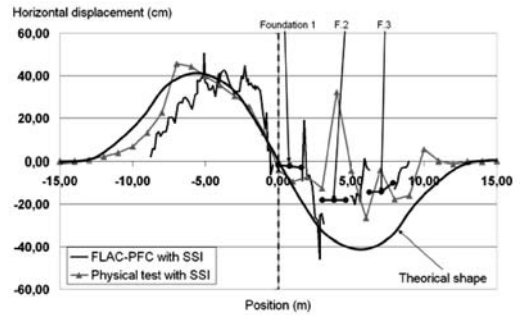


Figure 12. Horizontal displacement profiles (compared with the semi-empirical approach in greenfield condition).

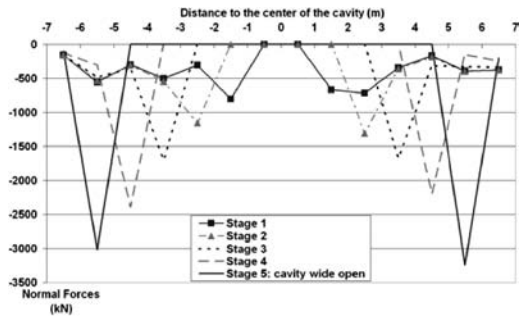


Figure 13. Vertical forces acting at the level of the roof of the cavity.

are largely stiffer than the soil which is generally not true in real situations where the deformability of the material constituting the walls leads to smaller stress concentration.

6 CONCLUSION AND PROSPECTS

This paper demonstrates that a coupled FLAC^{2D}-PFC^{2D} approach can be used to reproduce in a satisfying manner the soil-structure interaction phenomena induced by sinkholes.

Further research should improve the ability of the model to quantitatively describe the volume of the subsidence trough (smaller than the experimental values in the present analysis). Even if the efforts induced in the structure by the soil movements are complex, the coupled approach gives qualitatively similar results to the experimental observations. An in-depth analysis of the stresses and efforts induced in the structure is required to the global understanding of the phenomenon.

After improvement, the FLAC^{2D}-PFC^{2D} numerical model will be used for parametric studies in order to determine the influence of each parameters of the problem: geometry of the cavity and position with respect

to the building, mechanical characteristics of the soil mass and nature of the structure.

ACKNOWLEDGEMENTS

The authors would like to thank the French Ministry of Environment and Sustainable Development for partial funding of INERIS and its research project DRS02.

REFERENCES

Caudron M., Mathieu P., Emeriault F. et al Heib M. 2004. Effondrement de cavités souterraines et interaction avec les ouvrages en surface : approche expérimentale sur modèle analogique bidimensionnel, *Journées Nationales de la*

Géotechnique et de la Géologie pour l'Ingénieur, Lille, 28–30 June 2004, 435–442.

- Caudron M., Emeriault F., Kastner R. et al Heib M. 2006. Sinkhole and soil-structure interactions: Development of an experimental model. *International Conference on Physical Modeling in Geotechnics, Hong-Kong*, 04–06 August 2006.
- Deck O. 2002. Etude des conséquences des affaissements miniers sur le bâti. Propositions pour une méthodologie d'évaluation de la vulnérabilité du bâti. *PhD. Thesis, INPL, Nancy*, 241p.
- Itasca Consulting Group 2005. PFC^{2D} Manuals (Particles Flow Code in 2 Dimensions), Version 3.10, ICG, Minneapolis, Minnesota.
- Oteo C.S., Sagaseta C. 1982. Prediction of settlements due to underground openings, *Int. Symp. On Num. Meth. In Geomechanics, Zurich*, 13–17 September, 653–659.
- Potyondy D.O., Cundall P.A. 2004. A bonded-particle model for rock. *International Journal of Rock Mechanics & Mining Sciences*, 41:1329–1364.

Smoothed particle hydrodynamics for soil mechanics

H.H. Bui & R. Fukagawa

Department of Civil Engineering, Ritsumeikan University, Japan

K. Sako

Center for Promotion of the 21st COE Program, Ritsumeikan University, Japan

ABSTRACT: An elastic-perfect plastic model associated with the Mohr-Coulomb failure criterion is applied to describe the behavior of soil material in the framework of smoothed particle hydrodynamics (SPH). Numerical tests of dry soil collapse and erosion process in soil excavation by water jet are carried out in this study in order to verify our SPH models. Treatment of frictional boundary condition when applying SPH to simulate the behavior of soil material is also presented and discussed. As a fully Lagrangian and mesh free technique, SPH presents an advanced technique for simulation of soil material in comparing to the current traditional numerical approaches. Advantages of the method are its robustness, simple concept, ease of incorporating new physical effects and ability to handle large deformation in a pure Lagrangian frame.

1 INTRODUCTION

Smoothed particle hydrodynamics (SPH) was first developed to simulate astrophysical fluid dynamic problems (Lucy 1977, Gingold & Monaghan 1977) then it has been successfully applied to a vast range of problems. These include elastic-plastic flow (Libersky et al. 1991), quasi-incompressible flow (Monaghan & Takeda 1994), and fracture of brittle solids (Benz & Asphaug 1993), etc. SPH is fully Lagrangian and mesh free method, computational domain in SPH is represented by particles, typically fixed mass. Each particle carries all field variables information like density, pressure, velocity, etc., and moves with the particle velocity in Lagrangian frame. Therefore, particles themselves can be considered as geometrical grids of computational domain. SPH has some advantages over the grid based techniques because its concept is simple and it is relatively easy to incorporate complicated physical effects into the SPH formalism. Especially, it has a potential to handle the problems of extremely large deformation whereas the grid based techniques require additional computational effort.

In this paper, such above advantages of SPH will be applied to simulate the behavior of soil material in order to resolve the problem of grid distortion in the traditional FEM calculation. Modeling of dry soil and saturated soil are presented in which, the dry soil is assumed as an elastic-perfect plastic material and the stress states of solid particles in plastic flow regime

are described in terms of the Mohr-Coulomb failure criterion, the saturated soil is modeled by superimposing the dry soil and water into the same calculation domain, the interactions between solid soil particles and water is then calculated by means of the seepage force, which is introduced into the momentum equation as an external force. Simulations of dry soil collapse and erosion process in soil excavation by water jet are carried out in this research to verify our SPH models. Numerical results will be presented and discussed after some brief descriptions of simulation method.

2 SPH SIMULATION METHOD

2.1 Basic concept of SPH

The foundation of SPH is interpolation theory. The conservation laws of continuum mechanics, in the form of partial differential equations, are transformed into integral equations through the use of an interpolation function that gives the “kernel estimate” of the field variables at a point. The term “kernel estimate” refers to a weight function and defines how much of each field variable contributes to the field variable at a point.

Consider a function f , the kernel estimate of f can be defined using its values and a chosen kernel function W within a compact kernel support Ω , which is proportional to a smoothing length h . We thus write,

$$\langle f(x) \rangle = \int_{\Omega} f(x') W(x-x', h) dx' \quad (1)$$

where W = smoothing function having three following properties. The first one is the *normalization condition* that states,

$$\int_{\Omega} W(x-x', h) dx' = 1 \quad (2)$$

the second condition is the *Delta function property*,

$$\lim_{h \rightarrow 0} W(x-x', h) = \delta(x-x') \quad (3)$$

and the third condition is the *compact condition*,

$$W(x-x', h) = 0 \text{ when } |x-x'| > \kappa h \quad (4)$$

with κ is a constant and defines the influence domain of the kernel estimate. There are many possible choices of kernel functions, which satisfied (2)–(4). This research prefers to use the cubic spline interpolation function proposed by Monaghan et al. (1985).

The kernel estimation for the spatial derivative of f can be estimated by applying equation (1) and neglecting the surface integral term using the compact support property of W , leading to,

$$\langle \nabla \cdot f(x) \rangle = \int_{\Omega} f(x') \cdot \nabla W(x-x', h) dx' \quad (5)$$

Since the calculation domain in SPH is represented by a finite number of particles that carry individual mass and occupy individual space, the continuous integral equations (1) and (5) can be rewritten in the form of discretized particle approximation as follows,

$$\langle f(x_i) \rangle \approx \sum_{j=1}^N \frac{m_j}{\rho_i} f(x_j) W(x_i - x_j, h) \quad (6)$$

$$\langle \nabla \cdot f(x_i) \rangle \approx - \sum_{j=1}^N \frac{m_j}{\rho_j} f(x_j) \cdot \nabla W_{ij} \quad (7)$$

Equations (6) and (7) will be used to convert the partial differential equations into the SPH formulations.

2.2 Conservation equations

The conservation equations for continuum mechanics generally consist of a set of partial differential equations, which state the conservation of mass and momentum as follows,

$$\frac{D\rho}{Dt} = -\rho \frac{\partial v^\alpha}{\partial x^\alpha} \quad (8)$$

$$\frac{Dv^\alpha}{Dt} = \frac{1}{\rho} \frac{\partial \sigma^{\alpha\beta}}{\partial x^\beta} + f^\alpha \quad (9)$$

where α, β = the Greek superscripts used to denote the coordinate directions; ρ = density; v = velocity; $\sigma^{\alpha\beta}$ = total stress tensor; f^α = external force. Using the concept of SPH approximation as described in section 2.1, the system of partial differential equations (8)–(9) can be converted into the SPH formulations, which allow solving the motion of particles without using a grid system. Considering the continuity equation, the right hand side of equation (8) can be rewritten as,

$$-\rho \frac{\partial v^\alpha}{\partial x^\alpha} = - \left(\frac{\partial}{\partial x^\alpha} (\rho v^\alpha) - v^\alpha \cdot \frac{\partial \rho}{\partial x^\alpha} \right) \quad (10)$$

Replacing equation (10) into equation (8) and applying the SPH particle approximation to the gradients, the continuity density equation of particle i in the SPH formulation becomes,

$$\frac{D\rho_i}{Dt} = \sum_{j=1}^N m_j (v_j^\alpha - v_i^\alpha) \frac{\partial W_{ij}}{\partial x_i^\alpha} \quad (11)$$

Deriving the SPH formulations for particle approximation of momentum evolution is somewhat similar to the continuity density approach. The first term in the right hand side of equation (9) can also be rewritten as,

$$\frac{1}{\rho} \frac{\partial \sigma^{\alpha\beta}}{\partial x^\beta} = \frac{\partial}{\partial x^\beta} \left(\frac{\sigma^{\alpha\beta}}{\rho} \right) + \frac{\sigma^{\alpha\beta}}{\rho^2} \frac{\partial \rho}{\partial x^\beta} \quad (12)$$

applying the SPH particle approximation leads to,

$$\frac{Dv_i^\alpha}{Dt} = \sum_{j=1}^N m_j \left(\frac{\sigma_j^{\alpha\beta}}{\rho_j^2} + \frac{\sigma_j^{\alpha\beta}}{\rho_j^2} \right) \frac{\partial W_{ij}}{\partial x_i^\beta} + f_i^\alpha \quad (13)$$

Equations (11) and (13) will be used in this research as the conservation equations for both soil and water simulation; however, the calculation of stress tensor for water will be different from that of soil. For Newtonian fluids like water, the stress tensor consists of two parts: one part of isotropic pressure (p) and the other part of viscous shear stress (τ),

$$\sigma^{\alpha\beta} = -p \delta^{\alpha\beta} + \tau^{\alpha\beta} \quad (14)$$

The viscous shear stress is proportional to the shear strain rate denoted by ϵ through the viscosity μ ,

$$\tau^{\alpha\beta} = \mu \epsilon^{\alpha\beta} \quad (15)$$

where

$$\epsilon^{\alpha\beta} = \frac{\partial v^\beta}{\partial x^\alpha} + \frac{\partial v^\alpha}{\partial x^\beta} - \frac{2}{3} (\nabla \cdot v) \delta^{\alpha\beta} \quad (16)$$

The water pressure (p) appearing in equation (14) can be estimated using the approach proposed by Monaghan (1994) as,

$$p = B \left[\left(\frac{\rho}{\rho_o} \right)^\lambda - 1 \right] \quad (17)$$

where $\lambda = \text{constant}$, and $\lambda = 7$ is used in most circumstances; $\rho_o = \text{reference density}$; $B = \text{problem dependent parameter}$, which sets a limit for the maximum change of the density. If we choose B such that the density fluctuation of water is 1% and the sound speed of water is assumed to be,

$$c = \sqrt{\partial p / \partial \rho} \approx \sqrt{\lambda B / \rho_o} \quad (18)$$

then B will be calculated as,

$$B \approx 100 V_{typ}^2 \rho_o / \lambda \quad (19)$$

where $V_{typ} = \text{typical bulk velocity of water}$.

2.3 Soil constitutive modeling

The stress tensor of soil is composed of the isotropic pressure (p) and the deviatoric shear stress (s) as,

$$\sigma^{\alpha\beta} = -p \delta^{\alpha\beta} + s^{\alpha\beta} \quad (20)$$

The pressure (p) in SPH is normally calculated using “equation of state”, which has a function of density change. In the current research, the pressure equation for soil is derived as follows,

$$p = -K \frac{\Delta V}{V} = K \left(\frac{\rho}{\rho_o} - 1 \right) \quad (21)$$

where $\Delta V/V = \text{volumetric strain}$; $K = \text{bulk modulus}$; $\rho_o = \text{reference density}$. It is straightforward to calculate the pressure for soil using equation (21). However, simulation tests have shown that using the real value of K will result in a “stiff behavior” for soil. Therefore, K should be chosen as small as possible in order to ensure the nearly incompressibility condition and to avoid the stiff behavior. This study chooses $K = 50 \rho_o g H_{max}$.

The deviatoric shear stress in equation (20) can be estimated using the following equation,

$$s^{\alpha\beta} = 2G \bar{\epsilon}^{\alpha\beta} = 2G \left(\epsilon^{\alpha\beta} - \frac{1}{3} \delta^{\alpha\beta} \epsilon^{\gamma\gamma} \right) \quad (22)$$

where $G = \text{shear modulus}$; $\epsilon = \text{strain tensor}$; $(\dot{\cdot})$ denotes the time derivative. In order to get the material frame

indifferent strain rate, the Jaumann rate is adopted here with the following constitutive equation as,

$$\dot{s}^{\alpha\beta} - s^{\alpha\gamma} \omega^{\beta\gamma} - s^{\gamma\beta} \omega^{\alpha\lambda} = 2G \bar{\dot{\epsilon}}^{\alpha\beta} \quad (23)$$

where $\omega = \text{rotation rate tensor}$. The strain rate tensor and rotation rate tensor are defined as,

$$\epsilon^{\alpha\beta} = \frac{1}{2} \left(\frac{\partial v^\alpha}{\partial x^\beta} + \frac{\partial v^\beta}{\partial x^\alpha} \right); \quad \omega^{\alpha\beta} = \frac{1}{2} \left(\frac{\partial v^\alpha}{\partial x^\beta} - \frac{\partial v^\beta}{\partial x^\alpha} \right) \quad (24)$$

The plastic flow regime is determined by the Mohr-Coulomb failure criterion and the deviatoric shear stress components in this region are scaled back to the maximum shear stress defined by,

$$s_f = c + p \tan \phi \quad (25)$$

The above soil constitutive model used three basic soil parameters: cohesion (c), internal friction (ϕ) and shear modulus (G).

2.4 Modeling of saturated soil

Natural saturated soil consists of soil particles and water mixing together. To simulate this material using SPH, one has to assume that saturated soil is composed of two single layers, which are water layer and solid soil layer as shown in Fig.1. Using this assumption, the motion of particles on each layer will be solved separately using its own SPH governing equations. These two layers are then superimposed together and the interaction between particles from two different layers will be taken into account as follows. Considering the

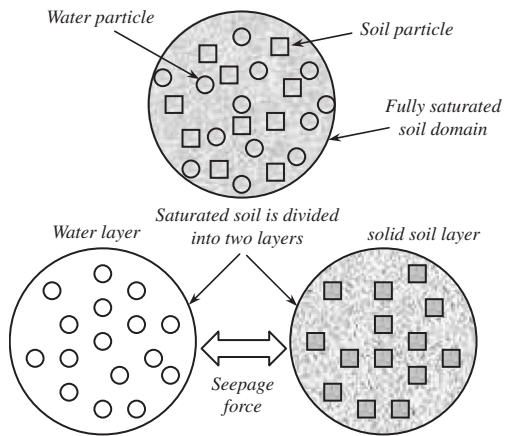


Figure 1. Schematic of saturated soil model in SPH simulation.

underground water flow, when water is seeping through the pores of a soil, viscous friction will produce a friction drag acting on the soil particles in the direction of water flow. Such force was called seepage force. The seepage force acts on the soil particles in addition to the gravitational force therefore, in this simulation the seepage force is introduced into the momentum equation as an external force when the soil and water particles are interacted each other as,

$$\begin{aligned} \frac{Dv_i^\alpha}{Dt} = & \sum_{j=1}^N m_j \left(\frac{\sigma_i^{\alpha\beta}}{\rho_i^2} + \frac{\sigma_j^{\alpha\beta}}{\rho_j^2} \right) \frac{\partial W_{ij}}{\partial x_i^\beta} + f_i^\alpha \\ & + \sum_{j=1}^M m_j \frac{f_j^{\text{seepage}}}{\rho_i \rho_j} W_{ij} \end{aligned} \quad (26)$$

where N = number of neighboring particles which have the same phase with particle i ; M = number of neighboring particles which are different phase from i . The seepage force is estimated as follows,

$$f^{\text{seepage}} = \rho_w g \frac{(v_{\text{water}} - v_{\text{soil}})}{k} \quad (27)$$

with k = soil permeability and it is specified through experiment, this paper chooses $k = 0.05$ cm/s.

2.5 Boundary conditions and implementation

Full exploitation of SPH has been hampered by the problem of particle deficiency near the solid boundary. To resolve this problem, Libersky (1993) has first proposed to use ghost particles. These particles are generated by reflecting the real particles, which are located within the distance of κh from the boundary, through the solid boundary. The ghost particles have the same properties with the real ones except the velocity. This method works well for the simulations of elastic-plastic flow, fluid flow; however, it is not enough to simulate the behavior of soil material whereas the friction force between the soil particles and the solid boundary is needed to implement. To simulate this force, this research proposed a new approach from which the frictional boundary condition can be estimated. Our approach is mainly based on the following two assumptions:

1. There is a line of virtual particles located right on the solid boundary. These particles will not contribute their properties into the SPH summations.
2. Both real particles and virtual particles are supposed to have a virtual radius, which equal to half of the initial smoothing length.

The above assumptions lead to the collisions between the real particles and the virtual particles when the real particles approaching the solid boundary. The

interaction between each real particle and virtual particle can be considered as the collision between two spherical particles that results in two forces in radial and tangential directions. The force in radial direction, so-called the normal force, can be estimated by using the Hertzian contact theory as,

$$F_n = k_n \times \delta_n^{3/2} \quad (28)$$

with k_n = constant and it is defined based on the material properties between two particles as,

$$k_n = \frac{4}{3} \frac{1}{\left(\frac{1-\vartheta_1^2}{E_1} + \frac{1-\vartheta_2^2}{E_2} \right)} \sqrt{r_1 r_2} \quad (29)$$

where r = radius of particle; ϑ = Poisson's ratio, E = Young's modulus; δ_n = overlap distance between two particles in radial direction.

The force in tangential direction, so-called the friction force, can be estimated by using the following equation as,

$$F_t = k_t \times \Delta \delta_t \quad (30)$$

where k_t = constant and it is taken approximate value to k_n ; $\Delta \delta_t$ = relative displacement in tangential direction. In order to limit the value of friction force obtained in equation (30), a Coulomb-type friction law is incorporated as follows. If the following relation is satisfied,

$$|F_t| \geq \mu |F_n| \quad (31)$$

then the friction force is given by,

$$\vec{F}_t = -\frac{\vec{V}_t}{|\vec{V}_t|} |\mu F_n| \quad (32)$$

where μ = wall friction coefficient, V_t = tangential component of relative velocity between two particles.

Our proposed boundary method is used not only for treatment of the frictional boundary condition, but also for preventing the penetration of particles through the solid boundary. This method can work well for even a complicated boundary.

2.6 Time integration

Equations (11), (13), (23) and (26) are integrated using a standard Leap-Frog (LF) algorithm with the following integration schemes,

$$\rho_i^{n+1/2} = \rho_i^{n-1/2} + \Delta t \cdot D\rho_i(t) \quad (33)$$

$$s_{\alpha\beta}^{n+1} = s_{\alpha\beta}^n + \Delta t \cdot Ds_i(t) \quad (34)$$

$$v_i^{n+1/2} = v_i^{n-1/2} + \Delta t \cdot Dv_i(t) \quad (35)$$

$$x_i^{n+1} = x_i^n + \Delta t \cdot v_i^{n+1/2} \quad (36)$$

where Δt = time step; n indicates the current time t ; $(n + 1)$ indicates the advanced time $(t + \Delta t)$. The stability of LF scheme is guaranteed by several criteria for time step, the first one is the Courant-Friedrichs-Levy (CFL) condition,

$$\Delta t \leq 0.25 \min(h_i / c) \quad (37)$$

and additional constraints due to the magnitude of particle acceleration f_i (Monaghan 1992),

$$\Delta t \leq 0.25 \min(\sqrt{h_i / f_i}) \quad (38)$$

and viscous diffusion (Morris et al. 1997),

$$\Delta t \leq 0.125(h_i^2 / \nu) \quad (39)$$

Finally, the time step Δt for simulation should be chosen as a minimum value of equations (37)–(39).

3 CALCULATIONS AND DISCUSSION

3.1 Simulation of dry soil collapse

Simulation of dry soil collapse using SPH is described in this section in comparison with SPH simulation for water flow. The same approach proposed by Monaghan (1994), except the treatment of boundary condition, is applied to describe the behavior of water particles. A total of 4500 water particles were used in this simulation to form a rectangular water column of 30 m in length and 15 m in width. The initial smoothing length of water particles was chosen to be 0.3 m. The process of water collapse after immediately releasing

the gate is shown in the upper four images of Fig.2 (left to right) at representative time. The particles keep an orderly configuration until they meet the right wall, forming the waves and finally staying at an equilibrium state.

In the dry soil collapse simulation, the soil constitutive modeling and the pressure calculation formulation, described in section 2.3, are implemented into the momentum equation in place of the formulations for water. The frictional boundary condition is also applied for the solid boundary. Initially, 2500 soil particles were arranged uniformly in a square volume with the initial smoothing length of 0.5 m. These particles have following properties: density 2.7 g/cm³, Young's Modulus 150 MPa and Poisson's ratio 0.3. The internal friction angle used in the Mohr-Coulomb failure criterion was taken as 27° and the cohesion of soil was assumed to be zero. The friction coefficient between the soil particles and the solid wall was chosen to be 0.3. The process of soil collapse is shown in the lower four images of Fig. 2 at representative times. It could be seen that the behavior of soil particles in this simulation are completely changed in comparison with the water particles. The reposed angle of soil collapse at the final state is found almost the same with the internal friction angle used in the Mohr-Coulomb failure criterion. Reasonable results have been obtained for the dry soil collapse simulation through SPH.

3.2 Erosion process in soil excavation by water jet

Simulation of erosion process in soil excavation by water jet is carried out on two different soil models, one is the dry soil and the other is the saturated soil. The dry soil is modeled by one particle layer, having the same material properties, filled in a rectangular reservoir of 0.5 m in length and 0.2 m in width. The particles on this layer have the same material properties with the particles used in the soil collapse simulation. The saturated soil is generated by overlapping

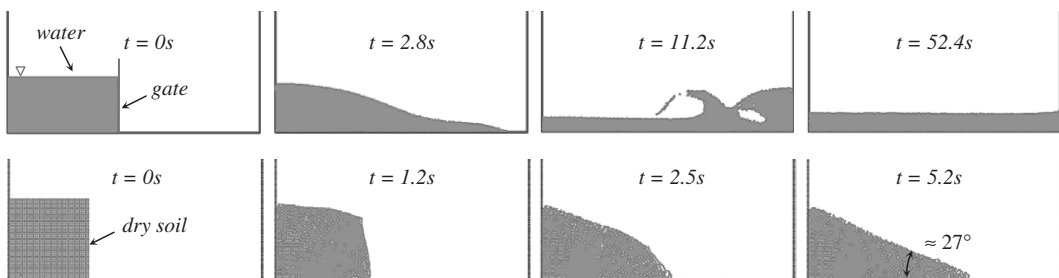


Figure 2. Snapshots of water and soil particle configurations in SPH simulation. The upper four images (left to right) represent the process of bursting dam while the lower ones show the results for soil collapse simulation. (The ghost boundary particles were used but not shown in this figure).

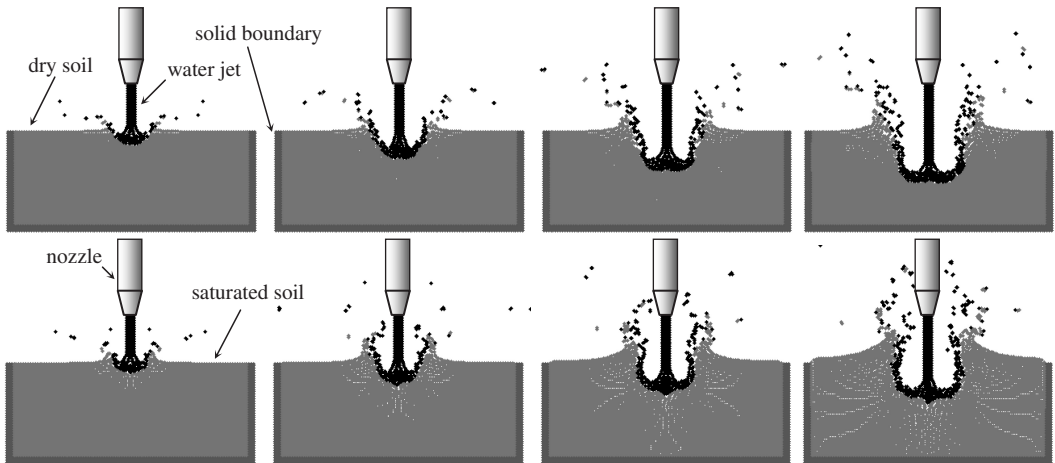


Figure 3. Snapshots of particle configurations in SPH simulation of excavation by water jet. The upper four images (left to right) show the erosion process of soil excavation on the dry soil model while the lower ones show the erosion process on the saturated soil model. The water jet has speed of 25 m/s and the diameter of nozzle in 2 cm. Time increases from left to right; $t = 0.005s, 0.01s, 0.015s$ and $0.02s$. (The ghost boundary particles were used but not shown in this figure).

the above soil layer and one water layer into the same calculation domain. The particles on the water layer have density of 1 g/cm^3 and viscosity of 0.001 Ns/m^2 . There are total of 4000 particles were generated regularly on each layer with the initial smoothing length of 0.005 m. The water jet is generated on the water layer using the same smoothing length and material properties with the water particles. Excavation process was done by ejecting the jet flow into the soil domain at a speed of 25 m/s.

The erosion process of soil excavation by water jet on the dry soil is shown in Fig.3 in comparison with the results on the saturated soil. The upper four images represent the results on the dry soil while the lower ones are the results for the saturated soil. As the seepage force was implemented into the momentum equation, transmission of energy from the water jet to the soil particles could be simulated. The soil volume was easily eroded by the jet flow and the soil particles were spattered together with the water particles. Furthermore, the erosion is also expanded during the excavation process due to the overflow of water in both simulations.

In comparison between two numerical results, it could be seen that the erosion process on the dry soil model could be done more easily than on the saturated soil model. This phenomenon can be computationally explained due to the presence of water layer on the saturated soil model. In the dry soil, the energy of water jet is directly transmitted to the soil particles through the seepage force; however, this energy has to share with the water particles in the water layer, which was overlapped with the dry soil layer to form the saturated soil model. The difference between two simulation results can also be seen in the behavior of soil particles in the

reservoir. The particles in the saturated soil tend to run over the reservoir after a long time of excavation while the particles in the dry soil are not. This again can be explained due to the effect of water layer in the saturated soil in which the seepage force is main factor.

4 CONCLUSIONS

The development of smoothed particle hydrodynamics to simulate the behavior of soil material has been described through this paper. Modeling of the dry soil and the saturated soil has been presented through the simulations of dry soil collapse and erosion process in soil excavation by water jet. Numerical results obtained in this study have shown that SPH can simulate the large deformation without difficulties. Reasonable results have been obtained when applying SPH to simulate the behavior of soil material. Although the calculations results in this paper have not been quantitatively compared with experimental data, the proposed approached are stable and the results are acceptable. We are encouraged by these preliminarily results obtained in this paper, but recognized the need for improvement to the constitutive modeling of soil material in order to get more accuracy of calculation results. Advantages of SPH are its robustness, simple concept, ease of incorporating new physics and ability to handle the large deformation in a pure Lagrangian frame.

REFERENCES

- Benz, W. & Asphaug, E. 1993. Explicit 3rd continuum fracture modeling with smoothed particle hydrodynamics,

- Proceedings of 24th Lunar and Planetary Science Conference in Lunar and Planetary Institute*: 99–100.
- Benz, W. & Asphaug, E. 1995. Simulating of brittle solid using smoothed particle hydrodynamics. *Computer Physics Communication* 87:235–265.
- Bui, H.H., Sako, K. & Fukagawa, R. 2006. Large deformation simulation of geomaterial using smoothed particle hydrodynamics (SPH), *National Congress of Theoretical and Applied Mechanics Japan* 55: 151–152.
- Colagrossi, A. & Landrini, M. 2003. Numerical simulation of interfacial flows by smoothed particle hydrodynamics. *Journal of Computational Physics* 191: 448–457.
- Cundall, P.A. & Strack, O.D.L. 1979. A discrete numerical model for granular assemblies. *Geotechnique* 29: 47–65.
- Gingold, R.A. & Monaghan J.J. 1977. Smoothed Particle Hydrodynamics: Theory and application to non-spherical stars, *Monthly Notices of the Royal Astronomical Society* 180: 375–389.
- Monaghan, J.J. 1994. Simulating free surface flows with SPH. *Journal of Computational Physics* 110: 399–406.
- Morris, J.P., Fox, P.J. & Zhu, Y. 1997. Modeling low Reynolds number incompressible Flows Using SPH. *Journal of Computational Physics* 136: 214–226.
- Libersky, L.D. & Petschek, A.G. 1991. Smoothed Particle Hydrodynamics with Strength of Material, *Proceedings of The Next Free Lagrange Conference* 395: 248–257.
- Libersky, L.D., Petschek, A.G., Carney, T.C. & Hipp, J.R. 1993. High strain Lagrangian hydrodynamics: A three-dimensional SPH code for Dynamic Material response. *Journal of Computational Physics* 109: 67–75.
- Liu, G.R. & Liu, M.B. 2003. *Smoothed Particle Hydrodynamics: A Meshfree Particle Method*. World Scientific.
- Lucy, L.B. 1977. A numerical approach to the testing of the fission hypothesis. *Astronomical Journal* 82: 1013–1024.
- Randels, P.W. & Libersky, L.D. 1996. Smoothed Particle Hydrodynamic: Some recent improvement and applications. *Computational Method in Applied Mechanics and Engineering* 139: 375–408.
- Takeda, H., Miyama, M. & Sekiya, M. 1994. Numerical simulation of viscous flow by Smoothed Particle Hydrodynamics. *Progress of Theoretical Physics* 92(5): 939–960.
- Tsuji, Y., Tanaka, T. & Ishida, T. 1992. Lagrangian numerical simulation of plug flow of cohesionless particles in horizontal pipe. *Powder Technology* 71, pp. 239–250.

Research on the pre-process of three dimensional composite element method for discontinuous rock

Sheng Qiang, Yang Zhang & Yueming Zhu

College of Water Conservancy and Hydroelectric Engineering, Hohai University, NanJing, China

Shenghong Chen

School of Water Resource and Hydropower Engineering, Wuhan University, Wuhan, China

ABSTRACT: Composite element method (CEM) is a new way to simulate the behavior of discontinuity in rock, which has the merits of generating mesh without considering the discontinuities. The pre-process of CEM means to treat with the relation between the mesh of structure and the faults and joints in it. The pre-process flow of CEM for jointed rock and the main algorithm are presented in this paper. Then the application of the corresponding program to the BaoZhusi complicated dam foundation shows the robustness of the pre-process.

1 INTRODUCTION

Discontinuity is the general term of faults, joints, beddings, etc. in the rock masses. The simulation of discontinuities is a crucial problem in the study of the deformation and stability of rock foundation, slope and underground cavern. Composite element method (CEM) is intended to solve the problem (Chen, S.H. & Qiang, S. 2004, He, Z.G. & Qiang, S. 2004, Qiang, S. & Chen, S.H. 2004). The main advantages of the composite element method is that it can be incorporated into the conventional finite element analysis procedure, and the mesh generation of the large scale rock structures with considerable number of discontinuities requiring explicit treatment in the calculation will not be restricted by the number, position and orientation of the discontinuities.

The main advantage of CEM is the convenient and effective pre-process compared with FEM. When analyzing rock structure, mesh may be generated firstly without considering the discontinuities. Then the inclination, direction and coordinates of corner points of the discontinuities should be inputted. After operation of pre-process, the information of intersection between discontinuities and mesh will be got. Because of the arbitrary of discontinuities, intersection situations may be very complex: an element may contain several discontinuities intersected with each other and an element may be divided into several odd blocks. The geometry information should be judged and recorded exactly so that CEM computation will run successfully. By this way mesh can be kept unchanged, which means more convenient to use such a method in the three dimensional situations.

There is no much profound innovation on the CEM pre-process theory, but it is perplexing to realize those functions and the workload is not less than writing the computation code. The application of pre-process program on the BaoZhusi complicated dam foundation shows the merits.

2 PRE-PROCESS FLOW

The purpose of CEM pre-process for jointed rock, which includes finding composite elements, getting relation between point and area or volume, identifying arbitrary block and defining the material domains etc. shown in [Figure 1](#), is to get the data that will be used in computation.

The composite element is defined as the element intersected with discontinuity, and the other ones in the mesh are still finite elements.

3 MAIN ALGORITHMS

The algorithm in the CEM pre-process is designed by such rules: less CPU time and easier realization. Sometimes a balance way has to be chosen if the two rules conflict.

3.1 Algorithm for finding composite element

The element intersected with discontinuities is regarded as a composite element. The operation between line and plane is easier than plane and plane or volume and plane (Wang, J.G. & Fu, R.N. 2003). Define the line between

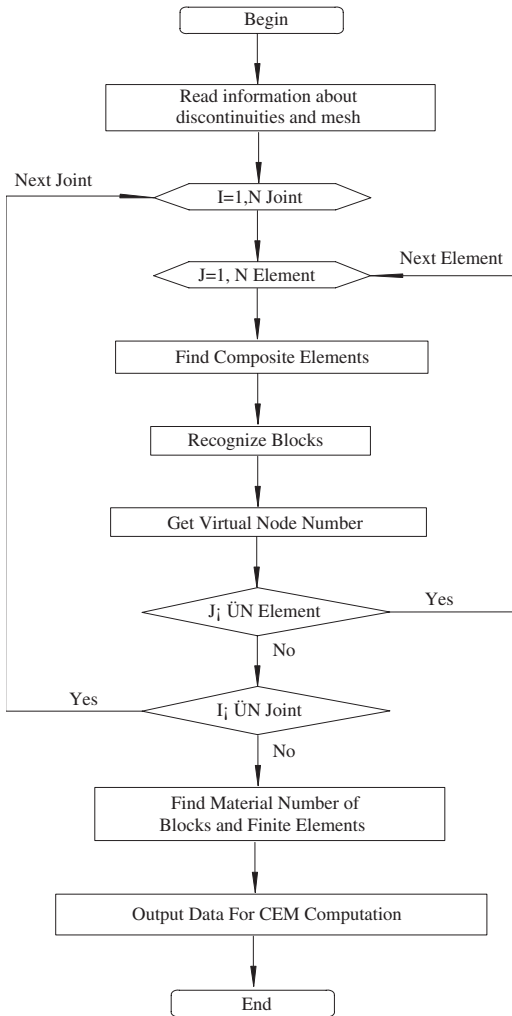


Figure 1. Main flow of CEM pre-process.

node A and node B in the mesh as line AB whose vector along X, Y, Z axes is:

$$\vec{AB} = (l, m, n) = (X_B - X_A, Y_B - Y_A, Z_B - Z_A).$$

So line AB may be expressed by parameter equation as follows:

$$\begin{cases} X = X_A + lt \\ Y = Y_A + mt \\ Z = Z_A + nt \end{cases} \quad (1)$$

Any discontinuity may be regard as one or more planes whose vector of the normal direction is:

$$\vec{F} = (A, B, C)$$

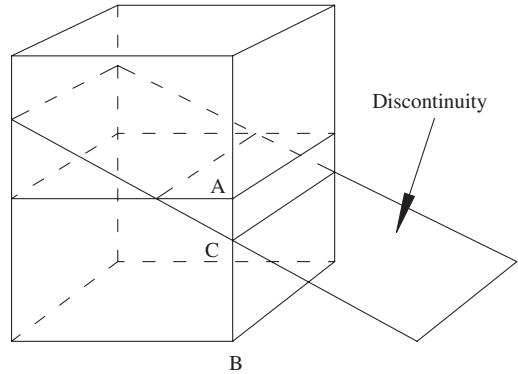


Figure 2. Line segment intersects with discontinuity.

So plane F may be expressed by equation as follows:

$$AX + BY + CZ + D = 0 \quad (2)$$

Intersecting node C will be got by cutting line AB by plane F (Figure 2). Parameter t_C is calculated by substituting equation (1) into equation (2):

$$t_C = -\frac{AX_A + BY_A + CZ_A + D}{Al + Bm + Cn} \quad (3)$$

Criterion 1: If the cross product of vector AB and vector F is zero, that is, the denominator of equation (3) is zero, which means line AB is in plane F or paralleled with it. At the same time, if the numerator of equation (3) is also zero, which means line AB is in plane F. Then line AB is defined as an effective line.

Criterion 2: If $t_C \in [0, 1]$, which means intersecting node C is between node A and node B, or coincide with one of them, that is, line AB intersects with plane F. Then line AB is defined as an effective line.

The number of effective lines in every element can be calculated according to criterion 1 and 2. Distinctly the element includes two or more effective lines should be a composite element.

3.2 Algorithm for finding the relation between point and polygon

Because the boundary of discontinuity is limited, it should be a polygon. The question whether a point is in a polygon or not will appear.

Several algorithms are mentioned in different masters (Chen, S.H. 2001, Sun, J.G. 1995), in which the following one is universal with the advantage of suitable for both convex and concave polygon.

For arbitrary polygon and point P, a horizontal radial with P as the start point can be drawn.

If the number of intersection points created by the radial and polygon is even (including zero), P is out of

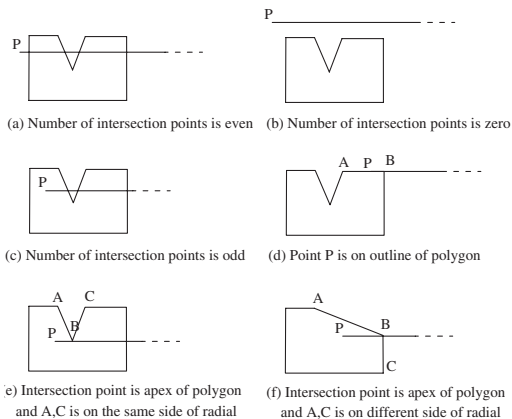


Figure 3. Relation between point and polygon.

the polygon, which are shown in Figure 3(a) and (b). Otherwise P is in the polygon (Figure 3(c)).

There are two special situations. First, the radial coincides with line AB of polygon, here whether P is in line segment AB should be judged further, referring to Figure 3(d). Second, the intersection point is on the apex B of polygon, here the relation between the radial and another endpoint A or C of the lines whose one endpoint is the apex. If point A and point C are on the same side of the radial, count one intersection point, else count two (Figure 3(e) and (f)).

3.3 Algorithm for identifying arbitrary block

Automatic identification method for three dimensional rock block systems has been presented, which provides some efficient algorithms for recognize rock block (Wang, W.M. & Chen, S.H. 1998). The new algorithm mentioned in this paper is easier to be understood and applied in program.

The initial block is the composite element itself. New points and lines will be created if discontinuities are intersected with the initial block. Check all faces on the block after every cutting.

If there is no new point on a certain face, so as one point on the face belongs to hanging side or lower side of the joint, the face belongs to the hanging side or lower side (Figure 4).

If there is new point on a certain face, then the face will be divided into two faces. Judge the lines on the two faces. If the endpoint of a line belongs to hanging side or lower side, the line should belong to hanging side or lower side. Sort anticlockwise the lines and points that belong to the same side.

As for the cutting face, which is the face between the two new blocks, belong to both sides (Figure 4). The outline of the cutting face is composed anticlockwise with the cutting lines that are the new lines on faces.

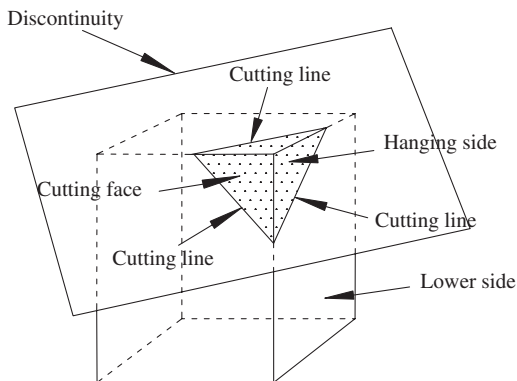


Figure 4. Identify blocks.

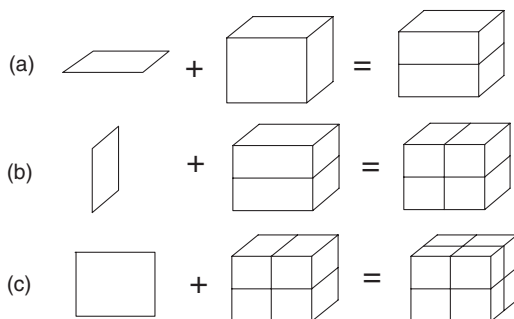


Figure 5. Element intersects with three discontinuities.

Apparently, the faces formed by the lines on hanging side or lower side should belong to the corresponding side naturally.

If an element intersects with several discontinuities, every discontinuity should cut the existed blocks separately. For example, a hexahedron element intersects with three joints (Figure 5). Two blocks will be created by the cutting of first joint, then two will become four after second joint, four will become eight after third joint at last.

Sometimes one or more joints may thin out in an element, which will make the block concave. Then the blocks cut devilishly must be glued.

Have to mention here, new virtual node number should be created for every new block according to the topological relation of various blocks. The virtual nodes of block are not the physical points, but the corresponding nodes to the element node. Therefore the shape of block will not affect its virtual node number.

3.4 Algorithm for finding material number

A rock structure model is usually divided into many material volumes by discontinuities, which contain

finite elements and composite element blocks. The material parameters of a finite element are same as the data of the material volume that contains it. But as for a composite element that includes several blocks of different materials, it is not an easy question. So designing an algorithm to find the material number for every finite element and composite element blocks is necessary.

First, confirm the model information about volumes, faces, lines and points. With the help of common software, such as ANSYS, a model including the necessary information can be created easily.

Second, suppose every volume contain a certain kind of material, and then the volume number should be the material number.

Third, get the shape center coordinates of finite element and composite element blocks. Find which volume the shape center is in, accordingly the finite element or the composite element block will get its material number that is just the volume number.

In the third step above, the problem to find the relation between a point and an arbitrary volume turns up. To solve the problem, the algorithm in section 3.2 is extended to the three dimensional situation, which will be always effective whatever the shape of volume is like. Defining the shape center point as P, a horizontal radial started with P can be drawn. Whether point P is in the volume or not can be judged according to the number of the intersection points created by the horizontal radial and the volume. If the number of intersection points is even (including zero), P is out of the volume, else in. Point P will not be on the face or line of volume because P is the shape center of finite element or composite element block, which reduces many complicated special situations and simplifies the judging greatly.

The algorithm is implemented as follows:

The horizontal radial may be expressed by parameter equation:

$$\begin{cases} X = X_p + lt \\ Y = Y_p \\ Z = Z_p \end{cases} \quad (4)$$

In the above equation $(l,0,0)$ is the vector of the radial that is calculated by:

$$(l,0,0) = (999999 - X_p, 0, 0) \quad (5)$$

Every volume is enclosed by many faces whose vector of the normal direction is. $\vec{F} = (A,B,C)$. So face may be expressed by equation as follows:

$$AX + BY + CZ + D = 0 \quad (6)$$

Parameter t is calculated by substituting equation (5) into equation (6):

$$t = -\frac{AX_p + BY_p + CZ_p + D}{Al} \quad (7)$$

Criterion 1: If A in equation (7) equal zero, which means the face is paralleled with X axes and the horizontal radial, so the intersection point number is zero.

Criterion 2: If $t \in (0,1)$, which means there is one intersection point created by the radial and the plane that the face is on. Here the outline of the plane is unlimited but the face is a polygon. Therefore a further judging should be done to find whether the intersection point is in the polygon or not with the algorithm in section 3.2. If it is in the polygon, the intersection number is surely one.

No special situation should be considered here.

Add the intersection point number on every face of the volume. If the total number of intersection points is odd, the shape center is in the volume, else out.

4 EXAMPLE OF APPLICATION

To certify the algorithms and program of the pre-process for discontinuous rock CEM, BaoZhusi gravity dam model with the base containing 11 faults and 1 material interface is established (Chen, S.H. & Qiang, S. in press). Model section with the thickness of 1 meter is shown in Figure 6. The 11 faults and 1 material interface divide the model into 12 material volumes.

Without considering the influence of the discontinuities, generate the mesh of the model with 4897 elements, referring to Figure 7.

Cutting the mesh with the 12 discontinuities, 479 composite elements are found, 969 blocks are created. Figure 8 shows some of typical composite elements and the blocks within.

The 12 material volumes containing finite elements and composite element blocks are shown in Figures 9–20.

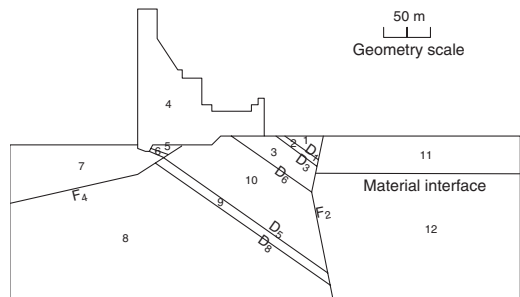


Figure 6. Material volume of BaoZhusi gravity dam section.

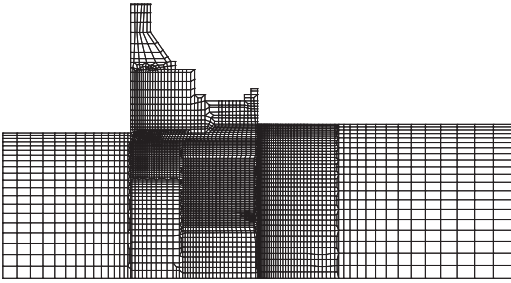


Figure 7. Composite element mesh.

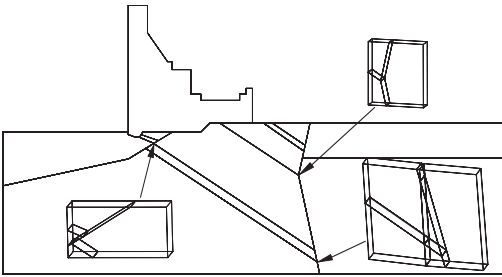
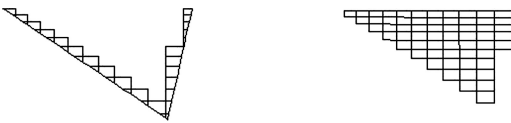
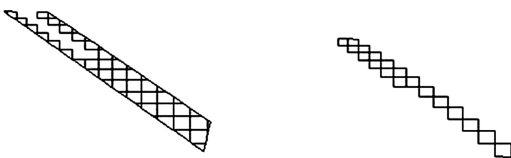


Figure 8. Typical composite elements.



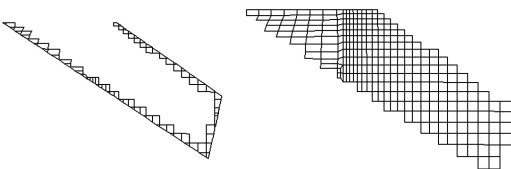
(a) Composite element blocks (b) finite elements

Figure 9. Elements in material volume 1.



(a) Composite element blocks (b) finite elements

Figure 10. Elements in material volume 2.



(a) Composite element blocks (b) finite elements

Figure 11. Elements in material volume 3.

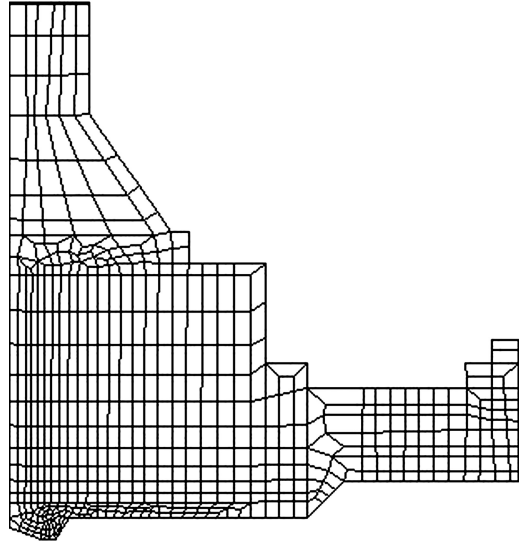
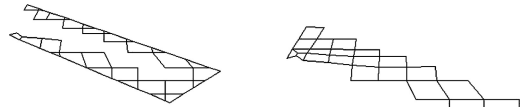


Figure 12. Finite elements in material volume 4.



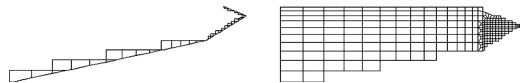
(a) Composite element blocks (b) finite elements

Figure 13. Elements in material volume 5.



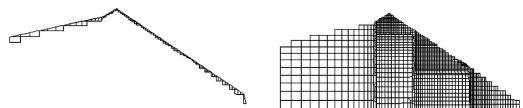
(a) Composite element blocks (b) finite elements

Figure 14. Elements in material volume 6.



(a) Composite element blocks (b) finite elements

Figure 15. Elements in material volume 7.



(a) Composite element blocks (b) finite elements

Figure 16. Elements in material volume 8.

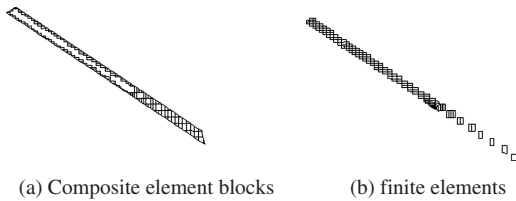


Figure 17. Elements in material volume 9.

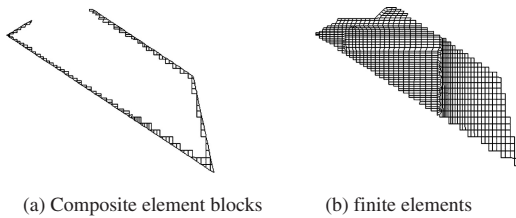


Figure 18. Elements in material volume 10.

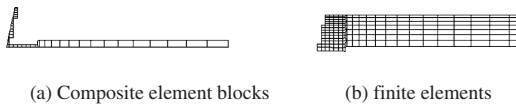


Figure 19. Elements in material volume 11.

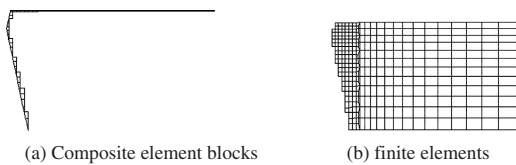


Figure 20. Elements in material volume 12.

5 CONCLUSIONS

The research presented in this paper illustrates the pre-process of composite element method for discontinuous rock mass. Compared with traditional finite element method, the main advantage of CEM is the high-activity pre-process. When analyzing rock structure, mesh may be generated firstly without considering the discontinuities. Then the inclination, direction and coordinates of corner points of the discontinuities should be inputted. The program of pre-process will find out the composite elements in the mesh, identify the blocks created by

joints intersecting with composite elements, value the virtual node number according to the topology of adjacent blocks, get the material number of every finite element and composite element blocks, output the necessary data for computation of CEM at last. The algorithms in the main flow are formulated separately.

Because of the arbitrary of discontinuities, intersection situations may be very complex: an element may contain several discontinuities intersected with each other and an element may be divided into several odd blocks. The geometry data structure is also complicated which should be recorded exactly to ensure the successful running of CEM computation.

The gravity dam with a challenging base studied in this paper shows the reliability and the advantage of the CEM pre-process program. It is easy to realize that the using of the composite element can simplify the pre-process greatly. The large scale discontinuities will not be necessarily modeled by the special regular elements, the mesh generation work can be concentrated on the other important aspects such as the structure configuration, the stress gradient, etc. In the practical application when there are many large-scale faults in a complicated three dimensional structure, this advantage should be very attractive.

REFERENCES

- Chen, S.H. 2001. *Stable analysis for complex rock foundation of high dam and high rock slope*. Beijing: China Water Power.
- Chen, S.H. & Qiang, S. 2004. Composite element model for discontinuous rock masses. *Int. J. Rock Mech. & Min. Sci.* 41(5): 865–870.
- Chen, S.H. & Qiang, S. et al. Three dimensional elastoviscoplastic composite element method of jointed rock masses and its application. *Int. J. Numerical and Analytical Methods in Geomechanics* (Accepted).
- He, Z.G. & Qiang, S. et al. 2004. Composite element method for jointed rock masses reinforced by hollow friction bolt. *Int. J. Rock Mech. & Min. Sci. Abstr.* 41(3): 464.
- Qiang, S. & Chen, S.H. 2004. Three dimensional elastoviscoplastic composite element model for jointed rock. *J. Rock Mech. & Eng.* 23(20): 3390–3396.
- Sun, J.G. & Yang, C.G. 1995. *Computer graphics*. Beijing: TsingHua University.
- Wang, J.G. & Fu, R.N. 2003. *Three dimensional analytic geometry*. Beijing: Beijing Normal University.
- Wang, W.M. & Chen, S.H. 1998. Automatic identification method for three-dimensional rock block systems. *J. Wuhan Univ. of Hydr. and Elec. Eng.* 31(5): 51–55.

Tunnels and caverns

The influence of the soil-structure interface on tunnel induced building deformation

J.N. Franzius

Geotechnical Consulting Group, London

D.M. Potts

Imperial College, London

ABSTRACT: Tunnel construction in an urban environment can deform overlying structures. This deformation is often estimated by assuming that a structure follows the greenfield settlement profile. The deformation of the building is, however, influenced by various building characteristics. This paper investigates how the nature of the building-soil interface affects tunnel induced building deformation. The tunnel construction beneath the building is simulated in a 2D Finite Element (FE) parametric study. The building is represented by an elastic beam while interface elements are included to model the behaviour between soil and building foundation. The paper discusses the application of both linear elastic and elasto-plastic constitutive models for the soil-structure interface.

1 INTRODUCTION

Estimating tunnel induced building deformation is a key issue in the planning and construction process of any new underground construction within an urban development. For recent and currently planned tunnel projects in London, a three stage approach was applied which, in the first two phases, evaluates the settlement from the expected greenfield settlement trough, described by a Gaussian curve (Mair et al., 1997). If necessary a more detailed analysis of the tunnel-soil-building interaction problem has to be carried out in the third phase. Such an assessment now often involves Finite Element (FE) analysis.

Over recent years a large number of numerical studies on tunnel induced settlement has been published showing a wide variety of approaches. The FE models range from simple two dimensional (2D) FE models with simplified buildings to detailed 3D analyses in which various details of the building and the tunnel construction method are modelled. Although this variety highlights the flexibility of FE analyses compared to other methods such as physical tests, there are difficulties in modelling tunnel construction, especially in stiff overconsolidated clay, such as London Clay (Franzius et al., 2005). It is therefore debatable how detailed soil-structure interaction problems have to be

modelled in order to be utilised in engineering practice (Franzius & Potts, 2005).

A relative simple model was presented by Potts and Addenbrooke (1997) in which the building was modelled as an elastic beam in a suite of plane strain FE analyses. The study revealed the importance of including the building's stiffness into the building damage assessment process. The conclusions from their study have been used to estimate tunnel induced settlement during construction of the Jubilee Line Extension in London (Mair & Taylor, 2001).

Based on their work, Franzius (2004) presented results from both 2D and 3D FE analysis which incorporated more details of the building and the tunnel construction. The study revealed that some of these building details have only a small influence on the tunnel induced building settlement (Franzius et al., 2006).

This paper focuses on how a variation in the properties of the interface between building and underlying soil affects the building deformation. Different constitutive models are adopted to model the interface and both normal and shear interface stiffness are changed independently. The study discusses the stress regime between building and soil for different constitutive interface models and shows how the introduction of building weight changes the mechanism at the soil-structure interface.

2 DETAILS OF ANALYSES

The 2D FE study was performed using the Imperial College Finite Element Programme (ICFEP). Reduced integration was used, with an accelerated modified Newton-Raphson solution scheme with an error-controlled substepping stress point algorithm for solving the nonlinear FE equations (Potts & Zdravkovic, 1999, 2001).

2.1 Geometry

The tunnel depth z_0 was 20 m with a tunnel diameter of $D = 4.146$ m. The building had a width of 100 m and was located centrally above the tunnel. Figure 1 shows the FE mesh adopted. Due to symmetry only half of the problem was modelled. The beam simulating the building is not visible in the mesh.

2.2 Building model

The building was modelled as an elastic beam with a Young's modulus E , a second moment of area I and cross sectional area A . These parameters were derived assuming that an n -storey building consists of $n + 1$ slabs with a vertical spacing of 3.4 m. Assigning a cross sectional area and Young's modulus for each slab, the overall values of E , I and A were calculated adopting the parallel axis theorem (Timoshenko, 1955) assuming the neutral axis to be the mid-height of the building. In this study a 5-storey building was used with a bending stiffness of $EI = 7.0 \times 10^8$ kNm²/m and an axial stiffness of $EA = 2.1 \times 10^7$ kN/m. More details of this building model are given in Franzius et al. (2006).

The building was modelled both with and without weight. Franzius et al. (2004) showed that the building weight only has a small influence on the structure's deformation compared to the effect of its own stiffness.

2.3 Tunnel construction

Tunnel construction was simulated over 15 calculation increments. The stress that act on the tunnel boundary

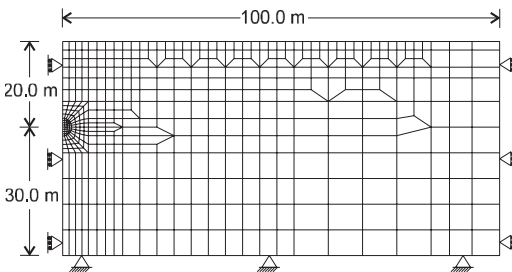


Figure 1. Finite element mesh.

within the soil was evaluated and then incrementally applied in the reverse direction. Elements within the tunnel boundary were not included in the analysis during this procedure. After each increment the volume loss V_L was calculated. The volume loss is the volume (per metre length) of soil moving into the tunnel divided by the original cross section of the tunnel (per metre running). Results were taken from that increment in which the desired volume loss of approximately $V_L = 1.5\%$ was achieved which was the case after the 7th increment.

2.4 Soil properties

The soil profile consists of London Clay represented by a non-linear elasto-plastic constitutive model. The non-linear pre-yield behaviour is based on the model described by Jardine et al. (1986) employing trigonometric functions to describe the reduction of G/p' and K/p' with increasing shear strain and volumetric strain, respectively. G is the secant shear modulus, K is the secant bulk modulus and p' is the mean effective stress. More details about this model and its input parameters can be found in Franzius et al. (2006).

A non-associated Mohr-Coulomb surface modelled the plastic behaviour with a cohesion of $c' = 5$ kPa, an angle of friction of $\phi' = 25^\circ$ and an angle of dilation of $\nu = 12.5^\circ$.

The initial stress conditions in the ground were controlled by the saturated bulk unit weight of the soil $\gamma = 20$ kN/m³ and by the depth of the water table of 2 m below ground surface. A hydrostatic pore water pressure distribution was applied with a zone of suction in the top 2 m of the clay. The coefficient of lateral earth pressure at rest was $K_0 = 1.5$.

2.5 Soil-structure interface

There are different approaches to model the soil-structure interface in FE analysis: the use of continuum elements (using standard constitutive laws); linkage elements (discrete springs); or special interface elements. The latter type, interface elements with zero thickness, have been implemented into ICFEP (Day & Potts, 1994). The shear strain γ_{if} and the normal strain ϵ_{if} within these elements is defined as the difference in displacement between the bottom and the top of the element, i.e.

$$\gamma_{if} = u^{\text{bottom}} - u^{\text{top}} \quad (1)$$

$$\epsilon_{if} = v^{\text{bottom}} - v^{\text{top}} \quad (2)$$

where u and v are the displacement in the longitudinal and the normal direction of the interface element.

It follows from these definitions that the dimension of interface strain is $[length]$ rather than being dimension-less.

ICFEP offers both elastic and elasto-plastic material laws to model the interface behaviour. In the linear elastic model the shear strain is linked with the shear stress by the interface shear stiffness K_s while the interface normal stiffness K_n links normal strain with normal stress. Note that the dimension of the stiffness moduli is [$force/length^3$]. The elastic constitutive matrix is such that normal and shear behaviour are uncoupled from each other.

The elastic-plastic material model used in this study adopts a Mohr-Coulomb failure criterion. The input parameters required are the cohesion c_{if} , angle of friction, ϕ_{if} and the angle of dilation ν_{if} . In this study the dilation was set to $\nu_{if} = 0^\circ$.

3 ELASTIC ANALYSES

Analyses with elastic interface elements were performed modelling a weight-less 5-storey building. In a first step the normal interface stiffness was varied from $K_n = 10^3$ to 10^7 kPa/m while the shear stiffness was kept to a low value of $K_s = 5$ kPa/m. Figure 2 shows the surface settlement profiles for these analyses between the centre line and the edge of the building. The graph shows that a low value of $K_n = 10^3$ kPa/m compensates the tunnel induced settlement leading to a wide shallow settlement trough. As the normal stiffness increases the settlement curve approaches the shape of the settlement trough obtained from a building analysis without interface elements. The settlement trough for greenfield conditions (i.e. no building present) is also shown for comparison.

Figure 3 plots the normal interface strain ϵ_{if} obtained from the same set of analyses. Normal strains reduce as K_n increases. However, all distributions of ϵ_{if} along the building have the same pattern (although the ϵ_{if} variations for $K_n = 10^6$ and 10^7 kPa/m are not visible in the scale of this graph). It can be seen that tensile normal

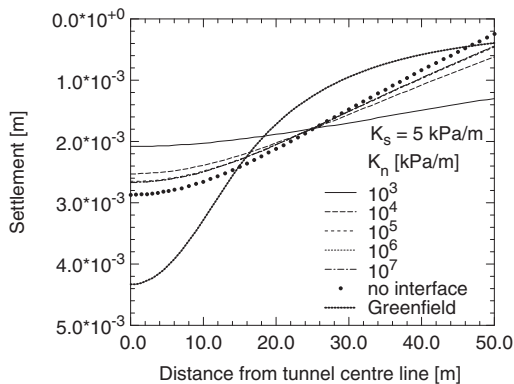


Figure 2. Building settlement profile for elastic analyses.

strains develop around the centre line of the building while compression can be found towards the edge of the structure. The position where the normal interface strain changes from tension to compression occur slightly outside the point where the building settlement in Figure 2 has the same magnitude as the greenfield settlement.

The interface shear strain in these analyses varied between 2.7×10^{-3} and 3.1×10^{-3} kPa/m. This relative small change (within 16%) shows that the shear strain is little affected when the normal interface stiffness is varied over an order of 4 magnitudes.

C Conversely, when changing the interface shear stiffness from 5 to 10^5 kPa/m while keeping the interface normal stiffness constant at $K_n = 10^5$ kPa/m the interface shear strain reduces from 3.1×10^{-3} to 4.3×10^{-6} kPa/m as shown in Figure 4. The normal interface

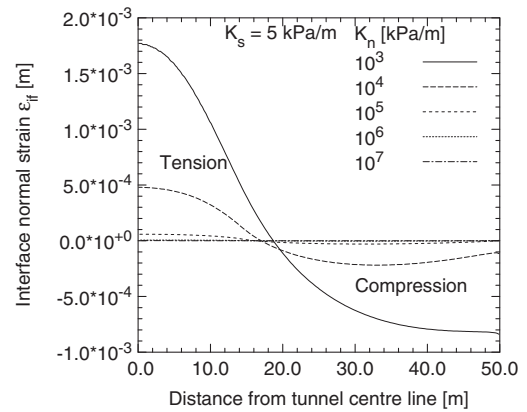


Figure 3. Normal interface strain along building for elastic analyses.

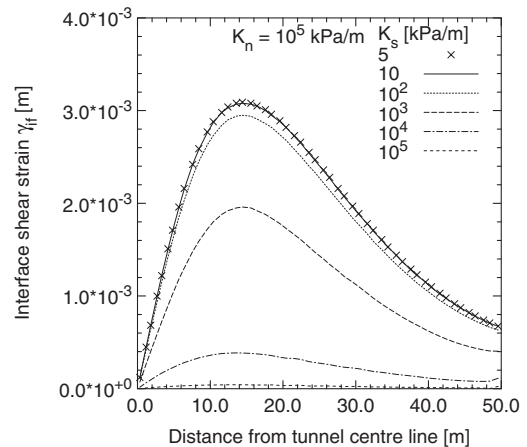


Figure 4. Interface shear strain along building for elastic analyses.

strain and the settlement profile remain relatively unaffected.

4 ELASTO-PLASTIC ANALYSES

Analyses with elasto-plastic interface elements between building and soil were performed to investigate the influence of both interface cohesion c_{if} and angle of friction ϕ_{if} . The elastic stiffness parameters were $K_n = 10^5$ kPa/m and $K_s = 10^4$ kPa/m. The elastic analyses showed that increasing these values would only marginally change the relative displacement between soil and structure. However, higher values of interface stiffness can lead to numerical instability depending on the difference in stiffness between interface and adjacent soil and/or beam elements and on the element size (Day & Potts, 1994).

Figure 5 shows the interface shear strain γ_{if} obtained from analyses with $\phi_{if} = 0^\circ$ and c_{if} varying between 0 kPa and 7.5 kPa (note that for numerical reasons values of $c_{if} = 10^{-3}$ kPa and $\phi_{if} = 0.001^\circ$ were used instead of 0 kPa and 0° , respectively). The same weightless 5-storey building as in the elastic analysis was modelled. The graph demonstrates that γ_{if} reduces as c_{if} increases. The curves for $c_{if} = 5$ kPa and 7.5 kPa coincide with the shear strain from the elastic analysis for $K_s = 10^4$ kPa/m (the same value as adopted in the elasto-plastic analyses), shown in Figure 4. This indicates that no plastic strain occurs for values of $c_{if} = 5$ kPa or greater.

Plastic strain, however, develops as c_{if} reduces to 2.5 kPa with a zone of plastic strain approximately between 4 m and 30 m distance from the tunnel centre line. As c_{if} decreases further to 0 kPa plastic strain develops along the whole width of the building. The

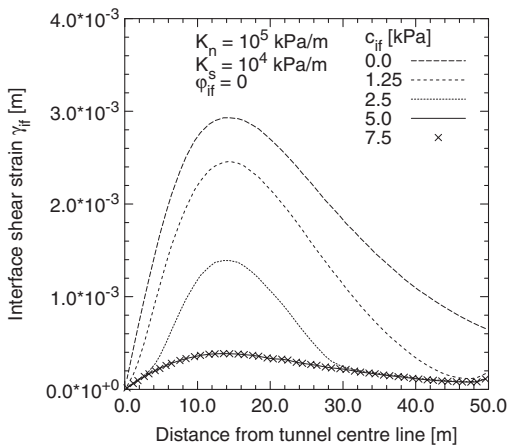


Figure 5. Interface shear strain along building for elasto-plastic analyses with varying interface cohesion.

results for $c_{if} = 0$ kPa are similar in pattern and magnitude to those obtained for $K_s = 5$ kPa in the elastic analysis, shown in Figure 4.

In the next set of analyses, c_{if} was kept constant at 2.5 kPa while ϕ_{if} was increased from 0° to 25° . Figure 6 shows the magnitude of γ_{if} along the building. One would expect that an increase of ϕ_{if} would lead to a reduction in plastic strain (i.e. the same pattern as observed for c_{if}). However, the opposite trend occurs. As ϕ_{if} increases, the peak interface shear strain also increases. Outside 20 m distance from the centre line, the behaviour is different and the interface shear strain reduces as ϕ_{if} increases.

To investigate this behaviour further, additional analyses were performed with a load of 10 kPa being applied to the building (note that all analyses presented up to this point included a weightless structure). The results are plotted in Figure 7. For $\phi_{if} = 0^\circ$ the distribution of shear strain is similar to that obtained from the corresponding weightless analysis (Figure 6). As ϕ_{if} increases, γ_{if} reduces – the opposite trend compared to the no-load scenario.

The reason for this behaviour can be explained when plotting the stress paths developing in the interface during tunnel excavation. Such a diagram is given in Figure 8 for the non-load scenario. The horizontal axis represents interface normal stress while the vertical axis denotes shear stress. Three suites of stress paths are given for points at $x = 0$ m, 10 m and 25 m distances from the tunnel centre line. Each data point represents the result of one increment of the FE analysis, corresponding to the stress removal at the tunnel-soil circumference. The initial point is for increment 0.

For the different geometric positions, stress paths are given for an elastic analysis with $K_n = 10^5$ kPa/m

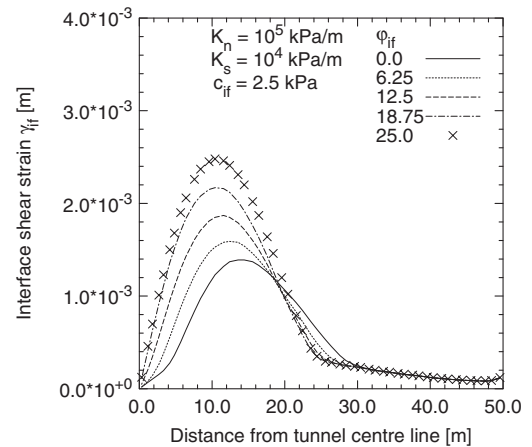


Figure 6. Interface shear strain along building for elasto-plastic analyses with varying angle of interface friction.

and $K_s = 10^4 \text{ kPa/m}$ and for elasto-plastic analyses with the same elastic parameters, a cohesion of $c_{if} = 2.5 \text{ kPa}$ and $\phi_{if} = 0^\circ, 12.5^\circ$ and 25° . The corresponding failure criteria are also plotted.

The stress paths for $x = 10 \text{ m}$ show the development of tensile normal stress, as expected from Figure 3 where tensile strain (positive sign) was found over approximately the first 20 m distance from the tunnel centre line. For the elasto-plastic cases plastic strain occurs when the stress paths reach the different failure criterions. For the $\phi_{if} = 0^\circ$ this occurs in the 6th increment, thereafter plastic strain develops. As ϕ_{if} increases, the failure criterion is reached in earlier increments: for $\phi_{if} = 12.5^\circ$ in increment 5 and for $\phi_{if} = 25^\circ$ already in the 4th step. Consequently, as ϕ_{if} increases from 0° to 25° , plastic strain develops over more and more increments.

This explains why in Figure 6 an increase in ϕ_{if} leads to an increase in plastic strain over a zone of 20 m distance from the tunnel centre line: In this zone tensile normal interface strain develops, and, consequently, the

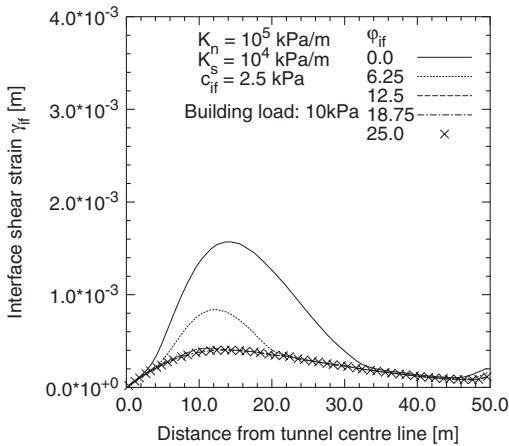


Figure 7. Interface shear strain along building with 10 kPa building load.

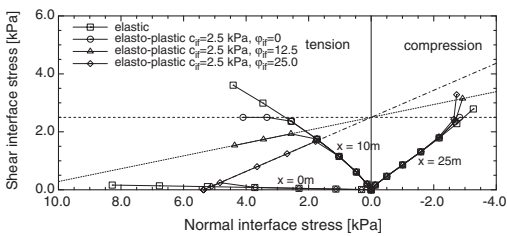


Figure 8. Interface stress paths for elastic and elasto-plastic analyses for weight-less building.

stress paths reach the failure envelopes with high angles ϕ_{if} at earlier stages than those with low values of ϕ_{if} .

For locations closer to the tunnel centre line, the stress paths become flatter. The stress path for $x = 0 \text{ m}$ (only the elastic and one elasto-plastic path are displayed) travels nearly horizontally (in theory nor shear stress should develop at $x = 0 \text{ m}$ due to symmetry; however, the results plotted are from the nearest integration point with a small value of x). As the elasto-plastic stress path encounters the failure criterion it travels down the failure surfaces until it eventually reaches the horizontal axis at a normal interface stress of $\sigma_{if} = c_{if}/\tan(\phi_{if})$. At this point it is not possible to exceed this normal stress magnitude. Instead the joint between structure and soil opens and plastic normal strain accumulates.

In the compressive zone (i.e. approximately 20 m from the tunnel centre line and beyond) a different behaviour can be found, as shown by the stress paths for $x = 25 \text{ m}$, shown in Figure 8. The stress path of the elasto-plastic analysis with $\phi_{if} = 0^\circ$ has the shortest distance to the failure criterion followed by the $\phi_{if} = 12.5^\circ$ case (both analyses reach the failure line in the last increment). The $\phi_{if} = 25^\circ$ case does not encounter the failure criterion and, consequently, no plastic strain develops at this position.

The application of building load shifts the initial stress condition prior to tunnel construction into the compressive stress regime. This situation is shown in Figure 9 which plots stress paths due to tunnel construction for a 5-storey building, subjected to a load of 10 kPa. The paths are presented for positions of $x = 0 \text{ m}$, 10 m and 25 m from the tunnel centre line. For clarity only results from the elastic analyses are represented (as they show the general direction of the stress paths). The stress paths have a similar shape as those from the no-load analyses. However, no tensile strain develops for the $x = 0 \text{ m}$ and 10 m paths as the initial stress situation is far enough in the compressive stress regime. In this context, an increase in ϕ_{if} leads to a larger distance for the stress path to travel before reaching the failure criterion. This explains the behaviour found in Figure 7 where plastic strain decreased as ϕ_{if} was increased.

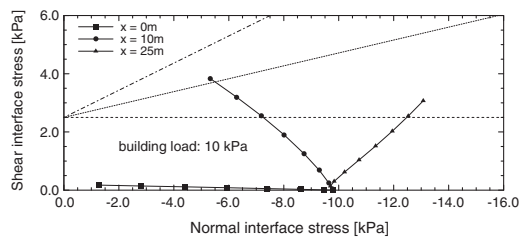


Figure 9. Stress paths for analyses with buildings subject to building load.

As noted above the situation when the stress path reaches the intersection of the failure criterion with the horizontal axis leads to the development of normal plastic strain, i.e. a gap opens between structure and soil. Figure 9 shows that such a scenario is unlikely to develop when a building load is applied in the analysis. The value of 10 kPa imposed on a 5-storey building is low and when a higher, more appropriate value was considered, the stress path was well within the compressive stress regime. It can therefore be concluded, that an open joint between building and soil is a consequence of assuming no building load – clearly an unrealistic scenario.

5 BUILDING DEFORMATION

The above analyses have shown that a gap between building and soil is unlikely to develop. The interface normal stiffness K_n has, therefore, only a minor influence on the deformation of the building, as long as an extremely low value is not adopted. The horizontal relative movement, in contrast, depends on the interface shear stiffness K_s . Assigning a low value of K_s allows slippage between the building and the ground. This slippage results in a vast reduction of horizontal strain within the building as Figure 10 shows. This graph compares the maximum horizontal strain in the 5-storey building obtained from an analysis with elastic interface elements of varying shear stiffness with the corresponding results from an analysis without interface elements by normalising them against each other. The figure shows that reducing K_s from 10^4 kPa/m to 10^2 kPa/m drastically reduces the horizontal strain (to below 10% of the non-interface value).

In their study, Potts & Addenbrooke (1997) showed that the horizontal strain experienced by a building is

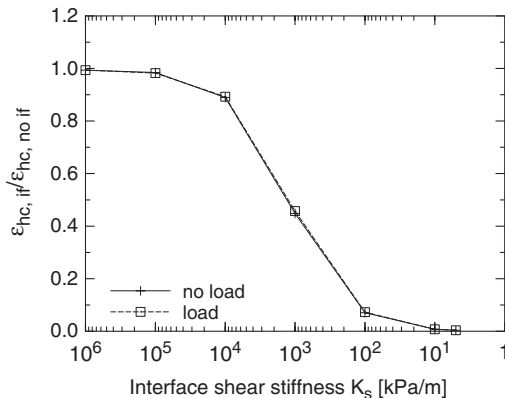


Figure 10. Decrease of horizontal building strain with reducing interface shear stiffness.

low when compared with greenfield values. For their building scenarios – which are comparable to the one presented here – the maximum horizontal building strain was below 5% of the corresponding greenfield value. Similar conclusions were drawn by Standing (2001) who presented horizontal building strain measurements during the construction of the Jubilee Line Extension in London.

The reduction in strain shown in Figure 10 has to be compounded with the decrease in horizontal strain due to the building stiffness. Compared to the vast reduction in horizontal strain due to the building's stiffness, the further reduction caused by slippage is of only small significance.

6 CONCLUSIONS

This paper presented a study of 2D FE analyses in which the tunnel-soil-building interaction was modelled by introducing interface elements between the base of the building and the soil. Both elastic and elasto-plastic constitutive models were assigned to the interface elements while the building was modelled as an elastic beam.

The study showed that when modelling the interface elements elastically, a change in normal interface stiffness changes the vertical settlement profile of the building while the horizontal movement between structure and soil is essentially unaffected. Conversely, when varying the interface shear stiffness, the relative horizontal displacement between building and soil changed while the building settlement profile was only marginally influenced. This indicates that vertical and horizontal building movement are relatively uncoupled from each other.

When modelling the building as weightless, introducing a low normal interface stiffness led to relatively large normal tensile strains between building and soil in a zone adjacent to the building and tunnel centre line (the building was concentric with the tunnel). In this zone a gap opened between the structure and the soil while further away from the tunnel/building centre line compressive strain occurred at the interface. Similar conclusions were drawn when modelling the interface elasto-plastically.

It was shown, however, that the introduction of a relatively small building weight is sufficient to change the normal interface stress adjacent to the centre line from tension into compression. In this situation it was concluded that no tension gap opens between the building foundation and the underlying soil.

It was concluded that allowing for full or partial slippage between building and soil only has a small effect on the horizontal building strain compared to the influence of the structure's own stiffness.

REFERENCES

- Day, R. A. & Potts, D. M. 1994. Zero thickness interface elements – numerical stability and application. *Int. Journal Num. Anal. Meth. Geomech.*, 18, 689–708.
- Franzius, J. N. 2004. *The behaviour of buildings due to tunnel induced subsidence*. PhD thesis, Imperial College, University of London.
- Franzius, J. N., Potts, D. M., Addenbrooke, T. I. & Burland, J. B. 2004. The influence of building self weight on tunnelling-induced ground and building deformation. *Soils and Foundation*, 44(1), 25–38.
- Franzius, J. N., Potts, D. M. & Burland, J. B. 2005. The influence of soil anisotropy and K_0 on ground surface movements resulting from tunnel excavation. *Geotechnique*, 55(1), 189–199.
- Franzius, J. N. & Potts, D. M. 2005. Influence of mesh geometry on three-dimensional finite element analysis of tunnel excavation. *Int. Journal of Geomech.*, 5(3), 256–266.
- Franzius, J. N., Potts, D. M. & Burland, J. B. 2006. The response of surface structures to tunnel construction. *Proc. of ICE, Geotechnical Engineering*, 159(1), 3–17.
- Mair, R. J., Taylor, R. N. & Burland, J. B. 1996. Prediction of ground movements and assessment of risk of building damage due to bored tunnelling. *Proc. of the Int. Symposium on Geotechnical Aspects of Underground Construction in Soft Ground, London*. 713–718. Balkema, Rotterdam.
- Mair, R. J. & Taylor, R. N. 2001. Elizabeth House: Settlement Predictions. *Chap. 14 of: Burland, J. B., Standing, J. R. & Jardine, F. M. (eds.), Building response to tunnelling*, Vol. 1. Thomas Telford, London.
- Potts, D. M. & Addenbrooke, T. I. 1997. A structure's influence on tunnelling-induced ground movements. *Proc. Instn. Civ. Engrs. Geotech. Engineering*, 125, 109–125.
- Potts, D. M. & Zdravkovic, L. 1999. *Finite Element analysis in geotechnical engineering. Vol. 1: Theory*. Thomas Telford, London.
- Potts, D. M. & Zdravkovic, L. 2001. *Finite Element analysis in geotechnical engineering. Vol. 2: Application*. Thomas Telford, London.
- Standing, J. R. 2001. Elizabeth House, Waterloo. *Chap. 30 of: Burland, J. B., Standing, J. R. & Jardine, F. M. (eds.), Building response to tunnelling*, Vol. 2. Thomas Telford, London.
- Timoshenko, S. 1955. *Strength of materials; Part 1: Elementary theory and problems*. 3rd edn. D. Van Nostrand, New York.

Morphological effects on settlements induced by shallow tunnelling

D. Segato & G. Scarpelli

Technical University of the Marche Region, Ancona, Italy

ABSTRACT: Stress and strain fields near the ground surface are strongly influenced by ground morphological conditions, so that sometimes, in the case of shallow tunnel design, numerical predictions of the induced subsidence are required to account for an initial stress which may not be simply geostatic. In this paper, this problem is studied with reference to a real tunnel excavated in a stiff clay deposit under the most intensively urbanized area of the city of Ancona (Italy). The results of the monitoring show that, displacements at the ground surface caused by tunnel excavation can be only explained if soil morphology is taken into account. In this particular problem, the morphological effect arise as a consequence of the sloping that characterize the ground surface at the beginning of the tunnel. A numerical, finite element model of the tunnel problem is presented to clarify such a behavior through parametric analysis.

1 INTRODUCTION

The correct formulation of boundary conditions, is a key parameter in analyzing any engineering problem. Numerical analysis of geotechnical problems is generally worked out using the plane strain condition hypothesis, since software supporting three dimensional models are still expensive in time and sometimes difficult to interpret. Dealing with tunnel analysis, the plane strain hypothesis is generally acceptable, in the cross plane, only far from the advancing front where the strain field, due to the presence of the soil core, becomes three dimensional.

The current method of analysis is to “force” the 2D numerical solution to take into account the presence of the front face using the convergence-confinement method introduced by Panet & Guenot (1982). At the excavation boundary a pressure reproducing the “at rest” condition is applied, which is then reduced through the deconfinement coefficient. For shallow tunnels excavated in urban areas, care must be taken in defining boundary conditions because the plane strain hypothesis may be inappropriate even far from the face: due to low covers and short lengths, the stress state is highly influenced by topographic effects. The presence of the slope standing above the portal allows a three dimensional state in the first part of the tunnel before the excavation takes place which will result in a preliminary strain field different from that expected in a 2D cross section analysis.

The more the soil element is close to the slope, the more this effect becomes important (resulting in a settlement up to three times greater in the present case

study). The result is that, while when dealing with support design the 2D simplification may be conservative, in settlement curve prediction the plane strain hypothesis may lead to an unsafe evaluation.

Bearing in mind the points mentioned above, in the following, a simplified (with reference to geometries, materials and boundary conditions) FEM model, is presented in order to enhance the comprehension of monitoring data from S. Martino Tunnel. Furthermore, the model is used for a sensitivity analysis with reference to the problem of the morphological effect.

2 ANALYSIS OF CASE RECORD

2.1 *Description of San Martino tunnel*

The San Martino tunnel has been driven through a stiff clay deposit beneath one of the main hills where the Ancona old city has expanded. It connect the port area (Vanvitelli building) with the city center (S. Martino square). [Figure 1](#) gives a schematic layout of the tunnel which is characterized by an about 100 m² excavation section and a 536 m length. The liner consists of a primary steel rib and jet grout lining at the advancing face and a secondary reinforced concrete internal layer cast in place at about a 2 diameter distance.

The tunnel ends were already present to a depth of 50 m and as such they served as bomb shelter during the Second War years. The former excavation section in these zones was about 85 m² and was supported by a brick lining.

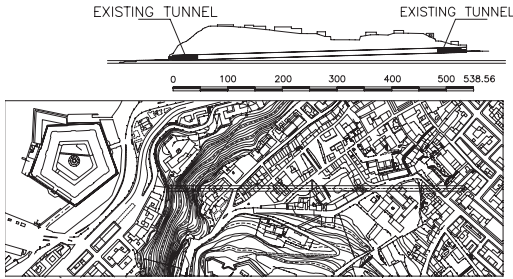


Figure 1. Tunnel layout.

The “Vanvitelli” side of the tunnel (left on fig. 1), has been studied in the present paper. It must be observed however that, except for the slope facing the sea which dipped 45° upward from the portal, the tunnel underlay, at an average height of 50 m, an intensely urbanized area.

Before the excavation started, a surface monitoring has been set and some holes along the tunnel axis were instrumented with both magnetic extensometers and slope indicators for vertical and horizontal displacements respectively. Piezometers were also installed for pore pressure measurements. In the following some result of topographic monitoring will be examined so as to identify the influence of morphological effect on the results.

2.2 Results of field monitoring

As the excavation progressed, surface monitoring showed the development of a zone along the tunnel center line where high vertical settlement was observed compared to adjacent sections. Such a behavior was not in agreement with internal convergence measurements, which in turn did not show unexpected volume loss, and neither was observed any local change in mechanical properties of the mass.

Figure 2 provides a plot of longitudinal settlements recorded after the excavation completion. Transverse settlement profiles taken parallel to the top slope edge and illustrated in figure 3 show a typical Gaussian trend; the theoretical settlement pattern based on the methods proposed by Peck (1969) and Mair et al. (1993) and matching each profile with the proper cover, indicate a subsidence volume increasing while approaching the slope. Plotting pore pressure and vertical settlement vs tunnel advancement allows an appreciation of how, the subsidence response is that of a drained continuum (fig. 4).

This can be explained as the consequence of the macro structural features of the clayey deposits crossed by the tunnel. It can be also noted that, even though

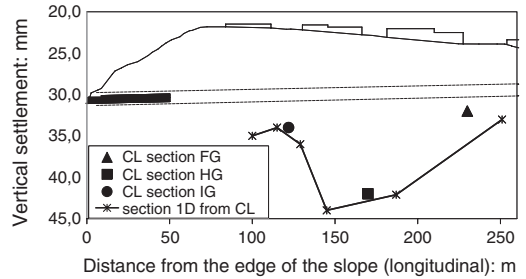


Figure 2. Longitudinal settlement profiles recorded along tunnel center line (CL) and one diameter aside.

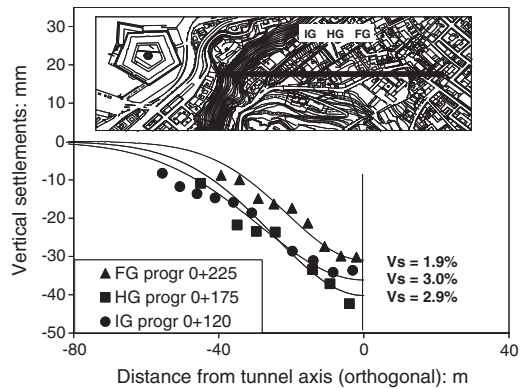


Figure 3. Measured and theoretical settlement troughs taken parallel to the slope edge, at different cross sections.

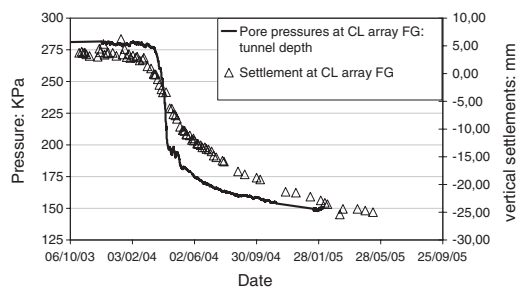


Figure 4. Pore pressure and measured vertical settlements at FG center line (CL) on FG.

the tunnel lining was water tight, for the whole observation period the pressure didn't come back to the former value as the hydrographic basin was of small extension.

Table 1. Summary of general soil properties.

Soil property	Stiff clay
Unit weight (kN/m ³)	20
OCR (at gravity loading stage)	3
K ₀	1.18
G ₀ (MPa)	150
E' (MPa)	360
E' _{50 ref} (MPa)	40
E' _{oed ref} (MPa)	30
c' (kPa)	80
ϕ' (deg)	26
Ψ (deg)	5

3 SOIL PROPERTIES FOR ANCONA STIFF CLAY

From the geomechanics point of view, in the considered mass portion, the two main soil strata can be identified from the ground surface:

- S: clayey sandy silt about 8 m thick;
- C: stiff overconsolidated clay deposit, typically found in the area dating back to the Pliocene period.

Due to the aim of the present study, it appeared to be useful to adopt models which have to be simple, but still are able to give a correct representation of the phenomena which are present in the soil mass. To reach this goal, the whole mass has been assumed as having the same mechanical properties of the C layer. For sake of simplicity, in the FE analysis, soil behavior has been modeled through the use of the so called Hard Soil model, an elastic/plastic relationship with deviatoric isotropic hardening which takes account for plastic deformations (both volumetric and distortional) and is implemented in the FE codes PLAXIS 7.2 and 3D Tunnel (Vermeer & Brinkgreve, 1998). In the HS model, the stress strain relationship is hyperbolic and the adopted tangent stiffness E' (which controls the material stiffness at each strain level) has been related to the shear stiffness at small strains G₀; this value has been chosen, on the base of a wide bibliography available on such materials (Scarpelli, 1995), equal to 150 MPa. From E', the reference stiffness values to be entered in the model are defined through FE simulation of triaxial CID tests and the comparison with tests results on real soil samples; it is pointed out that, being interested in small strain behavior, special care has been used in reproducing the initial part of q-ε curves.

Typically, stiff clays in the Ancona geological context have medium/high OC rates in the first 20 ÷ 25 m, decreasing with depth; in the following analysis, to represent the behavior of the soil element which is involved in subsidence phenomena, an OCR = 3 at the gravity loading stage has been taken for the whole mass which corresponds a 1.18 value for K_{0OC} (tab. 1).

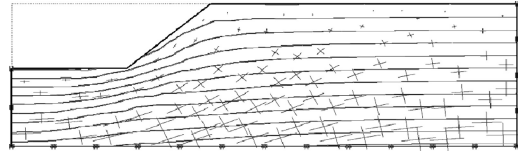


Figure 5. Mean stress contours and principal stress orientation along the tunnel axis.

4 DETAILS OF THE ANALYSIS

4.1 Preliminary morphological considerations

Since the free surface constituted by the slope in the first part of the tunnel, is a boundary condition for the principal stress flow, the shallow layer stress pattern will arrange parallel to this plane.

Owing to this fact, horizontal stresses in the driving direction taken at different distances from the slope top edge will be variable and generally different from that expected in K₀ conditions (which are instead reached far from the slope). It must be remembered that in this case, the final configuration of the principal stress field will be also dependent on the mass stress history. This will affect obviously the amount the K₀ value in the transverse direction, and will induce a rotation of principal stress thus modifying vertical and horizontal (in the driving direction) stresses in the mass (fig. 5). When in the considered case the plane strain excavation at different distances from the slope edge is analyzed, the variability of the out of plane stress (and strain) field can not be taken into account leading to an identical stress state and thus same transverse settlement trough.

4.2 Plane strain conditions

In order to match the 2D settlement trough, the FG array data were taken as reference and a simple FE problem model has been created which is showed in figure 6.

The tunnel excavation is simulated in a 2D green-field FE analysis. The parameters utilized for the HS model are reported in table 1, and formerly discussed. A circular excavation section has been considered with a 10 m diameter (D), an H vs. D ratio of 5 have been considered as cover height. Since the pore pressure drop recorded during monitoring can be associated to a generalized phreatic lowering, at the tunnel axis, (thus not affecting the shape of the settlement profile) for sake of simplicity the presence of the water was neglected.

Construction sequence was modeled using the convergence-confinement method. During the first phase of the analysis, a λ value equal to 0.5 has been used and in the following phase a circular lining

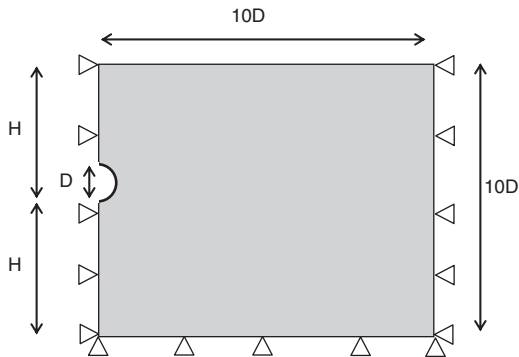


Figure 6. Plane strain model for FE analysis.

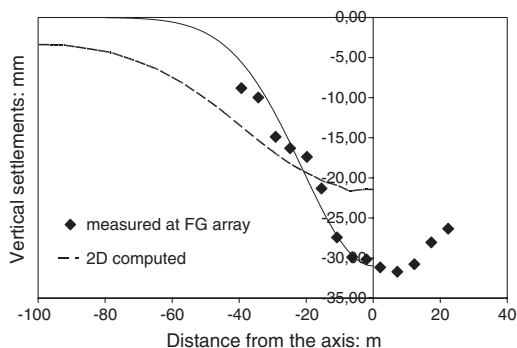


Figure 7. Comparison between vertical settlements measured at array FG and computed in plain strain conditions.

modeled by an elastic beam has been activated bringing the λ value up to a value of 1.0. Being the analysis in drained conditions, the volume (per running meter) of the surface settlement trough equal to that measured in the real case was taken as matching criteria.

A volume loss higher than that expected was calculated, which may be partially due to the inability of the hyperbolic relationship to reproduce the plastic softening of the stiff clay experienced by soil close to the tunnel profile and partially to the reduced excavation area used in the model. As the analysis purpose is to study the strain field far from the excavation area and being the mass mainly in pre failure conditions except a small area around the excavation, such an approximation was considered acceptable. The Calculated and measured settlement trough are illustrated in figure 7.

The inaccuracy of the matching between measured and computed settlement trough when the initial stress profile is characterized by high values of the coefficient of lateral earth pressure at rest K_0 , has been discussed by several authors (Addembroke et al., 1997; Gunn, 1993; Simpson et al., 1996; Lee & NG, 1996; Franzius, Potts & Burland, 2005) but a feature which is able to

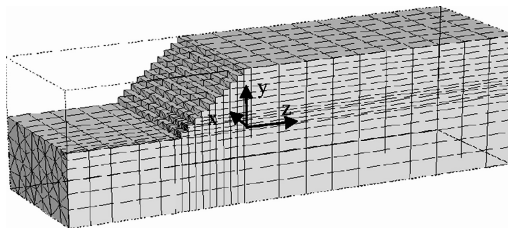


Figure 8. FE mesh for 3D analysis of San Martino tunnel excavation.

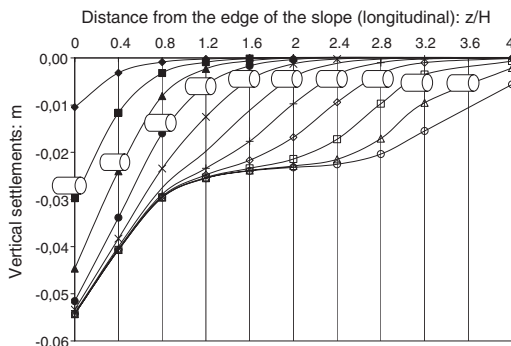


Figure 9. Evolution of the longitudinal settlement profile with tunnel progress for greenfield conditions with $H = 50$ m and $K_0 = 1.18$.

improve significantly the computed settlement profile has not yet been defined.

4.3 Three dimensional model

The 3D FE model shown in figure 8 has been developed using PLAXIS 3D Tunnel code by extruding the former 2D model and excavating the tunnel in the z direction. The 45° slope has been created after the gravity load phase by removing soil elements. In the following, coordinates will be referred to the origin of z axis set below the slope top edge and normalized to the height of the hill (50 m). The analysis has been carried on in drained conditions as for the previous case.

When introducing the third dimension in the problem, the convergence-confinement method in plane strain conditions has to be substituted by the step by step modeling sequence (Katzenbach & Breth, 1981).

Since the excavation sequence is not volume loss controlled, an excavation length of about 20 m (2D) with the contemporaneous activation of the lining has been chosen, which gives in plane strain conditions, the same radial convergence as in the 2D case. As the tunnel heading is advancing, the longitudinal settlement profile on the top of the slope develops as shown in figure 9. Different curves are given for every advancement step.

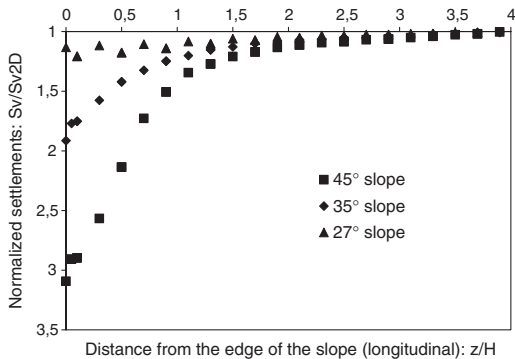


Figure 10. Longitudinal normalized settlement profiles for different slope inclination.

The figure demonstrates that for the reference case, in addition to the cumulative error curve shape across the tunnel face (which moves forward as the heading advances), a permanent influence zone $2H$ wide close to the slope edge is produced where settlements are amplified. In the 3D model this influence results in an amplification of the gaussian shape settlement curve approaching the slope top edge. It must be noted that similar behavior may be obtained if a volume loss is applied to the excavation section in a single step; this implies that the observed surface settlement trough may be attributed to the lack of confinement in the slope influence area.

4.4 Parametric analysis

A series of parametric analyses to investigate the influence of various parameters was carried out. The first one illustrates the influence of slope steepness. Three cases are shown in figure 10 where for an initial $K_0 = 1.18$, 45° , 35° and 27° sloping hill sides are considered and vertical settlement are normalized to the value recorded in plane strain conditions.

The figure highlights two effects: in this stress state conditions the effect of the slope on the settlement through is negligible for slopes under 27° . Furthermore, the extension of the influence area doesn't change being linked to the hill height H .

Since a link of the observed behavior with stress state can be guessed, a further set of analyses were conducted to evaluate the K_0 effect. The reference model with a 45° steep slope was studied at different initial stress states: $K_0 = 1.18$ ($OCR = 3$), $K_0 = 0.873$ ($OCR = 2$) and $K_0 = 0.562$ (NC). Besides two additional analysis were run: the first at $K_0 = 1.18$ for a material having an higher friction angle (35°) thus applying an $OCR = 5$ at the initial stage. The second one was again the case $K_0 = 1.18$ ($OCR = 3$), but a supplementary slope dipping 22° along the xy plane was introduced in the model.

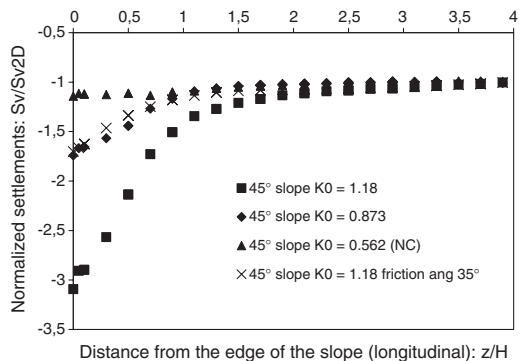


Figure 11. Longitudinal normalized settlement profiles for different initial stress states.

Results of this set of analysis are shown in figure 11. Again the extension of the influence area is still the same and inside it high K_0 values emphasize the slope effect being the NC case unaffected. The case with higher friction angle resulted in less influence in terms of maximum settlement ratio because of the smaller extension of the plastic zone around the excavation. When an additional surface is introduced, the stress rotation reduces again the influence of the main slope.

4.5 Synthesis of the results

The former results show an invariability in the extension of the influence zone regardless the initial stress state and the inclination of the slope.

If only the excess settlements with respect to the plane strain conditions is considered, it is possible to plot the normalized profile over the typical settlement profiles for spandrel type excavations for cantiliver walls. In figure 12, the computed excess profile for the case which have resulted sensitive to the influence zone are overlapped to the curves proposed by Hsieh & Ou (1998). It is interesting to note that the extension of the primary influence zone is the same as that predicted by the tunnel FEM analysis.

5 THE SAN MARTINO TUNNEL FEM MODEL

5.1 Settlements time history

Before comparing the fem model results with those of the case study, a consideration must be done concerning the settlement time history.

At the time the monitoring started, the mass had already been disturbed by the excavation of the bomb shelter in the first 50 m. The monitoring cannot account for the deformation phenomena already developed so the analysis results have to be processed before comparing prediction and measured data.

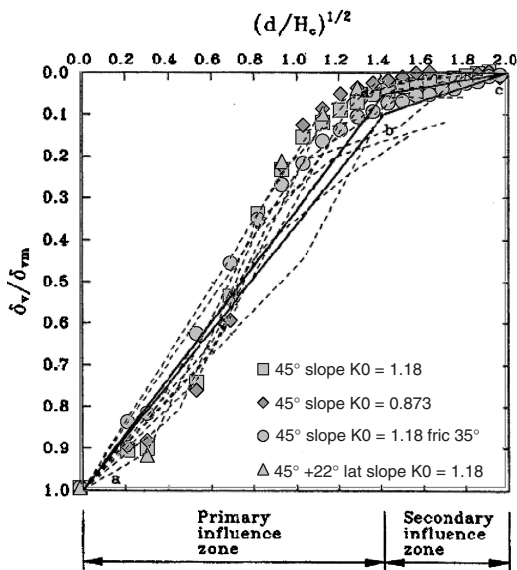


Figure 12. Longitudinal normalized excess settlement profiles from FEM analysis compared with Hsieh and Ou profiles (1998) for spandrel type excavations.

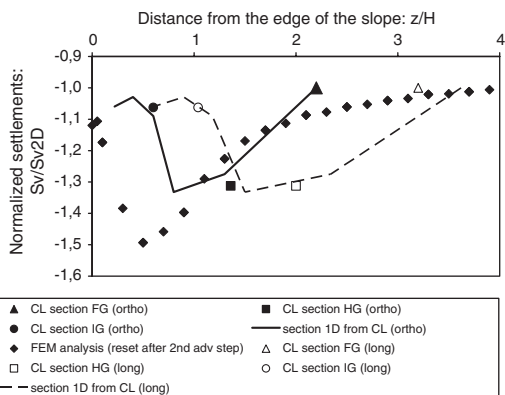


Figure 13. Longitudinal normalized calculated settlement profiles reset after two advancing steps compared with monitoring data.

5.2 FEM analysis results

The existing excavation section being comparable with that of the new tunnel, the FEM analysis settlements were reset after the first two advancement steps.

Due to the non-orthogonal arrangement between tunnel axis and slope edge a better matching between computed and measured settlements can be achieved if distance orthogonal to the slope edge is taken into account instead of distance along the tunnel axis (fig. 13).

6 CONCLUSIONS

A simplified tree dimensional numerical model was realized to investigate the results of monitoring from the excavation of S. Martino Tunnel in Ancona (Italy).

Morphological effects have been recognized playing an important role in the stress field reconstruction. A sensitivity analysis, based on the numerical model developed, allowed to identify an influence zone induced by the presence of a steep slope over the tunnel portal which extension is proportional to the eight of the slope itself. The study demonstrates that longitudinal settlement curve can be predicted by adopting the profiles proposed in literature for cantilever excavation.

REFERENCES

- Addembroke, T. I., Potts, D. M. & Putzrin, A. M. 1997. The influence of pre-failure soil stiffness on the numerical analysis of tunnel construction. *Geotechnique*, 47, No. 3: 197–204.
- Vermeer, P. A. & Brinkgreve, R. B. J. 1998. *Finite Element Code for Soil and Rock Analysis*. PLAXIS 7.0 and PLAXIS 3D Tunnel manual. Balkema.
- Franzius, J. N., Potts, D. M. & Burland, J. B. 2005. The influence of soil anisotropy and K_0 ground surface movements resulting from tunnel excavation. *Geotechnique*, 55, No. 3: 189–199.
- Gunn, M. J. 1993. The prediction of surface settlements profiles due to tunneling (eds. G. T. Houlsby and A. N. Schofield). *Predictive soil mechanics: Proc. of the Wroth Memorial symp.*, London: Thomas Telford, London.
- Hsieh, P.-G. and Ou, C.-Y. 1998. Shape of Ground Surface Settlement Profiles Caused by Excavation. *Canadian Geotechnical Journal*, 35, No. 6: 1004–1017.
- Katzenbach, R. & Breth, H. 1981. Nonlinear 3D analysis for NATM in Frankfurt Clay. *Proc. 10th Int. Conf. Soil. Mech. Found. Engng, Stockholm 1*: 315–318.
- Mair, R. J., Taylor, R. N. & Bracegirdle, A. 1993. Subsurface settlement profiles above tunnels in clays. *Geotechnique*, 43, No. 2: 315–320.
- Panet, M. & Guenot, A. 1982. Analysis of convergence behind the face of a tunnel. *Tunnelling 82*, The Institution of Mining and Metallurgy, London: 197–204.
- Peck, R.B. 1969. Deep excavations and tunnelling in soft ground. *Proc. of the 7th Int. Conference on Soil Mechanics and Foundation Engineering. State of the art*: 225–290. Sociedad Mexicana de Suelos A.C.
- Segato, D. 2005. Influenza della topografia sulla evoluzione dello stato deformativo del terreno nello scavo di gallerie a bassa copertura. *PhD Thesis*. Università Politecnica delle Marche.
- Scarpelli, G. 1995. Physical processes and related instabilities in overconsolidated clayey slopes. *Proc. 11th European Conference on Soil Mechanics and Foundation Engineering*. Copenhagen.
- Simpson, B., Atkinson, J. H. & Jovicic, V. 1996. The influence of anisotropy on calculations of ground settlements above tunnels. *Proc. Int. Symp. Geotechnical Aspects of Underground, Construction in Soft ground*, London: 591–594.

Eurocode-based ultimate limit state design of NATM tunnels using nonlinear constitutive models for sprayed concrete and soil

Herbert Walter

IGT – Geotechnik und Tunnelbau, Consulting Engineers, Salzburg, Austria

ABSTRACT: Numerical methods are a standard tool for the design of tunnels. An economic design of a sprayed concrete tunnel lining requires the application of constitutive models which cover the time-dependent properties of sprayed concrete and allow an “implicit design”: The constitutive model ensures, for each instant of time, stress states which are bearable by the material; if required the loads are redistributed to neighbouring regions as long as the overall collapse load is not reached. In order to perform an ultimate limit state design according to Eurocode 7 (EN 1997-1), partial safety factors on actions and resistances or strength parameters, respectively, have to be introduced in the analysis. Which of the Design Approaches of EN 1997-1 is applicable in connection with numerical methods is discussed and illustrated by means of the design of the primary lining of a metro station.

1 INTRODUCTION

With Eurocode 7 (EN 1997-1:2004) (CEN 2004a) being introduced as standard in Europe, its application in connection with numerical methods is being discussed (e.g. Schweiger 2005). Tunnels and other underground structures can be considered as retaining structures: The section about retaining structures of EN 1997-1 begins with “The provisions of this Section shall apply to structures, which retain ground comprising soil, rock or backfill and water. Material is retained if it is kept at a slope steeper than it would eventually adopt if no structure were present. Retaining structures include all types of wall and support systems in which structural elements have forces imposed by the retained material.” Following this definition, the design concept of the Eurocodes with its semi-probabilistic approach using partial safety factors should be applied to the design of underground structures.

In the following some characteristics of cyclically excavated underground with shotcrete as primary support in connection with their ultimate limit state design (ULS) will be highlighted. This type of structures is frequently analysed by means of two- or three-dimensional finite element or finite difference models. Applicability of the three Design Approaches of EN 1997-1 and their variants will be investigated. An “implicit design” using a constitutive model which itself limits the stress level to values bearable by the material at the current instant of time allows an economic design because the potential of stress redistribution within sprayed concrete and soil is utilised. The ultimate limit state design of the

primary lining of a metro station serves as an example and will be discussed in some depth.

2 ULTIMATE LIMIT STATE DESIGN OF NATM TUNNEL LININGS

2.1 Design concept of EN 1997-1

According to EN 1997-1, ultimate limit states have to be investigated: “Where relevant, it shall be verified that the following limit states are not exceeded: (...)

- internal failure or excessive deformation of the structure or structural elements, including e.g. footings, piles or basement walls, in which the strength of structural materials is significant in providing resistance (STR);
- failure or excessive deformation of the ground, in which the strength of soil or rock is significant in providing resistance (GEO); (...)

For these types of limit states, design actions E_d have to be smaller or equal to design resistances R_d . Both may depend on material parameters. Design actions and design resistances, respectively, are derived from representative values with the help of partial safety factors. In EN 1997-1 three different Design Approaches (DA) are listed with which an ULS design of a geotechnical structure can be performed. They differ in the way how partial safety factors are applied. Design Approach 1 requires two separate analyses which are denoted DA1-1 and DA1-2 in Table 1 below.

Table 1. Design approaches and partial safety factors.

Design approach	$\gamma_F = \gamma_E$		γ_R	$\gamma_{c'} = \gamma_{\phi'}$
	Permanent	Variable		
DA1-1	1.35	1.5	1.0	1.0
DA1-2	1.00	1.3	1.0	1.25
DA2	1.35	1.5	1.4	1.0
DA3	1.00	1.3	1.0	1.25

Table 1 contains partial safety factors for unfavourable actions, γ_F , for effects of unfavourable actions, γ_E , for earth resistance and bearing capacity, γ_R , and for material parameters cohesion c' and friction angle ϕ' , $\gamma_{c'}$ and $\gamma_{\phi'}$, respectively, as they are listed in Appendix A of EN 1997-1 for retaining structures (some of the partial safety factors have been omitted in the table for simplicity). One has to keep in mind that every country which introduces EN 1997-1 may prescribe the use of specific design approaches (depending on the type of structure, if appropriate) and may modify the safety factors of Appendix A.

EN 1997-1 permits to apply the safety factor for actions either directly to the actions, or to the effects of actions. Frequently, a design approach in connection with the application of partial safety factors to effects of actions is denoted with an asterisk, e.g. DA2* (using γ_E) versus DA2 (using γ_F) (Frank et al. 2004). This convention will also be used in this paper.

2.2 Characteristics of numerical models for cyclic excavation

One essential aspect of tunnels driven by cyclic excavation or NATM (New Austrian Tunneling Method) is that the excavation is usually immediately followed by support measures like applying anchors and/or a sprayed concrete lining. Especially in soft soil, the sprayed concrete lining plays a main role in supporting the structure being excavated.

2.2.1 Modelling excavation

Generally speaking, modelling excavation means modelling geometry changes. (This subsection is not only valid for tunnel excavation, but for excavations supported by retaining walls as well.) These geometry changes are considered as actions. The problem with this type of action – and with actions like dead load of the soil or earth pressure – is that there is no easy way of applying partial safety factors to these actions (Schweiger 2005, Schuppener & Vogt 2005). The only obvious option for factorising actions directly would be multiplying the forces acting on the boundary of the volume to be excavated by a partial safety factor before applying them to the surrounding soil when performing the actual excavation. Although such a procedure is possible – an analogous technique has

been implemented in various 2-D-finite element codes in order to simulate the so-called pre-relaxation – it requires special provisions which may not be available in the analysis tool at hand.

Additionally, like in slope stability analysis, increasing the dead load of the soil by a partial safety factor would not necessarily result in increased safety margins. In connection with numerical methods applying partial safety factors to effects of actions is favoured against applying partial safety factors directly to actions. Proceeding in this way has been recommended e.g. in FVS 2004, DIN 2005.

2.2.2 Sprayed concrete properties

Linings made of sprayed concrete exhibit a number of specific properties in addition to characteristics which are similar to those of concrete:

- Immediately after application, sprayed concrete has practically no stiffness and does not carry any loads (“stress-free application”).
- Stiffness and strength increase rapidly at young age
- Young sprayed concrete has high ductility in compression due to creep at high stress levels.

2.2.3 Implicit design of sprayed concrete linings

Considering running tunnels, established design procedures for 2-D-models are available which have been adapted to the design concept with partial safety factors in a straight-forward manner (FVS 2004). In these design procedures, sprayed concrete is simulated as linear elastic material, with different values for the stiffness in young age and later on.

For the design of tunnel intersections, like in the example below, relying on a linear elastic material model for sprayed concrete would result in uneconomic lining thicknesses and amounts of reinforcement. This is a result of overestimating the stresses in the sprayed concrete lining and of neglecting the potential of stress redistribution.

Advanced constitutive models for sprayed concrete cover all required features and allow an “implicit design”: Like nonlinear soil models, also the shotcrete model limits the stress level in accordance with pre-defined strength parameters.

In connection with an ULS design the question arises which partial safety factors for sprayed concrete have to be chosen in order to be in agreement with the requirements of EN 1997-1.

According to EN 1992-1 (CEN 2004b), the design resistance of reinforced concrete structures has to be calculated applying a partial safety factor for the compressive strength of concrete of $\gamma_c = 1.5$ and for the yield strength of the reinforcing steel of $\gamma_s = 1.15$. These requirements can be adopted for the nonlinear sprayed concrete model by scaling the time dependent failure envelope by a factor of 1/1.5.

However, this is correct only if the acting stresses are design stresses, i.e. stresses resulting from design actions (which themselves contain a partial safety factor). As already stated, applying partial safety factors on the effects of action is favoured in numerical analyses against partial safety factors applied directly on the actions. Stresses and strains result from characteristic actions, and the partial safety factor on actions has to be introduced immediately before comparison with the material resistances.

The first guess for an implementation would probably be: Let us – at the integration point level – increase the acting stresses by the partial safety factor on actions, and compare them with the stresses the failure envelope permits. Unfortunately, this does not work with most finite element programs: At the integration point level, the constitutive law yields stresses as functions of the strains. Limitation of the stress level to admissible values is automatically fulfilled by the constitutive law. Stresses and, as a result, sectional forces are limited to values bearable by the material. An artificially increased stress level is not possible. Increased strains cause additional plastification or rupture and, if possible, stress redistribution to other parts of the structure.

2.2.4 *Applicability of the design approaches*

Before deciding what to do instead, let us consider Table 1:

Design Approaches DA1-2 and DA3 have a nice property: The partial safety factor for permanent actions is 1.0. The higher safety factor for variable actions can be introduced in most cases by scaling the variable loads by the factor 1.5/1.35 in advance (factor 1.3 in Appendix A of EN 1997-1 is not consistent with the other partial safety factors) in order to incorporate the difference in safety factors between variable and permanent actions.

Hence, acting stresses at integration point level need not be factorised when using Design Approaches DA1-2 or DA3. The implicit design of the sprayed concrete lining can be applied directly, just by using an appropriately scaled failure envelope.

DA1-1 and DA2 would work with the implicit design of the lining; however, DA1-1* and DA2* are preferred for geotechnical problems, as already mentioned. In order to cope with these approaches, the following remedy has been taken: The failure envelope is scaled down by two factors: Firstly, by the safety factor for permanent actions, and secondly by the partial safety factor for the material sprayed concrete. This procedure is a deviation from EN 1997-1 in that the whole safety is put to the side of the resistances, and resembles the old global safety concept.

Design Approaches DA2 (and DA2*) specify partial safety factors greater 1.0 for resistances like bearing capacity and earth resistance. In numerical analyses, it is difficult to handle these resistances in a versatile

manner. It seems that the application of DA2 (or DA2*) in connection with continuum mechanics approaches is restricted to a limited number of problem types where the possible failure mechanisms are known beforehand.

Summarising, for retaining structures – including tunnel linings – analysed by numerical methods with nonlinear behaviour of the material of the retaining structure, there are restrictions on the use of the Design Approaches of EN 1997-1:

- Application of partial safety factors directly on actions is frequently not possible or would require sophisticated numerical implementation. As a result, Design Approaches should be used which do not contain safety factors on permanent actions (DA1-2, DA3), or the partial safety factor should be applied on the effect of actions (DA1-1*, DA2*).
- Application of partial safety factors on effects of actions (as required for DA1-1* and DA2*) does not work in connection with nonlinear constitutive relations which yield stresses as a function of strains. As a remedy, the strength parameters of the material of the retaining structure can be reduced twice, once for the effects of actions, and once for the safety required for the material.
- DA2 and DA2* are not generally applicable because the ground resistances bearing capacity, sliding resistance and earth resistance cannot be easily identified in continuum mechanics approaches.

3 EXAMPLE – METRO STATION

In the course of the extension of the metro line U2 in Vienna the station Taborstraße is under construction. Client is the “Wiener Linien”, the Vienna Transport Authority (Wiener Linien 2002). The line will go into operation in 2008.

The station consists of two parallel single track platform tunnels with a cross section of 74 m² each. The platform tunnels are linked by a connection tunnel (cross section 59 m²) from which an escalator tunnel (cross section 63 m²) provides access to the street level. Two shafts, a large one at the western end of the station and a small one at the eastern end between the platform tunnels, have been constructed as open cut prior to the platform tunnels. The tracks lie about 18 m below street level. The tunnels run partly below 5-7-storey-buildings, partly below streets. [Figure 1](#) shows a plan of the station.

The tunnels are driven through sediments of the Quarternary and Tertiary following an NATM excavation scheme. Each tunnel is subdivided into top heading, bench and invert. Primary support of the tunnels is a sprayed concrete lining with a thickness of 30 cm.

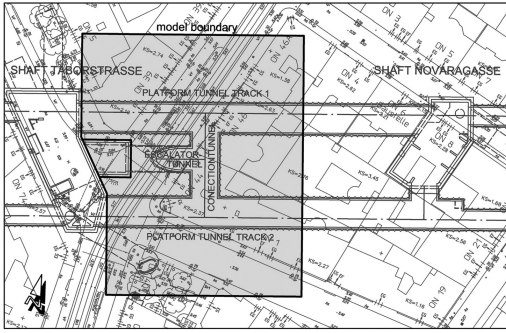


Figure 1. Station layout and model boundary.

The linings will be reinforced with two layers of wire mesh.

Three-dimensional finite element (FE) analyses have been performed in order to predict the settlements due to the excavation of the tunnels and to design the sprayed concrete lining (Walter 2006). Of special interest are the stress concentrations in the lining which develop at intersections in the course of the excavation process.

3.1 Constitutive relations, material properties

3.1.1 Soil

The soil has been modelled by linear volume elements using the Mohr-Coulomb-material model. Three different soil layers are distinguished. At a level of about 4 m below TOR the groundwater table (which has been lowered ahead of the construction) has been assumed.

The parameters have been chosen as cautious estimates of the mean value in the sense of EN 1997-1.

The soil above the level of the basements of the buildings has not been modelled. Instead, the dead load of the soil and the buildings, respectively, have been specified as distributed loads at the level of the basements.

3.1.2 Sprayed concrete

The sprayed concrete lining consists of layered shell elements. A constitutive model developed by Meschke and Mang (Meschke 1996, Meschke et al. 1996), and extended by additional creep and shrinkage terms, has been applied: It contains a strain-hardening Drucker-Prager loading surface with a time dependent hardening parameter in the compressive regime. Cracking of maturing sprayed concrete is accounted for in the framework of the smeared crack concept by means of three Rankine failure surfaces, perpendicular to the axes of principal stresses. The increase of elastic stiffness during hydration of sprayed concrete as well as the time-dependent increase of compressive strength, tensile strength, and yield surface are all considered.

The original Meschke-Mang-model describes creep effects with one single parameter, the viscosity. In the course of a research project the model has been adapted to experimental results by additional creep terms. Details of the model can be found in Walter (1997). The material parameters for sprayed concrete have been chosen in a way to match the time-dependent properties of sprayed concrete type SpC 25(56)/J2 (ÖVBB 2003). Different amounts of creep have been specified in the course of a parameter study. The values chosen for the analysis yield a relatively small amount of creep strains and little stress reduction due to creep. Thus, a conservative stress level is achieved.

The chosen material parameters for the described analyses have been described more in detail in Walter (2006).

3.2 Excavation sequence, discretisation in time

The excavation of the tunnels is modelled by removal of the finite elements representing the excavated soil. In order to keep the size of the model at a reasonable level two rounds, with a length of 1 m each, of the real excavation scheme have been combined to one fictitious round. In general, only one layer of finite elements has been used to simulate such a fictitious round. The size of the time steps in the analyses has been chosen as one time step per round, the size of one time step being 24 hours.

Sprayed concrete support is applied by stress-free activation of the shell elements simulating the newly added lining. It has been assumed that every newly excavated fictitious round is without sprayed concrete support and that the time of 24 hours is used just for excavation and mucking. The second round behind the face already contains sprayed concrete support. The sprayed concrete age at the end of this second round has been set to 18 hours, i.e. the hardening of the sprayed concrete starts 6 hours after the end of excavation and mucking. These assumptions result in a very conservative estimate of the deformations and the strength of the sprayed concrete support.

Perfect bond between soil and lining as well as between older and newer parts of the lining has been assumed.

Other means of support, like jet grouting, forepoling rods, lattice girders or temporary support of the face, have been neglected in the analyses.

3.3 Ultimate limit state design

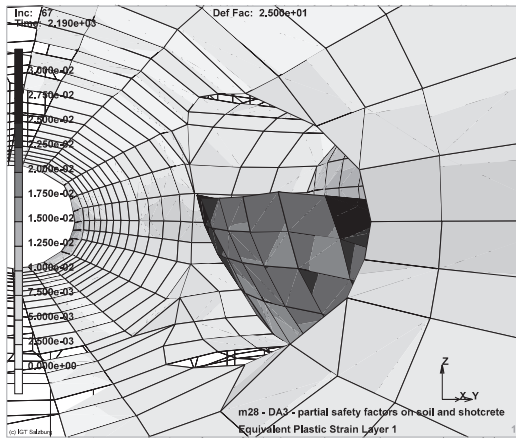
Considering design approaches DA1-2 (in this case equal to DA3) and DA1-1*, for the ULS-design of the metro station the following two sets of partial safety factors have been applied.

Both analyses showed convergence for all time steps investigated. On the following figures typical

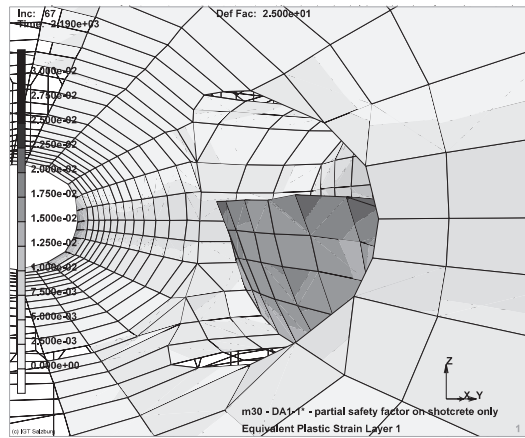
Table 2. Safety factors for the analyses.

Partial safety factor for	Analysis 1 (DA1-2, DA3)	Analysis2 (DA1-2, DA3)
Permanent actions	1.0	1.0
Soil strength parameters	1.25	1.0
Shotcrete strength Parameters	1.5	1.5*1.35≈2.0

results can be compared (more details can be found in Walter 2006): Figures 2a and 2b show equivalent plastic strains in the soil after a few rounds of excavation of the connection tunnel. The displacements are amplified by a factor of 25, the sprayed concrete lining is not displayed. Analysis 1 shows more pronounced displacements of the free surfaces at the face and larger plastic strains of the soil than analysis 2, as had to be expected. The face of the bench is less confined than the face of the top heading which results in larger deformations and plastic strains. Figures 3a and 3b

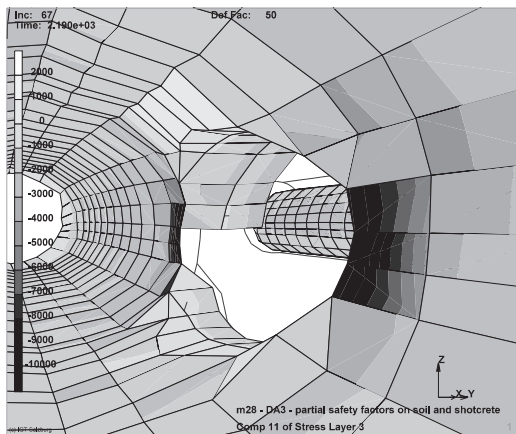


(a)

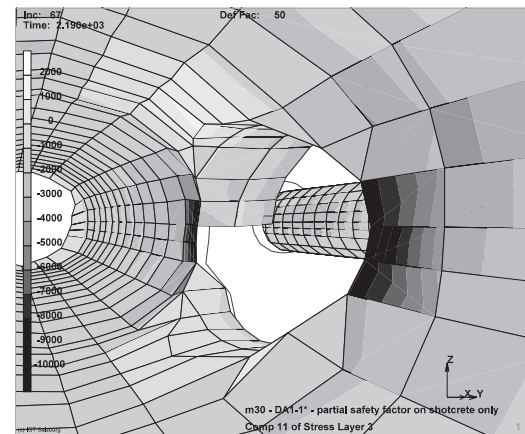


(b)

Figure 2. (a) DA1-2 and DA3: Equivalent plastic strains in the soil. Displacements of the soil. (b) DA1-1*: Equivalent plastic strains in the soil. Displacements of the soil.



(a)



(b)

Figure 3. (a) DA1-2 and DA3: Normal stresses in circumferential direction in the middle layer of the lining. Displacements of the lining. (b) DA1-1*: Normal stresses in circumferential direction in the middle layer of the lining. Displacements of the lining.

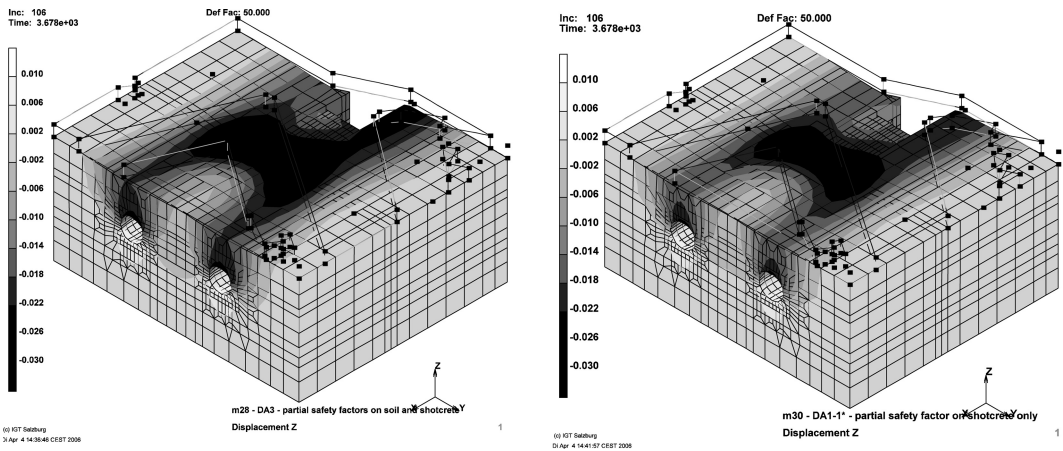


Figure 4. (a) DA1-2 and DA3: Vertical displacements at the end of excavation. (b) DA1-1*: Vertical displacements at the end of excavation.

show, for the same viewpoint and the same stage of excavation, the normal stresses in circumferential direction of the middle layer of the sprayed concrete lining. At the corners of the intersection, the relatively old and stiff sprayed concrete lining has to carry a considerable amount of additional loads due to the excavation of the connection tunnel. Comparison of the two analyses shows that in analysis 2 the sectional forces in the sprayed concrete lining are limited to smaller values than in analysis 1.

The overall stiffness is more influenced by the soil properties than by the sprayed concrete properties: The surface settlements after the end of excavation, depicted in figures 4a and 4b, show a considerably softer behaviour for the analysis with parameters according to DA1-2 and DA3 than with the second analysis matching DA1-1*.

4 SUMMARY AND CONCLUSIONS

It has been shown at the example of cyclic tunnel excavation that numerical simulation using nonlinear constitutive models for soil and retaining structure can be applied for an ultimate limit state design in the sense of Eurocode 7 (EN 1997-1). Care has to be taken in applying constitutive models which limit the stress level to values bearable by the material and therefore allow an “implicit design”: DA1-2 and DA3 (which are equal in the case of retaining structures) appear to be most appropriate for this type of analysis. DA1-1* can be useful if comparisons with the safety concept with global safety factors are requested or if the ultimate limit state is dominated by failure of the retaining structure and not by failure of the soil. In connection with an implicit design, instead of augmenting the effects of actions the strength parameters of the

retaining structure have to be reduced by a larger amount. DA2* contains safety margins on ground resistances which are difficult to implement in continuum models.

As an example, the construction of a metro station in soft soil has been investigated. Two analyses, one applying the partial safety factors of DA3, and one applying DA1-1*, have been compared. In both cases, convergence has been achieved in all analysis steps investigated. The overall behaviour of the structure is more governed by the soil than by the sprayed concrete. At tunnel intersections the stresses in the lining locally reach the specified strength limits and cause stress redistribution.

ACKNOWLEDGEMENTS

The analyses dealt with here were performed on behalf of the Vienna Transport Authorities (“Wiener Linien”) who kindly permitted to publish the results.

REFERENCES

- CEN 2004a. *EN 1997-1:2004 Eurocode 7: Geotechnical design – Part 1: general rules*; Brussels: European Committee for Standardisation.
- CEN 2004b. *EN 1992-1-1:2004 Eurocode 2: design of concrete structures – Part 1: General rules and rules for buildings*; Brussels: European Committee for Standardisation.
- DIN 2005. *DIN 1054:2005 Baugrund – Sicherheitsnachweise im Erd- und Grundbau*. Berlin: Normen.
- Frank, R. et al. 2004. *Designer’s Guide to EN 1997-1, Eurocode 7: Geotechnical design Part 1: General rules*. London: Thomas Telford.
- FVS 2004 (ed.). *RVS 9.32 Statisch-konstruktive Richtlinie: Geschlossene Bauweise im Lockergestein unter Behauung*,

- Vienna: Forschungsgesellschaft für das Verkehrs- und Straßenwesen.
- Meschke, G. 1996. Consideration of Ageing of Shotcrete in the Context of a 3-D Viscoplastic Material Model. *Int. Journal for Numerical Methods in Engineering* 39, 3123–3143.
- Meschke, G., Kropik, C. & Mang, H.A. 1996. Numerical Analyses of Tunnel Linings by Means of a Viscoplastic Material Model for Shotcrete. *Int. Journal for Numerical Methods in Engineering* 39, 3145–3162.
- ÖVBB 2003. *Richtlinie Spritzbeton, Anwendung und Prüfung*. Vienna: Österreichische Vereinigung für Betonbau und Bautechnik.
- Schuppener, B. & Vogt, N. 2005. Favourable and unfavourable actions in the verification of bearing capacity of footings. In *Proceedings of International Workshop on Evaluation of Eurocode 7*, Dublin: Trinity College.
- Schweiger, H.F. 2005. Application of FEM to ULS design (Eurocodes) in surface and near surface geotechnical structures. In *International Conference on Computer Methods and Advances in Geomechanics 2005*, 419–430.
- Walter, H. 1997. Application of a new shotcrete model in a 3-D-FE-analysis of a tunnel excavation. In S. Pietruszczak, G.N. Pande (eds.), *Numerical Models in Geomechanics, NUMOG 6; Proc. 6th intern. Symp. Montreal 2–4 July 1997*. Rotterdam: Balkema.
- Walter, H. 2006. Design of the primary support of an NATM excavation based on a nonlinear 3-D-FE-model. *Felsbau* 2, 2006, in print.
- Wiener Linien 2002. *U-Bahn-Linie U2. Bauabschnitt U2/2. Ausschreibungsunterlagen*. Vienna.

Numerical investigation of the failure of a shotcrete lining

R. Pöttler

ILF Consulting Engineers, Rum/Innsbruck, Austria

ABSTRACT: In the course of a 7-km-long railway tunnel, which is situated mainly in weathered chalk marl, covered by Tertiary over a length of about 500 m, the tunnel traverses a transition zone of chalk marl, weathered chalk marl and Tertiary. In a specific area with a length of 100 m, the deformation during tunnel drive did not cease and exceeded the predicted values considerably. About one year after the installation of the primary lining, cracks occurred in the shotcrete lining of the invert. Many different geotechnical models have been discussed to explain this special ground behaviour and the failure. Numerical calculations based on extensive geotechnical investigations were performed, aiming at detecting the cause of this failure. It was only when the real ground behaviour and reasons of failure had been understood that the secondary lining could be designed in an optimised way.

1 PROJECT

The tunnel is constructed according to NATM principles. Excavation of heading is followed by excavation of bench and invert. Between shotcrete lining and cast-in place inner lining a waterproofing membrane is installed. A drainage system will prevent any water pressure from acting on the lining. The inner lining has to take over the loads resulting from the traffic in the tunnel, the loads of the electrical–mechanical installations of tunnel and of the deterioration of shotcrete, as well as the loads of the primary shotcrete lining and of the anchors which will corrode with time.

In the area discussed, the tunnel is situated in the transition zone of Tertiary (TER) and weathered rock mass (RM) of chalk marl. The interface was predicted to be monotonous, both in longitudinal and transverse direction. Numerical analyses for verifying the stability of the tunnel were done prior to the construction based on the geotechnical report. The geotechnical parameters were verified and improved by back analyses. The main input parameters, for the finite element calculations, modulus of elasticity E , and the undrained parameters cohesion c_u and angle of friction φ_u could be determined quite well. Supervision of the tunnel drive was done by comparing and interpreting the geotechnical measurements on site with the calculated displacements.

2 EXCAVATION OF HEADING, BENCH AND INVERT

In the area discussed the overburden is about 25 m thick. According to the prognosis, the foundation of the

shotcrete lining of the heading was situated on rock mass. The FE model used for calculation is shown in Figure 1. The material law of Tertiary and of the rock mass is Drucker Prager. Input parameters are listed in Table 1. Differentiation in the chalk marl (TER1 to

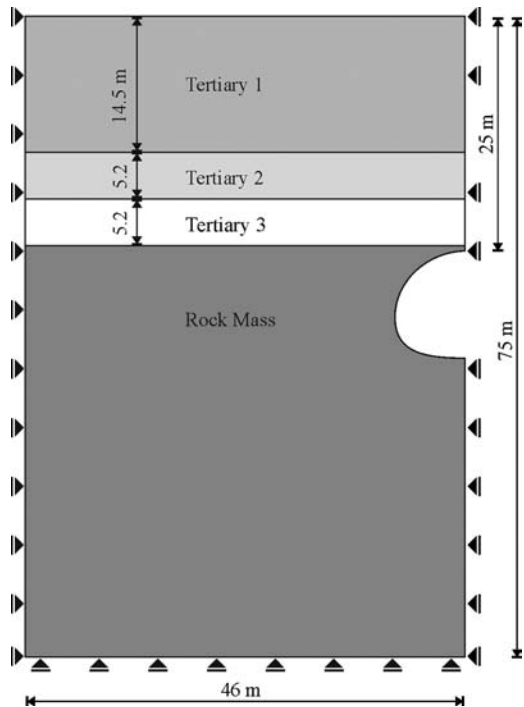


Figure 1. Numerical model for FE calculation.

Table 1. Geotechnical parameters for numerical analyses prior to excavation.

	E Load [MN/m ²]	E Unload [MN/m ²]	c_u [MN/m ²]	φ_u [°]	γ [MN/m ³]
TER1	6	18	0.010	25	0.020
TER2	16	48	0.015	25	0.021
TER3	80	240	0.015	25	0.021
RM	100	200	0.100	30	0.022

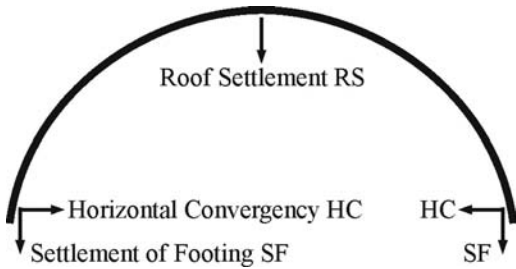


Figure 2. Observation of displacements.

TER3) takes into account that the weathering of rock mass nearer to the surface was expected to be higher.

The thickness of the shotcrete lining was 280 mm. In addition to the lattice girders, anchors with a length of 6 m spaced every 2 m × 2 m were installed. For the excavation of the heading the following ranges of displacements were calculated (Figure 2):

- Roof settlement (RS) 45 mm–50 mm
- Horizontal convergency (HC) 10 mm
- Settlement of footing (SF) 25 mm–30 mm

As there was no prognosis on long-term behaviour of the ground it was expected that displacements due to tunnel drive would cease 1–2 diameters behind the face. The normal force in the shotcrete lining was 2.1 MN/m, resulting in stresses of 3.5 MN/m² in the footing of the lining. Although these stresses are well below the sustainable stresses of the rock mass, additional numerical analyses were performed to investigate the influence of an enlargement of the shotcrete lining at the footing (“elephant footings” – Figure 3) up to 800 mm to reduce the stresses in the footing of the heading. This investigation was done by using the c/φ reduction method. As can be seen from Figure 4 there is only very little influence on the displacements of the lining. The x-axis shows the reduction factor (η), the y-axis shows the roof settlements. Figure 4 also shows that the factor of safety η , which can be calculated

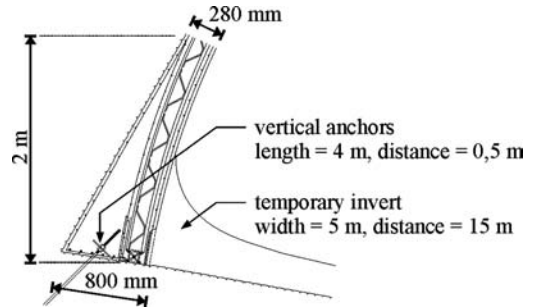


Figure 3. Additional support measures (elephant footing, vertical anchors).

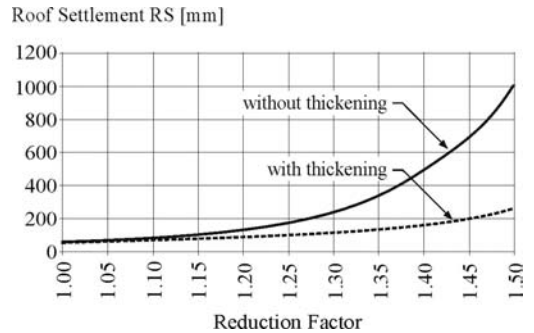


Figure 4. Result of c/φ reduction.

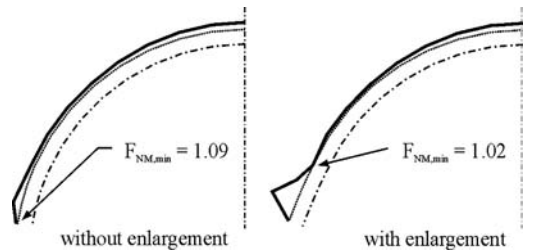


Figure 5. Calculated and measured roof settlement (RS).

$$\eta = \frac{\tan \varphi}{\tan \varphi - red} = \frac{c}{c - red}$$

is well over the required factor of safety according to the relevant standard. The difference of the partial factor of safety in the shotcrete lining F_{NM} (Pöttler 1992) with and without enlargement of the lining was less than 5% (Figure 5), F_{NM} being the factor of sustainable normal force and normal force. The sustainable normal force is calculated taking account of the bending moment and the shotcrete strength divided by the factor of safety according to the relevant standards (DIN 1045). Thus in case F_{NM} is higher than 1.00, there is a safety margin.

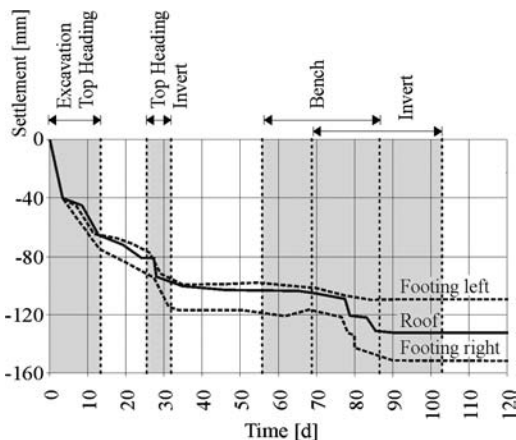


Figure 6. Measured displacements.

Table 2. Geotechnical parameters for adopted numerical analyses.

	E Load [MN/m ²]	E Unload [MN/m ²]	c_u [MN/m ²]	φ_u [°]	γ [MN/m ³]
TER1	6	18	0.010	25	0.020
TER2	16	48	0.015	25	0.021
TER3	80	240	0.015	25	0.021
RM	50	100	0.030	25	0.022

Enlargement of the shotcrete lining has only minor influence on the stress-strain behaviour of the tunnel. The same investigation was done for the placement of additional vertical anchors at the footing. This additional support measure also had no major influence on the overall stability of the heading. Therefore there was no reason to carry out both support measures from an engineering point of view.

In the course of the tunnel driving, the measured displacements became bigger than the calculated displacements (Figure 6). This was mainly because the transition zone of Tertiary and rock mass was located lower than in the prognosis. Numerical analyses with reduced values for the geotechnical parameters (Table 2) resulted in higher allowable displacements. No differentiation between RM1 and RM2 was done in the numerical model.

For the excavation of the heading the following ranges of displacements were calculated:

- Roof settlement (RS) 75 mm–85 mm
- Horizontal convergence (HC) –10 mm–60 mm
(- .. divergence)
- Settlement of footing (SF) 65 mm–80 mm

It was assumed that the displacements would cease 1–2 diameters behind the face. But the results of the measurements showed no abatement of displacements

at that distance (Figure 6). As the geotechnical parameters of the weathered rock mass have been assumed to be almost the same as for the Tertiary, from a geotechnical point of view the ground behaviour could not be explained. Additional support measures had to be installed based on engineering judgement to prevent a collapse of the tunnel. In a 1st step these consisted of enlarging the shotcrete lining at the footing, in a 2nd step of installing vertical anchors at the basement and in a 3rd step a temporary invert of the heading, 5 m wide and at a distance of 15 m. The 1st and 2nd step did not have any influence on the deformation behaviour of the heading. Thus the numerical investigations done at the beginning, showing no major influence of these support measures, have been proved. Deformations only ceased after installing, in the relevant section, a temporary invert arch in a 3rd step. Excavation of bench and invert had to be done close to the excavation of the heading. Also, in the invert a shotcrete lining with a thickness of 250 mm was installed.

3 STOP OF CONSTRUCTION WORK – ADDITIONAL GROUND INVESTIGATIONS

After the shotcrete invert had been placed, the work on site was stopped for about 1.5 years. During this time additional ground investigations were performed. As the tunnel was situated in karst, geological anomalies due to karst phenomena located in the vicinity of the tunnel had to be detected, which may have an influence on the permanent stability and serviceability of tunnel for a service life of 100 years. These investigation were done by geophysical measurements and drilling in an area of about 15 m around the tunnel (Pöttler 2004).

Using these investigations, it was possible to generate a realistic geological 3D model. The 3D model of the area under discussion is shown in Figure 7. A major discrepancy between the geological model in the prognosis stage and reality is evident. A main discrepancy is that the weathered rock mass is not situated in the area of the heading but under the invert. The surface of the weathered rock mass is quite irregular both in longitudinal and transversal direction.

4 UNPREDICTED EVENT

During this period of no construction, regular inspections of the shotcrete lining were undertaken by the site management. One year after the construction works had been stopped, cracks appeared in the invert lining and additional settlements occurred (Figure 8). The settlements could only be stopped when the tunnel was partly refilled with material and wooden columns placed to support the shotcrete lining of the heading.

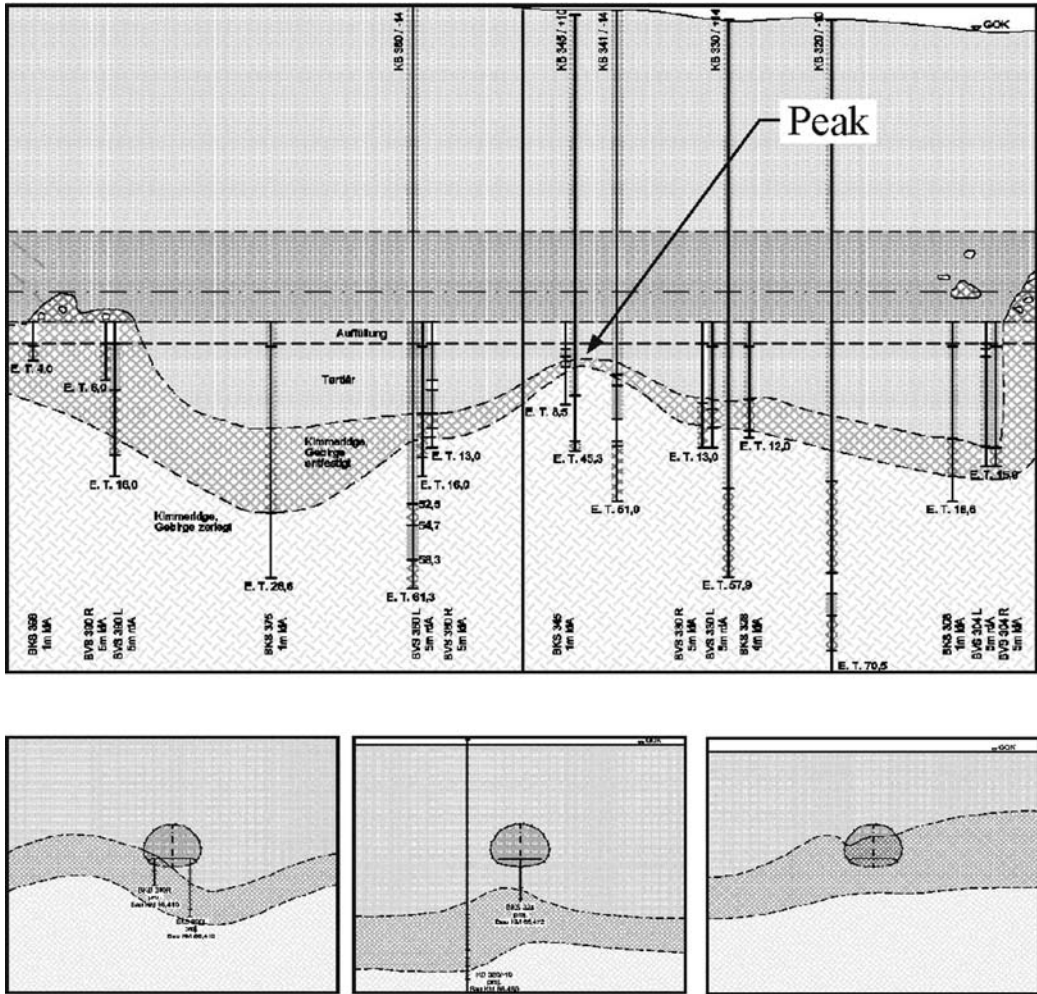


Figure 7. Geological situation in reality.

Due to the large settlements of up to 150 mm, the tunnel lining had to be reconstructed to provide enough space for installing the inner lining. Additional drilling had been performed to get even more information on the ground in this area. The main questions to be answered were:

- What is the reason for the unpredicted restart of movements?
- What is the realistic load on the inner lining caused by shotcrete deterioration?

Different scenarios to explain the behaviour of the tunnel have been discussed:

Scenario 1: Change of location of geological strata: The tunnel is situated in Tertiary and the weathered rock mass is about 10m below the invert. The same

geotechnical parameters as listed in Table 2 have been used for the numerical analyses. Taking account of the excavation sequence, the numerical analyses yielded the same results in terms of displacements which were measured (Table 3), therefore it could be assumed that the ground behaviour and the excavation process were modelled realistically.

But the numerical analyses showed no failure of the shotcrete lining in the invert section. The stresses in the shotcrete lining were considerably lower than the sustainable stresses. The actual location of the geological strata differed from the prognosis, but this could not be the reason for the unpredicted event.

Scenario 2: Influence of rock “peak”: As can be seen from Figure 4, the weathered rock mass forms a peak in the vicinity of the area where the crack in the

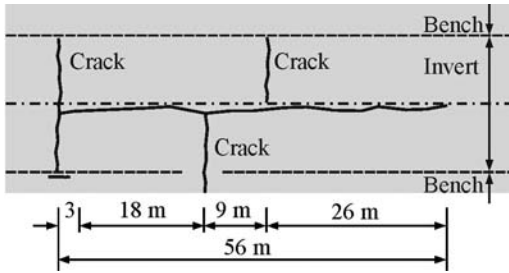


Figure 8. Cracks in the shotcrete lining of the invert.

Table 3. Comparison of numerical analyses and geotechnical measurements.

	RS [mm]	HC [mm]	SF [mm]
Numerical analysis	114	75	100
Measurements	125	80	125

shotcrete lining appeared. This geological situation was also analysed, assuming a great difference in the stiffness behaviour between Tertiary and rock mass. The modulus of elasticity of the rock mass was assumed to be 300 MN/m^2 . The influence of this rock “peak” on the stresses in the shotcrete lining was minor. No failure of shotcrete lining occurs.

Scenario 3: Influence of the rock “peak” and additional weathering of ground in the invert. It is assumed that the Tertiary under the shotcrete lining of the invert weathers due to water ingress from inside the tunnel, cohesion decreases to zero and the modulus of elasticity is considerably lower. This scenario is rather unrealistic as no water was in the tunnel and only a small wet zone of Tertiary of about 100 mm was detected when the shotcrete lining in the invert was replaced. The numerical analyses based on this model (Figure 9) showed that a failure of shotcrete lining would occur only if the weathered zone was very large.

Scenario 4: Influence of excavation procedure of the heading: The heading was driven without applying an enlarged footing of the shotcrete lining. Scenario 4 shows that because no enlarged footing was constructed, the amount of vertical displacement of the heading was so great that a loosening of the Tertiary at the crown occurred, resulting in the total load of overburden resting on the lining. The geotechnical parameters of the Tertiary have been proved and the numerical analyses based on these parameters made it possible to model the overall behaviour very realistically. These numerical analyses also showed that the influence of an enlargement of the footing of the lining has only minor influence on the behaviour and on the factor of

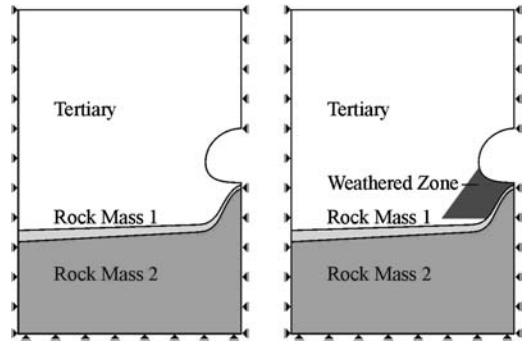


Figure 9. Numerical model for FE calculations.

safety. This was in addition proved by geotechnical measurements.

Scenario 5: Long-term behaviour of rock mass: The geological formation of the Tertiary and Chalk Marl does not show any aspects of creeping or swelling. The tunnel is situated well above the permanent groundwater level. No change in groundwater conditions occurred in the relevant period.

Scenario 6: Pore water pressure: The change of stresses and strains due to the excavation process also changes the pore water pressure and thus the effective stresses of the ground. In case of low permeability this process takes a long time. The permeability of the Tertiary is high so that this process, even if it had occurred, would have taken only a few days. From this point of view, the change of pore water pressure as the reason for the unpredicted event can be excluded.

Twelve different possible scenarios with different numerical methods and models were investigated to ascertain the reason for the failure and thus to be able to answer the two questions above in a satisfactory manner. Some of these scenarios are more unrealistic than the one described, such as heave of the tunnel due to groundwater and change of temperature. But every scenario that was brought up by an involved expert was discussed. None of the investigated twelve geotechnical models could answer the question in a satisfactory manner.

In summary, the discussion and investigation showed that a reason for the unpredicted event could not be identified, not even after a lot of additional numerical analyses and additional ground investigations. The dimensioning of the inner lining was therefore done in a very conservative way. The lining was designed so that it could sustain the entire loads of the overburden. The thickness of the lining is 550 mm, concrete grade B45 (DIN 1045) and reinforced by $23.2 \text{ cm}^2/\text{m}$ on both sides.

5 CONCLUSION

The prognosis of the geological situation was done based on the well-known geological mapping and additional drillings spaced every 500 m over the course of the tunnel. After problems as described appear, “experts” may state that a greater number of ground investigations have to be carried out before tunnel driving. It goes without saying that the better the ground investigations are before the construction starts, the lower the risk of an unpredicted event. The amount and quality of ground investigation representing the state of the art is found in the relevant standards. But even if the standard is met, like in the described case study, unpredicted events may occur. In this case study, the reason for the unpredicted event could not be defined in a proper way, although a far greater number of ground investigations were performed than ever done in a tunnelling project and although the geological situation was well known.

As numerical analyses were used to a great extent, and as there was time for a lot of discussion and meetings after the completion of the tunnel, at the end of

the process one had to become aware that, for the present, the limit of understanding and numerical modelling has been reached. It becomes evident that tunnelling in such ground conditions can be done only by an experienced team. The numerical analyses are helpful but not the only tool for success.

There was no complete collapse of the tunnel and no loss of life. This section of the tunnel was expensive, but all in all economic with regard to other possible and realistic scenarios. This was thanks to the proper work done on site by the client, construction company, site supervision and designer.

REFERENCES

- Pöttler, R. 1992. Die Standsicherheitsuntersuchung für die Kaverne der englischen Überleitstelle im Kanaltunnel. *Bautechnik* 69: 602–617.
- Pöttler, R. 2004. Die Beherrschung der Karst- und Erdfallproblematik bei Tunnelbauwerken. *Veröffentlichung des Instituts für Geotechnik der Technischen Universität Bergakademie Freiberg*. Freiberg.

Three-dimensional modelling for the widening of existing tunnels

G. Altamura & S. Miliziano

Dept. of Structural and Geotechnical Engineering, University of Roma “La Sapienza”, Italy

ABSTRACT: This paper presents the results of a number of three-dimensional numerical analyses regarding the simulation of the widening of existing tunnels using the pre-cutting technique. This technique consists in the construction, ahead of the generic tunnel face section to be widened, of a fibro-reinforced shotcrete shell, by filling up an opening which has been previously cut by a specifically designed machine. The shell is thus placed in advance, as a temporary lining, and it is completed before the tunnel widening excavation begins. Three-dimensional numerical analyses have been carried out to study the problem; different soil properties and two different modalities for carrying out the pre-cut, and its subsequent filling with shotcrete, have been considered. In the paper, the results of the analyses are presented in terms of evolution of the displacement fields during the widening excavation stages, highlighting the effects produced by the two different methods for the construction of the shotcrete shell.

1 INTRODUCTION

Increasing the capacity of motorways requires the widening of the existing tunnels. In general it is important to keep the roads in operation during the works, protecting the traffic. For soil with poor mechanical properties, in order to ensure the stability of the cavity, ground improvement in advance is required, ahead of the face, before the widening excavation starts. To this aim, a protective fibro-reinforced concrete shell – realized by filling an opening (the pre-cut) previously cut by a specifically designed machine – is placed ahead of the generic tunnel face section to be widened. An example of tunnel excavation adopting the pre-cutting technique is the construction of Baldo degli Ubaldi Station of the Rome Underground (Lunardi & Focaracci, 1998). Another example is the widening of the Nazzano tunnels on the Milan-Naples A1 highway in which case the works were carried out while maintaining the traffic load (Lunardi & Focaracci, 2003). The aim of this paper is to investigate the evolution of the stress-strain field around the wider tunnel during the construction stages associated with the pre-cutting technique. Three-dimensional (3D) numerical analyses were carried out to study the problem; in fact, 3D analyses are more appropriate in modelling tunnel excavation (Miliziano & Soccodato, 2003) and, in particular, tunnel widening by pre-cutting.

Different soil properties and two different modalities of realizing the pre-cutting and its subsequent filling with shotcrete were considered. Numerical analyses were also carried out by progressively reducing the cohesive strength of the soil, in order to evaluate, for

each of the two pre-cutting modalities, the minimum value of the cohesive strength which ensures stability.

In the following, the main construction stages which are necessary to widen a tunnel using the pre-cutting technique are briefly illustrated. After the description of the model used in the numerical analyses (geotechnical model, structural elements properties and simulation of construction steps), the results of the different analyses carried out are presented, compared and discussed with reference to the evolution of the displacement fields during the widening excavation steps.

2 THE PRE-CUTTING TECHNIQUE

Appropriate protective measures must be designed when construction works are to be carried out while maintaining the traffic load in the tunnel to be widened. A solution may be a steel protection shell placed inside the tunnel (see Fig. 1) which obviously means reducing the width of the lanes. The main steps of the widening process are shown in Figure 2. The first stage involves the realization of the mechanical pre-cut; it consists of a mechanical cut around and above the future permanent lining of the widened tunnel, slightly inclined outwards (Fig. 2a). The pre-cut is filled with fibro-reinforced shotcrete characterized by fast curing time, in order to secure good stiffness and strength properties in a short time (Fig. 2b). The soil is excavated and then the lining of pre-existing tunnel is removed (Fig. 2c). The last step of the construction cycle, before starting with a new pre-cut, is the erection of the permanent lining of the new tunnel (Fig. 2d).

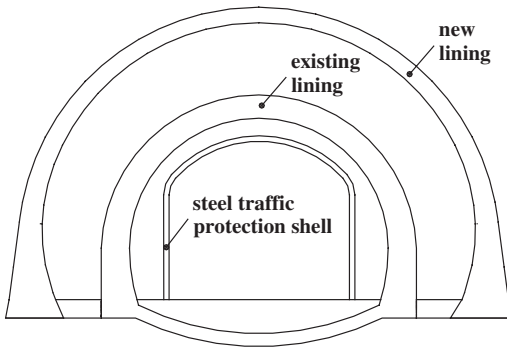


Figure 1. Cross section of the tunnel during widening.

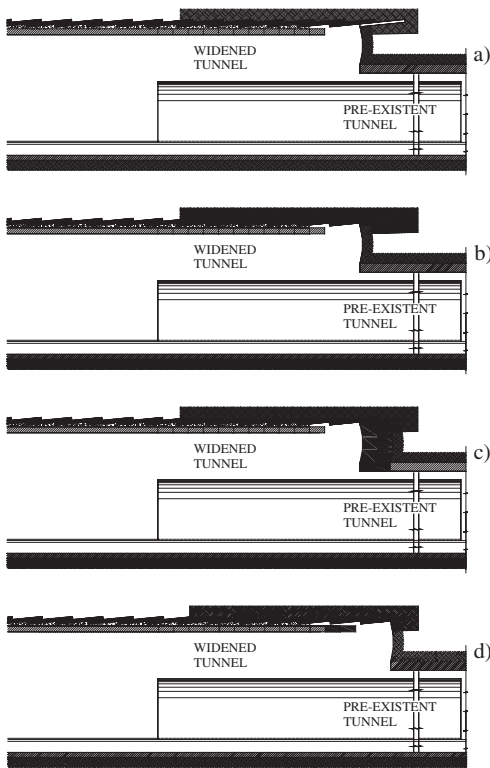


Figure 2. Main construction steps of widening.

The realization of a fibro-reinforced shotcrete shell is possible by filling up the whole pre-cut when the soils have appropriate mechanical properties (cohesion). Instead, in the presence of soils with poor mechanical strength (low cohesion), the shotcrete shell can be realized by progressively filling continuous but small openings which have been previously cut. When a single

tunnel is present, the construction of the new invert requires closing the tunnel to traffic for a short time. Instead, in the case of the widening of two twin tunnels, the widening works can be designed so as to guarantee the traffic flow in one of the two tunnels. Furthermore, depending on the geotechnical conditions, it may not be necessary to construct a new invert for the widened tunnel; in this case only a structural link between the final lining of the widened tunnel and the existing invert may be realized.

3 NUMERICAL MODEL AND ANALYSES

Finite difference numerical analyses of the widening of one of two twin tunnels were carried out using a commercial code, *FLAC^{3D}* (ITASCA, 2002). Figure 3 shows the mesh adopted to carry out the analyses. The transverse dimension of the mesh is 15 times the existing tunnel width, or 10 times the width of the widened tunnel. Preliminary numerical analyses were carried out to select the best longitudinal dimension of the mesh, which is the minimum size for which the effects of a perturbation at the boundaries of the excavation do not produce appreciable stress-strain effects on the reference (central) section. In the studied case there are two twin tunnels whose axes 24 m apart. The existing tunnels are about 12 m wide, and the widening consists in the excavation of about 3.5 m of soil around the tunnels, thus producing a final width of about 20 m.

The crown of the widened tunnels is 30 m below ground level. All soils were modelled as being elastic and perfectly plastic with the Mohr Coulomb yield criterion. The final lining is modelled with shell elements, glued to the mesh without interfaces. Prior to the widening stages, the construction of the existing tunnels was simulated by the following steps: removing the corresponding soil elements for an excavation length of 2 m, reaching equilibrium, and then installing the lining using shell elements. The two existing tunnels were excavated in succession. During the widening process (Fig. 4), the pre-cut was simulated by removing the corresponding soil elements (4 m long and 0.30 m thick). The construction of the fibro-reinforced shotcrete shell was modelled by activating the previously removed elements (during the pre-cutting stage). For the shotcrete shell, an elastic model was adopted, with an initial reduced stiffness. During the subsequent advancement of the widening (i.e., the next calculation cycle), the stiffness value corresponding to the final curing time was assigned to this section of the shotcrete shell (see Tab. 1).

The geometry of the pre-cut was modelled without the slight inclination in order to simplify the mesh, without however any major influence on the results (cf. Fig. 4 vs Fig. 2). The shotcrete shell was modelled as a longitudinal continuum. The widening of the tunnel

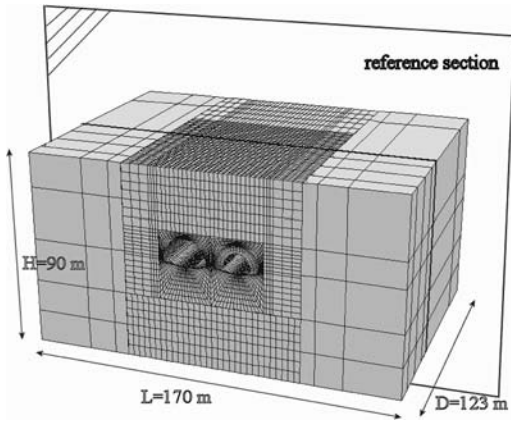


Figure 3. Mesh used in the analyses.

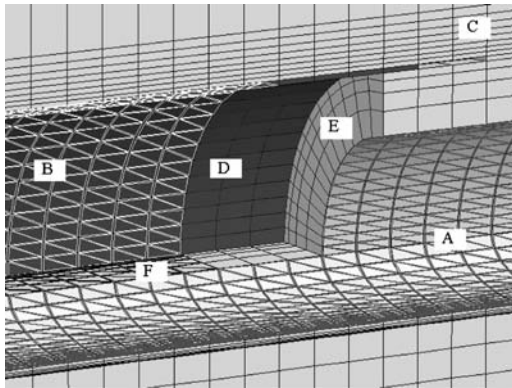


Figure 4. Widened tunnel during the pre-cutting phase; A: existing lining; B: new lining; C: pre-cutting, D: fibro-reinforced shotcrete shell.

Table 1. Properties of the soil and structural elements.

	Soil	Existing tunnel lining	Widened tunnel lining	Fibro-reinforced shotcrete	Link new lining-old invert
γ (kN/m ³)	20	24	25	24	24
E (MPa)	400	28500	33600	33600	22000
ν	0.2	0.2	0.2	0.2	0.2
φ (°)	36	–	–	–	–
c (kPa)	12–40	–	–	–	–
Model	Elasto-plastic	Elastic	Elastic	Elastic	Elastic
Thickness (m)	–	0.8 m	0.6 m	0.3 m	0.4 m

was modelled by removing the corresponding soil elements between shotcrete shell and existing lining shell, and then by deleting the existing lining. An excavation step consists of a 2 m advancement of the widening. The permanent lining is linked to the existing

invert by shell elements (Fig. 4). The widening simulation and the above described geometry were adopted in three different analyses. The first run was characterized by a soil cohesion of 40 kPa and the pre-cut stage was modelled by removing all corresponding soil elements at the same time. In the second run a lower cohesion value (12 kPa) was adopted. In the third run, with soil cohesion being maintained equal to 12 kPa, the pre-cut was modelled by removing the corresponding elements in successive steps. The simulation consists in removing approximately 2 m elements at a time, reintroducing them as an elastic medium, and then proceeding with the next approximately 2 m stretch until the entire shell is completed.

Table 1 summarises the main physical and mechanical properties that were adopted in the analyses.

4 RESULTS AND DISCUSSION

Figure 5 presents the settlements along three vertical lines located in the reference section, for four positions of the front of the excavation widening. Two vertical lines are located very close to the widened section of the tunnel, 2 m away from the extrados of the new lining; the third vertical line is located at the tunnel axis, above the crown. Results refer to the analysis with $c = 40$ kPa and the pre-cut realized in a single step (reference analysis).

Above the axis of the tunnel, the settlements are very small before the passage of the excavation front; then, the amount of settlements rapidly increases. At the end of the widening process, when the position of the excavation front is far away from the reference section, the settlements range from 22 mm to 13 mm, respectively near the crown and at the surface. Similar features may be observed for settlements at the edge of the tunnel; the maximum value is about 12 mm, at the crown. Settlements became negative (heave) with a maximum value of about 7 mm reached at about 10 m below the invert. Also in this case, the amount of displacements increases as the excavation proceeds. Due to the presence of the second tunnel located very close to the tunnel to be widened, results are not perfectly symmetrical. Settlement contours and displacement vectors are reported in Figure 6 at the end of the pre-cut, before filling with spritz beton. The displacements are essentially vertical; appreciable horizontal displacements are observed only near the pre-cut in the transverse section; therefore, no appreciable extrusion phenomena are observed. Heaves of the same order of magnitude as the settlements develop below the invert (see Fig. 6a). Similar results are reported in Figure 7 in the reference section when the front of the excavation is far away: displacements are essentially vertical and heaves at the invert are similar in magnitude to the settlements at the crown.

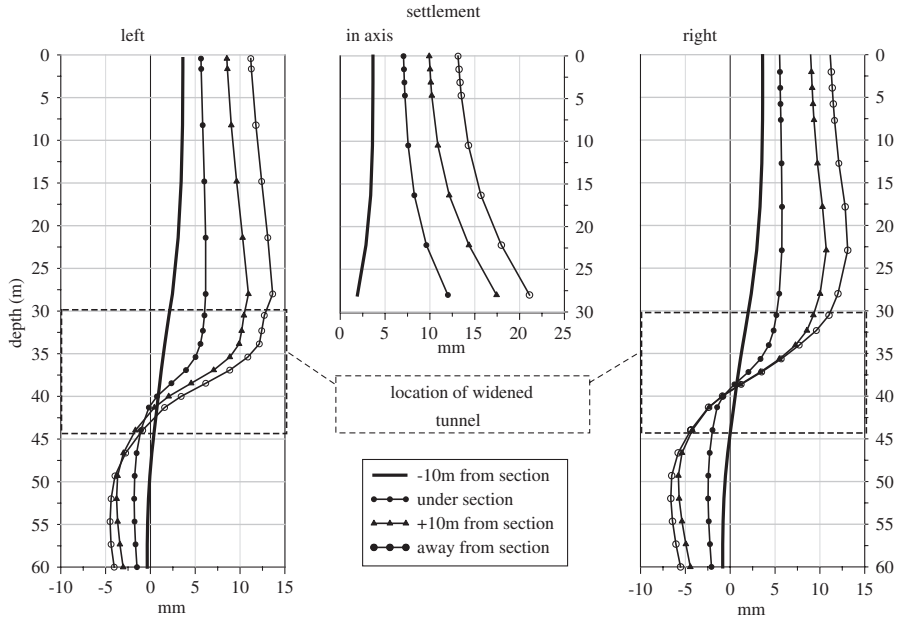


Figure 5. Settlement during excavation along three vertical lines placed around the widened tunnel.

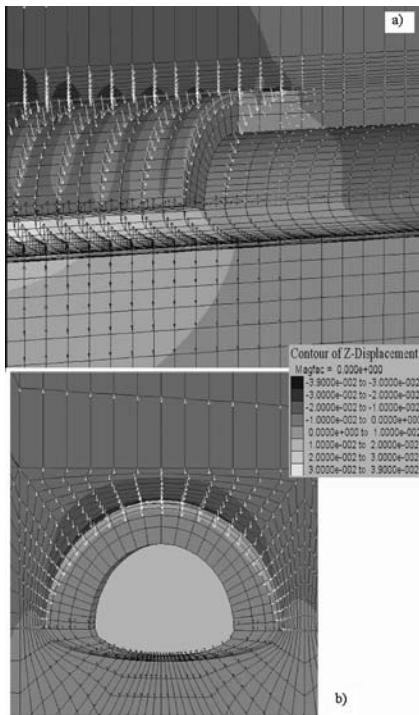


Figure 6. Settlement contours and displacement vectors on a longitudinal section (a) and on a transverse section (b) after pre-cutting.

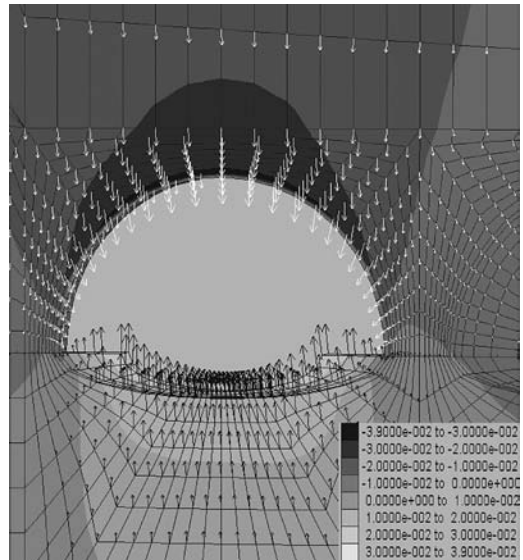


Figure 7. Settlement contours and displacement vectors on a transverse section when the widening is far away.

As soil strength decreases (cohesion from 40 kPa to 12 kPa), displacements increase; performing the pre-cut in small progressive steps rather than in a single stage appears to be effective in reducing displacements (Fig. 8). The extent of the plastic zone at the end of the construction of the shotcrete shell is reported in Figure 9

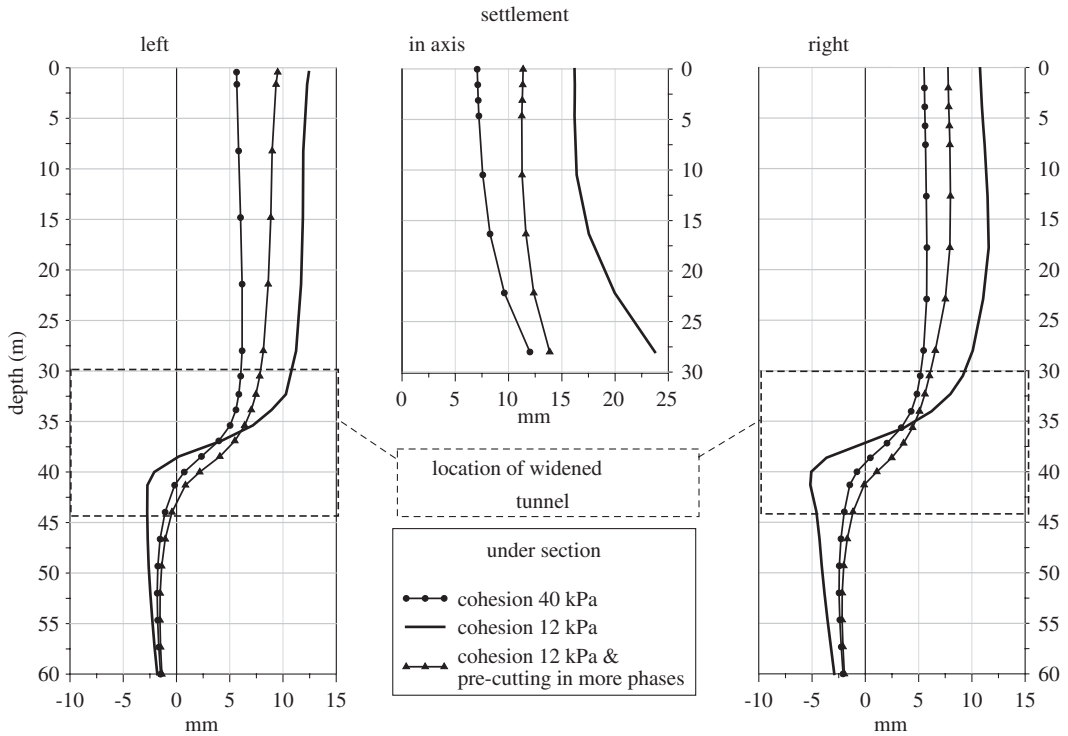


Figure 8. Settlement under reference section along three vertical lines placed around the widened tunnel, for three different simulations.

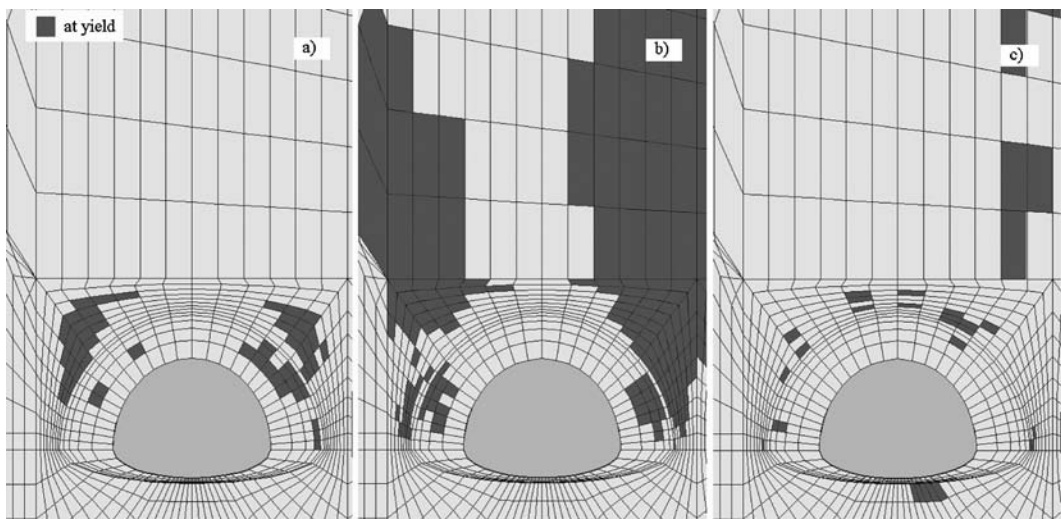


Figure 9. Zones in yield conditions just after simulating the construction of the fibro-reinforced protective shell; (a) $c = 40$ kPa (reference analysis); (b) $c = 12$ kPa; (c) $c = 12$ kPa and stepwise pre-cutting.

for the three different analyses carried out. As expected, the extent of the plastic zone increases as strength decreases; small cohesion associated with the single stage pre-cut (see Fig. 9b) produces two distinct and very large yield zones: conditions very close to collapse are reached and the distribution of plastic zones indicate the mechanism of failure. Progressive step-wise pre-cutting, is effective in limiting the extent of the yield zones (Fig. 9c) and in limiting the displacement field, also (Fig. 8): the maximum settlement at the crown drops from 24 mm to 14 mm (it is almost halved).

In order to evaluate the safety factors against failure (stability), the approach of progressively reducing the soil strength parameters was adopted. In detail, with reference to the two different pre-cutting modalities (pre-cutting the segment in a single stage or in progressive steps), the cohesive component of the strength was progressively reduced until collapse conditions were reached. The results obtained show that for pre-cutting in a single stage, a minimum soil cohesion of 11 kPa is needed; on the other hand, only 5 kPa of cohesion are sufficient to excavate the pre-cut in several steps (for each step, the length of excavation considered is about 2 m).

5 CONCLUDING REMARKS

In order to realistically simulate the construction process of the widening of an existing tunnel, the use of 3D analyses is undoubtedly appropriate. 3D analyses also provide information about the evolution of the state of stress and strain of the soil and of the different structural elements during each stage of the construction process. Furthermore, by progressively reducing the numerical values of the strength parameters of the soil, in a model where the real geometry is satisfactorily reproduced, the 3D analysis is able to furnish a useful estimate of the safety factor against failure and of the geometry of the mechanism at collapse.

Due to the high computational power of personal computers and to the continuous improvement in software interfaces, thanks to which both pre-processing (mesh generation) and post-processing (visualization of the results) operations are more user-friendly nowadays, 3D numerical analyses are being increasingly used in geotechnical engineering practice. For example, for the case presented in this paper, the calculation time was about 300 hours for each analysis using a 2.4 GHz Pentium processor.

With reference to the problem studied, the main conclusions are the following:

- in the widening of existing tunnels using the pre-cutting technique, the most delicate stage of the whole process is the pre-cutting excavation which is critical for stability and, also because induced displacements develop mostly in this stage;
- pre-cutting can be carried out in different steps, by progressively excavating a limited segment which is immediately filled with spritz-beton before excavating the next adjacent segment; this specific method ensures stability also when the excavation is carried out in soils having poor geotechnical properties; due to the significant reduction in the extent of the yield zones, pre-cutting in progressive steps is capable of limiting settlements;
- for the case at hand, in order to carry out the whole pre-cut in one single phase, the minimum soil cohesion is 11 kPa; on the other hand, only 5 kPa of cohesion are sufficient if the pre-cut excavation is carried out in several stages;
- when the mechanical properties of the soil were fairly good (high cohesion, sufficient self-supporting capacity), similar results in terms of displacement fields were obtained independently of the way in which the pre-cut was carried out; in this case, therefore, in order to minimize construction time, pre-cut excavations in a single phase are more convenient;
- displacements are essentially vertical in each construction stage; appreciable horizontal displacements are observed only very close to the tunnel; therefore, no appreciable extrusions are observed.

REFERENCES

- ITASCA Consulting Group (2002). FLAC3D (Fast Lagrangian Analysis of Continua) version 2.1. *User's manuals*. Minneapolis.
- Lunardi P. & Focaracci A. (1998). Design and construction of a station on the Rome Metro. *Tunnels & Tunnelling International*, 27–32.
- Lunardi P. & Focaracci A. (2003). Widening the load at Nazzano. *Tunnels & Tunnelling International*, 16–19.
- Miliziano S. & Soccodato F.M. (2003). Modellazione 2D e 3D di gallerie in ambiente urbano: valutazione del danno indotto sugli edifici in muratura. *XXI Convegno Nazionale di Geotecnica. Opere geotecniche in ambiente urbano*; L'Aquila.

Squeezing effects in the excavation of deep tunnels

D. Sterpi

Department of Structural Engineering, Politecnico of Milano, Milan, Italy

ABSTRACT: Difficult conditions in mechanized tunnelling can be met when the rock mass behaviour is time dependent and the so called squeezing condition develops. In this case, large radial pressures on the tunnel boring machine and on the supports are expected in the short and long term. The results of some finite element analyses, in plane strain and axisymmetric regimes, are here discussed concerning the full face excavation of a deep circular tunnel. An elasto-visco-plastic constitutive model that accounts for tertiary creep has been adopted and calibrated on the basis of laboratory test data. Some comments are drawn on the effects of tertiary creep and on the influence of the tunnel face advance on the closure of the opening and on the stress redistribution around it.

1 INTRODUCTION

The time-dependent behaviour of rocks is among the possible causes leading to difficult conditions in the tunnelling works. At great depth, the large deviatoric stresses induced around the opening during the excavation may lead to the so called squeezing condition (Barla, 1995). When this occurs, non reversible deviatoric strains develop at a constant or increasing rate, often combined with volumetric strains associated to plastic dilatancy. Large convergences and high pressure on the tunnel boring machine and on the supports are then expected in the short and long term (Einstein & Bobet, 1997).

This behaviour usually affects weak and altered rocks, but it can be observed also in hard rock masses at great depth (Dusseault & Fordham, 1993; Ladanyi, 1993; Malan, 2002).

A variety of results has been discussed in the literature, mainly focused on the constitutive models and on their calibration based on laboratory tests, and on numerical analyses (e.g. *Rock Mech. Rock Engng.*, 1996; *Italian Geotech. J.*, 2000).

A common drawback of the constitutive models for creep behaviour of rock masses is the calibration of their mechanical parameters, which would require seldom available data from in situ creep tests. These parameters could be identified through a back analysis, provided that an extensive measurement is made of closure and stress variation around the opening during the tunnelling works (Boiyd et al., 2002; Dalgıç, 2002). An alternative procedure could be to perform an easier laboratory testing, hence to calibrate the intact

rock parameters, and then to empirically relate them to the parameters characterizing the rock mass behaviour.

Here, the excavation process of a deep tunnel in squeezing conditions has been approached by means of the finite element method, aiming at evaluating the role of the tunnel face advance on the tunnel closure and on the stress redistribution around the opening. Two-dimensional analyses have been carried out in axisymmetric and plane strain conditions that concern, respectively, the longitudinal and cross sections of the tunnel.

An elasto-visco-plastic rheological model has been adopted that accounts for the time-dependent effects associated with tertiary creep (Gioda & Cividini, 1996). The parameters have been first calibrated on the basis of laboratory creep tests and then suitably corrected by means of empirical relations and of a measure of the rock mass weathering.

Some comments will be drawn on the contribution of tertiary creep in the prediction of the tunnel closure and on the effects of the advancing tunnel face in the short and long term conditions. A comparison between the results from plane strain and axisymmetric analyses will point out the limits of the plane strain analysis.

2 RHEOLOGICAL MODEL

When a rock sample is subjected to a deviatoric constant stress, time dependent deviatoric strains could develop even at low stress levels.

The nature of these strains depends on the stress applied: below a given threshold, they are fully

reversible and increase with decreasing rate (primary creep). For a stress level that overcomes the threshold, the deviatoric strains assume an irreversible nature (visco-plasticity) and increase with constant (secondary creep) or increasing rate (tertiary creep). The tertiary creep is responsible for the sample delayed failure.

Moving from the basic elasto-plastic constitutive model, consisting of an elastic element for the immediate, reversible, deviatoric and volumetric response and a yield condition $F(\underline{\sigma}) = 0$ for the time-independent failure, for a comprehensive rheological model a viscous component should be added, accounting for the time-dependent response which is deviatoric and only partially reversible (Fig. 1).

The visco-elastic element consists of a deviatoric dashpot and a deviatoric elastic substance, both connected with a plastic slider that imposes the limit $F^{ve}(\underline{\sigma})$ beyond which viscosity occurs. Under a constant stress the visco-elastic strains increase with time with decreasing rate, thus leading to an asymptotic value of strain that depends on the stiffness of the elastic substance. The viscosity of the dashpot governs the decay of the visco-elastic strain rate.

The visco-plastic element is the connection of a dashpot, that can carry only deviatoric stress, and a plastic slider, introducing the visco-plastic limit envelope $F^{vp}(\underline{\sigma}) = 0$. A constant stress exceeding this threshold induces secondary creep, as long as the parameters are constant. The strain rate depends on the value of viscosity and on the portion of deviatoric stress carried by the dashpot.

If a loss of viscosity or a reduction of the stress threshold are applied, the strain rate increases, yielding the tertiary creep phase and the eventual failure. The variation of these mechanical characteristics, between peak and residual values, is governed by the cumulated visco-plastic strains, similarly to what is customarily referred to as softening.

Due to its various features, such a constitutive model turns out to be characterized by a large number of parameters, even in the simplest case of isotropic material.

A simple model (Fig. 2) has been proposed in (Gioda & Cividini, 1996) neglecting the time-independent failure condition $F(\underline{\sigma})$ and the visco-elastic stress threshold $F^{ve}(\underline{\sigma})$.

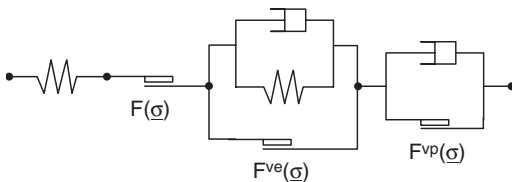


Figure 1. Rheological model accounting for elastic, plastic, visco-elastic and visco-plastic constitutive behaviour.

Figure 2 lists also the mechanical parameters associated with the model. Explicit reference is made to a visco-plastic non-associated envelope of Mohr-Coulomb type by specifying cohesion, friction angle and dilatancy. In the case of tertiary creep, these parameters must be characterized with reference to both peak and residual conditions and the two limit values of visco-plastic strains governing the onset and the completion of the visco-softening must be added to the set of parameters.

The constitutive equations in matrix form can be worked out considering an additive decomposition of the vector collecting the components of the total strain tensor:

$$\underline{\varepsilon} = \underline{\varepsilon}^{el} + \underline{\varepsilon}^{ve} + \underline{\varepsilon}^{vp} \quad (1)$$

The above components represent, respectively, the elastic, visco-elastic and visco-plastic strains, which depend on the applied stresses through the constitutive relations. It is convenient to express them through volumetric and deviatoric components of stress and strain:

$$\underline{\sigma} = \sigma_m \underline{\underline{m}} + \underline{s} \quad (2a)$$

$$\underline{\varepsilon} = \frac{\varepsilon_v}{3} \underline{\underline{m}} + \underline{e} \quad (2b)$$

where the entries of vector $\underline{\underline{m}}$ are equal to 1 or to 0 if they correspond to normal or shear stress. The three elements of the rheological model are described by their constitutive relations:

$$\underline{\sigma} = B^{el} \cdot \underline{\varepsilon}_v^{el} \cdot \underline{\underline{1}} + 2G^{el} \cdot \underline{e}^{el} \quad (3a)$$

$$\underline{s} = 2G^{ve} \cdot \underline{e}^{ve} + \eta^{ve} \cdot \dot{\underline{e}}^{ve} \quad (3b)$$

$$\underline{s}^{vp} = \eta^{vp} \cdot \dot{\underline{e}}^{vp} \quad (3c)$$

where the dot indicates the time derivative and \underline{s}^{vp} is the portion of the deviatoric stress carried by the

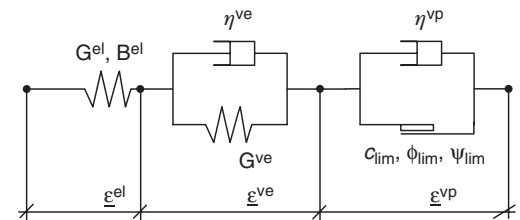


Figure 2. Simplified elasto-visco-plastic model and associated parameters.

visco-plastic dashpot. This can be determined by introducing the total stress carried by the plastic slider $\underline{\sigma}^{vp}$, which includes the entire volumetric stress component and fulfills the visco-plastic limit condition:

$$\underline{s}^{vp} = \underline{\sigma} - \underline{\sigma}^{vp} \quad , \quad (4a)$$

$$\sigma_m^{vp} = \sigma_m \quad , \quad (4b)$$

$$F^{vp}(\underline{\sigma}^{vp}) = 0 \quad . \quad (4c)$$

In addition, the visco-plastic flow rule requires that:

$$\underline{\dot{\epsilon}}^{vp} = \dot{\lambda} \cdot \left. \frac{\partial Q}{\partial \underline{\sigma}} \right|_{\underline{\sigma}^{vp}} \quad , \quad (5)$$

where $Q(\underline{\sigma})$ is the visco-plastic potential function and λ the visco-plastic multiplier. Its expression is readily worked out by substituting Equation (5) into Equation (2b), written for the visco-plastic strain rate, and multiplying by the transpose of vector $\underline{\dot{\epsilon}}^{vp}$:

$$\dot{\lambda} = \frac{(\underline{\dot{\epsilon}}^{vp})^T \cdot \underline{\dot{\epsilon}}^{vp}}{(\underline{\dot{\epsilon}}^{vp})^T \cdot \left. \frac{\partial Q}{\partial \underline{\sigma}} \right|_{\underline{\sigma}^{vp}}} \quad . \quad (7)$$

The finite element formulation of the elasto-visco-plastic problem and the iterative scheme for the time integration procedure is omitted here for sake of brevity (Gioda & Cividini, 1996).

3 IDENTIFICATION OF THE PARAMETERS

The rock mass parameters for the deep tunnel problem were obtained as a suitable correction of parameters calibrated on laboratory uniaxial creep tests on intact rock samples.

In presence of biaxial state of stress, the equations governing primary and secondary creep assume a simple analytical form, thus permitting a straightforward estimation of the associated mechanical parameters. On the contrary, the tertiary creep is defined by parameters that cannot be expressed in analytical form and should be calibrated by trial and error numerical analyses.

The lack of biaxial creep tests, as in the case at hand, forces to introduce some additional hypotheses. Assuming that the intact rock strength is known from standard laboratory testing, the shear strength

parameters, for instance cohesion and friction angle, are given. The ratio R_{CS} between the uniaxial stress that activates visco-plasticity and the rock unconfined compression strength can be estimated.

If one assumes that the difference between the thresholds of failure and of visco-plasticity is due only to a difference in the cohesive contribution, the parameter ϕ_{lim} is equal to the friction angle, while c_{lim} can be obtained by applying the same factor R_{CS} to the cohesion.

The symbols in Figure 3 show the variation of axial strain with time for 5 uniaxial compression tests on schist samples, carried out at different levels of constant load (Cristescu & Hunsche, 1998).

For this example, a value $\sigma_c = 54$ MPa was considered for the rock unconfined compression strength. From the experimental data the uniaxial stress σ_{lim} was estimated equal to 32 MPa, i.e. approximately 60% of the strength σ_c ($R_{CS} = 0.6$).

The results of the numerical simulation, represented in solid lines in Figure 3, were obtained with the values of parameters listed in Table 1. In the calibration, the two tests carried under the same stress, that yielded quite different results, were replaced by a single curve averaging them.

Note that the contribution of visco-elastic strains is not relevant compared with the purely elastic strains, since they reach approximately the 10% of the elastic strain in the tests conducted with low axial stresses. As a consequence, the tangential stiffness is much larger in the visco-elastic element than in the elastic one.

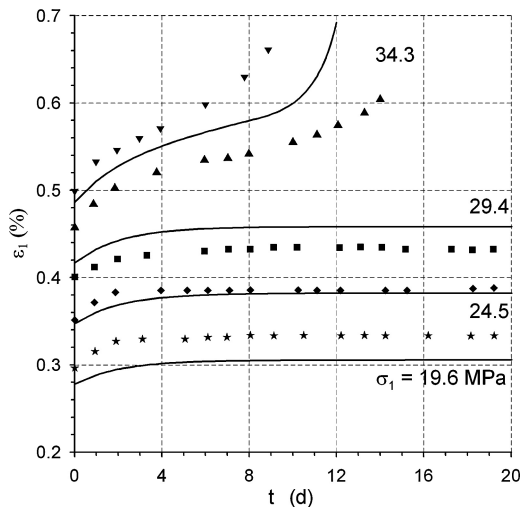


Figure 3. Experimental data (symbols) vs. numerical results (solid lines) for uniaxial creep tests on schist (laboratory data after Cristescu & Hunsche, 1998).

Table 1. Mechanical parameters for the intact rock and the in situ rock mass.

Material	Elastic		Visco-elastic		Visco-plastic (peak values)			Visco-plastic (residual values)				
	B^{el} (MPa)	G^{el} (MPa)	η^{ve} (MPa·d)	G^{ve} (MPa)	η^{vp} (MPa·d)	c_{lim} (MPa)	ϕ_{lim} (°)	ψ_{lim} (°)	η^{vp} (MPa·d)	c_{lim} (MPa)	ϕ_{lim} (°)	ψ_{lim} (°)
Intact rock	5880	2714	49470	23390	4800	7.88	37.6	20	2400	0	20	0
Rock mass	1470	678	49470	5848	706	1.16	32.3	14	353	0	20	0

Besides some discrepancies arising on the purely elastic component of the total axial strain, the curves well fit the test results for both visco-elastic and visco-plastic contributions, including the tertiary creep phase.

In order to estimate the values of the rock mass parameters, some additional information is necessary on the conditions in situ, which is often restricted to the assessment of the specific rock mass quality indexes. Usually, the squeezing potential of the rock mass is established on the basis of empirical relations between these indexes and the tunnel depth or the in situ stress (e.g. Singh et al., 1997; Hoek, 2001; Barla, 2002).

The Rock Quality Designation RQD and Rock Mass Rating RMR have been considered here as measures of the rock mass weathering and the values of, respectively, 70 and 48 have been assumed.

Empirical relations (Hendron, 1968) suggest reducing the stiffness by a factor of 0.25 when the rock mass is characterized by an index RQD = 70. This correction can be applied to the stiffness parameters belonging to both elastic and visco-elastic elements.

Resorting to Hoek-Brown criterion for the rock mass with RMR = 48, the unconfined compression strength and associated parameters can be worked out (Hoek, 1990). Adopting the same ratio R_{CS} of the intact rock and following the same procedure, the parameters c_{lim} and ϕ_{lim} can be estimated also for the rock mass.

A greater uncertainty affects the viscosity coefficients. The visco-elastic coefficient η^{ve} is not corrected here, since field data seem to point up that the visco-elastic strains develop in situ at a rate comparable or even lower than that measured in laboratory (Starfield & McClain, 1973; Chin & Rogers, 1987). While the visco-elastic coefficient influences only the strain rate, the visco-plastic coefficient governs also the strain magnitude. Therefore, like the parameter c_{lim} , it should be reduced with respect to the value characterizing the laboratory sample. For η^{vp} , the same reduction factor affecting c_{lim} is here suggested.

Finally, the residual condition of the rock mass can be considered the same that characterizes the laboratory sample. The visco-plastic coefficient only undergoes a reduction, applying the same factor found for the intact rock.

4 FINITE ELEMENT ANALYSIS OF A DEEP TUNNEL EXCAVATION

In order to verify the applicability of the rheological model to the analysis of a tunnel excavation, a simple representative problem has been considered, which could be solved by means of a 2-dimensional finite element model.

The problem consists of the full face excavation of a circular tunnel (radius $R = 4.5$ m), in a homogeneous, isotropic rock mass, subjected to an isotropic state of stress ($\sigma_0 = 10$ MPa). This choice may correspond to a tunnel depth of approximately 400 m.

A first series of 2-dimensional analyses has been carried out with reference to the tunnel longitudinal section, for which axisymmetric conditions apply. The face advance rate, here set equal to 6 m/day, is accounted for by removing a group of elements of total given length in a given time span. In the axisymmetric analysis, the explicit representation of the advancing tunnel face permits one to directly evaluate the face effects.

Figure 4 shows the adimensional tunnel closure in the section located at a distance of 20 m from the grid border, obtained from the various viscous analyses and from perfectly elastic and elastic perfectly plastic analyses. For the latter, the parameters c_{lim} , ϕ_{lim} of the rock mass in Table 1 have been assumed as strength parameters.

The negligible difference between elastic and visco-elastic solutions is the consequence of the high value of parameter G^{ve} compared with G^{el} .

For constant values of the visco-plastic parameters (VP analysis) the elasto-plastic solution is retrieved in the long term, since the viscous substance of the visco-plastic element acts only to delay the elasto-plastic solution governed by the slider. This solution, for the axisymmetric tunnel problem, always reaches convergence, i.e. a stable value of tunnel closure.

The results appear markedly different if tertiary creep is allowed for (VPS analysis). Note that, theoretically, the convergence is reached also in this case, but at a higher value of tunnel closure, which depends on the residual values of visco-plastic parameters.

The convergence of the tunnel closure to a stable value is pointed up also by the stress invariant path

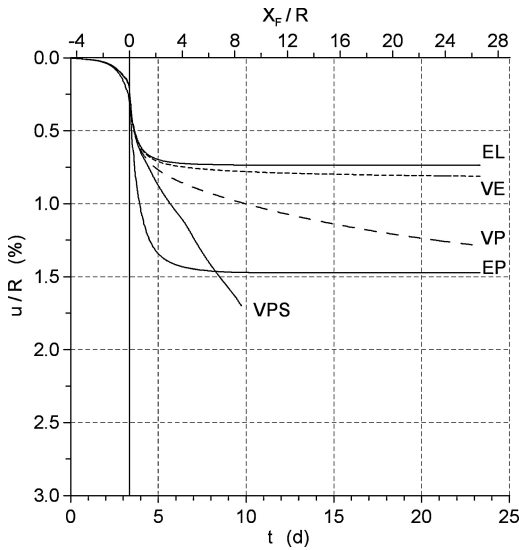


Figure 4. Tunnel closure with time and with distance X_F/R from the tunnel face, for axisymmetric analyses: elastic (EL), elasto-plastic (EP), visco-elastic (VE), visco-plastic with secondary (VP) and tertiary (VPS) creep (R = tunnel radius).

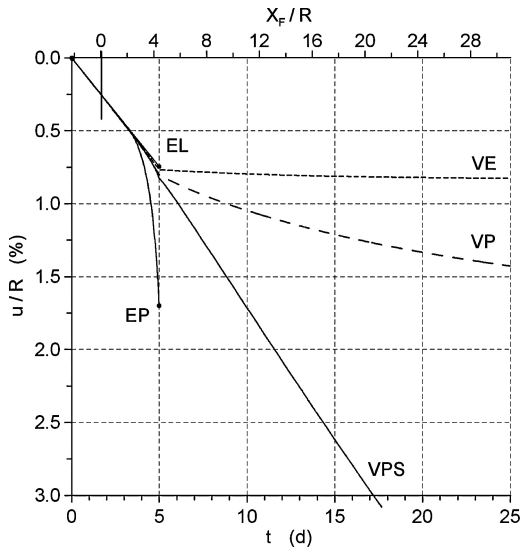


Figure 6. Tunnel closure with time and with distance from the tunnel face, for plane strain analyses (notations as in Fig. 5).

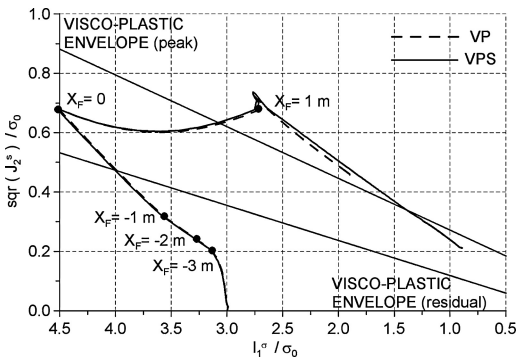


Figure 5. Stress invariant paths at a point close to the opening, for axisymmetric visco-plastic with secondary (VP) and tertiary (VPS) creep analyses (X_F : distance from the tunnel face).

induced at an integration point close to the opening during the excavation process (Fig. 5).

In the VP analyses, the stress path reaches the visco-plastic limit envelope (peak value), i.e. the exceeding portion of deviatoric stress carried by the dashpot vanishes, and the tunnel closure tends to a constant value. A different response is obtained if the visco-plastic envelope comes to the residual value (VPS analysis): in this case the viscous substance carries a large part of the deviatoric stress even in the long term, thus leading to a large tunnel closure.

The effect of the advancing tunnel face consists of a remarkable increase of isotropic stress, which attains a maximum value when the section at hand coincides with the face section. This yields a temporary increase of resistance in the vicinity of the tunnel face. Looking in detail at the variation of the various stress components, it could be observed that this effect is mainly due to a large increase in the stress component directed along the tunnel axis.

A series of analyses of the tunnel cross section has been also conducted, in plane strain conditions. This scheme entails to choose the time span in which the whole excavation takes place, i.e. to choose the rate of reduction of the ground pressure acting on the tunnel boundary. This rate depends on the actual advance rate and on the extent of the zone of influence of the tunnel face in the tunnel axis direction, which can be only roughly estimated. In this case, a length equal to 30 m was estimated, corresponding to approximately 3 times the tunnel diameter.

This led to a 5 days time span necessary to remove the ground pressure on the excavation boundary.

In addition, the pressure reduction is customarily applied linearly with time, whereas the effects of the advancing face on the tunnel section are increasingly relevant as the face approaches it and tend to gradually loose their relevance after the face has crossed.

Due to these approximations, the plane strain analyses lack of accuracy in the short term condition, within the zone of influence of the tunnel face. Conversely, they can provide a correct prediction of the long term condition, as shown for instance in Figure 6 in terms

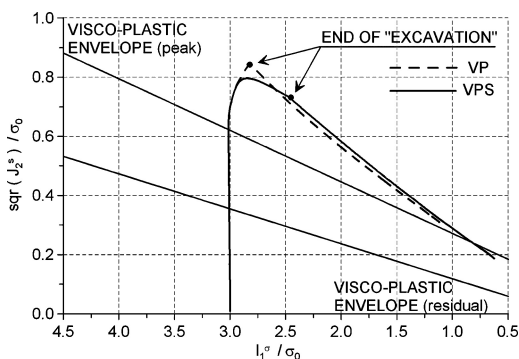


Figure 7. Stress invariant paths at a point close to the opening, for plane strain analyses (notations as in Fig. 6).

of tunnel closure. Note that the curves in the time range of 0–5 days coincide with the tunnel convergence-confinement curves.

As for the axisymmetric analyses, the variation of ground stresses induced by the tunnelling is shown with reference to the stress invariant path (Fig. 7).

The local effects of the face advance on the stress redistribution clearly appear by comparing Figure 5 with 7. In particular, the plane strain analyses do not indicate any increase of isotropic stress, but rather a decreasing value up to the end of the excavation, beyond which the path covers what already obtained with axisymmetric analyses.

5 CONCLUSIONS

The excavation process of a deep tunnel has been approached by means of the finite element method, aiming at evaluating the role of the tunnel face advance on the tunnel closure and on the stress redistribution around the opening, in the presence of squeezing rock.

Two-dimensional analyses have been carried out in axisymmetric and plane strain conditions and an elasto-visco-plastic rheological model that accounts for tertiary creep effects has been adopted.

The calibration of the mechanical parameters becomes a crucial point of the analysis. In fact, this should be carried out with reference to data from in situ creep testing. The lack of this information induces to resort to parameters obtained from laboratory tests that are suitably corrected by means of empirical relations and of a measure of the rock mass weathering. However, reliable empirical relations still have to be defined for the parameters describing the creep behaviour.

The numerical results show that the contribution of tertiary creep is crucial for the correct prediction of the tunnel closure.

The effects of the advancing tunnel face are relevant especially in the short term, but could affect also the long term conditions, whenever a constraint has to be applied in the proximity of the tunnel face, such as the action exerted by the TBM shield or by the tunnel supports. The axisymmetric scheme is definitely advisable in order to correctly predict the rock-structure interaction.

Finally, the constitutive model has shown a rather good potential for tunnel applications, provided that an accurate calibration of the mechanical parameters is carried out. Additional numerical analyses should be also required, introducing the effects of an internal support and evaluating the pressure that the surrounding rock is able to exert on it in the short and long term.

ACKNOWLEDGMENTS

The study is part of the National Research Project “Mechanized Tunnelling” (2001), coordinated by G. Barla and financially supported by the Italian Ministry of Education, University and Research.

REFERENCES

- Barla, G. 1995. Squeezing rocks in tunnels. *ISRM News Journal* Vol. II (3–4): 44–49.
- Barla, G. 2002. Tunnelling under squeezing rock conditions. In Kolymbas (ed), *Eurosummer-School in Tunnel Mechanics, Innsbruck 2001*: 169–268. Berlin: Logos Verlag.
- Boidy, E., Bouvard, A. & Pellet, F. 2002. Back-analysis of time-dependent behaviour of a test gallery in claystone. *Tunnelling Underground Space Techn.* 17: 415–424.
- Chin, H.P. & Rogers, J.D. 1987. Creep parameters of rocks on an engineering scale. *Rock Mech. Rock Engng.* 20: 137–146.
- Cristescu, N.D. & Hunsche, U. 1998. *Time effects in rock mechanics*. Wiley & Sons.
- Dalgıç, S. 2002. Tunneling in squeezing rock, the Bolu tunnel, Anatolian Motorway, Turkey. *Engng. Geol.* 67: 73–96.
- Dusseault, M.B. & Fordham, C.J. 1993. Time-dependent behaviour of rocks. In J.A. Hudson (ed), *Comprehensive rock engineering*: Vol. 3, 119–149. Pergamon Press.
- Einstein, H.H. & Bobet, A. 1997. Mechanized tunnelling in squeezing rock – From basic thoughts to continuous tunnelling. In Golsner, Hinkel & Schubert (eds), *Tunnels for people; Proc. 23rd ITA assembly, Wien*: 619–632. Rotterdam: Balkema.
- Gioda, G. & Cividini, A. 1996. Numerical methods for the analysis of tunnel performance in squeezing rocks. *Rock Mech. Rock Engng.* 29(4): 171–193.
- Hendron, A.J. 1968. Mechanical properties of rock. In K.G. Stagg & O.C. Zienkiewicz (eds), *Rock mechanics in engineering practice*: 21–53. Wiley & Sons.

- Hoek, E. 1990. Estimating Mohr-Coulomb friction and cohesion values from the Hoek-Brown failure criterion. *Int. J. Rock Mech. Min. Sci. & Geomech. Abstr.* 27(3): 227–229.
- Hoek, E. 2001. Big tunnels in bad rock (36th Terzaghi Lecture). *ASCE Int. J. Geotech. Geoenv. Engng.* 127: 726–740.
- Italian Geotechnical Journal* 2000. Special issue on Squeezing rock conditions in tunnelling, 34(1).
- Ladanyi, B. 1993. Time-dependent response of rock around tunnels. In J.A. Hudson (ed), *Comprehensive rock engineering*: Vol. 2, 78–112. Pergamon Press.
- Malan, D.F. 2002. Simulating the time-dependent behaviour of excavations in hard rock. *Rock Mech. Rock Engng.* 35(4): 225–254.
- Rock Mechanics and Rock Engineering* 1996. Special issues on Tunnelling in squeezing rock 29(3), 29(4).
- Singh, B., Goel, R.K., Jethwa, J.L. & Dube, A.K. 1997. Support pressure assessment in arched underground openings through poor rock masses. *Engng. Geol.* 48: 59–81.
- Starfield, A.M. & McClain, W.C. 1973. Project Salt Vault: a case study in rock mechanics. *Int. J. Rock Mech. Min. Sci. & Geomech. Abstr.* 10: 641–657.

Numerical modeling of tunnel lining at high temperature

M. Zaki Abd Elrehim

Civil Engineering Department, Minia University, Minia, Egypt

G. Swoboda

University of Innsbruck, Innsbruck, Austria

ABSTRACT: This paper presents a model to investigate the behavior of tunnels lining during fire on a structural level. Further emphasize has been drawn to the condition and stability of the supporting elements after fire. A numerical approach using the Finite Element Method is used to predict the lining internal forces before and after fire. The proposed modeling for investigating capacity of the tunnel lining during fire combines a heat transfer analysis and a non-linear structural analysis that includes type of fire, temperature-induced material degradation and ground-tunnel lining interaction. Two real case studies are considered. The influence of the fire protection systems on lining has been investigated and included in the numerical model. The results give more help to understand the structural behavior of tunnel lining under high temperature and also give guidelines that help the decision-makers to put the necessary regulation for tunnels' safety.

1 INTRODUCTION

The risk of tunnel fires increases as traffic volumes rise and in turn, as the number of tunnels continues to grow. Several accidents have recently tragically and clearly underlined the catastrophic effects that may be caused by tunnel fires. Fires in Mt. Blanc Tunnel (France/ Italy), the Tauern Tunnel (Austria), the Gotthard Tunnel (Switzerland), the Kaprun Tunnel (Austria), the Metro of Daegu (South Korea), and most recently in the Fréjus Tunnel (France/Italy) are instances of such incidents. These fire accidents gave rise to intensified multinational efforts to improve the safety level for tunnel users and for the tunnel structure itself (Haack 2005).

The implied hazards for users and the impact of the breakdown of vital infrastructure for months are considered to be more and more important. Tunnel lining made of Reinforced Concrete (R.C) can explosively spall at fires with high heat release rates and temperatures. Due to its economic and politic impact, the question's answer of whether and when a tunnel is reopened for traffic after a fire is very important.

For many years, structural fire performance studies for concrete members focused mainly on buildings; not much work has been done regarding tunnels although release rates are typically more severe in tunnel fires than in building fires.

2 MECHANICAL BEHAVIOR OF R.C AT HIGH TEMPERATURE

The mechanical characteristics of concrete and reinforcement, which include compressive and tensile strength, Poisson's ratio and modulus of elasticity etc., are highly influenced by high temperature. The changes depend on the peak temperature, the time and rate of heating, the type of concrete and reinforcement. Under fire conditions, material are subjected to transient processes and therefore the mechanical properties should be determined under transient temperature conditions and should be distinguished from other properties derived under steady state conditions. For high temperature experimental tests, three main test parameters should be considered: the heating process, the application of the load and the control of the strain (Schneider 1982).

During the last decades, many investigators have reported test results about compressive strength of normal and high strength concrete when subjected to elevated temperature. A comprehensive report about "Fire Design of Concrete Structures" had been reported by a group of investigators in Europe (CEB 1991). It was reported that the compressive strength decreases with the increase of the temperature and a set of design curves for normal and light weight concrete was suggested. Similar curves are also suggested by Eurocode 2

(Eurocode 2003). Both sets of design curves are illustrated in Figure 1 where a considerable reduction of concrete strength is noticed beyond 1200°C. Similar design curves for the concrete tensile strength and modulus of elasticity are reported by the CEB and the Eurocode where the general trend is the reduction of the strength and the modulus of elasticity with elevated temperature.

Experimental tests showed that all types of steel reinforcement sustain a reduction in its yield and ultimate strengths at high temperature. The typical relative elastic modulus of reinforcement is reduced gradually with the increase of temperature. The suggested design curves for the modulus of elasticity of steel at high temperature by (CEB 1991) and Eurocode 2 (Eurocode 2003) are shown in Figure 2. The accurate analysis of any structural element exposed to fire should include the material degradation due to high temperature.

3 EFFECTS OF FIRE ON TUNNEL LINING

Due to the characteristics of burning vehicles and the geometrical nature of tunnels, the fire impact in tunnels

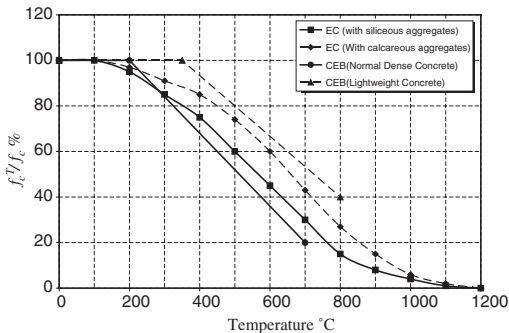


Figure 1. Reduction of compressive strength of concrete under elevated temperature.

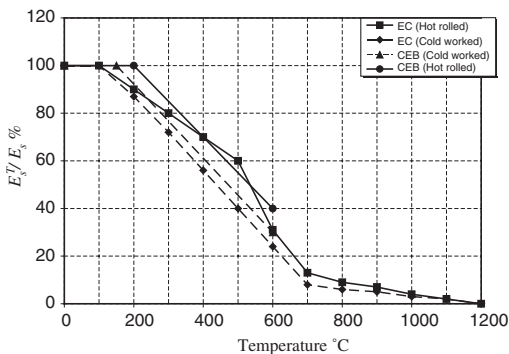


Figure 2. Reduction of elastic modulus of reinforcement under elevated temperature.

differs significantly from fires in buildings. In the event of a fire in an unprotected tunnel, the main damage occurs by concrete spalling due to the steep temperature gradient, in particular during the initial phase of the fire. Moreover, in case of burning vehicles, there is the very long duration of the fire involving extremely high temperatures of up to ca. 1200°C. Concrete spalling develops due to various damage mechanisms, resulting from the interaction between working loads and thermally induced additional strains (Both et al., 2003). At the later stages, of the fire a major issue is the material degradation, because an increase in structural demand and simultaneous decrease of structural capacity during fire event can result in serious structural damage.

3.1 Tunnel fire rating curves

Different fire rating curves are developed for tunnels representing extreme fire events. These curves are mainly used for structural fire rating (PIARC 1999), and are not a function of the size of the tunnel or ventilation system, or the burning of a single vehicle. Figure 3 shows the most fire rating curves used in Europe. These curves are classified by (Kusterle et al. 2004) as follows:

HC-curve: The Hydrocarbon-curve should be used in case of hydrocarbon fire. The maximum temperature reaches 1100°C without any cooling process.

HC-incr.-curve: The Hydrocarbon-increased-curve is similar to HC-curve with a maximum temperature of 1300°C.

RABT-curve: For cases of fire caused by benzene or petroleum products. The maximum temperature is 1200°C with cooling process.

EBA-curve: The curve is similar to RABT curve except that the cooling process will start after 60 min.

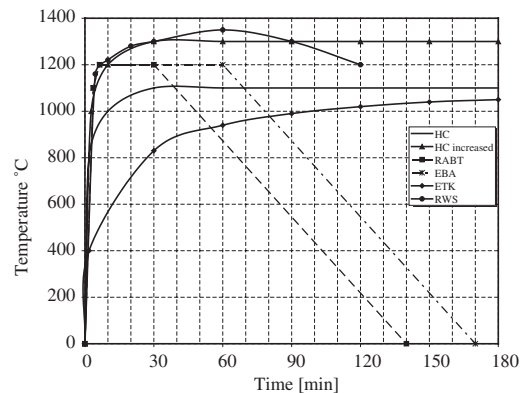


Figure 3. Temperature-Time curves used in European tunnels.

ETK-curve: The curve can be used for ordinary concrete structures and it is not recommended to be used in tunnelling.

RWS-curve: The curve was developed in the Netherlands, and simulates the burning of a fuel tanker with a fire load of 300 MW.

3.2 Temperature distribution in concrete

The temperature profile across the depth of any concrete member can be calculated using the analytical solution for a 1-D heat conduction problem. This solution however does not account for temperature dependency on the thermal properties of concrete and other nonlinearities. The temperature distribution through tunnel lining thickness is commonly calculated by laboratory tests by exposing concrete specimens to high temperature and measuring the temperature at different distances through the specimen.

Figure 4 illustrates the variations of temperature over the thickness of the concrete specimens at various times during heating and cooling phases. These curves and similar curves are used by many investigators for tunnel fire calculations (Kusterle *et al.* 2004). It should be noticed that the curves for times 30, 60 and 120 minutes describe the heating phase and the curves for times 180 and 240 minutes represent the cooling phase during and after fire extinguishing.

4 MODELING OF TEMPERATURE LOAD

The temperature load can be modelled in two steps; the first is the effect of temperature on the structural element itself which produces stresses and strains due to the temperature changes. The second step is to account for the material degradation which means the variation of concrete and steel mechanical properties such as the ultimate strength and the modulus of

elasticity. This can be achieved by using a two dimensional (2-D) layer-based model, Figure 5. In this model, the concrete section is divided into several layers depending on the temperature distribution. For every layer a constant temperature load and material properties are assigned. The Linearly varying Strain Triangular (LST) element can be used to simulate the concrete layers whereas the BEAM2 element is used to simulate the steel reinforcement.

The typical load vector for indirect loading such as temperature and shrinkage can be determined as follows:

$$f = \int_v B^T (D \epsilon^0 - \sigma^0) dv \quad (1)$$

where ϵ^0 and σ^0 are the initial strains and stresses respectively while the matrices D and B^T contain the material constants and the derivatives of the shape function respectively. It should be noticed that the initial strains and stresses as well as the D matrix and consequently the K matrix will be different for each layer and the resulting strains and stresses will take a linear distribution over the layer thickness.

During fire, the temperature changes across any layer with time. For an element i the elastic modulus changes with the temperature variation which means that stress redistribution takes place. At time t_1 , the stress of an element i will be:

$$\sigma_1^i = E_1 \epsilon^i \quad (2)$$

At time t_2 , the temperature and the elastic modulus change and the stress will be:

$$\sigma_2^i = E_2 \epsilon^i \quad (3)$$

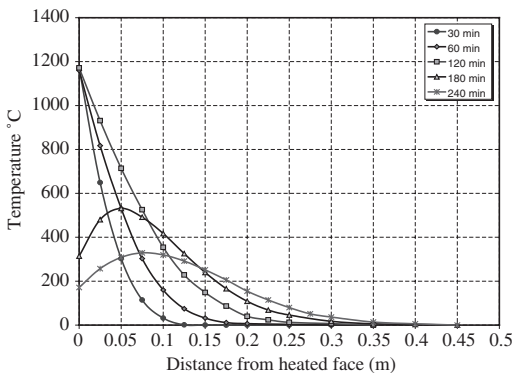


Figure 4. Temperature distributions in concrete section.

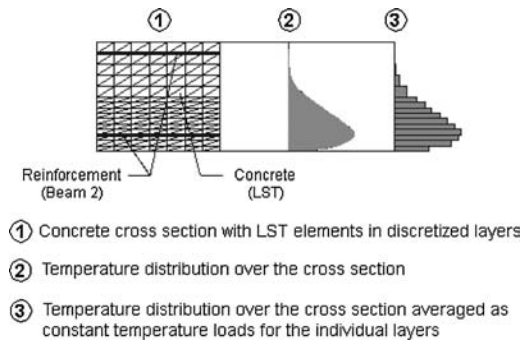


Figure 5. Modeling of temperature load.

Thus, the extra stress in this element to be redistributed will be:

$$\Delta\sigma^i = \sigma_1^i - \sigma_2^i = (E_1 - E_2) \cdot \varepsilon^i = (E_1 - E_2) \cdot \frac{\sigma^i}{E_1} \quad (4)$$

$$= \left(1 - \frac{E_2}{E_1}\right) \cdot \sigma^i$$

The respective redistribution factor $(1 - E_2/E_1)$ should be considered in the load cases.

5 APPLICATIONS AND CASE STUDIES

Two case studies with different construction methods and different site conditions will be considered.

5.1 Schönberg tunnel

In order to overcome the problem of traffic congestion in the town of Schwarzach located on the road Salzburg-Zell am See (Austria), a by-pass road with a length of 5170 m has been constructed. The by-pass includes a tunnel of 2988.6 m length which goes through the “Schönberg” mountain. The tunnel had to be constructed in a heavily jointed phyllite rock. A small pilot tunnel of diameter 3.6 m was excavated first using a Tunnel Boring Machine (TBM) for more geological investigation of jointed rock mass. Then, the NATM is followed to complete the tunnel profile using shotcrete outer lining of 20 cm thickness and inner lining of 25 cm thickness. The FE mesh used to get the lining stresses due to construction steps and typical situation (without temperature load) is illustrated in Figure 6.

Another 2D layer-based model is used to investigate the fire load case on tunnel lining, Figure 7. The inner lining is modeled using 10 layers of thickness 2.5 cm each and the outer lining is modeled using 4 layers of thickness 5 cm each. The relatively small elements sizes depict a very fine mesh in lining zone and enlarge gradually in the soil zone. Both concrete and soil elements are modeled using LST elements whereas the steel reinforcement is modeled using BEAM2 elements. Due to symmetry, only one half of the tunnel will be considered. The calculation is performed using FINAL code (Swoboda 2001) to simulate the fire load case on the tunnel.

The used fire scenario or rating curve was the relatively recent BEG-curve used for the calculation of fire on “Unterinntaltrasse” (Mauracher 2004). This curve is similar to EBA-curve, Figure 3, except that the cooling phase starts at 120 min. The considered load cases are:

- Loading 1: Dead load of tunnel lining.
- Loading 2: Temperature load from 0 to 60 min.

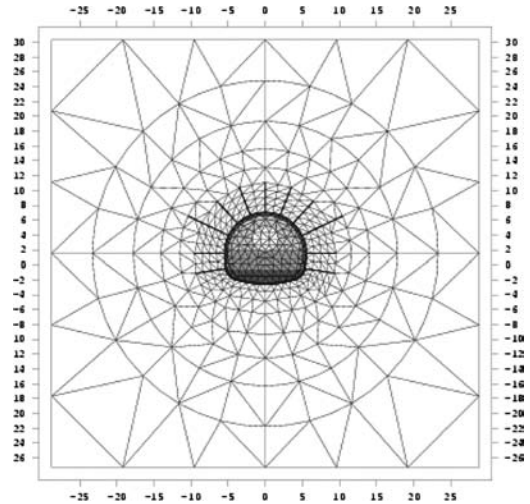


Figure 6. FE mesh for construction phase of Schönberg tunnel.

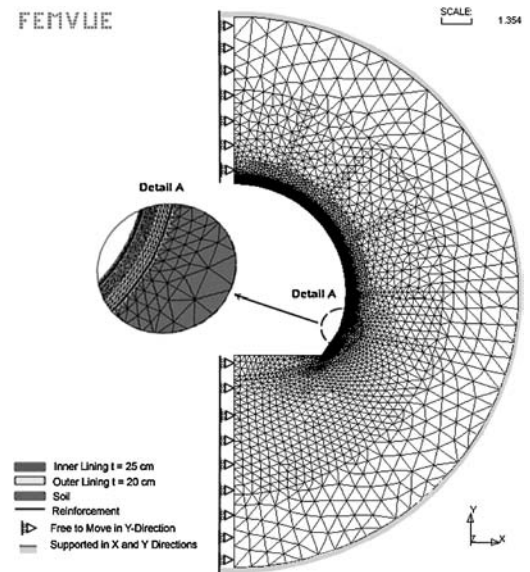


Figure 7. FE mesh for fire load case of Schönberg tunnel.

- Loading 3: Temperature load from 60 to 120 min.
- Loading 4: Temperature load after 120 min. (cooling or fire extinguishing).

During heating and cooling process, the temperature for each layer as well as the modulus of elasticity were calculated according to the experimental, (CEB 1991) and Eurocode 2 (Eurocode 2003) data.

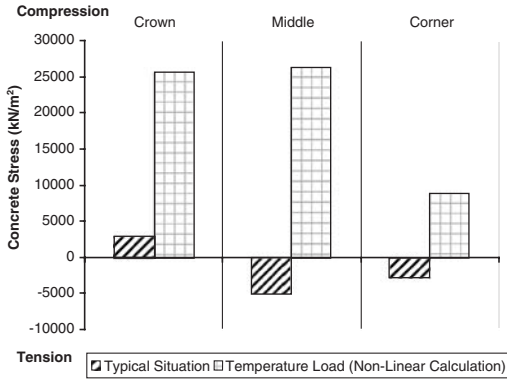


Figure 8. Comparison of principal stresses on lining.

The resulted additional lining stresses due to temperature load compared with typical situation at different cross sections are presented in Figure 8. The additional higher stress values due to fire loading are nearly five times the stresses of the typical situation. This dictates general review to check lining safety.

5.2 El-Azhar road tunnels

El-Azhar Road tunnels project in Cairo is located in the Fatimide area of Cairo which is one of the historical popular market center and features architectural treasures, with its mosques and ancient famous palaces such as Khan El Khalily. Tunnels had been constructed as one of the planned solution to overcome the problem of traffic jams especially in the congested city center zone. The project is composed of twin tunnels deigned to carry two lanes and two sidewalks in each direction. The total length of each tunnel is about 2.7 Km including nearly 1.0 Km portals. The tunnels had been driven using the bentonite slurry pressurized closed face Tunnel Boring Machine (TBM) with an external diameter of 9.40 m. The supporting rings are prefabricated reinforced concrete segments of 1.5 m width and 0.4 m thickness. FE plane strain analysis is performed with the help of a model containing the soil layers, water pressure and the construction sequences to get the primary stresses on concrete segments.

To investigate the effects of fire load on tunnel segments, a 2D layer-based model is used. Figure 9 shows a half symmetric cross section where the lining is simulated using 10 layers of thickness 2.5 cm each followed by 3 layers of 4 cm and the last one is 3 cm thickness to exactly simulate the reinforcement position. The same element types, the temperature rating curve, temperature distribution, material degradation and assignment of material properties for every layer in every loading case used in the previous case study is also used here.

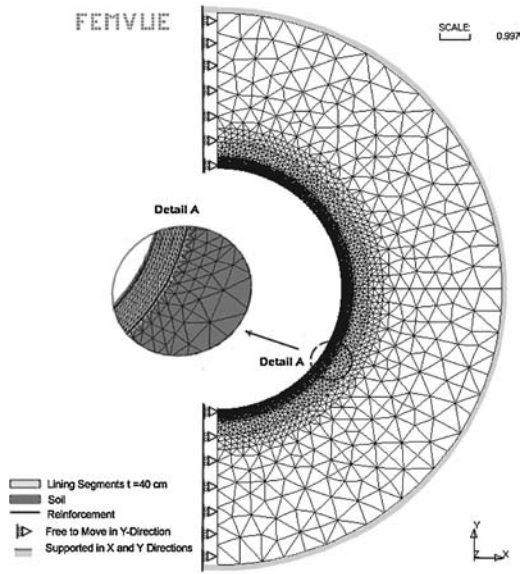


Figure 9. FE mesh for fire load case of El-Azhar tunnels.

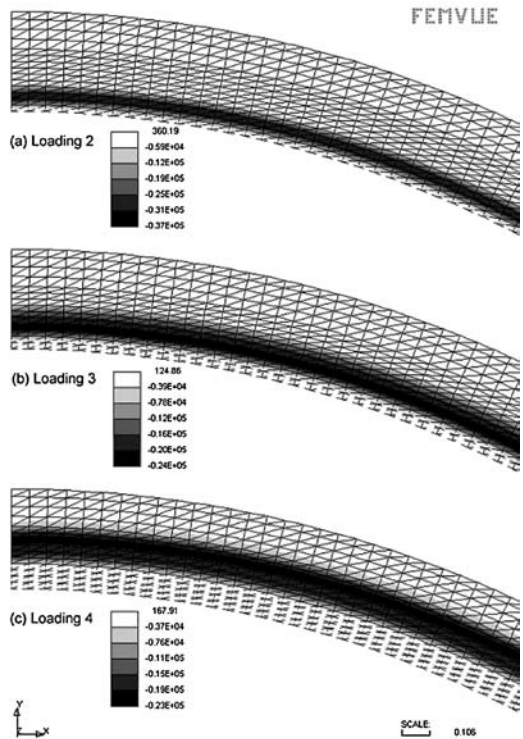


Figure 10. Principal stresses on lining (No isolation).

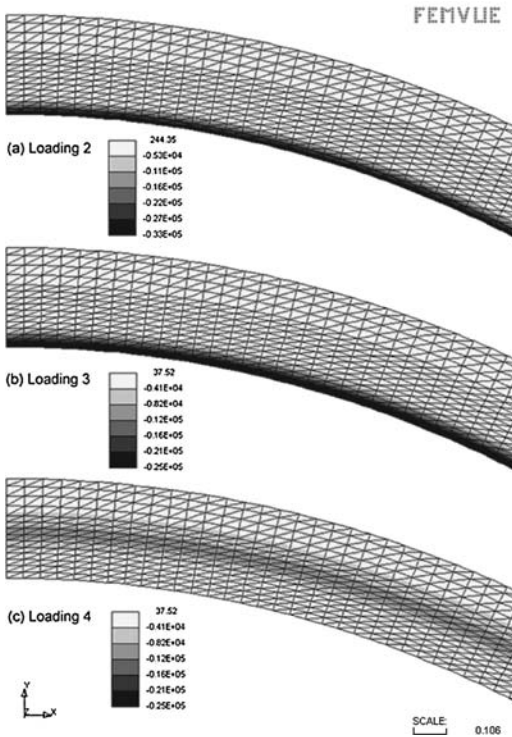


Figure 11. Principal stresses on lining (with isolation).

The relatively fine mesh used gave rise to LST elements to 7758 and BEAM 2 elements to 400 with a total of 8158. The number of freedoms to be determined in each loading step is 31622. Reviewing the resulting stress in concrete section and the forces in the reinforcement, the safety of tunnel lining is questionable. Figure 10 illustrates the development of principal stresses in concrete during and after fire. It should be noticed that some inner layers of concrete had been completely damaged. The capacity of the remaining section and the whole stability of tunnel lining are severely affected.

During construction, it was decided to protect the internal face of the concrete segments by using an isolation material, Fire Barrier 135 (NAT 1999). The experiments show that a thickness of 47 mm of Fire Barrier 135 prevents the temperature of the concrete at the interface to rise above 200°C. Another calculation is performed to investigate the effect of the isolation material on the developed stresses on lining during and after fire. The results are impressive due to a temperature of 200°C, only a relatively small amount of stresses had been developed in the concrete section and no damaged layers are recorded, Figure 11.

A comparison of concrete principal stresses at the crown of the tunnel due to fire load is illustrated in

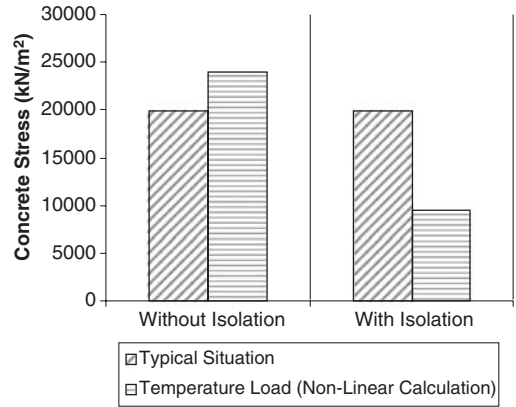


Figure 12. Comparison of crown compressive stresses.

Figure 12. Both cases of isolated and unprotected lining for each case are considered. The impact of using isolation materials to protect tunnel lining during fire is very clear. Further research for developing special types of concrete resisting more temperature load (Dorgarten *et al.* 2004) compared to the relatively expensive isolation material is highly recommended.

6 CONCLUSION

The Finite Element Method can be used to investigate the structural behavior of tunnel lining during and after fire. The proposed 2D layer-based model is capable of taking into account the material degradation due to temperature load. The non-linear fire calculations performed for the two case studies reflect the importance of checking the stresses developed in lining. The structural capacity of the remaining R.C section and the whole stability of tunnel lining are severely affected by fire. The impact of the fire protection systems on reducing the lining stresses is clarified. The analysis helps to answer the question of whether and when a tunnel is reopened for traffic after a fire and gives guidelines that help the decision-makers to put the necessary regulation for tunnels' safety.

REFERENCES

- Both, C., Wolsink, G.M. and Breunese, A.J. 2003. *Spalling of concrete tunnel linings in fire*. (Re) claiming the Underground Space, Saveur (ed.), Swets & Zeitlinger, Lisse.
- COMITE EURO-INTERNATIONAL DU BETON (CEB). 1991. *Fire design of concrete structure*. Lausanne.
- Dorgarten, H., Balthaus, H., Dahl, J. and Billig, B. 2004. *Fire-resistant Tunnel Construction: Results of Fire Behaviour Tests and Criteria of Application*. *Proceedings*

- of World Tunnel Congress and 13th ITA Assembly, Singapore.
- Haack, A. 2005. Standardisation and research about fire safety in European traffic tunnels. In Erdem & Solak (eds), *Underground Space Use: Analyses of the Past and Lessons for the Future*. London. Taylor & Francis Group.
- Kusterle W., Lindlbauer W. et al. 2004. *Brandbeständigkeit von Faser-, Stahl- und Spannbeton*. Straßenforschungsauftrag Nr. 3.269 des Bundesministeriums für Verkehr, Innovation und Technologie und auftrag der Eisenbahn – Hochleistungsstrecken AG, Wien.
- Mauracher, H. 2004. *Der Lastfall Brand im Tunnelbau*. Diplomarbeit. Innsbruck University, Austria.
- National Authority for Tunnels (NAT). 1999. *Project Documents*. Cairo, Egypt.
- PIARC Committee on Road Tunnels (C5). 1999. *Fire and smoke control in road tunnels*. Athens, Greece. World Road Association.
- prEN 1992-1-2: Eurocode 2. 2003. *Bemessung und Konstruktion Von Stahlbeton- und Spannbetontragwerken*, Teil 1–2: Allgemeine Regeln-Tragwerksbemessung für den Brandfall. Europäisches Komitee für Normung.
- Schneider, U. 1982. *Behavior of concrete at high temperature*. Berlin. Wilhelm Ernst & sohn.
- Swoboda, G. 2001. *Programmsystem FINAL, Finite Elemente Analysis linearer und nichtlinearer Strukturen*, in German, Version 7.1, Druck Universität Innsbruck, Austria.

A “multi-phase” model for finite element analysis of traction forces in bolts used in the reinforcement of tunnel walls

E. Bourgeois, C. Rospars & P. Humbert

Laboratoire Central des Ponts et Chaussées, Paris, France

P. de Buhan

Institut Navier, ENPC, Marne la Vallée, France

ABSTRACT: This paper presents a mechanical model, called “multiphase model”, designed to deal with ground reinforced by a network of regularly distributed linear inclusions. The main improvement of this model with respect to previous homogenization-based models for bolt-reinforced grounds lies in a better description of the mechanical interaction between the ground and the bolts, taken into account through the attribution of different kinematics for the ground and the reinforcements. The model has been implemented in a “research” version of the finite element code CESAR-LCPC, and used for the simulation of the construction of a tunnel under plane strain conditions. Results are compared with those obtained with two other approaches: the first one consists in treating the bolts as 1D bar elements, while the other is a standard homogenization procedure. Results show that, while the deformation pattern around the tunnel is more or less the same regardless of the model used, the tensile forces in the bolts predicted by the multiphase model appear to be in much better agreement with those given by the calculation with bar elements.

1 INTRODUCTION

The reinforcement of tunnels walls by bolts is a very effective way of improving their stability and reducing the strains in the surrounding ground. “Bolting” refers to a wide range of techniques, that have different objectives according to the ground: it is used to prevent block falls in tunnels built in rock masses, or to limit the strains induced around the tunnel for shallow tunnels in soft grounds. It is also worth recalling that the mechanical role of the bolts is different if bolts are sealed to the ground on their whole length or if they just act as anchors sealed on both ends: depending on the situation, bolts can be submitted to traction forces or to traction forces and bending moments.

In what follows, we deal with passive radial bolts grouted to a ground considered as a continuous material. The efficiency of the technique has given rise to considerable work aimed at providing design tools giving the optimal positions and number of bolts.

It was first suggested that the confining role of bolts could be taken into account by applying a fictitious pressure on the tunnel wall (Stille and et al., 1989, Peila, 1994), this fictitious pressure depending on factors such as the volume fraction of the bolts and on their traction resistance.

Another technique of modelling the efficiency of the bolts, available in most finite elements (or finite

differences) codes, consists in including in the model beam elements, in order to take into account the role of the bolts. In this approach, the preparation of the mesh may rapidly become tedious, especially for three-dimensional analysis (see Laigle, 2001, for instance), while at the same time the computational time may increase considerably.

This is why some authors have proposed to replace, for modeling purpose, the bolt-reinforced ground by a homogeneous material characterized by improved mechanical properties, in terms of resistance (Indraratna and Kaiser, 1990, Grasso and et al., 1991, Oreste and Peila, 1996) or both stiffness and resistance, with more or less detailed analyses of the ground-bolt interaction (Greuell, 1993, and after him Bernaud et al., 1995, Wong and Larue, 1998, among others). De Buhan and Sudret (2000) and Bennis and de Buhan (2003) have proposed a model belonging to this family, called “multi-phase model”, in which two distinct displacement fields and two distinct stress fields are taken into account for the ground and the bolts which are “diluted” in the equivalent homogenized medium. This model has given rise to a simplified version, in which both displacement fields are identical. This simplified version is now available in the standard version of the finite element software CESAR-LCPC, and was used to discuss the displacements of tunnel faces (Bourgeois et al, 2002), the

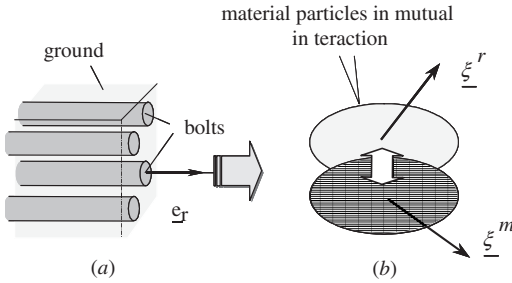


Figure 1. Principle of the multiphase model.

behaviour of a pile-reinforced embankment (Bourgeois and Borel, 2003) and of an experimental reinforced earth wall (Rospars et al., 2004).

Recently, the original model proposed by de Buhan and Sudret (2000) and Bennis and de Buhan (2003) has been implemented in a research version of the same finite element code. This communication presents the first results of this numerical tool, applied to the simulation of the construction of a tunnel, under plane strain conditions, using the convergence-confinement method. The more specific aim of the paper is to compare the forces in the bolts computed, for the same problem, by introducing bar elements in the mesh, by using the simplified homogenized model, and eventually the multiphase model.

2 MECHANICAL MODEL

The main features of the multiphase model are briefly recalled hereafter. More details can be found for instance in Bennis and de Buhan (2003) or Rospars et al (2005).

A ground reinforced by bolts can be described, at the scale of the bolts (“microscopic scale”), as a composite material whose constituents are located in geometrically separated domains (figure 1a). When the number of bolts is large enough, the multiphase model consists in adopting a different viewpoint: it is assumed that the reinforced ground as a whole, at a larger (or “macroscopic”) scale, can be seen as the superimposition in space of two continua, called “phases”. The “matrix phase” stands for the ground between the bolts, while the “reinforcement phase” stands for the network of bolts. According to such a description, two material particles are located simultaneously at every point of space, each attached to one of the phases, and in mutual mechanical interaction. Each phase has its own displacement field (figure 1b): we denote the displacement field for the “matrix phase” by ξ^m and the displacement field for the “reinforcement phase” by ξ^r .

Within this framework, and taking into account the fact that bolts are linear inclusions, the application of

the virtual work method and related principles lead to the definition of a stress tensor for each phase, and to the corresponding equilibrium equations. If we omit the volume forces (specific weight) for the sake of simplicity, these equations are:

$$\begin{aligned} \text{div } \underline{\underline{\sigma}}^m + \underline{\underline{I}} &= 0 \\ \text{div}(\sigma^r \underline{e}_r \otimes \underline{e}_r) - \underline{\underline{I}} &= 0 \end{aligned} \quad (1)$$

where $\underline{\underline{\sigma}}^m$ denotes the stress tensor associated with the “matrix phase”, and $\underline{\underline{I}}$ the force volume density exerted by the reinforcement phase on the matrix phase. It must be noted that the stress tensor associated with the “reinforcement phase” is uniaxial, and that the scalar σ^r can be interpreted as the axial force in the bolts calculated per unit area perpendicular to the direction of the bolts, defined by the unit vector \underline{e}_r .

The equilibrium equations are supplemented with boundary conditions. According to the multiphase model, these conditions are defined separately for the matrix and the reinforcement phases.

The last element of the model is the constitutive behaviour of both phases, that is :

- the constitutive law of the matrix phase, treated as an elastoplastic continuum endowed with the same characteristics of the ground:

$$\underline{\underline{\sigma}}^m = \underline{\underline{C}}^m : (\underline{\underline{\varepsilon}}^m - \underline{\underline{\varepsilon}}_p^m) \quad (2)$$

$$f^m(\underline{\underline{\sigma}}^m) \leq 0, \quad \dot{\underline{\underline{\varepsilon}}}_p^m = \dot{\lambda}^m \frac{\partial \underline{\underline{g}}^m}{\partial \underline{\underline{\sigma}}^m} \quad \text{with } \dot{\lambda}^m \geq 0 \quad (3)$$

where $\underline{\underline{\varepsilon}}^m$ denotes the strain tensor of the “matrix phase”, $\underline{\underline{\varepsilon}}_p^m$ its plastic component, $\underline{\underline{C}}^m$ the tensor of elastic moduli; while f^m and $\underline{\underline{g}}^m$ are the yield function and plastic potential, respectively, and $\dot{\lambda}^m$ the plastic multiplier.

- the constitutive law of the reinforcement phase, which is similar but simpler given the fact that the stress tensor is uniaxial, and therefore described by a unique scalar σ^r :

$$\sigma^r = A^r (\varepsilon^r - \varepsilon_p^r) \quad (4)$$

$$f^r(\sigma^r) \leq 0, \quad \dot{\varepsilon}_p^r = \dot{\lambda}^r \frac{\partial f^r}{\partial \sigma^r} \quad \text{with } \dot{\lambda}^r \geq 0 \quad (5)$$

where ε^r denotes the axial strain of the “reinforcement phase” along its direction, ε_p^r its plastic component. A^r is the axial stiffness of the reinforcement phase, that can be computed as the product of the Young’s modulus of the bolts constituent material (steel) by the reinforcement volume fraction. f^r is the yield function of the reinforcement phase, and $\dot{\lambda}^r$ the

plastic multiplier for the reinforcement phase (the flow rule being associated).

- the description of the matrix/reinforcement interaction, in the form of a relationship between the component of body force volume density I along the reinforcement direction, and the relative displacement of the reinforcement with respect to the matrix, projected onto this same direction, and denoted by:

$$\Delta = (\underline{\xi}^r - \underline{\xi}^m) \underline{e}_r \quad (6)$$

This relationship is of the elastoplastic type, that is:

$$I = c^I (\Delta - \Delta^p) \quad (7)$$

$$f^I(I) \leq 0, \quad \dot{\Delta}^p = \dot{\lambda}^I \frac{\partial f^I}{\partial I}, \quad \dot{\lambda}^I \geq 0 \quad (8)$$

where Δ^p is the plastic component of Δ , c^I a stiffness coefficient associated with the interaction, f^I the corresponding yield function, which controls the onset of an irreversible relative displacement between phases, and $\dot{\lambda}^I$ the plastic multiplier.

The main interest of the model with respect to a classical homogenization technique, in which the reinforced ground is modeled as one single equivalent continuum, lies in the introduction of the relative displacement Δ between phases. However, selecting the appropriate values of the interaction stiffness coefficient and the threshold value of I where an irreversible relative displacement between phases occurs, remains a difficult task, as will be illustrated hereafter.

3 NUMERICAL IMPLEMENTATION

The numerical implementation of the model in a 2D finite element code requires the introduction of a new type of elements, with three degrees of freedom per node (two displacements for the matrix, and one additional degree of freedom for the displacement of the reinforcement along its spatial direction).

The elementary stiffness matrix is the sum of three contributions attached to the matrix, reinforcement and interaction, respectively. In the non-linear regime, out-of-balance forces due to plastic strains in the phases or in the relative displacement, also lead to computing the sum of three independent contributions. However, the algorithm used to compute plastic strains is basically the same as for usual plasticity computations (Bennis, 2003).

Besides the implementation of the computation itself, special attention must be paid to the preprocessing of data, and to the post-processing of the

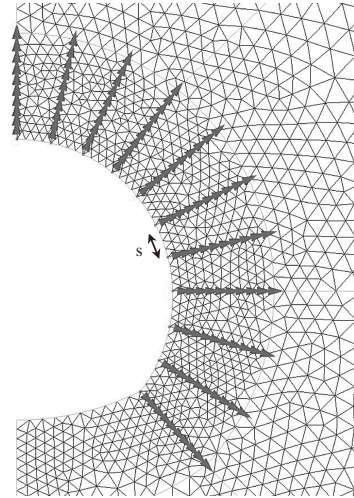


Figure 2. Detailed view of the mesh used for the numerical simulations.

specific results produced by the model (namely the additional displacement field in the reinforcement phase, the interaction force I , and the axial forces in the bolts that can be derived from the values of σ^r).

To date, the implementation has been carried out in a “research” version of the finite element software CESAR-LCPC, for two-dimensional analyses only. In its current state, the software makes it possible to take into account various spatial layouts of bolts, allowing for instance to model radial bolts in a tunnel vault.

4 EXAMPLE OF SIMULATION

4.1 Geometry and characteristics of the tunnel

The example discussed hereafter is a plane strain simulation of the excavation of a tunnel reinforced by radial bolts. The example is fictitious, and in order to illustrate the differences between the multiphase model and other modeling techniques, no lining is taken into account.

The meshed zone is included in a rectangle of 50 m in width by 100 m in height. The tunnel section is not circular, as shown by figure 2: the radius of the upper half is 5 m. The tunnel axis lies at a depth of 50 m. Rows of bolts are placed in the crown and in the walls. The mesh includes 8000 nodes and 4000 elements.

The tunnel construction is simulated by the succession of two steps:

- the first step sets the initial stress field, and a partial relaxation of the in situ stresses is exerted on the tunnel wall: the stress relaxation rate is 40%; there are no bolts in the ground;

- the second computation consists in activating the bolts and completing the stress relaxation simulating the excavation.

The ground behavior is described by a linear isotropic elasticity combined with the Drucker-Prager yield criterion (without hardening), with the following values of the parameters:

$$E = 150 \text{ MPa} , \nu = 0,25;$$

$$c = 120 \text{ kPa} ; \varphi = 26.3 \text{ degrees}; \psi = 0 \text{ degree}$$

Bolts are assumed to be made of a material with a Young's modulus of 200 GPa and their diameter is equal to 20 mm. It is assumed that the spacing between two bolted planes (in the direction of the tunnel axis) is equal to 2 m.

In what follows, all displacements are reset to zero at the beginning of the second step, and we compare the results obtained for three different models for the bolt-reinforced ground:

- in computation 1, bolts are taken into account by means of 11 rows of special linear elements providing additional stiffness in the direction of the bolts: these special elements are represented by triangular symbols in figure 2. Note that the analysis is carried out under plane strain conditions, which means that the inclusions are continuous in the direction perpendicular to the mesh plane (i.e. are modeled as plates rather than bolts).
- computation 2 resorts to a simple homogenization technique, which corresponds to the simplified version of the multiphase model, as already mentioned above, in which both phases are perfectly bonded.
- computation 3 uses the multiphase model. In this case, additional parameters are required for the simulation, namely the interaction coefficient as well as the maximum value of the interaction force. It is assumed here that there is no irreversible relative displacement between the matrix and the ground (which means that there is no limitation on the interaction force density I). As regards the value of the interaction coefficient, we started from the analytical estimate given by Sudret (1999), which relates this coefficient to the ground's shear modulus μ , reinforcement volume fraction η , and spacing s between two rows of bolts (see figure 2):

$$c^I = \frac{8\mu}{s^2(1-\eta)} \quad (9)$$

In what follows, to account for the progressive decrease of the shear modulus as plasticity occurs in the ground, we have assumed a reduced value corresponding to one sixth of the theoretical estimate. Computations are thus carried out with $c^I = 60 \text{ MPa.m}^{-2}$.

5 RESULTS

5.1 Displacements

In the first place, we compare the horizontal displacements computed in the ground surrounding the tunnel for the three computations. Figure 3 shows the contour lines of the computed horizontal displacement (for the three models, line 1 corresponds to 40 mm, line 2 to 35 mm, down to 5 mm for line 7).

In the results of computation 1, the contour lines show the variations of the displacements between two rows of bolts. (As mentioned before, the variations of the displacements between two bolted planes in the direction perpendicular to the mesh cannot be estimated in plane strain in the simulation with bar elements). The maximum computed horizontal displacement is 40 mm.

Computation 2 seems to underestimate the maximum horizontal displacement of the tunnel wall, since the maximum computed displacement is 25 mm. It is recalled that in this model, the displacement field is the same for the ground and the bolts that are "diluted" in it. This is a well-known feature of the simplified homogenization model.

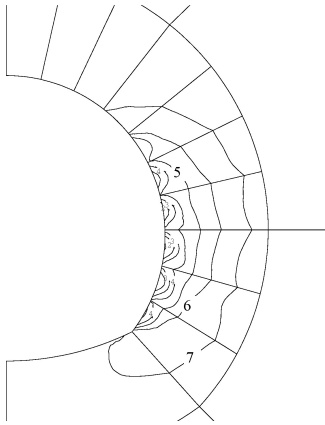
For computation 3, the figure shows the contour lines of the horizontal displacement computed in the matrix, which can be considered as an average value of the displacement in the ground between the bolts, and is no longer equal to the displacement of the reinforcement phase standing for the bolts. The introduction of an additional degree of freedom leads to computed displacements that are relatively close to those given by computation 1. In particular, the maximum value of the horizontal displacement is 33 mm.

More precisely, the wall displacement computed with the three models used here is shown in figure 4 (displacements are magnified by a factor 150). Computation 1 yields the only non-smooth profile, given that the heads of the bolts have smaller displacements. The calculation with the simplified homogenization procedure gives a good estimate of the displacements of the wall in the vicinity of the bolt heads, but the multiphase model gives in addition the amplitude of the displacements between the bolts.

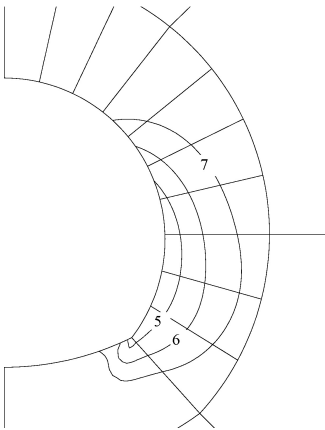
5.2 Traction forces in the bolts

Finally, we analyse the traction forces in the bolts derived from the different calculations. Bolt 1 is the bolt placed vertically in the crown. Results are also given for bolts 5 and 8, which are horizontal.

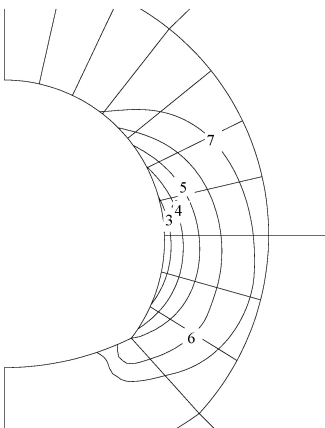
The main shortcoming of the simplified version of the multiphase model (computation 2), which is equivalent with the classical homogenization technique, lies in the fact that it leads to maximum values of the traction forces at the tunnel wall, thus overestimating the actual values (see notably bolt 5), which has important consequences from a practical design viewpoint.



a- Computation 1: special linear elements in the mesh



b- Computation 2: simplified homogenization approach



c- Computation 3: multiphase model ("matrix" phase)

Figure 3. Contour lines of the horizontal displacements.

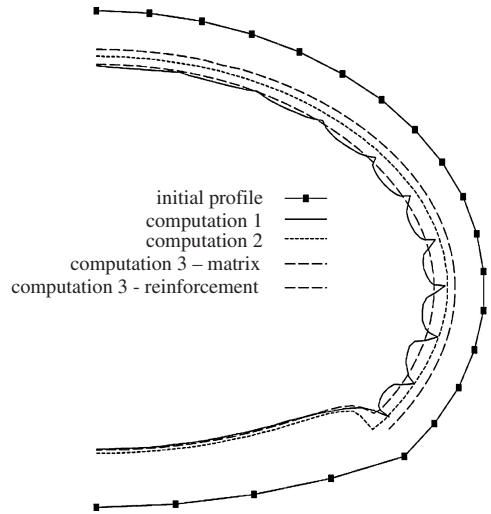


Figure 4. Displacements computed with the three models.

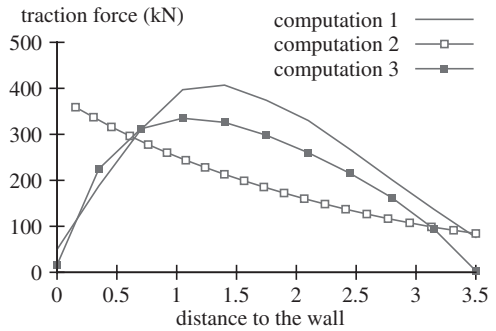


Figure 5. Traction force in bolt 8 (horizontal).

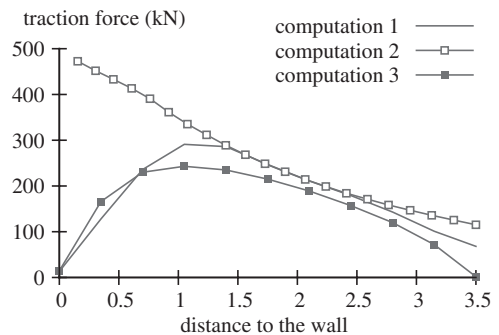


Figure 6. Traction force in bolt 5.

Conversely, the complete multiphase model (computation 3) leads to much more realistic estimates for the traction forces in the bolts, which appear to be much closer to the results obtained by a discretized

approach (computation 1), both in terms of the value and location of the maximum tensile force.

In the last place, the use of the multiphase model makes it possible to use less refined meshes, since it is no longer necessary to precisely specify the position of the bolts, when elaborating such a mesh. Moreover, it becomes much easier to undertake parametric studies on the various characteristics of the bolting system, without it being necessary to modify the mesh in each calculation.

6 CONCLUSION

Results show that the general strain pattern around the tunnel is more or less the same for all approaches. However, the simplified homogenization procedure leads to results that are acceptable for the displacements, but quite unsatisfactory as regards the evaluation of the traction forces in the bolts.

It is worth noting that the computation carried out with linear bar elements to account for the bolts cannot be considered as the reference computation, since it does not take into account the fact that the bolts do not provide a continuous reinforcement in the direction of the tunnel axis. A complete three-dimensional analysis, with an explicit description of the bolt-ground interface, would be necessary to get such reference solution, but this is obviously out of reach with current computation tools.

The multiphase model, though it does not provide the local variations of the displacements of the ground, may be, at least from a theoretical point of view, more representative of the actual mechanical system. In any case, it is encouraging to observe that computations 1 and 3, although based on different modeling techniques regarding the bolts, provide quite convergent results. In addition, the multiphase model allows for a significant reduction in the number of nodes needed to model a bolt-supported tunnel, thus leading to an important reduction of the computation times.

The next steps of the implementation as well as of the validation of the multiphase model would consist in incorporating this model into three-dimensional finite element analysis, and discussing the validity of the approach for the analysis of the failure of the bolting system. More specifically, the role played by the limited strength of the grout sealing the bolts to the ground, on the stability of tunnel faces remains to be investigated by such a numerical tool.

ACKNOWLEDGEMENT

The authors are thankful to O. Gastebled (Itech) for fruitful discussions during the preparation of the comparison between models.

REFERENCES

- Bennis M. & de Buhan P. (2003) A multiphase constitutive model of reinforced soils accounting for soil-inclusion interaction behaviour, *Math. Comp. Model.*, 37, 469–475.
- Bernaud D., de Buhan P., Maghous S. (1995). Numerical simulation of the convergence of a bolt-supported tunnel through a homogenization method. *Int. J. Num. An. Meth. Geomech.*, vol. 19, pp. 267–288.
- Bourgeois E., Garnier D., Semblat J.F. (2002) A 3D homogenized model for the analysis of bolt-reinforced tunnel faces, 5th Eur. Conf. Num. Meth. in Geotechnical Engineering NUMGE 2002, Mestat (ed), Presses de l'ENPC/LCPC, Paris, 573–578.
- Bourgeois E., Borel S. (2003) Modélisation numérique des fondations de la rocade d'Harfleur par une méthode d'homogénéisation, *Int. Symposium on Shallow foundations FONDSUP 2003*, Magnan et Droniuc (eds), Presses de l'ENPC/LCPC, 81–88.
- de Buhan P., Sudret B. (2000). Micropolar multiphase model for materials reinforced by linear inclusions, *Eur. J. Mech. A/Solids* 19, 669–687.
- Grasso P., Mahtab A., Ferrero A.M. & Pelizza S. (1991) The role of cable bolting in ground reinforcement. *Soil and Rock Improvement in Underground Works*, Milan, march, vol. 1, 127–128.
- Greuell, E. (1993) Etude du soutènement des tunnels par boulons passifs dans les sols et les roches tendres, par une méthode d'homogénéisation, thèse de l'Ecole Polytechnique.
- Indraratna B. & Kaiser P.K. (1990) Analytical model for the design of grouted rock bolts. *Int. J. for Num. and Analytical Meth. in Geomechanics*, vol. 14, 227–251.
- Laigle F. (2001) Conception des grandes cavernes souterraines: apport des modélisations numériques pour le projet CERN-LHC1, 1st Albert Caquot International Conference "Modelling and simulation in civil engineering: from practice to theory".
- Oreste P.P. & Peila D. (1996) Radial passive rockbolting in tunnelling design with a new convergence-confinement model. *Int. J. Rock Mech. Min. Sci. & Geomech. Abstr.*, vol. 33, no 5, 443–454.
- Peila D. (1994) A theoretical study of reinforcement influence on the stability of a tunnel face. *Geotechnical and Geological Engineering*, 12, 145–168.
- Rospars C., Bourgeois E., Humbert P., de Buhan P. (2004) Modélisation numérique de la construction d'un mur expérimental en Terre Armée à Bourron-Marlotte à l'aide d'un modèle homogénéisé. Colloque international de Géotechnique, Beyrouth, 19–22 mai 2004, 275–280.
- Rospars C., Bourgeois E., Humbert P., de Buhan P. (2005) Modélisation numérique des sols renforcés par un milieu continu homogénéisé. 16th ICSMGE, Osaka, 855–858.
- Stille H., Holmberg M., Nord G. (1989). Support of weak rock with grouted bolts and shotcrete, *Int. J. Rock Mech. Min. Sci. & Geomech.*, vol. 26, no 1, pp. 99–113.
- Sudret B. (1999). Modélisation multiphasique des ouvrages renforcés par inclusions. PhD thesis, ENPC, Paris
- Wong H. & Larue E. (1998) Modeling of bolting support in tunnels taking account of non-simultaneous yielding of bolts and ground. *Proc. Int. Conf. on the Geotechnics of Hard Soils – Soft Rocks*, Napoli, Italy, 1027–1038.

Abandonment of caverns in rock salt mass

K. Staudtmeister & D. Zander-Schiebenhöfer

Institut für Unterirdisches Bauen, Universität Hannover, Hannover, Germany

ABSTRACT: When abandoning and sealing a cavern in rock salt mass after storage or brine production operations the cavern will usually be filled with brine. Cavity closure by creep of the salt rock mass and thermal expansion of the brine lead to a pressure build-up, while infiltration of brine into the rock mass reduces the internal cavern pressure. The internal pressure development of the cavern has to be calculated by a simultaneous computation of the state variables of all three systems involved (rock matrix, temperature, pore space) assuming a coupling via the internal pressure of the cavern.

In order to cover all significant influencing factors the mechanical and thermal state variables of the rock matrix as well as the pore pressure distribution have to be taken into account. The description of the infiltration behaviour of the rock salt under stress conditions as existing under cavern abandonment conditions is based on the results of the laboratory tests as well as on the results of field tests.

The main goal of the paper is to compare the results of numerical computations with respect to different cavern configurations and abandonment conditions and to describe the effects of the results regarding the long-term behaviour.

1 INTRODUCTION

When considering the long-term behavior of plugged and abandoned solution mined caverns filled with brine the question arises, if these caverns will be safe at any point in time after plugging. Here safety has to be investigated in terms of stability of the rock mass and changes of the environment due to fluid migration or brine disposition.

As a consequence of the creep behavior of rock salt, the stressing of the rock mass and the geometrical layout of the cavern a pressure build up in the fluid due to volume convergence of the cavern will increase with time. This leads to a state of stressing especially at the cavern roof where the fluid (brine) pressure approaches a level equal to or above the initial (primary) stresses of the rock mass. Figure 1 shows a schematic sketch of this pressure increase and a possible equilibrium state. The factor x in figure 1 is close to $0.5 \cdot h$ for an impermeable rock mass. Observations in field tests and laboratory investigations however showed that a permeation of fluid occurs, which is dependent on the initial permeability and an increased secondary permeability. This fact may reduce the factor x significantly and leads to an infiltration area of brine around the cavern as shown qualitatively in the figure.

When taking into account an additional pressure build up due to the reheating of the brine, which may have a lower temperature than the rock mass at the time

of plugging, an intermediate state develops, before the final equilibrium is reached.

Figure 2 shows, that this intermediate state can lead to internal pressures significantly above the lithostatic state of stresses.

From a rock mechanical and engineering point of view the following questions have to be investigated and evaluated:

- Can the pressure build up lead to the formation of macroscopic fractures with subsequent rapid loss of fluid and loss of the rock mass integrity?

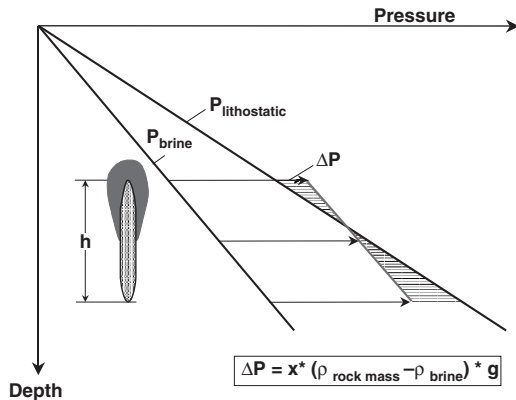


Figure 1. Pressure build-up in a sealed brine filled cavern.

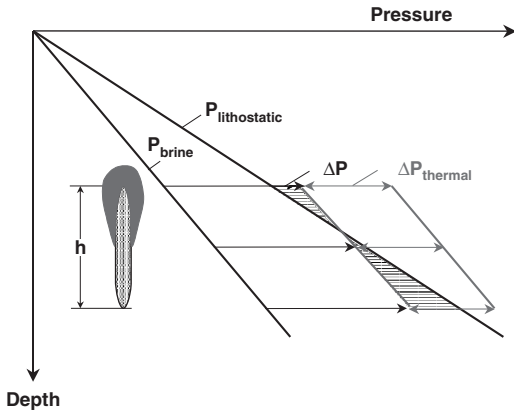


Figure 2. Influence of the thermal expansion of the brine.

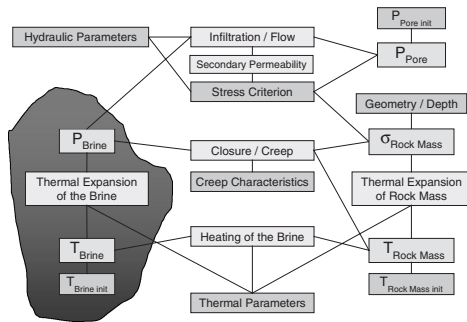


Figure 3. State variables and mechanisms during cavern abandonment.

- How can the interdependence between internal cavern pressure and fluid loss into the rock mass be described?
- What is the amount and extend of brine infiltration into the rock mass due to an increased secondary permeability?

2 BASIC MECHANISMS

In order to cover all significant influencing factors the mechanical and thermal state variables of the rock matrix as well as the pore pressure distribution have to be taken into account. Figure 3 shows the most significant variables and mechanisms. Further the pressure change in a sealed cavern is a coupled mechanism.

Cavity closure by creep of the salt rock mass and thermal expansion of the brine lead to a pressure build-up, while infiltration of brine into the rock mass reduces the internal cavern pressure. Therefore the internal pressure development of the cavern has to be calculated by a simultaneous computation of the state variables of all three systems involved (rock matrix, temperature,

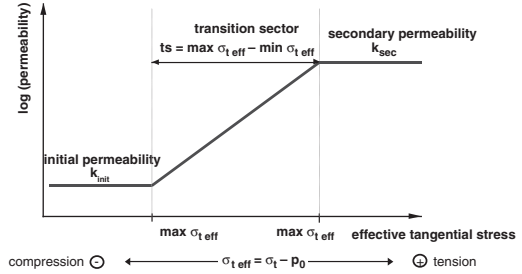


Figure 4. IUB criterion.

pore space) assuming a coupling of all the systems of state variables via the internal pressure of the cavern.

3 INFILTRATION CRITERIA

From laboratory tests different stress dependent criteria for permeability development in rock salt have been developed. The criteria describe the influence of the stress state in terms of σ_{teff} on the evolution of a raised or secondary permeability.

$$\sigma_{teff} = \sigma_t - p_0 \quad (1)$$

σ_t is the local tangential stress, which is the smaller stress component tangential to the flow direction. p_0 is the local pore pressure.

The IUB criterion states that a raised infiltration of the cavern fluid starts as soon as one component of the local principal stress state acting perpendicular to the spreading direction of the infiltration is lower in level than the internal cavern pressure acting at that point in time, which is equal to the pore pressure at the cavern boundary. The graphical representation of the criterion is shown in figure 4.

k_{init} and k_{sec} correspond to the initial permeability and secondary permeability, respectively. σ_{teff} is the difference between the minimal principal stress acting perpendicular to the flow direction and the pore pressure p_0 . $\sigma_{teff-min}$ and $\sigma_{teff-max}$ are the limits of the transition sector *TS* in which the development from an initial to a secondary permeability takes place.

Two alternative criteria are depicted in the figures 5 and 6. They show similar characteristics leading to an increase of permeability above a certain limit of tangential effective stress.

4 COMPUTATIONS

For the software implementations DARCY'S law is assumed for the brine flow. The treatment of the stress permeability criteria was carried out on the prerequisite that there is only a coupling from the stress state to the hydraulic parameters but not vice versa. Therefore the stress state can be treated as input parameter in the

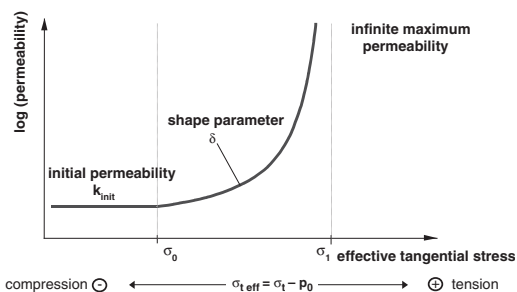


Figure 5. LMS criterion.

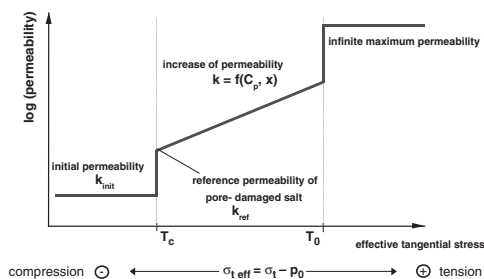


Figure 6. Generalised Stormont criterion.

form of the principal stresses for each element and time step. In the hydraulic calculations each time step the criterion is checked. The permeability at each point in time is taken into account according to the formulation of the chosen criterion. With respect to plugged cavern investigations the variables of state for the three different states of the rock mass (mechanical and thermal state of the rock mass and pore pressure state in the pore space of the rock mass) have to be calculated. As the pore pressures and the variables of state in the rock matrix are coupled from that point in time the cavern is plugged, they then have to be calculated simultaneously.

During the time of plugging the variables of state of each system (mechanical, hydraulical) are ruled by the condition of the pressure build up in the cavern. This internal cavern pressure build up is controlled by the balance of the pressure changes due to

- cavern volume convergence,
- thermal expansion of the brine in the cavern and
- the infiltrated volume of the brine into the rock mass.

In a plugged cavern the state variables of the three different systems (mechanical variables of state for the rock matrix, rock matrix temperature, pore pressure in the pore spaces) influence each other by changing the pressure level in the cavern. This is valid for every point in time simultaneously as soon as the cavern is sealed. This coupling can be expressed by a balance in terms of pressure changes in the cavern within each time interval from point in time t_{i-1} to t_i .

$$\Delta p_i = \Delta p_i^C + \Delta p_i^T + \Delta p_i^Q + \Delta p_i^S \quad (2)$$

with:

- Δp_i change of internal cavern pressure with respect to the end of the time interval
- Δp_i^C change of internal cavern pressure due to cavern volume convergence with respect to the end of the time interval
- Δp_i^T change of internal cavern pressure due to thermal expansion of the brine in the cavern as a consequence to the warming up with respect to the end of the time interval
- Δp_i^Q change of internal cavern pressure due to brine infiltration into the rock mass with respect to the end of the time interval
- Δp_i^S change of internal cavern pressure due to dissolution effects of salt in water under different pressure and temperature effects with respect to the end of the time interval

The theoretical determination of the individual pressure changes is described in /13/. For conditions of saturated brine at the time of plugging Δp_i^S can be neglected. The individual basic equations for heat conduction and finite element formulations are compiled in some basic literature (Carslaw & Jaeger 1978, Lewis & Schrefler 1987).

These changes in internal cavern pressure are calculated for every time interval. But, due to the time dependent material behavior of rock salt the solution for the variables of state with respect to the rock matrix have to be calculated by a time iteration scheme. Here an implicit Newton-Raphson formula is applied. After every completed time iteration the variables of state in the rock matrix are updated and the resulting changes of the internal cavern pressure are calculated again and updated. This second overlying iteration scheme for the determination of the cavern pressure change is continued until the calculated step by step changes in internal cavern pressure are below an error limit which is an input parameter.

Within this calculation process the pore pressures are always calculated simultaneously with the variables of state for the rock mass, because the permeabilities are assumed to be dependent of the rock matrix stresses via the tangential effective stress according to the three different criteria.

5 SENSITIVITY STUDY

5.1 Procedure

Within a sensitivity study the influences of the various boundary conditions and influencing parameters for a plugged and abandoned cavern filled with brine have been investigated. Starting with a reference model,

built for a typical cylindrical cavern, for each case study only one boundary value or parameter is varied. The investigated cases of cavern configurations are subdivided into four groups of study:

- geometrical parameters
- mechanical parameters
- hydraulic parameters
- thermal parameters

This paper gives by the way of example the results of the reference case and the variation of initial temperature conditions.

Geometric description

The assumed reference model is a cylindrical cavern with a radius of 25 m and a height of 300 m, giving geometrical volume of about 556,000 m³. The depth of the cavern roof is located at 1,000 m. The cavern is assumed to be a single cavern. The calculation model starts at a depth of 700 m and spreads downwards to the depth of 1,600 m.

Geologic description

The geologic formation is assumed to be entirely salt within a range of depth between 700 and 1,600 m. Geological layers other than salt are not considered in the calculation model.

Rock mechanical material parameters

The salt material is assumed to have a Young's Modulus of 20,000 MPa with a Poisson's ratio of 0.35. The creep behavior is described by the material law LUBBY2 with a set of parameters as shown in table 1, that represent a medium creep ability against the background of experience (Rokahr et al. 2002).

Hydraulic Description

The basic hydraulic parameters for the brine are taken into account as follows (Durup 1994):

- brine density $\rho = 1.208 \text{ t/m}^3$
- dynamic viscosity of the brine $\mu = 1.2 \cdot 10^{-3} \text{ Pa}\cdot\text{s}$
- compressibility of the brine in the cavern $\kappa = 2.7 \cdot 10^{-4} \text{ 1/MPa}$

Stress-Permeability Criterion

The permeability development with the tangential effective stress is described by the IUB-Criterion. Herein the following parameters are used:

Table 1. Reference parameter set for LUBBY2 material law.

Parameter	LUBBY2 – medium creep ability
$\bar{\eta} \frac{\kappa}{d} \cdot \text{MPa}$	$1.4 \cdot 10^{14}$
$m, \text{ 1/MPa}$	-0.31
$l, \text{ 1/K}$	-0.05

- Starting point for the development of a secondary permeability at tangential effective stresses σ_{teff} above 0 MPa.
- Maximum permeability is reached above $\sigma_{teff} > 2.5 \text{ MPa}$.
- Initial permeability is set to $k = 10^{-22} \text{ m}^2$.
- Induced secondary permeability to $k = 10^{-19} \text{ m}^2$.

Thermal description

The thermal conditions in the rock mass remain unchanged with time. The temperature of the brine in the cavern is considered equal at every depth to the state of temperature in the rock mass at the cavern wall. The brine in the cavern has already been reheated due to a long time interval with the cavern filled with brine. The coefficient of thermal expansion for the brine in the cavern is assumed with $\alpha_T = 4.75 \cdot 10^{-4} \text{ 1/K}$.

Primary state conditions

The primary state of stress is set equal to the stresses according to the overburden with the average density of the overburden $\rho_{salt} = 2.18 \text{ t/m}^3$. In the rock salt the primary state of stress is assumed to be isotropic, i.e. the primary stresses in all directions are equal at the same depth.

As for the primary pore pressures they are considered to be equal to the halmostatic pressure (i.e. equal to column of saturated brine) with the brine density $\rho_{brine} = 1.208 \text{ t/m}^3$. The primary state of rock temperatures is calculated from the assumption that the temperature in the rock mass at 1,000 m depth is 323 K and the temperature gradient with depth is 0.03 K/m.

Loading conditions

Prior to plugging of the cavern the internal pressure is equal to the brine column up to surface for approximately 3 years. This is necessary for the calculation of a realistic stress state of the rock mass for the point in time the cavern is plugged.

The investigated plugging interval is assumed with 100 years. This does not mean that caverns can only be plugged for 100 years. In case the calculations show still a pressure build up after this time interval of plugging, the investigated time has to be extended.

Calculation results

After plugging the most part of internal pressure build up in the cavern happens within the first 10 years. From then on only marginal internal cavern pressure changes occur. This can be observed in the principal stress vs. time spread out in figure 7 for a point in the cavern roof section. Close to the axis of symmetry two (tangential) stress components must be very similar. One principal stress component is equal to the internal cavern pressure. After approximately four years this stress component is equal to the circumferential stress component σ_φ . After this point in time the internal pressure exceeds

the circumferential stress. As proof of the coupling rule the internal cavern pressure at the cavern wall has to be equal to the pore pressure p_0 and vice versa.

Along with the build up of the internal cavern pressure the infiltration volume of brine develops as a result of two effects:

- First the pressure itself produces a higher pressure difference compared to the far field pressure and
- secondly the stress situation in the rock mass changes with the circumferential stress at the cavern wall being lower in level than the internal cavern pressure.

Consequently, due to the adopted tangential effective stress related permeability criterion, higher permeabilities are calculated for this specific area in the rock mass and hence the flow of brine is accelerated. Figure 8 shows the calculated values of the effective tangential stress for the rock mass along the cavern wall contour. After 100 years of plugging tensile tangential effective stresses (positive values) are produced over the upper 170 m of the cavern contour.

The zone of enhanced permeabilities expands into the rock mass with respect to time. This is shown in figure 9 at 100 years after plugging. In the roof section the zone of increased permeabilities at this point in time extends about 4.5 m into the rock mass.

Finally the cavern volume convergence rate and the accumulated brine infiltration volume have been calculated. While the rate of cavern volume convergence is down to below 0.1%/year, the flow rate of

brine infiltration is about $0.0016 \text{ m}^3/\text{d}$. In total about 100 m^3 of brine moved into the rock mass.

5.2 Variation of thermal initial condition

In this paper the following case will be presented in comparison with the reference case. It considers a pre-cooling of the rock mass as a consequence of a brine temperature at a temperature level of 30 K below the far field primary rock mass temperature during a time period of 10 years before plugging.

After 100 years of reheating/plugging the brine temperature approaches the level of the primary rock mass temperature up to 3.1 K. Principally, when temperature effects are included the plugging phase can be characterized by three phases.

In the *first phase* immediately after plugging the pressure in the cavern builds up faster than in the reference cavern configuration. About 10 years after plugging the peak level is reached. The area in the rock mass where the permeability is enhanced extends into the rock mass and downwards along the cavern contour. The greater the assumed initial gap of brine temperature with respect to initial primary rock mass temperature the higher this peak level of internal cavern pressure develops.

The maximum values of the tangential effective stress are higher compared with those for the reference cavern configuration and are increasing with the difference between brine temperature and primary rock mass temperature assumed at the beginning of sealing. For the chosen example $\Delta T = 30 \text{ K}$ the value for max σ_{teff} is 4.9 MPa. Figure 10 shows a plot for different points at the cavern contour versus time.

The *second phase* of the plugging interval starts around the point in time when the peak of the internal cavern pressure is reached. The build up rate due to thermal reheating declines, but the stresses immediately behind the cavern contour and along the cavern

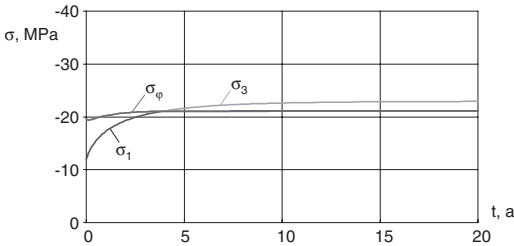


Figure 7. Principal stress components versus time.

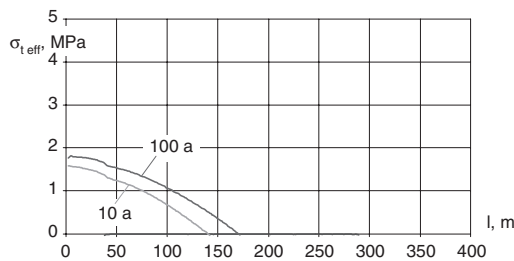


Figure 8. Effective tangential stress at cavern contour.

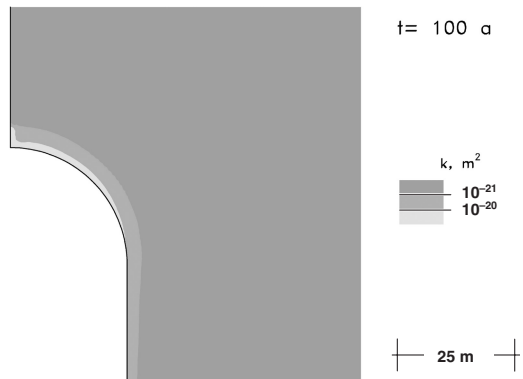


Figure 9. Zones of increased rock mass permeability.

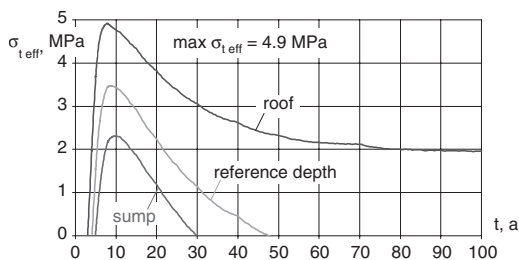


Figure 10. Tangential effective stress versus time.

height are of such a state that leads to volume enlargement of the cavern. At a specific point in time of plugging this divergent volume development consumes the pressure build up by thermal reheating. Thus the pressure in the cavern begins to decrease.

In the subsequent *third phase of plugging* the cavern volume convergence starts again from the deeper parts. While the cavern pressure is still decreasing, at a certain point in time, starting from the cavern sump the rock matrix stresses in the vicinity of the cavern wall become higher than the internal cavern pressure. At the same time the influence of the thermal induced cavern pressure build-up fades out, because the changes in temperature become smaller and smaller. The investigated plugging interval was assumed to be 100 years. At the end of this time interval the variables of state in terms of cavern internal pressure and rock mass temperature nearly reach the same level compared with the reference cavern configuration.

6 CONCLUSIONS

As part of a concept for an abandoned brine-filled cavern, confirmation is required that no macro-fracture can develop starting from the inner wall of the cavity. However, because brine infiltration into the rock cannot be prevented, the volume of infiltrating brine and its spread into the rock mass needs to be estimated.

It was revealed on the basis of the results of the laboratory tests that the effective tangential stress $\sigma_{t,eff}$ can

be utilized to describe zones of increased permeability in the salt rock to indicate the start and extent of an increased secondary permeability. Zones of these increased secondary permeabilities can then be localized as infiltration zones. The total amount of brine injected into the rock mass serves as a measure of the infiltration process.

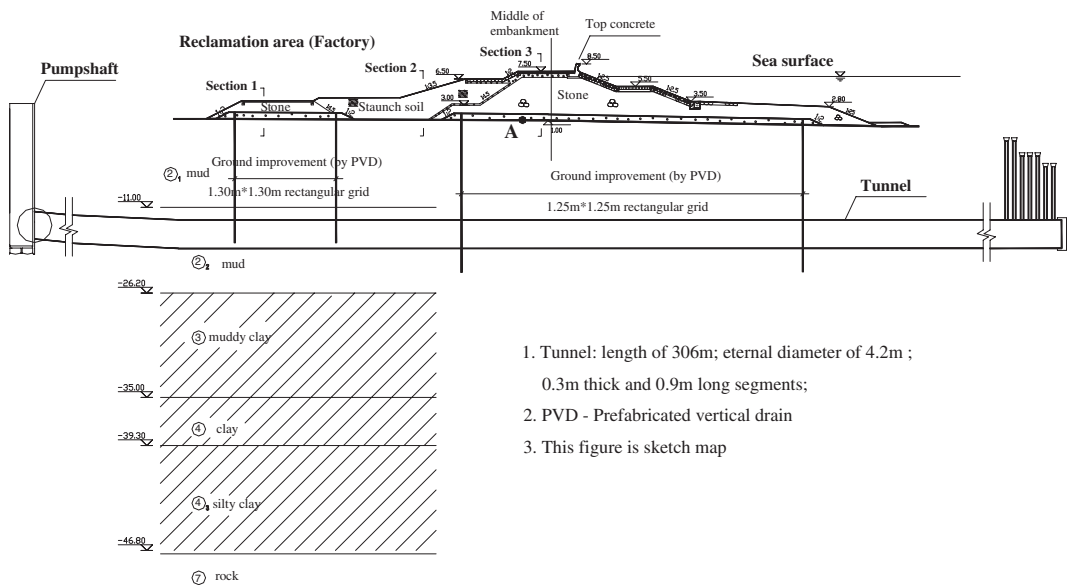
If the reheating is taken into account considerable higher values for the tangential effective stresses are calculated. At the same time the pressure build-up time for the maximum calculated cavern pressure is shorter. But the peak levels for the tangential effective stresses as well as for the internal cavern pressure are of an intermediate state. After the peak level of the cavern pressure is reached it decreases down to that level that has been calculated for the cavern configuration where the thermal effects of reheating are neglected.

The greater the temperature difference between brine and the far field rock mass at plugging time the higher the effective tangential stress will be. The extension of the zones of enhanced permeabilities are extended deeper into the rock and as well as deeper down along the cavern wall. But again this is intermediate with plugging time and will level with the long-term state for the same cavern configuration, if thermal aspects can be neglected.

Consequently every cavern, which is to be abandoned, needs to be investigated on a project-specific basis.

REFERENCES

- Carslaw, H.S. & Jaeger, J.C. 1978. *Conduction of Heat in Solids*. Oxford: Clarendon Press.
- Durup, G. 1994. SMRI Research and Development Project Report: Long-term Tests for tightness evaluations with brine and gas in salt (Field test No.2 with gas), SMRI Fall Meeting, Hannover.
- Lewis, R.W. & Schrefler, B.A. 1987. *The Finite Element Method in the Deformation and Consolidation of Porous Media*. Wiley & Sons.
- Rokahr, R.B. et al. 2002. High Pressure Cavern Analysis. Final Report of SMRI Research Project No. 2002-2 – SMRI.



1. Tunnel: length of 306m; external diameter of 4.2m ;
0.3m thick and 0.9m long segments;
2. PVD - Prefabricated vertical drain
3. This figure is sketch map

Figure 2. Profile of embankment, tunnel and distribution of the subsoil.

Table 1. Material properties adopted in the numerical analysis.

Layer		Mud	Muddy clay	Clay	Silty clay	Rock	Staunch soil
Constitutive model		Soft soil creep model			Mohr-Coulomb model		
Water content ω	(%)	63.4	63.3	47.4	31.7	—	—
Unit weight γ	(kN/m ³)	16.3	17.5	19.2	19	27	19.2
Young's modulus E	(MPa)	5.76	8.64	16.92	19.2	6.7E+04	16.82
Poisson's ratio ν		0.35	0.35	0.35	0.3	0.2	0.3
Cohesion c	(kPa)	8.7	10.2	20.1	9.1	35	17.7
Angle of shearing resistance ϕ	(°)	13.6	14.7	17.7	26	7.18	20.1
Permeability coefficient k_h	(m/d)	1.47E-04	2.59E-04	2.16E-03	4.00E-03	—	2.16E-03
Permeability coefficient k_v	(m/d)	1.47E-04	2.59E-04	2.16E-03	4.00E-03	—	2.16E-03
Modified compression index λ^*		0.06	0.05	0.037	—	—	—
Modified swelling index k^*		0.007	0.0075	0.006	—	—	—
Secondary compression index μ		0.0008	0.0008	0.0008	—	—	—

The in-situ measurements of settlement have been carried out. The measured data demonstrates that the post-construction settlement is quite large and will need long time to reach the stability.

2.2 Geological conditions

The tunnel studied here is the topside drainage tunnel shown in Figure 1. The profile of embankment and the tunnel is presented in Figure 2. The shield tunnel of 4.2 m in external diameter was lined with pre-cast

concrete segments of 0.9 m long and 300 mm thick. The total length of this tunnel is 306 m. The left head of the tunnel was fixed with the pump shaft and right one was located beneath the seabed. The distribution of subsoil is shown as Figure 2. The subsoil is characterized by a relatively low degree of consolidation and high water content, and the undrained shear strength is correspondingly low. The prefabricated vertical drain method (PVD) was employed to accelerate the dissipation of the excess pore pressure cause by the embankment filling in the vertical direction.

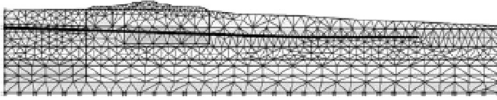


Figure 3. The finite element mesh used in numerical modeling.

3 NUMERICAL SIMULATION

Numerical analysis in the current investigation was conducted using the two-dimensional FEM PLAXIS (Brinkgreve and Bermeer, 1998). Fifteen node triangular elements were adopted in all finite element calculations.

3.1 Longitudinal settlement of tunnel

The behavior of the embankment stone is assumed to be governed by a linear-elastic relation with a Young's modulus $E = 4500$ MPa and a Poisson's ratio $\nu = 0.2$. The tunnel was assumed to be a very soft beam for its large slenderness ratio. The upper three layer soils were modeled using soft soil creep model to considering the creep behavior. The staunch soil of embankment and the lower two layers subsoil were supposed to be governed by an elastic perfectly-plastic constitutive relationship based on the Mohr-Coulomb criterion. Table 1 gives the parameters of the different material.

The dimensions of the mesh are given in terms of tunnel length and embankment height. The bottom boundary is fixed in all direction, and nodes on the two lateral boundaries are only allowed to move in vertical direction. The upper surface is free in displacement. Due to the pile foundation of the pump shaft, the pump shaft is assumed to be fixed; the left extent of mesh is located at the pump shaft. As for the consolidation boundary of the model, the bottom and two lateral boundaries are modeled as undrained. The finite element mesh used in numerical modeling is presented in Figure 3.

In the analysis, the embankment construction was modeled adopting consecutive filling to 1 m, 2.5 m, 4.2 m, 5.5 m, 6.5 m and 7.5 m similar to that followed during field construction.

3.2 Internal force of tunnel lining due to excessive settlement of embankment

In the analysis, three sections were chosen according to the different height of embankment. The locations of three sections are given in Figure 2. In order to consider the influence of the post-construction settlement of embankment, two simulations are carried out. One is that the embankment was modeled according to

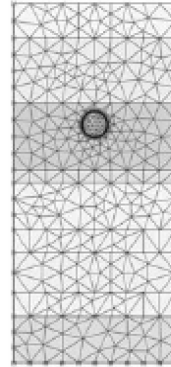


Figure 4. The finite element mesh used in numerical modeling.

the field construction process of the embankment. And in the other calculation, the embankment was assumed to be additional load according to its weight to obtain the force diagram of tunnel lining without influence of long-term behavior. Then the comparison between two calculations was presented.

The soils parameters, boundary conditions and the cases of simulation are all refer to that adopted in the modeling of longitudinal settlement. The finite element mesh used in numerical modeling is presented in Figure 4.

4 NUMERICAL MODELING RESULTS AND COMPARISON WITH MEASUREMENTS

4.1 Embankment base settlement

The monitoring program involved the measurements of (1) the vertical displacement of the embankment base and (2) the settlement of the tunnel. Only one set of the measurements was represented in Figure 2 corresponding to point A. Figure 5 compares the computed and monitored time-settlement curve of point A at the embankment base. The monitored data is from beginning of embankment construction to 233 days after completion of construction, total 653 days. Figure 5 shows a good agreement between the computed and monitored response and demonstrates that the post-construction settlement is quite large and will need long time to reach the stability.

4.2 Longitudinal settlement of tunnel

The settlement along tunnel is shown in Figure 6. The post-construction settlement of new-built embankment resulted in longitudinal differential settlement of tunnel. In Figure 6, one can find the maximum settlement

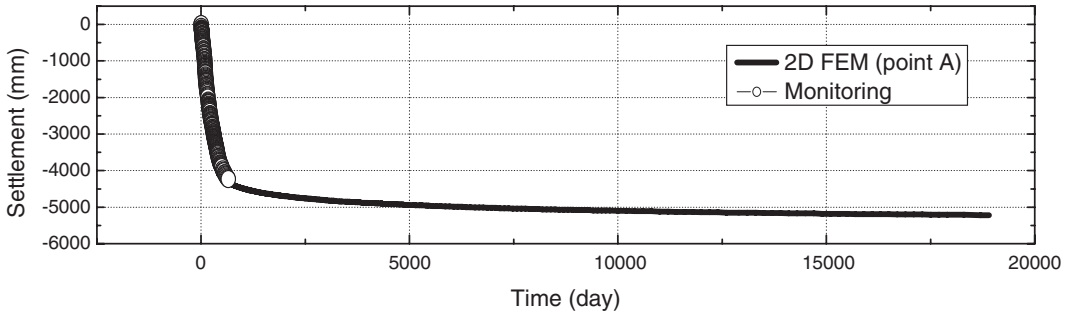


Figure 5. The time-settlement curve of point A.

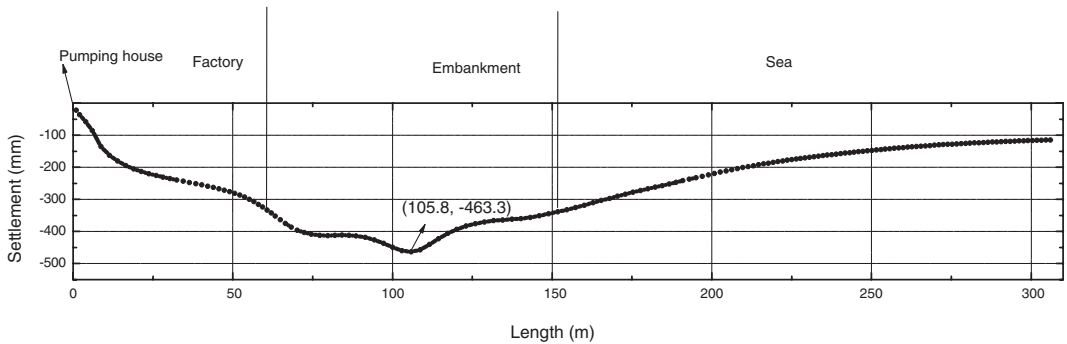


Figure 6. The final settlement trend along tunnel.

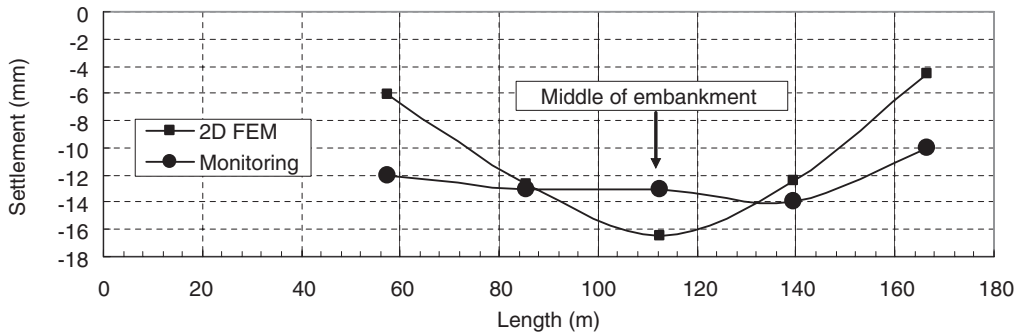


Figure 7. The comparison of calculated and measured tunnel settlement.

of 463.3 mm was attained at the location beneath the middle of embankment.

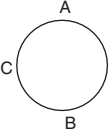
Figure 7 presents the comparison development between the computed and monitored settlements corresponding to 40 days after completion of tunnel construction. It shows a great agreement between the computed and monitored curve along the middle two quarters of the embankment base, which are of major

concern. However, the computed settlement is less than the monitored settlement near the embankment toes.

4.3 Internal force of tunnel lining due to excessive settlement of embankment

Table 2 gives the comparison of the bending moment and axial force of tunnel lining between with- and

Table 2. Bending moments and axial forces in the tunnel lining.

		M_{\max} (kN·m/m)			N_{\max} (kN/m)		
		Without	Considering		Without	Considering	
			Completion of tunnel	Stable state		Completion of tunnel	Stable state
Section 1	A	47.39	59.29	94.93	-210.59	-269.49	-232.66
	B	48.72	60.44	97.38	-238.63	-297.69	-261.63
	C	-49.68	-60.76	-96.69	-306.47	-382.46	-400.64
Section 2	A	78.98	79.74	136.95	-391.12	-370.03	-309.44
	B	80.48	80.94	141.74	-420.38	-399.48	-339.40
	C	-82.76	-81.05	-139.55	-542.88	-513.78	-541.51
Section 3	A	103.56	105.83	181.76	-530.62	-453.88	-374.53
	B	105.05	106.62	188.16	-559.86	-483.58	-405.83
	C	-108.26	-106.05	-183.65	-724.84	-631.87	-665.76

without-considering the influence of the embankment construction process corresponding to three sections.

It can be found that the bending moment and axial force distribution is similar regardless of considering the influence of the post-construction settlement of embankment or not. The maximum bending moment occurred at bottom of tunnel while the maximum axial force occurred at spring-line. The larger of the post-construction settlement of tunnel, the bigger increase of the bending moment of tunnel lining. However, compared to the bending moment, the axial force is less changed.

5 CONCLUSIONS

The influence on the shield tunnel of the post-construction settlement and additional load due to the excessive settlement of embankment in long term was studied based on numerical analysis and in-situ data. The main conclusions can be drawn as follows:

1. The long-term settlements of embankment in soft and compressible soils in coastland of Southeast China is quite large and need long time to reach the stability.

2. The post-construction settlement of new-built embankment resulted in large longitudinal differential settlement of tunnel crossing the embankment. And the maximum settlement occurred at the middle of embankment. Some actions have already been taken to diminish the differential settlement such as ground improvement beneath tunnel and design an original curvature for tunnel during the construction.
3. The post-construction settlement and differential settlement of tunnel can also result in the additional bending moment and axial force of tunnel lining besides the additional load of embankment.

REFERENCES

- Brinkgreve T.B.J. & Vermeer P.A. (1998). PLAXIS: finite element code for soil and rock analyses. Version 7. Plaxis B.V., the Netherlands
- Jin-Chun Chai et al. (2001). Simple method of modeling PVD-improved subsoil. *Journal of Geotechnical and Geoenvironmental Engineering*, Vol. 127, No. 11
- Samieh A.M. (2002). Analysis of earth embankments constructed on soft clay reinforced by stone columns. *Numerical Methods in Geotechnical Engineering*, Mestat (ed.), Paris

Excavation plan and preliminary support design of an underground control room using 3D analysis in soft and weathered rocks

F. Vahedi Fard & M. Talebi

Abgeer Consulting Engineers, Tehran, Iran

F. Jafarzadeh

Sharif University of Technology & Abgeer Consulting Engineers, Tehran, Iran

M. Dianat Nejad

Abgeer Consulting Engineers, Tehran, Iran

ABSTRACT: In this paper, proper and safe planning of excavation method and design of support system in very weak rocks with case study of control room of Silveh dam are discussed. Silveh earth-storage dam, with 102 m height; is under construction in North-West of Iran.

Due to numerous and various tectonic occurrences, the area of dam site is known as a high activity zone of Iran. In purposed location of control room, bedrock contains mostly weathered and crushed Shale and Schist. 60 m overburden and finite aquifers are another specific concern of this project.

In this paper by using 3D finite element modeling, different stages of excavation and support system installation have been analyzed for the explained control room. In this manner, stage excavation method (in accordance with NATM) is proposed. Finally, it is shown that allowable factor of safety is achievable by careful observing of all components of proposed support system. Plaxis 3D Tunnel software is applied for all of numerical modeling and analysis.

1 INTRODUCTION

Real estimation of mechanical parameters, analysis of materials behavior during and after excavation, using appropriate excavation methods based on material types and available technology and finally, adequate design and performance of preliminary and secondary support systems are most important considerations for underground projects. Reliable and accurate estimation of these factors could increase safety and construction rate and reduce costs and risk of projects. Among these parameters selection of appropriate analytical method has important role in design stage. For the most of tunnel projects, it seems that using of two-dimensional methods is suitable and compatible with real condition and the results are comparable with instrumentation outputs. Using three dimensional methods needs an extremely large number of numerical efforts and steps (Vermeer et al., 2001). However, for some underground projects application of three-dimensional (3D)

geometry is required. Underground control rooms and caverns are examples. The geometry of such structures makes it necessary to perform 3D analysis.

In this paper back analysis of an underground control room for a dam project is performed using 3D numerical method based on observed data and appropriate strength parameters and excavation details and sequences are proposed.

There are 3 main focuses of tunnel analyses (Vermeer et al., 2001), i.e.

- A tunnel heading stability
- B surface settlements
- C loads on lining.

The main focus will be on tunnel heading stability and loads on lining. For this purpose, a 3D sequential excavation is simulated and results have been discussed for optimizing excavation plan and preliminary support design with considering safety and cost.

2 CASE OF STUDY

2.1 Project specification

Silveh dam project is located in the Northwest of Iran on the Lavin River and mainly consists of:

- An embankment dam with a clay core, 102 m high and 750 m long at the crest elevation (1589.0 *masl.*);
- A diversion tunnel on the left bank with 5 m diameter and 841 m length;
- A ventilation shaft, 5 m diameter;
- A spillway on the right bank, 564 m long and 50 m wide and
- A control room in intersection of the access gallery and diversion tunnel, 12 m long and 13 m height.

The construction operation started on March 2004 with excavation of diversion tunnel. Due to complex geology and tectonic conditions, this tunnel has its share of problems during construction. Convergency measurements have been installed at 5 stations along diversion tunnel. Measured data showed that there was a considerable deformation in the walls at tunnel outlet, resulting in cracks in shotcrete. The preliminary strength parameters of materials have been modified by considering convergency measurement data in a 3D back analysis process (Ledema et al.).

In detailed design phase of project studies, a control room has been proposed in intersection of the access gallery and diversion tunnel, with 12 m long and 13 m height. Like diversion tunnel site, in this area, bedrock contains mostly unequal frequency of weathered and crushed Shale and Schist that has been induced by activity of major and minor existing faults in vicinity of dam site. These faults cause to crushing and intense reducing in bedrock quality. 60 m overburden and finite aquifers make other serious concerns for construction of this cave.

In this paper proper and safe excavation method and design of support system in very weak rocks with case study of control room of Silveh dam are discussed. Silveh earth-storage dam, with 89 m height and 750 m dam crest length; is under construction in North-West of Iran. At the moment water diversion system is carried out with excavating a tunnel with 841 m length located at the left abutment of dam valley. The valve chamber of Silveh dam is planed at control room located in intersection of the diversion tunnel with inspection gallery underneath of dam body axis. This chamber has spherical shape, 12 m length, and 13 m height of excavation (Abgeer Consulting Engineers, 1998 & 2004)

2.2 Site geology

The area is located in the Sanandaj-Sirjan geo-structural zone where both mountain ranges and the main faults

have Northwest-Southeast trend. Many tectonic activities such as strong folding and faulting accompanied by low metamorphism have affected this zone. Lavin fault is the main active fault of the concerned area passing along the Lavin River.

Control room is located in the left bank of the river and oblique faults branching out of the Lavin fault cross the diversion tunnel alignment. A thick overburden has covered the abutment and slopes; therefore, exact location of the faults cannot be determined easily.

The area consists of intercalation of Shale, Schist and dolomitic limestone. The rock mass, which is affected by faulting, folding and metamorphism are highly fractured and well jointed.

Three boreholes were drilled and 23 geo-electrical profiles carried out along and perpendicular to the diversion tunnel alignment. The specifications of major and minor faults were clarified based on the results of these explorations (Abgeer Consulting Engineers, 2002 & 2004).

3 EXCAVATION AND TEMPORARY SUPPORT SYSTEM

Due to poor quality of faulted zone in left abutment, an extensive soft rock support system has been foreseen during the detailed design stage. It will be proposed to excavate the control room in accordance with NATM method by sequential construction of top heading followed by bench and invert.

After each stage, shotcrete in section and front plane, radius grouting with 5 to 10 m depth and installation of steel frames at 0.5 m spaces are planed for temporary support of cave. Also, the drainage system has been proposed for increasing the short-term safety. Cross section of the control room is shown in Figure 1. (Abgeer Consulting Engineers, 2002 & 2004).

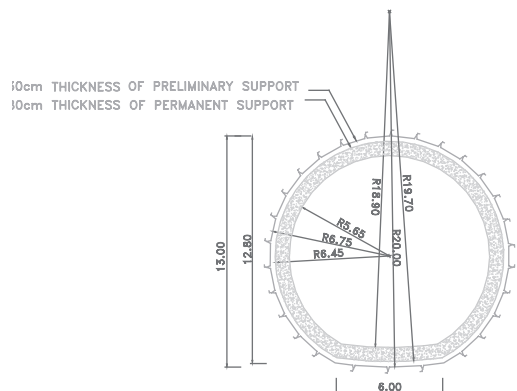


Figure 1. Designed section of the control room.

4 NUMERICAL ANALYSIS

4.1 Plaxis 3D tunnel

The Plaxis 3D tunnel program is a geotechnical finite element package specifically intended for the 3D dimensional analysis of deformation and stability in tunnel projects. In this program using of advanced constitutive models for simulation of the nonlinear, time-dependent and anisotropic behavior of soils and rock is possible (Brinkgreve et al., 2001). It offers a convenient option to create circular and noncircular tunnel sections composed of arcs and lines.

4.2 Geometrical model

Geometrical section of control room is shown in Figure 1. According to Figure 2, length of this room is about 10 m that is excavated in four 2.5 m stages.

Three dimensional wedge type elements with 15 nodes are used and total numbers of the elements were 1920 in numerical models. As seen in Figure 2, for increasing the accuracy of calculation, the FEM mesh is finer near tunnel and is coarser outward.

Geometrical section of control room simulated in this analysis has been presented in Figure 3. The section has been divided into 3 parts representing excavation stages (Abgeer Consulting Engineers, 1998 & 2004).

Sequential excavation has been presented in Figures 3 and 4. First, top segment then middle segment and finally lower segment of cave is removed accordingly excavation process. After each stage, temporary supporting was performed. Therefore, stability of control room along excavating is kept.

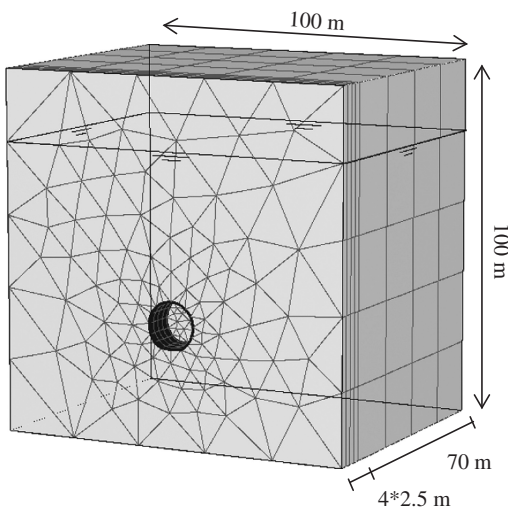


Figure 2. Generated mesh for numerical modeling.

4.3 Geotechnical parameters

Major parameters used in this paper are listed in Table 1. These parameters are based on field and laboratory geotechnical explorations. Ground water level is presumed in depth of 20 m below the ground surface. This assumption was presumed based on excavating in dry season.

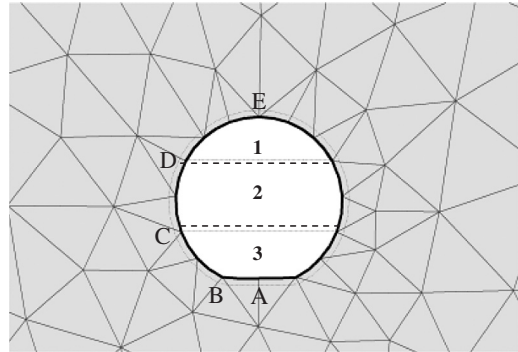


Figure 3. Geometrical section of control room.

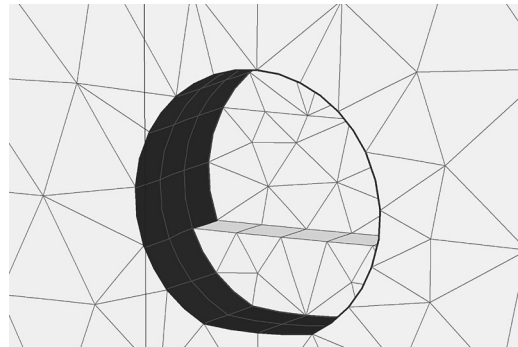


Figure 4. Sequential excavation modeling.

Table 1. Geomechanical parameters of material (resulted from back analysis).

Parameter/material type	High fractured, Schist and Shale
E_d (MPa)	294
Cohesion, c (MPa)	0.195
Friction angle, ϕ (Degree)	16
At rest parameter ratio, K_0	0.7
Natural density, γ (kN/m^3)	22
Saturation density, γ_{sat} (kN/m^3)	23
Poisson ratio, ν	0.3

To estimate the parameters, following cases was considered:

1. Sequential excavations of section of control room;
2. Shotcrete of section and front plane of tunnel after each stage;
3. Support installation at excavated section immediately after excavating;
4. Draining in order to decrease pore water pressure by constructing proper radial drainage;
5. Radial consolidation grouting, 5 to 10 m length.

The sequential excavations of front plane and tunnel were analyzed with the elastoplastic Mohr-Coulomb (MC) model. Its major parameters are cohesion, c ; and friction angle, ϕ . Other parameters of this model are Young's modulus, E ; and Poisson ratio, ν .

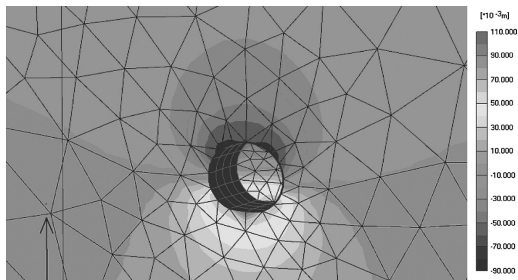


Figure 5. Vertical displacement contours at the end of excavation (max: 11 cm).

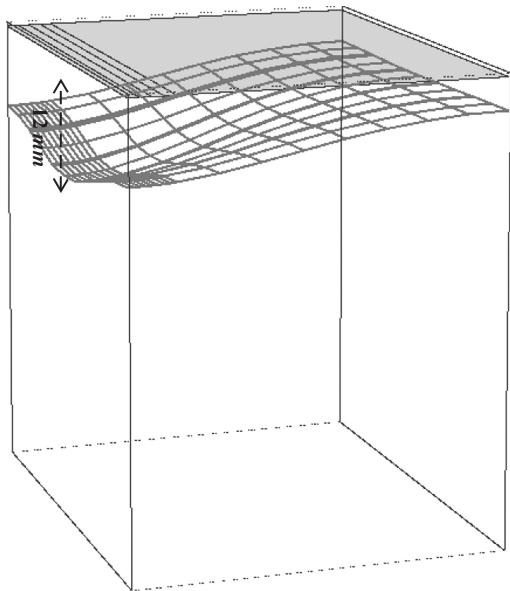


Figure 6. Settlement of ground level due to control room construction (max: 12 mm).

4.4 Results

Vertical deformation contours of control room at the end of excavation have been shown in Figure 5. As is clear from this figure, maximum displacement has been occurred in bottom of the cave and its value exceeds 11 cm upward demonstrating necessity of floor support installation. In top of the tunnel, maximum settlement is about 9 cm (Figure 5). Due to high depth of tunnel, displacement of ground level as can be seen in Figure 6, is low and equals to 12 mm.

In Figure 7, longitudinal deformation of tunnel heading has been shown at the end of the excavation process. Maximum corresponding value as can be seen in Figure 7, occurs at the center of front plane and equals to 24 cm toward removed zone. In Figures 8 and 9, vertical and total displacement contours at section passing from control room axis has been presented; respectively. This is clear that maximum movement take

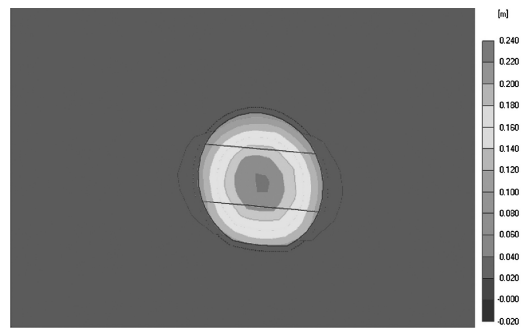


Figure 7. Heading longitudinal displacement at the end of construction (max: 24 cm).

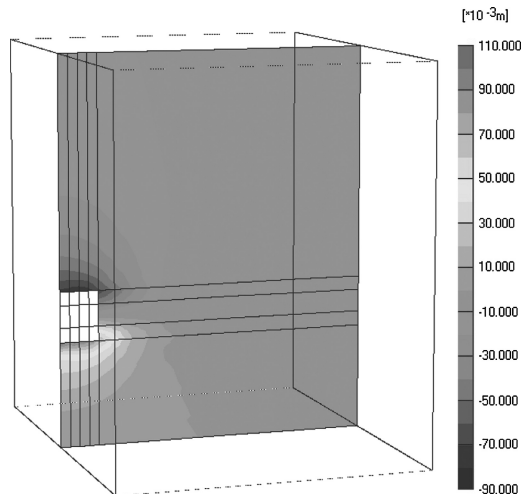


Figure 8. Vertical displacement at section passing from control room axis (max: 11 cm).

places at front plane. With regarding to results of analysis and wall improvement operation immediately after excavation, one of the most important subjects in evaluation of performance of tunnel construction is front plane behavior. This evaluation could not be observed in 2D analysis because 2D analysis is conducted by plane strain assumption that is unable to simulate longitudinal movement.

Therefore one of the most important results of this analysis is movement of front plane and its effect on excavation stability that can be modeled only in 3D analysis

Variations of maximum movement of supporting structure at the end of construction that can be seen in Figures 10 to 13 indicate that movements are relatively

small and in acceptable range. It should be mentioned that this maximum displacement occurs at the entrance of control room and decreases gradually toward the inside of chamber.

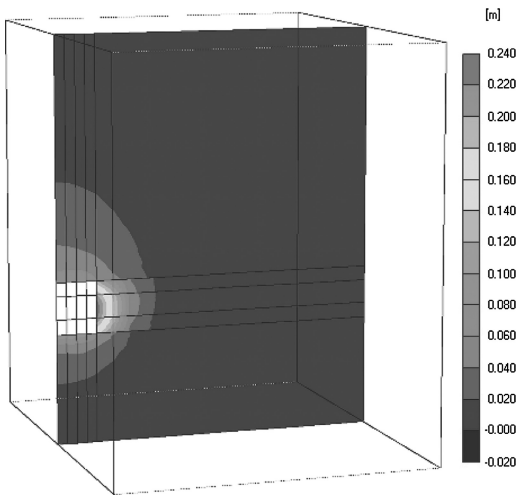


Figure 9. Total displacement at section passing from control room axis (max: 24 cm).

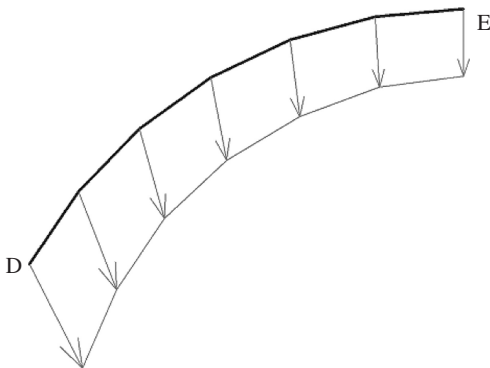


Figure 10. Crown support displacement at the end of construction (max: 14 cm).



Figure 11. Top bench support displacement at the end of construction (max: 17 cm).

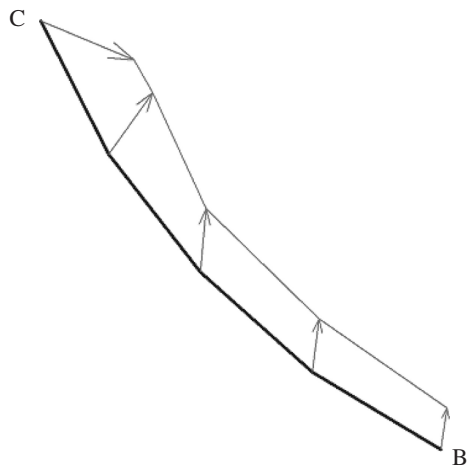


Figure 12. Bottom bench support displacement at the end of construction (max: 17 cm).



Figure 13. Invert support displacement at the end of construction (max: 11 cm).

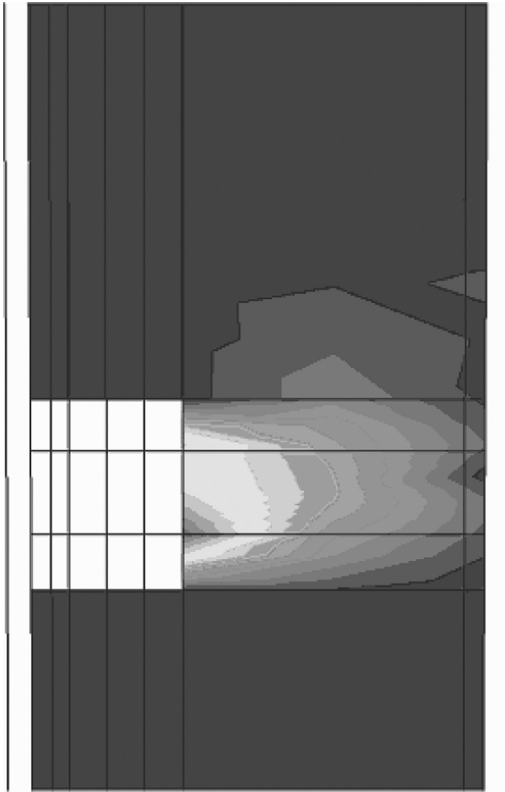


Figure 14. Displacement at section passing from control room axis in stability analysis (S.F. = 1.78).

5 SAFETY FACTOR

To investigate the stability of control room after excavating, stability analysis in order to determine of safety factor against failure was conducted. There is an option in Plaxis to compute safety factor. This option is Phi-c reduction in which strength parameters $\tan \phi$ and c of soil are successively reduced until failure of the structure occurs. In this approach, the factor of safety is defined as (Vermeer et al., 2002):

$$FS = \frac{\tan \phi_{real}}{\tan \phi_{failure}} = \frac{c_{real}}{c_{failure}} \quad (1)$$

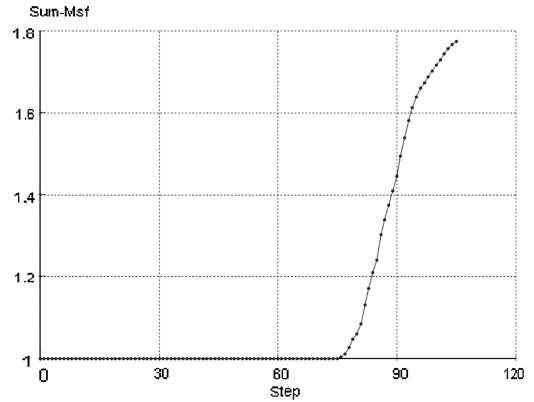


Figure 15. Performed calculation in stability analysis (S.F. = 1.78).

where $c_{failure}$ and $\tan \phi_{failure}$ are values at failure obtained by reducing the real shear strength parameters stepwise down to failure in an elastoplastic FE-analysis. According to results of this analysis, the factor of safety is about 1.78. The results are shown in Figures 14 and 15. As can be seen in Figure 14, critical instability is caused by front plane movement that has a significant effect on stability of excavation. This shows therefore that cave instability begins from front plane.

6 DISCUSSION AND CONCLUSION

In this paper, stability of temporary supports of control room with regard to real conditions and reports of Silveh dam project were investigated. Accordingly the following conclusions were obtained:

- It has been shown that a full 3D analysis of tunnel excavation is needed for the prediction of movement of front plane which can not be found in a 2D calculation.
- The current situation of control room located on fault axis, due to high tectonic activity has risky and unpredictable conditions. According to previous experience and results of analysis, construction of control room with 12 m height in this area is hard and dangerous. Accordingly, it is recommended to change (if possible) the location of control room and construct it in an area with better conditions. Otherwise, if the location of control room does not change, all practical concerns should be noticed and optimized along excavation process.
- Because of unpleasant effect of water in decreasing strength parameters that can clearly be seen in analysis, it is recommended that excavation process is conducted at dry seasons and excavating and

- supporting of control room with a proper schedule is completed from 2 to 3 months after beginning.
- In each section, excavation process is conducted in 3 stages including crown segment, bench segment and invert segment. After each stage, temporary support with regard to all proposed practical order is performed. Sequential excavations and supporting have significant effect on increasing safety of excavation and temporary stability of control room.
 - Due to safety problem, permanent support installation is necessary immediately after primary support installation.
 - Based on the details presented in this paper, permanent installation for control room is performed in three stages:
 - Steel ribs installation every 50 cm
 - Shotcrete
 - Radial consolidation grouting, 5 to 10 m length with regard to cement absorption.

For all presented numerical simulation results in this paper, it is assumed that all of the aforementioned stages are conducted in a convenient quality by an experienced contractor. Otherwise safety and stability is not satisfied.

Deformation control of the structure is very important for stability of the excavation in all sequences. Therefore, instrumentation and monitoring of the

structure is essential. Based on instrumentation observation and results, back analysis may be performed to update parameters and also primary and permanent support details.

REFERENCES

- Abgeer Consulting Engineers, 2002. Design of the diversion tunnel for Silveh embankment dam, Tehran, Iran.
- U.S army corps of engineers, 1997. Engineering and design tunnels and shafts in rock, Engineer manual 1110-2-2901.
- Abgeer Consulting Engineers, 2000 & 2004. Geological engineering report of Silveh embankment dam, Tehran, Iran.
- Ledeama, A., Romero, E. Systematic back analysis in tunnel excavation problems as a monitoring technique, Proc. 14th Int. Conf. Soil Mech. Found. Eng. 3, 1425–1428.
- Moller, S. C., Vermeer, P. A., Bonnier, P. G., 2003. A fast 3D tunnel analysis, Second MIT conference on computational fluid and solid mechanics, Boston, USA.
- Abgeer Consulting Engineers, 1998 & 2004. Site exploration and geotechnical investigation report for Silveh embankment dam, Tehran, Iran.
- Vermeer, P. A., Moller, S. C., Ruse, N., 2003. On the application of numerical analysis in tunneling. Post proceedings 12th Asian Regional Conference on Soil Mechanics and Geotechnical Engineering (12 ARC), Singapore, Vol. 2.
- Vermeer, P. A., Bonnier, P. G., Moller, S. C., 2002. On a smart use of 3D-FEM in tunneling. 8th Int. Symp. on numerical models in geomechanics, Rome, Italy.

Socorridos pumping station – numerical modelling

António Pedro & Jorge Almeida e Sousa

Department of Civil Engineering, University of Coimbra, Coimbra, Portugal

António Ambrósio & José Mateus de Brito

Cenorgeo, Lisbon, Portugal

ABSTRACT: The Socorridos pumping station is located in Madeira Island, Portugal, and is part of a system conceived to reutilize the water flow from a hydroelectric plant. This underground structure is 26 m high, 12 m wide and the rock mass at the site is of volcanic origin. In this article a brief description of the main characteristics of the project is presented and the results predicted by the design are compared with the values given by the instrumentation.

1 INTRODUCTION

The multi-purpose hydraulic system of Socorridos, located in Madeira Island, is composed of a vast network of reservoirs, tunnels and channels with the purpose of producing electric energy and supplying water to the region. The Socorridos pumping station belongs to this system and has four powerful pumps that, during low-consumption periods, send the water back to a reservoir located 460 m above in order to be reutilized by the turbines of an existent hydroelectric plant.

Due to its high complexity, particular care was assigned to the design and construction of the cavern for the pumping station (Fig. 1).

The main concerns were the geological and geotechnical characterization of the rock mass, the complete numerical modelling of the construction process and

the observation scheme to be adopted during the execution of the relevant works (Cenorgeo, 2005).

In this article, after a brief description of the project, special attention is given to the numerical modelling used for the design and to the confrontation of the predicted results with the observed ones during the construction works.

2 PROJECT CHARACTERISTICS

2.1 Location and geometry

Due to functional specifications, the location of the pumping station inside the volcanic rock mass was conditioned and so the portal is levelled with the embankment platform at the base of the slope, as seen in Figure 1a. Consequently, the cavern has a maximum cover of 22 m.

The dimensions of the cavern (Figs 2, 3), defined to allow the placement of the four pumps, as well as all the needed accessories, are 26 m (height), 12 m (width) and 44 m (length).

2.2 Geological-geotechnical characterization

Apart from the initial surface geological survey, the characterization of the rock mass included the execution of six rotary boreholes ($\phi 76$ mm). These allowed the recovering of rock samples for laboratory testing, the definition of the stratigraphy and the execution of six Lugeon tests and 20 dilatometer tests (LNEC), in order to characterize the permeability and the deformability of the rock mass, respectively.

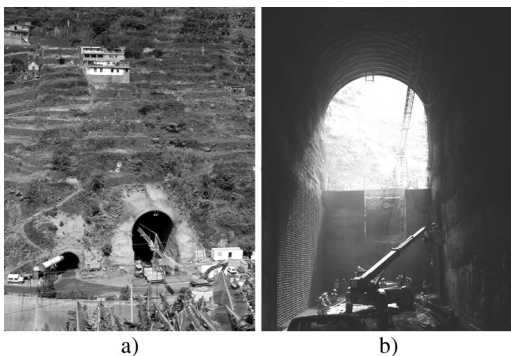


Figure 1. General view of the Socorridos pumping station – a) exterior; b) interior.

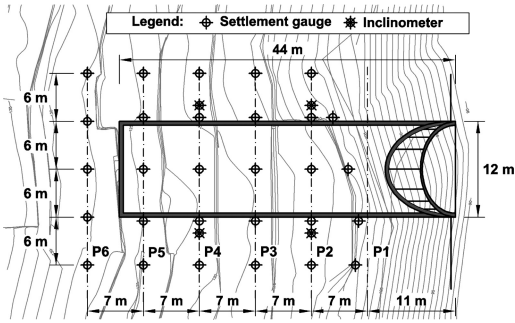


Figure 2. Top view and monitoring profiles.

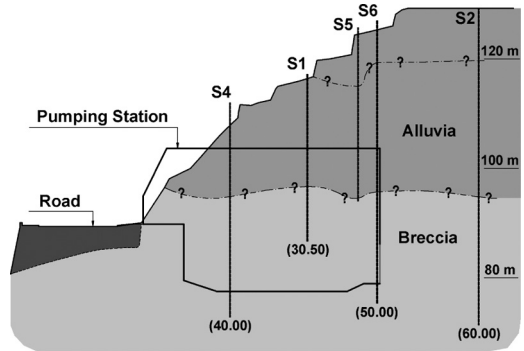


Figure 4. Geotechnical and geological profile.

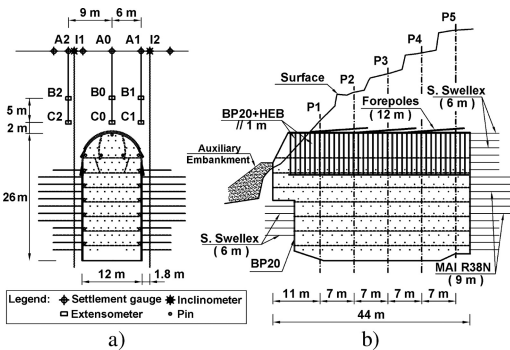


Figure 3. Geometry and instrumentation profiles – a) cross section; b) longitudinal profile.

With the recovered samples, 11 uniaxial compression tests were performed to evaluate the mechanical characteristics of the material. Further tests were conducted to determine its unit weight and porosity.

The rock mass zoning was established according to the geological survey, the results obtained during the drilling and the subsequent testing results and the experience of the designer in projects in similar materials.

Two distinct complexes with an almost horizontal interface were defined in the zone of the cavern excavation (Fig. 4). The first is located in the roof arch of the cavern and is constituted by consolidated and heterogeneous recent deposits – alluvia. The second, where most of the excavation is going to be performed, is composed of a mass of vulcanic breccia.

The geotechnical parameters defined as being the most representative ones for the two complexes are presented in Table 1 (Ambrósio et al. 2006).

2.3 Construction method and support system

Due to the geological and geotechnical characteristics of the hillside where the portal of the pumping station

Table 1. Geotechnical parameters.

Complex	γ (kN/m ³)	ϕ' (°)	c' (kPa)	E (GPa)	ν	K_0
Alluvia	21	32	60	1	0.38	0.65
Breccia	22	36	80	1.5	0.38	0.65

is located, the construction works started with its consolidation.

When this phase ended, the excavation of the station was started from the top by levels. Limits to the progression of the excavation were prescribed according to the geotechnical characteristics of the materials found during the works.

Because the roof arch has a small cover and is totally located in alluvia, the excavation of the cross section in the upper part of the cavern had to be done in more than one stage, as seen in Figure 3a. Firstly, a pilot tunnel was built with excavation steps of 1 m, which allowed to verify and validate the assumed geological and geotechnical conditions. Then, the complete top heading and the first bench were excavated, leaving a 12 m distance between each section.

The primary support used in the top heading (Fig. 3b) consisted in 20 cm thick of shotcrete with fibre reinforcement and steel ribs (HEB200) spaced 1 m, supported at the base by 9 m long rockbolts (self-boring MAI R38N). For the pilot tunnel, it was used a support consisting of shotcrete with fibres (15 cm thick) with HEB140 steel ribs spaced 1 m. All the upper zone of the cavern, excavated in recent deposits, was executed under the protection of a group of three sets of $\phi 73$ mm SCH40 forepoles, spaced 30 cm, each with a total length of 12 m.

The lower levels of the station were built in levels, 3 m high, allowing excavation steps of 3 m (12 m apart between different levels) in the longitudinal direction. The primary support for this part of the structure consisted of shotcrete with fibres (20 cm

thick) and a rockbolt mesh of 1.5×2.0 m, to prevent the rock mass from decompressing causing, eventually, blocks from falling. For the upper levels, self-boring, 9 m long MAI R38N rockbolts were adopted while for the lower levels, 6 m long Super Swellex bolts were chosen (Figs 3, 5b).

For the top walls, it was used shotcrete with fibres (20 cm thick). Also rockbolts were applied in the same pattern and kind as described for the transverse direction.

2.4 Instrumentation and observation

Considering the specific aspects of the project, the geotechnical and geological conditions of the site, and the spatial configuration of the cavern, an instrumentation plan was defined in order to allow: i) evaluation of safety during construction works; ii) comparison between the design assumptions and the observed behaviour; iii) extrapolation of the behaviour from the early stages of excavation to the later ones, in order to modify and adapt, if necessary, the construction methodology and the structural solutions according to the observed displacements of the rock mass.

In order to achieve this purpose, six instrumentation profiles were defined, with a distance of 7 m between them, which allowed measuring the following quantities: i) superficial settlements – 24 settlement gauges; ii) sub-surface vertical movements – six extensometer rods with two reading points each; iii) lateral movements – four inclinometers; iv) and convergences – through the use of several survey points. The location of these instruments is shown in Figure 3.

3 NUMERICAL MODELLING

3.1 General aspects

Due to the complex geometry and stratigraphy, 3D and 2D analyses were conducted in order to verify both the construction method and the chosen primary support. The 3D analyses were performed by the Finite Element Method software package PLAXIS 3D TUNNEL v1.2, which enabled the modelling of the soil-structure interaction and the complete excavation sequence. In Figure 5a, the finite element mesh used for stage 127 is shown. The entire calculation of the structure included a total of 142 phases, taking almost 16 hours to run (29000 elements mesh).

The behaviour of the rock mass was modelled by the Mohr-Coulomb model with the parameters presented in Table 1.

Particular care was given to the 3D modelling of the support where shell elements were used to model the vertical walls and the roof arch; solid elements were used to model the top walls and the forepoles and geotextile elements for rockbolts (Fig. 7).

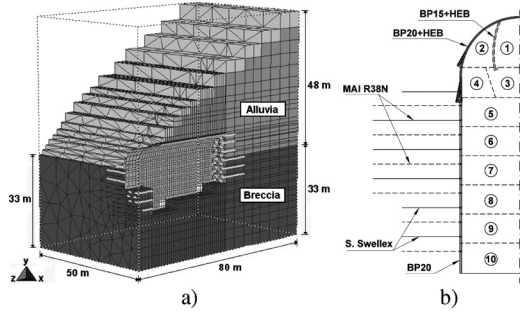


Figure 5. a) Finite element mesh (phase 127); b) adopted construction sequence.

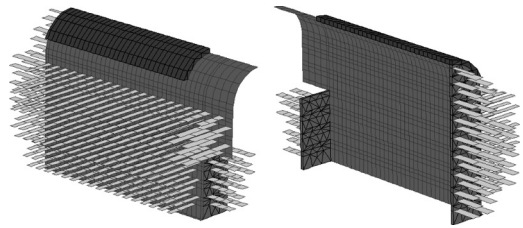


Figure 6. Primary support model of the pumping station.

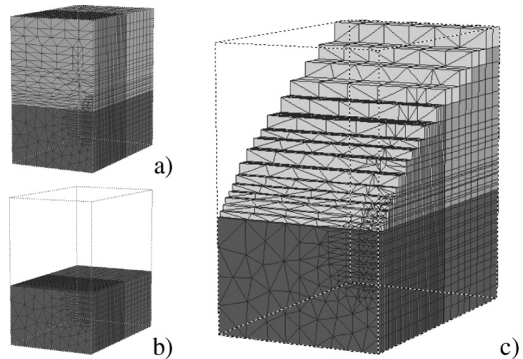


Figure 7. Terrain modelling – a) excavation; b) embankment; c) final aspect.

Tables 2 and 3 present the properties of all materials used to model the primary support.

The performed calculations characterized the expected displacements, used to define the warning levels for the structure, the stress state during the construction sequence and the forces in the structural elements of the support and, in particular, in the rockbolts.

Table 2. Rockbolts properties.

Designation	D _{ext} (mm)	e (mm)	A (mm ²)	EA (×10 ³)	Q _{fail} (ton)
MAI R38N	37	9.5	717	150.6	50
S. Swellex	54	3.0	480	100.9	17

Table 3. Structural elements properties.

Designation	γ (kN/m ³)	EA (×10 ⁶)	EI (×10 ³)	ν
BP20	24	5.80	19.3	0.2
BP15 + HEB	25	5.25	11.3	0.2
BP20 + HEB	25	7.44	31.3	0.2
Forepoles	–	1.60	85.3	0.2

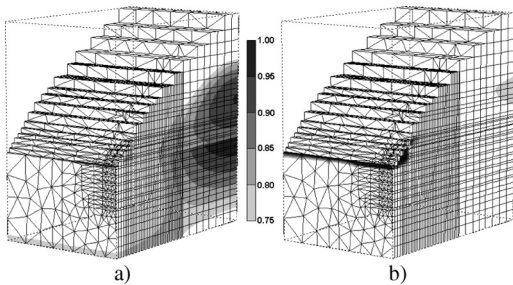


Figure 8. Relative shear stresses (initial stress state) – a) excavation model; b) embankment model.

3.2 Initial stress state

Because of the irregular terrain profile, it's difficult to simulate in PLAXIS 3D TUNNEL the initial stress state. To overcome this difficulty, two solutions were. In the first one, the initial stress state was determined by the unit weight of the terrain (and K0) for the whole mesh. Then, the alluvia were excavated in sequence until the desired terrain profile was obtained. In the second solution, the initial stress state was only generated for the breccia, followed by the staged construction of an embankment until the desired profile was reached (Fig. 7).

In Figure 8 the relative shear stresses for the two models are presented and it can be seen that the excavation procedure leads to higher stress levels and even to some plastification (Fig. 8a). The embankment model has, in general, lower stress levels, except near the portal zone where some of the stress points have reached the failure criterion (Fig. 8b).

3.3 Comparison between the two models

Eventhough the two models depart from different initial stress states, the results obtained after the

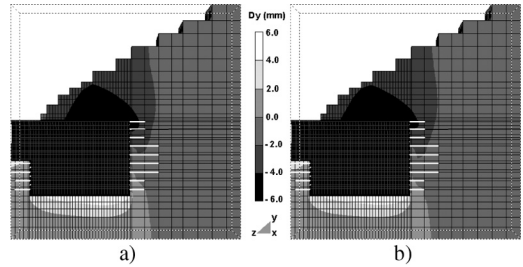


Figure 9. Vertical displacements – a) excavation model; b) embankment model.

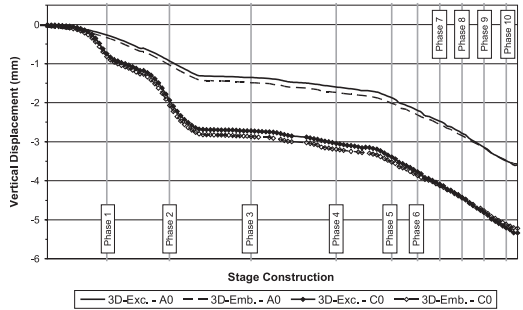


Figure 10. Evolution of vertical displacements – Profile P4.

excavation of the cavern were quite similar, especially for deformations.

The calculated vertical displacements for the last phase of the calculation are shown in Figure 9, where no significant differences between the two models can be pointed out. In both models, the maximum vertical displacement occurs at the top of the roof arch, in a section 15 m from the end of the cavern. Another important conclusion is that the excavation of the cavern doesn't seem to influence the stability of the hillside because no internal relevant displacements were obtained in the calculations.

From Figure 10 it is possible to conclude that the vertical displacements are similar for the two models, not only for the last phase but also during the complete excavation process. Another conclusion is that the largest percentage of displacements happens when the pilot tunnel is widened to the top heading. This effect tends to be reduced when the points are closer to the surface (point A0). After the conclusion of the top heading, it can be observed that the evolution of the displacements is almost constant in depth.

For horizontal displacements, a difference, although very small, resulted from the two calculations. The larger deformations were obtained when the terrain profile was generated by excavation (Fig. 11).

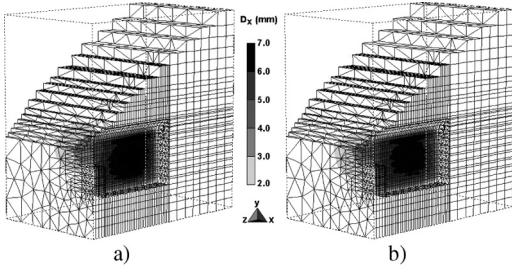


Figure 11. Transverse horizontal displacements – a) excavation model; b) embankment model.

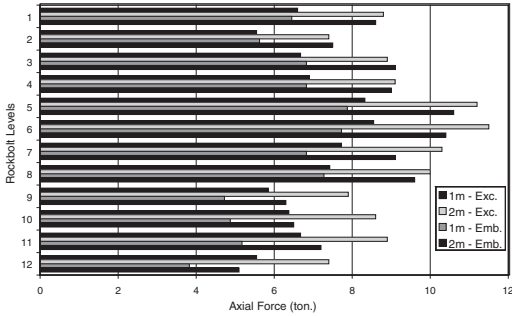


Figure 12. Axial force diagram for the rockbolts.

From the results of the 3D calculations, it can be concluded that rockbolts are indeed very important to maintain the stability of the vertical walls of the cavern. Due to this fact, several parametric studies were conducted in order to determine the influence of some parameters (both geotechnical and geometrical) in the rockbolt's mobilized axial force. In Figure 12 the result of one of these studies is shown for the two models. It can be concluded that if the rockbolt's spacing is changed from 1 to 2 m, the axial force becomes larger, but still far away from the failure loads (Table 2). It can also be seen that the mobilized forces are equivalent in both models, mainly in the upper levels. In the lower levels, the excavation model originates larger values.

From the economical and structural point of view, this parametric study allowed the designer to achieve an optimal solution for the bolt mesh.

4 COMPARISON BETWEEN THE PREDICTED AND OBSERVED RESULTS

As shown in the previous sections, no relevant differences between the two models were found and so the comparisons will only regard the observation data and the results given by the embankment model.

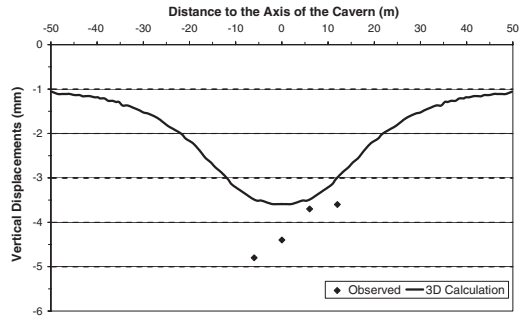


Figure 13. Surface settlement profile – profile P2.

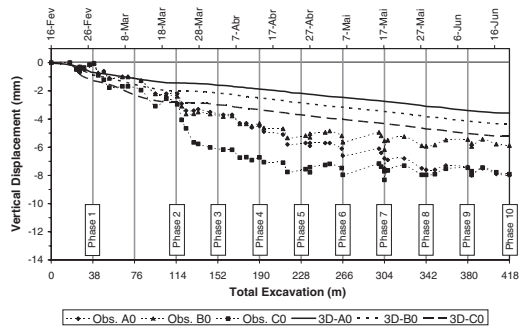


Figure 14. Evolution of vertical displacements (extensometer 0 – profile P4) with time.

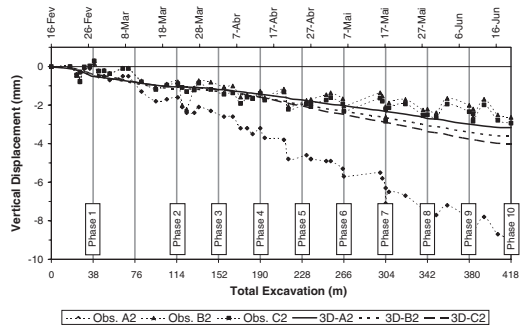


Figure 15. Evolution of the vertical displacements (extensometer 2 – profile P4) with time.

Figures 13 to 15 show both the vertical displacements yielded by the 3D calculation and the observation data from two profiles (P2 and P4).

The first figure has the results for profile P2. It can be concluded that the final displacements estimated by the numerical analysis agree well with those that have been observed (the latter ones are only a bit larger).

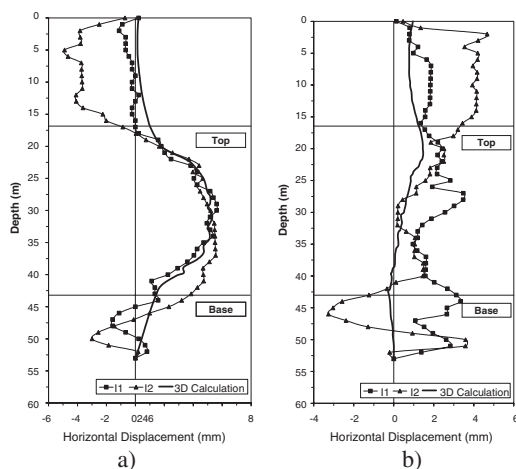


Figure 16. Inclinometer I1-2 a) x direction; b) z direction.

Figures 14 and 15 show the evolution of the vertical displacements for two distinct points of profile P4. At the axis (extensometer 0), the vertical displacements predicted by the calculation are smaller than the observed values. In extensometer 2, points B and C, the opposite occurs and the calculated displacements are larger. The biggest difference is found in point A, located at the surface, where the measured displacement was very large, especially when compared with the points at greater depths.

Finally, in Figure 16, the horizontal displacements recorded by the inclinometers located at profile P4 are compared with the results of the 3D numerical modelling.

In Figure 16a, the transverse horizontal displacement (x direction) are shown and good agreement between the calculations and the measured values can be seen, especially in the excavation zone where a maximum

displacement of 6.0 mm was obtained, against the 5.5 mm predicted by the numerical modelling.

The horizontal displacements in the longitudinal direction returned by the calculations were very small and in Figure 16b it is shown that they are in fact smaller than those obtained by the instrumentation.

5 CONCLUSIONS

The analysed project, concerning the Socorridos pumping station, presents a unique set of topographic, geotechnical, geological and geometrical characteristics. Due to this fact, special care was given to the geological and geotechnical characterization, to the numerical modelling of the construction sequence and to the observation system to monitor the construction works. After defining adequately the mechanical characteristics of the different formations, the 3D finite element analyses performed during design were able to predict with good accuracy the observed behaviour.

ACKNOWLEDGEMENTS

The authors would like to thank to Empresa de Electricidade da Madeira for authorizing the publication of this article.

REFERENCES

- Cenorgeo (2005). Aproveitamento de fins múltiplos dos Socorridos. Estação elevatória e túnel de restituição dos Socorridos. Projecto de execução (in Portuguese).
- Ambrósio, A., Brito, J.M., Rosa, S., Santos, J., Almeida e Sousa, J. & Pedro, A. (2006) *Estação elevatória e túnel de restituição dos Socorridos*, 10º Congresso Nacional de Geotecnia, Portugal (in Portuguese).

Deep excavations and retaining walls

Excavation-induced ground movements behind a single-propped wall

M.Z.E.B. Elshafie, R.J. Mair & K. Soga

University of Cambridge, Cambridge, United Kingdom

C.K. Choy

Geotechnical Consulting Group, United Kingdom

ABSTRACT: Ground movements behind a single-propped retaining wall were the focus of this study. This paper presents results from FE analysis of a single-propped wall in working conditions (typically with a Factor of Safety for strength = 1.5) in cohesionless dry soil. Assuming greenfield conditions a finite element study was conducted in which an elasto-plastic constitutive law was used to model the soil behaviour. The problem was solved in several stages with an increasing complexity of retaining wall construction. The ground movement values obtained were in good agreement with published field data. Settlements behind the wall extended up to 1.6 times the excavation depth. Horizontal movements were up to 2.5 times higher than the settlements and extended up to 3.5 times the excavation depth behind the wall. These conclusions provide guidance for practising engineers to assess the potential damage risk on structures adjacent to excavation sites.

1 INTRODUCTION

A substantial portion of the cost of excavations, especially in urban environments is related to the protection and/or repair of adjacent structures and utilities that may be damaged as a result of excavation-induced ground movements. The choice of a particular method of underground construction is often based, at least in part, on the potential ground movements associated with that scheme and the anticipated behaviour of nearby structures in response to those ground movements. So from the point of view of engineering design, planning and consultation purposes, the assessment of the degree of risk of damage, in terms of estimation of the magnitude and distribution of the excavation-induced ground movements, is highly important.

To estimate the total cost of a project involving underground construction more reliably, the engineer must evaluate the impact of the excavation on the surrounding properties. To perform this function, engineers require information that will enable them to do the following:

1. Estimate the range of typical ground movements for particular soil conditions and underground construction procedures.
2. Evaluate the response of the affected structures and utilities to the anticipated ground movements. This forms a basis for estimating the potential for

damage, selecting protection schemes and developing a system for monitoring and remedial measures.

The focus of this paper is devoted to Point 1. The conclusions drawn out from this study are based on the results that were obtained by the following sequence:

- a. Documented field data for cantilever retaining walls was compiled from the literature published over the last three decades.
- b. A finite element model was constructed using ABAQUS software. The inputs of the model were validated by the compiled field data.
- c. A centrifuge model for a cantilever retaining wall in dry sand was tested and the results were compared with field data and the finite element model from points a & b above.
- d. Using the same input parameters obtained from point b above, a prop was added at the top of the retaining wall. The prop was introduced in stages with increasing level of complexity until a reasonable simulation had been reached.

2 METHODOLOGY

The methodology followed in this study is described in [Sections 2.1 to 2.4](#) below. The sections correspond to the four points (a to d) mentioned above.

2.1 Field measurements of soil movements at greenfield sites

The first practical approach for estimating movements for in-situ wall systems was proposed by Peck (1969). Peck's chart defines three categories of behaviour, with the smallest movements indicated for sands, stiff clays. The maximum settlements near the wall for Category 1 (stiff clay and sand) are 1% of the excavation depth while those for Category 2 (very soft to soft clay) are 2% of the excavation depth.

Clough and O'Rourke (1990) updated the available data at that time in terms of the new wall construction technologies that had emerged since earlier periods. They had found that for in-situ walls in stiff clays, residual soils and sands:

- The value of the maximum wall deflections tend to average about 0.2% of the excavation depth and could reach 0.5% of the excavation depth.
- The soil settlements tend to average about 0.15% of the excavation depth.

Long (2001) reported that average maximum horizontal wall deflection (δ_{\max}) values for cantilever walls wholly embedded in stiff soils were about 0.4% of the excavation depth. He also considered maximum ground settlements behind the walls and found that average values were about 0.2% of the excavation depth.

The field data compiled over the past three decades, as summarised above, was used to validate the finite element model input parameters.

2.2 Finite element modelling

All geotechnical problems involving retaining structures are three-dimensional and ideally, a three-dimensional analysis of fully incorporating the structures' geometries, loading conditions and variations in ground conditions across the site should be undertaken. With current computer hardware this is not a practical proposition, except for a very limited number of cases. It is therefore necessary to make a number of simplified assumptions. It is common to conduct two-dimensional plane strain analyses. It is frequently assumed that there is an axis of symmetry about the centre-line of an excavation and that only a half section needs to be modelled. In this study construction process of a cantilever retaining wall was simulated using ABAQUS finite element software. The aim of this FE analysis was to construct a computational model that predicts the wall and soil deformations reasonably well when compared to field data.

2.2.1 Problem geometry, boundary conditions and initial conditions

The complete problem together with the finite element model adopted for analysis is shown in Figure 1.

The geometry of the problem (excavation depth and height of the retaining wall) was chosen so as to have a factor of safety (for strength) against overturning of about 1.5. In practice, walls are usually designed for such values for temporary works. The initial conditions for the model were:

- The density of the soil is 1800 kg/m³.
- Earth pressure coefficient at rest K_0 is 1.5 (simulating over-consolidated soil).

2.2.2 Soil constitutive model

2.2.2.1 Model elasticity

A porous elastic model (a built-in model in ABAQUS/CAE and ABAQUS/standard software) was used for modelling the elasticity of the soil elements. It is a stress-dependent isotropic elastic model in which the mean stress varies as an exponential function of volumetric strain.

The elastic part of the volumetric behaviour of porous materials is modelled using the following equations:

$$\delta\varepsilon_v = \left(\frac{\kappa}{vp'} \right) \cdot \delta p' \quad (1)$$

where $\delta\varepsilon_v$ = infinitesimal change in volumetric strain; κ = logarithmic bulk modulus; p' = effective mean stress and v = specific volume. The shear behaviour of the model is defined by:

$$G = \frac{vp' 3(1-2\nu)}{\kappa 2(1+\nu)} \quad (2)$$

where G = the shear modulus and ν = Poisson's ratio.

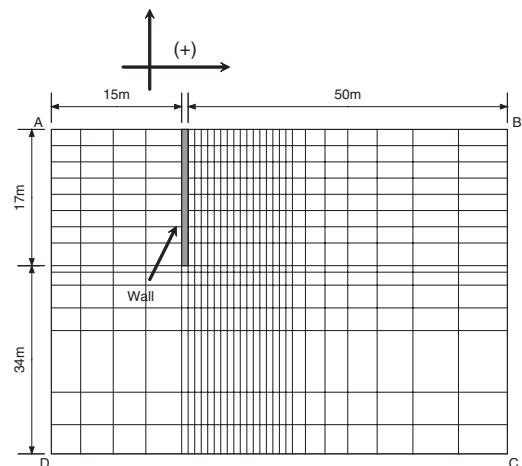


Figure 1. The mesh adopted in the FE analysis.

2.2.2.2 Model plasticity

The Drucker-Prager plasticity model (a built-in model in ABAQUS) was used to model soil plasticity, which has the following characteristics:

- The yield criterion is written as:

$$F = q - p' \tan \phi' = 0 \quad (3)$$

where q = deviatoric effective stress and ϕ' = critical state soil friction angle.

- It generally allows for soil dilation: the flow rule, defining the plastic straining, allows simultaneous plastic dilation (volumetric increase) and plastic shearing using a dilation angle ψ .

The effect of the dilation angle was found to be minimal behind the retaining wall; this is mainly because the shear strains, at 8 m-excavation depth, behind the wall are small in contrast to the strains at the bottom of the excavation where the angle of dilation is expected to have a large effect on the soil movements.

2.2.3 Simulating the excavation process

The excavation process was modelled by removing elements in front of the wall to the required depth of excavation. The excavation was divided into several steps and at the end of each step two metres of soil were excavated. (For further details see Elshafie, 2004).

2.2.4 Summary of model input parameters

The sand and concrete model properties adopted in the finite element analysis are summarised in Table 1. Two points need to be mentioned here: The first is that a typical value of κ used for sand is 0.015, but this lead to unrealistic soil settlement profiles due to the lack of small strain stiffness model in ABAQUS. Therefore, a modified value of 0.0015 was used. This value was obtained by comparing the FE results for soil and wall displacements with field data described earlier in the paper.

The second point is that two different soil friction angles (25° and 35°) were adopted while keeping all other input parameters the same. This was done to examine how the soil strength influenced the distribution and magnitude of soil displacements.

2.2.5 Finite element model results for a cantilever wall in dry sand at greenfield conditions

The surface settlement predictions in greenfield conditions are shown in Figure 2 with the x-axis representing the horizontal distance behind the wall (x) normalised by the depth of excavation (H) and the y-axis representing the soil settlement (S_v) normalised by the depth of excavation (H). The figure also shows the development of the soil settlement profile at different excavation depths. The soil settlements extended to a distance of 1.4 times the excavation depth with a cantilever shape

profile. At 8 m-excavation depth, the maximum settlement immediately behind the wall is about 0.2% H , which agrees quite well with field data that were presented in Section 2.

The horizontal soil surface displacements (S_h) versus the horizontal distance behind the wall are shown in Figure 3 with both axes normalised by the depth of excavation (H). The horizontal displacements were generally higher than the surface settlements and extended to a distance more than 3 times the excavation depth. Figure 3 shows a maximum horizontal displacement of 0.35% H compared to a maximum settlement of 0.19% H as shown in Figure 2.

The wall deflection (w) curves for the first eight-metres of excavation are shown in Figure 4, with the horizontal axis normalised by the excavation depth. The normalised maximum wall deflection of 0.37% H at 8 m-excavation depth compares well with the value reported by Long (2001) mentioned earlier.

2.3 Centrifuge model

A centrifuge test of a cantilever retaining wall in dry sand was performed on the 10-metre beam centrifuge at the Schofield Centre, Cambridge University. The model wall was 225 mm high and the test was carried out at a scaling factor of 75 (Elshafie et al., 2006). It is well worth noting here that the dry sand used in the

Table 1. Properties of the model materials.

Property	Sand	Concrete
Kappa (κ)	0.0015	–
Poisson's ratio (ν)	0.2	0.15
Dilation angle (ψ) (deg.)	17.5	–
Voids ratio (e)	0.6	–
Density (ρ)	1800 kg/m ³	2400 kg/m ³
Elastic modulus	–	20 GPa
Critical state friction angle (deg.)	25 & 35	–
Soil/concrete interface angle of friction (deg.)	–	25

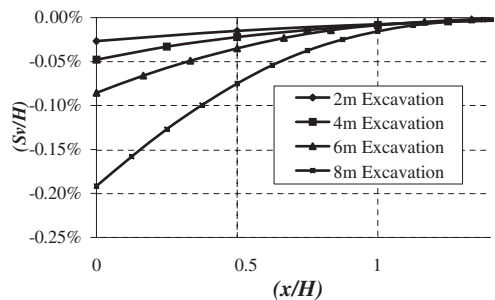


Figure 2. Normalised surface settlement versus normalised horizontal distance behind the wall.

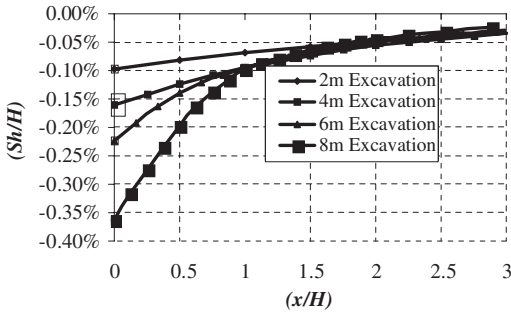


Figure 3. Normalised surface horizontal displacements versus normalised horizontal distance behind the wall.

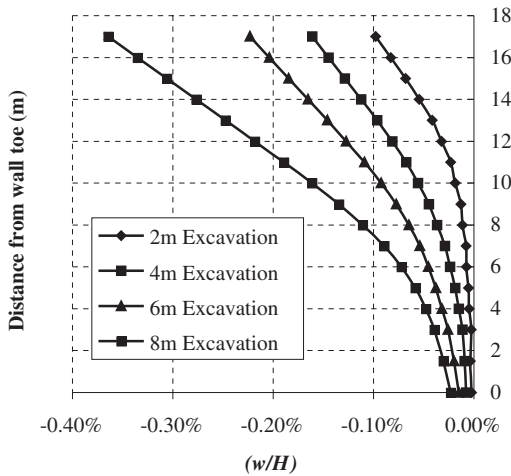


Figure 4. Normalised horizontal wall deflections along the wall.

centrifuge model had a critical state angle of friction of 32 degrees, whereas the finite element analyses performed earlier was for dry soil of angles of friction of either 35 or 25 degrees.

Figure 5 shows the comparison of soil surface settlement with the centrifuge test results and the finite element predictions at an excavation depth of 8 metres.

It is worth noting here that all the FE analyses were completed before any of the centrifuge tests were done.

The soil settlement profile obtained from the centrifuge results fits between the FE predictions using angles of friction of 25° and 35°. The curvatures of the curve for the centrifuge data and the FE prediction for $\phi' = 35^\circ$ show reasonably good agreement. The normalised maximum soil settlement recorded in the centrifuge test at a depth corresponding to 8 m in prototype is 0.28%H, which compares well with the field data mentioned earlier.

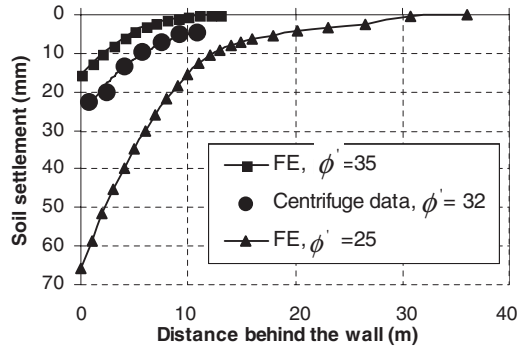


Figure 5. FE predictions – centrifuge test results comparison for soil settlement at an 8-metre excavation depth. (Prototype scale).

2.4 Single-propped wall

The same input parameters adopted for the cantilever wall were used for simulating the excavation for the single-propped wall. The prop was initially simulated simply by applying a zero displacement boundary condition. The prop was located at the top of the wall and was introduced in the analysis after four meters of excavation. This study aims to investigate the soil displacements from a single-propped wall at working conditions (i.e Factor of Safety (for soil strength) against overturning = 1.5). Therefore soil displacements are reported here for an excavation depth of 12 meters.

The normalised greenfield soil settlement profile is shown in Figure 6. The maximum settlement occurred at some distance (0.2~0.3 H) behind the wall with the curve having sagging and hogging zones. Generally the soil settlements were smaller than the cantilever wall and they extended up to 1.6 times the excavation depth (similar range of cantilever wall). The normalized horizontal displacements profile in Figure 7 shows a similar profile to the settlements with the values as large as 2.5 times the settlement values. Compared to the cantilever horizontal movement profile, the values of Figure 7 are smaller. The wall deflections at different excavation levels are shown in Figure 8. After the prop was installed, a ‘bulging’ appeared at a distance from the top of the wall and increased as the excavation went on. Before installing the prop, the wall deflects in a cantilever shape as seen in Figure 8 for the first four meters of excavation. Figure 9 shows the normalised wall deflections at an excavation depth of 12 meters.

Instead of using a zero-displacement option as described above, a ‘realistic’ prop was included in the analysis in order to simulate the excavation process realistically.

The prop was included in the analysis by using a structural element that had a circular cross-section

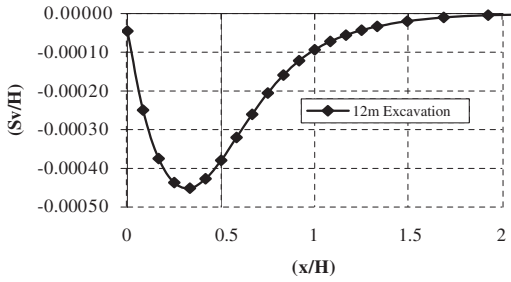


Figure 6. Normalised surface settlement versus normalised horizontal distance behind the wall. (prop simulated as no displacement boundary condition).

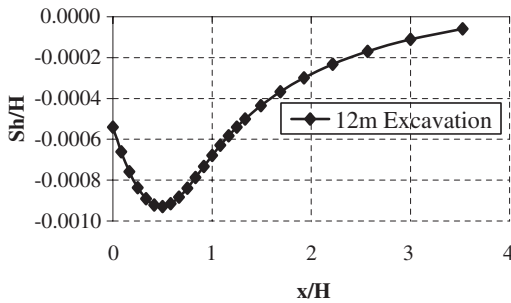


Figure 7. Normalised surface horizontal displacements versus normalised horizontal distance behind the wall. (prop simulated as no displacement boundary condition).

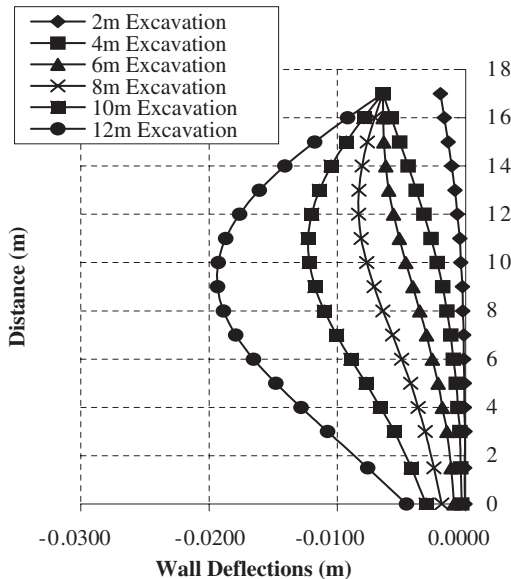


Figure 8. Wall deflections at different excavation levels (prop simulated as no displacement boundary condition).

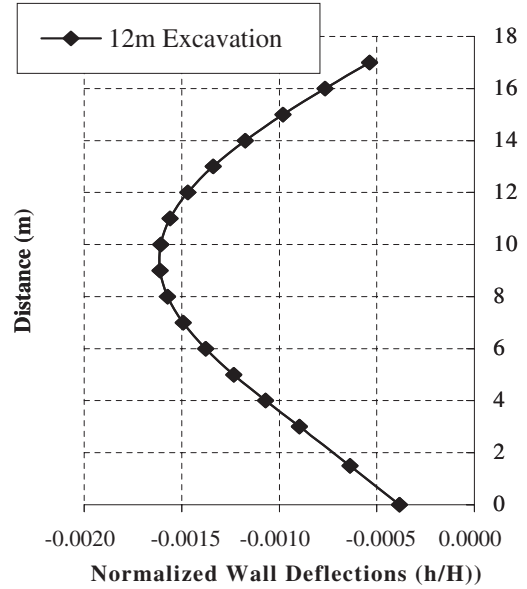


Figure 9. Normalised wall deflections at 12 m excavation level.

with a diameter of 0.25 m. The structural element has two ends, one connected to the retaining wall with the connection allowing rotation only. The other end was not allowed to rotate even though it was allowed to displace vertically only.

The normalised soil settlement, horizontal displacements and wall deflection can be seen in Figures 10 to 12. When the results are compared to the previous simulation results, the flexibility of the prop resulted in extra soil and wall deformations.

The soil maximum settlement and maximum horizontal displacement for the realistic prop are about an order of magnitude larger than the case of the rigid prop. The maximum wall deflection increased from 0.16% H to 0.22% H but showing less curvature compared to the rigid prop case.

The influence of the stiffness of the retaining wall was also studied. Figure 13 shows 10 case histories reported by Long (2001) for single propped walls in sand. The figure shows the normalized maximum wall deflections versus the system stiffness. The figure includes data points obtained from the finite element analysis for rigid prop and a realistic prop with the retaining wall thickness being 0.8 m as well as a data point for a realistic prop with the retaining wall thickness being 1.5 m. The system stiffness as defined by Clough and O'Rourke (1990) is calculated as follows:

$$\text{System Stiffness} = \frac{(EI)_{wall}}{\gamma_w s^4} \quad (5)$$

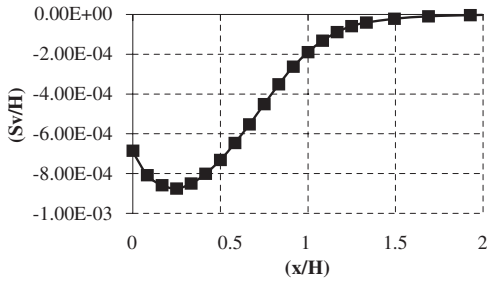


Figure 10. Normalised soil settlement at 12 m excavation depth versus normalised horizontal distance behind the wall (prop simulated as a structural element).

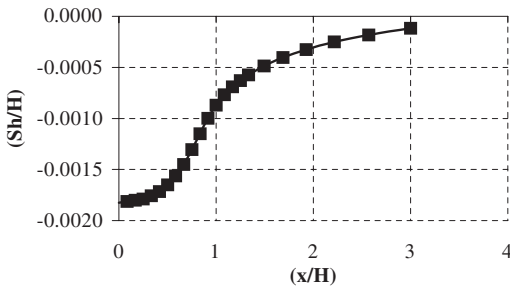


Figure 11. Normalised soil horizontal displacements at 12 m excavation depth versus normalised horizontal distance behind the wall (prop simulated as a structural element).

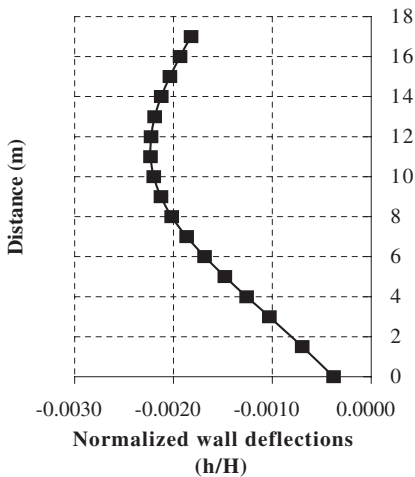


Figure 12. Normalised wall deflection (prop simulated as a structural element).

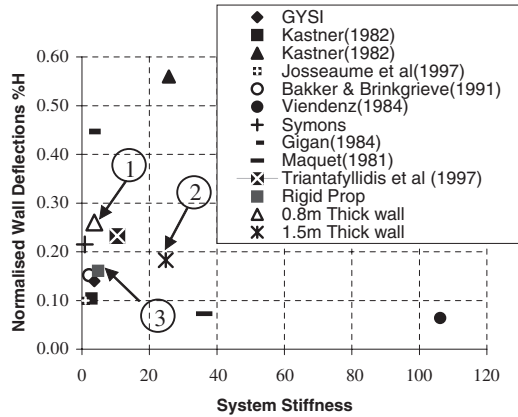


Figure 13. Comparison of FE results with field data.

where s is the distance between the props, γ_w is the unit weight of water and EI is the flexural rigidity of the wall. From the figure the average value of the normalised maximum wall deflections falls between 0.1 and 0.2% H if we exclude the exceptional cases reported by Kastner (1982) and Gigan (1984). It was reported by Long (2001) that for these cases, the excessive movements were due to an overly flexible retaining system, structural yielding of a sheet pile wall, failure of the propping system etc, so they can be treated as special cases.

Figure 13 shows three data points (marked 1, 2 and 3) of three analyses with different prop types and wall thickness. The three points compare well with the average maximum wall deflection from field data. Points 1 and 3 give the maximum wall deflection for a flexible and rigid prop respectively (The retaining wall thickness = 0.8 m was kept the same). It shows that stiffness of the prop can have a significant effect in wall deflections. Point 2 shows the maximum wall deflection for a 1.5 m thick retaining wall using the same realistic prop used to obtain point 1. Comparing points 1 and 2 shows that the wall deflections decreased with wall thickness but with a smaller effect compared to the prop stiffness.

3 CONCLUSIONS

Finite element analysis together with field measurements from previous construction sites in similar ground conditions together with centrifuge modelling provide valuable information for future designs. Based on the finite element analyses results, field data and centrifuge modelling data, a number of conclusions can be drawn about excavations retained by

single-propped walls in sand. At working conditions (for which the factor of safety for strength against overturning is 1.5):

- The maximum surface settlement was found to be within the range of 0.08~0.1%H (H = excavation depth).
- The settlements extended to about 1.6 times the excavation depth with the maximum settlement being in the range of 0.2~0.3 H.
- An important feature of the settlement profile is its sagging and hogging curvature which plays an important role in predicting likely damage for structures.
- The horizontal displacements at the ground surface were found to be around 2~2.5 times greater than the settlements and extended to about 3~3.5 times the excavation depth.
- The maximum horizontal wall deflection was found to have an average value of 0.2%H.

Clough, G.W. & O'Rourke, T.D. (1990). Construction induced movements of in situ walls. ASCE Geotechnical special publication No. 25 – Design and Performance of Earth Retaining structures, pp 439–470.

Elshafie, M.Z.E.B, Choy, C.K.C & Mair, R.J. (2006). Finite element and centrifuge investigations of excavation-induced ground movements. Accepted for publication in the International Conference on Physical Modelling in Geotechnics, Hong Kong.

Elshafie, M.Z.E.B. (2004). Effect of building stiffness on excavation-induced displacements. MPhil. Thesis, Cambridge University.

Long, M.M. (2001). Database for retaining wall and ground movements due to deep excavations. J. Geotech. And Geoenvironmental Engineering, ASCE 127, (3), pp 203–224.

Peck, R.B. (1969). Deep excavations and tunneling in soft ground. Proc. 7th ICSMFE, Mexico, state-of-the-art report volume 3, pp 225–290.

REFERENCES

ABAQUA/CAE User's manual, (2004), version 6.4, Hibbit, Karlsson & Sorensen Inc.

ABAQUS/Standard User's manual, (2004), version 6.4, Hibbit, Karlsson & Sorensen Inc.

Elastic-plastic flexure of embedded retaining walls

P.J. Bourne-Webb

Cementation Foundations Skanska, United Kingdom

D.M. Potts

Imperial College, London

S. Godden

Arup Geotechnics, London

D. Rowbottom

Formerly Corus Research and Development, United Kingdom

ABSTRACT: A number of cases have been examined using the finite element method, where the flexural behaviour of an embedded retaining wall has been considered. Steel sheet pile and reinforced concrete wall sections have been considered and modelled using simple and more realistic models. The study has concluded that the assumption of perfect plasticity in steel sheet piles does not capture the important effect of post-peak moment resistance softening which occurs in response to web buckling in steel sheet pile sections and current plastic rotation capacity values, proposed in Eurocode 3 should be treated with caution. In any event, the study has also shown that it is very difficult to mobilize wall plasticity, due to the well-known effect of bending moment reduction caused by wall flexure and soil arching effects. This effect, which can be captured reliably in calculation may lead to greater design economies than invoking full plastic design which is much more difficult to predict.

1 INTRODUCTION

The introduction of the Eurocode system will unify the procedures for limit state design across Europe. The limit state design approach is well established for conventional building structures but has not generally been applied to the design of earth retaining structures. One area of interest is the use of the limit state principles in the structural design of earth retaining walls. In particular, whether it is safe to allow the formation of plastic hinges in the wall at the Ultimate Limit State (ULS) and how to verify that the behaviour of the wall zone, undergoing plastic deformation is within acceptable limits. The following article presents some results from an extensive study of the impact of wall plasticity in soil-structure interaction problems involving steel sheet pile (SSP) and reinforced concrete (RC) embedded retaining walls. Conditions at the Serviceability Limit State (SLS) are not addressed in this paper.

2 DESCRIPTION OF WALL PLASTICITY

2.1 *Steel sheet pile sections*

The general requirements for the limit state design of steel structures are covered by Eurocode 3: Design of steel structures (EC 3), where Part 5 outlines the limit state principles relating to the structural design of bearing piles, sheet piles and other wall elements made from steel. The major European producers of steel sheet pile products have sponsored a number of projects in order to develop design rules consistent with the new codes and to assess how the development of wall plasticity may modify the behaviour of such wall systems when compared with established understanding.

Theoretically, the plastic moment, M_{pl} is defined as the bending moment resistance developed when the entire cross-section of the member is at yield, f_y . However, in practice, the bending resistance of SSP

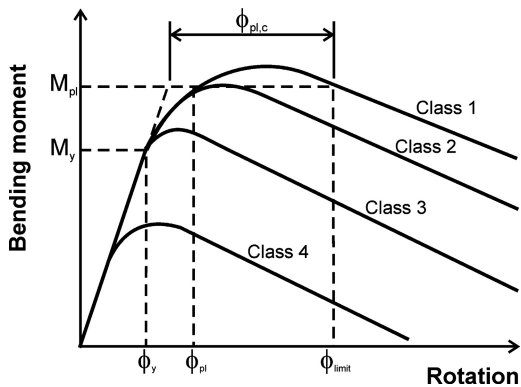


Figure 1. Idealised non-linear behaviour of SSP and member classification for plastic design of SSP.

can increase to a peak value a few percent higher than M_{pl} . As rotation within the member increases beyond that required to mobilise the peak resistance, buckling effects within the cross-section begin to dominate, Fig. 1 and the bending resistance reduces, tending to zero resistance at large rotations.

Plastic global analysis can only be used if the members are capable of forming plastic hinges with sufficient rotation capacity, $\Phi_{pl,c}$ (Fig. 1) to enable the required redistribution of bending moment to develop. Only members with cross-sections classified as Class 1 or 2 can be considered for use in plastic design. Class 3 and 4 sections have insufficient buckling resistance to enable the theoretical plastic moment resistance to be mobilised. While these classifications have been established for general steel sections for some time, no such work had been undertaken in relation to SSP sections and this was completed as part of the development of EC 3: Part 5 (Hartmann-Linden et al, 1997).

If moment redistribution and, therefore, plastic rotation is allowed to occur, then one of two approaches can be used to verify the member cross-section at the limit state being considered:

- 1 Assuming perfect plasticity, consider only Class 1 and 2 sections, with a separate check to verify that the rotation demand is less than the design rotation capacity. This approach is incorporated in Eurocode 3 and could be used in a Subgrade Reaction (SGRM) type calculation but is not considered appropriate for Finite Element (FEM) type models.
- 2 Use plastic-zone or plastic-hinge type models in combination with SGRM and FEM type models in which the plastic rotation demand is verified implicitly. In the FE calculations presented in this paper, a simplified plastic zone model has been used, in which the moment-curvature characteristic for the wall section is described explicitly rather than being calculated as part of the analysis.

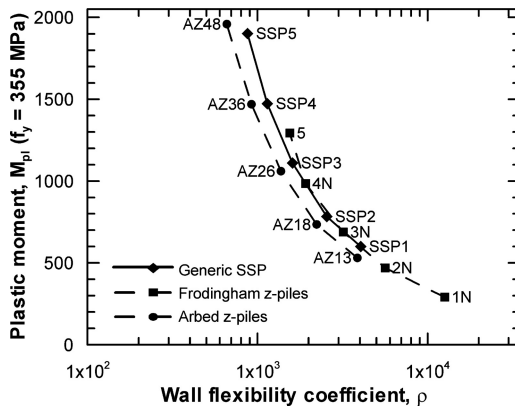


Figure 2. Comparison of generic SSP with commercially available sections, in terms of available moment resistance and wall system flexibility.

Based on the SSP bending data used to develop Eurocode 3, a set of generic SSP moment-rotation data was developed, which were representative of sections available commercially, Fig. 2 (Bornarel et al, 2001). The base data are presented in a non-dimensional form, which can then be scaled to the various generic SSP's, using the value of M_{pl} and EI associated with each section.

2.2 Reinforced concrete sections

The bending response of reinforced concrete (RC) sections is strongly influenced by the non-linear stress-strain behaviour of the concrete and depends on the amount of steel reinforcement. It is usual to design the section so that a ductile failure occurs, i.e. the tension steel yields as the ultimate concrete strength is mobilised. Given this, the moment-curvature response can be described in three idealised stages as follows:

- 1 Linear response up to first cracking of the concrete in tension ($f_{ct} \sim 0.1 f_c$).
- 2 Softer, near-linear response up to first yield of the tension steel.
- 3 Near perfectly plastic response until the onset of concrete crushing, when softening may develop.

As well as its immediate mechanical behaviour, concrete exhibits creep under constant load and the effective elastic modulus reduces depending on the loading conditions and environment the concrete is maintained under. Thus, the effective stiffness applicable at the ultimate strength, in the long-term, may be as little as 25% of the short-term, uncracked concrete stiffness. Typically, when reinforced concrete wall sections are modelled using the FEM, current practice is for linear elastic behaviour to be assumed with an effective stiffness modulus equal to the uncracked

concrete stiffness, in the short-term, reducing to 50% of this value in the long-term.

Moment-curvature characteristics representative of a range of rectangular section thickness and steel ratios were generated and for the analyses presented here, it was assumed that the bending capacity remained constant once the ultimate bending strength was reached (Godden, 2001).

2.3 Presentation of structural resistance

For this paper, resistance characteristics for the SSP and reinforced concrete wall sections are presented via ‘Structural curves’ (similar to Rowe, 1952) which have been developed by normalising the plastic moment resistance, M_{pl} for each wall section by the bending moment calculated using the limit equilibrium method, M^{LE} based on the procedures and factors-of-safety outlined in Eurocode 7 – Geotechnical design (EC7). This ratio is plotted against either the wall system flexibility coefficient, $\rho = (h + f)^4/EI$ (Rowe, 1952) or the revised flexibility coefficient, $\rho^* = (h + f)^4 E_{soil}/EI$ (Potts & Bond, 1994) where E_{soil} is the average soil stiffness over the height $(h + f)$ of the wall, based on the initial free-field stress state conditions modelled prior to excavation, h the exposed height of wall and f the wall embedment depth.

The structural curve for the generic SSP sections is compared to the equivalent curves for Arbed and Frodingham (recently discontinued) type z-pile sections, Fig. 2.

Structural curves for the reinforced concrete sections at the ULS are compared to the generic SSP in Fig. 3. Two examples (solid square symbols) of instantaneous curves illustrating the variation in system stiffness between the onset of cracking and the ultimate moment resistance are also shown (the initial stiffness already having been softened by 50% to allow for long-term creep effects).

2.4 Numerical implementation

The program ICFEP, developed at Imperial College over the last 25 years was used in this study. Within this program, one-dimensional, curved, 3-node iso-parametric Mindlin beam elements have been implemented with a tri-linear Elastic-plastic constitutive model which allows hardening or softening of the element force parameters to a residual value (Day, 1990, Potts & Zdravkovic, 1999). The data describing the moment-plastic curvature characteristic curves for the SSP and reinforced concrete sections have been used within a modified version of this model (Bourne-Webb, 2004) where the beam element constitutive model was modified to allow more complex moment-plastic curvature to be described using a user-defined piece-wise linear relationship.

Verification exercises, modelling a 4-point bending test were undertaken when testing the model. The

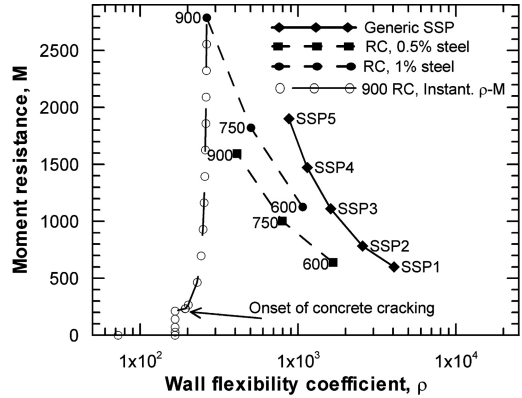


Figure 3. Comparison of RC sections and generic SSP in terms of available plastic moment resistance and wall system flexibility.

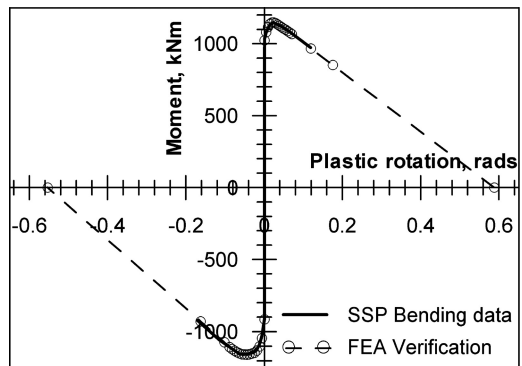


Figure 4. Verification of revised beam element model against generic plastic moment rotation response.

predicted response of a generic SSP is compared to the input data in Fig. 4 with good agreement. The FE model has been modified to extrapolate to zero to reflect the ongoing loss of section resistance at very large curvatures, beyond the range of the test data used to develop the generic base data for the model. Similar accord was found when testing the RC model.

3 INVESTIGATION OF WALL PLASTICITY

3.1 General aspects

The analyses discussed in this paper are drawn from PhD and MSc theses completed at Imperial College (Bourne-Webb, 2004 and Godden, 2001), where the basic model comprises a wall embedded to a depth of 20m bgl and a single prop located about 1m bgl. Varying ground conditions were considered and are summarised in Table 1.

Table 1. Summary of ground conditions assumed in analyses.

Description	γ	c'	ϕ'	K_0	FE Model	Reference
	kN/m ³	kPa	deg	–		
Dense sand	19	0	40°	~0.36	Lade's double cap model (Lade, 1977; Potts & Zdravkovic, 1999)	Bourne-Webb (2004)
Stiff Clay	20	5	23°	1.5	Mohr-Coulomb with pre-yield non-linear small strain model (Potts & Zdravkovic, 1999)	
Intermediate soils	20	0	25°	1, 2	Mohr-Coulomb with soil stiffness increasing linearly with depth (Potts & Zdravkovic, 1999)	Godden (2001)
	20	0	32°	0.5, 1		
	20	0	40°	0.5		

Zero pore water pressures (pwp) were initially assumed for the dense sand case and all the cases considered by Godden. Later analyses for the sand and all stiff clay cases incorporated differential pwp in order to examine plastic wall behaviour under such conditions. In the stiff clay cases, fully drained conditions were assumed as when only partial drainage during excavation was modelled, mobilisation of wall plasticity was not achieved until sometime after the excavation was completed.

3.2 Presentation of action effects

Each completed analysis produces a wealth of information and, in order to be able to present and compare the various results with clarity, bending moment demand curves (Rowe, 1952 called them 'operational curves') have been generated using the revised flexibility coefficient, ρ^* to define the wall system's stiffness and the moment ratio, M/M^{LE} . Where the bending moments, M are the maximum values predicted at various excavation stages.

It should be noted that normalising values, i.e. M^{LE} , are taken from the limiting equilibrium case (Factor-of-safety, FoS = 1), i.e. not for each level of excavation (varying FoS) as used by others (Rowe, 1952 and Potts & Bond, 1994). This was done for presentational purposes, to allow comparison with a single structural curve only. Therefore, while similar in form, the operational curves presented here differ somewhat from those presented in previous papers (Bourne-Webb, 2004).

3.3 Bending moment demand and wall plasticity

3.3.1 Analyses with zero and differential pwp

Comparison of bending moment demand and structural curves, such as those shown in Fig. 5 show that mobilisation of wall plasticity proved very difficult when dense dry sand was modelled (Bourne-Webb, 2004). It should be noted that the wall section was assumed to be elastic for the analyses used to generate the moment demand curves.

This was the case irrespective of the soil-wall interface shearing resistance assumption made and the results for a fully rough wall are shown in Fig. 5.

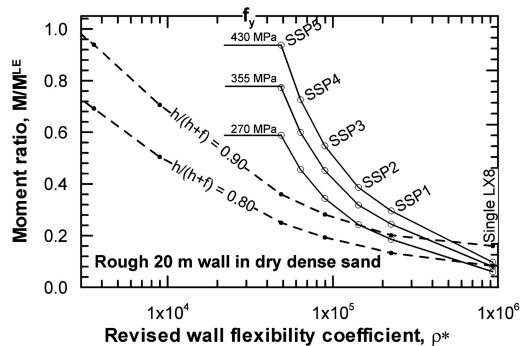


Figure 5. Potential for SSP wall plasticity through comparison of demand and structural curves.

Table 2. Occurrence of SSP wall plasticity (Godden, 2001).

$\nu\rho$ (deg)	K_0		
	0.5	1.0	2.0
25°	–	SSP 2	SSP 2 & 5
32°	SSP 2	SSP 2 & 5*	–
40°	none	–	–

*Moment demand just less than M_y in SSP5.

Full mobilisation of the theoretical plastic moment resistance is only predicted at excavation ratios larger than those allowed by an equivalent LE type calculation (In this case; $h^{LE}/(h + f) = 0.81$) and the weakest/most flexible SSP wall sections.

In relation to the occurrence of SSP wall plasticity, Table 2 summarises results for intermediate soils where the wall section was predicted to yield (Godden, 2001), i.e. bending moment, $M \geq M_y$ where $f_y = 355$ MPa. Based on these results, it would seem that, in the absence of differential pore water pressures, yield of the SSP sections will occur in the most flexible wall sections (except where high angles of shearing resistance are applicable) and stiffer SSP sections when lower shear strengths and/or higher initial stress conditions are applicable.

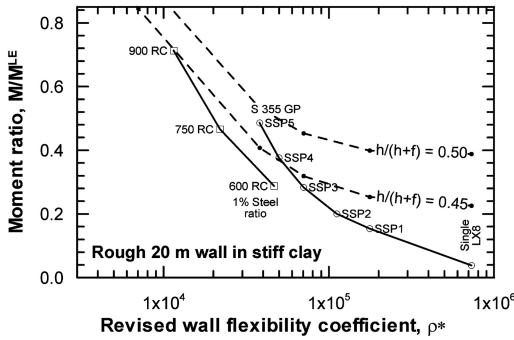


Figure 6. Moment demand and potential for wall plasticity during excavation in drained, stiff clay.

Following the assessment of wall behaviour in the absence of water pressures, differential pore water pressures acting on the wall were introduced into the analyses (Bourne-Webb, 2004). In all cases, the water level behind the wall was maintained 4 m below ground level (bgl) while on the dredge side of the wall the water level was maintained at or below the excavation level. Analyses were coupled and, initially, steady-state (fully drained) pore water pressure conditions were assured throughout the analysis by using large time steps.

In the presence of these differential pwp, plasticity can be mobilised in most SSP wall sections in dense sand and all SSP & RC sections in stiff clay (Fig. 6).

Unlike the cases discussed above, wall plasticity can be mobilised within the limiting depth defined by limit equilibrium considerations.

In the cases presented here, water pressures represent about 45% of the bending moment demand in the stiffest wall sections and this proportion increases with increasing wall flexibility (as a percentage of a reducing total). The very nature of hydrostatic loading means that water pressures cannot redistribute and this becomes important if wall plasticity is reached.

3.3.2 Partial drainage during excavation

A further examination of the effect of the pore water pressure assumption on the predicted wall system response has been made by examining the influence of undertaking excavation over a limited time span and allowing remaining excess negative pore water pressures to dissipate to an equilibrium condition. The predictions are then compared to the case presented earlier where drained pore water pressure conditions have been assumed throughout.

An analysis assuming drained conditions and an elastic wall section predicts a maximum moment, M_{drained} of about 2300 kNm/m at the end of excavation to 11.5 m (solid diamonds, Fig. 7). If instead excavation is assumed to occur over 150 days, the maximum bending moment at day 150 is about 25% of the equivalent value

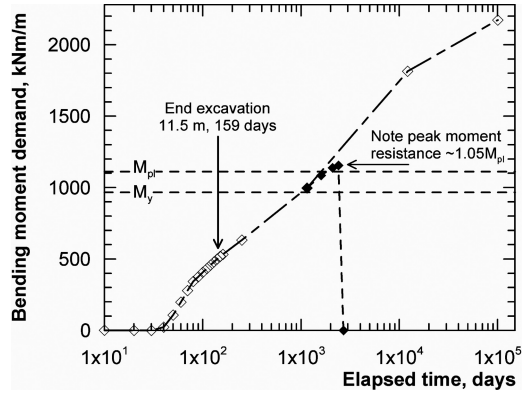


Figure 7. Comparison of predicted moment demand in SSP during excavation in stiff clay with partial drainage.

from the drained analysis. The plastic moment, M_{pl}^{355} is reached about 3 years after excavation is completed.

As in the drained analysis, when plasticity is allowed to occur (open diamonds in Fig. 7), the moment demand in the main span of the wall peaks at the maximum bending moment (about 1150 kNm/m; approx. $1.05 M_{\text{pl}}$) then the moment capacity in the plastic hinge zone drops to zero during the next time step (250 days).

3.4 Impact of wall model assumptions

3.4.1 Perfect-plasticity in SSP response

A realistic plastic moment-curvature response for SSP was introduced into the analyses. Generally, in the cases where plasticity could be mobilised in the wall, geotechnical failure was being approached and the rate of increase in moment demand was accelerating.

The rate in increase of moment demand with excavation depth was such that if the wall section yielded, then in the next increment of excavation the potential moment demand overshoot both the theoretical plastic and the peak moment resistances. When this happened, the wall system become unstable, as there was no further scope for stress redistribution and the section resistance moved onto the softening arm of the moment-curvature capacity response curve.

Because of the effects that the softening SSP beam element model invoked in the analyses, a set of analyses were undertaken to examine the differences between the assumption of perfect-plasticity and the strain hardening/softening behaviour of actual SSP walls. A wall with the same bending stiffness as the generic SSP 3 wall was assumed but with M_{pl} reduced to 350 kNm, in the dry sand case, to ensure mobilization of plasticity and allow comparison of the two wall plasticity assumptions.

The plastic bending moment-curvature response for these analyses are compared in Fig. 8. The analysis with the scaled generic SSP response predicts a

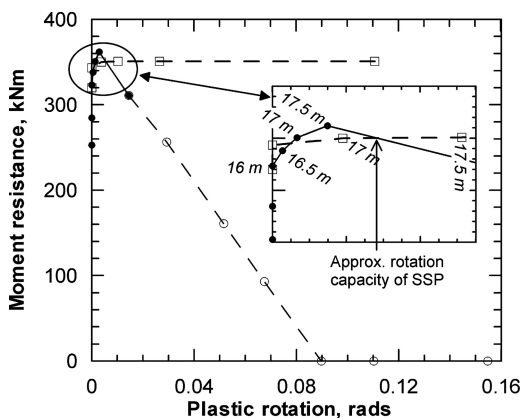


Figure 8. Comparison of perfectly plastic and generic SSP moment-curvature response at the ultimate limit.

maximum excavation depth of 17.5 m (coincidentally having mobilized the peak moment resistance), after which the SSP softens and the analysis was unable to reach an equilibrium condition. On the other hand, the perfectly plastic wall section enables excavation to reach a depth of 18.5 m but with very large plastic curvatures, larger than those that would be allowed under EC 3: Part 5 (lies approx. where the generic curve crosses the perfectly-plastic curve).

While these analyses demonstrate the effect of the two wall plasticity assumptions, the comparison is based on an inconsistent set of SSP stiffness and bending resistance parameters.

When the same exercise was repeated in the presence of differential pore water pressures, in which the section resistance did not need to be reduced artificially but it was found that an equilibrium state could not be established in the analyses.

The fixed hydrostatic loading drives the moment demand through the peak resistance and onto the softening curve within one excavation step.

3.4.2 Concrete stiffness assumptions

A RC wall section's characteristic properties are not constant and vary due to the onset of cracking, as bending moment demand increases and as a consequence of creep under constant load demand, with time. In the long-term, the effective Young's modulus of the section may reduce by between 50% and 80% depending on environmental and loading conditions (Godden, 2001).

RC wall sections with a realistic moment-curvature response, accounting for the effects of tensile cracking of the concrete were modelled. It was generally found that bending moments in these analyses were reduced and deflections increased when compared with analysis assuming a linear elastic wall section using uncracked concrete stiffness initially and a softened value (50% to 25% of the uncracked value)

long-term. This indicates that overall, the system stiffness in the former case is less than in the latter.

The assumption of an uncracked stiffness in the short-term does not reflect the true variation in stiffness that occurs as loading increases in this period.

4 EVALUATION AND CONCLUSIONS

4.1 Influence of wall flexure

The effect of wall flexibility should be allowed for in the assessment of embedded retaining walls, this is verified implicitly in continuum models while only flexural effects are recovered in spring type models. Empirical approaches can be used in limit equilibrium methods of calculation.

As a consequence of earth pressure redistribution and, hence, moment reduction, lower modulus wall sections could be used but this would be at the expense of greater deformation.

The magnitude of the wall flexibility effect depends on the degree of stability of the wall system (reducing as the wall approaches a state of limiting equilibrium) and whether there are differential pore water pressures present.

Reinforced concrete wall sections are characterised by section properties that vary with load and time. Further investigation of the effect of current assumptions with respect to the variation of concrete stiffness is recommended; although this is likely to be more important for deformation predictions than wall forces that currently appear to be conservative.

4.2 Wall plasticity in design of embedded walls

Piece-wise linear beam element models can be implemented in order to reproduce realistic structural behaviour at the ULS and allow for the implicit verification of plastic design of all types of wall section.

As SSP approach the theoretical plastic moment resistance, M_{pl} behaviour beyond this stage appears to be very sensitive to the rate of increase in moment demand as excavation proceeds (and soil pressures redistribute), and the presence of water pressures which provide a fixed loading which does not redistribute. It should be borne in mind that the peak resistance of SSP is only about 5% greater than M_{pl} and once this resistance is mobilized and a mechanism is formed, the wall resistance softens – accompanied by uncontrolled failure of the wall system.

For the time being, however, it is recommended that the full plastic rotation capacity suggested for SSP, in EC 3: Part 5 is not utilized. Moment resistance up to the first mobilization of the theoretical plastic moment, M_{pl} may be used safely with wall forces at the SLS being maintained at less than the moment at first yield of the sections, for verification of deformation limits.

Further investigation of the mobilization of plastic rotations in SSP, beyond this stage is recommended in order to verify that the plastic rotation capacity values in EC 3: Part 5 are in fact safe.

REFERENCES

- EN 1993-5, 'Eurocode 3 : Design of steel structures, Part 5 – Piling'.
- EN 1997-1, 'Eurocode 7: Geotechnical Design, Part 1 – General rules'.
- Bornarel, B. et al. 2001. *Advanced Design Tools for Steel Sheet Piling* – Draft Final report, internal and confidential.
- Bourne-Webb, P.J. 2004. *Analysis of embedded retaining walls at the Ultimate Limit State*. PhD thesis Imperial College of Science, Technology and Medicine, London.
- Day, R.A. 1990. *Finite element analysis of sheet pile retaining walls*. PhD thesis Imperial College of Science, Technology and Medicine, London.
- Godden, S.L. 2001. *Soil-structure interaction of embedded retaining walls: A numerical study*, MSc dissertation, Imperial College, University of London.
- Hartmann-Linden, R. Kort, A. Meyrer, M. Schmitt, A. Sedlacek, G. & van Tol, A.F. 1997. *Development of unified design rules for steel sheet piles and introduction in Eurocode 3, Part 5*, CEC Agreement 7210-SA 127/523/840, ECSC.
- Lade, P.V. 1977. *Elastic-plastic stress-strain theory for cohesionless soil with curved yield surfaces*. Intl. J. Solids & Stuct, Vol. 13, 1019–1035
- Potts, D.M. & Zdravkovic, L. 1999. *Finite element analysis in geotechnical engineering: Theory*. London: Thomas Telford.
- Potts, D.M. & Zdravkovic, L. 2001. *Finite element analysis in geotechnical engineering: Application*. London: Thomas Telford.
- Rowe, P.W. 1952. Anchored Sheet-Pile Walls. *Proceedings Institution of Civil Engineers*, Vol. 1, Part 1, 27–70 and Discussion 616–647.

Large scale excavation model test on single strutted sheet pile wall and back calculation of soil parameters

T.H. Tefera, S. Nordal & R. Sandven

Geotechnical division, Norwegian University of Science and Technology, Norway

ABSTRACT: The ground settlement and wall deformation of a single strutted sheet pile wall during different stages of excavation has been studied using a large scale model test in dry sand. The large scale model sheet pile wall was constructed in a sand bin 4 m×4 m in plan and 3 m deep. The influence of the side wall friction during the test was treated by separating the wall into three panel sections. The system reduces the influence of the side wall friction on the central panel which is instrumented. The different stages of excavation were modelled numerically using an elastoplastic soil model to back-calculate the soil parameters. The result shows that with a proper soil model the finite element method is a valuable tool in simulating the ground settlement, the wall deformation and the moment distribution in the wall. Special attention should be paid to the choice of the material model and the model parameters.

1 INTRODUCTION

Numerical methods are increasingly employed for analysis of excavation because of their advantages over classical methods. Actually the advancement and sophistication in the numerical solution techniques have exceeded the knowledge of the behaviour of materials defined by constitutive laws. Thus, one of the most difficult factors to consider in the numerical analysis of braced excavations is the constitutive behaviour of the soil. A number of researchers have reflected this issue (Grande 1998; Potts & Fourie 1986). As a consequence physical models are still extremely useful to investigate various boundary problems in geotechnical engineering practice. More particularly, they can validate theoretical and numerical studies, when similarity requirements are not predominant (Simonini et al. 1998).

This paper presents results from a well-defined large scale physical model test on a single strutted sheet pile wall (Tefera, 2004) in medium to loose dry sand and back calculation of soil parameters for the constitutive model used. The model used in the back calculation is the Hardening-Soil model implemented in the PLAXIS code. The back-calculation made focuses on the use of different sets of parameters for the chosen material model. The ground settlement, distribution of moments and deformation behaviour of the braced sheet pile wall and the strut load during different stages of excavation have been studied. Results from back-calculation are presented together with experimentally measured values.

2 TEST ARRANGEMENT

2.1 Model test bin

The model test facility at the Norwegian University of Science and Technology, NTNU, consists of a test bin 4 m by 4 m in plan and 3 m in depth, and equipped with a sand silo, a refill silo, a sand spreader, a crane, a bucket elevator and conveyors for transporting the model sand, [Figure 1](#). The size of the test bin allows realistic construction procedures and development of significant body forces. The sheet pile wall constructed in a sand bin consisted of series of structural aluminium box members type 6061, along with four structural support struts. The sand used in the study was local quarried sand from Hokksund, Norway. The sand was placed in the tank by pluviation from a mechanical spreader passing steadily back and forth over the tank. Pluviation (raining) is probably the method in the laboratory that not only provides reasonable homogeneous specimens with the desired relative density, but also simulates a soil fabric most similar to the one found in nature deposits formed by sedimentation.

The sand density (porosity) in the test tank is controlled by the diameter of 456 interchangeable nozzles located at the bottom of the mechanical spreader. The nozzle diameter can be varied between 7, 10, 16 or 20 mm, where the larger nozzle diameters give the lower densities. Previous studies conducted using the same sand has found satisfactory small variation in density from the bottom to the top of sand placed (Sandven

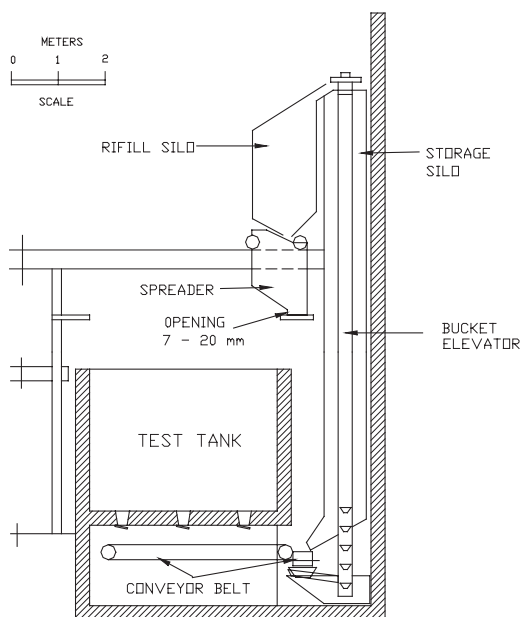


Figure 1. Cross section of test tank and sand handling arrangements.

Table 1. Common geotechnical properties of Hokksund Sand.

Grain density, (ρ_s)	2.71 g/cm ³
Maximum porosity, n_{max}	48.7%
Minimum porosity, n_{min}	36.4 %
Coefficient of uniformity, C_u	2.04

1992). Figure 1. shows a cross section of test tank and the associated sand handling arrangements. The Hokksund sand is medium/fine, uniform angular to semi angular quartz sand.

2.2 Hokksund sand

The Hokksund sand originates from a glacial deposit at Hokksund near Drammen, Norway. A laboratory test programme has been performed earlier (Sandven 1992) to determine the most common geotechnical properties of the material.

The material may be classified as quartz – rich, medium/fine, and uniform sand with cubical and angular grains. A summary of obtained parameters are shown in Table 1.

2.3 Sheet pile wall arrangement

The sheet pile wall was constructed with a series of aluminium box members type 6061, along with four support struts. The description of the sheet pile wall elements is given in Table 3. The struts were placed

Table 2. Density and porosity for different nozzle sizes.

Nozzle size openings (mm)	Density (kN/m ³)	Porosity (%)	Variations in porosity approximately
7	17.1	35.7	$n_{min} = 36.4$ $\pm 0.9\%$
10	16.6	37.6	$\pm 0.8\%$
16	16.0	39.9	$\pm 0.7\%$
20	15.1	43.2	$\pm 0.7\%$ $n_{max} = 48.7$

Note that the lowest porosity obtained in the bin is smaller than the nominal n_{min} from standard tests.

Table 3. Description of sheet pile wall element.

Type	Aluminium (6061)
Young's modulus (E)	69×10^9 Pa
Flexural rigidity (EI)	23.39 kNm ² /m
Axial stiffness (EA)	3.2×10^5 kN/m

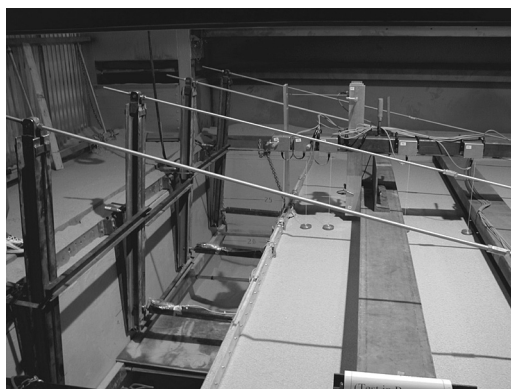


Figure 2. Partial view of the large scale model test set-up.

0.5 m from the top of the wall and spaced at 1.0 m intervals along the 4.0 m length of the wall. Four struts were used in the model. The aluminium members were placed length to length along the 4.0 m wide tank, 40 members were used to make up the wall. The height of the aluminium elements from the top of the wall to the bottom was 2.5 m.

2.4 Strut load arrangement

The strut loads were applied by a beam connected to the wall and in the other end to a vertical double channel beam through which the load can be controlled. At the top of the beam there is a metal eye device with a threaded rod (Fig. 2).

By tightening the nut to the rod a desired amount of strut force can be applied. The force in the strut was measured through a load cell installed at the beam connection.

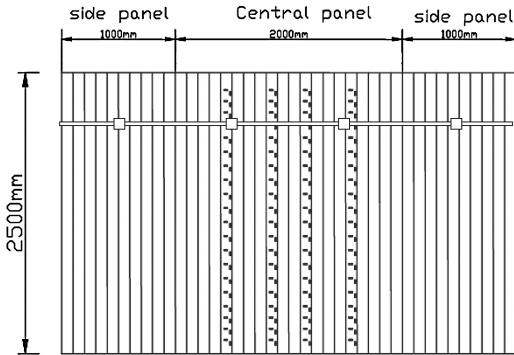


Figure 3. Independent sections of the articulated wall arrangement with location of strut load application and strain gauges along four individual wall members.

3 BOUNDARY CONDITIONS

The front and back walls of the sand bin was assumed not to affect the overall performance of the model sheet pile wall. The model base boundary condition was dealt with by two measures. The first measure was to place a 0.5 m layer of sand at the bottom of the bin to provide a non-restrictive soil-wall boundary interface at the base. This covered the whole 4 m × 4 m area of the tank. The second measure in the study was treated by separating the wall into three separate panel sections, Figure 3. The wall elements were grouped together into three panel sections, two being 1 m wide and a central panel 2 m wide, Figure 3. The three panel sections were able to move independently thus not restricting movement amongst them. This system reduced the influence of the side wall friction on the instrumented central panel section.

4 INSTRUMENTATION AND TEST PROCEDURE

4.1 Instrumentation

In the study, instrumentation was placed to measure-ground settlement, movement of the wall, bending moment in the wall and load on the strut. Displacements on the soil surface were measured by means of small weights on the surface from which thin steel wires went to special tailored potentiometers. A variable resistor is used to convert displacement to resistance/voltage. The basic principle of operation is that a moving wiper (sensor input) moves a contact along a resistor. The ends of the resistor are connected to a reference voltage. As the wiper moves, the potentiometer acts as a voltage divider and produces a voltage proportional to the position. The deformation transducers were calibrated and tested and were found to be convenient and reliable devices for the experiment. Eight deformation

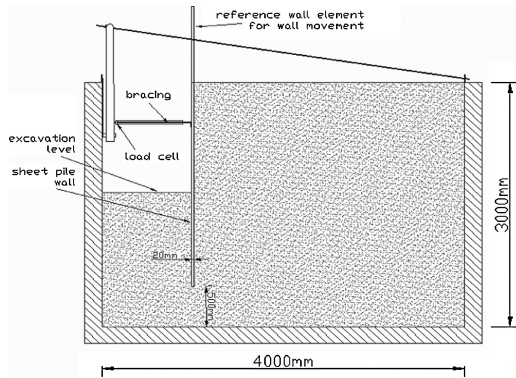


Figure 4. Section through the model showing the extended wall element and strut arrangement.

transducers were installed in the model. Five points monitored the surface settlement, one point on top of the model sheet pile wall monitored the vertical movement and another two points on the extended part of the model sheet pile wall determined top translation and rotation. The movement of the sheet pile wall buried in the sand were monitored using strain gauges glued on the instrumented sheet pile wall element. Twenty half Wheatstone bridge strain gauges were glued along the length of each of four wall elements in the central section of the wall, Figure 3. The strain gauges were calibrated for bending moment measurements in the wall. In the experiment four struts were used, i.e., one strut per meter of the model sheet pile wall. Figure 4 shows the location of the four struts used in the model test. The two struts in the central panel were instrumented using two HBM type U9B – 20 kN force transducers.

4.2 Test procedure

The large scale model single strutted sheet pile wall test was carried in two phases: Phase I Model construction, and Phase II Excavation and strutting. Phase I model construction has three stages. Stage(1) First stage of filling the test tank up to 0.5 m, Stage(2) Construction of the sheet pile wall, and Stage(3) Filling 2.5 m more sand in the test tank. Phase II Excavation and strutting was performed in 9 stages, see Table 4. In the excavation side of the model, there are three bottom holes (chutes) located at the bottom of the test tank, through which sand as allowed to drain out to simulate the excavation process. A series of tubes were installed in these bottom openings. The excavation process was carried out by removing parts of the tube corresponding to the desired excavation depth to drain the sand above that level. Careful horizontal manual shovelling of the sand to the draining tubes completed each excavation stage.

Table 4. Phase II, the excavation and strutting phase.

Stage	Excavation depth from top (m)
1	0.35
2	0.67
3	0.91
4	application of strut load (5 kN)
5	1.18
6	1.52
7	1.82
8	2.11
9	2.30

5 DESCRIPTION OF THE HARDENING-SOIL MODEL

The basis of a good prediction of stresses and deformation using the finite element method is the choice of a suitable constitutive model together with a careful assessment of the model parameters. The latter should be based on good quality soil investigation data. The constitutive model used in the back-calculation is called the Hardening-Soil model available in the PLAXIS code. The ground settlement, distribution of moments and deformation behaviour of the braced sheet pile wall and development of the strut load during different stages of excavation have been numerically simulated and studied.

The Hardening-Soil model is formulated in the framework of classical theory of plasticity. In the Hardening-Soil model the total strains are calculated using a stress-dependent stiffness, different for both virgin loading and un-/reloading stiffness. The plastic strains are calculated by introducing a two surface yield criterion. The hardening is assumed to be isotropic, depending on both the plastic shear and volumetric strain. For the frictional hardening, a non-associated and for the cap hardening, an associated flow rule are assumed. Hardening-Soil model has a relatively large number of parameters (Nordal, 2004), but some of them have default settings that are valid for a wide range of application. (Schanz et al., 1999, Brinkgreve, 2002).

6 BACK CALCULATION OF SOIL PARAMETERS

In the back calculation of soil parameters using PLAXIS, the domain analysed was the sand bin, Figure 5. The mesh consists of 643, 15-noded triangular soil elements with average element size of 13.6 cm. The sheet pile was modelled by 5-noded beam elements. Interface elements between the soil and the sheet pile wall were used on both sides of the wall with an interface strength reduction coefficient R_{inter} . This limits the interface vertical

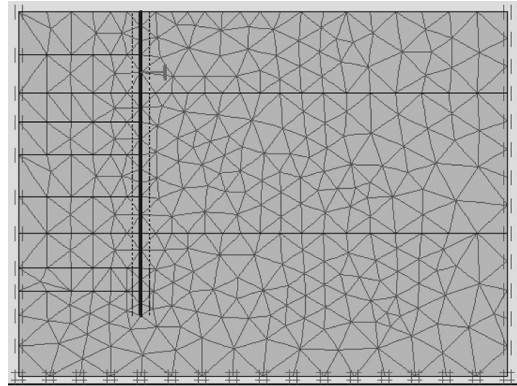


Figure 5. Finite element mesh, 3 m by 4 m used in the back calculation of soil parameters. for the numerical analysis with boundaries, 2.5 m long sheet pile wall, strut, soil elements and interface-elements.

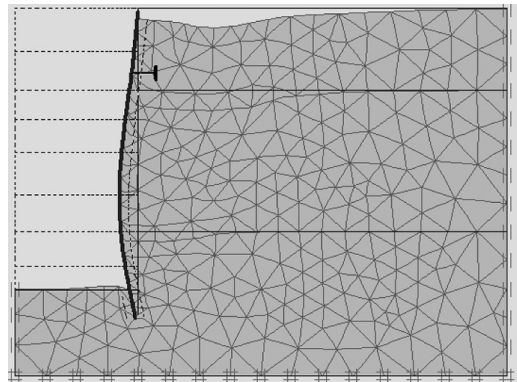


Figure 6. Deformed mesh showing the pattern of ground settlement and wall deformation at depth of excavation 2.30 m, displacements scaled up 5 times.

shear capacity to $\tan \delta = R_{inter} \cdot \tan \varphi$. A fixed-end anchor, which is a one-node elastic spring element with a constant spring stiffness, was used to model the strut load.

The actual construction sequence followed in the large scale model sheet pile wall test was also followed in the back-calculation.

6.1 Before application of the strut load

Three excavation stages were carried out before application of the strut load. Simulation results from two of these, to excavation depth 0.67 m and 0.91 m are presented in Figures 7 and 8.

The comparison of observed values and calculated values of horizontal wall movement, bending moment in the wall and settlement of the ground shows good

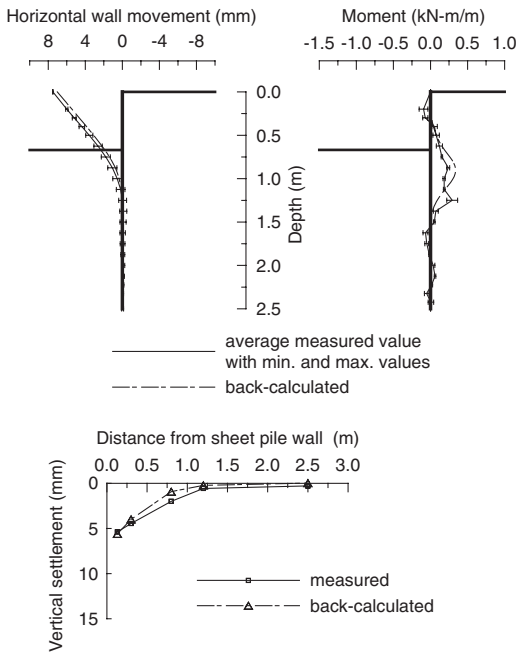


Figure 7. Observed and back-calculated horizontal wall movement, bending moment in the wall, and ground settlement at excavation depth 0.67 m, before application of strut load.

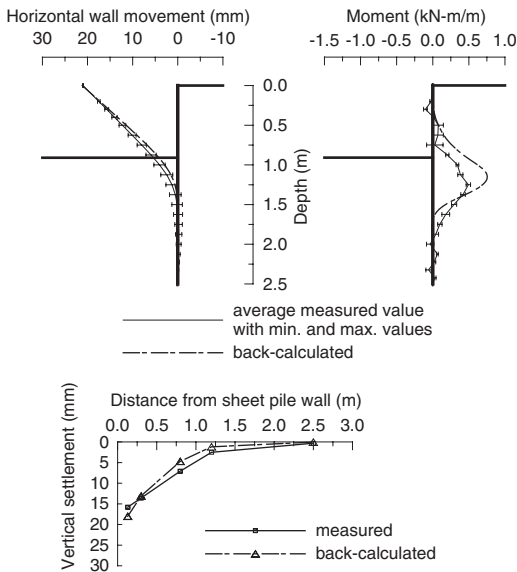


Figure 8. Observed and back-calculated horizontal wall movement, bending moment in the wall, and ground settlement at excavation depth 0.91 m, before application of strut load.

agreement. In the back-calculation relatively low interface strength reduction coefficient were used. $R_{inter} = 0.2$ and 0.3 for excavation depth 0.67 m and 0.91 m respectively.

6.2 After application of the strut load

Five excavation stages were carried out after application of the strut load of 5 kN/m. Simulation results from these excavation depths are presented in Figures 9–14.

In the simulation after application of strut load relatively higher interface strength reduction coefficient gives better fit with the observed horizontal wall movement. As the depth of excavation increases the simulation gives better fit with increased friction angle by 2° . A comparison of the measured and simulated strut load during the excavation process with one set of parameter, rough interface and increased friction angle by 2° , shows a reasonable fit until the last excavation phase, Figure 15.

The simulations show rather small inward wall movements when applying the 5 kN/m strut load, while the experimental measurements show a considerably larger inward movement of about 5 mm at the top of the wall. This discrepancy is somehow also reflected in the simulation results which follows after application of strut load.

7 DISCUSSION AND CONCLUSION

This paper presented results from a well-defined large scale physical model test on a single strutted sheet pile wall and back-calculation of soil parameters. In the paper a comparison of wall deformation, moment in the wall, ground settlement, and strut load from the model test and results from simulation using finite element method were made.

Comparing numerical simulations to measured wall behaviour, before application of strut load with relatively low interface strength reduction coefficient for the model parameters shown in Table 5, gives better result. With relatively higher interface strength reduction coefficient comparable results could be achieved by reducing the soil strength. As the depth of excavation increases after application of strut load, higher interface reduction coefficient gives better result. The observed discrepancies indicate that the simulation shows a response that is too stiff when the soil body is far from failure, and simulation that is too soft when failure is approached. Such behaviour suggest that the unloading stiffness parameters are too high while the stiffness in the final stage of loading towards Coulomb yielding is too low. The measure data in the last two stages of excavation, 2.11 m and 2.30 m, is best captured using rough interface and with slightly higher friction angle, 2° .

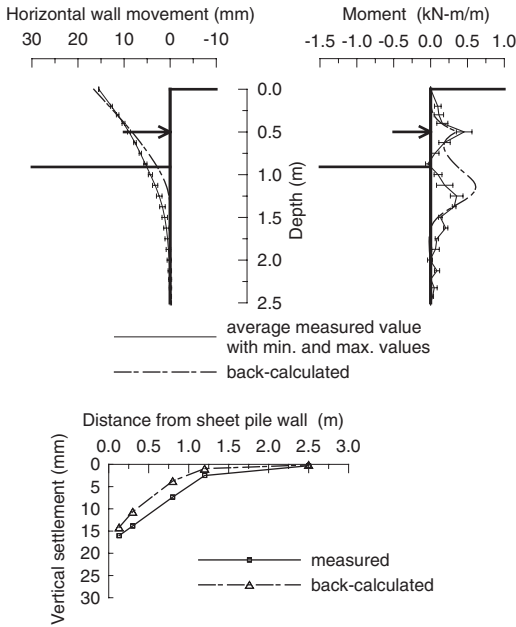


Figure 9. Observed and back-calculated horizontal wall movement, bending moment in the wall, and ground settlement at excavation depth 0.91 m, after application of strut load.

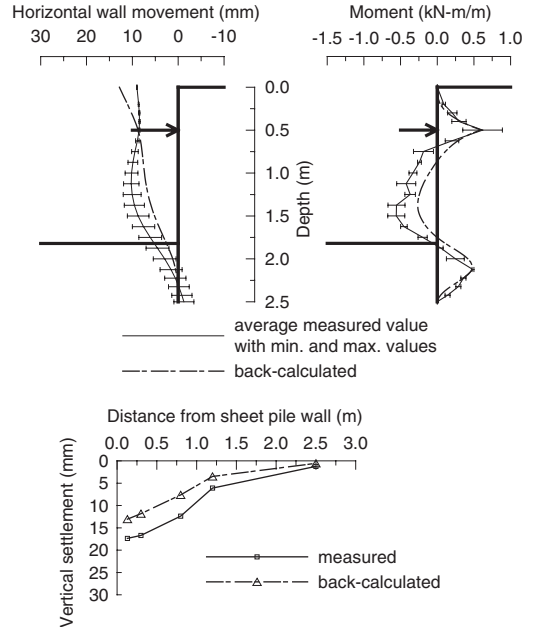


Figure 11. Observed and back-calculated horizontal wall movement, bending moment in the wall, and ground settlement at excavation depth 1.52 m.

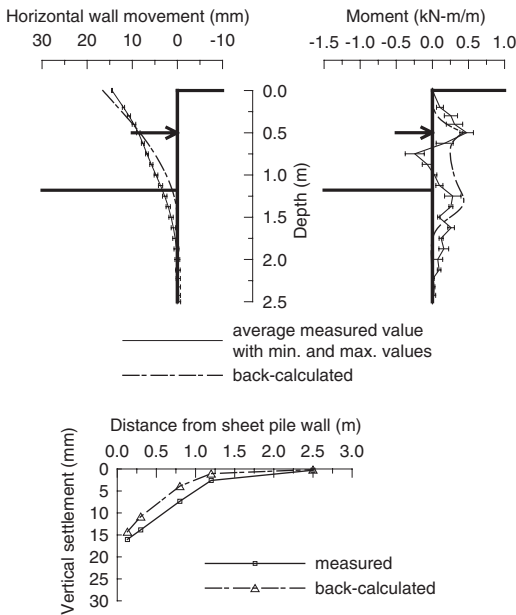


Figure 10. Observed and back-calculated horizontal wall movement, bending moment in the wall, and ground settlement at excavation depth 1.18 m.

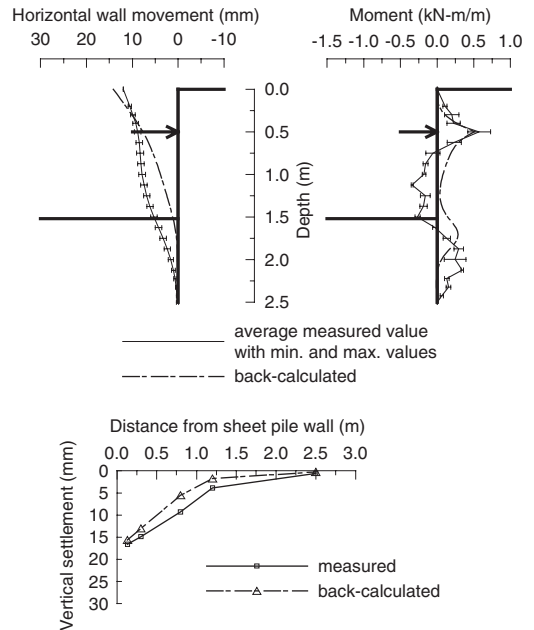


Figure 12. Observed and back-calculated horizontal wall movement, bending moment in the wall, and ground settlement at excavation depth 1.82 m.

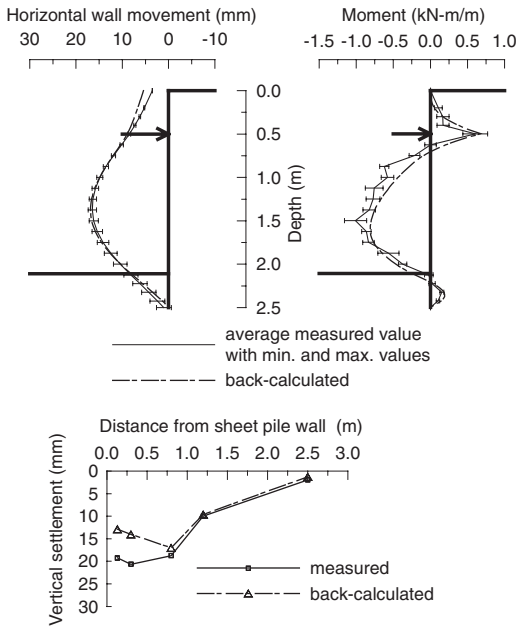


Figure 13. Observed and back-calculated horizontal wall movement, bending moment in the wall, and ground settlement at excavation depth 2.11 m.

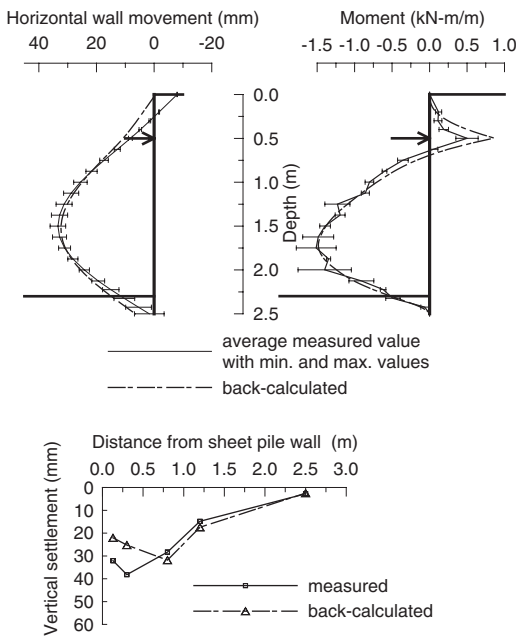


Figure 14. Observed and back-calculated horizontal wall movement, bending moment in the wall, and ground settlement at excavation depth 2.30 m.

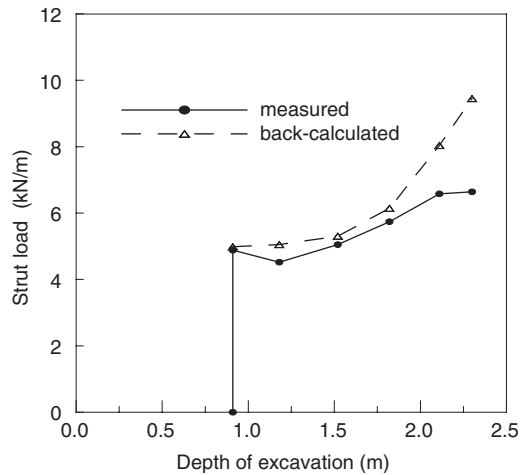


Figure 15. Observed and back-calculated values of the strut load for different stages of excavation.

Table 5. Summary of Hardening-Soil model parameters used in the back-calculation.

Unit weight, γ	15.1 kN/m ³
Cohesion, c'	0.05 kN/m ²
Friction angle, ϕ'	34°–36°
Dilatancy angle, ψ	2.5°
E_{50}^{ref}	20 MPa
E_{oed}^{ref}	25 MPa
E_{ur}^{ref}	100 MPa
R_{inter}	0.2–1.0
ν_{ur}	0.2
p^{ref}	100 kPa
Power, m	0.5

REFERENCES

- Brinkgreve, R.B.J., Vermeer, P.A., Editors, 1998, Plaxis material models manual. Plaxis B.V., The Netherlands.
- Grande, L. 1998, Some aspects on sheet pile wall analysis, soil-structure interaction. Darmstadt Geotechnics No. 4. Vol. 1: 193–211
- Nordal, S. 2004, Selection of parameters for Hardening Soil Model. International course on experienced PLAXIS users, Trondheim, Norway.
- Potts, D.M., Fourie, A.B. 1986, A numerical study of the effects of wall deformation on earth pressures. Int. J. Num. Anal. Meth. Geom. Vol.10: 382–405
- Sandven, R. 1992, Skirt foundations. Results from model test in sand bin. SINTEF Geotechnical Engineering Report. Contract No. T. 182422.
- Schanz, T., Vermeer, P. A., Bonnier, P. G. 1999, The hardening soil model: Formulation and Verification. Proc. Plaxis Symposium "Beyond 2000 in Computational Geotechnics", Amsterdam: 55–58. Rotterdam: Balkema.
- Tefera, T. H. 2004, Large scale model study and numerical investigation of sheet pile wall. PhD thesis. The Norwegian Univ. of Sci. and Tech. (NTNU), Trondheim.

Parametric FE study of loads and displacements of braced excavations in soft clay

Lars Andresen

Norwegian Geotechnical Institute (NGI), Oslo, Norway

ABSTRACT: A parametric finite element study has been carried out to calculate strut loads, bending moments and displacements of an undrained braced excavation in soft, essentially normally consolidated clay. The objective is to study how the factor of safety against basal heave affects the results. The material model used for the clay accounts for nonlinearity and anisotropy both in strength and stiffness. A strong correlation is found between the factor of safety against basal heave and the loads and displacements of the support system. Both loads and displacements increase with reduced bottom heave stability.

1 INTRODUCTION

The strut loads, moments and displacements of the supporting system for a braced excavation in clay generally increases with decreasing clay undrained shear strength or reduced bottom heave stability. This has been demonstrated through measurements by e.g. Peck (1969) and Flaate and Peck (1972). A strong correlation between wall displacements and bottom heave stability was found from field measurements and finite element parametric studies by Mana and Clough (1981). The effect of clay shear strength and depth of the clay layer on the strut loads and wall moment was demonstrated by Karlsrud and Andresen (2005) through a finite element parametric study.

The present work uses more of the results from the study presented by Karlsrud and Andresen (2005). Results, not only for the final excavation stage, but also for the intermediate excavation stages are used. The results are presented against the calculated factor of safety against basal heave for each stage. The objective is to establish a correlation between support system loads and displacements and the potential for basal heave.

The parametric study is carried out with the PLAXIS 2.D v. 8.2 (Plaxis, 2006) finite element code, and using a nonlinear anisotropic clay model implemented as a user defined soil model.

2 BASAL HEAVE

The factor of safety against basal heave for all cases and construction stages is calculated using the approach

proposed by Bjerrum and Eide (1956) and illustrated for isotropic clays in Fig. 1. In case of anisotropic shear strength, the factor of safety is calculated using the average shear strength $s_u^{ave} = 1/3(s_u^C + s_u^D + s_u^E)$. The shear strength in depth $H + 0.5 \cdot B_c/\sqrt{2}$ is used. N_c is the bottom heave stability number, depending on the ratio H/B_c between the excavation depth and the width of the bottom heave failure mechanism. N_c can be found from the classical diagrams, e.g. Skempton (1951) and Bjerrum and Eide (1956). The width of the failure mechanism is taken equal to the excavation width except for situations where the depth of the failure mechanism is limited by a firm layer. The factor of safety against basal heave obtained in this manner is

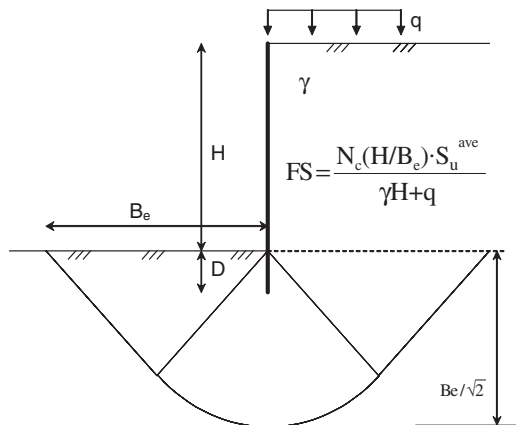


Figure 1. Calculation method for factor of safety against basal heave, after (Bjerrum and Eide, 1956).

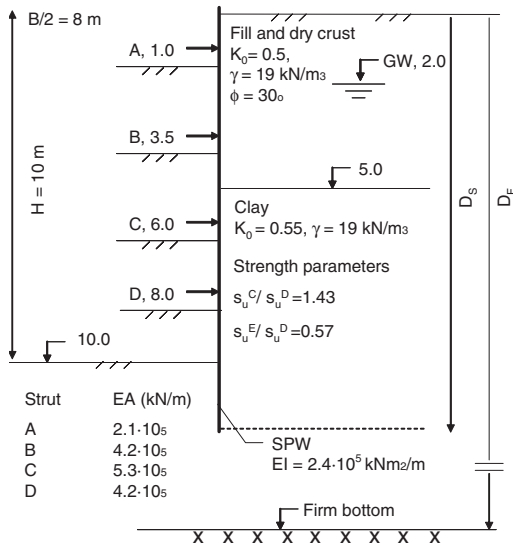


Figure 2. Illustration of the example problem.

not rigorously correct, however it serves as an index characterising the basal stability for a wide range of situations.

3 FINITE ELEMENT STUDY

Figure 2 shows the geometry and material parameters considered in the parametric study. The soil profile comprises a layer of fill and dry crust down to a 5 m depth, and soft clay below that depth. Initial pore pressures are hydrostatic from the groundwater table.

The excavation width and maximum depth are 16 and 10 m respectively. The sheet pile wall (SPW) is crosslot braced with four struts A–D. The excavation is performed sequentially with successive installation of the struts.

A series of cases have been calculated where the undrained shear strength s_u , the length of the wall D_s and the depth to the firm layer D_f are varied.

Half the symmetric problem was modeled in plane strain using 15-noded triangular elements to model the soil and 5-noded beam elements to model the wall. The bending stiffness of the SPW is given in Fig. 2. Interface elements were used to model the thin shearing zone between the wall and the soil. The lower boundary was taken at the depth of the firm layer with displacements fully fixed to model an assumed rough interface between the clay and the firm layer. The vertical (right) boundary was taken at a distance 50 m from the wall. The struts were modeled using spring anchors with axial stiffness given in Fig. 2. The struts were allowed to only carry a compressive force.

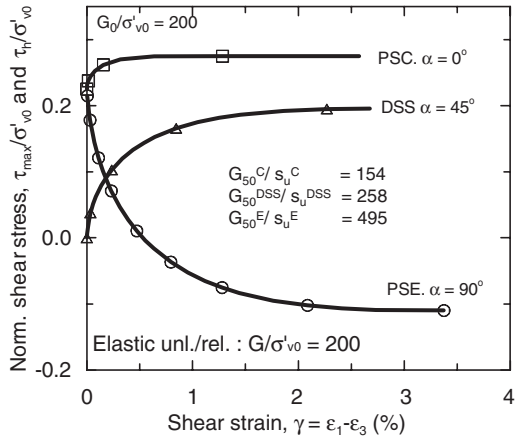


Figure 3. Example of NGI-ANI2 stress-strain relationship for case A1.

The fill and dry crust was modeled as a drained linear elastic – perfectly plastic material using the PLAXIS MC model with a Poisson's ratio $\nu = 0.3$ and with shear modulus $G = 10$ MPa. Full friction was assumed between the wall and the soil.

The soft clay from 5 m depth was modeled using the NGI-ANI2 constitutive model. This model is a modification of the ANISOFT model presented by Andresen and Jostad (2002) implemented as a user defined soil model (UDSM) in PLAXIS. The NGI-ANI2 model accounts for the nonlinear and anisotropic stress-strain relationship of clays using a framework of incremental hardening elastoplasticity and an anisotropic Tresca yield criterion. Input parameters are the undrained shear strengths, $s_u = \text{peak}[1/2(\sigma_1 - \sigma_3)]$ and corresponding shear strains at failure $\gamma_f = (\epsilon_1 - \epsilon_3)_f$ for plane strain compression (C), direct simple shear (DSS) and plane strain extension (E) mode of loading and an isotropic initial tangent shear modulus G_0 . Unloading/reloading is modeled as being elastic with stiffness given by G_0 .

For the base case the normalised undrained direct simple shear strength is $s_u^D/\sigma'_{v0} = 0.2$, where σ'_{v0} is the initial vertical effective stress, and with failure strains $\gamma_f^C = 0.75\%$, $\gamma_f^{DSS} = 2.0\%$ and $\gamma_f^E = 3.0\%$. For all cases the shear strengths in plane strain compression and extension are a factor of respectively 1.43 and 0.57 times s_u^D and with an initial tangent shear modulus $G_0/\sigma'_{v0} = 200$. An example of NGI-ANI2 stress-strain curves for the base case is given in Fig. 3. The assumed $K_0 = 0.55$ yields an initial (prior to construction work) maximum shear stress $\tau_0/\sigma'_{v0} = 0.255$. Material parameters for the different cases are given in Table 1. The clay stiffness may be characterised with the normalized secant shear modulus in direct simple shear at 50% mobilisation of shear strength $G_{50}^{DSS}/\sigma'_{v0}$.

Table 1. Case identification and main results.

Case identification	A1	A2	A3	B1	B2	B3	C1	C2	D1
s_u^{DSS}/σ'_{v0}	0.2	0.24	0.28	0.2	0.2	0.2	0.2	0.2	0.2
Safety factor, SF ^{a,b}	1.01	1.22	1.42	0.95	1.01	1.04	0.95	1.04	1.01
D _S (m)	12	12	12	15	20	20	12	12	12
G _D ⁵⁰ /s _u ^D	258	246	234	258	258	258	258	258	258
D _F (m)	20	20	20	15	20	30	15	30	20
Strut A (kN/m) ^b	*	5	25	10	*	*	12	*	9
Strut B (kN/m)	*	182	196	198	235	181	*	*	17
Strut C (kN/m)	604	351	260	273	417	454	588	615	493
Strut D (kN/m)	449	265	189	135	273	357	364	464	546
Toe (kN/m)	*	*	*	177	48	*	*	*	*
Sum (kN/m)	1053	803	670	793	973	992	964	1079	1065
K _{total} = 2 Σum/γH ²	1.11	0.85	0.71	0.83	1.02	1.04	1.01	1.14	1.12
Moment, M (kNm/m) ^b	793	323	133	594	631	568	729	807	681
Deflection, δ/H(%) ^b	1.88	0.85	0.51	0.49	0.79	0.94	1.70	1.89	1.73

^a SF against bottom heave defined in text ^b Final stage

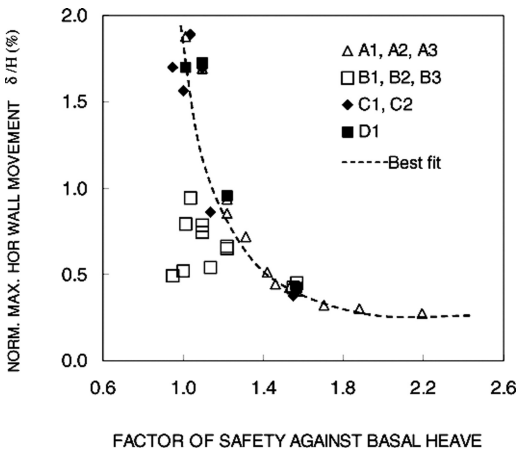


Figure 4. Relationship between normalized maximum horizontal wall movement and factor of safety against basal heave.

4 RESULTS

Table 1 gives the identification of the cases and the main results from the final excavation stage of all cases.

In Figs. 4–6 results from all but the first, cantilever, stage of excavation are plotted against the appropriate factor of safety against basal heave for each stage. The total strut force (sum of all active struts) is normalised by the sum of vertical total stresses against the wall above the excavation level, i.e. $K_{tot} = \Sigma F/0.5\gamma H^2$. The maximum horizontal wall displacement δ is normalised with the excavation depth H .

There is a strong correlation between the factor of safety against basal heave and strut force, wall moment and wall displacement. There is scatter in the results due to the fact that the cases involve both fixed and free end

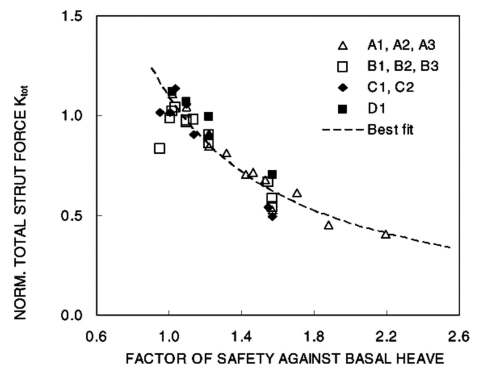


Figure 5. Relationship between normalized total strut force and factor of safety against basal heave.

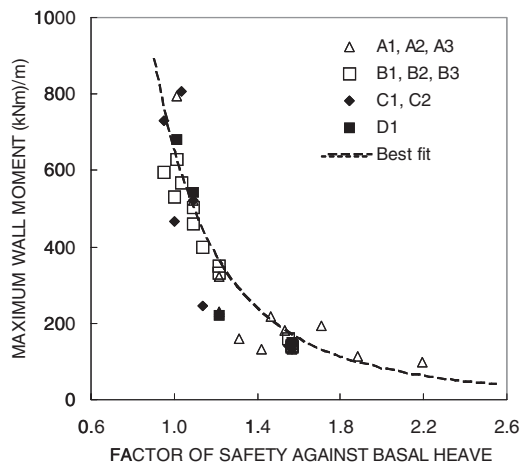


Figure 6. Relationship between wall moment and factor of safety against basal heave.

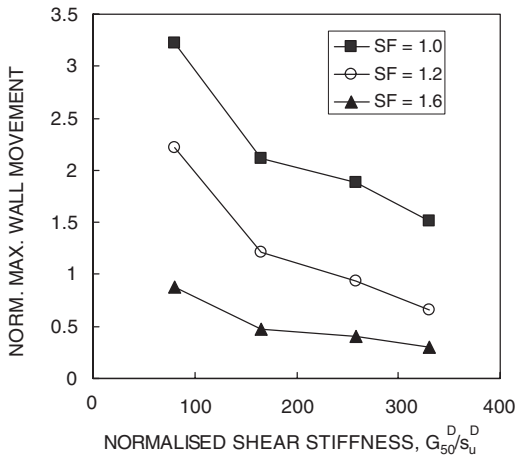


Figure 7. Relationship between normalised wall movement and normalised clay shear stiffness.

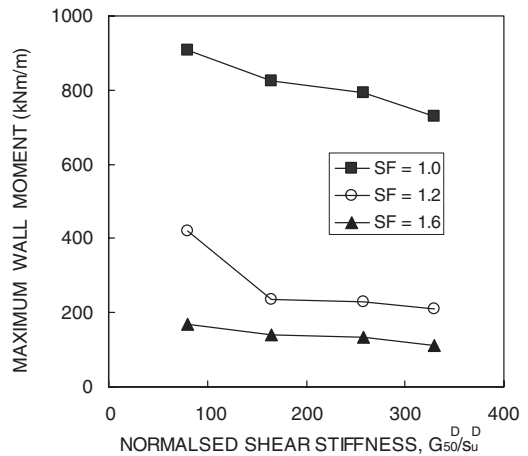


Figure 8. Relationship between wall moment and normalised clay shear stiffness.

walls, varying depth of soft clay to the firm layer, varying wall embedment and varying strut preloading. Strut force, wall moment and wall displacement all increase with decreasing basal heave stability. There is a large increase of both wall moment and displacement when the factor of safety against basal heave becomes lower than approximately 1.4. This indicates increasing zones of plasticity (yielding).

The wall displacements from the cases with longer walls (B1, B2, B3) and fixed ends (B1, B2) are considerably lower than for the free end walls at the same factor of safety against basal heave. The strong correlation between wall displacement and factor of safety against basal heave has been presented also by Mana and Clough (1981), however they did not find any significant difference between free end and fixed end walls. For the results of strut force and wall moment there is not a large effect of amount of wall embedment or wall end condition.

There is a small, but not very significant effect, on the results when the depth to the firm layer DF is reduced from 20 m to 15 m. Increasing the depth from 20 m to 30 m has essentially no effect. Resulting strut force from case D1 is somewhat above the trend due to the applied strut preloading to about 75% of the maximum load.

The results presented in Figs. 4–6 are all from cases with the same clay shear stiffness $G_{50}^{DSS}/S_u^{DSS} = 258$. The clay stiffness affects the support system load and displacement also. In Figs. 7–9 results are presented for the same case as A1 but where the shear stiffness has been varied. It is seen that for the same factor of safety against basal heave both wall displacement, moment and strut forces increases with decreasing clay stiffness.

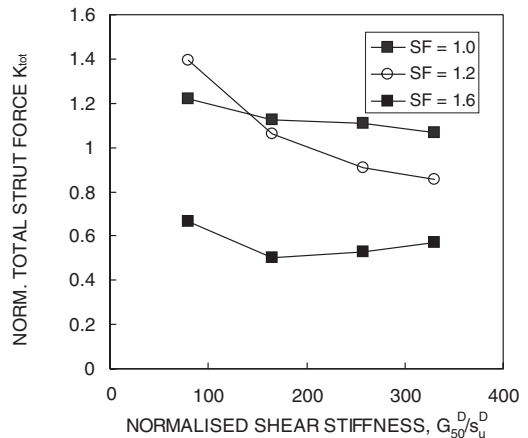


Figure 9. Relationship between normalised strut forces and normalised clay shear stiffness.

5 CONCLUSIONS

Results from the FE parametric study show that a strong correlation exists between the factor of safety against basal heave and the strut forces, wall moment and displacement. Results are obtained for several cases of support systems with the same wall bending stiffness and excavation width but with varying clay shear strength, clay shear stiffness and excavation depth, wall length, wall end condition and depth to firm layer. For problems of similar conditions as described herein, the relationships obtained can be used to estimate support system loading and displacements using the analytically calculated factor of safety against basal heave and the normalized clay shear stiffness.

ACKNOWLEDGEMENT

The writer would like to thank Norwegian Geotechnical Institute and the Research Council of Norway for funding the work.

REFERENCES

- Andresen, L. and Jostad H. P. (2002). A constitutive model for anisotropic and strain-softening clay. Proc. Num. Models in Geomechanics – NUMOG VIII, Italy, Rome, pp. 79–84.
- Bjerrum, L. and Eide, O. (1956). Stability of Strutted Excavations in Clay. Geotechnique, London, England, Vol. 6, No. 1, pp. 32–47.
- Flaate, K. and Peck, R.B. (1972). Braced cuts in sand and clay. Norwegian Geotechnical Institute Publ. 96, Oslo, Norway.
- Karlsrud, K. and Andresen L. (2005). Loads on Braced Excavations in Soft Clay Int. J. Geomech., Vol. 5, No. 2, Special Issue: Soft Clay Engineering and Soft Clay Improvement, pp. 107–114.
- Mana, A. I. and Clough, G.W. (1981). Predictions of movements for braced cuts in clay. J. Geotech. Eng. Div. ASCE. 107(6), pp. 759–777.
- Peck, R.B. (1969). Deep excavations and tunneling in soft ground. Proc. 7th Int. Conf. on Soil Mech. and Found. Engr. Mexico City, State-of-the-Art Volume. pp. 225–290.
- Plaxis (2006). PLAXIS v. 8.2 Prof. version, update pack 4, www.plaxis.nl
- Skempton, A.W. (1951). The Bearing capacity of clays. Proc. Building Research Congress. London. p. 180–189.

Numerical modeling of propped retaining walls – influence of parameters

H. Popa

Technical University of Civil Engineering, Geotechnical and Foundations Department, Romania

L. Thorel

Laboratoire Central des Ponts et Chaussées – Centre de Nantes, France

C. Gaudin

Centre for Offshore Foundations Systems, University of Western Australia, Crawley, Australia

J. Garnier

Laboratoire Central des Ponts et Chaussées – Centre de Nantes, France

ABSTRACT: Diaphragms walls are often used to support deep excavations, especially in urban areas. Their behavior is a critical point, taking into account the impact on the neighboring buildings. Design methods usually use limit equilibrium theory. These methods do not take into account the interaction parameters, some of them with great influence on the wall behavior, e.g. the relative wall – soil stiffness, the initial stress state in the ground, the wall – soil interface etc. A more reliable modeling can be obtained using the finite element method (FEM) which has been significantly improved over the past decade to model soil structure interactions. The paper presents the numerical modeling of a propped diaphragm wall. A parametric study is performed and the numerical results are compared with those obtained using limit equilibrium methods.

1 INTRODUCTION

Centrifuge and numerical modeling have been used independently for many years to study and predict the behaviour of geotechnical structures. However, by replicating faithfully the real in-situ conditions and by offering a very good control of the tests procedures and parameters, centrifuge modeling appears to be a useful tool to provide high quality data to calibrate numerical model. The two methods appear to be complementary and would surely benefit of a deeper interaction. This is illustrated in this paper where centrifuge results on tests performed on a cantilever wall were used to calibrate a numerical model which was afterwards used to investigate parameters influencing the behaviour of a propped retaining wall. During the last few years such interaction research has been conducted at the Laboratoire Central des Ponts et Chaussées (LCPC). The study refers to autostable diaphragm walls behavior and to their effects on neighboring foundations. The experimental models have been modeled afterwards by using FEM (Gaudin 2002; Popa, 2001, 2002, 2003), allowing to calibrate and validate the numerical model.

1.1 Numerical modeling

The model geometry (corresponding to the prototype) is shown Figure 1. The model size is imposed by the container used for the centrifuge tests. Even if these limits are closer to the wall than the usual ones for this type of construction (Mestat, 1997), the numerical results have validated this assumption (Gaudin, 2002). The horizontal displacement for the vertical boundaries of the numerical model is nil ($u = 0$), as well as the vertical displacement along the lower boundary ($v = 0$).

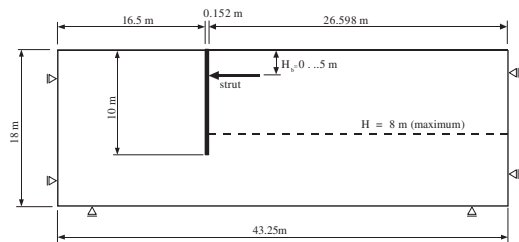


Figure 1. Geometry of the numerical model.

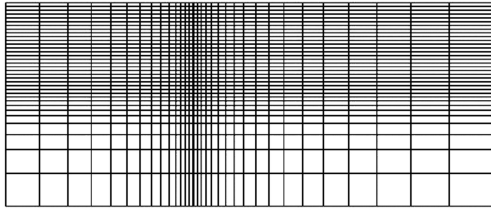


Figure 2. Finite elements mesh.

Table 1. Finite elements mesh characteristics.

No. groups	No. nodes	No. elements	Element type
40	3726	1217	1156 MBQ8 + 60 FDQ6 + 1 BB2

Table 2. Geotechnical characteristics.

E_s , MPa	ν	c , kPa	ϕ , °	ψ , °
75	0.275	2.6	39.4	16.7

where: E_s – soil elastic modulus; ν – Poisson coefficient; c – cohesion; ϕ – friction angle; ψ – dilatancy angle.

The model mesh and mesh characteristics are presented in Figure 2 and Table 1.

For both the soil and the wall, rectangular elements with 8 nodes (MBQ8) have been used.

For the soil – wall contact, special contact finite elements with 6 nodes (FDQ6) were used and for the strut a beam element between 2 nodes (BB2).

The strut position was modified in order to cover more than one depth value, varying from $H_b = 0 \dots 5$ m.

1.2 Material characteristics

The soil behavior (Fontainebleau sand) is described by an elastic – perfect plastic Mohr – Coulomb with non-associated failure criteria. The geotechnical parameters used for the calculation are presented in Table 2. The soil unit weight is $\gamma_d = 16,0 \text{ kN/m}^3$.

Due to the fact that the wall stiffness is much higher than the soil one, for the wall an elastic law has been adopted, characterized by an elastic modulus $E_p = 22350 \text{ MPa}$ and a Poisson coefficient $\nu = 0.3$. The wall stiffness was modified in order to take into account its influence on the results.

The soil – wall contact was modeled using a sliding interface with the same parameters for all calculations: elastic modulus $E_c = 75 \text{ MPa}$ and tensile strength $R_t = 0 \text{ MPa}$.

The strut was modeled by using a beam element initially characterized by an elastic modulus

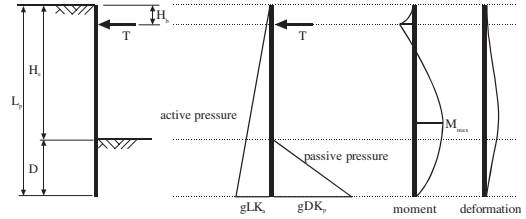


Figure 3. Static scheme for limit equilibrium methods LE1 and LE2.

$E_b = 24000 \text{ MPa}$ corresponding to reinforced concrete and a cross section $A_b = 0.1 \text{ m}^2$. The strut stiffness was modified in order to evaluate its influence on the wall behavior and the calculation results.

The numerical simulation has been performed using the FE code CESAR – LCPC, version 3.3.1. under Unix.

The calculations were performed in 2 dimensions (2D), modeling plane strains conditions, similar to the one achieved by the centrifuge modelling (Gaudin, 2002).

Note that the numerical model refers to the prototype retaining wall, that has been investigated at reduced scale by the centrifuge test.

1.3 Limit equilibrium calculation

The limit equilibrium calculation methods, known also as classical methods, are wide spread and used for diaphragm wall design (Delattre, 1999). This paper presents also some limit equilibrium computations for the same wall analyzed by FEM. The objective is to compare the results and to assess the influence of the various parameters. Three assumptions have been considered for the limit equilibrium calculations, called LE1, LE2 and LE3, presented hereafter.

1.3.1 Calculation LE1

For the LE1 calculation (simple passive earth pressure) the wall is considered simply propped on the strut and supported by the soil above the excavation bottom. (Figure 3).

In this assumption the limit passive earth pressure developed above the dredge line is reduced by a safety coefficient $F_s = 2$, resulting the design parameters, e.g. the wall embedment below the dredge line, D , the maximum bending moment, M_{max} and the axial force in the strut, T . This method is applicable for perfect rigid walls and, generally, it leads to an overestimation of bending moments and reactions for flexible walls.

1.3.2 Calculation LE2

LE2 calculation is similar to LE1 and uses the same static scheme (Figure 3). The difference between the

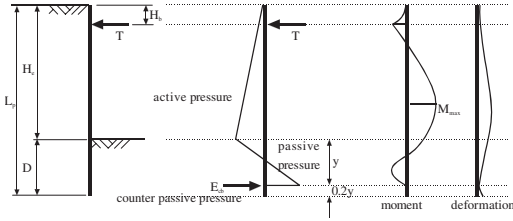


Figure 4. Static scheme for LE3 type limit equilibrium computation.

two computation methods is that the safety coefficient is taken equal to 1 for the passive earth pressure. It results the maximum bending moment and the strut axial force. The needed safety is obtained by multiplying the wall depth by $\sqrt{2}$.

1.3.3 Calculation LE3

In the third limit equilibrium computation the wall is considered to be embedded in the soil below the dredge line (this assumption is closer to the real wall behavior as indicated by FEM). In this case the soil embedment is ensured by a couple of earth pressures, passive earth pressure – counter passive earth pressure (Figure 4). The counter earth pressure is replaced by a force (E_{cb}) acting in the zero bending moment point.

2 STRUT DEPTH INFLUENCE

The FEM results for bending moment values are compared with those obtained from the limit equilibrium computations (LE1, LE2 and LE3). Figure 5 presents the ratio of the bending moment from the analytical calculation upon the one from the numerical analysis.

As shown on Figure 5 the differences are quite important between the two methods. The bending moments reports vary between 1.29 and 5.09. LE1 method (diminution of the passive earth pressure) overestimates drastically the bending moments for all configurations. LE3 method (embedded wall) gives the closest results to the numerical ones, but the differences are still high $M_{LE}/M_{FEM} = 1.29 \div 3.07$.

The maximum bending moments in the wall versus the strut or excavation depth is similar for the two computation methods (Figure 6).

The stability calculations using limit equilibrium methods give the embedment value considering the wall to be simply propped below the dredge line (LE1 and LE2) or embedded (LE3). The necessary wall length L_p is then compared to the fixed length (10 m) used for FEM (Figure 7), function of the strut and excavation depth.

It can be noted that only for a deep excavation (7 ÷ 8 m) the stability calculations give a necessary

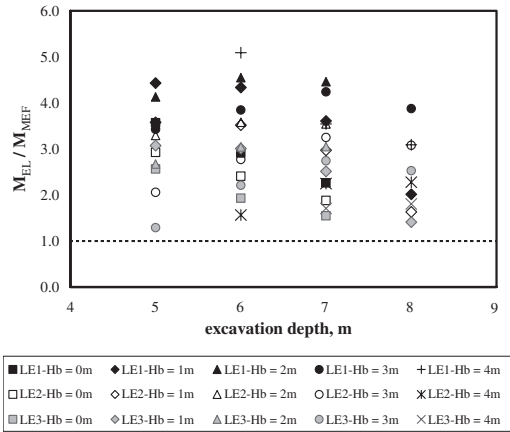


Figure 5. Bending moments in the wall in FEM and limit equilibrium method, function of the excavation depth.

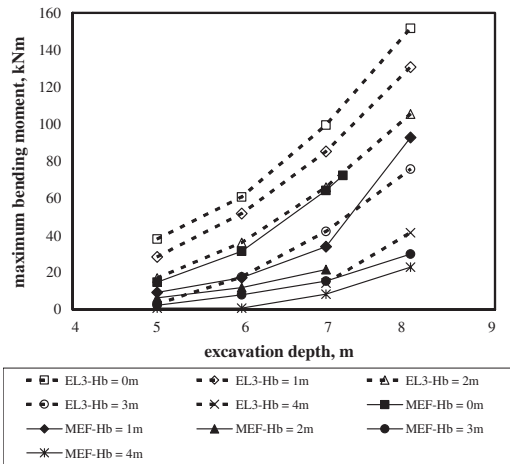


Figure 6. Maximum bending moments for limit equilibrium method and FEM, function of excavation depth.

wall length of about 10 m. The influence of the strut position on the wall depth is relatively low, being noted a small diminution when increasing the strut depth. Inversely, the excavation depth has an important influence and the relationship is almost linear (Figure 7).

Figure 8 presents 2 comparisons between the bending moments diagrams issued from LE3 and FEM computations for two cases for which the limit equilibrium wall depth is close to 10 m ($H_b = 0.0$ m, excavation depth 7.0 m, respectively $H_b = 4.0$ m, excavation depth 8.0 m).

The graphs on Figure 8 show a similar shape for LE3 and FEM bending moments and close maximum bending moment levels. As noted here above, the limit

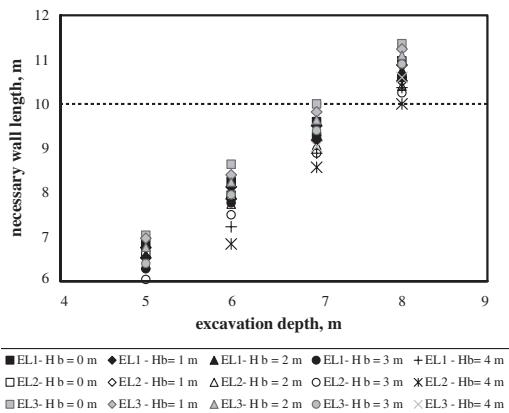


Figure 7. Wall depth as needed for stability purposes issued from limit equilibrium computations.

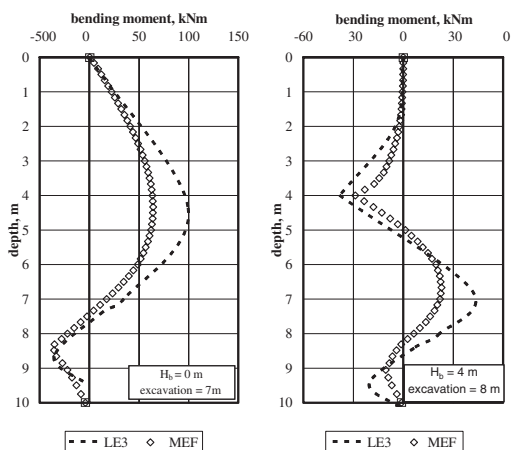


Figure 8. Comparison between LE3 and FEM bending moments.

equilibrium method overestimates the wall bending moments.

3 STRUT STIFFNESS INFLUENCE

In order to study the influence of the strut stiffness on the wall behavior, several numerical modeling were performed considering a stiffness varying from 282 to 90232 kN/m. The stiffness is computed using the following formula:

$$K_b = \frac{E_b A_b}{L_b}$$

where: E_b – strut elastic modulus; $A_b = 0.1 \text{ m}^2$ – strut cross section; $L_b = 26.598 \text{ m}$ – strut length.

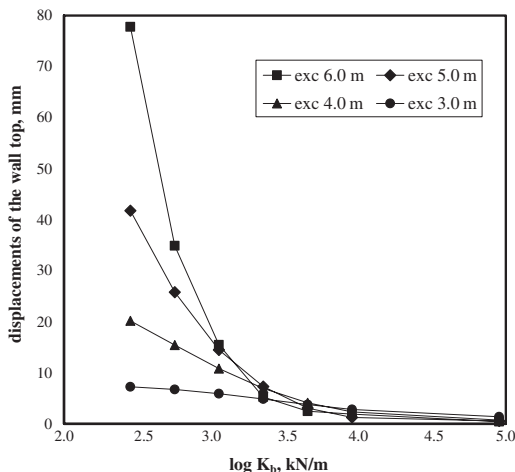


Figure 9. Horizontal displacements at top of the wall versus the strut stiffness.

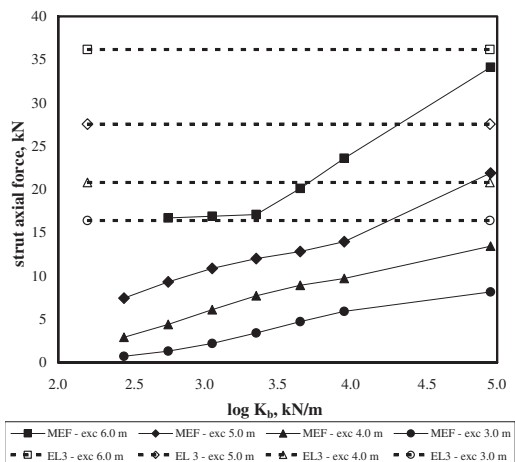


Figure 10. Strut axial forces versus strut stiffness.

The computations were performed using only one strut depth value H_b equal to 2.0 m.

Figure 9 shows the horizontal displacements of the top of the wall as a function of the logarithm of the strut stiffness. One can note an increasing displacement with the decreasing strut stiffness. Over 10000 kN/m of stiffness, the influence on the displacements becomes negligible.

The strut axial forces versus strut stiffness are shown in Figure 10 for various excavation depths. The graphs show also the values issued from the limit equilibrium computation (LE3). Comparing the values for the two calculation methods one can note that the differences depend strongly on the strut stiffness.

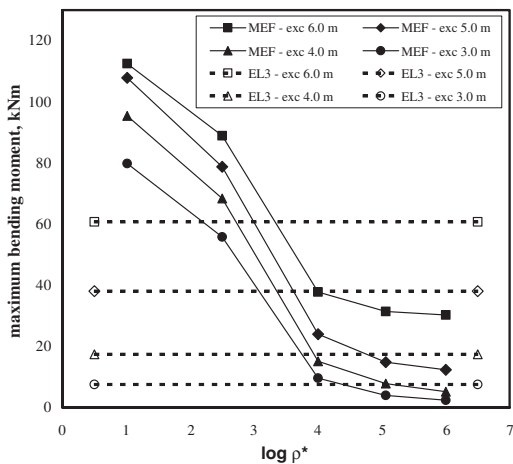


Figure 11. Wall bending moments versus wall stiffness.

The limit equilibrium calculation doesn't take into account the strut stiffness, indicating a constant value of the strut axial force for a given configuration, while the FEM computation shows a force diminution when the strut stiffness decreases. Only for high stiffness values the FEM and limit equilibrium results are closer.

4 WALL STIFFNESS INFLUENCE

In order to take into account the relative wall – soil stiffness, the results are expressed as a function of the flexibility characteristic, ρ^* computed as follows (Potts et Bond, 1994):

$$\rho^* = (L_p^4 E_s) / (E_p I_p)$$

where: $L_p = 10\text{ m}$ – wall depth; $E_s = 75000\text{ kPa}$ – soil elastic modulus; $E_p = \text{various values}$ – wall elastic modulus, kPa; $I_p = 292.6 \times 10^{-6}\text{ m}^4$ – wall inertial modulus.

The computations were performed for a strut depth H_b equal to 0.0 m.

Figure 11 shows the maximum bending moments function of ρ^* . For comparison purposes, on the same graphs are shown the results using the limit equilibrium method LE3.

It can be observed on the graphs a strong influence of the wall stiffness on the bending moments, for all excavation depth values. In fact, the relationship is similar for the various excavation depths that have been considered (from 3 to 6 m) and they are corresponding to those obtained by Potts and Bond (1994) on similar diaphragm walls.

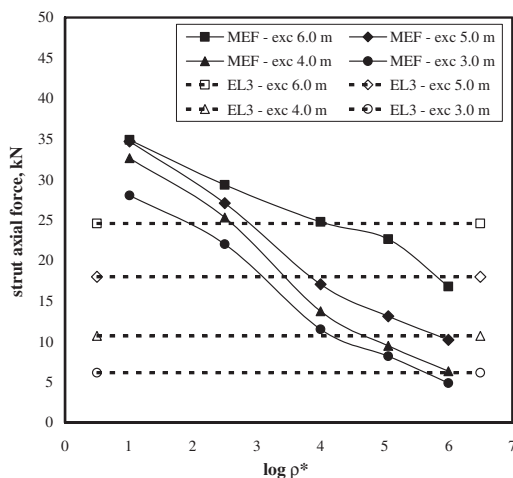


Figure 12. Axial forces in struts versus wall stiffness.

The numerical results are 2 to 10 times higher than the limit equilibrium ones (depths equal to 6 and, respectively, 3 m) for the very rigid walls ($\rho^* = 10.25$) and become 3 times lower for a very flexible wall ($\rho^* = 1000000$) than the LE3 values. It can be affirmed that for $\rho^* \geq 10^5$ the limit equilibrium calculation is more conservative.

The axial forces in the struts as function of the ρ^* characteristic for various excavation depths are shown Figure 12. LE3 results are also shown on the same graphs.

Comparing the results issued from numerical modeling and limit equilibrium computations one can note, once again, the strong influence of the wall stiffness, leading to important differences. For a rigid wall ($\rho^* = 10.25$) FEM results are 1,4 to 4,5 times higher than the limit equilibrium ones, while for very flexible wall ($\rho^* = 1000000$) is the contrary: the numerical values are 1.5 times lower than LE3 results. For $\rho^* \geq 10^5$ the limit equilibrium method is more conservative.

5 CONCLUSIONS

Modelling retaining structures represents a complex soil – structure interaction problem.

The study presented refers to finite element modeling for a single strutted diaphragm wall.

The numerical model used the same parameters which have proved to be reliable in the previous models based on centrifuge tests. The geometry and material are also the same as for the centrifuge tests.

A parametric study has been performed for the main interaction parameters: strut depth, strut stiffness, wall stiffness. The numerical results have been compared

with limit equilibrium results, considering several assumptions.

The strut depth seems to have the strongest influence on the wall behavior, especially concerning the horizontal displacements and the bending moments. The graphical representations show an optimum strut depth of about 2 ÷ 3 m for which minimum bending moments and displacements are obtained.

The strut stiffness has also an important influence on the wall behavior, especially for the horizontal displacements and for stiffness values lower than 10⁵ kN/m. The displacements increase when strut stiffness decreases, while the maximum bending moments decrease. The bending moments are less influenced than the displacements. The bending moments are, on the other hand, strongly influenced by the strut stiffness, when this one is higher than 600 kN/m.

The wall stiffness strongly influences all results. For example, in the case of bending moments, the numerical results are 2 to 10 times higher than the limit equilibrium ones (excavation depth of 6 m and, respectively, 3 m) for very rigid walls ($\rho^* = 10.25$) and 3 times lower for very flexible walls ($\rho^* = 10^6$). As well, in case of strut forces, for a rigid wall ($\rho^* = 10.25$) FEM results are 1,4 to 4,5 times higher than limit equilibrium ones, while for very flexible wall ($\rho^* = 1000000$) the results are inverse and the numerical values are 1.5 times lower than LE3 ones.

All those results would be helpful in order to design new centrifuge tests on propped diagram walls.

REFERENCES

- CESAR – LCPC. 1997. Manuel d'utilisation.
- Delattre, L. 1999. Comportement des écrans de soutènement. Expérimentations et calculs, *Thèse de doctorat*, ENPC – Paris, France, 492 p.
- Gaudin, C. 2002. Modélisation physique et numérique d'un écran de soutènement. Application à l'étude de l'interaction écran – fondation, *Thèse de doctorat*, LCPC, nov. 2002.
- Mestat, Ph. 1997. Maillage d'éléments finis pour les ouvrages de géotechnique. Conseils et recommandations, *Bulletin de liaison des laboratoires des Ponts et Chaussées*, vol. 212, pp.39–64, LCPC, nov–déc.
- Popa, H. 2001. Modélisations numériques 2D avec CESAR-LCPC d'un essai en centrifugeuse sur une paroi de soutènement, *Rapport de stage*, LCPC-Nantes, 59 pp.
- Popa, H. 2002. Modélisations numériques 2D avec CESAR-LCPC des essais en centrifugeuse sur des écrans autostables à proximité d'une fondation, *Rapport de stage*, LCPC-Nantes, 42 pp.
- Popa, H. 2003. Modélisations numériques 2D avec CESAR-LCPC des parois de soutènement autostables à proximité d'une fondation, *Rapport de stage*, LCPC-Nantes, 50 pp.
- Potts, D.M., Bond, A.J. 1994. Calculation of structural forces for propped retaining walls, *XIII ICSMFE*, 1994, New Delhi, India, pp. 823–826.

Elastoplastic joint element for the finite element analysis of the Hochstetten sheet pile wall

F. Elmi, E. Bourgeois, A. Pouya & C. Rospars

Laboratoire Central des Ponts et Chaussées, Paris, France

ABSTRACT: A four-node joint element has been introduced in the finite element code CESAR-LCPC, in order to model the contact between blocks in fractured rocks. We present here an attempt to model with this element the mechanical interaction between a retaining structure and the adjacent ground. The discussion is based on the comparison of numerical results with measures on a full scale monitored structure, the experimental sheetpile wall built in Hochstetten in 1994. The data available on the ground and the measures make it a reference for the validation of numerical simulation of retaining structures. Results show that simulations are in good agreement with measures, and that the new element provides a greater simplicity to the user of the code and an efficient way of modelling the soil-structure interaction.

1 INTRODUCTION

The use of the finite element method for the design of retaining walls remains rare, because simpler methods, for instance the subgrade reaction modulus method, give good results both in terms of bending moments and of horizontal displacement. However, such methods do not provide any information about the displacements induced in the surrounding ground by the construction of the retaining structure: therefore the prediction of the impacts of the excavation, and especially the vertical settlements induced by the excavation behind the wall, remains largely empirical.

One of the advantages of the finite element method is that numerical solutions include the displacements of all the nodes of the mesh, and thus give access to the displacements of the ground and not only those of the wall itself. However, finite element analyses often lead to results very different from the observed behaviour of real structures, or at least very dependent on the technique used in the simulation to model the mechanical interaction between the ground and the wall. As is well known, if no particular simulation technique is used to model the contact between the ground and the wall, the vertical response of the ground below the bottom of the excavation may lead to a displacement of the wall towards the supported ground, which is not realistic and makes the simulation results useless. It is therefore necessary to introduce a numerical technique to model the interaction between the wall and the ground, the difficulty being that it is not clear that the choice made for the interface has no interaction with the constitutive law of the ground.

Given the wide range of simulation tools available, and the fact that the determination of the parameters of the model used for the interface is not always well documented, it is advisable to validate them by checking the results against measures on full scale structures. The monitoring of an experimental sheetpile wall carried out in Hochstetten (Germany) in 1993 by the university of Karlsruhe (von Wolffersdorff, 1994a) provides a way of testing finite element techniques for the simulation of retaining walls. The wall was the basis of a prediction contest. Results obtained by different authors show that, if the overall behaviour and the horizontal displacements are well reproduced with simple models for the soil-wall interaction, the settlements behind the wall remain difficult to reproduce (Shahrour et al. 1995, Coquillay et al. 2005).

We discuss here the results obtained with special elastoplastic joint elements for the soil-wall interface. First, the formulation of the joint element (Goodman et al. 1968) is briefly recalled. The numerical implementation of the element in a “research” version of the finite element software CESAR-LCPC is briefly described. In the last place, the results obtained with the new element are compared with the results of simulations using a layer of thin elements.

2 FEATURES OF THE JOINT ELEMENT

2.1 *General presentation*

The explicit modelling of discontinuities using the FEM and the so-called joint elements goes back to the works of Goodman et al. (1968), Zienkiewicz et al.

(1970) or Ghaboussi et al. (1973). Goodman et al. (1968) proposed a zero-thickness element to model the discontinuities, in which the contact stresses and the relative displacements follow a linear relationship, with constant normal and tangential stiffness. Although it was originally developed for the simulation of joints in fractured rock masses, this element has been used to deal with problems of civil engineering involving discontinuities. It must be kept in mind that the discontinuities of the displacement along the interface between the ground and a concrete structure may be small in practice, but that the introduction of a joint element provides a convenient way of controlling (or rather limiting) the stresses that can be exerted at the interface between materials, and thus obtain more realistic stress distributions.

The joint element implemented in CESAR-LCPC is of the same type: it is a rectangular, four-node and zero thickness element. The degrees of freedom are the displacements of the nodes. The basic assumption of the model is that the behaviour of the joint can be expressed in terms of the normal stress σ and the shear stress τ acting on the surface of the joint between two adjacent blocks, on the one hand, and of the normal relative displacement u_n and the tangential relative displacement u_t , on the other hand.

Assuming that the relative displacement can be splitted into an elastic part and a plastic part, the constitutive law reads:

$$\begin{bmatrix} \sigma \\ \tau \end{bmatrix} = \begin{bmatrix} K_n & 0 \\ 0 & K_t \end{bmatrix} \left(\begin{bmatrix} u_n \\ u_t \end{bmatrix} - \begin{bmatrix} u_n^p \\ u_t^p \end{bmatrix} \right) \quad (1)$$

where u_n^p and u_t^p are the plastic parts of the normal and tangential relative displacements, and where the stiffness parameters K_n and K_t depend on the thickness of the real joint and of the material filling the space between adjacent rock blocks.

The plastic part of the relative displacement is described by an elastoplastic flow rule. The yield function adopted here is the Mohr-Coulomb function, the flow rule is non-associated. Denoting the yield function by f and the plastic potential by g , we have:

$$f(\sigma, \tau) = |\tau| - \sigma \tan \varphi - c \quad (2)$$

$$g(\sigma, \tau) = |\tau| - \sigma \tan \psi \quad (3)$$

where φ and ψ are the friction angle and the dilatancy angle respectively. The flow rules writes:

$$\begin{bmatrix} \dot{u}_n \\ \dot{u}_t \end{bmatrix} = \dot{\lambda} \begin{bmatrix} \frac{\partial g}{\partial \sigma} \\ \frac{\partial g}{\partial \tau} \end{bmatrix} \quad \text{with } \dot{\lambda} \geq 0 \quad (4)$$

where $\dot{\lambda}$ is the plastic multiplier, equal to zero if $f < 0$ and such that $\dot{f} = 0$ if $\dot{\lambda} > 0$. In the approach used here, a linear interpolation is used for the relative

displacements (and the normal and tangential stresses) along the joint element.

2.2 Numerical implementation

The numerical implementation of the stiffness of the joint elements is relatively simple. The implementation of the iterative procedure for the computation of the plastic relative displacements is also similar to the algorithms used for standard elements, though the adaptation must be carried out carefully.

From a practical point of view, the use of joint elements rise two specific difficulties:

- the introduction of the interface in the mesh; for the purpose of the study undertaken here, two specific tools have been designed: one makes it possible to introduce new nodes in an existing mesh along lines defined by the user (the difficulty is to define an algorithm robust enough to deal with intersections of joints), and the other is relatively simpler, and makes it possible to introduce joint elements at the interface between two sub-meshes and to assemble them in a third one;
- the initialization of the stress state in the joint element, which is likely to have a significant influence on the results (especially in the case of an excavation in front of a retaining wall).

Besides, given that we intend to use the model for the simulation of the excavation of the ground in several steps in front of a retaining wall, special care must be taken to ensure that the local stress state in the joint (σ , τ) is properly stored and retrieved between two successive computations.

2.3 Joint element features and expected performance

The normal stress in the joint is not zero, even if the normal stiffness is small and/or the normal component of the relative displacement becomes positive: the model does not account for unilateral contact – or joint opening, unless no traction stress is allowed by the yield function (i.e. unless the cohesion of the joint is zero, which should be avoided for numerical reasons). The joint element is therefore not means to reproduce the opening of the joint, seen as the loss of contact between two solids. In any case, the closure of the “open” joint can not be properly modelled. It follows that the joint element should not provide results very different from what can be obtained with small thickness elements. In practice, however, the joint element makes the mesh generation simpler (which can be significant to model real structures with complex construction process).

In the last place, the choice of the stiffness parameters of the joint remains to be discussed, keeping in mind that these parameters may have different meanings for a contact between rock blocks and for an

interface between a steel or concrete structure and a ground with much weaker characteristics.

3 THE EXPERIMENT AND THE SITE

The experimental wall under discussion hereafter was a 7-m long wall built in Hochstetten. Sheetpiles were vibrodriven down to a depth of 6 m in a sandy unsaturated ground. A row of three struts was placed to ensure its stability during the excavation (von Wolfersdorff, 1994a). The water table is located 5.5 m below the natural ground level. The experiment consisted in the following sequence :

- (0) installation of the sheet piles;
- (1) excavation of the ground in front of the wall down to a depth of 1 m;
- (2) excavation down to 1.75 m;
- (3) installation of three struts at a depth of 1.25 m, with an initial normal force of 10 kN each ;
- (4 to 6) excavation down to 3, 4 and 5 m;
- (7) application of a 10 kPa load at the ground surface, behind the wall, between 1 and 5 m from the wall head;
- (8) progressive shortening of struts until the normal force reached a constant value, corresponding to the limit state of the ground behind the wall.

The monitoring devices made it possible to measure earth pressures on both sides of the wall, bending moments in the wall, horizontal displacements of the wall and of the ground at a distance of 80 cm behind it. Measures also included settlements behind the wall, and forces in the struts. Given the large number of data, and their dispersion, comparisons are made with averaged values of the measures considered as reliable. Results of the experiment have been made public after the prediction contest by von Wolfersdorff (1994b), and reproduced by Shahrouf et al. (1995) and Coquillay (2005).

The ground is a fine to medium sand, with a density index of 58.4 and a dry volume weight of 15.7 kN/m³; the volume weight is 16.5 kN/m³ in the unsaturated zone and 19.8 kN/m³ in the saturated zone. Pressuremeter tests showed that the site is made of three layers: the first two meters are made of fine and slightly silty sand; between 2.3 and 4 m, the ground is a fine and slightly silty sand with gravels, and below 6 m tests showed the presence of a layer of sandy gravel.

4 FINITE ELEMENT SIMULATION OF THE HOCHSTETTEN PILE WALL

4.1 Finite element simulation

The sheet pile wall is modelled in plane strain. For comparison of joint elements with previous simulations,

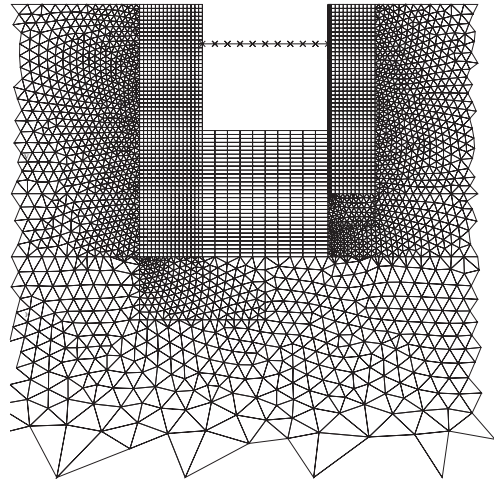


Figure 1. Detailed view of the central part of the mesh used for the numerical simulations – the apparent density is related to the fact that the elements used are linear.

we adopt the same choices as Mestat et Arafati (1998) and Coquillay et al. (2005) when possible:

- the mesh includes the monitored wall and the opposite wall used for the reaction of the struts. Dimensions of the mesh are 45 m × 15 m. It includes 8000 elements and 5400 nodes (figure 1). Since only a four-node version of the joint element is available at present, the mesh is made of “linear” elements (4-node rectangles and 3-node triangles);
- sheet piles are modelled with 4-node rectangle elements, with an elastic behaviour and a thickness notably larger than the actual thickness of the sheet-piles: equivalent constitutive parameters are chosen to reproduce the rigidity of the real wall with respect to bending and to traction. The interface between the piles and the ground is modelled by four rows of joint elements (one on each side of the two walls);
- struts are represented by bar elements, with a reduced section (0.02 m²) to take into account the horizontal spacing between struts. The horizontal displacement is zero on the vertical boundaries, and both displacements are zero on the lower boundary;
- computations are carried out in effective stresses, and the initial stress field is geostatic, with a volume weight of 16.5 kN/m³ above the water table ($0 < z < 5.50$ m) and 9.8 kN/m³ below ($z > 5.50$ m). The coefficient of earth pressure at rest is given by $K_0 = 0.35$. The parameters obtained above correspond to depths between 1 and 4 m, and have been adopted for the whole numerical model, except for the cohesion, set to zero below the water table. The simulation itself consists in the sequence of steps described in section 4. The initial normal force in the strut is taken into account, in step 3, by a force

applied at both ends of the bar element before activating the corresponding stiffness. Step 8 is not reproduced in the simulation presented here.

4.2 Choice of the parameters

The prediction contest showed considerable discrepancy in the parameters used by the participants, although the same test results were provided to all participants. These differences result in part from the fact that models used for the soil were different. However, even with the same soil model (linear elasticity with Mohr Coulomb plasticity) different parameters were chosen, because of the influence of the model used for the soil-wall interface, and also because the geotechnical survey included several types of tests (triaxial tests and plate loading tests).

We have adopted the same friction and dilatancy angles as Mestat and Arafati (1998), then performed a parametric study to find the values of the other parameters that give the best agreement between the computed displacements and the measures.

We compare the results obtained with the parameters resulting from the parametric study with previous analyses by Mestat and Arafati (1998) and by Coquillay et al. (2005).

Mestat and Arafati used a mesh with 800 elements (8-node rectangles) and 2600 nodes, and modelled the interface is by a 0.5 cm thick layer of elements with a Coulomb friction behaviour, with $\varphi = 20$ degrees and no plastic volume change. The sand is described with a Mohr-Coulomb model.

Coquillay et al. (2005) used the same mesh and interface model as Mestat and Arafati (1998), but adopted for the sand the model proposed by Fahey and Carter (1993), which associates the Mohr-Coulomb model with a non-linear elastic law (such a model makes it possible to describe both layers with the same parameters, because elastic moduli depend on the stress state). The parameters used by the different authors are given in table 1.

The friction angle is very high for the sand of the site, and the Young's modulus providing the best results are not too different from those adopted by Mestat and Arafati (1998).

However, the friction angle of the interface is significantly different depending on the model used: the value adopted by Mestat and Arafati is roughly the half of the friction angle in the sand, whereas the simulation with the joint elements provides better results if the friction angle associated with the interface is 2/3 of the friction angle in the sand.

4.3 Horizontal displacement of the wall

Figures 2 to 4 shows the horizontal displacements of the wall for construction steps 3, 5 and 7.

Table 1. Parameters used by Mestat & Arafati (1998) and Coquillay et al. (2005).

Upper layer (depth < 5,5 m)					
	E (MPa)	ν	c (kPa)	φ (deg)	ψ (deg)
Mestat	30	0,25	3	41,6	11,6
Coquillay	—	—	3,5	40,6	11,5
Elmi	33	0,25	3	41,6	11,6
Lower layer (depth > 5,5 m)					
	E (MPa)	ν	c (kPa)	φ (deg)	ψ (deg)
Mestat	45	0,25	0	—	—
Coquillay	—	—	3,5	40,6	11,5
Elmi	50	0,25	3	41,6	11,6
Interface					
	c (kPa)	φ (deg)	ψ (deg)	model used	
Mestat	1	20	0	thin elements	
Coquillay	1	20	0	thin elements	
Elmi	3	28	0	joint elements	

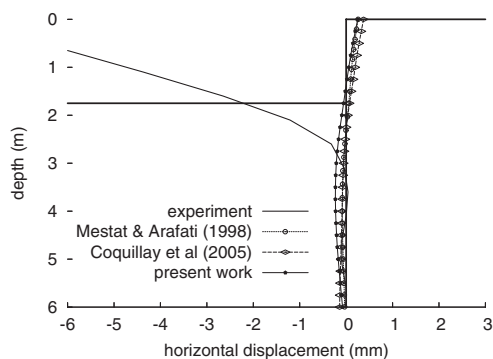


Figure 2. Horizontal displacements for step 3.

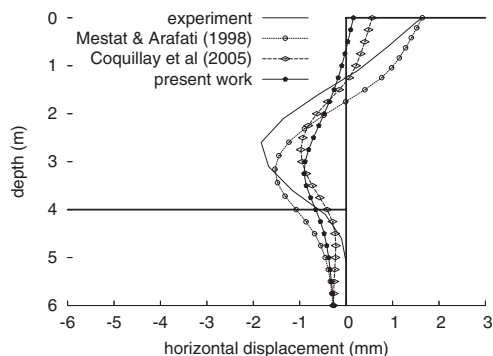


Figure 3. Horizontal displacements for step 5.

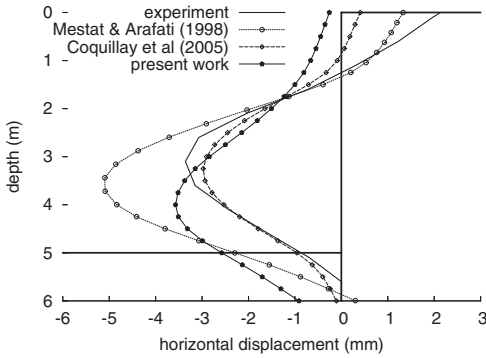


Figure 4. Horizontal displacements for step 7.

For all three simulations, the results for step 3 are not satisfactory. This has already been discussed in previous analyses: the initial stress state is probably very different from the geostatic distribution assumed here, because pile installation by vibrodriving is very likely to have a significant impact on the horizontal earth pressure on the wall. New simulations with an improved estimation of the horizontal in situ stress have not been undertaken yet (it seems that measures are available from step 1 onwards). After the first steps of excavation, the influence of the initial state becomes progressively less significant, because stresses are controlled by the momentum balance and the resistance of the sand, which explains why computations are in better agreement with measures for steps 5 and 7.

The results show some common features of the simulations by Mestat & Arafati (1998) with thin elements and the simulations carried out with joint elements: the horizontal displacement of the wall toe tends to be overestimated, and the maximum displacement position is below the maximum measured displacement. For step 7, the joint elements give a maximum horizontal displacement smaller than that obtained by Mestat and Arafati (1998), which can be related to the difference between the values of the friction angle of the interface in the two models.

It can be pointed out that the use of a more advanced constitutive model for the sand allowed Coquillay et al. (2005) give results globally better than those of the other simulations (as regards the value of the maximum displacement, its position, as well as the movement of the wall toe).

4.4 Settlements behind the wall

Figures 5 to 7 shows the horizontal displacements of the wall for construction steps 3, 5 and 7.

The main weakness of finite element simulation of retaining walls lies in the fact that the settlements behind the wall (and more generally the vertical

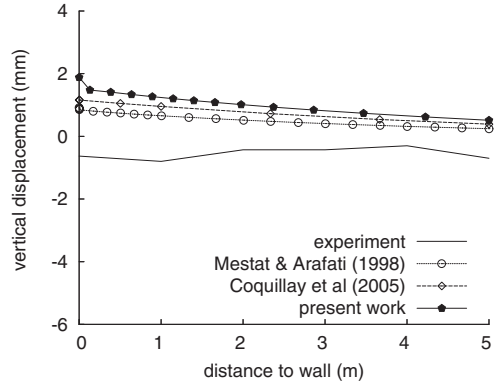


Figure 5. Settlements behind the wall for step 3.

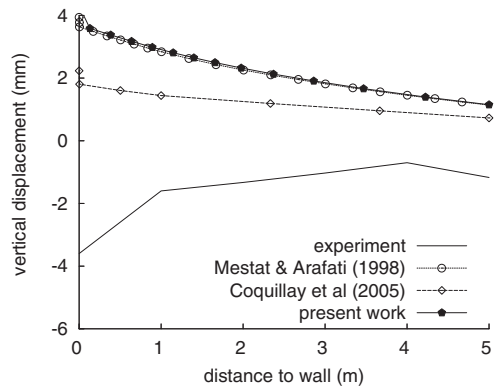


Figure 6. Settlements behind the wall for step 5.

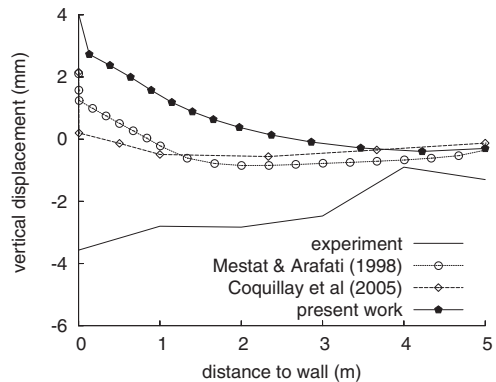


Figure 7. Settlements behind the wall for step 7.

displacements) are often poorly estimated. The reason for this shortcoming is that the excavation process adds up to exerting on the remaining ground a vertical force equal to the weight of the removed materials,

and directed upwards. If a simple constitutive model is used for the surrounding ground, the computed displacements show a heave of the bottom of the excavation and of the ground behind the wall: this is commonly observed in simulations carried out using a linear elasticity associated with a perfect plasticity. This explains why the analysis by Coquillay et al. (2005) provides results that are on the whole more satisfactory than the other approaches.

Horizontal displacements obtained with joint elements are closer to the measures than those obtained by Mestat and Arafati (1998), probably because of the stronger value of the dilatancy angle in the interface. On the other hand, the estimated vertical displacement are relatively less satisfactory.

It must be recalled that the joint model involves two elastic parameters, the normal and tangent stiffnesses of the joint, that cannot easily be related to the properties of the ground. The computations presented here correspond to a normal stiffness 100 times larger than the tangent stiffness; however, the vertical displacement behind the wall remains poorly estimated.

5 CONCLUSION

Comparing simulation results with measures on a real monitored structure rises specific difficulties for the identification of the material parameters, but remains the better way of evaluating the capabilities of a modelling technique, namely the joint elements for the simulation of retaining structure in the case under discussion here.

From a practical point of view, joint elements are relatively easy to introduce in the mesh and involve a small number of parameters. However, the determination of the elastic stiffnesses remains an experimental challenge. In the case discussed here, which corresponds to a wall submitted to loads that remain far from failure, the results are reasonably good and the iteration procedure associated with plastic strains is stable and fast, which seems to indicate that the element is robust and can be used for retaining structures in spite of the fact that it was primarily designed to deal with fractures in rocks.

As expected, results remain qualitatively similar to what can be obtained with thin elements. However, the model used for the interface seems to interact with the model used for the ground, in such a way that parameters of both models cannot really be chosen independently. In the case presented here, the variation of the ground parameters presented in table 1 remains acceptable, but the value of the friction angle of the interface is significantly different. This is a strong concern if displacements must be evaluated with some accuracy.

Some additional comments can be made:

- the initial stress state has a major influence on the simulation results, at least in the early steps of the construction process, and it would be fruitful to investigate this question further;
- the discussion here is focused on the displacements, but it remains to discuss whether or not the bending moments in the sheetpile wall and the normal force in the strut given by the computations are acceptable for design purpose;
- the results obtained with an advanced constitutive model for the sand by Coquillay et al. (2005) seem to indicate that the soil-structure interaction itself is not the only problem that must be paid attention in the modelling of retaining structures;
- computations are carried out in plane strain, which adds up to assuming that the excavation is of infinite length: in itself, this assumption is likely to have a greater influence on the results than the choice of the models for the ground and the interface, or the choice of the parameters for these models – in the case presented here, a three-dimensional finite element simulation could be undertaken to investigate this question.

REFERENCES

- Coquillay S., 2005. *Prise en compte de la non-linéarité du comportement des sols soumis à de petites déformations pour le calcul des ouvrages géotechniques*, PhD. thesis, ENPC.
- Coquillay S., Bourgeois E., Mestat Ph., 2005. A non-linear elastic-perfectly plastic model for the simulation of the Hochstetten sheet pile wall. 11th International Conference of IACMAG, Turin, Italy, June 19–24, 2005.
- Fahey M., Carter, J., 1993. A finite element study of the pressuremeter test in sand using a nonlinear elastic plastic model. *Canadian Geotechnical Journal*, 30: 348–362.
- Goodman E., Taylor L., Brekke L., 1968. A model for mechanic of jointed rock, *Journal of soil mechanics and foundation division ASCE*, V. 94, No. SM3, pp. 637–659.
- Mestat Ph., Arafati N., 1998. Modélisation par éléments finis du comportement rideau de palplanches expérimental de Hochstetten, *Bulletin des Laboratoires des Ponts et Chaussées*, n° 216, 19–39.
- Shahrou I., Ghorbanbeigi S., von Wolffersdorff P.A., 1995. *Comportement des rideaux de palplanche: expérimentation en vraie grandeur et prédictions numériques*, *Revue Française de Géotechnique*, V. 71, pp. 39–47.
- von Wolffersdorff P.A., 1994a. Sheetpile wall verification test – Document for the prediction. *Rapport de l'Université de Karlsruhe*, 85 pages.
- von Wolffersdorff P.A., 1994b. Results of the field test and evaluation of the predictions and subsequent calculations. *Workshop Sheet Pile Test Karlsruhe*, Delft University, Holland, 91 pages.

Numerical modelling of a diaphragm wall production process in Rotterdam compared to monitoring data

H.P. Neher & A. Lächler

Ed. Züblin AG, Zentrale Technik, Tunnelbau, Stuttgart

ABSTRACT: The installation of diaphragm walls causes state changes and thus displacements in the adjacent ground. A diaphragm wall construction in Rotterdam, the Netherlands, is accompanied by an extensive monitoring program to analyse the underlying mechanisms. Displacement and stress data are produced during the construction of the diaphragm wall panels and the excavation of the pit. In this paper the installation of the diaphragm wall panels is modelled using the Finite Element Methode (FEM) with an elastic-ideal-plastic model that includes the Mohr-Coulomb yield criterion (the Mohr-Coulomb model). The calculation results are discussed and compared with recorded monitoring data.

1 INTRODUCTION

In the framework of the RandstadRail rapid transit project in the Netherlands, the two existing lines “Erasmuslijn” (metrolijn in Rotterdam) and “Hofpleinlijn” (railway track between Den Haag and Rotterdam) are connected with a new rail link called “Statenwegtracé” in Rotterdam (see Figure 1). This link consists of two single track tunnels, each with a total length of 2.94 km. Around 80% of the total length is constructed as a hydro shield driven tunnel with segmental lining (outside diameter 6.5 m), while the remain 20% is constructed as a cut-and-cover tunnel.

Within the scope of a research project funded by the German Ministry of Education and Research, a monitoring program was conceived and gauges were installed on the west side of the excavation pit for the station Blijdorp (see Figure 1). Pore and earth pressures as well as deformations (vertical and horizontal) are monitored in the ground and on the surface during the construction of the diaphragm wall and the subsequent excavation of the pit. In addition, temperatures and pressures are recorded inside the diaphragm wall during concreting. As well, the deflection of the diaphragm wall is monitored during the entire excavation process. Moreover, strut forces are recorded. The research project is conducted by the Institute of Soil Mechanics and Foundation Engineering of the Ruhr-University Bochum, Germany (RUB) and the Geotechnical Department of the Ed. Züblin AG.

2 GEOLOGY

A geological cross section of the Station Blijdorp is given in Figure 2. The underground of Rotterdam can

be subdivided into 4 sub-horizontal layers. At the station Blijdorp, the anthropogenic sand fill is 4.5 to 6.0 m thick, underlain by soft soils from the Holocene. These peaty and clayey deposits called “Westland Formatie”

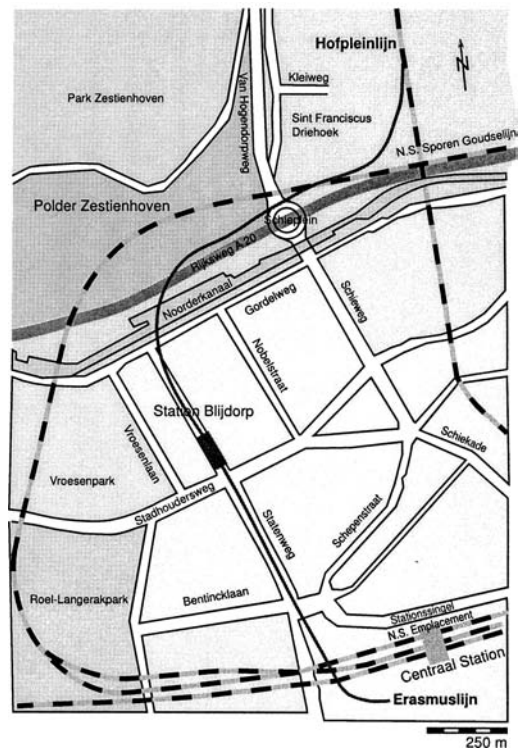


Figure 1. Plan view of Statenwegtracé.

are of fluvial origin and very heterogeneous. They reach depths beyond 15.0 to 18.0 m NAP. The sand layer beneath called "Formatie van Kreftenheye" has a thickness of about 17.0 to 22.5 m at this location. Below the sand layer lies the "Formatie van Kedichem", which consists of sand, peat, clay and loam layers. Both the "Formatie van Kreftenheye", and the "Formatie van Kedichem" are Pleistocene formations. The phreatic groundwater level averages about 2.5 m below NAP (Normaal Amsterdams Peil).

As shown in Figure 2, the diaphragm wall panels have a depth of 41.0 m and are footed in the "Formatie van Kedichem". The width of the panels varies between 1.2 and 1.5 m. In order to stabilise the excavation of the 22.8 m wide pit, four sets of struts are placed at different depths. A fifth set of struts is installed at a depth of 8.75 m. This is done during retrieval of previously placed struts.

3 MONITORING PROGRAM

Figure 3 shows a plan view of the station Blijdorp construction site. A detailed location plan of the monitoring gauges is given in Figure 4. The devices are installed in 5 rows (axes *a*, *b*, *c*, *d* and *e*) parallel to the diaphragm wall with varying spacings. In the orthogonal direction there are 7 axes (axes, I, II, ..., VI and VII) having a constant spacing of 3.95 m. Ground surface deformation is recorded at the intersecting points of the axes.

Additional information is recorded along the two main axes (axis II and axis VI). Vertical and horizontal displacements, pore pressures and lateral earth pressures are recorded in the ground at the locations

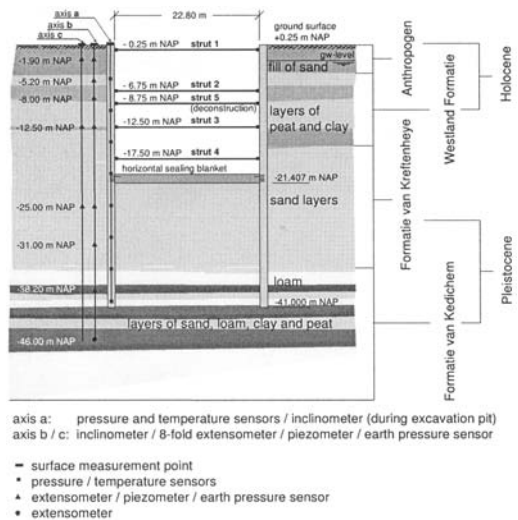


Figure 2. Geological cross section at station Blijdorp.

93 to 96. Slurry and wet concrete pressures as well as respective temperatures are recorded along axis *a* before and during concreting the panels L34 and S36. The depths of the gauges are shown in Figure 2. In the middle of the diaphragm wall (axis *a*) sensors are placed at a vertical spacing of 5 m down to a depth of 40.0 m NAP. Thus, changes in pressure and temperature are recorded at 8 points in each panel. After concreting the panels, the inclinometer tube is built into a steel pipe to record the deflection of the diaphragm wall during the excavation of the pit. The monitoring data from the piezometers and ground pressure cells are recorded at 7 different depths. Moreover, vertical displacements are obtained from 8-fold extensometers, located at the same depths. Horizontal displacements are recorded with inclinometers. The locations of the data recording instruments in axis *c* are similar

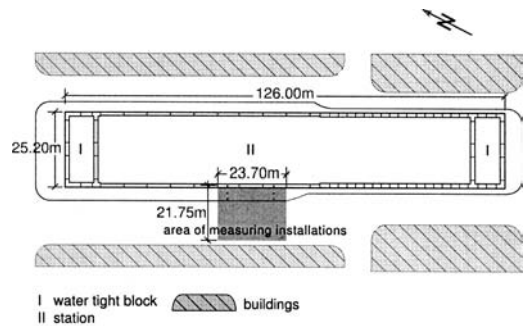


Figure 3. Plan view of the station Blijdorp excavation.

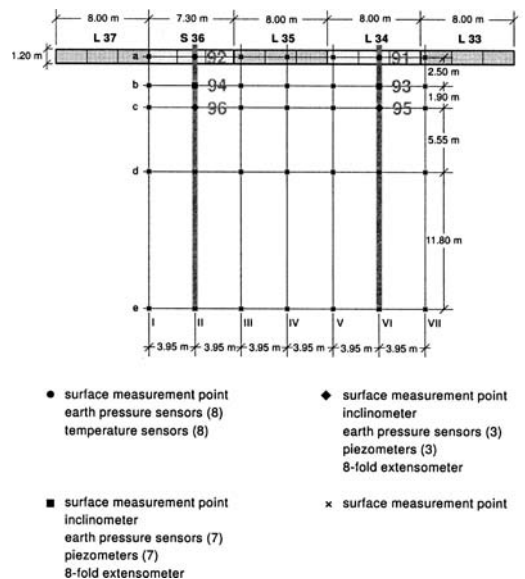


Figure 4. Location map of the monitoring instruments.

to those in axis *b*. However, piezometers and pressure cells are installed only at depths of 1.9 m, 12.5 m and 25.0 m. The position of the different data recording instruments in the ground is shown in Figure 2.

4 NUMERICAL MODELLING

The diaphragm wall installation is simulated using the FEM with an elastic-ideal-plastic constitutive model that includes the Mohr-Coulomb yield criterion (see next section). An overview of the construction process is shown in Figure 5. The obtained numerical values will be compared with the recorded data.

4.1 Finite element model

The FE-program TOCHNOG is used for the numerical simulation. The 3D model consists of 21000 hexahedron elements (23472 nodes) with a linear interpolation function. It is 62.0 m wide, about 71.0 m deep, and 46.7 m long. The width is subdivided into three regions. Due to an assumed symmetry condition in the center of the excavation, only half of the pit width (11.4 m) is considered. The modeled diaphragm wall is 1.2 m wide and behind the wall the mesh extends for 49.4 m. Figure 6 shows a section through the diaphragm wall with the adjacent monitoring field.

Vertical rollers define the boundary conditions at the model base. Horizontal rollers are applied along the vertical edges. The hydraulic head is assumed for all layers at -2.5 m NAP (-2.75 m below surface level). An existing second water level in the Pleistocene sand layer with a lower hydraulic head is not modelled to simplify matters. Moreover, drained soil behaviour is assumed for all soil types, including the soft layers (clay 2b, peat 3a and clay 4a). The simplification of drained soil behaviour for the soft soil layers is justified, because almost no pore pressure changes are recorded during the construction of the diaphragm wall in the piezometers.

4.2 Simulation of installation

The installation of the guide wall is modelled after the generation of the in situ stress state. Thereafter, the sequential construction steps of panels A32, L33, L34, L38, L35, L37 and S36 are simulated. The panels are excavated in three stages (left, right and middle stitch) except for panel L32 (one stitch). Moreover, only half of panel L38 is modelled. Each stitch excavation process is simulated with 10 segments. The same segments are then used to model the concreting phase. The hydrostatic slurry pressure is modelled as a surface load and applied when the segments are removed. The pouring of the concrete is simulated by increasing the surface load, starting from the bottom of the trench. Up to a critical height, here assumed with 8.5 m (see (Lächler et al. 2006)), the wet concrete pressure is hydrostatic. As of reaching that critical level, the wet concrete pressure is modelled bilinearly (first section as hydrostatic wet concrete pressure second section

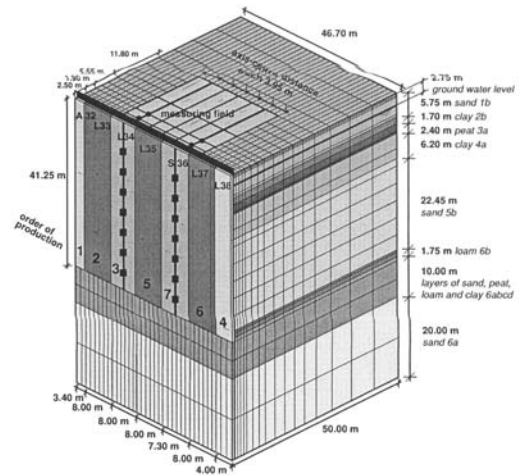


Figure 6. Part of the finite element model.

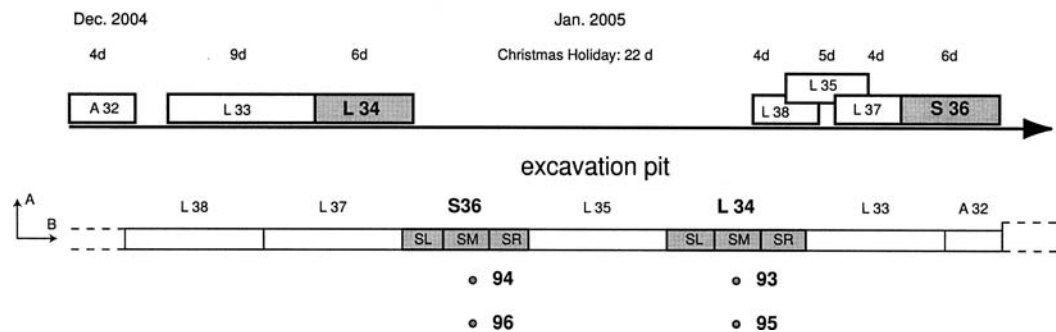


Figure 5. Production stages of the diaphragm wall.

Table 1. Numerical simulation stages.

Step	Description
1	Generation of in situ stress state
2	Guide wall installation
3	Stepwise excavation of panel A32 in 1 stitch, including activation of slurry pressure
4	Stepwise concreting of panel A32,
5	Stepwise excavation of panel L33 in 3 stitches, including activation of slurry pressure
6	Stepwise concreting of panel L33
7	Stepwise excavation of panel L34 in 3 stitches, including activation of slurry pressure
8	Stepwise concreting of panel L34
9	Stepwise excavation of panel L38 in 3 stitches, including activation of slurry pressure
10	Stepwise excavation of panel L35 in 3 stitches, including activation of slurry pressure
11	Stepwise concreting of panel L38
12	Stepwise excavation of panel L37 in 3 stitches, including activation of slurry pressure
13	Stepwise concreting of panel L35
14	Stepwise concreting of panel L37
15	Stepwise excavation of panel S36 in 3 stitches, including activation of slurry pressure
16	Stepwise concreting of panel S36

slope as hydrostatic slurry pressure). The final shape of the wet concrete pressure line is thus for the top part hydrostatic down to the critical depth of 8.5 m. Subsequently the slope of the wet concrete pressure is parallel to the hydrostatic slurry pressure. An overview on the numerical simulation stages is given in Table 1.

5 CONSTITUTIVE LAW AND MATERIAL PARAMETERS

All soil layers are modelled using an elastic-ideal-plastic constitutive model with the Mohr-Coulomb yield criterion. The Mohr-Coulomb model is briefly introduced and the material parameters for all soil layers are given.

5.1 Mohr-Coulomb model

The Mohr-Coulomb model is a linear-elastic ideal-plastic constitutive law. The total strain is divided into an elastic and a plastic part. The mechanical soil behaviour is characterized with Hooke's linear elasticity up to the yield stress f . The yield stress f is defined by Mohr-Coulomb's criterion (see Figure 7), using the effective strength parameters c' and ϕ' .

$$f = \tau - c' - \sigma' \cdot \tan \phi' \tag{1}$$

The soil behaviour is linear-elastic below the yield surface, defining the yield condition. Stress states

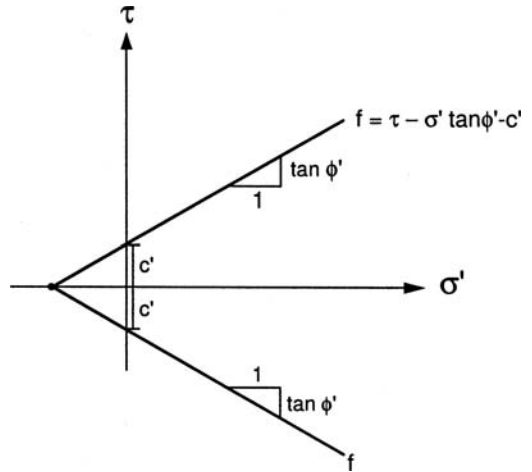


Figure 7. Mohr-Coulomb yield condition in a σ' - τ -diagram.

Table 2. Material parameters for the Mohr-Coulomb model.

Layer	γ_r [kN/m ³]	E [kN/m ²]	ϕ' [°]	c' [kN/m ²]
Sand 1b	19.5	60000	29.0	1.0
Clay 2b	15.8	12000	15.0	10.0
Peat 3a	10.5	8000	13.5	10.0
Clay 4a	15.0	16000	15.0	10.0
Sand 5b	20.0	80000	29.0	0.0
Loam 6b	21.5	60000	24.5	4.0
Layers 6abcd	21.5	60000	13.0	3.5
Sand 6a	20.0	120000	29.0	0.0

upon the yield surface generate ideal-plastic deformations. Stress states above the yield surface are not possible. A plot of the Mohr-Coulomb yield condition in a σ' - τ -diagram is given in Figure 7. Compression is defined positive.

The input parameters of the Mohr-Coulomb model are the Young modulus E and the Poisson ratio ν for the description of the elastic soil behaviour. The effective cohesion c' , the effective friction angle ϕ' as well as the dilatancy angle ψ are needed to describe the plastic soil behaviour. The use of a dilatancy angle implies a non-associated flow rule for the plastic strains.

Figure 7 shows, that soils with an effective cohesion are theoretically able to sustain tensile stresses. However, generally soils do not bear any tensile stress. Therefore, a so-called "tension cut-off" criterion is used to cap the tensile area of the Mohr-Coulomb model in the calculation.

5.2 Material parameters

Table 2 shows the material parameters of the soil layers for the Mohr-Coulomb model. The poisson ratio ν is assumed to be 0.33, the dilatancy angle ψ is 0.0°

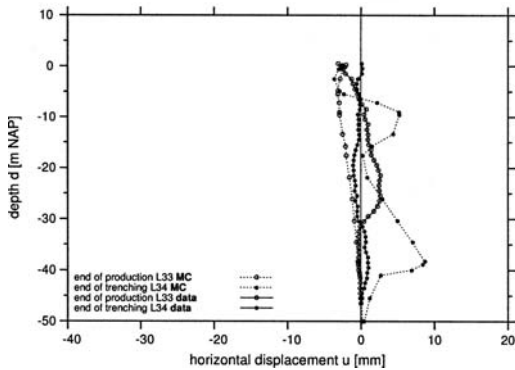


Figure 8. Comparison between inclinometer data and calculation at location 93 (panel L34) during trenching.

for all soil types. The specific soil weight γ_r and the effective cohesion c' as well as the effective friction angle ϕ' are selected according to given subsoil evaluations. However, the Young's modulus E (un/reloading) is based on subsoil evaluations and experience. In comparison to the calculations performed in (Lächler et al. 2006) the Young's modulus E is adjusted (clay 2b, peat 3a, clay 4a, loam6b and layers6abcd). The adjustment is done, to get a better agreement between the recorded data and the calculation results.

6 DISCUSSION OF DATA AND CALCULATION RESULTS

This simulation deals with the detailed construction process of the panels A32, L33, L34, L38, L35, L37 and S36 at Station Blijdorp. The calculated and recorded horizontal displacements at location 93 and location 94 (see Figure 4) are exemplarily illustrated and discussed.

6.1 Horizontal displacements during trenching

Figures 8 and 9 compare the calculated and recorded horizontal displacements at location 93 (1.9 m behind panel L34) and 94 (1.9 m behind panel S36) during trenching, respectively. Negative displacements denote a movement away from the trench, whereas positive displacements point into it.

According to Figure 8, modelling the construction of the panels A32 and L33 causes movements away from the trench of panel L34. The maximum displacement of about 3 mm occur in the soft soil layers (clay 2b, peat 3a and clay 4a). The recorded data show displacements with no major pointing direction. Recorded small displacement changes after the completion of trenching panel L34 point mainly away from the trench. This behaviour could not be modelled so

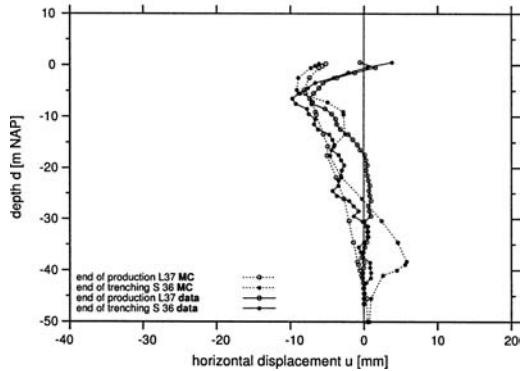


Figure 9. Comparison between inclinometer data and calculation at location 94 (panel S36) during trenching.

far. In the soft soil layers as well as in the sand 5b and the loam 6a smaller movements (up to 9 mm) into the trench are calculated. Whereas, in the fill displacements away from the trench are obtained.

The calculation results for the location 94 (see Figure 9) show a similar behaviour. The construction of the panels A32, L33, L34, L38, L35 and L37 causes movements away from the trench of panel S36. The maximum displacement is with 8 mm in the soft soil layers larger than before. The fact, that both panels (L35 and L37) next to panel S36 are constructed before, whereas only one panel (L33) is produced before panel L34, explains the larger movements. During trenching panel S36 movements into the trench are calculated for all layers except for the fill. But they are all smaller than those at location 93. The recorded data show in the soft soil layers also movements away from the trench, caused by the installation of the panels A32, L33, L34, L38, L35 and L37. The deeper layers basically show no displacements. During trenching panel S36 small displacement changes away from the trench are recorded once again.

The calculated displacements can be explained with the help of Figure 10, where, the total horizontal (earth and water pressure) and the hydrostatic slurry pressure assumed in the calculation are plotted versus depth. The resulting horizontal pressure is pointing out of the trench down to a depth of about 5 m. Below this depth the resulting pressure is pointing inward. Thus, the general behaviour of the calculation result during trenching of the panels L34 and S36 is reasonable. Note, that the total horizontal pressure, at least in the sand 5b, is actually lower, because of the lower ground water level in the second aquifer.

6.2 Horizontal displacements during concreting

Figures 11 and 12 compare the calculated and recorded horizontal displacements at location 93 (1.9 m behind

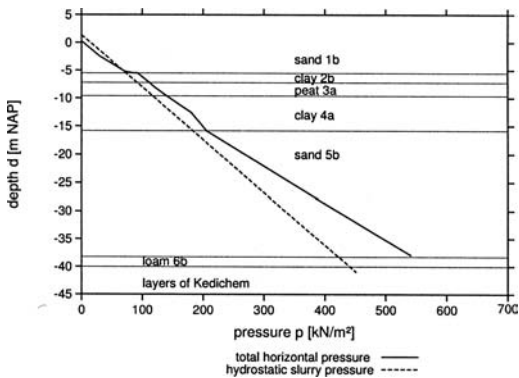


Figure 10. Comparison between total horizontal and the hydrostatic slurry pressure versus depth.

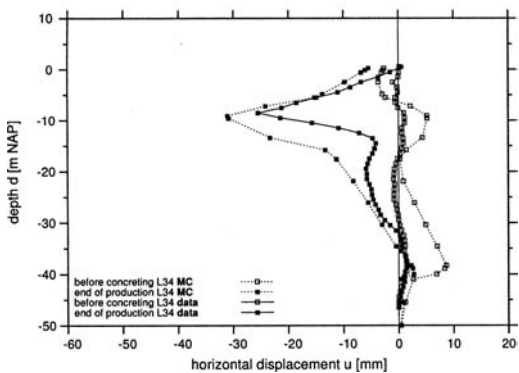


Figure 11. Comparison between inclinometer data and calculation at location 93 (panel L34) during concreting.

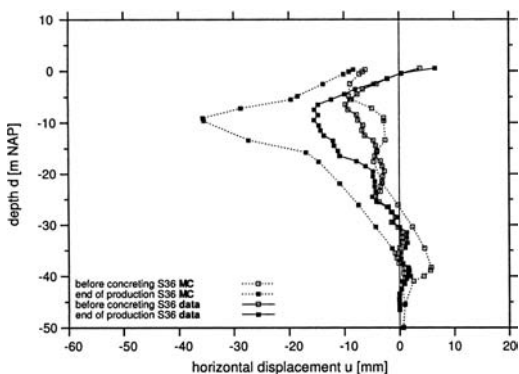


Figure 12. Comparison between inclinometer data and calculation at location 94 (panel S36) during concreting.

panel L34) and 94 (1.9 m behind panel S36) during concreting, respectively. Again, negative displacements denote a movement away from the trench, whereas positive displacements point into it.

The effect of concreting on horizontal displacements qualitatively agrees between the calculated and the recorded data. In both cases the wet concrete pressure causes movements away from the trench. Moreover, the maximum horizontal displacements occur for both, the recorded and the calculated data, in the soft soil layers. However, the calculated displacements are larger than the recorded. This is especially the case for the location 94. At location 93 the calculated and the recorded displacements match quite well.

7 SUMMARY

The present paper shows, that modelling the successive construction of diaphragm wall panels is at least qualitatively possible with a basic constitutive law and simplified assumptions. The numerical simulation can cover the examined horizontal displacements during concreting. But the small horizontal displacements during trenching are not well predicted. This is probably linked to the fact, that only one phreatic water level is adopted in the calculations, and the insitu earth pressure at rest may be different from the assumed. Thus, the difference between the total horizontal pressure and the slurry pressure insitu is not that large as shown in Figure 10. Nevertheless, the basic approach of modelling the successive construction of diaphragm wall panels shown in this paper is reasonable.

ACKNOWLEDGEMENT

The research is supported by the German Ministry of Education and Research grant 19W2086B. The authors are responsible for the content.

REFERENCES

- Lächler, A., H. P. Neher, and G. Gebeyehu (2006). A comparison between monitoring data and numerical calculation of a diaphragm wall construction in Rotterdam. In T. Triantafyllidis (Ed.), *Proceedings of the International Conference on Numerical Modelling of Construction Process in Geotechnical engineering for Urban Environment*, Bochum, Germany, pp. 83–95. Taylor & Francis Group plc, London, UK.
- van Zanten, D. C., M. de Vries, and H. M. A. Pachen (2004). Door de rotterdamse ondergrond met twee boortunnels. *Geotechniek* 8(3), 68–75.

Back analysis on a deep excavation in Stockholm with finite element method

J.Q. Ma

College of Highway, Chang'an University, Xi'an, China

B.S. Berggren & P.E. Bengtsson

Swedish Geotechnical Institute, Linköping, Sweden

H. Stille & S. Hintze

Royal Institute of Technology, Stockholm, Sweden

ABSTRACT: A deep excavation section from the South Link in Stockholm is analyzed with 2D PLAXIS. The excavation, protected by anchor back-tied sheet pile walls, is 12-m-deep and 43-m-wide in soft soils overlying bedrock. Except wall installation, six soil excavations, five anchor preloading stages and seven consolidation analysis stages are presented in a Mohr-Coulomb model. The back-calculated lateral displacements in the numerical model are about 15% less than the monitored in the middle and lower parts of the test section, while about 20% larger in the upper part. The analysis results for the stage of soil excavation are closer to the monitoring results than for the stage of anchor preloading. The magnitude of settlement behind the sheet pile wall in the numerical model is less than that of the monitoring result. Negative soil volume strain is selectively used to discuss a possible mechanism with significant settlement increase.

1 INTRODUCTION

For excavation works in urban areas, braces and tiebacks normally replace the lateral restraint that is provided by materials, which are to be removed. The performance of braced excavation has been extensively studied since the end of the 1960s (Peck 1969, Stille 1976, Finno et al. 1989, Clough & O'Rourke 1990, Ou et al. 1993, Potts & Zdravkovic 2001, Finno et al. 2002, Ng et al. 2004). However, it is still a practical way to design a deep excavation in soft clay on the base of both empirical and numerical analysis results. The design should be updated according to observational results, since many factors may contribute to an unacceptable movement during excavation (Boone 2003): base stability, soil type, elastic compression and rebound to unloading, consolidation of loose sands and soft clays, structural stiffness, construction procedures and workmanship. Any one of these factors may play a key role in controlling the overall movement of a braced deep excavation. Experiences from well-instrumented case histories are always the base for both empirical design and numerical analysis.

A tested section 1/840N analyzed here is from the South Link Infrastructure Project in Stockholm. The excavation, with its dimensions of 12 m depth and 43 m width, were performed in soft soils overlying

crystallized rock. Excavation activities are simulated with 2D PLAXIS. The numerical analysis results are compared with monitored behavior.

2 PROJECT DESCRIPTION

The South Link 10 (SL10) project comprises a 460 m long underground structure including 40 m of rock tunnel, a cut and cover concrete tunnel and tunnel ramps. Section 1/840 N is one of the deepest excavation sections in the project SL10.

2.1 Geotechnical conditions

The geotechnical conditions can be simply expressed as soils overlying bedrock. The soils consist of a fill deposit overlying a sequence of glacial clay. The glacial clay is mainly composed of soft clay, with about 1 m thick dry crust as the top layer. There are interlayers of silt and sand in the soft clay. Granular soil, about 1 m thick, overlies the bedrock of unweathered gneiss. The groundwater level is 2 m below ground surface.

The soft clay exhibits an undrained shear strength of 16 kPa, with an increase of 2 kPa/m below +10 m. The soft clay is lightly overconsolidated, with its overconsolidation ratio (OCR) varying from 1.4 at the surface to 1.0 at a level of +6 m and below.

2.2 Retaining wall

The steel sheet pile wall is commonly used in Scandinavian. The sheet pile wall is keyed into bedrock and back-tied with 5 levels of anchors, with an inclination of 45° (Fig. 1). The grout part of the anchors is mainly fixed into the bedrock. The vertical intervals of the anchors vary from 2.5 m to 3.0 m. The area of the toe of the sheet piling steel wall is sealed by jet grouting (Hintze 2002, Jonsson 2002, Hintze et al. 2000).

2.3 Excavation procedures

The excavation activities in test section 1/840N are presented in stages. The sheet pile wall is first installed. Excavations inside the sheet pile wall are conducted in stages, which are alternated by the installation of anchors, respectively. The excavation is briefly shown as excavation I through VI from top to final excavation level (Fig. 1).

2.4 Instrumentation

Instrumentation in the test section includes one inclinometer, one settlement marker, three anchor load jacks and three water level wells in the granular soil (Fig. 2).

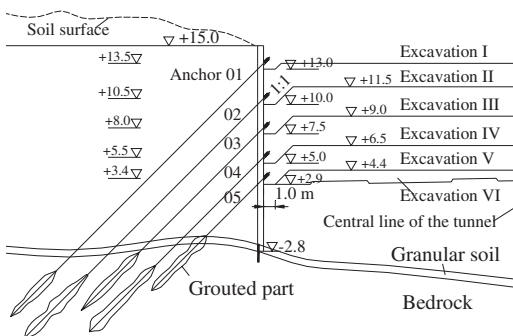


Figure 1. Procedures of excavation in test section 1/840N.

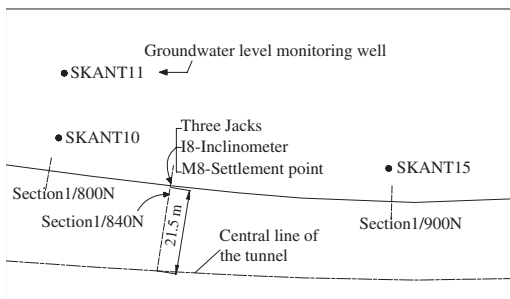


Figure 2. Plan showing the locations of the instruments.

The inclinometer I8 (Fig. 2), with its toe fixed into bedrock, is 2.0 m outside the sheet pile wall and installed vertically. Its sensors I8-1 through I8-8 (Fig. 3), with an interval of 2.0 m, are located from -0.8 m to +13.2 m. The settlement point M8 is located 1.0 m outside the sheet pile wall. Three jacks are for anchor 01, 03 and 05 (Fig. 1), respectively.

3 OBSERVED RESPONSE

3.1 Lateral displacement

The horizontal displacement of the inclinometer I8 during construction was recorded after preloading of anchor 01, which corresponds to stage 3 in the numerical model. The results are shown in figure 3. Data from 1998-12-01 and 1998-12-02 should be considered abnormal condition of measuring system.

3.2 Settlement

The data from M8 is read after 1998-11-23, which is corresponding to the period prior to excavation III. The settlement increases generally at a constant rate before excavation IV. Then, the increase rate significantly lowers until the end of 1999. At the end of excavation, the maximum settlement is 106 mm.

3.3 Anchor loads

The loads of the anchors were recorded after anchor 02 was preloaded. The loads of anchor 01 and 03 were adjusted during the excavation.

3.4 Pore water pressure in the granular soil layer

The pore pressure head of the wells SKANT 10 and 11 correspond to ground water level about +12.5 m, and at SKANT 15 about +6.5 m.

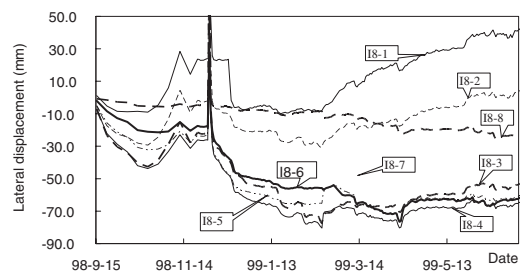


Figure 3. Lateral displacement of I8 in section 1/840N.

4 BACK ANALYSIS WITH PLAXIS

4.1 Model description

4.1.1 Geometry model and elements

A 2D Mohr-Coulomb model (SL01) with PLAXIS 8.2 is used to represent the three-dimensional problem and the excavation process is simplified as a symmetrical problem, though this kind of simplification may induce certain errors (Potts & Zdravkovic 2001). The model includes a representative division of the subsoil into distinct soil layers, sheet pile wall and anchor system, construction stages and surcharge on the surface. A 15-node triangular element is chosen to get an accurate calculation of stresses and failure loads (Brinkgreve 2002). The element distribution of mesh is moderately generated and refined around anchors, interface between sheet pile wall and retained soil. The total number of elements in the model is 1472.

4.1.2 Geotechnical properties

Geotechnical properties used in the numerical model are shown in table 1. All five distinct geotechnical layers are simplified as horizontal. From level +15 m to +14 m there is a relatively loose fine soil fill. The surface of the bedrock is at -2.8 m. Groundwater is 2.0 m below the surface. The water level is updated according to the above monitoring results.

4.1.3 The sheet pile wall

The length of the sheet pile wall is 17.8 m and its toe is totally fixed into rock. Its main properties are shown in table 2.

Table 1. Geotechnical parameters used in numerical model.

Parameter	Friction angle [°]	Cohesion [kN/m ²]	Young's modulus [kN/m ²]	Permeability [m/day]
Fill	35	1	6000	1
Dry crust	0	30	15000	0.0001
Soft clay	0	16	4900	0.0001
Till	38	0.5	35000	0.1
Bedrock	45	200	2000000	0.00001

Table 2. Properties of sheet pile wall.

Type	Axial stiffness [kN/m]	Flexural rigidity [kNm ² /m]	Weight [kN/m/m]	Equivalent thickness [m]
LX32	5.0×10^6	1.5×10^5	1.41	0.603

4.1.4 Ground anchors

Data of the anchor rods is shown in table 3. The anchor rod is simulated as an elastic node-to-node anchor. Maximum force is given as 1.0×10^{15} kN. Axial stiffness of the geogrid is 1.0×10^8 kN/m. Preloads of the anchors are given either according to monitoring results or deduced from design values with a ratio analogy from the monitored anchors.

4.1.5 Lateral pressure coefficient

The influence of the overconsolidation on the lateral coefficient k_0 is considered in the numerical model. Based on the equation of $K_0 = (1 - \sin \varphi)OCR^{\sin \varphi}$ (Mayne & Kulhawy 1982), the value of K_0 is given from 1.38 to 1.0 from ground surface to the elevation of +6 m.

4.1.6 Surface load

With temporary transportation load considered, the surface distribution load is given as varying from 30 kN/m² to 10 kN/m².

4.1.7 Stages in the numerical model

Except wall installation, six soil excavations, five anchor preloading stages and seven consolidation analysis stages are presented in model SL01 (Fig. 4). Anchor installation is included in its preceding excavation stage respectively, while anchor preloading is simulated as a separated stage. It is assumed that only 67% of the shear strength of the retained soil can be mobilized along the soil-wall interface, since many cases show ground movements caused by retaining wall installation (Poh & Wong 1998, Dawkins 2001, Finno et al. 2002, Thorley & Forth 2002). For simplicity, if a stage is followed by a consolidation calculation, only result from the later is presented.

4.2 Analysis results

The calculated lateral displacements are shown in figure 5. As mentioned above, the displacement pre-stage 3 has not been tested. For comparison with numerical results, the lateral displacement of stage 2

Table 3. Properties of the anchors in test section 1/840 N.

Anchor	Elevation [m]	EA* [kN]	c-c* [m]	Grouted length [m]	Rod length [m]
01	13.5	1.7×10^5	2.8	5.5	25.0
02	10.5	2.4×10^5	2.2	7.5	21.3
03	8.0	3.5×10^5	1.9	7.0	15.0
04	5.5	3.8×10^5	1.9	8.0	13.0
05	3.4	3.1×10^5	2.1	6.5	7.0

*EA: Axial stiffness; c-c: horizontal spacing.

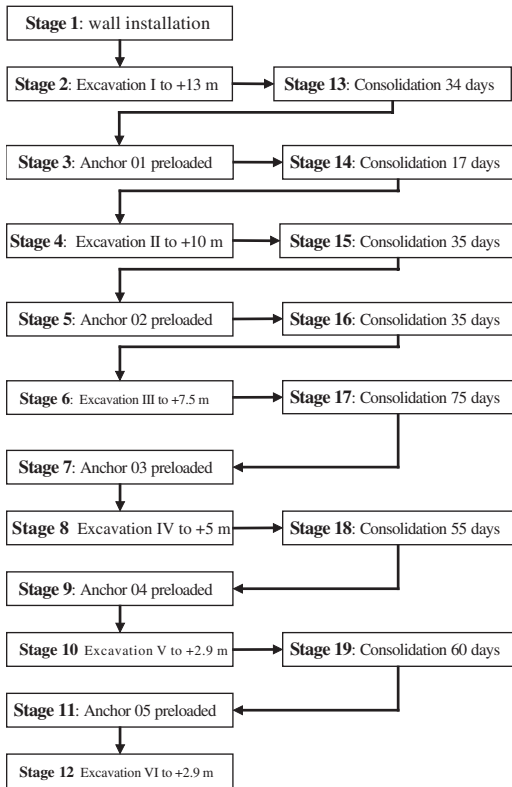


Figure 4. Stages in numerical model.

from numerical results is added to the monitoring results in terms of stages.

Maximum settlement on the surface is compared with monitoring results in figure 6.

5 DISCUSSION ON THE ANALYSIS RESULTS

5.1 Compared with monitoring results

Although the use of finite element modelling for excavations is a robust method, routinely used in engineering environments, it is impossible to include every detail from a practical project in a numerical model. The major challenges for applications of finite element analysis in excavations in urban areas are material modeling, assessment of material parameters and the interaction between soil and construction. Some distinct parameters are selectively simulated in a numerical model. Another fact is that projects are typical one of a kind (Schreppers & Horrigmoe 2005). A numerical analysis usually needs practice check.

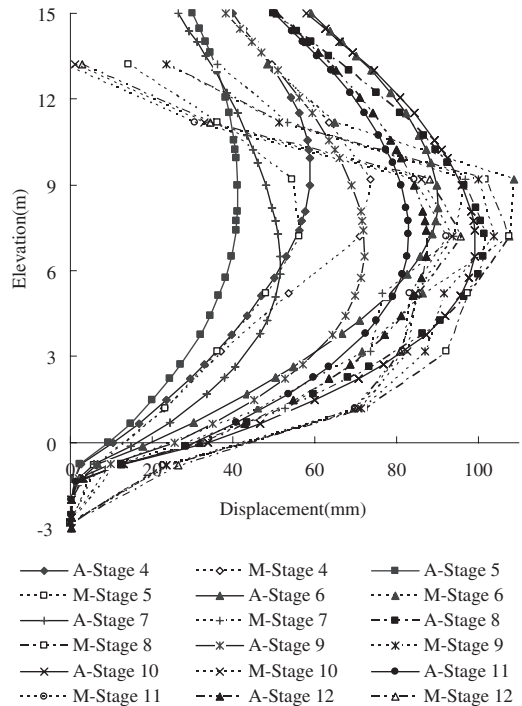


Figure 5. Comparison between analysis (A) and monitoring (M) results.

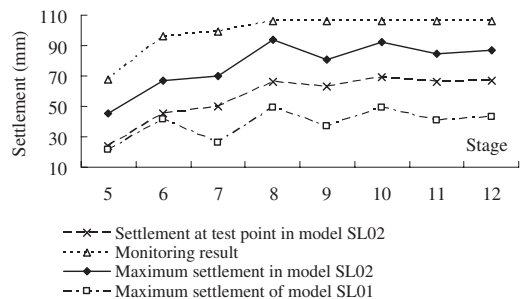


Figure 6. Settlements of analysis and monitoring.

The numerical analysis results are checked in terms of stages. Figure 5 shows that the soil is generally subjected to elastic deformation and the lateral displacement is decreased in the stage of anchor pre-stressing. This situation may be partially different from the practical deformation nature of the soft soil. Figure 5 shows that the middle part of the inclinometer does not vary in a similar smooth mode as in the numerical model.

However, figure 5 shows that the monitoring results are generally well approximated by numerical

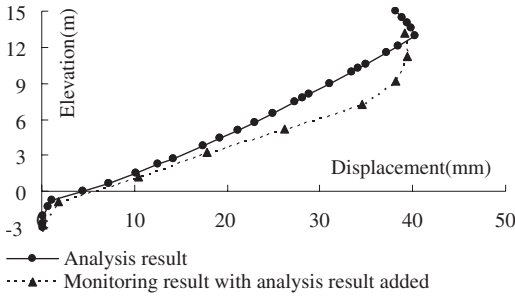


Figure 7. Comparison of lateral displacements of numerical analysis in stage 2 and the corresponding monitoring data.

results in terms of stage, though the following differences are clear.

First, for the upper part of the section, the calculated lateral displacements are larger than those of the monitoring results.

For the middle part of the section, the calculated displacements in stages 4 through 7, and stage 9, are less than those of the monitoring results, while it is reverse versa in stage 10.

For the lower part of the section, the calculated displacements are less than those of the monitoring results, and this feature is significant in stage 9 through 12.

The difference between the monitoring results and the numerical ones in the lower part may be related to the different reference point for inclinometer and for the numerical analysis. The effect of the reference point is checked by the comparison between the first monitoring data and numerical result of stage 2 (Fig. 7). Compared to the lateral displacement tendency, the characteristic of cantilever deformation is more typical for the numerical result than for the monitoring behavior. For the lower part of the sheet pile wall, the monitored displacements are larger than those calculated, in which the wall deforms as an ideal elastic beam with its toe totally fixed, but the difference is insignificant.

5.2 Lateral displacement feature in stages

One of the features of a deep excavation procedure is of being conducted in stages. The response of the retained soils to the stage construction is always changeable. The ground movement may suddenly increase at an intermediate stage of construction, but not gradually as excavation proceeded to full depth (Finno et al. 1989). In figure 5, both the numerical analysis and the monitoring results indicate that the increment of lateral displacement from preceding stages varies among stages.

There is no simple increasing tendency of lateral displacement through construction stages, and the

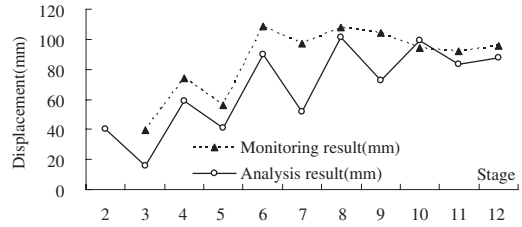


Figure 8. The maximum lateral displacement of monitoring and numerical analysis results in stages.

increasing tendency varies in different parts of the test section. The largest displacements occur in the middle part of a stage. For all stages, the largest displacements occur in stage 6 in the monitoring results while in stage 8 in the numerical model (Fig. 8). Of the displacement increment in a stage, the displacement increases significantly in stage 4, 6 and 8 from their preceding stage, while the displacement decreases in stage 5, 7, 9, 11 from their preceding stage, respectively (Fig. 8). This feature is even significant in the numerical results.

After stage 6, displacement increment from preceding stage is either insignificant or even negative. After stage 8, the magnitude of the largest displacement from monitoring results decreases, while this trend appears after stage 10 in the numerical model (Figs. 5, 8). This tendency should be attributed to the occurrence of bedrock. As the distance from dredging level to the bedrock is less than the depth of dredge level, the beneficial influence of the bedrock on the movement of the soil-retaining wall system increases.

5.3 Influence of preload in anchors

Stages representing preloading of anchors are simulated as independent stages in the numerical model. There is no time spare for consolidation in anchor preloading stages. This is different from the practical situation. The most important factor in those stages is the magnitude of the preload. The behavior of the retained soil is readily influenced by the magnitude of the preload. This is illustrated by the zigzag shape of the maximum lateral displacement in both numerical and monitoring data in terms of stages (Fig. 8). The influence of the preload on the lateral displacement is more significant for numerical model than for monitoring results, though the influence is similar in stage 3 through 6.

As mentioned above, preloads given in the numerical model are based on monitoring results of anchor 01, 03 and 05. The load value decreases significantly in stage 5 and 6 for anchor 01, in stage 8 for anchor 02 and 03, in stage 10 for anchor 03, and in stage 12 for anchor 04. Lateral displacement increases significantly

in stage 4, 6 and 8 for both numerical and monitoring results (Figs. 5, 8). This implies that the decreasing of anchor preload also plays a key role in the lateral displacement increasing.

Monitoring results show that the preload in anchor 01 is perfectly kept after stage 7. This has not only effectively controlled lateral displacement of the upper part in test section, but also incurs negative lateral displacement from preceding stages (Fig. 5). The tendency is more significant in monitoring results than in numerical analysis results.

5.4 Magnitude of surface settlement

Based on case studies, Clough & O'Rourke (1990) and Ou et al. (1993) concluded that the maximum ground surface settlement usually occurs very close to the face of the wall for the case with relatively large wall deflection at the initial stage of excavation, and the maximum ground surface settlement usually occurs at some distance from the retaining wall for the case with relatively small wall deflection at the initial stage of excavation. The distance where the maximum ground surface settlement occurs does not vary with excavation depth (Ou et al. 1993). In the model SL01, the location of the maximum settlement point on surface varies between 5 m and 7 m from the sheet pile wall. This is similar to the cases with relatively small wall deflection at the initial stage of excavation. Although it is noted that the computed point of maximum settlement may be too far away from the wall as in a Mohr-Coulomb model simulation (Ng et al. 2004), and there is not enough data to discuss the shape of surface settlement due to excavation, the monitoring point is not corresponding to the maximum settlement location in model SL01.

The settlements in model SL01 are much smaller than the monitoring values. Although some cases show that the numerical analysis result of settlement is less than that of practice if a Mohr-Coulomb model is used (Simpson et al. 1979, Ng et al. 2004), some causes for this case may exist.

Another numerical model (SL02) is used to discern the potential reason for the larger monitoring result. In model SL02, all the parameters are the same as in model SL01 except soil volume strain being selectively applied to partial soil in stage 5 and stage 7. The application of soil volume strain is partially given to granular soil and a small part of the soft clay around anchor rods. This incurs less than 10% difference between the two models in lateral displacement. However the settlement increases significantly as shown in figure 8, and the maximum settlement is around 25% less than the monitoring result. This implies that the settlement may be related to the soil losing during anchor installation and water seepage through sheet pile wall, though there is no record available supporting this assumption.

6 CONCLUSIONS

The results of this study show that the deformation of the soil-anchor-sheet pile wall system can be preliminarily simulated with a Mohr-Coulomb model of the PLAXIS code, provided that the preloads in anchors, the pattern and value of the surcharge on surface and groundwater level are respectively updated according to their monitoring results.

Both numerical and monitoring results show that the lateral displacement increase mainly in the first three excavation stages (I through III). The beneficial influence of the bedrock becomes significant when the distance from excavation level to bedrock is less than to ground surface.

The settlements in the model SL01 are much smaller than the monitored values. The result of model SL02, in which soil volume strain being selectively applied, implies other factors, such as soil losing, may cause significant settlement increase.

REFERENCES

- Boone, S.J. 2003. Design of deep excavations in urban environments, *A thesis submitted in conformity with the requirements for the degree of Doctor of Philosophy*, Graduate Department of Civil Engineering, University of Toronto, 2003.
- Brinkgreve, R.B.J. (Ed) 2002. *PLAXIS – Finite Element Code for Soil and Rock Analyses: Users Manual – Version 8*. Rotterdam: A.A. Balkema, Netherlands.
- Clough, G.W. & O'Rourke, T.D. 1990. Construction induced movements of in situ walls. *Proceedings on Conf. on Design and Performance of Earth Retaining Structures, ASCE, Geotechnical Special Publication No. 25*: 439–470.
- Dawkins, W.P. 2001. Investigation of wall friction, surcharge loads, and moment reduction curves for anchored sheet-pile walls. *ERDC/ITL TR-01-4*.
- Finno, R.J., Bryson, S. & Calvello, M. 2002. Performance of a Stiff Support System in Soft Clay. *J. Geotech. and Geoenviron. Engrg., Vol. 128*: 660–671.
- Finno, R.J., Atmatzidis, D.K. & Perkins, S.B. 1989. Observed performance of deep excavation in clay. *J. Geotech. Eng., ASCE, Vol. 115(8)*: 1045–1064.
- Hintze, S. 2002. Prediction and impact on nearby structures during deep excavation for the Southern Link Road Construction. *Proc. 2nd International Conference on Soil Structures Interaction in Urban Civil Engineering, IABSE Congress, Zurich, Switzerland*.
- Hintze, S., Ekenberg, M. & Holmberg, G. 2000. Southern Link Road Construction: Foundation and Temporary Constructions. *Proc. 16th IABSE, Switzerland*.
- Johnson, L. 2002. Numerisk analys av rörelser i spontvägg. *Master Thesis*. Division of Soil and Rock Mechanics. Royal Institute of Technology. Stockholm. Sweden (In Swedish).
- Krajewski, W. & Reul, O. 2004. Deep Excavation in Stiff Clay: Comparison between Numerical Analyses and In-situ-measurements. *Proceedings of NUMOG IX*

- (*Numerical Models in Geomechanics*), Ottawa, Canada, 25–27 August 2004.
- Mayne, P.W. & Kulhawy, F.H. 1982. K_0 -OCR Relationships in Soil. *J. Geotech. Engrg. Division, ASCE*, 108(6): 851–872.
- Ng, C.W.W., Simons, N. & Menzies, B. 2004. *A short course in soil-structure engineering of deep foundations, excavations and tunnels*. London: Thomas Telford.
- Ou, C.Y., Hsieh, P.G. & Chiou, D.C. 1993. Characteristics of ground surface settlement during excavation. *Can. Geotech. J.*, Vol. 30: 758–767.
- Peck, R.B. 1969. Deep excavations and tunneling in soft ground. *Proc. 7th Int. Conf. on Soil Mech. and Found. Engrg., State-of-the-Art Rep., State-of-the-Art Vol.*: 225–290.
- Poh, T.Y. & Wong, I.H. 1998. Effects of Construction of Diaphragm Wall Panels on Adjacent Ground: Field Trial. *J. Geotech. and Geoenviron. Engrg.*, Vol. 124(8): 745–756.
- Potts, D.M. & Zdravkovic, L. 2001. *Finite element analysis in geotechnical engineering: Application*. London: Thomas Telford.
- Schreppers, G.-J.M.A. & Horrigmoe, G. 2005. A Review of FEA technology issue confronting the civil engineering industry. *NAFEMS World Congress*, 2005, May 17–21st, Malta.
- Simpson, B., O’Riordan, N.J. & Croft, D.D. 1979. A computer model for the analysis of ground movements in London clay. *Géotechnique*, Vol. 29(2): 149–175.
- Stille, H. 1976. Behavior of anchored sheet pile walls. *A thesis*, Department of Soil and Rock Mechanics, Royal Institute of Technology.
- Thorley, C.B.B. & Forth, R.A. 2002. Settlement due to Diaphragm Wall Construction in Reclaimed Land in Hong Kong. *J. Geotech. and Geoenviron. Engrg.*, Vol. 128: 473–478.

Design of a deep building pit with numerical and limit equilibrium methods

V. Račanský

Institute of Geotechnics, Brno University of Technology, Czech Republic

R. Thurner

Keller Grundbau, Söding, Austria

C. Kummerer

Keller Fondazioni S.r.l., Verona, Italia

ABSTRACT: For the design of a deep excavation, different methods were applied in order to investigate the deformation behaviour and the stability of the structure. Especially the uncommon geological situation with a layer consisting of gravel underlain by a soft clay layer and a groundwater table close to the ground surface and its lowering during excavation required comprehensive geotechnical analyses. The ground failure mode was investigated by using different models, namely the finite element method with PLAXIS and the limit equilibrium method. In the finite element method the stability of the excavation support was investigated by means of the ϕ/c -reduction method. Special attention was paid to the dimensions of the jet grouting body and the prestressed anchors, respectively. The effects of varying the depth and the width of the retaining wall and the prestress forces were studied in detail.

1 INTRODUCTION

This calculation is based on an existing project which was realized in Italy in a close vicinity to the lake “Lago di Garda”. The project consisted of the deep excavation of a building pit and the underpinning of adjacent buildings for an underground car park. The construction site was located in a gap site of a street running parallel with the lake shore in approx. 50 m distance. The site with the maximum dimensions of 70×20 m was next to existing structures such as a school building on one side and the apartment buildings on the other side. The plan view can be seen in Figure 1. For the calculation purposes a section F–F’ was selected, as it was the most significant one.

The design of the underpinning structure was done with traditional methods – the Limit Equilibrium

Method. The design resulted into two different variants, which are differing in terms of the dimensions of the base of the retaining wall. Both variants, later referred to as design 1 (large base) and design 2 (small base), met the requirements of the calculation standards, but with different problems regarding the construction on site. Moreover, ground water cut-off elements were requested for controlling the water flow towards the excavation. The models can be seen in Figure 2, where the variants without ground water cut-off construction are drawn with solid lines and with ground water cut-off structures are plotted with dashed lines. The aim of this paper is to back-analyze the design derived from the traditional methods by means of the Finite Element Method, especially with respect to their deformations and safety factors, as this approach gives

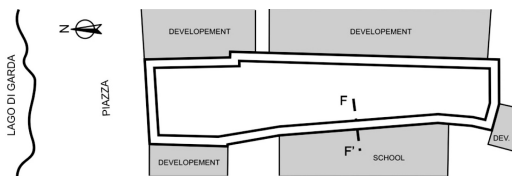


Figure 1. Plan view of the building pit.

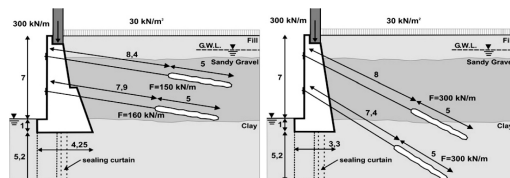


Figure 2. Cross sections of large (left hand side) and small base design.

Table 1. Mechanical properties – Hardening soil model.

Hardening soil		Clay	Fill	Sandy gravel
Type		Drained	Drained	Drained
γ_{unsat}	[kN/m ³]	21	18	18
γ_{sat}	[kN/m ³]	21	20	21
k_x	[m/day]	0,007	1,000	1,420
k_y	[m/day]	0,007	1,000	1,420
E_{50}^{ref}	[kN/m ²]	7500	15000	40000
$E_{\text{ocd}}^{\text{ref}}$	[kN/m ²]	7500	15000	39915
Power (m)	[-]	0,90	0,70	0,50
c_{ref}	[kN/m ²]	15	3	0,5
φ	[°]	25	30	35
ψ	[°]	0,0	0,0	3,0
$E_{\text{ur}}^{\text{ref}}$	[kN/m ²]	30000	60000	160000
$\nu_{\text{ur}}^{(\text{nu})}$	[-]	0,200	0,200	0,200
p^{ref}	[kN/m ²]	100,00	100,00	100,00
R_f	[-]	0,90	0,90	0,90

a more comprehensive view of the overall behaviour. A comparison of the two different models (with different dimensions and different pre-stress forces) in combination with different ground water cut-off walls are investigated in this paper. The results of the FEM-analyses are compared with the Limit Equilibrium Methods.

2 GEOTECHNICAL PROPERTIES AND MATERIAL PARAMETERS

The parameters for the calculation were derived from the soil investigations (Tab. 1). As the geotechnical report did not indicate all the parameters for performing the analyses, some additional assumptions had to be made based on local experience.

For the calculation the following constitutive models predefined in PLAXIS V8.2 were chosen for different elements of the structure.

The Hardening soil model was used for modelling the soil behaviour as a more appropriate soil response on the excavation is given.

Mohr-Coulomb model was used for modelling the behaviour of the jet-grouted structure. A distinction of two different jet-grouted materials was done because the properties of the jet grouting (JG) procedure are largely influenced by type of soil. One material type is JG-Sandy Gravel for the jet grouting columns produced in sandy gravel layer and the other material type is JG-Clay for jet grouting columns in clay and fill layers. The properties of these materials can be seen in Table 2. PLAXIS allows using the tension cut-off option to define maximum tension stresses for jet grouted material. The maximum allowable tensile stresses were defined as 1/8 of maximal compression strength.

The strip footing (dimensions 0.7 × 1.0 m) of the existing wall which was to be underpinned was

Table 2. Mechanical properties of jet grouted soil.

Mohr-Coulomb		Jet grouted sandy gravel	Jet grouted clay
Type		Drained	Drained
γ_{unsat}	[kN/m ³]	22	22
γ_{sat}	[kN/m ³]	22	22
k_x	[m/day]	0	0
k_y	[m/day]	0	0
E_{ref}	[kN/m ²]	20000000	5000000
ν	[-]	0,20	0,20
c_{ref}	[kN/m ²]	1000	250
φ	[°]	35	25
ψ	[°]	0	0

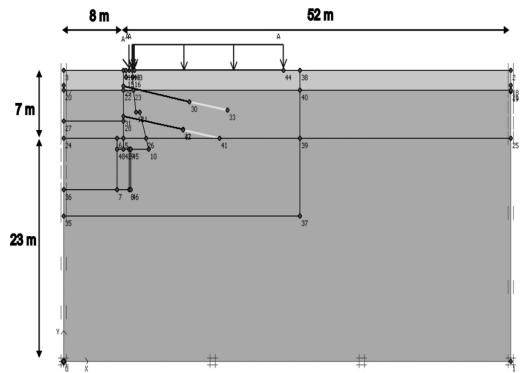


Figure 3. Geometry model.

modelled as linear elastic material with the same mechanical properties as JG-Clay. This is a necessary detail in order to overcome the problem of load transfer to subsoil.

Ground anchors were modelled as a combination of a node to node anchor for its free length and a geogrid for its bonded length with following properties:

Node to node anchor (as 3 tendons Ø 0.62 mm):

$EA = 3e4 \text{ kN/m}$

Geogrid:

$EA = 3e5 \text{ kN/m}$

3 GEOMETRY AND CALCULATION PHASES

The Geometry of the calculated area was taken from Figure 2. Two different files were prepared for the PLAXIS calculation. The geometry in the first file was done for the large base design and the other file was done for the small base design. In each file it was possible to activate suitable clusters in order to model different variants of cut-off walls.

In Figures 3 & 4, the geometry model and generated mesh for design 1 is depicted. Care was taken during the mesh generation process in order to generate

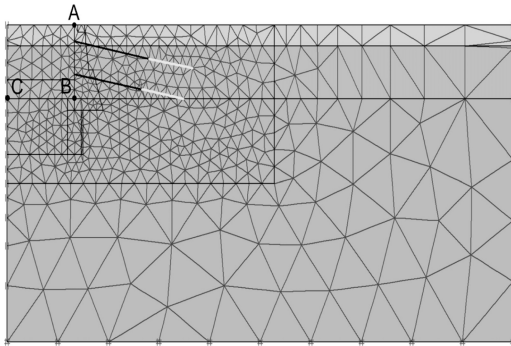


Figure 4. Generated mesh.

similar meshes in both files. This is important for comparability of calculations. In areas of expected large deformations and tension gradients the finer mesh was generated. Both models have 960 elements.

The calculation was divided into several calculation phases. These phases followed the construction phases on the site and are listed below:

- Phase 1: Activation of the existing loads and foundation elements.
- Phase 2: Activation of jet grouted column construction – switching appropriate clusters from existing soil to jet grouted material.
- Phase 3: (Reset displacements to zero) Ground water lowering to the level of the 1st excavation (–2.0 m).
- Phase 4: 1st excavation to –2.0 m.
- Phase 5: Anchor installation and pre-stressing.
- Phase 6: Ground water lowering to the level of the 2nd excavation (–5.2 m).
- Phase 7: 2nd excavation to –5.2 m.
- Phase 8: Anchor installation and pre-stressing.
- Phase 9: Ground water lowering to the level of the 3rd excavation (–7.0 m).
- Phase 10: 3rd excavation to –7.0 m.

These phases were followed by the phi-c reduction calculation for the determination of the safety factor. The results of these calculations are summarized in the next chapter.

4 CALCULATION RESULTS

The calculations for all variants are summarized below in Table 3, where deformations of selected points and calculated safety factors ΣM_{sf} from phi-c reduction can be found.

4.1 Displacements/factor of safety

In Table 3 the deformation for the investigated variants is shown. The variant with a reduced level of

Table 3. Displacements of different points and factor of safety. Point A – top point of the wall, point B – foot of the wall, point C – centre of the excavation pit (horizontal displacements are zero – symmetry axis).

		Displacements [mm]					
		A		B		C	
Variant		Hor.	Ver.	Hor.	Ver.	Ver.	ΣM_{sf}
Without cut-off elements	Large base	66	34	48	34	88	1,38
	Small base	74	46	49	46	91	1,25
Cut-off curtain	Large base	56	21	47	21	86	1,40
	Small base	60	29	43	29	85	1,35
Cut-off wall	Large base	42	8	35	7	84	1,41
	Small base	41	11	33	11	82	1,48
Cut-off wall pre stress level 50%	Large base	49	8	37	8	85	1,41
	Small base	55	11	39	11	82	1,48

Remark: horizontal displacements: + values towards excavation; vertical displacements: + values settlements.

anchor pre-stress force, set to 50% of original value gained from Limit Equilibrium Design method, was included into the study. All cases prove the fact that the small base design gives a larger settlement than large base one. This is clearly caused by the size of the foundation base. Settlements of the design 2 (small base) variants are roughly 35% higher than settlements of the design 1 (large base) variants. The influence of the size of the foundation base on the horizontal displacements of the underpinning structure is smaller as expected. Furthermore, it is evident that the ground water cut-off structures are reducing the calculated settlements and that with larger dimensions of sealing structure smaller deformations are obtained. Another fact which can be seen is that the vertical deformations of the upper point A and of the lower point B of the wall are the same. This is due to the fact that the jet grouted wall is very stiff and thus the vertical contraction of the wall due to the induced force is negligible.

4.2 Anchor forces

The evaluation of the anchor forces is given for the design with cut-off walls only. The development of the anchor forces for the large and the small base variant was observed. For comparison the calculations were run with reduced pre-stress anchor forces by half as well. This value is normally the lower bound limit when pre-stressing of anchors is applied. The development of the anchor forces can be seen in Figures 5 & 6. The anchor forces in all construction steps and in selected steps of phi-c reduction are shown. In all cases, an increase of forces in anchors

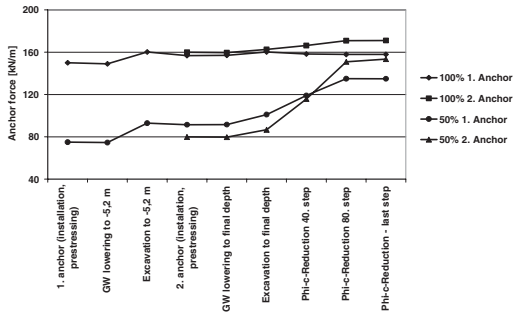


Figure 5. Development of anchor forces after the installation (design 1).

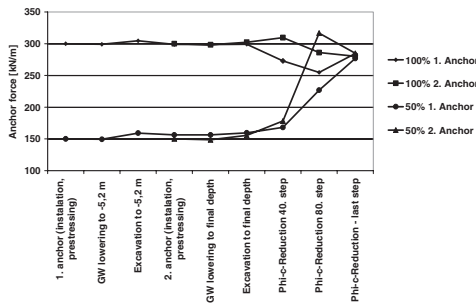


Figure 6. Development of the anchor forces after the installation.

can be seen. This increase is bigger in case of design 1 (maximum increase 34.8%) compared with design 2 (maximum increase 6.3%). The increase of the anchor force is caused by displacement of the anchor head relative to anchor bond part. This relative displacement of the mentioned areas depends not only on the amount of the displacement of the wall but as well on the direction. The anchors in small base variant are much more inclined and so the displacement of the wall is much more tangential to the anchors and the increase of the force is not so large.

Another matter of fact is that the increase of forces is much greater applying only 50% of the pre-stressing force. This means that the structure has more “freedom” to find its balanced position. This is linked up increase in anchor forces.

The other interesting fact is verifying development of anchor forces in phi-c reduction. It can be observed that the forces are probably approaching to some “limit” value, which does not depend on the pre-stressing level.

4.3 Horizontal effective stresses

Looking at the horizontal effective stresses allows understanding the behaviour of the structure and pronounces some basic facts about the anchors. In Figure 8,

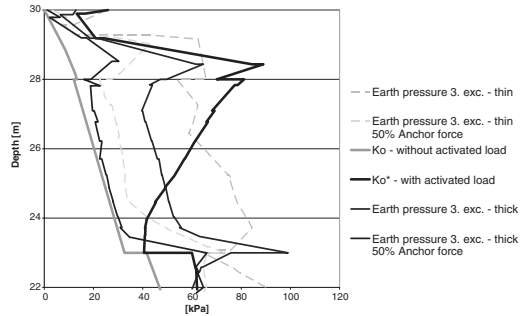


Figure 7. Horizontal effective stresses.

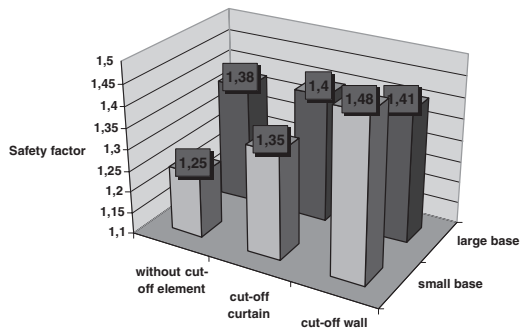


Figure 8. Safety factor (ΣM_{sf} PLAXIS).

the effective horizontal stresses on the back of the underpinning structure after last excavation step are plotted for the large and small base option and as well for different anchor forces, respectively. For the better understanding, K_0 was depicted (initial horizontal stresses before the load is activated), and of K_0^* (initial horizontal stresses after all surcharge load is activated but before any excavation steps is done). It can be seen that in the upper part of the wall there is a decrease in horizontal effective stresses compared to the K_0^* – activated load line. This is due to the fact that in upper part the surcharge influence is larger and the movement of the wall towards the excavation pit unloads the soil and this yields a decrease of horizontal effective stresses. Pre-stressing of the first anchor row counteracts against this unloading, but this effect is smaller in the upper part of the wall. In lower part of the wall, the same effects are in place, but in different magnitude. Because the surcharge influences are smaller in the lower part, also the unloading effect caused by movement of the wall towards the excavation pit is smaller. This unloading effect is counterweighted by the effect caused by anchor pre-stressing. That causes the fact that in lower part of the wall, the horizontal effective stresses are bigger than K_0^* – activated load line.

The graphs of horizontal effective stresses for different levels of pre-stressing forces are compared. Pre-stress forces were reduced to 50% of its original level. With the lower pre-stress forces, horizontal effective stresses are significantly smaller. This leads, together with the facts presented in part 4.4 about safety factors to the following conclusions. The larger the anchor forces are, the larger are the effective horizontal stresses. That means increasing the pre-stress forces increases the utilization of the material of the structure (both, jet grouted and steel) and doesn't increase the safety factor of the structure. The influence of increased pre-stress forces can be only seen in reducing of the displacements, otherwise high pre-stressing forces seem to be unjustified.

4.4 *Phi-c reduction*

Running phi-c reduction calculation allows to calculate the ΣM_{sf} factor which is analogous and comparable to the safety factor known from Limit Equilibrium Method. Calculated values of ΣM_{sf} are given in Table 3 and are visualized in Figure 8.

In addition to the analyses of the phi-c reduction (ΣM_{sf} – safety factors), further calculations were made with modified soil strength parameters reduced by corresponding value of ΣM_{sf} factor in order to check two facts. As a first fact, a control of the phi-c reduction calculation can be obtained. In case it was correct, the result of the calculation with reduced parameters should be just on the verge of the failure (from safety point of view). So values of ΣM_{sf} close to 1.0 in the calculation with reduced strength parameters are likely. As a second aspect, it was considered to control if any of the previous phases is more critical than the last phase. In case that some phase would be less stable than the last one, the calculation of this phase with reduced parameters should not converge and the calculation should fail.

5 LIMIT EQUILIBRIUM CALCULATIONS – SAFETY CONSIDERATIONS

Limit equilibrium calculations were done with an in-house software called UFA. It was not possible to model entirely the same geometry of the structure as in PLAXIS because the input possibilities in UFA are limited in comparison to PLAXIS. This geometrical unevenness of the models can influence the comparison of calculated results, but should not be a critical factor. With UFA only two variants – large and small base design without water cut-off wall – were modelled. For design 1 without ground water cut-off, the calculated value of the safety factor against sliding is 1.59 (compared with the PLAXIS “safety factor” 1.38). For design 2 without ground water cut-off, the

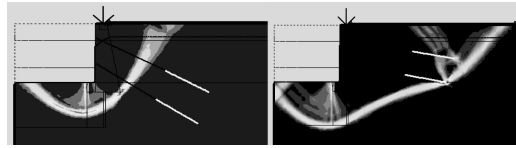


Figure 9. Critical slip surfaces in the last calculation step (100 steps totally calculated) of phi-c reduction in PLAXIS.

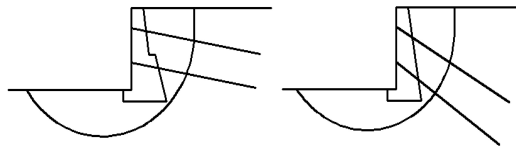


Figure 10. Critical slip surfaces in UFA (redrawn).

calculated value of the safety factor against sliding is 1.35 (compared with the PLAXIS “safety factor” 1.25). The safety factors are in better agreement for the small base design than for the large base one.

For finding the explanation, the shapes of the critical slip surfaces were compared. As depicted in Figures 9 & 10, the shapes of the slip surfaces for design 2 are nearly the same and both have circular shape. On the other hand, in case of design 1 the shapes of the slip surfaces differ quite substantially. In case of limit equilibrium method, a circular slip surface crosses the ground anchors, but in case of FEM calculation a slip surface touches ends of the anchors and has a polygonal shape. With the limit equilibrium method the shape of the slip surface is given. Furthermore in this method there is no interaction between stresses and strains and so the development of the strains before the failure occurs doesn't change the stresses (forces) acting on the soil body. On the other hand in case of the finite element method, stresses and strains are related by constitutive law. So for example if the magnitude of the strains is increased by initiation of a slide failure the stresses (forces) in the anchors are changed as well. In case of the large base design, the increase in strains caused by the initiated sliding mechanism increased forces in the anchors. These increased forces acted against this initiated slide mechanism and did not allow this mechanism to propagate. That resulted in “pushing out” the slip surface behind anchors and eventually to the failure, as shown on Figure 9 (left).

In order to confirm the above presented thoughts it should be possible to find circular shape of the initiated slip surface crossing the ground anchors in some calculation steps of phi-c reduction prior to the last one. In Figure 11 a plot of the total strains at step 45 out of 100 of the phi-c reduction calculation is given. The shape of the slip surface is very similar to the

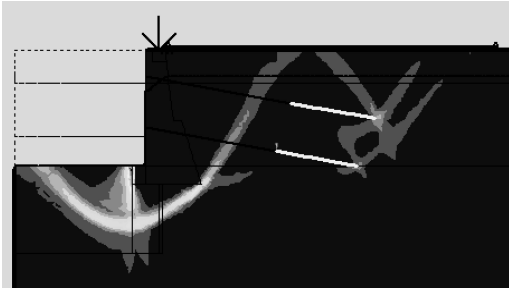


Figure 11. Critical slip surfaces in PLAXIS (step 45 of ϕ -c reduction).

shape obtained from the limit equilibrium method. In successive steps, the slip surface was pushed out to the final position as shown on Figure 9 (left).

6 CONCLUSIONS

Although the two designs initially considered for realizing a deep excavation in difficult soil and ground water conditions have fulfilled the same calculation code requirements, their behaviour with respect to displacements is quite different. Settlements of the small base design are roughly 35% larger than settlements of the model with the larger base. Moreover the effects of the pre-stress forces on the displacements and the horizontal effective stresses were investigated.

It can be shown that the increased anchor forces yield larger effective horizontal stresses. There was no influence of anchor pre-stress forces observed on safety factor of the structure. The effect of higher anchor forces can be seen only in reduction of the horizontal displacements. From the safety considerations it can be concluded that the calculated safety factors based on the ϕ -c reduction and on the limit equilibrium method are in reasonable agreement. But it must be remarked that the limit equilibrium method does not take in to account the interaction between stresses and strains. When this interaction is considered then the additional stresses (forces) are generated during the activation of the slide failure and these can alter the shape of the slip failure surface. Using limit equilibrium method for design of underpinning structures one has to be aware of possible shortcomings, especially problems with excessive displacements and with the shape of the slip surface. As the large base design resulted as the one with the minor risk, it was chosen for the actual realization.

REFERENCES

- Brinkgreve, R.B.J. (2005). PLAXIS, *Finite element code for soil and rock analyses, user manual*.
- Kummerer, C., Schweiger, H.F., Falk, E. (2001). *Finite element analysis of a deep excavation employing jet grouting techniques: results from a case study*. Proc. IACMAG 2001, Tucson.

Numerical modelling of earth pressure loading of the vertical stem of L-shaped retaining walls

M. Achmus

*Institute of Soil Mechanics, Foundation Engineering and Waterpower Engineering,
 University of Hannover, Germany*

ABSTRACT: The influence of system and boundary conditions on the earth pressure acting on the vertical stem of a L-shaped retaining wall is analysed with a numerical model. It is found that only in rare cases, namely with very high wall and subsoil stiffnesses, is the design load due to German regulations reached. In most cases the earth pressure is significantly lower than the average of active earth pressure and earth pressure at rest. A connection is found between the average rotation of the vertical wall stem and the magnitude of the earth pressure load. On this basis a concept for a more sophisticated, but still simple-to-use new design method is outlined.

1 INTRODUCTION

L-shaped walls are simple to construct and thus often used as earth retention constructions. Since the usual approaches of the design for overall stability (e.g. bearing capacity, sliding) are believed to be reliable and sufficiently accurate, questions remain concerning the magnitude of the earth pressure acting on the vertical stem of the wall (Fig. 1).

For the overall stability design a substitute retaining wall is usually considered. This consists of the wall itself

and the soil behind the stem and above the wall base. Active earth pressure is assumed to act on the virtual wall back, progressing upwards from the heel of the foundation. The angle of wall friction δ is to set equal to the inclination of the backfill surface β . The assumption of active earth pressure is justified even if the wall deformations in service are small, since before reaching the failure state larger deformations would occur.

In contrast to this, the actual earth pressure load acting in service has to be applied for the design of the vertical wall stem. Due to the existence of the horizontal base it is to be assumed that at least in the lower part of the wall an earth pressure larger than the active earth pressure is effective. To account for this, in the old German regulation DIN 4085 of 1987 a trapezoid distribution of the earth pressures had to be assumed, which leads to an increase of the design wall bending moments when compared with the classical triangular earth pressure distribution.

The actual magnitude and distribution of the earth pressure on the vertical stem is not generally clarified, see, for example, Arnold (2001). Due to the current German regulation DIN 4085 the average of active earth pressure and earth pressure at rest (in the following called increased earth pressure) is to be applied in classical (triangular) distribution. Here the angle of wall friction δ is to set equal to the surface inclination β . Thus the following earth pressure coefficients apply:

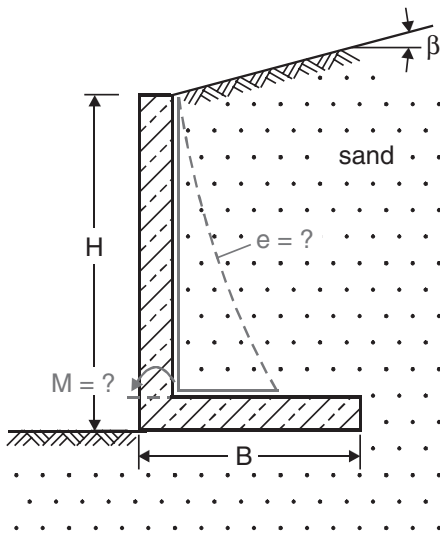


Figure 1. Schematic sketch of a L-shaped retaining wall.

$$k_{ah} = \frac{\cos^2 \varphi'}{\left(1 + \sqrt{\frac{\sin(\varphi' + \beta) \sin(\varphi' - \beta)}{\cos^2 \beta}}\right)^2} \quad (1)$$

$$k_{oh} = \frac{\sin \varphi' - \sin^2 \varphi'}{\sin \varphi' - \sin^2 \beta} \cos^2 \beta \quad (2)$$

Considering this, the maximum wall bending moment M at a depth z below the wall top due to the soil dead weight amounts to:

$$M(z) = \frac{1}{6} \gamma z^3 \frac{1}{2} (k_{ah} + k_{oh}) \quad (3)$$

On the basis of numerical investigations Goh (1993) proposed to apply active earth pressure in the upper half of the wall and to increase the pressure in the lower half from the active value in the middle of the wall to increased earth pressure for rough walls, or earth pressure at rest for smooth walls at the bottom. This leads to lower bending moments compared to the current German regulation approach.

It is obvious that the wall displacements, and therefore the actual earth pressure magnitude, is dependent on the wall geometry (height H , width B or ratio B/H), the wall stiffness and the stiffnesses of the backfill and the subsoil material (see Achmus & Rouili 2004, Arnold 2004). In this paper the influences of these parameters are quantified by numerical modelling. On this basis, a concept for a new design method is outlined.

2 NUMERICAL MODELLING

The Plaxis programme code (Brinkgreve & Vermeer 2002) was used for the numerical modelling. Medium dense sand is considered as backfill material. Since the dependence of the earth loading on the wall deformations is to be analysed, an accurate consideration of the stress-deformation behaviour of sand is very important.

2.1 Material law for sand

The Hardening Soil (HS) material law implemented in the Plaxis code is applied (see Schanz et al. 1999). This elastoplastic material law accounts in a realistic manner for the stress-dependence of the soil stiffness for oedometric and deviatoric stress paths as well as for unloading and reloading states. Using three reference stiffness modules and a parameter m as input parameters, the stress-dependency is modelled as follows (here cohesion is set to zero):

$$E_{(\sigma_3)} = E_{ref} \left(\frac{\sigma_3}{\sigma_{ref}} \right)^m \quad (4)$$

The reference stiffness modulus $E_{oed,ref}$ is determined by oedometer tests, and the modules $E_{50,ref}$ and

Table 1. Parameters of the Hardening Soil (HS) material law used for medium dense sand.

Unit weight	$\gamma = 17 \text{ kN/m}^3$
Stiffness parameters ($\sigma_{ref} = 100 \text{ kN/m}^2$)	$E_{oed,ref} = 25 \text{ MN/m}^2$ $E_{50,ref} = 25 \text{ MN/m}^2$ $E_{ur,ref} = 100 \text{ MN/m}^2$ $m = 0,65$
Shear parameters	$\varphi' = 35^\circ$ $c' = 0$ $\Psi = 2,5^\circ$

$E_{ur,ref}$ are determined in conventional triaxial tests by loading and un-/reloading, respectively.

With two yield surfaces shear hardening as well as compression hardening is accounted for. The shear yield surface is of the Mohr-Coulomb type. Plastic deformations are determined via a non-associated flow rule with a dilatancy angle Ψ . The failure surface is defined by the shear parameters, i.e. angle of internal friction φ' and cohesion c' . Plastic deformations at oedometric stress paths are determined using a cap yield surface with associated flow rule. For a detailed description of the Hardening Soil (HS) material law reference is made to Schanz et al. (1999).

Beside the unit soil weight γ a total of seven parameters are necessary to describe the stress deformation behaviour of the soil. For the numerical calculations presented in the following, the parameters typical for a medium dense sand given in Table 1 have been used.

2.2 Validation

For the validation of the material law chosen, the deformation dependency of earth pressure acting on a rigid wall was modelled. For this problem, comparisons with experimental results documented in the literature are possible.

In the upper part of Fig. 2 the system modelled is shown schematically. A wall with a height of 5 m was considered. The soil behind the wall was applied in 5 steps in layers of 1 m thickness. Between wall and soil an interface was defined with a maximum wall friction angle of $\delta = 29,3^\circ$. The wall movement was controlled by the stiffness of two anchor elements supporting the wall. The stiffnesses were in each case chosen in such a way that a combination of translatory and rotational movement of the rigid wall occurred. In the lower part of Fig. 2 the earth pressure distributions obtained with three different displacement modes (θ = wall rotation angle) are shown.

As assumed, an approximately linear increase of the earth pressure is obtained with depth. The coefficient

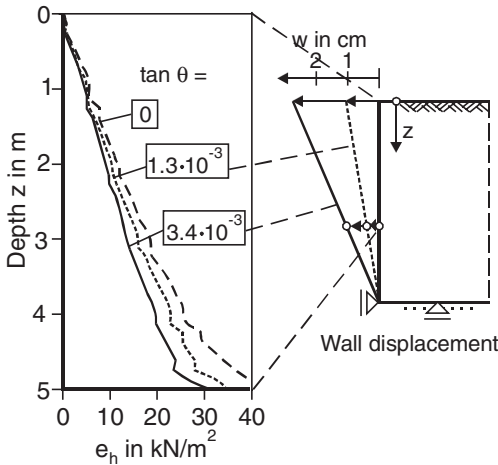
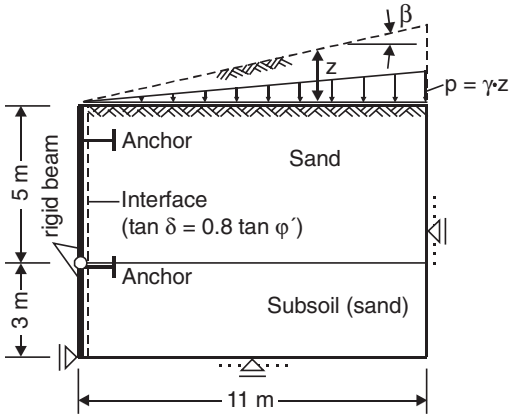


Figure 2. Earth pressure problem. System (top) and earth pressure distributions for different displacement modes (below).

of horizontal earth pressure can be determined by the following equation:

$$k_h = \frac{E_h}{0.5 \gamma H^2} = \frac{\int_{z=0}^{z=H} e_h dz}{0.5 \gamma H^2} \quad (5)$$

In Fig. 3 the calculated earth pressure coefficients for the case of a horizontal surface ($\beta = 0$) are presented dependent on the wall rotation $\tan \theta$. From the at-rest state the earth pressure decreases with increasing wall rotation, reaching a minimum value corresponding to the active state at a rotation of about $\tan \theta = 0.5$ to 0.6%.

For the base rotation mode wall rotations between 0.2 and 0.6%, dependent on the relative density, are

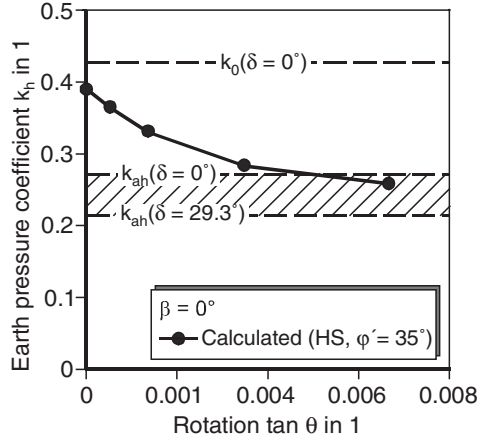


Figure 3. Calculated dependence of the earth pressure coefficient from the wall rotation (surface inclination $\beta = 0$).

usually assumed to be necessary to reach the active limit state in sand, see for example, Fang & Ishibashi (1986). For translatory displacement normally even smaller maximum wall displacements apply. For pure translatory displacement in medium dense sand, Ishihara et al. (1995) determined a ratio of displacement to wall height of about 0.4%.

Altogether, good agreement of the calculated displacement-dependency of the earth pressure with existing experience can be stated. There is a tendency to slightly overestimate the displacement necessary to reach the active state. For the determination of a deformation-dependent earth pressure approach for L-shaped walls, the modelling will thus presumably give results lying on the safe side.

2.3 Modelling of the L-shaped wall system

First, an L-shaped wall with a height of 5 m, a base width of 3.25 m ($B/H = 0.65$) and a wall thickness of $d = 0.4$ m is considered as a basic system. The configuration corresponds to the system shown in Fig. 1.

The subsoil was modelled down to a depth of 5 m below the wall base. Medium dense sand was assumed for both backfill and subsoil material. Wall stem and base were modelled by beam elements. Young's modulus of reinforced concrete was assumed with $E_b = 3 \cdot 10^4$ MN/m². Elements with a wall friction angle of $\delta = 0.84$, $\phi' = 29.3^\circ$ were applied between wall and soil interface.

In analogy to the earth pressure problem modelling, a stepwise application of the backfill soil in layers of 1 m thickness was simulated.

In Fig. 4 the wall displacement is given together with the earth pressure loading of the vertical stem obtained.

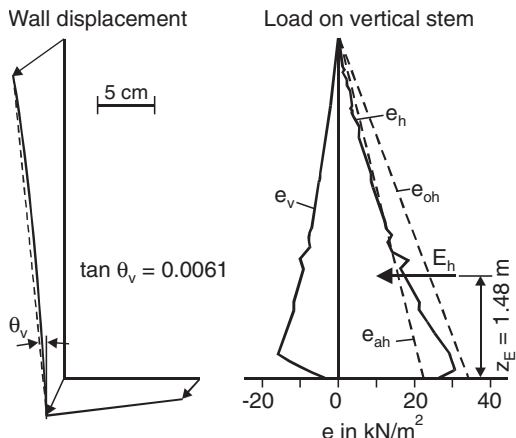


Figure 4. Calculation results for the basic system ($H = 5\text{ m}$, $B/H = 0.65$, $d = 0.4\text{ m}$).

In the upper part of the wall the pressure corresponds to active earth pressure, while it increases in the lower part and locally nearly reaches the earth pressure at rest. This general distribution was also obtained in centrifuge tests reported by Djerbib et al. (2001).

The resultant load acts at $z_E = 1.48\text{ m}$ above the wall toe ($z_E/H = 0.30$). The earth pressure coefficient calculated with Equation (5) is $k_h = 0.301$ and is thus about 10% larger than the active earth pressure coefficient for $\delta = 0$ ($k_{ah} = 0.271$). It is significantly smaller than the increased earth pressure coefficient of 0.349 which has to be used due to the German regulation. The k_h -value calculated corresponds with a horizontal displacement on the wall top of 4.61 cm and of 1.57 cm on the wall base, which yields an average rotation of the vertical wall stem of $\tan \theta_v = 0.0061$.

3 PARAMETRIC STUDY

To investigate the connection of the system and boundary conditions and the magnitude of the earth pressure loading of the vertical wall stem, a parametric study was carried out with the numerical model.

In all cases the earth pressure distribution was similar to that shown in Fig. 4. The height of the point of action of the resultant load always lay in the bandwidth $0.29H \leq z_E \leq 0.33H$. As a good and conservative approximation, the height of the point of action can be assumed at one third of the wall height, i.e. $z_E \approx 0.33H$. In the following only the horizontal earth pressure coefficient is considered as a measure for the magnitude of the earth pressure load and the resultant maximum bending moment of the wall stem.

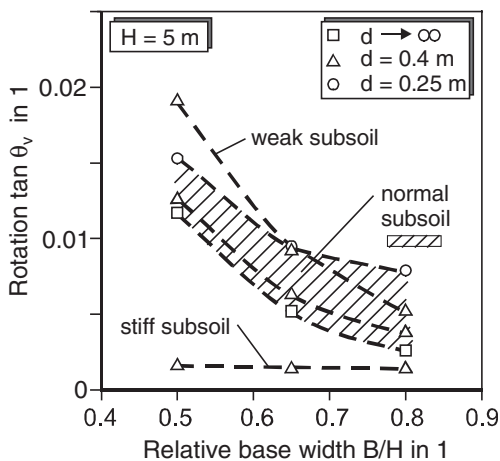
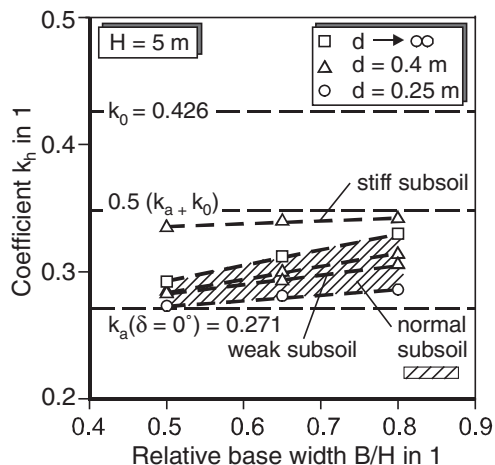


Figure 5. Earth pressure coefficient k_h (top) and average rotation of the vertical stem $\tan \theta_v$ (below) dependent on system and boundary conditions ($H = 5\text{ m}$).

3.1 Variation of wall geometry and subsoil stiffness

First, the width of the wall base B and the wall thickness d , i.e. the stiffness of the wall, was varied for the wall height $H = 5\text{ m}$ of the basic system. The results for the earth pressure coefficient k_h are given in Fig. 5 (top).

An increasing coefficient with increasing wall width and increasing wall stiffness is found. Also, a higher width B leads to a lower overall rotation of the wall, and a higher wall stiffness leads to a smaller bending deformation of the vertical wall stem. Thus, both effects reduce the average rotation of the vertical wall stem $\tan \theta_v$. This dependence is depicted in Fig. 5 (below).

Additionally, the stiffness of the subsoil was varied. For a weak subsoil an oedometric stiffness modulus of $E_s = 10\text{ MN/m}^2$ was assumed, and for a stiff subsoil

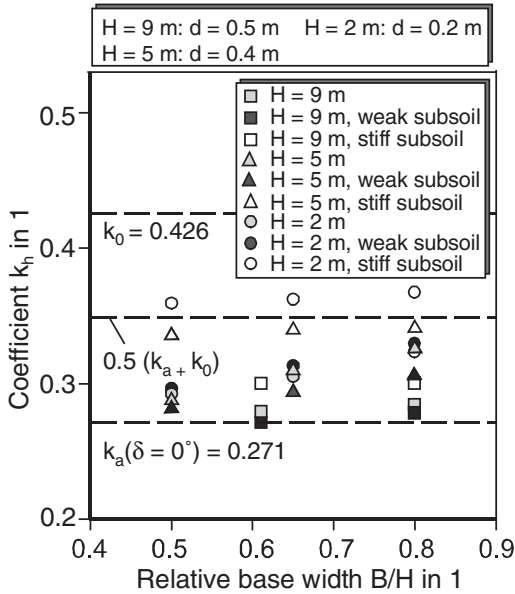


Figure 6. Earth pressure coefficients k_h for $H = 2, 5$ and 9 m.

$E_s = 200 \text{ MN/m}^2$. The results (only for $d = 0.4$ m) are also given in Fig. 5. Again it is found that a stiffness increase leads to an increase of the earth pressure coefficient and to a reduction of the rotation $\tan \theta_v$.

From the numerical investigation it is found that for the considered wall height of 5 m only in rare cases, namely with very stiff subsoil, very stiff wall and relatively large width of the wall base, does a loading in the magnitude of increased earth pressure originate.

Subsequently, the height of the L-shaped wall was also changed. Results for wall heights of 2 m, 5 m and 9 m are presented in Fig. 6. There is a tendency for small wall heights slightly higher earth pressure coefficients, but with that also smaller wall rotations to arise.

The earth pressure coefficient and the average rotation of the vertical stem are influenced by the same parameters. A direct connection between these two values can be presumed. In Fig. 7 the calculated earth pressure coefficients are given dependent on the corresponding wall rotations $\tan \theta_v$. The results for all wall geometries and subsoil stiffnesses investigated in the parametric study are given with the exception of the unrealistic values obtained with the assumption of a rigid wall ($d \rightarrow \infty$).

A clear dependence of the two values is evident, and this is nearly independent of the system and boundary conditions.

3.2 Variation of surface inclination

The calculation results presented in section 3.1 are valid for a horizontal surface of the backfill material

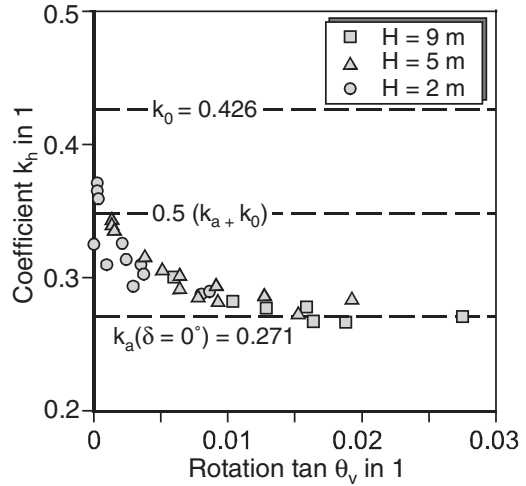


Figure 7. Dependence of the earth pressure coefficient k_h on the average rotation of the vertical stem $\tan \theta_v$.

($\beta = 0^\circ$, see Fig. 2 top). In a further step the parametric study was extended to surface inclinations $\beta > 0$.

A special problem in this context is to determine the earth pressure at rest in the numerical model. Equation (2) for the coefficient k_{0h} is purely empirical and must thus not necessarily be confirmed in numerical calculations. If a comparison with analytical results should be carried out, the deviations must be taken into account. For this reason the earth pressure problem presented in section 2.2 was also considered for cases with $\beta > 0$.

In a first step the triangular soil block shown in Fig. 2 (top) was applied stepwise in triangular layers. However, with this procedure unrealistically high earth pressures were obtained for the at-rest state (rigid wall and rigid anchors). The reason is a stress redistribution inside the triangular soil block, inducing a concentration of the vertical pressures beneath the wall. To avoid this effect, the surface inclination was considered via a triangular load $p = \gamma z$ acting on the horizontal surface (see Fig. 2 top).

From the exemplary presentation of the deformation-dependence of the earth pressure coefficient for $\beta = 10^\circ$ in Fig. 8 it is evident that this procedure gives realistic results for the earth pressure at rest, i.e. k_{0h} -values comparable with the analytical approaches. There is a tendency for the earth pressure at rest to be slightly overestimated. This trend is the more intensive, the higher the surface inclination β is. This has to be kept in mind in the evaluation of the results for L-shaped walls presented in the following.

The same parameter variations presented in section 3.1 for $\beta = 0^\circ$ were carried out for L-shaped walls with surface inclinations of $8^\circ, 15^\circ$ and 25° . The calculated

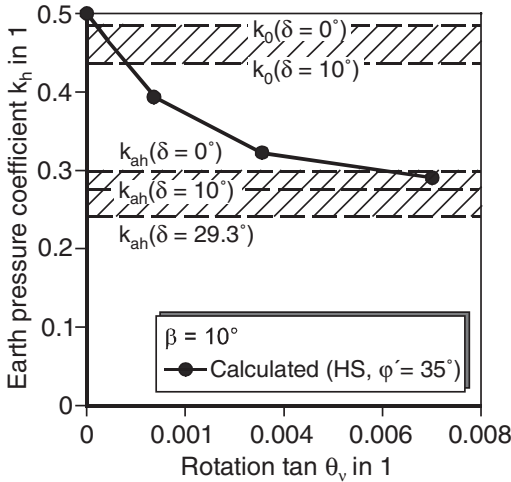


Figure 8. Deformation-dependence of the earth pressure coefficient for $\beta = 10^\circ$.

earth pressure coefficients dependent on the rotation of the vertical wall stem are given in Fig. 9. The analytical earth pressure coefficients determined by Equation (2) are also shown. The connection between k_h and the rotation $\tan \theta_v$ is also confirmed for an inclined surface.

In contrast to the case $\beta = 0$, for $\beta > 0$ with very small wall rotations earth pressure coefficients are obtained which are higher than the increased earth pressure to be applied due to the German regulation DIN 4085. However, the reason for this is the overestimation of the earth pressure at rest compared with the analytical approach discussed above. Taking this into account, it seems reasonable to assume that also for an inclined surface increased earth pressure is the maximum load occurring only in cases with very small wall rotations. In almost all cases a smaller, and from a certain limit rotation, active earth pressure is to be expected.

4 CONCLUSIONS

Due to current German regulations the vertical wall stem of L-shaped walls is to be designed for increased earth pressure in classical distribution. The results of the numerical modelling prove that this approach is realistic only for very stiff systems, i.e. very high wall and subsoil stiffnesses. In most cases the loading will therefore be overestimated. Similar results were obtained from Arnold (2004), who also carried out numerical investigations and found that the resultant earth pressure is strongly dependent on the stiffness of the subsoil and the wall width.

A promising design approach results from the determined dependence of the earth pressure coefficient

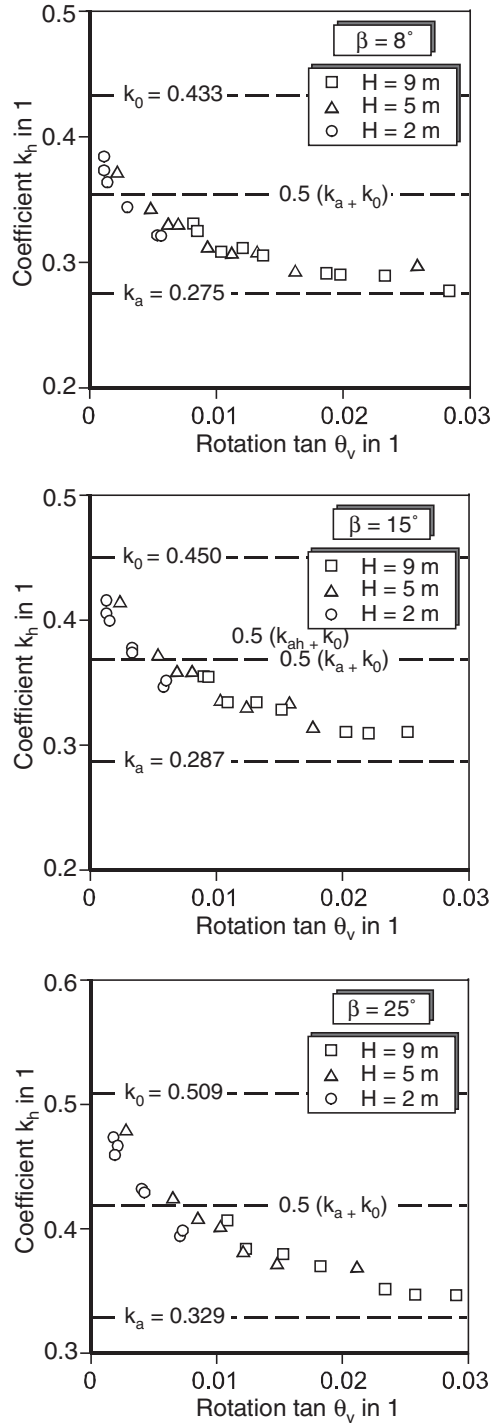


Figure 9. Dependence of the earth pressure coefficient k_h on the average rotation of the vertical stem $\tan \theta_v$, for $\beta = 8, 15$ and 25° .

on the average rotation of the vertical wall stem. With a usual settlement calculation and by calculation of the bending deformation of the vertical stem the average rotation can be easily estimated. Dependent on this value, the earth pressure coefficient to be applied can be determined (see also Achmus & Rouili 2004). This new approach is more sophisticated than the old one, but still simple to use.

Due to the calculated results, a wall rotation of $\tan \theta_v = 0.01$ to 0.015 is necessary to reach the state in which active earth pressure can be applied. Increased earth pressure is to be applied only if $\tan \theta_v = 0$, and for cases with $0 \leq \tan \theta_v \leq 0.01$ (0.015) a linear interpolation between these limit values may be carried out.

These results were derived for medium dense sand as backfill material. There is no doubt that the values need verification by experimental tests. But, in combination with experimental results, the results of the numerical study can form the basis for a new, and in most cases more economic, design approach for the vertical stem of L-shaped walls.

REFERENCES

- Achmus, M. & Rouili, A. 2004. Untersuchung zur Erddruckbeanspruchung von Winkelstützwänden. *Bautechnik* 81, H. 12 (December), pp. 942–948 (in German).
- Arnold, M. 2001. Modellversuche zum Erddruck auf Winkelstützwände. In: *Mitteilungen des Instituts für Geotechnik der Universität Dresden*, H. 9, pp. 23–34 (in German).
- Arnold, M. 2004. Zur Berechnung des Erd- und Auflastdrucks auf Winkelstützwände im Gebrauchszustand. *Mitteilungen des Instituts für Geotechnik der Universität Dresden*, H. 13 (in German).
- Brinkgreve, R.B.J. & Vermeer, P.A. 2002. *Plaxis Version 8* (Handbook). Balkema, Rotterdam.
- Djrbib, Y., Hird, C.C. & Touahmia, M. 2001. Centrifugal model tests of uniform surcharge loading on L-shaped retaining walls. *15th Int. Conf. on Soil Mechanics and Foundation Engineering, Istanbul*, Vol. 2, pp. 1137–1140.
- Fang, Y.S. & Ishibashi, I. 1986. Static earth pressures with various wall movements. *Journal of Geotechnical Engineering*, Vol. 112, No. 3, pp. 317–333.
- Goh, T.C. 1993. Behaviour of cantilever retaining walls. *Journal of Geotechnical Engineering*, Vol. 119, No. 11, pp. 1751–1770.
- Ishihara, K., Arakawa, T., Saito, T., Hada, M. & Huang, Y. 1995. Study on the earth pressure by using a large-size soil box with a movable wall. *Proc. of the 30th Japan National Conf. on SMFE*, pp. 1717–1720 (in Japanese).
- Schanz, T., Vermeer, P.A. & Bonnier, P.G. 1999. The hardening soil model: Formulation and verification. In: *Beyond 2000 in Computational Geotechnics – 10 Years of Plaxis*. Balkema, Rotterdam.

Embankments

The pre-failure deformation of an embankment predicted by two kinematic hardening models

A. Grammatikopoulou

Geotechnical Consulting Group, formerly Imperial College, London, UK

L. Zdravkovic & D.M. Potts

Imperial College, London, UK

ABSTRACT: This paper presents a comparison of the pre-failure behaviour of an embankment when its clay foundation is modelled with two kinematic hardening models. The paper shows that the pre-failure deformations are not only influenced by non-linearity but also by the stiffness response predicted in both compression and extension paths.

1 INTRODUCTION

Nowadays it is well known that the pre-failure behaviour of overconsolidated clays is highly non-linear and inelastic from the early stages of loading. However, conventional elasto-plastic models (e.g. the Modified Cam Clay model (MCC)) do not predict satisfactorily these features of behaviour.

A family of soil models, known as the kinematic hardening models (e.g. Mroz et al. (1979), Al-Tabbaa and Wood (1989), Stallebrass & Taylor (1997)), seem to provide an improvement over simple elasto-plastic constitutive models. These models allow for plasticity and non-linearity to be invoked within the conventionally defined yield surface, through the introduction of a number of kinematic surfaces. Models based on this framework are usually extensions of existing constitutive models for normally consolidated clays – for example the two-surface “bubble” model (Al-Tabbaa and Wood (1989)) is an extension of the MCC model.

Grammatikopoulou et al. (2002) presented a comparison of the pre-failure behaviour of an embankment predicted by the two-surface “bubble” model and the Modified Cam Clay model. The results of the analyses showed that the pre-failure movements were strongly influenced by non-linearity, a feature not adequately realised by the MCC model. The two-surface “bubble” model was shown to predict highly non-linear pre-failure behaviour; however, it also predicted an abrupt transition from elastic to elasto-plastic behaviour (Grammatikopoulou et al. (2002)). This resulted in the model being unable to predict a smooth stiffness degradation curve.

This feature of behaviour has been improved by modifying the hardening modulus of the model and in this way a new model has been formulated, the modified two-surface model (Grammatikopoulou et al. (2005)).

This paper investigates the behaviour of an embankment when its clay foundation is modelled with the two-surface “bubble” model and the modified two-surface model. The same undrained strength profile is assigned to both models and the pre-failure behaviour of the embankment is examined.

2 BOUNDARY VALUE PROBLEM ANALYSED

For the present study the geometry of the same embankment analysed by Grammatikopoulou et al. (2002) was also adopted. This was part of a research programme undertaken by Laval University, Canada, in order to study the behaviour of embankments on a soft clay deposit at Saint Alban, Quebec. The embankment analysed in this paper, test embankment A, was built to failure (La Rochelle et al. (1974)).

2.1 *Ground conditions at Saint-Alban*

The typical soil profile at Saint-Alban consists of approximately 2 m of weathered clay crust, overlying a soft silty marine clay deposit, which extends to a depth of approximately 13.7 m. This is underlain by a deep layer of dense sand, extending to depths of more than 24 m. The clay layer beneath the crust is lightly overconsolidated with an overconsolidation ratio *OCR* of approximately 2. The water table is located at a depth of

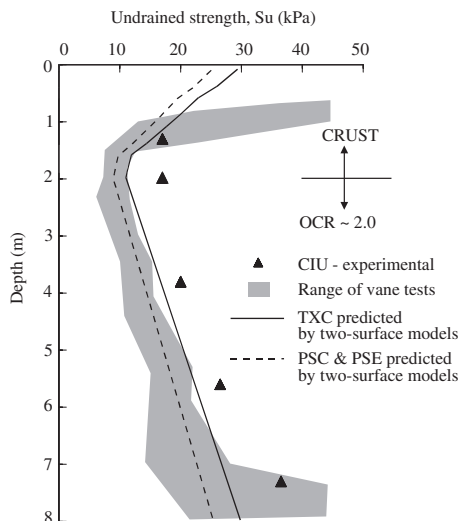


Figure 1. Undrained strength profiles for the clay at Saint-Alban (data after La Rochelle et al. (1974)).

0.7 m below the ground surface. The bulk unit weight of the soil is 19 kN/m^3 above the water table and 16 kN/m^3 below it. The undrained strength profile at the site was measured from field vane tests and isotropically consolidated undrained triaxial tests (CIU) (La Rochelle et al. (1974)) and can be seen in Figure 1. The field vane tests show an increased undrained strength at the crust.

2.2 Geometry of test embankment A

A plan view and a typical cross section of the test embankment A can be seen in Figure 2. The figure shows the dimensions of the embankment corresponding to an embankment height of 4.6 m (this was the failure height indicated by limited equilibrium stability analysis, performed before the embankment construction). In the event, failure of the embankment occurred at a lower height, i.e. 3.9 m. The three sides of the embankment with a slope of 2:1 and a 1.5 m high berm ensured that the failure would be confined to the fourth side, which had a slope of 1.5:1. The fill material was a uniform medium to coarse sand.

3 CONSTITUTIVE MODELS USED IN THE ANALYSES

3.1 Clay deposit

The clay deposit was modelled with a version of the two-surface “bubble” model and with the modified two-surface model.

The two-surface “bubble” model (Al-Tabbaa and Wood (1989)) employs a single kinematic yield surface, within the Modified Cam Clay bounding surface, see

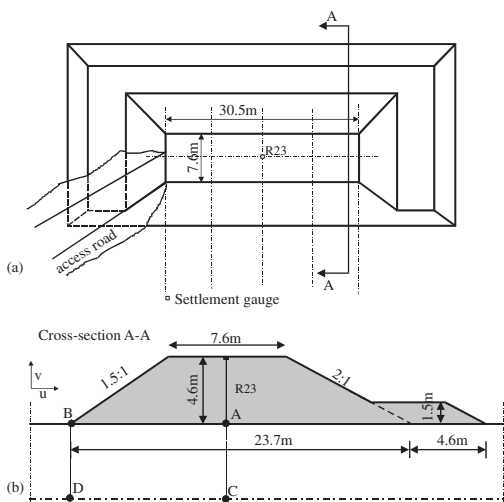


Figure 2. Test embankment A (a) plan view (b) cross section A-A.

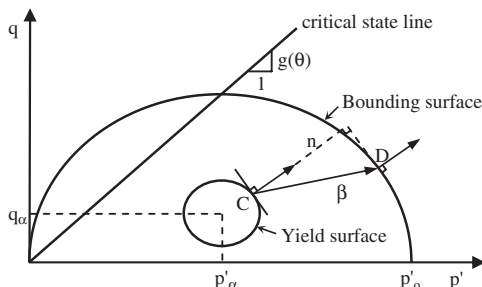


Figure 3. 2-SKH and M2-SKH models: Representation of the kinematic yield and bounding surfaces in triaxial stress space.

Figure 3. The kinematic yield surface encloses the region within which the behaviour is elastic. The behaviour becomes elasto-plastic once the stress state touches the kinematic surface, in which case the kinematic surface is dragged along the stress path, see Figure 3. The model has been generalized and implemented into the finite element program ICFEP, and a number of improvements have been made (Grammatikopoulou (2004)). These include a variety of shapes of the yield and plastic potential surfaces in the deviatoric plane. This was essential, since the circular shape of the yield and plastic potential surfaces (and hence the failure surface) assumed in the original model does not represent well the failure conditions of most soils. This version of the two-surface kinematic hardening “bubble” model is denoted here as the 2-SKH model.

Early trials using the 2-SKH model showed that it predicts a non-smooth elasto-plastic transition with a sudden drop in stiffness once yielding is initiated (Grammatikopoulou et al. (2002)). This feature of behaviour is attributed to the adopted hardening modulus and proves to be a deficiency when simulating pre-failure non-linearity in the small strain range. This was overcome by adopting a new improved hardening modulus, which results in a smooth elasto-plastic transition. In this way a new model was formulated, namely the modified two-surface model (M2-SKH). For more details on the new model the reader is referred to Grammatikopoulou (2004) and Grammatikopoulou et al. (2005). Appendix 1 gives some basic equations common to both models.

3.2 Fill material

The fill material was modelled as a linear elastic material with a Mohr-Coulomb yield surface and a non-associated flow rule.

4 MODEL PARAMETERS

4.1 Clay deposit

The clay deposit was modelled with the 2-SKH and the M2-SKH models and the parameters are given in Appendix 1. The derivation of the parameters can be found in Grammatikopoulou (2004). For the M2-SKH model there is only one parameter that is different from the parameters of the 2-SKH model and that is the parameter α in the new hardening modulus (instead of the parameter ψ used in the 2-SKH model). This parameter was chosen so that both models predicted similar stress-strain curves in triaxial compression. Figure 4 plots the stiffness-strain and stress-strain curves obtained from single element finite element analyses, modelling an undrained triaxial compression test at a depth of 2.0 m (J is the deviatoric stress, which is equal to $J = q/\sqrt{3}$ and E_d is the corresponding deviatoric strain). This figure shows that the 2-SKH model predicts a sudden drop in stiffness once the stress state touches the yield surface, whereas the M2-SKH model predicts a smooth stiffness degradation curve. Hence, it is difficult to predict exactly the same response for both models, since the 2-SKH model predicts lower values of stiffness than the M2-SKH model in the initial part of the small strain range. It has to be noted that significant differences in stiffness in the initial part of the small strain range in Figure 4a plot as relatively small differences in the stress-strain curves of Figure 4b.

An effective stress ratio, K_o , of 0.67 was assumed for the clay layer and an OCR profile reducing from the ground surface to a depth of 2 m and then remaining constant with depth at a value of 2.0 was adopted. The above parameters result in the same undrained

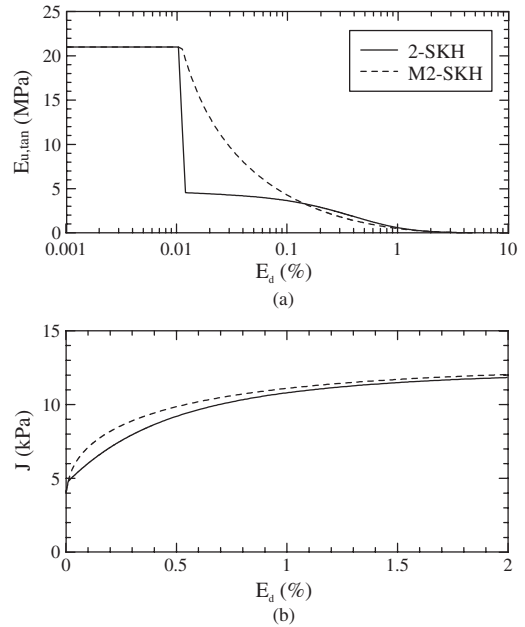


Figure 4. Predictions of the 2-SKH and M2-SKH models for an undrained triaxial compression test at a depth of 2.0 m (a) stiffness-strain curve (b) stress-strain curve.

strength profile for both models. The resulting profiles in triaxial compression (TXC) and in plane strain compression (PSC) and extension (PSE) can be seen in Figure 1 (these profiles were back calculated so that the analyses predicted the correct failure height of 3.9 m).

4.2 Fill material

A Young's modulus, E' , of 10000 kPa and a Poisson's ratio, μ' , of 0.3 were assumed for the fill material. The angle of shearing resistance, ϕ' , was determined from triaxial tests on samples of the fill (La Rochelle et al. (1974)) and was equal to 44° and the angle of dilation, ν' , was assumed equal to 22°.

5 FINITE ELEMENT ANALYSES

5.1 Analyses details

Two analyses were performed, one in which the clay layer was modelled with the 2-SKH model and one in which it was modelled with the M2-SKH model. Both analyses were carried out undrained.

The finite element mesh adopted can be seen in Figure 5. The analyses were plane strain and used eight noded isoparametric quadrilateral elements with 2×2 integration. A modified Newton-Raphson scheme, with an error controlled sub-stepping stress

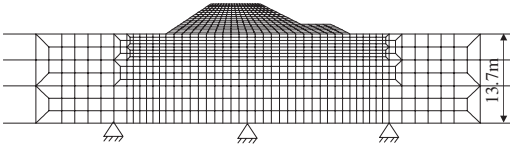


Figure 5. Finite element mesh.

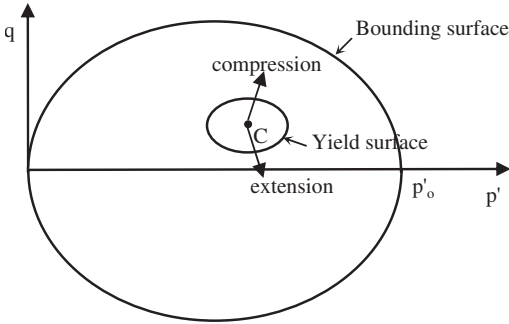


Figure 6. Schematic diagram showing the kinematic surface centred around the current stress state C.

point algorithm, was used as the non-linear solver (see Potts & Zdravkovic (1999)). The building of the embankment was simulated with the construction of successive layers, until failure occurred.

In both cases it was assumed that at the start of the analyses the kinematic surface was centred around the initial stress state, see Figure 6. This has implications with respect to the relative stiffness predicted in compression and extension paths. On initial loading the models predict the same elastic stiffness in both compression and extension. However, on further loading the stress state reaches the kinematic surface and since in these models the hardening modulus depends on the relative position of the kinematic and bounding surfaces, a softer response is predicted in a compression path than in an extension path. In the kinematic hardening models a different stiffness response between compression and extension paths is always predicted (the exception being the case where the kinematic surface is centred around an isotropic initial stress state). This will be shown to have a significant effect on the pre-failure behaviour of the embankment.

5.2 Analyses results

Both analyses predicted the same failure height, as expected, since the same undrained strength was prescribed for both models.

Figure 7 compares the vertical settlement measured at settlement gauge R23 (point A in Figure 2) with the predictions of the analyses. Both predictions compare well with the measured response.

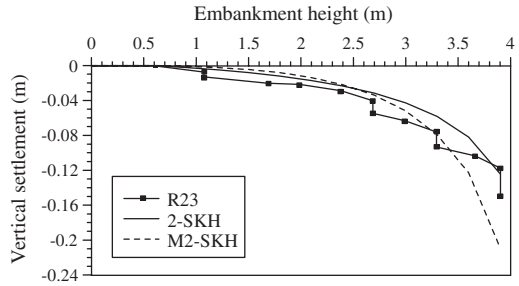


Figure 7. Comparison between observed and predicted vertical settlement at the centreline of the embankment.

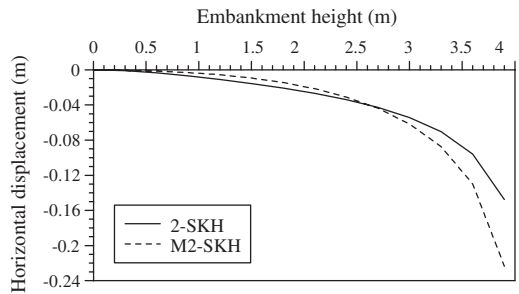


Figure 8. Horizontal displacement at the toe of the embankment versus embankment height predicted by the two models.

Figure 8 plots the horizontal displacement at the toe of the embankment (point B in Figure 2) against the embankment height. Both Figures 7 and 8 show that the analysis with the M2-SKH model predicts smaller movements than the analysis with the 2-SKH model, up to an embankment height of ~ 2.7 m. For higher embankment heights the M2-SKH model predicts larger movements than the 2-SKH model.

The fact that the M2-SKH model predicts smaller movements than the 2-SKH model in the initial stages of the embankment construction, where the strains are still small, is not surprising. As shown in Figure 4, due to the non-smooth elasto-plastic transition the 2-SKH model predicts lower values of stiffness than the M2-SKH model once the stress state becomes elasto-plastic and up to strains of $\sim 0.1\%$. However, the fact that the M2-SKH model predicts larger movements after a certain embankment height (~ 2.7 m) is in contrast with the stress-strain curve predicted in Figure 4. Figure 4b shows that the M2-SKH model predicts an overall stiffer response than the 2-SKH model.

This behaviour can be explained by examining typical stress paths followed by soil elements along a potential failure surface of the embankment, see Figure 9. It can be seen that the stress path, imposed by the construction of the embankment changes from

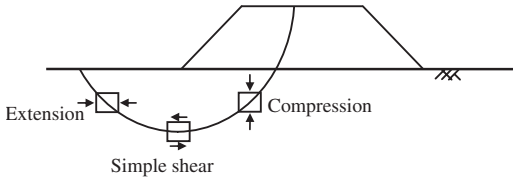


Figure 9. Stress paths followed by soil elements along the failure surface beneath an embankment (after Bjerrum (1973)).

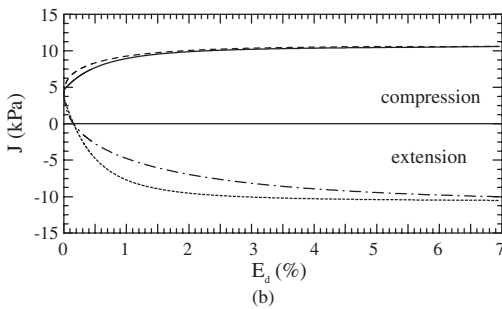
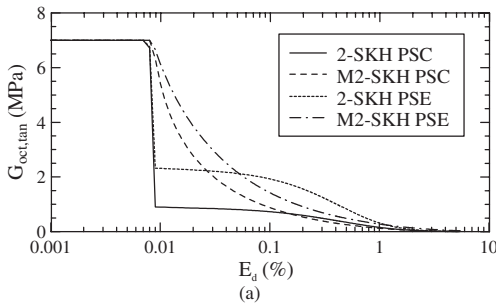


Figure 10. Predictions of the 2-SKH and M2-SKH models for a plane strain compression (PSC) and extension (PSE) test at a depth of 2.0 m (a) stiffness-strain curve (b) stress-strain curve.

a compression path to an extension path (Bjerrum (1973)). Hence, the stiffness of the soil in both compression and extension is important.

Figure 4 plots the response for a triaxial compression test. However, since the analyses are plane strain, what is of relevance here is the response under plane strain conditions.

Figure 10 plots the stiffness-strain and stress-strain curves predicted by the two models for single element analyses modeling plane strain compression (PSC) and plane strain extension (PSE) at a depth of 2 m ($G_{oct} = dJ/dE_d$). It can be seen that for each model the stiffness in compression is softer than the stiffness in extension, once the stress state touches the kinematic yield surface, as expected.

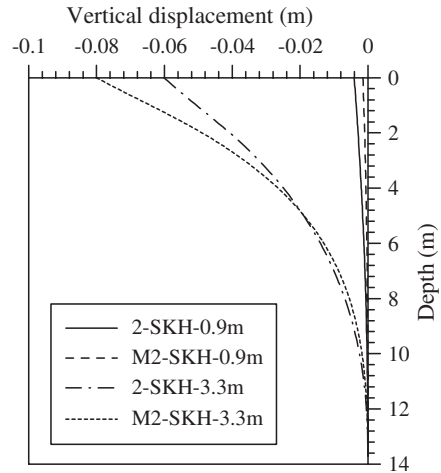


Figure 11. Vertical displacement at the centreline of the embankment for embankment heights of 0.9 m and 3.3 m.

Inspection of Figure 10 shows that the predicted response by the two models in plane strain compression is similar to the response predicted in triaxial compression in Figure 4. However, the response predicted in plane strain extension is different, and although the response of the M2-SKH model is initially stiffer, it soon changes to become softer than the response of the 2-SKH model. This observation can explain the behaviour encountered in the embankment analyses (Figures 7 and 8), in which the M2-SKH model shows an initially stiffer behaviour than the 2-SKH model, which as the embankment height increases becomes softer than the response predicted by the 2-SKH model.

Figure 11 shows the vertical movements below the centreline of the embankment (line AC in Figure 2) against depth for two embankment heights, 0.9 m and 3.3 m. Figure 12 presents the distribution of horizontal movements under the toe of the embankment (line BD in Figure 2) with depth for the same embankment heights. Comparison of the movements predicted by the models, for an embankment height of 0.9 m, shows that the M2-SKH model predicted significantly smaller movements than the 2-SKH model. For an embankment height of 3.3 m the M2-SKH model predicted larger vertical movements than the 2-SKH model up to a depth of 5 m and larger horizontal movements up to a depth of 10 m.

Table 1 summarises the percentage differences between the maximum vertical movement, beneath the centreline, and the maximum horizontal movement, beneath the toe of the embankment, predicted by the two models, for four embankment heights.

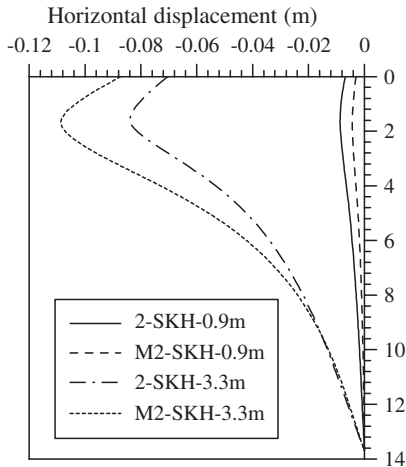


Figure 12. Horizontal displacement at the toe of the embankment for embankment heights of 0.9 m and 3.3 m.

Table 1. Percentage difference between the maximum movements predicted by the 2-SKH and M2-SKH models.

Embankment height (m)	0.9	1.8	2.4	3.3
$\frac{ v_{2-SKH}^{\max} - v_{M2-SKH}^{\max} }{ v_{2-SKH}^{\max} } \cdot 100$	62.7	35.9	10.4	-33.1
$\frac{ u_{2-SKH}^{\max} - u_{M2-SKH}^{\max} }{ u_{2-SKH}^{\max} } \cdot 100$	49.9	20.4	-1.0	-30.2

v: vertical movement below the centreline of the embankment.

u: horizontal movement below the toe of the embankment.

6 SUMMARY AND CONCLUSIONS

This paper examines the pre-failure behaviour of an embankment when the soft clay deposit on which it is founded is modelled with two kinematic hardening models; a version of the two-surface “bubble” model (Al-Tabbaa & Wood (1989)) (2-SKH model) and the modified two-surface model (M2-SKH model). The latter is an extension of the former; it adopts a new hardening modulus, which overcomes the non-smooth elasto-plastic transition predicted by the original model. The conclusions that can be drawn from this comparison are the following:

- When the same undrained strength is prescribed to both models, then these predict the same failure height of the embankment. However, each model predicts a different deformational behaviour.
- The pre-failure deformations are not only influenced by non-linearity, but also by the stiffness response in both compression and extension paths.

- For similar stress-strain curves in compression the models predict a different response in extension. This, combined with the drop in stiffness predicted by the 2-SKH model, results in the M2-SKH model predicting smaller movements than the 2-SKH model, up to an embankment height of ~2.7 m, and larger movements than the 2-SKH model for higher embankment heights.
- These results have important implications for the use of kinematic hardening models in practice. It is common practice to derive model parameters and examine the predicted response for compression paths. However, since in most cases any kinematic hardening model predicts a different stiffness response between compression and extension paths, it is important that in the evaluation of the models the predicted response against extension paths is equally examined.

ACKNOWLEDGEMENTS

The research presented in this paper was funded by an EPSRC grant. Their support is gratefully acknowledged.

REFERENCES

- Al-Tabbaa, A. & Wood, D.M. 1989. An experimentally based “bubble” model for clay. *Int. Conf. Num. Models Geomech.*, NUMOG III, Edt. A. Pietruszczak G. N. Pande: 91–99.
- Bjerrum, L. 1973. Problems of soil mechanics and construction on soft clays and structurally unstable soils. *8th Int. Conf. Soil Mechanics and Foundation Engineering* 3: 111–159.
- Grammatikopoulou, A., Zdravkovic, L. & Potts, D.M. 2002. The effect of a kinematic yield surface on the predicted behaviour of an embankment. *Int. Conf. Num. Models Geomech.*, NUMOG VIII, Edt. A. Pietruszczak G. N. Pande: 553–559.
- Grammatikopoulou, A. 2004. *Development, implementation and application of kinematic hardening models for over-consolidated clays*. PhD thesis, Imperial College, London, UK.
- Grammatikopoulou, A., Zdravkovic, L. & Potts, D.M. 2005. General formulation of two kinematic hardening constitutive models with a smooth elasto-plastic transition. Accepted for publication in the *International Journal of Geomechanics, ASCE*, in September 2005.
- La Rochelle, P., Trak, B., Tavenas, F. & Roy, M. 1974. Failure of a test embankment on a sensitive Champlain Clay deposit. *Canadian Geotech. Jnl.* 11(1): 142–164.
- Mroz, Z., Norris, V.A. & Zienkiewicz, O.C. 1979. Application of an anisotropic hardening model in the analysis of elasto-plastic deformation of soils. *Geotechnique* 27(1): 1–34.
- Potts, D.M. & Zdravkovic, L. 1999. *Finite element analysis in geotechnical engineering: Theory; Vol.1*. Thomas Telford.

Stallebrass, S.E. & Taylor, R.N. 1997. The development and evaluation of a constitutive model for the prediction of ground movements in overconsolidated clay. *Geotechnique* 47(2): 235–253.

APPENDIX 1

Bounding surface:

$$F_b = \left(p' - \frac{p'_o}{2} \right)^2 + \frac{1}{2} \frac{\mathbf{s} : \mathbf{s}}{g^2(\theta_b)} - \frac{p_o'^2}{4} = 0$$

Kinematic yield surface:

$$F_y = (p' - p'_a)^2 + \frac{1}{2} \frac{(\mathbf{s} - \mathbf{s}_a) : (\mathbf{s} - \mathbf{s}_a)}{g^2(\theta_y)} - R^2 \frac{p_o'^2}{4} = 0$$

where p' is the mean effective stress, \mathbf{s} is the deviatoric stress tensor, p'_o is the mean effective stress at the intersection of the current swelling line with the isotropic compression line, p'_a and \mathbf{s}_a are the mean effective stress and the deviatoric stress tensor at the centre of the kinematic surface, R is the ratio of the size of the kinematic surface to that of the bounding surface. The functions $g(\theta_b)$ and $g(\theta_y)$ define the shape of the bounding and kinematic surfaces in the

deviatoric plane, where θ_b and θ_y are the values of the Lode's angle for the bounding and yield surfaces respectively.

In the analyses presented here a Mohr-Coulomb hexagon was adopted as the deviatoric shape of the yield surface, hence:

$$g(\theta) = \frac{\sin \varphi'}{\cos \theta + \frac{\sin \theta \sin \varphi'}{\sqrt{3}}}$$

where φ' is the angle of shearing resistance. The plastic potential surface was assumed to have a circular deviatoric shape.

The parameters common to these versions of the two models are: $\lambda^* = 0.215$ and $\kappa^* = 0.005$, the slopes of the isotropic normal compression and the elastic part of the swelling line in $\ln v - \ln p'$ space respectively, $\varphi' = 27^\circ$, the angle of shearing resistance at the critical state, $R = 0.06$, the ratio of the size of the history surface to that of the bounding surface, G_e , the elastic shear modulus, (see Grammatikopoulou et al. (2002)). In the 2-SKH model an extra parameter, which controls the hardening modulus, is required and this is $\psi = 1.5$. In the M2-SKH the extra parameter in the hardening modulus is $\alpha = 20.0$.

Numerical modelling of Murro test embankment with S-CLAY1S

M. Koskinen

Helsinki University of Technology, Finland

M. Karstunen

University of Strathclyde, Glasgow, Scotland, UK

ABSTRACT: The structure of most natural soft soils is anisotropic and apparently bonded. The apparent bonding gives the soil additional resistance to yielding, resulting in an increased value of undrained shear strength. It is commonly assumed that the undrained shear strength under an embankment increases with time due to consolidation. However, underneath Murro test embankment in Finland measurements suggest that in some layers the undrained shear strength had decreased during eight years of consolidation, whereas the disturbed undrained shear strength has increased. This kind of behaviour can be explained with a recently proposed soil model S-CLAY1S that accounts for plastic anisotropy and destructuration. In this paper, the behaviour of Murro test embankment is modelled with the S-CLAY1S model and compared with observations.

1 INTRODUCTION

Soft clay deposits cover a large portion of the coastal areas of Finland, in which most of the population is concentrated. Therefore, a great deal of construction takes place on soft soils. In 1993 the Finnish Road Administration commissioned an instrumented test embankment in Murro, near the town of Seinäjoki, in Western Finland (Koskinen et al. 2002b). Murro clay is relatively homogenous silty clay with undrained shear strength of less than 30 kPa throughout the deposit. The clay contains sulphur that makes it black and gives it a special odour. The observed settlement of the two-meter high test embankment ten years after construction was 81.6 cm and the primary consolidation is still going on.

Extensive series of field and laboratory tests were carried out prior to the construction of the test embankment, as well as eight years after. The field tests included field vane tests, static-dynamic penetration tests and CPTU tests (Koskinen et al. 2002b). In the laboratory, oedometer tests and triaxial tests were carried out on both undisturbed and reconstituted samples (Karstunen & Koskinen 2004a). The field vane tests carried out prior to construction of the test embankment (Fig. 1a), showed that underneath a 1.6 m thick dry crust there was a 4.5 m thick layer with an undrained shear strength of 12 kPa. From the depth of 4.5 m the undrained shear strength increased nearly linearly down to the depth of 14 meters, from which depth downwards the deposit exhibited virtually constant undrained

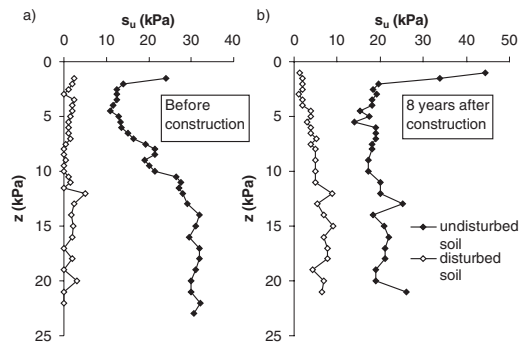


Figure 1. Field vane test results in Murro test embankment a) prior to construction and b) eight years after construction.

shear strength of 30 kPa. The results of a field vane test carried out eight years later (Fig. 1b), showed that the undrained shear strength of the softest layer had increased from 12 kPa to 18 kPa. However, the undrained shear strength measured below that layer seemed to be around 20 kPa, and has therefore, in fact decreased. This is in contrast with the common assumption that the undrained shear strength increases in time due to consolidation. Furthermore, the field vane measurements (Fig. 1) show that the remoulded undrained shear strength had increased in the whole soil profile during the 8 years of consolidation.

The reduction of the undrained shear strength under an embankment, described above, can be explained with

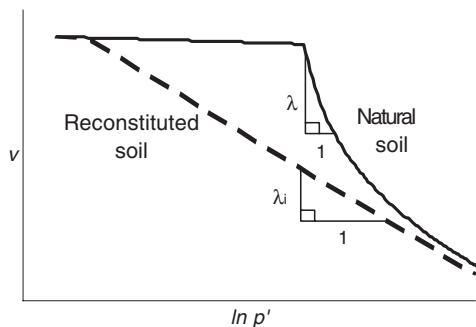


Figure 2. Behaviour of natural (structured) and reconstituted (unstructured) clays.

the existence of structure that most natural soft soils appear to exhibit. The structure consists of two components: fabric (i.e. arrangement of particles and particle contacts), which expresses itself as anisotropy, and apparent interparticle bonding as demonstrated e.g. by sensitivity. The apparent bonding gives the soil additional resistance to yielding, resulting in a higher value of undrained shear strength than without the bonding present. Plastic straining modifies fabric, and causes gradual degradation of bonding, called destructuration. A soil, where the destructuration process is complete, or where the bonding is otherwise absent, is referred to as destructured or unstructured soil.

When a normally consolidated sample, where the bonds have been removed (for example by reconstituting it), is loaded along a K_0 stress path (K_0 is the coefficient of earth pressure at rest), it would follow a straight line in the $\ln p' - v$ plane, where p' is the mean effective stress and v the specific volume, respectively. This line is called the intrinsic compression line (ICL), with a slope of λ_i (see Figure 2). In contrast, a sample where the bonding is still present, would yield at a higher stress than the unstructured sample, and the normal compression line (NCL) would then converge towards the intrinsic compression line in the $\ln p' - v$ space as the strains increase and the bonding is gradually destroyed. Therefore, for a natural sample, the apparent gradient of the normal compression line (λ) is higher than the intrinsic gradient. This phenomenon is schematically shown in Figure 2. In addition, the rate of destructuration, represented by the apparent value of λ , was found to depend on the stress ratio $\eta = q/p'$ (where q is the deviator stress), so that the higher the stress ratio the higher the value of λ (Koskinen & Karstunen 2004).

The combined effect of anisotropy and destructuration can be modelled with a constitutive model called S-CLAY1S (Koskinen et al. 2002a). Earlier studies have shown that this relatively simple critical state model

embedded in standard elasto-plastic framework is able to perform satisfactorily for stress path tests and undrained tests on several natural soft Finnish clays (Koskinen et al. 2002a, Karstunen & Koskinen 2004a, 2004b). S-CLAY1S accounts for the initial and plastic strain induced anisotropy with an inclined yield surface, and the additional strength given by any apparent bonding. The effect of the latter is modelled via a so-called intrinsic yield curve, a concept originally proposed by Gens and Nova (1993). In the following, the behaviour of Murro test embankment was simulated with the S-CLAY1S model using the commercial finite element code PLAXIS Version 8 (Brinkgreve 2002), in which the S-CLAY1S model had been implemented in as a user-defined model (Wiltafsky 2003).

2 GEOMETRY AND INPUT DATA

The Murro test embankment is 30 m long, 10 m wide and 2 m high. The inclination of the slopes is 1:2. Based on the site investigations, symmetry of the embankment could be assumed in calculations. The ground water table is at the depth of 0.8 m. The construction was completed in two days.

The embankment was modelled with the linear elastic-perfectly plastic Mohr Coulomb model using the following values for the embankment material: Young's modulus $E = 40000 \text{ kN/m}^2$, Poisson's ratio $\nu' = 0.35$, friction angle $\phi' = 40^\circ$, dilatancy angle $\psi' = 0^\circ$, cohesion $c' = 2 \text{ kN/m}^2$ and unit weight $\gamma = 19.6 \text{ kN/m}^3$, which are typical values for crushed biotite gneiss. The simulations were not found to be sensitive to these values, as the behaviour is dominated by the underlying soft clay. The values for soil constant and state variables in the clay layers differ from the earlier calculations by Karstunen et al. (2005), as at that time very little laboratory data was available on e.g. the intrinsic properties.

The subsoil was divided into eight layers, for which the values chosen are shown in Tables 1–3. The values assumed for parameters describing initial state are shown in Table 1, where e_0 is initial void ratio, K_0 the lateral earth pressure at rest, α_0 the initial inclination of yield curve and x_0 the initial amount of bonding. On the top there is a 1.6 m thick overconsolidated dry crust layer. Below the dry crust there are seven very soft, nearly normally consolidated, layers. In order to model the overconsolidation profile of the deposit as accurately as possible, the overconsolidation in the dry crust was defined using overconsolidation ratio (OCR) and in the layers below by using pre-overburden pressure (POP), defined as the difference between the vertical preconsolidation stress and the in situ vertical effective stress. Just like for the "standard" models in PLAXIS, the user is allowed to use either one (OCR or POP) with the S-CLAY1S user-defined model. The

Table 1a. Layers and initial state for Murro clay.

Layer	Depth m	γ kN/m ³	e_0	x_0
1	0.0–1.6	16.12	1.522	2.7
2	1.6–3.0	15.47	1.893	6.5
3	3.0–6.7	14.47	2.425	6.3
4	6.7–10.0	15.07	2.081	6.3
5	10.0–15.0	15.66	1.784	4.5
6	15.0–18.0	15.93	1.584	3.1
7	18.0–21.5	16.24	1.627	11.7
8	21.5–23.0	17.29	1.204	4.5

Table 1b. Initial state for Murro clay.

Layer	OCR	POP kPa	K_0	α_0
1	7.2	–	1.25	0.69
2	–	13	0.37	0.63
3	–	4	0.34	0.69
4	–	3	0.34	0.69
5	–	7	0.37	0.63
6	–	2	0.43	0.54
7	–	1	0.43	0.54
8	–	3	0.43	0.54

Table 2. Conventional soil constants for Murro clay.

Layer	λ_i	κ	M	ν'	k_y 10 ⁻⁴ m/day	k_x 10 ⁻⁴ m/day	c_k
1	0.18	0.023	1.7	0.15	155	201	0.25
2	0.18	0.028	1.6	0.15	4.87	6.33	0.87
3	0.25	0.041	1.7	0.15	3.88	5.18	1.06
4	0.21	0.039	1.7	0.15	2.50	3.25	0.89
5	0.22	0.030	1.6	0.15	3.03	3.95	0.64
6	0.16	0.027	1.4	0.15	2.64	3.43	0.47
7	0.17	0.028	1.4	0.15	5.12	6.66	0.74
8	0.11	0.012	1.4	0.15	2.37	3.08	0.09

Table 3. Values of the additional parameters for S-CLAY1S.

Layer	μ	β	a	b
1	61	1.00	10	0.2
2	47	1.02	10	0.2
3	28	1.00	10	0.2
4	32	1.00	10	0.2
5	43	1.02	10	0.2
6	55	0.95	10	0.2
7	47	0.95	10	0.2
8	283	0.95	10	0.2

in situ K_0 values, listed in Table 1, were determined for the almost normally consolidated layers (layers 2–8) based on Jaky's simplified formula, whereas the K_0 value for the overconsolidated dry crust (layer 1) was

determined based on the equation proposed by Mayne & Kulhawy (1982):

$$K_0^{OC} = (1 - \sin \phi') \cdot OCR^{\sin \phi'} \quad (1)$$

The values for the standard soil constants in Table 2 (where κ is the slope of swelling line and M the slope of critical state line) were determined in a conventional manner from triaxial and oedometer tests on natural samples on each layer. The value of ν' was taken as 0.15 which is typical value for clay type of soils. The values for λ_i were determined from tests on reconstituted samples.

The values for permeabilities (k_x , k_y) and c_k , the change of permeability (a parameter used for all soil models in PLAXIS, see Brinkgreve 2002) were determined using Constant Rate of Strain oedometer tests and compression permeometer tests. The ratio 1.3 between horizontal and vertical permeability for all layers was obtained based on permeabilities measured on some horizontal samples from layers 2, 3 and 4.

The values for the initial state and additional parameters needed for S-CLAY1S, shown in Tables 1 and 3 (α_0 , x_0 , μ , β , a and b), were determined in a manner described by Wheeler et al. (2003) and Koskinen et al. (2002a). Parameter μ controls the rate at which the yield curve tends towards the stress ratio dependent target value and parameter β controls the relative effectiveness of plastic volumetric and shear strains in the process. Parameter a controls the absolute rate at which the amount of bonding is degrading and parameter b controls the relative effectiveness of plastic volumetric and deviatoric strains in the destructuration process. Experimental data for determining those was only available for layers 3 and 4. The values a = 10 and b = 0.2 were used for all the layers (Karstunen & Koskinen 2004a) and are similar to the values found for some other Finnish clays (Koskinen et al. 2002a). Parametric studies should be conducted in order to see how sensitive the predictions are to changes in a and b values. None of the parameters have been optimised in any way and the numbers in Tables 1–3 represent values that one would derive based on well-defined standard procedures.

In generating the mesh, 15-noded triangular elements were used. The mesh was refined below the embankment and the final analyses were done with a mesh containing 17495 nodes and 2159 elements. The boundary conditions for consolidation were assumed to be open at the ground surface and at the bottom of the mesh. In terms of displacement, the lateral boundaries were fixed in horizontal direction and the bottom boundary was fixed in both vertical and horizontal directions. In order to ensure the accuracy of the results, the sub-stepping at the user-defined subroutine was controlled by giving parameter StepSize values of –0.1,

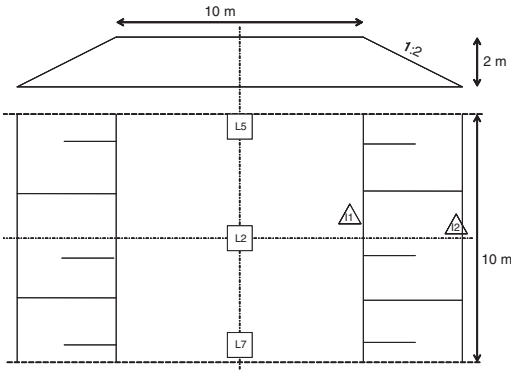


Figure 3. Layout of some of the instrumentation on Murro test embankment.

as suggested by Wiltafsky (2003). The value limits the maximum size of the strain increment during each sub-iteration. The simulations were done as large strain analyses.

3 RESULTS OF THE CALCULATIONS

In this paper, the main focus is on settlements, horizontal displacements and the effect of destructuration. Three settlement plates were installed underneath the centre line of the embankment, as shown in Figure 3. Plate L2 is situated underneath the centre of the embankment and L5 and L7 both are along the central axis, 5 m on either side of L2, as shown. The inclinometers are located on the crest of the embankment (I1) and on the toe of the embankment (I2), also shown in Figure 3.

The predicted settlement with time under the centre-line of the embankment is shown in Figure 4. The results from settlement plates L2, L5 and L7 are also shown. Interestingly, the highest value of settlement was not measured at the centre point of the embankment but 5 m away from the centre in settlement plate L7, which suggests that the subsoil is perhaps not as homogenous as assumed. However, the differences in the settlements measured in the three points are of the order of 8 cm, which is about 10%.

The settlement predicted by the S-CLAY1S model is in a good agreement with the observations. However, the calculated time-settlement curve suggests that the settlements are slightly slowing down, whereas the observed settlements in all three points suggests that the embankment keeps on settling with a constant rate so far (Fig. 4). This could be due to creep effects, which are not accounted for in the analysis. Nonetheless, both the calculated and observed time-settlement curves suggest that the primary consolidation is still continuing.

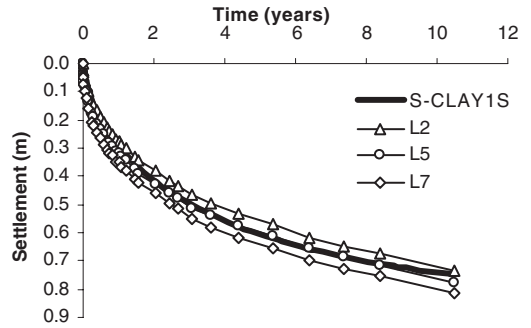


Figure 4. Observed settlements and settlements calculated with S-CLAY1S in linear time scale.

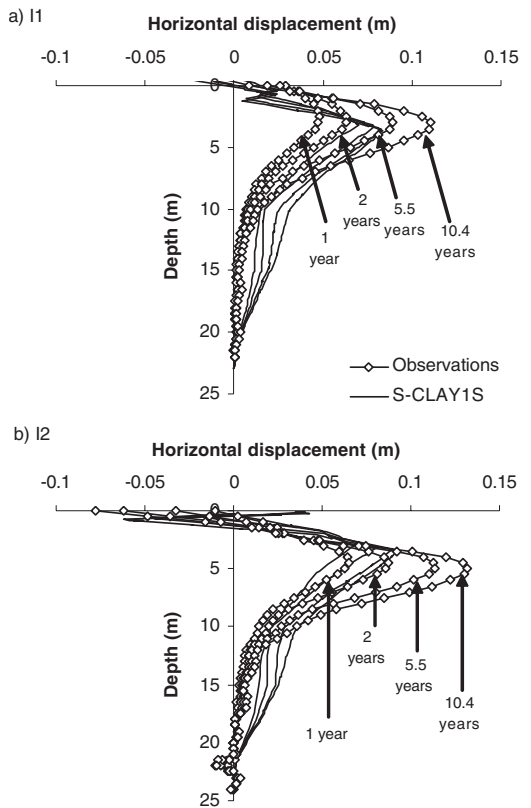


Figure 5. Horizontal displacements of Murro test embankment a) on the crest and b) on the toe of the embankment.

The predicted settlement after ten years of consolidation is 74.5 cm, whereas the maximum settlement measured after ten years of consolidation with plate L7 is 81.6 cm.

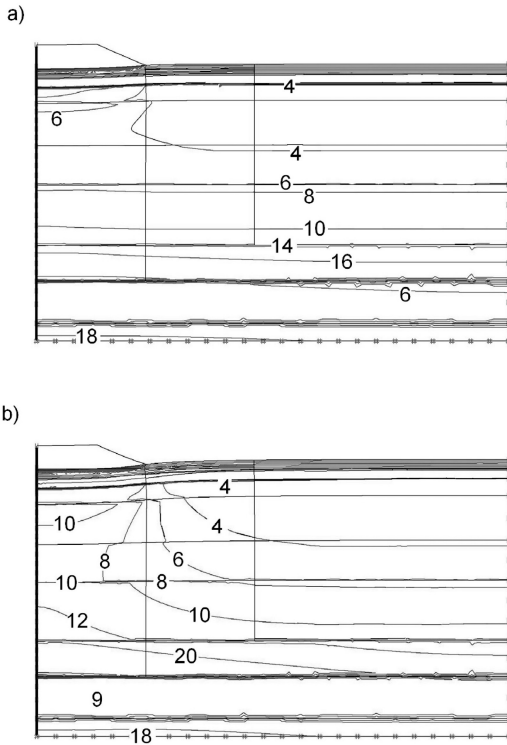


Figure 6. Contours of parameter p'_{mi} (kPa) calculated with program PLAXIS using the S-CLAY1S model for Murro clay a) one year and b) 10.4 years after construction of the test embankment.

Figure 5 shows the horizontal displacements at different times after construction underneath the crest (Fig. 5a) and the toe (Fig. 5b) of Murro test embankment. Underneath the crest of the embankment the magnitude of the maximum horizontal displacement is slightly underestimated but the depth of the maximum horizontal displacements is reasonably well predicted with S-CLAY1S at ten years after construction (Fig. 6a). However, the development of the displacements with time is predicted rather poorly. According to the predictions, the horizontal displacements develop very rapidly after construction. In contrast, the observed horizontal displacements develop overall at much slower rate, but the rate is increasing with time. These differences could again be partially due to time effects. Furthermore, below the depth of 7.5 m, the predicted horizontal displacements are notably in excess of the observed ones.

The horizontal displacements under the toe of the embankment ten years after construction are slightly underestimated with S-CLAY1S (Fig. 5b). Also, the depth of the maximum horizontal displacement is

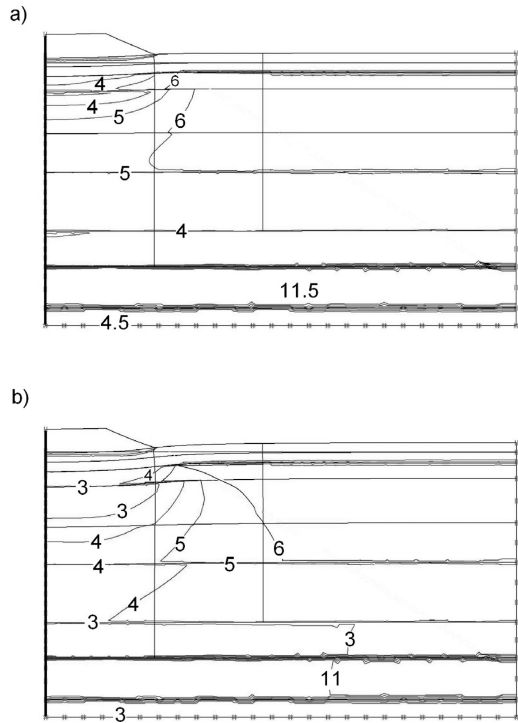


Figure 7. Contours of parameter x calculated with program PLAXIS using the S-CLAY1S model for Murro clay: a) one year and b) 10.4 years after construction of the test embankment.

slightly underestimated. A further interesting point in Figure 5b is that the soil immediately underneath the toe is moving towards the centreline. This is reproduced by the prediction. The rate of the horizontal displacements is predicted more realistically than under the crest of the embankment. Below the depth of 7.5 m the predicted horizontal displacements are again larger than the observed ones.

Destruction process can be studied by inspecting evolution of state variables p'_{mi} (size of the intrinsic yield surface), x and p'_m (size of the natural yield surface) in time. In Figure 6, contour plots of p'_{mi} are shown at 1 year and 10.4 years after construction. It can be seen that the value of p'_{mi} increases in time throughout the soil profile. This would suggest a systematic increase in the remoulded undrained shear strength, in agreement with Figure 1b.

Figure 7 presents the evolution of parameter x . A notable amount of destruction is predicted, e.g. in layers 2, 3 and 4 the initial value of x_0 was 6.3...6.5, but already after one year the value has decreased to 4...5 underneath the embankment, and after ten years the value of x has dropped to approximately 3 underneath

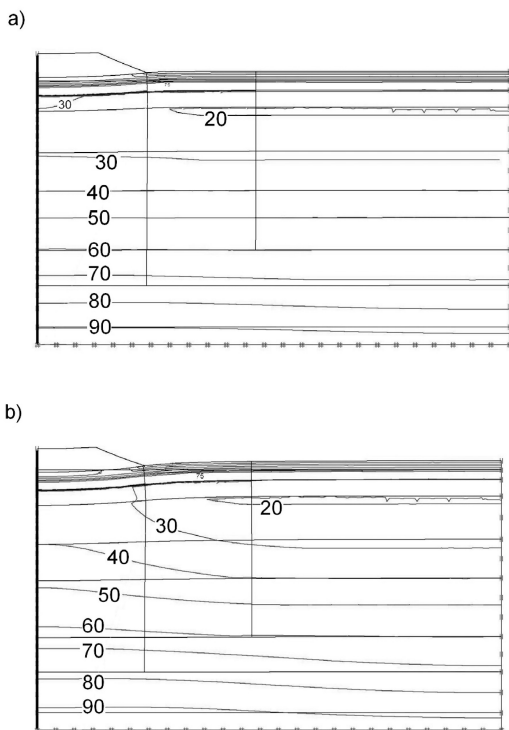


Figure 8. Contours of parameter p'_m (kPa) calculated with program PLAXIS using the S-CLAY1S model for Murro clay: a) one year and b) 10.4 years after construction of the test embankment.

the embankment. In parallel, the contour line representing $x = 6$ has moved outwards from the centreline of the embankment.

Figure 8 shows the prediction of the size of the natural yield curve p'_m at 1 year and 10.4 years after construction. The size of the natural yield curve p'_m (and hence the undrained shear strength) seems to increase slightly with time in the subsoil, which is in contrast to what was observed in field vane tests. The predicted values of undrained shear strength depend on the values assumed for constants a and b .

4 CONCLUSIONS

The settlements and horizontal displacements of Murro test embankment in Seinäjoki, Finland were calculated with a recently proposed elasto-plastic model S-CLAY1S that accounts for plastic anisotropy and destructuration, using the finite element code PLAXIS. The parameters for the calculations were derived using the extensive laboratory data collected

from the soil profile, and were not optimised in any way.

Observations of settlements, horizontal displacements and pore pressures have been collected now for more than ten years at Murro test embankment. Field vane tests were carried out prior to construction and through the test embankment eight years after construction. When the results were compared, it was noticed that the undrained shear strength had in fact decreased during consolidation in part of the subsoil underneath the embankment. This is in contrast to what is commonly assumed in geotechnical design. In parallel, the remoulded undrained strength had increased for the whole profile. These phenomena might be explained with destructuration.

The settlements calculated with S-CLAY1S were in very good agreement with the observed ones. The horizontal displacements were reasonably well predicted, apart from the development of the magnitude of displacements with time. This issue need to be investigated further.

Additionally, destructuration was studied underneath the embankment roughly by examining calculated contour plots of size of the intrinsic yield curve p'_{mi} , amount of bonding x and size of the yield curve p'_m for natural soil at different times. However, the observed decrease in the undrained shear strength could not be modelled, which could be due to use of the same values in all layers for parameters a and b controlling rate of destructuration.

In addition to further parametric studies concerning the parameters a and b , the future work will include studying the time effects with an objective to incorporate the effect of creep within the S-CLAY1S model.

ACKNOWLEDGEMENTS

This work was carried out as a part of projects funded by the Academy of Finland (Grants 53936 and 210744). The experimental programme was funded by the Finnish Road Administration. The work presented was carried out as part of a Marie Curie Research Training Network "Advanced Modelling of Ground Improvement on Soft Soils (AMGISS)" (Contract No MRTN-CT-2004-512120) supported the European Community through the program "Human Resources and Mobility".

REFERENCES

- Brinkgreve, R.B.J. 2002. PLAXIS – Finite element code for soil and rock analyses. Users manual. Lisse: Balkema.
- Gens, A., Nova, R. 1993. Conceptual bases for a constitutive model for bonded soils and weak rocks. Proc. Int. Symp. of Hard Soils – Soft Rocks, Athens: 485–494.
- Karstunen, M., Krenn, H., Wheeler, S.J., Koskinen, M. & Zentar, R. 2005. The effect of anisotropy and destructuration

- on the behaviour of Murro test embankment. *ASCE Int. J. of Geomechanics* 5, No. 2, 87–97.
- Karstunen, M. & Koskinen, M. 2004a. Anisotropy and destructuration of Murro clay. In Jardine, R.J. et al. (eds.) *Advances in geotechnical engineering – The Skempton Conference: Vol. 1*, 476–487. London: Thomas Telford.
- Karstunen, M. & Koskinen, M. 2004b. Undrained shearing of soft structured natural clays. In *Proc. of IX International Symposium on Numerical Models in Geomechanics (NUMOG IX)*, 25–27 August, Ottawa, Canada: 173–179. Leiden: Balkema.
- Koskinen, M. & Karstunen, M. 2004. The effect of structure on the compressibility of Finnish clays. *SGF Report 3:2004, Proc. of XIV Nordic Geotechnical Meeting*, 19–21 May 2004, Ystad, Sweden. Vol. 1, A-11–A-22 Linköping: Swedish Geotechnical Society.
- Koskinen, M., Karstunen, M., Wheeler, S.J., 2002a. Modelling destructuration and anisotropy of a natural soft clay. *Proc. of 5th European Conference on Numerical Methods on Geotechnical Engineering (NUMGE02)*, 4–6 September, Paris, France, pp. 11–20. Paris: Presses de l'ENPC/LCPC.
- Koskinen, M., Vepsäläinen, P., Lojander, M., 2002b. Modelling of anisotropic behaviour of clays. *Test embankment in Murro, Seinäjoki, Finland*. Finnish Road Administration, Finnra reports 16/2002, 62 + 5 p.
- Mayne, P.W., Kulhawy, F.H., 1982. K_0 -OCR relationship in soil. *Journal of Geotechnical Engineering* 18(GT6), 851–872.
- Wheeler, S.J., Nääätänen, A., Karstunen, M., Lojander, M., 2003. An anisotropic elasto-plastic model for soft clays. *Canadian Geotechnical Journal* 40(2), 403–418.
- Wiltafsky, C., 2003. *S-CLAY1S, User Defined Soil Model for Plaxis – Documentation*. University of Glasgow.

Numerical design, installation and monitoring of a load transfer platform (LTP) for a railway embankment near Rotterdam

A.E.C. van der Stoel

CRUX Engineering BV, Amsterdam, The Netherlands & Royal Military Academy, Breda, The Netherlands

J.M. Klaver & A.T. Balder

CRUX Engineering BV, Amsterdam, The Netherlands

A.P. de Lange

Voorbij Funderingstechniek BV, Amsterdam, The Netherlands

ABSTRACT: To connect the city of Rotterdam (the Netherlands) to the city of Barendrecht by means of a new Lightrail, a bridge approach to cross a highway had to be built on extremely soft ground. To minimise the expected settlement and to reduce construction time an innovative foundation with High-Speed-Piles (HSP) and a geosynthetic reinforced mattress was designed and built (piled embankment). The design was performed using both British Standard BS8006 and PLAXIS 2D and 3D numerical simulations. A monitoring program was set up to measure the pile forces and the forces in the geogrid. This paper deals with some specific aspects of the (numerical) design and draws conclusions on the validity of the design methods. Results show that grid forces are generally lower when calculated with the FEM compared to BS8006 when relatively high embankments are considered. Monitoring results showed that the load carrying system was activated at small geogrid strains, leading to extremely small deformations and high durability. Due to the maximum embankment height of 8.7 m no traffic loads were measured in the geogrids. This, in combination with the conservative BS8006 design, lead to an extremely high safety factor when comparing calculated and measured forces.

1 INTRODUCTION

To connect the suburb Carnisselande – Barendrecht to the city of Rotterdam the Lightrail “Carnisselandelijn” was constructed. To cross the highway A15 (Nijmegen-Rotterdam) and the parallel freight railway (Betuwe-line) an 8.7 m high and 350 m long curved embankment had to be built, see figure 1.

The subsoil mainly consists of clay and peat deposits embedded with sand layers of varying thickness and strength. The total depth of poor soil layers varies from 14 to 17 m. A sketch of the subsoil conditions is shown in figure 2.

Consolidation by means of preloading combined with sand and vertical drainage would have been an adequate solution. However, a number of conditions made it necessary to develop a new foundation system that met the following requirements:

- The need to reach the load bearing sand layer (Pleistocene), 17 meters below existing grade,
- Preventing seepage of silt water from the subsoil,
- High groundwater table should not be disturbed,

- Construction passes through a nature reserve, the embankment base had to be limited,
- Initiation of Lightrail service as soon as possible.

2 DESIGN CONCEPT

2.1 Geogrid mattress on piles

Due to partially lower bearing capacity of the soil, the chosen foundation system had to be opted for these



Figure 1. Overview.

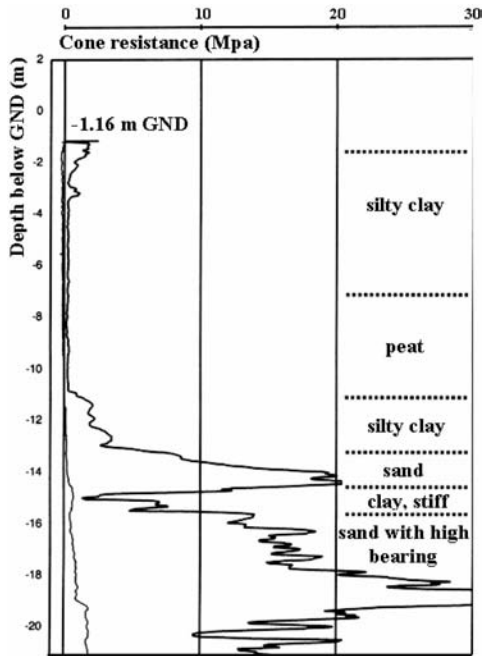


Figure 2. Typical CPT result on construction site.

subsoil conditions, as it is economically not viable to explore every weakness in the changing subsoil. To minimise installation and maintenance cost, a foundation system was designed consisting of Voton® High Speed Piles (HSP piles) with a maximum design load of 250 kN overlain by a geogrid reinforced mattress. 9,200 HSP piles with a diameter of 180 mm and 135 piles with a diameter of 273 mm (installed in a section with lower cone resistance) and an average length of 15.8 m were installed in a square grid of 0.8–1.6 m. The pile cap was enlarged with reinforced concrete to 0.3–0.5 m. To transfer the load from the embankment into the piles, two or three layers of geogrid with a short term strength of 40–180 kN/m where laid with vertical spacing of 0.3 m transverse to the dam axis. Gravel was used as stone aggregate between the geogrids. The embankment was constructed with sand. Figure 3 shows the concept of the settlement free embankment with HSP pile system.

An advantage of the pile system is the control of and adaptability to the soil conditions during installation. Pile length can immediately be adjusted on the spot whenever insufficient bearing capacity is encountered during installation. For the same purpose pile diameter can be adapted quite easily.

2.2 Design approaches

Design of the geogrids was based on specific project requirements in accordance with Rotterdam Municipal

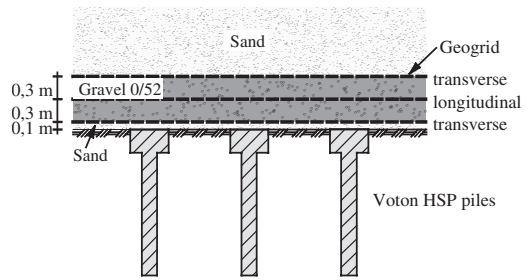


Figure 3. Constructed foundation system with geogrid mattress overlying HSP piles.

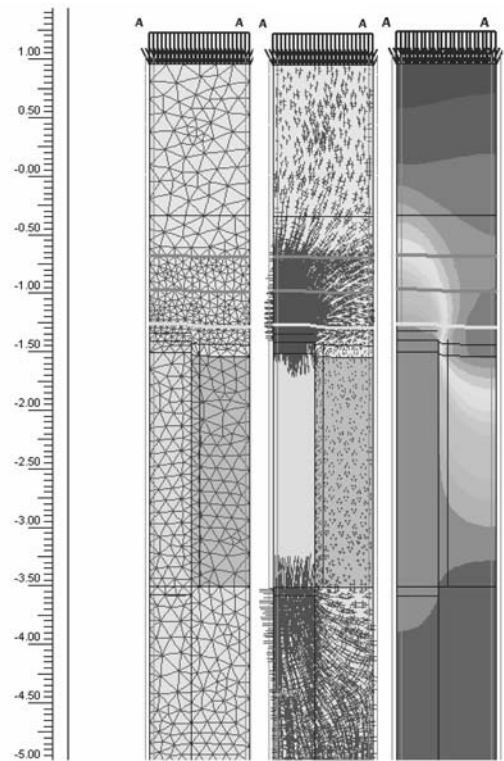


Figure 4. PLAXIS 3D axial-symmetric pile – mattress model (l > r: mesh, arching stresses and displacement pattern).

Works Department based on BS 8006 (1995) and numerical calculations (finite elements) using the PLAXIS software. A series of calculations have been made beforehand comparing different design approaches, being British Standard 8006, Terzaghi, Terzaghi & Heijnen, Bush-Jenner and Hewlett & Randolph. For the PLAXIS model a 3D axial symmetric (Figure 4) and a 2D plane strane (Figure 5) model were used to respectively calculate the surcharge load and lateral sliding load.

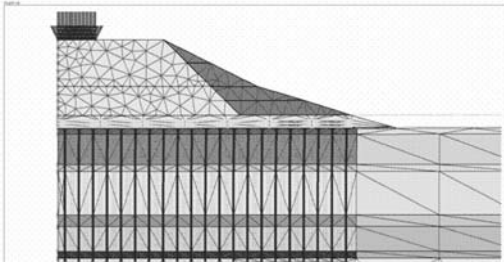


Figure 5. Principle of PLAXIS 2D plane strain pile – mattress mesh/model.

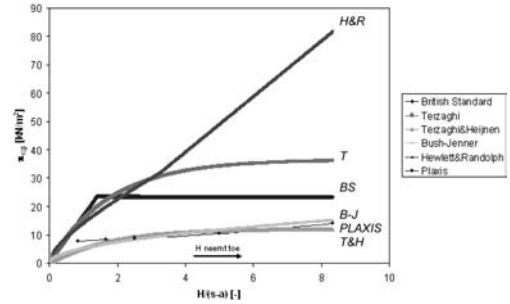


Figure 7. Vertical stress on subsoil for different design approaches.

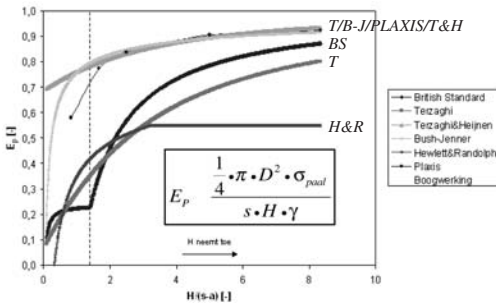


Figure 6. Pile efficiency (E_p) for different design Approaches.

Parameters used for the calculations were: $\gamma = 17.0[\text{kN/m}^3]$, $\phi = 35[^\circ]$, $c' = 17[\text{kN/m}^2]$ (Terzaghi & Heijnen), $K_n = 1.0[-]$ (Terzaghi en Terzaghi & Heijnen) and for the geometry different s and a values were used; here presented are $s = 1.6[\text{m}]$ and $a = 0.4[\text{m}]$. For the geogrids a stiffness of $2,000 \text{ kN/m}$ was used. To reduce the length of the paper, BS8006 symbols are use for forces, etc.

2.3 Applicability of models

Based on the calculations, graphs were created to show Pile efficiency (Figure 6), vertical stress on the subsoil (Figure 7), reinforcement loads T_{rp} and T_{ds} (Figure 8) and the summation of T_{rp} and T_{ds} (total tensile load on reinforcement; Figure 9) are shown as a function of the ‘standardised embankment height’ $H/(s-a)$.

From the figures 6 and 7 the following conclusions can be drawn:

- the results of the different analytical methods show a large scatter, especially with relatively small embankment heights;
- when $H/(s-a) > 5$ the differences diminish, except for the results of Hewlett & Randolph;
- the Bush-Jenner method and the PLAXIS calculations show similar results, i.e. the proposed Bush-Jenner mechanism shows large similarities with FEM;

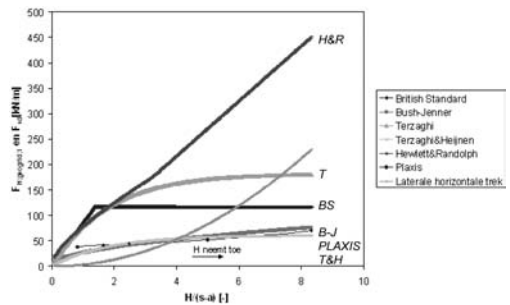


Figure 8. Reinforcement loads T_{rp} (vertical tensile load) and T_{ds} (tensile load needed to resist lateral thrust of embankment fill).

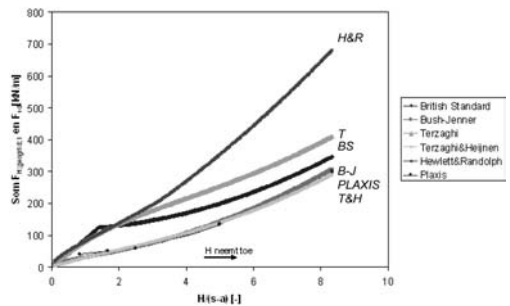


Figure 9. $T_{rp} + T_{dp}$ (summation vertical tensile load in the reinforcement).

- based on Bush-Jenner, British Standard and PLAXIS the effect of arching starts at $H/(s-a) \approx 1.4$.

From the figures 8 and 9 the following conclusions can be drawn:

- the results of the different analytical methods show a similar large scatter as with pile efficiency, especially with relatively small embankment heights;

Table 1. Comparison of calculation results (kN/m).

		PLAXIS	BS8006
Forces by	Longitudinal	25	90
Membrane effect	Transverse	25	90
Additional	Longitudinal	145	230
horizontal force			
Maximum total		170	320
force			

- the tensile load needed to resist lateral thrust of embankment fill T_{ds} , for relatively large embankment heights has a large influence on the total forces;
- the Bush-Jenner, Terzaghi & Heijnen en PLAXIS approach show the lowest tensile forces.

Based on the above calculations, the conclusion could be drawn that the Bush-Jenner method and PLAXIS show similar results. BS8006 tends to overestimate the tensile forces compared to these methods. Because of the relative large influence of the tensile load needed to resist lateral thrust of embankment fill with high embankments, this difference however decreases with an increase of the embankment height.

2.4 Design of Barendrecht project

For the Barendrecht project, for several reasons (a.o. not much experience with LTP, very heterogeneous soil, large embankment heights) a combination of BS8006 and PLAXIS calculations was chosen for the design approach.

As can be seen from table 1, different geogrid strengths were required, based on the calculation procedure. To optimise the design three geogrid layers with a tensile strength of 180 kN/m where chosen at the maximum embankment height 8.7 m. By reducing the allowable strain to 5%, the allowable installed long term strength is 107 kN/m in transverse and 69 kN/m in longitudinal direction.

BS8006 and PLAXIS results differ significantly, especially considering the relative large height of the embankment. Although it was expected that BS8006 overestimated the forces considerably, for safety reasons BS8006 design was executed. By means of a monitoring program the design results were verified.

3 GEOTECHNICAL MONITORING PROGRAM

3.1 Introduction to the program

An extensive monitoring program was installed to ensure that the actual geogrid forces would not exceed the calculated forces, the construction would suffer only the required limited deformation and to validate the design methods. This program provided

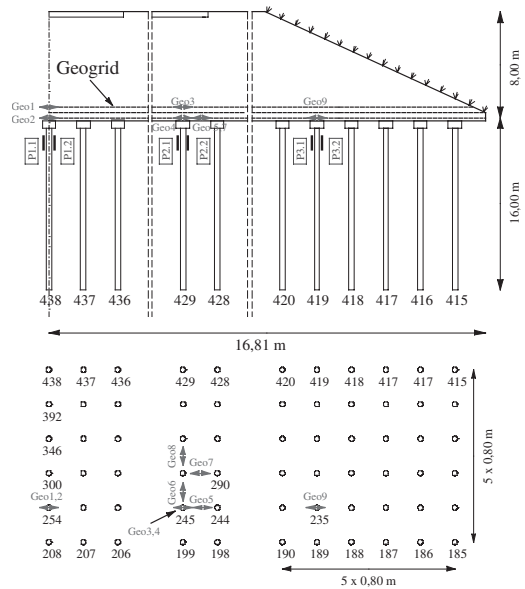


Figure 10. Installed monitoring section.

information about the load transfer and deformation characteristics and consisted of:

- settlement plates;
- inclinometers;
- pore water pressure meters;
- geogrid strain gauges;
- pile strain gauges.

Inclinometers and pore water pressure meters were mainly installed to monitor the installation phase of the HSP piles (soil displacing system). Settlement plates were used to verify the project requirements and the general process. The measured settlements were extremely small, showing the high resistance and small deformation characteristics of the construction. Almost no settlement was measured after construction of the embankment, thus showing that the load transfer concept with geosynthetics overlying the HSP piles is successful in reducing deformations. Special observation of the geogrid strains and forces that were transferred into the pile was necessary, because in design phase lower forces than the required geogrid forces were chosen.

3.2 Installation of geogrid and pile strain gauges

In one measurement section three piles with each two strain gauges were installed using vibrating wire strain gauges to measure axial forces as well as bending moments transverse the embankment axis, see figure 10. Due to the high heterogeneity of the soil, a section with limited subsoil bearing capacity and high

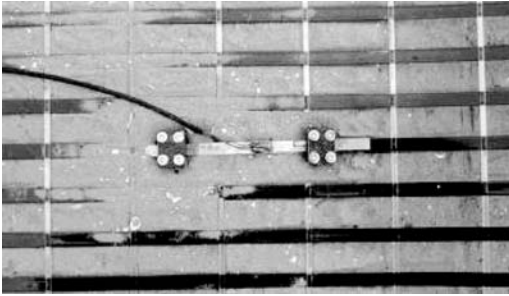


Figure 11. Installed geogrid measurement device.

static load (embankment height) was chosen. Forces in the geogrids were measured on nine locations at different levels as indicated in figure 10. Strain gages in geogrids were installed on top of the pile caps as well as in between the piles in longitudinal and transverse direction. Information about the existing strains as well as strain development during embankment construction is required to be able to give information about the load transfer in the compound system. Due to the construction of HSP piles, strain gauges have been connected to the reinforcement cage before installation. The reinforcement was pushed into the fresh concrete afterwards.

Attaching of strain gages directly to the surface of the geogrid is difficult. Additionally the rheological behaviour of geosynthetics is leading to a difficult interpretation of geogrid strains and forces, as strain increases under constant loading. It is possible to calculate the existing forces in the geogrid from the geosynthetic isochrones when only small strains are recorded (Fannin, 1991). To ensure that the monitoring results indicate the existing forces, 0.1 mm thick steel strips to which the strain gauges were attached, were used to measure the forces in the geogrids (Bussert et al., 2004), see figure 11.

The stiffness of the steel strip assured stress-strain behaviour similar to that of the geogrids, thus minimizing the effect of disturbance for the global geogrid stress-strain behaviour. The connection between the geogrid and the measurement device was made by steel blocks and additional gluing; long term stability was proven successfully prior to installation.

3.3 Discussion of measurement results

As high quality data was necessary to proof the load deformation and the load transfer characteristics in the structure, measurement started immediately after installation of the monitoring devices. Installation of the piles in the monitored section started in May '04, followed by construction of the geogrid mattress. The construction in the monitored section was completed in June 2004. Figure 12 indicates the measured pile forces.

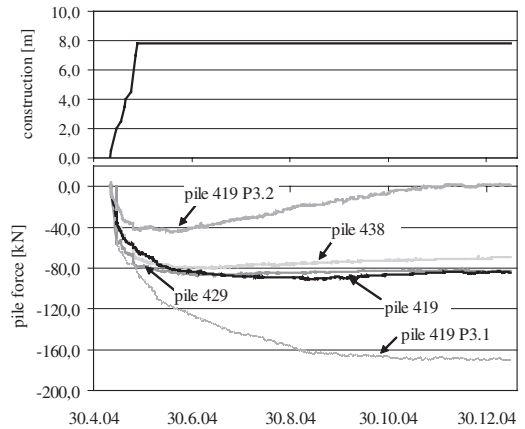


Figure 12. Calculated pile forces.

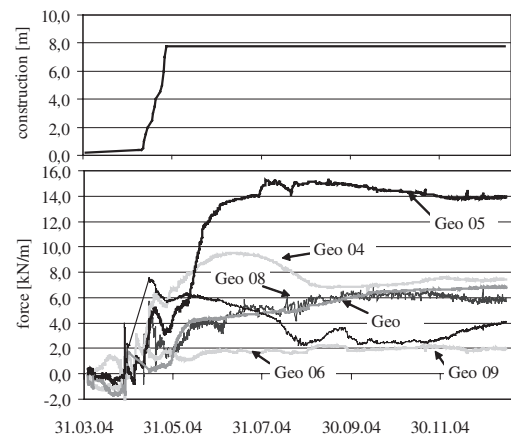


Figure 13. Geogrid forces calculated from measured strains.

With increasing embankment height the measured strains indicate increasing pile forces. Pile 438 and 429 do not show any effect of bending and are loaded axially. At the end of the construction phase, the pile load is equal to the overburden pressure by taking the contributing area into account. The average pile force of Pile 419 is nearly equal to the others; the difference between both strain gauges indicate pile bending, taking place during several months. Towards the end of 2004 bending nearly stopped, showing the behaviour of the construction at rest. Bending of the pile might be caused by the installation process or horizontal forces from the embankment slope (Bussert et al., 2004a).

As usual, determination of geogrid forces is a little bit more complex, leading to more deviations in the measured values. After compaction of the soil layer overlying the geogrids, nearly similar geogrid forces are measured, independent of the geogrid location, see figure 13.

After completion of the embankment, geogrid strains are increasing as the subsoil between the piles consolidates. Due to consolidation the membrane effect of the geogrids is activated and forces, which are not directly transferred by arching towards the pile caps into the piles, are transferred via the geogrids in the piles. The activated increase in pile forces is due to the low vertical loading of the geogrids (75% of the embankment load is directly transferred into the pile), is very small and takes place during a longer period of time. The mean values of tension forces in the three geosynthetic layers can be calculated from the measurement results and are equal to 28.7 kN/m and 33.2 kN/m longitudinal and transverse the embankment axis. The relative large influence of the tensile load needed to resist lateral thrust of embankment fill which was predicted, is oddly enough not measured at all.

The measured geogrid forces are slightly higher than the calculated forces with PLAXIS for the membrane effect and they are much smaller than the forces calculated by the totals of BS8006/PLAXIS. By measuring overall geogrid forces no distinction between membrane and horizontal forces can be made. Therefore only the difference between measured forces in longitudinal and transverse direction can be taken as additional horizontal forces.

No increase in strain was measured due to traffic loading. Therefore it seems that a specific embankment height exists, for which traffic load does not need to be taken into account in the geogrid design. For economical reason this should be examined more thoroughly in future research.

From the measurements it can be deduced, that pile forces are similar to the theoretical pile force distribution. Additional and more extensive measurements are necessary to fully comprehend the load transfer mechanism in the geogrids.

4 EXPECTED LONG TERM BEHAVIOUR

Maximum measured strain in a single geogrid layer was found to be 0.45%, from which a geogrid force of 15.1 kN/m could be calculated. The expected increase in strain in 120 years using the isochrones would lead to an overall strain of 0.67%. The expected strain increase of 0.22% is significantly lower than the allowed increase of 5% after completion of the construction. The difference is mainly due to the limited utilisation of the geogrids. Under the measured loads, only small creep occurs. It is proposed to determine a safety factor for geogrid creep, under smaller strains actually used.

5 CONCLUSION

With the constructed foundation system of HSP piles overlain by a geogrid mattress a fast, economical and



Figure 14. Embankment after completion of the construction.

limited settlement construction was achieved. Based on the predictions, the conclusion could be drawn that the Bush-Jenner method and PLAXIS show similar results. BS8006 tends to overestimate the tensile forces compared to these methods.

The installed measuring system indicates that the predicted pile loads and geogrid strains are (much) smaller than expected. The combination of geogrids with small vertical spacing seems to lead to a compound material with increased strength at lower strains. The relative large influence of the tensile load needed to resist lateral thrust of embankment fill which was predicted, is oddly enough not measured at all. The measured strains indicate that the executed design leads to a safe construction. Because of the large difference between measurements and predictions however an economical optimization is possible and desirable.

ACKNOWLEDGEMENTS

A special word of appreciation goes out to Florian Bussert of the Institute of Geotechnical Engineering and Mine Surveying, Clausthal University of Technology, Germany, for his contribution to the monitoring analysis.

REFERENCES

- Balder, A.T. & Stoel, A.E.C. van der, (2005) CRUX Engineering BV internal study/report on design optimisation of LTPs.
- BS8006 (1995): Code of Practice for Strengthened/Reinforced Soils and other Fills, British Standards Institution, London, 1995.
- Bussert, F., Meyer, N., de Lange, A., de Kant, M. (2004): "Messtechnische Überwachung eines Bahndammes auf einer geokunststoffbewehrten Tragschicht über HSP-Pfählen", IGB, TU Braunschweig, Heft Nr. 77.
- Bussert, F., Meyer, N., de Lange, A.P., van der Stoel, A.E.C. (2004a): Bemessung und Überwachung einer geokunststoffbewehrten Tragschicht auf HSP-Pfählen, Bautechnik, Vol. 81, No. 12, 12/ 2004.

- Empfehlung 6.9: Bewehrte Erdkörper auf punkt- oder linienförmigen Traggliedern, Entwurf Juli 2004, Kapitel 6.9 für die Empfehlungen für Bewehrungen aus Geokunststoffen (EBGEO).
- Fannin, R.J., Herman, S. (1991): "Creep Measurements on Polymeric Reinforcement", Geosynthetics '91, Atlanta, USA, www.voton-hsp.com
- Heijnen, W.J. (2001) "Notitie Terzaghi axiaal-symmetrisch" CUR C112.
- Hewlett, W.J. Randolph, M.F. and Aust, M.I.E. (1998) "Analysis of piled embankments" Ground Engineering, Vol. 21, No. 3, April 1988, pp. 12–18.
- Han, J. and Gabr, M.A. (2002) "Numerical Analysis of Geosynthetic-Reinforced and Pile-Supported Earth Platforms over Soft Soil" Journal of Geotechnical and Geoenvironmental Engineering, January 2002, pp. 44–53.
- Kempton, G. Russel, D. Pierpoint, N.D. and Jones, C.J.F.P. (1999) "Two- and Three-Dimensional Numerical Analysis of the Performance of Piled Embankments", pp. 1–7.
- Klaver, J.M. & Stoel, A.E.C. van der (2004) CRUX Engineering BV internal study/report on LTP design.
- Lawson, C. (2001) "Basal reinforced piled embankments with steep reinforced side slopes" Ten Cate Nicolon, Malaysia, Geotechnics.
- Lawson, C.R. "Serviceability limits for low-height reinforced piled embankments".
- Russell, D. and Pierpoint, N. (1997) "An assessment of design methods for piled embankments" Ground Engineering, pp. 39–44.
- Stoel, A.E.C. van der, De Lange, A.P., Bussert, F. & Meyer, N., Railway embankment on "high speed piles" – Design, installation and monitoring, Eighth International Conference on Geosynthetics, September 2006, Yokohama Japan.

Results of the settlement prediction exercise of an embankment founded on soil improved by stone columns

Ph. Mestat, J.P. Magnan

Laboratoire Central des Ponts et Chaussées (LCPC), Paris, France

A. Dhouib

GTM Construction – Vinci, Paris, France

ABSTRACT: A settlement prediction exercise has been organized by the LCPC during the International Symposium on Ground Improvement (ASEP-GI 2004, 9–10 september, Paris, France). Predictions refer to an embankment built on improved fine soils by means of stone columns. 17 predictions have been compared with the field measurements and the validity of calculations is discussed. This paper presents the final analysis and concludes this settlement prediction exercise.

1 INTRODUCTION

Although numerous experiences have already been gained on modelling the behaviour of embankments on soft ground, problems still arise designing embankments on improved soil. The existence of stone columns or improved areas complicates the design and leads to empirical approaches, tri-dimensional numerical modelling or homogenized media. For practical design, it is important to validate these approaches.

The Laboratoire Central des Ponts et Chaussées has organized an international competition to calculate the behaviour of an embankment built on improved fine soils by means of stone columns.

Improvement of the fine silty alluvial soils by stone columns is considered in order to limit the settlements of the embankment.

This exercise is not really a class A prediction because the measurements were obtained before the organization of the competition, but only the organizers knew the measurements. The embankment was built in 2003 and has been well instrumented. The calculation parameters have been given from the LCPC interpretation of the results of a geotechnical campaign: oedometer tests, triaxial tests, pressuremeter test, scissometer test. The characteristics of the stone columns were also given. Nevertheless, some parameters were not fixed: for example, the values of Young's modulus and the Poisson's ratio in the case of numerical computations by finite element method (FEM) or discrete element method (DEM). Each participant used FEM or DEM had to determine the values of these parameters.

Predictions were asked for the settlements with stone columns at different stages of the embankment construction: 40, 160 and 200 days. All calculation methods were allowed.

Before to present and to discuss the previsions, we describe the data of the exercise, the embankment test and the computation approaches used.

2 DATA OF THE EXERCISE

2.1 *Geometry and soil properties*

The geometry of the embankment is shown in [figure 1](#). The embankment is 9 m high at the end of the construction and the width at the top is 35 m. The fill material is gravel with a density of 20 kN/m³.

The embankment is lying on silty fine-grained soils with a depth of 5.5 m and under that there are sandy soils. The incompressible substratum is located at 9 m depth. The ground water table is 1 m under the surface.

The subsoil is divided in four geotechnical layers. The layers and geotechnical data are summarized in [figure 2](#).

The stages of construction are defined in [table 1](#).

2.2 *Characteristics of the stone columns*

The geometry and geotechnical characteristics of the columns are given in [figure 3](#). The mesh is triangular and the distance of axes is 2.15 m. The mechanical properties of the columns were also fixed.

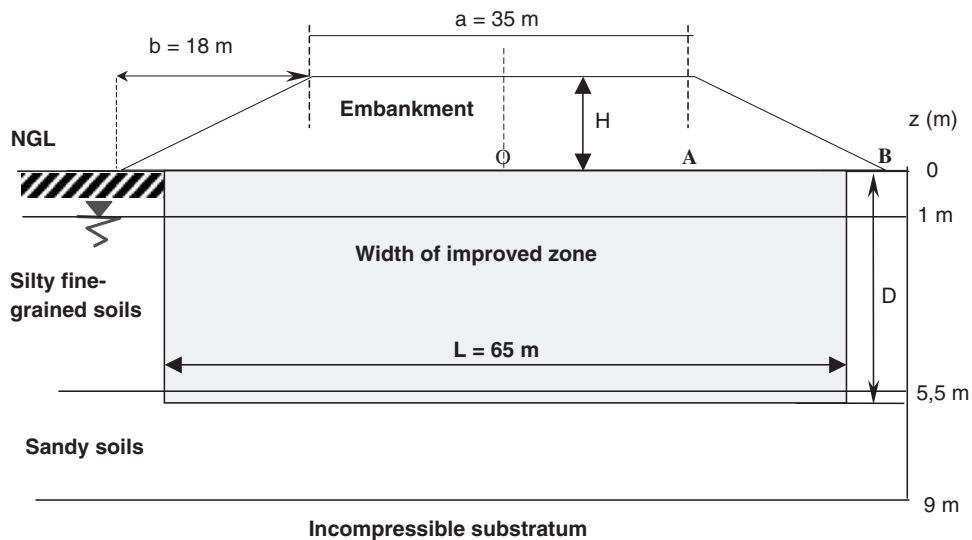


Figure 1. Cross section of the embankment in the improvement zone.

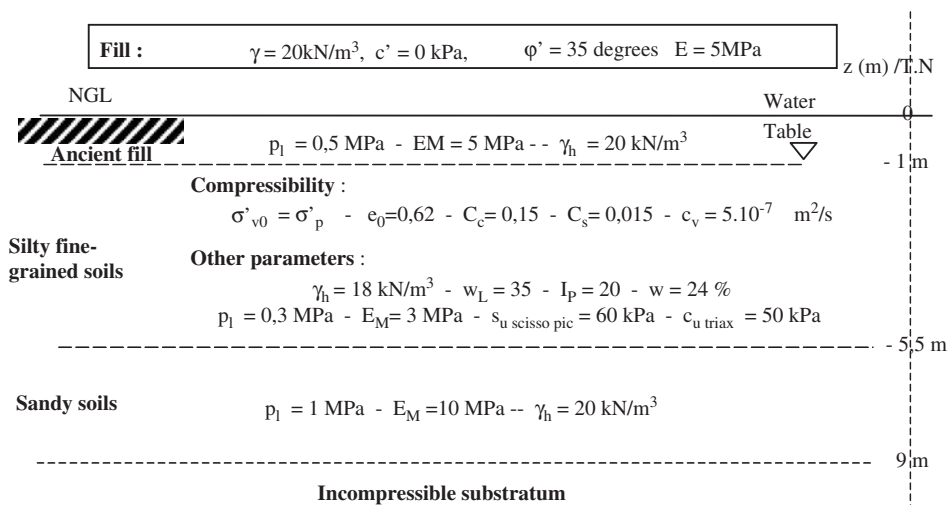
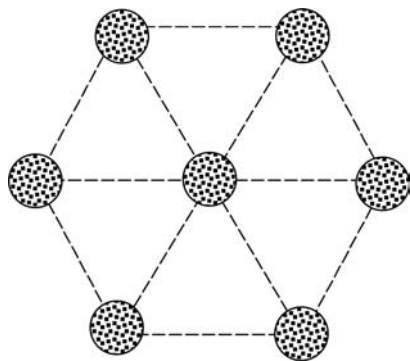


Figure 2. Geotechnical properties of the soils and fill material.

Table 1. Stages of construction.

Stage	Phase	H (m)	T (day)
0	Initial state	0	0
1	End of embankment construction (phase 1)	6	40
2	Beginning of embankment construction (phase 2)	6	160
3	End of embankment construction (phase 2)	9	200



Stone columns

Material : $\phi' = 38$ degrees ; $c'=0$ kPa
 $E_M = 30$ MPa - $E_{\text{plaque}} = 15$ MPa

Geometry : Length = 6m Diametre = 0,9m

Triangular mesh – Distance of axes = 2,15 m

Figure 3. Characteristics of the stone columns.

Table 2. List of participants.

Participants	N°	Calculation methods
Den Haan (The Netherlands)	1	FEM 2D (PLAXIS)
B. Klobe (Germany)	2	Priebe's method
CSTC (Belgium)	3	FEM 2D (PLAXIS)
J.-P. Rajot, N. Neyret (France)	4	FEM 2D (CS2P)
R. Goubet (France)	5	Priebe's method
F. Baguelein (France)	6a	Priebe's method
	6b	Combarieu-Baguelein's method
J. Wehr, I. Herle (Germany)	7	GRETA software
I. Herle, J. Wehr, S. Bazgan (Germany)	8	FEM 2D (PLAXIS)
R. Katzenbach, M. Itershagen (Germany)	9	FEM 2D (PLAXIS)
G. Bertaina (France)	10a	Priebe's method
	10b	Priebe's method and empirical corrections
E. Antoinet, B. Page (France)	11a,b,c	DEM (FLAC3D)
S. Bretelle (France)	12	FEM 2D (PLAXIS) and Priebe's method
O. Combarieu (France)	13	Combarieu's method
S. Burlon (France)	14a,b	Priebe's method
	14c	Non linear elastic behaviour
	14d	Method of slices
	14e	Alamgir et al.'s method
	14f	Homogenized method
	14g,h	FEM
M. Bouassida, Z. Guétif Fessi (Tunisia)	15a	Linear elasticity
	15b	Poroelastic model
	15c	Homogenized model
	15d	Balaam and Booker's method
	15e	Priebe's method
	15f	Chow's method
	15g	French rules DTU 13.2. (pressiometric data)
K. Pühringer, H.F. Schweiger, R. Thurner (Austria)	16	FEM 3D (PLAXIS)
D. Remaud, E. Bourgeois (France)	17	FEM 3D (CESAR-LCPC)

3 CALCULATION METHODS

17 participants have sent predictions to the organizing committee of the ASEP-GI symposium.

The calculation methods used were:

- finite element method;
- discrete element method;
- special methods proposed in the literature (Alamgir et al., Balaam and Booker, Chow, Priebe, Combarieu or Baguelein's method).

With parametric studies, we have analyzed 34 predictions. Table 2 presents all the approaches used by the participants.

3.1 Numerical calculations

Eight numerical calculations were done with three commercial available programs: PLAXIS, CESAR-LCPC and FLAC3D.

The analysis is based on the plasticity theory and rarely on the consolidation theory. The construction sequence was taken into account.

The embankment and the columns have been modeled with an elastic-perfectly plastic Mohr-Coulomb model. The behaviour of the silty fine-grained soil has been described by the Mohr-Coulomb model, or the modified Cam Clay model, or the Soft Soil Model.

The problem was handled in a plane-strain state for the homogenized approach or wall equivalent approach. In these approaches, the symmetry has been taken into account, and only a half of the problem was modeled (figure 4). In the three-dimensional approach, the geometry is assumed periodical and only a slice is considered with rows of stone columns (figure 5a and b).

3.2 Special methods proposed in the literature

Other calculation methods were based upon combinations between a simplified theoretical approach (elastic or plastic) and empirical correction factors.

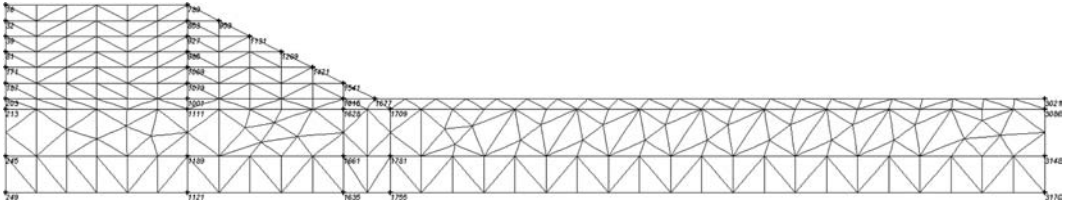


Figure 4. Example of PLAXIS2D model for the calculation of experimental embankment on stone columns coupled with Priebe's method.

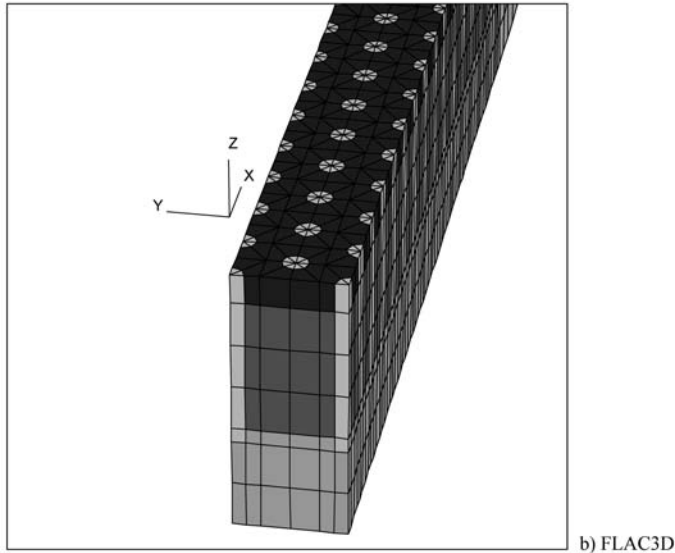
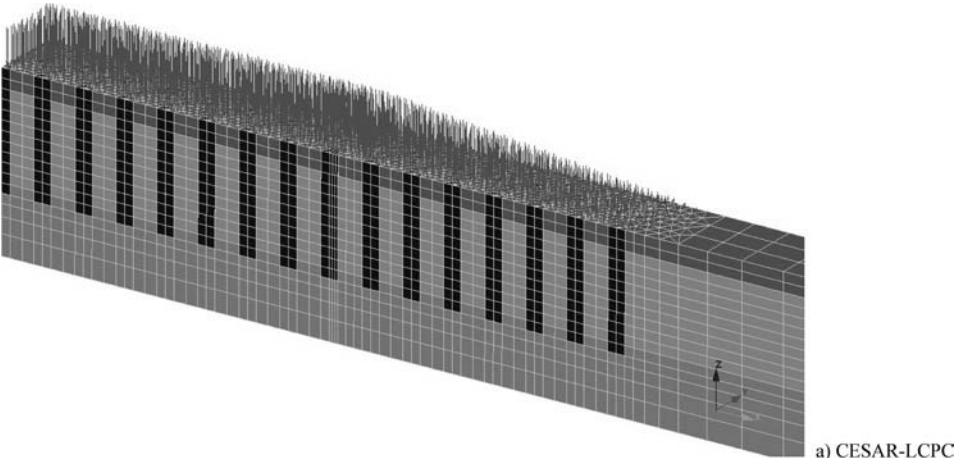


Figure 5. Views of the 3D models used for the calculation of experimental embankment on stone columns: a) CESAR-LCPC; b) FLAC3D

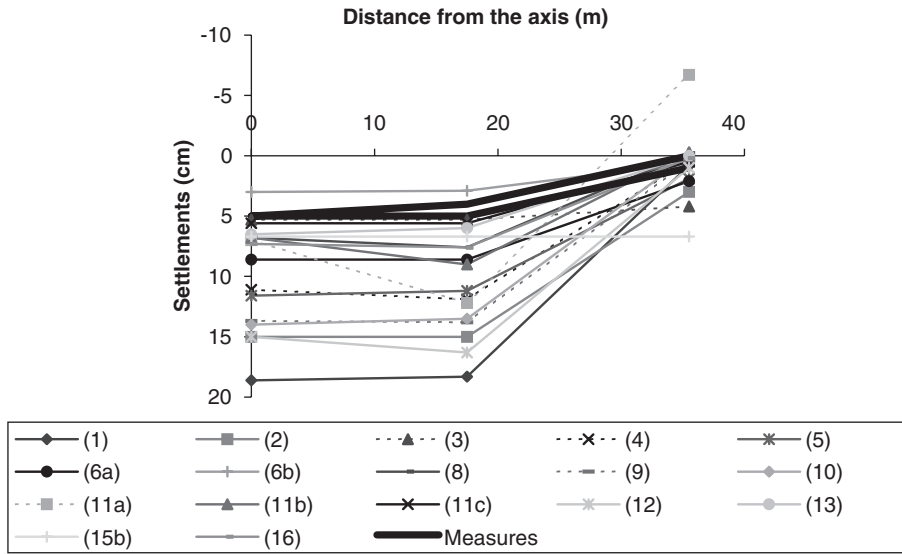


Figure 6. Comparison between calculated and measured settlements (t = 40 days).

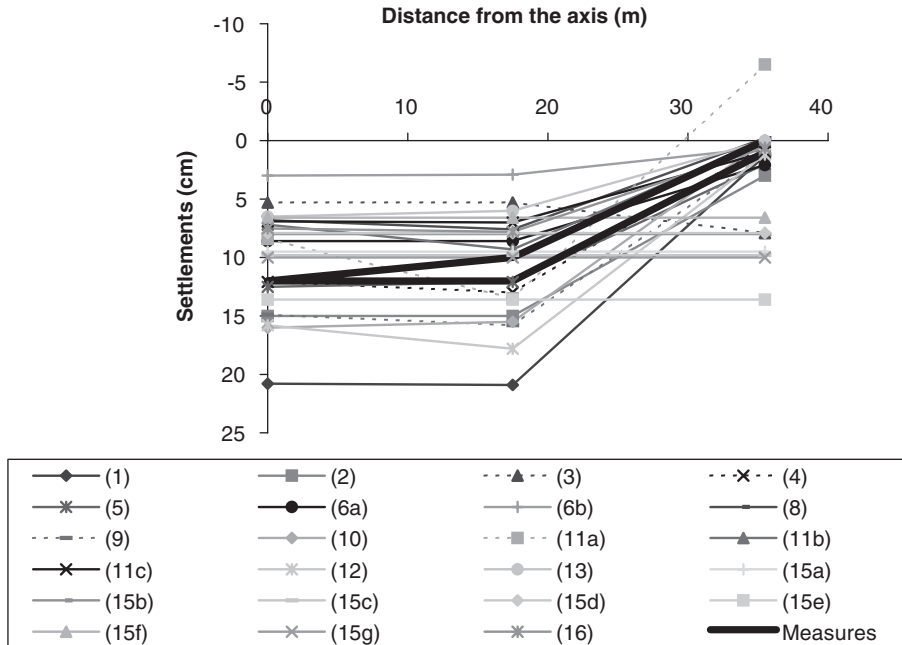


Figure 7. Comparison between calculated and measured settlements (t = 160 days).

4 RESULTS

This paper doesn't present these methods, because the length is short and many participants have not well described the used method (Mestat et al., 2004 and list of references at the end of this paper).

The curves of calculated and measured settlements at the surface under the embankment are presented in the figures 6 and 7.

The calculation results for 40 days are not satisfactory (figure 6). Except one prediction, all the results overestimated the measurements of surface settlement. For $t = 160$ days, the measurements were clearly an average of the predictions.

The measurements of settlements were the following (figure 1):

- 5 cm at the point O ($t = 34$ days) and 12 cm ($t = 158$ days);
- 4–5 cm at the point A ($t = 34$ days) and 10–12 cm ($t = 158$ days);
- 0–1 cm at the point B ($t = 34$ days) and 0–1 cm ($t = 158$ days).

The prediction contest showed considerable discrepancy in the results provided by the calculations, although the same data were given to the participants. These differences result in part from the fact that the models used for the group of columns and their interactions were different and the values of parameter seem to be very conservative in certain predictions. It appears that the modelling of the transfer of load from columns to soil mass through shear is not satisfactory.

The comparison leads to the following conclusion: the more complex model (FLAC3D) and a simple approach (1D) with “good” parameters provided the better previsions.

5 CONCLUSIONS

Comparing simulation results with measures on a real monitored structure remains the better way of evaluating the capabilities of a calculation method.

An evaluation has been made of the calculation methods applied to the surface settlements of soil improved by stone columns.

In general poor agreement has been found between the measurements and the predictions. At short time all the calculated results overestimated the measurements. After 150 days we observe a large scattering of results.

The main explanation of this scattering is the poor modelling of the soil-structure interaction. More researches and studies have needed to taken into account better models for the interaction between the soil mass and the columns and for the group effect.

Finally this exercise shows that the calculation of settlement of improved soil by stone columns is complicated and remains a problem for the practical applications. This conclusion should question the geotechnical engineers and lead to establish adapted design rules.

REFERENCES

- Mestat Ph., Dhoubi A., Magnan J.-P. & Canépa Y. 2004. Résultats de l'exercice de prévision des tassements d'un remblai construit sur des colonnes ballastées. In French. *Int. Symp. PARAM 2002, FONDSUP 2003, ASEP-GI 2004*, vol. 2, Presses de l'ENPC/LCPC, 599–612.
- Antoinet E. & Page B. 2004. Exercice de calcul du tassement de colonnes ballastées – Utilisation du logiciel FLAC3D. In French. *Int. Symp. PARAM 2002, FONDSUP 2003, ASEP-GI 2004*, vol. 2, Presses de l'ENPC/LCPC, 613–620.
- Baguelin F. 2004. Exercice de calcul du tassement de colonnes ballastées. In French. *Int. Symp. PARAM 2002, FONDSUP 2003, ASEP-GI 2004*, vol. 2, Presses de l'ENPC/LCPC, 621–628.
- Bertaina G. 2004. Exercice de calcul du tassement de colonnes ballastées. In French. *Int. Symp. PARAM 2002, FONDSUP 2003, ASEP-GI 2004*, vol. 2, Presses de l'ENPC/LCPC, 629–634.
- Combarieu O. 2004. Exercice de calcul du tassement de colonnes ballastées. In French. *Int. Symp. PARAM 2002, FONDSUP 2003, ASEP-GI 2004*, vol. 2, Presses de l'ENPC/LCPC, 635–638.
- Rajot J.-P. & Neyret N. 2004. Exercice de calcul du tassement de colonnes ballastées. In French. *Int. Symp. PARAM 2002, FONDSUP 2003, ASEP-GI 2004*, vol. 2, Presses de l'ENPC/LCPC, 639–642.
- Remaud D. & Bourgeois E. 2004. Exercice de calcul du tassement de colonnes ballastées avec CESAT-LCPC. In French. *Int. Symp. PARAM 2002, FONDSUP 2003, ASEP-GI 2004*, vol. 2, Presses de l'ENPC/LCPC, 643–646.

Deformation analyses of land reclamation and a test construction with finite element method

M.M. Hassan, M. Lojander & J. Takala

Soil Mechanics and Foundation Engineering, HUT, Espoo, Finland

ABSTRACT: Realistic prediction of deformations of natural soft soil deposits is still a challenge in geotechnical engineering. Toukoranta, situated in the eastern part of Helsinki, was favored by the City of Helsinki for dwelling purposes. The area was fully reclaimed from sea in 1985 and left 10 years. In order to build safely and economically, ground improvement was necessary. To study the area the City of Helsinki arranged a test embankment with an adjacent excavation in 1995. Finite element calculations are a useful tool for the optimization of the design and to obtain a realistic prediction of the deformations. This article presents finite element simulation of reclamation and the test construction. Long-term consolidation settlement because of reclamation and short horizontal displacements caused by the test construction are presented and compared with observed measurement.

1 INTRODUCTION

Realistic prediction of deformations of natural soft soil deposits is still a challenge in geotechnical engineering. It gains even more importance as urban areas all over the world become more and more congested. For socio-economic development today's construction projects are frequently built on those areas, which were considered unsuitable for construction work couple of decades ago.

Toukoranta is situated in the eastern part of Helsinki near the outlet of the river Vantaa. The area was favored for dwelling purposes by The City of Helsinki from the early eighties as the area is near to the downtown of Helsinki. The original ground level was under sea more than 1 m. The area was considered completely unsuitable for building purposes because of underlain soft soils, thereby served mainly as filling area. Filling operation was started around 1963 and continued about 10 years. The City of Helsinki fully reclaimed the area by placing filling material over frozen sea in 1985 and approximately 0.85 km² area was recovered for 8000 inhabitants. Ground improvement was necessary for future construction because of high compressibility and low undrained shear strength of soft soil. For ground improvement and for future construction, The City of Helsinki arranged a test embankment with an adjacent excavation to study the area at the end of 1995. Inclinometers were installed around the test construction and horizontal displacements were measured from November 1995 to February 1996 (Gulin and Wikström, 1997).

This study focuses on numerical simulation of long term vertical settlement by the reclamation and horizontal displacements induced by the test construction. Finite element calculations are a useful tool for the optimization of the design and to obtain a realistic prediction of the deformations. Finite element simulations have been performed using PLAXIS with Mohr-Coulomb (MC) and Soft Soil Creep (SSC) model.

2 SOIL PROFILE AND TEST CONSTRUCTION

2.1 Soil profile

To determine the geotechnical properties of soil deposit in-situ and laboratory testing were performed. For laboratory testing undisturbed soil samples were collected in July 2004. Index properties determination, incremental loading oedometer testing and triaxial testing were performed in laboratory and all the laboratory testing was carried out in The Laboratory of Soil Mechanics and Foundation Engineering, Helsinki University of Technology from August to December 2004 (Hassan, 2006). [Figure 1](#) presents the geological profile of the area based on in-situ site investigation and laboratory tests. The deposit is roughly divided into five layers-fill layer, organic clay layer, clay layer, silt and sand layer. The thickness of the soil layers varies from location to location as well as the bottom rock level. Thickness variation indicates that additional site and laboratory investigation will provide more accuracy to construct

geological profile of the deposit to obtain a high degree of precision in simulation.

The top layer filling was started around 1963 and mainly composed of waste deposit of earth and blasted rock masses. The exact filling thickness from 1963 to 1973 and settlement are unknown. The City of Helsinki fully reclaimed the area by placing filling material over frozen sea in 1985. After the full reclamation, the finished thickness of the fill layer was approximately 4 m. Sea level is considered as groundwater level, which is located approximately 2.5 m below the formation level and assumed constant throughout the simulation. The next soil layer is distinguished as organic clay layer. This layer was deposited some 8000 years ago into the Lithorina Sea. The natural water content (w_0) of the organic clay layer varies from 100 to 130% and has 6 to 9% organic content. Liquid limit (w_L) of this layer is more than 150% and plasticity index I_p is more than 100%. Void ratio (e) of this layer is high and varies from 3 to 4. Undrained shear strength was determined with Swedish Fall Cone test and varies from 20 to 30 kPa. Below the organic clay layer, there is another clay layer with natural water content between 70 and 100%. Liquid limit (w_L) of this layer is 100% and plasticity index I_p is 71%. Void

ratio of this layer varies from 2 to 3. Near the bottom, occasional silt and sand layers are found and the bottom layer is uncompressible layer and is considered as rock layer.

2.2 Test construction

Figure 2 shows the geometry of the test structures. The base dimensions of the embankment and the excavation were $12.5 \times 35 \text{ m}^2$ and $15 \times 35 \text{ m}^2$ respectively. The distance between the embankment and the excavation was 27.8 m. Both the embankment and the excavation were constructed in two stages. The first stage of construction was started approximately on the first week of October 1995 and completed within 7 days. After the first stage operation the embankment was 1.4 m high and the excavation reached 1.2 m deep with 1:1 slope. The first stage operation lasted for more than one and half month. The second stage of the operation was started on the middle of November 1995 and this operation took approximately 10 days. The final height of the test embankment was 1.9 m and the excavation depth were 1.7 m with 1:1 slope. Inclinometers were installed around the test construction and inclinometer locations are presented in Fig. 2.

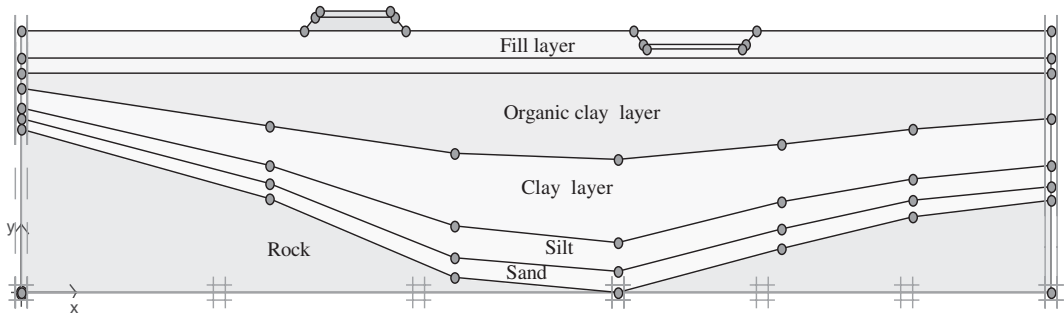


Figure 1. Geometry and geological profile of the area.

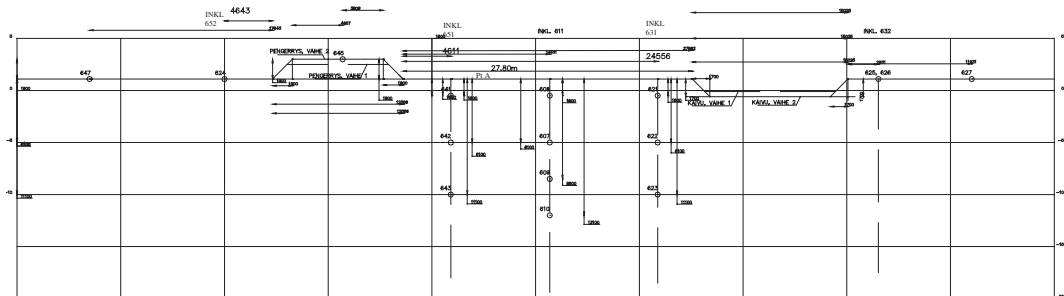


Figure 2. Geometry of the test structure and inclinometer locations of the studied area.

3 FINITE ELEMENT CALCULATION

3.1 Initial information

Plane strain conditions have been considered for calculation, i.e. no three-dimensional effects are considered. Fifteen noded triangular elements have been used in simulation. The finite element mesh has a width 126 m and covered the soil deposit down to the bedrock (Fig. 3). The lateral boundaries have been fixed in horizontal direction and the bottom boundary has been fixed both in horizontal and vertical direction. Consolidation boundary has been opened at the ground surface and on the bottom of the mesh. The bottom rock layer has been considered as free drainage layer with high permeability.

Modeling order used for calculation is presented below:

1. Calculation of the initial stresses
2. Adding load of reclamation
3. Calculation of 10 years of consolidation

4. Adding load of the first stage of test construction
5. Consolidation of next 44 days
6. Adding load of the second stage of test construction
7. Consolidation of next 90 days.

Filling operation was started a long time before 1985 though in FE simulation it has been assumed that the reclamation of the whole area is done in a single operation to simplify the calculation. After that a consolidation phase of 10 years was performed. The next calculation steps simulate the test construction phases.

Two different models have been used for calculation. Mohr-Coulomb (MC) model has been used to model fill layer, sand layer, whereas the organic clay layer, clay layer and silt have been modeled with Soft Soil Creep (SSC) model. Tab. 1 to 4 presents the general material parameters and specific material model parameters. Fill layer is composed of different material and material properties presented in Tab. 4 of fill layer are approximated values. SSC material model parameters were evaluated and modified from laboratory test

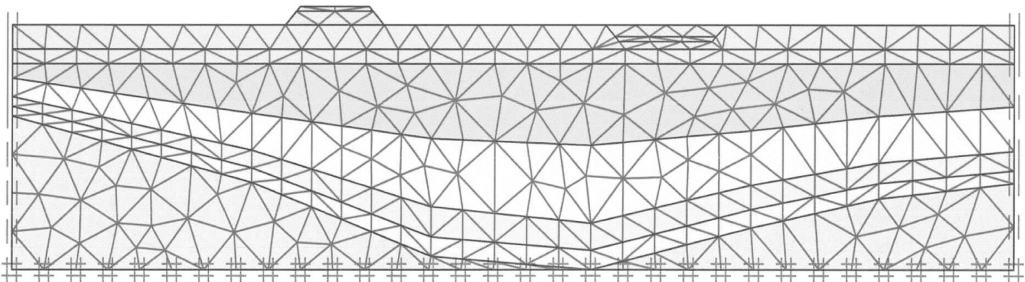


Figure 3. Finite element mesh for numerical solution.

Table 1. The layers and overconsolidation conditions used in PLAXIS.

Layer number	Soil type	Thickness (Pt A Fig. 2)m	Material model	POP, kPa
1	Fill layer	4	MC	Not used
2	Organic clay layer	8.4	SSC	0
3	Clay layer	8	SSC	0
4	Silt	2.8	SSC	0
5	Sand	2	MC	Not used
–	Embankment	–	MC	Not used

Table 2. Parameters of Soft Soil Creep model part 1.

Layer number	γ_{dry} kN/m ³	γ_{wet} kN/m ³	k_x m/day	k_y m/day	C_k	λ^*	κ^*	μ^*
2	3.0	13.0	3.456E-5	3.456E-5	1.0	0.197	0.015	0.024
3	13.5	14.5	5.184E-6	5.184E-6	1.0	0.221	0.02	0.013
4	17.5	18.5	8.64E-5	8.64E-5	1.0	0.045	0.0064	0.0095

Table 3. Parameters of Soft Soil Creep model part 2.

Layer number	ν_{ur}	K_0^{nc}	c' kN/m ²	ϕ'°	ψ°	e_{init}
2	0.15	0.694	2.0	27.7	0	3.429
3	0.15	0.694	2.0	27.7	0	2.451
4	0.15	0.692	2.0	27.7	0	0.902

Table 4. Parameter of Mohr-Coulomb model.

Layer number	γ_{dry} kN/m ³	γ_{wet} kN/m ³	k_x m/day	k_y m/day	ν	E kN/m ²	c' kN/m ²	ϕ'°	ψ°
1	14.0	16.0	1.0	1.0	0.35	3.0E+4	10.0	30	0
5	16.0	18.0	5.0	5.0	0.35	3.0E+4	1.0	30	0
Embankment	16.0	18.0	1.0	1.0	0.35	4.0E+4	1.0	34	0

results (Hassan, 2006). Symbols used in the following tables are according to PLAXIS manual.

3.2 Results and discussion

The first objective of this study is to calculate the long-term vertical settlement because of the reclamation. It is mentioned earlier that the reclamation was started a long time before 1985, therefore consolidation settlement because of reclamation is an approximate solution. Point A (Fig. 2) is chosen on the surface of the formation ground level and at the middle of the studied area where soil deposit is thickest. Consolidation time frame of this back analysis is 10 years. Figure 4 shows the vertical settlement from 1985 to 1995 and maximum vertical settlement of Pt A is approximately 1.13 m. The clay layers mainly contribute this settlement because of high compressibility of these layers. Settlement distribution is found approximately 1 m around the thickest deposit. Accuracy in settlement distribution requires three-dimensional analyses with accurate geological profile, stress distribution and proper boundary condition, but in this study three-dimensional analyses are not considered.

Observed horizontal displacements of the inclinometers (Gulin and Wikström, 1997) and calculated horizontal displacements corresponding time February 1996, are presented in Fig. 5. Inclinometer locations are presented in Fig. 2. Observed and calculated maximum horizontal displacements for clay layers are fairly close for this small time frame. Inclinometer 651 was installed 4.6 m from the toe of the embankment and calculated maximum horizontal displacement of inclinometer 651 in the middle of the organic clay layer is 101 mm and observed reading is approximately 93 mm. Inclinometer 631 was located 24.5 m from the toe of the embankment and observed maximum horizontal displacements of inclinometer 631 was 75 mm whereas

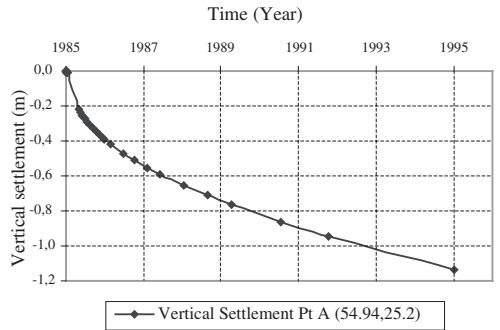


Figure 4. Simulation results – consolidation settlement versus time.

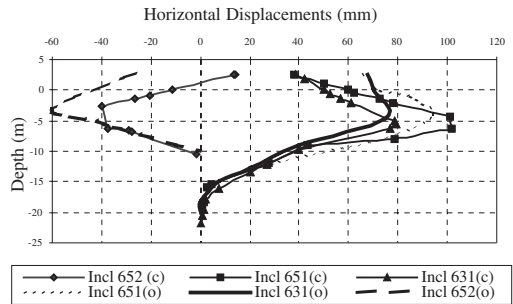


Figure 5. Calculated (c) and observed (o) horizontal displacement.

calculated one is approximately 79 mm. Discrepancy found between the calculated and observed horizontal displacements at the fill layer. Inclinometer 652, located 4.6 m of the other side of the embankment, showed approximately -26 mm horizontal displacement at the

formation ground level in contrast calculated displacement is 13 mm. Also calculated and observed horizontal displacements readings of other inclinometers of the fill layer are not fairly close. Limitations of fill layer modeling are material heterogeneity, material parameters, varying thickness of deposit, bottom rock level and imposed lateral boundary condition in FE analysis. Gulin and Wikström (1997) also pointed out that during the test construction the fill layer unevenly penetrated into the clay layers. These might lead to errors found in horizontal displacements of fill layer.

4 CONCLUSION

Numerical back-analysis of reclamation and test construction on soft soil is presented. The simulation has been performed with MC and SSC model. Numerical solution of long-term consolidation settlement is approximately 1.13 m approximately where the soil deposit is thickest. Horizontal displacements of calculated and observed are found close in the clay layers though differences in horizontal displacements of fill layer are noticeable. Initially it was assumed that primary consolidation would be completed with in the specified 10 years time frame, but it is found that simulation requires more time to complete primary consolidation. Therefore further investigation is underway with Soft Soil model for clay layers, more realistic material parameters of fill layer, more precise

geological profile, time frame and imposed lateral boundary conditions to reduce errors and to obtain more realistic deformation prediction.

ACKNOWLEDGEMENT

The work presented was carried out as part of a Marie Curie Research Training Network "Advanced Modelling of Ground Improvement on Soft Soils (AMGISS)" (Contract No MRTN-CT-2004-512120) supported the European Community through the program "Human Resources and Mobility". The authors would like to acknowledge the support provided by the City of Helsinki. Also the authors would like to thank Professor Pauli Vepsäläinen for his valuable comments and discussion.

REFERENCES

- Gulin, K. & Wikström, R. 1997. Stabilization of horizontal movements in weak organic clay layers. Proceedings of the Fourteenth International Conference on Soil Mechanics and Foundation Engineering, Hamburg, Germany, pp. 1689–1692
- Hassan, M.M. 2006. Deformation behaviour and permeability of soft Finnish clay. Master's Thesis, Helsinki University of Engineering and Technology, Finland.
- PLAXIS 2002. PLAXIS, Finite element code for soil and rock analyses, user manual version 8.2. Rotterdam: Balkema.

Slopes and cuts

Factors of safety by limit equilibrium and strength reduction methods

Y.M. Cheng & W.B. Wei

Department of Civil and Structural Engineering, Hong Kong Polytechnic University, Hong Kong

T. Lämsivaara

Tampere University of Technology, Finland

ABSTRACT: The factors of safety and the locations of critical failure surfaces obtained by limit equilibrium method and strength reduction method are compared for various slopes. For simple homogenous soil slopes, it is found that the results from these two methods are generally in good agreement. There are however cases where great differences between the two methods may occur in some special circumstances which should be considered in analysis.

1 INTRODUCTION

Limit equilibrium method (LEM) is well known to be a statically indeterminate problem and assumptions on the internal forces distribution are required for the solution of the factor of safety. Morgenstern (1992) among others has however pointed that for normal problems, the factors of safety from different methods of analyses are similar so that the assumptions on the internal force distribution $f(x)$ are not major problems except for some particular cases.

LEM requires trial failure surfaces and optimization analysis to locate the critical failure surface which is a difficult N-P type global optimization problem. Many different proposals have been suggested in the past and detailed discussions on various methods in locating critical failure surface have been provided by Cheng (2003). While most of these methods can work for normal problems, they may be trapped by the presence of local minimum in the solution and Cheng (2003) has encountered several interesting problems which are trapped by the presence of local minima with the use of classical gradient type optimization methods. The use of modified simulated annealing method by Cheng (2003) is one of the few successful methods which can escape from local minimum and the method has been used for many major problems in several countries.

Many researchers have compared the results between strength reduction method (SRM) in finite element analysis and limit equilibrium method and it is found that generally the two methods will give similar factors of safety. Most of the studies are however limited to homogenous soil slopes and the geometry of the problems is relatively regular with no special

feature (presence of thin layer of soft material or special geometry). Furthermore, there are only limited studies in the comparisons of critical failure surface from LEM and SRM as factors of safety appear to be the primary goal of studies. In this paper, the two methods are compared under different conditions and both the factors of safety as well as the locations of the critical failure surfaces are considered in the analyses. In the present study, non-associated flow rule (SRM1 and dilation angle = 0) and associated flow rule (SRM2 and dilation angle = friction angle) which are the upper and lower limit of the flow rule are applied in the SRM analyses.

2 STABILITY ANALYSIS FOR A SIMPLE AND HOMOGENEOUS SOIL SLOPE

Firstly, a homogeneous soil slope with a slope height equal to 6 m and slope angle equal to 45 degree is considered, Figure 1.

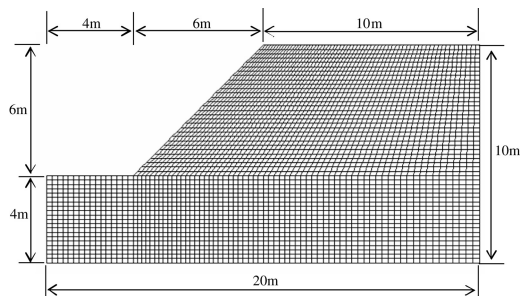


Figure 1. Discretization of a simple slope model.

In the parametric study, different shear strength properties are used and LEM, SRM1 and SRM2 analyses are carried out. The cohesion of the soil varies from 2, 5, 10 to 20 kPa while the friction angle varies from 5, 15, 25, 35 to 45 degree respectively, but the density, elastic modulus and Poisson ratio of the soil are kept to be 20 kN/m³, 14 MPa and 0.3 respectively in all the analysis. Actually, the authors have found that the results are not sensitive to the density of soil and this parameter is hence kept constant in the study. The results of analyses are shown in Table 1. As shown in Figure 1, the size of the domain for SRM analyses is 20 m in width and 10 m in height and there are 3520 zones and 7302 grid points in the mesh for analysis. Morgenstern-Price's method which satisfies both moment and force equilibrium is adopted and the critical failure surface is evaluated by the modified simulated annealing technique as proposed by Cheng (2003).

From Table 1 and Figure 2 it is found that the factors of safety and critical failure surfaces as determined by SRM and LEM are very similar under different combinations of soil parameters. Most of the factor of safety values obtained by SRM differ by less than 7% with respect to LEM solutions except for case 16 ($c = 20$ kPa, $\phi = 5$ degree) where the difference is up to 12.8%. The differences between LEM and SRM by Saeterbo Glamen et al. (2004) are more than those in the present study and the authors suspect that it is due to

Table 1. Factors of safety by LEM and SRM.

Case	Cohesion (kPa)	Phi (degree)	factor of safety (LEM)	factor of safety (SRM1, non-associated)	factor of safety (SRM2, associated)
1	2	5	0.25	0.25	0.26
2	2	15	0.50	0.51	0.52
3	2	25	0.74	0.77	0.78
4	2	35	1.01	1.07	1.07
5	2	45	1.35	1.42	1.44
6	5	5	0.41	0.43	0.43
7	5	15	0.70	0.73	0.73
8	5	25	0.98	1.03	1.03
9	5	35	1.28	1.34	1.35
10	5	45	1.65	1.68	1.74
11	10	5	0.65	0.69	0.69
12	10	15	0.98	1.04	1.04
13	10	25	1.30	1.36	1.37
14	10	35	1.63	1.69	1.71
15	10	45	2.04	2.05	2.15
16	20	5	1.06	1.20	1.20
17	20	15	1.48	1.59	1.59
18	20	25	1.85	1.95	1.96
19	20	35	2.24	2.28	2.35
20	20	45	2.69	2.67	2.83

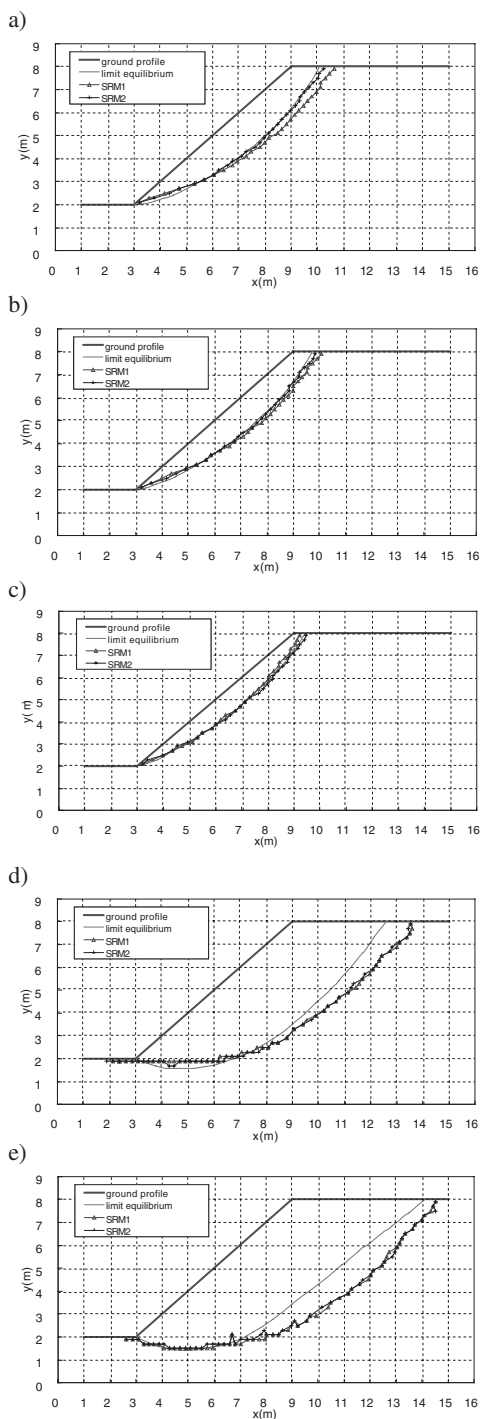


Figure 2. Slip surface comparison with increasing friction angle, $c = 2$ kPa, $\phi = 15$ (a), 25 (b) and 45 (c) and increasing cohesion ($\phi = 5$ degree), $c = 2$ (a), $c = 10$ (d) and $c = 20$ (e).

the use of manual location of critical failure surfaces by Saeterbo Glamen et al. (2004) while the authors adopted global optimization method with a very fine control in obtaining the minimum factors of safety.

Based on Table 1 and Figure 2, some conclusions can be made as follows:

1. Most of the FOS values obtained from SRM are slightly larger than those obtained by LEM with only few exceptions.
2. When the SRM is implemented, the FOS values with the use of associated flow rule (SRM2) are slightly above those with the use of non-associated flow (SRM1), and the differences in the factors of safety increases with increasing friction angle. These results are reasonable and are expected.
3. When the cohesion of the soil is small, the differences of FOS between LEM and SRM (SRM1 and SRM2) are greatest for higher friction angles. When the cohesion of the soil is large, the differences of FOS are greatest for lower friction angles. This result is somewhat different from that by Dawson (1999) who pointed out that the differences are greatest for higher friction angles.
4. The failure surfaces from LEM, SRM1 and SRM2 are similar in most cases. In particular, the critical failure surfaces obtained by SRM2 appear to be closer to those by LEM than those based on SRM1.
5. The right end of the failure surface gets closer and closer to the crest of the slope when the friction angle of the soil is increasing which is also a well known result. This behavior is more obvious for those failure surfaces obtained from SRM1.
6. For SRM analyses, when the friction angle of soil is small, the differences of slip surfaces between SRM1 and SRM2 are greatest for smaller cohesion. When the friction angle is large, the differences of slip surface between SRM1 and SRM2 are greatest for higher cohesion (Figure 2).
7. It can also be deduced from the results that the potential failure volume of the slope gets smaller with increasing friction angle but gets greater with increasing cohesion which is also a well known behavior that when the cohesive strength is high, the critical failure surface will be a deeper failure surface.

Although there are some minor differences in the results between SRM and LEM in this example, in general the results by these two methods are in good agreement and the results suggest that the use of LEM or SRM is satisfactory in general.

3 STABILITY ANALYSIS OF A SLOPE WITH A SOFT BAND

A special problem with a soft band is constructed by the authors. The geometry of the slope is shown in

Figure 3 and the soil properties are shown in Table 2. It is noticed that the soil parameters are particularly low for soil layer 2 which has a thickness of 0.5 m only and slope failures in similar conditions have actually occurred in Hong Kong (Fei Tsui Road slope failure in Hong Kong).

In order to consider the size effect (boundary effect) in SRM, three different numerical models are developed to perform SRM using Mohr-Coulomb analysis and the lengths of the domains are 28 m, 20 m and 12 m respectively. In these three SRM models, various maximum element sizes have been tried until the results are not sensitive to the number of elements used for analysis. Since the factors of safety from this special problem have great differences with those from LEM, the authors have tried several well known commercial programs and obtained very surprising results from them. For the locations of the critical failure surfaces, the results from the three SRM models (using different programs) and LEM are generally in good agreement with minor differences. Majority of the critical failure surfaces lie within layer 2 which has very small shear strength parameters and this result is as expected.

From Table 3, it is surprising to find that different programs produce drastic different results for the factors of safety even though the locations of the critical failure surface from these programs are very close. For the cases as shown in Figure 1 and other cases analyzed by the authors, the results are practically insensitive to the domain size (from parametric study by the authors) while the case as shown in Figure 3 are very sensitive to the size of domain for programs

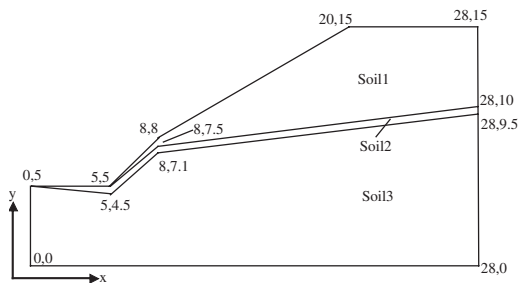


Figure 3. A slope with a thin soft band.

Table 2. Soil properties for Figure 3.

Soil name	Cohesion (kPa)	Friction angle (degree)	Density (kN/m ³)	Elastic modulus (MPa)	Poisson ratio
Soil1	20	35	19	14	0.3
Soil2	0	25	19	14	0.3
Soil3	10	35	19	14	0.3

A (SRM1 and SRM2) and B (SRM2). Results from program C appear not to be sensitive to the domain size but is relatively sensitive to the dilation angle which is different from the previous results. SRM1 results from program B is also not sensitive to the domain size but SRM2 results behave differently. Results from program A appear to be over-estimated as the soil parameters for the soft band are low, but the results from this program are not sensitive to the dilation angle which are similar to all the other examples in the present study. For SRM1, the results from program B and C appear to be reasonable as the results are not sensitive to the domain sizes while for SRM2, the authors view that results from program C may be better as the results are less sensitive to the dilation angle. It is also surprising to find that program D cannot give any result to this problem after many different trials but the program work properly for all the other examples in this study.

Besides the special results as shown above, the factors of safety from 28 m domain analysis appear to be large for programs A and B as the soil parameters for soil layer 2 are very small. In fact, it is not easy to define an appropriate factor of safety for this problem. If the cohesive strength of the top soil is reduced to zero, the factor of safety can be roughly estimated as 0.57 from $\tan \phi / \tan \beta$, where β is the slope angle. It can be viewed that for LEM, the cohesive strength 20 kPa

Table 3. FOS by SRM from different programs. The values in each cell are based on SRM1 and SRM2 respectively. (min. FOS = 0.927 from Morgenstern-Price's analysis)

Program/FOS	12 m domain	20 m domain	28 m domain
A	1.03/1.03	1.30/1.28	1.64/1.61
B	0.77/0.85	0.84/1.06	0.87/1.37
C	0.82/0.94	0.85/0.97	0.86/0.97
D	No solution	No solution	No solution

for soil 1 help to bring the factor of safety to 0.927 and a high factor of safety for this problem is not reasonable. Allowing for tension crack would reduce the factor of safety close to 0.57. Obviously it would be dangerous to adopt factor of safety values of the order 1.3 to 1.64 given by some of the analysis using SRM.

When the soil properties of soil layer 2 are changed to the soil properties of soil layer 3, the results are practically independent of the domain size and all programs can give similar results. The results from LEM and the results from programs B and C using unassociated flow rule are basically consistent and can be considered as the estimations of the factors of safety. This interesting case has illustrated the limitation of using both SRM and LEM method when there is a thin layer of soft material and great care and judgment are required for acceptance of the results of analysis. The problems as shown in Table 3 may be purely the limitations of some of the commercial programs instead of the limitation of SRM, but it also illustrate that it is not easy to compute a good value for this special type of problem for SRM. The results are highly sensitive to different nonlinear solution algorithms (which are however not always clearly explained in the commercial programs). In this respect, LEM appears to be a better solution for this special type of problem. Great care, effort and time are required to achieve a reasonable result from SRM for this special problem and the result should also be compared with LEM before the final acceptance.

If the soil properties of soil 2 and 3 are interchanged so that the third layer soil is the weak soil, the factors of safety from SRM2 are 1.33 (with all programs) for all the three different domain sizes while the factor of safety from LEM is 1.29 from Morgenstern-Price's analysis. The locations of the critical failure surface from SRM and LEM for this case are very similar. It appears that the presence of a soft band instead of major differences in soil parameters will create the difficulties in SRM analysis.

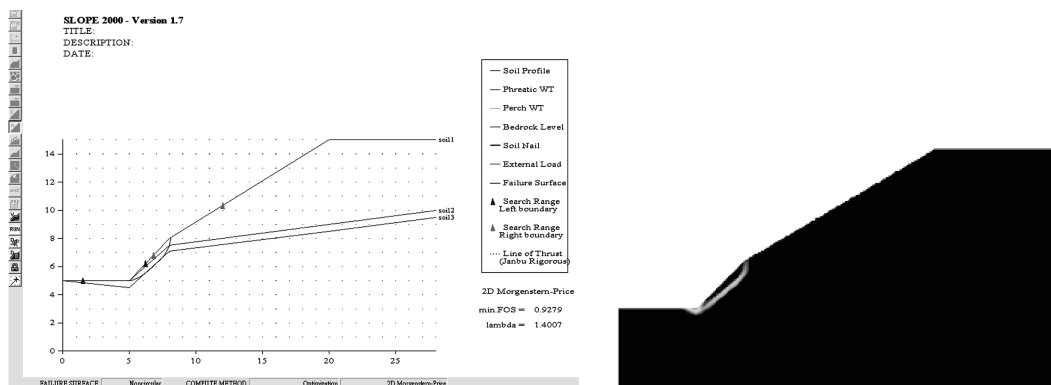


Figure 4. Locations of critical failure surfaces from LEM and SRM for soft band problem.

4 LOCAL MINIMUM IN LEM AND SRM

For LEM, it is well known that many local minima may exist besides the global minimum and this is also the difficulty in locating critical failure surface by classical optimization method. The comparisons of LEM and SRM with respect to local minimum has not been considered in the past but is actually a very important issue which is illustrated by the following example. In SRM, there is no local minimum as the formation of shear band will attract strain localization in the solution process. To investigate this problem, a relatively simple slope with a total height of 17 m and one soil layer is discussed. The soil parameters are $c' = 5 \text{ kPa}$ and $\phi' = 30^\circ$ while unit weight is 20 kN/m^3 . Using LEM, the global minimum factor of safety is obtained as 1.33 (Figure 5) but several local minima are found with factors of safety ranging 1.38 to 1.42. It can be viewed that there are several failure surfaces which are potential failure mechanisms with virtually the same probability of failure with the concept of LEM. From SRM, only 1 factor of safety is found to be 1.33 which is equal to the global minimum from LEM. Other possible failure mechanism cannot be determined from SRM easily. It may thus well be, that the SRM analysis yields a local failure surface of less importance, while a more severe global surface remains undetected. If slope stabilization is carried out only for this failure surface, failure surfaces as shown by Figure 5 will not be considered

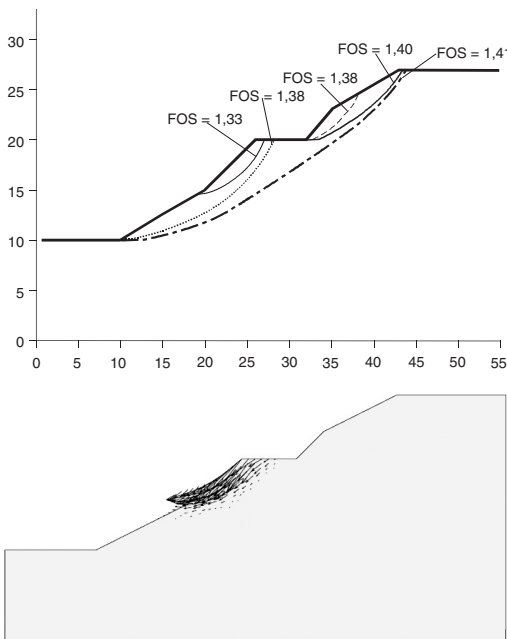


Figure 5. Global and local minima by LEM/SRM analysis.

in SRM and no stabilization measures will be carried out for these locations. In this respect, LEM is a better tool to the engineers in slope stability analysis.

5 DISCUSSION AND CONCLUSIONS

While most of the researchers concentrate on the factors of safety between LEM and SRM, the authors have also compared the locations of critical failure surfaces from these two methods. In simple and homogenous soil slope, the differences of the FOS and locations of critical failure surfaces from SRM and LEM are small and both methods are satisfactory for engineering use. It is found for the analyzed example that when the cohesion of the soil is small, the difference of FOS is greatest for higher friction angles. When the cohesion of the soil is large, the difference of FOS is greatest for lower friction angles. For the effects of flow rule, the FOS and locations of critical failure surface are not greatly affected by the choice of the dilation angle which is important for the adoption of SRM in slope stability analysis. The critical slip surfaces from finite element analyses appeared to be closer to those by limit equilibrium method when associated flow rule was applied.

For SRM, the authors have studied the effects of dilation angle and found it to be small but still noticeable. Drastic different results are determined from different computer programs for the problem with soft band which illustrates that SRM is highly sensitive to the method of modeling and nonlinear equation solution process (may not be the fault of SRM). For this special case, the authors have also found that the factor of safety determined by some of the programs was very sensitive to the size of elements, tolerance of analysis and number of iteration allowed and a parametric study on the effects of these factors is strongly suggested as a routine process. For soft band problems limit equilibrium method calculations with a reliable global optimization tool is also strongly suggested to be carried out as a check of the results from the strength reduction method. Although the problems for SRM in this special problem may not be the fault of SRM, the authors view that SRM has to be used with great care for a problem with soft band.

Through the present study, the two limitations of SRM are established: sensitive to nonlinear solution algorithms/flow rule for some special cases and the inability to determine other critical failure surfaces. For general problem, it is possible that the use of SRM may miss the location of the next critical failure surface (with a very small difference in the FOS but a major difference in the location of critical failure surface) so that the slope stabilization measures may not be adequate. If SRM is used for routine analysis and design of slope stabilization measures, these two

major limitations have to be overcome and the authors suggest that LEM should be carried out as a reference. If there are great differences between the results from SRM and LEM, great care and engineering judgment should be exercised in assessing the proper solutions. There is one practical problem in applying SRM to slope with soft band. When the soft band is very thin, the number of elements required to achieve a good solution is extremely large so that very significant computer memory and time are required. Cheng (2003) has tried a slope with 1 mm soft band and has effectively obtained the global minimum factor of safety by simulated annealing method. If SRM is used for a problem with 1 mm thick soft band, it is extremely difficult to define a mesh with good aspect ratio unless the number of element is tremendous. For SRM, the authors have used about 1 hour for a small problem (several thousand elements) and several hours for a large problem (over ten thousand elements) for program B while program A requires 1–3 days (small to large mesh). If a problem with 1 mm thick soft band is to be modeled with SRM, the computer time and memory required will be based on the experience from the present study be extremely high and SRM is practically inapplicable. The authors are also not aware of any successful application of SRM to slope with very thin soft band. In this respect, LEM is more efficient than SRM for this special type of

problem as it can be solved very quickly by the limit equilibrium method (Cheng 2003).

It can be concluded that both LEM and SRM have their own merits and limitations and the use of SRM is not really superior to the use of LEM in routine analysis and design. Both methods should be viewed as providing an estimation of the factor of safety and the probable failure mechanism but engineers should also appreciate the limitations of each method and solution routines in the programs they are using in the assessment of the results of analysis.

REFERENCES

- Cheng, Y.M. Locations of Critical Failure Surface and some Further Studies on Slope Stability Analysis, *Computers and Geotechnics*, vol. 30, p. 255–267, 2003.
- Dawson, E. M., Roth, W. H. & Drescher, A. (1999). Slope stability analysis by strength reduction. *Geotechnique* 49, No. 6, 835–840.
- Morgenstern, N.R. The Evaluation of Slope Stability – A 25 Year Perspective, Stability and Performance of Slopes and Embankments –II, *Geotechnical Special Publication No. 31, ASCE*, 1992.
- Saeterbo Glamen, M.G., Nordal, S. & Emdal, A. (2004). Slope stability evaluations using the finite element method. NGM 2004, *XIV Nordic Geotechnical Meeting*. Volume 1. p. A49–A61.

Slope safety factor calculations with non-linear yield criterion using finite elements

Johan Clausen & Lars Damkilde

Esbjerg Institute of Technology, Aalborg University Esbjerg, Esbjerg, Denmark

ABSTRACT: The factor of safety for a slope is calculated with the finite element method using a non-linear yield criterion of the Hoek-Brown type. The parameters of the Hoek-Brown criterion are found from triaxial test data. Parameters of the linear Mohr-Coulomb criterion are calibrated to the same triaxial data and the corresponding safety factor is calculated. Of the two safety factors the Hoek-Brown factor is the lower. Triaxial tests carried out with a wide stress range indicate that the failure envelope of soils is indeed non-linear, especially at low confinement stresses. As standard triaxial tests are carried out at much higher stress levels than present in a slope failure, this leads to the conclusion that the use of the non-linear criterion leads to a safer slope design.

1 INTRODUCTION

Slope stability is usually assessed using the linear Mohr-Coulomb criterion, which means that the angle of friction is constant in the entire stress range. However experimental evidence suggests that the failure criterion should not be linear, especially in the range of small normal stresses, (Baker 2004). This fact can have a significant impact on the safety of slopes as the slope failures are often shallow and hence associated with small normal stresses along the slip line. In itself this does not disqualify the Mohr-Coulomb criterion entirely, as reasonable results can be found if the Mohr-Coulomb parameters are calibrated to test data obtained by triaxial testing at the applicable normal stress levels. But in standard triaxial tests the pressure is usually much higher than the pressure along the slip line, and because of this the safety of slopes can be overestimated when applying the Mohr-Coulomb criterion, see e.g. (Jiang et al. 2003).

The preferred method of assessing slope stability has for many years been some type of limit formulation, where the slip line giving the lowest safety factor is sought out with the aid of an optimizing algorithm. With the proper numerical algorithm this is possible with both the Mohr-Coulomb criterion as well as non-linear yield criteria, see e.g. (Jiang et al. 2003).

As opposed to this approach the elasto-plastic finite element method is an alternative which is gaining ground, at least in academia, see e.g. (Duncan 1996), (Griffiths & Lane 1999) and (Zheng et al. 2005). An advantage of slope safety calculations with the

finite element method is that they are relatively easy incorporated in already existing finite element code, including commercial codes. The location of the slip line along which the slope fails is not rigorously defined with the finite element method but can be found by visualizing the displacements or the plastic strains at failure. It is also possible to employ a non-associated flow rule in order to better capture the dilative behaviour of real soils, as opposed to the limit formulations, where the flow rule must be associated. The associated flow rule overestimates the dilation effects of soils, although this usually has little impact on the safety factor, as the slope failure is relatively unconfined.

In this paper the soil will be treated as a linearly elastic – perfectly plastic material. The plastic integration needed to update the stresses in each Gauss point is done by return mapping on the basis of a method outlined in (Clausen et al. 2006). An elaboration on the plastic integration of the Hoek-Brown yield criterion will be available in (Clausen & Damkilde in prep.).

2 THE CONCEPT OF SLOPE SAFETY

Traditionally the strength of soils is expressed as a Mohr-envelope, $S(\sigma)$, in $\sigma - \tau$ space, see [Figure 1](#). Here σ and τ are the normal and shear stress on a section of the material, respectively. The envelope defines the relation between the maximal shear and normal stress which the soil can endure before yielding occurs. If the Mohr circle representing the stress state at a point in the soil is located in such a way that

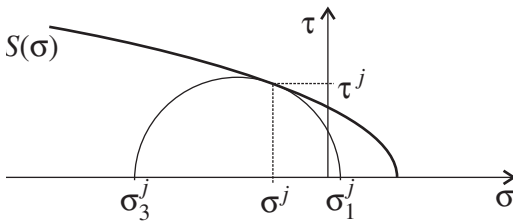


Figure 1. A Mohr-envelope in $\sigma - \tau$ space. A Mohr circle representing a stress state of yield is shown.

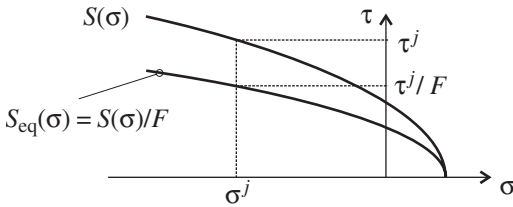


Figure 2. The actual Mohr-envelope, $S(\sigma)$ and the Mohr-envelope needed to maintain equilibrium, $S_{eq}(\sigma)$.

the strength envelope is its tangent the material is yielding at that point. This is illustrated on Figure 1.

The safety of a slope is usually assessed by calculation of a safety factor. Several definitions of the safety factor exist, see e.g. (Gunnaratne 2006). In numerical applications the most frequently used definition is that which is some times referred to as the stability number (Taylor 1948), in which the safety factor is defined as the ratio between the actual shear strength of the soil to the shear strength needed to maintain equilibrium, $S_{eq}(\sigma)$

$$F = \frac{S(\sigma)}{S_{eq}(\sigma)} \quad (1)$$

This relation is illustrated on Figure 2.

2.1 Reduced Mohr-Coulomb parameters

The simplest Mohr envelope is the linear Mohr-Coulomb strength envelope, see Figure 3 given by

$$S_{MC}(\sigma) = c - \sigma \tan \varphi \quad (2)$$

where c is the cohesion and φ is the friction angle.

The Mohr-Coulomb envelope needed to maintain equilibrium, also shown on Figure 3, is given by

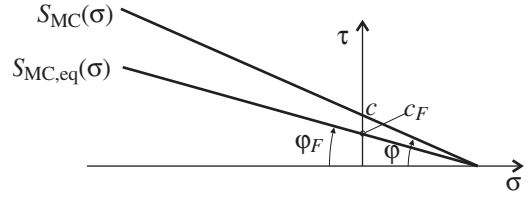


Figure 3. The Mohr-Coulomb strength envelope, $S_{MC}(\sigma)$ and the corresponding envelope needed to maintain equilibrium.

$$S_{MC,eq}(\sigma) = \frac{S_{MC}(\sigma)}{F} = \frac{c - \sigma \tan \varphi}{F} \quad (3)$$

$$= c_F - \sigma \tan \varphi_F$$

where the reduced parameters c_F and φ_F are given by

$$c_F = \frac{c}{F} \quad \text{and} \quad \varphi_F = \arctan \left(\frac{\tan \varphi}{F} \right) \quad (4)$$

2.2 Reduced parameters in a non-linear Mohr envelope

As an example of a non-linear Mohr envelope consider the envelope suggested by Hoek & Brown (1997). This particular envelope is chosen as it is a close approximation to the Hoek-Brown yield criterion presented in section 3.2

$$S_{HB}(\sigma) = A \sigma_c \left(\frac{\sigma_t - \sigma}{\sigma_c} \right)^B \quad (5)$$

Here A and B are dimensionless parameters, σ_c is the uniaxial compressive strength and σ_t is the value of the normal strength for which $S_{HB}(\sigma_t) = 0$. The envelope is similar to the one depicted on Figures 1 and 2. The reduced envelope needed to maintain equilibrium is given by

$$S_{HB,eq}(\sigma) = \frac{S_{HB}(\sigma)}{F} = A_F \sigma_c \left(\frac{\sigma_t - \sigma}{\sigma_c} \right)^B \quad (6)$$

with the reduced parameter

$$A_F = \frac{A}{F} \quad (7)$$

The rest of the parameters are unchanged.

3 RELATION BETWEEN MOHR ENVELOPES AND YIELD CRITERIA

For use in the finite element method the yield criterion must be expressed in stresses related to coordinate axes, rather than as the normal and shear stress on an arbitrary plane. Therefore the yield criterion parallels to the Mohr envelopes will be presented. Both of the applied criteria are independent of the intermediate principal stress. For this reason and for simplicity the graphical representation leaves out this stress component, although all stress components are included in the finite element analyses.

3.1 The Mohr-Coulomb criterion in principal stress space

The Mohr-Coulomb criterion in principal stresses, see Figure 4, corresponding to the envelope of Eq. (2) is given as

$$f_{MC} = \frac{\sigma_1 - \sigma_3}{2} + \frac{\sigma_1 + \sigma_3}{2} \sin \varphi - c \cos \varphi = 0 \quad (8)$$

3.2 The Hoek-Brown criterion in principal stress space

To represent the non-linear strength behaviour of the soil in the principal stress space, the Hoek-Brown yield criterion is used, see (Hoek & Brown 1997)

$$f_{HB} = \sigma_1 - \sigma_3 - \sigma_c \left(1 - m \frac{\sigma_2}{\sigma_c} \right)^n = 0 \quad (9)$$

where σ_c is the uniaxial compressive strength, m is a dimensionless parameter and n is a curvature parameter. It should be noted that the original Hoek-Brown parameter s here have been fixed to a value of $s = 1$, which is adequate for the present analysis. The Hoek-Brown criterion can be seen on Figure 5.

Contrary to the linear Mohr-Coulomb case it is not possible to explicitly express Eq. (9) as a Mohr envelope in the $\tau - \sigma$ space which means that the Equations (9) and (5) are not identical. The Mohr envelope is needed in the parameter reduction because of the safety factor's definition in terms of the shear strength, cf. Eq. (1).

The uniaxial compressive strength, σ_c is present in both criteria and the Mohr parameter σ_t is found from the Hoek-Brown parameters as

$$\sigma_t = \frac{1}{2} \sigma_c (\sqrt{m^2 + 4} - m) \quad (10)$$

The dimensionless parameters A and B are found by regression, see e.g. (Hoek & Brown 1997). The

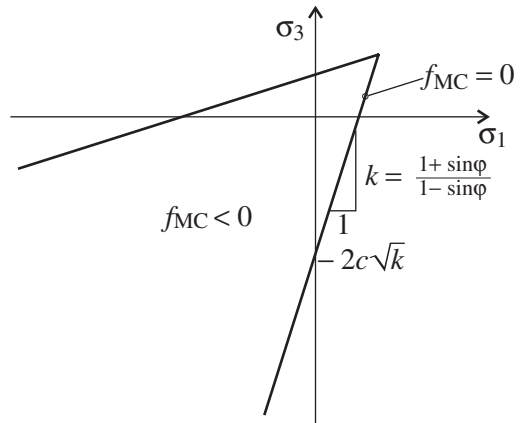


Figure 4. The Mohr-Coulomb criterion in principal stress space.

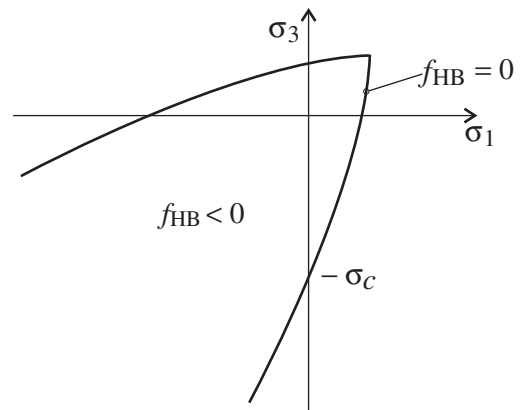


Figure 5. The Hoek-Brown criterion in principal stress space.

translation from the $\sigma_1 - \sigma_3$ stress pairs into $\sigma - \tau$ stress pairs needed for the regression can be found from the equation of the yield criterion with the relations given in (Balmer 1952).

$$\sigma = \sigma_1 - \frac{\sigma_1 - \sigma_3}{\partial \sigma_3 / \partial \sigma_1 + 1} \quad (11)$$

$$\tau = \frac{\sigma_1 - \sigma_3}{\partial \sigma_3 / \partial \sigma_1 + 1} \sqrt{\frac{\partial \sigma_3}{\partial \sigma_1}} \quad (12)$$

With f_{HB} given by Eq. (9) the derivative $\partial \sigma_3 / \partial \sigma_1$ is calculated by

$$\frac{\partial \sigma_3}{\partial \sigma_1} = 1 + nm \left(1 - m \frac{\sigma_1}{\sigma_c} \right)^{n-1} \quad (13)$$

4 SLOPE SAFETY BY FINITE ELEMENTS

The procedure used in this paper for determining F is outlined below and is a reduction scheme similar to the one applied by Brinkgreve & Vermeer (1998).

After satisfying equilibrium for the selfweight with the true material parameters a series of steps is repeated until equilibrium can no longer be satisfied. In each series of steps the material parameters are reduced gradually by a current safety factor F_i according to Eqs. (3) and (6). Index i denotes the step number with $i = 0$ signifying the establishing of equilibrium with the true material parameters, i.e. $F_0 = 1$. The procedure is outlined in Table 1.

A few comments should be tied to each of the steps in Table 1:

1. The series of current safety factors must be predetermined and the numerical distance between each factor must be reasonably small to determine the factor of safety accurately.
2. Step 2 will be elaborated upon in the following sections.
3. In the equilibrium iterations the stresses are updated according to principles of the return mapping scheme with a method outlined in (Clausen et al. in press).

4.1 Strength reduction for a Mohr-Coulomb material

The reduced material parameters of step 2 in Table 1 is found by inserting the current safety factor, F_i in Eq. (4). Equilibrium iterations are then carried out with these reduced parameters inserted in Eq. (8).

4.2 Strength reduction for a Hoek-Brown material

As mentioned in Section 3.2 there is no explicit relation between Eqs. (9) and (5). This implies that the material parameter reduction, step 2 in Table 1, is not as straight forward as in the Mohr-Coulomb case. The reduction procedure is outlined in Table 2. Some comments should be attached to steps 1 and 2 in Table 2:

1. The reduced non-linear Mohr-envelope is found by inserting the current safety factor, F_i in Eqs. (6) and (7).
2. In step 2 a number of stress points are transformed from $\sigma - \tau$ space into the principal stress space. This is done on the basis of Figure 6. The principal stresses are given by

$$\begin{aligned} \sigma_1 &= C + r & \text{with} & & C &= \sigma - \tau \tan \phi \\ \sigma_3 &= C - r & & & r &= \frac{\tau}{\cos \phi} \end{aligned} \quad (14)$$

Table 1. Procedure for calculating the safety factor.

1. The current safety factor F_i is chosen, $F_i > F_{i-1} \geq 1$
2. Reduced material parameters are established from F_i
3. Equilibrium iterations are performed IF global equilibrium can be satisfied go to step 1 ELSE take the factor of safety as $F = F_i$ END IF

Table 2. Procedure for reducing the Hoek-Brown material parameters, see step 2 of Table 1.

1. A reduced Mohr envelope is found from
 $S_{HB,i}(\sigma) = S_{HB}(\sigma)/F_i$
2. A number of stress points in principal stress space is generated on the basis of $S_{HB,i}(\sigma)$.
3. The parameters of a reduced Hoek-Brown criterion, $f_{HB,i}$ is found by regression analysis on the generated stress points.

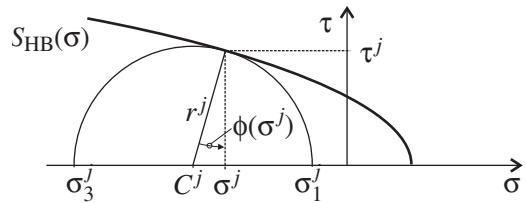


Figure 6. Calculation of principal stress points.

Here the centre and radius of the circle are denoted C and r , respectively. The instant friction angle is found by differentiation of Eq. (5)

$$-\tan \phi = \frac{d\tau}{d\sigma} \Rightarrow$$

$$\phi = \arctan \left(AB \left(\frac{\sigma_t - \sigma}{\sigma_c} \right)^{B-1} \right) \quad (15)$$

5 NUMERICAL EXAMPLE

Ahmad & Peaker (1977) carried out unconsolidated undrained triaxial tests on marine soft Singapore clay. Parameters of the Mohr-Coulomb and the Hoek-Brown yield criteria are calibrated against the reported test results. The regression is carried out by minimizing the

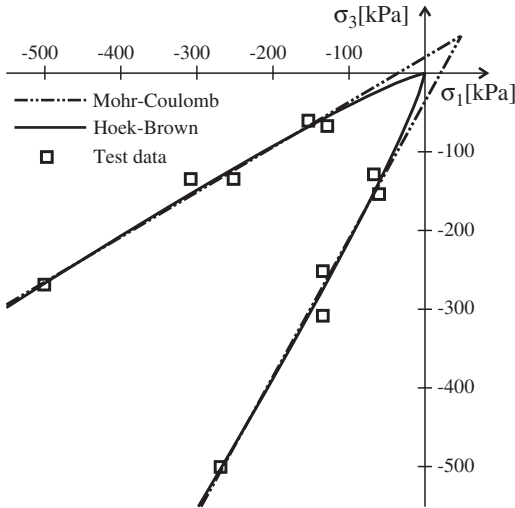


Figure 7. The Mohr-Coulomb and Hoek-Brown criteria fitted to test results.

Table 3. Calibrated yield parameters.

Yield criterion	Parameters
Mohr-Coulomb	$c = 13.5 \text{ kPa}$ $\varphi = 15.8^\circ$
Hoek-Brown	$\sigma_c \approx 0 \text{ kPa}$ $m = 66.5$ $n = 0.735$

sum of squares of the error of the fit. Effective stresses from the test results and the best fit of the two criteria can be seen in Figure 7.

In the range of the experimental test data the criteria are seen to be almost identical whereas significant differences can be seen in the range of small principal stresses. Attention should be drawn to the fact that the Mohr-Coulomb criterion predicts a tensile strength whereas this is not the case for the Hoek-Brown criterion. The resulting parameters are shown in Table 3. In addition to these parameters a selfweight of $\gamma = 15.5 \text{ kN/m}^3$, a modulus of elasticity, $E = 20 \text{ MPa}$, and a Poisson's ratio of $\nu = 0.26$ are assigned to the material.

It should be noted that σ_c can not be set to zero, cf. Eqs (9) and (5). For this reason it is set to a small value to represent zero uniaxial compressive strength, here $\sigma_c = 0.002 \text{ kPa}$.

5.1 Comparison between Hoek-Brown criterion and the non-linear Mohr envelope

To obtain the non-linear Mohr envelope of Eq. (5) ten $\sigma - \tau$ stress pairs in the experimental data range was formed from Eqs. (11) and (12). The parameter σ_t was found from Eq. (10) and the material parameters

Table 4. Calibrated yield parameters of the non-linear Mohr envelope, S_{HB} .

Envelope	Parameters
S_{HB}	$\sigma_t \approx 0 \text{ kPa}$ $A = 4.17$ $B = 0.7932$

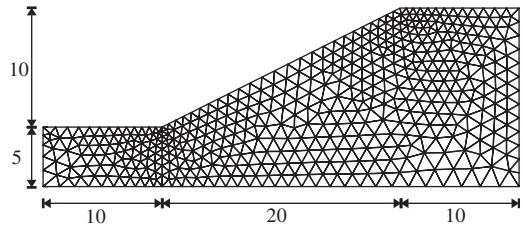


Figure 8. Geometry and element mesh of the analyzed slope. Measurements in m.

Table 5. Calculated slope safety factor.

Yield criterion	Safety factor
Mohr-Coulomb	1.47
Hoek-Brown	1.19

A and B was obtained by regression. The parameters for the Mohr envelope can be seen in Table 4.

A plot of S_{HB} translated into principal stresses by Eq. (14) can not be distinguished from the plot of f_{HB} with the resolution offered on Figure 7, which reveals a good agreement between the two expressions.

5.2 Safety factor calculation

The calculation of the safety factors is carried out on a slope of inclination 1:2 with geometry and element mesh as shown on Figure 8. A total of 902 six-noded linear-strain triangular elements with a total of 3818 degrees of freedom are used. The deformations are taken to be plain strain but the stress component out-of-plane is included in the finite element calculations. Failure was reached in about 35 steps for both materials.

The resulting safety factor for the two materials can be seen in Table 5. It is seen that the Hoek-Brown safety factor is significantly lower than the corresponding Mohr-Coulomb safety factor. The reason for this can be seen in Figure 9, where the stress contours for the smallest principal stress, σ_3 is outlined together with the position of the slip lines. It is seen that the locations of the slip lines are almost identical and that they are located predominantly between the contours of $\sigma_3 = -72 \text{ kPa}$ and $\sigma_3 = -30 \text{ kPa}$. From Figure 7 it is seen that the Hoek-Brown and the Mohr-Coulomb

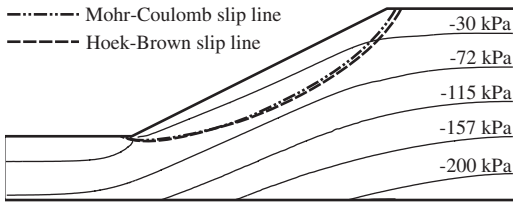


Figure 9. Slip lines and contour curves of smallest principal stress, σ_3 . Compression is negative.

Table 6. Reduced material parameters cf. Tables 3 and 5.

Yield criterion	Reduced parameters		
Mohr-Coulomb	$c = 9.2 \text{ kPa}$	$\varphi = 10.9^\circ$	
Hoek-Brown	$\sigma_c \approx 0 \text{ kPa}$	$m = 57.5$	$n = 0.732$

criteria differ significantly at these stress levels, whereas the two criteria almost coincide at stress levels $-500 \text{ kPa} < \sigma_3 < -150 \text{ kPa}$.

The reduced material parameters corresponding to a reduction by the safety factors in Table 5 are shown in Table 6.

6 CONCLUSIONS

A finite element methodology for calculating the slope safety factor with a non-linear yield criterion is presented. For a non-linear Hoek-Brown criterion it is not possible to translate explicitly between the formulations in $\sigma - \tau$ space and the principal stress space as opposed to the linear Mohr-Coulomb criterion. For this reason the parameter reduction is carried out by repeatedly fitting the yield criterion to a reduced Mohr envelope. In an example Mohr-Coulomb and Hoek-Brown parameters are fitted against the same test data and the safety factor of a slope is calculated. As the stresses in the slope are low compared to the

stresses at which the test data are obtained, the Hoek-Brown criterion predicts a lower slope safety than the corresponding Mohr-Coulomb criterion.

REFERENCES

- Ahmad, S. & K.R. Peaker 1977. Geotechnical properties of soft marine singapore clay. In *Proceedings of the International Symposium on Soft Clays*, pp. 3–14. Bangkok, Thailand.
- Baker, R. 2004. Nonlinear mohr envelopes based on triaxial data. *Journal of Geotechnical and Geoenvironmental Engineering* 130(5), 498–506.
- Balmer, G. 1952. A general analytic solution for mohr's envelope. *Proceedings-American Society for Testing and Materials* 52, 1260–1271.
- Brinkgreve, R. & P. Vermeer 1998. *Plaxis, Finite Element Code for Soil and Rock Analyses, Version 7*. A.A. Balkema, Rotterdam.
- Clausen, J. & L. Damkilde In prep. Finite element implementation of the hoek-brown yield criterion.
- Clausen, J., L. Damkilde, & L. Andersen 2006. Efficient return algorithms for associated plasticity with multiple yield planes. *International Journal for Numerical Methods in Engineering* 66(6), 1036–1059.
- Duncan, J.M. 1996. State of the art: Limit equilibrium and finite-element analysis of slopes. *Journal of Geotechnical Engineering* 122(7), 577–596.
- Griffiths, D. & P. Lane 1999. Slope stability analysis by finite elements. *Géotechnique* 49(3), 387–403.
- Gunaratne, M. 2006. *The Foundation Engineering Handbook*. Taylor & Francis.
- Hoek, E. & E.T. Brown 1997. Practical estimates of rock mass strength. *International Journal of Rock Mechanics and Mining Sciences* 34(8), 1165–1186.
- Jiang, J., R. Baker, & T. Yamagami 2003. The effect of strength envelope nonlinearity on slope stability computations. *Canadian Geotechnical Journal* 40, 308–325.
- Taylor, D. 1948. *Fundamentals of Soil Mechanics*. John Wiley, New York.
- Zheng, H., D. Liu, & C. Li 2005. Slope stability analysis based on elasto-plastic finite element method. *International Journal for Numerical Methods in Engineering* 64(14), 1871–1888.

A study on interslice force function and line of thrust in slope stability analysis

K. Aryal

Norwegian Road Authorities, Region West, District Office Bergen, Norway

L. Grande & R. Sandven

Geotechnical Engineering Division, Norwegian University of Science and Technology, NTNU, Trondheim, Norway

ABSTRACT: This paper presents a study of interslice force function which is used in slope stability analysis. The study was performed by both limit equilibrium (LE) and finite element (FE) analyses, where Morgenstern-Price, as LE method and PLAXIS software code, as FE method, were utilized. Moreover, a discussion has been presented among other LE methods, which differ basically from their assumptions for the inter slice force function. Additionally, an evaluation of line of thrust has been presented and discussed based on the pseudo-static analysis of a surcharged simple 10 m high slope.

The study reveals that the interslice force function can neither be a constant nor it follows a well defined pattern as assumed in LE analysis. The variation will largely depend on the geometry and loading conditions. This will have further effect on the factor of safety (FOS). However, the FE analysis shows a considerable difference in the interslice force function as compared to the sine function in LE (Morgenstern-Price) analysis. This shows a limitation in LE analysis which is unable to capture the localized interslice forces.

1 INTRODUCTION

Since many years, advanced limit equilibrium (LE) methods have been used for slope stability analysis. These methods consider both normal and tangential forces acting on slices. These forces are computed by dividing the entire sliding mass into a reasonable number of slices. Furthermore, the FOS is based on an assumed interslice force function where the computation is carried out by an iterative procedure (Janbu 1957).

Today, stability computations have been equally possible by the introduction of finite element (FE) codes. Among them, PLAXIS is the one which has been used here for the study of the force function.

2 LIMIT EQUILIBRIUM METHODS

2.1 The interslice force function

The interslice force function is defined as the ratio of tangential to normal forces acting on a slice. This function varies according to the assumptions made.

The fundamental difference in the assumptions has been summarized in Table 1.

Morgenstern-Price method (1965) assumes an arbitrary function ($f(x)$) with a scale factor (λ). Similarly, Janbu's GPS method (1957) relates the function to the inclination of the line of thrust. Likewise, Spencer (1967) assumed a constant function throughout the sliding surface. However, Sarma (1973) relates the relationship similar to the Mohr-Coulomb expression for shear strength.

Moreover, the function in Lowe-Karafiath (1960) method is assumed as a tangent to the average inclination of the slope and the sliding plane. However, the

Table 1. Interslice forces and relationships (Aryal 2006).

Morgenst-Price	$T = f(x) \lambda E$
Janbu GPS	$T = E \tan \alpha_t - h_t (dE/dx)$
Lowe-Karafiath	$T = E \tan \theta$, where $\theta = \frac{1}{2}(\alpha_1 + \beta)$
Corps of Engrs.	$T = E \tan \theta$, where $\theta = \frac{1}{2}(\alpha_1 + \alpha_2)$
Sarma	$T = ch + E \tan \phi$
Spencer	$T = E \tan \theta$

Corps of Engineers method (1970) considers the function as the average angle of the entry and exit points of the sliding surface.

2.2 The line of thrust

The line of thrust is defined along the point of application of the resultant of interslice forces. According to Janbu (1957), this line of thrust may fluctuate from 1/3 to 2/3 of the slice height from the base in active and passive conditions respectively.

Thus the assumption for the interslice force function in GPS method depends on the inclination of the line of thrust. The line of thrust and forces considered in the advanced LE methods are illustrated in Figure 1.

3 MODEL GEOMETRY AND INPUTS

The geometry and input parameters used in the study is shown in Figure 2. The model was analyzed in three different software programs SLOPE/W, SLIDE and PLAXIS. The first two softwares are based on LE principles.

The model was analyzed by selective LE method (M-P) and FE method (PLAXIS) assuming a dry slope

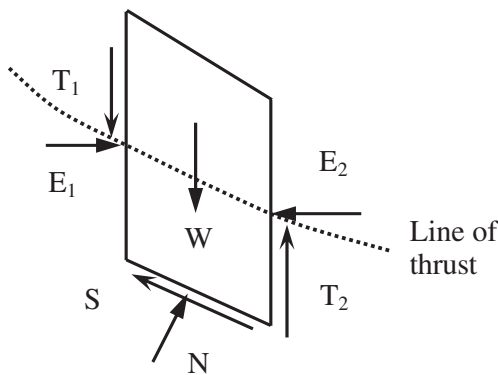


Figure 1. Forces considered in LE methods.

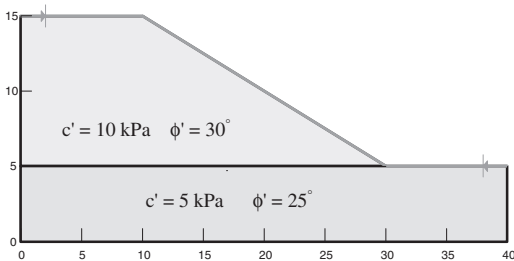


Figure 2. Slope model and input parameters (Aryal 2006).

with surcharge, $q = 50 \text{ kPa}$ at the crest and earthquake coefficient, $\alpha_h = 0.25$ (Aryal 2006).

The purpose of selecting typical soil properties similar to silty clay is to study the comparative difference in circular shear surface analysis using the software codes. The results related to the interslice force function and the line of thrust are presented and discussed here.

4 MODEL ANALYSIS RESULTS

4.1 Results of interslice force function

The interslice forces (T, E) were determined from the PLAXIS simulation at 1 meter interval. The ratio of these forces, $T/E = \lambda.f(x)$ were plotted together with similar results obtained from SLOPE/W and SLIDE for the M-P method.

Figure 3 shows the analysis results and comparison of the interslice force function for the analyzed load conditions. The slope profile and the shear surface (SS) obtained from PLAXIS simulations are also indicated by the dotted lines.

Mohr-Coulomb material model was selected in both SLOPE/W and SLIDE. Similarly, half-sine function (sine function but half cycle) was assumed. The interslice force function looks almost identical. SLOPE/W found exactly the same shape as half-sine function at the scale factor, $\lambda = 0.8$, whereas SLIDE shows a marginal difference in shape at a lower value of λ .

PLAXIS finds an irregular and contrast function with considerable difference at the crest and toe of the slope. The reason for the higher interslice shear force at the crest is the loaded surcharge. In the middle of the SS, the function is almost matching with the LE method. Since the function may vary with geometry and loading conditions, it is hard to generalize. Nevertheless, the study shows that interslice forces are not the same in LE and FE analyses, especially at the crest and toe of the slope (Aryal 2006).

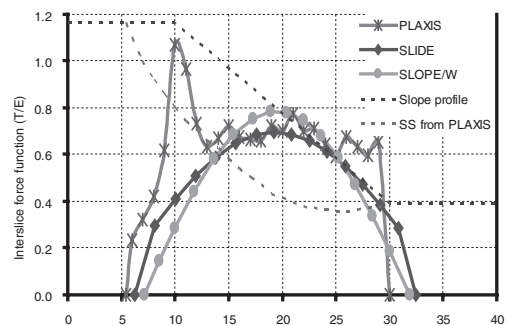


Figure 3. Comparison of interslice forces (Aryal 2006).

4.2 Results of line of thrust

The plot in Figure 4 shows the location of the line of thrust obtained from SLIDE (M-PM) and PLAXIS simulations. Moreover, the dotted lines indicate the CSS and slope profile.

The points of application of interslice resultant force are not the same in FE and LE analyses. In PLAXIS, the point was considered at the location where the normal force was found. However, the option for automatic generation of the line of thrust was utilized in SLIDE. Even if the location for the line of thrust may not show similar pattern for different geometry and loading conditions, it can be noticed the considerable disagreement between LE and FE computations.

The LE (M-PM) analysis gives the line of thrust lower at the crest; slightly higher in the middle and unreasonably high at the toe. This finding indicates that the sine function does not represent the static situation very well at the toe (Aryal 2006).

Ideally the thrust line in Janbu's GPS method should be located between 0.2h and 0.4h from the base of the shear surface, where h is the height of the slices (Abramson et al. 2002). Janbu (1973) states, "the line of thrust should be located somewhat lower than h/3 in the active zone (crest) and higher than h/3 in the passive zone (toe) for cohesive soils".

5 EFFECTS ON FACTOR OF SAFETY

The FOS primarily depends on the normal stress at the shear surface as seen from equations 1 and 2. Moreover, the normal stress is also a function of the interslice shear force as given in Equation 3.

$$F_m = \frac{\sum(c'l + (N - ul) \tan \phi')}{\sum W \sin \alpha} \quad (1)$$

$$F_f = \frac{\sum [\{ c'l + (N - ul) \tan \phi' \} \sec \alpha]}{\sum \{ W - (T_2 - T_1) \} \tan \alpha + \sum (E_2 - E_1)} \quad (2)$$

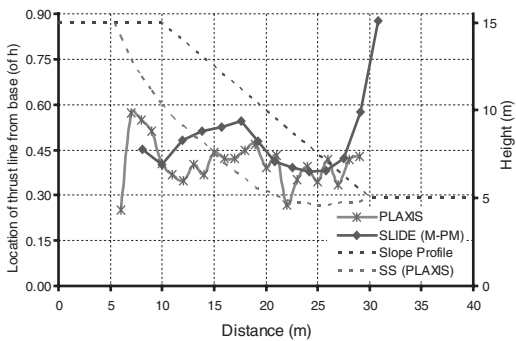


Figure 4. Location of the line of thrust (Aryal 2006).

$$N = \frac{1}{m_\alpha} \left\{ W - (T_2 - T_1) - \frac{1}{F} (c'l - ul \tan \phi') \sin \alpha \right\} \quad (3)$$

The LE based Morgenstern-Price method iterates for the FOS until the moment equilibrium (Equation 1) and the force equilibrium (Equation 2) give a constant value. This FOS can be found at the intersection point in Figure 5. Lower interslice shear force generally gives higher normal force (Equation 3). If this is the case, the FOS will be overestimated observing at Equations 1 and 2.

In addition to the half-sine function, constant and variable functions were also studied in both SLOPE/W and SLIDE softwares. However, the change in FOS was found insignificant (<0.5%) in Morgenstern-Price method for circular shear surface. This shows that selection of interslice force function in LE analysis may have no change in the FOS if the moment equilibrium curve has no change in gradient (Aryal 2006).

However, another study (SLOPE/W 2002) shows that interslice force function causes significant shifting in the force equilibrium FOS. If the moment equilibrium FOS also shifts upwards, as shown in Figure 5, the intersecting point will have higher FOS compared to the previous one.

From the studies, it can be concluded that the effect of interslice force function is a case dependent. If one of the curves is parallel to the axis, there is no any effect on the FOS for Morgenstern-Price method. On the other hand, there can be considerable shifting of both curves resulting change in FOS.

As seen in Figure 3, PLAXIS computes more accurately the interslice forces under the surcharge location than LE software. The application of surcharge load will definitely increase in interslice shear force which has nicely been captured in PLAXIS. In such condition, the higher interslice shear force will lower the

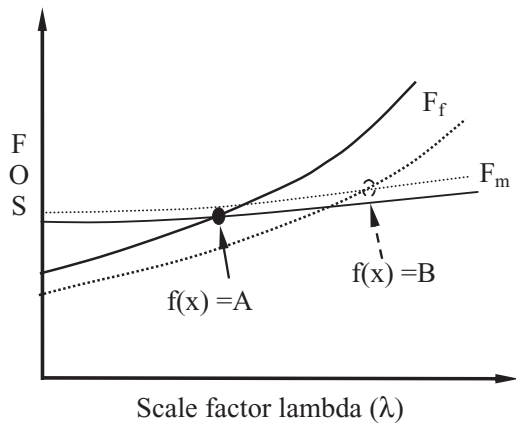


Figure 5. Effect on FOS due to f(x) (SLOPE/W 2002).

FOS. This situation is observed at the crest and toe of the simple slope referring again to Figure 3.

Thus the difference in the interslice force function and the line of thrust found in LE and LE analysis will have variations in the FOS. This explains why the LE based methods compute higher FOS than the FE based ones. The ultimate differences in FOS can easily be understood considering the difference in the base normal force.

6 CONCLUSIONS

The interslice force function can neither be a constant nor a well defined pattern as assumed in LE methods. The variation will largely depend on the geometry and loading conditions. This will have an effect in the FOS.

The FE analysis in PLAXIS shows a consideration difference in the interslice force function as compared to the assumed sine function in LE (Morgenstern-Price) analysis. Thus the LE methods are unable to capture the localized interslice forces.

The line of thrust is not similar in SLIDE and PLAXIS. The assumed sine function in Morgenstern-Price method gives exceptionally unrealistic thrust line at the toe. Thus the LE methods are found less accuracy to compute forces especially at the crest and toe of a slope. Due to these differences, the FOS in LE analysis differs from those obtained from FE analysis.

7 SYMBOLS AND ABBREVIATIONS

α	inclination of the sliding plane
α_1	inclination at the entry point
α_2	inclination at the exit point
α_t	inclination of the line of thrust
β	slope inclination angle
ϕ	internal friction angle
ϕ'	effective friction angle
λ	scale factor
θ	inclination of interslice resultant force
c	apparent (total) cohesion
c'	effective cohesion

h	average height of a slice
h_t	height from mid point of the slice to dE
dE	change in interslice normal force
l	length of slice along sliding surface
$m\alpha$	factor based on slope α
u	pore pressure
E	interslice normal force
F_f	force equilibrium FOS
F_m	moment equilibrium FOS
N	normal force
S	shear force (strength)
T	interslice shear force
W	weight of the slice

REFERENCES

- Abramson, L.W., Lee, T.S., Sharma, S., and Boyce, G.M. (2002). *Slope Stability Concepts*. Slope Stabilisation and Stabilisation Methods, Second edition, published by John Wiley & Sons, Inc., pp. 329–461.
- Aryal, K. (2006). *Slope stability evaluation by LE and FE methods*. Ph D thesis, Norwegian University of Science and Technology, NTNU
- Corps of Engineers (1970). *Slope Stability manual. EM 1110-2-1902*, Washington, DC: Department of the Army, Office of the Chief Engineers.
- Janbu, N. (1973). *Slope Stability Computations*. Embankment Dam Engineering, Casagrande Volume, pp. 47–86.
- Janbu, N. (1957). *Earth pressure and bearing capacity calculations by generalised procedure of slices*. Proceedings of the 4th International Conference, SMFE, London, 2, pp. 207–12.
- Lowe, J., and Karafiath, R.V. (1960). *Stability of Earth Dam upon Drawdown*. Proceedings of the of the first Pan American Conference on Soil Mechanics and Foundation Engineering, Mexico City, pp. 537–52.
- Morgenstern, N.R. and Price, V.E. (1965). *The Analysis of the Stability of General Slip Surfaces*. Geotechnique, Vol. 15, No. 1, pp. 77–93.
- Sarma, S.K. (1973). *Stability Analysis of Embankment and Slopes*. Geotechnique, Vol. 23 (3), pp. 423–33.
- SLOPE/W (2002). *Stability Analysis*. Users Guide Version 5, GeoSlope Office, Canada. www.geoslope.com.
- Spencer, E. (1967). A method of Analysis of the Stability of Embankments, Assuming Parallel Interslice Forces. Geotechnique, Vol. 17, pp. 11–26.

Sensitivity analyses of global stability in sanitary landfills

I. Petrovic & D. Kovacic

University of Zagreb, Faculty of Geotechnical Engineering, Varazdin, Croatia

T. Ivsic

University of Zagreb, Faculty of Civil Engineering, Zagreb, Croatia

F. Veric

Geoekspert, Zagreb, Croatia

ABSTRACT: The global stability of landfills is influenced by many factors including wide range of parameters. To establish the influence of selected parameter on global factor of safety, the sensitivity analysis was carried out. Three main groups of parameters were defined: strength parameters of waste and bottom liner, geometrical parameters (slope of disposed waste, position and shape of failure surface, appearance of tension cracks) and variations of leachate level. In addition, global factor of safety was also analyzed using stress state data along the failure surface obtained by finite element method. This procedure establishes a relatively new approach compared to the well-established limit equilibrium methods.

1 INTRODUCTION

Global stability of the sanitary landfill is one of the dominant problems in the landfill design from the geotechnical point of view. In order to ensure the stability of landfill the design considerations should include the stability of waste, bottom liner and drainage layers, as well as the stability of foundation soil.

The stability of landfill is affected by the wide range of parameters. Similar to common geotechnical design for embankment stability, the design situations for landfill consider the geometry of the design section, the strength parameters of main materials and the influence of possible pore pressures (leachate in waste). In order to estimate the influence of single parameters on the global stability, the sensitivity analyses were performed. Three main groups of variable parameters were studied encountering basic unfavorable design scenarios: the strength parameters (cohesion and friction angle of waste and bottom liner), leachate level (due to possible clogging of drainage system) and geometrical issues like the slope of dumped waste, the appearance of tension crack in slope and the contribution of the edge embankment to global stability.

2 METHODS AND BASIC PARAMETERS

The design stability of landfills is usually verified by common limit equilibrium methods. Although the

applicability of these methods for waste landfill is often questioned, their routine use in many geotechnical applications makes them still a popular tool for common design. Actually, the main goal in most geotechnical design analyses is not to exactly replicate all physical conditions, but to simulate crude stability mechanisms and apply an adequate margin of safety against unfavorable event.

The limit equilibrium methods are based on rigid body static principles. They do not consider the deformations of the real body and stress-strain compatibilities. Due to these reasons the distribution of stresses along the sliding plane may not be realistic in many cases. To overcome this deficiency, and still remain in “practical” design domain, the hybrid procedure can be used. The more realistic stress distribution is obtained by stress-strain FEM analysis and then the average factor of safety is obtained using calculated mobilized stresses along the sliding plane and appropriate strength values.

The stability analyses in this paper are performed by both methods. As a representative for limit equilibrium method the Janbu-simplified method is chosen, which is often routinely used for the polygonal sliding surfaces. The analyses are made by program package Slope/W (later referred as Method 1), and critical sliding surfaces are obtained. The stress state in landfill body is obtained by program package Sigma/W, using finite element method in elasto-plastic analysis.

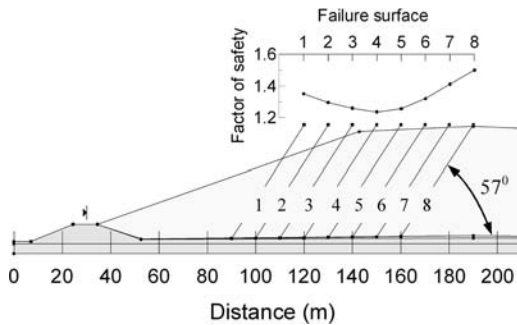


Figure 1. The analyzed landfill section with polygonal failure surfaces.

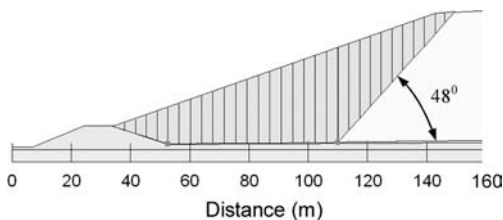


Figure 2. The position and shape of the most critical failure surface.

The resulting stresses are returned to Slope/W program and average factor of safety for the same critical sliding surface is obtained using Finite Element Stress option in that program (Method 2).

The basic data for the analyses are obtained from design documentation of waste landfill Jakusevec in the City of Zagreb in Croatia.

The analyzed sliding surfaces were chosen as polygonal surfaces with bottom part passing through bottom liner and upper part passing through waste. The slope of the waste part of sliding surface is inclined to horizontal at an angle $45 + \phi'/2$ (Rankine's active state plane). The referent geometry of analyzed landfill cross section is shown in Figure 1. The position of sliding surface with minimal factor of safety (No. 4) is also shown.

Although the assumption of Rankine active plane is common in design procedures, additional analysis was made to investigate the most critical inclination of failure surface in waste body. The bottom position and the inclination of failure surface were varied (the range of angles was $45-65^\circ$) and the most critical surface is shown in Figure 2. The bottom point is closer to the surface No. 3 from Figure 1 and the inclination is much lower (48° for Janbu method). It seems that the redistribution of forces is not too significant, since the minimal factor of safety is only about 4% lower than with

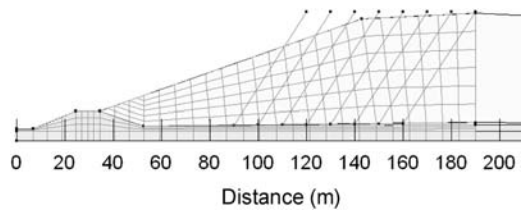


Figure 3. The finite element mesh for Method 2.

the Rankine plane assumption. For the rest of analyses the surfaces presented in Figure 1 were used.

The mesh of finite elements with overlapped failure surfaces used in Method 2 is shown in Figure 3.

The range of strength parameters for waste was selected to represent the common suggested design values (Ivšić et al. 2004). The values for bottom liner are selected as a conservative choice of geomembrane-clay residual interface strength.

The following referent values and range of values are used in the analyses:

Referent parameters:

- waste: $\gamma = 13 \text{ kN/m}^3$; $c' = 19 \text{ kPa}$; $\phi' = 24^\circ$
- bottom liner: $\gamma = 20 \text{ kN/m}^3$; $c' = 0$; $\phi' = 12^\circ$

Range of parameters:

- waste: $c' = 5.5-19 \text{ kPa}$; $\phi' = 24-33^\circ$
- bottom liner: $\phi' = 10-13^\circ$

The referent parameters for elasto-plastic stress-strain analysis were:

- waste: $E = 1000 \text{ kPa}$; $\nu = 0.3$; $c' = 19 \text{ kPa}$; $\phi' = 24^\circ$
- bottom liner: $E = 7800 \text{ kPa}$; $\nu = 0.3$; $c' = 0$; $\phi' = 24^\circ$

3 RESULTS OF ANALYSES

3.1 Variation of strength parameters

The results of analyses (factors of safety) for the variation of waste and bottom liner friction angles are presented in Figure 4. As expected, the factors of safety become greater as the strength parameters rise. Also, a general observation is that the Method 2 (finite element stresses) gives significantly higher values of safety factor.

In order to obtain the relative values of presented results, the factors of safety are normalized to reference value ($F_S = 1.236$) from the Janbu method. These normalized results are summarized in Figure 5, and the following can be deduced:

- in the analyzed range of waste friction angles the change of factors of safety was about 20%, giving an average of 2.2% per unit degree of waste friction angle.

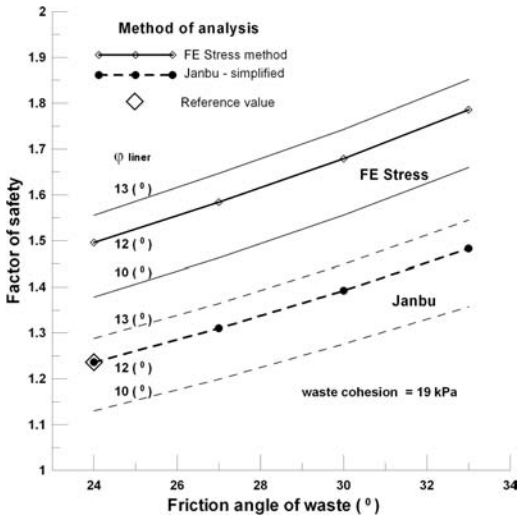


Figure 4. Factor of safety in relation to friction angle of waste (with range of values of bottom liner friction angle).

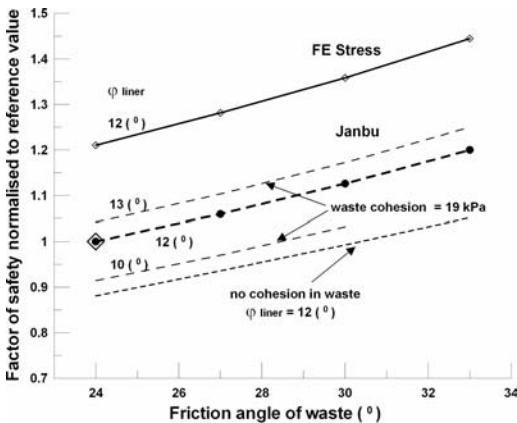


Figure 5. Factor of safety in relation to friction angle of waste – normalized values (summary of main results).

- the range of safety factors for the variation of bottom liner friction angles is from 0.91 to 1.04 of reference values, giving about 4% of variation per unit degree of bottom liner friction angle.
- the results for simultaneous change of both parameters can be estimated from the presented graphs.
- the safety factors curves for Method 1 and Method 2 are approximately parallel, so the same unit variations are obtained. The Method 2 consistently gives about 20% higher factors of safety, which will be commented later.

The results for waste cohesion variation (not presented in figures) show that for the analyzed range of waste

Table 1. Variation of safety factor within the range of strength parameters (comparing to reference value).

Parameter	Change of safety factor (%)	
	Method 1	Method 2
Waste cohesion	–8 to 10*	–7 to 9*
Waste friction angle	+20	+18–20*
Bottom liner friction	–9 to 4	–10 to 3
Loss of waste cohesion	–12	–12

* Range of results due to bottom liner friction variation.

cohesion extreme difference of 8–10% is obtained, depending on bottom liner friction angle. This gives the average variation of 0.65–0.75% per 1 kPa of cohesion.

It is understood (e.g. König & Jesberger 1997) that the cohesion of waste originates from fibrous waste components. During damping and compacting of waste all the components are mixed giving quasi homogeneous material with macroscopic average cohesion and friction angle. In situation when fibrous components are missing, or on the contact plane of older and new waste where the “waste homogenization” cannot occur, the cohesion part of waste strength is lost. This situation was also analyzed and the results in Figure 5 show that the factor of safety without waste cohesion is more than 12% lower than the reference value with $c' = 19$ kPa. Summary of variation results is presented in Table 1.

3.2 Change of leachate level

It is quite common case that rise of leachate level, especially after prolonged period of heavy rain, becomes a triggering mechanism of failure event in waste landfills (Koerner & Soong 1999). Excess pore pressures generated due to rise of leachate level have detrimental effect on the effective stresses in waste body which finally results with lower shear strength of waste.

Therefore, the analysis of changes in leachate level on factor of safety value is performed. In this analysis the strength parameters of waste were fixed to the referent values, while the strength parameters of bottom liner were changed in the mentioned range. The leachate level was raised in 5 meters increments, in range from 0 to 15 meters with respect to the bottom liner.

The results of analysis show nonlinear changes in factor of safety value due to rise of leachate level. Method 1 shows that acceptable values of factor of safety are obtained only for higher values of friction angle in bottom liner (namely 12° and 13°), up to 5 meters height of leachate level. Method 2 gave acceptable factor of safety values up to almost 10 meters height of leachate level regardless of the friction angle

value of bottom liner. It was also noticed that Method 2 yields higher factor of safety values than Method 1 for all values of leachate levels, as well as for the all values of friction angle in bottom liner.

From normalized factor of safety values (the results are normalized with respect to the factor of safety value obtained for case with dry waste body) it turned out that for leachate level of 15 meters both methods gave 20 to 25% reduced factor of safety.

Obtained results indicate that the increase of leachate level in waste body greatly reduces the global factor of safety. Consequently, it is crucial in the design of landfill to ensure high quality drainage system which will last during the operational as well as in the post closure time of landfill.

3.3 Variation of landfill geometry parameters

In the process of landfill design it is important to define the geometric features of the landfill in such way that mechanical stability of landfill is ensured. Some of the geometry parameters which must be defined prior to construction of the landfill are inclination of waste slope and edge embankment height.

The inclination of waste slope was varied in range from 1:2 to 1:3 with increments of 0.25, while the strength parameters of waste and bottom liner were fixed at referent values. During the analysis the embankment was excluded from analysis in order to simulate the worst case scenario. The results of analysis show that change in waste slope inclination gives nonlinear change in factor of safety values. In order to obtain the relative values of results, the factors of safety are normalized to reference value ($F_S = 1.236$) from the Janbu method. From these results it was noticed that the change in inclination of waste slope from 1:2 to 1:3 gives 20% higher factor of safety value.

The influence of edge embankment height to global stability was also analyzed. As a retaining structure in the toe of the landfill, the embankment has favorable effect on the factor of safety value. The change of embankment height was varied from 0 to 10 meters, in increments of 1 meter. The strength parameters of waste were fixed at referent value, while the strength parameters of bottom liner were changed in previously defined range. The obtained results show that change of factor of safety values in this analysis was also nonlinear. As expected, the factor of safety values became greater while increasing the embankment height.

The obtained results are normalized to reference value ($F_S = 1.073$), which is the factor of safety value for the case without embankment. Normalized values revealed that maximum height of embankment (in this case 10 meters) yields change in factor of safety value, with respect to referent value, of about 25%, regardless of the friction angle value of bottom liner. The average change per unit degree of embankment

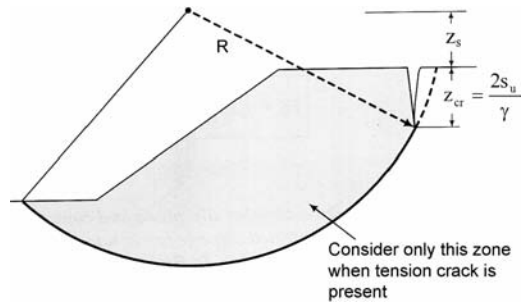


Figure 6. Appearance of tension cracks in waste body.

height is 2.5%. This high percentage of change suggests that embankment height could be very important design parameter.

In addition, the influence of tension cracks to global stability was checked, simulating possible appearance of cracks in upper zone of landfill. The depth of tension cracks was varied from 5 to 25 meters, in increments of 5 meters, while the strength parameters of waste and bottom liner were fixed at referent values. It was also assumed that cracks could be filled with water from 0 to 100% of its depth. For dry and 50% saturated cracks the results show increasing of safety factor with deepening of crack. This happens because the appearance of tension crack reduces active forces which act on failure surface. For fully saturated cracks the hydrostatic pressure cancel out the positive effect of reduced active forces. The additional destabilizing moment M_w caused by hydrostatic pressure is defined with equation 1.

$$M_w = \frac{1}{2} \gamma_w z_{cr}^2 \left(z_s + \frac{2}{3} z_{cr} \right) \quad (1)$$

where γ_w is unit weight of water, z_s is vertical distance from slope crest to the center of failure surface and z_{cr} is defined according to Figure 6.

The relative values of results, normalized to reference value ($F_S = 1.212$) which is the factor of safety value for the fully saturated tension crack, are presented in Figure 7. From Figure 7 it could be noticed that, for maximum depth of tension cracks, factor of safety value rise for about 11% and 18% for dry and 50% saturated tension cracks, with respect to the referent value. Fully saturated tension cracks give 15% decrease in factor of safety value, with respect to the referent value.

Due to the modeling difficulties which appeared during the tension crack analysis for all geometrical analysis only Method 1 was carried out.

Summary of variation results is presented in Table 2.

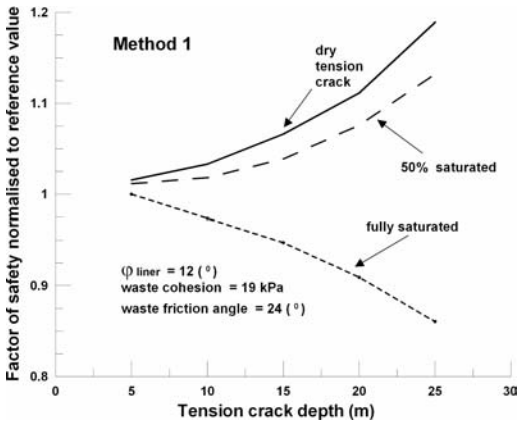


Figure 7. Factor of safety vs. crack depth (normalized curves).

Table 2. Variation of safety factor within the range of geometrical parameters (comparing to reference value).

Parameter	Change of safety factor (%) Method 1
Waste inclination	-20%
Embankment height	+25%
Tension cracks	+18%*; +11%**; -15%***

* Dry tension crack.

** 50% saturated tension crack.

*** Fully saturated tension crack.

4 COMPARISON OF METHODS

The analyses of strength parameters and leachate level variation with both methods have shown that the factors of safety obtained by Method 2 are significantly higher than the factors in Method 1.

The difference in factors of safety comes from different stress distribution which is shown in Figures 8–9. The presented stress distribution curves are obtained from the analyses results for sliding surface No. 4 (Fig. 1) and referent strength parameters of waste and bottom liner.

The normal stresses along the sliding surface are generally similar for both methods. They are practically identical in middle part of sliding surface where the bottom of surface is horizontal and the weight of overburden is normal to the failure plane (in this part the assumptions for methods of slices are fulfilled). Some slight differences occur in the sloping parts of sliding surface where the influence of shear stresses in Method 2 becomes evident.

The basic difference is in distribution of mobilized shear stresses as shown in Figure 9. For limit

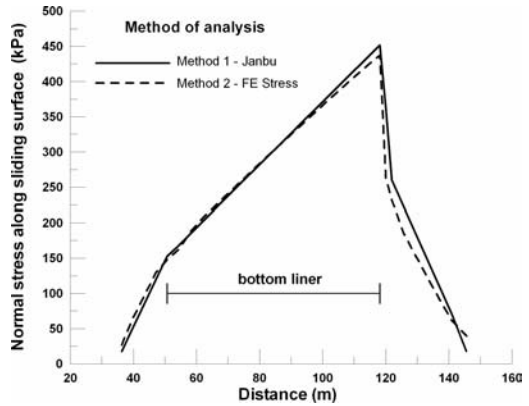


Figure 8. Distribution of normal stresses along the sliding surface.

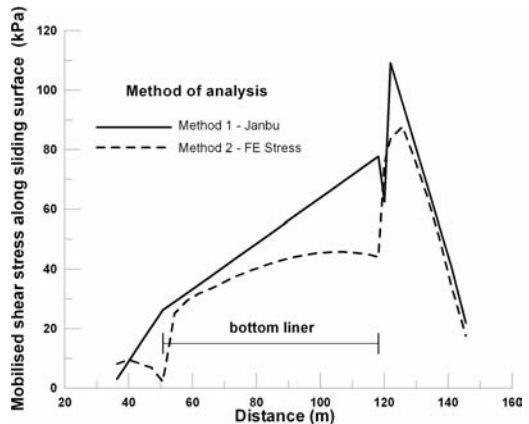


Figure 9. Distribution of mobilized shear stresses along the sliding surface.

equilibrium methods the mobilized shear stresses are obtained from strength distribution and average factor of safety. In finite element method the deformation compatibility must be satisfied and the stresses are redistributed to satisfy this condition. This redistribution results in much lower mobilized stresses in bottom part of sliding surface (also retained by the edge embankment). In the waste part of sliding body the mobilized stresses are similar. Since the shear strength in both methods is proportional to normal stresses (generally similar in both methods), the difference in average safety factor comes from difference in mobilized shear stresses.

In Janbu simplified method the effect of interslice shear forces is neglected. In practice, the average overall empirical correction factor may be applied to the calculated factor of safety as compensation. For

the presented geometry of failure surfaces the correction factor of about 1.09 is valid. Multiplying the values of safety factor from Janbu method with this correction factor gives 9% higher values than those presented in Figures 4–5. By this, the presented difference between methods becomes lesser, but still more than 10% higher results are obtained by Method 2.

5 CONCLUSIONS

Waste landfill is unique type of object. Proper design of waste landfills requires interdisciplinary approach of wide variety of experts. Between them, the geotechnical engineer has important role to ensure mechanical stability of waste landfill for proper functioning of all landfill components.

Sensitivity analyses were performed for variation of common parameters and critical design situations. The rate of influence of selected parameter on global factor of safety was determined.

The following conclusions can be drawn from the presented results:

- The results of strength parameters variation in common range demonstrate that factor of safety is most sensitive to change in bottom liner friction angle (for the given geometry of critical sliding plane)
- Rise of leachate level in waste body has strong influence on factor of safety value. For leachate height of 15 meters, in comparison to “dry tomb” landfill, the factor of safety value is reduced to more than 20%
- Inadequate temporary or final waste inclination could cause failure of waste body. Change of waste inclination from 1:3 to 1:2 reduces factor of safety value for 20%. It should be also noticed that the inclination of 1:2 can be considered as an upper bound of inclination for waste slopes
- Fully saturated tension cracks, due to high hydrostatic pressure, cause drop of the factor of safety

- values. Dry or 50% saturated tension cracks have beneficiary influence to the factor of safety values
- Embankment height has beneficial effect to factor of safety value. For embankment height of 10 meters, in comparison to the case without embankment, factor of safety value is increased for about 25%
- Conventional limit equilibrium methods give conservative results of safety factors. It is recommended to perform a stress-strain analysis in order to obtain more realistic stress distribution in landfill profile. The stresses from this analysis can than be used to calculate the average factor of safety along the selected failure surface which is comparable to conventional procedure

REFERENCES

- Ivsic, T. et al. 2004. Overview of parameters for stability analyses on waste disposal sites. *Građevinar* 56(2004)11: 665–674 (in Croatian).
- Jones, D.R.V. & Dixon, N. 2003. Stability of Landfill Lining Systems: Report No. 1 – Literature Review (R&D Technical Report P1-385/TR1). Bristol: Environment Agency.
- Jones, D.R.V. & Dixon, N. 2005. Landfill lining stability and integrity: the role of waste settlement. *Geotextiles and Geomembranes* 23: 27–53.
- Koerner, R.M. & Soong, T. 1999. Assessment of Ten Landfill Failures Using 2-D and 3-D Stability Analysis Procedures: 2. Österreichische geotechniktagung.
- Konig, D. & Jesberger, H.L. 1997. Waste Mechanics, Report of the ISSMFE TC5 on Environmental Geotechnics, Bochum.
- Krahn, J. 2004. Stability Modeling with SLOPE/W. Calgary: GEO-SLOPE/W International Ltd.
- Petrovic, I. 2005. Mechanical stability problems of waste landfills. Zagreb, M.Sc. Thesis, University of Zagreb, Faculty of Civil Engineering.

Numerical analysis of the behaviour of a cut slope in stiff clays by finite difference method

P. Lollino & F. Santaloia

National Research Council, Irpi, Bari, Italy

A. Amorosi & F. Cotecchia

Technical University of Bari, Italy

ABSTRACT: This paper concerns the instability process occurring on a cut slope in stiff clays located at the north of the town of Lucera (Southern Italy). This unstable slope lies between a hospital at the top and an abandoned quarry at the toe, which was active until the end of the 1970s. A first landslide was triggered around 1980 and was characterized by a subsequent retrogressive activity. This paper presents the results of a coupled elasto-plastic finite difference analysis of the slope behaviour carried out with FLAC^{2D}, outlining a possible interpretation of the landslide mechanism. The input data have been defined according to field surveys and laboratory investigations on the involved clays. The numerical results show that during the excavation stages the negative excess pore water pressures due to undrained unloading allowed for a temporary slope stability and that subsequently the process of pore pressure equalization caused the slope failure.

1 INTRODUCTION

The equalization of negative excess pore water pressures due to excavation in clay deposits has been recognized as a possible cause for delayed failure of slopes. In particular, this process has been shown to control “first-time” landslides in stiff overconsolidated clays, long time after excavation (Skempton 1970, 1977, Vaughan & Walbancke 1973, Chandler & Skempton 1974, Chandler 1984). According to these Authors, in the short term, undrained unloading causes a temporary decrease of the pore pressures within the portion of the slope influenced by the excavation and therefore induces a stabilizing effect of the slope. In the long term, the slow equalization of the negative excess pore pressures with the new boundary conditions defined by the excavation can eventually be responsible for the slope failure. This process depends on several factors, such as the consolidation properties of the soil, the geometry of the problem, the stress state of the soil, the hydraulic conditions within the slope (Chandler 1984, Potts et al. 1997). In recent years, several authors have dealt with this problem by means of numerical studies, highlighting the need to use coupled numerical techniques for an appropriate prediction of the time-dependent stress-strain response of the slope (Potts et al. 1997, Adachi et al. 1999, Hoshikawa et al. 1999).

The present paper discusses a numerical analysis of the failure process occurred within a slope in stiff clays

which had previously been subjected to excavation at the toe due to quarrying, between the first decades of the past century and the 1970s (Lucera landslide, South Italy). A first landslide occurred around 1980, i.e. some years after the quarry had been abandoned. Recently, a retrogressive evolution with a wider and deeper failure surface has involved the parking area of a public hospital located on the top of the hill.

An interpretation of the 1980 landslide mechanism is proposed in this paper based upon field and laboratory investigations and numerical analyses. The slope behaviour has firstly been studied by means of geological and geomorphological investigations, in-situ monitoring and laboratory testing of the soils. Thereafter, a coupled elasto-plastic finite difference numerical analysis has been carried out with the code FLAC^{2D} (ICG 2000) in order to investigate the influence on the slope behaviour of the variations with time of the pore pressure regime following the excavation.

2 EVOLUTION OF THE GEOLOGICAL AND GEOMORPHOLOGICAL SETTINGS

The instability process involves the stiff clays outcropping on the northern slope of the Lucera hill (Figure 1). These clays belong to the Sub-Apennine Clay Formation (Pliocene-Early Pleistocene) and are overlain by alluvial sands and conglomerates, lying at the top of the

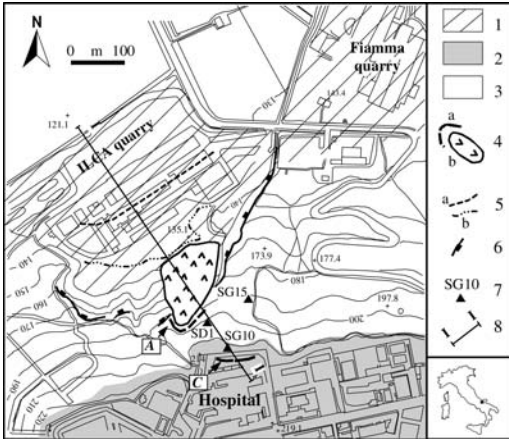


Figure 1. Geological-geomorphological map of the study area. Key: 1) fill of the quarry, 2) terraced alluvial deposits, 3) Sub-Apennine Clays, 4) landslide (a-crowns; b-landslide body), 5) toe of the slope (a-1954, b-1975), 6) current quarry front, 7) boreholes discussed in the paper, 8) line of section shown in Figure 2.

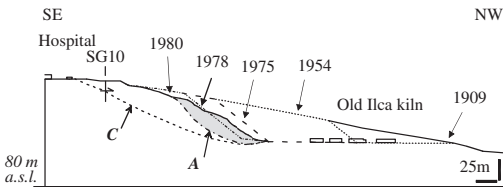


Figure 2. Evolution of the slope profile between 1909 and 1980 (A and C refer to failure surfaces shown in Figure 1; landslide body A is highlighted in grey).

hill (Terraced alluvial deposits; Pleistocene). Several continuous coring boreholes, of depth ranging between 10 and 75 m, were drilled throughout the slope and equipped with either piezometers or inclinometers (Figure 1). Undisturbed samples were also taken from different depths during the coring of the boreholes.

The unstable slope lies below a hospital at the top of the hill, which was built during the 1980s, and an abandoned quarry is present at the toe (Figure 1). The rate of the quarry excavation, which lasted from the first decades of the past century to the end of the 1970s, has been defined by means of the analysis of multi-year aerial photos, historical data and topographical maps (Figures 1 and 2, Santaloia et al. 2004). At the end of the seventies, when the quarry front reached the maximum height of about 50 m, the slope excavation was stopped and the quarry was abandoned without any retaining structure (Figure 2). Around 1980, a rotational landslide, 25 m deep, here named landslide A, occurred in the slope where the quarry front was highest (Figures 1 and 2, Santaloia et al. 2004). In 1998, a more extended

and deeper mass movement developed as a retrogression of the first sliding process (landslide C in Figures 1 and 2).

The pore water pressure regime has been monitored by means of piezometers: the water table is found at a depth between 5 and 10 m below ground level within the top area of the slope and at 2–3 m below ground level at the toe of the slope.

3 GEOTECHNICAL PROPERTIES OF THE SOIL

The soil variability in the slope is quite limited and the slope can be considered a stiff grey clay deposit of fairly uniform geotechnical properties. The mean values of the index properties and of the mechanical properties of the soil samples tested in the laboratory are reported in Table 1. The clay is overconsolidated, of medium plasticity (IP = 24%), with a relatively low void ratio ($e = 0.58$) and an undrained shear strength, c_u , of about 180 kPa at 20 m depth. The value of the coefficient of permeability, k , as measured by means of oedometer testing, has been found to be in the range $5\div7 \times 10^{-11}$ m/s; the consolidation coefficient, c_v , is approximately equal to 1.2×10^{-7} m²/s and the swelling coefficient, c_{vs} , is about 3×10^{-7} m²/s. Consolidated-undrained triaxial tests (CIU) have been carried out on undisturbed samples taken at various depths along borehole SG15 (Figure 1), while one consolidated-drained test (CID) has been performed on an undisturbed sample taken down borehole SD1 (see Figure 1). Figure 3 shows the q - p' stress paths resulting from the tests. The peak shear strength envelope, according to the Mohr-Coulomb failure criterion, is characterised by intercept cohesion $c' = 30$ kPa and friction angle $\phi' = 22^\circ$. The shear behaviour of the soil is scarcely brittle, with a post-peak decay beginning from a strain level in the range $\epsilon_a = 8\div10\%$. The elastic parameters have been estimated according to the undrained triaxial test data. The decay in shear stiffness, G , with shear strain, ϵ_s , as resulting from seven triaxial tests, is plotted in Figure 4. The shear modulus generally reduces from values in the range $G = 40\div60$ MPa at a strain level of about $\epsilon_s = 0.02\div0.03\%$, to values ranging between 10 and 30 MPa at $\epsilon_s = 0.1\div0.3\%$, and decreases further at larger strain levels.

4 NUMERICAL ANALYSIS OF THE SLOPE BEHAVIOUR

4.1 Model assumptions

In order to study the influence on the activation of the first mass movement (landslide A) of the process of equalization of the negative excess pore pressures

Table 1. Index properties and mechanical properties of the Lucera clay.

γ_d kg/m ³	IP %	e	G OCR kPa	ν	c'_p kPa	ϕ'_p k m/s	ψ °
1740	24	0.58	5.5	2×10^4	0.25	30	$22 \cdot 7 \times 10^{-11}$
				7×10^4			
				14×10^4			

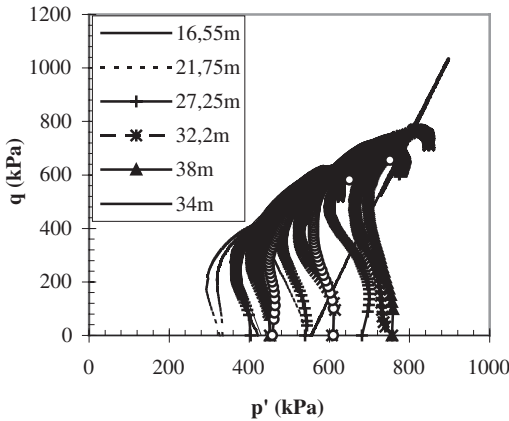


Figure 3. Consolidated undrained and drained triaxial tests on Lucera clay.

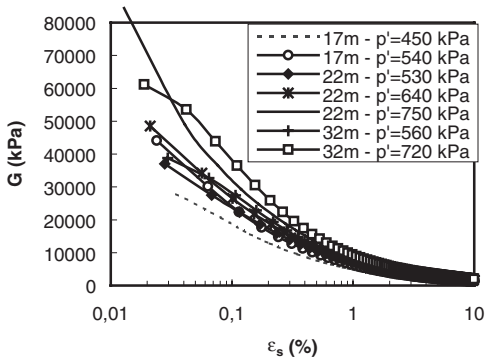


Figure 4. G - ϵ_s curves from undrained triaxial tests on Lucera clay.

resulting from the quarry excavation, a plane-strain numerical analysis has been performed with the finite difference code FLAC^{2D} (ICG 2000). The grid, formed of quadrilateral elements, is shown in Figure 5 and corresponds to section 1 in Figure 1. Coupled elastoplastic behaviour of the soil mass has been assumed in the analysis. A non-associated elastic-perfectly plastic model with a Mohr-Coulomb yield surface has been used to model the clay behaviour. The observed values

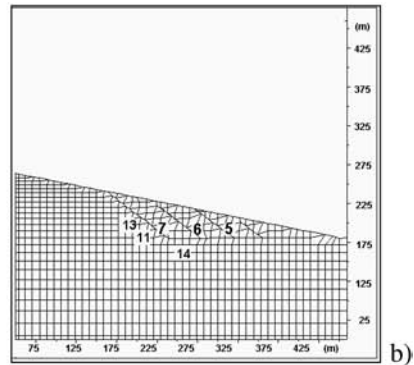
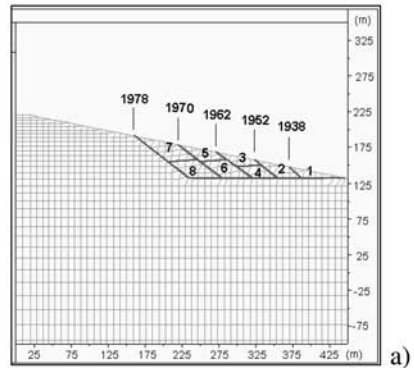
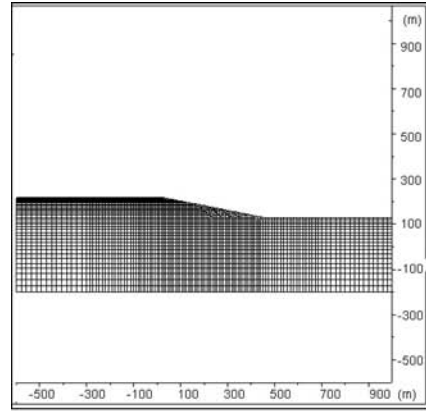


Figure 5. Grid adopted for FLAC^{2D} analysis; 5a. excavation stages simulated in the analysis; 5b. location of the monitoring gridpoints.

of intercept cohesion and friction angle at peak have been adopted as strength parameters for the soil (see Table 1), since the clay is scarcely brittle and at first-time failure. The coefficient of permeability has been assumed equal to that measured in the oedometer tests

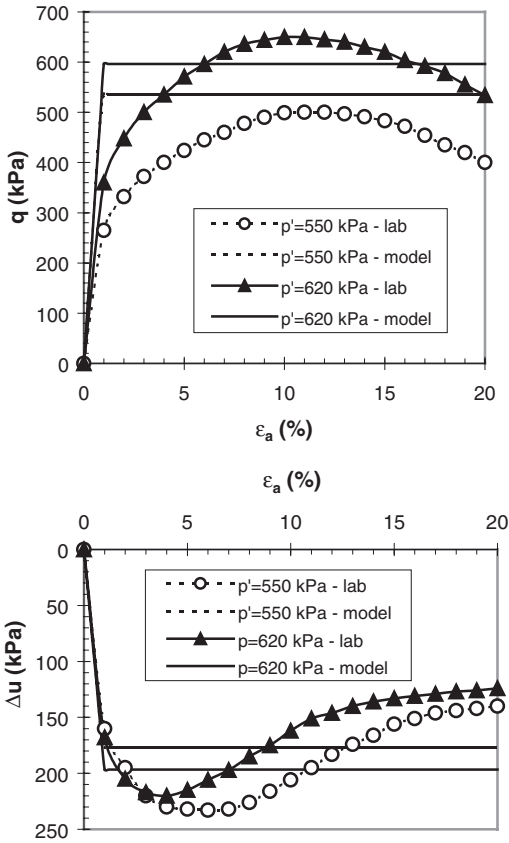


Figure 6. Comparison between observed and simulated curves of undrained triaxial tests on Lucera clay.

($k = 7 \times 10^{-11}$ m/s). To account for the increase in shear stiffness with depth, the grid has been divided into three layers, each characterised by increasing values of the shear modulus (Table 1). In particular, the mean value of G measured in the triaxial tests for $\varepsilon_s = 0.1\div 0.3\%$ has been chosen for the shallowest layer, which is the one mainly involved in the failure mechanism (see Figure 4). The value of the swelling coefficient, c_{vs} , implicitly adopted in the analysis is resulted to be consistent with the value observed in laboratory. A poisson ratio, ν' , equal to 0.25 has been assumed in the whole grid. Figure 6 reports a comparison between the clay behaviour observed in two CIU triaxial tests and the corresponding numerical back-predictions. The plot shows that the curves are in good agreement, despite the relatively simple constitutive model adopted.

The first stage of the numerical analysis was aimed at modelling the initial (elastic) equilibrium conditions under gravity loading. In order to define the initial steady-state pore water pressure regime, a seepage

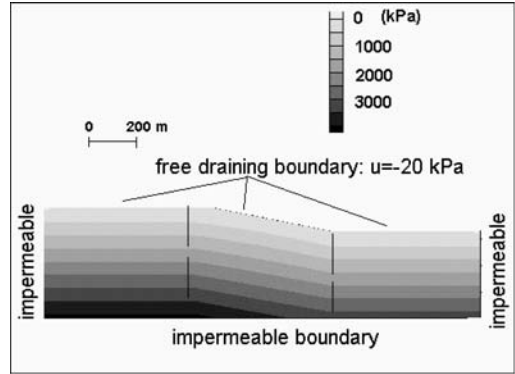


Figure 7. Steady-state pore pressure distribution assumed in the analysis.

calculation has been performed in accordance with the boundary conditions assumed to apply before the beginning of the quarrying activity. The pore pressure distributions at both the side boundaries of the model have been assumed to be hydrostatic. A piezometric level at 8 m depth has been assumed to exist at the top of the slope, at 60 m distance from the crest, whereas a piezometric level at 2 m depth has been considered at the toe of the slope, in accordance with the field measurements. A free-draining surface boundary, with a suction $u_b = -20$ kPa, has been imposed both on the original ground surface and along the excavation boundary, according to field measurements performed in clay deposits of southern Italy (Piscitelli & Urciuoli 2002, Gullà et al. 2004). The resulting steady pore water pressure distribution is reported in Figure 7. The comparison between the calculated values of the pore pressure and those recently measured by two piezometers (SD2 and SG16 in Figure 1) within the slope, assuming steady state conditions, has been found to be acceptable. The excavation process, from 1920 to 1978, has been simulated according to the rate of the quarry activity, as reconstructed by means of the available data (Figures 2 and 5a). Each stage of the excavation has been modelled by removing the corresponding elements and by simulating both an undrained calculation and a subsequent coupled consolidation, which has been developed with time intervals consistent with the rate of the excavation process.

4.2 Results

The results of the analysis are consistent with the observed behaviour of the slope. In particular, they show that during the cultivation of the quarry the slope was stable, although the consolidation process was already in progress. As indicated in Figure 8, which shows the contours of cumulated shear strains predicted at the

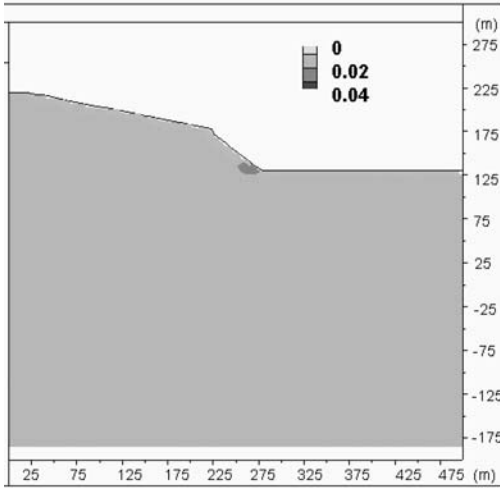


Figure 8. Contours of cumulated shear strains predicted at the end of the consolidation analysis of the 4th excavation stage (1962).

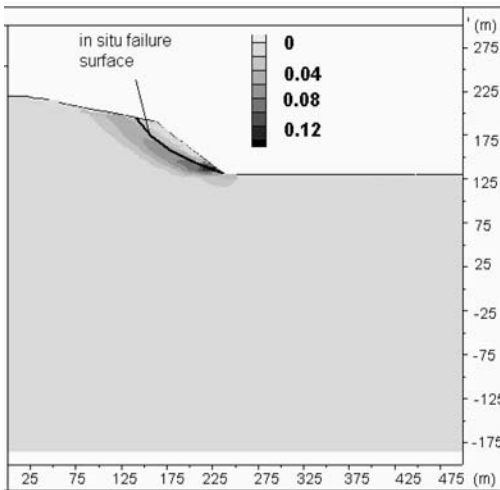


Figure 9. Contours of cumulated shear strains predicted during the last consolidation analysis (1980).

end of the consolidation analysis of the 4th excavation stage (1962), a small shear zone is calculated in the area of the current toe of the slope. A clear collapse mechanism, indicated by a shear zone connecting the toe and the top of the slope, is instead predicted during the consolidation analysis following the last excavation stage, at a timestep approximately corresponding to 1980 (Figure 9). Figure 9 reports the contours of the shear strains calculated at this stage, which agree well

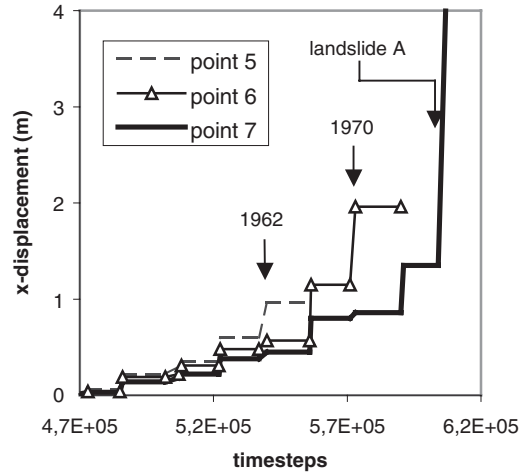


Figure 10. Calculated horizontal displacements against timesteps for three monitoring points.

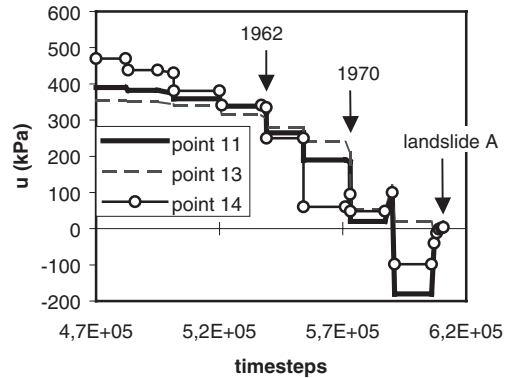


Figure 11. Calculated pore water pressures against timesteps for three monitoring points.

with the shape of the failure surface deduced from in-situ observations. This result confirms that landslide A can be identified as a first-failure mechanism of the slope.

The evolution with time of the behaviour of the slope is well illustrated in Figures 10 and 11, the first reporting the horizontal displacements calculated for gridpoints located at the toe of three stages of the quarry face (1962, 1971, 1978; Figure 5b) against timesteps and the second reporting the pore pressures calculated for three gridpoints within the slope against timesteps. Figure 10 highlights that during the consolidation stages of the analysis for each position of the slope profile a significant increment of the displacement of the toe occurs. The rate of increment suggests a tendency of

the slope to a long-term failure, which is not reached during the quarrying activity, due to the on-going excavation process. During the last consolidation stage (1975–1980), the displacement of the toe of the final slope profile (gridpoint 7) experiences a dramatic acceleration which clearly indicates failure conditions according to the FLAC^{2D} iteration procedure. Figure 11 shows the effect of the undrained unloading in terms of negative variations of the pore pressures calculated for the undrained stages of the analysis. Thereafter, during the subsequent consolidation stages, a process of partial equalization develops.

5 CONCLUSIONS

A finite difference analysis of the behaviour of the Lucera slope has been carried out with FLAC^{2D} to validate an interpretation of the landslide process occurred within the slope, according to which the failure has been triggered by the equalization of the negative excess pore pressures induced by the quarry excavation at the toe. The results of the numerical study, which has been defined according to geological and geomorphological investigations, in-situ monitoring and laboratory testing of the soils, have confirmed the proposed hypothesis and have shown that the collapse was a first-failure mechanism of the slope. The analysis has also pointed out that the risk of failure, for slopes in stiff clays subjected to excavation at the toe, must account for the time necessary for negative consolidation to develop. Also the study has shown that, in general, to predict the time development of this class of processes, numerical procedures which account for the soil-water coupling effects within the soil mass must be developed.

REFERENCES

- Adachi, T., Oka, F., Osaki, H., Fukui, H. & Zhang, F. 1999. Soil-water coupling analysis of progressive failure of cut slope using a strain softening model. In Yagi, Yamagami & Jiang (eds), *Slope Stability Engineering*: 333–338. Rotterdam: Balkema.
- Chandler, R.J. 1984. Delayed failure and observed strengths of first-time slides in stiff clays: a review. *Proc. IV Intern. Symp. Landslides, Toronto*, 2: 19–25.
- Chandler, R.J. & Skempton, A.W. 1974. The design of permanent cutting slopes in stiff fissured clays. *Géotechnique* 24(4): 457–464.
- Gullà, G., Niceforo, D., Ferraina, G., Aceto, L. & Antronico, L. 2004. Monitoring station of soil slips in a representative area of Calabria (Italy). In Lacerda, W.A., Ehrlich M., Fontoura, S.A.B. & Sayão, A.S.F. (eds), *Landslides: Evaluation and Stabilization; Proc. IX Intern. Symp. Landslides, Rio de Janeiro, 28 June–2 July 2004*. Rotterdam: Balkema.
- Hoshikawa, T., Nakai, T. & Nishi, Y. 1999. Coupled excavation analyses of vertical cut and slopes in clay. In Yagi, Yamagami & Jiang (eds), *Slope Stability Engineering*: 333–338. Rotterdam: Balkema.
- ITASCA Consulting Group 2000. *FLAC Version 4.0, User's Guide*, Minneapolis, USA.
- Piscitelli, F. & Urciuoli, G. 2002. Regime delle pressioni neutre in frane di colata in argille varicolori. In Evangelista A. & Pellegrino A. (eds), *Campi sperimentali per lo studio della stabilità dei pendii*: 27–34. Benevento: Hevelius.
- Potts, D.M., Kovacevic, N. & Vaughan, P.R. 1997. Delayed collapse of cut slopes in stiff clay. *Géotechnique* 47(5): 953–982.
- Santaloia, F., Lollino, P., Amorosi, A., Cotecchia, F. & Parise, M. 2004. Instability processes of stiff clayey slopes subjected to excavation. In Lacerda W.A., Ehrlich M., Fontoura S.A.B. & Sayão A.S.F. (eds), *Landslides: Evaluation and Stabilization; Proc. IX Intern. Symp. Landslides, Rio de Janeiro, 28 June–2 July 2004*. Rotterdam: Balkema.
- Skempton, A.W. 1970. First-time slides in overconsolidated clays. *Géotechnique* 20(3): 320–324.
- Skempton, A.W. 1977. Slope stability of cuttings in brown London Clay. In *Proc. 9th Int. Conf. Soil Mech. Found. Engng.*, Tokyo, 3: 261–270.
- Vaughan, P.R. & Walbancke, H.J. 1973. Pore pressure changes and the delayed failure of cutting slopes in overconsolidated clay. *Géotechnique* 23(4): 531–539.

Simulation of a large excavation using a Hoek-Brown model

Thomas Benz

University of Stuttgart & Federal Waterways Engineering and Research Institute, Karlsruhe, Germany

Regina Kautner & Radu Schwab

Federal Waterways Engineering and Research Institute, Karlsruhe, Germany

ABSTRACT: The Hoek-Brown criterion is widely used in practice to evaluate the strength of rock masses. It starts from the properties of intact rock and introduces factors to reduce these properties on the basis of joint characteristics within the rock mass. In this paper, the 2002 edition of the Hoek-Brown criterion is used as the failure envelope of a nonlinear elastic-perfectly plastic constitutive model. The nonlinear elastic part of the proposed model takes into account the closure of cracks in the small stress domain, which is a significant feature of a rock mass' deformation characteristics in typical civil engineering applications. Numerical results from the proposed model are presented in a case study. In this, the model is calibrated in back-analyzing laboratory and in-situ borehole dilatometer test data obtained for the new Minden lock excavation. In the example, the influence of crack closure and rock mass strength on slope deformation and failure is studied.

1 INTRODUCTION

This paper is concerned with the numerical simulation of rock masses using the Hoek-Brown (HB) failure criterion in a nonlinear elastic – perfectly plastic constitutive model. The brief description of the model and its numerical implementation found in the first part of this paper follows a practical application in its second part: The new Minden navigable lock excavation in siltstone/claystone.

In the past, the deformation characteristics of rock masses has been studied by numerous researchers (Eberhardt et al. 1998). Based on the stress–strain behavior shown in Figure 1, Bienawski (1967) for example, defines five stages in the stress–strain behavior of rock masses: (a) Crack closure gradually occurs until the normal stress reaches a threshold value σ_{cc} . During crack closure, stiffness increases as pre-existing cracks successively close. Crack closure is particularly important to near-surface structures; (b) Linear elastic behavior is encountered once the majority of existing cracks is closed; (c) Stable micro-fracturing is found after the crack initiation stress σ_{ci} is reached; (d) Crack growth becomes then unstable for stresses exceeding the threshold value σ_{cd} . The threshold stress σ_{cd} marks at the same time the stress at which volumetric strains reverse; (e) Rock masses may show either ductile or brittle failure depending on geology, confining

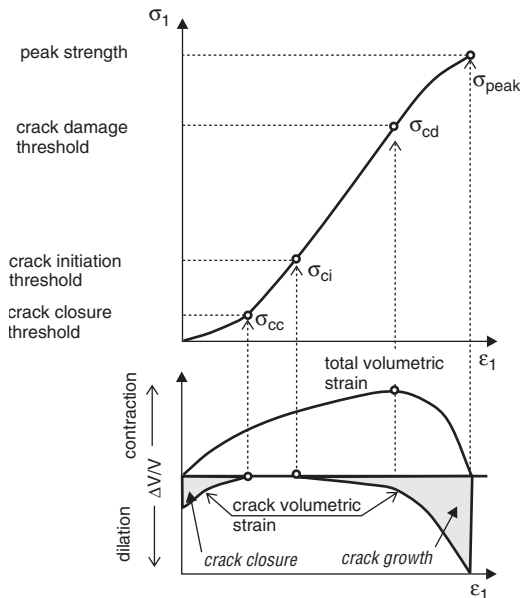


Figure 1. Behavior of fractured rock in uniaxial compression (after Eberhardt et al. 1999)

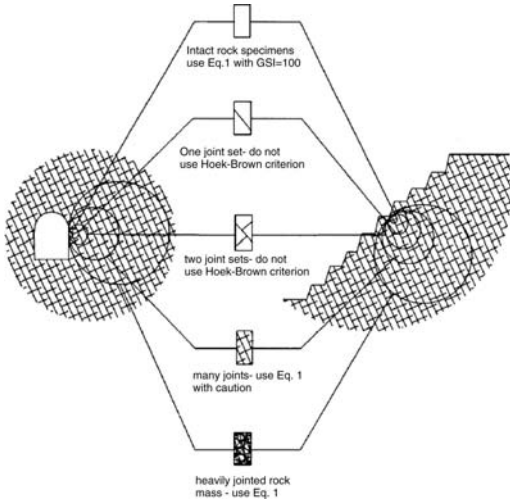


Figure 2. Diagram showing the idealized transition from intact to heavily jointed rock masses with increasing sample size (modified after Hoek 2004).

pressure, and temperature. In the proposed constitutive model, crack closure (a) is simulated by means of a simple nonlinear elastic law. After crack closure, the model is linear elastic up to failure. After failure, the rock is assumed to be perfectly plastic. As failure criterion serves the HB criterion.

The HB criterion was derived from studies on the behavior of jointed rock masses (Hoek and Brown 1980) and is often used in practice. The criterion starts from the properties of intact rock and then introduces factors to reduce these properties on the basis of joint characteristics within the rock mass. The original criterion was subsequently changed in order to adapt it to the behavior of weak rock masses, as well. In the following, the generalized HB criterion (2002-Edition) presented in Hoek et al. (2002) is used. In their paper, Hoek et al. also derive equivalent parameters for the Mohr-Coulomb (MC) failure criterion using a best-fit procedure within a given stress domain. However, there is no direct theoretical relationship between the HB and the MC criterion. Any attempt to estimate equivalent cohesion and friction values in gravitational stress fields will thus be inaccurate. The curvilinear HB criterion automatically accommodates changing stress fields, the MC criterion does not.

Although rock masses typically show both, inherent anisotropy and stress induced anisotropy caused by the evolution of crack systems in an inhomogeneous stress field, the HB criterion was initially introduced to predict failure in quasiisotropic rock masses (Figure 2). The constitutive model proposed here is likewise isotropic. In the following, the sign convention of soil mechanics is used: Compressive stress and strain

is taken as positive. Tensile stress and strain is taken as negative. All stresses are taken to be effective values.

2 THE CONSTITUTIVE MODEL AND ITS IMPLEMENTATION

2.1 Governing equations of the HB criterion

The generalized HB criterion is expressed as:

$$\sigma_1 = \sigma_3 - \sigma_{ci} \left(m_b \frac{\sigma_3}{\sigma_{ci}} + s \right)^a \quad (1)$$

where σ_1 and σ_3 are the maximum and minimum effective stresses at failure respectively, m_b is the value of the Hoek-Brown constant m_i for the rock mass,

$$m_b = m_i \exp \left(\frac{GSI - 100}{24 - 14D} \right) \quad (2)$$

σ_{ci} is the uniaxial compressive strength of intact rock and s and a are constants which depend upon the rock mass characteristics given by the following relationships:

$$s = \exp \left(\frac{GSI - 100}{9 - 3D} \right) \quad (3)$$

$$a = \frac{1}{2} + \frac{1}{6} \left(\exp \left(\frac{-GSI}{15} \right) - \exp \left(\frac{-20}{3} \right) \right) \quad (4)$$

The Geological Strength Index (GSI), introduced by Hoek (1994) provides a system for estimating the reduction in rock mass strength under different geological conditions. The Geological Strength Index takes into account the geometrical shape of intact rock fragments as well as the condition of joint faces. Finally, D is a factor that quantifies the disturbance of rock masses. It varies from 0 (undisturbed) to 1 (disturbed), depending on the amount of stress relief, weathering and blast damage as a result of nearby excavations. For the significance of the parameters and their values see (Hoek 2004).

2.2 Yield surface and plastic potential

The Hoek-Brown failure surface in principal stress space is shown in Figure 3. Taking into account a strength reduction factor (RF), which reduces material strength for $RF > 1.0$, the model's yield surface is written as:

$$f = \sigma_1 - \sigma_3 - \frac{\sigma_{ci}}{RF} \left(m_b \frac{\sigma_3}{\sigma_{ci}} + s \right)^a \quad (5)$$

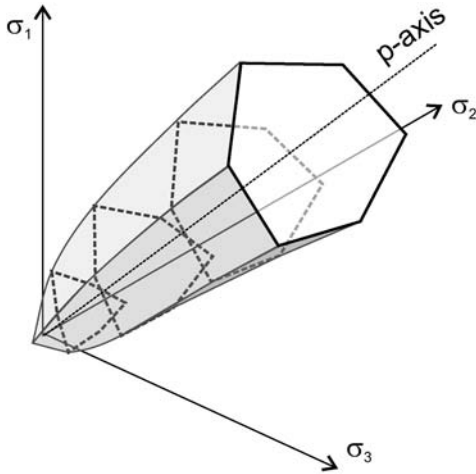


Figure 3. Hoek-Brown criterion in principal stress space.

Trial stresses outside the yield surface are returned to it with a Drucker-Prager potential:

$$g = q - p \left(\frac{6 \sin \psi_{mob}}{3 - \sin \psi_{mob}} \right) \quad (6)$$

where p and q are the Roscoe invariants and ψ_{mob} is the mobilized angle of dilatancy. With increasing minor principal stress, the initial angle of dilatancy ψ is reduced to 0 in a linear manner. The minor principal stress at which zero volumetric plastic flow is reached and the initial angle of dilatancy ψ are model parameters.

2.3 Elastic stiffness

The simulated pre-failure rock mass behavior consists of: (a) a nonlinear crack closure domain and (b) a linear domain. Stable plastic crack propagation and the gradual stiffness degradation associated to it is neglected in the model proposed. The nonlinear stress-strain behavior can be simulated by piecewise linear, hyperbolic or exponential stiffness approximations (Lahaie et al. 2002, Kaselow and Shapiro 2003). The piecewise linear approximation shown in Figure 4 is adopted here. Poisson's ratio is assumed constant.

2.4 Implementation issues

The maximum allowable tensile stress for which the HB criterion is defined calculates as:

$$\sigma_{Tens} = -\sigma_{ci} \frac{s}{m_b} \quad (7)$$

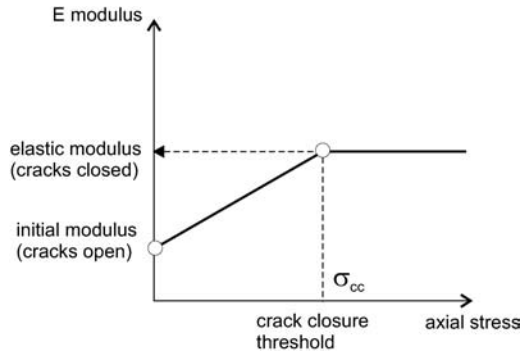


Figure 4. Stress dependant stiffness in the open crack domain.

For tensile stresses below the maximum allowable one, the yield surface is undefined. Therefore, the first stress return for trial stresses outside the yield surface is always conducted to a circumscribed Drucker-Prager yield surface.

3 MODEL APPLICATION – THE NEW MINDEN LOCK EXCAVATION

3.1 The new Minden navigable lock

The so called ‘Schachtschleuse’ Minden, built 1913, is located at Germany’s Mittelland Canal. The lock chamber has a length of 85 m and a width of 10 m. In order to adapt the Minden lock to the new ship generation (2100 t ships), a new lock chamber is projected in close vicinity of the existing lock. For the construction of the new lock a 25 m wide, 250 m long and 18 m deep excavation pit is necessary.

The soil profile (from top to bottom) is made up of an up to 15 m thick layer of inhomogeneous fill, followed by a 3.5 m thick layer of quaternary sands and gravels of sometimes very high density. The bottom layer is composed of tertiary fine grained clastic sedimentary rocks (siltstone/claystone), which usually show a weathering profile.

The excavation pit has a slope of about 10 m height in the sedimentary rock. The face angle is 70°. After the interpretation of the geological general information, the examination of photos from the old lock’s excavation pit, and existing soil data that have been acquired in the near vicinity, a preliminary exploration program was carried out. The exploration program comprised 6 boreholes and 6 cone penetration tests. In the boreholes, 8 water pressure tests and 9 dilatometer tests were conducted at different depths to determine the permeability and the stiffness parameter of the rock. In the laboratory, rock samples were tested for their unconfined compressive strength (UC-tests).

Three sets of discontinuities were observed in the drill cores, which results in a orthogonal joint structure: the bedding planes which decline with values between 0 and 12, a vertical joint family and one which declines under an angle of 45. According to DIN EN ISO 14689-1, spacing of the bedding is characterized as “thin” (200 to 60 mm) and joint spacing as “medium” (600 to 200 mm).

3.2 Model parameter selection

The new Minden lock excavation is located in a relatively homogeneous rock layer (Figure 7). All parameters and tests discussed in the following refer therefore to that specific rock layer only. Based on geological evidence, the Hoek-Brown constant m_i is assumed as 8. The uniaxial compressive strength σ_{ci} of the siltstone/claystone is determined as 2000 kPa. The rock mass disturbance D depends on the respective experiment or calculation. It is assumed that $D = 0.0$ for unconfined compression tests, $D = 0.2$ for dilatometer tests, and $D = 0.7$ for the excavation. The Geological Strength Index (GSI) equals 100 for samples subjected to unconfined compression. In situ, the discontinuities described above reduce the strength index to GSI ≈ 55 –65. The GSI value is later verified in the numerical simulation of dilatometer tests. First, however, the model’s stiffness parameters are quantified in a back-analysis of unconfined compression tests.

Back-analysis of unconfined compression tests

From unconfined compression tests, the linear elastic stiffness for the model proposed is determined to 208 MPa (cracks closed). Its initial stiffness is quantified to 10 MPa (cracks opened). Figure 5 shows the unconfined compression tests used in the stiffness determination. These tests can be basically grouped in two sets. Both sets have approximately the same stiffness in the linear domain. However, their nonlinear

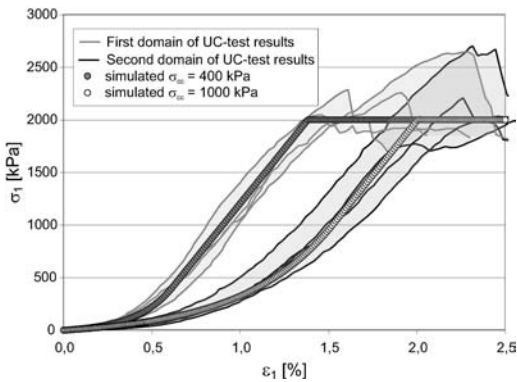


Figure 5. Simulation of unconfined compression tests.

behavior at the onset of testing is significantly different. These differences might be explained and modelled by a variation of the threshold stress σ_{cc} at which all pre-existing cracks are closed. From the back-calculation, σ_{cc} is found to vary between 400 kPa and 1000 kPa.

Back-analysis of dilatometer tests

Knowing most of the model’s strength parameters and having calibrated all its stiffness parameters, the GSI value can now be calibrated from dilatometer test data. Figure 6 shows two test results and their simulation with the strength index GSI = 55. The difference in the two calculated stress–strain curves is solely due to the above discussed variation in the threshold stress σ_{cc} .

3.3 Analysis of the new Minden lock excavation

In the following, a simplified calculation of the new Minden lock excavation is presented. The rock is actually not dry like assumed in the calculation. The actual geometry is also more complex than the one shown in Figure 7. However, for the purpose of demonstrating the possibilities of the constitutive model, the simplified calculation seems adequate. The finite element

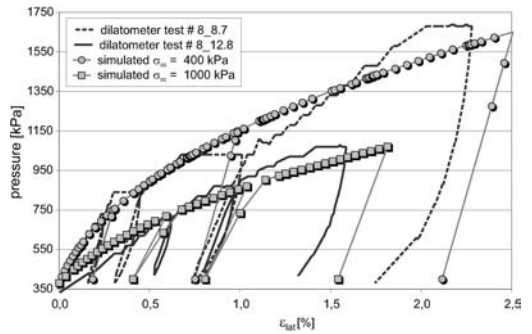


Figure 6. Simulation of dilatometer tests.

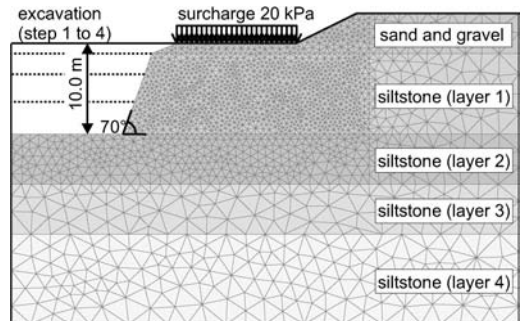


Figure 7. Geometry and finite element mesh used in the excavation analysis.

code used in the 2D plane strain analysis is Plaxis V8 (Brinkgreve 2002). Calculation results are compared to results obtained in an equivalent linear elastic – perfectly plastic analysis using the MC failure criterion. The equivalent MC strength parameters ($\varphi = 31.2^\circ$, $c = 39\text{ kPa}$) have been obtained by the method proposed in Hoek et al. (2002). Note that these parameters are less conservative than these used in the preliminary design as presented in Kautner and Herten (2006).

Slope failure

Slope failure is reached in the HB calculation by factorizing material strength by means of the factor introduced in Equation 5. In successively decreasing material strength until failure, finally the limit state is found. This scheme is basically identical to the well known φ - c reduction scheme used in the equivalent MC calculation. However, the level of safety, quantitatively expressed in the strength reduction factor and the factor of safety obtained in the φ - c reduction are not directly comparable. In the example, the HB calculation gave a strength reduction factor of 1.2. The factor of safety found in the MC analysis is 1.5. As the equivalent MC parameters can only poorly fit the HB criterion in the highly nonlinear domain around the apex of the yield surface, it is yet reasonable that

the HB analysis reaches failure first. Figure 8 shows the respective shear strain distributions at failure. Obviously, the HB calculation gives a much steeper failure surface.

Figure 9 highlights the failure mechanisms for different GSI values by visualizing incremental displacements at failure. The strength reduction factor (RF) is now below 1.0 for GSI = 40 and 3.5 for GSI = 70. The failure mechanism for GSI = 70 resembles the one observed in the equivalent MC calculation shown before.

Slope deformation

Figure 10 illustrates calculated horizontal slope deformations for unreduced material strength. Again, results from the equivalent linear elastic – perfectly plastic MC analysis are compared to results from the nonlinear elastic – perfectly plastic HB analysis. In the latter, the threshold stress σ_{cc} is set to the limiting values found in the backanalysis of the unconfined compression tests. Both, deformation pattern and deformation magnitude is different in the HB and the equivalent MC analysis. In the HB analysis, the variation of σ_{cc} leads to a variation in horizontal displacements in the same order of magnitude as the input is varied.

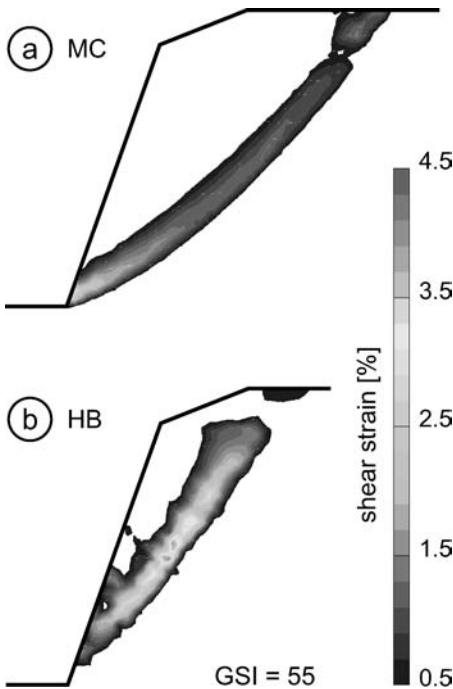


Figure 8. Shear strain distribution at failure (a – MC criterion, b – HB criterion).

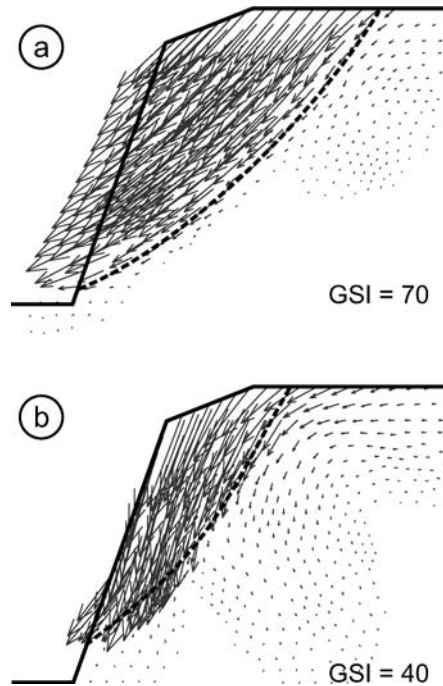


Figure 9. Influence of the GSI on the failure mechanism.

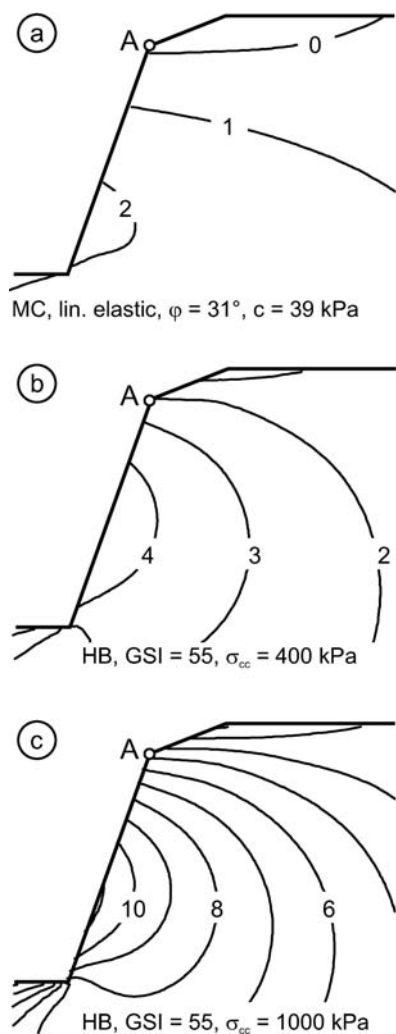


Figure 10. Horizontal slope displacements in [mm] (a – MC criterion, b – HB criterion with $\sigma_{cc} = 400$ kPa, c – HB criterion with $\sigma_{cc} = 1000$ kPa).

4 CONCLUSIONS

The nonlinear elastic-perfectly plastic constitutive model introduced in this paper could be successfully applied in the back-analysis of various test data. The model's strength parameters are easy to determine as its failure envelope is the well known Hoek-Brown criterion. Representative unconfined compression tests are sufficient to determine its stiffness parameters as well. In the example, the simulation of dilatometer

tests could be used to narrow down the uncertainties of the applied in situ Geological Strength Index.

Analysis of a 10 m slope showed significant differences in the failure mechanism and deformation characteristics obtained by the new model compared to those of an equivalent linear elastic – perfectly plastic analysis with the Mohr-Coulomb failure criterion. In the comparison, the equivalent Mohr-Coulomb parameters, which were fitted in the governing stress region turned out to be inadequate. For small minor principal stress, cohesion is most likely overrated whereas the angle of friction is taken too small. For design purposes, strength reduction should thus be incorporated in the Hoek-Brown analysis directly as for example shown in Equation 5.

The siltstone/claystone mainly addressed in this paper showed distinct nonlinear features at the onset of loading (crack closure). The simple nonlinear elastic law introduced was found sufficient to model the deformation characteristics in the crack closure domain. The non-linear law's impact in the simulation of dilatometer tests and slope deformation problems is considerable. Experimental scatter in dilatometer tests could partly be explained by a scatter in the threshold stress σ_{cc} .

REFERENCES

- Bienawski, Z. T. (1967). Mechanics of brittle rock fracture. *Int. J. of Rock Mech. Minn. Sci.* 4 (4), 395–423.
- Brinkgreve, R. (Ed.) (2002). PLAXIS, 2D Version 8. AA. Balkema.
- Eberhardt, E., D. Stead, B. Stimpson, and R. S. Read (1998). Identifying crack initiation and propagation thresholds in brittle rock. *Can. Geotech. J.* 35, 222–233.
- Hoek, E. (1994). Strength of rock and rock masses. *ISRM News Journal* 2 (2), 4–16.
- Hoek, E. (2004). Practical rock engineering – an ongoing set of notes available on the Rocscience website, www.rocscience.com.
- Hoek, E. and E. T. Brown (1980). Empirical strength criterion for rock masses. *J. Geot. Engr. Div, ASCE* 106 (GT9), 1013–1035.
- Hoek, E. C. Carranza-Torres, and B. Corkum (2002). Hoek-brown failure criterion – 2002 edition. In *Proc 5th North Amer. Symp. – NARMS-TAC*, Toronto, Canada.
- Kaselov, A. and S. A. Shapiro (2003). Elastic properties of anisotropic rocks under hydrostatic load. In *Proc. 65th Conf. EAGE*, Stavanger, Norway.
- Kauther, R. and M. Herten (2006). Optimierte Baugrunderkundung für den Neubau des Weserschleuse Minden. In *Proc. 13 Darmstädter Geotechnik Kolloquium*, Darmstadt, Germany, pp. 161–170.
- Lahaie, F., C. J. Bean, and A. Khasar (2002). Nonlinearity in the elastic moduli-porosity. *Geophysical Prospecting*, in press.

Investigation of interaction of landslide soil with the piles of a double-row construction with the help of the finite-element method

S. Matsiy & Ph. Derevenets

Kuban State Agrarian University, Krasnodar, Russia

S. Shiyan

PI «UkrGazNIIProject», Ukraine

ABSTRACT: The investigation results of landslide soil interaction with the piles of a double-row retaining construction in an elastic-plastic statement with the help of the finite-element method have been given. The stress-strain state of landslide soil during squeezing between the piles has been analysed taking into consideration the construction configuration. The dependences of the critical landslide pressures have been obtained from soil non-squeezing and pressure of the first row and the second row on the piles on the construction configuration and soil properties. The investigation results have been used in the engineer protection from the landslide displacement of the section of the North-Caucasian railway in the city of Sochi.

1 INTRODUCTION

The relaxed sections of the slopes are often strengthened with the help of the rows of the cast-in-place piles restrained in steady soils. Sometimes, the multi-row pile constructions are used.

The matters connected with the investigation of the interaction of the landslide soil with the buttress elements, in particular the pile ones, of the one-row retaining structures have been studied by K. Sh. Shadunts (1962), T. Ito & T. Matsui (1975), L. K. Ginsburg (1979), S. I. Matsiy (1991) et al. Some sources (Ginsburg et al. 1990, NIISK of Gosstroy of the USSR 1986, Adashi 1988) contain the investigation results of the double-row pile constructions work. But at present, the simplifications and presumptions (a substitution of the arched form of the plastic deformation zone by the trapezoidal form, a stiff-plastic model of the squeezing process, a neglect of soil friction on a pile and an interaction of the pile rows, etc.) cause significant errors in the pile landslide construction design.

2 RESEARCH TECHNIQUE

The computation was performed with the help of the *PLAXIS* finite-element analysis package. The investigation was performed taking into consideration the following conditions and admissions. The following plane problem was considered: a fragment of the double-row construction with the checkerboard arrangement of the

piles in the horizontal plane (Figure 1). Piles fastening was a rigid one. Soil behaviour was described by the Mohr-Coulomb model. As the numeric investigations are made for the landslide clay soils, the angle of dilatance ψ is accepted as being equal to zero. Limit pressure of the landslide soil on a construction from the soil non-squeezing condition between the piles was considered as a difference of landslide pressure in front of the construction and bearing pressure of soil behind it.

In the computation diagram, the piles are given as one of the symmetrical halves of the «tunnel» of the circular section. The tunnel-pile lining material is assigned rather high values of bending stiffness and normal stiffness allowing disregard of the strains of the pile itself. In order to model the soil operation in the

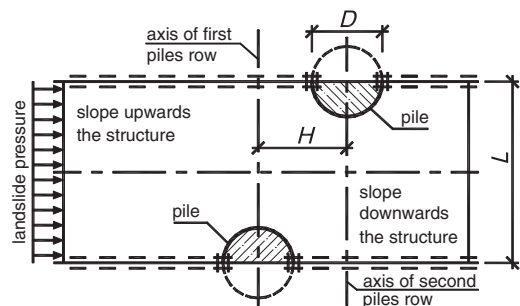


Figure 1. Design model of the task of soil squeezing between the piles.

contact with the pile with the possibility of soil creeping or separation, the contact surfaces («*the interfaces*») are applied to «*the tunnels*». Landslide pressure was modeled by a distributional load along the left boundary of the design model.

The whole design area was divided into elements of «*medium*» fineness. Mesh refinement was made in the construction influence area. An additional refinement of the finite element mesh was carried out within measurable distance of the piles with the use of the round «*tunnel*» without lining and contact surfaces.

A number of parameters of the design diagram of the double-row pile construction and the intervals of their change was identified:

pile diameter D , m	0.72
pile spacing in the row L/D ,	1.125–5.0
distance between the rows H/D ,	0.125–4.0
cohesion c , kPa	5–60
angle of friction φ , $degree$	0–20
deformation module E , kPa	10
friction coefficient on a pile η ,	0.6

An influence of each factor depending on the distances between the piles was estimated. A load in each numerical experiment was increased step-by-step (automatic step-by-step loading) till soil body destruction in the space between the piles and the soil plastic yield.

3 ANALYSIS OF STRESS–STRAIN STATE

The stress–strain state of the soils interacting with two rows of the piles was investigated when the distances between the piles in the row and between the rows were different. The fields of relative deformations, the longitudinal and transverse displacements of soil as well of the Moor-Coulomb «*plastic points*» were investigated. The soil displacements directions are accepted as the longitudinal and transverse ones in relation to a landslide pressure vector.

A deformation process of the soils of the space near the piles under the influence of the landslide load, which was increased from zero to the limit value, was considered. The soil properties are characteristic for the majority of the landslide soils of Krasnodar Region, which are represented by loams. Cohesion c is accepted as being equal to 20 kPa , the angle of internal friction is $\sigma = 10^\circ$. Depending on the configuration of the double-row construction, the following main types of soil interaction with the piles have been identified.

Single row of piles (broken). When the distances $H = (0.13–0.63)D$ between the rows are small and pile spacing is $L = 1.5D$, a mutual influence between the adjacent piles of the first row and the second one is observed. A size of the compacted soil wedge being formed near the piles of the first row is considerably larger than near the piles of the second row. Soil is

deformed according to the form of the flow of the piles of the first row initially, then of squeezing between the rows. In the limit state between the pile elements, the characteristic zones of plastic deformations take place in the form of «*the lobes*» (Figure 2-a), which are known from the earlier investigations (Matsiy, 1991). Plastic deformations near the piles of the second row expand from the top of the compacted soil wedge to the lateral surface of the piles of the first row. When spacing of the elements L is increased up to $(2.5–3.0)D$, such mechanism of interaction of soil with the piles is observed in case of large distances between the rows H , up to $(1.63–1.88)D$.

One-and-a-half row construction. When pile spacing is $L = 1.5D$ and the distances between the rows H are from $0.75D$ to $1.25D$ together with the mutual influence of the adjacent piles of the first row and the second one, the mutual influence between the piles of the first row have been identified. Soil is deformed when it is squeezed firstly in gaps of the first row, then between the rows. The characteristic «*lobe*» areas of plastic deformations of the soil (Figure 2-b) expand from the top of the compacted soil wedge of the second row to the back surface of the piles of the first row. At the moment of the soil plastic yield, the interlocking «*lobe*» deformations take place near the piles of the first row. The plastic deformation intensity is the largest one near the «*lobes*» of the second row. When pile spacing in the row L is increased up to $2.0D$, *one-and-a-half* type of soil interaction with the piles is realized when a distance between the rows is $H = (1.5–2.5)D$. When pile spacing L is large, up to $2.5D$, a transit to other types of soil interaction with the piles is observed.

Double-row construction. When the distance between the piles in the row is $L = 1.5D$ and between the rows is $H = (1.5–2.5)D$, a mutual influence between the piles of the second row is observed. Soil is deformed while flowing and squeezing between the piles of the first row initially, then between the rows and later on between the piles of the second row. The sizes of the compacted wedge in front of a pile of the second row (Figure 2-c) are considerably larger. The shear surfaces take place from the lateral surface of the piles of the first row to the top of the compacted wedge of the pile of the second row as well as from the lateral surface of the piles of the second row to the top of the wedge behind the piles of the first row. A characteristic area is formed in the shape of a quadrangle; when it has been formed, «*the lobes*» of plastic deformations expand in front of the piles of the first row. When the piles are arranged very close to each other in the row $L = 1.125D$, it has the form of a rhomb (Derevenets, 2005). If pile spacing L exceeds $(1.5–2.0)D$, a rupture of the mutual «*lobe*» plastic zones of the second row and a transition to the *one-and-a-half* type of interaction of soil with the piles take place.

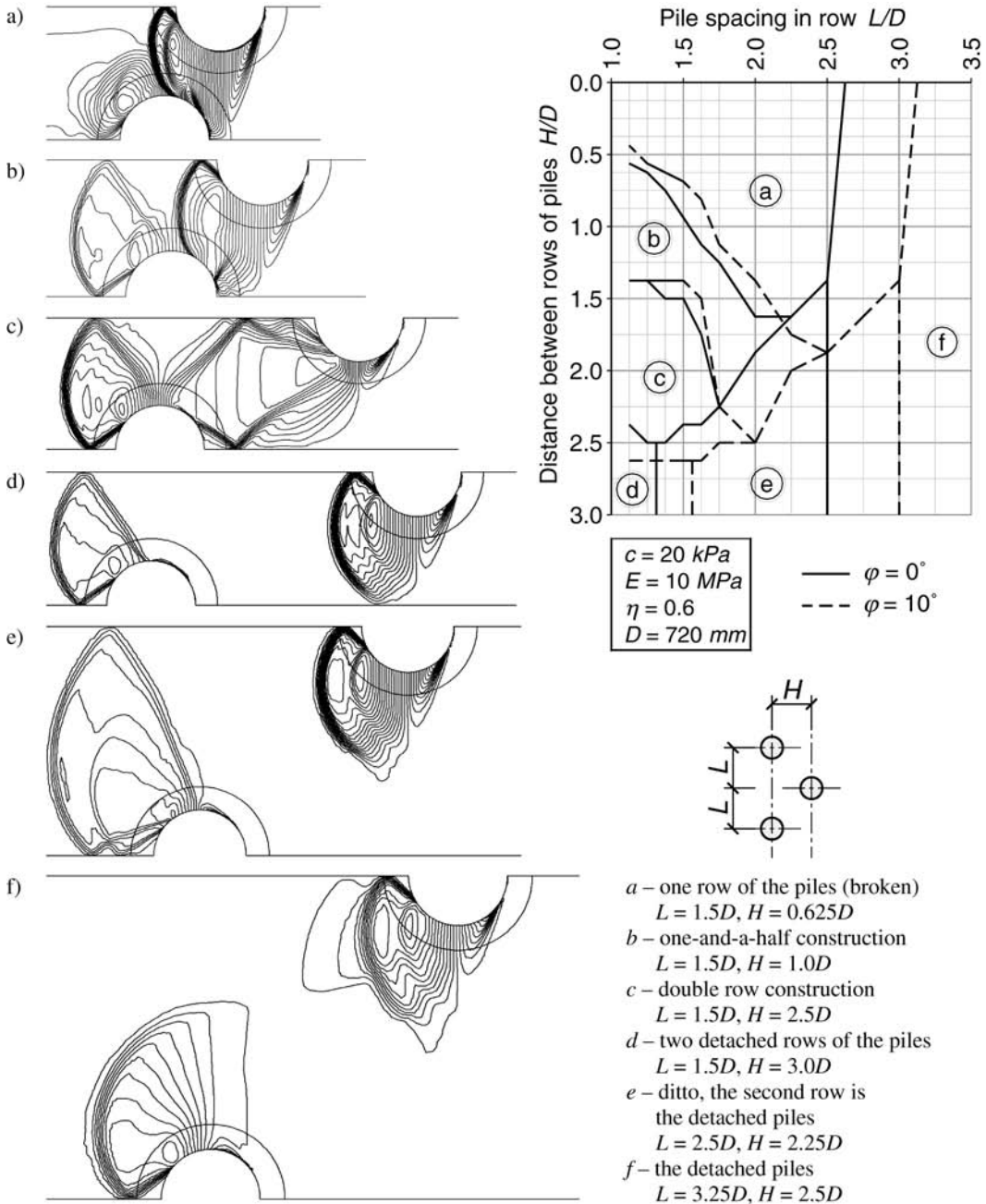


Figure 2. Transverse displacement of soil for various types of interaction with the pile rows depending on a configuration of the retaining construction.

Two detached rows of the piles. When pile spacing L is up to $2.0D$ and the distance between the rows is $H > 2.5-2.75D$, the joint areas of plastic deformations between the rows are divide (Figure 2-d). When the

piles are arranged too close to each other $L = 1.125D$, the «lobes», which determine soil pressure (Derevenets, 2005), are formed behind the piles of the first row. When pile spacing in the row L exceeds $1.5D$ with the

same distances between the rows, a rupture of the joint «lobe» zones near the piles of the second row takes place. The second row of the piles starts operating as a row of the *detached abutments* (Figure 2-e). Further increase of pile spacing L up to $3.0D$ results in operation of the piles as the *detached rows* with smaller distances between the rows H up to $(1.5-1.75)D$.

Detached piles. When pile spacing value is $L = (2.5-3.0)D$, the interaction between the piles of the first row is absent. When spacing L exceeds $3.0D$, a separation of the joint plastic deformation areas takes place near the adjacent piles of the first row and the second one; the local «lobe» area are formed near the piles of both rows (Figure 2-f).

The given types of interaction of the landslide soils with the piles are specific for the stress-strain state of soil by squeezing between two rows of the piles and by other values of its physicommechanical characteristics. The limit values of the distances between the piles in a row and between the rows are slightly changed (the diagram in Figure 2).

4 ANALYSIS OF PRESSURE LIMITS

As a result of the computation of the double-row pile constructions, the diagrams of critical pressure of soil squeezing (Figure 3-a) and a distribution of pressures between the rows (Figures 3-b...d) have been obtained.

If pile spacing is small $L = (1.125-1.5)D$ and a distance between the pile rows H is increased up to $(0.0-0.5)D$, a value of squeezing pressure as well as a value of pressure limit on the piles is reduced. A difference of pressures on the piles between the rows is increased practically proportionally. When a value of the distance between the rows H exceeds $0.5D$, a non-linear decrease of pressures on the piles of both rows takes place. By soil squeezing together with the mutual influence of the rows, an interval between the piles of the first row is involved. With $H = (1.50-1.75)D$, critical pressure of squeezing is minimal, and a difference of the limit pressures on the piles is maximal. When a value of the interval between the piles is $H = (1.25-1.50)D$, a jump of the difference of pressures on the piles is observed. At this moment, a transition of operation of the *one-and-a-half row* construction to the *double-row* construction takes place.

When the distance between the rows H is increased from $1.5D$ to $2.75D$, a non-linear increase of the pressure limit of squeezing and pressures on the piles takes place. A difference of pressures on the piles of the adjacent rows is slightly reduced. It is explained by a step-by-step involvement of the rows. The second row provides a soil reaction creation behind the first row and, consequently, an increase of resistance to squeezing here.

When a value of the interval between the rows H exceeds $2.75D$, the joint areas of plastic deformations of the adjacent rows are separated. The squeezing pressure values and the distribution of pressures on the piles depend on the distance H between the piles no more. The pile rows operate as the *detached* ones.

When pile spacing in the row L exceeds $1.5D$ and the value of the distance between the rows H is up to $(2.0-3.5)D$, critical landslide pressure and pressure on the first row of the piles are increased nonlinearly. When the distances H between the rows are large, their values are not changed. Pressure limit on the second row of the piles with H up to $0.75D$ is decreased, and with H from $0.75D$ to $2.0D$ it is increased up to the previous values and then is changed no more. When L exceeds $1.5D$ and H exceeds $2.0D$, a value of pressure on the second row of the piles does not depend on pile spacing and the distance between the rows.

5 APPLICATION

The investigation results are used in justification of a project connected with protection of the dwelling facilities and the section of the railway against landslide displacements. The landslide section with the width of $0.5-1.0\text{ km}$ and the absolute marks of $8-100\text{ m}$ is situated in the suburbs of the Central district of the city of Sochi and is surrounded by the private buildings. The section is contoured by the natural steep slope of the mountain from the south and the southwest. There is groundwork of Tuapse-Adler railway at the foot of the mountain slope. The ancient landslide adjustment movements and the modern ones have been noted on the slope.

An arrangement of four tiers of the retaining walls employing the cast-in-place piles with the diameter of 1200 mm is envisaged in order to strengthen the landslide slope. The piles of every tier are arranged in two rows in check disposition. According to the results of the geotechnic survey, the following physicommechanical properties of the landslide soil are adopted: unit weight $\gamma = 19.2\text{ kN/m}^3$; cohesion $c = 23\text{ kPa}$; angle of internal friction $\varphi = 10^\circ$. Landslide body thickness is 6 m in the most characteristic cross section. A calculation of the moments in the construction units with various distances between the rows H (Figure 4) has shown that its optimal value is $1.5D$ (1.8 m).

A pile construction calculation for non-squeezing of the soil has been carried out for the main load combination (483 kN/m) and the specific load combination (575 kN/m). The results of the calculation according to the well-known methods and the methods being suggested are given in Table 1.

One should note that the well-known methods of the calculation of the distances between the piles do not take into account the dependences of the landslide

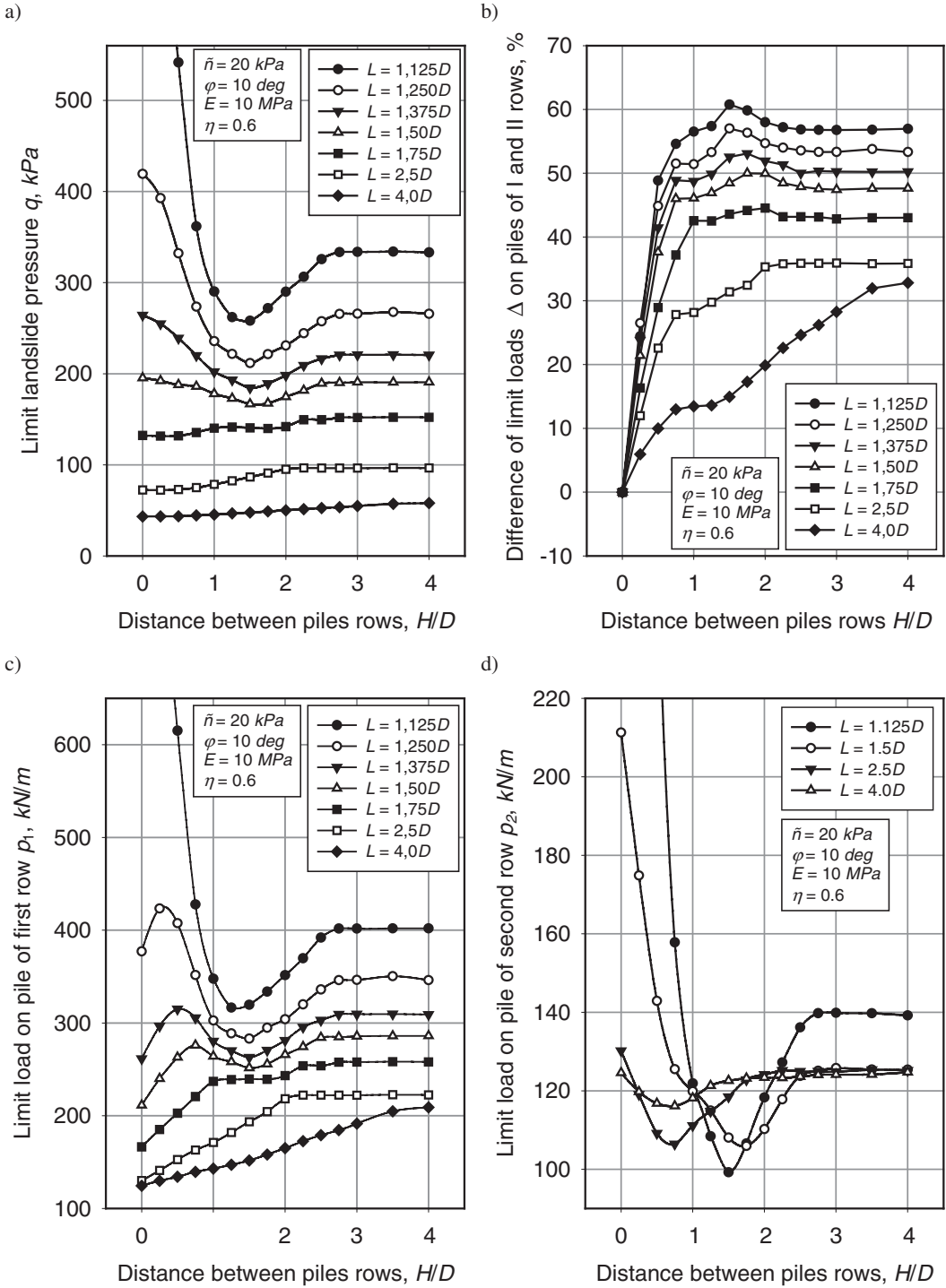


Figure 3. Critical squeezing pressure (a); difference of pressure limits on the piles of I and II rows (b); landslide pressure limit on the piles of I (c) and II (d) rows.

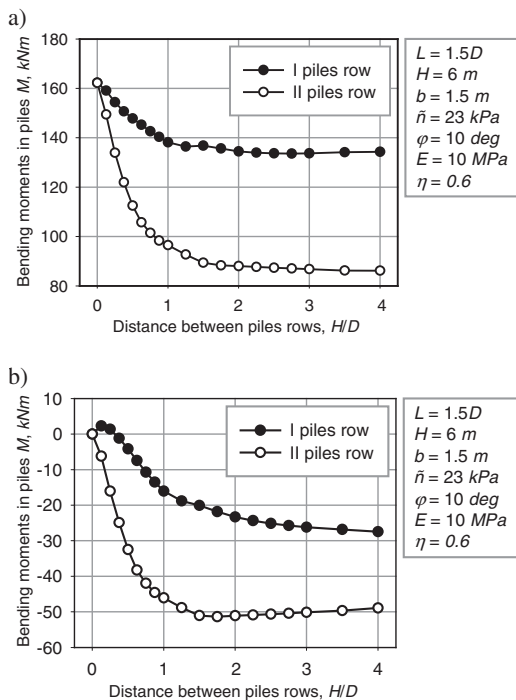


Figure 4. Moments in conventional embedding of the pile (a) and on the level of grillage (b).

Table 1. Construction configuration determination.

Methods	Pile spacing in a row, m when the loads are combined	
	Main	Specific
Ito and Matsui (1975)	1.88 (1.57D)	1.73 (1.44D)
Ginsburg (1979)	3.92 (3.27D)	3.43 (2.86D)
Suggested technique	4.18 (3.48D)	3.60 (3.00D)

pressure limit on the quantity of the rows of the piles. That's why the required distances between the piles turn to be insupportably small or overstated ones.

Thus taking into consideration the features of the interaction of the soils with the piles of the multi-row retaining constructions, more efficient antilandslide structure has been designed with the distances of 3.5 m between the piles in the row and 1.8 m between the rows.

6 CONCLUSION

The following facts have been ascertained as a result of the investigation of the landslide soil interaction

with the piles of the double-row retaining construction with the help of the finite-element method:

- Under the influence of the landslide pressure during soil squeezing in the space between the piles, the characteristic areas of plastic deformations are formed that determine the features of interaction of soil with the piles. On the basis of their analysis, the following classification of the retaining constructions has been suggested:
 - one row of the piles (a straight row or a broken one),
 - one-and-a-half row construction,
 - double-row construction,
 - two detached rows of the piles,
 - detached abutments.
- The limit distances between the piles in a row and between the rows have been ascertained from the condition of the joint resistance to soil squeezing in case of various strength properties of the landslide soil.
- We have obtained the dependences of the landslide pressure limits and the pressure on the piles on element spacing in the row, the distances between the rows and strength properties of the soils, which have the characteristic extremes and give an opportunity to make a rational choice of configuration of a double-row construction, taking into consideration the minimal pressure on the piles.

REFERENCES

- Shadunts, K.Sh. 1962. On buttress structure calculation, *DIIT proceedings, Geotechnics issues 5*: 24–42.
- Ito, T. & Matsui, T. 1975. Methods to estimate lateral force acting on stabilizing piles. *Soils and Foundations* 15(4): 43–59.
- Ginsburg, L.K. 1979. *Antilandslide retaining structures*, Moscow: Stroyizdat.
- Matsiy, S.I. 1991. Landslide soil interaction with piles. *Abstract of the thesis*. Sankt-Peterburg.
- Ginsburg, L.K. et al. 1990. Force distribution between the rows of the piles of the antilandslide construction. *Basements, foundations and mechanics of soils 2*: 7–11.
- NIISK of Gosstroy of the USSR, 1986. *Design guidelines on buried engineering structures arrangement*. Moscow: Stroyizdat.
- Adashi, T. et al. 1988. Model tests on the preventive mechanism of landslide stabilizing piles. *Doboku gakkoy rombun*; *Proc. of JSCE*. 400: 243–252.
- Derevenets, Ph. N. 2005. Investigation of interaction of landslide soil with the piles of a double-row retaining construction with the help of the finite-element method. *City agglomerations on the landslide areas. Proceedings of the third international conference, Volgograd, December 14–16, 2005*. Volgograd: the Volgograd State University of Architecture and Civil Engineering.

Numerical analysis of an open excavation close to an embankment on improved ground

José A. Barco, Jorge Cañizal, Jorge Castro, Almudena da Costa, César Sagaseta
University of Cantabria, Santander, Spain

ABSTRACT: A numerical study of an embankment (12 m high) on a reinforced earth wall (14 m high) is presented. The embankment is located on a hillside, and the ground was improved with stone columns to increase stability. An open excavation (11 m deep) supported with an anchored wall, unforeseen during the design stage, was undertaken close to the toe once the embankment construction had started. The multiple interactions between excavation, wall, anchors, improved ground, reinforced earth and embankment, are analyzed in the paper. The global stability of the slope was studied by means of slip circle limit analysis and compared with ϕ -c reduction analysis by finite element methods. The same finite element model was used to analyze the stresses and deformations due to the embankment construction and open excavation. The results are compared with the measured vertical and horizontal displacements, total stresses and pore pressures.

1 INTRODUCTION

The design and construction of embankments on soft soils is still a challenging problem in geotechnical engineering. Difficulties arise from: (1) the low strength of the soft soil, severely limiting the working load with an adequate safety for short term stability; (2) its high deformability, inducing large total and differential settlements that are developed slowly due to the low permeability.

These problems are more and more common due to the ever increasing cost of land occupation, leading to the use of marginal sites, as in the case presented in this paper. It is a very populated and industrialized zone in a narrow valley, where the design of a highway should not affect all the industrial, agricultural and residential uses of the land near the river. The highway was then located on the hillside, but near its lower part, in order to enable communication with the existing roads.

2 DESCRIPTION OF THE PROBLEM

The problem concerns the construction of a highway section on a hillside in Arbuio, in the outskirts of Bilbao (Spain) (see Figure 1). A high embankment (14 to 20 m) was needed to connect a bridge and a cut section. The lateral extension of the base was limited by an industrial plant. The design solution involved a reinforced soil wall at the embankment toe. The foundation ground had to be improved by excavation and back-substitution to a depth of 6 meters.

However, the excavation needed for this solution posed many problems, due to a canal located very close to the wall. The required excavation clearly implied more serious problems than the embankment itself. Finally, it was decided to limit the depth of excavation to 3 m, and to reinforce the ground below this elevation with stone columns.

The main purpose of the stone columns in this case was to increase the average strength of the soil. The drainage effect was not needed, because of the relatively high permeability of the ground. However, it was considered as an extra safety measure, to avoid excess pore water pressures in low permeability lenses. The extension of the treated area is 6400 m² with 830 columns. The columns were installed from a platform, after the shallow back-substitution described.

The columns were constructed by the dry-bottom feed method. In the initial design, a column diameter



Figure 1. General view of the site.

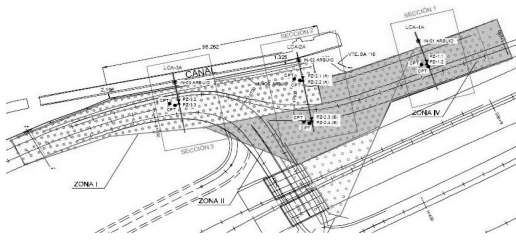


Figure 2. Plan view of the instrumentation.

of 1 m was assumed, with a replacement ratio, a_s , of 0.10. However, the first control measurements indicated an average diameter of 0.7 m, meaning a substantial reduction of the replacement ratio ($a_s = 0.05$).

The situation was further complicated by an open excavation, started at the same time. This excavation, supported by an anchored concrete wall, was located downhill (see Figure 3). In the design stage, it was considered that the distance to the embankment was enough to avoid a significant influence. However, it was thought reasonable to analyze further the mutual effects of the two works.

Because of these facts, it was decided to instrument the embankment, in order to study the new situation and analyze possible solutions if needed.

Figure 2 shows the instrumentation layout. The instruments were concentrated in 3 sections. Each section consists of:

- a transversal continuous settlement profile,
- an inclinometer, near the reinforced earth wall,
- one cluster of instruments (two in Section 2), with 2 piezometers in a borehole (each one in the middle of a less permeable layer) and 2 total vertical pressure cells, one on the column and the other on the soil, in the midpoint between columns.

This paper presents the results of Section 3. This was the section where the influence of the open excavation was more important. Both finite element and limit equilibrium analyses were carried out.

3 ANALYZED SECTION

In section 3 (Figure 3), the excavation slope was 2(V):1(H), and the reinforced earth wall is 14 m high and 10 m wide. The width of the backfill is 23 m and its height 8.5 m. In this section, the embankment is split into two separate parts. In the lower part, it has negligible height above the reinforced earth wall. The width of the stone column treated area is 20 m and the length of the columns is 11.8 m, reaching the bedrock.

The foundation soil corresponds to the contact between the alluvial deposits of the valley and the colluviums covering the hillside. It has been divided

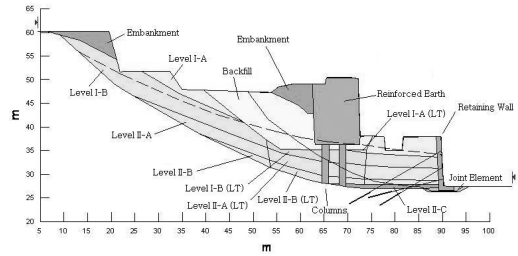


Figure 3. Transverse cross-section for Section 3.

in three levels with sublevels. The strength and deformational properties taken for the analyses are shown in Table 1. These parameters were obtained from different tests, such as triaxial compression, oedometer and plate loading tests.

4 STAGED CONSTRUCTION SEQUENCE

The required construction sequence for the embankment was determined based on a simple one-dimensional analysis of the consolidation. Vertical and radial flows were uncoupled by the Carrillo equation. The coefficient of consolidation of the soil was taken as $2 \times 10^{-3} \text{ cm}^2/\text{s}$ for vertical and radial flow (due to the colluvial nature of the soil, no anisotropy was considered).

This analysis was used to evaluate the relative influence of the change in column diameter from 1.0 m to 0.7 m. The load factor, N_c , is used:

$$N_c = \frac{p_a}{c_u} \quad (1)$$

where p_a is the applied vertical pressure. A value of N_c about 6.0 means foundation failure. For each loading step, the soil shear strength was evaluated from the current vertical effective stress, σ'_0 , according to the Ladd and Eggers (1974) expression:

$$c_u = k\sigma'_0 OCR^\alpha \quad (2)$$

with $k = 0.2$, $\alpha = 0.8$ and initially $OCR = 3.0$. A safety factor of 2.0 against failure was required, meaning a load factor less than 3.0.

Figure 4 shows the design for a column diameter, d_c , of 1.0 m. Construction was made in ten equal loading steps, waiting two weeks between them (total construction time 126 days). The decrease of N_c due to the gain in c_u with consolidation in each step is more noticeable when the preconsolidation pressure is reached (at about an embankment height of 8 m), according to eq. (2).

This sequence had to be modified for the change in column diameter (Figure 5). The last steps were delayed

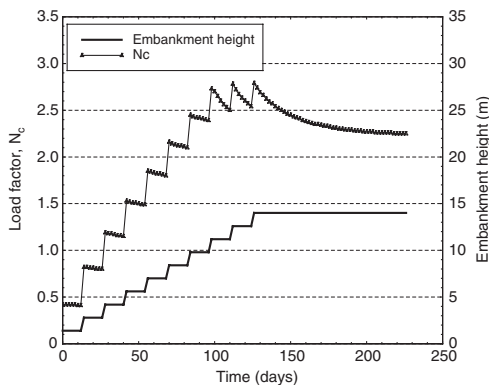


Figure 4. Construction rate and load factor for $d_c = 1.0$ m.

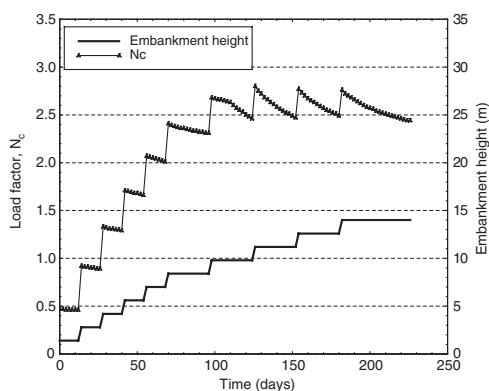


Figure 5. Construction rate and load factor for $d_c = 0.7$ m.

to four weeks, extending the construction period to 182 days. With this arrangement, the load factor was still kept below the limit value.

5 MODELLING

5.1 Excess pore pressures

With the above described construction sequence and c_v values, no significant excess pore pressures were anticipated. Hence, the soil around the columns was considered as drained during all the process.

This was later confirmed by the instrumentation (Figure 6): for an applied load of 260 kPa, the maximum measured excess pore pressure was 10 kPa, indicating a consolidation rate higher than 95% during the embankment construction.

5.2 Shear strength

The use of an average strength for the improved ground was not practical in this case, because averaging the

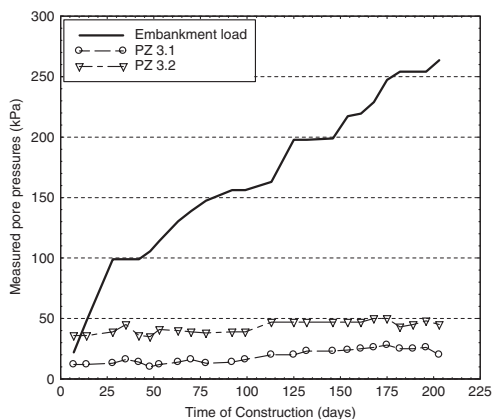


Figure 6. Pore pressures measured between columns.

Table 1. Mechanical parameters for the soil layers considered.

Soil level	γ (kN/m ³)	c' (kPa)	ϕ (°)	c_u (kPa)	E (MPa)
Concrete wall	15	250	0		20000
Reinforced earth	22	100	32		75
Embankment	20	10	32		25
Stone columns	18	0	40		50
Backfill	20	10	32		25
Level I-A	21	25	26	42	4.5
Level I-B	20	25	26	60	4.5
Level II-A	21	0	35	75	8
Level II-B	21	20	35	75	12
Level II-C	18	0	40		50
Interface	22	0	45		500
Bedrock	22	—	—		1000

product ($\sigma' \tan \phi$) was difficult due to the large transverse variations of the effective stress σ' across the reinforced earth wall. So, the original properties were kept for the soil, and an equivalent friction angle was used for the columns, concentrated in two large gravel trench elements, 1.5 m wide. These two elements were located near the toe and heel areas below the reinforced soil wall.

In all the soil mass treated with columns, the soil was considered to be fully drained at all stages. In the rest of the soil, drained or undrained conditions were assumed, depending of the load stage.

Table 1 shows the values of the parameters.

The equivalent friction angle of the columns was selected to produce the same total shear strength along a horizontal plane, at a depth representative of the position of the failure surface.

The frictional component of the strength depends of the vertical effective stress at the depth of the failure surface. Hence, a difference arises between finite

element analyses and limit equilibrium by slip line methods (Barksdale and Bachus, 1983). In the analysis with finite elements, the stress transfer between soil and columns is considered by the compatibility of the respective deformations, inducing a stress concentration on columns. However, in the method of slices, the vertical stress is evaluated as the weight of the soil column above it, with no stress transfer between slices. So, a higher value of the equivalent friction angle for the columns is needed to match the correct value of the product ($\sigma' \tan \phi$).

The actual shear resistance along a horizontal failure surface across the treated area of width B per unit length of embankment is:

$$T_r = T_{rc} + T_{rs} = a_r B \sigma'_c \tan \phi_c + (1 - a_r) B (c_s + \sigma'_s \tan \phi_s) \quad (3)$$

where a_r is the replacement ratio. Subscripts c and s refer to the columns and the soil, respectively. The effective stresses at a depth z are:

$$\begin{aligned} \sigma'_c &= \mu_c q + \gamma_c z \\ \sigma'_s &= \mu_s q + \gamma_s z \end{aligned} \quad (4)$$

where μ_c and μ_s are the stress concentration factors, linked by the equilibrium condition:

$$a_r \sigma'_c + (1 - a_r) \sigma'_s = q \quad (5)$$

If the columns are modelled by a set of n 2-D trenches of width b , the total shear force would be:

$$T_m = T_{mc} + T_{ms} = nb \sigma'_c \tan \phi_{mc} + (B - nb) (c_s + \sigma'_s \tan \phi_s) \quad (6)$$

The equivalent column friction ϕ_m is obtained from the equality of T_r and T_m . For a slip line method, the effective stresses in eq. (6) are evaluated without consideration of the concentration factors ($\mu_c = \mu_s = 1$ in eq. 4).

The obtained equivalent friction angle for the trenches representing the columns are shown in Table 2, both for finite element and slip line analyses. The stress concentration factors are taken from Balaam and Booker (1981), Priebe (1995) and as measured (see Figure 7). For this purpose, a soil strength of $c = 25$ kPa and $\phi = 25^\circ$, and a column/soil modulus ratio of 6.0 were taken.

From the above results, the equivalent column friction angle was selected as 40° for the limit equilibrium and 25° for the F.E. analyses.

Table 2. Concentration factors and equivalent column friction for limit equilibrium (L.E.) and finite element (F.E.) analyses.

	Stress factors		ϕ_{mc}	
	Column, μ_c	Soil, μ_s	L.E.	F.E.
Balaam & Booker 1981	3.5	0.86	44.8°	24.3°
Priebe 1995	2.86	0.90	42.7°	25.6°
Measured	2.5	0.92	41.3°	26.5°

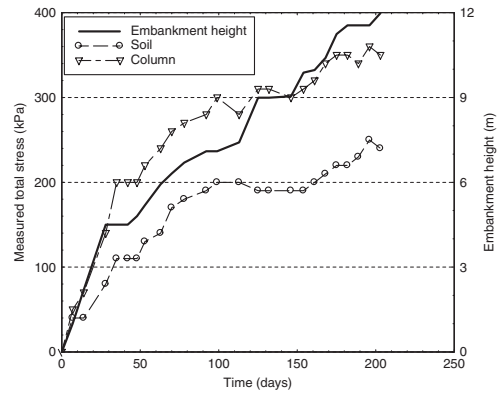


Figure 7. Measured total stresses on the columns and the soil.

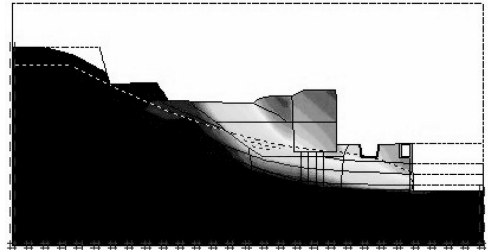


Figure 8. Failure mechanism.

6 STABILITY ANALYSIS

The global stability of the embankment was calculated by means of limit equilibrium with Morgenstern-Price method (program SLOPE-W) and finite elements, with the c - ϕ reduction procedure (PLAXIS) (Figure 8). The obtained safety factors are compared for short term (S.T.) and long term (L.T.) in Table 3. Two assumptions have been considered for the excavation located downhill, with or without anchors.

The agreement between the two methods is reasonable, with a tendency to give slightly smaller values

Table 3. Obtained factor of safety.

Situation	Limit Equilibrium		Finite Element	
	S.T.	L.T.	S.T.	L.T.
Anchors	1.66	1.71	1.50	1.69
No anchors	1.34	1.35	1.20	1.30

with the numerical analysis, and it is found in most cases (Sagaseta and Da Costa, 2005).

7 NUMERICAL ANALYSIS OF THE CONSTRUCTION PROCESS

7.1 Earth pressure on the retaining wall

During the construction, one of the important questions arisen was how much the construction of the embankment influences the pressure on the anchored wall. Although the embankment is outside the active soil wedge, the anchors induce a greater extension of the affected area. This is not considered in conventional analyses (Coulomb) for the wall, but is clear from finite element analyses, and also from simple calculations using elastic solutions for the stress distribution due to the embankment load (see Table 4).

These results indicate that the limit equilibrium (Coulomb) analysis assumes the soil in active state and it could not capture the interaction between the wall and the embankment. This interaction takes place via the deformations, due to the stiffness of the anchoring system. In the “elastic” solution, the wall is implicitly assumed to be fixed, i.e. the anchors have infinite stiffness, and so the solution is an upper bound for the earth pressures. However, this upper bound is in this case very close to the actual situation.

The increase of ground pressures took the anchor forces beyond their allowable limits. It was then decided to install an additional anchor system, and to loose the existing ones at the same time.

7.2 Ground displacements

The displacements obtained from the numerical analysis during construction were compared with the measured ones. Particularly, the situation when the embankment reached a height of 6 m was analyzed in detail, and the results were used to predict the foregoing movements for H = 6 to 12 m.

Figure 9 shows the calculated and measured settlements at the base of the reinforced earth wall. The average settlement is 60 mm, roughly uniform across the central part of the base of the embankment. These value and distribution were reasonably matched by the numerical calculations.

Table 4. Earth pressures on the retaining wall.

Embankment height (m)	Mean earth pressure (kPa)		
	Coulomb	Elastic	F.E.M.
0	39	—	—
6	39	48	47
12	39	57	56

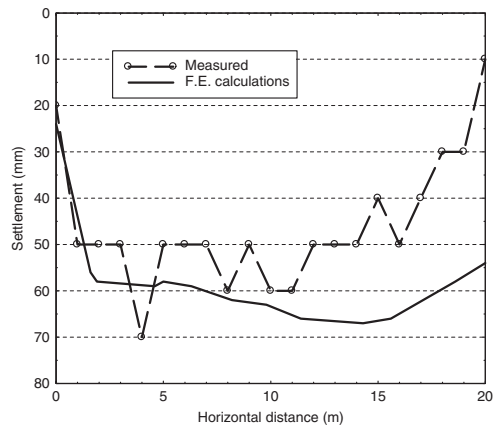


Figure 9. Surface settlements for H = 6.0 m.

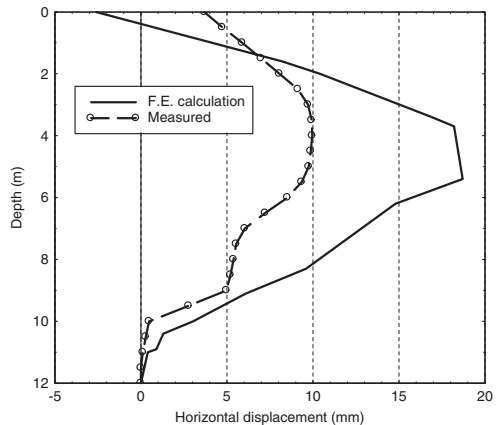


Figure 10. Deep horizontal displacements for H = 6.0 m.

The horizontal displacements measured by the inclinometer at the embankment toe are plotted in Figure 10. In contrast with the settlements, although the pattern of variation of displacements with depth is well reproduced, their absolute values are overpredicted in the calculations by a factor of about 2.

The plastic zones are very small in extension, and most of the displacements are of elastic nature. So, the only way to match the results is by assuming a

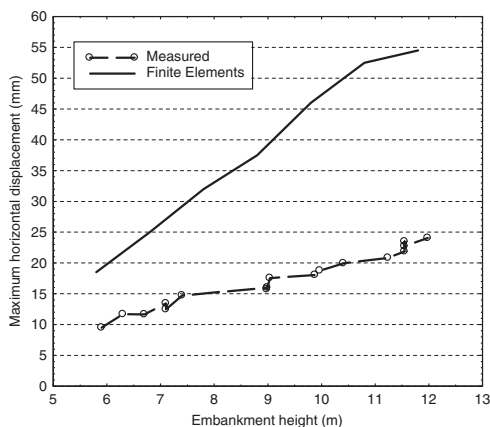


Figure 11. Evolution of maximum horizontal displacement for $H = 6\text{--}12\text{ m}$.

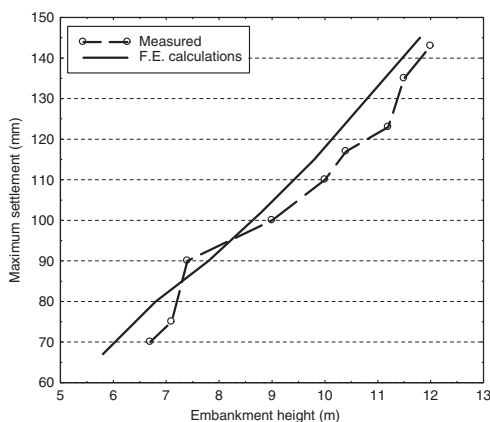


Figure 12. Evolution of maximum settlement for $H = 6\text{--}12\text{ m}$.

horizontal modulus higher than the vertical, with an anisotropy ratio of about 2.0.

The above trends keep during the embankment raising from 6 to 12 m. Figure 12 shows the evolution of the maximum settlement, and Figure 11 the maximum horizontal displacement. Both variations are fairly linear with embankment load, according to the elastic nature of the deformation. Again, the settlement values are well predicted, but the calculated horizontal displacements are twice than the measured ones.

The reason because the soil is twice stiffness in the horizontal direction could be in a increase of horizontal stiffness due to the column construction. In the dry method of installation, the horizontal forces induced by the vibrator can increase the lateral stresses, and also the corresponding stiffness. In the wet method, the increase and further dissipation of excess pore

pressures can mask this phenomenon. Kirsch (2004) has obtained a similar increase in modulus, measured with pressuremeter tests before and after the column installation.

8 CONCLUSIONS

A real case of complex interaction between several geotechnical structures has been analyzed with a numerical model. The case includes an embankment with reinforced earth toe, on a sloping soil reinforced with stone columns, and with an excavation supported by an anchored wall at short distance downhill. The analysis, in close comparison with the instrumentation results, indicates that the distribution of loads between columns and soil follows the generally accepted rules. Finding an equivalent strength for the columns is not straightforward, and it depends on how the analysis of stability handles the stress transfer between columns and soil.

Although the limit analyses indicate that the separation of the excavation from the embankment was enough to avoid interactions, the deformation analysis showed that the deformations are mutually affected. In an anchored system, these deformations produce changes in the earth pressures.

Finally, the numerical analysis of the construction gives a reasonable agreement for the settlements along the process, but the horizontal displacements are over-predicted by a factor of 2.0. The soil lateral stiffening during column installation could explain this feature.

Part of the work presented herein is within a research project, supported by the Spanish Ministry of Public Works (Ref. 03 A634), on stone column use under road embankments. The case described is in the Kadagua motorway, and the Authors are grateful to the professionals in charge of the work for their support.

REFERENCES

- Balaam, N.P. and Booker, J.R. 1981. Analysis of rigid rafts supported by granular piles. *Int. J. Num. Ana. Methods in Geomechs.* 5: 379–403.
- Barksdale, R.D. and Bachus, R.C. 1983. Design and Construction of Stone Columns. *Report FHWA/RD-83/026*. Nat. Techn. Information Service, Springfield, Virginia.
- Kirsch, F. 2004. Experimentelle und numerische Untersuchungen zum Tragverhalten von Rüttelstopfsäulengruppen. Dissertation. Technische Universität Braunschweig.
- Plaxis 2002. Finite Element Code for Soil and Rock Analyses. Plaxis B.V., the Netherlands.
- Priebe, H.J. 1995. Design of vibro replacement. *Ground Engineering* 28 (10): 31–37.
- Sagaseta, C. & Da Costa, A. 2005. Dimensionamiento frente a Estado Límite Último usando métodos numéricos. *2^{as} Jornadas Hispano-Lusas de Geotecnia*. 3–11. Lisbon.
- Slope/w 2001. Slope Stability Analysis Software. Geo-Slope International Ltd., Canada.

Shallow foundations

Undrained bearing capacity and mechanisms of collapse of square footings under vertical and moment loads

S. Gourvenec

Centre for Offshore Foundation Systems, University of Western Australia, Perth, Australia

ABSTRACT: Shallow foundations are typically required to carry a combination of vertical and moment loads and undrained bearing failure is a fundamental consideration. Many structures are founded on shallow foundations of low aspect ratio and idealisation to conditions of plane strain is inappropriate. Analytical studies have addressed the response of circular footings to uniaxial vertical loading and combined vertical and moment loading in the past but square and rectangular foundation geometry has been largely overlooked. This paper reports results from a suite of finite element analyses addressing the undrained bearing failure of square footings subjected to vertical and moment loading. Ultimate limit states and the kinematic mechanisms accompanying failure observed in the finite element analyses are presented in the context of other available solutions for strip, circular and square footings.

1 BACKGROUND

Exact solutions for the undrained vertical bearing capacity of strip and circular footings on idealized plastic material are well established. Expressed in terms of bearing capacity factor $N_c = q_u/s_u$, where q_u is the limiting vertical stress and s_u the representative undrained shear strength, $N_c^{\text{strip}} = 5.14$ (Prandtl 1921) and $N_c^{\text{circle}} = 6.05$ (for a rough soil/footing interface) (Cox et al. 1961). Very little work has addressed vertical bearing capacity of square footing and no exact solution has been identified.

Conventionally a shape factor of 1.2B/L is relied on to account for variation in bearing capacity due to edge effects, giving maximum $N_c = 6.17$ for a three-dimensional footing (Skempton 1951, Brinch Hansen 1970); 3% larger than the exact solution for a circular footing. To date, no exact solution has been identified for a square footing to enable a similar comparison. However, Levin (1955) suggested the bearing capacity for a square footing would lie slightly below that for a circular footing of equivalent area. This would lead to an increased over prediction of capacity of a square footing if relying on conventional shape factors.

Recent studies have proposed revised bearing capacity factors based on bound solutions for rough square footings but the range is significant ($5.52 < N_c < 6.56$) (Michalowski 2001, Salgado et al. 2004, Gourvenec et al. 2006). One of the problems in identifying a converging bound solution is the uncertainty over the kinematic mechanism accompanying failure; particularly the occurrence of diagonal and/or orthogonal

symmetry. This is addressed in detail by Gourvenec et al. (2006).

Moment capacity of a shallow foundation is typically assessed using the effective width principle (Meyerhof 1953); whereby the capacity of a strip footing under a vertical load and moment, expressed as a vertical load applied at an eccentricity e/B , is assumed to be equivalent to that of a footing of reduced width $B' = B - 2e$ under the vertical load centrally applied. For a square or rectangular footing only the width is modified, on the assumption that the bearing length of footing is unaffected by the load eccentricity (when applied in the plane of the footing's width).

Represented in VM load space, the interaction is symmetrical with the maximum moment capacity ($N_{cM} = M_{\text{ult}}/ABs_u = 0.64$) predicted under a vertical load of half the uniaxial capacity. In the absence of vertical load, or at ultimate vertical load, no moment capacity is available. As limiting moment capacity is a function of the applied vertical load (since $M = Ve$) moment capacity increases in the same proportion as vertical capacity. For example for a square footing, $s_c = 1.2$ leading to $N_{cM}^{\text{square}} = 0.77$. The VM interaction diagram remains symmetrical with M_{ult} at $V = 0.5 V_{\text{ult}}$ ($= 0.5 * 1.2 * 5.14 * As_u$) and $M = 0$ at $V = V_{\text{ult}}$ and $V = 0$. (Maximum moment capacity for a circular footing predicted by the effective area principle is lower, $N_{cM}^{\text{circle}} = 0.59$, as the effective length is also affected by the eccentricity. (See Taiebat and Carter 2002).

No exact solution for failure under combined VM loading has been found to date against which to verify the

effective width or area principle. The problem in identifying an exact solution with plasticity theory is separation of the footing from the soil interface, inevitable under moment loading at low vertical load, violates the normality condition. Houlsby and Puzrin (1999) and Salencon and Pecker (1995) discuss alternative approximate analytical solutions for strip footings under vertical and moment loading although the main focus concerns inclined eccentric loads. No analytical solutions have been proposed for three-dimensional footing geometry. Taiebat and Carter (2002) compared the effective area rule for circular footings with predictions of limiting vertical and moment loads from finite element analyses. To date square (and rectangular) footings have not been considered.

Reduction in moment capacity at low vertical loads as predicted by the effective width principle indicates no tensile capacity at the footing-soil interface. In some circumstances (particularly offshore) passive suction is developed beneath a footing plate providing tensile capacity. Therefore moment can be resisted even at low vertical loads. Assuming unlimited tensile capacity can be mobilized along the footing-soil interface, upper bound plasticity solutions exist for pure moment capacity for strip and circular footings but not for a square footing ($N_{EM}^{strip} = 0.69$, $N_{EM}^{circle} = 0.67$, Murff and Hamilton 1993, Randolph and Puzrin 2003). No analytical solution has been derived for combined moment and vertical load interaction for fully bonded conditions even for the simple case of a strip footing. Interaction diagrams have been derived numerically for strip (Bransby and Randolph 1998) and circular (Gourvenec and Randolph 2003) footings, but to date square (or rectangular) footing geometry has not been considered.

2 THIS STUDY

Undrained ultimate limit states of square footings under a range of vertical and moment loading are investigated with finite element analyses. Cases of a footing with unlimited tensile capacity and zero-tensile capacity along the footing-soil interface are considered. Failure envelopes and kinematic mechanisms accompanying failure are presented and compared with results from plane strain models. For the footing with unlimited tensile capacity, ultimate limit states for a circular footing from a previous study are also presented. All finite element analyses were carried out with the software ABAQUS (HKS 2004).

2.1 Finite element model

2.1.1 Mesh

The mesh represents a half-footing of width B cut through one of the orthogonal planes of symmetry

(Figure 1). The footing was represented as a discrete rigid body on the surface of the mesh. The mesh extends $3B$ from the edges of the footing and $2.5B$ beneath the footing. Zero-displacement boundary conditions prevent out-of-plane displacements of the vertical boundaries, and the base of the mesh is fixed in all three coordinate directions.

A number of different mesh densities were investigated to achieve a time-efficient model without compromising accuracy. The mesh shown in Figure 1 comprises approximately 12,000 first order fully integrated hexahedral hybrid elements. The hybrid element formulation uses a mixture of displacement and stress variables (as opposed to solely displacement) to approximate the equilibrium equations and compatibility conditions. Hybrid elements are recommended for modeling the response of near incompressible materials (such as is appropriate for undrained soil conditions).

A plane strain mesh was constructed using quadrilateral first order fully integrated hybrid elements. The same geometry and discretisation as the plane of symmetry (i.e. the front face) of the three-dimensional mesh was used and equivalent boundary conditions, soil conditions and analysis procedures were modeled.

2.1.2 Material properties

Simple soil conditions were represented with an isotropic linear elastic-Tresca plastic constitutive model with uniform undrained shear strength with depth, s_u . (Note that ABAQUS adopts a von Mises flow rule with the Tresca failure criterion to avoid problems in defining the relative plastic strain magnitudes at the vertices of the hexagonal Tresca surface in the deviatoric plane.) The conditions considered are intended to represent a fine grained material subjected to a period of loading sufficiently short that no drainage will take place. Constant stiffness index $E_u/s_u = 1000$, Poisson's ratio $\nu = 0.49$, and buoyant unit weight $\gamma' = 8 \text{ kN/m}^3$ were prescribed. Although soil self-weight was used in the analysis, the nature of the problem considered, i.e. a surface footing resting on an isotropic homogeneous soil without drainage, leads to the calculated bearing capacity being unaffected by the value of γ' .

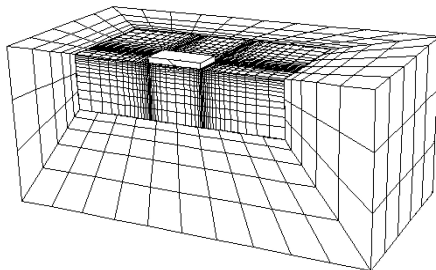


Figure 1. Finite element mesh for square footing analyses.

A contact surface was provided along the footing/soil interface to enable slip (when limiting shear strength was exceeded) and separation (when tensile stresses were developed). To represent the footings with unlimited tensile capacity common nodes were shared along the footing/soil interface preventing slip or separation.

2.2 Scope and loading method

Constant ratio displacement probe tests and displacement-controlled swipe tests were carried out to identify failure envelopes under vertical and moment loading. The foundation was subjected to controlled displacements, as opposed to directly applied loads, to enable post-failure conditions to be observed. The reference point for the applied displacement was taken as the midpoint of the foundation base.

Probe tests were carried out at constant ratios of rotation to vertical displacement (θ/u). The probe tests give rise to load paths that move from the origin across the failure envelope, initially at gradients determined by the elastic stiffness but with the gradients changing due to internal plastic yielding as the paths approach the failure envelope. Once the failure envelope is reached, each load path travels around the failure envelope until it reaches a point where the normal to the failure envelope matches the prescribed displacement ratio.

Swipe tests (introduced by Tan 1990) were also carried out to identify the failure envelopes. The footing was first brought to failure with uniaxial vertical displacement followed by a rotational swipe (θ) at constant embedment. The benefit of the swipe test is that a complete failure locus on a certain plane can be determined in a single test. Previous studies of strip and circular footings have confirmed that swipe paths track very close to the failure envelopes in the VM (and VH) plane with good agreement between constant ratio displacement probe tests (e.g. Bransby and Randolph 1998, Gourvenec and Randolph 2003).

3 RESULTS

3.1 Validation of FE model

A vertical bearing capacity factor of $N_c = 5.31$ was obtained from the plane strain finite element analysis, over predicting the exact solution by just 3% (Prandtl 1921). A much finer plane strain mesh was also constructed using 1,500 elements, two and a half times as many elements as the coarser mesh. The finer mesh gave a vertical bearing capacity factor $N_c = 5.27$, only a 0.5% increase in accuracy, indicating that the coarser mesh was sufficiently fine.

A vertical bearing capacity factor $N_c = 5.91$ for a square footing was predicted with the three dimensional

finite element model. Although no exact solution exists for benchmarking the three-dimensional model, the predicted capacity falls between numerically derived lower and upper bounds for a square footing $5.52 \leq N_c \leq 6.22$ (Salgado et al. 2004). Assessment of the true vertical bearing capacity of square (and rectangular) footings is considered by Gourvenec et al. (2006).

Under moment loading, the plane strain models predicted $M_{ult} \sim 8\%$ higher than the analytical solutions for both zero-tension and unlimited tension interface conditions. The larger discrepancy in the prediction of moment capacity compared with vertical capacity, results from the difficulty of representing a circular failure mechanism with quadrilateral elements.

The observed failure mechanisms conformed to those expected under uniaxial vertical bearing and pure moment providing additional confirmation that the finite element model was representing the intended conditions.

3.2 Ultimate limit states under combined vertical load and moment

3.2.1 Footing interface with zero tensile capacity

Figure 2 shows the load paths from the constant ratio displacement probe tests and the swipe test for the square footing with no tensile resistance. The probe paths correspond to ratios of rotation to vertical displacement $\theta/u = 0$ (pure vertical displacement), 1, 3 and 8. The swipe path provides good fit to the failure surface indicated by the probe tests. The swipe path terminates following mobilisation of the maximum moment capacity at $V \sim 0.5 V_{ult}$. The failure envelope for $V < 0.5 V_{ult}$ can be inferred from the high moment load path ($\theta/u = 8$), although it may cut inside the true failure envelope.

Figure 3 compares failure envelopes of the square and strip footings. For $V > 0.5 V_{ult}$ the swipe path is adopted and for $V < V_{ult}$ the highest moment constant ratio displacement probe load path is shown. The shape of the envelopes is similar with the moment capacity factor for the square footing falling consistently above that for the strip footing. The failure envelopes predicted by the effective width principle are also shown

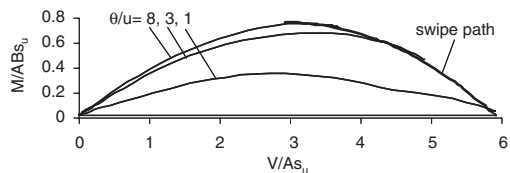


Figure 2. Constant ratio displacement load paths and displacement-controlled swipe path for square footing under vertical and moment loading.

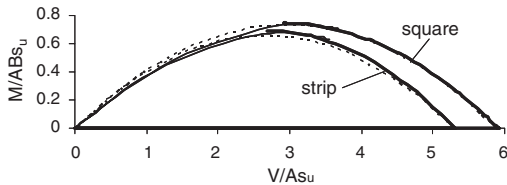


Figure 3. Failure envelopes in vertical and moment load space for strip and square footings.

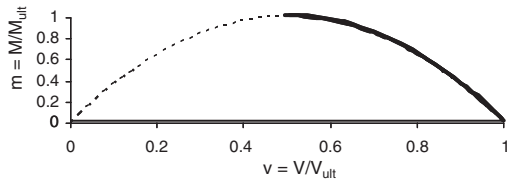


Figure 4. Normalised failure envelopes in vertical and moment load space for strip and square footings.

in Figure 3. A good fit is observed for both the plane strain and square footings for $V > 0.5 V_{ult}$.

Figure 4 shows the interaction presented in Figure 3 in terms of loads normalised by the respective uniaxial vertical or ultimate moment load $v = V/V_{ult}$ and $m = M/M_{ult}$. The normalised failure envelopes for the strip and square footings are coincident and in agreement with the effective width solution. Therefore ultimate limit states under combined vertical and moment loading for a square footing could be predicted by simply scaling the plane strain effective width solution by the appropriate limit states V_{ult} and M_{ult} . The shape of the envelope in normalised load space can be conveniently expressed algebraically by a parabolic curve;

$$m = 4v - 4v^2 \quad (\text{Eqn 1})$$

Figure 5 shows the kinematic mechanisms at the mid-plane cross-section accompanying failure of the square footing under uniaxial vertical load and under two different combinations of combined moment and vertical load. Figure 5a shows resultant displacement contours and displacement vectors at failure under pure vertical load. The displacement contours indicate a modified Prandtl mechanism with a shallower central wedge beneath the footing and additional sliding wedges between the central wedge and the shear fan zones (Kusakabe 1986). For the conditions modelled in this study the central triangular wedge creates an angle of approximately 23° with the footing as opposed to 45° as in Prandtl's plane strain solution (Prandtl 1921). The region of displaced soil around the square footing occupies a much smaller area than that around a strip footing of equal breadth. For example the failure mechanism

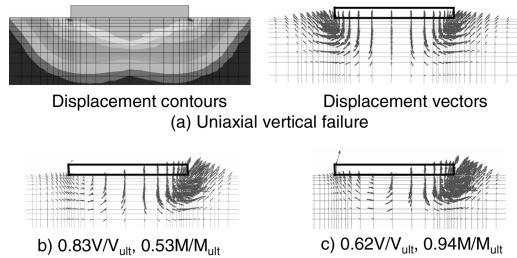


Figure 5. Failure mechanisms of square footing under vertical and moment loading.

of the square footing extends approximately $0.53B$ beneath and $0.58B$ to either side compared with $0.81B$ and $1.25B$ for a strip footing. The vertical failure mechanism is also shown in terms of displacement vectors for comparison with the combined loading cases shown in Figures 5b and c. The combined load cases refer to compressive vertical load and clockwise moment. As the component of moment increases a scoop mechanism is observed beneath the upward moving portion of the footing. Beneath the downward moving portion of the footing the vertical failure mechanism (as seen in Figure 5a) remains largely unchanged. The mechanisms correspond to the terminating points of the load paths shown in Figure 2 for imposed constant ratio displacement probes $\theta/u = 3$ and 8 . Almost no moment capacity was mobilised under an imposed displacement $\theta/u = 1$ and is therefore not included in Figure 5. A wedge-scoop mechanism is also observed at failure of a strip footing under equivalent loading conditions (Gourvenec & Randolph 2003).

Figure 6 shows plan views of the displacement vectors at failure of the square footing under (a) uniaxial vertical load and (b) combined moment and vertical loading at a constant displacement ratio $\theta/u = 8$. It is clear that the vertical failure mechanism, or the portion of the failure mechanism governed by vertical capacity, is axisymmetric while the rotational failure occurs in-plane.

Figure 7 illustrates the separation of the footing from the soil interface at the end of the displacement probes $\theta/u = 3$ and 8 .

3.2.2 Footing interface with tensile capacity

Figure 8 shows the failure envelopes under vertical and moment loading for the plane strain and square footings fully bonded to the soil interface. Results for a fully bonded circular footing from a previous study are also shown (Gourvenec and Randolph 2003).

The unlimited tensile capacity along the footing-soil interface leads to mobilisation of the maximum moment at zero vertical load for each of the footing geometries. The maximum moment capacity of the circular footing is similar to that for the strip footing while greater

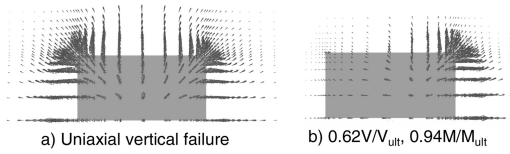


Figure 6. Plan view of displacement vectors at failure of square footing.

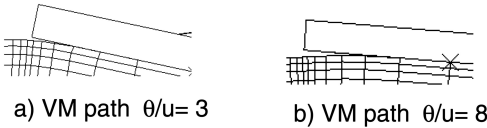


Figure 7. Separation along footing-soil interface under vertical and moment loading.

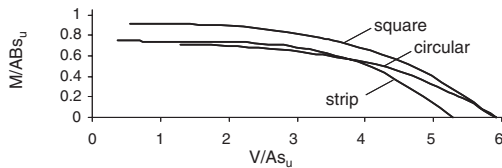


Figure 8. Failure envelopes in vertical and moment load space for strip, square and circular footings.

moment capacity is available with the square footing. Conversely the vertical bearing capacity of the circular footing is similar to that of the square footing and greater than that of the strip footing. The similarity of vertical bearing capacity of the three-dimensional footings is expected as the failure mechanism is essentially axisymmetric as opposed to in-plane for the strip footing. The moment capacity of the square footing is higher than the circular (or plane strain) footing due to the additional out-of-plane shear.

A footing with unlimited tensile capacity will fail under pure moment with a rotational ‘scoop’ mechanism. Upper bound solutions for moment capacity of strip and circular footings based on a plane circular or spherical scoops respectively are established (Murff and Hamilton 1993, Randolph and Puzrin 2003). No upper bound solution has been derived for a square footing, but logic may suggest a cylindrical rotational failure. If this were the case then a relatively straightforward upper bound could be derived from the work done on the circumferential slip plane (as in the plane strain solution) and in the circular segments in the out-of-plane direction. Observations from the finite element analyses carried out for this study show that the assumption of a prismatic cylindrical scoop is too simplistic and would be likely to lead to an unconservative estimate of moment capacity.

Figure 9a shows the rotational scoop beneath the square footing at the mid-plane cross-section as

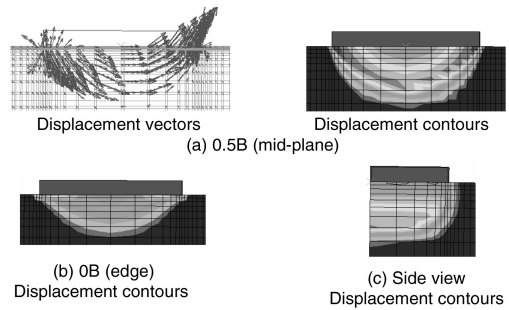


Figure 9. Failure mechanism under pure moment of square footing with unlimited tensile capacity.

resultant displacement vectors and contours of resultant displacements. The depth of the scoop is $0.288B$ beneath the footing-soil interface, giving the centre of rotation $0.212B$ above foundation level. This coincides with the optimal scoop mechanism for a plane strain footing with a moment capacity factor $N_{cM} = M_{ult}/ABs_u = 0.69$ (Murff and Hamilton 1993). Figure 9b shows the rotational failure observed under the edge of the footing (in the plane of applied moment) and shows that the mechanism is no longer circular. At the edge of the footing the scoop is approximately 20% shallower than at the mid plane. The side view of the displacement contours shown in Figure 9c illustrates the variation of the depth of the rotational mechanism with proximity to the edge of the footing.

Figure 10 shows the failure envelopes for the strip, square and circular footings in normalised vm load space. The normalised envelopes for the three-dimensional footings are a similar size, and plot inside the envelope for the strip footing. As the normalised envelope for the strip footing is largest, scaling the envelope derived for plane strain conditions by the appropriate uniaxial limit states for three-dimensional footing geometry would be unconservative. Gourvenec and Randolph (2003) proposed a simple power law to describe the shape of normalised failure envelopes

$$v = (1-m)^p \quad (\text{Eqn 2})$$

Where $p = 0.23$ for a strip footing and 0.27 for a circular footing for uniform Tresca material as modelled in this study (the exponent also varies with shear strength profile). The power law given in Eqn 2 also describes the shape of the normalised failure envelope for the square footing geometry with $p = 0.30$. The fitted curves are shown in Figure 10 as broken lines.

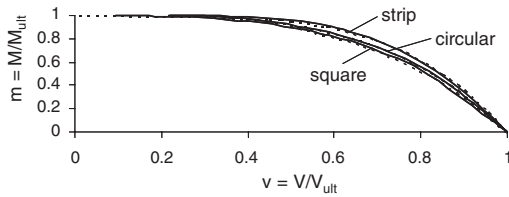


Figure 10. Normalised failure envelopes in vertical and moment load space for strip, square and circular footings.

4 FINAL REMARKS

The purpose of this study was to predict undrained limit states of square footings under combined vertical and moment loading and observe the accompanying failure mechanisms. Footings with zero-tensile capacity and with unlimited tensile capacity were considered.

As would be expected the capacity of the square footing was consistently higher than that of the strip footing for both interface conditions. Uniaxial vertical capacity and ultimate moment (for the zero-tension interface) increased in approximately equal proportion ($\sim 15\%$) which led to a good fit with predictions by the effective width rule. For the footing interface able to sustain unlimited tension an increase in maximum moment capacity of $\sim 30\%$ was observed. Although no established procedure is available for footings with unlimited tension with which to compare the predicted VM limit states, the failure envelope was shown to conform to a simple power law also appropriate for strip and circular footings.

The observed failure mechanisms indicated a composite wedge-scoop mechanism with the scoop portion becoming more pronounced with increasing moment. For all combinations of loading the wedge portion developed axisymmetrically and the scoop portion occurred in-plane. For the footing with unlimited tensile capacity the failure surface was barrel-shaped with the depth of the scoop diminishing towards the edges of the footing, indicating an upper bound based on a prismatic cylindrical scoop would be unconservative.

ACKNOWLEDGEMENT

The work described here forms part of the activities of the Special Research Centre for Offshore Foundation Systems, established under the Australian Research Council's Research Centres Program. This support is gratefully acknowledged.

REFERENCES

- Bransby, M.F. and Randolph, M.F. (1998). Combined loading of skirted foundations. *Geotechnique* 48(5):637–655.
- Cox, A.D., Eason, G. and Hopkins, H.G. 1961. Axially symmetric plastic deformation in soils. *Proc. Royal Soc. London, Ser. A*, 254, 1–45.
- Gourvenec, S.M. and Randolph, M.R. (2003). Effect of strength non-homogeneity on the shape and failure envelopes for combined loading of strip and circular foundations on clay. *Geotechnique*, 53(6): 575–586.
- Gourvenec, S., Randolph, M.F. and Kingsnorth, O. (2006) Undrained bearing capacity of square and rectangular footings. *Int. J. Geomech.*
- Hansen, B.J. (1970). A revised and extended formula for bearing capacity. *Danish Geotechnical Institute Bulletin* 28, Copenhagen.
- HKS (2004). *Abaqus Users' Manual, Version 6.5*, Hibbit, Karlsson and Sorensen, Inc.
- Houlsby, G.T. and Puzrin, A.M. (1999). The bearing capacity of a strip footing on clay under combined loading. *Proc. Royal Soc. Lond., Ser. A*: 455: 893–916.
- Kusakabe, O., Susuki, H. and Nakase, A. (1986). An upper bound calculation on bearing capacity of a circular footing on a non-homogeneous clay. *Soils and Foundations*, 26(3):143–148.
- Levin, E. (1955). Indentation pressure of a smooth circular punch. *Q. of Appl. Math.*, 13(2):133–137.
- Meyerhof, G.G. 1953. The bearing capacity of foundations under eccentric and inclined loads. *Proc. 3rd ICSMFE*, Zurich, 1, 440–445.
- Michalowski, R.L. (2001). Upper bound load estimates on square and rectangular footings. *Geotechnique*, 51, (9):787–798.
- Murff, J.D. and Hamilton, J.M. 1993. P-ultimate for undrained analysis of laterally loaded piles. *J. Geot. Eng. Div., ASCE*, 119(1), 91–107.
- Prandtl, L. 1921. Eindringungsfestigkeit und festigkeit von schneiden. *Angew. Math. U. Mech* 1(15).
- Randolph, M.F. and Puzrin, A.M. (2003). Upper bound limit analysis of circular foundations on clay under general loading. *Geotechnique* 53(9): 785–796.
- Salençon, J. and Pecker, A. (1995) Ultimate bearing capacity of shallow foundations under inclined and eccentric loads – I: Purely cohesive soil, *Eur. J. Mech. A* 4: 349–375.
- Salgado, R., Lyamin, A.V., Sloan, S.W. and Yu, H.S. (2004). Two- and three-dimensional bearing capacity of foundations in clay". *Geotechnique*, 54(5):297–306.
- Skempton, A.W. 1951. The bearing capacity of clays. *Proc. Building and Research Congress*, London 1, 180–189.
- Taiebat, H.A. and Carter, J.P. 2002. Bearing capacity of strip and circular foundations on undrained clay subjected to eccentric loads. *Geotechnique* 52(1), 61–64.
- Tan, F.S. (1990). *Centrifuge and theoretical modelling of conical footings on sand*. PhD Thesis, Cambridge University, UK.

Advanced FE versus classical settlement analyses

J. Hintner, P.A. Vermeer & C. Baun

Institute of Geotechnical Engineering, University of Stuttgart, Germany

ABSTRACT: According to Eurocode 7 the elasticity based settlement analysis is still state of the art in geotechnical engineering. On the other hand numerical methods have become available these days and the question arises whether or not such results comply with the classical methods based on the elasticity theory. To answer these questions numerical analyses have been performed for a strip footing as well as circular footing on sand as well as clay. The computations for the sand have been carried out with two different constitutive models, namely an elastoplastic and a hypoplastic one. Both models are advanced in the sense that stiffnesses are highly non-linear, including small-strain stiffness. It is shown that both models predict very similar footing settlements. However they highly exceed the predictions from classical calculations when the thickness of the compressible layer is high compared to the width of the footing. Finally it is shown that the classical idea of limit depth is well explained on the basis of small-strain soil stiffness.

1 INTRODUCTION

The estimation of settlements on the basis of the elasticity theory is well accepted in the geotechnical engineering practice. The considered classical methods are the oedometer method and the adjusted elasticity method. This study comprehends the comparison between these classical methods and numerical calculations for a strip footing as well as circular footing on sand as well as clay.

The datas for the soils are taken from the dense and loose Hostun-sand and the NC-Kaolin. The numerical calculations for the sand have been carried out with two completely different constitutive soil models, namely the elastoplastic Hardening-Soil model developed at the University of Stuttgart and the hypoplastic model developed at the University of Karlsruhe. Both models are nowadays extended to include small-strain stiffness effects. Both models have been calibrated on the basis of high quality experimental data such from oedometer and triaxial tests.

Within this study it will be shown that the two soil models give a good agreement regarding the deformation behaviour of the footing. The importance of considering the small-strain stiffness for simulating the real behaviour of the soil will be shown. It will also shown that numerical results at least for plane strain problems no longer depend on the mesh sizes when taking high stiffnesses at low strain level into account. Finally it will presented that the limit depth in classical settlement analysis is correct.

2 CLASSICAL METHODS

2.1 Oedometer method

According to Eurocode 7 (Orr & Farrell 1999) the oedometer method is the preferred method for settlement analysis. It is based on computing the stresses at selected points in the ground beneath the foundation from elasticity theory, calculating the strains in the ground from stresses using stiffness moduli from oedometer tests, and then integrating the strains to find the settlement.

This method takes the non-linear behaviour and the stress dependency of the soil into account, but is based on the assumption that foundations impose more or less one-dimensional compression. The limit depth considered in settlement analysis is the point where the vertical stress is not more than twenty per cent of the effective vertical pressure of the overburden (Tomlinson 1995, German code of practice DIN 4019 1979).

2.2 Adjusted elasticity method

The adjusted elasticity method (Tomlinson 1995) is based on calculating the settlement using the equation:

$$s = \frac{1 - \nu^2}{E} \cdot \Delta q \cdot b \cdot f \quad (1)$$

where E = Young's Modulus; ν = Poisson's ratio; Δq = net foundation pressure; b = width of foundation; and f = influence factor.

The selected E value should represent the non-linear behaviour and the stress dependency of the soil. For this study the representative E value is determined from oedometer test by converting the constrained modulus into a Young's Modulus via the Poisson ratio $\nu = 0.3$. In contrast to the oedometer method this method is considering the lateral strain in the ground however the adjusted elasticity equation should only be used if in the ground no significant yielding occurs. In the case of deep compressible soils the lowest level considered in the settlement analysis is based on the same assumption as for the oedometer method.

3 CONSTITUTIVE SOIL MODELS

The elastoplastic Hardening-Soil model goes back to the double hardening model as published by Vermeer (1978). Schanz (1998) created a similar model by using a Mohr-Coulomb type yield surface instead of a Matsuoka & Nakai type one and by introducing user-friendly input parameters. Most recently this model was extended by Benz (2006) to account for small-strain soil behaviour. Both the HS model and the HS-small model, i.e. the newest extension by Benz have been implemented in the Plaxis finite element code.

The hypoplastic model as also used in this study goes back to the original work of Kolymbas (1991). In 1996 a hypoplastic model with a predefined limit state surface was published by von Wolfersdorff. Later this constitutive model was extended by Niemunis & Herle (1997) to include the so-called small-strain stiffness.

4 ANALYSIS FOR THE SAND

4.1 Input datas for the sand

The calculations of a strip footing as well as circular footing have been performed considering the loose and the dense Hostun-sand. This sand is well documented by Desrues et al. (2000) and Biarez & Hicher (1994). For the footings on sand it is assumed that there is no groundwater and that the soil is normally consolidated. As one may see from Figure 1 the footings are embedded one meter in the ground and the width or the diameter of the footings are one meter.

The classical methods in this study are based on the use of stiffnesses as obtained in the oedometer test. In accordance to the empirical approach by Ohde (1939) the oedometer curves are described by Equation 2:

$$E_{oed} = E_{oed}^{ref} \left(\frac{\sigma'_z}{p_{ref}} \right)^m \quad (2)$$

where E_{oed}^{ref} = reference value of oedometer stiffness; σ'_z = vertical pressure; p_{ref} = reference pressure; and

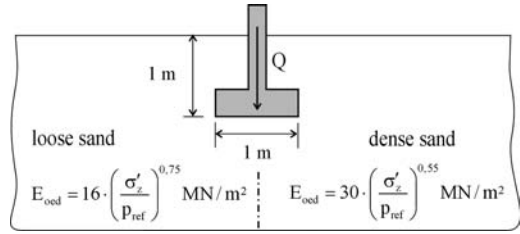


Figure 1. Geometry of the strip and circular footing.

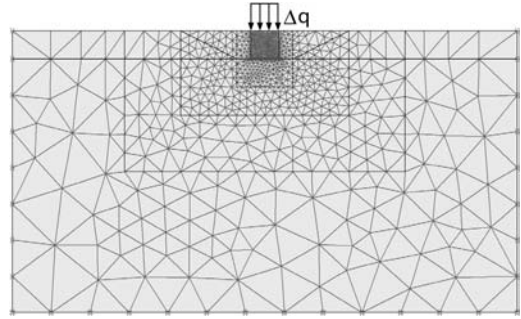


Figure 2. FE mesh of the strip footing.

m = exponent. The stiffness moduli for the classical methods are given in Figure 1 at a reference stress p_{ref} of 100 kN/m^2 .

The stress dependency of the stiffness as specified in Equation 2 is also implemented in the HS model. The numerical calculations for the strip footing were performed with a plane strain mesh (Fig. 2) and those for the circular footing with an axisymmetric mesh. The ground is represented by 6-noded triangular elements. The boundary conditions of the finite element mesh are as follows: The ground surface is free to displace, the side surfaces have roller boundaries and the base is fixed. The simulation has been carried out in analogy to a possible construction sequence with first excavating a pit, constructing the footing and filling on the sides. After this the displacement is set to zero and loading by applying the net foundation pressure Δq begins. Δq for both the classical and the numerical analyses is the same. Δq is the effective vertical soil pressure at the level of the footing reduced by the overburden pressure at this level. To achieve this for numerical analyses the footing block and the soil have the same unit weight. The fineness of the mesh is high adjacent to the footing and is getting coarser outwards. The mesh size is big in such a way as there is no influence from the boundaries. Between soil and foundation full contact is assumed, so no interface elements are used.

As already noted, FE calculations have been carried out with the HS-small model and the hypoplastic

model, both models extended by high stiffnesses at low strain level. The soil parameters were obtained by calibrating them on the bases of oedometer and triaxial tests. As one may see from Figures 3–5 the numerical simulations for both models are fitting very well the experimental curves, especially for the dense sand. Looking at the triaxial test for the loose sand one may see the stiffer behaviour of the hypoplastic model compared to the HS-small model. The parameters for the HS-small model as well as hypoplastic model are shown in Tables 1 and 2. Please note that the stiffnesses for the HS-small model are given at $p_{ref} = 100 \text{ kN/m}^2$.

The footings behave rigid as the linear elastic parameters of concrete with $E = 30,000 \text{ MN/m}^2$ and $\nu = 0.2$ are set to them.

4.2 Load-settlement curves

Figure 6a, b show the load-settlement curves for the strip footings on dense sand as well as loose sand. Figure 7a, b show the load-settlement curves for the circular footings resting on dense sand as well as loose sand. The curves have been carried out using the classical methods shortly explained in chapter 2, the HS-Small model and the hypoplastic model with small-strain stiffness. One may easily see that the classical analyses underpredict the settlements obtained by numerical analyses. For the classical methods one can observe that the rate of settlement decreases with loading. In contrast for the numerical analysis the rate of settlement increases when the load increases. The decreasing rate of settlement in classical analyses is due to the use of constrained moduli obtained in oedometer tests. There the rate of strains also decreases during loading.

Analysing the classical methods it is visible from the Figures 6, 7 that the adjusted elasticity method gives nearly twenty up to twenty five percent more settlement compared to oedometer method. Of course this could be expected since the adjusted elasticity method takes the lateral elastic strains into account.

The representative E value or E_{oed} value respectively for the adjusted elasticity method is obtained from stresses one meter beneath the foundation. To quantify how good this assumption is one may also derive a representative E value by backcalculating from settlement obtained by the oedometer method. This is done using Equation 1 and specifying $\nu = 0$. Remember an elastic soil with $\nu = 0$ deforms one-dimensional under vertical loading. For this case the adjusted elasticity method gives the same settlement as the oedometer method. Now when taking the backcalculated E value into account the adjusted elasticity method with $\nu = 0$ gives 23% more settlement compared to oedometer method. So for this study the chosen representative E value from stresses one meter beneath the foundation is quite a good choice.

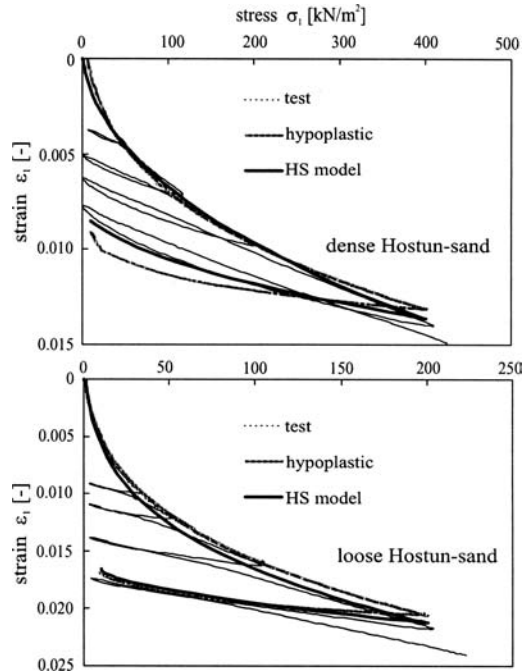


Figure 3. Oedometer test: Comparison between experimental data and numerical simulations.

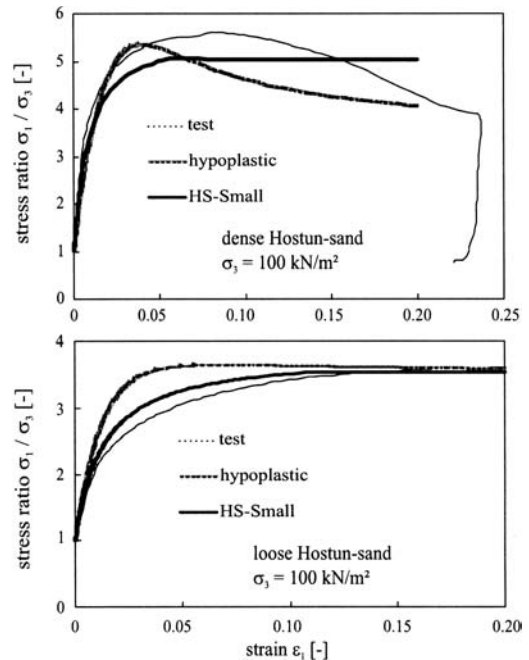


Figure 4. Drained standard triaxial test: Comparison between experimental data and numerical simulations.

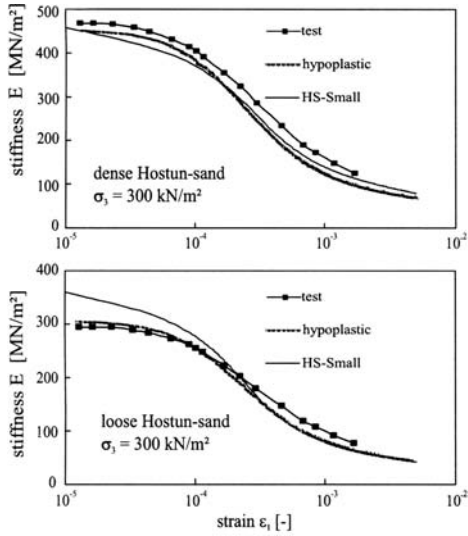


Figure 5. Triaxial test for small deformations after Biarez & Hicher (1994) and numerical simulations.

Table 1. Parameters for the HS model.

HS basic model		Loose	Dense Hostun-sand
γ	[kN/m ³]	15.0	17.0
ϕ'	[°]	34.0	42.0
ψ	[°]	0.0	16.0
c'	[kN/m ²]	0.0	0.0
E_{50}^{ref}	[MN/m ²]	12.0	30.0
E_{oed}^{ref}	[MN/m ²]	16.0	30.0
m	[-]	0.75	0.55
E_{ur}^{ref}	[MN/m ²]	60.0	90.0
ν_{ur}	[-]	0.25	0.25
Parameters for small-strain stiffness			
E_0^{ref}	[MN/m ²]	170.0	270.0
$\gamma_{0.7}$	[-]	0.0002	0.0002

Table 2. Parameters for the hypoplastic model.

HS basic model		Hostun-sand
h_S	[MN/m ³]	3800.0
ϕ_c	[°]	32.0
e_{c0}	[-]	0.91
e_{c0}	[-]	0.61
e_{c0}	[-]	1.09
n	[-]	0.29
α	[-]	0.134
β	[-]	1.35
Parameters for small-strain stiffness		
R	[-]	0.00006
m_R	[-]	5.0
m_T	[-]	2.0
β_r	[-]	0.5
χ	[-]	2.0

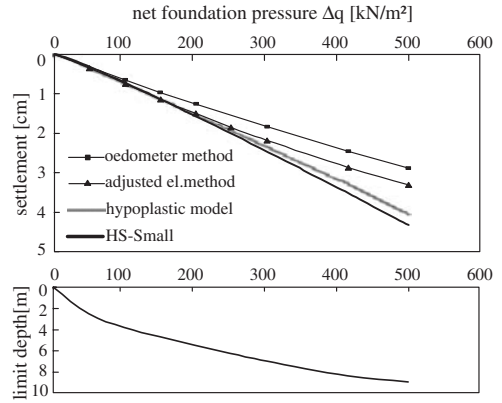


Figure 6a. Load-settlement curves and limit depth for the strip footing on dense sand.

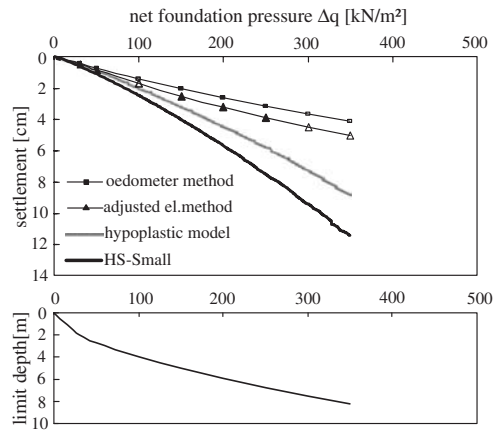


Figure 6b. Load-settlement curves and limit depth for the strip footing on loose sand.

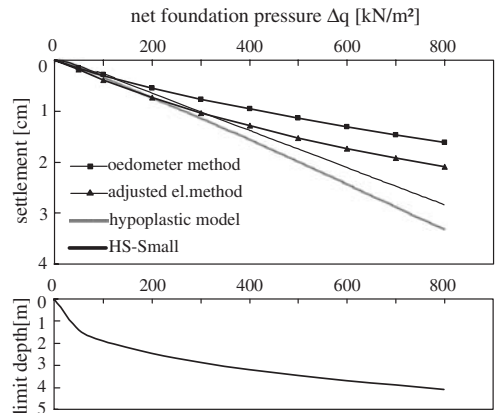


Figure 7a. Load-settlement curves and limit depth for the circular footing on dense sand.

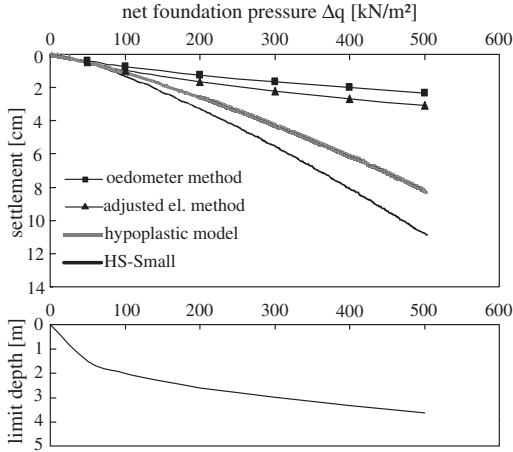


Figure 7b. Load-settlement curves and limit depth for the circular footing on loose sand.

The classical methods give only elastic settlements, plastic strains are considered with numerical methods and so the numerical calculations exceed the predictions from classical analyses in the case of loose sand up to three times whereas in the case of dense sand the factor between is less than two. Regarding the unfactored ultimate bearing capacity q_f for the strip footing with $q_f = 730 \text{ kN/m}^2$ for the loose sand and $q_f = 2700 \text{ kN/m}^2$ for the dense sand it is obvious that the rate of settlement in loose sand is higher due to higher plastic straining. This effect is more significant for the circular footing with $q_f = 890 \text{ kN/m}^2$ for the loose sand and $q_f = 3330 \text{ kN/m}^2$ for the dense sand since the problem is three-dimensional.

Basically it can be noted that the settlements of the two numerical models agree very well despite the different constitutive formulation especially for the dense sand. For the loose sand the hypoplastic model is behaving stiffer and this corresponds to the stiffer behaviour already noted in the numerical simulation of the triaxial test.

The limit depth used in classical methods is given in the Figures 6, 7. These charts are derived according to the German code of practice DIN 4019 (1979) or Tomlinson (1995). It is clear that the classical analyses match the numerical analyses till a certain limit depth. It follows that classical methods are acceptable for situations with a limit depth as given in Table 3. For limit depths higher than the given numerical analyses are considered. For layered soils the limit depth can also be a physical limit e.g. a much stiffer layer. In Table 3 this limit depth is given as a function of the width b of the footing. One can imagine if the thickness of the compressible layer is not much higher than the width of the footing the behaviour of the soil is close to the

Table 3. Limitations of the classical methods.

		Loose	Dense
<i>Strip footing</i>			
Oedometer method:	h_{limit}	$<2b$	$<2.5b$
Adjusted elasticity method:	h_{limit}	$<2.5b$	$<4.5b$
<i>Circular footing</i>			
Oedometer method:	h_{limit}	$<1b$	$<2b$
Adjusted elasticity method:	h_{limit}	$<1.5b$	$<3b$

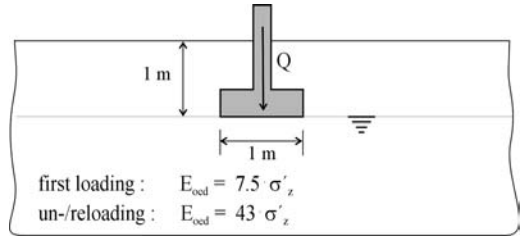


Figure 8. Geometry of the strip and circular footing for the clay.

behaviour of soil in the oedometer test. Whereas if the layer is much higher than b soil behaviour is far away from oedometric behaviour. The use of numerical methods is recommended.

5 ANALYSIS FOR THE CLAY

5.1 Input data for the clay

The determination of settlements for weak clay has been performed considering data from the NC-Kaolin by Biarez & Hicher (1994) and Bard (1993). The clay is preloaded by a small uniformly distributed surface load of $\sigma'_z = 10 \text{ kN/m}^2$. The groundwater table is at the level of the footing. The clay is fully saturated till the surface level. The suction due to capillary effect is not taken into account neither in the classical methods nor in the numerical analysis. As one may see from Figure 8 the footings are embedded one meter in the ground and the width or the diameter of the footings are one meter. For clays the stiffness exponent yields $m = 1$ and Equation 2 reduces to following equation:

$$E_{\text{oad}} = \alpha \cdot \sigma'_z \quad \text{with} \quad \alpha = E_{\text{oad}}^{\text{ref}} / p_{\text{ref}} \quad (3)$$

The stiffness moduli for the classical methods are given in Figure 8 for first loading and unloading-reloading since the soil is slightly preloaded. As can be seen stiffness of soil is much higher during un-/reloading compared to first loading. Similar to the sand the numerical calculations for the strip footing were performed with a plane strain mesh and those for the circular footing with an axisymmetric mesh. The simulation has been

carried out in accordance to a construction sequence as also used for the sand. Preconsolidation is modeled specifying the initial stress state using the Pre-Overburden Pressure (Brinkgreve 2002) with $POP = 10 \text{ kN/m}^2$.

FE calculations have been carried out with the HS-small because the hypoplastic model previous used is only suitable for coarse material. The soil parameters were obtained by calibrating them on the bases of oedometer and triaxial tests. As one may see from Figures 9–11 the numerical simulations are fitting very well the experimental curves. The parameters for the HS-small model are given in Table 4.

5.2 Load-settlement curves

Figure 12a, b show the load-settlement curves for the strip footing as well as the circular footing on clay. Again the oedometer method gives the lowest settlement, but not at low load level. This deviation comes from the choice of the representative stiffness modulus E_{oed} from stresses that arise one meter below the footing for all load levels. For low load levels this point should be closer to the footing since the limit depth is not much deeper than one meter. By plotting the stiffness modulus over depth (Vermeer et al. 2006) one may observe how the preconsolidation

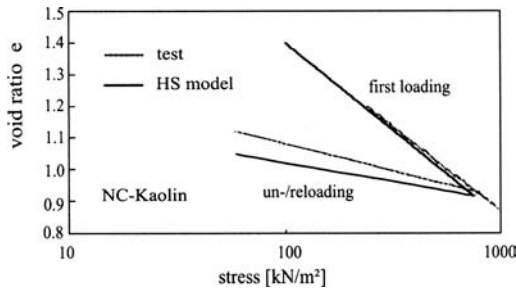


Figure 9. Oedometer test: Comparison between experimental data and numerical simulation.

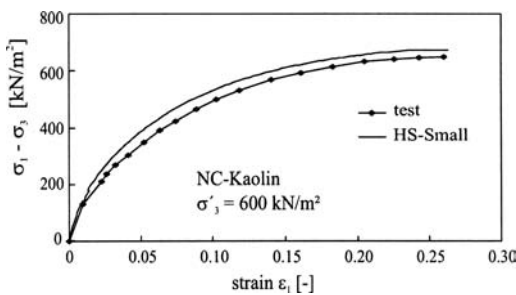


Figure 10. Triaxial test: Comparison between experimental data and numerical simulation.

pressure influences the shape of the curve. For low load levels soil stiffness one meter below the footing is still in the unloading-reloading part of the oedometer curve whereas the soil closer to the footing behaves soft since the vertical effective pressure is beyond the pre-consolidation stress. For higher loads this point should be deeper than one meter because the representative E_{oed} value accounts only for the soft behaviour of the soil and not for stiff behaviour in deeper regions since there the vertical effective pressure is below the pre-consolidation stress.

In comparison to the analysis in sand the classical load-settlement curves show a nearly bilinear shape with an increasing rate of settlement. The bilinearity of the curves is effected by the preconsolidation. Considering load levels higher than the given in Figures 12, 13 the rate of settlement would decrease again. Compared to sand it seems that the prediction in clay with classical methods is more successful. This arises, as the compressibility of clay is dominant when looking at the ratio of stiffnesses:

$$\begin{aligned} \text{Clay: } E_{oed}/E_{50}/E_{ur}/E_0 &\approx 1/2/10/100 \\ \text{Sand: } E_{oed}/E_{50}/E_{ur}/E_0 &\approx 1/1/3/9 \end{aligned}$$

From the load-settlement curves one can see that the oedometer method predicts the numerical analysis

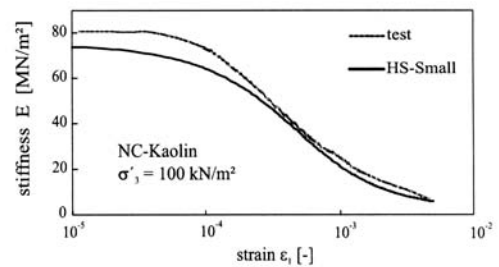


Figure 11. Triaxial test for the small deformations after Biazar & Hicher (1994) and numerical simulation.

Table 4. Parameters for the HS model.

HS basic model		NC-Kaolin
γ/γ'	[kN/m ³]	17.0/7.0
ϕ'	[°]	21.0
ψ	[°]	0.0
c'	[kN/m ²]	0.0
E_{50}^{ref}	[MN/m ²]	1.5
E_{oed}^{ref}	[MN/m ²]	0.75
m	[-]	1.0
E_{ur}^{ref}	[MN/m ²]	8.0
ν_{ur}	[-]	0.2
Parameters for small-strain stiffness		
E_0^{ref}	[MN/m ²]	80.0
$\gamma_{0,7}$	[-]	0.0002

till a limit depth of $2.5b$ for strip footing and $1.5b$ for circular footing. The elasticity method for the strip footing matches the numerical analysis for the shown load levels. For circular footing the use of this method is still considerable when the limit depth is not beyond $2.5b$.

6 VERTICAL DISPLACEMENT OVER DEPTH

Figures 13, 14 show the vertical displacement over depth as resulting from the HS model, the HS-Small model and the hypoplastic model with small-strain stiffness. It is visible that for the strip footing (Fig. 13) the influence of small-strain stiffness, as implemented in the HS-Small and the hypoplastic model, is considerable regarding the magnitude of the settlement and the

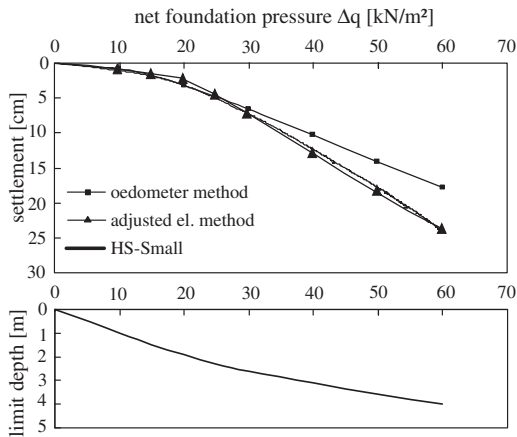


Figure 12a. Load-settlement curves and limit depth for the strip footing on clay

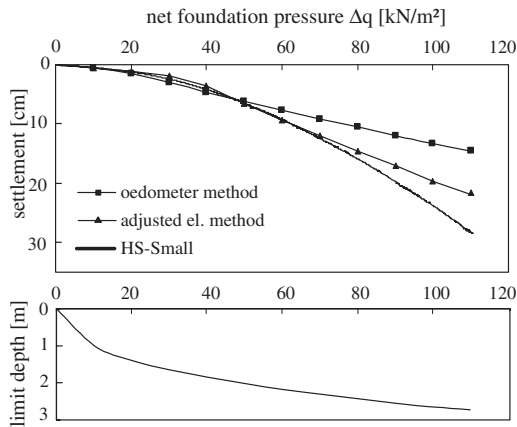


Figure 12b. Load-settlement curves and limit depth for the circular footing on clay.

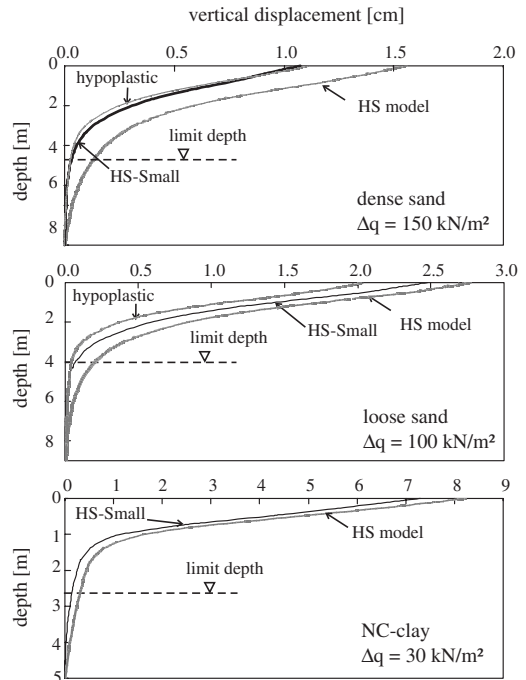


Figure 13. Vertical displacement over depth for strip footing.

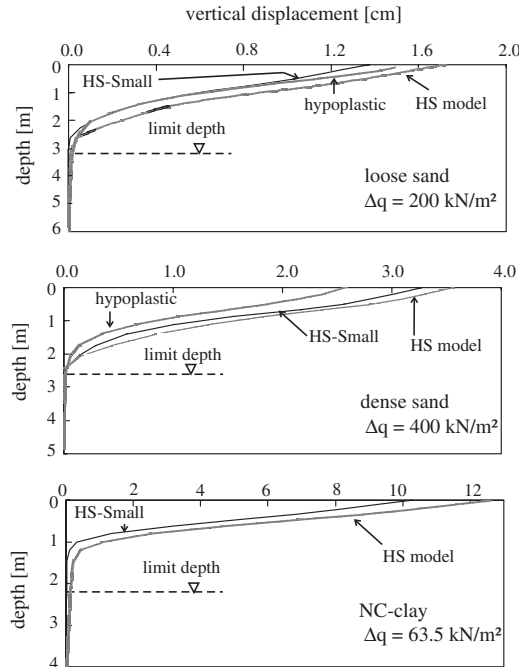


Figure 14. Vertical displacement over depth for circular footing.

shape of the curves. It can be seen that below a certain depth the vertical displacement tends to be negligible when small-strain stiffness is inside the model. One can observe that this depth is in good agreement with the limit depth in classical settlement analysis. This is not a surprise since at that depth the additional stress is low compared to the vertical initial stress. Therefore the strain of the soil is very low and stiffness is within the range of small-strain stiffness. Regarding the circular footing (Fig. 14) it can be seen that small-strain stiffness is not that important to consider since the HS and the HS-small model give nearly the same results. This is in contrast to the strip footing. But looking at the additional vertical stresses over depth one may observe that the stress gradient below the circular footing is higher compared to the strip footing.

It can be pointed out that the idea of considering a limit depth in classical settlement analysis is correct. Moreover the 20% rule for this limit depth would seem to be realistic. If the small-strain stiffness is neglected, the use of this limit depth should even be considered in numerical analyses, at least for plane strain problems.

7 CONCLUSIONS

In the framework of this study the settlements as calculated by classical methods have been compared with results of numerical analyses. It turns out that the classical methods underestimate settlements, at least with a limit depth beyond the given limitations in Table 3 and Chapter 5.2.

One of the classical methods is the so-called oedometer method which assumes one-dimensional compression. This method typically yields the smallest settlements. The so-called adjusted elasticity method takes the lateral strain into account. Therefore the settlements are slightly larger but care must be taken in choosing the representative E value. The classical methods do not account for plasticity. The deviation to the numerical analysis becomes high especially when the load is close to the design bearing capacity. Another interesting feature is that the prediction in NC clayey soils is more successful with the classical methods since the behaviour in such soils is dominated by the compression.

It was shown that the two completely different constitutive numerical models give a good agreement regarding the load-settlement curves and the vertical displacement over depth. Taking the effect of the high stiffnesses at low strain level into account the depth showing vertical displacement to be negligible is in good agreement with the limit depth according to the German code of practice or Tomlinson (1995). Another advantage of small-strain stiffness inside the model is that numerical results at least for plane strain problems depend no longer on the mesh sizes.

The authors will mention that in this study the calculations have been carried out using parameters from laboratory testing. Naturally soils have some cementation and therefore stiffnesses are higher. Having the real parameters this would effect the numerical results as well as classical ones.

ACKNOWLEDGEMENT

The authors are indebted to Dr. Peter A. von Wolffersdorff of Baugrund Dresden for his support in determining the hypoplastic parameters and to Thomas Benz of the Federal Waterways Engineering and Research Institute for developing the HS-Small model.

REFERENCES

- Benz, T. 2006. Small-Strain Stiffness of Soils and its Numerical Consequences, *Ph.D. Thesis*. Mitteilung des Instituts für Geotechnik der Universität. In print.
- Bard, E. 1993. Comportement des Matériaux granulaires secs et à liant hydrocarbone, *Ph.D. Thesis*. École Centrale de Paris – Laboratoire de Mécanique, Sols, Structure et Matériaux.
- Biarez, J. & Hicher, P.-Y. 1994. Elementary Mechanics of Soil Behaviour. Balkema.
- Brinkgreve, R.B.J. 2002. Plaxis – Finite Element Code for Soil and Rock Analyses. Rotterdam: Balkema.
- Desrués, J. & Zweschper, B. Vermeer, P.A. 2000. Database for Tests on Hostun RF Sand, Forschungsbericht des Instituts für Geotechnik der Universität Stuttgart: Heft 13.
- DIN 4019, Part 1 1979. Subsoil; analysis of settlements for vertical and centric loading. Berlin: Beuth Verlag.
- Kolymbas, D. 1991. An outline of hypoplasticity. *Archive Applied Mechanics* 61: 143–151.
- Niemunis, A. & Herle, I. 1997. Hypoplastic model for cohesionless soils with elastic strain range, *Mechanics of Cohesive Frictional Materials*, Vol. 2: 279–299.
- Ohde, J. 1939. Zur Theorie der Druckverteilung im Baugrund. *Der Bauingenieur* Vol. 20:451–459.
- Orr, T.L.L. & Farrell, E.R. 1999. Geotechnical Design to Eurocode 7. London: Springer-Verlag.
- Schanz, T. 1998. Zur Modellierung des mechanischen Verhaltens von Reibungsmaterialien. *Habilitation*. Mitteilung des Instituts für Geotechnik der Universität, Heft 45.
- Tomlinson, M.J. 1995. Foundation Design and Construction Sixth Edition. Longman.
- Vermeer, P.A. 1978. A double hardening model for sand. *Geotechnique* 28: 413–433.
- Vermeer, P.A., Hintner J., Baun C. 2006. Die Setzungsanalyse von Flachgründungen, In H. Schad (ed), 5. *Kolloquium Bauen in Boden und Fels, Ostfildern, 24–25 January 2006*: 351–362. Ostfildern: TAE.
- Von Wolffersdorff, P.-A. 1996. A hypoplastic constitutive relation for granular materials with a predefined limit state surface. *Mech. of Cohes. Frict. Mater.*, Vol. 1: 251–271.

Foundation analyses with unsaturated soil model for different suction profiles

Ayman A. Abed & Pieter A. Vermeer

Institute of Geotechnical Engineering, Universität Stuttgart, Germany

ABSTRACT: The well-known Barcelona Basic Model is considered to be a robust and suitable model for unsaturated soils and has thus been implemented into the Plaxis finite element code. After verifying its results by analytical solutions the unsaturated-saturated groundwater flow code PlaxFlow is used to calculate suction profiles required for the deformation analyses. This paper provides results of numerical analyses of a shallow foundation resting on an unsaturated soil using the implemented model. The unsaturated soil is considered to have common suction profiles. Special attention is given to the effect of suction variation on soil behaviour.

1 INTRODUCTION

Unsaturated soil is characterized by the existence of three different phases, namely the solid phase, the liquid phase and the gas phase. The important consequence is the development of suction at the solid-water-air interface. Suction increases with continuous drying of the soil and vice versa suction will be reduced upon wetting of the soil. The relation between the suction and the water content is named the Soil-Water Characteristic Curve (SWCC). Figure 1 gives a graphical representation for two different soils, namely clayey silt and fine sand. This curve plays a key role in unsaturated groundwater flow calculations and unsaturated soil deformation analyses. It can be seen from Figure 1 that suction plays a more important rule in the case of fine-grained soil than in the case of coarse-grained

sand. Indeed at the same water content, clay exhibits much more suction than sand. For that reason, one can expect more suction related problems for foundations on clay than on sand.

Soil shrinkage is a well recognized problem which is associated with suction increase, i.e. soil drying. On the other hand, soil swelling and soil structure collapse is considered as a main engineering problem during suction decrease under constant load, i.e. soil wetting. These phenomena would affect the foundations if no special measures would have been taken during the design process. The damage reparation costs level could reach high numbers e.g. as much as \$9 billion per year in the USA alone, as reported by Nelson & Miller (1992).

In the past many empirical procedures have been proposed to predict soil volume changes due to suction variations, but during the last fifteen years research attention has shifted to more theoretical models. In combination with robust constitutive models the FE method gives the designer a nice tool to understand the mechanical behaviour of unsaturated soils and it offers the opportunity to reach better design criteria.

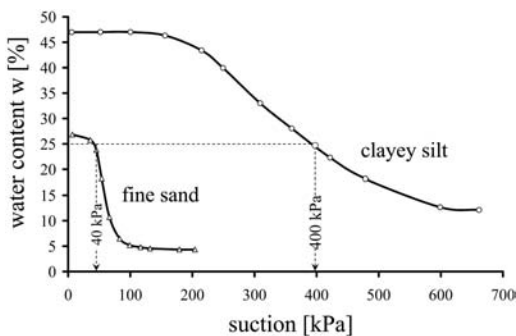


Figure 1. Soil-Water Characteristic Curves for clayey silt and fine sand.

2 UNSATURATED SOIL MODELLING

In surveying the literature one can classify the modelling methods into empirical and theoretical approaches.

2.1 Empirical methods

Empirical methods are based on direct fitting of test data for clays or silts. Especially poorly graded silts

(loess) are renowned as collapsible soil. These empirical methods are mostly based on data from one-dimensional compression in the oedometer apparatus. These tests give only clear information about the sample initial conditions and final conditions but no information about the suction variation during the saturation process. A nice review and evaluation of these methods can be found for example in the paper by Djedid et al. (2001).

As an example, Equation 1 is proposed by Kusa & Abed (2003) to predict the swelling pressure σ_{sw} in (kPa) as a function of the liquid limit w_L (%) the initial water content w_n (%) and the free swelling strain ε_0 (%). This strain is defined as the ratio of the soil sample height after saturation (without any external load) and the initial sample height before saturation.

$$\sigma_{sw} = 5.3 w_L + 3.3 w_L \cdot \ln \frac{\varepsilon_0}{w_n} \quad (1)$$

It is believed that such empirical correlations give only satisfactory results as long as they are applied to the same soils as used to establish the particular considered correlation. This reduces their use to a very narrow group of soils.

2.2 Theoretical methods

This category uses the principles of soil mechanics together with sophisticated experimental data for the formulation of a constitutive stress-strain law. An early attempt was made by Bishop (1959). He extended the well-known effective stress principle for fully saturated soil to unsaturated soil. Bishop proposed the effective stress measure

$$\sigma' = \sigma - u_a + \chi \cdot (u_a - u_w) \quad (2)$$

where σ is the total stress with compression reckoned positive, u_a is the pore air pressure, u_w is the pore water pressure and χ is a factor related to degree of saturation. It yields $\chi = 0$ for dry soil and $\chi = 1$ for saturated soil. According to Bishop the effective stress always decreases on wetting under constant total stress. As the effective stress decreases an increase in the volume of the soil should be observed in accordance with the above definition of effective stress. However, experimental data often shows additional compression on wetting which is opposite to the prediction based on Bishop's definition of effective stress. Many critics were expressed regarding the use of a single effective stress measure for unsaturated soil and there has been a gradual change towards the use of two independent stress state variables.

It was proposed by Fredlund et al. (1977) to use the net stress $\sigma - u_a$ and the suction s as two independent stress state variables to describe the mechanical

behaviour of the unsaturated soil, where $s = u_a - u_w$. In this study pore air pressure is considered to be atmospheric and soil suction is equal to negative pore water pressure. In the rest of this paper the terms suction and negative pore water pressure have the same meaning. On integrating the two stress measures into critical state soil mechanics, an elastoplastic constitutive model for unsaturated soil has been developed by Alonso et al. (1987) and later by Gens et al. (1990). Later other constitutive models have been proposed, but many of them remain in the framework of the Alonso and Gens model, which became known as Barcelona Basic Model (BBM).

3 BARCELONA BASIC MODEL

The BB-model is based on the Modified Cam Clay model for saturated soil with extensions to include suction effects in unsaturated soil (Gens et al. 1990). This model uses the net stresses $\sigma - u_a$ and the suction s as the independent stress measures. Many symbols have been used for the net stresses such as σ'' and σ^* . The latter symbol will be used here. It is assumed that the soil has different stiffness parameters for changes of net stress and changes of suction.

3.1 Isotropic loading

For isotropic unloading-reloading the rate of change of the void ratio is purely elastic and related to the net stress and the suction:

$$\dot{e} = \dot{e}^c = -\kappa \cdot \frac{\dot{p}^*}{p^*} - \kappa_s \cdot \frac{\dot{s}}{s + p_{atm}} \quad (3)$$

where κ is the usual (modified) swelling index and κ_s is the suction swelling index, p_{atm} is the atmospheric pressure and p^* is the mean net stress

$$p^* = \frac{1}{3}(\sigma_1 + \sigma_2 + \sigma_3) - u_a \quad (4)$$

In terms of volumetric strain equation (3) reads

$$\dot{\varepsilon}_v = \dot{\varepsilon}_v^c = -\frac{\dot{e}}{1+e} = -\frac{\kappa}{1+e} \cdot \frac{\dot{p}^*}{p^*} + \frac{\kappa_s}{1+e} \cdot \frac{\dot{s}}{s + p_{atm}} \quad (5)$$

where compressive strains are considered positive. For primary loading both elastic and plastic strains develop. The plastic component of volumetric strain is given by the equation

$$\dot{\varepsilon}_v^p = \frac{\lambda_0 - \kappa}{1+e} \cdot \frac{\dot{p}_{p0}}{p_{p0}} \quad (6)$$

where λ_0 is the usual (modified) compression index and p_{p0} is the preconsolidation pressure in saturated state. The above equation is in accordance with critical state soil mechanics, but we write p_{p0} instead of p_p and λ_0 instead of λ to emphasize that they relate to the saturated state. The difference with critical state soil mechanics is the yield function

$$f = p^* - p_p \quad (7)$$

where p_p is the suction dependent preconsolidation pressure

$$p_p = p^c \cdot \left(\frac{p_{p0}}{p^c}\right)^{\frac{\lambda_0 - \kappa}{\lambda - \kappa}} \quad (8)$$

where p^c is a reference pressure and

$$\lambda = \lambda_\infty - (\lambda_\infty - \lambda_0) \cdot e^{-\beta \cdot s} \quad (9)$$

λ is the suction dependent compression index. Hence, for full saturation we have $s = 0$, $\lambda = \lambda_0$ and $p_p = p_{p0}$. The larger the suction the smaller the compression index λ . In the limit for $s = \infty$ the above expression yields $\lambda = \lambda_\infty$. The index ratio λ_∞/λ_0 is typically in the range between 0.2 and 0.8.

The constant p^c is mostly in the range from 10 to 50 kPa. The constant β controls the rate of decrease of the compression index with suction; it is typically in the range between 0.01 and 0.03 kPa⁻¹. The monotonic increase of soil stiffness with suction is associated with an increase of the preconsolidation pressure p_p according to Equation 8. In order to study Equation 6 in more detail, we consider the consistency equation $\dot{f} = 0$, as it finally leads to Equation 6. In terms of partial derivatives the consistency equation reads

$$\dot{f} = \frac{\partial f}{\partial p^*} \cdot \dot{p}^* - \frac{\partial p_p}{\partial s} \cdot \dot{s} - \frac{\partial p_p}{\partial \varepsilon_v^p} \cdot \dot{\varepsilon}_v^p = 0 \quad (10)$$

with

$$\frac{\partial f}{\partial p^*} = 1 \quad (11)$$

$$\frac{\partial p_p}{\partial s} = \frac{\lambda - \lambda_\infty}{\lambda - \kappa} \cdot p_p \cdot \beta \cdot \ln \frac{p_p}{p^c} \quad (12)$$

$$\frac{\partial p_p}{\partial \varepsilon_v^p} = \frac{1 + e}{\lambda - \kappa} \cdot p_p \quad (13)$$

It follows from the above equations that

$$\dot{\varepsilon}_v^p = -\frac{\lambda - \lambda_\infty}{1 + e} \cdot \beta \cdot \ln \left(\frac{p_p}{p^c}\right) \cdot \dot{s} + \frac{\lambda - \kappa}{1 + e} \cdot \frac{1}{p_p} \cdot \dot{p}^* \quad (14)$$

This equation is in full agreement with Equation 6, but instead of p_{p0} it involves the stress measures s and p^* . Equation 14 shows the so-called soil collapse upon wetting. Indeed, upon wetting we have $\dot{s} < 0$ and the above equation yields an increase of volumetric strain, i.e. $\dot{\varepsilon}_v^p > 0$ even at constant load, i.e. for $\dot{p}^* = 0$.

3.2 More general states of stress

For the sake of convenience, the elastic strains will not be formulated for rotating principal axes of stress and strain. Instead, restriction is made to non-rotating principal stresses. For such situation Equation 5 can be generalized to become

$$\dot{\sigma}_i^* = D_{ij} \cdot (\dot{\varepsilon}_j^e - K_s^{-1} \cdot \delta_j \cdot \dot{s}) \quad \text{for } i, j = 1, 2, 3 \quad (15)$$

where $\dot{\varepsilon}_i^e$ is a principal elastic strain rate, σ_i^* is a principal net stress, $\delta_j = 1$ for $j = 1, 2, 3$ and

$$K_s^{-1} = \frac{\kappa_s}{3 \cdot (1 + e) \cdot (s + p_{atm})} \quad (16)$$

$$D_{ij} = \frac{E}{(1 - 2\nu) \cdot (1 + \nu)} \cdot \begin{bmatrix} 1 - \nu & \nu & \nu \\ \nu & 1 - \nu & \nu \\ \nu & \nu & 1 - \nu \end{bmatrix} \quad (17)$$

where ν is the elastic Poisson ratio. Young modulus is stress dependent:

$$E = 3 \cdot (1 - 2\nu) \cdot K \quad \text{with} \quad K = \frac{1 + e}{\kappa} \cdot p^* \quad (18)$$

The term $K_s^{-1} \cdot \delta_j \cdot \dot{s}$ in Equation 15 represents the contribution of suction loading-unloading (drying-wetting) to the elastic strain rates, whereas the other term represents the net stresses loading-unloading contribution.

For formulating the plastic rate of strain, both the plastic potential and the yield function have to be considered. For the BB-model the yield function reads

$$f = q^2 - M^2 \cdot (p^* + p_s) \cdot (p_p - p^*) \quad (19)$$

where M is the slope of the critical state line, as also indicated in Figure 2, and

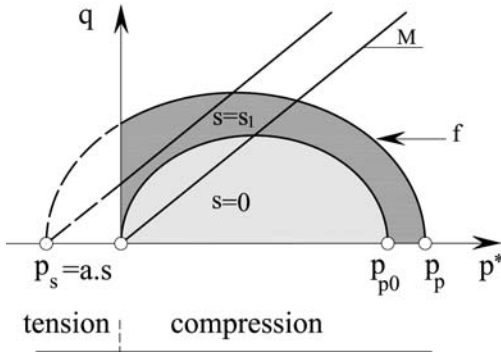


Figure 2. Yield surface of Barcelona Basic Model.

$$q = \frac{1}{\sqrt{2}} \sqrt{(\sigma_1 - \sigma_2)^2 + (\sigma_2 - \sigma_3)^2 + (\sigma_3 - \sigma_1)^2} \quad (20)$$

$$p_s = a \cdot s \quad (21)$$

It can be observed from Figure 2 that p_s reflects the extension of the yield surface in the direction of tension part due to apparent cohesion. The constant a determines the rate of p_s increase with suction.

At full saturation with $s = 0$ the yield function in Equation 19 reduces to the Modified Cam Clay (MCC) yield function. In contrast to the MCC-model, the BB-model has a non-associated flow rule, which may be written as

$$\dot{\varepsilon}_i^p = \Lambda \cdot \frac{\partial g}{\partial \sigma_i} \quad (i = 1, 2, 3) \quad (22)$$

where $\dot{\varepsilon}_i^p$ stands for a principal rate of plastic strain, Λ is a multiplier and g is the plastic potential function.

$$g = \alpha \cdot q^2 - M^2 (p^* + p_s) \cdot (p_p - p^*) \quad (23)$$

The flow rule becomes associated for $\alpha = 1$, but Gens et al. (1990) recommend to use

$$\alpha = \frac{M(M-9)(M-3)}{9(6-M)} \cdot \frac{\lambda_0}{\lambda_0 - \kappa} \quad (24)$$

In this way the crest of the plastic potential in p^* - q -plane is increased. Finally it leads to realistic K_0 -values in one-dimensional compression, whereas the associated MCC-model has the tendency to overestimate K_0 -values (Roscoe & Burland 1968).

In combination with Equation 15 and 22 the consistency condition $\dot{f} = 0$ yields the following expression for the plastic multiplier.

$$\Lambda = \frac{1}{H} \cdot \frac{\partial f^T}{\partial \sigma_i^*} D_{ij} \dot{\varepsilon}_j + \frac{1}{H} \cdot \left(\frac{\partial f}{\partial s} - K_s^{-1} \cdot \frac{\partial f^T}{\partial \sigma_i^*} D_{ij} \delta_j \right) \cdot \dot{s}$$

with

$$H = -\frac{\partial f}{\partial \varepsilon_v^p} \cdot \frac{\partial g}{\partial p^*} + \frac{\partial f^T}{\partial \sigma_i^*} \cdot D_{ij} \cdot \frac{\partial g}{\partial \sigma_j^*} \quad (25)$$

4 GROUNDWATER FLOW

Ground water flow is governed by the ground water head $h = y + u_w/\gamma_w$, where y is the geodetic head and u_w/γ_w is the pressure head which will be denoted as ψ for the sake of simplicity. γ_w is the unit pore water weight. In most practical cases there will not be a constant ground water head, but a variation with depth and consequently ground water flow.

Indeed, in reality there will be a transient ground water flow due to varying rainfall and evaporation at the soil surface. This implies transient suction fields and footing settlements that may vary with time. For most footing, settlements variations will be extremely small, but they will be significant for expansive clays as well as collapsible subsoil. In order to analyse such problems, we will have to incorporate ground water flow. Flow in an isotropic soil is described by the Darcy equation

$$q_i = -k_{rel} \cdot k_{sat} \cdot \frac{\partial h}{\partial x_i} \quad (26)$$

where q_i is a Cartesian component of the specific discharge water, k_{sat} is the well-known permeability of a saturated soil and k_{rel} is the pore pressure head-dependent relative permeability. Gardner (1958) proposed a simple but suitable exponential relative permeability function of the form

$$\begin{aligned} k_{rel} &= e^{\alpha \cdot \psi} & \text{for } \psi < 0 \\ k_{rel} &= 1 & \text{for } \psi \geq 0 \end{aligned} \quad (27)$$

where α is a fitting parameter. It is worthy to point out that the pressure height ψ has a negative value in the unsaturated zone. Figure 3 shows a graphical representation of Equation 27 for $\alpha = 2 \text{ m}^{-1}$.

In order to do ground water flow calculations, one has to supplement Darcy's equation 26 with a continuity equation of the form

$$\frac{\partial q_i}{\partial x_i} + C \cdot \frac{\partial h}{\partial t} = 0 \quad (28)$$

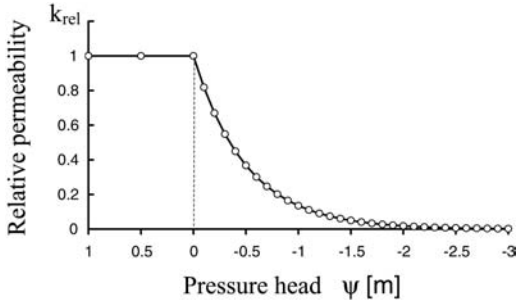


Figure 3. Gardner permeability model.

where repeated subscripts stand for summation. C is the effective storage capacity, which is often expressed as (Brinkgreve et al. 2003)

$$C = C_{sat} + n \cdot \frac{dS_r}{ds} \quad (29)$$

where C_{sat} is the saturated storage capacity, n the porosity and S_r the degree of saturation. The latter is a function of pore pressure head ψ , Russo (1988) proposed the following equation which is compatible with Gardner model (1958)

$$S_r = S_{res} + S_e \cdot (S_{sat} - S_{res}) \quad (30)$$

S_{res} is the residual degree of saturation, S_{sat} is the degree of saturation at full saturation which is usually taken as 1 and S_e is the effective degree of saturation given as

$$S_e = \left[(1 - 0.5 \cdot \alpha \cdot \psi) \cdot e^{0.5\alpha \cdot \psi} \right]^{\frac{2}{2+m}} \quad (31)$$

where m is a fitting parameter.

Strictly speaking soil deformation implies changing soil porosity n and pore fluid flow cannot be separated from soil deformation. For many practical problems, however, the soil porosity remains approximately constant and flow problems may be simulated without consideration of coupling terms.

In order to solve the differential equations 26 and 28, boundary conditions are required. For studying footing problems, one would need the water infiltration or the rate of evaporation at the soil surface, q . PlaxFlow finite element code has been used to calculate suction in unsaturated zone. In the following section, the numerical results of PlaxFlow are checked by analytical solutions in the case of one dimensional unsaturated groundwater flow.

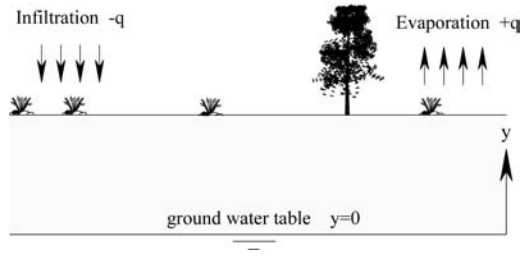


Figure 4. Boundary conditions used in Gardner solution.

4.1 Analytical solution for one dimensional unsaturated stationary groundwater flow

For one dimensional vertical steady flow Equation 28 reduces to Equation 32 in terms of pore pressure head ψ

$$\frac{\partial}{\partial y} \left[k_{sat} \cdot k_{rel}(\psi) \cdot \left(\frac{\partial \psi}{\partial y} + 1 \right) \right] = 0 \quad (32)$$

Gardner (1958) gave an analytical solution for the differential Equation 32 with infiltration or evaporation boundary conditions at soil surface, as shown in Figure 4. Using Equation 27 for the permeability function, the solution is given as

$$\psi = \frac{1}{\alpha} \cdot \ln \left[\left(\frac{q}{k_{sat}} + 1 \right) \cdot e^{-\alpha \cdot y} - \frac{q}{k_{sat}} \right] \quad (33)$$

Please note that Gardner used negative values for q to indicate infiltration and positive values to indicate evaporation.

4.2 Verification of the numerical results

A silty soil with saturated permeability of $k_{sat} = 1$ m/day and $\alpha = 2 \text{ m}^{-1}$ has been used to compare PlaxFlow numerical results with the analytical solution of Equation 32. Figure 5 shows the finite element mesh and boundary conditions used in the verification examples. Six noded triangular elements are used with closed vertical boundaries to recover 1-D conditions. The ground water table is at 3.0 depth and a Neumann type boundary condition is applied at the soil surface.

The problem has been solved for three common practical situations, namely hydrostatic conditions with $q = 0$, evaporation with $q = 0.002$ m/day and infiltration with $q = -0.1$ m/day. The hydrostatic conditions represent pore pressure distribution in unsaturated soil which has no interaction with surface water, for example a soil directly underneath a raft foundation. Evaporation represents soil moisture decrease due to temperature increase during a dry season and

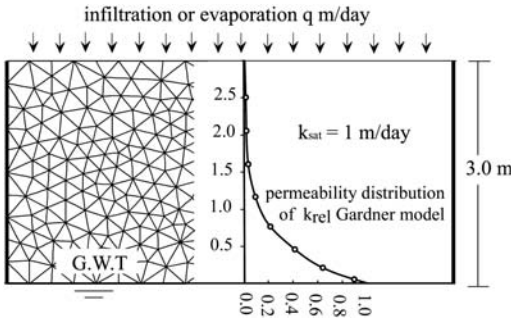


Figure 5. Finite element mesh and boundary conditions used in numerical calculations.

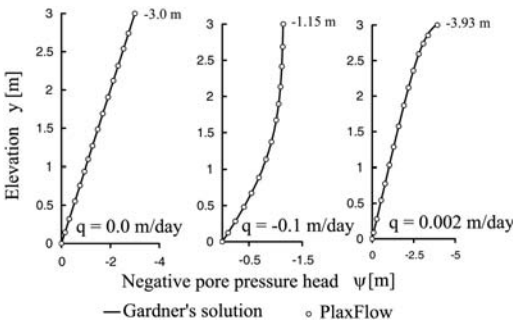


Figure 6. Analytical versus numerical results.

infiltration represents soil moisture increase due to rainfall for instance.

Figure 6 shows very good agreement between analytical and numerical results for this particular kind of problems. At the same time it gives a nice idea about negative pore water pressure profiles in such common cases. These profiles are used as input for deformation analyses using the Barcelona Basic Model.

5 DEFORMATION ANALYSES

Figure 7 shows the geometry, the boundary conditions and the finite element mesh for the problem of a rough strip footing resting on partially saturated clay of 3.0 meters thickness followed by a very stiff sand layer. The material properties shown in Table 1 are the same as those given by Gens (1990), except for the preconsolidation pressure p_{p0} and the reference pressure p^c . For the sake of convenience, a constant (mean) value of 17.1 kN/m^3 has been used for the soil weight above the phreatic line. For the initial net stresses K_0 -value of 1 has been used.

The finite element mesh consists of 6-noded triangles for the soil and 3-noded plate element for the

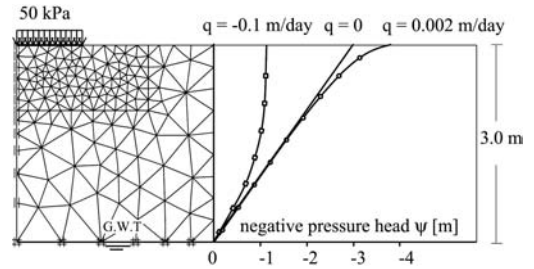


Figure 7. Finite element mesh, initial and boundary condition for deformation analysis.

Table 1. Material and model parameters.

e_0	0.9	[-]	β	0.0164	$[\text{kPa}^{-1}]$
λ_0	0.14	[-]	ν	0.15	[-]
κ	0.015	[-]	κ_s	0.01	[-]
p_{p0}	30	$[\text{kPa}]$	a	1.24	[-]
M	0.82	[-]	p^c	10	$[\text{kPa}]$
λ_∞	0.036	[-]			

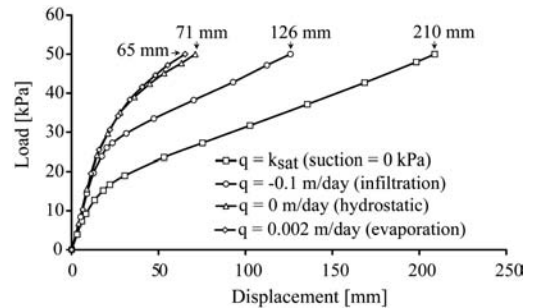


Figure 8. Load-settlement curves for footing on unsaturated soil with different suction profiles.

strip footing. The flexural rigidity of the plate was taken to be $EI = 10 \text{ MN}\cdot\text{m}^2$ per meter footing length. This value is representative for a reinforced concrete plate with a thickness of roughly 20 cm. The footing is loaded by a uniform pressure of 50 kPa and the corresponding settlements are determined for unsaturated soil with suction profiles satisfy those calculated in section 4.2. in addition an analysis without suction is to be considered. Computed load-settlement curves are shown in Figure 8. Loading the soil during dry season results in a stiff behaviour due to high suction values caused by continuous evaporation.

Nevertheless, it is only slightly different from loading the soil with hydrostatic suction distribution, both analyses yield about 70 mm footing settlement. In contrast, rainfall will reduce soil stiffness dramatically leading to final settlement of 126 mm which is two

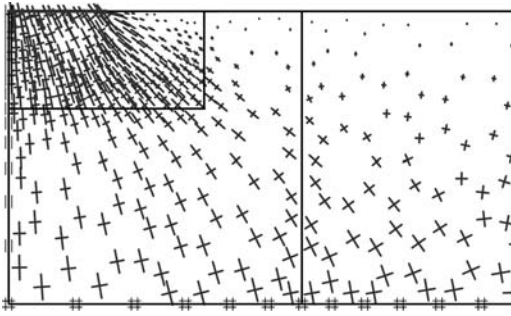


Figure 9. Principal stresses for hydrostatic pore pressure distribution at the end of loading.

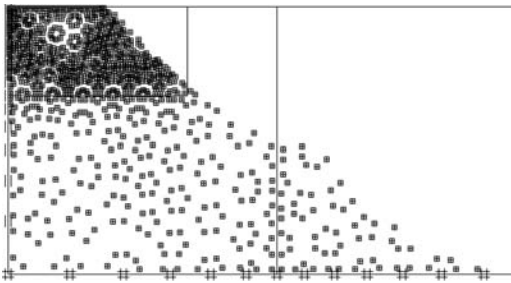


Figure 10. Hardening points distribution for hydrostatic pore pressure conditions at the end of loading.

times higher than the previous cases. When soil reaches full saturation it loses all suction contribution to stiffness which weakens the soil more and more. Loading the soil in such condition will result in settlement of 210 mm which is about four times higher than the settlement in the case of dry soil.

Figure 9 shows the principal stresses distribution at the end of loading in the case of hydrostatic suction profile. The distribution suggests that for a continuous clay layer with depth, a deeper finite element mesh will be preferred.

A typical plastified zone below the footing is indicated in Figure 10.

The previous calculations consider that we are loading the soil with a specific suction profile and this profile stays constant during and after construction. In reality, after construction on unsaturated soil, the decisive factor for footing movement will be suction variation with the variation of environmental factors such as temperature and rainfall. These variations lead to different phenomena such as soil shrinkage associated with soil drying and soil swelling or even soil structure collapse upon wetting. Soil potential for swelling or collapse should be given enough attention during design to avoid any unexpected consequences. A

detailed numerical study on unsaturated soil deformation and stability in the case of shallow foundations can be found in a recent paper by Vermeer & Abed (in press).

6 CONCLUSIONS

The present study addresses the effect of evaporation and infiltration on negative pore water pressure values in the unsaturated zone. This has been clarified using a simple 1-D vertical unsaturated flow model which has been solved analytically and numerically. Furthermore, the effect of changing suction on soil mechanical behaviour has been illustrated by studying the settlement of shallow footing on unsaturated soil with different suction profiles. The study gives clear idea about the strong influence of suction on soil stiffness. Further studies about soil deformation especially during wetting under constant load will improve too much our understanding for the mechanics of unsaturated soils and pave the way to incorporate such relatively new science in the real geotechnical engineering practise.

ACKNOWLEDGEMENT

We are grateful to Dr. Peter van den Berg of GeoDelft, the Netherlands for providing support to this study. We are also indebted to Dr. Klaas Jan Bakker of the Plaxis company for fruitful discussions on unsaturated soil behaviour.

REFERENCES

- Abed, Ayman. A. & Kusa, Issa. D. 2003. *Effect of swelling pressure on the soil bearing capacity*. Master thesis. Syria: Al-Baath University.
- Alonso, E.E., Gens, A. & Hight, D.W. 1987. Special problem soils: General report. *In proc. 9th Euro. Conf. on Soil Mech. and Found. Engin.* Vol.3:1087–1146. Rotterdam: Balkema.
- Bishop, A.W. 1959. The principle of effective stress. *Teknisk Ukeblad* 39:859–863.
- Brinkgreve, R., Al-Khoury, R. & van Esch, J. 2003. *PLAXFLOW User Manual*. Rotterdam: Balkema.
- Djedid, A., Bekkouche, A. & Mamoune, S.M. 2001. Identification and prediction of the swelling behaviour of some soils from the Telmcen region of Algeria. *Bulletin des Laboratoires des Ponts et Chaussées* 233 (July–August).
- Fredlund, D.G. & Morgenstern, N.R. 1977. Stress state variables for unsaturated soils. *Journal of the Geotechnical Engineering Division* 103: 447–466.
- Fredlund, D.G. & Rahardjo, H. 1993. *Soil Mechanics for Unsaturated Soils*. John Wiley & Sons.
- Gardner, W.R. 1958. Some steady-state solutions of the unsaturated moisture flow equation with applications

- to evaporation from a water table. *Soil Science* 85: 228–232.
- Gens, A., Alonso, E.E. & Josa, A. 1990. A constitutive model for partially saturated soils. *Géotechnique* 40:405–430.
- Nelson, J.D. & Miller, D.J. 1992. *Expansive Soils*. John Wiley & Sons.
- Roscoe, K.H. & Burland, J.B. 1968. On the generalized stress-strain behaviour of ‘wet’ clay. *Engineering Plasticity*. Cambridge University Press.
- Russo, D. 1988. Determining soil hydraulic properties by parameter estimation: On the selection of a model for the hydraulic properties. *Water Resources Research* 24:453–459.
- Vermeer, P.A. & Brinkgreve, R. 1998. *PLAXIS User Manual*. Rotterdam: Balkema.
- Vermeer, P.A. & Abed, A.A. (in press). Numerical simulation of unsaturated soil behaviour. *In proc. First Euro Mediterranean Conference on Advances in Geomaterials and Structures, Hammamet, 3–5 May 2006*. Tunisia.

Piles

Numerical modelling of laterally loaded short pile

S.W. Lee, A.R. Pickles & T.O. Henderson

Geotechnical Consulting Group (Asia) Ltd, Hong Kong

ABSTRACT: Design of laterally loaded short piles is normally based on empirical relationships derived from laboratory and full-scale tests. Finite element analysis (FEA) offers an alternative means to study the mobilisation of soil resistance around the pile and the associated failure mechanism. A series of three-dimensional FEA have been carried out to model laterally loaded single short pile, and the results compared against published laboratory and centrifugal model tests for flat ground and near slope conditions. The parameters investigated include the pile geometry, sand relative density, pile location relative to slope crest line and direction of lateral force. The results of FEA are also compared with theoretical solutions, for which relatively good agreements have been achieved. The behaviour of pile rotating about a fixed point and the variation of mobilised lateral soil resistance down the pile are highlighted and discussed against the assumptions adopted in theoretical solutions.

1 INTRODUCTION

Structures such as transmission towers, highway overhead signs, quays and train gantries are subject to high lateral loadings from wind force, wave action and traction forces. These structures are often supported by large diameter piers with high stiffness, which behave as short rigid piles. A short rigid pile fails by rotation, mobilising passive resistance on the opposite pile faces above and below the point of rotation. The moment-carrying capacity of the pile is therefore the principal design requirement, as the lateral force acts at a lever arm at the pile head. If the pile is constructed near a slope, the lateral soil resistance will be reduced due to the reduction of initial confining pressure acting around the pile on the slope side.

Theoretical approaches, based on the modulus of subgrade reaction and the elastic continuum reaction, have been used widely for predicting the ultimate lateral resistance of piles. Laman et al. (1999) argued that the theoretical approaches are inappropriate for short piles, which have relatively small depth/breadth ratios. Most of the current design approaches for short piles have been based on empirical relationships derived from full-scale tests and conventional laboratory model tests. However, the empirical relationships are either too arbitrary or only suitable for homogeneous soil condition.

This paper presents the results of three-dimensional (3D) finite element (FE) modelling on laterally loaded single short pile in cohesionless soil. The FE modelling simulated published conventional (earth's gravity) and centrifugal model tests, for which the pile was embedded in flat ground and near a slope, respectively. The

influences of the pile geometry, sand relative density, the pile location relative to crest of the slope and the direction of lateral force have been investigated. The FE programme Plaxis 3D Foundation has been used.

2 LITERATURE REVIEW

Figure 1 shows a pile subjected to lateral loading. The failure mechanism of the pile is related to the pile stiffness. If a pile is sufficiently rigid, i.e. a short pile, the soil resisting the lateral movement of the pile will fail first before the pile itself. If a pile is flexible, i.e. a long pile, a plastic hinge will develop on the pile first

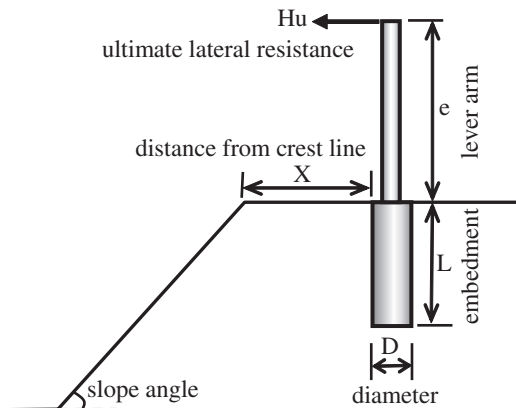


Figure 1. A pile subjected to lateral loading.

before the soil failure. Matlock & Reese (1960) proposed a stiffness factor (T) to assess the rigidity of a pile, i.e. whether it is a short or long pile. In cohesionless soils, the stiffness factor is defined as $T = \sqrt[5]{E_p I_p / n_h}$, where E_p is the pile Young's modulus, I_p the pile moment of inertia and n_h the coefficient of subgrade reaction. If the embedment depth of a pile is less than $2T$ then it behaves as a short rigid pile, whereas with an embedment depth of greater than $4T$ the pile behaves as a long flexible pile.

The literature review concentrates on the ultimate lateral resistance (H_u) of a short rigid pile embedded in cohesionless soil. Hansen (1961) considered the variation of lateral soil resistance with depth, based on earth pressure theory. By solving the equilibrium of horizontal force and moment of an unrestrained laterally loaded pile, the point of rotation of the pile is first determined (by trial and error) and then the H_u -value is calculated. Using a similar concept, Poulos & Davies (1980) proposed a conventional statics approach to estimate H_u , for the cases of uniform and linearly varying soil resistance with depth. Broms (1964) simplified the variation of lateral soil resistance with depth by assuming 1) no active earth pressure acting at the back of the pile; and 2) passive resistance in front of the pile equals to three times Rankine passive pressure. By taking moments about the pile toe, H_u is expressed as $H_u = (0.5\gamma' DL^3 K_p) / (e + L)$, where γ' is the soil effective unit weight and $K_p = (1 + \sin\phi / 1 - \sin\phi)$. Broms' method is useful for the initial design of a pile, if the soil has uniform characteristics. However, Poulos & Davies (1980) argued that Broms' assumption of passive resistance equal to three times Rankine passive pressure may be conservative in some cases. Reese & Van Impe (2001) presented the use of p - y curves to estimate the ultimate lateral soil resistance per unit pile length.

For a pile constructed at the crest line of a slope, Gabr & Borden (1990) proposed a three-dimensional wedge equilibrium analysis to estimate ultimate lateral soil resistance. The soil resistance is derived by assuming the pile as a translating rigid body moving into the soil. The soil in front of the pile will be in a passive state and the soil at the back in an active state. The angles of the wedge from the horizontal and vertical are determined by iteration so as to reach the minimum soil resistance. Reese & Van Impe (2001) presented analytical solutions to estimate the ultimate soil resistance of a rigid pile constructed in sloping ground, based on the p - y curve principle. UIC/ORE (1957) recommended a slope-reduction factor of 0.85 (pulled toward slope) and 0.95 (pulled away from slope) to the H_u -value in flat ground, if the distance of the pile from the slope crest line is less than the pile embedment depth. Chae et al. (2004) carried out 3D FE analyses for a single short pile located near a slope with an angle of 30° from the horizontal. The FE results suggested that to nullify the

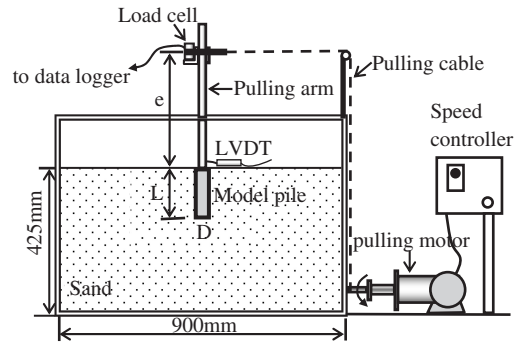


Figure 2. Nazir & Lee's (2004) conventional model test.

effect of the slope, the pile had to be located $4D$ (four times pile diameter) distance away from the slope crest line.

3 FINITE ELEMENT MODELLING

3.1 Pile in flat ground

Nazir & Lee (2004) present a series of conventional (earth's gravity) model tests on unrestrained single short piles subjected to lateral load in dense and loose gravelly sand. Figure 2 shows the schematic view of the model test. The model pile was made of mild steel. A geared motor was used to pull the model pile at a pre-determined pulling lever arm (e) via a load cell measuring the applied lateral load. The lateral displacement at the pile head was measured. The model pile diameter (D) was 40 mm and the three pile embedments (L) of 120 mm, 160 mm and 200 mm were adopted, corresponding to L/D ratios of 3, 4 and 5 respectively. The selected pulling lever arm over pile embedment ratios (e/L) ranged between 1 and 4. The γ' for the dense and loose gravelly sand was 16.2 and 14 kN/m³ respectively, and the peak friction angle (ϕ) was 48° and 39° respectively. The particle size distribution ranged between 0.1 and 4 mm.

Figure 3 shows a FE mesh modelling Nazir and Lee's model test where $L/D = 5$ and $e/L = 1$. Only half of the model domain was simulated, taking advantage of the symmetry with respect to the centre plane parallel to the loading direction. The gravelly sand was modelled as a Mohr-Coulomb material. Table 1 summarises the Mohr-Coulomb input parameters for the dense and loose sand. The secant Young's modulus value at 50% of maximum shear stress (E_{50}) was back-calculated from the direct shear box tests carried out by Lee (1996), based on the corresponding stress level at the mid-depth of the model pile. It is noted that the FE modelling is primarily aimed at predicting the ultimate lateral resistance of the model pile, not the load-displacement

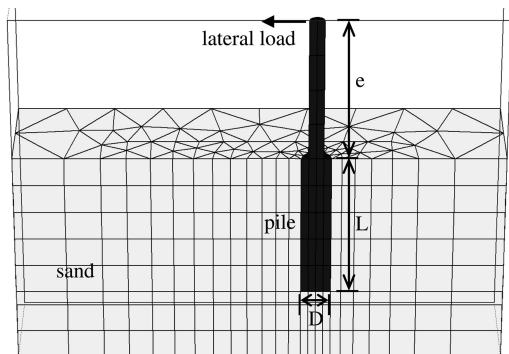


Figure 3. 3D mesh of Nazir & Lee's (2004) model test.

Table 1. Mohr-Coulomb input parameters.

Property	Dense	Loose	Pile
γ' (kN/m ³)	16.2	14	78
ϕ (°)	48	39	–
E_{50} (kPa)	4100	1900	$2.1E + 8$
Poisson's ratio, ν	0.3	0.3	0.15
Coef earth pressure at rest, K_0	0.26	0.37	1.0
Coef of interface, R_{int}	0.7	0.7	–

relationship of the laterally loaded pile. An interface was modelled between the pile and the surrounding sand, allowing for slip or a gap to develop between the sand and pile. The interface shear strength ($\tan\phi_{int}$) was input as 0.7-time the shear strength of the surrounding sand, i.e. $\tan\phi_{int} = 0.7\tan\phi_{soil}$. In the FE model a lateral point load was applied at the pre-specified lever arm above the pile head and the load was gradually increased. The ultimate lateral resistance (H_u) was defined as the point when the analysis failed to converge, and this normally associated with large slipping and gap development at the pile/sand interface.

3.2 Pile near slope

Dickin & Nazir (1999) carried out centrifuge modelling for a short pile embedded near a slope, see Figure 1. The centrifugal acceleration was 50 g and the slope angle was 36° from the horizontal. The model pile diameter (D) was 20 mm, the embedment (L) 80 mm and the pulling lever arm (e) 240 mm. In prototype, the D, L and e correspond to 1 m, 4 m and 12 m, respectively. The distance of the model pile from the slope crest line (X) was varied from 0 mm to 120 mm (0 to 6 m in prototype). The lateral pulling force was applied in two directions, either toward or away from the slope. The centrifuge tests were carried out in a fine, dry and dense sand, with a γ' of 16.4 kN/m³, ϕ of 46° and grain sizes

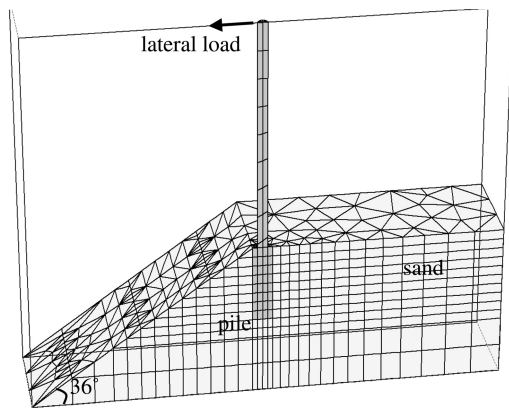


Figure 4. 3D mesh of Dickin & Nazir's (1999) centrifuge test.

ranging from 0.125 to 0.25 mm. In the centrifuge tests, a constant rate of displacement was applied to the lever arm head via a load cell, and the tests were terminated when the pulling force peaked.

Dickin and Nazir presented a series of triaxial test results for the dense sand, under different confining stresses (σ'_3). Taking the confining stress in the centrifuge at the mid-depth of the model pile, the secant Young's modulus at 50% of the maximum stress ratio (σ'_1/σ'_3), i.e. E_{50} , was back-calculated to be approximately 38,000 kPa. In the FE modelling a constant E-value of 38,000 kPa was adopted in the Mohr-Coulomb model, without considering the non-linear stress-strain behaviour of the sand from small strain. A Poisson's ratio (ν) of 0.3 and K_0 of 0.28 were assumed. The pile was modelled as a linearly elastic steel material, with an E-value of 210 GPa, γ' of 78 kN/m³ and ν of 0.15. An interface was included between the pile and the surrounding sand, allowing for slipping or gap development at the interface. The interface strength was specified as 0.7 times the sand strength, i.e. the interface friction angle was 32°. Figure 4 shows the FE mesh. Only half of the domain was modelled, taking advantage of the symmetry with respect to the centre plane parallel to the loading direction. In the FE modelling the gravity acceleration was increased to 50 g to model the centrifugal acceleration. A lateral force was applied at the lever arm head and gradually increased to pull the model pile. The ultimate lateral force (H_u) was defined as the point when the analysis failed to converge.

4 DISCUSSION OF FE PREDICTION

4.1 Pile in flat ground

Figure 5 compares the conventional model test results to the FE predictions for the tests carried out in the dense

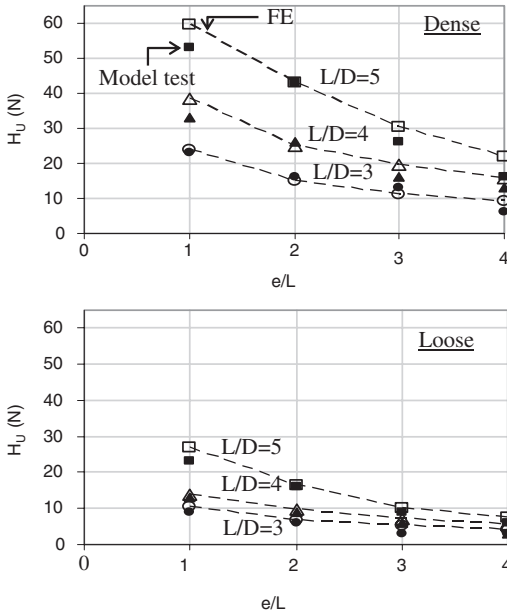


Figure 5. H_u comparison between model tests and FE results.

and loose sand. The ultimate lateral resistance (H_u) is plotted against the lever arm over pile embedment ratio (e/L), for different pile embedment over pile diameter ratios (L/D). The model test results are shown as individual solid symbols and the FE predictions as a dashed line with open symbols. Good agreement between the model test results and the FE predictions were observed, though the FE model tended to slightly over-predict the measured H_u -values. The predicted H_u -values were 95%–120% and 100%–120% of the model test results in the dense sand and loose sand respectively. The H_u -values in the dense sand were about two times the corresponding H_u -values in the loose sand.

Figure 6 shows the predicted displacement vectors for the analysis in the dense sand with $L/D = 5$ and $e/L = 1$. It is noted that the pile rotated at about $0.3L$ from the pile toe. Above the rotation point, the pile moved in the direction of pulling (forward), whereas below the rotation point the pile kicked backward. Ground heave was predicted in front of the pile, within an area $3D$ from the pile edge.

Figure 7 shows the predicted horizontal stress (σ_{xx}) contours around the model pile for the analysis in the dense sand with $L/D = 5$ and $e/L = 1$. It is noted that the largest σ_{xx} was predicted at $0.4L$ from the ground level in front of the pile and at $0.9L$ from the ground level at the back of the pile. The σ_{xx} contours ranged $10\text{--}80\text{ kPa}$ and $10\text{--}90\text{ kPa}$ for the region in front of and at the back of the pile respectively. In the region

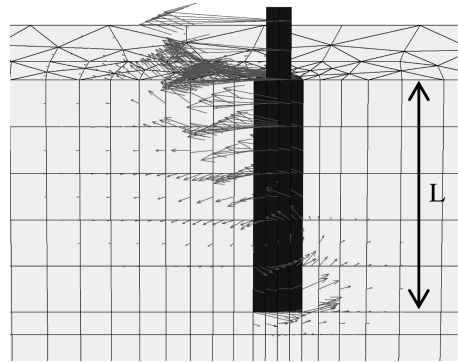


Figure 6. Predicted displacement vectors in the dense sand.

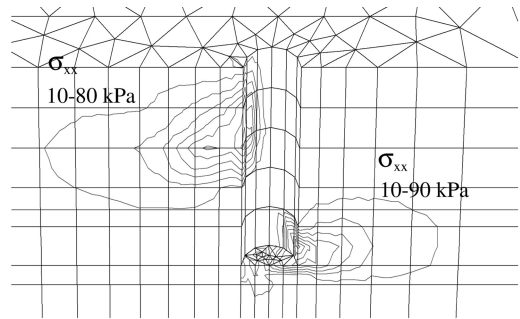


Figure 7. Predicted horizontal stress (σ_{xx}) around the pile.

of the rotation point, at $0.7L$ from the ground level, negligible change in σ_{xx} was predicted. For the corresponding test in the loose sand (not shown in this paper), the pattern of the σ_{xx} contours resembled that in the dense sand. However, the σ_{xx} magnitude in the loose sand was smaller, being $5\text{--}35\text{ kPa}$ and $5\text{--}40\text{ kPa}$ for the region in front of and at the back of the pile respectively.

Figure 8 shows the distribution of σ_{xx} with depth, for the analysis in the dense and loose sand with $L/D = 5$ and $e/L = 1$. In the chart, the σ_{xx} values in front of and at the back of the pile have been plotted on the same side of the abscissa axis. The Broms' assumption of three times Rankine passive pressure ($3K_p\sigma'_{yy}$) is also superimposed on the charts, where σ'_{yy} is the effective vertical stress.

For the dense sand, from the ground level to the region above the rotation point, the FE predicted larger σ_{xx} values, being 2–2.5 times Broms' three times Rankine pressures. In the region around the rotation point (from 0.12 m to 0.16 m depth), the FE predicted negligible σ_{xx} , compared to the Broms' linearly increasing σ_{xx} distribution. Below the rotation point, the FE predicted larger σ_{xx} values than those given by

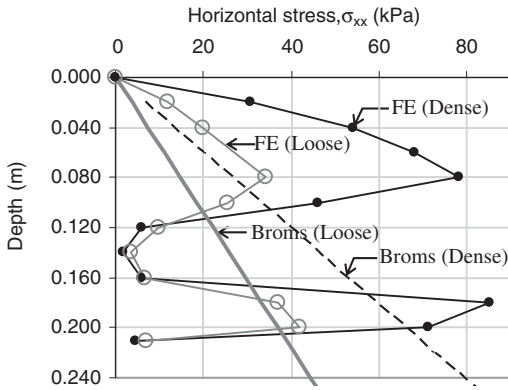


Figure 8. Distribution of σ_{xx} in the dense and loose sand.

Broms, being 10%–30% larger. When integrating the σ_{xx} -profile over the pile embedment depth of 0.2 m, it was found that the horizontal resistance force given by the FE was 25% larger than the Broms' assumption. Poulos & Davies (1990) commented that Broms' assumption of passive resistance equal to three times the Rankine passive pressure may be conservative in some cases. The FE predictions in the dense sand appear to support the Poulos and Davies' comment.

For the loose sand, from the ground level to the region above the rotation point, the maximum σ_{xx} predicted was 35 kPa, about twice Broms' assumption at the same depth. Below the rotation point the FE's σ_{xx} was 10% larger. When integrating the σ_{xx} -profile over the pile embedment depth of 0.2 m, the horizontal resistance force given by the FE was 5% larger than the Broms' assumption. Considering that the 5% discrepancy is small, the FE predictions in the loose sand appear to support the Broms' assumption of passive resistance equals to $3K_p\sigma'_{yy}$.

4.2 Pile near slope

Figure 9 compares the centrifuge results with the FE predictions. The H_u (in the model scale) is plotted against the X/L ratio ranging between 0 and 1.5. The model H_u value is multiplied by 2500 (50^2) to convert it to the prototype value. For the centrifuge results, if $X/L < 0.5$, H_u was smaller when the pile was pulled toward the slope than pulled away from the slope. If $X/L > 0.5$ the effect of the slope was in the opposite way, i.e. H_u larger when the pile is pulled towards the slope. At $X/L > 1.5$, the centrifuge results show that pulling towards the slope gave a 20% higher H_u than pulling away from the slope.

The FE predictions fall within the range of the centrifuge results. However, the FE shows that pulling towards the slope always gives a lower H_u than pulling away from the slope. At $X/L > 1.5$ the H_u values for

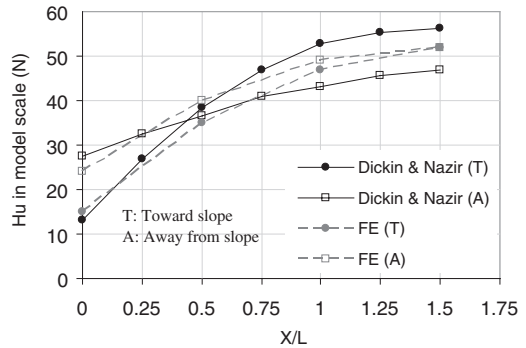


Figure 9. Comparison between centrifuge and FE results for a pile near slope (X : distance from crest line; L : embedment).

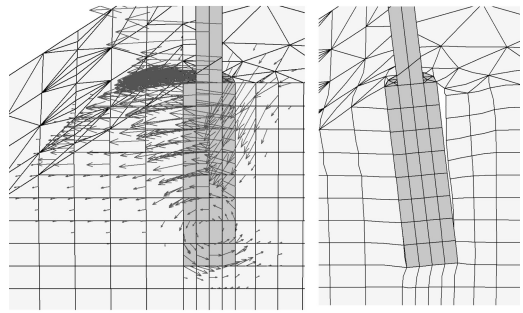


Figure 10. Predicted displacement vectors and deformed mesh for the case $X/L = 0$.

both the directions of pulling become similar at 52 N, and the effect of the slope is negligible. For the model pile located at the slope crest line (i.e. $X/L = 0$), the slope effect reduces the H_u to 30% of that in flat ground ($=15/52$) if pulled towards the slope, and 45% ($=24/52$) if pulled away from the slope.

Figure 10 shows the predicted displacement vectors when the pile failed, for the case $X/L = 0$. The rotation point was predicted at a distance $0.2L$ from the pile toe. Outward and slightly upward displacements were predicted on the slope in front of the pile, whereas the soil behind the pile head moved downward forming a depression. The same figure shows the deformed mesh when the pile failed. A gap opened behind the pile at the pile/sand interface and a depression was formed. In the FE modelling when a substantial gap appeared at the pile/sand interface behind the pile, the analysis was approaching the maximum H_u value.

Figure 11 shows the predicted horizontal stress (σ_{xx}) around the model pile when it failed, for the selected case $X/L = 0$. At the mid depth of the pile front the maximum mobilised σ_{xx} was 300 kPa, which was about 1.5 times the Rankine passive pressure. The slope effect has reduced the confining pressure in front of the pile,

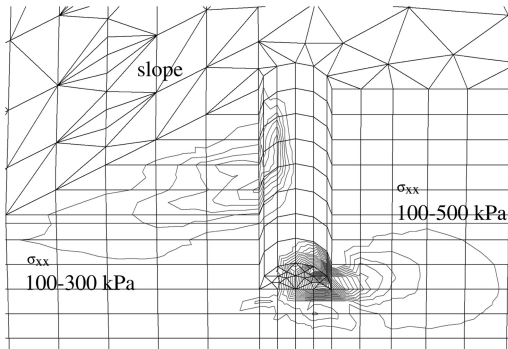


Figure 11. Predicted σ_{xx} around the pile near slope for $X/L = 0$.

reducing the maximum mobilised passive pressure from the conservatively assumed three times Rankine passive pressure in flat ground to 1.5 times. At the pile toe, a larger passive pressure was predicted at the back of the pile, the maximum being 500 kPa. This is equivalent to 1.24 times the Rankine passive pressure. A failure region developed both in front (upper half) and at the back (the toe region) of the pile, due to the pile rotation at $0.2L$ distance from the toe. The failure region became smaller, as the pile distance to the slope crest line increased (not shown in the paper). These predicted phenomena were similar to those predicted by Chae et al. (2004).

5 CONCLUSION

A series of 3D FE analyses were carried out to investigate the mobilisation of soil lateral resistance down a short rigid pile when subjected to a lateral force applied at a lever arm. Relatively good agreement has been achieved between the FE predictions and the conventional and centrifuge model tests. In flat ground, the predictions suggest that the Broms' assumption of passive resistance equals to three times Rankine passive pressure may be conservative in dense sand, whereas in loose sand the predictions agree with the Broms' assumption. When a pile is constructed at the crest line of a slope, the ultimate lateral resistance is predicted to reduce to 30% of that in flat ground (if pulled towards slope) and 45% (if pulled away from slope). This is due

to the reduction of initial confining pressure around the pile as a result of the slope. The effect of a slope on the lateral resistance of the pile is negligible when the pile is located at a distance 1.5 times the pile embedment from the slope crest line. The point of rotation for the pile is predicted to be located at 0.7 to 0.8 times the pile embedment from the ground surface for both flat ground and near slope conditions. When carrying out the FE analyses it was found that interface elements between the pile and surrounding soil were required to simulate the behaviour of a laterally loaded pile more realistically.

REFERENCES

- Broms, B.B. (1964). Lateral resistance of piles on cohesionless soil. *J. Soil Mech. Found. Div. Am. Soc. Div. Eng.* 90(SM3): 123–156.
- Chae, K.S., Ugai, K. & Wakai, A. (2004). Lateral resistance of short single piles and pile groups located near slope. *Int. J. Geomechanics ASCE* 4(2): 93–103.
- Dickin, E.A. & Nazir, R. (1999). Moment-carrying capacity of short pile foundations in cohesionless soil. *J. Geotech. & Geoenv. Engrg. ASCE* 125(1): 1–10.
- Gabr, M.A. & Borden, R.H. (1990). Lateral analysis of piers constructed on slopes. *J. Geotech. Engrg. ASCE* 116(12): 1831–1850.
- Hansen, J.B. (1961). Ultimate resistance of rigid piles against transverse forces. Danish Geotechnical Institute Report 12: 5–9.
- Laman, M., King, G.J.W. & Dickin, E.A. (1999). Three-dimensional finite element studies of the moment-carrying capacity of short pier foundations in cohesionless soil. *Computers and Geotechnics* 25(3): 141–155.
- Lee, S.W. (1996). Behaviour of horizontally loaded short piles in sand. Final year project of BEng course, University Technology Malaysia (in Malay language).
- Matlock, H. & Reese, L.C. (1960). "Generalised solutions for laterally loaded pile" *J. Soil Mech. Found. Div. Am. Soc. Div. Eng.* 86(5): 63–91.
- Nazir, R. & Lee, S.W. (2004). Horizontal load capacity of single piles in sand. *Proc. of 1st Malaysian Geotechnical Conference, Kuala Lumpur, March: 277–282.*
- Plaxis 3D Foundation. Plaxis three-dimensional finite element programme. Netherlands: Plaxis bv.
- Poulos, H.G. & Davies, A.G. (1980). *Pile Foundation Analysis and Design*. John Wiley & Sons.
- Reese, L.C. & Van Impe, W.F. (2001). *Single piles and pile groups under lateral loading*. Rotterdam: Balkema.
- UIC/ORE (1957). Calculation of catenary masts and foundations. Interim Report No.1, International Union of Railways/Office for Research and Experiments, Utrecht, The Netherlands.

Modelling piles under multi-directional loading conditions

N.H. Levy

Centre for Offshore Foundation Systems, University of Western Australia, Perth, Australia

I. Einav

School of Civil Engineering, University of Sydney, Sydney, Australia

ABSTRACT: The behaviour of pile foundations subjected to single directional lateral and axial loading has been substantially investigated in the past. However, the response of a pile subjected to a change in lateral loading direction or inclined loading (i.e. combined axial and lateral loading) has not been treated adequately. There is an increasing demand for a design method that considers the interaction between the responses of the pile-soil system when loads are applied in more than one direction, particularly for pile foundations that are installed offshore, which incur substantial lateral and torsional loads. This paper presents a multi-directional Winkler system that is modeled using an energy based variational (EBV) method, considering interaction at each depth along the pile using a series of local yield surfaces.

1 INTRODUCTION

The response of piles subjected to lateral or axial loading has been investigated in detail and established methods exist for determining this response (Fleming et al. 1992, API 1993). These methods generally model the soil as non-linear elastic, which limits their use to monotonic loading. In recent years the soil has been represented as an elasto-plastic medium with a yield or ultimate soil pressure defined as a function of depth (Murff 1975, Guo & Randolph 1997, Guo & Lee 2001, Hsiung 2003, Einav 2005). The concept of using a continuous field of yield surfaces to create a smooth non-linear curve was introduced by Einav (2005) for both axial and lateral loading.

The current paper presents an energy based variational (EBV) approach to solve the pile-soil system using the method presented by Einav (2005) for dissipative soil. A general model is presented for multi-directional loading based on the yield surface model presented by Levy et al. (2005). This model allows inclined loading to be modeled considering the interaction between the lateral and axial pile deformations. This type of model is also useful for the loading of piles in unaligned lateral directions, where the residual displacements from loading in previous lateral directions (“recent load history”) are taken into account for subsequent loading (Levy et al. 2006).

In this paper we extend our pile model of recent load history to a model with infinite yield surfaces at each point along the length of the pile. In this way we

benefit from the more realistic damping capabilities of multi-surface plasticity when compared to single surface plasticity. It is shown that the new model predicts a stronger effect of recent load history when smaller pile displacements are applied, but equivalent results in large displacements.

2 THE MODEL

The EBV approach allows all information regarding the geometry and constitutive assumptions of the pile-soil interaction problem to be encapsulated within two potential functionals (which are defined explicitly). For rate independent isothermal deformations the energy and dissipation potentials must satisfy the following equation:

$$\delta W = \delta \Psi + \Phi, \quad \Phi \geq 0 \quad (1)$$

where δW is the change in virtual work, $\delta \Psi$ is the change in internal energy and Φ is the change in mechanical dissipation (which is strictly non-negative).

The change in virtual work is defined as:

$$\delta W = \sum_i \int_0^L r_i(z) \delta u_i(z) dz \quad (2)$$

where r is the unbalanced force vector and δu is the change in displacement vector, each having a length n

defined by the number of perpendicular directions being considered (i.e. including x, y and/or z where x and y are perpendicular lateral directions and z represents the axial direction). The symbol L represents the length of the pile and z is the depth below the pile head. The unbalanced force vector is generally defined as zero along the length of the pile and as the imposed external forces at the pile head. If required a non-zero force could be applied along the pile length to represent lateral soil movement.

The internal energy is defined as the sum of the contributions from the pile and soil as follows:

$$\Psi = \Psi_p + \Psi_s \quad (3)$$

where the subscripts P and S refer to the pile and soil respectively.

The pile is assumed to deform in an elastic manner according to Euler-Bernoulli beam theory and is defined for a circular pile as (Reddy 2002, Einav 2005):

$$\Psi_p = \frac{E_p}{2} \int_0^L \left[I_p \left(\frac{d^2 u_x(z)}{dz^2} \right)^2 + I_p \left(\frac{d^2 u_y(z)}{dz^2} \right)^2 + A_p \left(\frac{du_z(z)}{dz} \right)^2 \right] dz \quad (4)$$

where E_p is the Young's modulus of the pile (assumed constant along the pile for simplicity), I_p is the moment of inertia of the pile about the axis of bending (for a circular pile $I_{xx} = I_{yy} = I_p$), A_p is the cross-sectional area of the pile. The x, y and z terms are included when required according to the loading conditions and the functions u_x , u_y and u_z represent the x, y and z components of the total displacement vector u , which has a length n .

2.1 Single yield surface soil model

The soil is modeled at each depth along the pile using independent Winkler springs, one each in the perpendicular directions, and a multi-dimensional yield surface.

In this model the soil resistance force (f_i) in each direction i is the same as the spring force (χ_i), which is defined by a linear force-displacement relationship with the elastic displacement and has spring stiffness E_{si} . The spring stiffness can also be referred to as the modulus of subgrade reaction and can be defined as a function of the pile and soil properties. The soil resistance force f_i can be defined by:

$$\begin{aligned} f_i(u_i, \alpha_i, z) &= \chi_i(u_i, \alpha_i, z) \\ &= E_{si}(z)(u_i(z) - \alpha_i(z)) \end{aligned} \quad (5)$$

where α_i is the plastic displacement in the i direction and the elastic displacement is defined as the total displacement minus the plastic displacement.

The components of the unbalanced force can now be defined as (for derivation see Einav 2005):

$$r_i(z) = \frac{d\Psi_p}{du_i(z)} + f_i(u_i, \alpha_i, z) \quad (6)$$

The soil energy density function ψ_{si} in each direction i is defined as:

$$\psi_{si}(u_i, \alpha_i, z) = \frac{E_{si}(z)}{2} (u_i(z) - \alpha_i(z))^2 \quad (7)$$

The soil energy potential Ψ_s is then defined as:

$$\Psi_s = \sum_i \int_0^L \psi_{si}(u_i, \alpha_i, z) dz \quad (8)$$

The change in energy potential can be defined as:

$$\delta\Psi = \sum_i \left(\frac{d\Psi_p}{du_i(z)} \delta u_i(z) + \frac{d\Psi_s}{du_i(z)} \delta u_i(z) \right) \quad (9)$$

The yielding behaviour of a soil subjected to lateral loading can be defined using the Randolph-Houlsby mechanism (Randolph & Houlsby 1984, Einav & Randolph 2005). As the limiting reaction will be the same in all lateral directions, a circular yield surface is suitable to define this behaviour.

It is less obvious how the soil will behave when subjected to combined lateral and axial loading. Levy et al. (2005) presented an elliptical yield surface for this behaviour but suggested that further research was required to refine this shape.

The general form of the dissipation function, assuming an elliptical relationship between the lateral and axial directions, will be as follows:

$$\Phi = \int_0^L \sqrt{\sum_i (f_{ui} \delta \alpha_i)^2} dz \quad (10)$$

where f_{ui} is the ultimate soil resistance force in the i direction.

A set of yield functions can be obtained from the dissipation potential using a set of degenerate Legendre transformations. The local elastic behaviour is bounded by a three dimensional ellipsoidal yield function (y) defined by the following:

$$y(z) = \sum_i \left(\frac{\chi_i}{f_{ui}} \right)^2 - 1 = 0 \quad (11)$$

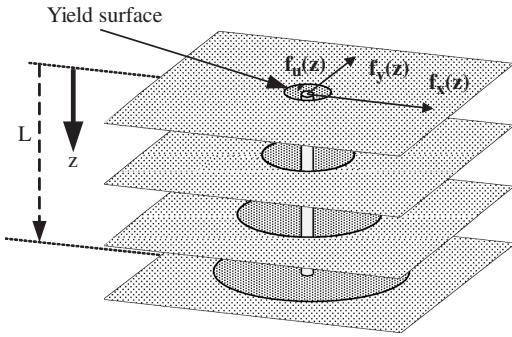


Figure 1. Schematic representation of a two dimensional single yield surface interaction model.

An example of this type of model is presented in Figure 1 for two dimensional lateral loading, where $f_u = f_{ux} = f_{uy}$. This can be extended to three dimensions and an ellipsoidal yield surface, as expressed in Equation 11.

2.2 Soil model 2 – continuous yield surfaces

An elasto-plastic non-linear force versus displacement relationship can be represented using the EBV approach. Rather than having a single spring-slider element in a given direction Einav (2005) presented a continuous Masing-Iwan model. This model consists of a group of spring-slider elements arranged in series with each element having a different spring stiffness and slider threshold depending on a local internal variable η that signifies the amount of yielding at each point along the length of the pile. Initially, before the occurrence of any yielding, η is 0, but as yielding in a soil layer progresses, η tends to 1. In this one-directional model, each value of η marked a single spring and a single one-directional slider.

In this paper we extend this model to two dimensions by considering an additional spring per internal coordinate η and representing the yielding by a two-dimensional yield surface rather than the slider.

Distribution functions are defined for the spring stiffness (H) and yield threshold (k) in each direction i and these must satisfy the following condition:

$$\int_{\eta=0}^1 H_i(\eta) d\eta = \int_{\eta=0}^1 k_i(\eta) d\eta = 1$$

The spring forces are defined for each internal variable η in a direction i as:

$$\chi_i(u_i, \alpha_i, z, \eta) = E_{si}(z) H_i(\eta) (u_i(z) - \alpha_i(z, \eta)) \quad (12)$$

The total soil resistance force at depth z in the i direction is defined as the integral of all the spring forces over the internal variable η :

$$f_i(u_i, \alpha_i, z) = \int_{\eta=0}^1 \chi_i(u_i, \alpha_i, z, \eta) d\eta = E_{si}(z) \left(u_i(z) - \int_{\eta=0}^1 H_i(\eta) \alpha_i(z, \eta) d\eta \right) \quad (13)$$

Therefore the soil free energy function can be defined as:

$$\psi_{si} = \frac{E_{si}(z)}{2} \int_{\eta=0}^1 H_i(\eta) (u_i(z) - \alpha_i(z, \eta))^2 d\eta \quad (14)$$

The dissipation function can be defined as:

$$\Phi = \int_0^L \int_{\eta=0}^1 \sqrt{\sum_i (k_i(\eta) f_{wi} \delta \alpha_i)^2} d\eta dz \quad (15)$$

The yield surfaces are defined as:

$$y(z, \eta) = \sum_i \left(\frac{\chi_i}{k_i(\eta) f_{wi}(z)} \right)^2 - 1 = 0 \quad (16)$$

3 EXAMPLES

The multi-dimensional EBV model provides a versatile approach to solving the cases of both simultaneous and staged loading in different directions. An example of each of these cases will be presented here.

3.1 Simultaneous lateral and axial loading

The case of simultaneous lateral and axial loading was presented by Levy et al. (2005) using the differential equations defined for each loading in each direction and a two-dimensional elliptical yield surface to couple the soil forces. These differential equations can be derived from the energy potentials (Einav 2005) and therefore this situation can be defined using the single yield surface model. Sensitivity analyses were completed on the influence of pile flexibility and the inclination of the imposed displacement. For the case of a 20 m length, 2 m diameter solid circular steel pile embedded in normally consolidated clay the applied

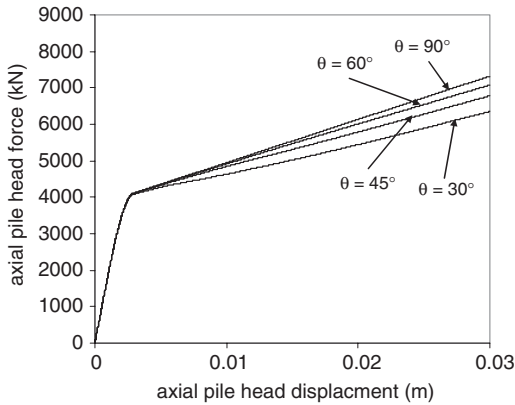


Figure 2. Axial pile head force versus displacement for inclined loading (from Levy et al. (2005)).

axial force versus the pile head displacement is shown in Figure 2 for various displacement inclinations from the horizontal (θ).

The results from this study suggest that the inclination of the applied load will influence the axial pile behaviour. A greater lateral load will cause the pile to displace further in the vertical direction. A sensitivity analysis on the pile flexibility shows that a more flexible pile will be influenced more in the axial direction by an inclined load.

This influence was shown to be less prominent for the lateral pile behaviour, with an applied axial load having minimal effect.

This study was presented as a starting point for this type of yield surface interaction model. The results show trends that agree with previous studies on inclined loading (Shahrour & Meimon 1991, Anagnostopoulos & Georgiadis 1993). Currently work is being undertaken to refine the yield surface shape to provide a more realistic representation of the interaction mechanism.

3.2 Staged two dimensional lateral loading

A pile subjected to monotonic lateral loading will behave the same in any direction using the EBV model. This model can be applied when a pile is loaded in a lateral direction and then in a different direction on the horizontal plane. Levy et al. (2006) coined the term “recent load history” to describe the soil-pile response in these conditions. As this term suggests loading history influences the behaviour of a pile during subsequent loading.

Levy et al. (2006) presented a numerical example of a pile loaded in a given direction, unloaded to zero and then loaded in a new direction. The study explores the influence of the pile flexibility, magnitude of the

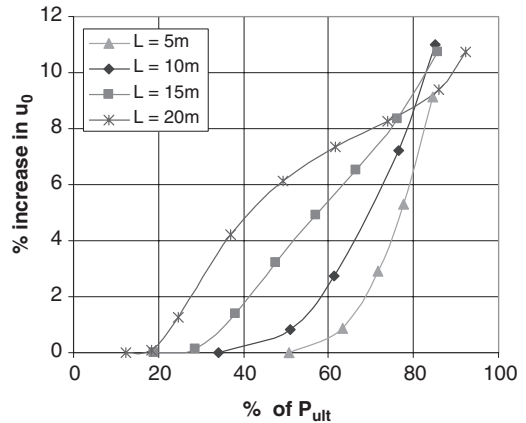


Figure 3. Percentage increase in resultant displacement relative to monotonic loading conditions ($\theta = 90^\circ$) (from Levy et al. 2006).

applied load and the angle between loading stages on the pile behaviour. An example of a steel pile with a diameter of 2 m and 20 mm wall thickness embedded in normally consolidated clay is presented below. Figure 3 shows the influence of the magnitude of loading during initial loading (as a percentage of the pile capacity, P_{ult}) on the resultant pile head displacement (u_0), as a percentage increase from the displacement achieved for monotonic lateral loading. The change in loading direction (θ) for this case was 90° and four different pile lengths were considered.

This plot suggests that the more a pile is loaded initially the greater the increase in the final pile head displacement. It also shows that a longer, (i.e. more flexible) pile will be influenced more by previous loading. This is because more stored energy is frozen along the length of the pile as a result of the yielding such that after unloading a more significant plastic displacement remains further from the zero position.

An even more astonishing factor is presented when examining the resultant load-displacement response. A typical load-unload-reload curve is shown in Figure 4 where Stage I is initially loading to a given force ($P/P_{ult} = 0.75$) in the x direction, Stage II is unloading to zero force and Stage III is loading at 90° (in the y direction) to the same P/P_{ult} as Stage I. The shape of the curve of Stage III is markedly different than that of Stage I, ending with additional displacement as summarised in Figure 3.

3.3 Extension to continuous yield surface model

In this section we extend the above model to the case of continuous yield surfaces. This allows a non-linear

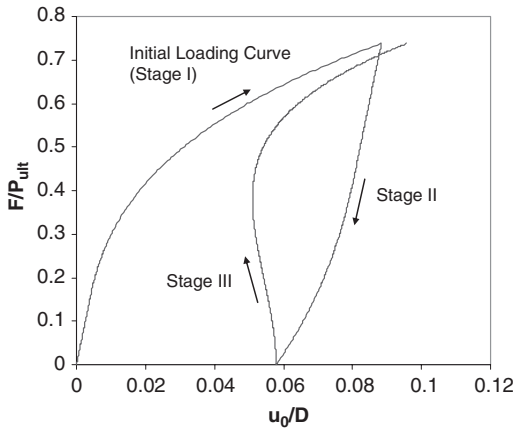


Figure 4. F/P_{ult} versus u_0/D at the pile head for $P/P_{ult} = 0.75$.

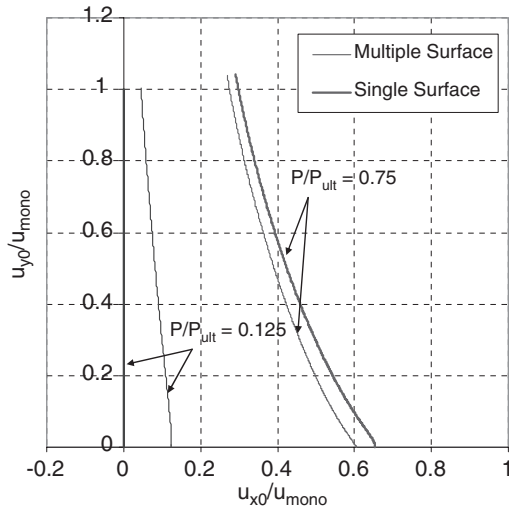


Figure 5. Evolution of pile head displacement determined using a single and multiple yield surface models.

force displacement profile to be considered, which will represent the soil in a way that more closely resembles the curves defined from physical testing results (API 1993).

The continuous yield surface model allows the behaviour of the soil during unloading of a pile to be better represented. The analysis discussed in the previous section for staged lateral loading was repeated using the continuous yield surface model. A comparison between the pile head location as suggested by the two alternative models is shown in Figure 5.

At large loads the behaviour of the pile does not vary significantly between the two models. As the soil

has reached the yield value over a section of the pile some plastic deformation will remain after unloading. In contrast, for the case where $P/P_{ult} = 0.125$ the single yield surface model does not reach yield at any point along the pile and therefore the pile will return to its original position after unloading. Due to the gradual yielding the multiple yield surface model does exhibit a plastic displacement. Since it is well established that the fundamental constitutive stress-strain behaviour of clays presents small strain non-linearity the multiple yield surface model is more representative, accounting for the additional damping in the soil. It is shown that the new model predicts a stronger effect of recent load history when smaller pile displacements are applied, but similar results in larger displacements.

4 CONCLUSIONS

A model is presented in the paper that enables an analysis of the behaviour of a pile loaded in multiple directions. This model allows different soil conditions to be considered as well as many loading combinations. This type of interaction model has enormous potential to consider the interaction between loading directions and design piles more efficiently.

REFERENCES

- Anagnostopoulos, C., & Georgiadis, M. (1993). Interaction of axial and lateral pile responses. *Journal of Geotechnical Engineering*, 119(4), 793–798.
- API. (1993). Recommended practice for planning, designing and constructing fixed offshore platforms – Working stress design, 20th edition. *API-RP-2A*.
- Einav, I. (2005). Energy and variational principles for piles in dissipative soil. *Geotechnique*, 55(7), 515–525.
- Einav, I., & Randolph, M. F. (2005). Combining upper bound and strain path methods for evaluating penetration resistance. *International Journal for Numerical Methods in Engineering*, 63(14), 1991–2016.
- Fleming, W. G., Weltman, A. J., Randolph, M. F., & Elson, W. K. (1992). *Piling Engineering*, E & FN Spon, New York & London.
- Guo, W. D., & Lee, F. H. (2001). Load transfer approach for laterally loaded piles. *International Journal for Numerical and Analytical Methods in Geomechanics*, 25(11), 1101–1129.
- Guo, W. D., & Randolph, M. F. (1997). Vertically loaded piles in non-homogeneous media. *International Journal for Numerical and Analytical Methods in Geomechanics*, 21(8), 507–532.
- Hsiung, Y. -M. (2003). Theoretical elastic-plastic solution for laterally loaded piles. *Journal of Geotechnical and Geoenvironmental Engineering*, 129(5), 475–480.
- Levy, N. H., Einav, I., & Randolph, M. F. (2005). Modelling combined loading of piles with local interacting yield

- surfaces. *International Symposium on Frontiers in Offshore Geotechnics*, Perth, Australia, 873–879.
- Levy, N. H., Einav, I., & Randolph, M. F. (2006). Effect of Recent Load History on Laterally Loaded Piles in Normally Consolidated Clay. *The International Journal of Geomechanics*, (submitted).
- Murff, J. D. (1975). Response of axially loaded piles. *Journal of Geotechnical Engineering Division, ASCE*, 101(3), 356–360.
- Randolph, M. F., & Houlsby, G. T. (1984). Limiting Pressure on a Circular Pile Loaded Laterally in Cohesive Soil. *Geotechnique*, 34(4), 613–623.
- Reddy, J. N. (2002). *Energy Principles and Variational Methods in Applied Mechanics*, John Wiley & Sons, Inc., Hoboken, New Jersey.
- Shahrour, I., & Meimon, Y. (1991). Analysis of the behaviour of offshore piles under inclined loads. *International Conference on Deep Foundations*, 277–284.

Nonlinear analysis of laterally loaded piles by a pseudo three-dimensional FE model

Dj. Amar Bouzid

Department of Civil Engineering, Engineering Institute, University Yahia Fares of Médéa, Quartier Ain D'Hab, Médéa, Algeria

B. Tiliouine

Seismic Engineering and Structures Dynamics Laboratory, National Polytechnic School, Algiers, Algeria

P.A. Vermeer

Geotechnical Institute, University of Stuttgart, Germany

ABSTRACT: A pseudo 3D FE model has been developed to simulate nonlinear response of single piles under lateral loading. This procedure called Nonlinear Vertical Slices Model (NVSM) takes advantage of finite element 2D numerical solutions in plane stress for building approximate 3D solutions by replacing the inter-slices interactions by fictitious body forces. The pile/soil continuum slices are successively analyzed by the combination of the explicit 2D finite element and finite difference method in a process satisfying both iterative natures of the VS Model and the nonlinear soil assumed to follow Drucker-Prager yield criterion. First, the nonlinear FE VS computational strategy is briefly outlined and then a computer code called Pile3D-NVSM for laterally loaded piles is presented. The paper ends by the validation of the code by problems involving both elastic and elasto-plastic soils.

1 INTRODUCTION

Pile foundations are commonly used to transfer loads from a structure to deep soil strata in cases where shallow foundations are judged inappropriate as they undergo excessive settlement or fail.

As geotechnical engineers are often asked to provide load-displacement response as well as lateral load capacity of horizontally loaded piles, a considerable amount of research encompassing many empirical, analytical and numerical methods has been published on the problem of laterally loaded piles in the last three decades (Banerjee & Davies 1978, Poulos & Davis 1980, Randolph 1981, Verruijt & Kooijman 1989 and Amar Bouzid 1997). Each technique has its own advantages and drawbacks. Although, empirical Winkler spring models are satisfactory for uniform homogeneous soils, these models suffer from difficulties in modeling soil/pile interaction properly when non-homogeneous or layered soil are involved. On another hand, analytical or semi-analytical approaches are very useful as a considerable computational advantage can

be achieved for elastic analyses, however for analyses which incorporate non-linear behavior, or in cases where the loading conditions are relatively complicated, these approaches present some difficulties.

In dealing with a soil/pile interaction problem involving horizontal loading, the full 3D FE analysis is the most rigorous method that can treat all components of the soil/pile system together, providing thus a realistic response of the system. However, engineering costs still remain prohibitive, as processing results requires a large amount of calculation time, especially when soil non-linearity is considered, making the 3D FE model unfeasible and uneconomical as it requires excessive computer resources.

As far as simplicity with efficiency in modeling is concerned, it is certainly desirable, if not mandatory to search for alternatives that may reduce both the large computational effort and the amount of data. To achieve this goal, this paper describes a pseudo 3D FE model for the analysis of laterally loaded single piles. This procedure called Vertical Slices Model takes profit of finite element 2D numerical solutions in plane stress

for building approximate 3D solutions by replacing the inter-slices interactions by fictitious body forces. The pile/soil continuum slices are successively analyzed by the combination of the explicit 2D finite element and finite difference method in a process satisfying both iterative natures of the model itself and the soil nonlinearity.

2 METHOD OF ANALYSIS: NONLINEAR FE VERTICAL SLICES MODEL FOR PILE ANALYSIS

2.1 Linear background of the FE VSM

The technique called finite element vertical slices model is based on discretization of the 3D soil/pile medium into a series of vertical slices, each slice represented by 2D boundary value problem. This procedure involves the combination of the finite element (FE) method and the finite difference (FD) method for analyzing the vertical pile and the surrounding soil substructured into vertical panels. The theory on which the present approach is based, has been presented elsewhere by Amar Bouzid et al. (2005) for problems involving other structures interacting with soil. Hence, the pseudo 3D model is not detailed herein, only a brief description is presented.

The 3D soil/pile problem depicted in Figure 1 shows the vertical slices acted upon by external forces.

Each individual slice (Fig. 1) in this approach is ruled by the following equilibrium equations:

$$\frac{\partial \sigma_x}{\partial x} + \frac{\partial \tau_{yx}}{\partial y} + b_x = 0, \quad (1)$$

$$\frac{\partial \tau_{xy}}{\partial x} + \frac{\partial \sigma_y}{\partial y} + b_y = 0$$

The key element in the FE vertical slices model is the significance of the body forces b_x and b_y in the equation (1). These forces have been interpreted as fictitious forces transmitted to the slice under consideration by shear forces from slices at the left and at the right. For an arbitrary slice i , this can be mathematically expressed as:

$$b_x = \frac{\tau_{zx_i}^l - \tau_{zx_i}^r}{t_i}, \quad b_y = \frac{\tau_{zy_i}^l - \tau_{zy_i}^r}{t_i} \quad (2)$$

where t_i is the slice thickness.

Using the combination of the finite element method and the finite difference method, each slice should be resolved according to the updating iterative process:

$$S_i^j a_i^j = H_i^{pr^j} + H_i^{fl^{j-1}} + P_i \quad \text{for } j = 1, 2, \dots, j_{max} \quad (3)$$

where j denotes for the iteration number and j_{max} is determined by a certain convergence criterion.

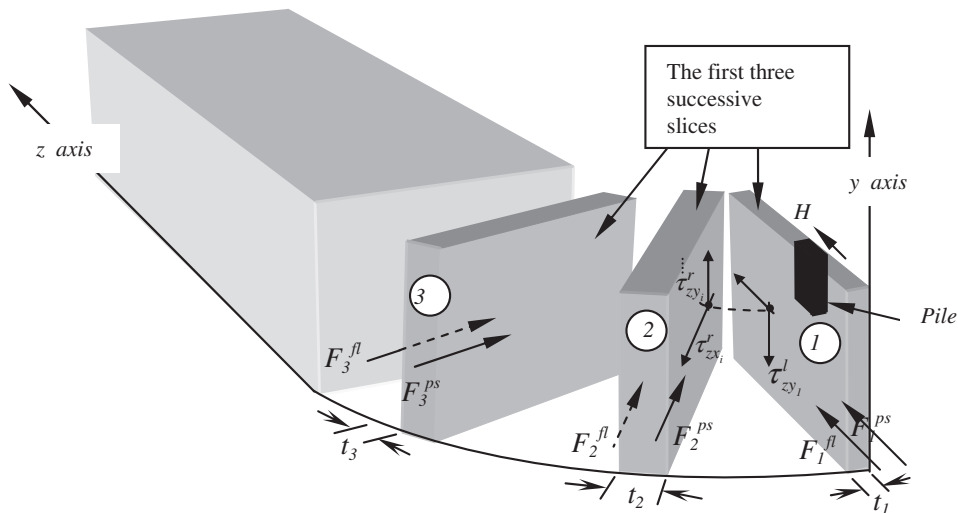


Figure 1. The VSM showing the external forces acting on the first slice containing the pile and the two successive slices.

a_i^j is the nodal displacement vector in the slice i , s_i^j is the element stiffness matrix embodying the contribution to the slice i itself, H_i^{prj} is the body load vector induced by the displacements in the preceding slice $i - 1$, H_i^{prj} is the body load vector induced by the nodal displacements in the following slice $i + 1$ and P_i is the vector of applied loads.

2.2 Soil model

The inelastic state represents an area of great importance in soil mechanics, because the deformation of the soil in the elastic range is usually small and does not represent the realistic stress range.

As far as the correct simulation along with simplicity in numerical modeling are concerned, the well known Drucker-Prager yield criterion is chosen for modeling the soil behavior. The Drucker-Prager criterion formulated in 1952 (Drucker & Prager 1952), is a simple modification of the Von-Mises criterion involving the influence of the hydrostatic pressure on failure (Chen & Han 1987). The yield function of the Drucker-Prager model can be expressed as (Chen & Mizuno 1990):

$$f(I_1, J_2) = \alpha I_1 + \sqrt{J_2} - k = 0 \quad (4)$$

where α , k are material parameters, I_1 is the first stress invariant and J_2 is the second deviatoric stress invariant. The yield function is represented in principal stress space by a right-hand circular cone with its axis equally inclined to each of the coordinate axes and its apex is in the tension octant.

The parameters α and k are calculated as functions of the material parameters of the Mohr-Coulomb failure criterion, namely soil cohesion c and soil internal friction angle ϕ .

These parameters are determined as follows:

$$\alpha = \frac{2 \sin \phi}{\sqrt{3}(3 - \sin \phi)}, \quad k = \frac{6c \cos \phi}{\sqrt{3}(3 - \sin \phi)} \quad (5)$$

2.3 Computational strategy in the Nonlinear FE Vertical Slices Model (NVSM)

Apart from the iterative nature of the elastic version of the VSM due to the coupling between slices, the nonlinear vertical slices model should account for another level of iterative process due to the soil nonlinearity. Furthermore, as the loading on the pile is carried out step by step, the elasto-plastic relationships are incremental. Hence, each slice in the soil/pile discretised

medium has to be solved according to a more refined bi-iterative updating process:

$$S_j \Delta a_i^{j,m} = \Delta P_i + \Delta H_i^{prj} + \Delta H_i^{pr^{i-1}} - E_i^{j,m-1} + G_i^{j,m-1} \quad (6)$$

for $m = 1, 2, \dots, m_{max}$ et $j = 1, 2, \dots, j_{max}$

where j denotes the global iteration number of the iterative process related to the coupling of slices, and m is the iteration number related to nonlinear nature of soil assumed to follow Drucker-Prager model.

$E_i^{j,m-1}$ is the vector that accounts for unconverged equilibrium in the previous load step, and $G_i^{j,m-1}$ is the pseudo load vector accounting for plastic strains.

2.4 Computer code Pile3D-NVSM

The theoretical developments of the NVSM for the problem of laterally loaded single piles have been encoded in a Fortran computer program called Pile3D-NVSM.

The incremental and the iterative analysis are performed as follows. The initial stresses due to self-weight are calculated for all elements in each slice of the discretised medium. The horizontal stress σ_x in an element is assumed to be equal to $K_0 \sigma_y$, in which σ_y is the vertical stress in the element and K_0 is the coefficient of lateral earth pressure at rest. Shear stresses are set equal to zero for all elements. The horizontal load is then applied in increments on the first slice containing the pile. The analysis is carried out slice by slice and the VSM iteration procedure normally terminates when a convergence criterion reaches a pre-set limit.

Having determined the correct displacement increments in all slices that constitute the modeled continuum, the FE computation follows the usual way in checking the yield criterion at every sampling point in each slice. The residual force vector is evaluated from plastic strain increments at yielding points. This vector will be added to the other load components for the next plasticity iteration. The convergence is assumed to have taken place when the largest term in the residual force vector becomes sufficiently small. After the nonlinear convergence at the end of each increment, the incremental nodal displacements and the element stresses in soil and pile elements are added to the previous total values to get the nodal displacements and element stresses at the end of the increment. The Pile3D-NVSM output can show the pile displacements, pile rotations, shear forces and bending moments at the end of each load increment.

3 ANALYSIS OF LATERALLY LOADED SINGLE PILES

3.1 Mesh of soil/pile medium

Taking account of symmetry of the soil/pile system, the slice finite element mesh used for the computer code Pile3D-NVSM is shown in Figure 2. The analysis can be made by cutting the soil surrounding the pile into vertical slices of different thicknesses. The first slice that contains a half of the pile has a thickness of r_0 , where r_0 is the radius of the pile. In order to represent smooth lateral boundaries, all the nodes along the two vertical sides are given roller supports. All nodes on the bottom limit of the slice are restrained against any movement, representing thus rough, rigid base conditions.

The slice finite element mesh of Figure 2 consists of 584 eight-noded elements modeling the soil and 40 eight-noded elements modeling the pile. The side boundaries of the mesh in the vertical plane were located at a distance of $25d$ in the back and in front of the pile ($d = 2r_0$ is the pile diameter). The vertical extent is placed at $0.5L_p$ under the pile tip. Those distances from the pile boundaries have virtually no effect on the finite element results.

In order to have a compromise between a reasonable accuracy in modelling and the number of iterations

for reaching convergence, a limited parametric study has been undertaken to set the mesh boundaries in the z direction and to determine the appropriate number of slices. The parametric study involves essentially the variation of pile head displacement as a function of lateral extent Z in the z direction for different slice thicknesses and for various pile slendernesses. It was finally concluded that a lateral distance of $Z = 40r_0$ and a slice number of $N_s = 21$ have practically no effect on the lateral pile behavior. The slice of pile has a thickness r_0 , and the same thickness of $2r_0$ has been attributed to the other slices.

3.2 Validation of the proposed method for single piles embedded in both linear and nonlinear soils

To verify the proposed method of analysis, a homogeneous elastic medium is investigated first. The elastic results obtained by Pile3D-NVSM are compared with those obtained by other methods that are available in the literature (Boundary element method, FE method and Subgrade reaction theory).

For this case the pile has a length 25 times its diameter $L_p/d = 25$, the soil has a constant modulus of elasticity E_s and the value of Poisson's ratio was taken as 0.5.

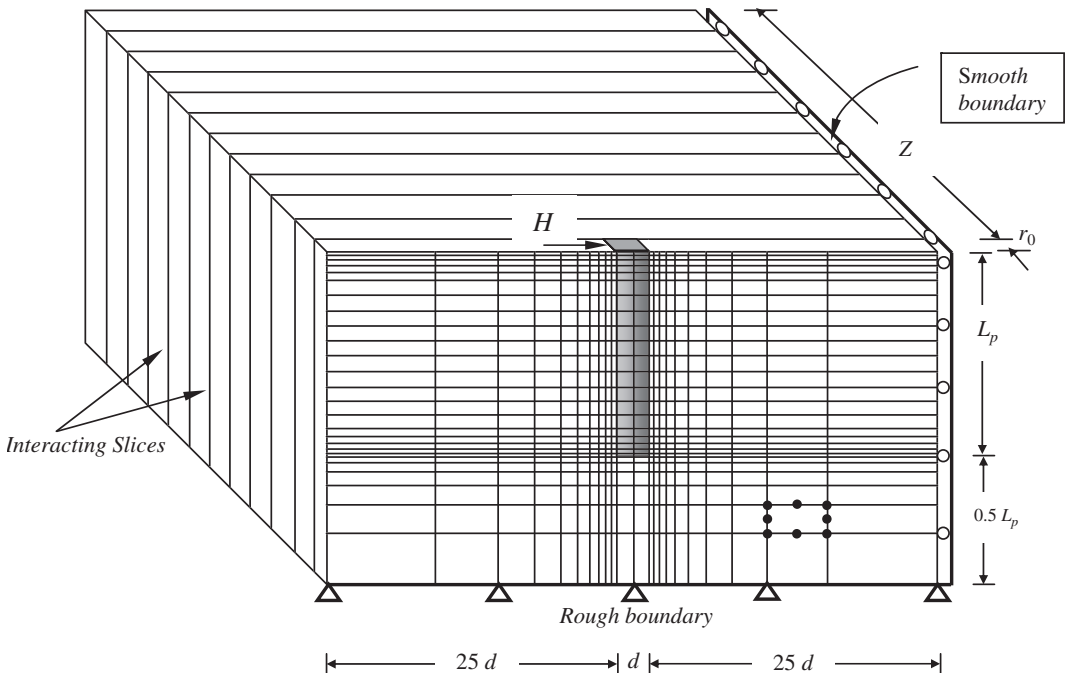


Figure 2. Finite element mesh for the computer code Pile3D-NVSM.

The dimensionless pile head displacements are shown in Figure 3, as a function of the flexibility factor K_R . The line marked with crosses in this Figure, represents the data obtained when the soil is represented by a series of linear springs, with subgrade modulus E_s . The general agreement between the results of Verruijt and Kooijman, those of Poulos and Davis, and those obtained by the computer program Pile3D-NVSM is good, although the displacements obtained by the proposed method are slightly lower at large values of K_R .

The maximum bending moment occurring in the pile is shown in Figure 4. As it can be seen from this Figure the agreement between the present method, Poulos and Verruijt and Kooijman is very good for the entire range of flexibility factor.

As a second verification, the case of a pile in an elastic Gibson's soil with a linearly increasing modulus of elasticity is considered ($G_s = mz$, where m is the rate of increase of G_s with depth).

For this soil profile the non-dimensional pile head displacement is expressed by $ur_0^2 m^* / H$ where $m^* = m(1 + 3\nu_s/4)$ and ν_s is the soil Poisson's ratio.

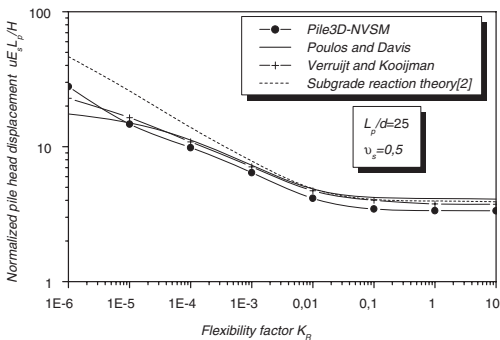


Figure 3. Comparison of pile head deflection in a homogeneous soil.

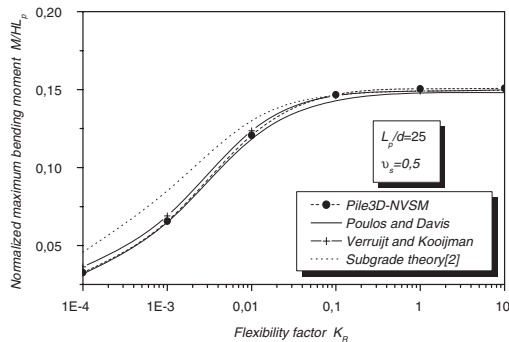


Figure 4. Comparison of the maximum bending moment in a homogeneous elastic soil.

The variation of the normalized pile head deflection is plotted against the pile/soil stiffness E_p/m^*r_0 in Figure 5.

As can be observed, the agreement between the results of Verruijt and Kooijman, Randolph, Banerjee and Davies, and those obtained by Pile3D-NVSM is very close, although the finite element displacement of Randolph at small values of E_p/m^*r_0 (<1000) are slightly smaller than those predicted by the other methods. As in the case of a pile embedded in a homogeneous soil, the spring model overestimates the displacements for the full range of the flexibility factor.

The comparisons of Figures 3, 4 and 5 demonstrate that the finite element vertical slices model is successfully able to model the laterally loaded piles embedded in different types of soil.

To further substantiate the performances of Pile3D-NVSM results in problems involving elasto-plasticity, research in the literature led us to investigate the work of Faruque and Desai (1982) for a laterally loaded single pile in a nonlinear medium. This paper was intentionally chosen for two reasons. Firstly, because it has been carried out using the FE method and secondly, the Drucker-Prager yield criterion has been chosen as a soil model. Moreover, Faruque and Desai used full three-dimensional FE method to analyze square cross-section piles, which is perfectly appropriate to the vertical slicing model, thus eliminating the need of computing the equivalent pile elements Young's modulus from the actual pile flexural rigidity $(EI)_p$.

By means of full 3D FE analysis, these authors studied a square cross-section pile under horizontal loading. The soil strength and stiffness properties along with pile geometric characteristics are given in Table 1.

The 3D FE mesh was 3.66 m in width, 10.36 m in breadth and 27.43 m in depth. This mesh contains 105 eight-noded brick elements. This type of elements generally fails to give accurate results, as it has stiff behavior due to the linear approximation of the displacement field (comparable to the 2D noded element).

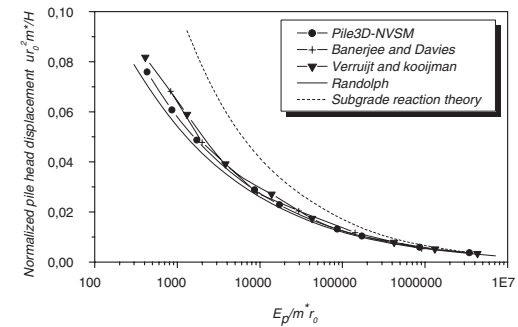


Figure 5. Comparison of pile head displacement in an elastic Gibson's soil.

Table 1. Soil-pile properties (Faruque & Desai 1982).

Material	Properties
Pile	$L_p = 18.3 \text{ m}$ $d = 0.61 \text{ m}$ $E_p(\text{1st case}) = 20.67 \times 10^7 \text{ kPa}$ $E_p(\text{2nd case}) = 20.67 \times 10^4 \text{ kPa}$ $\nu_p = 0.25$
Soil	$E_s = 1000 \text{ kPa}$ $\nu_s = 0.33$ $c = 7.65 \text{ kPa}$ $\phi = 0.0$

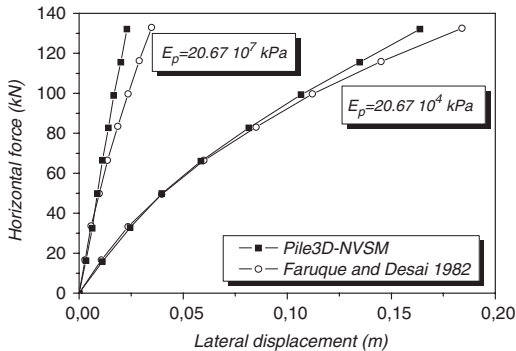


Figure 6. Load-displacement response of a pile in nonlinear medium.

Despite, the insufficient number of elements used for modeling such a problem and despite numerical inaccuracies that characterize the eight-noded brick element, the work of Faruque and Desai constitutes a good reference of comparison through which the user can have a global assessment of NVSM results, as these authors used the full 3D FE method and the same yield criterion chosen in this paper. Figure 6 illustrates the variation of pile head lateral displacement with the increasing applied horizontal force for both approaches in comparison. As can be clearly seen, although a good agreement is obtained in the range of small displacements, a slight deviation is observed in the range of great displacements for the two pile stiffnesses considered. This is probably due to numerical inaccuracies of Faruque and Desai's modelling. In deed, they used a very coarse mesh with a less performant element in modeling a problem mainly characterized by a flexural behavior.

4 CONCLUSIONS

In recent years it has become possible to compute solutions with increasingly complex descriptions in

both geometry and soil properties. However, the use of complex constitutive laws in 3D FE codes is restricted by time and cost.

In dealing with a soil/pile interaction problem, the full three-dimensional finite element analysis is the most rigorous method that can provide information and answers. However, engineering costs still remain prohibitive, as processing results requires a large amount of calculation time, especially when soil nonlinearity is considered, making the method inappropriate for practical design.

In order to reduce calculations time and computer resources, a pseudo 3D FE model for laterally loaded piles has been presented in this paper. Based on this model, the computer code Pile3D-NVSM has been validated in comparison with other numerical methods involving both linear and nonlinear soils.

In view of the excellent results obtained, and considering its potential to save time over a full 3D FE analysis, the pseudo 3D FE method with the relatively simple criterion of Drucker-Prager has been a worthy alternative for the analysis of a pile under lateral loads.

REFERENCES

- Amar Bouzid, Dj. 1997. Analyse semi-analytique par éléments finis des pieux isolés sollicités horizontalement dans un milieu à comportement non-linéaire. Thèse de Magister, Ecole Nationale Polytechnique, Alger, Algérie.
- Amar Bouzid, Dj., Vermeer, P.A. & Tiliouine, B. 2005. Finite element vertical slices model: Validation and application to an embedded square footing under combined loading. *Computers and Geotechnics* 32(2): 72–91.
- Banerjee, P.K. & Davies, T.G. 1978. The behaviour of axially and laterally loaded single piles embedded in non-homogeneous soil. *Géotechnique* 28(3): 309–326.
- Chen, W.F. & Han, D.J. 1988. *Plasticity for structural engineers*. Springer-Verlag, Berlin.
- Chen, W.F. & Mizuno, E. 1990. *Nonlinear analysis in soil mechanics: Theory and implementation*. Developments in geotechnical engineering 53, Elsevier Science Publishers B.V., the Netherlands.
- Drucker, D.C. & Prager, W. 1952. Soil mechanics and plastic analysis of limit design. *Quart. Applied Mathematics* 10: 157–162.
- Faruque, M.O. & Desai C.S. 1982. 3D material and geometric nonlinear analysis of piles. *Proc. 2nd International Conference on Numerical Methods for Off-shore Piling, Austin, Texas*.
- Poulos, H.G. & Davis, E.H. 1980. *Pile Foundation Analysis and Design*. Wiley: New York.
- Randolph, M.F. 1981. The response of flexible piles to lateral loading. *Géotechnique* 31(2): 247–259.
- Verruijt, A. & Kooijman, A.P. 1989. Laterally loaded piles in a layered elastic medium. *Géotechnique* 39(1): 39–46.

Numerical modelling of the combined axial and lateral loading of vertical piles

K. Abdel-Rahman & M. Achmus

*Institute of Soil Mechanics, Foundation Engineering and Waterpower Engineering,
University of Hannover, Germany*

ABSTRACT: In offshore technology large diameter steel pipes are often used for pile foundations. Especially when used as foundation elements for offshore wind energy converters, such piles experience not only vertical, but also substantial horizontal loading. In this paper the interaction between axial and lateral forces acting on vertical steel pipe piles in sand is investigated by means of numerical modelling. A three-dimensional finite element model was developed with a non-linear elasto-plastic material law for the sand. It is found that for axial tension loads the decrease of axial pile stiffness due to horizontal loads has to be taken into account. For axial compression loads as well as for horizontal loading the interaction effects are of minor importance and can be neglected in the design.

1 INTRODUCTION

Tripod or jacket foundations can be applied for offshore wind energy converters planned in the German part of the North Sea at large water depths from 30 up to 50 m. For these structures, driven steel pipe piles are used as foundation elements. The piles are driven through a pile sleeve fixed at the corner points of the foundation structure. After pile driving, the connection is carried out by means of grouting.

The loads applied to these quasi-vertical piles differ greatly from typical onshore and also offshore structures, with more substantial lateral loading. These loads result from the combined actions of vertical dead load and horizontal loads due to wind and wave action.

Current design practice involves separate analysis of the axial and lateral responses of piles and does not consider the effect of interaction between the different load directions. This paper deals with the interaction effects for piles embedded in sand, since in the German North Sea sand soils are to be expected in most cases.

Several results of investigations concerning the behaviour of piles in sand subjected to combined axial and lateral loading (inclined loading) were reported in the literature, e.g. by Yoshimi (1964), Das et al. (1976), Chari & Meyerhof (1983), Ismael (1989) and Sastry & Meyerhof (1990). In some investigations combined horizontal load and vertical compression load are concerned, in others oblique tensile loads are considered. From these investigations, it seems that the pile response to horizontal loading is only slightly

affected by a vertical load, whereas horizontal loads significantly affect the vertical pile response. This was also determined by Ismael (1989), who investigated the behaviour of bored piles subjected to axial and oblique pulls.

In this paper, the results of a numerical study on the behaviour of vertical piles in sand under inclined compression and tension loads are presented. For this a three-dimensional finite element model was used.

2 FINITE ELEMENT MODELLING

For the investigation of the behaviour of vertical piles under combined loading conditions a three-dimensional (3D) numerical model was developed. The finite element programme ABAQUS (Abaqus 2005) was applied. An advanced computer system with parallel processor technology was used to minimize the computation time.

Steel pipe piles with a length of 20.0 m and a wall thickness of 2 cm were considered. Two different outer diameters $D = 2.0$ and $D = 3.0$ m were chosen in order to study the effect of pile geometry.

The most important issue in geotechnical numerical modelling is the simulation of the soil's stress-strain-behaviour. An elasto-plastic material law with Mohr-Coulomb failure criterion was used to describe the behaviour of medium dense sand. The soil stiffness is represented here by a stiffness modulus for oedometric compression E_S and a Poisson's ratio ν .

To account for the non-linear soil behaviour, a stress dependency of the stiffness modulus was implemented as follows:

$$E_s = \kappa \sigma_{at} \left(\frac{\sigma_m}{\sigma_{at}} \right)^\lambda \quad (1)$$

Here $\sigma_{at} = 100 \text{ kN/m}^2$ is a reference (atmospheric) stress and σ_m is the current mean principal stress in the considered soil element. The parameter κ determines the soil stiffness at the reference stress state, and the parameter λ rules the stress dependency of the soil stiffness.

The material parameters used in the calculations are given in Table 1.

The material behaviour of the piles was assumed to be linear elastic with the parameters $E = 2.1 \cdot 10^5 \text{ MN/m}^2$ (Young's modulus) and $\nu = 0.2$ (Poisson's ratio) for steel. The considered pile geometries are given in Table 2.

Due to the symmetric loading condition only a half-cylinder representing the sub-soil and the pile could be considered. The discretized model area had a diameter of twelve times the pile diameter. The bottom boundary of the model was extended by six times the pile diameter below the base of the pile. With these model dimensions the calculated behaviour of the pile is not influenced by the boundaries (Fig. 1).

Eight-node continuum elements were used for the soil as well as for the pile. The frictional behaviour in the boundary surface between pile and soil was modelled by contact elements, where the wall friction angle was set to $\delta = 0.67\phi'$.

The finite element calculation is executed stepwise. At first, for the generation of the initial stress state the whole model area is discretized using soil elements only. Subsequently, the pile is generated by

replacing the soil elements located at the pile position by steel elements and activating the contact conditions between pile and soil.

Finally, the vertical load and the horizontal load are applied simultaneously and increased gradually until the required maximum loads are reached.

The piles were subjected to loads with various inclinations ($\alpha = 0.0, \pm 30.0^\circ, \pm 60.0^\circ, \pm 90.0^\circ$) measured from the horizontal direction, whereby the positive sign of α stands for compression loads and the negative sign for tension loads (Fig. 2).

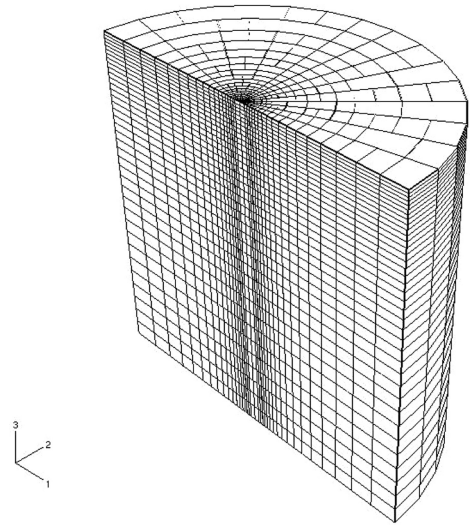


Figure 1. Finite element model.

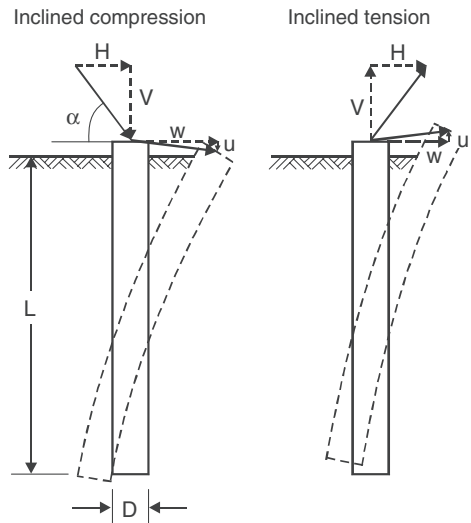


Figure 2. System and denominations.

Table 1. Material parameters used for medium dense sand.

Unit buoyant weight γ'	11.0 kN/m ³
Oedometeric stiffness parameter κ	400
Oedometeric stiffness parameter λ	0.60
Poisson's ratio ν	0.25
Internal friction angle ϕ'	35°
Dilation angle ψ	5°
Cohesion c'	0.1 kN/m ²

Table 2. Pile properties.

Case	Diameter D (m)	Wall thickness (m)	Length L (m)
1	2.0	0.02	20.0
2	3.0	0.02	20.0

3 NUMERICAL MODELLING RESULTS

3.1 Generalities

In order to investigate the influence of combined axial and lateral loading, the load inclination α was varied in seven steps between -90° (pure axial compression) over 0° (pure horizontal loading) to 90° (pure axial tension). For the problem concerned, the pile head displacements in the horizontal and vertical direction are of major interest. A comparison of the H - w - and V - u -curves (ref. to Fig. 2) clearly shows the effect of the vertical load on the horizontal load-deformation behaviour and vice versa. Hence, these curves are given in the following for different load inclinations. In this respect, a distinction is made between inclined compression load (i.e. axial compressive load and horizontal load) and inclined tension load.

3.2 Results for piles under inclined compression loads

The horizontal load deformation behaviour for the pile with a diameter of 2 m is shown in Fig. 3. Due to these results, the horizontal displacement is nearly independent of the load inclination and thus independent of a vertical load acting together with the horizontal load. Similar results were found experimentally by Sastry & Meyerhof (1990), who carried out model tests with inclined compression loads.

Instead, the vertical displacement (settlement) of the pile is affected by a horizontal load. In Fig. 4 the calculated dependence of settlement and vertical load for different load inclinations is given for the pile with a diameter of 2 m. The horizontal load has a

favourable effect, since it leads to a stiffer behaviour in the vertical direction. For instance, for a vertical force of 2 MN the settlement is reduced by about 25% for $\alpha = -60^\circ$ and even by about 50% for $\alpha = -30^\circ$ compared to the pure compression case.

Figures 5 and 6 show the load-displacement curves for a pile with a diameter of 3 m. There is a tendency for similar results as for the case $D = 2$ m to be obtained. For the larger diameter, a small stiffening effect of the horizontal behaviour is obtained with increasing axial load. However, this effect is of minor importance.

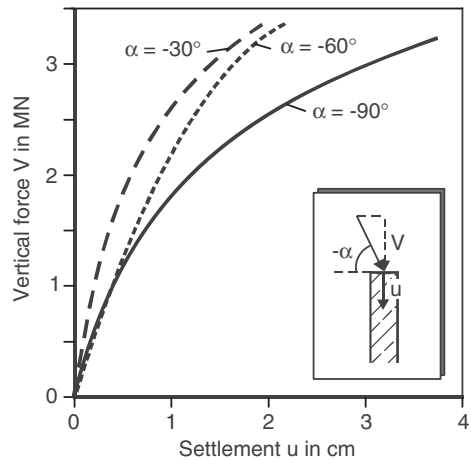


Figure 4. Settlement of the pile top dependent on vertical load (inclined compression, $D = 2.0$ m, $L = 20.0$ m).

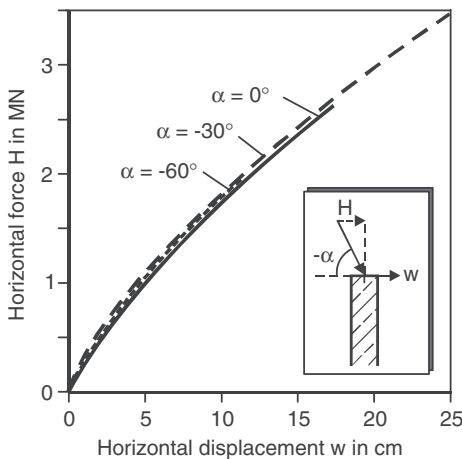


Figure 3. Horizontal displacement at the pile top dependent on horizontal load (inclined compression, $D = 2.0$ m, $L = 20.0$ m).

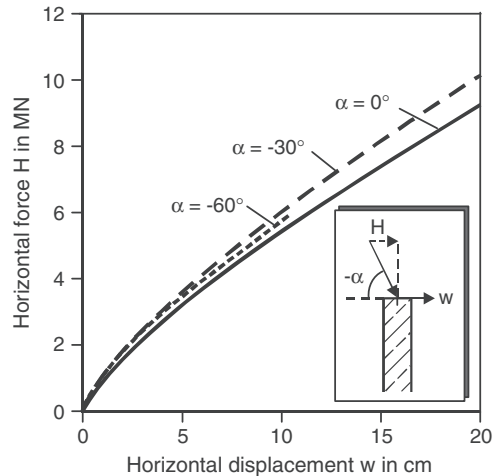


Figure 5. Horizontal displacement at the pile top dependent on horizontal load (inclined compression, $D = 3.0$ m, $L = 20.0$ m).

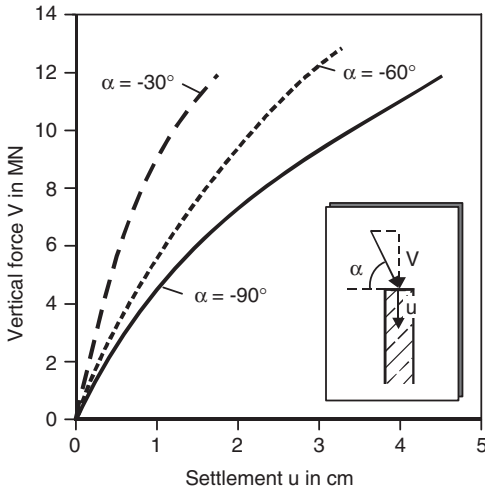


Figure 6. Settlement of the pile top dependent on vertical load (inclined compression, $D = 3.0$ m, $L = 20.0$ m).

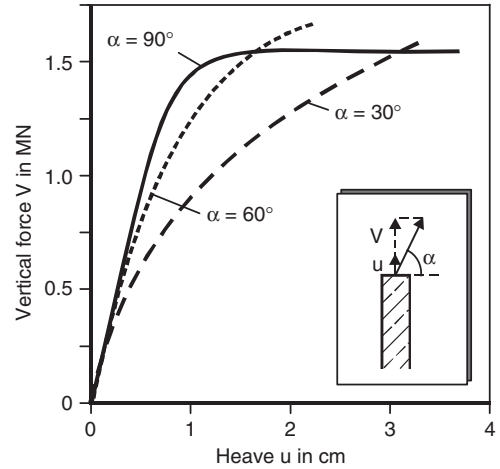


Figure 8. Pile heave dependent on vertical load (inclined tension, $D = 2.0$ m, $L = 20.0$ m).

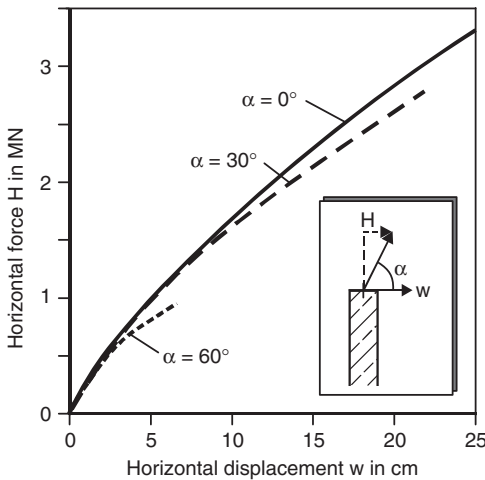


Figure 7. Horizontal displacement at the pile top dependent on horizontal load (inclined tension, $D = 2.0$ m, $L = 20.0$ m).

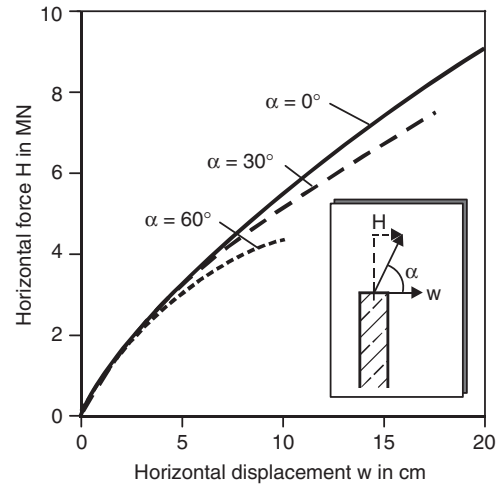


Figure 9. Horizontal displacement at the pile top dependent on horizontal load (inclined tension, $D = 3.0$ m, $L = 20.0$ m).

3.3 Results for piles under inclined tension loads

In Fig. 7 the horizontal load-displacement behaviour with variable axial tensile loads is presented for the pile with a diameter of 2 m. As for the inclined compression case, at first there is no significant influence of the vertical load on the H - w -curve. But, from a certain load level which is dependent on the load inclination, the curves for inclined loads deviate from the curve for pure horizontal loading. Larger horizontal displacements then apply, i.e. the horizontal pile stiffness is decreased.

The respective vertical load-displacement curves for the case with $D = 2$ m are shown in Fig. 8. Here again, as for the inclined compression load, a significant influence of the horizontal load is found. The vertical pile stiffness is distinctly reduced when compared to the case with pure axial tension. But, on the other hand, a horizontal load increases the ultimate vertical pile capacity. Thus, the unfavourable effect of decreased stiffness is joined by the favourable effect of increased capacity.

Figures 9 and 10 show the load-displacement curves obtained for the pile with a diameter of 3 m under

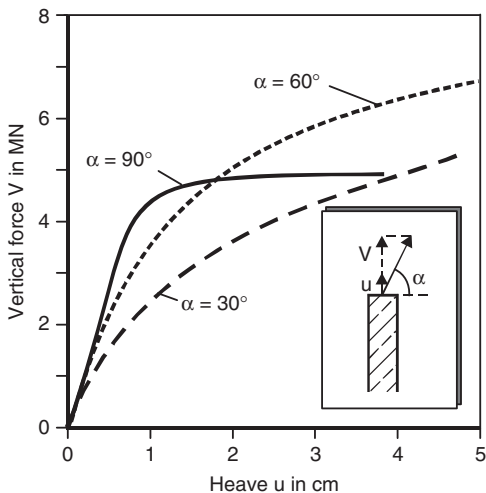


Figure 10. Pile heave dependent on vertical load (inclined tension, $D = 3.0\text{ m}$, $L = 20.0\text{ m}$).

inclined tension loads. The results tend to be similar, which means that the general behaviour described above applies independent of the pile diameter.

The vertical load, above which a significant impact on the horizontal load-deformation behaviour begins, corresponds to the load above which a distinct increase of the pile heave is to be noticed. Thus, the reason for the deviation in the H - w -curves is obviously that the pile capacity for tension load is smaller than the horizontal pile capacity in the cases considered. If the vertical load approaches the ultimate load, this ultimate load becomes decisive for the combined ultimate load.

4 ANALYSIS OF THE NUMERICAL RESULTS

4.1 Piles under inclined compression loads

The results from the numerical modelling show a positive effect of a horizontal load on the pile settlement behaviour. A substantial reason for this is that in the upper part of the pile large horizontal stresses act on the 'passive' side in front of the pile due to the horizontal load. On the passive side bedding reactions are induced, which are much larger than the horizontal stresses in the 'at rest' state. Compared to this, the decrease of horizontal stresses on the active side (behind the pile) is a minor effect. The same applies below the point of rotation of the pile, with the stress increase now on the other side of the pile.

This is elucidated by the presentation of the vertical shear stresses acting on the pile in the plane of symmetry, i.e. in the loading plane, given in Fig. 11.

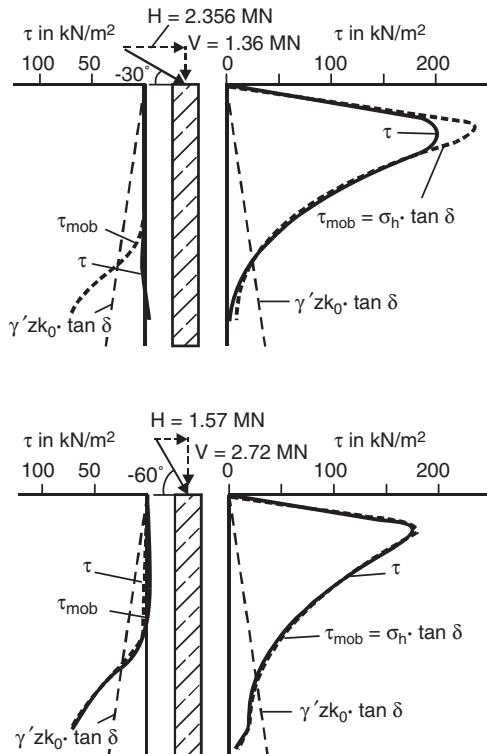


Figure 11. Shear stress distribution along the pile in the loading plane for two inclined compression loading cases ($D = 2.0\text{ m}$, $L = 20.0\text{ m}$).

The upper part gives the results for $\alpha = -30^\circ$ and a load level, at which the mobilizable skin friction (horizontal load multiplied by the coefficient of friction $\tan \delta$) is not fully utilized. The shear stresses behind the pile (on the active side) are very low, but high shear stresses act in front of the pile. These stresses are much higher than the maximum shear stresses for pure axial loading, which can be assumed to increase linear with depth z according to the equation $\tau_{max} = \gamma z k_0 \tan \delta$.

The lower part of Fig. 11 gives the shear stress distributions for $\alpha = -60^\circ$ and a higher loading level. The mobilizable shear stresses on both sides of the pile are fully utilized. Hence, the resultant shaft resistance of the pile is significantly larger than for the case of pure compression load.

Another reason for the increased vertical pile stiffness obtained is a prestress effect due to the horizontal load. In the region near the soil surface in front of the pile, where the maximum shear stresses occur, the soil is moved upwards by the horizontal load. To carry the vertical load, a pile needs a relative displacement to mobilize the skin friction. This displacement is

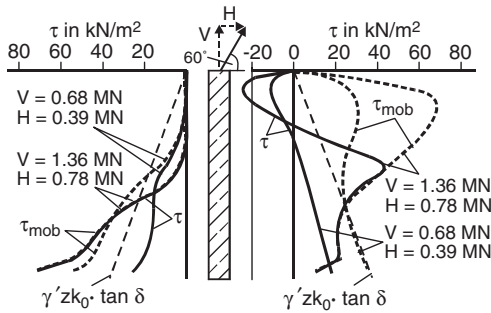


Figure 12. Shear stress distribution along the pile in the loading plane for inclined tension loading cases ($D = 2.0\text{ m}$, $L = 20.0\text{ m}$).

partly induced by the horizontal load, i.e. fewer pile settlements are necessary to carry a certain load.

4.2 Piles under inclined tension loads (oblique pull)

For vertical tension loads, the interaction between horizontal and vertical loads leads to unfavourable effects. The vertical pile stiffness and – beyond a certain load level – also the horizontal pile stiffness is reduced.

The stiffness decrease in the vertical direction results from negative skin friction induced by the horizontal load. This is elucidated in Fig. 12, where the shear stresses acting on the pile in the loading plane are shown for a load inclination of $\alpha = 60^\circ$ and two different loading levels. The horizontal displacement of the pile corresponds to a vertical upwards directed displacement of the soil body in front of the pile. This displacement is larger than the pile heave due to tension load, so that negative skin friction, i.e. an additional tensile load on the pile, occurs. Accordingly, the pile heave is increased.

In principle, negative skin friction is only a problem of serviceability, i.e. deformations, but not a problem of ultimate capacity. If a large pile heave occurs due to high tensile load, the direction of the relative displacements between pile and soil is reversed, so that ‘positive’ shear stresses can be utilized. Thus, the ultimate load for the combined action of vertical and horizontal load is also larger for the inclined tension load case than for the case with pure tensile loading, since the mobilizable skin friction is increased by the horizontal force. However, the pile heaves belonging to the ultimate state are much larger than the heave belonging to the ultimate capacity for pure tension loading (see Figs. 8 and 10).

Ismael (1989) also stated that theoretically larger vertical pile capacities occur under inclined tension

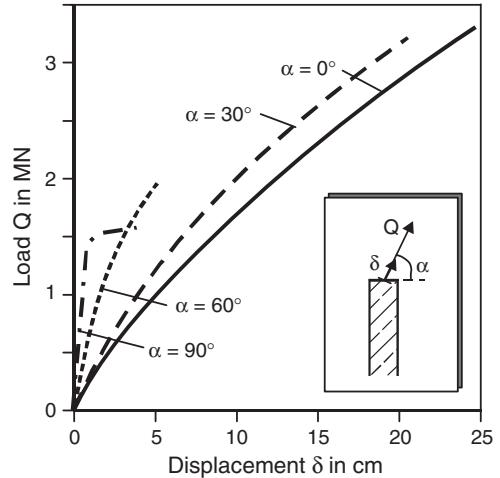


Figure 13. Load-displacement curves for oblique pull ($D = 2.0\text{ m}$, $L = 20.0\text{ m}$).

load. However, he mentioned that this was never observed in field tests. The reason for that could be that this capacity increase will only be observed for very large displacements, which may not have been reached in field tests.

In Fig. 13 the results obtained are presented in the form of an ‘oblique pull’ curve. Here the displacement in the direction of loading is given dependent on the resultant load. This kind of presentation is usually chosen when the behaviour of piles for the anchoring of moorings is considered.

The result is that the anchoring becomes the stiffer, the larger the load inclination, i.e. the vertical portion of the load, is. However, the resultant capacity becomes the lowest for pure vertical loading. This was also found experimentally by Das et al. (1976).

However, the piles considered here and also the piles investigated by Das et al. are relatively short with ratios of pile length to pile diameter of around 10. Due to this, the vertical capacity of the piles is lower than the horizontal capacity. If a long pile with a higher vertical than horizontal capacity is considered, the stiffness as well as the capacity of the mooring anchor increases with the load inclination α (see, for example, Ismael 1989).

5 CONCLUSIONS

According to the numerical calculation results, piles in sand under combined axial compression and horizontal load behave more favourably than purely horizontally or purely axially loaded piles.

The horizontal pile stiffness is almost unaffected by a vertical compression load acting simultaneously.

Thus, the design of pile bending with usual methods without consideration of interaction (e.g. p-y curve method) seems justified.

In the vertical direction with a compression load an increase of pile stiffness and capacity is induced by a horizontal load. The pile design without consideration of the interaction effects thus lies on the safe side.

Different conditions apply for combined axial tension and horizontal load. The vertical pile stiffness is significantly reduced by a horizontal force. This must be taken into account in the pile design. However, in principle this is a problem of negative skin friction, and hence not a problem of ultimate pile capacity.

For the design in the horizontal direction, interaction effects can also be neglected for axial tension loads. Since the actual tension load has sufficient safety related to the ultimate tension load (determined without interaction effects), no significant influence on the horizontal stiffness occurs. This is ensured by the pile design in the axial direction.

To summarize the results, the interaction between horizontal and vertical load must only be considered in the determination of axial displacements due to tension loads.

However, the question of how cyclic loads affect the interaction behaviour remains open. The loads on foundations of offshore wind energy converters are of extremely cyclic nature. For piles of tripod and jacket structures, the horizontal as well as the vertical load are to a great extent cyclic, with the latter even varying between tension and compression. This leads to an accumulation of displacements and to a change of the load-bearing behaviour in both directions. For instance, in the horizontal direction a reduction of soil stiffness with cyclic loading is to be expected.

The effect of cyclic loading on the interaction behaviour should be investigated. A numerical or analytical analysis alone is not sufficient here, i.e. experimental tests are indispensable.

ACKNOWLEDGMENTS

The results presented in this paper were obtained within the framework of the FORWIND research group funded by the Government of the State of Lower Saxony, Germany. The support is gratefully acknowledged.

REFERENCES

- Abaqus 2005. User's manual, Version 6.4.
- Amde, A.M., Chini, S.A. & Mafi, M. 1997. Model study of H-piles subjected to combined loading. *Geotechnical and Geological Engineering*, 15, pp. 343–355.
- Chari, T.R. & Meyerhof, G.G. 1983. Ultimate capacity of single rigid piles under inclined loads in sand. *Canadian Geotechnical Journal*, 20, pp. 849–854.
- Das, B.M., Seeley, G.R. & Raghu, D. 1976. Uplift capacity of model piles under oblique loads. *Journal of the Geotechnical Engineering Division*, ASCE, 102(9), pp. 1009–1013.
- Ismael, N.F. 1989. Field tests on bored piles subject to axial and oblique pull. *Journal of Geotechnical Engineering*, 115(11), pp. 1588–1598.
- Meyerhof, G.G. 1995. Behaviour of Pile Foundations under Special Loading Conditions. 1994 R.M. Hardy Keynote Address. *Canadian Geotechnical Journal*, 32, pp. 204–222.
- Sastry, V.V.R.N. & Meyerhof, G.G. 1990. Behaviour of flexible piles under inclined loads. *Canadian Geotechnical Journal*, 27(1), pp. 19–28.
- Shahrour, I. & Meimon, Y. 1991. Analysis of behaviour of offshore piles under inclined loads. *International Conference on Deep Foundations*, pp. 227–284.
- Yoshimi, Y. 1964. Piles in cohesionless soil subject to oblique pull. *Journal of the Soil Mechanics and Foundations Division*, ASCE, 90(6), pp. 11–24.

Analysis of piled raft foundations with piles of different lengths subjected to horizontal and vertical loadings

H.S.W. Chow & J.C. Small

*Department of Civil Engineering, The University of Sydney,
NSW, Australia*

ABSTRACT: Analysis of the behaviour of piled raft foundations subjected to horizontal and vertical loadings has been of particular interest in foundation engineering. The behaviour of piled rafts subjected to vertical loadings has been extensively investigated by numerous researchers. However, the behaviour of piled rafts subjected to horizontal loadings has not received much attention. When the raft is subjected to non-uniform loadings, the differential settlements and tilting will be of great importance. The use of different sizes of piles under a non-uniformly loaded raft can reduce the settlements and tilts. In this paper, Finite Layer techniques are used for the analysis of piled rafts. This technique accounts for the complex soil-structure interaction that governs the behaviour of the foundation and the lateral resistance of the soil on the piles and raft. The behaviour of piled rafts supported by piles of different lengths will be examined when the raft is subjected to both vertical and horizontal loads.

1 INTRODUCTION

Piled rafts have been used as the foundation for tall buildings on soft soil such as clay to limit excessive settlements. Such foundations have been proven to be an economic way to reduce both the overall and differential settlements. In the design of a piled raft foundation, part of the working load is carried by the raft and the remaining load is carried by the piles. Thus, the behaviour of the foundation system is governed by the raft-pile-soil interaction.

In past decades, different techniques have been developed for the analysis of piled raft foundations. Approaches which modeled the piles as a series of spring and the raft as a thin plate were used by Clancy & Randolph (1993), Poulos (1994) and Viggiani (1998). Three dimensional finite element techniques have been used by Katzenbach & Reul (1997) and Reul & Randolph (2003, 2004).

The finite layer technique was developed by Small & Booker (1986) to determine the deflections of a horizontally layered soil. This technique can take into account the interaction effects among the pile and raft elements. The method was used for the analyses of piled raft foundations subjected to vertical loads by Ta & Small (1996) and horizontal loads by Zhang & Small (2000), and was extended for the analysis of piled raft foundations with non-identical piles subjected to non-uniform loads by Small et al. (2004) and Chow & Small (2005a, b).

This paper presents a finite layer approach to examine the behaviour of piled raft foundations when the raft is subjected to both horizontal and vertical non-uniform loads. When the raft is loaded non-uniformly, longer piles should be used underneath the heavily loaded area to minimize settlements and tilting of the foundation.

2 METHOD OF ANALYSIS

Analysis of the piled raft foundation is carried out by separating the foundation system into an isolated piled raft and a layered soil system as shown in Figure 1. The piles are rigidly attached to the raft at the nodes on the raft. The finite element method is used to analyse the raft and piles and the finite layer method is used to analyse the layered soil.

The raft is subjected to external vertical and horizontal forces, and contact and shear stresses that exist between the raft and soil. The contact stresses between the raft and soil are represented by rectangular blocks of uniform pressure and the shear stresses are represented by a series of uniform rectangular shear stress.

The pile group is subjected to the interface forces between the pile and soil. The loads acting on the pile are transferred from the piles to the soil through shear and lateral earth pressure along the pile shafts and the normal contact and shear stresses at the pile base. The normal contact and shear stresses acting along the pile shaft are approximated as a series of ring loads applied

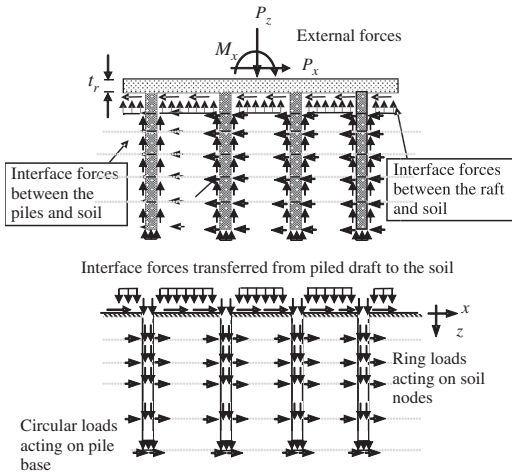


Figure 1. Forces acting on the piled raft.

at the soil interface in both vertical and horizontal directions. The force at the pile base is approximated as a uniform circular load with the same diameter as the pile base.

2.1 Types of interaction

Complex soil-structure interaction plays an important role in the design of a piled raft foundation as the loads are shared between the piles and raft. The raft and piles load the soil and cause it to deform. There are four different types of interaction that need to be computed in the analysis:

- (1) Pile-Pile Interaction – deflection of an unloaded pile caused by loading of an adjacent pile
- (2) Pile-Soil Interaction – deflection of an unloaded soil surface caused by loading of the pile
- (3) Soil-Pile Interaction – deflection of an unloaded pile caused by loading the soil surface
- (4) Soil-Soil Interaction – deflection of the soil surface caused by another loaded soil area

3 ANALYSIS OF PILED RAFT

An example is presented to demonstrate the use of the finite layer method for the analysis of a piled raft foundation. A square piled raft is supported by piles of different lengths as shown in Figure 2. The piles are embedded in a 30 m thick layer of clay. Piles underneath the central region of the raft are twice as long as the piles along the edge. Parameters used in the analysis are given in Table 1.

Two cases were analysed by the present (finite layer (FL)) method and results were compared with a 3D

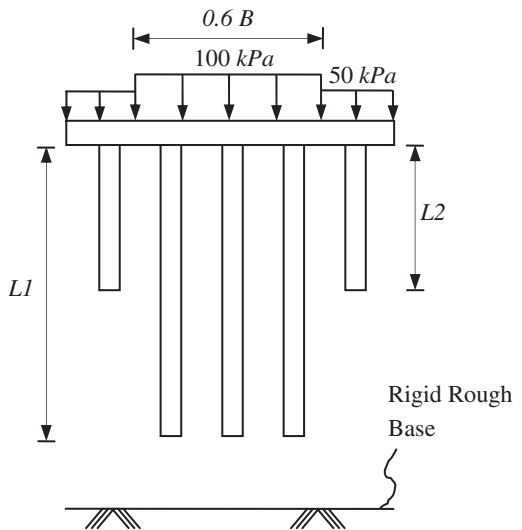
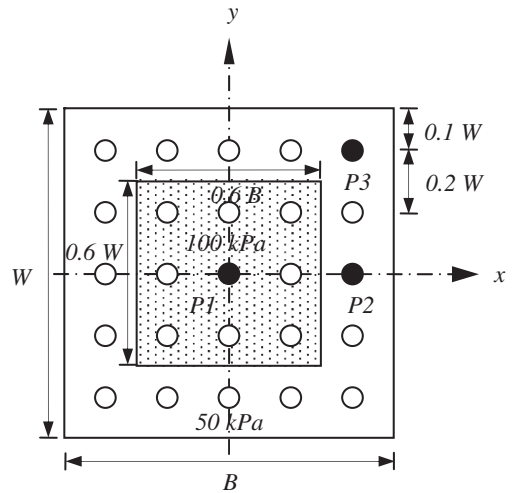


Figure 2. Configuration of piled raft.

finite element (FE) method to examine the behaviour of the raft. The raft is subjected to uniform pressures of 100 kPa and 50 kPa at the central and edge regions of the raft respectively. Uniform pressures were applied horizontally in case 1 and vertically in case 2.

For the finite layer analysis, the whole raft is modeled and the pile has a circular cross section. However, for the finite element analysis, a quarter of the raft is modeled to save computation time and the piles are modeled by square elements with the same cross sectional area as the circular piles in the finite layer analysis. Figure 3 shows the mesh of the piled raft used for the finite layer analysis.

Table 1. Parameters used in the piled raft analysis.

Parameters and dimensions	Soil	Pile (L1/L2)	Raft
Young's modulus, E (MPa)	10	25,000	25,000
Poisson's ratio, ν	0.35	–	0.15
Thickness of raft, t_r (m)	–	–	0.5
Dimensions of raft, $B \times W$ (m)	–	–	25×25
Diameter of piles, D (m)	–	0.5	–
Length of piles, L (m):	–	16/8	–

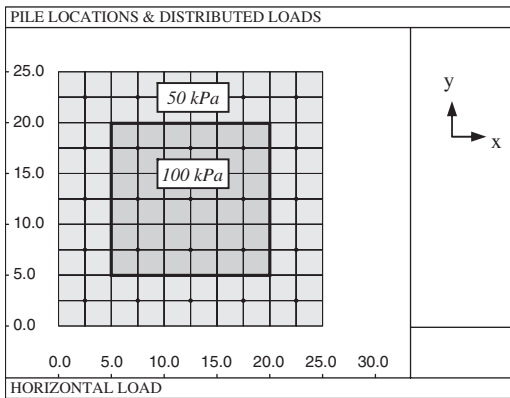


Figure 3. Mesh of the piled raft for finite layer analysis.

3.1 Comparisons with finite element results

3.1.1 Case 1: Horizontal loads

The raft is subjected to horizontal loads in the x-direction. Figure 4 shows the deformed mesh of the piled raft obtained from the finite element analysis and Figure 5 shows the contours of x-displacement obtained from the finite layer analysis.

The raft is undergoing large x-displacements compared to the vertical displacements. The deformed mesh of the finite element analysis shows that the raft displaces fairly uniformly laterally and the piles are bending at the top.

A comparison of the horizontal (x-direction) and vertical displacements along the centre line of the piled raft is shown in Figures 6a and 6b respectively.

Figure 7 shows the horizontal displacements (x and y directions) and compression (relative to pile base) along the pile shaft at different pile locations.

When horizontal x-load is applied to the raft, the centre pile only moves in the direction of the applied load while piles at the corner move horizontally (x

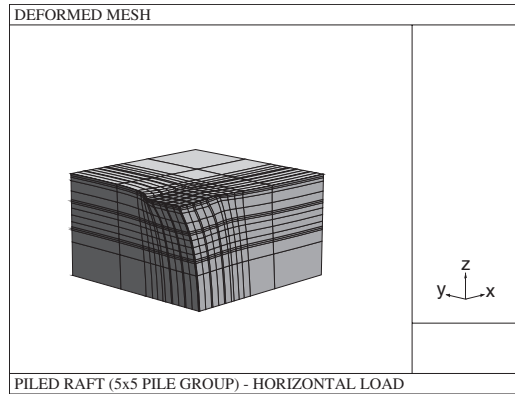


Figure 4. Deformed mesh of piled raft subjected to horizontal load.

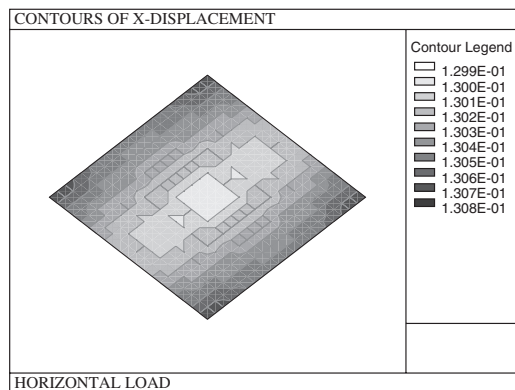


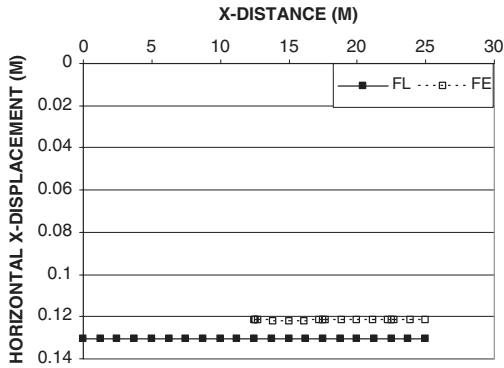
Figure 5. Contours of horizontal X-displacement for piled raft subjected to horizontal loads by finite layer analysis.

and y) and vertically (z), and piles at the edges move horizontally in the direction of load and vertically.

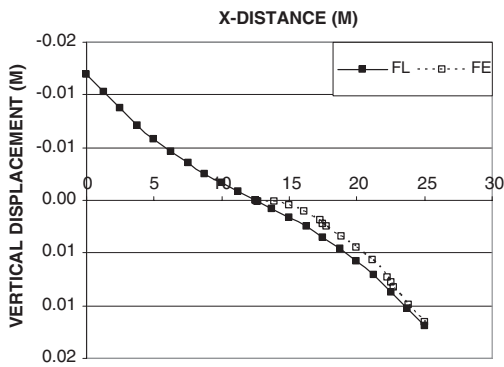
The horizontal displacements obtained from the finite layer method agreed reasonably well with the finite element results. However, the compression of the piles was slightly different. Such a difference could be due to the connection of the pile to the raft. As the pile is attached to the raft at the node in the finite layer analysis, the load applied to the pile head is assumed to be a point load. However, in the finite element method, the pile is attached to the raft element and the load is evenly applied over the area of the pile head.

3.1.2 Case 2: Vertical loads

In this case, the raft is subjected to the load with the same magnitude as in case 1 but in the vertical direction. Figure 8 shows the deformed mesh of the raft obtained from the finite element analysis and Figure 9



(a) Horizontal x-displacement along the centre line of the raft.



(b) Vertical displacement along the centre line of the raft.

Figure 6. Comparison of raft displacements between Finite Layer and Finite Element method when the raft is loaded horizontally.

shows the contours of vertical displacement obtained from finite layer analysis.

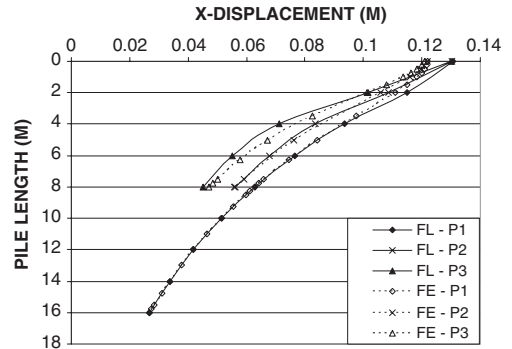
Figure 10 shows a comparison of horizontal and vertical displacements along the centre line of the raft between the two methods. The finite layer results are slightly different from the finite element results. The horizontal displacement of the raft is relatively small compared with the vertical displacements.

Comparisons of the horizontal displacements and compression (relative to pile base) of the piles between the two methods are shown in Figure 11.

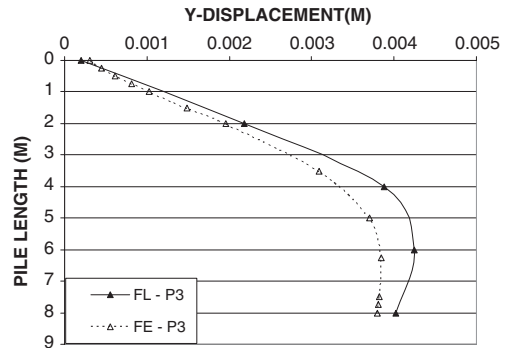
When vertical load is applied to the raft, piles at the centre move vertical downwards only, piles at the edges move horizontally in the x-direction and vertically, and piles at the corners move horizontally in both the x and y directions and vertically.

The pile at the centre compressed more than the edge and corner piles, this implies that the centre pile is carrying a higher load than the piles at other locations.

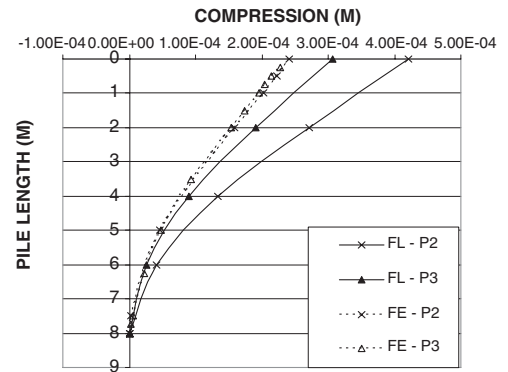
The horizontal displacements and compression of the piles obtained from the finite layer analysis are



(a) Horizontal x-displacement of piles along pile shaft.



(b) Horizontal y-displacement of the corner pile along pile shaft.



(c) Compression of the corner and edge piles (relative to pile base).

Figure 7. Comparisons of horizontal displacements and compression of piles at different locations; raft subjected to horizontal loads.

slightly different from the finite element analysis due to the pile being attached at a node in the finite layer method and to an element in the finite element method as mentioned in case 1.

For both cases 1 and 2 where the raft is subjected to horizontal and vertical loads respectively, the

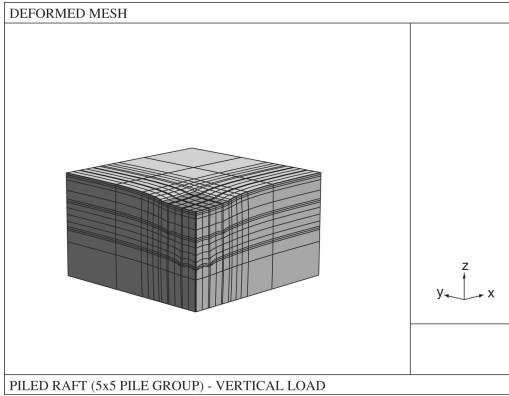


Figure 8. Deformed mesh of piled raft subjected to vertical load from finite element analysis.

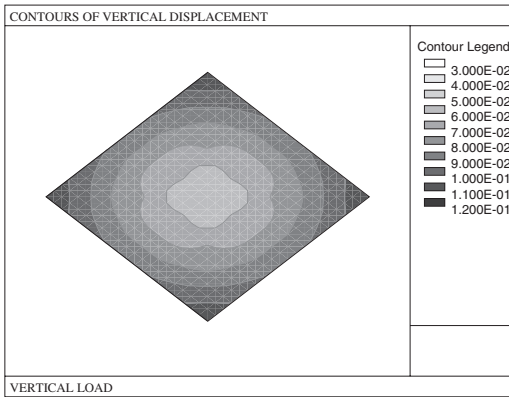


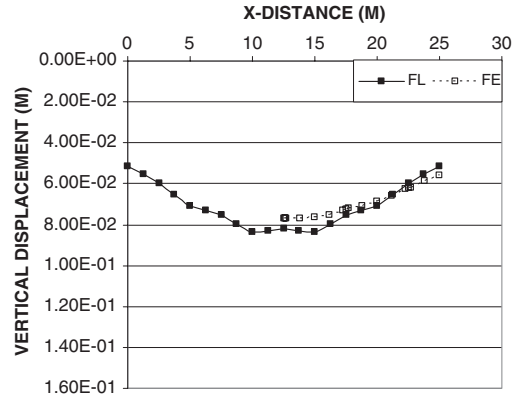
Figure 9. Contours of vertical displacement for piled raft subjected to vertical loads by finite layer analysis.

displacement of the raft obtained from the finite layer results are slightly different from the finite element results due to the following:

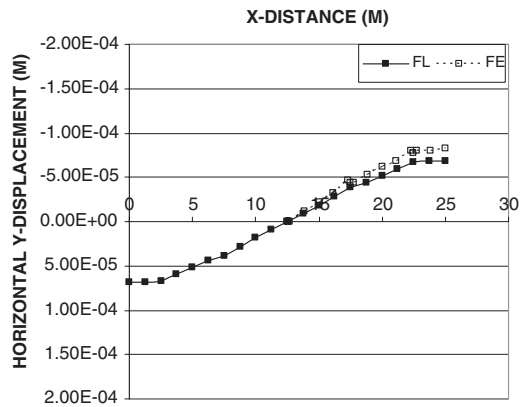
- (1) Boundary conditions of the soil layers – the soil layers are fixed on both sides in the finite element analysis whereas the soil layers are of infinite extent in the finite layer analysis.
- (2) Connection of piles to the raft – the pile is attached to the raft element in the finite element analysis, whereas, the pile is attached to the node on the raft in the finite layer analysis.

4 CONCLUSION

In this paper, the finite layer method is used for the analysis of a piled raft foundation. This technique takes



(a) Vertical displacement along the centre line of the raft.



(b) Horizontal displacement along the centre line of the raft.

Figure 10. Comparison of raft displacements between Finite Layer and Finite Element method when the raft is loaded vertically.

into account the soil-structure interaction and the lateral resistance of the soil. Solutions obtained from this method are in good agreement with the full 3D finite element analysis.

When the raft is subjected to vertical loads only, its contributions to the horizontal displacement of the raft and piles are relatively small. However, when the raft is subjected to horizontal loads, the raft will deform horizontally and vertically.

This method has the advantage that the computation time is less and does not require creation of complicated meshes as would be required for finite element solutions. It is applicable to the analysis of piled raft foundations with piles of different lengths and diameters and subjected to uniform or non-uniform loadings in both horizontal and vertical directions. The soil may also be horizontally layered.

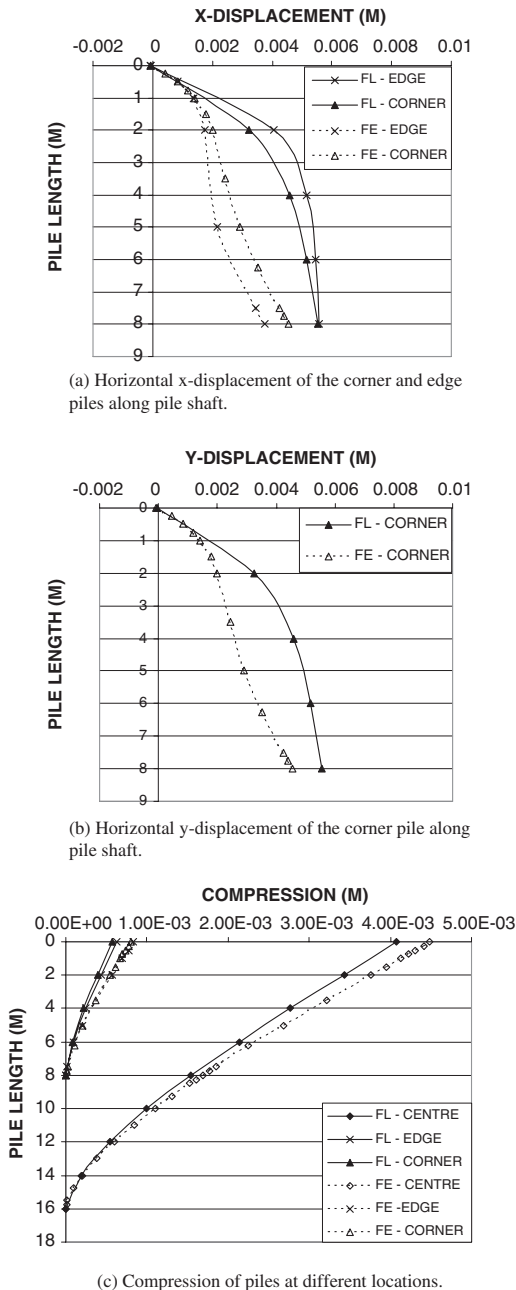


Figure 11. Comparisons of horizontal displacements and compression of piles at different locations; raft subjected to vertical loads.

REFERENCES

- Chow, H. & Small, J.C. 2005a. Behaviour of piled rafts with piles of different lengths and diameters under vertical loading. *Geotechnical Special Publication No. 130-142, Geo-Frontiers 2005*, Austin, USA, 841–855.
- Chow, H. & Small, J.C. 2005b. Finite layer analysis of combined pile-raft foundations with piles of different lengths. *Proceedings of the 11th International Conference of IAC-MAG*, Turin, Italy, 2: 429–436.
- Clancy, P. & Randolph, M.F. 1993. An approximate analysis procedure for piled raft foundations. *Int. J. for Numerical and Analytical Methods in Geomechanics*, 17(12): 849–869.
- Katzenbach, R. & Reul, O. 1997. Design and performance of piled rafts, *Proceedings of the 14th Int. Conf. on Soil Mech. and Found Eng., Hamburg*, 4: 2253–2256.
- Poulos, H.G. 1994. An approximate numerical analysis of pile-raft interaction. *Int. J. for Numerical and Analytical Methods in Geomechanics*, 18(2): 73–92.
- Reul, O. & Randolph, M.F. 2003. Piled rafts in overconsolidated clay: comparison of in-situ measurements and numerical analyses. *Géotechnique*, 53(3): 301–315.
- Reul, O. & Randolph, M.F. 2004. Design strategies for piled rafts subjected to nonuniform vertical loading. *J. of Geotechnical and Geoenvironmental Eng., ASCE*, 130(1): 1–11.
- Small, J.C. & Booker, J.R. 1986. Finite layer analysis of layered elastic materials using a Flexibility Approach, Part 2 – Circular and Rectangular Loadings. *Int. J. for Numerical Methods in Eng.*, 23: 959–978.
- Small, J.C., Zhang, H.H. & Chow, H. 2004. Behaviour of piled rafts with piles of different lengths and diameters. *Proceedings of the 9th Australia New Zealand Conference on Geomechanics*, Auckland, 1: 123–129.
- Ta, L.D. & Small, J.C. 1996. Analysis of piled raft systems in layered soils. *Int. J. for Numerical and Analytical Methods in Geomechanics*, 20: 57–72.
- Viggiani, C. 1998. Pile groups and piled raft behaviour. *Deep Foundations on Bored and Augered Piles, BAP III*, van Impe and Haegman (eds.), Balkema, Rotterdam, 77–90.
- Zhang, H.H. & Small, J.C. 2000. Analysis of axially and laterally loaded pile groups embedded in layered soils. *Proceedings of the 8th Australia New Zealand Conference on Geomechanics*, Hobart, 1: 475–483.

Prediction of pile group response using a simplified non-linear finite element model

Bryan A. McCabe

Department of Civil Engineering, National University of Ireland, Galway, Ireland

Barry M. Lehane

Department of Civil and Resource Engineering, University of Western Australia, Perth, Australia

ABSTRACT: This paper presents predictions from a finite element 2-D axisymmetric modelling approximation for a small pile group employing the BRICK constitutive (non-linear) soil model, and examines the suitability of this model to the prediction of the response of a pile group at a soft clay site near Belfast, Northern Ireland. The study indicates that, despite some limitations, this approach captures both the non-linearity of the load-displacement behaviour and the relative stiffnesses of group piles much better than commonly used linear elastic predictions.

1 INTRODUCTION

An ideal analysis of a closely spaced pile group would be capable of capturing the following facets of its behaviour:

- (i) potential changes in shear stiffness of the soil close to a pile group due to other neighbouring installations
- (ii) consideration of the unified response of the pile group – soil system
- (iii) large pile groups with non-standard pile geometries and pile layouts
- (iv) the highly non-linear stiffness response exhibited by many soils.

Despite recent significant theoretical advances, such as the Strain Path Method (Baligh 1985) and the Contact Surface Method (Einav & Klar 2003), a thorough understanding of the local effective stress changes associated with single pile installation remains elusive. Additional stress changes on group piles imposed by neighbouring installations are even more uncertain, and useful experimental data are quite scarce (Koizumi & Ito 1967, O'Neill et al 1982, McCabe & Lehane 2003).

In determining the load-settlement behaviour of a pile group, each of the items (ii), (iii) and (iv) referred to above imposes significant drains on computational resources, to the extent that complete consideration of all three is currently not an option for geotechnical practice. Finite Element Analysis is the most rigorous and versatile analysis tool available, but the computational effort required limits its use to all but the simplest

of applications. Various pile group analysis methods have evolved from dilutions of items (ii) and (iv); these are summarized by Randolph (1994) and others.

This paper examines the role played by soil stiffness non-linearity in the prediction of pile group response by using the OASYS SAFE finite element programme. The model output is interpreted in the context of data from a programme of full scale load tests on instrumented driven single piles and pile groups at a soft estuarine silt site near Belfast, Northern Ireland (McCabe & Lehane 2006).

2 BELFAST PILE TEST PROGRAMME

2.1 Site characterization

An instrumented pile test programme was conducted by the authors (while both at Trinity College Dublin, Ireland) at a geotechnical test bed near Belfast. The site comprises approximately 7.5 m of lightly over-consolidated estuarine organic soft silty clay (known locally as *sleech*), for which typical properties are shown in Table 1. The *sleech* is overlain by ≈ 1.0 – 1.5 m of granular made ground and underlain by medium dense sand at ≈ 8.5 m depth.

Small-strain stiffness measurements (using Hall effect transducers) from K_0 consolidated undrained triaxial tests on 54 mm diameter Geonor piston samples indicated the marked reduction in shear stiffness with strain shown in Figure 1. In this figure, the secant shear stiffness G_{sec} is normalized by the mean effective stress at the commencement of shearing (p'_0).

Table 1. Typical properties of the sleetch.

Clay friction (%)	20 ± 10
Fines content (%)	90 ± 5
Water content (%)	60 ± 10
Plasticity index (%)	35 ± 5
Organic content (%)	11 ± 1
Peak vane strength (kPa)	22 ± 2
Yield stress ratio	1.1 to 2.0
Friction angle (°)	33 ± 1

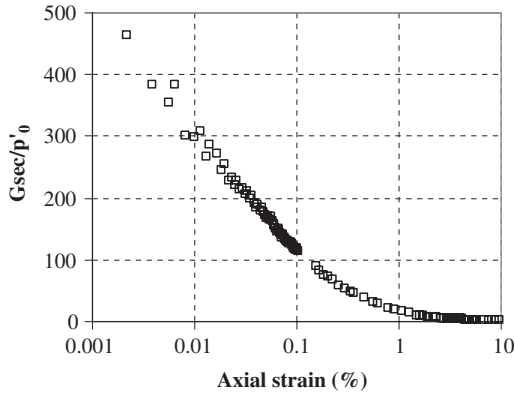


Figure 1. Variation of G_{sec}/p'_0 with axial strain.



Figure 2a. Pile group configuration.

2.2 Pile and load test details

Precast square concrete piles, 250 mm in width (B), were driven to a depth of 6.0 m in the *sleetch*. Reference is made to the single pile S1 and pile groups G1 and G2 as described in McCabe & Lehane (2006). The groups comprised four ‘corner’ piles driven at the corners of a square of 1.0 m side after a ‘centre’ pile had been installed at the centre-point of the square (Figure 2a). The average centre to corner pile spacing to width ratio (s/B) was 2.8.



Figure 2b. Load test arrangement.

The single piles and pile groups were loaded in compression using conventional Kentledge dead weight (Figure 2b). The group piles were loaded through a pre-fabricated steel cap standing ≈ 0.5 m free of the ground surface (Figure 2a). All pile heads were equipped with load cells and displacement transducers. Load tests were carried out using a maintained load test procedure, with increments not exceeding 15% of pile capacity, in conjunction with a threshold ‘creep’ rate of 0.24 mm/hr.

3 OASYS SAFE FINITE ELEMENT MODEL

3.1 Validation of axisymmetric model

An axisymmetric model of pile group G1 was set up in OASYS SAFE, in which the axis of the centre group pile coincided with the axis of symmetry of the model space (Figure 3). The four corner piles could not be defined in discrete locations, so their spacing from the pile group centre was represented by the circumference of a cylinder of radius 2.8 B . It is acknowledged that the load-displacement behaviour of the corner piles cannot be modelled in this way, but it was anticipated (and subsequently verified) that the influence they would have on the centre pile would nevertheless be realistic. The centre pile (of square cross-section) was modelled as a circular pile with an equivalent shaft area.

Shaft load on the corner piles was modelled by applying shear stresses to the cylindrical surface, with appropriate scaling for the difference in surface area between four discrete pile shafts and the cylindrical surface. Base load on the corner piles was modelled by applying vertical pressures to a circular annulus at a depth of 6.0 m, with equivalent scaling for base area.

Initial trials with the model, assuming a linear elastic soil, indicated that the load-displacement response predicted by SAFE for a single pile (i.e. when no load is placed on the corner piles) was in excellent agreement with predictions using the analytical linear elastic solution of Randolph & Wroth (1978). Likewise,

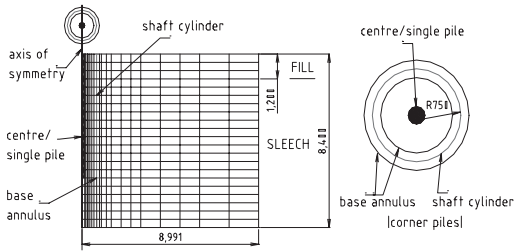


Figure 3. SAFE finite element mesh.

when the centre and corner piles were loaded together in a linear elastic soil, the load-displacement response of the centre pile of the SAFE group was found to agree very well with PIGLET (Randolph 2002) predictions. Both rigid and flexible caps were modelled. These outcomes gave confidence that the approximate model used was a reasonable method of accounting for the interactive loads and settlements to which an interior group pile might be subjected.

4 OASYS BRICK SOIL MODEL

The BRICK constitutive model (Simpson 1992) is a non-linear elastic plastic soil model; the 3-D version described in Lehane & Simpson (2000) was employed here. OASYS provide a single element programme for this model in addition to its inclusion in the SAFE finite element code. The BRICK model requires specification of:

- (i) prior stress/strain history of the deposit,
- (ii) tangent shear stiffness (G_t) degradation with shear strain (γ), referred to as 'string data' and
- (iii) compressibilities at very low strains and at higher strains.

The material's friction angle (ϕ') is a function of the specified G_t vs. γ variation; see Simpson (1992).

Before applying the BRICK model to the FE problem, its ability to replicate measured triaxial behaviour was assessed using the single element BRICK programme.

The stress history of the *sleech* was modelled as normal consolidation ($K_0 = 0.5$) with subsequent swelling to the current *in-situ* overconsolidation ratio of 1.2 (which was representative of the average value in the *sleech* encountered by the piles). The BRICK modelling of the triaxial test also accounted for the loss in effective stress induced by sampling; see Figure 4.

The development of an S-shaped relationship between tangent shear modulus (G_t) and shear strain (γ) was based upon a measured seismic shear modulus (G_s) of 10.5 MPa combined with the triaxial data presented in Figure 1.

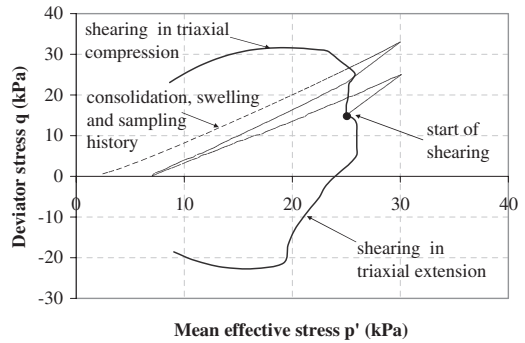


Figure 4. BRICK predictions of triaxial behaviour.

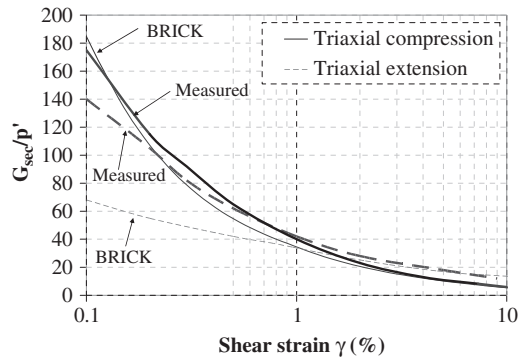


Figure 5. BRICK predictions of triaxial stiffness.

The final G_t - γ relationship chosen was that which offered the best prediction of the measured triaxial behaviour – to include the angle of friction, undrained stress path and the undrained strength γ (Figure 4), and estimate of G_{sec}/p' as a function of γ (Figure 5). Reasonable matches were obtained. Some deviation between the measured and predicted G_{sec}/p' values in triaxial extension is noted. This is partly because of the assumption in BRICK that the shear stiffness varies with the mean effective stress level (p') at all strain levels (noting that G_0 varies approximately with $p'^{0.5}$).

This S-shaped curve was then converted into the 'string format' shown in Table 2 (G_0 = initial shear modulus).

Other parameters derived from triaxial and oedometer testing are presented in Table 3. The values of β_g and β_ϕ were not measured, but the output was found to be relatively insensitive to their values. The reader is referred to Simpson (1992) and Lehane & Simpson (2000) for a full description of these parameters.

Table 2. BRICK string data.

Step	G_r/G_o	Shear strain (γ) (\equiv 'string length')
1	0.95	0.000001
2	0.80	0.000015
3	0.47	0.0001
4	0.15	0.0004
5	0.075	0.0009
6	0.035	0.004
7	0.025	0.011
8	0.015	0.03
9	0.005	0.06
10	0	0.1

Table 3. BRICK parameters.

Parameter	Value	Details
$\lambda/1 + e$	0.104	λ = Slope of normal consolidation line in void ratio (e) – mean effective stress (p') space
$\kappa/1 + e$	0.020	κ = Slope of recompression line in $e-p'$ space
ν	0.0017	Small strain equivalent of λ, κ defined as p'/K_{max} (K_{max} = small strain bulk modulus)
ν	0.2	Poisson's ratio
M	1.3	Drucker-Prager failure criterion
β_g, β_ϕ	1.0	Effect of overconsolidation on soil stiffness

5 STAGES OF ANALYSIS

The SAFE/BRICK analysis was carried out in a number of distinct stages to recreate as closely as possible the sequence of events occurring at the site from soil deposition to pile loading. These stages are identified below:

- (i) 'Deposition' of sileech from ground level to the rigid (sand) boundary at 8.5 m depth
- (ii) Transformation of the top 1.2 m of material to 'made ground', treated as an elastic Mohr Coulomb material with drained Young's modulus $E = 25$ MPa and friction angle $\phi' = 33^\circ$
- (iii) Transformation of appropriate elements along the axis of symmetry into a linear elastic material with the properties of concrete
- (iv) Compressive pile loading was applied by imposing pressure loads on line elements (on the head of the centre pile and along corner pile shaft cylinder and base annulus) and noting the corresponding displacements. The load-displacement behaviour reported in subsequent figures is relative to the start of stage (iv).

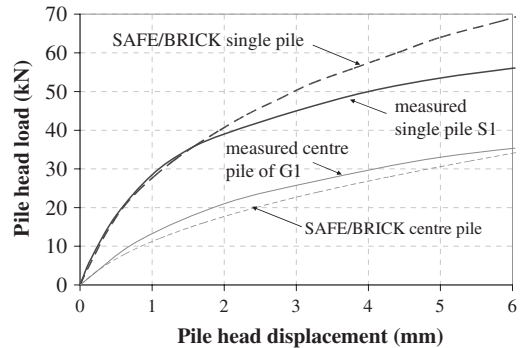


Figure 6. Belfast load tests – measurements and SAFE/BRICK predictions.

5 SAFE/BRICK RESULTS

5.1 Single pile S1

A direct comparison between the measured load-displacement behaviour of single pile S1 and the corresponding SAFE/BRICK prediction is presented in Figure 6.

The exactness of the agreement is somewhat fortuitous, given that the installation of the piles is not modelled in SAFE/BRICK (i.e. the piles are wished-in-place piles). Nevertheless, the single pile stiffness is captured reasonably well up to 40 kN or approximately two-thirds of the single pile's capacity. Deviation between prediction and measurement at higher loads is partly due to the fact the SAFE/BRICK makes no provision for slip at the interface between pile and soil. Importantly, the non-linear shape of the load-displacement curve is captured very well.

5.2 Pile group G1

Figure 6 also presents measurements and SAFE/BRICK predictions of the load-displacement response of the centre pile of group G1. The non-linearity of the centre pile's behaviour is modelled as well as that of the single pile, and the measured 'relative' stiffnesses are also reflected accurately to loads well in excess of typical working levels.

The significance of this result can be put in context by comparing the non-linear predictions in Figure 6 with the linear elastic PIGLET predictions in Figure 7. The PIGLET predictions assume a rigid pile cap, which is consistent with the uniform settlement experienced by all five piles of G1. Under a typical working load of ≈ 30 kN, the single pile head displacement is predicted correctly when a constant shear modulus (G) of 3.5 MPa is assigned to the soil. However, at the same load per pile head, and with the same value of G assumed for the soil within group G1, Figure 7

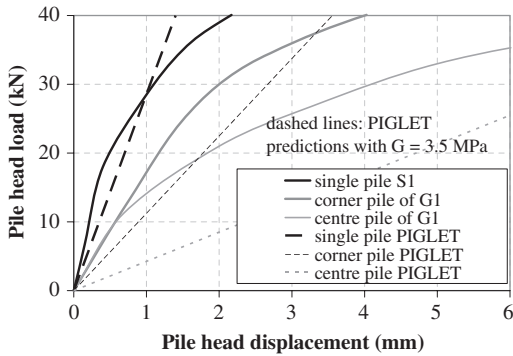


Figure 7. Belfast load tests – measurements and PIGLET predictions.

illustrates that PIGLET overpredicts the settlement of the centre pile by 75% and an corner pile ‘average’ by 33%. These overestimates lead to a predicted group stiffness efficiency (η_g) of 0.25 compared to the measured efficiency of 0.45 ± 0.05 (McCabe & Lehane 2006). Such a gross underestimate of stiffness is a consequence of the assumption of a linear elastic soil stiffness in PIGLET, which leads to overestimates of the extent to which piles interact under load.

Castelli & Maugeri (2002) recognized the importance of soil stiffness non-linearity and proposed the following expression for stiffness efficiency, based on a modified ‘equivalent pier’ approach:

$$\eta_g = [D/D_g]^\varepsilon \quad (1)$$

where D is the diameter of one pile and D_g is the diameter of the plan area of a pile group ($D_g = 2[A_g/\pi]^{0.5}$; A_g = plan area of group). The empirical constant ε was back-figured from a database of pile group load tests, with the authors recommending $\varepsilon = 0.15$ for design. However, application of eqn. (1) leads to an unconservative $\eta_g = 0.79$. The foregoing clearly illustrates the difficulties associated with a realistic prediction of pile group settlement, and that realistic predictions are only likely to be obtained when non-linear constitutive soil models are used in conjunction with an undiluted continuum analysis such as Finite Element modelling.

While this simple SAFE/BRICK model is only capable of predicting load interaction and not installation effects, it still models the measured pile stiffnesses well. The success of the prediction suggests that the centre pile is not subject to significant additional installation effects over and above a single pile. McCabe & Lehane (2006) have already demonstrated this experimentally at the Belfast site by two independent methods: (i) total stress sensors on the centre pile of G1 monitored

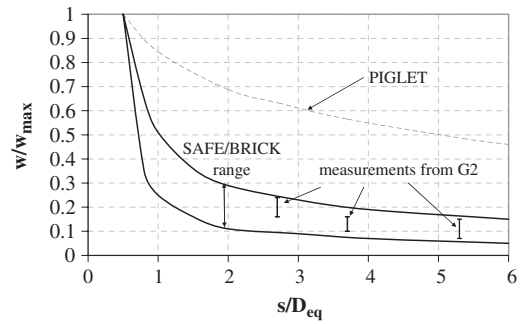


Figure 8. Interaction factors – measurements and PIGLET predictions.

before, during and after group installation and (ii) by loading one corner pile of a new group (G2) alone and comparing with the single pile (S1).

5.3 Interaction factors

When loaded piles are in close proximity, their displacement fields may overlap. The displacement interaction between piles is quantified by interaction factors (α), where:

$$\alpha = w/w_{\max} \quad (2)$$

with w_{\max} the displacement at the head of any loaded pile and w is the displacement that this induces on a neighbouring pile. McCabe & Lehane (2006) present measurements of α , determined by loading one corner pile of group G2 and monitoring the displacements on the load-free piles.

However, α measurements are very scarce, and approximations to α for design are often made by trying to predict the decay of displacement w/w_{\max} in the ground around an isolated single pile – obviously without the ‘reinforcement’ to the ground that nearby piles would provide.

The measured values of α are shown in Figure 8 as a function of the spacing normalized by the equivalent diameter of a circular pile ($D_{eq} = 2B/\pi^{0.5}$), where $s/D_{eq} = 0.5$ represents the pile-soil interface.

The range plotted reflects small variations in α with load level. Corresponding predictions of w/w_{\max} around a single pile using PIGLET and the SAFE/BRICK non-linear model are also included.

It is clear that the SAFE/BRICK model produces a more realistic estimate than PIGLET of the steep decay of w/w_{\max} with displacement from a pile, and is consistent with trends shown by 2-D finite element analyses performed by Jardine et al (1986). Within the range of values attributed to the SAFE/BRICK predictions in Figure 8, the value of w/w_{\max} was

found to reduce with both depth and increasing load level – trends that would require further more detailed investigation.

6 CONCLUSIONS

This paper highlights the strong bearing that soil stiffness non-linearity has on the load displacement performance of a pile group. In particular, it illustrates that a 2D simplification of a pile group coupled with an accepted non-linear constitutive model can yield more realistic predictions than linear elastic models or other empirical analyses.

REFERENCES

- Baligh, M.M. 1985 Strain Path Method, *Journal of Geotechnical Engineering Division*, ASCE 111, No. GT9, 1108–1136
- Castelli, F. & Maugeri, M. 2002 Simplified Nonlinear Analysis for the Settlement Prediction of Pile Groups, *Journal of Geotechnical and Geoenvironmental Engineering*, 128(1), 76–84
- Einav, I. & Klar, A. 2003 An Approach for Nonlinear Contact Surface Analysis and Application to Pile Installation, *Proceedings BGA International Conference on Foundations, Innovations, Observations, Design and Practice*, Dundee, 259–268
- Lehane, B.M. & Simpson, B. 2000 Modelling Glacial Till under Triaxial Conditions using a BRICK Soil Model, *Canadian Geotechnical Journal*, Vol. 37, 1078–1088
- Jardine, R.J., Potts, D.M., Fourie, A.B. & Burland, J.B. 1986 Studies of the Influence of Nonlinear Stress Strain Characteristics in Soil-Structure Interaction, *Geotechnique*, 36(3), 377–396
- Koizumi, Y. & Ito, K. 1967 Field Tests with Regard to Pile Driving and Bearing Capacity of Piled Foundations, *Soils and Foundations* 7, No. 3, 30–53
- McCabe, B.A. & Lehane, B.M. 2003 Stress Changes associated with Driving Pile Groups in Clayey Silt, *Proceedings XIII European Conference in Soil Mechanics and Geotechnical Engineering*, Vol. 2, 271–276
- McCabe, B.A. & Lehane, B.M. 2006 Behaviour of Axially Loaded Pile Groups Driven in Clayey Silt, *Journal of Geotechnical and Geoenvironmental Engineering*: ASCE, Vol. 132, No. 3, 401–410
- O'Neill, M.W., Hawkins, R.A. & Audibert, J.M.E. 1982 Installations of Pile Group in Overconsolidated Clay, *Journal of Geotechnical Engineering Division*, ASCE, Vol. 108, No. GT11
- Randolph, M.F. 1994 Design Methods for Pile Groups and Piled Rafts, *XIII International Conference in Soil Mechanics and Foundation Engineering, New Delhi*, Vol. 5, 61–82
- Randolph, M.F. 2002 *PIGLET: Analysis and Design of Pile Groups Users' Manual, Version 4–2*, University of Western Australia, Australia
- Randolph, M.F. & Wroth, C.P. 1978 Analysis of Deformation of Vertically Loaded Piles, *Journal of Geotechnical Engineering Division, ASCE 104*, No. 12, 1465–1488
- Simpson, B. 1992 Retaining Structures: Displacement and Design: 32nd Rankine Lecture, *Geotechnique*, 42, No. 4, 541–576

Numerical investigation into stress and strain development around a displacement pile in sand

J. Dijkstra¹, W. Broere^{1,2} & A.F. van Tol^{1,3}

¹Delft University of Technology, Delft, The Netherlands

²A. Broere BV, Amsterdam, The Netherlands

³GeoDelft, Delft, The Netherlands

ABSTRACT: This paper presents two methods for the modelling of the stress and strain developments in the soil due to the installation of a displacement pile using the finite element method. The first is a workaround to incorporate the pile installation phase into a small strain finite element method, in this case PLAXIS. The second is a simulation of the installation in an Arbitrary Lagrangian Eulerian numerical scheme. The results of both methods are compared with experimental results of a jacked pile in sand.

1 INTRODUCTION

Displacement piles, such as concrete prefabricated piles, are often used for pile foundations. During the installation of a displacement pile the soil around the pile is pushed away and distorted. For a driven pile the process is even more complex, due to vibrations caused by the installation process. In engineering practice the installation effects are accounted for in the empirical or analytical design method. For more complex geotechnical constructions, especially in cases with complex load combinations or strong interaction with neighbouring structures, the use of the finite element method is common, in order to reach an optimal and economical design.

However, when the modelling of displacement piles is attempted in finite element code, the installation phase is often not taken into account. The occurrence of large shear strains and a significant stress increase (see e.g. Salgado et al. 1998), combined with the limited knowledge of the material behaviour around a displacement pile, complicates the calculations and leads to large differences between predictions and measurements.

The total Lagrangian and updated Lagrangian description are most used in geotechnical finite element applications. The difference between the two is found in the definition of the reference state for the body: at $t = 0$ for the total Lagrangian or small strain approach and the current geometry in the updated Lagrangian formulation. The weakness of both methods is the inability of tracking large deformations in the body. The numerical integration scheme for acquiring the

displacements is only accurate or even stable for limited distortion of the elements. However, in that regard the updated Lagrangian method is an improvement upon the total Lagrangian method.

Incorporation of pile installation effects in an small strain numerical scheme are published by Van Niekerk (1996) and Van Baars and Van Niekerk (1999). They published a numerical method to calculate tension piles while taking in account the installation effects by loading the boundary of the mesh and additional traction loads. However in both publications no insight is given in the magnitude of the additional loads, only a remark that horizontal stress should be between 1–2 times the vertical stress.

To overcome the mesh distortions rezoning/remeshing of the distorted elements is an option. This technique requires the remapping of all variables on the new mesh, which can be a cause of additional errors. Hu & Randolph (1998) presented a method which incorporate regular updating of the mesh and interpolation of the stress and material parameters.

Another method to allow for large displacements is the Arbitrary Lagrangian-Eulerian (ALE) scheme. In an ALE approach the grid is not fixed to the material or in space, the grid can move arbitrary, i.e. the material flows independent from the grid. Element shapes can be independently optimized from deformations, therefore no mesh distortions will occur. For a full overview one is referred to Gadala (2004) and its cited references. This method is successfully implemented by Van den Berg (Van den Berg 1994, Van den Berg et al. 1996), who developed a constitutive model within the ALE-framework to simulate the cone penetration test.

Although this model is most promising, it relies on the numerical stability of the Drucker-Prager constitutive model. It proved to be difficult to obtain stable solutions for the Mohr-Coulomb model. More recently similar calculations are made with a commercial FEM program (ABAQUS) which incorporates the ALE scheme. Susila & Hryciw (1996) and Sheng et al. (2005) published simulations of cone/pile penetration in sand. Again the Drucker-Prager constitutive model is used by Susila & Hryciw (1996). However, Sheng et al. (2005) published calculation results for a critical state model (CAM-Clay). They also reported that the implementation of a flat pile tip seemed to result in numerical unstable calculations. Therefore a conical shape of the pile tip is used.

A special variety of the ALE method is the particle-in-cell or material point method (Więckowski et al. 1999 and Więckowski 2004). Calculations in this method are split into two phases. First the mesh is deformed in the Lagrangian phase. This allows for the calculation of the strain and stress increments. Secondly, in the convective phase, a new position of the computational mesh is chosen, and the velocity field is mapped from the body particles to the mesh nodes. The method shows to be very powerful in solving difficult large strain frictional problems, like the silo problem.

In the following analysis a simple scheme to incorporate the pile installation phase in a commercially available small strain scheme (Plaxis, Brinkgreve et al. 2004) is proposed. Next the simulation of the installation phase itself is attempted in an ALE environment offered by the freely available Tochnog package.

The first approach aims at the development of a numerical model that includes the effects of pile installation and subsequently calculates the bearing capacity of the pile. However, it should also provide a correct prediction of the load-settlement curve. The second approach is aimed at a better simulation of the installation process itself and focuses on the development of stresses and strains around the pile as the method does not allow for the subsequent derivation of a load displacement curve.

For the time being stress wave effects are excluded from both analyses. This implies the study is restricted to jacked displacement piles in sandy soils, as no others soils are considered.

The numerical results are compared to a centrifuge pile load test performed by GeoDelft (Allard 1996), as for this test all data was readily available. In this test a 0.5 m diameter pile was continuously jacked into a uniform saturated sand layer. The velocity during this test was chosen sufficiently small that no excess pore pressures were generated. During the entire test both the total jack force and the base load were recorded, and the shaft friction has been calculated from these measurements. Although the total load capacity and the ratio of shaft friction over total

load capacity can be determined from the test, it offers no data to determine the load-settlement curve for the pile after installation. To this end, a separate source for the load-settlement behaviour of displacement piles has been found in the pile load tests documented by Plantema (1948). He presents the results for a large number of good quality load tests on a similar sized pile jacked into place, which resemble the test conditions in the centrifuge better than most (driven) pile load field tests.

2 NUMERICAL SCHEME

2.1 *Small strain*

For the calculation in the small strain scheme the pile and soil are modelled by 15-noded triangular elements in a axisymmetric mesh. The boundaries are taken such that their influence is negligible. The pile is already embedded at installation depth at the start of the calculation, as Plaxis V8 does not allow for simulation of the whole installation process. Between the pile and soil elements an interface element is applied.

In order to overcome the limitations of the code the pile installation process is simulated directly after the initial stress generation by increasing the volume of the pile cluster by volumetric strains or by prescribed displacements at the pile-soil boundary. After that the material of the pile cluster is replaced by the linear elastic concrete material and the interface between soil and pile is activated. The stress state obtained in this way is maintained, but all displacements are reset to zero. If prescribed displacements are used in the first phase, a slight relaxation of the stress occurs as the pile cluster material is activated and the prescribed displacements deactivated. The last method offers more flexibility, as the horizontal and vertical displacement component can be set independently.

In initial calculations with the Mohr-Coulomb model, in which dilatancy and pile expansion is not taken into account, the mesh-dependency and influence of the interface are investigated. From this analysis it is found that a mesh consisting of 16 elements over the height of the pile and four elements over the radius of the pile tip and including interfaces between pile and soil is the sufficiently fine to model the problem.

The influence of the interface strength reduction is considered next. The pile-soil friction δ has been measured in model tests and corresponds with an interface reduction factor of approximately 0.75.

In order to overcome numerical problems during the first pile expansion phase no dilatancy has been used in this phase and dilatancy of the pile-soil interface has been activated only during the simulation of the pile load test. In all calculations after the pile expansion, a pile load test has been simulated and the

bearing capacity has been determined at failure, as well as after 10 mm of pile settlement.

2.2 ALE

Another method to simulate the pile installation process prior to the “bearing capacity” calculations is to use a numerical scheme which is better suited to large strains. The Arbitrary Lagrangian Eulerian scheme allows this as the mesh can move independently from the material. Here the method of Van den Berg (1994) is followed. The mesh is chosen to be fixed and the material flows through the mesh, strictly speaking the method is Eulerian, although still a special version of ALE.

For the present calculations the open source package Tochnog (<http://tochnog.sourceforge.net/>) has been used. In this package stress and strain fields are assumed to be continuous over the whole element and the unknowns are stored in the nodes as opposed to in the integration points. The latter is the case in most other finite element applications. Additionally in Tochnog the nodal and material displacements can be uncoupled, thereby creating an Eulerian description.

The full penetration of the displacement pile in sand is simulated. The mesh and geometrical boundary conditions are given in Figure 1. The soil is pushed along the pile, instead of the pile being pushed into the soil. Therefore, a partially embedded pile, 5 m embedment, with a prescribed slide geometry at the boundary of the pile is added. The strength reduction

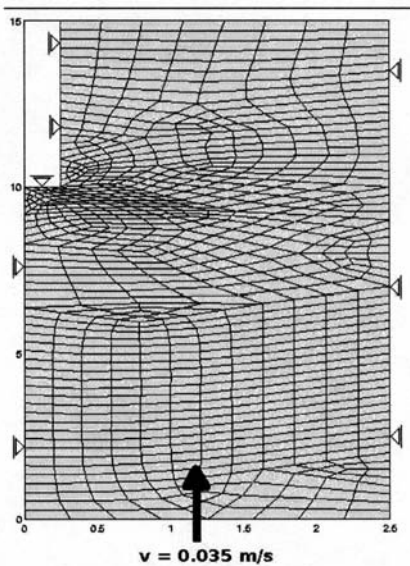


Figure 1. Mesh and geometrical boundary conditions for ALE calculation, measures in meters.

of this slide geometry is set at 0.75, equal to the small strain calculations. At the lower side of the mesh a material velocity of 0.035 m/s is applied. This rather low velocity is derived from the model penetration velocity during pile installation in the model test. The total prescribed displacement is 15 meters. The initial vertical and horizontal stress is -50 kPa, resulting in an initial $K_0 = 1$.

Only during the calculations a realistic K_0 is reached. However, no additional measures are taken to model pile installation other than the Eulerian scheme and the large prescribed displacements. It is not attempted to simulate the subsequent pile load test.

3 CONSTITUTIVE MODEL

3.1 Small strain

In order to improve the obtained load-settlement curve of the pile used, a hyperbolic model with a separate unloading-reloading modulus is suggested by several authors (e.g. Wehnert & Vermeer 2004). In the current study the Hardening Soil (HS) model Brinkgreve et al. (2004), is used. Parameters for the model have been derived from the Mohr-Coulomb parameters, which are reported for the pile load test on the assumption that the E_{50} for the HS model is equal to the Young's modulus E of the MC model at the tip of the pile, and that the unloading-reloading modulus E_{ur}^{ref} is $3 \cdot E_{50}^{ref}$. The resulting parameters are again listed in Table 1. The phreatic level is equal to the surface level, simulating fully saturated conditions.

The calculations with the HS model and pile expansion are made for fine meshes with interfaces.

Table 1. GeoDelft centrifuge test soil parameters for the MC and HS models.

Name	Symbol	MC model	HS model	Unit
Saturated volumetric weight	γ_{sat}	20	20	kN/m ³
Cohesion	c	1	0.1	kPa
Friction angle	ϕ	37	37	°
Dilatation angle	ψ	7	7	°
Young's modulus	E	$1 \cdot 10^4$	–	kN/m ²
Poisson ratio	ν	0.3	0.2	–
Reference stiffness	E_{50}	–	$1.1 \cdot 10^4$	kN/m ²
Oedometer reference stiffness	E_{oed}	–	$9.6 \cdot 10^3$	kN/m ²
Unloading reference stiffness	E_{ur}	–	$3.3 \cdot 10^4$	kN/m ²
Power	m	–	0.5	–

An interface strength reduction factor of 0.75 has been used. For the pile expansion process first the volumetric strain method is investigated and subsequently the prescribed displacements.

3.2 ALE

Some authors report stability issues with the Mohr-Coulomb model in an ALE environment (e.g. van den Berg, 1994). Therefore, the pile penetration tests in Tochnog are performed with the Drucker-Prager model. An additional tension cut is added to prevent tension in the material. The input data is taken from Table 1. Again in this case the phreatic level is set on the surface level, simulating fully saturated conditions. A dilatancy angle of 8° is used, as this does not introduce numerical errors in contrast to the small strain analysis, where a high dilatancy would lead to numerical errors and premature failure of the calculations.

4 RESULTS

4.1 Small strain

The results from the calculations using volumetric strains to simulate pile installation are given in Figures 2 and 3. Here the volumetric strain, interface strength reduction and the dilatancy of the soil are varied. As can be seen from the graphs, the cases with 50% volumetric strain yield load capacities close to the load capacity observed in the centrifuge test, at a vertical displacement of 100 mm. Also, the load-settlement curve shows a clear failure load capacity, instead of an ongoing increasing load capacity with increasing deformation.

Still, the distribution of the total load over shaft friction and base resistance is not in accordance with the centrifuge test. The shaft friction is invariably too high, the base resistance still low. A possible cause is the relatively high prestressing around the shaft as compared to the amount of prestressing near the pile tip.

This can be improved with prescribed displacements at the interface between pile and soil. This allows for different amounts of expansion to be used in the horizontal and vertical directions, in contrast to the method using volumetric strains. The load-displacement curves for several combinations of prescribed displacements are given in Figure 4. The resulting shaft resistance and base resistance are very sensitive for the magnitude of the prescribed horizontal displacement (Δu_x), variations of vertical displacements (Δu_y) have much less influence on the results.

The shaft friction found with $\Delta u_y = 50$ mm is too high, although, the base resistance is close to that observed in the centrifuge test. Therefore it was decided to perform several calculations with prescribed horizontal displacements less than 50 mm. Figure 5 shows

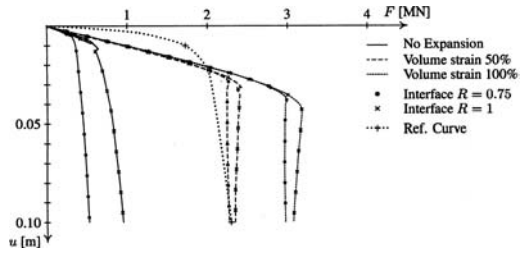


Figure 2. Load-displacement curves for meshes with an initial volume strain of the pile volume, fine meshes with interfaces ($R = 1$ and 0.75) along the pile, for HS material with $\psi = 0^\circ$.

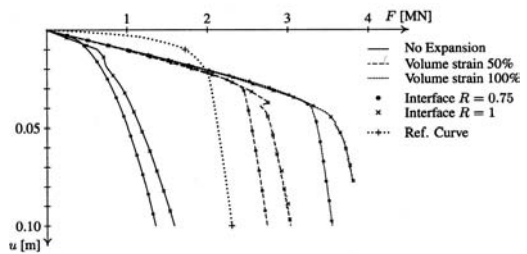


Figure 3. Load-displacement curves for meshes with an initial volume strain of the pile volume, fine meshes with interfaces ($R = 1$ and 0.75) along the pile, for HS material with $\psi = 4^\circ$.

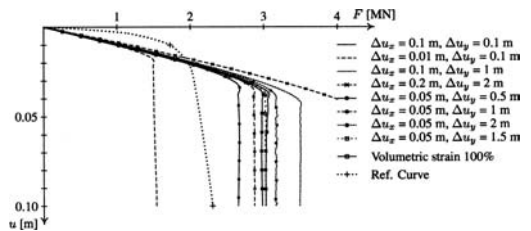


Figure 4. Load-displacement curves for meshes with an initial prescribed displacement Δu at the border of the pile volume, compared to the case of 100% initial volume strain, fine meshes with interfaces ($R = 0.75$) along the pile, for HS material with $\psi = 0^\circ$.

the load-settlement curves for these cases. The case with a horizontal prescribed displacement of 15 mm and a vertical prescribed displacement of 1.5 m fits the centrifuge test results best. Both the shaft friction and base resistance are predicted to within 5%.

4.2 ALE

Figures 6(a) and 6(b) shows the distribution of the vertical and shear stress after 3.5 meters of displacement

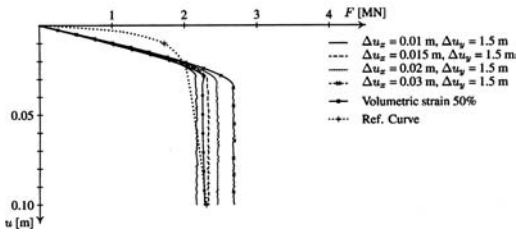
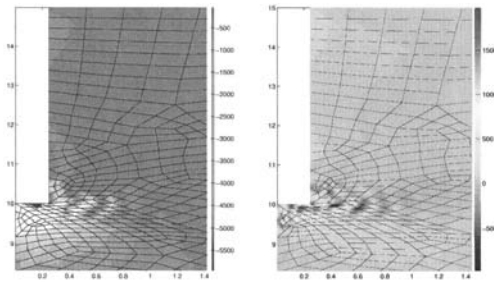


Figure 5. Load-displacement curves for meshes with an initial prescribed displacement Δu at the border of the pile volume, compared to the case of 50% initial volume strain, fine meshes with interfaces ($R = 0.75$) along the pile, for HS material with $\psi = 0^\circ$.

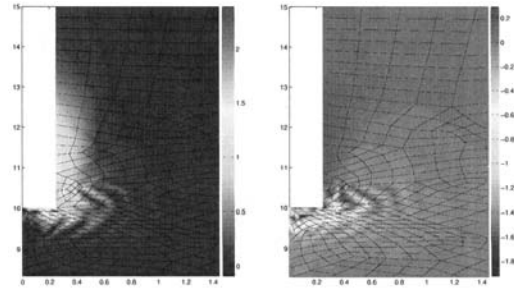


(a) Vertical effective stress after 3.5 meters of displacement, magnitude in kPa
(b) Shear stress after 3.5 meters of displacement, magnitude in kPa

Figure 6. Calculated stress from ALE simulations.

respectively. In Figures 7(a) and 7(b) the shear and volumetric strain are depicted for the same situation. The stress plots clearly show a stress concentration directly under the pile tip and on the pile corner. Directly under the pile tip a vertical stress of 6 MPa is readed. The overall stress distribution is similar to the small strain calculations. After full pile installation, i.e. after 15 meters of pile displacement, the bearing capacity of the pile tip is derived from the vertical stress distribution and the area of the pile tip. The mean stress per element is multiplied with it's area. This yields a pile tip bearing capacity of 1.25 MN, or approximately 97% of the experimentally observed value. When the shaft resistance is derived from the mobilized shear stress in a similar manner a shaft capacity of 1.1 MN is found for the first 5 meters, as only an embedment of 5 meters is modelled. If a linear extrapolation to the remaining 10 m is made, the total shaft capacity is estimated at 2 MN. This overestimates the experimental results by 78%.

In the plot of the shear strains it becomes apparent that after 3.5 meters of pile displacement the soil near



(a) Shear strain after 3.5 meters of displacement (1 = 100 %)
(b) Volumetric strain after 3.5 meters of displacement (1 = 100 %)

Figure 7. Calculated strains from ALE simulations.

the upper part of the mesh is still undisturbed. In Figure 7(a) it can be seen that the height of the disturbance zone is indeed 3.5 meters. The same is observed in the plot of the volumetric strains. The maximum magnitude of the strains is exceeding 150%.

5 DISCUSSION

Both models leave something to be improved. In the ALE environment it is difficult to get results using advanced soil models, or even the MC-model, and it is problematic to include a free soil surface. In small strain FE code large strains are not considered and the installation process is modelled very schematically at best.

This suggests that a combination of the best of both models could be a viable option, using the ALE large strain approach to determine the stress change due to the pile installation and a small strain/Lagrangian approach to deal with the complex soil models and model the pile load test. An implementation of the Material Point Method could be the solution that offers this combination. For the current engineering practice, however, combining the ALE and small strain method could be a short term solution.

6 CONCLUSIONS

In the small strain model a calculation scheme was selected in which the stress increase due to pile installation is modelled with a few relatively simple steps. First the initial stress field is calculated for the axisymmetrical situation in which no pile is present. In this situation, prescribed displacements are applied to the volume of soil that will represent the pile. At the pile shaft, a prescribed horizontal displacement equal to

7.5% of the pile radius is applied. At the pile tip, a prescribed vertical displacement equal to 7.5 times the pile radius is applied. After this prescribed displacement is applied, the properties of the soil volume representing the pile are replaced by the properties of the concrete pile and all calculated displacements are reset. These two steps combined simulate the pile installation. After pile installation a load is applied to the top of the pile and the load capacity is calculated.

In the Arbitrary Lagrangian Eulerian environment the complete pile installation phase is simulated by 15 meters of prescribed displacements. From the final vertical and shear stress distribution the tip and shaft resistance has been determined. The modelling of the pile test itself is not attempted.

The results of both methods indicate the need for improvements. The combination of the stress change found in the pile installation simulation in the ALE calculations with the capability of the more complex soil models in the small strain methods could offer a solution to the current engineering problems.

REFERENCES

- Allard, M. (1996). Centrifuge tests on tension piles, co-351600/91. Technical report, GeoDelft.
- Baars, S. v. & Niekerk, W. v. (1999). Numerical modelling of tension piles. In *International Symposium on Beyond 2000 in Computational Geotechnics*, pp. 237–246.
- Berg, P. v. d. (1994). *Analysis of soil penetration*. Ph. D. thesis, Delft University of Technology.
- Berg, P. v. d., Borst, R. d. & Huétink, H. (1996). An eulerian finite element model for penetration in layered soil. *International Journal for Numerical and Analytical Methods in Geomechanics* 20(12), 865–886.
- Brinkgreve, R., Broere, W. & Waterman, D. (2004). *Plaxis 2D – Version 8*. Plaxis B.V.
- Gadala, M. (2004). Recent trends in ALE formulation and its applications in solid mechanics. *Computer methods in applied mechanics and engineering* 193, 4247–4275.
- Hu, Y. & Randolph, M. (1998). A practical numerical approach for large deformation problems in soil. *International Journal for Numerical and Analytical Methods in Geomechanics* 22(5), 327–350.
- Niekerk, W. v. (1996, April). Berekening van op trek belaste alleenstaande palen. Technical report, Plaxis Gebruikersbijeenkomst.
- Plantema, G. (1948). Results of a special loading test on a reinforced concrete pile, a so-called pile sounding; interpretation of the results of deep soundings, permissible pile loads and extended settlement observations. In *Proceedings of the Second International Conference on Soil Mechanics and Foundation Engineering*, Volume IV, pp. 112–118.
- Salgado, R., Mitchell, J. & Jamiolkowski, M. (1998). Calibration chamber size effects on penetration resistance in sand. *Journal of Geotechnical and Geoenvironmental Engineering* 124(9), 878–888.
- Sheng, D., Dieter Eigenbrod, K. & Wriggers, P. (2005). Finite element analysis of pile installation using large-slip frictional contact. *Computers & Geotechnics* 32(1), 17–26.
- Susila, E. & Hryciw, R. (1996). Large displacement fem modelling of the cone penetration test (cpt) in normally consolidated sand. *International Journal for Numerical and Analytical Methods in Geomechanics* 27(7), 585–602.
- Wehnert, M. & Vermeer, P. (2004). Numerical analyses of load tests on bored piles. In *Numerical Methods in Geomechanics – NUMOG IX*, pp. 505–511.
- Więckowski, Z. (2004). The material point method in large strain engineering problems. *Computer methods in applied mechanics and engineering* 193, 4417–4438.
- Więckowski, Z., Youn, S. & J.H., Y. (1999). A particle-in-cell solution to the silo discharging problem. *International Journal for Numerical Methods in Engineering* 45, 1203–1225.

Axisymmetric and 3D analyses of pile test using FEM

V. De Gennaro, I. Said & R. Frank

Ecole Nationale des Ponts et Chaussées (CERMES, Navier Institute), Paris, France

ABSTRACT: This study focuses on the modelling of the mechanical behaviour of single piles in sand during pile tests. The Finite Element Method (FEM) is used to simulate pile test. Numerical analyses are performed using axisymmetric and 3D geometries. Two specific points are addressed: (i) the reproduction of the installation effects prior to the loading phase in the case of jacked and driven piles and (ii) the simulation of the loading phase accounting for an accurate description of the interface behaviour. The validity of the approach is verified against field data results from an available pile test.

1 INTRODUCTION

Soil-structure interaction problems such as shallow and deep foundations often involve interface behaviour. In the case of deep foundations such as vertical piles the soil-structure interaction includes the shaft capacity mobilised at the interface layer existing between the pile and the surrounding soil and the base resistance at pile tip. These are the two factors that define the axial capacity of the structure.

In this paper results on the modelling of the mechanical behaviour of a single pile in sand during pile tests are presented. The general strategy adopted to simulate the pile test is first described. This includes: (i) the definition of the mechanical properties of soils and interfaces moving from field and laboratory data, (ii) the definition of the initial conditions following the installation process and (iii) the constitutive and numerical modelling of the soil-pile interface (where almost all the non linearity of the problem is concentrated). The first point deals with the choice of the relevant geotechnical data. The second point is tackled adopting the design method proposed by Jardine & Chow (1996) for jacked and driven piles. The third point copes with the formulation of a constitutive model for the interface. For axisymmetric FE calculations MEPI model (De Gennaro & Frank 2002) is considered to reproduce the elastic-plastic behaviour of the pile-sand interface. The model, implemented in the FEM code CESAR-LCPC, is associated to 8-nodes thin layer element (Desai et al. 1984). For 3D calculations an oriented failure criterion based on Mohr-Coulomb failure condition and non-associated ideal plasticity (i.e. elastic perfectly-plastic behaviour) is adopted (Frank et al. 1982). The model is associated to a 20-nodes element. Existing differences between

the two models is briefly outlined. Results of FE calculations adopting both axisymmetric and the 3D configurations are then compared with field data from pile test. Special emphasis is put on the role of the non-associativity in the interface constitutive modelling and on the effect of interface dilatancy.

2 PILE TEST

The pile test analysed is that performed by Chow (1997) in Dunquerque. Measurements were obtained using a displacement pile fully instrumented designed at Imperial College by Bond (1989). We summarise in the following paragraphs the geotechnical data and the test conditions considered in view of numerical analyses using FEM.

2.1 Geotechnical data

The horizons encountered in Dunquerque consisted of a top layer of hydraulic fill up to about 4 m depth and the Flandrian sand formation from 4 m to 30 m depth. The Flandrian sand horizon is interrupted at 7.6 m depth by an organic layer, 0.6 m thick. The water table was found at a depth of 4 m (Chow 1997).

Densities were assessed by means of CPT tests, that revealed dense sand ($I_D = 0.75$), with a net reduction in density in the organic layer. The hydraulic fill had $I_D = 1$, the corresponding bulk densities were $\gamma = 17.1 \text{ kN/m}^3$ above the water table for the hydraulic fill, and $\gamma = 19.9 \text{ kN/m}^3$ below the water table, within the Flandrian sand formation. The instrumented pile is sketched in Figure 1. The cylindrical steel pile was 0.102 m in diameter and 7.4 m in length. The pile tip was close-ended with a 60° conical shape. Four instrumented clusters allowed the simultaneous measurements of axial load, total radial stress σ_r and shear stress σ_{rz} .

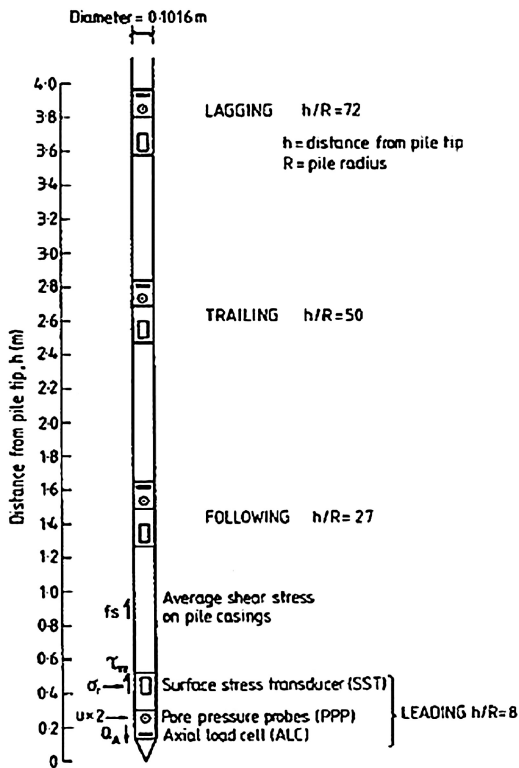


Figure 1. The Imperial College instrumented pile (Chow 1997).

The clusters were spaced about 1 meter along the shaft, starting from a distance of 0.2 m from the pile tip. Data treatment of the axial loads recorded in the four clusters allowed to calculate the average shear stress f_s between two clusters.

2.2 Installation effects

Following Chow (1997), pile installation was performed by means of successive jack strokes using a hydraulic jack. During each stroke pile head was displaced at a constant rate of 600 mm/min. Once the installation performed, a period of stress equalization of about 15 hours was observed. This time was assessed as the time necessary to get almost complete stabilization of the radial effective stress. An overall increase of the radial effective stress $\Delta\sigma'_{rc}$ after installation was found in the four clusters at the end of the equalization period. Values of $\Delta\sigma'_{rc}$ were comprised between 5 kPa and 117 kPa moving from the top cluster down to the bottom cluster (near the pile tip), respectively.

In order to consider this installation effect on the radial stress, Jardine & Chow (1996) and Chow (1997) proposed the following empirical formula to quantify

the final value (after equalization) of the radial stress along the pile shaft:

$$\sigma'_{rc} = 0.114 q_b (\sigma'_{vo})^{0.2} (h/R)^{-0.33} \quad (1)$$

where h is the vertical distance from the pile tip, R the pile radius, σ'_{vo} the effective vertical stress, σ'_{rc} the radial effective stress at the end of installation and q_b the net cone resistance from CPT.

Note that installation effects on the shaft friction (i.e. residual shear stresses) were not considered in the following analyses. The numerical calculations presented in the next sections only accounted for the installation effects on the radial stress, described by equation (1). The quantification of the installation effects on residual shaft friction will certainly deserve further studies.

3 FEM MODELLING

Finite element analyses were performed using CESAR-LCPC code (Humbert, 1989). Both axisymmetric and 3D numerical modelling were performed, with the aim to compare results in terms of load-settlement curves. In both cases simulations required a specific treatment of the interface layer, in terms of constitutive models and contact finite elements. Details of the assumptions related to numerical and constitutive modelling will be discussed further in the next sections.

3.1 Constitutive modelling

During simulations, Flandrian sand from Dunkirk was considered elastic perfectly-plastic, obeying the Mohr-Coulomb failure criterion. The mechanical parameters for the Flandrian sand were obtained from the triaxial data by Kuwano (1996), reported by Chow (1997). The elastic parameters were: $E_s = 200$ MPa and $\nu_s = 0.3$. At failure, neglecting cohesion, the internal friction angle was $\varphi' = 37^\circ$ and the dilatancy angle was $\psi' = 12^\circ$. Linear elasticity was considered for the IC steel pile, with $E_p = 195$ GPa and $\nu_p = 0.28$.

For the soil-pile interface modelling, two constitutive laws were considered. The first law (Oriented Criterion, OC) involves elastic perfectly-plastic behaviour, assuming the Mohr-Coulomb failure criterion and non-associativity (Frank et al. 1982). The second constitutive law for the interface was that proposed by De Gennaro & Frank (2002), admitting non-associated elastic-plastic behaviour (MEPI model).

Both interface laws consider the two components of stresses σ_n and τ , perpendicular and parallel to the interface layer as the conjugate stress variables of the normal and vertical relative displacements of the interface (state variables). The two stress components are calculated in each integration point as a projection on the directions perpendicular and parallel to the interface

layer of the general stress tensors acting in this point. Uncoupled linear elastic behaviour is considered in the tangential and perpendicular directions to the interface. The normal stiffness K_n and the tangential stiffness K_t allow to define the stress-displacement relationships in elasticity. Following the classical finite element approach, stresses and strains at the interface are correlated directly by a constitutive matrix. It's easy to verify that interface elastic stiffness K_n and K_t can be derived considering the interface thickness t as a scaling factor. If a linear elastic behaviour is admitted fictitious values of the Young's modulus E and the Poisson's coefficient ν are then obtained (e.g. Hohberg & Schweiger 1992, Sharma & Desai 1992). Referring now to the plastic behaviour, the OC law admits the plastic parameters of the standard Mohr-Coulomb failure criterion (i.e. cohesion c' , friction angle φ' and dilatancy angle ψ').

For the sake of space only the general features of MEPI model are outlined, more details can be found in the given reference. Plastic hardening is introduced by means of an extended Mohr-Coulomb yield locus including deviatoric hyperbolic hardening. The plastic tangential displacement u_t^p is the hardening variable. The plastic flow is derived from the original Cam clay model, considering the classical plastic potential function suggested by Schofield & Wroth (1968). Basically MEPI model needs three friction parameters to be determined: the coefficient of friction at failure μ_f , the initial friction coefficient μ_o (elastic domain) and the friction coefficient μ_{co} at phase transformation (contractancy/dilatancy threshold). Two additional parameters are needed to control the hardening function and the evolution law of dilatancy. Zero dilatancy rate at large tangential displacements is one of the key behavioural features introduced in MEPI model. This avoid unrealistic increase of the normal stress due to excessive dilatancy during interface shearing

For both constitutive laws data from Kuwano (1996), who performed some interface direct shear tests on Flandrian sand, were used to identify the constitutive parameters. The parameters are summarised in Table 1.

3.2 Axisymmetric modelling

Pile test modelling entailed the discretisation of the soil-pile system by eight-node rectangular isoparametric finite elements.

3.3 Axisymmetric modelling

Pile test modelling entailed the discretisation of the soil-pile system by eight-node rectangular isoparametric finite elements. Given the geometry of the problem (Fig. 1), the axisymmetric finite element mesh was defined by taking a radial vertical section cut of the pile and the soil (Fig. 2a). The extension of the investigated domain was

Table 1. Constitutive parameters.

Parameters	Interface MEPI	OC	Soil MC
E (MPa)	–	1.5	200
ν	–	0.11	0.3
φ' (°)	–	28	37
ψ' (°)	–	10	10
K_n (kPa m ⁻¹)	288000		
K_t (kPa m ⁻¹)	144000		
μ_f	0.51		
μ_{co}	0.1		
μ_o	0.01		
A	0.003		
B	15		
t (mm)	3		

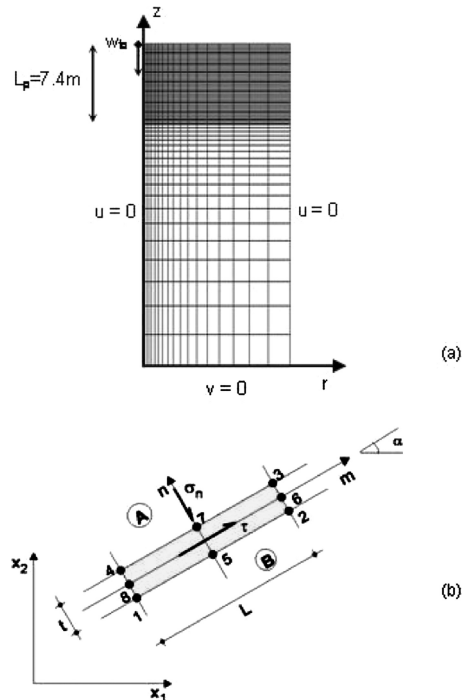


Figure 2. (a) Axisymmetric mesh and boundary conditions; (b) 2D interface element.

set at 30 m in the vertical direction and 22 m in the radial (horizontal) direction (moving from the pile axis), in order to reduce boundary effects on the numerical results obtained. Standard displacement constraints were imposed on the outer boundaries, that is: radial displacements equal to zero on the vertical boundary and vertical displacements equal to zero on the bottom boundary.

The soil was discretised by means of 1352 axisymmetric isoparametric 8-nodes elements, 100 pile elements and 50 interface elements. The total number of

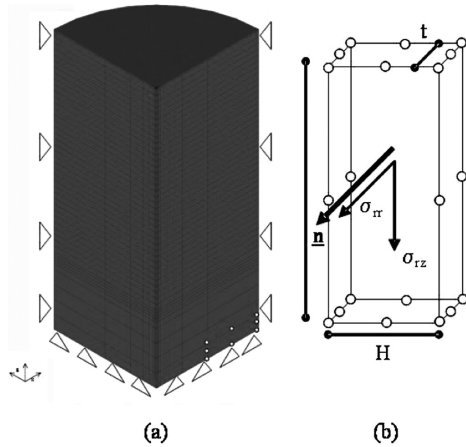


Figure 3. (a) 3D mesh and boundary conditions; (b) 3D interface element.

nodes was 4389. The interface layer was $t = 3$ mm in width (12 times D_{50} of the sand) and its behaviour was simulated using eight-nodes thin-layer elements oriented parallel to the pile shaft (i.e. $\alpha = 90^\circ$) (Fig. 2b). The aspect ratio L/t of the interface elements ($L/t = 48$) was chosen in order to better reproduce the jinterface behaviour and avoid numerical ill-conditioning related to the degeneration of the Jacobi matrix components (e.g. Pande & Sharma 1979, Hohberg & Schweiger 1992, De Gennaro & Frank 2005). In order to describe the interface behaviour the MEPI model or the OC law were associated to these elements.

3.4 3D modelling

The mesh used for the 3D modelling of the pile test is shown in Figure 3a. Symmetry conditions with respect to the pile axis in terms of loading and geometry allowed the analysis of a sector representing one fourth of the entire three-dimensional space.

The boundary limits of the cylindrical-shaped domain were extended at 1.25 times the pile length below the pile tip and 15 times the pile diameter in the radial direction. A total of 2256 parallelepiped 20-nodes elements were used for the soil, including 37 interface elements. The pile was discretised by means of 188 triangular 15-nodes elements. The total number of nodes was 10979.

In analogy with the axisymmetric case, the interface layer was simulated by means of 3D thin-layer elements oriented parallel to the pile shaft (Fig. 3b). This condition was fulfilled assuming the normal vector $\underline{n} = (n_x; n_y; 0)$, where n_x and n_y are the components of the normal vector in the x-axis and y-axis, respectively. The aspect ratio relevant to the simulation of the interface layer is again the ratio L/t . With the same arguments already discussed for the axisymmetric case, numerical ill-conditioning depends on the modification of some

elements of the Jacobi matrix where the ratio L/t appears. An aspect ratio $L/t = 67$ was found to ensure a consistent response of the interface elements in terms of mobilized shear curves. The interface thickness was assumed equal to 3 mm as in the axisymmetric calculations. The mechanical behaviour of the interface layer was reproduced using the OC law and the two components of stress σ_{rr} and σ_{rz} (Fig. 3b) acting in the interface layer. The same mechanical parameters adopted for the axisymmetric analyses were assumed (Table 1).

4 RESULTS

All the analyses were performed after previous initialisation of the state of stress to the effective stresses derived from the pore pressure profile (with the water table at 4 m depth).

For the axisymmetric analyses equation (1) was considered to initialise the values of the radial stress along the pile shaft and take into account the effect of jacking. The installation effect on radial stress due to jacking was disregarded in the 3D analyses. The change in base resistance Q_p after installation was imposed assuming the value of the axial load obtained at the end of the equalization period ($Q_p = 50$ kN, Chow 1997). During the initialisation phases only the soil was considered, no interface constitutive models were introduced.

Moving from the initial conditions obtained during the previous numerical modelling, compression loading was performed imposing a total vertical displacement of 8 mm to the pile head by successive increments. Before the compression loading interface models were activated in the interface thin-layer elements. For axisymmetric analyses both interface constitutive laws were used. In 3D analyses only the OC law was used to simulate the interface behaviour. Results of the analyses carried out are presented in the next two sections.

4.1 Axisymmetric analysis

Figure 4 shows the results of axisymmetric analyses in terms of average shear stress and normal stresses mobilised along the pile shaft during the pile test. FEM predictions in terms of mobilised average shear stress are compared with the experimental measurements obtained from the four instrumented clusters located along the IC pile (Fig. 4a). The agreement between numerical prediction and field measurements is rather satisfactory, in particular when MEPI model was used to describe the interface behaviour. Note that the experimental curves start from a residual negative shear stress due to the relaxation of the soil-pile system after jacking. As mentioned earlier, shear stress changes on the pile shaft due to jacking were neglected in FEM calculations during the initialisation phase.

The scatter between measured and predicted values increases when the OC law is used for the soil-pile

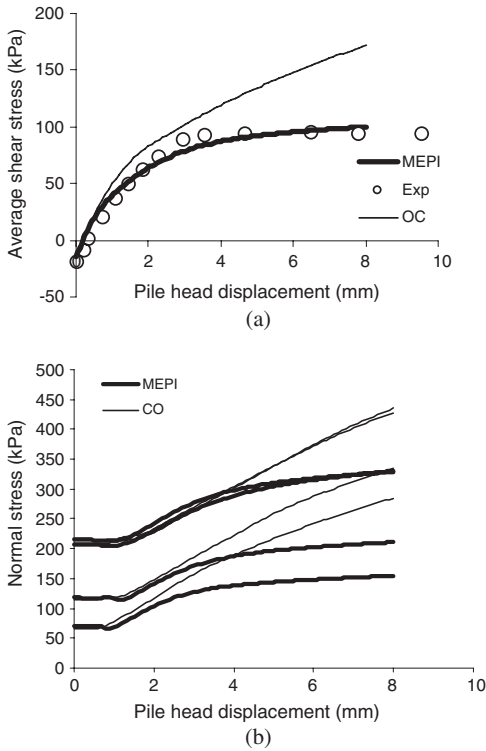


Figure 4. Loading phase (axisymmetric condition): (a) shear stress mobilised along the pile shaft, (b) evolution of the normal stresses along the pile shaft.

interface. Increasing values of the average shear stress at the interface and absence of shear stabilisation at failure are observed. Figure 4b furnishes a key of interpretation of this situation. Increasing shear stresses result from the over-predicted dilatancy of the interface layer. In other words, the highly dilatant behaviour predicted by the Mohr-Coulomb non-associated criterion, constrained by the surrounding soil stiffness, results in a continuous increase of the radial stress (normal to the pile shaft) and, consequently, of the shear stress. This situation is not encountered in the case of numerical simulations obtained using MEPI model since the latter allows for dilatancy stabilisation at large relative tangential displacements.

Figure 5 shows the results of the numerical prediction of the axial capacity of the pile during the test. Pile head load (Q_T) and base resistance (Q_P) are plotted vs pile head displacement and are compared with results from the numerical simulations.

Although values are slightly underestimated, the predicted total load-settlement curve compares well with the experimental one, showing similar trend.

The result obtained assuming the OC law at the interface also compares quite well with field data, even

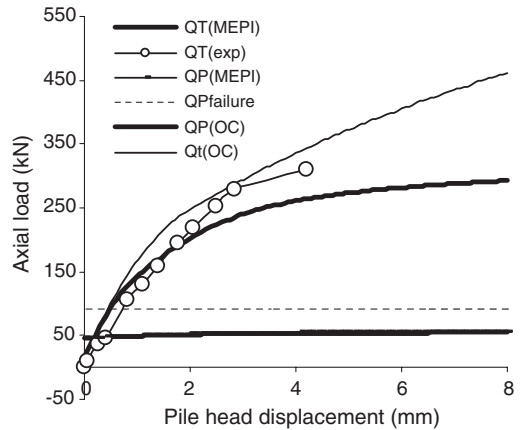


Figure 5. Loading phase (axisymmetric condition): load-settlement curves and base resistance predictions.

though the general trend of the load-settlement curve seems to suggest that failure condition (plateau) is far to be attained. Again the effect of the constrained dilatancy is believed to be at the origin of this behaviour.

As a concluding remark, a big scatter appears between the measured Q_P at failure (about 92 kN) and the predicted one (about 50 kN), the latter corresponds to the same value imposed during the initialisation phase. It's readily apparent that no mobilisation of the base resistance is predicted by the numerical simulations, irrespective of the interface model adopted. It seems likely that the base load is transferred to a highly compressible material, whereas the overall effect of jacking is very likely the opposite, resulting in a densification and a reduced compressibility of the soil below the pile tip.

4.2 3D analysis

Results of the 3D analysis of the same pile test are presented in Figure 6 in terms of pile head load (Q_T) and base resistance (Q_P) plotted vs the pile head displacement. As already mentioned, 3D numerical analysis was carried out assuming only the OC law for the interface layer. The results are in good agreement with that obtained performing the same calculation assuming axisymmetric conditions. It can be observed that also in this case numerical prediction over-estimates the total capacity of the driven pile. Furthermore, no signs of stabilisation on a final plateau (failure condition) are apparent. The over-predicted dilatant behaviour of the interface seems to be again at the origin of such a behaviour.

Surprisingly, the base resistance Q_P predicted using the 3D numerical modelling is well captured. The mobilisation of the base resistance during loading is readily apparent from the curve in Figure 6.

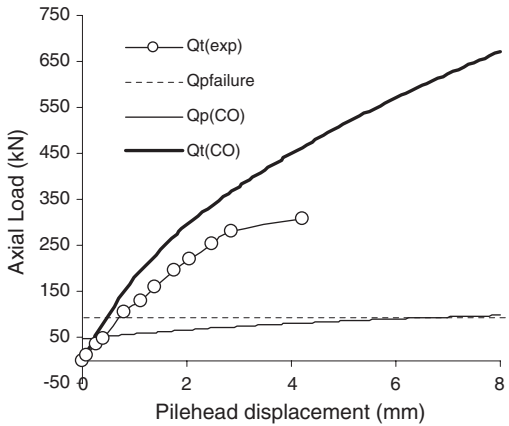


Figure 6. Loading phase (3D condition): load-settlement curves and base resistance predictions.

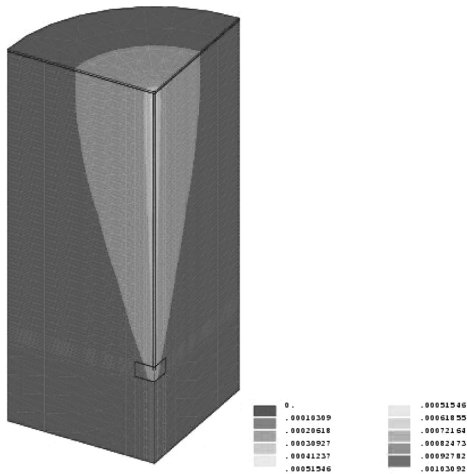


Figure 7. Total displacement field (values in meters).

At the end of the simulation of the pile test the predicted base resistance value is practically equal to the experimental value.

We conclude showing in Figure 7 the total displacement field around the pile for an imposed pile settlement of about 1 mm. By inspecting the curves of mobilised shear stress and the load-settlement curves we can recognise that the total displacement field can be assumed roughly representative of the serviceability state of the structure. The vertical settlement of about 1 mm corresponds to 1/3 of the mobilised total load Q_T . As expected, displacements are localised around the pile. The extension of the zone increases approaching the surface, we also observe a rapid decrease of the displacements following the radial direction. Displacements are zero at about 7 diameters from the pile axis.

5 CONCLUSION

The numerical analyses of the compression test of an instrumented pile jacked into sand have been presented. Both axisymmetric and 3D conditions were analysed using FEM.

A specific treatment of the interface layer in terms of constitutive and numerical modelling has been proposed and its importance has been clearly illustrated. The proposed approach predicts results in good agreement with the pile test data.

A further step will consist in implementing and validating MEPI model in the 3D version of CESAR-LCPC code. To this scope, a generalisation of the model to the 3D space will be necessary.

Installation effects were tentatively accounted considering empirical relationship available in literature. Only the change in radial stress around the pile, consecutive to jacking was considered in this study. Similar correlations could be used to reproduce the installation effects in terms of residual skin friction.

REFERENCES

- Bond A.J. 1989. Behaviour of displacement piles in overconsolidated clays, *PhD Thesis*, Imperial College, London.
- Chow F.C. 1997. Investigations in the behaviour of displacement piles for offshore foundations, *PhD Thesis*, Imperial College, London.
- De Gennaro, V. & Frank, F. 2002. Elasto-plastic analysis of the interface behaviour between granular media and structure. *Computers and Geotechnics* 29, 547–572.
- De Gennaro V. & Frank R. 2005. Modélisation de l'interaction sol-pieu par la méthode des éléments finis. *Bull. de Liaison des Laboratoire des Ponts et Chaussées*, 256–257: 107–133.
- Desai, C.S., Zaman, M.M., Lightner, J.G. & Sirirwardane H.J. 1984. Thin-layer element for interfaces and joints. *Int. J. Numer. Anal. Methods Geomech.* 8, 19–43.
- Frank R., Guenot, A. & Humbert, P. (1982). Numerical analysis of contacts in geomechanics. *Proc. 4th Int. Conf. on Num. Meth. in Geomechanics*, Edmonton, May 31–June 4: 37–45.
- Hohberg, J.-M. & Schweiger, H. 1992. On the penalty behaviour of thin-layer elements. *Proc. 4th Int. Symp. on Num. Models in Geom. (NUMOG IV)*, Swansea, UK, 241–248.
- Humbert, P. 1989 CESAR-LCPC, un code général de calcul par éléments finis. *Bull. liaison Labo. Ponts et Chaussées*, 160, févr.-mars, 112–116.
- Jardine, R.J. Chow, F.C. 1996. *New design methods for offshore piles*. MTD publication No. 96/103 CPMT, London, UK.
- Pande, G.N. & Sharma, K.G. 1979. On joint/interface elements and associated problems of numerical ill-conditioning. *Int. J. Numer. Anal. Methods Geomech.* 3, 293–300.
- Schofield, A.N. & Wroth, P. (1968). *Critical state soil mechanics*. McGraw-Hill, European Civil Engineering series, London.
- Sharma K.G. & Desai C.S. 1992. Analysis and implementation of thin-layer element for interfaces and joints. *J. of Engin. Mechanics*, ASCE 118 (12): 2442–2462.

Interpretation of pile load test failure using FEM simulation

S.A. Tan & T.Y. Bui

Centre for Soft Ground Engineering, Department of Civil Engineering, National University of Singapore, Singapore

ABSTRACT: This paper examines two cases of instrumented piles that did not performed as intended. The first case is an O-cell test of a 1500 mm large diameter bored pile. The pile could not be loaded by the O-cell to its required test load of 1.5 times working load of 18.5 MN. The upper part of the shaft resistance was not fully mobilized at the end of test. The second case is the simulation of a conventional top loaded 1200 mm bored pile installed by the slurry method that has a significant soft toe layer resulting in a plunging failure at 2.5 times its working load at 25 MN. Using the FEM model to simulate the pile response, brittle plunging failure can be illustrated that correspond to the measured pile response at the time of failure. Also the model can be extended to see how the pile would have performed if there were no soft toe at the base of the pile.

1 INTRODUCTION

Fully instrumented pile load test is an effective way to verify the pile performance and evaluate the uncertainties of in-situ soil profiles and parameters, and load transfer characteristic that are much dependent on pile installation effects. Types of pile load tests in common practice include static load test, statnamic and pseudo-static tests, Osterberg-cell test and dynamic pile test. The essential information provided by a pile load test includes the load-settlement responses, axial load distribution, shear stress load transfer characteristics and structural integrity of the pile as constructed. With reliable vibrating wire strain gages and telltales embedded in bored piles, detailed information on the pile/soil load transfer response can be obtained in a proper instrumented pile load test.

For the ultimate pile load test to 3 times working load, when the shaft resistance is fully mobilized, and end bearing resistance is adequately mobilized, the determination of unit shaft friction of the soil layers and unit end bearing from the instrumented data to validate the pile design is fairly straightforward. However, when the tested pile fails prematurely, either as a result of soft toe created during installation; or when the loading system is inadequate and the pile cannot be loaded to ultimate capacity, the interpretation and extrapolation of the test data to ultimate pile capacity can be quite difficult.

This paper illustrates how the pile response can be simulated in the FEM modeling to give insight into the failure mechanisms, and how the test result can be extended numerically when the capacity of test setup had been exceeded.

The FEM study of the pile load test is conducted using 3-dimensional axisymmetric finite element analysis by means of the commercial computer program PLAXIS version 8.2 (2002). Undrained analysis is performed and Mohr-Coulomb soil model with 15 node elements is adopted for the relatively stiff soils and weak rocks where the pile end was embedded. Medium mesh setting was used with the boundary at 30 m away from the test pile to ensure minimal boundary effects on the analysis. To enhance accuracy in the analysis, the meshes 5 m around the test pile area are further refined.

It is well known that for that while loading a pile, the shaft friction will first be mobilized, the pile movement will increase almost linearly with the load increase. When the shaft friction is fully mobilized, the end bearing of the pile will be increasingly mobilized to take the part of the load that exceeded the capacity of shaft friction. Normally the load settlement curve will begin to show a sharper bend at this location of the load settlement curve of the pile. Since end bearing involves the volumetric compression of the soil bulb around the pile toe, plunging response of the load settlement curve is quite unlikely to occur in piles with good toe condition. A sharp plunging behavior is indicative of piles with poor end bearing problem (like a soft toe).

2 CASE STUDY

2.1 Description

The proposed extension of AYE expressway involved a working load O-Cell test of a 1.5 m diameter bored

Table 1. Soil profile and properties.

Depth to	Name	γ (kN/m ³)	$\bar{\nu}$	E_{ref} (kN/m ²)	c_u (kN/m ²)
1.2	Fill	18	0.3	2000	10
2.7	S/YB/S/Silt01	16	0.4	6000	16
4.2	S/YB/S/Silt02	16	0.3	15000	40
5.7	VS/RB/S/Silt01	18	0.3	24000	80
7.2	VS/RB/S/Silt 02	16	0.3	48000	160
10.2	VS/RB/S/Silt03	18	0.2	60000	160
11.7	VS/RB/S/Silt04	18	0.3	79500	212
13.2	VS/RB/S/Silt05	18	0.2	88500	236
16.2	VD/RB/S/Silt	19	0.2	117000	312
17.7	H/RB/C/Silt01	20	0.2	150000	400
23.96	H/RB/C/Silt02	20	0.2	130000	350
25.6	VD/RB/S/Sand	20	0.2	150000	400
32.6	H/RB	20	0.2	200000	500
37.6	VD/S	20	0.2	120000	500

pile in a Jurong Formation residual soil in Singapore. The load test stop short of the specifications of 1.5 WL (18.5 MN). To address concern over the load test interpretation, a FEM model of the O-Cell test was done to estimate what would be the test pile performance if it had been loaded to 1.5 WL in a conventional top down load test with kentledge system.

The 1.5 m diameter test pile is a cast-in-situ concrete bored pile of 24.6 m long. The O-cell was installed at 7.0 m above the pile tip where it was estimated that soil resistance above and below this level would be nearly equal. The O-cells were pressurized to push the pile upwards and downwards, with load applied in the Quick Load Test Method as given in ASTM D1143 (1978). Altogether 6 loading increments up to 10.5 MN were applied to the O-cell, at which point the O-cell had reached its maximum capacity.

The subsurface soil profile belongs to the Jurong Formation of Singapore consisting of weak sedimentary rocks and residual soils of sedimentary origin (Leung, 1996). The soil profile and properties at the site is summarised in Table 1.

2.2 FEM study

Figure 1 shows the finite element mesh adopted in the present study. The O-cell part of the pile is simulated as solid elements of about 100 mm thick in accordance with the extension range of the O-cell assembly. When the O-cell assembly is not in operation such as in the case of static load test with load applied at the pile top, the material properties of the O-cell are made identical to those of pile materials (i.e. concrete). When the O-cell is in use, its material properties are deactivated so that the interaction between the shaft upward and downward movement as well as the tip movement of the pile can be de-coupled.

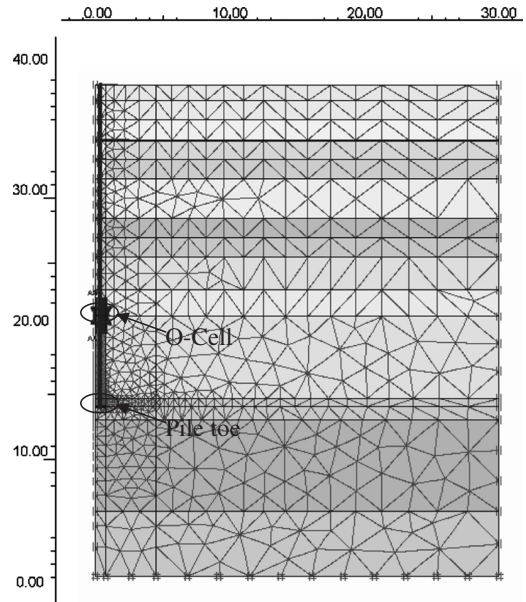


Figure 1. Finite element mesh of the O-cell load test.

Three assumptions made to reconstruct the equivalent head-down load-settlement curve at the pile top from an O-cell load test results are as follows:

- The shaft resistance-movement curve for upward movement of the pile is the same as the downward movement of a conventional head-down static pile load test.
- The end bearing load-movement curve obtained from an O-cell test is the same as the end bearing-load movement component curve of a conventional head-down test.
- The pile is assumed to be rigid so that the top and bottom have the same movement but sustaining different loads.

By adding the shaft resistance to the end bearing at the same movement, a single point on the head-down equivalent load-settlement curve is obtained. The equivalent head-down load-settlement curve can then be determined by repeating this step for all data. If either the upper pile shaft resistance or the lower pile end bearing has reached its ultimate state before the other, hyperbolic extrapolation is usually applied by constructing the linear regression equation to fit the movement/load versus movement curve of either component that needs to be extrapolated. The virtue of the application of FEM analysis is that the load applied by O-cell on either component of the pile can be simulated to increase continually even if one or the other component has reached its largest measured value.

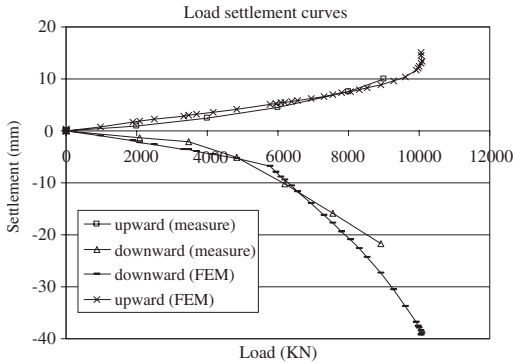


Figure 2. Load settlement curve for O-cell load test.

The elastic compression of the test pile can be determined accurately based on the readings of strain gauges installed along the test pile. It is assumed that a linear distribution of load transfer exists between gauges. This is considered sufficiently accurate as there are 8 levels of strain gauges in the test pile PTP1 and the distance between the gauges is adequately small.

2.3 Results and discussion

Figure 2 shows a comparison between the back-analyzed load-movement curves with the measured ones. It can be seen that the result from FEM analysis and measured curves can be matched very well.

The feature of shaft friction curve and end bearing curve are also shown clearly in this Figure. When the upper part of the pile moves about 10 mm, the shaft friction is already nearly fully mobilized. The load movement curve of the upper part of the pile shows a plunging response at this point. In contrast the load movement curve of the lower part of the pile does not show any plunge. A bend at movement of about 5 mm showed that the end bearing starts to be mobilized at that point.

This feature showed that when the load test stopped due to insufficient test capacity, it is not always reasonable to extrapolate the result using any hyperbolic curve because this mathematical extrapolation had no means of producing plastic plunging failure of shaft resistance.

It is more rational and reasonable to use back-analyzed FEM model for pile load test extrapolation than any hyperbolic curve fitting method. In the present case, both the components of O-cell load-movement curves are extrapolated by increasing the uplift force and the push-down force to 10.5 MN in the FEM O-cell model. It can be conserved that the capacity of the shaft resistance of upper part has been reached when loaded to 10.5 MN while the end bearing of lower part is still increasing at a load of 10.5 MN.

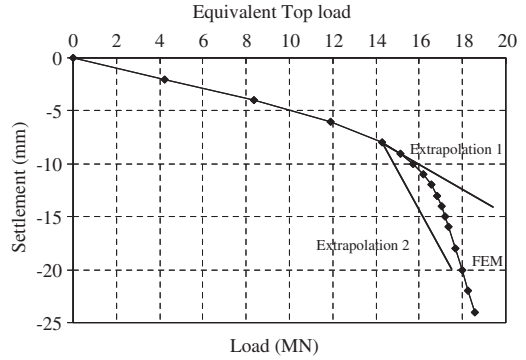


Figure 3. Equivalent top down load settlement curve.

The equivalent pile top head-down load-movement curve is illustrated in Figure 3. The first hyperbolic curve is named Extrapolation 1 which uses the hyperbolic extension of the measured upper shaft resistance beyond the last measured point. The second hyperbolic curve named Extrapolation 2 ignores the contribution of the upper part of the shaft resistance from the O-cell test beyond the last measured point. It can be seen that the Extrapolated curve gave either too high or too low a result when compared to the result from FEM analysis. Finite element simulations reflect a rational plastic yielding trend in the test.

3 CASE STUDY 2

3.1 Description

The simulation of a conventional top loaded 1200 mm bored pile installed by the slurry method with total embedded length of 27.3 m is considered next. Pile instrumentation consisted of 32 vibrating wire type strain gauges (VWSGs) at 11 different levels and 3 tell-tale extensometers at about 10 m, 21 m and 27 m below pile top. Figure 4 showed the layout of the instrumentation.

The pile has a significant soft toe layer that resulted in a plunging failure at 2.5 times its working load (2500 tons). The measured data showed that the pile was carried by shaft friction only in the very stiff clays up to a pile head settlement of 19 mm; until it failed suddenly by brittle shearing at the pile shaft when all the shear stresses had reached peak values simultaneously. With very little end bearing the pile unloaded and plunges downwards by another 80 mm. The FEM model with estimated soil parameters using the Mohr-Coulomb soil model can model the pile response up to peak load just before plunging failure. Also the model can be extended to see how the pile would have performed if there were no soft toe at the base of the pile.

The soil profile and properties at the site is summarised in Table 2.

3.2 FEM study

The pile was modeled with 200mm soft toe which was modeled as an elastic soil with Young's modulus value of 1000kPa. In order to get more accuracy for the analysis, the mesh around the pile toe was made very fine. The interface element of the concrete pile part was modeled outside the pile (in the soil side) whereas it was modeled inside the soft toe (in the soft toe part) because the soft toe material is much softer

than the soil around it. Figure 5 shows the finite element mesh adopted in the present study.

3.3 Results and discussion

Figure 6 shows a comparison between the back-analyzed load-movement curves with the measured ones of both the pile top and the pile toe. It can be seen that the measurement data and the result from back analysis matched very well. The FEM model of this pile illustrated the brittle failure response at the loading test at about 2400 tons. It can be seen that the

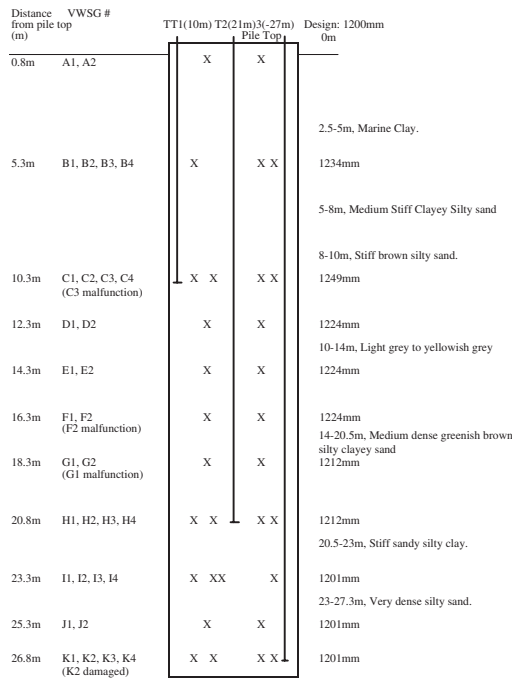


Figure 4. Instrumentation of pile test.

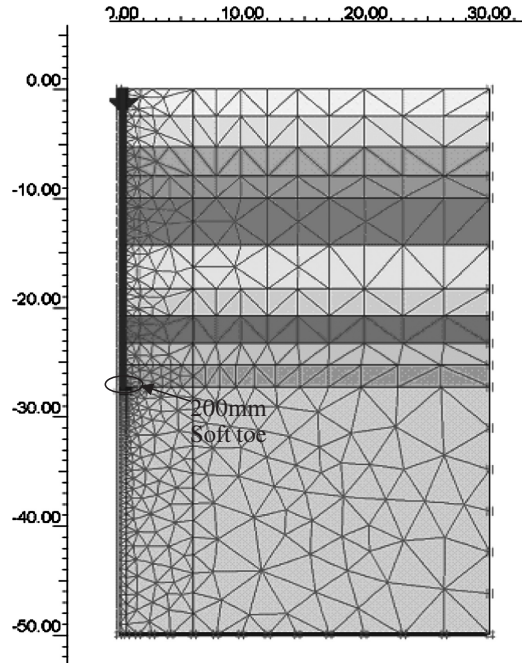


Figure 5.

Table 2. Soil profile and properties.

Depth to	Name	γ (kN/m ³)	ν (kN/m ³)	E_{ref} (kN/m ²)	c_{ref} (kN/m ²)	ϕ_i [°]
2.5	01a Backfilled Soil	19	0.3	15000	0.1	32
5.3	01b Marine Clay	17	0.4	15000	27	0
8.0	02a Medium stiff Clayey Silty Clay	18	0.3	50000	90	0
10.0	02b Stiff Brown Silty sand	18	0.3	50000	90	0
14.3	02c Light Grey to yellowish grey silty Clayey Sand	18	0.3	50000	90	0
18.3	03 Medium Dense Greenish brown silty clayey Sand	19	0.3	75000	140	0
20.3	04 Medium Dense Greenish brown silty clayey Sand	19	0.3	150000	250	0
23.3	05 Stiff Sandy Clayey Silty	20	0.3	400000	150	38
25.3	06 Very Dense Silty Sand	20	0.3	550000	350	40
50.0	07 Very Dense Silty Sand	20	0.3	550000	350	40

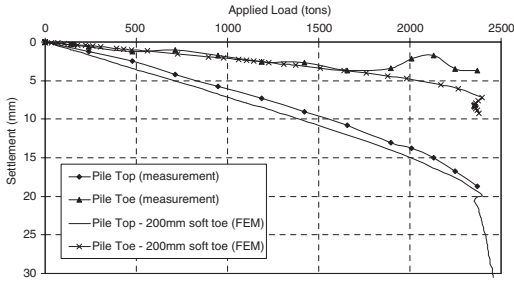


Figure 6. Load-settlement curves comparison.

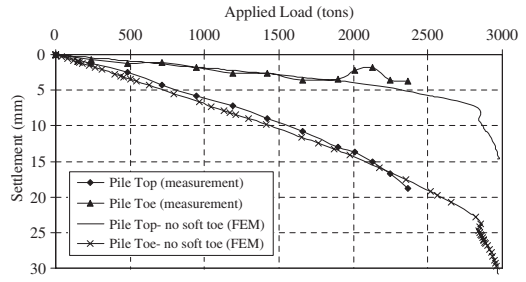


Figure 8. Load settlement curves in the case of no soft toe.

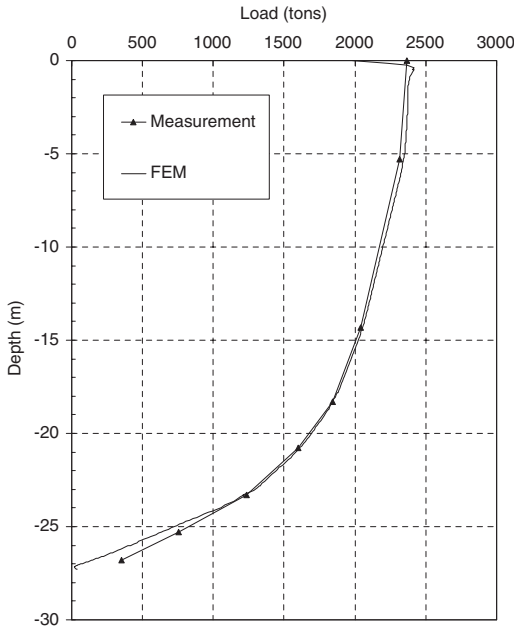


Figure 7. Load transfer curve at failure.

Mohr-Coulomb soil model can produce a good simulation of the pile load test response up to peak load just before plunging failure.

The good match between the measurement and the FEM result can be seen in the comparison of the load transfer curve at failure as shown in Figure 7, where negligible toe bearing is measured. It showed that FEM analysis can model the soft toe condition very well.

The FEM model can also be extended to see how the pile would have performed if there were no soft toe at the base of the pile. Figure 8 showed the load

settlement curve of the pile load test without a soft toe condition. It can be seen that the pile in that case can support the load test of about 2850 Tons. And then the pile will yield more gradually and not plunge suddenly as in the soft toe case.

4 CONCLUSION

A study of two cases of instrumented piles in Singapore that did not perform as intended using FEM had been carried out to illustrate how FEM modeling can be used to understand the unexpected pile load test performance. The following findings can be inferred:

- The FEM model can simulate quite accurately the O-cell load test or Conventional load test to failure in a pile load test.
- Using FEM to extrapolate the response of further load applied to the pile load test give a more reasonable prediction than any hyperbolic extrapolation method, as plastic yielding of soil resistance cannot be properly accounted for in hyperbolic curve fitting.
- Soft toe plunging failure in pile load testing can be properly simulated in FEM analysis.

REFERENCES

ASTM D1143. 1978. *Standard Test Method for Piles under Static Axial Load*. American Society for Testing Materials.

Leung, C.F. 1996. Case studies on rock-socketed piles. *Geotechnical Engineering*, 27, 51–67.

Osterberg, J.O. 1989. New device for load testing driven piles and drilled shafts separates friction and end bearing. *Proceedings International Conference on Piling and Deep Foundations*, 421–426.

PLAXIS 2002. *Plaxis Computer Program*, Version 8.2 manual.

Different aspects of large deformation contact formulations applied to pile-soil FE-analysis

Kathrin A. Fischer & Daichao Sheng

School of Engineering, The University of Newcastle, NSW, Australia

Numerical descriptions of the installation of displacement piles typically involve material nonlinearities, large deformations and frictional contact. Additionally, large relative sliding as well as surface separation and closure at the pile-soil interface must be taken into account.

Traditional finite element descriptions of geotechnical problems are indeed very accurate concerning material nonlinearities, but not so concerning geometry and boundary nonlinearities. For example, joint elements or prescribed constraints, which are commonly used to model soil-structure interaction, are only valid for small displacements and are not appropriate for soil-structure interaction involving large frictional sliding, separation and reclosure, such as those encountered in pile installation and in cone penetration tests. Therefore, large deformation contact formulations, commonly used in various applications of mechanical engineering, have recently been adapted to model soil-structure interaction in geotechnical problems (Sheng et al. (2005) and Sheng et al. (2006)).

Sheng et al. (2005) and Sheng et al. (2006) have successfully used the simple node-to-segment (NTS) contact discretisation (Wriggers and Simo (1985)) to model the stability of sheet-pile retaining walls and the installation of displacement piles. Nevertheless, there are a number of issues remain unsolved. These problems include, but are not limited to, the discretisation of sharp corners (as part of the pile geometry for instance), the mesh distortion at large deformation and the stability and efficiency of the solution schemes. In addition, the NTS technique is only valid for linear elements which are seldom used for soil modelling.

This paper addresses some of the issues concerning frictional contact formulations for soil-structure interaction. In particular, several possibilities for smoothing sharp corners will be discussed. Alternative contact discretisation techniques will also be discussed. One interesting approach amongst others might be the mortar method which originates from the domain decomposition technique firstly introduced by mathematicians as Bernardi et al. (1992). The idea is to couple generally nonconforming meshes by defining a so-called mortarfunction on the intersection of the contacting bodies. Recent developments adapt this successfully to large deformation frictional contact problems as given in Puso and Laursen (2004) and Fischer and Wriggers (2006) for example. Since the NTS formulation can only be used with linear discretisations of the contact partners, the big advantage of this method is that it can be coupled consistently with shape functions of higher order. If such a method is incorporated into a geomechanical context, a wider range of complex soils-structure interaction problems can be analysed.

1 INTRODUCTION

The simulation of pile installation is still an unsolved problem since it is deemed to be a complex nonlinear mechanical problem.

If the whole installation process should be modeled within a FE analysis as detailed as possible, large deformations, large relative movement as well as contact and separation between the pile and the soil have to be taken into account. This demands the inclusion of a contact formulation which is able to transfer the stresses as accurate as possible from one contact surface to the other. Therefore we choose a so-called NTS formulation based on the master-slave concept of Hallquist

(1979). The derivation of the finite element model of this concept and its adaption to geotechnical problems are described in detail Sheng et al. (2006).

First applications of this formulation to the geomechanical field lead to predictions of pile resistance during the installation process, which otherwise could not be obtained for nonlinear soil models so far. However, the discrete FE-description requires improvements since the pile resistance shows oscillations instead of a smooth increase.

Therefore, we compare the results of the NTS formulation with the mortar type formulation given in Fischer and Wriggers (2006). With this smooth, weak (integral) contact description one is able to overcome

well-known problems in contact simulations. For similar mortar approaches we refer to Yang et al. (2005) for instance.

Instead of exchanging the NTS for the mortar type formulation, another approach might be to change the geometry of the pile by smoothing the vertex between the pile tip and the shaft for instance.

2 PILE INSTALLATION SIMULATION

2.1 Pile installation in soil

A pile installation problem as given in figure 1 is computed by using quadrilateral axi-symmetric elements with 4 nodes and 4 integration points for the soil and the pile as well. Therefore the finite element program *SNAC*, which was developed by the Newcastle Geotechnical Research Group see Abbo and Sloan (1998) is used. The soil is modeled by the modified Cam clay model, while the pile is treated as an elastic material. The material parameters and the finite element mesh are given in figure 1 as well. Contact is discretised with NTS-elements where the soil is defined as slave surface while the pile is used as the master surface. The frictional behaviour between pile and soil is assumed to follow COULOMB's friction model with $t_T = \mu t_N$.

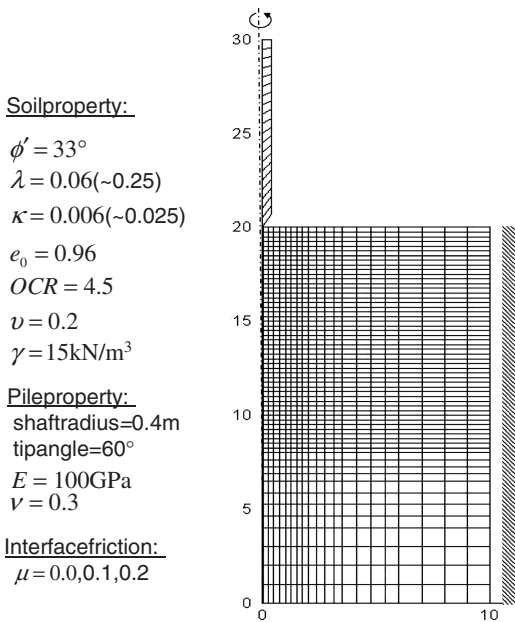


Figure 1. Mesh and boundary conditions for the pile installation (4-noded quadrilateral elements with 4 integration points).

The penalty parameters within the contact formulation are chosen to be equal in normal and tangential direction with $\epsilon_N = \epsilon_T = 10^6 \text{ kN/m}^3$. They can be interpreted as an elastic bedding between the contacting surfaces. Besides, they establish a linear dependance between the contact pressure p_N and the normal gap g_N and as well between the tangential contact stress t_T and the tangential gaps g_T .

$$p_N = \epsilon_N g_N \quad t_T = \epsilon_T g_T \quad (1)$$

Note that the derivation of the tangential quantities changes due to stick/slip changes.

The pile is initially located above the ground surface. Gravity loading is first applied to the soil to establish the initial in-situ stress states prior to the pile installation. Once the initial stress is established, all nodal displacements are set to zero and the void ratio e_0 of the soil is set to the given value. The pile is then pushed into the soil to a depth of 6 m by prescribing the displacements at its top boundary.

The resulting pile resistance in vertical direction is then plotted for three different frictional coefficients. As depicted in figure 2, the resistance increase with the increase of the friction coefficient μ and the penetration of the pile. However oscillations of the pile resistance can be observed during the whole installation process, no matter which friction coefficient is chosen. These oscillations occur whenever a slave node is released from vertical compression beneath the conical end. The high vertical compression becomes a shear force as soon as the slave node passes the transition point, see figure 3. This shear force is restricted by the friction law and so a sudden drop of the total resistance can be observed. Afterwards the resistance increases again until the next slave node slides above the vertex.

This sudden rearrangement of stresses can even lead to divergence of the entire problem if the forces are highly concentrated at this vertex.

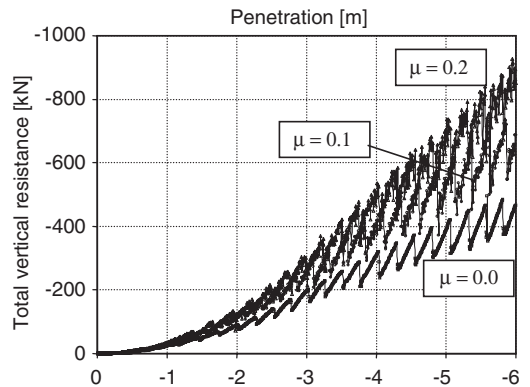


Figure 2. Pile resistance during push-in installation.

This singularity problem is well-known in finite element analysis. Simo and Meschke (1993) described this behaviour as zig-zagging and attributed it down to the relatively coarse mesh they used. It cannot be solved by mesh refinement which will likely lead to mesh distortion. Although these oscillations are a discretisation problem, also observed in extrusion simulations Voyiadjis and Foroozesh (1991), we have to investigate other possibilities to overcome this concentrated amount of nonlinearities in pile installation simulations.

2.2 Pile installation in nonlinear elastic material by using the NTS element

Obviously, the observed oscillations stem from the contact discretisation. Hence we want to focus on the smoothing of the contact stress transmission by firstly excluding any side effects from the model. Therefore the soil is replaced by a simpler hyperelastic material, the so-called Neo-HOOKEian material. Here the stresses depend nonlinearly on the strain measure which itself depends nonlinearly on the displacements due to large deformations. The linearisation of this model leads to the linear elastic law of HOOKE.

The pile is assumed to be nearly rigid by using YOUNG's modulus $E = 2.1 \cdot 10^8 \text{ kN/m}^2$ and $\nu = 0.3$, whereas the soil is represented by a soft material with $E = 10^4 \text{ kN/m}^2$. To avoid locking effects and ill-conditioning due to material characteristics, this soft material is meant to be perfectly compressible ($\nu = 0.0$). Furthermore, the pile and the soil (substitute) are assumed to be weightless. Also plain strain instead of axi-symmetry is assumed. The computation is done for $\mu = 0.1$. The mesh, the boundary constraints and the penalty parameters have been retained unchanged as given in the pile-soil simulation in subsection 2.1.

For this computation, the finite element analysis program *FEAP*, which was basically developed at the University of Berkeley, California, was used. Zienkiewicz and Taylor (2000) give a review about the structure and the handling of this program.

The simplifying assumptions seem to have not a lot in common with the former problem, but they simplify

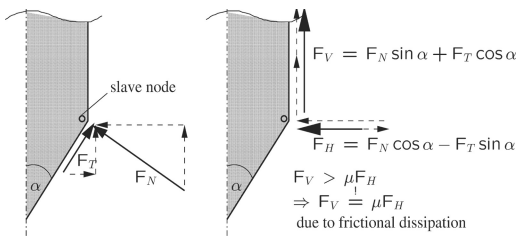


Figure 3. Turnaround and rearrangement of normal pressure and tangential friction stress at the transition point.

the problem as much as possible to achieve fast results due to good convergence without getting loss of the regarded oscillation problem. As figure 4 shows oscillations occur here as well.

Hence this model provides a starting basis in search for other improving contact discretisation techniques.

2.3 Pile installation in nonlinear elastic material by using the mortar type element

The mortar discretisation technique differs from the NTS formulation by setting up contact constraints variationally. The variational contact discretisation can be combined easily with higher order shape functions by using the same shape functions for the contact discretisation. The possibility of a consistent coupling is a great advantage since the strong NTS formulation can only be used consistently in a linear approximation.

The mortar type formulation discussed in Fischer and Wriggers (2005) and Fischer and Wriggers (2006) is already incorporated in *FEAP* and therefore it is used in the following. Herein, a numerical integration is performed by summing up the contact constraints evaluated at GAUSS points. Therefore a fixed number N of GAUSS points is put inside each non-mortar (slave) segment s . The discretisation of the variational contact formulation C_c is given as follows.

$$C_c = \int_{\Gamma_c} (\delta g_N p_N + \delta g_T t_T) d\Gamma$$

$$\approx \bigcup_{s=1}^M \sum_p^N (\delta g_{N_{s_p}} p_{N_{s_p}} + \delta g_{T_{s_p}} t_{T_{s_p}}) \cdot A_{s_p} \cdot w_p \quad (2)$$

Herein, $\delta g_{N_{s_p}}$ and $\delta g_{T_{s_p}}$ are the variations of the normal and the tangential gap functions. A_{s_p} describes the transformation of the segment length l_p and w_p is the weighting of the associated GAUSS point p . Whenever the contact constraint is not fulfilled ($g_{N_{s_p}} > 0$ or $p_{N_{s_p}} < 0$) at a certain GAUSS POINT p , $p_{N_{s_p}}$ and $t_{T_{s_p}}$ are

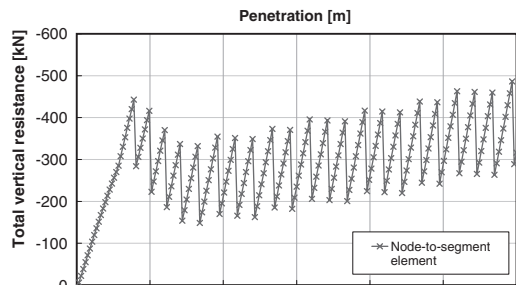


Figure 4. Pile installation in Neo-HOOKEian material using NTS-contact-elements.

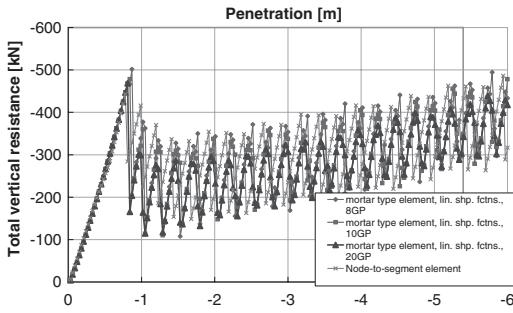


Figure 5. Pile installation in Neo-Hookeian material using mortar type elements, linear approximation.

set equal to zero, so that no contribution is delivered to the global equation system.

The computation is rerun with the mortar type formulation using linear shape function for different numbers of GAUSS points, namely 8, 10 and 20. Still the same material and contact parameters as in the previous example are used.

For a small number of GAUSS points (8) the vertical resistance oscillates within the same thresholds as the NTS results as depicted in figure 5. An increase of integration points reduces the amplitude by a reduction of the upper threshold by around 10%. The lower threshold remains at the same level.

However, the oscillations are still significant. This is due to stress concentration close to the vertex. Thus, the move of the GAUSS point lying close to the vertex is sufficient to create the drop of resistance. The slight reduction of the upper threshold derives from the better stress distribution via the integral formulation. However, the difference is slight, because the singular stress concentrations cannot be distributed well.

For this reason, we now have a closer look at the vertex and try to smooth it in the following subsection.

2.4 Pile installation in nonlinear elastic material by refining the mesh

The vertex should now be smoothed which comes along with mesh refinement. By creating the new mesh, we paid attention to retain the significant geometry of the pile cone as good as possible, see figure 6 a) and b). In the first instance this smoothing seems to be an unacceptable interference in the geometry of the investigated problem. But it can be motivated by the viscous behaviour of fluids for instance. Viscous behaviour leads to a void once the lower end of the pile shaft comes into contact with the fluid, see figure 7. Due to this void a drop of resistance can be observed at its initialization. After the void is established and the soil contacts the shaft a little bit further up the shaft, the resistance increases smoothly.

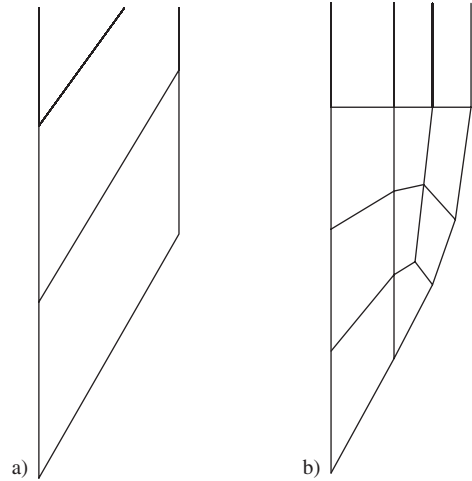


Figure 6. a) Origin mesh used for the pile tip, b) Refined mesh at the pile tip to obtain a smooth transition between pile tip and shaft.

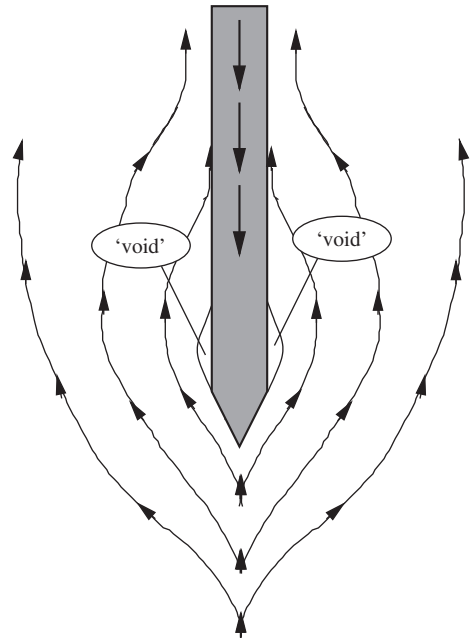


Figure 7. Appearance of a void at the vertex due to viscous flow.

Another reasonable explanation for smoothing the vertex is that perfect singularities which would lead to infinite stresses, do not exist in reality.

Indeed the amplitude of the oscillations can be reduced clearly by around 80%, compared to the

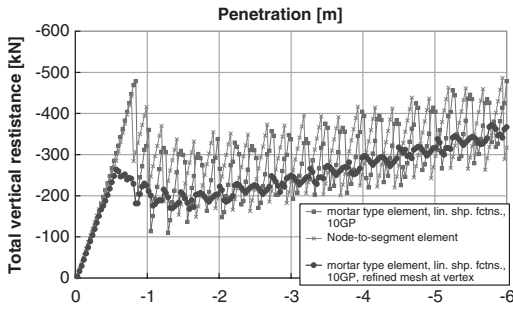


Figure 8. Pile installation in Neo-Hookeian material using mortar type elements, refined mesh at vertex.

amplitude of the NTS computation, see figure 8. Figure 6(b) depicts that the former vertex between shaft and cone is now distributed to several vertexes with smaller angles. So it is obvious that the resistance still includes oscillations even though the amplitude decreases significantly due to the distribution of the vertex over a larger area.

Further smoothing and mesh refinement can of course lead to a smoother resistance, but with cost of more computation time. Thus, it is of interest to find a more efficient solution.

2.5 Pile installation in nonlinear elastic material by inverting slave and master surface

The exchange of master (mortar) and slave (nonmortar) surface brings the pile to be the surface where the slave nodes, respectively the GAUSS points are situated. Hence the contact geometry is described now in terms of the normal and tangential direction of the soft surface of the soil (substitute) and therefore it depends on its deformations as well. This surface is smooth and deformable and the way of bordering the vertex depends strongly on the material model as already mentioned. Thus, by using this surface as reference surface for projection, the transmission of contact stresses adapts to the limited characteristics of the material. This makes sense since the contact formulation acts only as transmitter of strains-stress relations of material characteristics. So the stress transfer via the contact surface can only be as accurate as the stress-strain relation of the material model. Note that whenever a soft material is used as projection surface, a stable convergence can only be guaranteed if the linearisation of the master (mortar) geometry is carefully included in the stiffness matrix.

The computation is now done by using the mortar type element for contact discretisation. This has the advantage that the mesh can retain unchanged since several (20) GAUSS points per non-mortar segment trace the pile surface accurately. In contrast to this, mesh

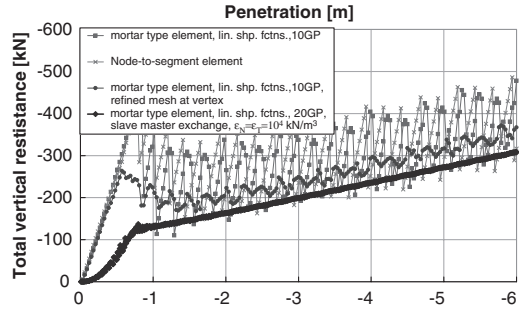


Figure 9. Pile installation in Neo-Hookeian material using mortar type elements, slave master exchange.

refinement would be necessary by using NTS-elements.

In doing so, one is able to obtain a smooth vertical resistance as expected, see figure 9. The curve depicts one peak when the vertex dips into the soil (substitute) the first time and afterwards the increase proceeds smoothly with further installation. The curve is situated at the lower threshold of the oscillations which were obtained by all previous computations.

In this simulation the penalty parameters must be adapted to the stiffness of the projection surface as mentioned in Wriggers (2002), otherwise the computations fail due to the new geometrical relations on the contact surface.

The location of the smooth resistance curve at the lower threshold is reasonable since the repeating steep increase of the resistance and its sudden drop were traced back to the slack flow of stress concentration at the vertex. Since this singularity does not exist in reality, the oscillations do not exist. Nevertheless the base value has to be constant which is given by the lower threshold. This lower threshold is independent of discretisation and the choice for the penalty parameters.

These characteristics of the vertical total resistance is even confirmed by recomputations with the NTS and the mortar type element due to subsections 2.2 and 2.3 using the same penalty parameters as given here ($\epsilon_N = \epsilon_T = 10^4 \text{ kN/m}^3$).

3 CONCLUSIONS

The presented different simulations yield to the conclusion that the oscillations of the total vertical resistance are caused by the well-known problem of handling singularities. Even though these oscillations occur, their lower threshold is independent of discretisation and therefore it can be interpreted as the real resistance.

However, it turned out that the finite element contact simulation by using the pile as non-mortar (slave)

surface in combination with the mortar type element yields the best results.

Furthermore, the simulations have shown that finite element contact simulations including large deformations and sliding demand a lot of experience and understanding about the meaning and handling of contact variables like the penalty parameters and the possibilities of discretising contact surfaces.

A next step should be to adapt the mortar type formulation to *SNAC*, so that the presented results could be confirmed for real soil behaviour. Afterwards this contact discretisation technique can be extended, so that it can be used in the context of higher order solid elements which are usually used in soil simulations to avoid locking. This would mean a great progress in geomechanical finite element simulations since higher order soil elements could be consistently coupled with contact formulations for the first time.

REFERENCES

- Abbo, A. J. and S. W. Sloan (1998). *SNAC Users Manual*.
- Bernardi, C., Y. Maday, and A. Patera (1992). A new conforming approach to domain decomposition: the mortar element method. In H. Brezis and J. L. Lions (Eds.), *Nonlinear partial differential equations and their applications*, pp. 13–51. New York: John Wiley & Sons.
- Fischer, K. A. and P. Wriggers (2005). Frictionless 2d contact formulations for finite deformations based on the mortar method. *Computational Mechanics* 36(3), 226–244.
- Fischer, K. A. and P. Wriggers (2006). Mortar based finite frictional contact formulation for curved surfaces using the moving friction cone. *Computer Methods in Applied Mechanics and Engineering* in press.
- Hallquist, J. (1979). Nike2d: An Implicit, Finite Deformation, Finite Element Code for the Analysing the Static and Dynamic Response of Two-dimensional Solids. Report UCRL 52678, UC-Lawrence Livermore National Laboratory.
- Puso, M. A. and T. A. Laursen (2004). A mortar segment-to-segment frictional contact method for large deformations. *Computer Methods in Applied Mechanics and Engineering* 193(45–47), 4891–4913.
- Sheng, D., K. D. Eigenbrod, and P. Wriggers (2005). Finite element analysis of pile installation using large slip frictional contact. *Computers and Geotechnics* 32, 17–26.
- Sheng, D., D.-A. Sun, and H. Matsuoka (2006). Cantilever sheet-pile wall modelled by frictional contact. *Soils and Foundations* 46 in press.
- Simo, J. C. and G. Meschke (1993). A new class of algorithms for classical plasticity extended to finite strains application to geomaterials. *Computational Mechanics* 11, 253–278.
- Voyiadjis, G. Z. and M. Foroozesh (1991). A finite strain, total LAGRANGIAN finite element solution for metal extrusion problems. *Computer Methods in Applied Mechanics and Engineering* 86, 337–370.
- Wriggers, P. (2002). *Computational Contact Mechanics*, pp. 101–104, 284–286. John Wiley & Sons Ltd.
- Wriggers, P. and J. C. Simo (1985). A Note on Tangent Stiffness for Fully Nonlinear Contact Problems. *Comm. Appl. Num. Meth.* 1, 199–203.
- Yang, B., T. A. Laursen, and X. Meng (2005). Two dimensional mortar contact methods for large deformation frictional sliding. *Int. J. Numer. Meth. Engng.* 62, 1183–1225.
- Zienkiewicz, O. C. and R. L. Taylor (2000). *The Finite Element Method* (5 ed.), Volume 1 and 2. Oxford: Butterworth-Heinemann.

Numerical analyses of pile foundation in complex geological conditions

Y. El-Mossallamy

Ain Shams University, Cairo, Egypt

c/o ARCADIS Consultants, Darmstadt, Germany

ABSTRACT: Deep foundations using large diameter bored piles nowadays are applied widely to support heavy structures such as bridges, industry constructions and high rise buildings. The structural serviceability requirements can be fulfilled with relatively fewer piles in an economic manner. Although large diameter bored piles are successfully applied in most subground conditions, their behavior in moderately to completely weathered rock and in residual soils is not sufficiently clarified. The results of pile load tests for a bridge foundation using Osterberg-cell technique in weathered rock will be demonstrated. The conducted analyses to re-calculate the pile load tests and to simulate the behavior of the bridge foundation to consider the pile group action will be illustrated and discussed in detail.

1 INTRODUCTION

There is relatively good experience regarding the behavior of bored piles in cohesive and cohesionless soils. Realistic design values for skin friction and tip resistance are given in most standards and design recommendations. The DIN 4014 gives values of the shaft skin friction and base resistance depending on either the undrained cohesive strength of the soil in case of clayey soils or depending on the results of the static cone penetration test (soil density) in case of cohesionless soil. Most of the standards (e.g. DIN 4014) correlate the bearing capacity of bored piles in rocks with their uniaxial compressive strength. These correlations can be suitable for unweathered to slightly weathered rock where the behavior of the rock mass depends mainly on the quality of the intact rock. In moderately to completely weathered rock as well as rock that is decomposed to residual soil, the load-settlement behavior of bored piles depends on the whole rock formation matrix considering the rock joint system and the shear strength along the presented joints and discontinuities more than on the quality of the intact rock pieces.

The aim of the presented work is to study the behavior of large diameter bored piles in moderately to completely weathered rock and residual soils considering the results of a case history of a bridge foundation in Germany. Deep foundation using large diameter bored piles was required for the 5-span highway bridge (Fig. 1). The bridge has a total length of about 450 m with a maximum span of about 169 m.

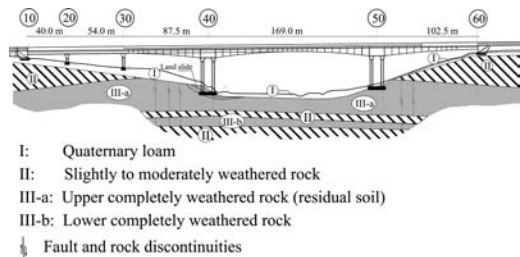


Figure 1. Bridge layout and subsoil conditions.

The bridge is a part of the new federal highway A38 to establish a new connection between west and east Germany (from Kassel to Halle). This bridge was planned to cross a deep valley (Weidatal) with a height of about 50 m (Dürrwang et al. 2005). The 5 span continuous prestressed concrete rigid frame consists of two completely separated structures that carry three lanes of traffic each.

The subsoil mainly consists of Quaternary formations of silt down to a depth of about 10 m. Below the Quaternary soil; there is a layer of completely weathered limestone and residual soils (silt and clay) with a thickness of about 30 to 40 m. A sublayer of a slightly to moderately weathered limestone bank with a thickness of about 6 m (Fig. 1) divides the completely weathered layer in an upper and lower sublayers. Moderately to slightly weathered rock formations of limestone and dolomite were found in large depths of about 40 to 50 m beneath the ground surface. The first

design suggested a deep foundation that reaches the lower rock formation with a total pile length of about 50 m. As a special proposal, the bridge piers were suggested to be founded on large diameter bored piles that should be socketed 2 m in the above mentioned slightly to moderately weathered limestone bank reducing the required pile length to only 25 to 30 m.

2 PILE LOAD TEST

To ascertain the adequacy of the pile bearing capacity and determine appropriate design values, at first pile load tests were conducted on large diameter bored piles. The tested piles are socketed in the suggested bearing layer of the slightly to moderately weathered limestone bank (see Fig. 2). To avoid the need for a large reaction system, multiple Osterberg-cells were applied to conduct the load test.

The Osterberg-cells (Osterberg 2001) is a very well established static pile load test where the pile is used as a test pile and as the reaction system at the same time avoiding the need of extra reaction system. The loading system consists of a hydraulic jack (Osterberg-cell also O-Cell) that is installed at a certain depth along the pile shaft. During the test, the O-Cell is inflated with water pushing the upper part of the pile and mobilizing the skin friction along it. At the same time the lower pile part is pushed downward mobilizing the skin friction and base resistance of this part. The pile load test using this technique can be done up to relatively large loads (more than 50 MN) without the need of any external reaction system. Using only one O-Cell can lead to test results where only one part of the pile reaches its ultimate capacity. Therefore, multi cells were applied at different depths (Figs. 2 and 3) to load the pile segments in different combinations to reach the ultimate capacity of all segments.

The pile load tests were carried out using two O-Cells that were installed in the different geotechnical subground layers (Fig. 2). The pile performance has been monitored extensively with geotechnical measurement devices such as a load cell at pile tip to measure directly the pile tip resistance. Telltales are attached at the upper and lower plates of the O-Cells as well as at the load cell at the pile base to get information on the displacements of the different pile segments during the test. Strain gages along the pile shaft were installed to measure the skin friction of different layers (Fig. 3). Results of the conducted geotechnical investigations just beside the pile load tests at pier 50 are illustrated in figure 2. The results of the conducted dynamic penetration test -according to the German standard: DIN 4094- show that the alluvial sand and gravel is dense to very dense. The measured values of the standard penetration test in the residual soil (silt and clay) range between 30 and 50. Therefore,

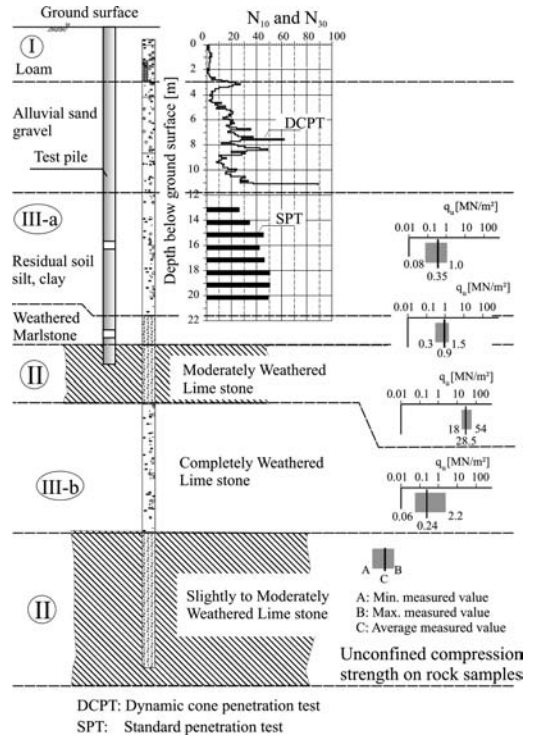


Figure 2. Instrumentation of pile load test.

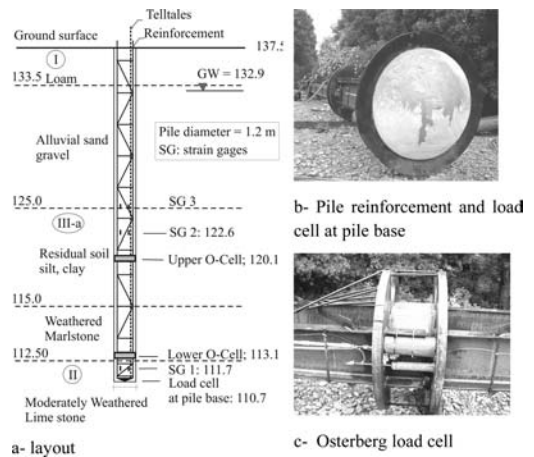


Figure 3. Pile load test.

the consistency of the cohesive residual soil can be estimated as very stiff to hard.

The results of the conducted unconfined (uniaxial) compression tests on samples of the different subground layers are given in figure 2. The residual soil has values of unconfined compression strength between

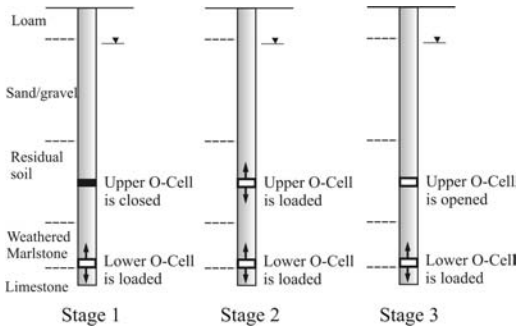


Figure 4. Load stages of the pile load test.

80 and 1000 kPa (kN/m²) with an undrained cohesion of 40 to 500 kPa. These values correlate well with the measured values of the SPT and lie in the existing experience with cohesive soils (Peck et al. 1974). The uniaxial compressive strength of the bearing layer (moderately weathered limestone) varied between 18 and 54 MPa (MN/m²) with an average value of about 28.5 MPa. Therefore, according to the German recommendation FGSV (1992) this rock can be classified as slightly to moderately weathered rock. Details of one of the two conducted pile load tests are given in figure 3. The O-Cells were chosen to be able to apply loads up to 12 MN for each cell corresponding to a total load of about 50 MN. The results of the two load tests are rather comparable to each other. Figure 3b shows the applied pile reinforcement (rigid steel frame of double U profiles) with the installed O-Cells. Figure 3b shows also the load cell used to measure directly the loads transmitted at the pile base. The O-Cell is shown in more details in Figure 3c.

The load test is carried out in three stages (Fig. 4). In the first stage, the upper O-Cell is shut and the lower one is loaded to its maximum value to estimate the skin friction and base resistance of the lower pile segment. In the second stage; both O-Cells are loaded applying the same pressure. This stage gives information on the skin friction development in the upper pile segment. In the third stage, the upper O-Cell is kept open and the lower O-Cell is loaded to measure the skin friction along the middle pile segment.

A realistic estimation of the elastic modulus of the pile material is required to calculate the normal forces along the pile shaft. Using the measurements of the strain gages, the development of the skin friction in different subground layers can then be determined. The second load stage can be considered as a huge compression test on the middle pile segment. The pile's elastic shortening is given as the difference between the measured displacements (using the tell-tales) at the lower plate of the upper O-Cell and the upper plate of the lower O-Cell. The pile's elastic

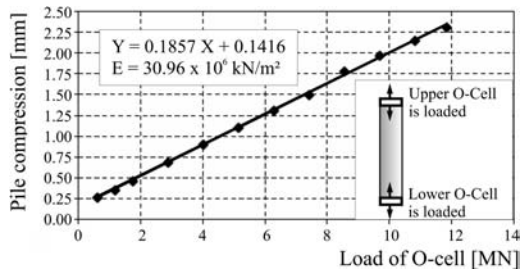
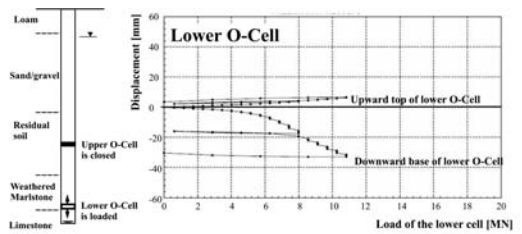
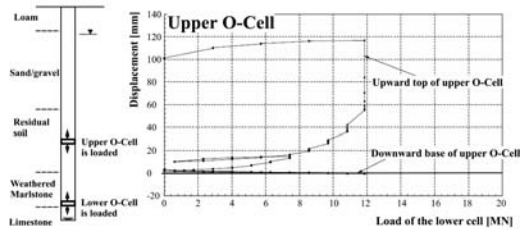


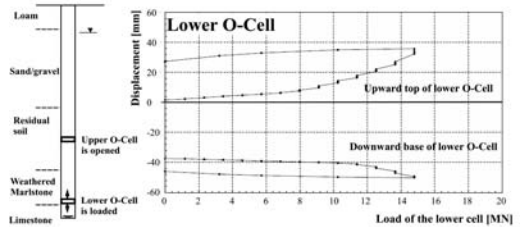
Figure 5. Determine the elastic modulus of the pile material.



Stage 1: Upper Osterberg-cell is closed and lower cell is loaded



Stage 2: Both upper and lower Osterberg-cells are loaded



Stage 3: Upper Osterberg-cell is opened and lower cell is loaded

Figure 6. Results of the multi-Osterberg load test.

shortening is shown in figure 5. These results are used to calculate the in-situ elastic modulus of the pile material. An elastic modulus of about 31000 MPa is determined for the pile concrete.

Figure 6 summarizes the results of the three applied load stages.

Figure 7 represents the evaluated skin friction in the different layers as well as the measured pile base resistance in the bearing stratum. The measured ultimate skin friction in the alluvial sand and gravel layer

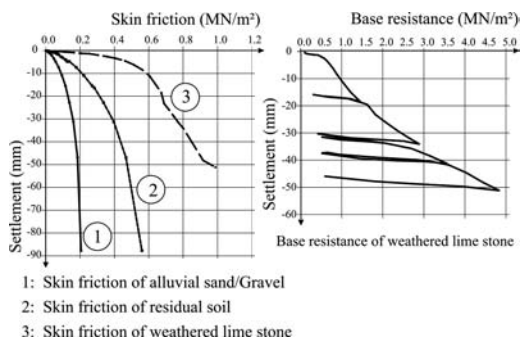


Figure 7. Pile skin friction and base resistance.

reaches about 200 kPa. This value is larger than the maximum value given in DIN 4014 for cohesionless soil but still lies in the expected range according to experience (e.g. Kempfert 1982 and Dürrwang 1997). In the contrary the measured ultimate skin friction in the residual soils with a value of about 600 kPa reaches about 10 times the corresponding value for cohesive soils according to DIN 4014. This high value of skin friction in completely weathered rock and residual soils were measured by other load tests on large diameter bored piles (Dürrwang 1997 and Moormann 2005). These high values are due to the structure of completely weathered rock and residual soils on one hand and the conventional sedimented cohesive soils on the other hand. The residual soils show a dominant dilation performance that leads to increasing the horizontal stresses during shearing by pile loading. The increased horizontal confinement stresses cause a large increase of the ultimate skin friction.

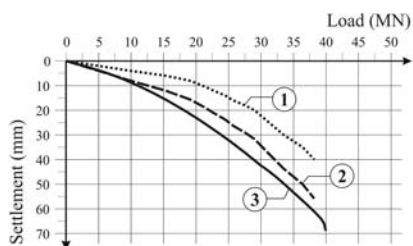
The ultimate skin friction in the slightly to moderately weathered lime stone reaches 1000 kPa and lies higher than the given value according to DIN 4014. The ultimate pile base resistance reaches about 4.8 MPa and lies beneath values given by DIN 4014. These results show that the correlation between pile capacity in weathered rock and the uniaxial compressive strength of the intact rock is not accurate to estimate the ultimate capacity of bored piles in such rock formations.

3 NUMERICAL MODELLING OF THE PILE LOAD TEST

As no possibility does exist to take into account—in an adequate manner—the effect of pile installation by theoretical means, the numerical model as well as soil parameters applied to design the piled foundation of the bridge were first calibrated and adjusted to the results of single pile load tests. The bridge foundations were then designed using the same numerical

Table 1. Geotechnical parameters of the different soil layers.

Soil parameter	Alluvial sand/gravel	Residual soil	Moderately weathered limestone
E [MN/m ²]	60	100	180
ν [-]	0.3	0.3	0.3
γ / γ' [kN/m ³]	20/10	21/11	22/12
Ultimate pile skin friction [kPa]	180	450	990
Ultimate pile base resistance [kPa]	—	—	4800



Measurements:

- 1- Summation of all segments of the test results without considering the elastic shortening of the whole pile
- 2- Summation of all segments of the test results with considering the elastic shortening of the whole pile

Finite element calculation:

- 3- With considering the elastic shortening of the whole pile and additional soil deformation due to loading at pile head

Figure 8. Total load-settlement behavior of the test piles.

model and the determined soil and pile/soil parameters. Table 1 summarizes the estimated soil parameters according to the conducted soil investigation considering the results of the pile load tests.

The results of the load test using multi O-Cells give information on pile segments. Therefore, the first design step is to calculate an equivalent top-loaded load-settlement curve from the results of the pile segments. Figure 8 shows the equivalent load-settlement curve that is calculated directly from the pile load test (line 1). Line 2 represents the equivalent load-settlement curve considering the elastic deformation of the pile material. Line 3 demonstrates the calculated equivalent load-settlement curve applying axisymmetric finite element analyses using the parameters of the soil and pile/soil as given in table 1. The soil is modeled as linear elastic and the pile soil interface applying Mohr-Coulomb as failure criterion with the measured ultimate skin friction as an equivalent

shear strength of the interface. The good correspondence between line 2 and 3 supports the used numerical model and pile/soil parameters.

4 BEHAVIOR OF BRIDGE FOUNDATION

The 5 span prestressed concrete rigid frame is founded on piers (Fig. 1) with two completely separated superstructures which are founded on the same foundation (Fig. 9 and Fig. 10). Therefore, the internal stresses of the superstructure depend mainly on the stiffness of the pier foundations and the resulting differential settlements between the different axes.

A structural study (Fig. 9) considering the stiffness of both superstructure and foundations was carried out in the design stage. This study has shown that the deformation behavior of the superstructure in case of separated foundation of pier 50 (Fig. 9b) is better than that in case of coupled foundation (Fig. 9a). Therefore, the pier foundation was conducted in two separated foundations as shown in figure 10.

The structural design of the superstructure depends mainly on the determined stiffness of the foundations. The three dimensional feature of the foundation has a dominant effect on the foundation behavior and should be considered in a realistic manner. Therefore, a three dimensional analyses to study the foundation behavior under working conditions was carried out. Figure 11 demonstrates the used three dimensional finite element model to simulate the behavior of the foundation (pier 50).

It can be recognized from figures 8 that the pile behavior under working conditions is mainly elastic. Due to a lack of enhanced information regarding the stress-strain behavior of the whole rock formation matrix, it was decided in the design stage to apply a conventional elastic model to simulate the stress-strain behavior of the subground. This simple constitutive law with the corresponding elastic parameters of the subground based on the conducted pile load tests and the re-calculation of the test results is more realistic for design purposes.

Figure 12 represents some results of the conducted analyses. The expected settlements of the pier foundation range between 1.2 cm in the construction stage and 1.7 cm at the end of construction. Considering the measured time-settlement behavior of the single pile during the load test, the time dependent part of the foundation settlement under working conditions is estimated to be negligible. Corresponding foundation stiffness was calculated according to the conducted deformation analyses. The superstructure then was designed depending on the determined foundation stiffness. The construction of the bridge was begun at the end of 2004. The construction period is about two years. The construction of the first half of the bridge

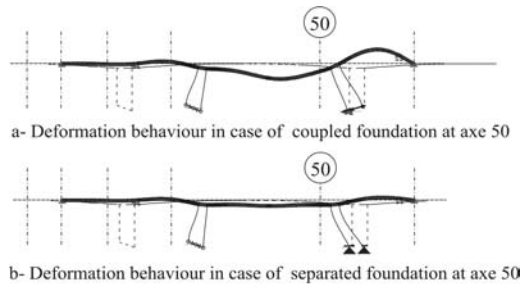


Figure 9. Foundation with geological conditions (axis 50).

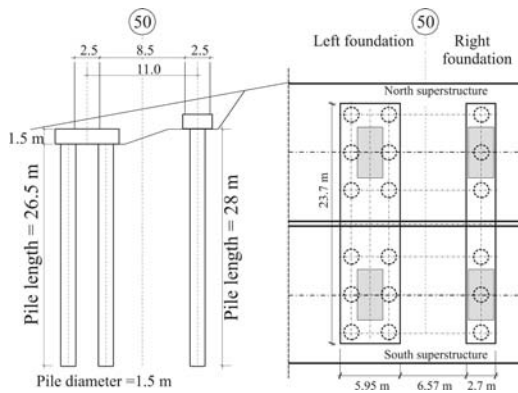


Figure 10. Layout of the foundation (axis 50).

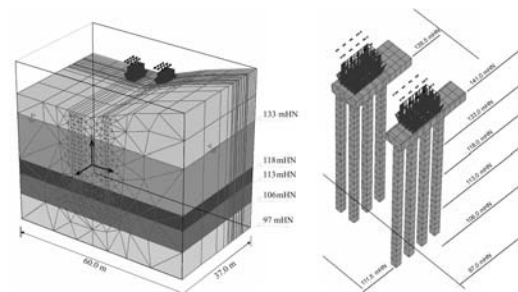
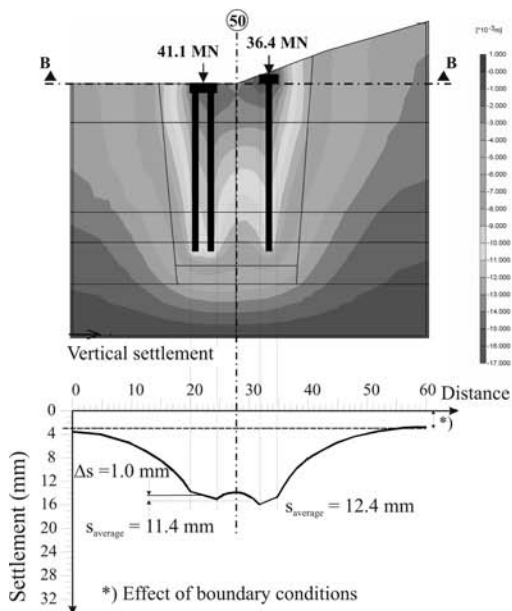


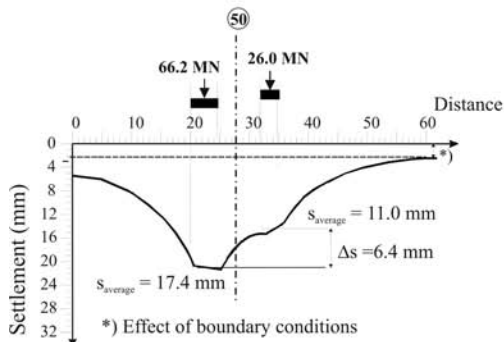
Figure 11. Layout of the used three dimensional model.

was almost completed at the end of 2005. Therefore the applied load on the foundation amounts to about 50% of the total design load. The corresponding measured settlement of pier 50 is about 5 mm and agrees well with the estimated value of about 12 mm under the complete load of the two superstructures (load case: during construction).

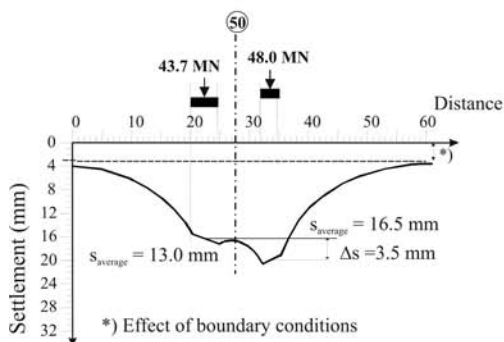
The simulation of the behavior of a single foundation pile was also carried out applying the same three dimensional numerical model with the same soil and pile parameters. A comparison between the settlement



Load case: During construction



Load case: End of construction (max. Load on left foundation)



Load case: End of construction (max. Load on right foundation)

Figure 12. Deformation behavior of pier 50.

Table 2. Pile group action.

Load case	Left foundation	Right foundation
During construction	2.8	2.3
End of construction (max. load of left foundation)	2.6	2.8
End of construction (max. load of right foundation)	3.0	2.3

of the pile groups and that of the corresponding single pile under the same average load gives an idea on the so-called pile group action which is the settlement of the pile group divided by the settlement of the single pile under the corresponding average load. Table 2 summarizes the calculated values of the pile group action for both pile groups beneath pier 50.

The pile group action ranges between 2.3 and 3 depending on the applied load level and the interaction between the two separated foundations. In general, the pile group action depends on many factors such as the pile length, pile spacing, the number of piles in the pile group, the arrangement of the piles within the pile group, on the stiffness of the pile cap and on the applied load level.

5 CONCLUSION

The behavior of large diameter bored piles in weathered rock formations depends on the weathering degrees and on the behavior of the whole rock mass and not only on the uniaxial compressive strength of the intact rock pieces. The presented pile load tests show that the ultimate pile capacity (skin friction and base resistance) in these rock formations is too higher than the estimated values according to standards and design recommendations. Pile load tests in such complex geological conditions are the most appropriate method to get realistic design parameters and to optimize the foundations. The O-Cell load test can be applied in an economic manner to realize the required pile load tests.

The pile group action regarding the settlement of the pile group related to that of the corresponding single pile under the same average load of the pile group is a decisive design criterion for important construction on pile groups. In such cases an appropriate three dimensional analyses are needed to obtain a realistic estimation of the group behavior. The applied model and the required parameters should be evaluated through back-calculation of the pile load test. Other pile group action is the so called "pile group efficiency" that is defined as the ultimate capacity of the pile group compared with the ultimate capacity of the

corresponding single pile time the number of piles in the pile group. This pile group efficiency can be considered larger than unity for most cases of pile groups in weathered rocks. The deformations under working conditions (serviceability requirements) can be considered as the most governing design criteria of large diameter bored piles in weathered rock.

REFERENCES

- Dürrewang, R. (1997): *Pfahltragfähigkeiten im Grenzbereich Lockerboden/Fels*; Geotechnik Heft 3/97.
- Dürrewang, R., Hecht, T., Johmann, S. und El-Mossallamy, Y. 2005. *Die Gründung der Weidatalbrücke; Pfahlprobelastungen mit der Osterbergzelle*, Pfahlsymposium 2005, Braunschweig, pp. 377–388.
- FGSV, Forschungsgesellschaft für Straßen- und Verkehrswesen 1992. *Merkblatt zur Felsbeschreibung für den Straßenbau*. FGSV, Arbeitsgruppe Erd- und Grundbau, Köln.
- Kempfert, H.-G. (1982): *Vergleichende Auswertung von Probebelastungen der DB an Großbohrpfählen in nicht-bindigem Untergrund*; Geotechnik 1982, Heft 1.
- Moormann, Chr. (2005) *Pfahltragverhalten in festen und veränderlich festen Gesteinen*, Mitteilung des Institutes für Grundbau und Bodenmechanik, Universität Kassel, Heft Nr. 18, pp. 249–273.
- Osterberg, J. O. 2001. *Load testing high capacity piles – what have we learned?* Proceedings of the Fifth International Conference on Deep Foundation Practice, Singapore, April 2001.
- Peck, R.B., Hansen, W.E., Thornburn, T.H., (1974). *“Foundation Engineering”*, 2nd edition, John Wiley&Sons, Inc., New York.

Reliability and probability analysis

Implementation and validation of a simple probabilistic tool for finite element codes

Stefan van Baars

University of Technology Delft, The Netherlands

ABSTRACT: Both a circular slip surface stability calculation (Bishop or Fellenius) and a FEM calculation (c-phi reduction) produce a safety factor but not a probability of failure or reliability index. The major problem with the probabilistical calculations is that variable soil parameters create a correlated and therefore also variable failure mechanism. The question is how much the value of the calculated probability of failure is influenced by this correlation. The Monte Carlo method leads, because of the many slip surface calculations, to the most accurate calculation of the probability of safety. The disadvantage of this method is that it is far too time consuming for daily FEM calculations. The idea is therefore to replace the Monte Carlo approach by another approach with only a limited amount of calculations. In this paper several methods are discussed and validated. An indication is given about the error, the number of necessary stability calculations and the optimal estimation points for an additional stability calculation. In this way a minimum number of FEM calculations is needed to obtain a certain desired accuracy.

1 INTRODUCTION

According Bea (2005) many people (mainly in the USA) have worked on the field of probabilistical geotechnical engineering (Wu 1974, Meyerhof 1976, Vanmarke 1977, Baecher 1979, Harr 1987, Wu et al 1989, Whitman 1984, 2000, Bea 1990, Ronold, Bjerager 1992, Christian et al 1994, Lacasse, Nadim 1994, Morgenstern 1995, National Academy of Engineering 1995, Kulhawy 1996, Kulhawy, Phoon 1996, Tang et al 1999, Duncan 2000, Vick 2002, Lacasse 2004, Christian 2004).

However, the field of probabilistical geotechnical engineering in combination with finite element modelling (FEM) is until now rather underdeveloped. In Europe a few institutes have studied on methods to calculate the probability of failure of a geotechnical structure using FEM. These institutes are Graz University of Technology (Peschl, Schweiger, Pöttler and Turner), University of Manchester (Hicks), the Dutch Ministry of Public Affairs (H.L. Bakker) and the Delft University of Technology (Waarts and independently the author).

Also other Dutch institutes like GeoDelft (Calle) and TNO (Waarts) have studied this subject. In the Netherlands this research is driven by a special reason. For the safety check of the 3500 km of main dikes, besides a calculation of the safety factor, nowadays also a risk analysis is required.

Both a circular slip surface stability calculation (Bishop or Fellenius) and a FEM calculation (c-phi reduction) produce a safety factor but not a probability of failure or reliability index. The major problem with the calculation of the probability of failure is that variable soil parameters create a correlated and therefore also variable failure mechanism. The question is how much this correlation influences the value of the calculated probability of failure. Therefore four different probabilistical approaches were studied:

1. an analytical linear approximation based on a single slip surface calculation
2. various approximations using stability calculations (point estimate method)
3. a single point approximation (reliability method)
4. a Monte Carlo calculation of the probability of safety

The first approach is rather simple, but neglects the correlation. The second approach is in other words a sort of linearisation of the non-linear safety factors. The third one is, more or less, the same as the second, because it also needs point estimates, but needs only one final point for the probability analysis.

The fourth one is because of the many slip surface calculations, the most accurate estimation. The corresponding disadvantage is that a Monte Carlo calculation is far too time consuming for daily FEM

calculations. The idea is therefore to replace the Monte-Carlo method by a point estimate method or reliability method. For a few different dike profiles is studied with slip surface calculations how much the error of the first three approaches versus the MonteCarlo approach can be.

2 NON-LINEARITY

The problem of non-linearity can be explained by the following example of an embankment. The structure contains three layers: below a stiff clay ground surface, in the middle a medium clay layer of 3 m thick and on top a soft clay layer of 2 m thick. All three layers have a unit weight of $\gamma = 17 \text{ kN/m}^3$.

The 5 m high embankment has a slope of 1 to 3 (hor.-vert.), see Figure 1.

The three soil layers each have an independent undrained cohesion, which can be described as a normally distributed function:

$$c_{u,i} = N(\mu_{c_{u,i}}; \sigma_{c_{u,i}}) \quad (1)$$

For the values, see Table 1.

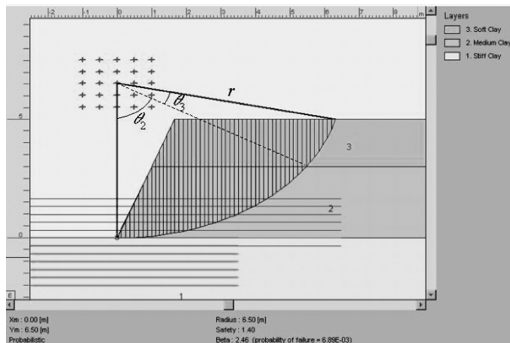


Figure 1. Geometry of example.

Table 1. Undrained cohesion per layer.

Layer number (i)	c_u per layer: (type)	$\mu (c_u)_i$ [kPa]	$\sigma (c_u)_i$ [kPa]
3.	Soft clay	2	2
2.	Medium clay	24	3
1.	Stiff clay	26(2)*	4

* See example about double failure mode.

3 CALCULATION METHODS

3.1 Monte Carlo

In the used Monte Carlo calculation, 100,000 independent drawings for each of the three uncorrelated undrained cohesion values are made, leading to a rather accurate total distribution of the probability density function of the Safety Factor SF of the geotechnical structure.

3.2 Linear-analytical solution

Another simple method to predict the probability of failure of the structure is the linear analytical solution. The average Safety Factor is:

$$\mu_{SF} = \sum_{i=1}^n (\alpha_i \mu_{c_{u,i}}) \quad \text{where: } \alpha_i = \frac{r^2 \theta_i}{S} \quad (2)$$

and the corresponding standard deviation is:

$$\sigma_{SF} = \sqrt{\sum_{i=1}^n (\alpha_i \sigma_{c_{u,i}})^2} \quad (3)$$

where:

n = number of distributed soil parameters (layers)

i = soil layer number

θ_i = angle of the slip surface in the i -th soil layer

S = Solicitation

= driving moment caused by weight of failing soil mass

$\mu_{c_{u,i}}$ = average undrained cohesion of the i -th layer

By calculating the reliability index

$$\beta = -\frac{\mu_{SF} - 1}{\sigma_{SF}} \quad (4)$$

the probability of failure can be found:

$$P_f = \Phi(\beta) \quad (5)$$

This solution is a linear solution and neglects the 2nd order influence of the changing slip surface by the changing soil parameters. This method is only possible if the exact position of the slip surface is known, which is the case for a Fellenius/Bishop slip circle method, but is not the case for a finite element method. There the angles and radii are unknown.

3.3 First Order Point Estimate Method (FO-PEM)

Another method which works well both for circular slip plain models and for finite element models is the Point

Estimate Method. The Safety Factor is regarded as a function of the distributed soil parameters. The most simple approximation is a linear or 1st order prediction:

$$SF_{x_1, x_2, \dots, x_n} = C_0 + \sum_{i=1}^n C_i x_i \quad \text{where: } x_i = \frac{c_{u,i} - \mu_{c_{u,i}}}{\sigma_{c_{u,i}}} \quad (6)$$

This first order prediction needs $n + 1$ point calculations. One for determining C_0 (which is μ_{SF}) at $x_i = 0$ $i \in n$ and one for each C_i , so for each soil variable, for example $x_i = -2 \cap x_{j \neq i} = 0$ $i, j \in n$.

In this way the four safety factors are found for the example with three layers:

$$\begin{aligned} SF_{0,0,0} \quad SF_{-2,0,0} \quad SF_{0,-2,0} \quad SF_{0,0,-2} &\Rightarrow \\ C_0 = SF_{0,0,0} & \\ C_1 = \frac{\delta SF_{x_1,0,0}}{\delta x_1} = \frac{SF_{-2,0,0} - SF_{0,0,0}}{-2} &\text{ etc.} \end{aligned} \quad (7)$$

3.4 Advanced First Order Point Estimate Method (A-PEM)

The 1st order method can be improved by estimating the non-linearity in the function by only one extra calculation ($n + 2$ points). This can be for example, $x_i = -1$ $i \in n$, giving $SF_{-1,-1,-1}$. If the function of the safety factor would be linear, then the following factor should be one:

$$R = \frac{SF_{0,0,0} - SF_{-1,-1,-1}}{\sum_{i=1}^n C_i} \quad (8)$$

However, in most cases this factor is not one. To reduce the parameters C_i , with this factor would be a too strong reduction, especially for many parameters, so a reduction of:

$$\frac{1}{R^n}$$

would be more appropriate, but this needs some more research. This leads to the following advanced first order prediction:

$$SF_{x_1, x_2, \dots, x_n} = C_0 + \sum_{i=1}^n R^n C_i x_i \quad \text{where: } x_i = \frac{c_{u,i} - \mu_{c_{u,i}}}{\sigma_{c_{u,i}}} \quad (9)$$

3.5 Probability of failure

The probability density function of each parameter is described by:

$$f_{c_{u,i}} = \frac{1}{\sqrt{2\pi}\sigma_{c_{u,i}}} e^{-\frac{1}{2}\left(\frac{c_{u,i} - \mu_{c_{u,i}}}{\sigma_{c_{u,i}}}\right)^2} \quad (10)$$

or:

$$f_{x_i} = \frac{1}{\sqrt{2\pi}} e^{-\frac{1}{2}x_i^2} \quad (11)$$

The probability of failure is defined by the summation of this probability density function over the area with a safety factor $SF < 1.00$, so:

$$P_f = \iiint_{SF_{x_1, x_2, \dots, x_n} < 1.00} f_{x_1, x_2, x_3} dx_1 dx_2 \dots dx_n \quad (12)$$

The only difference between the different first order calculations is the area over which the probability density function is integrated.

Only for non-correlated probability density functions the combined probability density function can be split in the independent probability density functions of each independent parameter:

$$f_{x_1, x_2, \dots, x_n} = f_{x_1} \cdot f_{x_2} \cdot \dots \cdot f_{x_n} \quad (13)$$

3.6 Advanced First Order Reliability Method (A-FORM)

This method is in fact the same as the linear analytical solution, but the factors α_i are measured with fluctuations of the individual soil parameters, giving:

$$\alpha_i = \frac{\partial \mu_{SF}}{\partial \mu_{c_{u,i}}} \quad \text{so: } \alpha_i = \frac{C_i}{\sigma_{c_{u,i}}} \quad (14)$$

This results in a single point reliability index:

$$\beta = -\frac{\mu_{SF} - 1}{\sigma_{SF}} = -\frac{C_0 - 1}{\sqrt{\sum_{i=1}^n (RC_i)^2}} \Rightarrow P_f = \Phi(\beta) \quad (15)$$

In this way the probability of failure is found without integrating over the total probability density function.

4 EXAMPLES

4.1 Single Failure Mode

To test the different methods, the example with the three soil layer embankment is calculated for all previous mentioned methods. The bars in Figure 2 show the Monte Carlo distribution and the straight line the Linear-Analytical Solution. All data can be found in Table 2.

The Monte Carlo simulation is close to the real answer and is therefore used as reference. The Linear solution is the best approximation, but can not be

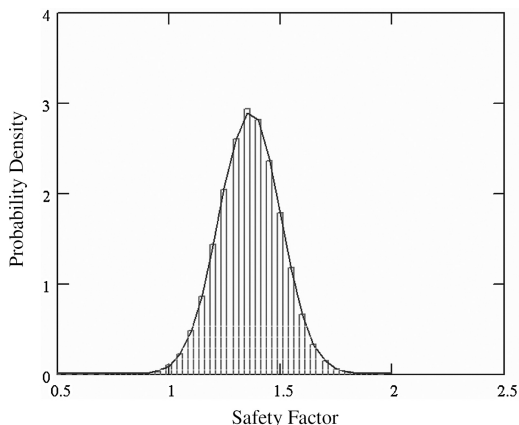


Figure 2. Probability density function of the safety factor.

Table 2. Probability of failure according several methods (Single Failure Mode).

Probability of failure (Single Failure)	Monte Carlo	Linear Anal	FO-PEM	A-PEM	A-FORM
μ_{SF}	1.388	1.389	–	–	1.388
σ_{SF}	0.137	0.137	–	–	0.139
$P(SF < 1.00)$	0.21%	0.23%	0.26%	0.26%	0.26%
Error	–	11%	26%	26%	26%

implemented in Finite Element Models, since the length of the slip plane through each soil layer is in those models unknown. The Point Estimate Models (FO-PEM & A-PEM) and the First Order Reliability Method (A-FORM) show more or less the same reasonable approximations. Both PEM predictions are the same because the reduction factor $R = 1$.

The Linear Solution and the Point Estimate Models show good results because there is in this case only one failure mechanism, which is failure of the embankment (layer 2 and 3) with a circular slip plane through the toe of the dike ($x = 0, y = 0$).

4.2 Double Failure Mode

Suppose the ground layer (1st layer) has not an average undrained cohesion of 26 kPa, but of 20 kPa. In this case the probability of a second failure mechanism is strongly increased, which is a deep slip circle failure in the first layer, see Figure 3.

For: $r \gg h$ one can state for the load (Solicitation):

$$S \approx \gamma hr \frac{1}{2} r \approx \frac{1}{2} \gamma hr^2 \quad (16)$$

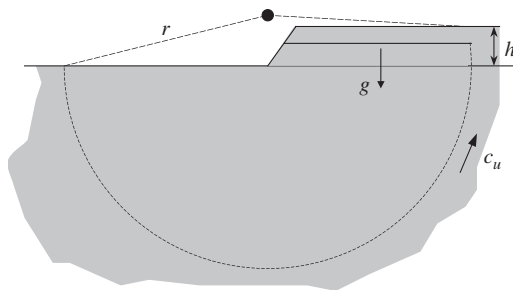


Figure 3. Deep slip surface.

and for the soil strength (Resistance) along the slip plane:

$$R \approx \pi r c_u r \approx \pi c_u r^2 \quad (17)$$

This means failure is initiated when:

$$SF = \frac{R}{S} < 1 \Rightarrow c_u < \frac{\gamma h}{2\pi} \quad (18)$$

This means the embankment foundation will fail if its undrained cohesion is lower than:

$$c_u < \frac{5 \cdot 16}{2\pi} \approx 12.7 \text{ kPa} \quad (19)$$

The corresponding reliability index and probability of failure are:

$$\begin{aligned} \beta &= -\frac{\mu_{c_u} - c_u}{\sigma_{c_u}} = -\frac{20 - 12.7}{4} = -1.817 \\ \Rightarrow P_f &= 0.0346 \end{aligned} \quad (20)$$

This probability of failure is much larger than what can be expected based on the slip circle corresponding to the average values. This extra failure mechanism causes a large non-linearity in the failure distribution, see Figure 4, showing a probability density function for the linear prediction versus a Monte Carlo prediction with 100,000 simulations.

The Monte Carlo and PEM simulation clearly discover the extra mechanism (and that is why alterations of the variables of at least 2σ are made), but the linear solution doesn't. Only the advanced PEM approximation and the advanced FORM give a reasonable prediction here. It is remarkable that these methods give the same results. The description of the safety factor in the Advanced PEM is:

$$SF = 1.388 + 0.198x_1 + 0.115x_2 + 0.010x_3 \quad (21)$$

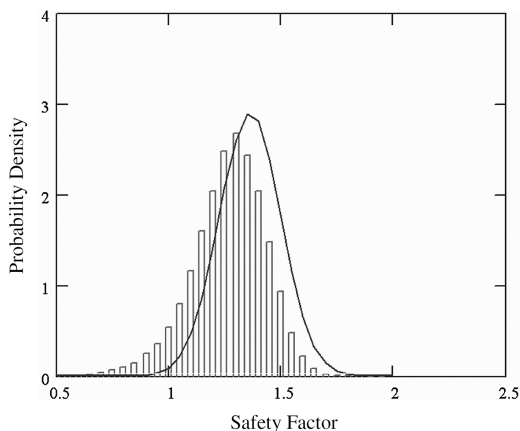


Figure 4. Probability density function of the safety factor.

Table 3. Probability of failure according several methods (Double Failure Mode).

Probability of failure (Double Failure)	Monte Carlo	Linear anal.	FO-PEM	A-PEM	A-FORM
μ_{SF}	1.293	1.389	–	–	1.388
σ_{SF}	0.166	0.137	–	–	0.229
$P(SF < 1.00)$	5.04%	0.23%	7.89%	4.5%	4.5%
Error	–	95%	56%	10%	10%

The used reduction factor of $R = 0.83$ is clearly smaller than one. This means that only non-linear functions can describe this failure plane ($SF = 1$) more accurately.

5 ADVANCED RESEARCH

The first steps for future research are improving the methods described in this paper and implementing these in slip surface models and finite element models.

Another step which has to be made is to study the affect of having several random input variables, such as c , ϕ , γ , instead of only c_u . A more complex step will be to implement the inhomogeneous soil layer behavior in vertical and two horizontal directions. Especially the 2nd horizontal direction will be complex, since most slip surface stability models and finite element programs are 2-dimensional.

6 CONCLUSIONS

The advanced first order reliability method gives the same results as the advanced point estimate method. The first method saves an amount of work by not making a n -th order integration over the probability density functions. Therefore the advanced first order reliability method (A-FORM) gives, in an easy way, the most accurate prediction of the probability of failure, for both the single and double failure modes. This method can be easily implemented in all finite element codes and slip circle models.

REFERENCES

- Bakker, H.L. Failure probability of river dikes strengthened with structural elements, *16th International Conference on Soil Mechanics and Geotechnical Engineering, Osaka, Japan*, Millpress, Rotterdam, ISBN 90-5966-027-7, Sep. 2005
- Bea, R. Reliability and human factors in geotechnical engineering, *Journal of Geotechnical and Geoenvironmental Engineering*, Nov. 2005
- De Boer, A., Waarts, P.H. Full stochastic analysis of a cofferdam, *Safety and Reliability*, Swets & Zeitlinger, Lisse, ISBN 90-5809-551-7, 2003
- Peschl, G., Schweiger, H.F., Pöttler, R., Thurner, R. Reliability analysis in geotechnics with deterministic finite elements – a simplified approach for practical applications in tunneling, *Int. Conf. on Probabilistics in Geotechnics Graz, Austria*, Verlag Glückauf Essen, Sept. 2002

Inverse analysis of an embankment using the Ensemble Kalman Filter including heterogeneity of the soft soil

A. Hommels & F. Molenkamp

Delft University of Technology, Delft, The Netherlands

ABSTRACT: Geomechanical models are indispensable for reliable design of engineering structures and processes and hazard and risk evaluation. Model predictions are however far from perfect. Errors are introduced by fluctuations in the input or by poorly known parameters in the model. To overcome these problems an inverse modelling technique to incorporate measurements into the deterministic model to improve the model results can be implemented. This allows for observations of on-going processes to be used for enhancing the quality of subsequent model predictions.

In geomechanics several examples of inverse modelling exist where the improved model of the system is obtained by minimizing the discrepancy between the observed values in the system and the modelled state of the system within a time interval. This requires the implementation of the adjoint model. Even with the use of the adjoint compilers that have become available recently, this is a tremendous programming effort for the existing geomechanical model system.

The Ensemble Kalman filter is being implemented to overcome this problem. The Ensemble Kalman filter analyses the state of the system each time data becomes available. The Random Finite Element Method is used to simulate the heterogeneity of the subsurface.

Very promising results of a conceptual example, based on the construction of a road embankment on soft clay, are presented. The Ensemble Kalman filter is not only used for a straight forward identification of the elastic modulus E and the K_0 parameter of several soil layers below the embankment, but also incorporates by means of the Random Finite Element Method the variation of the parameters throughout a soil layer.

1 INTRODUCTION

1.1 *Inverse modelling*

In geotechnical engineering context inverse modelling or back analysis consists in finding the values of the mechanical parameters, or of other quantities characterizing a soil or rock mass, that when introduced in the stress analysis of the problem under examination lead to results (e.g. displacements, stresses etc.) as close as possible to the corresponding in situ measurements. The optimal state of the system is obtained by minimizing the discrepancy between the observed values in the system and the forecasted or modelled state of the system within a certain time interval. In the eighties and the nineties, several articles concerning inverse analysis in geomechanics using the Maximum Likelihood and the (Extended) Bayesian method were published (Gens et al. 1996, Honjo et al. 1994a,b). Recent developments in other fields of science have shown a new powerful technique indicated as the Ensemble Kalman filter. In a filter, the state of the system is analysed each time data becomes available.

1.2 *Geological uncertainty*

Usually in the field of geomechanics the Finite Element Method is used for numerical simulations. In this method, one particular value for a certain parameter is assigned to the soil mass or a soil layer, which remains constant throughout the mass or the layer. However, in nature, this is not really the case: properties of natural soils will vary through depth and often also in horizontal extent due to for example different loading conditions or different depositional conditions. One way to deal with this uncertainty is the Random Finite Element Method. This technique incorporates the spatial correlation between the properties using Monte Carlo simulations in order to represent the proper stochastic properties.

The general formulations of the Ensemble Kalman filter and the Random Finite Element Method will be discussed in the next sections. In Hommels et al. 2005 the effectiveness of the Ensemble Kalman filter using the Finite Element Method has been proven. In this paper the Ensemble Kalman filter will be combined with the Random Finite Element method in a conceptual

case study. The sensitivity of the analyses to the number of Monte Carlo simulations is also considered.

2 THEORY

2.1 Basic principles

The true state of the subsurface at time step k can be described by a state vector $x^t(k)$. The elements of the state vector are filled with stresses but possibly also strains or other state parameters. The superscript “ t ” denotes that $x^t(k)$ is the “true” state; the exact value is probably unknown. To obtain insight in the true state, a model is developed to make a forecast or to model $x^f(k+1)$ at time step $k+1$:

$$x^f(k+1) = M(x^f(k)) \quad (1)$$

The superscript “ f ” denotes that $x^f(k)$ is a “forecast” of the true state $x^t(k)$ at time step k , which is in the best case a good approximation. In the context of the shallow subsurface, the state vector can partly be filled with displacements u . M denotes the dynamical model operator, which describes for instance the constitutive model of the soil, e.g. the soil parameters Young’s modulus E and Poisson’s ratio ν in the simplest elastic case. If there are uncertainties in the parameters, which have to be updated, the state vector $x^f(k)$ is also filled with the uncertain parameters.

Since models are never perfect:

$$x^t(k) = x^f(k) + \eta(k) \quad (2)$$

in which $\eta(k)$ is the unknown model error in the k -th forecast with $E\{\eta^j\} = 0$ (E denotes expectation) and $E\{\eta^2\} = P$, which is the model error covariance matrix.

Some entities of the state are compared with data from an observational network, for example the measurements y^o of the surface displacements. All available data for time step k are stored in an observation vector $y^o(k)$. The superscript “ o ” denotes that $y^o(k)$ is an “observation”. There is a difference $\varepsilon(k)$ between the “true” state $x^t(k)$ and the actual “observed” data $y^o(k)$:

$$y^o(k) = H(k)x^t(k) + \varepsilon(k) \quad (3)$$

where $H(k)$ is the linear observational operator. The observations are assumed unbiased ($E\{\varepsilon\} = 0$) and $E\{\varepsilon^2\} = R$, which is the measurement error covariance matrix.

The final goal of inverse modelling methods is to improve the state vector; at each time step k measurements become available, with an error $\varepsilon(k)$ as small as possible.

2.2 Extended Kalman filter

In a filter, the state of the system is analysed each time data becomes available. This is done in a two-step approach. In the first step, the time update step, the modelled values are calculated for the time measurements will come in. Also the forecasted (or modelled) error covariance matrix P^f is calculated as well as the Kalman gain K , which is a kind of weighting factor between the measured values and the modelled values. The Kalman gain K is independent of the measurements. In the second step, the measurement update step, the measurements will come in and the assimilated state vector $x^a(k)$ using the Kalman gain are calculated as well as the assimilated error covariance matrix P^a . The simplest filter is the linear Kalman filter. However the linear Kalman filter is designed for linear systems and therefore not very useful in geomechanics. It is possible to derive approximate filters using linearization techniques for non-linear systems. Again, assume that the system can be described by a state vector x , and the physical process is governed by the non-linear stochastic equation:

$$x^f(k+1) = f(x^t(k), u(k)) + G(k)w(k) \quad (4)$$

in which $u(k)$ is the system input, $G(k)$ is the noise input matrix and $w(k)$ is the process noise with zero mean and covariance matrix Q . In the time update step, the equations can be written as:

$$x^f(k+1) = f(x^a(k), u(k)) \quad (5)$$

$$P^f(k+1) = F(k)P^a(k)F^T(k) + G(k)Q(k)G^T(k) \quad (6)$$

where

$$F(k) = \left(\frac{\partial f}{\partial x} \right)_{x_{ref}} \quad (7)$$

The measurement update equations can be written as follows:

$$x^a(k+1) = x^f(k+1) + K(k+1) \{y^o(k+1) - H(k+1)x^f(k+1)\} \quad (8)$$

$$P^a(k+1) = \{I - K(k+1)H(k+1)\} P^f(k+1) \quad (9)$$

And the Kalman gain is given by:

$$K(k+1) = \frac{P^f(k+1)H^T(k+1)}{H(k+1)P^f(k+1)H^T(k+1) + R(k+1)} \quad (10)$$

2.3 Ensemble Kalman filter

Evensen introduced the Ensemble Kalman filter (EnKF) in 1994 and the theoretical formulations as well as an overview of several applications are described in Evensen (1994, 2003). The EnKF was designed to resolve two major problems related to the use of the extended Kalman filter (EKF). The first problem relates to the use of an approximate closure scheme in the EKF, and the other one to the huge computational requirements associated with the storage and forward integration of the error covariance matrix P . For further details the reader is referred to the references.

In the Ensemble Kalman filter, an ensemble of possible state vectors, which are randomly generated using a Monte Carlo approach, represents the statistical properties of the state vector. The algorithm does not require a tangent linear model, which is required for the EKF, and is very easy to implement.

At initialisation, an ensemble of N initial states $(\xi_N)_0$ are generated to represent the uncertainty at time step $k = 0$. In the measurement update step, the matrix $E^f(k + 1)$ defines an approximation of the covariance matrix $P(k + 1)$.

The time update equations for the Ensemble Kalman filter for each estimate of the state are:

$$\xi_i^f(k + 1) = f(\xi_i^a(k)) + G(k)w(k) \quad (11)$$

$$x^f(k + 1) = \frac{1}{N} \sum_{i=1}^N \xi_i^f(k + 1) \quad (12)$$

$$E^f(k + 1) = [\xi_1^f(k + 1) - x^f(k + 1), \dots, \xi_N^f(k + 1) - x^f(k + 1)] \quad (13)$$

In the measurement update step:

$$P(k + 1) = \frac{1}{N - 1} E^f(k + 1)(E^f(k + 1))^T \quad (14)$$

Equation (11) is never really calculated due to huge computational requirements, as mentioned before, but is split up:

$$K(k + 1) = \frac{E^f((E^f)^T H)}{(N - 1) \left(H \frac{1}{N - 1} E^f((E^f)^T H^T) + R \right)} \quad (15)$$

$$\xi_i^a(k + 1) = \xi_i^f(k + 1) + K \{ y_o(k + 1) - H \xi_i^f(k + 1) + \mathcal{E} \} \quad (16)$$

where \mathcal{E} is for each ensemble member a randomly added measurement error.

2.4 Random Finite Element Method

The Random Finite Element Method (RFEM) combines the finite element analysis with the random field theory generated using the local average subdivision method (Fenton & Vanmarcke 1990). A brief description will be given.

In the Finite Element Method the uncertainty of a material is defined by its mean μ and its standard deviation σ . For the introduction of more spatial variability, the introduction of an additional statistical parameter, the spatial correlation length θ , is required. The spatial correlation length defines the distance beyond which there is minimal correlation and can be determined from for example CPT-data. A large value of θ indicates a strongly correlated material, while a small value indicates a weakly correlated material. Now the random field can be generated and in the Random Finite Element Method, this is done using the local average subdivision (LAS) (Fenton & Vanmarcke 1990), based on a standard normal distribution (mean μ is zero and the standard deviation σ equals one) and a spatial correlation function ρ . LAS generates a square random field by uniformly subdividing a square domain into smaller square cells, where each cell has a unique local average, which is correlated with surrounding cells. For an isotropic field, where θ is equal in all directions, the Gauss-Markov correlation function ρ is given by

$$\rho(\tau) = \exp \left(-\frac{2}{\theta} |\tau| \right) \quad (17)$$

in which τ is the lag vector. The random field for a certain parameter E for cell i , based on a standard normal distribution, can then be transformed into for example a normal distribution:

$$E_i = \mu_E + \sigma_E Z_i \quad (18)$$

in which μ_E is the mean and σ_E is standard deviation of parameter E ; Z_i is the local average value for cell i .

There are an infinite number of possibilities for the random field, based on the given set of statistics of μ , σ and θ . Again Monte Carlo simulations are used to express the spatial distribution (Hicks & Samy 2002).

2.5 Monte Carlo simulations

Since both the Ensemble Kalman filter and the Random Finite Element Method are based on Monte Carlo simulation, these simulations are combined in order to save computational effort. However enough realizations are required to ensure a good representation of probability density of the state estimate.

3 CASESTUDY

3.1 Loaded soil column

Consider a soil column consisting of 16 elements, which are 1 meter in length. Each element has a random stiffness EA , calculated using LAS. The column is axially loaded at element number 16.

The true state value of the element axial stiffness vector EA is 16 kN and based on this value the measurements are generated. The measurement noise is normally distributed with zero mean and standard deviation 0.01.

The stiffness EA of the soil has a normal distribution, with mean $\mu = 16\text{ kN}$ and standard deviation $\sigma = 2$. The total length of the column is 16 meter and the spatial correlation length θ equals 3. During 100 timesteps the load is increased from 0.5 kN to 1.1 kN.

3.2 Update process

In figure 1, the results of the update of the stiffness, for one element is shown. The assimilated values tend to approach the value of the true state, but it takes a while due to the random field assumption.

At the start of the update or assimilation process, the uncertainty of parameter EA is very large. The range of the ensemble members is shown in figure 2. In figure 3, the range of the ensemble members is shown after 100 loading steps. One can see that there has been a large reduction of the parameter uncertainty. The true state can be found, for both loading steps, between the range of the ensemble members and therefore the filter is performing well. In figure 4, the different distributions for loading step 1 and loading step 100 are shown. Again the large reduction of the uncertainty is shown. The distribution at loading

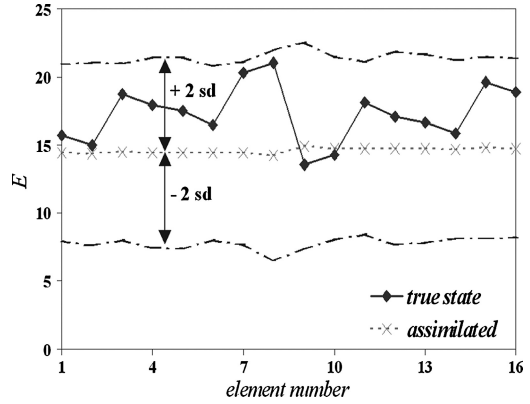


Figure 2. Uncertainty of parameter E at loading step 1.

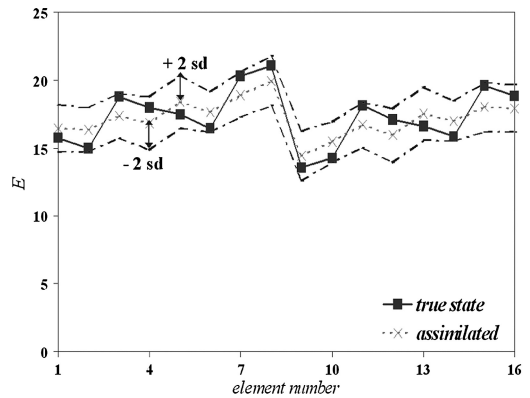


Figure 3. Uncertainty of parameter E after 100 loading steps.

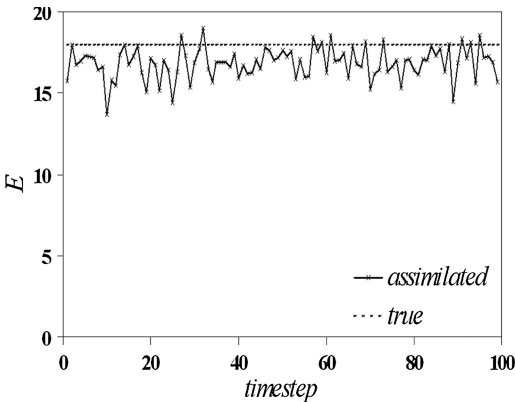


Figure 1. The update process of parameter E for several time steps.

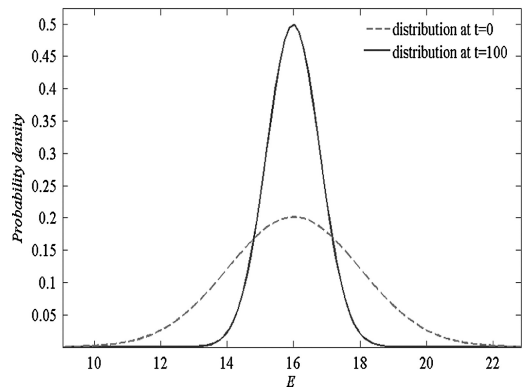


Figure 4. Comparison of starting and final distribution of E .

step 100 is much smaller than the distribution at time step 1. Therefore the uncertainty about the value of the stiffness EA has decreased.

3.3 Sensitivity to the number of MC realisations

In principle, a higher number of Monte Carlo realisations will give a better estimate of the parameter. However often not a very large amount is required to obtain good results. In figure 5 the update of each element after 100 loading steps for a different number of Monte Carlo realisations is shown. A number of 500 MC realizations gives a slightly better estimate than for 100 MC realizations. However, the difference is very minimal. One can then choose for a lower amount of MC realizations, which will save computation time.

In figure 5 it is also shown that the true state is never fully reached, not even for 500 MC realizations. This is due the fact that the observation points are limited to 4 points. If the observation points were “traveling” throughout the material, the estimation would be much better, because then the true state is observed at least once. However this is hardly ever the case in the “real” world and therefore not simulated here.

3.4 Embankment

The authors are working on an a case study of the construction of a road embankment where the Ensemble Kalman filter in combination with the Random Finite Element Method will be applied to determine several uncertain parameters of the shallow

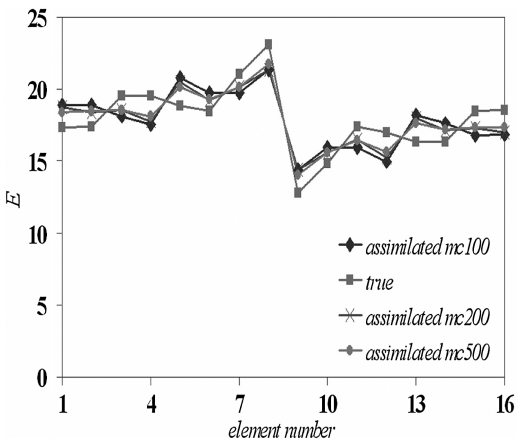


Figure 5. Comparison of different amount of Monte Carlo simulations.

subsurface. During the presentation the first results will be shown.

4 CONCLUSIONS

The Ensemble Kalman filter has already proven to be effective in the field of geomechanics using the standard finite element code (Hommels et al. 2005). In this paper the effectiveness of the ensemble Kalman filter in combination with the Random Finite Element Method is shown.

After 100 loading steps, the parameter uncertainty has been decreased significantly. The true state will never be fully reached if there are a limited amount of observation points at fixed places.

The analysis is slightly sensitive to the amount of Monte Carlo realizations. It is shown that not a very high amount of realizations is necessary to obtain a good representation of the probability density of the state estimate.

REFERENCES

- Evensen, G. 1994. Sequential data assimilation with non-linear quasi-geostrophic model using Monte Carlo methods to forecast error statistics. *Journal of Geoph. Research*, vol. 99, C5/10, p.143–162.
- Evensen, G. 2003. The Ensemble Kalman filter: theoretical formulation and practical implementation. *Ocean dynamics*, vol. 53, 4, p. 343–367.
- Fenton, G. A. and Vanmarcke, E.H. 1990. Simulation of random fields via local average subdivision. *Journal of Geotech. Engng., ASCE*, 116, 8, p. 1733–1749.
- Gens, A., Ledesma, A. and Alonso, E. 1996. Estimation of parameters in geotechnical back analysis – II. Application to a tunnel excavation problem. *Computers and Geotechnics*, vol. 18, 1, p. 29–46.
- Hicks, M.A. and Samy, K. 2002. Influence of heterogeneity on undrained clay slope stability. *The Quarterly Journal of Engineering Geology and Hydrogeology*, vol. 35, 1, p. 41–49.
- Hommels, A., Molenkamp, F., Heemink, A.W and Nguyen, B. 2005. Inverse analysis of an embankment on soft clay using the Ensemble Kalman Filter. Proceedings of the Tenth Int. Conf. on Civil, Structural and Env. Eng. Computing, B.H.V. Topping (Editor), Civil-Comp Press, Stirling, United Kingdom, paper 252.
- Honjo, Y., Liu, W.T. and Soumitra, G. 1994a. Inverse analysis of an embankment on soft clay by extended Bayesian method. *Int. Journal for Num. and Anal. Methods in Geomechanics*, vol. 18, p. 709–734.
- Honjo, Y., Wen-Tsung, L. and Sakajo, S. 1994b. Application of Akaike information criterion statistics to geotechnical inverse analysis: the extended Bayesian method. *Structural safety*, vol. 14, p. 5–29.

System reliability assessment of friction drilled shafts in gravel soils

A.M. Harraz & M.M. El-Meligy

Structural Engineering Department, Mansoura University, Mansoura, Egypt

ABSTRACT: Most design equations used to predict the skin friction values of drilled shafts are based on test results in sands and clays where the concrete-soil interface is much smoother and does not take into account the effect of soil dilation which is much higher in gravels compared to sand. The objective of this paper is to conduct system reliability analyses on friction shafts to study the probability of failure and determine the reliability indices and partial factors of safety of these kinds of shafts. A parametric study was conducted using finite element technique. The response surface methodology is used to link between the finite element analyses phase and the reliability analyses. As a result of this study, two limit state functions, ultimate bearing capacity and serviceability functions were developed. It is found that soil dilation, soil angle of internal friction and soil modulus are the most important parameters controlling the probability of failure of friction shafts in gravelly soils.

1 INTRODUCTION

Drilled shafts have become the preferred deep foundation element in many areas around the world because soil conditions are usually unfavorable to driven piles, scour depths on the ephemeral river channels are quite large, and the increased confidence in the bearing layer afforded by the drilled shaft construction process. A related issue of concern to designers is the performance of groups of drilled shafts in gravelly soils under load. AASHTO standards call for groups to be designed in cohesionless soils using a reduction factors times the individual capacity of each shaft (AASHTO 1998). Traditionally, the design process is either based on one conventional safety factor or based on multi safety factors or the so called partial safety factors. Recently, this new concept of partial safety factors has been employed in some codes of practice (Eurocode 1 1991). However, the determination of partial safety factors was based somehow on empirical judgment not on mathematical basis.

2 DETERMINISTIC ANALYSES

2.1 Analytical approach

All methods for determining the skin friction of drilled shafts are based upon the general equation:

$$Q_s = f_s A_s \quad (1)$$

where Q_s = kin friction capacity, f_s = shaft resistance per unit area, and A_s = surface area of the sides of the

shaft in contact with the soil. For differing layers of soils, Q_s consist of contributions from each layer. The methods that follow are focused on determining f_s for cohesionless granular soils.

2.1.1 Tomlinson 2001

The unit skin resistance is calculated by Tomlinson (Tomlinson 2001):

$$f_s = K \sigma' \tan \delta \leq 110 \text{ [kN/m}^2\text{]} \quad (2)$$

where σ' = average effective overburden pressure over the depth of a soil layer, K = coefficient of horizontal soil stress, and δ = soil-pile friction interface angle obtained from laboratory shear box tests.

2.1.2 Meyerhoff 1976

Meyerhoff gives the unit side resistance as:

$$f_s = \frac{N}{100} \text{ tsf} \quad (3)$$

where N = average number of blows from standard penetration test (SPT N-value), not corrected for overburden pressure. (Meyerhoff 1976)

2.1.3 Reese and O'Neill 1989 (AASHTO METHOD)

The unit side resistance for a given layer is given by Reese and O'Neill and adopted by AASHTO as:

$$f_s = \xi \sigma' \quad (4)$$

where $\xi = K \tan \delta$ in equation (2) and is given by the function

$$\xi = 1.5 - 0.135z^{0.5}; 0.25 \leq \xi \leq 1.20 \quad (5)$$

σ' = vertical effective stress at the middle of a layer, and z = depth to the middle of a layer in feet. (Reese & O'Neill 1989)

2.1.4 Kulhawy 1989

The unit side resistance is found using the general equation:

$$f_s = K \sigma' \tan \delta \quad (6)$$

where δ can be expressed as a function of angle of internal friction, ϕ' . The ratio δ/ϕ' is a function of construction technique and for good construction techniques equals 1. For poor slurry construction techniques where sufficient care was not taken to ensure that all of the slurry was expelled from the hole or the slurry was mixed together with and infiltrated the sides of the hole, δ/ϕ' is reduced to 0.8 or lower. (Kulhawy 1989)

2.1.5 Rollins, Clayton, Mikesell, and Blaise 1997

Rollins et al. expanded on Reese & O'Neill's method (AASHTO method) by suggesting ξ factors for gravelly soils (Table 1) (Rollins et al. 1997).

where z = depth to the center of the layer. Their results were based upon uplift tests (Rollins et al. 1997).

2.2 Field test approach

There are many tests performed on axially loaded drilled shaft in clayey, silty or sandy soils, but there are few tests conducted on gravelly soils. This is because the heavy equipments (pump and jacks) needed for field tests in these kind of soils due to the large capacity of shafts. In these kinds of testing, shafts are instrumented with strain gauges, load cells, and displacement sensors. The advantages of performing field tests are to develop a real load displacement and load transfer curves. These load test results have served to create and validate the equations used to predict shaft capacity. However, these tests are always expensive and need a big effort and special equipments (Walsh et al. 2002).

Table 1. ξ values (Rollins et al. 1997).

(%) Gravel	ξ
Less than 25%	$\xi = 1.5 - 0.135z^{0.5}; 0.25 \leq \xi \leq 1.2$
25% to 50%	$\xi = 2.0 - 0.0615z^{0.75}; 0.25 \leq \xi \leq 1.8$
Greater than 50%	$\xi = 3.4e^{-0.0265z}; 0.25 \leq \xi \leq 3.0$

2.3 Finite element approach

Finite Element Method (FEM) is another analytical method used for the design of axially loaded shafts. There are four basic components of finite element: mesh generation, failure criterion, calibration, and boundary conditions. The selection of the size and number of elements of the mesh is important because they define where stresses and strains will be calculated. To obtain a valid solution to a problem using the finite element method it is necessary to develop a proper mesh. The results obtained from the FE analysis can be highly dependent on the failure criterion that is used. Establishing boundary conditions is of great importance when using the FEM, especially when modeling soil. The advantage of the finite element method is that it performs analyses based on the stress and strain characteristics of the materials used in the design. The form of the solution does not have to be assumed in order to solve the problem. The disadvantages of this method are that it is very complicated and the analysis time is very large. Another disadvantage of finite element is the difficulty in modeling soil properties with great precision. Due to the complexity of FE, it is more of a research tool than a tool used in design practice.

3 SYSYEM RELIABILITY ANALYSES

3.1 Methodology

The system failure event F_{sys} can be expressed in terms of minimal unions of intersections as (STRUREL 1997)

$$F_{sys} = \bigcap_{(i)} \bigcup_{(j)} (F_{ij}) \quad (7)$$

where

$$F_{ij} = \{g_{ij}(X) \leq 0\} \quad (8)$$

denotes the j -th failure event in the i -th intersection of the system, and $g_{ij}(X)$ is the j -th failure event in the i -th intersection of the system, and (X) is the vector of basic random variables with dimension n . According to the probability theory unions correspond to series systems and intersections to parallel systems. The exact evaluation of the probability of unions of events is prohibitively expensive. However, bounds have been proposed by several authors (e.g.; Ditlevsen 1979). The computation of the probability of intersection which is the key to system reliability analysis requires first performing the probability distribution transformation (Hohenbichler & Rackwitz, 1981)

$$u = T^{-1}(x) \quad (9)$$

where u = vector of independent standard normal variables (realization of U) and x = a realization of X . Then, for large reliability index β , the failure probability can asymptotically determined as (Hohenbichler et al. 1987)

$$P(f) = P\left(\bigcap_{j=1}^m F_j\right) \approx \Phi_k(\beta; R) C_{SORM} \quad (10)$$

where $\Phi_k(\beta; R)$ = k-dimensional normal integral with β a vector of the local reliability indices the components of which are given by (Rangannathan 1990)

$$\beta_j = -\alpha_j^T u^* \quad (11)$$

and R = matrix of correlation coefficients with elements $\{\alpha_i^T \alpha_j\}$, α_i = normalized gradients of the k active limit state surfaces in the joint β -point u^* (the design point in u -space) for which (El-Meligy & Abedelatif, 1999)

$$\beta = \min\{\|u\|\} \text{ for } \left\{ u : \bigcap_{j=1}^m g_j(U) \leq 0 \right\} \quad (12)$$

C_{SORM} = correction factor accounting for curvatures of the active failure surfaces in the joint β -point u^* . The generalized reliability index is defined as (El-Meligy & Rackwitz, 1998)

$$\beta_E = -\Phi\left(P\left(\bigcup g_{ij}(U) \leq 0\right)\right) \quad (13)$$

3.2 Partial safety factors (PSF)

Generally, the partial safety factor can be defined as the factor by which the variable is multiplied in order to achieve a target reliability index ; i. e.,

$$\gamma_{li} = \frac{x_i^*}{x_{c,i}} \quad (14)$$

$$\gamma_{si} = \frac{x_i^*}{x_{c,i}} \quad (15)$$

where, γ_{li} = partial safety factor for the loading variable, γ_{si} = partial safety factor for the strength variable, $x_{c,i}$ = characteristic value of the random variable x_i^* = design value of the random variable which can be calculated as (Harraz et al. 1998)

$$x_i^* = F_i^{-1}[\Phi(-\alpha_i \beta_T)] \quad (16)$$

where, $F_i^{-1}[\]$ = distribution function of the random variable under consideration, β_T = target reliability

index, α_i = normalized sensitivity of the reliability index with respect to the random variable x_i in the u -space; i. e.,

$$\alpha_i = \frac{\partial \beta}{\partial u_i} \frac{1}{\|\alpha\|_{\|u\|}} \quad (17)$$

and $\|\cdot\|$ indicates Euclidean norm. If α_i has a positive sign this means that the random variable is a strength variable; otherwise, it is a loading variable. Clearly, a partial safety factors, in this concept, is dependent on the probability distribution and sensitivity of the random variable under consideration as well as on the target reliability index (Rackwitz & Fiessler, 1987).

4 IDENTIFICATION OF UNCERTAINTIES

4.1 System uncertainties

As for most systems considerable amount of uncertainty exists in the assessment of drilled shaft safety. In general, the uncertainty may be categorized in three groups; namely, system properties, system geometry, and loading.

The reinforced concrete and soil are the two main materials that comprise the drilled shaft foundations. Generally, three major sources of uncertainties associated with soil properties can be identified (Vanmarcke 1977). The first source is the in-situ variability that may be due to the variation of the mineral composition, stress history and process of stratification. The second source of uncertainties is the result of measurement errors. The difference between the measured and the actual values is mainly due to sample disturbance, test imperfections and human factors. The statistical uncertainty that is due to the limited number of tests and samples required for the evaluation of subsurface conditions is the third source of uncertainty. The variability in reinforced concrete properties is the result of many factors; among others are the inherit variability of constituents and quality control. Generally, in soil mechanics problems the variability in system geometry does not contribute too much. The load variability depends on the considered type of loading; dead load, live load, earthquake load, etc. An additional source of uncertainty results from the difference between the actual behavior of the component or system and the behavior of the mechanical model for the same component or system. This source of uncertainty is mainly due to the simplifications in the mechanical model. The above-mentioned sources of uncertainties are compiled in the reliability analysis through the stochastic model, which contains the probability distributions and statistical moments (El-Meligy 2002).

5 PROPOSED ALGORITHM

The proposed algorithm for the reliability assessment of drilled shaft is summarized as follows:

1. Prepare the mechanical as well as the stochastic models.
2. Perform the required numerical experiments using ABAQUS code (ABAQUS 1998). Then, using regression analysis find in closed form the limit states considered in the assessment; i.e., the shaft bearing capacity and settlement.
3. The system reliability package STRUREL (STRUREL 1996) is used for system reliability analysis.
4. In the first run use STRUREL to perform sensitivity analysis for the random variables with respect to the failure probability for each limit states and for the system as well.
5. Based on the sensitivity analysis reduce the stochastic model by replacing the unimportant random variables by deterministic variables at their mean values.
6. Perform the reliability analysis using SYSREL based on the reduced stochastic model in order to determine the reliability indices and the sensitivity coefficients required for the evaluation of the partial safety factors.

Get the partial safety factors using the aforementioned sensitivity coefficients and based on the target reliability indices of EUROCODE 1991.

6 CASE STUDY

6.1 Case study description

A real pull out field test that was performed in January 1997 at Mapleton, Utah, USA was chosen as a case study for this paper. The percent of gravel ranges from 68% in the gravelly materials to 2% in the silty sand soil areas (Rollins et al. 1997). The main objective of this test was to determine the skin friction values between soil and shaft. The shaft diameter is 0.62 m and has a length of 3.9 m.

6.2 Finite element model

Finite element analyses using the program ABAQUS (1998) were performed on a 3-D finite element model with 8-node elements. The boundary conditions include infinite (continuous) elements to reduce the effect of stress concentrations. The mesh shown in Figure 1 represents the results of several mesh refinement runs (Harraz et al 2005). In this mesh, the soil and shaft were discretized. The behavior of the reinforced concrete shaft was modeled as linear elastic. The soil was modeled as an elastic-perfectly-plastic, Drucker-Prager-Type material with volumetric dilation (Chen &

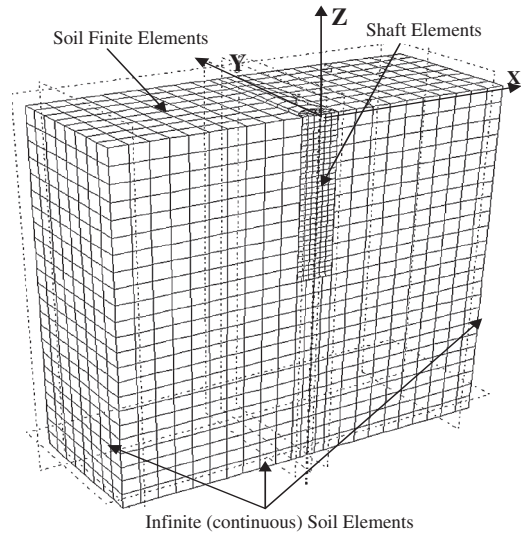


Figure 1. Half symmetry of shaft and soil discretization mesh.

Table 2. Soil parameters at Mapleton (Harraz et al. 2005).

Parameter	Values
ϕ°	42
ψ°	42
c (kPa)	23.85
E (kPa)	1.0×10^5
$\gamma(\text{kN/m}^3)$	19.6
k	1.0
f	1.0
L (m)	3.9

Baladi, 1985). Friction elements with a coefficient of friction, f , were used to represent the interaction between the soil and the shaft. Harraz et al (2005) developed the best soil set to fit this real field load-displacement curve as shown in Table 2 using in situ and laboratory data as well as FEM. Where, ϕ = soil angle of internal friction, Ψ = soil dilation, c = soil cohesion, E = soil modulus, γ = soil unit weight, k = initial coefficient of lateral earth pressure at rest, f = coefficient of friction between soil and shaft, L = shaft length. The finite element results showed also that the initial coefficient of lateral earth pressure, k , soil Poisson's ratio, ν , and concrete shaft modulus have neglect effect on the skin friction values. (Harraz et al. 2005)

6.3 Stochastic model

A sensitivity analyses performed by the authors using STRUREL showed that the soil cohesion, c , and soil

Table 3. Reduced stochastic model.

Random variable	Units	Probability distribution	Mean	Coefficient of variation
ϕ	degree	Normal	42	0.25
Ψ	degree	Normal	42	0.25
E	kPa	Normal	1×10^5	0.25
γ	kN/m ³	Normal	19.6	0.20
L	meter	Normal	3.9	0.10
c	kPa	Constant	23.85	—
f	—	Constant	1.0	—

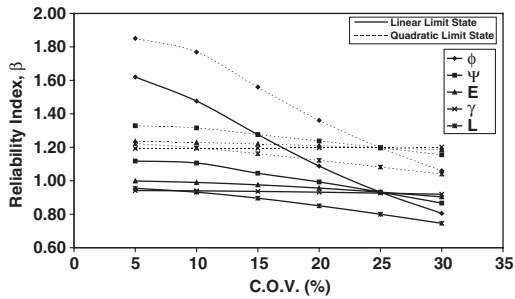


Figure 2. Effect of coefficient of variation of all variables on system reliability.

shaft friction, f , have the lowest normalized sensitivity factors in the model. This implies that we need to consider these two random variables as constants. Table 3 shows the reduced stochastic model. Random variables are assumed to be uncorrelated.

6.4 Discussion of results

Two limit states were developed for shaft bearing capacity and settlement. Linear and quadratic functions were used for each limit state. A parametric study was performed using STRUREL to study the change of coefficient of variation of each variable on the system reliability indices and probability of failures. Figures 2, 3 show the effect of the basic random variables on the system reliability and probability of failure; respectively, for both the linear and quadratic limit states. It can be seen that the effect of nonlinearity is considerable. Moreover, the effect of the variability of ϕ is larger than the effect of the variability of any other random variable. That is due to the high sensitivity of the reliability with respect to ϕ in comparison with the other variables. Figures 4–8 show the effect of the variability of ϕ , Ψ , E, γ , and L; respectively, on the partial safety factors of the basic random variables using target reliability equals to 3.8. Generally, the increase of the variability of a random variable results in decrease of its partial safety factor and increase in the partial safety factors of the other variables.

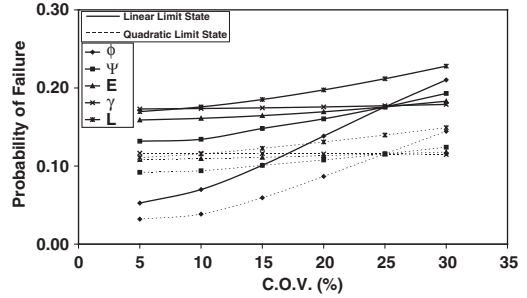


Figure 3. Effect of coefficient of variation of all variables on system probability of failure.

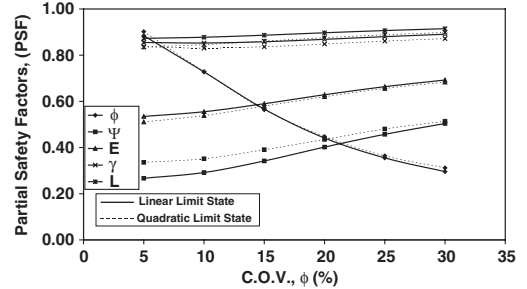


Figure 4. Effect of coefficient of variation of ϕ on System PSF.

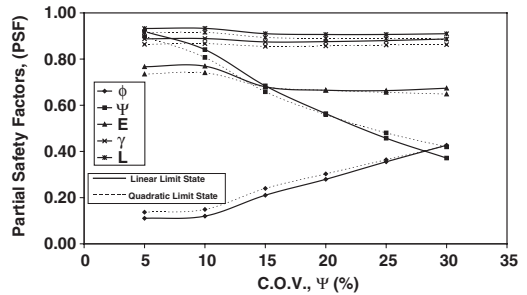


Figure 5. Effect of coefficient of variation of Ψ on system PSF.

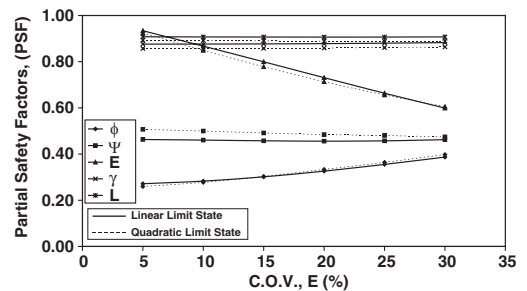


Figure 6. Effect of coefficient of variation of E on system PSF.

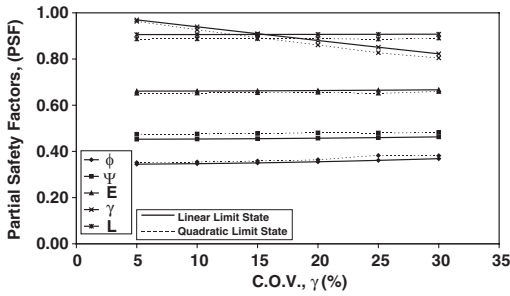


Figure 7. Effect of coefficient of variation of γ on system PSF.

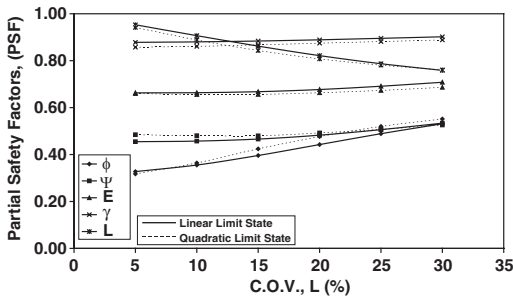


Figure 8. Effect of coefficient of variation of L on system PSF.

Table 4. Partial safety factors ($\beta_T = 3.8$).

Variable	Partial safety factors	
	Linear limit state	Quadratic limit state
ϕ	0.36	0.36
Ψ	0.46	0.48
E	0.66	0.66
γ	0.88	0.86
L	0.91	0.89

Table 4 shows the partial safety factors for each variable for linear and quadratic limit states functions. From Table 4, it is clearly shown that ϕ and Ψ play the most important role in system reliability of skin friction drilled shaft foundations in gravelly soils.

7 CONCLUSIONS

An algorithm has been proposed for the system reliability assessment of skin friction drilled shaft foundations in gravelly soils. The algorithm enables the inclusion of the probabilistic concept in soil mechanics and foundation codes of practice. The large number of random

variables, which can be prohibitively expensive, is reduced based on the normalized sensitivity of the variables. The partial safety factors required for the codified design of friction shafts are determined according to the target reliability levels recommended by EUROCODE. The partial safety factors are determined corresponding to the system failure. It is found that the soil angle of internal friction, soil dilation, and soil modulus are the most important random variables. The results and findings in this paper are only related to the considered example. Generalization of the results requires more intensive work. More intensive research and data collection are required to determine the most appropriate stochastic models for the important random variables.

REFERENCES

- AASHTO 1998. *AASHTO LRFD Bridge Design Specifications*. American Association of State Highway and Transportation Officials, Washington, D. C., 2nd edition.
- ABAQUS/Standard User's Manual 1998. (Version 5.8), Computer Software. Hibbit, Karlsson, & Sorensen, Inc, 1998.
- Chen, W. F & Baladi, G.Y. 1985. *Soil Plasticity: Theory and Implementation*. Published by Elsevier, New York.
- Ditlevsen, O. 1979. Narrow Reliability Bounds for Structural Systems. *Journal of Structural Mechanics*, vol. 7, No. 4: 453–472.
- El-Meligy, M. & Rackwitz, R. 1998. On a Reliability-Based Approach for Design of Shallow Foundations. *Proceeding of the 3rd International Conference On Computational Stochastic Mechanics*, Santorini, Greece, 14–17 June 1998, 575–583.
- El-Meligy, M. & Abdelatif, S. 1999. Probabilistic Analysis of Piles: An Insight into Partial Safety Factors. *Proceeding of the 3rd International Conference on Civil and Architecture Engineering*, Military Technical College, Cairo, Egypt, 9–11 March, 1999, GT3.
- El-Meligy, M. 2002. System Reliability Assessment of Cantilever Retaining Walls. *Proceeding of the 2nd International Conference on Geotechnical and Geoenvironmental Engineering in Arid Lands*, King Saud University, Riyadh, Saudi Arabia, GEO2002, 6–9 October, 2002.
- EUROCODE 1. 1991. *European Committee for Standardization*.
- Harraz, A.M., El-Meligy, M. & Dif A. 1998. Reliability Analysis of Tunnels. *Alexandria Engineering Journal*, vol. 37, no. 6: C135–C144.
- Harraz, A.M., Houston, W.N., Walsh, K.D., Perry, C. & Houston, S.L. 2005. Comparison of Measured and Predicted Skin Friction Values for Axially Loaded Drilled Shaft Foundations in Gravelly Soils. *Proceeding of the Geo-Frontier 2005, the Geo-Institute Conference on Geotechnical Engineering Applications*, Austin, Texas, January 24–26.
- Harraz, A.M., Houston, W.N., Houston, S.L. & Walsh, K.D. 2005. Parameters Controlling the Capacity of Axially Loaded Drilled Shaft Foundations in Sand, Gravel, and

- Cobbles. Proceeding of the 16th International conference of Geomechanics, Osaka, Japan, September 12–15, 1987–1991.
- Hohenbichler, M., and Rackwitz, R. 1981. Non-Normal Dependent Vectors in Structural Safety. *Journal of Engineering Mechanics*, ASCE, vol. 107, no. 6, 1227–1249.
- Hohenbichler, M., Gollwitzer, S., Kruse, W. and Rackwitz, R. 1987. New Light on First- and Second-Order Reliability Methods. *Structural Safety*, vol. 4, 267–284.
- Kulhawy, F.H. 1991. *Drilled Shaft Foundations*, *Foundation Engineering Handbook*. 2nd (ed). Edited by H.Y. Fang, Van Nostrand Reinhold, New York, NY.
- Meyerhoff, G.C. 1976. Bearing Capacity and Settlement of Pile Foundations, *Journal of the Geotechnical Engineering Division*, vol. 102, No. GT3, March 1976, 197–228.
- Rackwitz, R. & Fiessler, B. 1987. Structural Reliability under Combined Random Load Sequences. *Computer & Structure*, vol. 9, 484–494.
- Rangannathan, R. 1990. Reliability Analysis and Design of Structures. 1st (ed), Tata Mcgraw-Hill Publishing Company Limited, New Delhi.
- Reese, L.C., & O'Neill, M.W. 1989. New Design Method For Drilled Shafts From Common Soil and Rock Tests. *Foundation Engineering: Current Principles and Practices*, ASCE, vol. 2, June 1989.
- Rollins, K.M., Clayton, R.J., Mikesell, R.C., & Blaise, B.C. 1997. *Drilled Shaft Side Friction in Gravelly Soils*. Report No. UT-90.02, January 1997.
- STRUREL 1997. *A Structural Reliability Analysis Program System*, Users Manual, RCP GmbH, Munich, Germany.
- Tomlinson, M.J. 2001. *Foundation Design and Construction*. 7th (ed), Prentice Hall, London.
- Vanmarcke, E.H. 1977. Probabilistic Modeling of Soil Profiles. *Journal Geotechnical Engineering Division*, ASCE, vol. 103, no. GT11, November, 1977, 1227–1246.
- Walsh, K.D., Houston, W.N., Houston, S.L., Harraz, A. & Perry, C. 2002. Drilled Shaft Bridge Foundation Design Parameters and Procedures for Bearing in SGC Soils *Interim Report for Project No. KR001870TRN*, Arizona, USA.

Artificial intelligence

A neural network equivalent of hardening soil model of PLAXIS

S.I. Drakos & G.N. Pande

Centre for Civil & Computational Engineering, Swansea University, Swansea

ABSTRACT: This paper presents a Neural Network based Constitutive Model (NNCM), which is an equivalent of the Hardening Soil Model (HSM) available in the commercial software PLAXIS. The primary aim is to study the feasibility of developing a User Defined material module from the raw experimental data obtained from testing of soils. Instead of using real triaxial test data for any particular soil, synthetic data were generated by choosing a set of parameters, typical of sands, for the HSM. The technique of data enrichment proposed by Shin & Pande (2002) was adopted to obtain a good performance of the NNCM. To model a realistic behaviour of soils under different loading/unloading/reloading conditions, the length of strain trajectory in strain space, ξ , has been introduced as an independent input parameter. Four different stress paths in triaxial space were used for training. Two geotechnical problems, viz. a foundation and an excavation were analysed using the HSM. The stress paths at some typical points in these structures were predicted using the trained NNCM and compared with that obtained from the HSM. Good agreement was found. A secondary aim of the study was to check if NNCM equivalents of complex constitutive models were computationally more efficient than the original models. This aim, however, could not be achieved in this study due to lack of time.

1 INTRODUCTION

Appropriate constitutive models of soils are the key to a successful prediction of the behaviour of geotechnical structures. A large number of models based on various constitutive theories have been proposed in the last three decades. All of them assume a-priori, a mathematical framework of the model and the material parameters corresponding to the assumed framework have to be identified from physical material tests. Many material parameters in complex constitutive theories have no physical meaning, are difficult to determine and have to be identified by trial and error from numerical simulations.

Neural Network based Constitutive Models (NNCMs) do not require a-priori stipulation of any mathematical framework. They also do not require identification of any material parameters, although desired material parameters can be identified from virtual tests on the trained NNCM [Shin & Pande, 2003]. NNCMs simply learn the complex relationship between stresses and strains from the physical test data presented to it for training. Following the pioneering work of Ghaboussi and his co-workers (1998), Shin & Pande (2000) have shown that the NNCMs can also be trained from the monitored load-displacement response of 'structures' having non-uniform field of stress and strain. Monitored response may be from a test on an arbitrarily shaped specimen with known boundary conditions in an

experimental configuration or may be from a field or in-situ test. In either case, trained NNCMs can be interrogated to obtain material parameters, if required. Such NNCMs embedded in a finite element code are also the basis of 'self-learning finite element' procedures, proposed by Shin & Pande (2000) and Pande & Shin (2002). There are, thus, distinct advantages in adopting NNCMs for the analysis and design of geotechnical structures.

The triaxial tests data of soils do not contain information relating to shear stress-shear strain response explicitly. To overcome this, Shin & Pande (2002) used a data enrichment scheme which involved transformation of test data (stresses & strains) along arbitrarily rotated axes to generate shear stress – shear strain response. This scheme has been used here and found to be effective. In the previous research papers, NNCMs have been developed for geomaterials under monotonic loading only. Apart from problems of cyclic and transient loading, unloading and reloading can take place even in a quazi-static geotechnical problem. To account for this, in this paper, a new input parameter, viz. the length of strain trajectory, ξ , has been introduced. This parameter, is called 'intrinsic time' and has previously been used in 'endochronic' theories of material behaviour proposed by Valanis (1982) and his co-workers and Bazant (1982) and his co-workers. Results of the study indicate much improved predictions of stress-strain response under loading re-loading conditions in practical problems from NNCMs trained from synthetic data.

2 NEURAL NETWORK BASED CONSTITUTIVE MODEL

2.1 Neural network based constitutive model methodology and architecture

A neural network is composed of causes (inputs), the hidden layer and the effects (outputs). The aim of neural network training is to find out the complex relationship between the causes and the effects. A neural network can be used to simulate stress-strain response of any material by using appropriate data. In this case, the components of strain become the causes whilst the resulting stresses are the effects. Description of stress-strain behaviour by a NNCM does not require checking for plastic flow, computation of flow vector, updating and reconstitution tangential stress integration matrix. Full details are contained in the publications of the senior author and his co-workers. Here a brief description will be given for completeness and continuity.

Total (as distinct from incremental) stress vector can be computed from the corresponding strain vector as follow:

$$\sigma = \text{NNCM}(\varepsilon) \quad (1)$$

Where:

$$\varepsilon = \{\varepsilon_x, \varepsilon_y, \varepsilon_z, \gamma_{xy}, \gamma_{yz}, \gamma_{xz}\} \quad (2)$$

$$\sigma = \{\sigma_x, \sigma_y, \sigma_z, \tau_{xy}, \tau_{yz}, \tau_{xz}\} \quad (3)$$

Here, NNCM stands for a neural network trained from stress-strain data. Alternatively, a NNCM can be trained with pairs of incremental strain and incremental stress data at various stress levels.

In many geotechnical problems, soils are subjected to cyclic and transient loads. Even in quasi-static problems many elements are subjected to unloading and reloading. For constitutive models to be valid, in such situations, it is proposed to adopt 'intrinsic time' (Bazant, 1982, Valanis, 1982) or length of strain trajectory, ξ , as an independent input parameter. Mathematically, ξ , is defined as follows:

$$\xi = \int d\xi \quad (4)$$

Where, $d\xi$ is an increment of deviatoric strain defined as

$$d\xi = d\varepsilon_{ij} - \delta_{ij} \varepsilon_{kk} \quad (5)$$

Intrinsic time, ξ , is a monotonically increasing positive parameter. The above definition can be changed to include volumetric strain as well as real time.

The NNCM adopted in this paper has strain increments, stresses and 'intrinsic time' as the input variables. Increments of stress are the output variables. For two-dimensional analyses, the optimal architecture of the NN is presented in figure 1. It is constituted by 9 input nodes two hidden layer of 18 and 8 nodes respectively and 4 output nodes. In order to train the neural network the resilient backpropagation (RPROP) algorithm is used. RPROP was first proposed by Reidmiller (1993) and implemented by Shin (2001). It is a local adaptive learning scheme based on the standard backpropagation framework.

2.2 Data enrichment

The strain-stress pairs from the triaxial tests are actually principal stresses and strains since no shear stresses/strains are involved. If such data were used for training, NNCM will have to extrapolate wherever shear stress/strain components are involved. This will lead to large inaccuracies in stress-strain response of the NNCM.

To overcome this limitation, Shin & Pande (2002) proposed a data enrichment strategy. They created additional data by transformation of stress and strain in which the shear components will naturally be non-zero. In the two dimensional case, the transformation of a principal stress vector by an angle θ measured anticlockwise from the X axis is as follows:

$$\sigma_x = A + B \cos(2\theta) \quad (6)$$

$$\sigma_y = A - B \cos(2\theta) \quad (7)$$

$$\tau_{xy} = B \sin(2\theta) \quad (8)$$

Where:

$$A = 0.5(\sigma_1 + \sigma_2) \quad (9)$$

$$B = 0.5(\sigma_1 - \sigma_2) \quad (10)$$

For strains

$$\varepsilon_x = C + D \cos(2\theta) \quad (11)$$

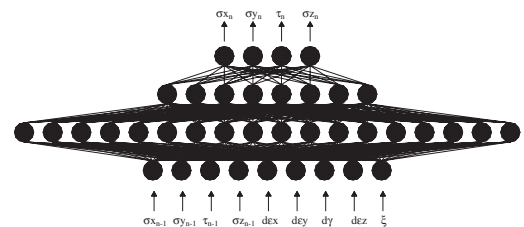


Figure 1. Architecture of NNCM [9-18-8-4] for two-dimensional analysis.

$$\varepsilon_y = C - D \cos(2\theta) \quad (12)$$

$$\gamma_{xy} = 2D \sin(2\theta) \quad (13)$$

Where:

$$C = 0.5(\varepsilon_1 + \varepsilon_2) \quad (14)$$

$$D = 0.5(\varepsilon_1 - \varepsilon_2) \quad (15)$$

This method produces a large amount of training data depending on the number of transformations chosen to generate data. Among the expanded data there are many duplicated strain-stress pairs so an additional process of 'data pruning' is adopted. In this paper an incremental angle, $\Delta\theta$ equal to 5° was used in order to rotate the strain-stress axes from -45° to $+45^\circ$.

3 TRIAXIAL TEST SIMULATION

3.1 Data generation

As stated in the abstract of the paper, the main goal of this research is to study the feasibility of developing User Defined models based on experimental data. However, in place of using real experimental data for any material, we have chosen to generate data (these are termed as 'synthetic' data) from the well known constitutive model, the Hardening Soil model available in the commercially available software, PLAXIS. For this purpose typical parameters for sand have been arbitrarily chosen and are shown in Table 1. For the definition of various variables, the reader should refer to PLAXIS software manuals.

The triaxial test paths corresponding to conditions of Loading in Compression (LC), Loading in Extension (LE), Unloading in Compression (UC) and Unloading in Extension (UE) have been simulated under stress controlled drained conditions using PLAXIS software with HSM. These stress paths, in deviatoric stress, q , and effective mean stress, p' , space are shown in figure 2. Three different confining pressures of 50, 100 and

150 kPa were used for each of the above stress paths. In engineering practice, if such test data were available for a soil, one would perhaps term them as 'extensive'. These stress-strain data obtained from these simulations were then used for training the NNCM.

Plots of q versus axial strain, ε_{yy} , as predicted by the trained NNCM and the original HSM data used for training, for various stress paths are shown in figures 3 and 4. An excellent match is seen confirming

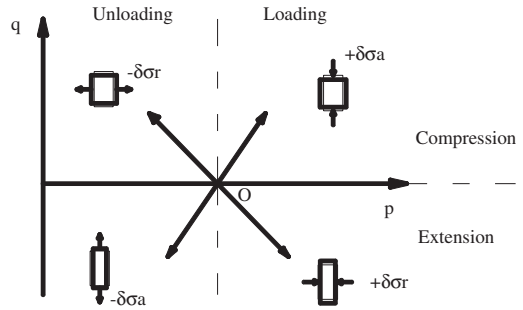


Figure 2. Stress paths in $q - p'$ space used for generating synthetic data.

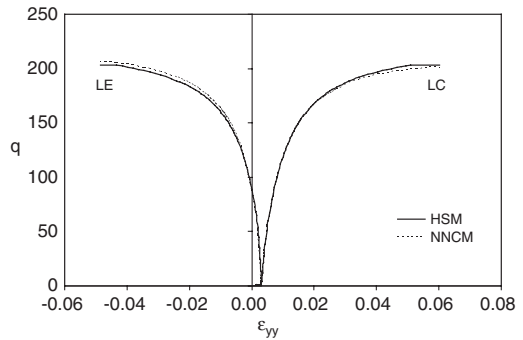


Figure 3. Graph of q versus ε_{yy} under LC and LE conditions for a confining pressure of 100 kPa.

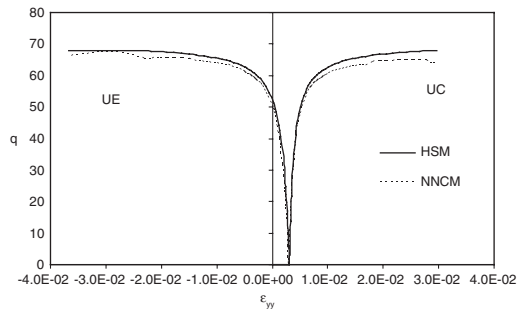


Figure 4. Graph of q versus ε_{yy} under UC and UE conditions for a confining pressure of 100 kPa.

Table 1. Arbitrary sand parameters.

E_{50}^{ref} (for $p_{ref} = 100$)	20000
E_{ur}^{ref} (for $p_{ref} = 100$)	60000
E_{oed}^{ref} (for $p_{ref} = 100$)	20000
Cohesion c'	0.0
Friction angle φ'	30
Dilatancy angle ψ	0
Poisson ratio ν	0.2
Power m	0.5
K_0^0	0.5
Tensile strength	0
Failure ratio	0.9

that NNCM has been adequately trained. This, however, is not surprising since prediction of response is made for the confining pressure which was also used in training data. We need to check if the response at confining pressures within the training range as well as outside that used in training is also reasonable. This issue is discussed in the next section of the paper.

4 MODEL VALIDATION

In the part of the paper, we present the prediction of the trained NNCM for two additional triaxial tests with confining pressures of 10 & 200 kPa which are out of the range of the training data. For these tests the predictions of the NNCM were poor. NNCM was then re-trained using additional data generated for the four stress paths described earlier and for confining pressures of 1 kPa and 200 kPa. The graphs of q versus ϵ_{yy} are presented in the figures 5 and 6 for the HSM, trained and re-trained NNCMs. This confirms that extrapolation by NNCM is always of poorer quality than interpolation, Pande & Shin (2004).

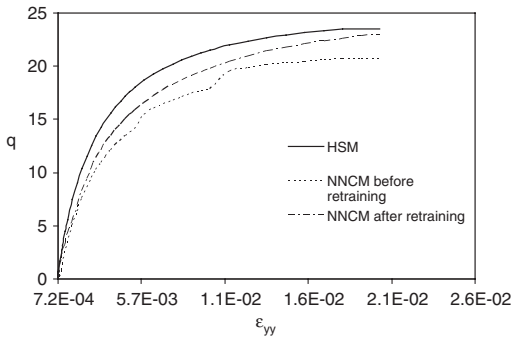


Figure 5. Graph of q versus ϵ_{yy} under LC conditions for a confining pressure of 10 kPa.

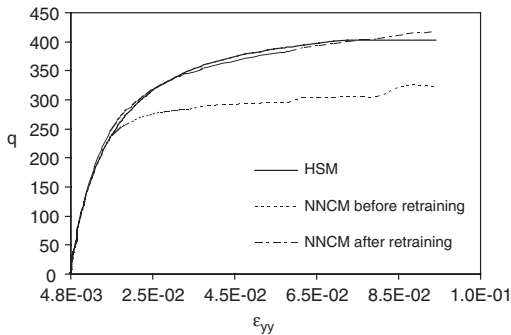


Figure 6. Graph of q versus ϵ_{yy} under LC conditions for a confining pressure of 200 kPa.

5 NUMERICAL EXAMPLES

The stress paths imposed in real problems are obviously different from those under the aforementioned four stress paths. The aim of this section is to compare NNMC and HSM predictions in typical geotechnical problems. For this purpose, we have chosen two

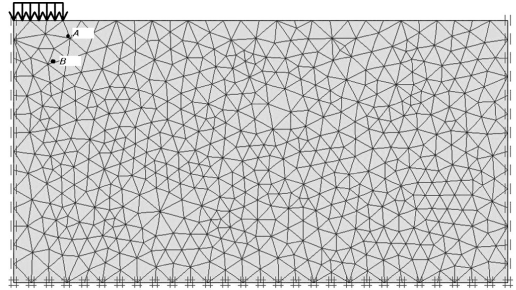


Figure 7. Geometry and monitoring points of the foundation problem.

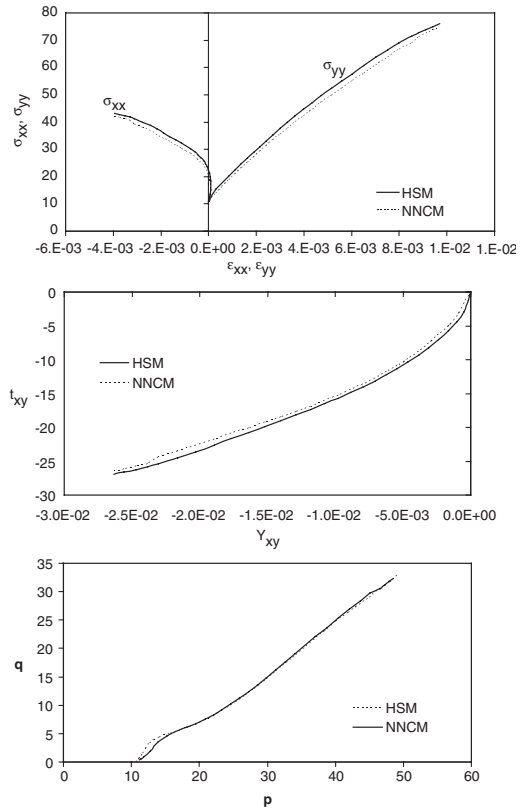


Figure 8. Various stress paths at point A in foundation problem.

examples. In the first example a foundation problem has been considered whilst in the second a problem of excavation has been studied. The soil parameters for a both problems are taken from table 1. PLAXIS FE code has been used in order to solve the above geotechnical problems. Plane strain and drained condition was assumed for the calculations.

5.1 Foundation problem

In figure 7 the geometry of the foundation problem is presented. Six node triangular isoparametric elements have been used for the analysis. A uniform load of 150 kPa has been incrementally applied and the resulting strain–stress curves at two monitoring points, A & B, marked on the figure, for NNCM and HSM are shown in figures 8 and 9.

5.2 Excavation problem

In this example, analysis of a 10 m × 4 m deep excavation behind a sheet piled wall was carried out in one

stage. After the calculation for the initial conditions, excavation load is applied. The geometry of the problem and the locations of monitoring points are presented in figure 10. As mentioned earlier, three confinement pressures were initially used to generate data for the training of the NNCM. If this NNCM is used for the prediction of stresses corresponding to

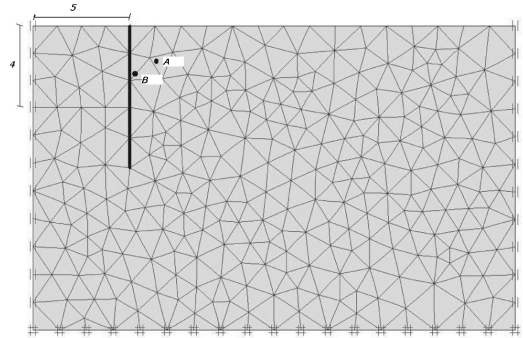


Figure 10. Geometry and monitoring points of the retaining problem.

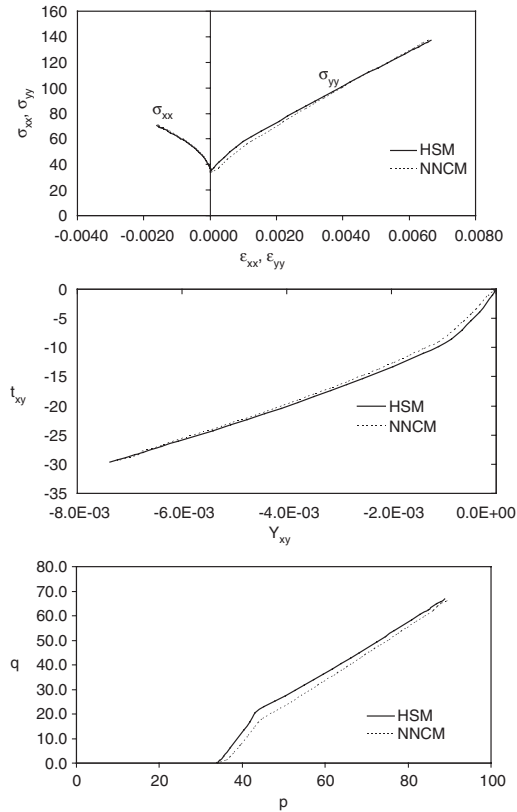


Figure 9. Various stress paths at point B in foundation problem.

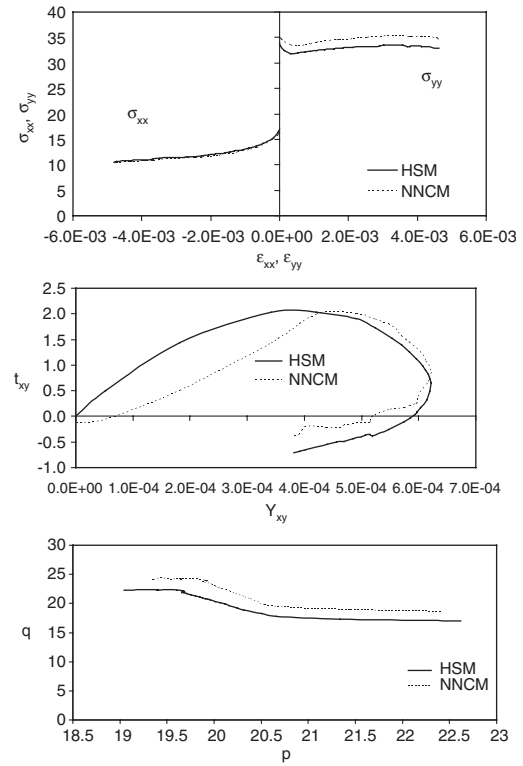


Figure 11. Various stress paths at point A in excavation problem.

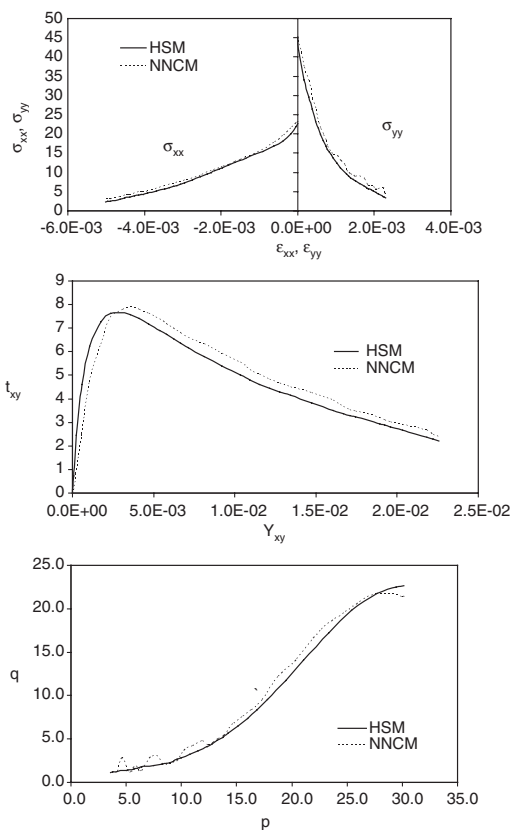


Figure 12. Various stress paths at point B in excavation problem.

the strains at monitoring point A, predictions were found to be inaccurate. However, when the NNCM trained with five sets of confining pressure data was used, accurate response corresponding closely to HSM was obtained, see figure 11 & figure 12. The reason for this is obvious. In the excavation problem, at some points, the confining pressure is small. The initially trained NNCM had to extrapolate the response at low confining pressures whilst after re-training with five sets of pre-consolidation pressures, it had only interpolate or extrapolate only in a small zone beyond the data used in its training.

6 CONCLUSIONS

In this paper, a Neural Network based Constitutive Model which is an equivalent to the Hardening Soil Model of PLAXIS has been presented. Four triaxial

stress paths with five initial confining pressures were used to generate synthetic data. The performance of the NNCM has been validated against stress paths experienced by some critical points in typical problems of foundations and excavation. It is expected that in the near future, the analyst would be able to develop a constitutive model based on experimental data, without invoking a constitutive theory and need for identification of material parameters. Need for engineering judgment in selection of appropriate data will, however, be a paramount factor.

REFERENCES

- Bazant, Z. P., Ansal, A. M. & Krizek, R. J., Endochronic models for soils, Chapter 15, *Soil Mechanics – Transient & Cyclic Loads*, Edited by G. N. Pande & O. C. Zienkiewicz, J. Wiley & Sons, 1982.
- Ghaboussi J., Pecknold D. A., Zhang M., Haj-Ali R. M., Auto progressive Training Of Neural Network Constitutive Models. *Int. J. Numer. Meth. Engng.* 1998; 42: 105–126.
- Pande, G. N. & Shin, H.S., Artificial intelligence v. equations, *Proceedings of Institute of Civil Engineers*, Vol. 156, pp 39–42, 2004.
- Pande, G. N. & Shin H.S., Finite element with artificial intelligence, *Proceeding of The Eighth International Symposium on Numerical Models in Geomechanics (NUMOG VIII)*, edited by G.N. Pande & S. Pietruszczak, Rome, Italy, April 2002, pp. 241–246.
- Riedmiller, M. & Braun, H. (1993), A direct adaptive method for faster backpropagation learning: the RPROP algorithm, *Proceedings of the IEEE, International Conference on Neural Networks*, San Francisco, CA, March 28–April 1.
- Shin, H.S. & Pande, G.N., Identification of elastic constants of orthotropic materials from structural test, *Computers and Geotechnics*, Vol 30, pp. 571–577, 2003.
- Shin, H.S. & Pande, Enhancement of data for training neural network based constitutive models for geomaterials, *Proceeding of The Eighth International Symposium on Numerical Models in Geomechanics (NUMOG VIII)*, edited by G.N. Pande & S. Pietruszczak, Rome, Italy, April 2002, pp. 141–146.
- Shin, H.S. & Pande, Intelligent finite elements in masonry research, *Proceeding of International Symposium on Computer Methods in Structural Masonry (STRUMAS V)*, edited by T.G. Hughes & G.N. Pande, Rome, Italy, 2001, pp. 221–230.
- Shin H.S. Neural Network Based Constitutive Models for Finite Element Analysis. 2001, Ph. D. thesis, Department of Civil Engineering, University of Wales Swansea.
- Shin, H.S. & Pande, On self-learning finite element codes based on monitored response of structures, *Computers and Geotechnics*, Vol. 27, pp. 161–178, 2000.
- Valanis, K.C. & Read, H. E., A new endochronic plasticity model for soils, Chapter 14, *Soil Mechanics-Transient & Cyclic Loads*, Edited by G. N.Pande & O. C. Zienkiewicz, J. Wiley & Sons, 1982.

Application of artificial neural networks in solving inversion problem of surface wave method

T. Akhlaghi

University of Tabriz, Tabriz, Iran

ABSTRACT: Surface wave method is an in-situ nondestructive testing procedure for estimation of elastic moduli and layers thicknesses of layered structures such as pavements and natural soil deposits. In this research “*Matlab*” has been employed for applying artificial neural networks in solving inversion problem of surface wave test dispersion curve and estimating the soil profile. Multi layer neural networks along with back propagation training procedure are used to carry out the required inversion process. The networks are trained using the Steepest Descent Gradient Algorithm, Conjugate Gradient Algorithm and Levenberg–Marquardt Algorithm. Eight training functions have been employed and assessed in three, four and five layer networks. The most optimized network with the least error rate and iteration number for convergence was selected and tested for certainty. By employing the selected optimum network, a number of real cases have been studied and the results obtained have been compared with the available actual data. The results show very good match indicating that the selected back propagation neural network is capable of providing a useful tool for carrying out the inversion process of surface wave method.

1 INTRODUCTION

The surface wave method is a new nondestructive seismic technique for in-situ evaluation of elastic moduli and layers thicknesses of layered systems such as pavements and natural soil deposits. The method is based on the dispersive characteristics of surface (Rayleigh) waves in layered media, i.e., waves of different wavelengths propagate with different velocities. The methodology of the surface wave test is simple and has the potential to be fully automated.

The procedure for conducting the surface wave method, which is referred to as spectral analysis of surface wave method by some researchers, can be divided into three phases: (1) data collection in the field; (2) evaluation and construction of the experimental dispersion curve; and (3) inversion of the dispersion curve for determining the stiffness profile of the system. Elastic waves are generated by an impact source on the surface of the system, detected by a pair of receivers, and recorded by an appropriate transient recording device. Figure 1 shows a schematic diagram of the surface wave testing setup. The dispersion curve for a single receiver spacing is obtained from the relationships for phase velocity and wavelength for an arbitrary frequency component. The test is repeated for several receiver spacings to cover a broad range of wavelengths and in two directions to

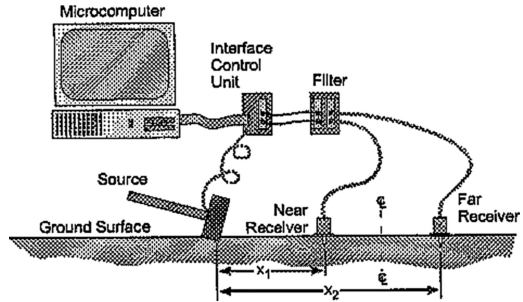


Figure 1. Schematic diagram of surface wave test setup.

minimize the effects of dipping layers and the internal phase of the instrumentation. The dispersion curves for all receiver spacings and two directions are fully filtered and statically combined to derive an average dispersion curve for the system.

The objective of the surface wave method is to obtain the experimental dispersion curve that describes the relationship between the velocity of wave propagation (phase velocity) and wavelength (or frequency). Then, through an inversion process, the profile of the layers stiffness and thickness of the layered system is obtained. Typical results of the field measurements are shown in Figure 2. Determination of the dispersion curve is

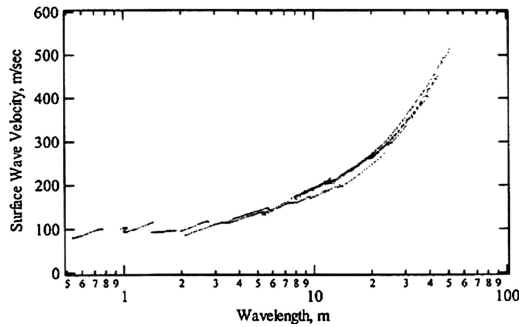


Figure 2. Typical results of surface wave field measurements.

a simple and mostly automated task. The inversion process, however, is complex. Most of the inverse techniques developed thus far are based on numerical methods. These methods are almost time-consuming and greatly dependent on the experience of the user. Also the inversion process has been automated for special conditions only, such as pavements and soil profiles where the shear modulus increases with depth. There is a need to develop methods for efficient inversion of the dispersion curve under general conditions.

This paper describes the application of neural networks to perform the inversion process for surface wave method using “*Matlab*” program. Various back propagation and general regression neural network models were studied. These models accept a description of the dispersion curve as input, and provide the results as output ratios describing the stiffnesses and layers thicknesses of the system.

2 ARTIFICIAL NEURAL NETWORKS

Artificial neural networks are biologically inspired analogues of the human brain. They are composed of many operationally simple but highly interconnected processing units. The processing units themselves have certain functional similarities to biological neurons, and their organization bears at least superficial resemblance to the organization of neurons in the brain.

The type of calculation performed by a neural network is determined by the architecture of the network. The most common architecture used for mapping, classification and forecasting is the multi-layer, feed-forward network (Hecht-Nielsen 1989). These networks consist of several layers of processing elements. The processing elements pass information in the form of signal patterns from the input layer of the network through a series of hidden layers to the output layer. The signals travel along connections whose strengths are adjusted to amplify or attenuate the signal as it

propagates through the network. Each processing element sums the signals arriving at its inputs from the previous layer, performs a nonlinear transformation on the collective signal, and passes the transformed signal on to each of the processing elements in the succeeding layer. Thus, the output signal pattern that results from a given input signal pattern is uniquely determined by the distribution of connection strengths throughout the network. In that respect, the “knowledge” contained in the network is stored as the connection strengths.

The neural network gains its knowledge through training. Training of feed-forward networks is commonly accomplished using a supervised learning method. In supervised learning, a set of training examples (consisting of input-output pairs) is iteratively presented to the network. The input signals are propagated through the network, and the resulting outputs are compared to the target outputs. A learning algorithm is employed to adjust the connection strengths so as to minimize the differences between the calculated and target outputs.

The back propagation learning algorithm has become the de facto standard for training multi-layer, feed-forward networks. After each training example is presented to the network, the differences between the calculated and target output patterns are computed and propagated backwards through the network using the existing network connection strengths. The individual connection strengths are then adjusted in the direction that reduces the error apportioned to them. If training is successful, after many iterations (using training examples each time or reusing a limited set of training examples in a different order), the connection strengths attain values that globally minimize the output error (commonly expressed as the root mean square or arithmetic mean) for all inputs.

3 NEURAL NETWORK TRAINING

Back propagation and general regression neural network models are trained using a training set. This training set consists of training patterns, each of which is a data pattern consisting of input variables and correct output variables. The inputs in these models are the dispersion curves data. The dispersion curves used to instruct the neural networks are synthetic dispersion curves constructed using the exact dynamic stiffness matrix method developed by Kausel & Roesset (1981) and computerized by Manochehri (2003).

The dispersion curves in the training set can be defined either in terms of dimensionless velocity versus dimensionless frequency or dimensionless velocity versus dimensionless wavelength. The dimensionless values of the parameters are used to enable application of the database to a much wider range of soil profiles. The

Layer No.	Thickness	Shear wave velocity (Ground surface)	Mass density	Poisson's ratio
1	d_1	V_{S1}	ρ_1	ν_1
2	d_2	V_{S2}	ρ_2	ν_2
3	d_3	V_{S3}	ρ_3	ν_3
4	∞	V_{S4}	ρ_4	ν_4

Figure 3. Idealized soil profile and layers parameters.

dimensionless velocity and dimensionless wavelength are respectively given by the following relations:

$$V'_{phase} = V_{phase} / V_{S1} \quad (1)$$

$$\lambda'_{phase} = \lambda_{phase} / d_1 \quad (2)$$

where V_{S1} and d_1 are the shear wave velocity and thickness of the surface layer, V_{phase} and λ_{phase} are phase velocity and corresponding wavelength in the dispersion curve, respectively.

The training data considered contain a four-stratum soil profile, as shown in Figure 3. One hundred nineteen training cases were developed each with 76 inputs. All the curves are defined for the same set of 76 dimensionless pair of data (dimensionless wavelength-dimensionless shear wave velocity) in the range from 5–20 with step of 0.2 for the dimensionless wavelength.

The effects of mass density and Poisson's ratio on the dispersion characteristics of surface waves are small. Nazarian & Stokoe (1984) has shown numerically that the effects of these two parameters, in most practical cases, are less than 5%. Therefore, to simplify the inversion process, it is assumed that mass density and Poisson's ratio for each layer are known parameters. Reasonable values are assigned to these parameters based upon past experience. In the present work, these parameters have been assumed to be $\nu = 0.4$ and $\rho = 2000 \text{ kg/m}^3$. Also shown in Table 1 are the various values required for each of the five output parameters used in the construction of the corresponding dispersion curve of the given soil profile.

The corresponding output for each training case is the soil profile. This profile is described by two thickness ratios, d_2/d_1 and d_3/d_1 , and three shear wave velocity ratios, V_{S2}/V_{S1} , V_{S3}/V_{S1} and V_{S4}/V_{S1} . The training sets were developed so that the dispersion curves matched various combinations of these output parameters. Implementation of the neural network in the field for backcalculation of the soil profile using the surface wave method requires the thickness and the shear wave velocity to be known. The experimental dispersion

Table 1. Output training parameters.

d_2/d_1	d_3/d_1	V_{S2}/V_{S1}	V_{S3}/V_{S1}	V_{S4}/V_{S1}
1.2	1.3	1.2	1.5	2.0
1.4	1.6	1.4	1.8	2.5
1.6	1.9	1.6	2.1	3.0
1.8	2.2	1.8	2.4	3.5
2.0	2.5	2.0	2.7	4.0
2.2	2.8	2.2	3.0	4.5

curve is then normalized according to the relations (1) and (2), and input to the neural network. Finally, the neural network provides output defining the soil profile.

4 BACK PROPAGATION NEURAL NETWORK

A back propagation network is made up of interconnected nodes arranged in at least three layers. The input layer receives the input data patterns, and passes them into the network. The number of input nodes equals the number of input data values. The output layer produces the result. The hidden layers have no direct connection to input or output.

During training, back propagation networks process patterns in a two step procedure. In the first or forward phase of back propagation learning, an input pattern is applied to the network, and the resulting activity is allowed to spread through the network to the output layer. The desired results are then compared to the actual results produced by the network. This comparison results in an error for each node in the output layer. In the second or backward phase, the error from the output layer is propagated back through the network to adjust the interconnection weights between layers. This process is repeated until the network's output is sufficiently accurate. Back propagation learning is this process of adapting the connection weights. After instruction, a back propagation network can process unknown input data. An unknown input pattern can be applied, and the network produces a corresponding pattern at the output.

In this paper, the *Matlab* 6.5 software has been used for development of the network and performance of its training, evaluation and assessment. Normal three-, four- and five-layer back propagation networks were tested. These networks in company with learning algorithms such as Steepest Descent Gradient (SDG) Algorithm, Conjugate Gradient (CG) Algorithm and Levenberg-Marquardt (LM) Algorithm were used to evaluate the training data. To train the networks, a test set of 35 normalized dispersion curve in company with their soil profile were developed and used. After running the program, the error for each case was calculated and the number of neurons in hidden layers

Table 2. Mean squared error for test set.

Model B. P.	Learning algorithm	Training function	Epochs	MSE
3-layer	SDG	<i>traingdx</i>	28750	0.388234
4-layer	SDG	<i>traingdx</i>	21750	0.29405
5-layer	SDG	<i>traingdx</i>	19250	0.25504
3-layer	CG	<i>trainscg</i>	4380	0.099985
4-layer	CG	<i>trainscg</i>	1592	0.099900
5-layer	CG	<i>trainscg</i>	1243	0.099966
3-, 4- and 5-layer	LM	<i>trainlm</i>	-	-

determined. The mean squared error (*MSE*) was used to evaluate the performance of the network due to different number of intermediate neurons (in the hidden layers). Examination of the outputs from the neural network models indicates that these models are capable of matching the dispersion curve inputs with the correct soil profile. The *MSE* is given by the following:

$$MSE = \frac{\sum (A - P)^2}{n} \tag{3}$$

where *A* = actual output value, *P* = output value by the neural network, and *n* = number of cases in the training set.

The lower values of the *MSE* indicate that the neural network is working better. Table 2 shows the *MSE* values for the test set for each model.

Eight instructive functions have been used, including: Batch Gradient Descent (*traingd*), Batch Gradient Descent with Momentum (*traingdm*), Steepest Gradient Descent with Variable Learning Rate (*traingdx*), Fletcher-Reeves Conjugate Gradient (*traincgf*), Polak-Ribiere Conjugate Gradient (*traincgp*), Powell-Beale Conjugate Gradient (*traincgb*), Scaled Conjugate Gradient (*trainscg*) and Levenberg-Marquardt (*trainlm*) algorithms. After instructing the network all instructive algorithms have been assessed in three, four and five layer networks. Among these networks, the most optimized one with the least error rate and iteration number to be converged was studied and investigated. It was noticed that the Scaled Conjugate Gradient (SCG) algorithm is the best and fastest one among the others and therefore this algorithm was selected as the optimum one to be utilized in the network training. Levenberg-Marquardt algorithm was also applied but as the network was so large, the computer confronted with run out of memory. Considering the methods to decrease the memory for algorithm, again computer failed to run the program because of great dimensions of network. Therefore, according to the *Matlab*'s recommendation, the other algorithms were used.

Table 3 compares the results between neural network calculations and the actual examining values for

Table 3. Neural network output parameters' error values.

Test data	d_2/d_1	d_3/d_1	V_{s2}/V_{s1}	V_{s3}/V_{s1}	V_{s4}/V_{s1}
TEST-1	-0.0735	-0.1796	0.1867	-0.0204	-0.0149
TEST-2	0.0235	0.2826	-0.1257	0.0677	-0.0348
TEST-3	-0.1972	0.0583	0.0813	0.0980	-0.0135
TEST-4	0.2445	-1.1585	-0.1320	-0.0154	-0.0463
TEST-5	-0.3148	0.2218	-0.0681	0.3976	-0.014

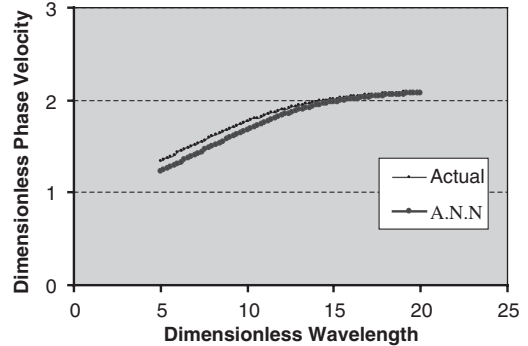


Figure 4. Dispersion curves of neural network results and actual examining data.

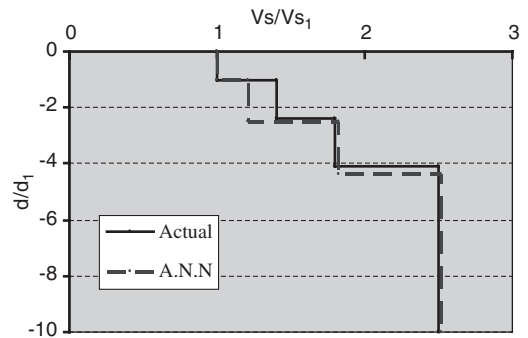


Figure 5. Soil profiles of neural network results and actual examining data.

5 test data. Figures 4 and 5 show artificial neural network's results with actual examining data in the form of dispersion curve and plot of soil profile in 5-layer network (5-90-80-70-119) using Conjugate Gradient algorithm in TEST-1 (for instance).

Figures 6 and 7 also show the trained neural network results in company with actual site dispersion curve and soil profile (for instance).

These dispersion curve and soil profile have been determined using surface wave test and exploration logs conducted at the site. The site is located at Sacarya in Turkey (Rosenblod & Stokoe 1999). As can be seen from the Figures, the agreement between the calculated neural network results and the actual data is reasonably good. This agreement was also

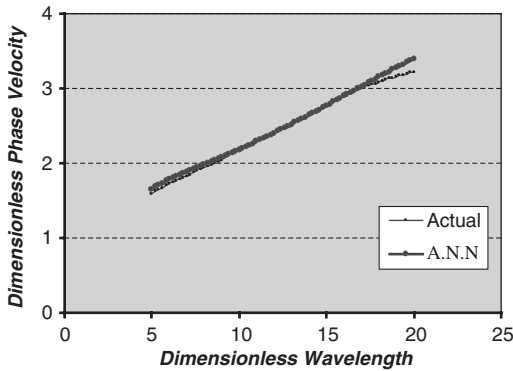


Figure 6. Dispersion curves of neural network results and actual site data.

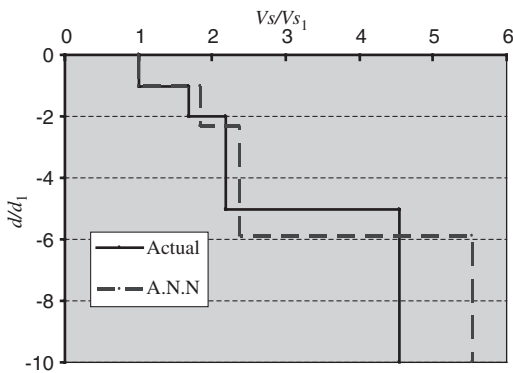


Figure 7. Soil profiles of neural network results and actual site data.

seen in all other cases studied as well. The results indicate that back propagation SCG model with five layers provides good results in analyzing the dispersion data obtained by surface wave method.

5 CONCLUSIONS

Investigations and results on back propagation neural networks show that these networks are capable of estimating the soil profile under study. The networks studied in this research work inverse the surface waves dispersion curve in order to find out the corresponding four-stratum modeled soil profile.

According to the observed results, among applied networks in this study, five layer back propagation network with Scaled Conjugate Gradient (SCG) training algorithm produced the best estimation in accordance with these dispersion curves. Using dispersion curves data obtained from the tests carried out on real sites to

train the neural networks, made it possible to use this method for real sites.

One of disadvantages of neural network methods to inverse dispersion curves is lack of recognition of the soil layer number and it can be removed by training the network according to assumed soil layers. It means that we can not use a trained neural network for four-layer soil system in a five-layer soil profile. In the case of using neural networks for more soil layer profiles, we need to increase the training data suitable with that profile. Increasing the range of problem, network will need to learn more complex points which will in turn lead to bigger networks, and several more examples will be needed to train the network. Also faster training algorithms will be required in order to complete the set of training data within a reasonable period of time.

REFERENCES

- Akhlaghi, T.B. & Cogill, W.H. 1994. Application of the free plate analogy to a single-layered pavement system. *Insight, the Journal of the British Institute of Non-Destructive Testing*, 36(7): 514–518.
- Demuth, H.B. & Beale, M. 2002. *Neural Network Toolbox, user's guide*. Natick, MA: The MathWork, Inc.
- Hecht-Nielsen, R. 1989. *Neurocomputing*, Addison-Wesley, New York.
- Hossain, M.M. & Drenevich, V.P. 1989. Numerical and Optimization Technique Applied to Surface Waves for Backcalculation of the Layered Media, *Nondestructive Testing of Pavements and Backcalculation Moduli, STP 1026*, A.J. Bush and G.Y. Baladi, Eds., ASTM, Philadelphia, 649–669.
- Kartam, N., Flood, I. & Garrett, J.H. 1997. *Artificial Neural Networks for Civil Engineer, Fundamentals and applications*. ASCE, New York, NY.
- Kausel, E. & Roesset, J.M. 1981. Stiffness Matrices for Layered Soils. *Bull. of the Seismological Soc. of America*, 54(1): 431–438.
- Manochehri, A.R. 2003. Investigation of effective parameters on the theoretical dispersion curve in a multi-layer medium. MSc thesis, Urmia University, Urmia, Iran.
- Meier, R.W. & Rix, G.J. 1993. An Initial Study of Surface Wave Inversion Using Artificial Neural Network, *Geotechnical Testing Journal*, 16(4): 425–431.
- Nazarian, S. & Stokoe, K.H. 1984. In Situ Shear Wave Velocity from Spectral Analysis of Surface Waves. *Proc. of The 8th World Conference On Earthquake Engineering*, Vol. 3: 31–38.
- Nazarian, S. & Desai, M.R. 1993. Automated Surface Wave Method: Field Testing. *Journal Of Geotechnical Engineering*, ASCE, 119(7): 1094–1111.
- Rosenblad, B. & Stokoe, K.H. 1999. Shear Wave Velocity Profiling by the SASW Method at Selected Strong-Motion Stations in Turkey. *Second International Conference on Earthquake Geotechnical Engineering*, Lisbon, Portugal.
- Yuan, D. & Nazarian, S. 1993. Automated Surface Wave Method: Inversion Technique. *Journal Of Geotechnical Engineering*, ASCE, 119(7): 1113–1126.

Simulating the seismic response of an embankment using soft computing techniques

E.C. Georgopoulos & Y. Tsompanakis
Technical University of Crete, Greece

N.D. Lagaros & P.N. Psarropoulos
National Technical University of Athens, Greece

ABSTRACT: Geotechnical earthquake engineering can generally be considered as an “imprecise” area due to the unavoidable uncertainties and simplifications. Therefore, relatively accurate predictions, using advanced *Soft Computing (SC) techniques*, can be tolerated rather than solving a problem conventionally. Artificial Neural Networks (ANNs), being one of the most popular SC techniques, have been used in many fields of science and technology, as well as, an increasing number of problems in engineering. In the present study the application of ANNs is focused on the simulation of the seismic response of an embankment. Typically, the dynamic response of an embankment is evaluated utilizing the finite-element method, where nonlinearity of geo-materials can be taken into account by an equivalent-linear procedure. This extremely time-consuming process is replaced by properly trained ANNs.

1 INTRODUCTION

Uncertainties and approximations are inherent in geotechnical earthquake engineering practice. Therefore, realistically accurate approximation methods can be applied very effectively. On the other hand, advances in computational hardware and software resources since the early 90's resulted in the development of new non-conventional data processing and simulation methods. Techniques based on *Metamodels* that belong to Soft Computing (SC) methods are gaining popularity very rapidly lately in various time-consuming, large-scale applications in structural and geotechnical engineering. Among SC methods, Artificial Neural Networks (ANNs) has to be mentioned as one of the most eminent approaches of the so-called intelligent methods of information processing.

From among general problems that can be analyzed by means of ANNs the simulation and identification problems can be classified as follows:

- *simulation* is related to direct methods of structural or geotechnical analysis, i.e., for known inputs (e.g., excitations of mechanical systems (MS)) and characteristics of structures, geo-structures, or materials outputs (responses of MS) are searched;
- *inverse simulation* (partial identification, for example, of an unknown excitation) takes place if inputs

correspond to known responses of MS and excitations are searched as outputs of ANNs; and

- *identification* is associated with the inverse analysis of structures, geo-structures and materials, i.e., excitations and responses are known and MS characteristics are searched.

Over the last decade an increasing number of articles presenting ANN applications in geotechnical earthquake engineering has been published. Most of these studies are focused on liquefaction potential under seismic excitations (Chouicha et al. 1994, Goh 1994, Wang & Rahman 1999, Baziar & Nilipour 2003), which is an extremely computationally intensive task and therefore suitable for ANNs. Recently, some of the studies in this field are examining the applicability of ANNs in soil dynamic analysis (Hurtado et al. 2001, Garcia et al. 2002, Paolucci et al. 2002, Garcia & Romo 2004, Kerh & Ting 2005).

In the present study the application of ANNs is focused on the simulation of the seismic response of an embankment. The embankments (water dams, tailings dams, solid waste landfills, etc.) usually constitute important large-scale geo-structures, the safety and serviceability of which are directly related to environmental and social-economical issues (Psarropoulos et al. 2006a). This kind of structures became subject of systematic research following the Northridge (1994) and

Kobe (1995) earthquakes, after which extended investigations took place to examine the failures, occurred in embankments due to seismic actions.

Usually, the dynamic nonlinear response of an embankment is evaluated utilizing the finite-element method. This strategy has been also used in the present study, where nonlinearity of materials is taken into account by a time-consuming equivalent-linear procedure. Since a large number of dynamic analyses are required in order to simulate the dynamic behavior of the embankment under various seismic excitations, in order to reduce the aforementioned computational cost, a specially tailored back propagation ANN has been used. Initially, the ANN is trained utilizing available information generated from selected dynamic analyses of the geo-structure. In the sequence, the trained ANN is used to accurately predict the response of the examined geo-structure to various seismic excitations replacing the conventional analysis procedure. The results demonstrate the efficiency of the proposed methodology for treating large-scale problems in geotechnical earthquake engineering.

2 SEISMIC RESPONSE OF EMBANKMENTS

As most of the failures of embankments are related to slope instabilities (either of the embankment mass or of the supporting soil), seismic slope stability analysis is certainly a critical component of the design process. Recent practice is based on three main families of methods that differ primarily in the accuracy with which the earthquake motion and the dynamic slope response are represented.

The most accurate methods are considered to be the *stress-deformation methods*, which are typically performed using dynamic finite-element analysis. In general, these methods are used to describe the nonlinear behavior of the material with the highest possible accuracy, but they require sophisticated constitutive models involving a large number of parameters that cannot be easily quantified in the laboratory or in situ. Because of their complexity, these methods are usually excluded from the seismic design of embankments. On the other hand, simplified seismic stability procedures are widely used in geotechnical practice. A crude index of seismic slope stability (or instability) is the *factor of safety* evaluated in a pseudo-static fashion in the realm of conventional limit-equilibrium analysis. Finally, an alternative family of methods utilizes displacement-based approaches to predict permanent slope displacements induced by earthquake shaking.

The key issue in limit-equilibrium methods is the selection of a proper seismic coefficient, as the latter controls the pseudo-static forces in the soil masses, whereas in the displacement-based methods permanent

displacements are calculated using either acceleration time histories (Newmark 1965) or seismic coefficients (Makdisi & Seed 1978). Thus, it becomes evident that slope stability methods require an accurate estimation of the acceleration levels induced on the embankment under examination. Therefore, pertinent response analyses incorporating the “*local site conditions*” should precede any kind of seismic slope stability analysis. The term “local site conditions” is used here to describe not only soil conditions (stratigraphy, geomorphology, topography) of the site, but the geometric and mechanical properties of the embankment as well.

Records and analyses of valleys and hills have shown that local site conditions of a site, either in two or in three dimensions, may alter substantially the ground motion (Gazetas et al. 2002) by: (a) amplifying the ground motion, (b) elongating its duration, and (c) generating differential motions, phenomena which will be referred hereafter to as “aggravation”. Recent analyses have shown that geomorphic and topographic conditions may profoundly aggravate the surface ground motion in the presence of low levels of material damping, while material nonlinearity may substantially suppress aggravation by diminishing scattered body waves, especially horizontally propagating surface waves (Psarropoulos et al. 2006b). Therefore, in most cases aggravation depends not only on the geometrical and mechanical properties of a surface formation, but also on the amplitude of the excitation.

The aim of the present study is to examine in more detail the aggravation of horizontal acceleration and to investigate the relationship between this aggravation and the potential nonlinear behavior of soil. To accomplish this goal, two-dimensional (2-D) finite element equivalent-linear numerical simulations have been performed utilizing specially tailored ANNs to examine the nonlinear dynamic response of a typical embankment. The main parameters examined are the characteristics of the seismic excitation. Results indicate that local site conditions may play a significant role in the seismic response of an embankment, depending on the circumstances. However, as the material behavior of the geo-structure is directly related to the characteristics of the seismic excitation, this role cannot be judged a priori as beneficial or detrimental for the overall response of the geo-structure.

3 ARTIFICIAL NEURAL NETWORKS

An ANN is an information processing paradigm that is inspired by the biological nervous systems, such as the brain process information network. It is composed of a large number of highly interconnected processing elements (neurons) working in unison to solve specific problems. As in biological systems, learning involves

adjustments to the synaptic connections that exist between the neurons. ANNs, with their remarkable ability to derive meaning from complicated or imprecise data, can be used to extract patterns and detect trends that are too complex to be noticed by either humans or conventional computational techniques.

An ANN is configured for a specific application, such as pattern recognition or data classification, through a learning process. ANNs, like human beings, learn by example. A trained ANN provides a rapid mapping of a given input into the desired output quantities, thereby enhancing the efficiency of the analysis process. This major advantage of a trained ANN over a conventional procedure, under the provision that the predicted results fall within acceptable tolerances, is that it leads to results that can be produced in a few clock cycles, representing orders of magnitude less computational effort than the conventional procedure.

In this work a fully connected network with one hidden layer is used. The learning algorithm, which was employed in this study for the ANN training, is the well-known Back Propagation (BP) algorithm. The BP algorithm progresses iteratively, through a number of epochs. On each epoch the training cases are submitted in turn to the network and target and actual outputs are compared and the error is calculated. This error, together with the error surface gradient, is used to adjust the weights, and then the process is repeated. Training stops when a given number of epochs elapses, or when the error reaches an acceptable level, or when the error ceases to decrease (user-defined convergence criteria). The ANN training comprises the following tasks: (i) select the proper training set, (ii) find a suitable network architecture

and (iii) determine the appropriate values of characteristic parameters such as the learning rate and momentum term; two user defined BP parameters that effect the learning procedure.

4 NUMERICAL STUDY

In order to examine more thoroughly the effectiveness of ANNs in computationally expensive dynamic finite-elements problems, the 2-D numerical model, shown in Figure 1, was investigated. The discretization of the finite element model is presented in Figure 2. The embankment is founded on stiff rock. Shear-wave velocity of the embankment soil material at small strain levels was set equal to 250 m/s and unit weight of the soil was considered to be 10 kN/m³. While the geometry and the properties of the model remained constant, the seismic excitations varied during the analyses.

The simple embankment examined herein can be regarded as a relatively small-scale earth embankment, the dynamic behavior of which has thoroughly been examined in the past by other researchers (Gazetas 1987). Assuming plane-strain conditions, the seismic response of the embankment examined was evaluated using QUAD4M code (Hudson et al. 1994), which is capable of performing 2-D equivalent-linear finite-element analyses. As shown in Figure 2, the model was discretized with three-noded triangular finite elements. The size of the finite elements was tailored to the wavelengths of interest. Material non-linearity for soil was taken into account approximately by an iterative procedure, according to which the values of material stiffness and material damping

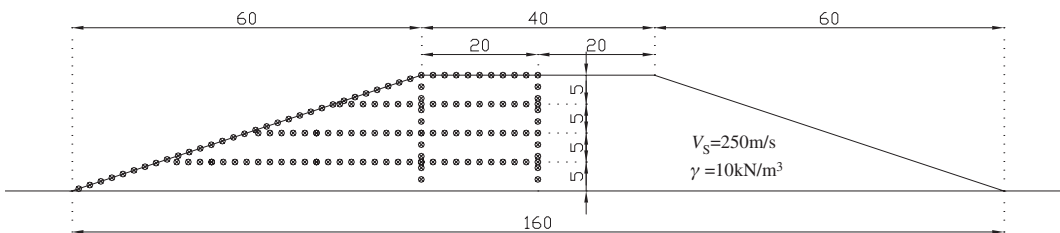


Figure 1. Geometry and material properties of the examined embankment. Bullets represent the position of the “receivers”.

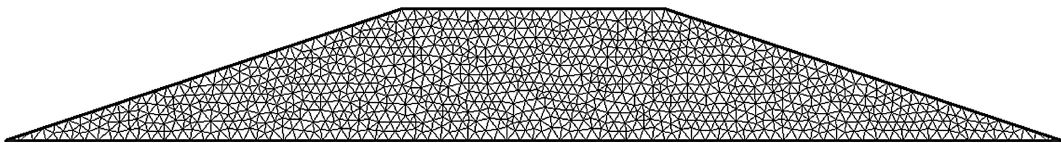


Figure 2. Discretization of the embankment into three-noded triangular finite elements.

are consistent with the level of maximum shear strain. Stiffness degradation and damping increase for the soil were based on the curves proposed by Idriss & Sun (1992).

A suite of characteristic accelerograms has been used as seismic excitations: namely 43 recorded earthquake motions (presented in Table 3) and 3 idealized pulses. The three pulse excitations were simple Ricker pulses with a varying central frequency: $f_0 = 2, 3, 4$ Hz, respectively. Furthermore, in order to cover a sufficient range of nonlinear behavior (strains) of the soil, all input motions were scaled to peak ground acceleration (PGA) ranging from 0.01 g to 0.5 g. Thus, five cases were examined:

- Case I (essentially linear behavior): 0.01 g
- Case II (almost linear behavior): 0.05 g
- Case III (low level of nonlinearity): 0.1 g
- Case IV (medium level of nonlinearity): 0.2 g
- Case V (high level of nonlinearity): 0.5 g

The use of ANN in this study was motivated by the fact that the finite-element models are time-consuming: approximately 30 minutes for a “simple” run (linear run (Case I) with a short duration Ricker pulse) of the examined 2-D model of Figure 2 (with 850 nodes and 1540 elements) at a Pentium IV PC with 2.53 GHz CPU processor and 1 GB RAM. While, for a more “complex” run (a real record with larger duration and/or for a higher level of nonlinearity) the computing time increased significantly, up to 60 minutes. On the other hand, the computational cost for the calculation of an ANN prediction in all cases was only a few seconds.

Therefore, the need for an efficient computational tool for the simulation of the seismic response of large-scale geo-structures is indisputable. The ANN software used in this study has been developed by one of the authors (Lagaros & Papadarakakis 2004). For the needs of the present paper, the ANN-based simulation has been compared with the results of non-linear finite element models obtained using QUAD4M. The ANN has been used for the prediction of the seismic response in terms of peak ground horizontal accelerations at the embankment’s surface, as well as in the embankment’s body. For this reason the embankment has been separated into zones, as it is presented in Figure 1, where the “receivers” for recording the local seismic response had been placed. The total number of the receivers was 138, placed at the left half of the embankment, because of the symmetric shape of the geo-structure.

The ANN configurations used were properly trained in order to predict the acceleration for new earthquake records. The records used were identified using a set of Intensity Measures (IMs). The term *Intensity Measure* is used to denote a number of

commonly used ground motion parameters, which represent the amplitude, the frequency content, the duration or any other important ground motion parameter. In addition, IMs can be classified as only record dependent, or as both structure and record dependent.

A significant number of different IMs can be found in the literature. In the present investigation, in addition to the IMs available in Kramer (1996), the A95 parameter (Sarma & Yang 1987) was used. This parameter defines the acceleration level of a record below which 95% of the total Arias Intensity (I_a) is contained. For instance, if the entire accelerogram yields a value of I_a equal to 100 then the A95 parameter is the threshold of acceleration such that integrating all the values of the accelerogram below it one gets $I_a = 95$. The most significant IMs were used in this study, after examining various combinations of them for each “load-case”, in order to provide the best possible training to ANN metamodels.

4.1 Ricker pulse excitations

Initially, the embankment was excited with the three Ricker pulses and the five different maximum acceleration levels, resulting to 15 models in total. The input data for the ANN metamodel were the coordinates of the receivers, which are positioned in an axial distance 2 m at x-axis and at y-axis (at the surface and inside the body of the embankment) and several IMs that described efficiently the Ricker pulse. The output was the seismic response of each receiver for the specific Ricker pulse.

The ANN that has been used for the prediction of the embankment’s response excited by the Ricker pulses consisted of three layers: the input layer with seventeen nodes (receiver’s coordinates $-x, y$, $PGA, PGV, PGD, PGI/PGA, A_{RMS}, V_{RMS}, D_{RMS}$, characteristic intensity, specific energy density, cumulative absolute velocity, acceleration spectrum intensity, velocity spectrum intensity, effective design acceleration, A95 parameter and predominant period), the hidden layer and the output layer with one node (response). After an initial investigation about the number of the hidden layer’s nodes, the ANN configuration resulted in a [17-50-1] architecture.

The ANN model trained with the Ricker input data was used to evaluate embankment’s response for a Ricker pulse with 2.5 Hz predominant frequency and its performance was very satisfactory. The maximum tolerance between the computed by QUAD4M and the predicted through the ANN (for all Cases I to V) are presented in the diagram of Figure 3. The results shown in Figure 3 can also be presented in a table form, according to the percentage of the absolute value of the tolerance between the computed and the predicted value of the seismic response, as it is depicted in Table 1.

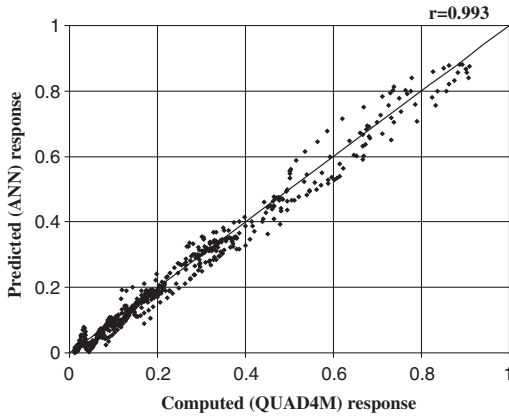


Figure 3. Computed versus Predicted seismic response for the entire embankment (Ricker Pulse).

Table 1. Percentage of receivers that exceeds different levels of tolerance for the entire embankment (ricker Pulse).

Tolerance (%)	No of receivers	Receivers (%)	Total Receivers (%)
0 to 5	216	31.3	31.3
5 to 10	139	20.1	51.4
10 to 20	156	22.6	74.0
20 to 30	46	6.6	80.7
30 to 40	31	4.4	85.2
40 to 50	23	3.3	88.5
50 to 60	7	1.0	89.5
60 to 70	11	1.5	91.1

Furthermore, in order to evaluate more efficiently the performance of ANN metamodel, a coefficient of correlation was used, which was defined as follows:

$$r = \frac{\sum_{i=1}^m (x_i - \bar{x})(y_i - \bar{y})}{\sqrt{\sum_{i=1}^m (x_i - \bar{x})^2 \sum_{i=1}^m (y_i - \bar{y})^2}} \quad (1)$$

where x_i and \bar{x} are the recorded and the averaged response values; y_i and \bar{y} are the ones estimated by ANN and their averaged value; and m denotes the number of ANN training data sets. This coefficient may have a positive or negative value, therefore, its square value r^2 can be used instead in order to represent the degree of correlation of the recorded data and their approximation by the ANN metamodel. In Figures 3 to 5 the mean value (for all receivers and Cases) of the correlation parameter is depicted.

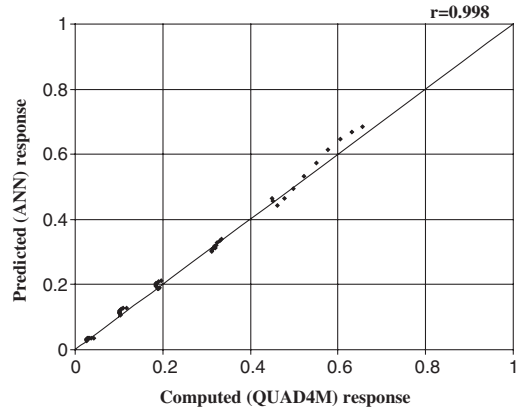


Figure 4. Computed versus Predicted seismic response for the upper boundary of the embankment (Ricker Pulse).

Table 2. Percentage of receivers that exceeds different levels of tolerance for the upper boundary of the embankment.

Tolerance (%)	No of receivers	Receivers (%)	Total receivers (%)
0 to 5	26	47.2	47.2
5 to 10	14	25.4	72.7
10 to 15	15	27.2	100.0

It was observed that a higher discrepancy between the predicted and the calculated values of the seismic response occurred for the receivers that were located inside the embankment's body. If the internal receivers are ignored then the accuracy for the external receivers is much better, as it is clearly shown in Figure 4 and Table 2.

4.2 Earthquake excitations

The next stage was to use, instead of relatively simple Ricker pulses, records derived from real earthquakes. The earthquake data from the 43 records used for ANN training are presented in Table 3. For each earthquake record the aforementioned five acceleration levels have been used. Following the same considerations as for the Ricker pulses case and after an extensive investigation a [16-20-1] architecture was used for the prediction of the geo-structure's response. After considering various possible IMs combinations, the input layer in this case consisted of sixteen nodes (coordinates $-x$, y -, PGA , PGV , PGD , PGV/PGA , characteristic intensity, specific energy density, cumulative absolute velocity, acceleration spectrum intensity, velocity spectrum intensity, sustained maximum acceleration, sustained maximum velocity, effective design acceleration, A95 parameter and predominant period)

Table 3. Earthquake records for the training of the ANN.

Earthquake's name (Region)	Year of occurrence	Number of records
Lefkada, Greece	1973	1
Mexico City, Mexico	1981	4
Kalamata, Greece	1986	1
Northridge, USA	1994	14
Kobe, Japan	1995	9
Aigio, Greece	1995	1
Kocaeli, Turkey	1999	7
Parnitha, Greece	1999	4
Lefkada, Greece	2003	2

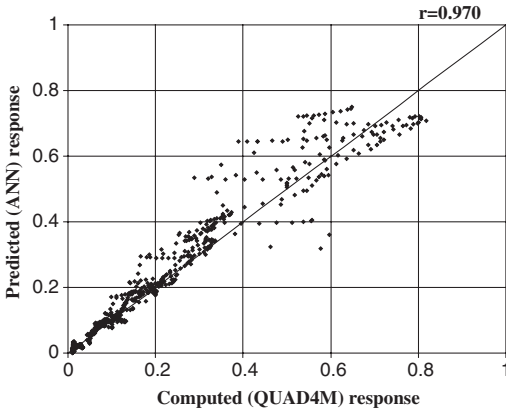


Figure 5. Computed versus Predicted seismic response for the entire embankment (Sepolia record).

Table 4. Percentage of receivers that exceeds different levels of tolerance for the entire embankment (Sepolia record).

Tolerance (%)	No of receivers	Receivers (%)	Total Receivers (%)
0 to 5	144	20.8	20.8
5 to 10	149	21.5	42.4
10 to 20	157	22.7	65.2
20 to 30	96	13.9	79.1
30 to 40	33	4.7	83.9
40 to 50	33	4.7	88.7
50 to 60	20	2.9	91.5
60 to 70	14	2.0	93.6

in order to provide the more important input data and therefore enhance the predictions of the ANN.

After its training the ANN metamodel was used to predict the response for Sepolia record (Parnitha earthquake, Greece, 1999). This record was chosen due to the fact that its IMs were similar to those of the earthquakes used for the ANN training (an ANN can

interpolate, but not extrapolate). As it can be seen in Figure 5 and Table 4 in this case nonlinearity affects more the performance of ANN. Nevertheless, even in this case, which is more computationally intensive, ANN approximate with a relative high level of accuracy the seismic response of the embankment, especially for the external receivers.

5 CONCLUSIONS

In the present implementation of ANNs the objective was to investigate their ability to capture the dynamic nonlinear response of an embankment under various seismic excitations and reduce the excessive computational cost. In general, ANN achieved a slightly better approximation of the response for the receivers that are positioned at the crest and the upper part of the embankment than for the receivers that are positioned inside the embankment. Furthermore, comparing the results obtained via ANN for the Ricker pulses and the earthquake records it is obvious that when the embankment material behaves linearly or with a moderate level of nonlinearity then the response of the embankment is approximated very accurately by the ANN-based metamodel. When a severe earthquake occurs, then high nonlinearity deteriorates the accuracy of ANN predictions. However, they can still be considered very satisfactory, while in this case the computational gains are even more than in the linear case. In conclusion, ANN presented a very good performance in marginal computing cost and their applicability in the field is very promising.

REFERENCES

- Baziar, M.H. & Nilipour, N. 2003. Evaluation of liquefaction potential using neural-networks and CPT results. *Soil Dyn. & Earthquake Engng* 23(7): 631–636.
- Chouicha, M.A., Siller, T.J. & Charlie, W.A. 1994. An Expert-system approach to liquefaction analysis: 2. Evaluation. *Computers & Geotechnics* 16(1): 37–69.
- Garcia, S.R., Romo, M.P., & Sarmiento N. 2002. Modeling ground motion in Mexico City using artificial neural networks. *Geofisica International* 42(2): 173–183.
- Garcia, S.R. & Romo, M.P. 2004. Dynamic soil properties identification using earthquake records: a NN approximation. *Proceedings of the 13th World Conference on Earthquake Engineering, Vancouver, B.C., Canada August 1–6, 2004*. Paper No. 1817.
- Gazetas, G., Kallou, P.V., & Psaropoulos, P.N. 2002. Topography and soil effects in the MS 5.9 Parnitha (Athens) earthquake: the case of Adames. *Natural Hazards* 27: 133–169.
- Gazetas, G. 1987. Seismic response of earth dams: some recent developments. *Soil Dyn. & Earthquake Engng* 1(6): 3–47.

- Goh, A.T.C. 1994. Seismic liquefaction potential assessed by neural networks. *ASCE J. of Geotech. Engng* 120(9): 1467–1480.
- Hudson, M., Idriss, I.M., & Beikae, M. 1994. *User's Manual for QUAD4M*. Center for Geotechnical Modeling, Department of Civil and Environmental Engineering, University of California, Davis, CA, USA.
- Hurtado, J.E., Londono, J.M. & Meza, M.A. 2001. On the applicability of neural networks for soil dynamic amplification analysis. *Soil Dyn. & Earthquake Engng* 21: 579–591.
- Idriss, I.M. & Sun, J.L. 1992. *User's manual for SHAKE91*. Center for Geotechnical Modeling, Department of Civil and Environmental Engineering, University of California, Davis, USA.
- Kerh, T. & Ting, S.B. 2005. Neural network estimation of ground peak acceleration at stations along Taiwan high-speed rail system. *Engng Appl. of Artifi. Intel.* (18): 857–866.
- Kramer, S.L. 1996. *Geotechnical earthquake engineering*. Prentice Hall, New Jersey.
- Lagaros, N.D. & Papadrakakis, M. 2004. Improving the condition of the jacobian in neural network training, *Adv. in Engng Soft.* 35(1): 9–25.
- Makdasi, F.I. & Seed, H.B. 1978. Simplified procedure for estimating dam and embankment earthquake induced deformations. *ASCE J. of Geotech. Engng Div.* 104: 849–867.
- Newmark, N.M. 1965. Effects of earthquakes on dams and embankments. *Geotechnique* 15(2): 139–160.
- Paolucci, R., Colli, P. & Giacinto, G. 2002. Assessment of seismic site effects in 2-D alluvial valleys using neural networks. *Earthquake Spectra* 16(3): 661–680.
- Psarropoulos, P.N., Tsompanakis, Y. & Karabatsos, Y. 2006a. Effects of local site conditions on the seismic response of municipal solid waste landfills. *Soil Dyn & Earthquake Engng* (in press).
- Psarropoulos, P.N., Tazoh, T., Gazetas, G. & Apostolou, M. 2006b. Linear and non-linear valley amplification effects on seismic ground motion. *Soils & Foundations* (in press).
- Sarma, S.K. & Yang, K.S. 1987. An evaluation of strong motion records and a new parameter A95. *Earthquake Engng & Struct. Dyn.* 15: 119–132.
- Wang, J. & Rahman, M.S. 1999. A neural network model for liquefaction-induced horizontal ground displacement. *Soil Dyn. & Earthquake Engng* 18(8): 555–568.

Hybrid neural network and genetic algorithm approach to the prediction of bearing capacity of driven piles

H.I. Park, J.W. Seok & D.J. Hwang

Institute of Construction Technology, Samsung Corporation, Sungnam-si, Kyunggi-do, Korea

ABSTRACT: Although numerous investigations have been performed over the years to predict the behavior and bearing capacity of piles, the mechanisms are not yet entirely understood. The prediction of bearing capacity is a difficult task, because large numbers of factors affect the capacity and also have complex relationship with each others. Therefore, it is extremely difficult to search the essential factors among many factors, which are related with ground condition, pile type, driving condition and others, and then appropriately consider complicated relationship among the searched factors. The present paper describes the application of Artificial Neural Network (ANN) in predicting the capacity including its components at the tip and along the shaft from dynamic load test of the driven piles. The results of this study indicate that the neural network model serves as a reliable and simple predictive tool for the bearing capacity of driven piles.

1 INTRODUCTION

Although numerous investigations for the behavior and bearing capacity of piles have been conducted over the years, the mechanisms of these behavior and bearing capacity of piles have yet to be entirely understood. The problem is that many parameters affect the pile behavior, which is difficult to quantify and involve considerable uncertainty. Kraft (1991), Brucy et al. (1991), Baik (2002) and Cho (2003) illustrated that the more important parameters are the soil condition (the type of soil, density, shear strength, and others), information related to pile (diameter, penetration depth, whether the tip of pile is open-ended or closed-ended, and others), and other information (driving method, driving energy, set-up effect and others).

Although many methods predicting pile resistance have been presented, these methods cannot appropriately consider the various parameters affecting pile resistance. Moreover, these methods over-simplify pile resistance and do not appropriately consider the characteristics of the soil, pile type, and information about the driving. Because of these weaknesses, a pile load testing is accepted as the best way to provide accurate pile capacity, but it is restricted by time and cost, despite of its reliability. Consequently, an alternative method that can predict pile capacity is necessary to determine the amount of pile to install in preliminary design.

Recently, artificial neural network (ANN) has been successfully applied to many applications in geotechnical engineering (Goh, 1994; Lee and Lee, 1996;

Rahman et al., 2001). In particular, neural networks have been used to predict static pile capacity (Lee and Lee, 1996; Teh et al., 1997). ANN has been found to be very useful in learning complex relationships between multidimensional data.

Although ANN is an effective algorithm for solving complex engineering problems, only few approaches are available to design the network and most of them rely on iterative procedures. The design of network architecture mainly consists of the appropriate selections of a training algorithm, network layers, number of neurons of each layer, and the transfer functions between layers. To make an ANN more efficient, the convergence speed must be improved and the computational complexity of ANN reduced. The convergence speed and computational complexity of network are generally affected by the number of neurons in each layer. And the network performs poorly as the model become larger and more complex. In general, the structure of ANN is designed by the trial and error approach, which runs repeatedly to find the network architecture. There is no general framework for the selection of the optimum ANN architecture and its parameters (Chung and Kusiak, 1994; Kusiak and Lee, 1996).

Genetic algorithm (GA) is an evolutionary search algorithm based on the mechanics of natural selection and natural genetics and can search a large number of combinations, because of interdependencies and redundancies between variables (Goldberg, 1989). GA is a very effective and robust approach for solving a wide range of problems in science and engineering.

This study considers the use of hybrid ANN/GA in applications in science and engineering. Yu and Liang (2001) presented a hybrid approach involving ANN and GA to solve job-shop scheduling problem. The computational ability of the hybrid approach, ANN's computability and GA's searching efficiency, is strong enough to deal with complex scheduling problems. Therefore, in this study, the advantages of ANN and GA are used together in a hybrid approach to design an optimal ANN model to predict pile resistance.

The present paper describes the application of ANN in the prediction of the resistance of driven piles. The structure of the proposed ANN model is obtained by the hybrid design method based on ANN and GA. The proposed model is trained using the results of the dynamic load test (Cho, 2003) performed at various sites in Korea. The effect of each parameter on the value of pile resistance is investigated using the proposed model.

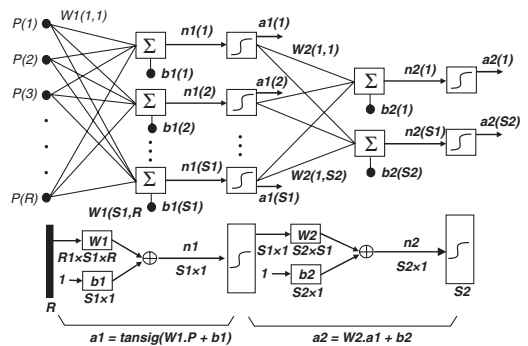
2 ARTIFICIAL NEURAL NETWORK (ANN)

Artificial neural networks are promising computational techniques capable of mapping and capturing all features and sub-features embedded in a large set of data that yields a certain output. A network that has successfully captured the governing relationships between input and output data can be used as a prediction tool for cases where the output solution is not available. The input variables comprise the input layer to the network and the output layer contains the target output vector (the solution of the problem).

An example of typical back-propagation artificial neural network is shown in Figure 1. A network can have several layers. The output of each intermediate layer is the input to the following layer. Each layer has a weight matrix W , a bias vector B , and an output vector a . Each element of the input vector P is connected to each neuron input through the weight matrix W . The i th neuron has a summer that gathers its weighted inputs and bias to form its own scalar output $n(i)$. The various $n(i)$ taken together form an S -element vector n . Finally, the neuron layer outputs form a column vector a .

The layers of a multilayer network have different functions. The layer that receives the inputs is called the input layer and the layer that produces the network output is called the output layer. All other layers are called hidden layers. A hidden layer, usually placed between the input and output layers, is usually employed to assist the network in the learning process. The most commonly used transfer functions are the linear, the log-sigmoid, and the tan-sigmoid function (Rahman et al., 2001).

In this study, the training data sets (inputs and target outputs) were normalized according to Equation 1



$R =$ No. of input parameter; $S1 =$ No. of hidden nodes; $S2 =$ No. of output nodes

Figure 1. The architecture of artificial neural network (Rahman et al., 2001).

and Equation 2. Processing of the training data was performed so that the processed data was in the range of -1 to $+1$. The output of the network will be trained to produce outputs in the range of -1 to $+1$, and we convert these outputs back into the same units that are used for the original targets.

$$pn = \frac{2(p - \min p)}{(\max p - \min p)} - 1, tn = \frac{2(t - \min t)}{(\max t - \min t)} - 1 \quad (1)$$

where p = matrix of input vectors; t = matrix of target output vectors; pn = matrix of normalized input vectors; tn = matrix of normalized target output vectors; $\max p$ = vector containing the maximum values of the original input; $\min p$ = vector containing the minimum value of the original input; $\max t$ = vector containing the maximum value of the target output; and $\min t$ = vector containing the minimum value of the target output.

The normalized data were then used to train the neural network (to get the final connection weights). The data from the out neuron have to be post processed to convert the data back into unnormalized units according to Equation 2.

$$t = 0.5 \cdot (tn + 1) \cdot (\max t - \min t) + \min t \quad (2)$$

The normalized output is then obtained by propagating the normalized input vector through the network as follow:

$$tn = W2 \times \log \text{sig}(W1 \times pn + b1) + b2 \quad (3)$$

where $W1$ = weight matrix representing connection weights between the input layer neurons and hidden layer; $b1$ = weight matrix representing connection weights between the hidden layer neurons and the

output neuron; $W2$ = bias vector for the hidden layer neurons; and $b2$ = bias for the output neuron. The log-sigmoid function, logsig is defined as:

$$\text{log sig}(X) = 1/[1 + \exp(-X)] \quad (4)$$

An example of typical back-propagation artificial neural network is shown in Fig. 1. A network can have several layers. The output of each intermediate layer is the input to the following layer. Each layer has a weight matrix W , a bias vector B , and an output vector a . Each element of the input vector P is connected to each neuron input through the weight matrix W . The i th neuron has a summer that gathers its weighted inputs and bias to form its own scalar output $n(i)$. The various $n(i)$ taken together form an S -element vector n . Finally, the neuron layer outputs form a column vector a .

3 STRUCTURAL DESIGN OF ANN USING GA

In the proposed approach, a trained neural network (NN) was employed to model the complex relationships among the parameters related to the resistance of driven pile, whereas genetic algorithm (GA) was applied to determine a set of optimal architecture of NN.

The hybrid approach involving ANN and GA was developed and implemented. It consists of two unit: an NN prediction unit and a GA optimization unit. First, an initial population, which contains a number of sets including information about the structure of ANN, is randomly generated. Then the individuals stored in it are fed into a NN-based prediction unit. The predicted quality measures, which related to objective function, are used to indicate the fitness of the individuals. Secondly a GA-based optimization unit is used to establish the best architecture of NN. In the following sections, the key issues of the design and development of NN prediction unit and GA optimization are discussed.

3.1 Creation of initial population

The hybrid ANN-GA approach starts with the generation of an initial population, which contains a predefined number of chromosomes (strings). Each chromosome is composed of binary strings that include the design information of ANN's structure. For example, a chromosome used in this study is presented in Figure 2.

This chromosome is composed of the eighteen binary strings. First seven binary strings in the chromosome include the information about the selection of input parameters. Six binary strings deal with the input variables used for the network architecture, with the 0 code indicating that a variable cannot be

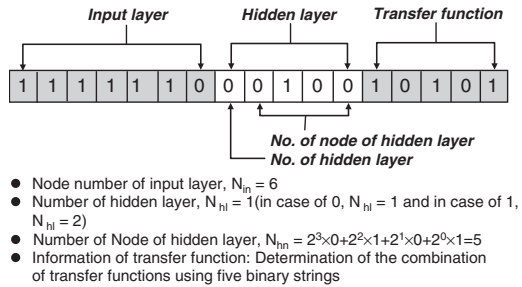


Figure 2. Design information about the structure of ANN included in chromosome.

used and with the 1 code indicating that a variable can be used. There are eight input variables, in this chromosome; six binary strings present that the first six inputs should be kept, and the last two inputs removed. The information about hidden layer and transfer function is included in the other ten binary strings.

3.2 Genetic operation

A GA is an optimization procedure that operates on sets of design variables. Each set is called a string and it defines a potential. Each string consists of a series of characters representing the values of the discrete design variables for a particular solution. The fitness of each string is the measurement of the performance of the design variables as defined by the objective function. In its simplest form, a genetic algorithm consists of three operations: (1) reproduction, (2) crossover, and (3) mutation (Goldberg, 1989). Each of these operations is described below.

The reproduction operation is the basic engine of Darwinian natural selection by the survival of the fittest. The reproduction process promotes the information stored in strings with good fitness values to survive into the next generation. The next generation of offspring strings is developed from the selected pairs of parent strings exposed to the application of explorative operators such as crossover and mutation.

Crossover is a procedure in which a selected parent string is broken into segments, some of which are exchanged with corresponding segments of another parent string. In this manner, the crossover operation creates variations in the solutions population by producing new solution strings that consist of parts taken from a selected parent string.

The mutation operation is introduced as an insurance policy to enforce diversity in a population. It introduces random changes in the solution population by exploring the possibility of creating and passing features that are nonexistent in both parent strings to the offsprings. Without an operator of this type, some

Table 1. Test result obtained by dynamic load tests (Cho, 2003).

Site	Diameter (m)	Tip type	Penetration depth (m)	EMX (kN · m)	Elapsed time (day)	Soil type		Shaft resistance (kN)	Tip resistance (kN)
						Shaft	Tip		
Po-Hang	0.508	Closed or open	9.6~18.3	41.2~60.8	0~28	6	8	451~2502	1423~2031
	0.406	Closed or open	10.5~14	20.6~43.2	0~27			216~1030	1236~1835
Kwang-Yang	0.508	Closed or open	23~24.2	50.0~94.2	0~11	3	8	613~1988	2384
		Closed or open	24.2	58.9	0			1232	1867~1986
	0.406	Closed or open	24.1~24.6	54.9~95.2	0~13			636~1754	1704~2442
	0.355	Closed or open	22~23.7	41.2~60.8	0~12			725~1484	1664~1903
	0.323	Closed or open	24~24.4	51.0~78.5	0~20			785~1589	1501~1942
	0.400	Closed or open	23.3~23.6	24.5~56.9	0			42~949	1053~2228
	0.273	Closed or open	24	42.2~62.8	0~13			668~1117	1356~1617
	0.508	Closed or open	20.4~22.8	44.1~102	0~27			343~1689	1880~2741
Si-Heung	0.406	Closed or open	20.5~21.6	30.4~77.5	0~25	3	7	308~1350	1495~2376
	0.406	Closed or open	26.1~29.1	42.2~74.6	0~5			1031~2841	391~1617
Yong jong-Do	0.400	Closed or open	26~28.1	42.2~66.7	0~4	5	8	332~1717	1324~2075
	0.610	Closed or open	31.3~42.8	59.8~99.1	0~18			1	7
Dong-Hae	0.406	Closed or open	34.7~39.6	54.9~65.7	0~9	7	8	385~2865	394~2076
	0.350	Closed or open	14.7~25	15.7~33.4	0~35			154~1372	157~500
Pusan	0.450	Closed or open	21.5~29	26.5~61.8	0~12	1	1	172~1398	313~1319

possibly important regions of the search space may never be explored.

3.3 Definition of objective function

The objective function for each chromosome is computed by Equation 1. The objective function of the *i*th chromosome, $ObjV(i)$ is composed of the error function, E_i , calculated as the difference between measured values and predicted values, and the penalty function, P_i , calculated on the basis of the complexity of structure of ANN. The complex structure of an ANN model increases the probability that the value of the error function will decrease, but generality is more likely to decrease due to overfitting. Therefore, the penalty function, P_i , is included in the objective function to control the decrease of generality.

$$ObjV(i) = E_i + P = \left(\sum_{k=1}^{N_{mea}} \frac{|T_k - t_k|}{T_{max}} \right) / N_{mea} + \alpha \cdot \left(\frac{N_n^i / N_{max} + CW^i / CW_{max}}{2} \right) \quad (5)$$

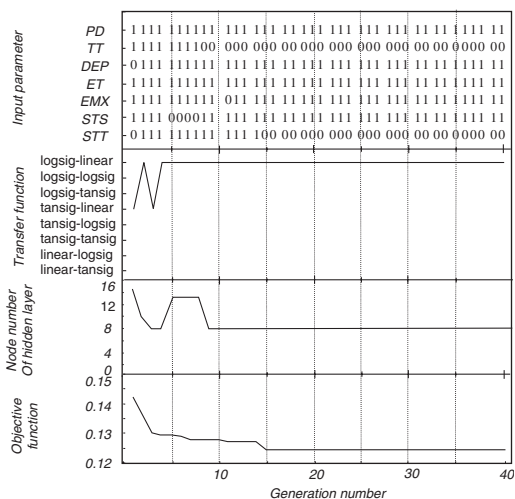
where $\alpha = 0.01$; N_{mea} = the total number of measured data; T_{max} = the maximum value among measured values; $T_k = k$ th measured value; and $t_k = k$ th predicted value; N_n^i = total number of nodes used in the *i*th chromosome; N_{max} = the maximum number of nodes that can be applied to the structure of ANN in this study; CW^i = total number of connections used in the *i*th chromosome; and CW_{max} = the maximum number of connections that can be applied to the structure of ANN in this study.

Table 2. Classification according to soil types near the shaft and the tip of pile.

Classification of soil	Value
Clay	1
Silt - Clay	2
Silt	3
Sand - Clay	4
Sand - Silt	5
Fine Sand	6
Sand	7
Sand - Gravel	8

165 dynamic load tests were preformed for seventy seven piles in five different areas of Korea, as illustrated in Table 1 (Cho, 2003).

As shown in this Table, the pile resistance was assumed to be affected seven parameters which are the soil type near the tip and shaft, the diameter of the pile, the driven depth, the tip condition of the pile (open-ended or closed-ended), the penetration depth of the pile, and the elapsed time after the end of initial strike. The applied dynamic load tests were performed by using a Pile Driving Analyzer (PDA) according to ASTM D 4945 (Crowther, 1988). The value of bearing capacity was evaluated by CAPWAP, which used the force and velocity data obtained with the PDA as input. In this study, the soil type near the tip and shaft of a pile was classified as shown in Table 2.



PD=pile diameter; TT=tip type of pile; PD=penetration depth; EMX=driving energy
STS=soil type of pile shaft; STT=soil type of pile tip

Figure 3. The search results of optimal neural network.

5 DATA BASE FOR ANALYSIS

Hybrid NN/GA approach is presented to design the optimal ANN model which estimate the resistance of driven pile. In this research, the following value are used for design parameters related to this approach which population = 1000, mutation probability = 0.005, crossover rate = 0.3, maximum node number of hidden layer = 16. Figure 3 shows the search results of optimal neural network to estimate resistance of driven pile. As shown in Figure 3, optimal neural network architecture was searched in 15 generation. In this figure, the variation of the combination of input parameters and transfer functions and node number of hidden layer is shown according to generation based on the optimal architecture of neural network.

After computation experiments with the hybrid ANN/GA approach, the best results were obtained with the structure of ANN model (5 × 12 × 1), which had a single hidden layer with eight neurons, an input layer with six neurons, and log-sigmoid (1/(1 + e⁻ⁿ)) and linear transfer functions for the hidden layer neurons and output layer neurons, as shown in Figure 3. Remained six parameters excluding the tip type of pile and the soil type near the tip of pile are used in this input layer of the model. Figure 4 shows the relationship between the output targets (measured values) and predicted values obtained through the training and testing process. High coefficient of correlations (R²) are obtained for both training and testing sets of data.

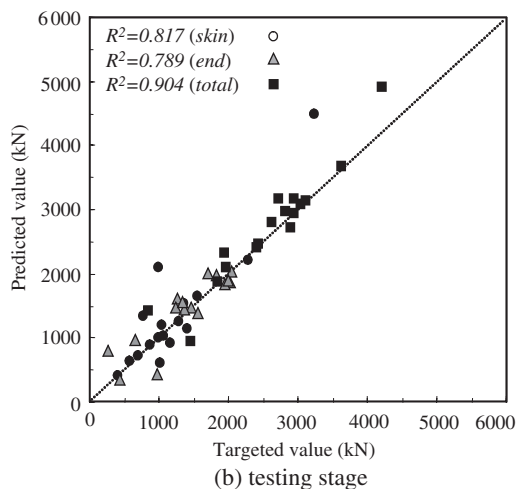
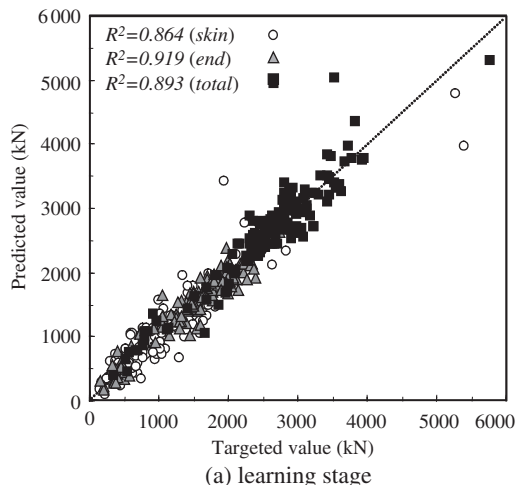


Figure 4. Comparison of predicted and measured pile resistance.

6 CONCLUSION

The objective of this paper was to demonstrate the feasibility of using ANN to predict the shaft resistance, the tip resistance, and the total resistance of driven piles installed in many sites located in South Korea in various soil types. In order to propose a simple and effective ANN model to predict the pile resistance, the hybrid NN/GA approach that combines the characteristics of GA and NN to overcome the shortcomings of NN structure design was applied. The appropriate combination of input variables, hidden layer, the number of neuron of hidden layer, and transfer function was obtained by optimization using the hybrid NN/GA approach.

REFERENCES

- Baik, K. 2002. Optimum Driving Method for Steel Pipe Piles in Sands. *J. of Civil Engineering*, 22(1-C): 45–55.
- Beringen, F. L. 1979. Results of Loading Tests on Driven Piles in Sand. *Recent Developments in the Design and Construction of Piles*, 213–225. London
- Brucy, F., Meunier, J. & Nauroy, J. F. 1991. Behavior of Pile Plug in Sandy Soils during and after Driving. *Proc. 23rd Annual Offshore Technology Conf.*, 1: 145–154.
- Chan, W. T., Chow, Y. K., and Liu, L. F. 1995. Neural Network: A Alternative to Pile Driving Formulas. *Comp. and Geotechnics*.
- Cho, C. W. 2003. The Characteristics of the Set-up Effect of Driven Piles. *J. of Korean Geotechnical Society, JKGS*, 19(4): 235–246.
- Chung, Y. & Kusiak, A. 1994. Grouping Parts with a Neural Network. *J. of Manufacturing System*, 13(4): 262–275.
- Crowther, C. L. 1988. *Load Testing of Deep Foundations. The Planning Design and Conduct of Pile Load Tests*, John Wiley & Sons.
- De Nicolar, A. & Randolph, M. F. 1997. The Plugging Behavior of Driven and Jacked Piles in Sand. *Geotechnique*, 47(4): 841–859.
- Goh, A. T. C. 1994. Seismic Liquefaction Potential assessed by Neural Networks. *J. Geotech. Engrg. Div., ASCE*, 120(9): 1467–1480.
- Goldberg, D. E. 1989. *Genetic Algorithms in Search, Optimization and Machine Learning*, Addison-Wesley, USA.
- Klos, J. & Tejchman, A. 1981. Bearing Capacity Calculation for Pipe Piles. *International Conference on Soil Mechanics and Foundation Engineering, Stockholm*, 2: 751–753.
- Kraft, L. M., Jr. 1991. Performance of Axially Loaded Pipe Piles in Sand. *J. Geotech. Engrg.*, 117(2): 272–296.
- Kusiak, A. & Lee, H. 1996. Neural Computing based Design of Components for Cellular Manufacturing. *International Journal of Production Research*, 34(7): 1777–1790.
- Lee, I. M. & Lee, J. H. 1996. Prediction of Pile Bearing Capacity Using Artificial Neural Networks. *Computers and Geotechnics*, 18(3): 189–200.
- Nauroy, J. F. & Le Tirant, P. 1983. Model Tests on Piles in Calcareous Sands, *Proc. Conf. on Geotech. Practice in Offshore Engrg.*, Austine, 356–369.
- Rahman, M. S., Wang, J., Deng, W. & Carter, J. P. 2001. A Neural Network Model for the Uplift Capacity of Suction Caissions. *Computers and Geotechnics*, 28: 269–287.
- Szechy, C. H. 1959. Tests with Tubular Piles. *AcTa Technica of the Hungarian Academy of Science*, 24: 181–219.
- Yu, H. & Liang, W. 2001. Neural Network and genetic algorithm based hybrid approach to expanded job-shop scheduling, *Computers and Industrial Engineering*, 39: 337–356.

Application of evolutionary programming techniques in geotechnical engineering

M. Rezania & A.A. Javadi

University of Exeter, Exeter, Devon, UK

ABSTRACT: Analysis of many geotechnical engineering phenomena is a complex problem due to the heterogeneous nature of soils and the participation of a large number of factors involved. During the past few years artificial neural networks (ANNs) have been the most widely used pattern recognition techniques in modeling of complex geotechnical engineering problems; however they suffer from a number of drawbacks. In this paper the application of a new evolutionary polynomial regression (EPR) method to a number of geotechnical engineering problems is presented. Like ANN, this method can operate on large quantities of data in order to capture the nonlinear interaction between variables of the system. In addition, it provides a structured representation of the data, which allows the user to gain additional information on how the system performs. Capabilities of the EPR methodology are illustrated by application to a number of complex practical geotechnical engineering problems which are difficult to solve or interpret using conventional approaches. The merits and limitations of the proposed method are discussed in detail.

1 INTRODUCTION

Many geotechnical engineering problems lack a precise analytical theory or model for their solutions. This is usually because the engineering properties of soil and rock exhibit varied and uncertain behavior due to the complex and imprecise physical processes associated with the formation of these materials (Jaksa 1995). This is in contrast to most other civil engineering materials like steel or concrete which have greater homogeneity and isotropy. In order to cope with the complexity of geotechnical problems traditional forms of engineering design solutions have been widely developed. The information has been usually collected, synthesized and presented in the form of design charts, tables or numerically developed empirical formulae.

In recent years, by pervasive developments in computational software and hardware, several alternative computer aided pattern recognition and data classification approaches have been emerged and developed. The main idea is that a pattern recognition system (e.g. neural network, fuzzy logic or genetic programming) learns adaptively from experience and extracts various discriminants, each appropriate for its purpose. Although there are other general purpose data-driven techniques, artificial neural networks (ANNs) are the most widely used pattern recognition methods that have been introduced to model complex geotechnical engineering problems and capture nonlinear interactions

between various soil (and rock) parameters in a system. So far ANNs have been applied to a wide range of geotechnical applications such as pile bearing capacity (Goh 1996, Abu-Kiefa 1998), site characterizations (Juang et al. 2001), soil behavior (Zhu et al. 1998), liquefaction potential (Juang & Chen 1999, Baziar & Nilipour 2003), slope stability (Lu & Rosenbaum 2003), foundation settlement (Shahin et al. 2002b), underground openings (Benardos & Kaliampakos 2004), and many others. The basic architecture of neural networks has been covered widely (e.g. Lippmann 1987, Flood & Kartam 1994). A neural network consists of a number of interconnected processing elements, commonly referred to as neurons. The neurons are arranged into two or more layers and interact with each other via weighted connections. The data are presented to the neural network using an input layer; and an output layer holds the response of the network to the input. The input/output relationship is captured by repeatedly presenting examples of the input/output data sets to the ANN and adjusting the model coefficients (i.e., connection weights and biases) in an attempt to minimize an error function representing the difference between the actual outputs and the outputs predicted by the model.

Although it has been shown by various researchers that ANNs offer great advantages in the analysis of many geotechnical engineering phenomena, but they have their own drawbacks. One of the disadvantages

of the ANN is that the optimum structure of the network (such as number of inputs, hidden layers, transfer functions, etc.) must be identified a priori, which is usually done through a time consuming trial and error procedure. Furthermore, the main disadvantage of the neural network-based models is the large complexity of the network structure, as it represents the knowledge in terms of a weight matrix which is not accessible to user understanding. In addition, as ANNs perform function approximation through large parameterization and the use of simple functional structures (transfer functions); parameter estimation and overfitting problems represent other major disadvantages of a model constructed by ANN (Giustolisi 2002). In this paper, the application of a new evolutionary polynomial regression (EPR) method to a number of geotechnical engineering problems is presented.

2 EVOLUTIONARY POLYNOMIAL REGRESSION

2.1 Overview

Evolutionary polynomial regression is a data-driven hybrid method for a multi-model approach based on evolutionary computing, aimed to search for polynomial structures representing a system. A general EPR expression may be given as:

$$y = \sum_{j=1}^m f(X, a_j) + a_0 \quad (1)$$

where y = estimated output of the system; a_j = a constant value; f = a function constructed by the process; X = matrix of input variables; and m = length (number of terms) of the polynomial expression (Giustolisi & Savic, in press). The general functional structure represented by $f(X, a_j)$ is constructed from elementary functions by EPR using a Genetic Programming (GP) strategy. The GP is employed to select the useful input vectors from X to be combined. The building blocks (elements) of the $f(X, a_j)$ structure are defined by the user based on understanding of the physical process. While the selection of feasible structures to be combined is done through an evolutionary process; the parameters a_j are estimated by the least square (LS) method.

2.2 Some features of EPR

EPR is a technique for data-driven modeling. In this technique, the combination of the genetic programming to find feasible structures and the least square method to find the appropriate constants for those structures implies some advantages. In particular, the GP allows

a global exploration of the error surface relevant to specifically defined objective functions. By using such objective (cost) functions some criteria can be selected to be satisfied through the searching process. These criteria can be set in order to (a) avoid the overfitting of models; (b) push the models towards simpler structures; and (c) avoid unnecessary terms representative of the noise in data. EPR shows robustness and in every situation can get a model truly representative of data.

The interesting feature of EPR is in the possibility of getting more than one model for a complex phenomenon. Each different model can be trained according to a specific cost function. A further feature of EPR is the high level of interactivity between the user and the methodology. The user physical insight can be used to make hypotheses on the elements in the function $f(X, a_j)$ and on its structure (Equation 1). Selecting an appropriate objective function, assuming pre-selected elements in Equation 1 (based on engineering judgment), and working with dimensional information enable refinement of final models (Giustolisi & Savic, in press).

3 APPLICATION OF EPR IN GEOTECHNICAL ENGINEERING

Two examples are presented to illustrate the capabilities of the EPR approach in capturing nonlinear interaction between input and output variables in geotechnical systems. The accuracy of every proposed model for each particular phenomenon is evaluated based on the coefficient of determination (COD) and root mean square error (RMSE) which are calculated as:

$$COD = 1 - \frac{\sum_N (Y_m - Y_p)^2}{\sum_N (Y_m^2) - \left(\sum_N Y_m\right)^2 / N} \quad (2)$$

$$RMSE = \left(\frac{\sum_N (Y_m - Y_p)^2}{N} \right)^{0.5} \quad (3)$$

where Y_m = actual measured value; Y_p = predicted value; and N = number of samples.

3.1 Pile bearing capacity

Piles have been used for many years as a major type of structural foundation. However the estimation of bearing capacity of pile foundations has been a difficult problem due to the contribution of different factors that affect the behavior of piles and the uncertainties

Table 1. The range of values for the parameters.

Parameter	Minimum value	Maximum value
φ_s (degree)	28	39
φ_t (degree)	31	41
σ'_v (kN/m ²)	38	475
L (m)	3	47.2
A (m ²)	0.0061	0.6568
Q (kN)	75	5604

involved in determination of these factors. Theoretical approaches are mainly based on simplifications and assumptions; therefore, in-situ testing has been accepted as the most reliable means of calculating the bearing capacity of these structures. However, this is not necessarily the most economical method. During recent years, the prediction of the load capacity of piles, particularly those based on pile driving data, has been examined using artificial neural networks (Goh 1994, 1995a, b, 1996, Chan et al. 1995, Lee & Lee 1996, Teh et al. 1997, Abu-Kiefa 1998). The ANN-based (black box) models have been able to successfully capture the input-output relationship for the given set of data but they do not provide a transparent relationship that can be used in engineering practice.

In this research, several EPR models have been developed using the same database of the in situ pile tests presented in Abu-Kiefa (1998). Five variables were selected to be the model inputs. These inputs were the angle of shear resistance of the soil around the shaft (φ_s), the angle of shear resistance at the tip of the pile (φ_t), the effective overburden pressure at the tip of the pile (σ'_v), the pile length (L) and the equivalent cross-sectional area of the pile (A). The model had one output representing the total pile capacity (Q). The range of values for each parameter, used in the development of the EPR models, is listed in Table 1.

The data set was divided in two subsets: a training set used for model construction (78%) and a test set used for testing of the developed model (22%). It is important to emphasize that the test set was never used in the model construction phase, thereby allowing evaluation of the generalization capabilities of the models. In this way, an unbiased performance indicator was obtained on real capability of the models. The EPR analysis was conducted with various combinations of different number of generations, different functions, different multi-objective optimization strategies and different number of terms in order to obtain a number of potential relationships describing the pile bearing capacity as a function of the selected input parameters. Among the relationships obtained, three were chosen according to their performance on both training and testing sets. The COD and RMSE values for

Table 2. COD and RMSE values for the selected EPR models.

Model	Training set		Testing set	
	COD	RMSE (kN)	COD	RMSE (kN)
4	0.87	456	0.81	536
5	0.87	457	0.8	544
6	0.88	447	0.81	526

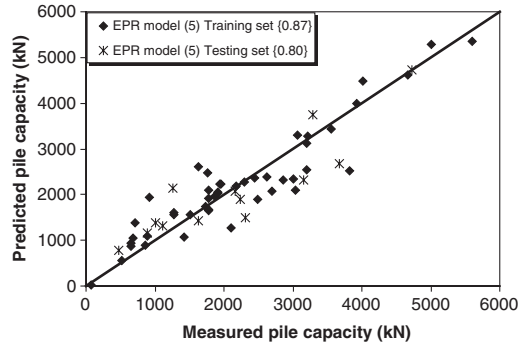


Figure 1. Predicted versus measured pile bearing capacities for both training and testing cases, using EPR model (5).

the selected models are summarised in Table 2. The selected models are:

$$Q = 26.84 \frac{\varphi_t \sigma_v'^2}{\varphi_s^2 L} + \frac{1069440.88}{\varphi_s} + 837.44 \frac{\varphi_s^2 \sigma_v' A}{\varphi_t^2 L} + 15.46 \varphi_s^2 - 50042.76 \quad (4)$$

$$Q = \frac{20497002}{\varphi_s^2} + 999.40 \frac{\sigma_v'^2}{\varphi_s^2 L} + 869.47 \frac{\varphi_s^2 \sigma_v' A}{\varphi_t^2 L} + 1201.40 \varphi_s - 59412.38 \quad (5)$$

$$Q = \frac{68859831.74}{\varphi_s^2} - \frac{4188724.23}{\varphi_s} + 238.16 \frac{\varphi_s^2 A}{\varphi_t} + 0.87 \varphi_s \sigma_v' - 0.19 \varphi_s^2 L + 63032.92 \quad (6)$$

It was observed that the EPR was able to learn the complex relationship between pile capacity and the main contributing factors with a very high accuracy. For example Figure 1 shows the comparison of the results for the training and validation sets, obtained from EPR model (5). It can be seen that the trained model can predict the pile bearing capacity and generalize the learning to unseen cases with a very good accuracy.

3.2 Settlement of shallow foundations on granular soils

Determination of settlement of shallow foundations on granular soils is another complex geotechnical engineering problem due to the complex and heterogeneous nature of soils and the participation of several factors related both to the soil and foundation properties. Due to the complexity of the problem, several researchers have attempted to model this phenomenon using different techniques. As a result, a considerable number of theoretical, empirical and numerical methods have been developed to predict the settlement of shallow foundations on cohesionless soils. In past few years ANN has been the most widely used method for determination of shallow foundation settlement based on field data (Sivakugan & Eckersley 1998, Shahin et al. 2002a, b, 2003a, b, 2005). However, these methods cannot provide a well formulated scheme which can be used by practicing engineers and non-academic people.

In the present study, EPR models were developed using a database of 173 SPT-based case histories, collected from the literature that involved field measurements of settlement of shallow foundations on granular soils. The input parameters were considered as the foundation width (B), foundation net applied pressure (q), soil compressibility represented by average SPT blow count (N), foundation length (L) and foundation embedment (D_f). Settlement was the single output variable. The range of values for each parameter, used in the development of EPR models, is listed in Table 3.

The whole database of the case histories was divided into two sub-sets; the training set used for model construction (81%) and the test set used for testing of the developed model (19%). Having done different analyses with different criteria, several EPR models were obtained. Among the models obtained, the three best models are presented here.

$$S_c = 2.31 \frac{Bq}{N^2} - 25.55 \frac{BD_f}{N^2} - \frac{7.88}{L} + 9.93 \quad (7)$$

$$S_c = 2.16 \frac{Bq}{N^2} - 22 \frac{BD_f}{N^2} + 0.01 \frac{q^2}{N^2} - \frac{10.04}{L} + 9.41 \quad (8)$$

Table 3. The range of values for the parameters.

Parameter	Minimum value	Maximum value
B (m)	0.9	55
L (m)	0.9	101
q (kPa)	18.32	697
N	4	60
D_f (m)	0	10.7
S_c (mm)	0.6	121

$$S_c = 0.05 \frac{q^2}{N^2} + 32.56 \frac{B}{N} - 3.65 \frac{B^2 LD_f}{qN^2} - 0.05 \frac{Bq^2}{L^2 N^2} \quad (9)$$

Table 4 shows the values of COD and RMSE calculated for the three selected models. It is shown that, again, for this geotechnical problem, EPR was able to capture the complex relationship between input and output variables with a very high accuracy.

In order to assess the performance of the proposed method in providing improved predictions of settlement of shallow foundations, the results of the model presented by Equation (8) were compared with those obtained using a number of commonly used empirical methods including the methods proposed by Schmertmann et al. (1978), Schultze & Sherif (1973) and also a neural network based model (Shahin et al. 2002b). The results of settlement prediction (for the validation part of the EPR model), obtained using the aforementioned methods are presented in Figure 2. The values of the COD calculated for each method are shown in {} in the legend.

The results show that the method of Schmertmann et al. (1978) appears to overpredict small settlements of about 0–20 mm. The method of Schultze & Sherif (1973) generally provides reasonable predictions for settlements of up to 20 mm but underestimates larger

Table 4. COD and RMSE values for the selected EPR models.

Model	Training set		Testing set	
	COD	RMSE (mm)	COD	RMSE (mm)
7	0.91	7.8	0.95	5.8
8	0.92	7.4	0.94	6.4
9	0.91	7.7	0.84	10.1

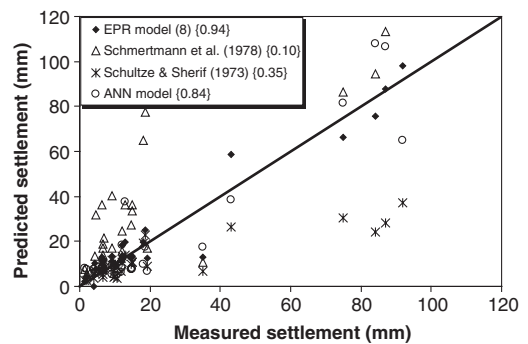


Figure 2. Predicted versus measured settlement for testing cases, using EPR model (8) and conventional methods.

settlements. It is shown that, in some cases, the application of the traditional methods could lead to error of more than 400%. The ANN model performs better than the traditional methods although it has some problems with accurate prediction of small settlements. The proposed EPR model appears to outperform the conventional methods. It also provides a considerable improvement over the ANN-based model both in terms of the accuracy and ease of use in engineering practice.

4 SUMMARY AND DISCUSSION

Current practice in geotechnical engineering often involves the use of subjective or empirical techniques to evaluate imprecise field or experimental data that involve complex relationships between various geotechnical parameters. The traditional methods usually suffer from the lack of physical understanding. Furthermore, the simplifying assumptions that are usually made in the development of the traditional methods may, in some cases, lead to very large errors. In recent years, a number of alternative pattern recognition methods (such as neural networks) have begun to be used in the analysis of engineering problems. These methods have the advantage that they do not require any simplifying assumptions in developing the model. However, the neural network models suffer from a number of shortcomings including their inability to present an explicit relationship between the input and output parameters.

In this paper, a new approach has been introduced for the analysis of complex geotechnical problems using evolutionary polynomial regression. The capabilities of EPR methodology have been illustrated by application to two practical geotechnical engineering problems including prediction of pile bearing capacity and settlement of shallow foundations on granular soils.

The results show that the EPR models provide a significant improvement over the existing models. Furthermore, the proposed EPR models generate a transparent and structured representation of the system. An additional advantage of the EPR approach is that there is no need to assume a priori the form of the relationship between the input and output parameters. The explicit and transparent structures obtained from the proposed EPR method can allow physical interpretation of the problem which gives the user an insight into the relationship between input and output data. For design purposes, the EPR models, presented in this study, are simple to use and provide results that are more accurate than the existing methods. In the EPR approach, no preprocessing of the data is required and there is no need for normalization or scaling of the data. Another major advantage of the EPR approach is that as more data becomes available, the quality of the prediction can be easily improved by retraining the

EPR model using the new data. However, it should be noted that the EPR models should not be used for extrapolation i.e. for new cases where one or more parameters fall outside the range of the parameters used in training (see Tables 1, 3), the predicted results should be taken with caution and allowance should be made for the uncertainty.

5 CONCLUSION

In this study the feasibility of using a new evolutionary polynomial regression (EPR) method to capture non-linear interactions between input and output variables in complex geotechnical engineering systems was demonstrated. The method provides a structured representation of the data, which allows the user to gain additional information on how the system performs. The capabilities of this method were illustrated by application to two practical geotechnical problems. Based on the results, the EPR method was found to be very reliable and accurate.

REFERENCES

- Abu-Kiefa, M.A. 1998. General regression neural networks for driven piles in cohesionless soils. *J. Geotech. & Geoenv. Engrg.* 124(12): 1177–1185.
- Baziar, M.H. & Nilipour, N. 2003. Evaluation of liquefaction potential using neural-networks and CPT results. *J. Soil Dyn. Earthquake Engrg.* 23: 631–636.
- Benardos, A.G. & Kaliampakos, D.C. 2004. Modelling TBM performance with artificial neural networks. *J. Tunnelling & Underground Space Tech.* 19(6): 597–605.
- Chan, W.T. Chow, Y.K. & Liu, L.F. 1995. Neural network: An alternative to pile driving formulas. *J. Computers & Geotechnics*, 17: 135–156.
- Flood, I. & Kartam, N. 1994. Neural networks in civil engineering II principles and understanding. *J. Computing in Civil Engrg.*, 8(2): 149–162.
- Giustolisi, O. 2002. Some techniques to avoid overfitting of artificial neural networks. *Hydroinformatics; Proc. 5th intern. conf., Cardiff, 1–5 July 2002*. London: IWA publishing, 2: 1465–1477.
- Giustolisi, O. & Savic, D.A. 2006. A symbolic data-driven technique based on evolutionary polynomial regression. *J. Hydroinformatics* 8(3): (in press).
- Goh, A.T.C. 1994. Nonlinear modelling in geotechnical engineering using neural networks. *Australian Civil Engrg. Trans.* 36(4): 293–297.
- Goh, A.T.C. 1995a. Back-propagation neural networks for modeling complex systems. *Artificial Intelligence in Engrg.* 9: 143–151.
- Goh, A.T.C. 1995b. Empirical design in geotechnics using neural networks. *Geotechnique* 45(4): 709–714.
- Goh, A.T.C. 1996. Pile driving records reanalyzed using neural networks. *J. Geotech. Engrg.* 122(6): 492–495.
- Jaksa, M.B. 1995. The influence of spatial variability on the geotechnical design properties of a stiff, overconsolidated clay. PhD thesis, The University of Adelaide, Adelaide.

- Juang, C.H. & Chen, C.J. 1999. CPT-based liquefaction evaluation using artificial neural networks. *Computer-Aided Civil and Infrastructure Engng.* 14: 221–229.
- Juang, C.H., Jiang, T. & Christopher, R.A. 2001. Three-dimensional site characterisation: neural network approach. *Geotechnique* 51(9): 799–809.
- Lee, I.M. & Lee, J.H. 1996. Prediction of pile bearing capacity using artificial neural networks. *Computers & Geotechnics* 18(3): 189–200.
- Lippmann, R.P. 1987. An introduction to computing with neural nets. *IEEE Acoustics, Speech and Signal Processing Magazine* 4(2): 4–22.
- Lu, P. & Rosenbaum, M.S. 2003. Artificial neural networks and grey systems for the prediction of slope stability. *Natural Hazards* 30(3): 383–395.
- Schmertmann, J.H., Hartman, J.P. & Brown, P.B. 1978. Improved strain influence factor diagrams. *J. Geotech. Engrg. Div.* 104(8): 1131–1135.
- Schultze, E. & Sherif, G. 1973. Prediction of settlements from evaluated settlement observations for sand. *Soil Mech. & Foundation Engrg.; Proc. 8th intern. conf., Moscow*, 1(3): 225–230.
- Shahin, M.A. Jaksa, M.B. & Maier, H.R. 2002a. Artificial neural network-based settlement prediction formula for shallow foundations on granular soils. *Australian Geomechanics* 37(4): 45–52.
- Shahin, M.A. Jaksa, M.B. & Maier, H.R. 2005. Neural network based stochastic design charts for settlement prediction. *Canadian Geotech. J.* 42(1): 110–120.
- Shahin, M.A. Maier, H.R. & Jaksa, M.B. 2002b. Predicting settlements of shallow foundations using artificial neural networks. *J. Geotech. Geoenv. Engrg.* 128(9): 785–793.
- Shahin, M.A. Maier, H.R. & Jaksa, M.B. 2003a. Neural and neurofuzzy techniques applied to modelling settlement of shallow foundations on granular soils. In D.A. Post (ed.), *Modeling and simulation, MODSIM; Proc. intern. congress, Townsville, Queensland*, 4: 1886–1891.
- Shahin, M.A. Maier, H.R. & Jaksa, M.B. 2003b. Settlement prediction of shallow foundations on granular soils using B-spline neurofuzzy models. *Computers & Geotechnics* 30(8): 637–647.
- Sivakugan, N. Eckersley, J.D. & Li, H. 1998. Settlement predictions using neural networks. *Australian Civil Engrg. Trans.*, 40: 49–52.
- Teh, C.I. Wong, K.S. Goh, A.T.C. & Jaritngam, S. 1997. Prediction of pile capacity using neural networks. *J. Computing in Civil Engrg.* 11(2): 129–138.
- Zhu, J.H. Zaman, M.M. & Anderson, S.A. 1998a. Modeling of soil behavior with a recurrent neural network. *Canadian Geotech. J.* 35(5): 858–872.

Miscellaneous

Some experiences developing software for seepage with phreatic surfaces

M. Mavroulidou & M.J. Gunn

Faculty of Engineering, Science and The Built Environment, London South Bank University, London, UK

R.I. Woods

School of Engineering, University of Surrey, Guildford, Surrey, UK

ABSTRACT: Geotechnical engineers need versatile numerical tools for the successful solution of seepage problems involving phreatic surfaces. The paper reviews and assesses techniques used for the numerical modelling of this category of problems, for both steady-state and transient conditions. This is based on experience gained through the development of a finite element computer model for seepage with phreatic surfaces. It is shown that the results from the various methods may differ significantly, especially for transient seepage analyses. A realistic modelling of flow in the unsaturated zone was found to improve the quality of the results. The study also led to conclusions on some additional points of interest to the numerical modeller, concerning other factors potentially affecting the quality of the results.

1 INTRODUCTION

In the geotechnical engineering field both analytical and numerical solutions are used to estimate flow rates and pore water pressures associated with seepage in the presence of phreatic surfaces. Calculation of steady state flow rates and drawdowns for both confined and unconfined problems is often based on the assumption of predominantly horizontal flow (Dupuit's assumptions). Under these assumptions, transient seepage can also be modelled as a sequence of steady states. When applied to transient flow, the Dupuit-Forchheimer assumptions, can lead to the one-dimensional, transient Boussinesq equation, which can be linearised. Thus, a number of analytical solutions can be obtained. For the majority of problems, however, use of numerical techniques such as finite differences or finite elements will be required. Two distinct approaches to modelling unconfined flow have been used with numerical models. Both approaches involve strong non-linearities, making their numerical solution challenging.

The first approach assumes that water flow below the phreatic surface is of primary importance and idealises the flow domain as one confined to the saturated zone only (Taylor & Brown 1967, Bathe & Khosghoftaar 1979). The phreatic surface is treated as a geometrical boundary between a completely saturated and a completely dry zone in which any flow is ignored (free boundary approach). Although real soils do show a decline in hydraulic conductivity with

increasing suction, it is clear that most previous workers have used the former approach as an artifice to eliminate (or greatly reduce) flows above the phreatic surface.

When time dependent movement of the phreatic surface is modelled the usual approach is to apply a flow term uniformly distributed along the phreatic surface, to account for the volume of water released or absorbed by the soil as the phreatic surface moves (e.g. Bathe et al. 1982). The specific yield of the soil is used to quantify this term. According to this approach, any subsequent flow above the phreatic surface is, in effect, ignored.

A different approach, which will be referred to as the variably saturated domain approach, considers continuity of flow between the saturated and the unsaturated zones. The position of the phreatic surface emerges as a by-product of the calculation. This approach is more realistic, as it does not introduce any arbitrary boundary assumptions between the zones above and below the phreatic surface. Moreover, it can give an estimate of suctions in the zone above the phreatic surface. However, it involves complications with added unknown soil parameters, especially if a coupled flow-soil deformation analysis is desired. In the latter case, an appropriate constitutive model for partially saturated soils would also be required. An additional complexity is that these functional relationships have to be determined separately for every soil and are difficult to obtain in practice.

For practising geotechnical engineers the main question is whether there is any need for such increased complexities in the modelling of seepage with phreatic surfaces. To assess this, the writers have developed two finite element seepage programs. The first is based on the free boundary approach and can provide solutions of steady-state unconfined seepage problems. The second is based on the variably saturated domain approach. The paper compares the two methods based on results of steady seepage through flow domains of different geometries and material properties. Results of transient flow are also presented and compared with previously published solutions. Some additional points of interest to the numerical modeller are also discussed.

2 METHODOLOGY

2.1 Free boundary approach model

The governing equation for steady-state fluid flow through saturated porous media is:

$$\frac{\partial}{\partial x}(K_x \frac{\partial h}{\partial x}) + \frac{\partial}{\partial y}(K_y \frac{\partial h}{\partial y}) + \frac{\partial}{\partial z}(K_z \frac{\partial h}{\partial z}) = 0 \quad (1)$$

where h = total head; K_x , K_y , K_z = hydraulic conductivities in the x , y and z directions respectively.

Equation 1 is written with respect to the main axes of hydraulic conductivity. For the derivation of Equation 1 flow was assumed to obey Darcy's law. For homogeneous and isotropic soils Equation 1 reduces to Laplace equation.

Having physically neglected the flow in the unsaturated zone, the free surface becomes not only a zero pressure isobar, but also the limit of the flow domain. In steady-state flow, this means that the phreatic surface also constitutes the upper streamline which is expressed mathematically by the boundary condition that the flux normal to the surface should be zero. The other boundary condition to be satisfied along the free surface, is that water pressure along it is zero. Note the non-linearity introduced by the free surface boundary conditions according to this approach: the location of the free surface depends on the head distributions; the head distributions depend in turn on the free surface location.

To develop the computer program, the variable mesh technique was used, which re-adjusts the geometry of the mesh as part of the iterative process (Taylor & Brown 1967). The Gauss-Seidel iterative procedure was used for the solution of the matrix equations.

The iterative procedure can be described as follows: (a) An initial guess of the free surface position is made before the iterative process starts. Zero-flux boundary conditions are imposed along the assumed free surface (i.e. the phreatic surface is assumed to be a flowline).

This gives a first numerical solution; (b) the second boundary condition that a free surface should satisfy is checked, namely that the free surface must be an equipotential line of zero pressure. This is equivalent to checking whether the total head equals the elevation head on the free surface nodes (within the specified tolerance); (c) if this condition is not satisfied, the iterative procedure is repeated, starting with the updated position of the free surface (and hence that of the flow domain), after the coordinates of all internal nodes have been readjusted accordingly.

2.2 Variably saturated domain approach

The basic equation governing flow of water through the soil is:

$$\frac{\partial}{\partial x}(K_x(\psi) \frac{\partial h}{\partial x}) + \frac{\partial}{\partial y}(K_y(\psi) \frac{\partial h}{\partial y}) + \frac{\partial}{\partial z}(K_z(\psi) \frac{\partial h}{\partial z}) = (\theta S_s + C(\psi)) \frac{\partial h}{\partial t} \quad (2)$$

where h = total head; K_x , K_y and K_z = hydraulic conductivities in the x , y and z directions respectively; ψ = pressure head; θ = volumetric moisture content; S_s = elastic storage coefficient; and $C(\psi)$ = moisture retention capacity, representing the rate at which the soil absorbs or releases water as a function of the negative pressure head. It is determined by the slope of the moisture retention curve (relating volumetric water content to pressure head).

The latter two quantities are responsible for defining elemental water content changes for saturated and unsaturated conditions respectively. For the derivation of Equation 2 Darcy's law was assumed to be valid in both saturated and unsaturated zones. For steady seepage where $\partial h / \partial t = 0$, the right hand side of Equation 2 vanishes.

The dependence of the hydraulic coefficients on pressure head variations causes Equation 2 to be non-linear. Picard iteration is used for the linearisation of the non-linear systems of equations.

To describe the form of the volumetric water content and hydraulic conductivity variation in the unsaturated zone (defined experimentally) the program offers the choice between some of the most widely used expressions (Brutsaert's 1966, Brooks & Corey's 1966, Gardner's 1958 and Van Genuchten's 1980).

The finite element program developed according to the variably saturated domain approach can perform both two- and three- dimensional analyses using linear or quadratic quadrilateral and parallelepiped elements respectively. It can handle soil anisotropy and heterogeneity (layered soils), existence of seepage faces, hysteresis of the hydraulic properties and hence falling, rising and fluctuating water table conditions. The program has been validated against analytical,

analogue, numerical and experimental results, as well as case studies found in the literature.

3 NUMERICAL ANALYSES

3.1 Analyses performed at the validation stage

The first conclusions concerning the comparative assessment of the two methods as well as factors affecting the quality of the results were derived at the verification/validation stage. The investigation was carried out in order to choose the most appropriate method (or to exclude potentially inappropriate methods), before applying the code to problems for which the solution is unknown.

3.1.1 Free boundary approach model

When linear quadrilateral elements were used, instability problems concerning the seepage face exit point location were observed. This resulted to unacceptable exit point positions. These findings are in agreement with Taylor & Brown's (1967), Kazda's (1978), Gioda & Cividini (1986) and Cividini & Gioda's (1989) observations, while they contradict suggestions by Griffiths (1990).

Note that this instability was not observed when linear triangular elements were used. The probable reason why triangular elements perform better than quadrilateral in this case, is the better distribution of nodal flow between the two adjacent triangular elements. This way, the error in the exit point flux calculation is minimised. (The problem with the modelling of the exit point in the free boundary approach is that it belongs

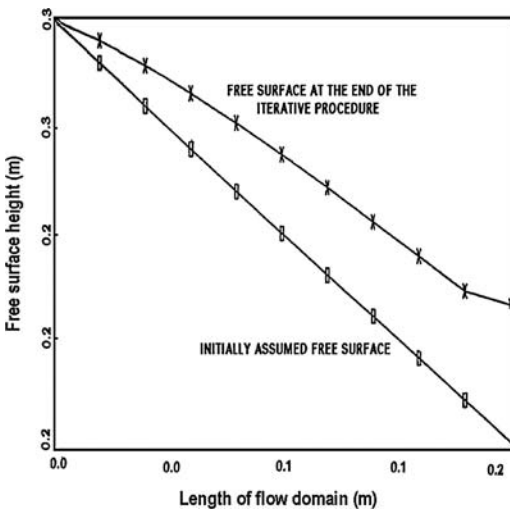


Figure 1. Unacceptable exit point locations obtained from the variable free boundary approach model.

both to the phreatic surface and the seepage face. Being a point of the phreatic surface, it is assigned zero flux – or it is expected to justify the zero flux condition, while being a point of the seepage face, in which water exits the dam, it has clearly a non-zero flux).

3.1.2 Variably saturated domain model

The study included comparisons of results between two methods used for the discretisation of the element time-dependent storage matrix (namely lumped or consistent formulation) and different forms of mathematical functions to model the hydraulic property variations in the unsaturated zone. A study of hydraulic property hysteresis effects and the appropriateness of various hysteresis models was also performed (Mavroulidou 1999). Due to space limitations only a summary of the findings is provided here:

(a) Consistent versus lumped formulation

Results showed that the lumped formulation gave slightly superior results with respect to the consistent formulation. Nevertheless, the overall improvement of the results when using the lumped formulation was not so important, to suggest that the consistent formulation of the time-dependent matrix should be avoided for reasons of accuracy. Note that the lumped formulation has often been suggested as a way to improve the numerical stability (e.g. Cooley 1983 and Milly 1985). However for the range of problems solved at the validation stage, no instability problems were encountered when the consistent formulation was used (Mavroulidou 1999).

(b) Models for the hydraulic property curves

In most cases studied at the validation stage, all functions gave a reasonable fit to the experimental data of the soil hydraulic properties, despite some differences in the exact form of the curves. Consequently, all hydraulic curve models gave substantially the same numerical results for the seepage problems solved at the validation stage, despite these differences (Mavroulidou 1999). However, for general applications, it is advisable that before using a function, a plot is always made of the curve that it produces. This is necessary in order to check if its form is appropriate for a given soil and the ranges of suctions involved in a particular problem.

(c) Modelling hysteresis

The results accounting for hysteresis improved the numerical predictions in cases of reversals in the boundary conditions (Mavroulidou 1999).

3.2 Further applications to geotechnical problems

A series of consistent comparisons of the two methods were made for steady state problems (Mavroulidou 1999, Mavroulidou et al. 2006). These included

investigations of the effect of scale, material properties and heterogeneity (idealised core dams). For the sake of brevity, only some indicative results and the summary of findings are presented here. The geometry and boundary conditions of the selected problems are shown in Figures 2a, 2b and 3. The hydraulic conductivity (permeability) variation in the unsaturated zone for the homogeneous and heterogeneous domains is shown in Figures 4 and 5 respectively. The

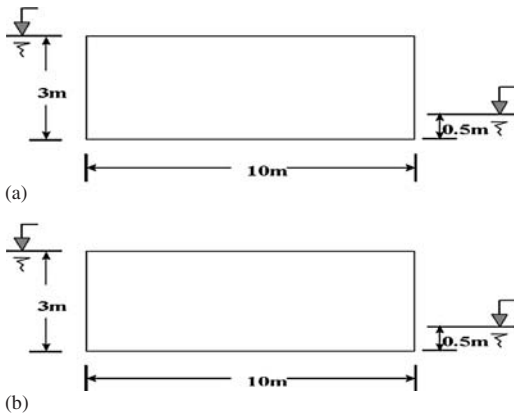


Figure 2. (a) Small rectangular section. (b) Large rectangular section.

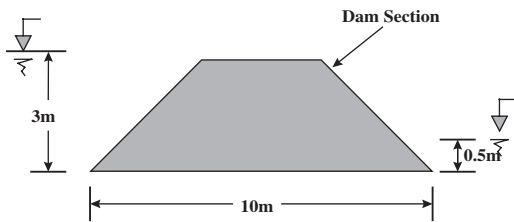


Figure 3. Small sloping edge dam section.

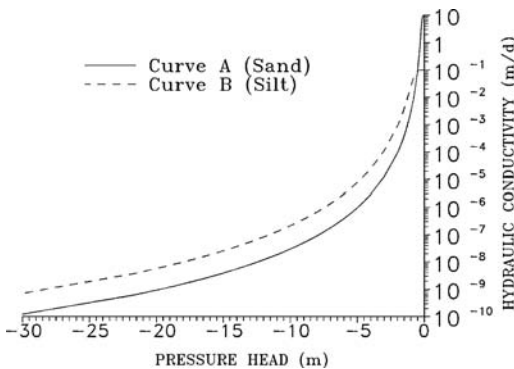


Figure 4. Homogeneous dams: hydraulic conductivity variation in the unsaturated zone.

curves were produced based on the empirical formulae mentioned above, in which typical parameters for various types of soils were used. The results of the free boundary approach are represented by a single figure for all homogeneous soil analyses (Fig. 6). This is also the case for the core dam analyses (Fig. 10). This is because when the free boundary approach is used, the results give the same relative water table position, irrespective of the material assumed or the domain dimensions (i.e. the water table coordinates are proportional to the section dimensions but always pass through the same relative section coordinates). No flow vectors are represented in the free boundary analyses figures as all flow above the water table is discarded by definition. Figures 7 and 8 represent material effects in small homogenous sections according to the variably saturated domain approach. Figure 9 represents a large homogenous section analysis according to the variably saturated domain approach to investigate potential scale effects. Figures 11–13 represent results from the variably saturated domain approach to show material effects in small dams with cores of different hydraulic

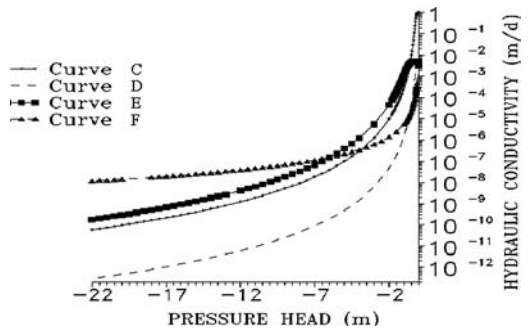


Figure 5. Core dams: hydraulic conductivity variation in the unsaturated zone.

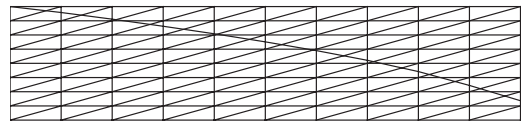


Figure 6. Free boundary approach. Homogeneous section 3×10 m.

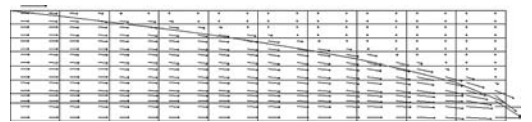


Figure 7. Variably saturated approach. Homogeneous section 3×10 m; saturated hydraulic conductivity $K = 10$ m/d (curve A).

properties (the latter are shown in Fig. 5). From the above mentioned figures it can be noticed that:

(a) Steady state analyses

In homogeneous domains, the water table configurations as obtained by the two approaches are in

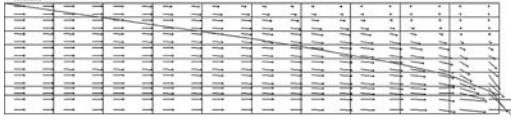


Figure 8. Variably saturated approach. Homogeneous section 3×10 m; saturated hydraulic conductivity $K = 0.1$ m/d (curve B).

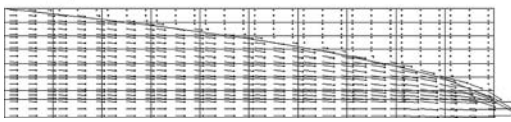


Figure 9. Variably saturated approach. Homogeneous section 30×100 m; saturated hydraulic conductivity $K = 0.1$ m/d (curve B).

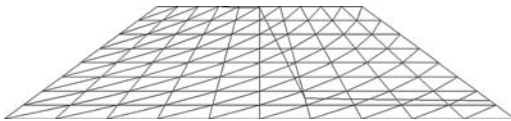


Figure 10. Free boundary approach. Core dam section 3×10 m; dam saturated hydraulic conductivity $K = 1$ m/d; core saturated hydraulic conductivity $K = 0.005$ m/d.

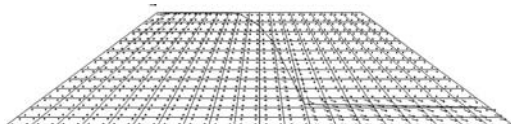


Figure 11. Variably saturated approach. Core dam section 3×10 m; dam saturated hydraulic conductivity $K = 1$ m/d (curve C); core saturated hydraulic conductivity $K = 0.005$ m/d (curve D).

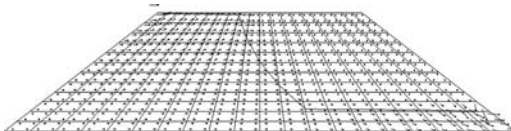


Figure 12. Variably saturated approach. Core dam section 3×10 m; dam saturated hydraulic conductivity $K = 1$ m/d (curve C); core saturated hydraulic conductivity $K = 0.005$ m/d (curve E).

reasonable agreement irrespective of material. Note that when the variably saturated domain approach is adopted a slightly higher number of iterations might be needed for steeper hydraulic conductivity functions (Fig. 4, curve type A). The water table has the same relative position (i.e. in proportion to scale) for both bigger and smaller homogeneous domains. Nevertheless, the results from the variably saturated domain program show that the water table is not the upper flow line (which is the assumption made according to the free boundary approach). This is in agreement with Papagiannakis & Fredlund's (1984) findings. The unsaturated flow components are shown to be more important in small rather than in large flow domains (c.f. Figs. 8 and 9) and in soils showing more gradual changes in hydraulic conductivity with respect to suction and which do not dry out completely, rather than for soils with steep hydraulic conductivity-suction functions that reach very low hydraulic conductivities (c.f. Figs. 7 and 8).

Conversely, for the heterogeneous domains (idealised core dams), the water table configuration as provided by the two approaches is not the same (Figs. 10–13). In general, the variably saturated domain approach results give lower water table configurations. Steep hydraulic conductivity functions for the core material (Figs. 11 and 13) tend to give results closer to the free boundary approach results.

(b) Transient seepage

For the transient flow case, previously published results were used to compare the two methods, as the free boundary approach program only handles steady state flow. Figure 14 represents results from a problem of rapid drawdown in a homogeneous square cross section (Bathe et al. 1982). The geometry and boundary conditions of the problem are also shown in Figure 14. The assumed hydraulic properties were selected to be consistent with those adopted in Bathe et al. (1982).

The results of the two analyses do not agree. Although the final steady state configurations of the phreatic surface are similar, the free boundary approach seems to underestimate significantly the time needed for the steady state to be reached (Fig. 14). It gives considerably lower water table

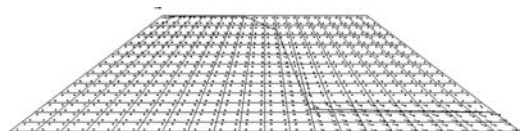


Figure 13. Variably saturated approach. Core dam section 3×10 m; dam saturated hydraulic conductivity $K = 1$ m/d (curve C); core saturated hydraulic conductivity $K = 0.005$ m/d (curve F).

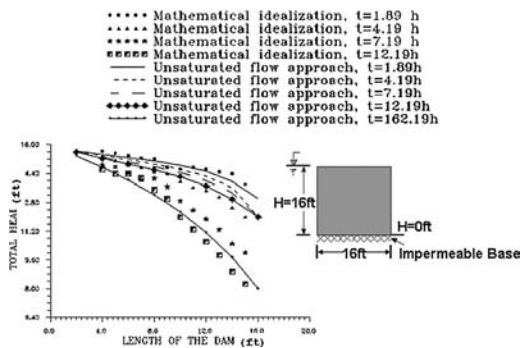


Figure 14. Comparison of transient analysis results.

configurations for all time steps except the initial, as compared to those derived by the variably saturated domain approach. Note that the variably saturated approach results were found to agree satisfactorily with experimental results for similar boundary value problems and material properties (Mavroulidou 1999, Mavroulidou et al. 2003).

This discrepancy can be explained by the fact that the free boundary approach neglects all water retained by and flowing through the unsaturated zone. Instead, it assumes instantaneous flow of the water stored or released by the soil when rise or fall of the water table occurs. Moreover, it assumes a uniform distribution of the volume of water released during desaturation. This is a poor representation of the physics involved in seepage with a moving phreatic surface. The importance of accounting for a varying storage coefficient in the unsaturated zone was demonstrated in Mavroulidou et al. (2003). This was further supported by results of case studies of pumping under transient flow conditions. In these studies, the variably saturated method was also found to improve predictions with respect to solutions assuming constant soil coefficients (Mavroulidou et al. 2005).

It is acknowledged that, strictly mathematically speaking, differences between the two methods were expected, as the respective mathematical problems to be solved are not exactly the same (e.g. different boundary conditions and property variation). The purpose of this paper however, was precisely to show how different ways of modelling the same physical problem may lead to more realistic solutions, and a better representation of the physics involved.

4 CONCLUSIONS

The study drew conclusions based on the writers' experience developing software for problems of seepage in the presence of phreatic surfaces. These

covered aspects of interest to both the numerical modeller and the geotechnical engineer. It was shown that the variably saturated domain approach was overall superior to the free boundary approach: it did not suffer the severe numerical instabilities the latter was subject to and gave a better representation of the physics of flow with phreatic surfaces. It therefore gave better agreement with experimental results or field studies. This was particularly true for the solution of transient problems. Therefore, numerical tools based on the variably saturated domain approach show promise in providing improved solutions of seepage in the presence of phreatic surfaces.

REFERENCES

- Bathe, K.-J., & Khoshgoftaar, M. 1979. Finite element free surface seepage analysis without mesh iteration. *International Journal for numerical and analytical methods in geomechanics* 3: 13–22.
- Bathe, K.J., Sonnad, V. & Domigan, P. 1982. Some Experiences Using Finite Element Methods for Fluid Flow Problems. In *Proceedings of the 4th conference on finite element methods in water resources*, Hannover.
- Brooks, R.H. & Corey, A.T. 1966. Properties of Porous Media Affecting Fluid Flow. *ASCE Journal of the Irrigation and Drainage Division* 92(2): 61–88.
- Brutsaert, W. 1966. Probability laws for pore-size distributions. *Soil Science* 101: 85–92.
- Cividini, A. & Goda, G. 1989. On the variable mesh finite elements analysis of unconfined seepage problems. *Géotechnique* 39(2): 251–267.
- Cooley, R.L., 1983. Some new procedures for numerical solution of variably saturated fluid problems. *Water Resources Research* 19(5): 1271–1285.
- Gardner, W.R. 1958. Some steady-state solutions of the unsaturated moisture flow equation with application to evaporation from a water table. *Soil Science* 85(4): 228–232
- Goda, G. & Cividini, A. 1986. An analysis of unconfined steady state seepage. In *Proceedings of the European Conference on Numerical Methods in Geomechanics ECONMIG 86*, Stuttgart.
- Griffiths, D.V. 1990. Discussion on the paper, On the variable mesh finite elements analysis of unconfined seepage problems, by Cividini, A., Goda, G.. *Géotechnique* 40(3): 523–526.
- Kazda, I. 1978. Free surface seepage flow in earth dams. In Brebbia, C.A., Gray, W.G. and Pinder G.F. (eds), *Finite Elements in Water Resources, Proceedings of the Second international conference on Finite Elements in Water Resources*, Plymouth: Pentech Press.
- Mavroulidou, M. 1999. *Numerical modelling of seepage in the presence of phreatic surfaces*. PhD Thesis. University of Surrey: Guildford.
- Mavroulidou, M., Gunn, M.J. & Woods, R.I. 2003. Impact of storage coefficient on the numerical modelling of trench drainage. *Computers and Geotechnics* 30(8): 683–693.
- Mavroulidou, M., Gunn, M.J. & Woods, R.I. 2005. Numerical modelling of pumping processes involving

- moving phreatic surfaces. *ICE Journal of Geotechnical Engineering* 158(2): 83–93.
- Mavroulidou, M., Gunn, M.J. & Woods, R.I. 2006 An assessment of the free boundary approach for the numerical modelling of seepage in the presence of phreatic surfaces (accepted for publication subject to amendments in *ICE Journal of Geotechnical Engineering*).
- Milly, P.C.D. 1985. A mass-conservative procedure for time-stepping in models of unsaturated flow. *Advances in Water Resources* 8: 32–36.
- Papagiannakis, A.T. & Fredlund, D.G. 1984. A steady state model for flow in saturated-unsaturated soils. *Canadian Geotechnical Journal* 21: 419–430.
- Taylor, R. & Brown, C.B. 1967. Darcy Flow Solutions with a Free Surface. *A.S.C.E. Journal of the Hydraulics Division*, 93: 25–33.
- Van Genuchten, M.T. 1980. A closed form equation for predicting the hydraulic conductivity of unsaturated soils. *Soil Science Society of America Journal* 44: 892–898.

Flow-deformation due to two-phase flow: A loose coupling simulation

A. Chinkulkijniwat

School of Civil Engineering, Suranaree University of Technology, Thailand

S. Semprich

*Institute for Soil Mechanics and Foundation Engineering, Geotechnical Group Graz,
Graz University of Technology, Austria*

ABSTRACT: TOUGH2-FLAC3D coupling is employed to simulate flow and deformation due to two-phase flow induced by the application of air pressure into subsoil. The NATM compressed air tunnelling is of interest in this paper, thus test results from an in-situ air flow test in Essen, Germany are used to verify the TOUGH2-FLAC3D simulation. The comparison shows good agreement between the calculation results and the corresponding test results.

1 INTRODUCTION

In tunnelling construction under certain conditions, water inflow at the tunnel face during tunnelling construction can be prevented by applying a certain magnitude of air pressure into the tunnel space. The magnitude of air pressure must be equal or greater than the magnitude of groundwater pressure at a level of tunnel invert which leads to a linearly increase of pressure difference between air pressure and groundwater pressure. The pressure difference causes an air flow into the surrounding soil. Two-phase flow in an upward direction takes place both at the tunnel face and along the shotcrete lining.

Determination of air consumption due to tunnelling construction has been studied at the Institute for Soil Mechanics and Foundation Engineering at Graz University of Technology for couple of years, e.g. Chinkulkijniwat et al. (2005). However, a surface movement has not yet concerned. In this paper, the surface movement due to tunnelling construction is of interest. There are many reports have been argued that applying of air pressure in the tunnel space during tunnelling construction can reduce a magnitude of surface settlement, e.g. Weber (1983). The interaction between fluid flow and mechanics, which is so-called a fluid-mechanical interaction, is an explanation of the reduction of surface settlement due to compressed air tunnelling construction.

Basically there are three algorithms to perform a numerical simulation for the fluid-mechanical interaction, the full coupling, the loose coupling, and the one way coupling. The loose coupling simulation has been

chosen in this study. Comparing to the one way coupling, the loose coupling is considered more accuracy. Advantage of the loose coupling over the full coupling is an ease in implementation. Moreover, it opposes less limitation to modify the code. Therefore, further extension on the capability of the code is very straightforward. In order to perform loose coupling simulation for fluid-mechanical interaction, two numerical codes are needed, one for mechanical simulation and the other for fluid flow simulation. In this paper, TOUGH2 (Pruess et al. 1999) and FLAC3D (ITASCA 2002) are used for fluid flow and mechanics, respectively. This paper examines whether the loose coupling simulation can capture the feature of flow and deformation due to the application of air pressure to the subsoil (Chinkulkijniwat, 2005). The results for field test according to Kramer & Semprich (1989) is used in this paper to verify the calculation results.

2 METHODOLOGY

2.1 Assumptions

Unsaturated soils consist of three components including a solid and two fluids: water and air. Three phases, including solid, liquid, and gas, represent mixture of components. Liquid is a mixture of water and dissolved air. Gas is a mixture of air and vapour water. Solid is soil skeleton. Unsaturated soils are considered as a multiphase, isothermal, deformable system whose voids are filled partly with liquid and partly with gas. Each fluid phase composes of two components, i.e. water

and dissolved air in liquid phase and vapor and air in gas phase. The mechanical behavior of unsaturated soils is governed by the effective stress (Bishop 1959).

$$\sigma' = \sigma - p_g + \chi(p_g - p_l) \quad (1)$$

where σ' = effective stress; σ = total stress; p_g = gas pressure; p_l = liquid pressure; and χ = Bishop's effective stress parameter. In this paper, the effective stress is the difference between total stress and the average pore pressure. Thus Equation 1 can be rewritten as

$$\sigma' = \sigma - \{S_l p_l + (1 - S_l) p_g\} \quad (2)$$

where S_l = degree of liquid saturation. A small magnitude of deformation is assumed consequently an elastic model is applicable. Deformation due to mechanical response is then translated to the increment or decrement in porosity due to the balance of mass as shown in Equation 3.

$$\frac{d\phi}{dt} = (1 - \phi)\Delta\varepsilon_v \quad (3)$$

where ϕ = porosity; and ε_v = volumetric strain. According to Leverett (1941), the capillary pressure function must be modified with the current fluid conductivity and porosity as:

$$p_{cL} = p_c \sqrt{\frac{\phi}{\phi_i}} \quad (4)$$

where p_{cL} = Leverett's corrected capillary pressure; p_c = calculated capillary pressure; and ϕ_i = initial porosity.

2.2 Coupling algorithm

According to the use of loose coupling, two numerical simulators are employed. The TOUGH2-FLAC3D coupling is conducted as introduced by Rutqvist et al. (2002), i.e. sequential execution and data transfer via a set of external ASCII files. TOUGH2 is developed to handle non-isothermal, multiphase, multicomponent fluid flows in 3-dimensional porous and fracture media. However, mechanical simulation is not possible in a stand alone TOUGH2 simulation. FLAC3D is developed to perform mechanical simulation in soils and rocks. Although FLAC3D can also handle the fluid-mechanical interaction for single-phase fluid flow, a simulation of two-phase fluid flow is not possible with a stand alone FLAC3D simulation. The sequential coupling of two codes is more time consumed in comparison with having a single code. However, the big

advantage of the coupling TOUGH2 and FLAC3D is that both of them are world widely used and well tested in their respective fields. Additionally, source code is available for TOUGH2. Thus modification of the code as well as implementation of the constitutive transport equations is possible. In FLAC3D, an embedded programming language a so-called FISH enables the user to define any new variables and functions. FLAC3D can communicate with TOUGH2 via this feature.

In order to let two numerical simulators: FLAC3D and TOUGH2, communicate each other, knowledge of their corresponding meshes and data structure store in the meshes must be established. A finite difference mesh in FLAC3D generated by the user consists of elements and nodal points. An element is the smallest geometric domain within which the change in a phenomenon (e.g., stress versus strain) is evaluated. A nodal point is points at the corners of the corresponding element. In FLAC3D, state variables which are the vector quantities are stored at the nodal points and the state variables which are the scalar and tensor quantities are stored at the element centroids. However, the input variables can be submitted into the FLAC3D mesh only through the FLAC3D nodal points. Regarding to TOUGH2 mesh, TOUGH2 does not use nodal points but elements. Therefore all the state variables in TOUGH2 are stored at the element centroids.

The effective stress at each FLAC3D element is calculated based on Equation 2. Thus, variables that FLAC3D needs from the TOUGH2 simulation are the degree of liquid saturation S_l , the pressure of liquid phase p_l , and the pressure of gas phase p_g . The capillary pressure can be calculated from the difference between pressure of liquid phase and pressure of gas phase. The degree of gas saturation S_g , can be calculated by deducting the degree of liquid saturation S_l from 1.

An increment in porosity is calculated from a volumetric strain as written in Equation 3. A volumetric strain increment is stored at a FLAC3D element centroid, therefore an updated porosity represent at the corresponding element centroid. The updated porosity after the FLAC3D simulation run is then sent to a corresponding TOUGH2 element. Figure 1 is schematic diagram shows how to send the information from TOUGH2 mesh to the j th FLAC3D node and the information from FLAC3D mesh to the i th TOUGH2 element.

The TOUGH2-FLAC3D coupling is initiated with TOUGH2 simulation run. TOUGH2 is executed between t_0 and t_1 until convergence is reached. At each TOUGH2 element, porosity is assumed constant during this time step. Then FLAC3D is executed for mechanical simulation for the same period of time step. The effective stress at each FLAC3D element is calculated. To the end of each time step, an increment in porosity is calculated from a volumetric strain as

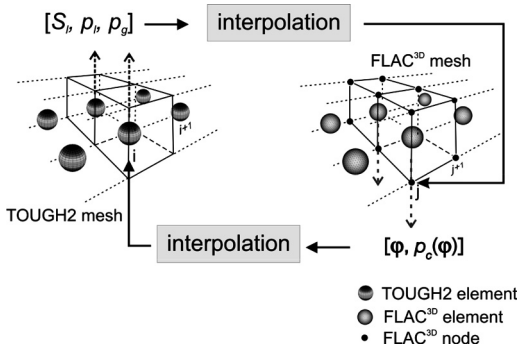


Figure 1. Communication between TOUGH2 and FLAC3D.

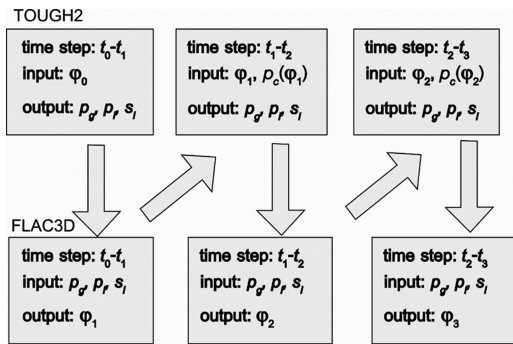


Figure 2. TOUGH2-FLAC3D coupling procedures.

written in Equation 3. TOUGH2 is then executed for a next time step. The updated porosity after the FLAC3D simulation run is then sent to a corresponding TOUGH2 element. TOUGH2 is again executed between t_1 and t_2 until convergence is reached. These procedures are repeated until the simulation time reach a time specified by the user. Figure 1 shows numerical procedures of the coupling TOUGH2 and FLAC3D.

Between fluid flow and mechanical simulations in Figure 2, interpolation is needed to map inputs and outputs from one mesh to the other. It is because the variables are submitted into FLAC3D mesh through its nodal points, while TOUGH2 mesh uses only elements. Moreover, even the outputs from FLAC3D are at a FLAC3D elements, in loose coupling, the computational grid mesh used in each simulation codes is not necessary the same therefore interpolation is also needed. In this study, a weighted distant interpolation is used for interpolation inside the domain. At the boundaries of the model, the closest point is searched and assigned to the destination, point by point.

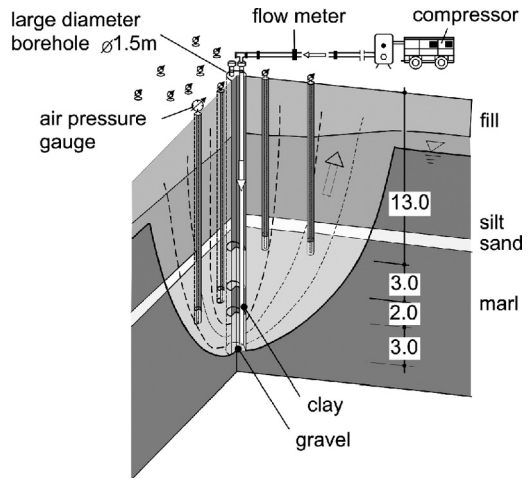


Figure 3. In-situ air flow test in Essen (Kramer & Semprich, 1989).

3 VERIFICATION

3.1 In-situ air flow test in Essen

In this topic, an example dealing with two-phase flow and deformation due to the application of air pressure into the soil domain are demonstrated and verified. The in-situ air flow test in Essen carried out by the German contractor Bilfinger + Berger Bauaktiengesellschaft (Kramer & Semprich 1989) is chosen.

Simultaneously with a tunnelling construction project in Essen, Germany, an in-situ air flow test was carried out to investigate the fluid conductivity of gas phase and the deformations due to two-phase flow induced by the application of compressed air. Figure 3 shows a schematic diagram of the experimental set up. The certain magnitude of air pressure was introduced into the ground via a borehole of 1.5 m diameter. Inside of the borehole a steel pipe is installed and the annular between the pipe and the ground is filled with clay throughout its length except at a depth from 13 to 16 m and a depth from 18 to 21 m below the ground surface where gravels are filled in the annulus as shown in Figure 3.

During the test the rate of air supplied by a compressor, the pore pressure in the ground in vicinity of the borehole, and the ground surface displacement were monitored. As shown in Figure 3, a number of piezometers were installed in vicinity of the borehole to monitor the magnitudes of pore pressure according to the application of air pressure. The ground surface displacement was controlled by geodetic leveling. Thirteen level rods were installed at different distances from the borehole. According to Kramer & Semprich (1989), the Essen subsoil consists of four distinct layers

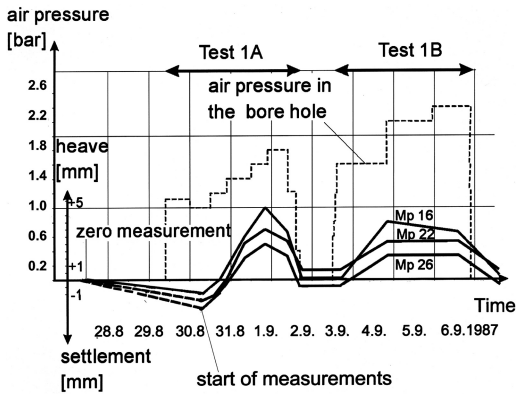


Figure 4. Vertical displacement at the ground surface during the experiment (Kramer & Semprich, 1989).

including an approximate 3 m thickness of fill, an approximate 7–8 m thickness of silt beneath the fill, an approximate 1.2 m thickness of sand beneath the silt, and a thick layer of marl which is rather weathered in the upper region and pronounced joints further down. The groundwater table is at about 4.7 m below the ground surface.

In total, three sets of different tests were carried out. Two of them were carried out by varying depth where the air pressure was applied into the soil. In a test so-called 1A, the air pressure was applied at a depth between 13 and 16 m from the ground surface. In a test so-called 1B, the air pressure was applied at a depth between 18 and 21 m from the ground surface. In the third test, the soil was grouted and the air pressure was applied into the soil at a depth between 11 to 14 m from the ground surface through a second large diameter borehole. Details of the experiment are elaborately described in Kramer & Semprich (1989). Period of the test 1B which is considered here took about 3.5 days. In this test, air pressure was applied three stepwise $p_a = 160 \text{ kN/m}^2$, $p_a = 220 \text{ kN/m}^2$, and $p_a = 235 \text{ kN/m}^2$ within 3.5 days.

Figure 4 shows beside another the magnitudes of ground surface displacement read from three level rods at 1.7 m (Mp16), 11.9 m (Mp22) and 16.1 m (Mp26) horizontally apart from the borehole. Figure 5 shows beside another the time series curve for the rate of air losses read during the experiment 1B. Due to an ease in simulation, only the first pressure level $p_a = 160 \text{ kN/m}^2$ is concerned in this study.

Figure 6 shows beside another, the magnitudes of pore pressure read from four piezometers during the experiment. The symbols represent locations of the piezometers. The magnitudes of pore pressure read from these piezometers are depicted beside the corresponding symbols.

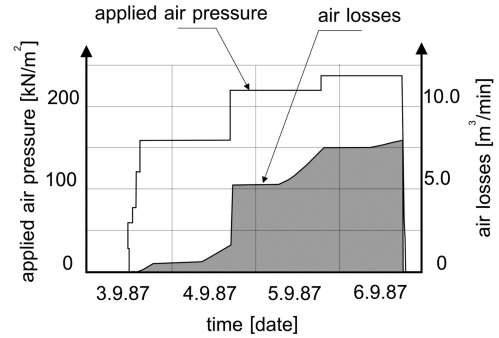


Figure 5. Rate of air losses during the test 1B (Kramer & Semprich, 1989).

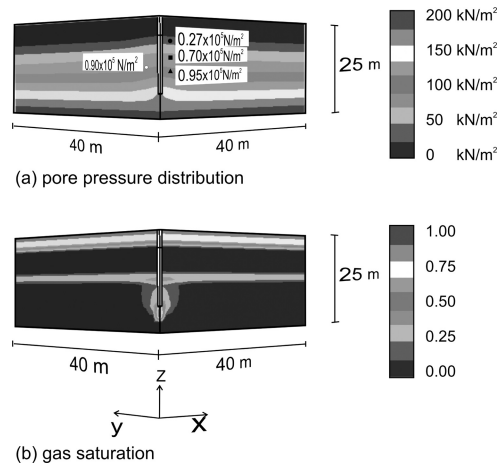


Figure 6. Pore pressure distribution and gas saturation.

Table 1. Physical and mechanical properties of subsoil layers in Essen.

	Subsoil layer			
	Fill	Silt	Sand	Marl
Grain density [g/cm^3]	2.72	2.90	2.72	2.79
Dry density [g/cm^3]	1.74	1.68	1.74	1.87
Young's modulus [MPa]	20	12.5	21.2	14.3
Poisson's ratio []	0.33	0.35	0.32	0.40
		(0.37)		

The physical and mechanical properties of all the soil layers are shown in Table 1. The lower half part of silt is weaker in stiffness than that of the upper one and the stiffness properties of this lower half part are written in parentheses in the table.

Table 2. Fluid related properties of subsoil layers in Essen.

	Subsoil layer			
	Fill	Silt	Sand	Marl
$K [\times 10^{-12} \text{m}^2]$	4.95	0.495	9.90	2.48
$S_{lr} []$	0.20	0.20	0.05	0.15
$p_o [\text{kPa}]$	4.0	30.0	4.0	12.0
$n []$	5.0	2.0	2.86	2.5

The fluid related properties of each subsoil layer are represented in term of model parameters written in Table 2. The model parameters are according to van Genuchten equation and van Genuchten-Mualem equation which are written in Equation 5 and Equation 6, respectively. Equation 5 represent soil-water retention characteristics while Equation 6a and 6b represent fluid conductivity of liquid and gas phase, respectively. It is noted according to Kramer & Semplich (1989) that high anisotropy between horizontal and vertical fluid conductivity should be aware.

$$p_c = p_o [S_e^{-n/n-1} - 1]^{1/n} \quad (5)$$

$$k_l = K \{ S_e^{0.5} [1 + (1 - S_e^{n/n-1})^{1-1/n}]^2 \} \quad (6a)$$

$$k_g = K \{ (1 - S_e)^{0.5} (1 - S_e^{n/n-1})^{2(1-1/n)} \} \quad (6b)$$

where p_o = air entry pressure; k_l = fluid conductivity; k_g = gas conductivity; n = model parameter related to pore size distribution; K = intrinsic permeability; and S_e = effective saturation which is expressed as written in Equation 7.

$$S_e = (S_l - S_{lr}) / (S_{ls} - S_{lr}) \quad (7)$$

where S_{lr} = residual liquid saturation; and S_{ls} = maximum liquid saturation.

3.2 Numerical modelling

According to the use of loose coupling method for the simulation of fluid-mechanical interaction, two numerical models are created separately. Details of the numerical model in FLAC3D is first presented and followed by the details of the numerical model in TOUGH2. To the end, the results calculated from the coupling TOUGH2-FLAC3D simulation are presented and compared with the corresponding experimental results.

Figure 7a shows the FLAC3D mesh to simulate the problem. The width of the model in transverse

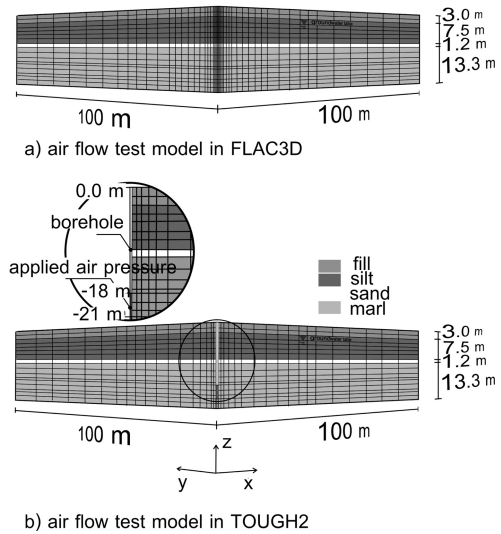


Figure 7. Air flow test model in FLAC3D and TOUGH2.

direction (x) and longitudinal direction (y) are respectively 100 m. The height of the model is 25 m. The mesh discretization along the transverse direction is the same as that along the longitudinal direction. Taking advantage of the axisymmetry of the problem, only one-fourth of the geometry is considered and the symmetry axes are simulated by boundary conditions with roller displacement. The roller displacement type boundary is also prescribed on all remained boundaries of the model except the upper and lower boundaries. The upper boundary is prescribed as a free deformed boundary while the lower boundary is prescribed as a fixed boundary. According to the subsoil conditions described in the previous section, the groundwater table is at 4.75 m beneath the upper boundary. The mesh is discretized in vertical direction such that the soil layers and the groundwater table can be taken into account. In horizontal direction, the mesh is discretized such that the size of elements in vicinity of the borehole is rather small but becomes bigger as increasing distance from the borehole.

Figure 7b shows the TOUGH2 mesh to simulate the problem. Once again taking advantage of the axisymmetry of the problem, only one fourth of the geometry is considered and the symmetry axes are simulated by the impermeable type boundary. Dirichlet conditions are prescribed to all remained boundaries of the model. The dimensions of the model are the same as those of the FLAC3D model. The discretization of the mesh is done under the same consideration as done in the FLAC3D mesh.

The initial conditions are first prescribed to the TOUGH2 model according to the geometry described

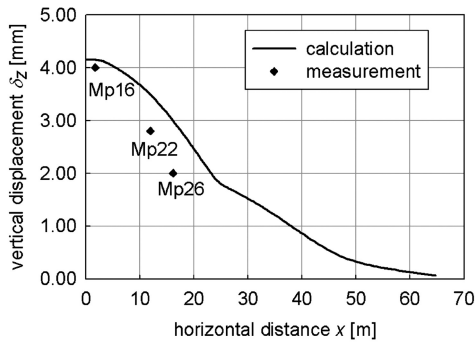


Figure 8. Surface displacement due to the first air pressure level in the test 1B.

in the previous section. Due to the small displacement found from the experimental results, linear elastic behavior is assumed for the whole domain.

3.3 Results

Figure 6 shows the calculated pore pressure and gas saturation after 27 hours of the application of the air pressure $p_a = 160 \text{ kN/m}^2$ into the borehole. The distribution of pore pressure after 27 hours of applying the air pressure $p_a = 160 \text{ kN/m}^2$ into the borehole is shown in Figure 6a. The magnitude of pore pressure increases significantly in vicinity of the borehole but retains its magnitude of hydrostatic pressure at certain distance apart of the borehole. The magnitudes of pore pressure measured from 4 piezometers are also shown in Figure 6a. As can be found from Figure 6a, good agreement between measured and calculated pore pressures is a conclusion. The distribution of gas saturation after 27 hours of applying the 160 kN/m^2 of air pressure into the borehole is shown in Figure 6b. A bulb like shape of desaturation zone in marl layer is found. In marl layer, high degree of gas saturation can be found at vicinity of the air injection zone. However, it is only a small area of the marl layer is desaturated. In sand layer, because of its relatively high value of fluid conductivity, the desaturation zone spreads over a whole sand layer. However, in silt layer, the desaturation zone does not exist due to its low value of fluid conductivity and high value of air entry pressure.

Figure 8 is the comparisons between the surface displacement measured from the experiment and that calculated from the loose coupling simulation at 27 hours after applying the 160 kN/m^2 air pressure into the borehole. The blue diamonds are experimental results extracted from Figure 4. Keeping in mind that each soil layer is assumed homogeneous and isotropic, good agreement between the experimental results and the numerical results can be concluded even the

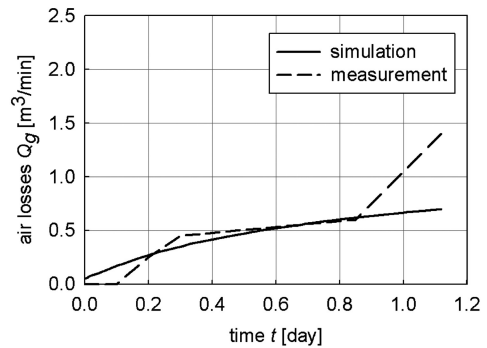


Figure 9. Rate of air losses due to the first air pressure level in the test 1B.

magnitude of surface displacement given by the numerical simulation is somewhat higher than that found from the experiment.

Figure 9 shows the comparisons between the rate of air losses measured from the experiment and that calculated from the numerical simulation. To the end of the first pressure step in the experiment 1B, the simulation yields somewhat 50% of that found from the experiments. It is worth reminding that the numerical model assumes that the soil layers oppose isotropic properties. However, as reported by Kramer & Semprich (1989), high anisotropy between horizontal and vertical fluid conductivity might be encountered. Moreover, the continuum medium is assumed in the model, whereas it is reported that the fractured media type might be found after 13 m below the ground surface. By ignoring those attributes of the ground conditions, difference between the experimental results and the simulation results is expected.

4 CONCLUSION

The calculation results from TOUGH2-FLAC3D coupling simulation show good in agreement with the corresponding test results indicating that the TOUGH2-FLAC3D coupling can capture the feature of flow and deformation due to the application of air pressure to the subsoil. The next step is to implement an elasto-plastic model for unsaturated soils into FLAC3D and extend the simulation to explain surface settlement due to compressed air tunnelling construction.

REFERENCES

- Bishop, A.W. 1959. The principal of effective stress. *Teknisk Ukeblad* 106(39): 859–863.
- Chinkulkijniwat, A. 2005. Multiphase Flow in Unsaturated Soils and the Induced Deformation with Respect to

- Compressed Air Tunnelling. Ph.D. Thesis, Graz University of Technology, Geotechnical Group Graz, Vol. 27.
- Chinkulkijniwat, A., Steger, G., Semprich, S. 2005. Unsaturated hydraulic properties for compressed air tunnelling by inverse modelling. Proc. 16th Int. Conf. Soil Mech. and Geotech. Eng, Osaka, 12–16 September 2005. Rotterdam: Millpress.
- ITASCA Consulting Group Inc. 2002. Fast Lagrangian Analysis of Continua in 3 Dimensions Version 2.10 – User's Manual. Minnesota: ITASCA Consulting Group Inc.
- Kramer, J. & Semprich, S. 1989. Erfahrungen über Druckluftverbrauch bei der Spritzbetonbauweise. Taschenbuch für den Tunnelbau. Essen: Verlag Glückauf GmbH.
- Leverett, M.C. 1941. Capillary behavior in porous solids. Trans. AIME 142: 152–168.
- Pruess, K., Odenberg, C., Moridis, G. 1999. TOUGH2 User's Guide Version 2.0. Earth Science Division, Ernest Orlando Lawrence Berkeley National Laboratory.
- Rutqvist, J., Wu, Y.S., Tsang, C.F. Bodvarsson, G. 2002. A Modeling approach for analysis of coupled multiphase fluid flow, heat transfer, and deformation in fractured porous rock. Int. J. of Rock Mechanics & Mining Sciences 39: 429–442.
- Weber, J. 1983. Erfahrungen mit Druckluftvortrieben in Spritzbetonbauweise beim Münchener U-Bahn-Bau, STUVA Tagung 1983 in Nürnberg. Forschung und Praxis 32: 184–192.

Identification of characteristic coefficient of seepage in inhomogeneous and anisotropic rock masses

Y. Zhu, D. Sun, & W. Cen
Hohai University, Nanjing, China

S. Semprich
Graz University of Technology, Graz, Austria

ABSTRACT: The fractured rock masses can be considered as inhomogeneous and anisotropic permeable media. The optimal fitting for calculated and measured water level and seepage discharge of measuring points is made. The reverse problem to identify the coefficient tensors of permeability of the rock masses is transformed into an equivalent mathematical minimizing problem. To improve the convergence of iterative calculation, an effective term for penalty is added to the expression of the minimum optimization function. Hereby, the solution to three-dimensional complicated reverse problems can directly be obtained on computer. Finally, the solution of a complicated practical example is presented in detail.

1 INTRODUCTION

In general, the property of seepage of rock masses mostly depends on the permeability of texture surfaces of fractures. Due to complicated causes, large time-scale and uncertainties of texture surfaces of fracture, the properties of permeability of rock masses are discrete, and with wide range of the value of parameters. For general seepage problem in engineering, the rock masses can be considered as strongly inhomogeneous and anisotropic permeable continuum, the coefficient tensors of permeability are required to express the macroscopical properties of permeability. However, up to now there is still no any test method or numerical method to decide the coefficient tensors of permeability accurately in theory.

In order to obtain the geological structure and characteristics of permeability of rock masses, enormous work is required to do, like geological exploration, water pressure test, observation data of groundwater head, sometimes it is also necessary to observe exit points of groundwater of openings and outflow points of natural spring. These observation data represent the comprehensive characteristics of permeability involving all kinds of influence factors. Hereby, according to a certain algorithm, to inverse the coefficient tensors of permeability and parameters of boundary conditions is very important in solving seepage problem and design seepage control on the basis of observation data. Recently, inverse analysis has been received increasing concern.

Due to the facts that in engineering practice just short-term and discontinuous observation data of water level of borehole and strongly discrete results of water pressure test are obtained, the finite element method and optimization theory are adopted in our algorithm proposed by authors, which can successfully perform the reverse analysis of identification of coefficient tensors of permeability in different parts of seepage domain. There are a lot of difficulties in inversion analysis, like large-scale of inversion problem, great number of unknown parameters, wide range of values of parameters. In order to overcome these problems, some procedures are adopted including the procedure of nodal virtual flux is used to get the free table and most possible algorithms are used to improve the convergence of iterative calculation, an effective term for penalty is added to the minimum objective function, so that the solution to three-dimensional complicated reverse problems can be obtained. Two examples in this paper show that the procedures proposed can satisfactorily handle the reverse analysis of identification of coefficients of permeability tensor in inhomogeneous and anisotropic seepage domain.

2 THEORY

2.1 *Coefficient tensors of permeability*

The property of fractured rock masses is strongly heterogeneous and anisotropic. Due to the width of texture

surfaces of fracture is much smaller compared to the characteristic size of project, like dam bottom width, tunnel diameter, slope height, rock masses can be considered as inhomogeneous and anisotropic equivalent continuum media, whose property of permeability can be described by coefficient tensor of permeability. The corresponding Darcy's law is described by equation (1), and in general the direction of velocity vector is not consistent with the direction of hydraulic gradient.

$$V_i = -k_{ij}I_j \quad (1)$$

Where, V_i denotes the component of velocity; I_j denotes the component of hydraulic gradient; k_{ij} denotes coefficient tensor of permeability with six independent components, whose matrix form is described by equation (2). The goal of this paper is to inverse the coefficient tensors of permeability and relevant parameters in different parts of seepage domain.

$$k_{ij} = \begin{bmatrix} k_{xx} & k_{xy} & k_{xz} \\ & k_{yy} & k_{yz} \\ sym & & k_{zz} \end{bmatrix} \quad (2)$$

2.2 Solving seepage problem using FEM

For the Darcy's seepage problem shown by figure 1, the FEM governing equation in the domain Ω_1 below the free surface ABCD can be described by equation (3) according to the variational principle.

$$[K]\{H\} = \{Q\} \quad (3)$$

Procedure of nodal virtual flux in fixed grid can be used to solve the seepage problem with free surface, the virtual seepage domain Ω_2 above the free surface is also taken into account, iterative form is shown as equation (4).

$$[K]\{H\}_i = \{Q\} - \{Q_2\}_{i-1} + \{\Delta Q\}_{i-1} \quad (4)$$

Where, i is index of iterative step, $\{Q_2\}$ is the equivalent nodal virtual flux in virtual seepage domain contributed by known water head boundary condition, $\{\Delta Q\}$ denotes nodal virtual flux. Due to arrays $\{Q_2\}$ and $\{\Delta Q\}$ are depended on the array of nodal water head, $\{H\}$, the iteration method is required to solve equation (4).

2.3 Inversion method for coefficient tensors of permeability

The general idea for inverting seepage problem is to search a set of parameters in the probable range of values determined by the known conditions, then termination criterion is reached when the measured values on site are

fitted 'best' well with the calculated values of them, hereby, the reverse analysis of identification of parameters of seepage domain becomes a mathematical optimization problem shown in equations (5) and (6).

$$Re(\{k\}) = \sum_{t=1}^T \sum_{i=1}^M \omega_{i,t} [\varphi_{i,t}^m - \varphi_{i,t}^c(\{k\})]^2 = Min \quad (5)$$

$$\underline{k}_j \leq k_j \leq \bar{k}_j, j = 1, 2, \dots, N \quad (6)$$

Where, $(\{k\})$ denotes the quadratic sum of difference between calculated and measured values of water head, $\{k\} = [k_1, k_2, \dots, k_N]^T$ denotes the array of unknown parameters with the number of N , $\omega_{i,t}$ denotes the weight coefficient of point i at time t , $\varphi_{i,t}^c$ and $\varphi_{i,t}^m$ denote the calculated and measured value of water head at time t , respectively, \underline{k}_j and \bar{k}_j denote the probable lower and upper limit value of parameter, k_j which can be determined according to the property of hydrological geology of rock mass and results of water-pressure test.

A number of techniques are available to solve the optimization problem, for example complex method. Due to the seepage problem is an unsteady-state flow through porous media, in general the solution to complicated reverse problems of seepage defined by equations (5) and (6) is difficult to obtain. A simplified method is to choose some typical measurement times, like T_0 times, which can be approximated to steady state seepage, so the unsteady-state seepage in T measurement times is substituted by steady state seepage in T_0 times solved according to equations (6) and (7).

$$Re(\{k\})_t = \sum_{i=1}^M \omega_{i,t} [\varphi_{i,t}^m - \varphi_{i,t}^c(\{k\})]^2 = Min \quad (7)$$

Where, $Re(\{k\})_t$ denotes the quadratic sum of error of water head involving t times.

The optimum solutions with the number of T_0 can be assumed as:

$$\{k\}_t = [k_{1,t}, k_{2,t}, \dots, k_{N,t}]^T, t = 1, 2, \dots, T_0 \quad (8)$$

We can also assume that k_j^0 is the estimated optimum value of, k_j , and we have:

$$E_k = \sum_{t=1}^{T_0} \sum_{j=1}^N \omega_{j,t} (k_j^0 - k_{j,t})^2 = Min \quad (9)$$

Where $\omega_{j,t}$ is weight coefficient of j th parameter at t th measurement time. And we have:

$$\frac{\partial E_k}{\partial k_j^0} = 0, j = 1, 2, \dots, N \quad (10)$$

Then we obtain the terminal inversion solutions of characteristic coefficients described in equation (11).

$$k_j^0 = \frac{1}{T_0} \sum_{i=1}^{T_0} k_{j,i}, j = 1, 2, \dots, N \quad (11)$$

In general, the seepage problem is with free surface besides with the characteristics of inhomogeneous and anisotropic, so the calculated value of water head $\varphi_{i,t}^c(\{k\})$ must be calculated iteratively. Moreover, the permeability parameters is with wide range of value and with discrete characteristic, and the non-diagonal elements of tensor k_{ij} maybe negative, which cause the stability solving equation (4) is not very well, even iterative computations fail to converge in optimization problem described by equation (6) and (7), the inversion calculation has to break. In order to overcome this problem, a feasible procedure is to redefine the objective function $Re(\{k\})_t$ in equation (7), we have:

$$Re(\{k\})_t = \sum_{i=1}^M \omega_{i,t} [\varphi_{i,t}^m - \varphi_{i,t}^c(\{k\})]^2 + P(\{k\}) \quad (12)$$

Where, additional term $P(\{k\})$ is penalty correction term in minimum objective function, which will be in effect through a relative large value of objective function is chosen at the unknown parameter point when the solving process of equation (4) is unstable. So the inversion process can go on smoothly.

This procedure has proved to be a very powerful tool in automatically searching optimum results of inversion problem shown in equations (6) and (12).

In the solving process of inversion problem of seepage in rock mass described above, equation (13) or (14) can be regarded as the convergence criteria.

$$\max(\Delta k_{1,t}, \Delta k_{2,t}, \dots, \Delta k_{N,t}) \leq \varepsilon_k \quad (13)$$

$$Re(\{k\})_t \leq \varepsilon_R \quad (14)$$

where, $\Delta k_{i,t} = |k'_{i,t} - k^{j-1}_{i,t}|$ denotes the absolute value of difference between inversion value of i th parameter in j th step and that in $(j - 1)$ th step at t th measurement. ε_k is the maximum tolerance error of undermined parameter between two successive iterative steps, ε_R denotes the tolerance error of accumulative quadratic sum of calculated and measured values of water head.

3 EXAMPLES

3.1 Example of flow through embankment

An isotropic seepage problem with free surface is shown in figure 1, its upstream water level and downstream water level are 6.0m and 1.0m respectively, which can be solved by procedure of nodal virtual flux. The whole embankment can be regarded as

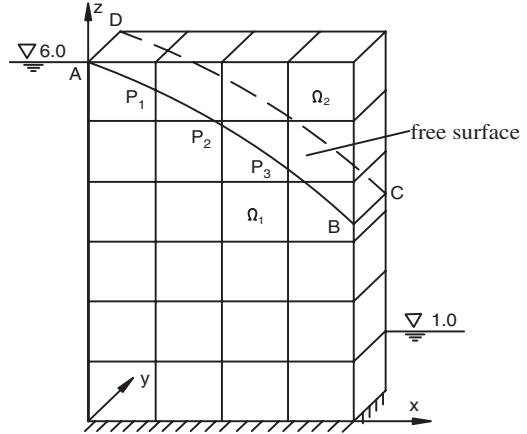


Figure 1. A seepage flow problem with free surface.

computation domain, which is divided into 4×6 grids. And computation domain is divided into two subdomains according to the permeability of materials, in where the x -value is less than or equal to 1.0 the coefficient of permeability k_1 is equal to 1.0, in where x -value is greater than 1.0 the coefficient of permeability k_2 is equal to 5.0. The thickness of the domain in Y -direction is equal to 1.0. Three sides of $Z = 0$, $Y = 0$ and $Y = 1.0$ are impervious boundaries. Using finite element method the flow through embankment can be simulated, the coordinates of three points P_1 , P_2 and P_3 in free table are (1.0,0.0,4.96), (2.0,0.0,4.27), (3.0,0.0,3.49). In first case we assume that the calculated water heads at the three points of P_1 , P_2 and P_3 as measured values, our reversion algorithm is used to identify the characteristic coefficients of domain, after 9 iteration steps we get the results of $k_1 : k_2 = 1.0 : 5.006$ and $Re(k_1, k_2) = 1.6 \times 10^{-5}$ ($\varepsilon_R = 1.0 \times 10^{-4}$ is chosen). In second case we assume that the calculated water heads at the two points of P_2 and P_3 as measured values, after 14 iteration steps the results of $k_1 : k_2 = 1.0 : 5.003$ and $Re(k_1, k_2) = 2.0 \times 10^{-6}$ ($\varepsilon_R = 1.0 \times 10^{-5}$ is chosen) are obtained. In third case just assume the calculated water head at point P_2 as measurement value, after 7 iteration steps we can get the results of $k_1 : k_2 = 1.0 : 5.116$ and $Re(k_1, k_2) = 8.0 \times 10^{-6}$ ($\varepsilon_R = 1.0 \times 10^{-5}$ is chosen). One can see the genuine solutions are generally yielded in these three cases. We choose k_1 and k_2 with the uniform probable upper and lower limit values of $\underline{k}_1 = 0.01$, $\bar{k}_1 = 100.0$ and $\underline{k}_2 = 0.05$, $\bar{k}_2 = 500.0$ which are smaller or larger two orders of magnitude than genuine solutions and uniform initial value of $(k_1, k_2) = (100.0, 0.05)$ is used to inverse.

When the material of embankment is homogeneous and anisotropic, the coefficient of permeability is assumed as equation (15).

Table 1. The inverse value of coefficient tensor of permeability of homogeneous anisotropic embankment.

Parameter	k_{xx}	k_{xy}	k_{xz}	k_{yy}	k_{yz}	k_{zz}
True value	2.0	-0.3	-0.5	3.0	0.5	1.0
Upper limit value	0.02	-30.0	-50.0	0.03	0.05	0.01
lower limit value	200.0	-0.03	-0.05	300.0	50.0	100.0
Initial value	0.02	-30.0	-0.005	0.03	50.0	0.01
Inversion value	2.0	-0.32	-0.49	2.89	0.49	0.99
Error	0.0	0.02	-0.01	0.11	0.01	0.01

$$k_{ij} = \begin{bmatrix} k_{xx} & k_{xy} & k_{xz} \\ & k_{yy} & k_{yz} \\ sym & & k_{zz} \end{bmatrix} = \begin{bmatrix} 2.0 & -0.3 & -0.5 \\ & 3.0 & 0.5 \\ sym & & 1.0 \end{bmatrix} \quad (15)$$

Using finite element method the flow through the embankment is simulated and the free surface locations are $z = 5.57, 5.09$ and 4.62 at where $y = 0, x = 1.0, 2.0$ and 3.0 . In first case, when traditional method defined by equations (5) and (6) is used to identify the coefficients of permeability, the optimum solutions cannot be achieved due to automatic combination of 6 elements in tensor k_{ij} is too bad to converge. However when our improved inversion method defined by equations (6) and (12) is used, the optimum solution can be obtained smoothly shown in table 1. And the locations of free surface are simulated are $z = 5.58, 5.09$ and 4.62 at the three measurement points. One can see inverse values are quite similar to the measured values.

3.2 Inverse analysis for initial seepage field of Dachaochan underground hydropower station

Dachaoshan hydropower station is located in the lower and middle reach of Lancang River in Yunnan province of China. The pivot is composed of a RCC gravity dam with 115 m in height, group of openings on the right bank and other hydraulic structures. Before dam construction the groundwater levels of near and far river reach of initial seepage field are mainly subjected to the change of water level of river and rainfall respectively.

The plant is located in the hard basalt between the Longtang Trench and Qingmiao Trench, and the distance between two trenches is about 450 m, the slope is about 35° , the trend of basaltic layer is $N50 \sim 70^\circ E$, the angle to the direction of axis of main plant is about 45° , and slope is $20 \sim 25^\circ$. The faults are well developed in rock masses, namely, F_{217}, F_{168} and F_{114} etc., and the permeability of them are slightly weak except few faults. The unit water absorption ω obtained by water pressure test is $0.0075 \sim 0.0095$ L/min · m · m. The style of groundwater is fissure phreatic water. For the case of this project the migration condition is to infiltrate from

Table 2. The ω -values of the rock mass obtained through in situ water-pressure test L/min · m · m.

Serial number	Borehole number	Weakly weathered	Slightly weathered	Fresh rock
1	ZK417	0.04603	0.0089	0.00024
2	ZK419	0.0296	0.0213	0.00018
3	ZK423		0.0049	0.00543
4	ZK428	0.3478	0.07857	0.005775
5	ZK431	0.0302	0.08093	0.00533
6	ZK432	0.5855	0.00843	0.000438
7	ZK433	0.2209	0.2061	0.00632
8	ZK434		0.0045	0.0059
9	ZK435	0.5059	0.01645	0.00573
10	mean value	0.2523	0.04779	0.00393
11	relative ratio	64.198	12.16	1.0

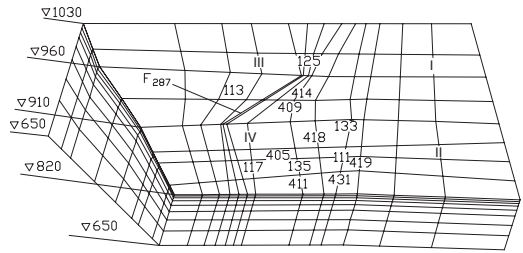


Figure 2. The calculation domain and element mess for back analysis to determine seepage parameters.

both slopes to riversides due to the higher groundwater level on both slopes. Table 2 shows the results of water pressure test in the boreholes of Zk417, Zk419 and Zk435 and so on all together 9 boreholes in the weakly weathered, slightly weathered and fresh rock layer, the ratios of relative permeability of them are 64.198:12.16:1.0. According to equation (16) the value of ω obtained from water pressure test can be converted to comprehensive average coefficient of permeability in rock masses, so the coefficient of permeability k in these three rock masses are $0.65 \times 10^{-5}, 7.95 \times 10^{-5}$ and 4.20×10^{-4} cm/s respectively.

$$k = 2.65 \times 10^{-4} \omega \ln(R/r_0) \quad \text{cm/s} \quad (16)$$

Where, $r_0 = 3.75$ cm and $R = 2000$ cm are radius of borehole and influence radius of infiltration in water pressure test.

The flow domain is shown in figure 2. Qingmiao Trench is regarded as downstream side of domain, about 300 m away from left side of Longtang Trench is regarded as upstream side of domain, and width of upstream-downstream direction is about 700 m. The width is about 500 m from inside of the slope to middle plane of river; elevation of base of domain is 650 m, and the elevation of top of inside of slope is 1030 m. In order

Table 3. The upper and lower possible limit values, initial values, and reverse values of the identified parameters.

Undetermined parameters	Lower bound	Upper bound	Initial value	Inversion value
k_1	1.0	50.0	1.0	17.99
k_2	-20.0	20.0	20.0	17.15
k_3	-20.0	20.0	20.0	19.38
k_4	0.01	100.0	0.01	78.76
k_5	-20.0	30.0	30.0	28.75
k_6	0.01	100.0	0.01	90.89
k_7	1.0	50.0	1.0	1.19
k_8	0.1	10.0	10.0	2.58
k_9	10.0	5000.0	10.0	363.26
k_{10}	650.0 m	1020.0 m	1020.0 m	935.43 m

to insure the precision of calculated water heads, there is at least one layer of virtual element above free surface. The top of the domain can be considered as probable seepage surface, the base, upstream and downstream sides, along with middle plane of river are considered as impervious boundary. The zone of river-bed where water level is relatively deep can be regarded as known water head boundary with average water head of 818.5 m. Assume the water head along the inside of the domain presents linear distribution with elevation (water head of base at the elevation of 650.0 m is determined by inversion analysis, and the result obtained is 935.43 m, see table 3). According to the data of geological exploration the permeability of upstream and downstream rock masses are different, the natural slope of groundwater surface of near river reach is just 0.05, while that of far river reach increases vastly to 0.3~0.72, even to 0.84. In the model of inversion analysis the flow domain shown in figure 2 can be considered as heterogeneous and isotropic media. According to the location of Longtang Trench, the borderline between near and far river reach, four degrees of weathering of rock mass and faults of F_{217} , the domain can be divided into 17 subdomains, namely, 1~4th subdomains are located in the I zone, 5~8th subdomains are located in the II zone, 9~12th subdomains are located in the III zone, 13~16th subdomains are located in the IV zone, 17th subdomains is located in the fault of F_{217} . The coefficient of permeability of every subdomain is determined by the inversion analysis. In rectangular coordinate system, X axis is parallel to the axis of main plant building, and directs to river bed; Y axis is perpendicular to the axis of main plant building and directs to upstream, Z axis directs upward, and origin is at the zero altitude. There are 102 unknown elements in 17 coefficient tensors of permeability of subdomains. In order to simplify the inversion model, first the meshes are relative rough, then the relationships of relative ratio of permeability obtained from the water pressure test in every degree weathering rock masses are taken into account, and assume that the tangential permeability of fault belt F_{217}

Table 4. The coefficient tensors of permeability of the subdomains (10^{-7} cm/s).

Zone number	Coefficient of permeability					
	k_{xx}	k_{yy}	k_{xz}	k_{yy}	k_{yz}	k_{zz}
1	0.149	0.142	0.161	0.654	0.239	0.755
2	1.817	1.731	1.957	7.952	2.903	9.177
3	9.591	9.141	10.331	41.983	15.326	48.449
4	14.939	14.239	16.091	65.394	23.872	75.466
5	0.386	0.368	0.415	1.688	0.616	1.948
6	4.689	4.469	5.050	20.525	7.492	23.686
7	24.755	23.594	26.664	108.362	39.557	125.051
8	38.559	36.751	41.533	168.788	61.615	194.783
9	0.176	0.168	0.190	0.771	0.281	0.890
10	2.141	2.041	2.306	9.373	3.422	10.816
11	11.308	10.775	12.176	49.485	18.064	57.106
12	17.608	16.783	18.966	77.079	28.137	88.950
13	0.454	0.433	0.490	1.989	0.726	2.296
14	5.527	5.268	5.953	24.192	8.831	20.918
15	29.178	27.810	31.428	127.724	46.625	147.395
16	45.448	43.318	48.954	198.947	72.624	229.587
17	301.59	0.0	0.0	30.160	0.0	301.59

Table 5. The measured and inverse values of the piezometric levels (m).

Point number	Measured data	Calculated data	Error
ZK111	824.14	820.99	-3.15
ZK113	915.86	915.98	0.12
ZK117	822.38	821.62	-0.76
ZK125	946.47	949.74	3.27
ZK133	843.87	844.78	0.91
ZK135	819.98	819.31	-0.67
ZK405	827.70	829.14	1.44
ZK409	848.62	847.72	-0.90
ZK411	820.36	819.66	-0.70
ZK414	924.17	923.98	-0.19
ZK419	820.09	819.33	-0.36
ZK431	819.79	818.91	-0.88

is greater one order of magnitude than the normal permeability. And due to the analogy in geologic structure, there are proportional relationships between the coefficient tensors of permeability of both sides of Longtang Trench and between near and far river reach. The number of unknown variables reduces from 103 to 10, namely, k_1, k_2, \dots, k_{10} , where, $k_1 \sim k_6$ are the relative ratios among six independent elements in I zone, k_7 and k_8 are the scale factors of the coefficient tensor of permeability of both sides of Longtang Trench and near and far river reach, k_9 is the scale factor of tangential relative permeability of fault belt F_{217} , and k_{10} is the water head on the boundary of slop side with the elevation of 650 m.

The probable upper and lower limit values, initial values and optimum solutions of 10 independent variables are shown in table 3. The optimum solutions are not unique theoretically because there are only observation data of water level of borehole. And only relative

ratios can be obtained by inversion calculation. Inversion solutions of coefficient tensors of permeability of 17 subdomains shown in table 4 are obtained by considering the inversion solutions of $k_1 \sim k_9$ shown in table 3, the properties of fracture structures, the results of water pressure test shown in table 2 and equation (16). One can see that the calculated water head of 13 boreholes adopted in inversion calculation are fitted very well with the measured values of them.

4 SUGGESTIONS

Because in equation (4) the vector of nodal water head $\{H\}$ will not change when all coefficient tensors of permeability of domain are enlarged or reduced in same scale simultaneous, so just the relationship of ratio among the parameters of permeability can be obtained by inversion analysis only with the convergence criterion of the calculated values of water head are fitted best well with the measured values, that is to say there is a problem that the inversion solution is not unique. In order to overcome this problem, additional prescribed flux condition is required. It is also feasible to supply some known coefficient tensors of permeability of subdomains. As for how to achieve the genuine solution, the authors based on their experiences in practice engineering put forward some powerful suggestions shown as following.

First, the inversion analysis should be performed on the basis of observation data of initial seepage field before construction, which can lead to less amount of work to be done. The observation data of geological exploration and results of tests etc. should be fully used to determine the flow domain, some known boundary conditions, reasonable subzone and probable upper and lower limit values of determined parameters.

Second, at the present time the inversion analysis has been implemented on the basis of steady Darcy's flow theory, and the groundwater flow in drought period quite agrees with steady Darcy's flow theory.

Third, it is necessary to measure the overflow region and the flux. And the location of seepage overflow region and flux in geological exploration and excavation are useful to improve the accuracy. On the basis of ratios among the determined parameters and measured seepage flux are known, the genuine solution can be achieved with the convergence criterion of the best fitted seepage flux.

Fourth, besides routine work of water pressure test, one should pay attention to choose appropriate locations in one or two typical subdomains, in where to determine the coefficient tensor of permeability of rock mass by water pressure test. Then the optimum solution of coefficient tensor of permeability can be directly obtained by inversion analysis according to the initial observation data of water head.

Fifth, the permeability of rock mass is influenced not only by geological structure of fractured media but also greatly by the weathering. For example, the permeability of completely weathered rock on the surface is greater two orders of magnitude than that of fresh rock of deep layer in Dachaoshan underground hydropower station. So in inversion analysis this ratio relationship of relative permeability obtained by water pressure test can be used to reduce the number of undetermined parameters.

Sixth, if the directions of major coefficients of permeability can be obtained by geological structure of rock mass and water pressure test, the directions of local coordinate axes, namely, r , s and t axis, can be chosen to be same with the directions of major coefficients of permeability. Then the number of unknown independent elements in coefficient tensor of permeability in local coordinate system can be reduced from 6 to 3. Then the coefficient tensor of permeability of rock mass in global coordinate system k_{ij} can be calculated by equation (17) corresponding to that in local coordinate system k'_{lk} .

$$k_{ij} = k'_{lk} a_{il} a_{jk} \quad (17)$$

Where, a_{ij} denotes cosine value of the angle of axes in global coordinate system to axes in local coordinate system.

ACKNOWLEDGMENTS

Support from the Ministry for Science and Technology in China and the Federal Ministry of Education, Science and Culture in Austria for the bilateral scientific technological co-operation between Hohai University in Nanjing and Graz University of Technology in Graz is greatly acknowledged.

REFERENCES

- Zhu B. et al. 1984. Optimum Design of Structure Theory and Application. Waterpub, China.
- Zhu Y. 1991. Review of Seepage through fractured media. *Advances in Science and Technology of Water Resources* **11**(2): 16–25.
- Zhu Y. et al. 1992. Some adaptive techniques for solution of free surface seepage flow through arch dam abutments. In *Proceedings the Internal Symposium on Arch Dams*. Nanjing, China.
- Zhu Y. et al. 1996. On solution of Complicated seepage field in surrounding rock mass of underground power station openings. *Journal of Hydraulic Engineering* (9): 79–85.
- Zhu Y. & Liu W. 1991. Back analysis of complicated seepage field for earth and rockfill dam. *Journal of Hohai University* **19**(6): 49–56.

Numerical determination of soil deformations around a penetrating object in 2D and 3D models

S. Farhangi, D.J. Richards & C.R.I. Clayton

School of Civil Engineering and the Environment, University of Southampton, UK

ABSTRACT: Various numerical methods have been employed to determine soil deformations around penetrating objects. However, due to extensive computational resource requirements for 3D analysis, soil deformations are usually estimated from 2D analysis. The adequacy of estimating soil deformations around a 3D penetrating object with a 2D plane-strain analysis has been evaluated in this paper using FLAC^{3D} and FLAC programs. The modelling strategy and the use of interface elements in these programs for simulating penetration were outlined. The comparison of strain paths determined from 3D and 2D analyses illustrates the existence of an out of plane deformation component and shows that soil deformations around a 3D geometry with a finite width cannot be estimated solely by a plane-strain analysis. In addition, it is observed that new modelling techniques such as the explicit finite difference formulation can be used to analyze three-dimensional penetration problems.

1 INTRODUCTION

Many geotechnical topics are associated with penetration, including foundation elements (e.g. push-in piles, caissons), in-situ devices (e.g. cones, dilatometers), and samplers. An understanding of the influence of the penetration process on the stress-strain behaviour of soil is essential for a rational design of foundation elements, interpretation of in-situ tests and assessment of sampler disturbances. A range of techniques have been developed to examine the stress changes that occur within the soil as penetration takes place.

Various experimental and analytical techniques have been adopted to evaluate the influence of the penetration process on soil behaviour. Experimental techniques used to evaluate the stress-strain behaviour of soil during penetration includes visual inspection of soil displacements during penetration processes (Butterfield et al. 1970, White et al. 2003); triaxial (Siddique 1990) and chamber tests (Houlsby & Hitchman 1988, Fahey et al. 1989). A range of analytical techniques have also been proposed to provide an insight into the complex soil behaviour during penetration, including bearing capacity (Skempton 1951), cavity expansion (Vesic 1972), strain path (Baligh 1984) and shallow strain path methods (Sagaseta et al. 1997). The requirement for an exposed surface elevation makes the visual inspection methods more appropriate for examining two-dimensional penetration problems. The triaxial test also requires a known

stress or strain history to be applied to the specimen, which is often unknown in many penetration problems. The results of pressure chamber tests may be complicated by boundary effects. Analytical techniques also suffer from a range of limitations, such as the requirement for a pre-defined failure mechanism in the bearing capacity method, neglecting the dependency of deformations on the direction of penetration in the cavity expansion method and ignoring the influence of interface adhesions in the strain path and shallow strain path methods (Farhangi 2006).

Numerical techniques have been the subject of research in mechanical engineering and methods have been developed to simulate penetration/indentation problems (Anderheggen & Renau-Munoz 2000). In soil mechanics, a wide range of numerical techniques (i.e. finite element and finite difference methods) have been employed to analyze soil penetration problems over the last two decades (Griffiths 1982, Teh 1987, Kioussis et al. 1988, Budhu & Wu 1992, Van den Berg 1994, Abu-Farsakh et al. 1998, Hu & Randolph 1998, Liyanapathirana et al. 2000, Yu et al. 2000, Susila & Hryciw 2003). However, the majority of these analyses were limited to two-dimensional geometries and most of these methods were not capable of simulating the flow of soil around a penetrating object (i.e. large deformations). In addition, due to modelling constraints, the interface between the soil and penetrating object has been modelled as either rough or smooth and the influence of interface adhesion has not been assessed on the behaviour of the soil.

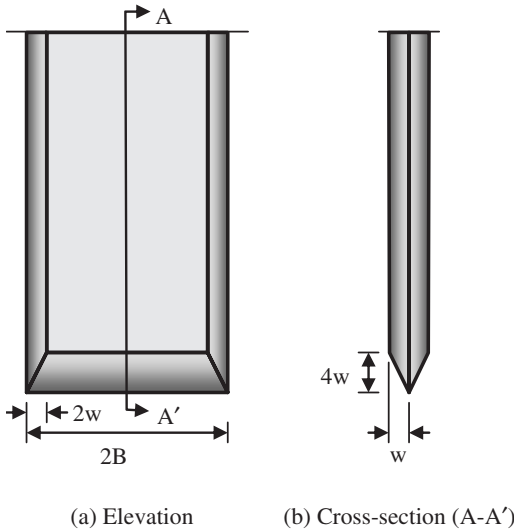


Figure 1. Schematic view of the *chisel*.

In this paper, the penetration of an idealized geometry, termed the *chisel* (Figure 1), into a mass of soil has been analyzed in both two and three dimensional models. The modelling strategy implemented to analyze the penetration of a *chisel* in FLAC and FLAC^{3D} is outlined. The strain paths for a soil element close to the centreline of the *chisel* in the three-dimensional model have been compared with those for a corresponding element in the two-dimensional model. The results of this evaluation are also presented.

2 CONTACT LOGIC IN FLAC

FLAC and FLAC^{3D} (Fast Lagrangian Analysis of Continua) are two and three dimensional explicit finite difference programs used in this study to analyze soil penetration (Itasca 2004). Although, the constitutive formulation adopted in FLAC at each step is small-strain, large-strain calculations are performed by updating the mesh geometry and consequently the stress tensors as displacements occur. FLAC is also time-marching code (i.e. one step is equal to one iteration in the calculation cycle) enabling the steady-state penetration process to be readily simulated.

A contact logic (Frank et al. 1982) is used to model the interface between two objects by specifying normal and shear (k_n , k_s) springs between opposite sides of the interface plane. FLAC and FLAC^{3D} however, employ slightly different techniques to calculate the interface forces.

The interface elements used in FLAC are doubled as shown schematically in Figure 2(a). Nodes on either sides of the interface (e.g. interface node P)

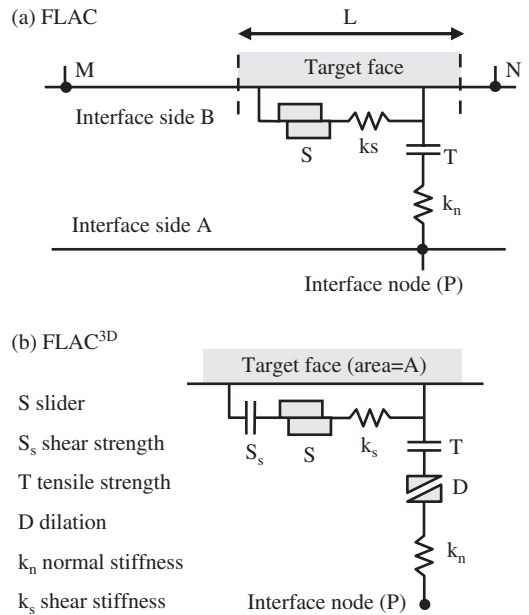


Figure 2. Interface parameter in (a) FLAC and (b) FLAC^{3D}.

are checked in turn for contact on the “target face”, which is defined as half the distance of the interface node (P) from the nearest left-side (M) and right-side (N) nodes on the opposite side. At any time step, the incremental relative displacement in the shear and normal directions are used to determine the shear and normal forces acting on across the contact length (L).

FLAC^{3D} uses one-sided interface elements shown schematically in Figure 2(b). An interface node (P) is checked for interpenetration with any other face (i.e. target face) that comes into contact during each iteration cycle. In a process similar to FLAC, the shear force acting across the contact area (A) is determined from the relative incremental displacement in the direction of shear. The normal force however, is calculated from the absolute normal penetration distance of an interface node into the target face.

Potyondy (1961) proposed to express the interface resistance with the Coulomb failure envelope. FLAC codes use the same criterion to limit the shear force on the interface element by specifying an effective cohesion and friction angle. FLAC’s interface logic was used to simulate sliding and separation of two objects in these penetration analyses.

3 2D PENETRATION MODEL

FLAC was used to simulate the undrained penetration of the *chisel* geometry in 2D models (i.e. plane-strain analysis). The penetration of the *chisel* was simulated

by assigning a constant vertical velocity to the *chisel*. Models with prescribed velocities were stepped through the analyses until the intended length of penetration (L) was achieved by the *chisel* (i.e. the initial and final positions of the *chisel* tip were $z = +L/2$ and $z = -L/2$ respectively). As the *chisel* penetrated, the soil elements were deformed and displaced around the sliding *chisel*.

The mesh representing the soil had two features. First, the mesh columns were aligned with imaginary flow streamlines which would form around the *chisel* if placed in a fluid flow field, in order to use complete quadrilateral elements (rather than truncating elements adjacent to the boundaries) through out the entire model. This alignment also reduced the occurrence of modelling problems during large deformations (Itasca 2002b). Secondly, the density of elements was increased in all directions towards the initial position of the *chisel* tip. This was due to the requirement for a finer mesh adjacent to the tip, where significant distortions due to penetration were envisaged. Other parameters defined for the penetration models were:

- 1 The *chisel* geometry had a half-thickness of $w = 4.2$ mm;
- 2 Elastic and Tresca constitutive models were reused to represent the *chisel* and soil respectively;
- 3 The initial in-situ soil stress was isotropic and equal to the vertical stress applied across the upper boundary (i.e. initial equilibrium);
- 4 Double-sided interfaces were defined between the plane of symmetry ($x = 0$) and soil, the plane of symmetry and *chisel*, and the soil and *chisel*;
- 5 Boundary fixities were defined as rollers on the bottom ($z = -H$) and far-right ($x = A$) boundaries, as illustrated in Figure 3(a).

Alternating boundary conditions for soil on a line of symmetry ($x = 0$) was represented by an auxiliary sub-grid (termed the *mirror*) as illustrated in Figure 4(a). During the penetration process, the grid points on the left boundary of the soil were constrained in the horizontal direction while they were below the tip of the advancing *chisel*. As the *chisel* tip passed these grid points, they were allowed to move along the *chisel* boundary in both the horizontal and vertical directions.

4 3D PENETRATION MODEL

Three-dimensional penetration models were developed using the FLAC^{3D} program. In common with the 2D models, penetration was simulated by assigning a constant vertical velocity to the *chisel*. The constitutive models and initial in-situ/applied stresses for the 3D models were identical to those specified for

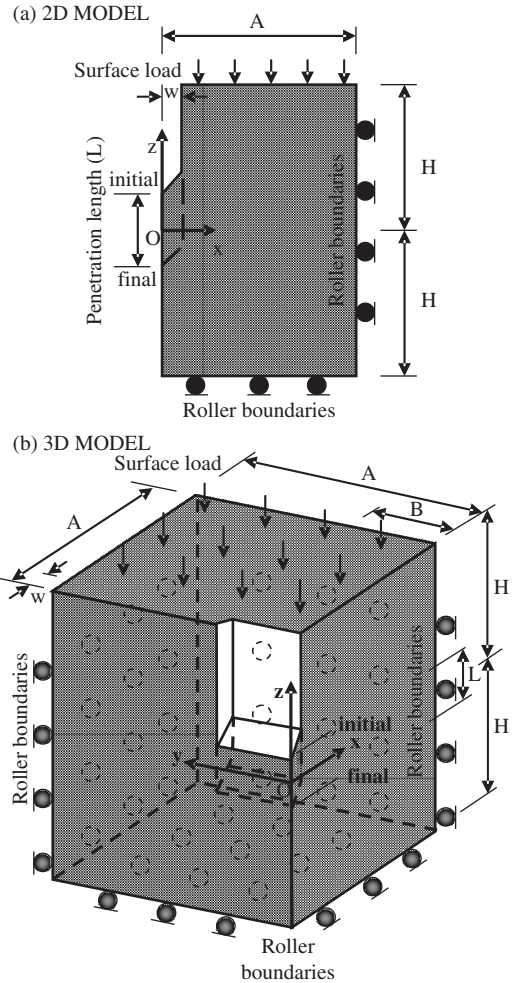


Figure 3. Boundary conditions in (a) 2D and (b) 3D penetration models.

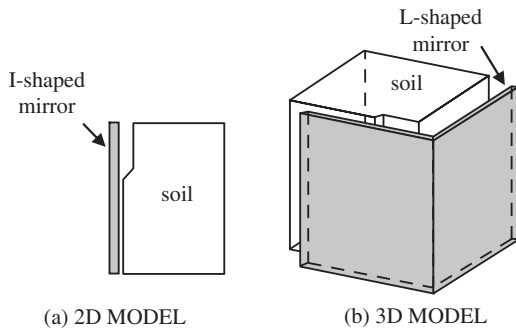


Figure 4. Mirror auxiliary sub-grids in (a) 2D and (b) 3D penetration models.

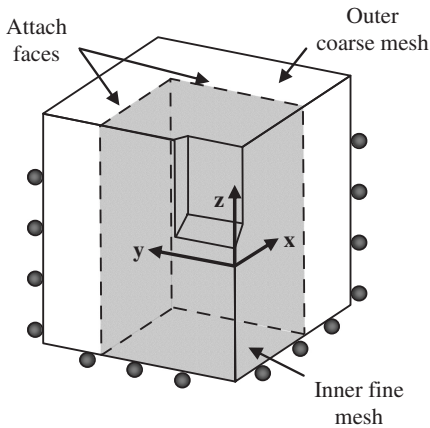


Figure 5. Location of attach faces between fine and coarse meshes.

the 2D models. Other parameters defined in the 3D models were:

- 1 The *chisel* had a width of $B = 12w$ ($w = 4.2\text{ mm}$);
- 2 One-sided interfaces were defined on the planes of symmetry ($x = 0$ and $y = 0$), and on the *chisel*;
- 3 Boundary fixities were defined as rollers on the bottom ($z = -H$) and far-lateral boundaries ($x = A$ and $y = A$), as illustrated in Figure 3(b).

Boundary conditions for the soil grid points on the symmetry planes ($x = 0$ and $y = 0$) were controlled by an L-shaped *mirror*, as illustrated in Figure 4(b). The *mirror* sub-grid did not allow the soil grid points to move inside the planes of symmetry, however, as penetration occurred (i.e. the *chisel* moved downwards) the soil grid points were allowed to move in all other directions.

Meshing was a more elaborate process in the 3D penetration models, as primitive grid shapes (e.g. bricks, wedges or tetrahedrons) from the $\text{FLAC}^{3\text{D}}$ mesh library were deformed and attached together to generate the model geometry. The mesh columns were aligned along streamline as discussed for the 2D models. The mesh density in the soil was also increased gradually towards the location of the *chisel* tip. For a more effective use of the available computing power, an inner finer sub-grid was attached to an outer coarse sub-grid (Itasca 2002a). The location of attached faces between the fine and coarse meshes are shown in Figure 5. In addition, a fine mesh was also used at the surface of the soil, as this area experienced high distortions during the penetration.

5 RESULTS AND DISCUSSION

In common with all numerical analyses, it is necessary to assess carefully the influence of the various

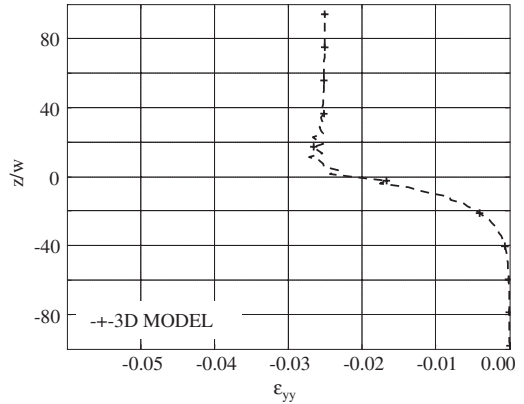


Figure 6. Strain path for ϵ_{yy} around the *chisel* in 3D models.

modelling parameters on the calculated results. Details such as the penetration rate, position of the boundaries, grid density and penetration length may all affect the stability of the model, and were examined in detail (Richards et al. 2005).

The soil behaviour during penetration was assessed by evaluating the computed strain paths. The strain path is a graphical means for highlighting changes in soil strain levels during the penetration process. A strain path shows the cumulative strain increments ($\epsilon = \sum \epsilon_{inc}$) plotted for a particular soil element against its normalized relative vertical position, z/w (relative to the position of the penetrating *chisel* tip). Strain paths were presented for an element located at $P_0(x_0 = 10w, y_0 = 2w, z_0 = 0)$ in all outputs. Although P_0 should have been chosen on the *chisel* plane of symmetry ($y = 0$), in order to evade the artefacts of the interface, P_0 was offset $2w$ from the centreline ($y_0 = 2w$). The strain paths for longitudinal ϵ_{yy} , lateral (ϵ_{xx}), vertical (ϵ_{zz}) and shear (ϵ_{xz}) strains have been evaluated in 2D and 3D models and are discussed in the following paragraphs.

The strain path for the longitudinal (ϵ_{yy}) strains was determined in the 3D model. The strain path for the ϵ_{yy} strains was extensive ($\delta\epsilon_{xx} < 0$) with minimum strain values occurring at $z/w = 10$, as shown in Figure 6. The longitudinal strain declined slightly from this point until the $z/w = 40$ level, where it then became relatively constant.

The strain path for the lateral (ϵ_{xx}) strains had a similar pattern in both the 2D and 3D penetration models, as shown in Figure 7(a). The ϵ_{xx} strain path consisted of three sections: extension ($\delta\epsilon_{xx} < 0$), compression ($\delta\epsilon_{xx} > 0$) and re-extension with the peak compression and extension strain values occurring at $10w$ above and below the tip level.

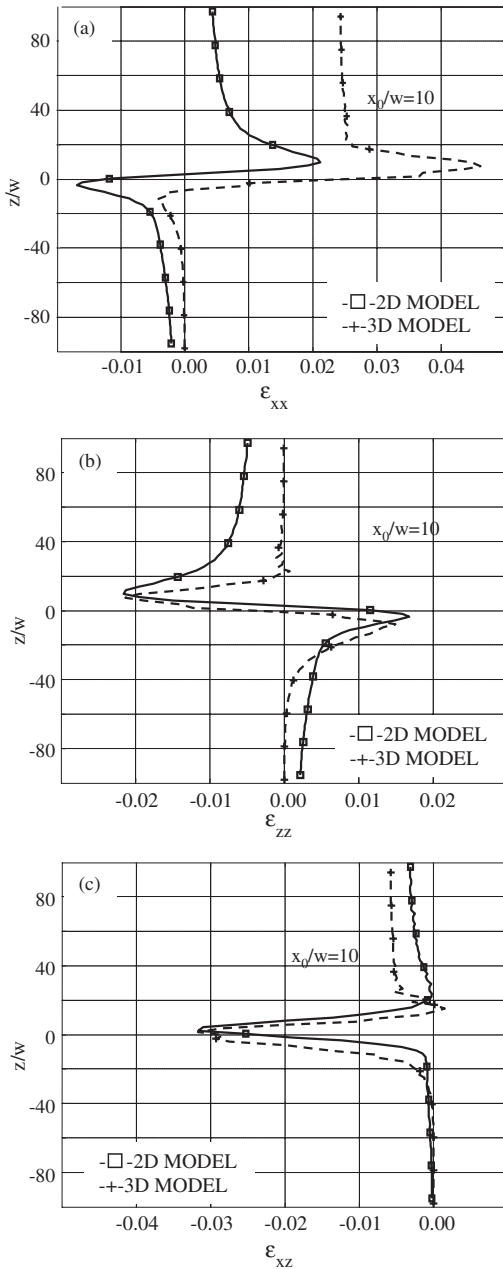


Figure 7. Comparison of strain path for (a) ϵ_{xx} , (b) ϵ_{zz} , and (c) ϵ_{xz} around the chisel.

The strain path for vertical (ϵ_{zz}) strains determined in the 2D analyses were markedly different from those obtained from the 3D models, as shown in Figure 7(b). In the 2D analyses, the absolute value of vertical strain at any level above the tip was higher

than the strain value at the corresponding level below the tip. In the 3D analyses however, vertical strains above the tip were approximately equal to strain values at the corresponding level below the tip.

Figure 7(c) shows that the strain paths for shear (ϵ_{xz}) strains determined in both the 2D and 3D penetration analyses. The peak shear strains were attained as the soil elements passed the tip level. The shear strains reduced slightly from the tip level until $z/w = 20$, before then increasing.

As soils are non-linear (Atkinson 2000), the history of changes they undergo affects their current stress-strain behaviour. The estimation of soil behaviour in a three-dimensional penetration problem, with a two-dimensional model could hence lead to significant errors in the behaviour predicted for soils around a penetrating object.

6 CONCLUSIONS

The discrepancies between the strain paths determined from the 2D and 3D analyses indicated that the deformations generated around the chisel during penetration could only be successfully evaluated by performing a three-dimensional analysis. In contrast to the lateral (ϵ_{xx}) and shear (ϵ_{xz}) strains that had a similar pattern in the 2D and 3D analyses, there was a difference between the vertical (ϵ_{zz}) strains determined from the 2D and 3D models. It was shown that, the strain reversal and return of soil elements to their initial vertical position could not be predicted by the 2D plane-strain analyses. As the stress-strain relationships for soils are generally inelastic-nonlinear, differences in the strain-history of the soil could lead to unrealistic estimation of stresses.

These analyses also showed that the advanced modelling techniques such as the explicit finite difference formulation adopted in FLAC can be used to model three-dimensional penetration problems.

REFERENCES

- Abu-Farsakh, M.Y., Voyiadjis, G.Z. and Tumay, M.T. 1998. Numerical analysis of the miniature piezocone penetration tests (PCPT) in cohesive soils. *International Journal for Numerical and Analytical methods in Geomechanics*, 22(10): 791–818.
- Anderheggen, E. and Renau-Munoz, J.F. 2000. A parallel explicit solver for simulating impact and penetration of a three-dimensional body into a solid substrate. *Advances in Engineering Software*, 31(12): 901–911.
- Atkinson, J.H. 2000. Non-linear soil stiffness in routine design. *Geotechnique*, 50(5): 487–508.
- Baligh, M.M. 1984. *The strain path method*. Dept. of Civil Engineering, Massachusetts Institute of Technology, Cambridge, Massachusetts, Research Report R84-01.
- Budhu, M. and Wu, C.S. 1992. Numerical analysis of sampling disturbances in clay soils. *International Journal for*

- Numerical and Analytical Methods in Geomechanics*, 16(7): 467–492.
- Butterfield, R., Harkness, R.M. and Andrawes, K.Z. 1970. A stereo-photogrammetric method for measuring displacement fields. *Geotechnique*, 20(3): 308–314.
- Fahey, M., Been, K., Horsfield, D. and Jefferies, M.G. 1989. Discussion: Calibration chamber tests of a cone penetrometer in sand. *Geotechnique*, 39(4): 729–731.
- Farhangi, S. 2006. *A numerical study of spade cell penetration*. PhD Thesis, School of Civil Engineering and the Environment, University of Southampton, UK, Southampton.
- Frank, R., Guenot, A. and Humbert, P. 1982. Numerical analysis of contacts in geomechanics. *Numerical Methods in Geomechanics; Proc., Edmonton, Alberta, Canada, Balkema, Rotterdam*: 37–45.
- Griffiths, D.V. 1982. Elasto-Plastic Analyses of Deep Foundations in Cohesive Soil. *International Journal for Numerical and Analytical Methods in Geomechanics*, 6: 211–218.
- Houlsby, G. T. and Hitchman, R. 1988. Calibration chamber tests of a cone penetrometer in sand. *Geotechnique*, 38(1): 39–44.
- Hu, Y. and Randolph, M.F. 1998. A practical numerical approach for large deformation problems in soil. *International Journal for Numerical and Analytical Methods in Geomechanics*, 22(5): 327–350.
- Itasca. 2002a. *FLAC 3D ver. 2.1, Fast Lagrangian Analysis of Continua in 3 Dimensions User's guide*. Minnesota: Itasca Consulting Group Inc.
- Itasca. 2002b. *FLAC ver. 4.0, Fast Lagrangian Analysis of Continua User's guide*. Minnesota: Itasca Consulting Group Inc.
- Itasca. 2004. *Itasca: Software*. Available from: <http://www.itascacg.com/index.html>, [Accessed May 2005].
- Kiousis, P.D., Voyiadjis, G.Z. and Tumay, M.T. 1988. A large strain theory and its application in the analysis of the cone penetration mechanism. *Journal for Numerical and Analytical Methods in Geomechanics*, 12(1): 45–60.
- Liyanapathirana, D.S., Deeks, A.J. and Randolph, M.F. 2000. Numerical modelling of large deformations associated with driving of open-ended piles. *International Journal for Numerical and Analytical Methods in Geomechanics*, 24(14): 1079–1101.
- Potyondy, J.G. 1961. Skin friction between various soils and construction material. *Geotechnique*, 11: 339–353.
- Richards, D.J., Clayton, C.R.I. and Farhangi, S. 2005. Two-dimensional analysis of soil behaviour around a penetrating object. *Canadian Geotechnical Journal (submitted 12/12/2005)*.
- Sagaseta, C., Whittle, A.J. and Santagata, M. 1997. Deformation analysis of shallow penetration in clay. *International Journal for Numerical and Analytical Methods in Geomechanics*, 21(10): 687–719.
- Siddique, A. 1990. *A numerical and experimental study of sampling disturbance*. PhD thesis, Department of Civil Engineering, University of Surrey, Guildford.
- Skempton, A.W. 1951. The Bearing Capacity of Clays. *Building Research Congress, Division I*: 180–189.
- Susila, E. and Hryciw, R. D. 2003. Large displacement FEM modelling of the cone penetration test (CPT) in normally consolidated sand. *International Journal for Numerical and Analytical Methods in Geomechanics*, 27(7): 585–602.
- Teh, C.I. 1987. *An analytical study of cone penetration test*. PhD thesis, Hertford College, University of Oxford, Oxford.
- Van den Berg, P. 1994. *Analysis of soil penetration*. PhD thesis, Strategic Research Department of Geotechnics, Delft University of Technology, Delft.
- Vesic, A.S. 1972. Expansion of Cavities in Infinite Soil Mass. *ASCE Journal of Soil Mechanics and Foundations*, 98(3): 265–290.
- White, D.J., Take, W.A. and Bolton, M.D. 2003. Soil deformation measurement using particle image velocimetry (PIV) and photogrammetry. *Geotechnique*, 53(7): 619–631.
- Yu, H.S., Herrmann, L.R. and Boulanger, R.W. 2000. Analysis of steady cone penetration in clay. *ASCE Journal of Geotechnical and Geoenvironmental Engineering*, 126(7): 594–605.

CIP-based numerical simulation for large deformation problems considering the interaction between geomaterial and rigid body

K. Sawada, S. Moriguchi, A. Yashima & M. Goshima
Gifu University, Gifu, Japan

S. Inoue & Y. Nishida
Protec Engineering Inc., Niigata, Japan

ABSTRACT: Numerical methods based on Lagrangian framework, such as FEM, have widely used in order to predict the deformation of geomaterials. Large deformation, however, induces a significant numerical error due to the distortion of numerical mesh in Lagrangian scheme. A CIP-based numerical method for large deformation problems of geomaterial is proposed in a series of this study. In the method, geomaterials are assumed to be a fluid that has shear strength based on the Mohr-Coulomb's failure criterion. From previous study, effectiveness of the numerical method was validated using results of real phenomena and model test. The efficacy of proposed method for interaction problems between solid and geomaterials, however, is not investigated in detail. In order to describe the interaction between geomaterials and rigid body, the numerical method is modified and some numerical simulations are conducted in this study. The effectiveness of the modified method for interaction problems is discussed based on numerical results.

1 INTRODUCTION

In recent years, based on rapid development of computing power, it is possible to predict behaviors of geomaterial using numerical simulation. It is, however, still difficult to solve large deformation problems using traditional methods based on continuum mechanics with Lagrangian mesh framework, such as the Finite Element Method (FEM). Although, some other numerical methods such as the Arbitrary Lagrangian-Eulerian (ALE) method (Hughes et al., 1981) has been applied to deformation analysis of geomaterials, it is still incapable of treating extreme large deformation problems.

There is different way to simulate behavior of geomaterials at large deformation region. Trunk et al. (1986), Sousa and Voight (1991), Uzuoka et al. (1998), Hadush et al. (2001) and Moriguchi et al. (2005) proposed numerical methods based on fluid dynamics with non-Newtonian fluid models for the deformation analysis of geomaterials. In these works, geomaterials are assumed to be viscous fluids. The proposed methods can treat large deformation of geomaterials in the framework of Eulerian method. Additionally, Moriguchi et al. (2005) proposed fluid model with the Mohr-Coulomb failure criterion, and it was confirmed that deformation of geomaterials can be described using the friction angle and the cohesion in the framework

of fluid dynamics. Moriguchi et al. (2005) conducted simulation of real geomaterial flow to validate the proposed method. According to the simulated results, it was confirmed that the method was effective to predict flow behavior and traveling distance of sediment.

The method based on fluid dynamics can describe behavior of geomaterial, however, the method cannot solve interaction problem between geomaterial and solid. It is important to describe interaction between geomaterial and solid for design of infrastructures. In this study, the method proposed by Moriguchi et al. (2005) is modified to solve interaction problem, and numerical simulations related to interaction problem between geomaterial and rigid body are conducted.

2 CONSTITUTIVE MODEL

In this study, geomaterials are assumed to be the Bingham visco-plastic fluid. The behavior of the Bingham fluid can be expressed in one-dimensional condition as follow,

$$\tau = \eta_0 \dot{\gamma} + \tau_y \quad (1)$$

where τ is the shear stress, η_0 is viscosity after yield, $\dot{\gamma}$ is the shear strain rate and τ_y is shear strength. From

Equation 1, an equivalent Newtonian viscosity of the Bingham fluid can be obtained. The equivalent viscosity η' is expressed by following equation.

$$\eta' = \frac{\tau}{\dot{\gamma}} = \eta_0 + \frac{\tau_y}{\dot{\gamma}} \quad (2)$$

Figure 1 shows behavior of the Bingham fluid and the concept of the equivalent viscosity. As shown in Equation 1, the shear stress of the Bingham fluid is described as a linear function of shear strain rate. Shear strength of the Bingham fluid is expressed as intercept of the liner function. In Figure 1, a solid line describes the behavior of the Bingham fluid, and a dashed line expresses the behavior of an equivalent Newtonian fluid. The equivalent viscosity η' is described as the gradient of the dashed line. In other words, η' is an apparent viscosity of the Bingham fluid. If the shear strain rate increases, the dashed line moves in the direction of (A) as shown in Figure 1, and the equivalent viscosity coefficient becomes smaller. On the contrary, when the shear strain decreases and the dashed line moves in the direction of (B) then the equivalent viscosity coefficient becomes larger.

The infinite value of the equivalent viscosity arises when shear strain rate equals to zero. It is impossible to treat such infinite value in numerical calculations. In order to avoid the numerical difficulty, the maximum value for the equivalent viscosity is defined as below,

$$\begin{aligned} \eta' &= \eta_0 \dot{\gamma} + \frac{\tau_y}{\dot{\gamma}} & \text{if } \eta' < \eta_{\max} \\ \eta' &= \eta_{\max} & \text{if } \eta' < \eta_{\max} \end{aligned} \quad (3)$$

where η_{\max} is maximum equivalent viscosity. Using this concept, the Bingham model is described as a bilinear model as shown in Figure 2. The relationship between the equivalent viscosity and the shear strain rate is described in Figure 3. As shown in Figure 3, η_{\max}

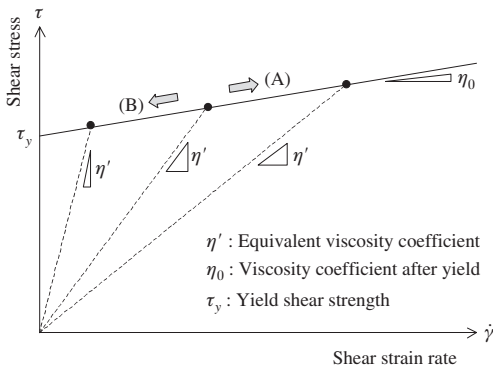


Figure 1. Equivalent viscosity of the Bingham model.

and η_0 defines the maximum and minimum value of the equivalent viscosity. In the simulation conducted in this study, the equivalent viscosity η' is constant value in one calculation step, and η' is updated step by step. In the calculation for η' in two and three-dimensional condition, the shear strain rate $\dot{\gamma}$ is defined using second invariant of shear strain tensor V_{ij} as follow,

$$\dot{\gamma} = \sqrt{\frac{1}{2} V_{ij} V_{ij}} \quad (4)$$

in which,

$$V_{ij} = \frac{1}{2} \left(\frac{\partial u_i}{\partial x_j} + \frac{\partial u_j}{\partial x_i} \right) \quad (5)$$

where u_i is the velocity vector.

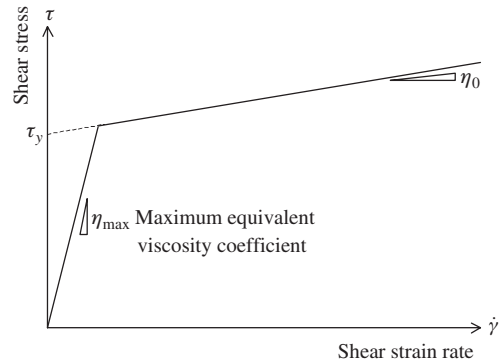


Figure 2. Bi-linear Bingham model.

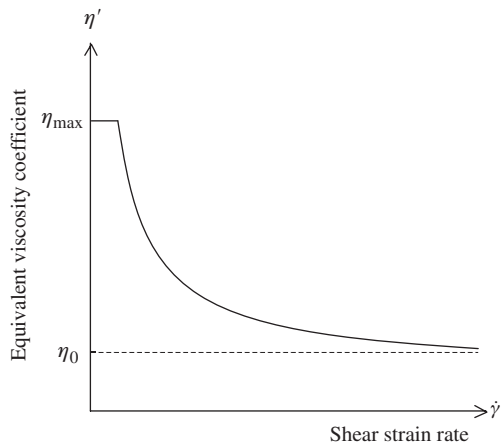


Figure 3. Relation between equivalent viscosity coefficient and shear strain rate.

Using the equivalent Newtonian viscosity, the behavior of the Bingham model can be expressed in the numerical analysis. The original Bingham model, however, cannot describe deformation behavior of geomaterials perfectly. In order to express the shear strength of geomaterial, Moriguch et al. (2005) introduced the Mohr-Coulomb failure criterion into the Bingham model. The Mohr-Coulomb failure criterion is described as follows,

$$\tau_y = \sigma_n \tan \phi + c \quad (6)$$

where τ_y is the shear strength of geomaterial, σ_n is the effective stress, ϕ is the internal friction angle and c is the cohesion. Substituting the shear strength derived from Equation 6 into Equation 1, the modified Bingham model with shear strength of geomaterial is given as below,

$$\tau = \eta_0 \dot{\gamma} + \sigma_n \tan \phi + c \quad (7)$$

In this study, there is no concept of the effective stress, because numerical framework is based on fluid dynamics. Therefore, the hydrostatic pressure p is used as a substitute for the normal stress σ_n as follows,

$$\tau = \eta_0 \dot{\gamma} + p \tan \phi + c \quad (8)$$

Using the modified Bingham model in Equation 8, the equivalent viscosity is described as follow,

$$\eta' = \eta_0 \dot{\gamma} + \frac{p \tan \phi + c}{\dot{\gamma}} \quad \text{if } \eta' < \eta_{\max} \quad (9)$$

$$\eta' = \eta_{\max} \quad \text{if } \eta' \geq \eta_{\max}$$

The equivalent viscosity derived from Bingham model with the Mohr-Coulomb failure criterion is obtained by above equations. Finally, the equivalent viscosity is introduced into the constitutive model for Newtonian fluid. The constitutive model for Newtonian fluid is described by the following equation.

$$\sigma_{ij} = -p \delta_{ij} - \frac{2}{3} \eta V_{kk} \delta_{ij} + 2\eta V_{ij} \quad (10)$$

where σ_{ij} is the stress tensor. By substituting the equivalent viscosity η' for η , the constitutive model used in this study is given as below,

$$\sigma_{ij} = -p \delta_{ij} - \frac{2}{3} \eta' V_{kk} \delta_{ij} + 2\eta' V_{ij} \quad (11)$$

3 NUMERICAL METHOD

3.1 Governing equation

In this study, following equations are used as governing equations.

$$\frac{\partial p}{\partial t} + u_j \frac{\partial p}{\partial x_j} = -\rho C_s^2 \left(\frac{\partial u_k}{\partial x_k} \right) \quad (12)$$

$$\frac{\partial u_i}{\partial t} + u_j \frac{\partial u_i}{\partial x_j} = \frac{1}{\rho} \frac{\partial \sigma_{ij}}{\partial x_j} + b_i \quad (13)$$

$$\frac{\partial \varphi^m}{\partial t} + u_k \frac{\partial \varphi^m}{\partial x_k} = 0 \quad (14)$$

where u_i is the velocity vector, ρ is the density, C_s is the sound speed, b_i is the body force vector and φ^m is the density function. Density functions are defined in each element to distinguish different kind of materials. If $\varphi^m = 1$, the element is filled up with the material m , and if $\varphi^m = 0$, there is no material m in the mesh. Equation 12, 13 and 14 show the equation related to the pressure, the law of linear conservation of momentum and advection equation of the density function, respectively. By using the constitutive model shown in Equation 11, the law of linear conservation of momentum is described as follow,

$$\frac{\partial u_i}{\partial t} + u_j \frac{\partial u_i}{\partial x_j} = -\frac{1}{\rho} \frac{\partial p}{\partial x_i} - \frac{2}{3} \frac{1}{\rho} \frac{\partial}{\partial x_i} (\eta' V_{kk}) + \frac{1}{\rho} \frac{\partial}{\partial x_i} (\eta' V_{ij}) + b_i \quad (15)$$

For Newtonian fluid, generally, the spatial derivative of viscosity is not considered. The value of the equivalent viscosity, however, depends on the distribution of velocity and pressure as shown in Equation 9. This means that the equivalent viscosity η' has the spatial derivative. Therefore, the spatial derivative of η' is considered in Equation 15.

Changes of velocity and pressure can be expressed by the governing equations. However, changes of density, viscosity and sound speed are not expressed. In this study, value of density, viscosity and sound speed are calculated using density function. The density, viscosity coefficient and the sound speed in each element are calculated as follows,

$$\rho = \sum \varphi^m \rho^m \quad (0 \leq \varphi^m \leq 1) \quad (16)$$

$$\eta = \sum \varphi^m \eta^m \quad (0 \leq \varphi^m \leq 1) \quad (17)$$

$$C_s = \sum \varphi^m C_s^m \quad (0 \leq \varphi^m \leq 1) \quad (18)$$

where, ρ^m, η^m and C_s^m is the density, viscosity, and sound speed of the material m .

In this study, the governing equations are solved using CCUP (CIP and Combined, Unified Procedure) method (Yabe and Wang, 1991).

3.2 Equation considering motion of rigid body

Objective of this study is to describe the interaction between geomaterial and solid. Therefore it is necessary to consider an effect of solid motion. For describing an interaction problem between fluid and rigid body, a framework was proposed by Xiao (1999). In order to represent the interaction, following additional term was introduced to the law of linear conservation of momentum.

$$\frac{\partial u_i}{\partial x_i} = \frac{U_i - u_i}{\Delta t} \varphi^r \quad (19)$$

where U_i is the velocity of rigid body and φ^r is density function of rigid body. This term works only inside of the rigid body ($\varphi^r = 1$). By introducing this term into advection term of the law of linear conservation of momentum, Equation 17 is developed as below,

$$\begin{aligned} \frac{\partial u_i}{\partial t} + u_j \frac{\partial u_i}{\partial x_j} = & \left[-\frac{1}{\rho} \frac{\partial p}{\partial x_i} - \frac{2}{3} \frac{1}{\rho} \frac{\partial}{\partial x_i} (\eta' V_{kk}) \right. \\ & \left. + 2 \frac{1}{\rho} \frac{\partial}{\partial x_j} (\eta' V_{ij}) + b_i \right] (1 - \varphi^r) + \frac{U_i - u_i}{\Delta t} \varphi^r \end{aligned} \quad (20)$$

Additionally, Poisson equation of pressure is also developed as follow,

$$\begin{aligned} \frac{\partial}{\partial x_i} \left(\frac{(1 - \varphi^r)}{\rho^n} \frac{\partial p^*}{\partial x_i} \right) = & \frac{p^* - p^n}{\Delta t^2 \rho^n C_s^2} \\ & + \frac{1}{\Delta t} \frac{\partial \{ (1 - \varphi^r) u_i^n + U_i \varphi^r \}}{\partial x_i} \end{aligned} \quad (21)$$

In this study, the numerical framework mentioned above is used to solve interaction problem between geomaterial and rigid body.

3.3 Calculation method of the rigid body

In this study, not only behavior of geomaterial but also motion of the rigid body should be calculated. Motion of the rigid body can be separated into two part, translation motion and rotational motion, so that we can calculate translation velocity and rotational

velocity respectively. By integrating force acting on surface of the rigid body, translation acceleration is calculated. In this study, translation acceleration is calculated using density function of rigid body, as below,

$$\frac{\partial V_i}{\partial t} = \frac{1}{M} \int \frac{\partial u_i}{\partial t} \rho \varphi^r dV \quad (22)$$

where V_i is the translation velocity vector of the rigid body, u_i is the velocity vector of geomaterial and M is the mass of the rigid body. By using above equation, it is possible to calculate the force exerted on rigid body from geomaterial without considering position of surface of rigid body. Based on same thinking, rotational angular acceleration of rigid body can be described as follow,

$$\frac{\partial \Omega_k}{\partial t} = \frac{1}{I} \int R_i \frac{\partial u_j}{\partial t} e_{ijk} \rho \varphi^r dV \quad (23)$$

in which

$$R_i = x_i - X_i \quad (24)$$

where Ω_k is angular velocity of the rigid body, I is the inertia moment, e_{ijk} is the permutation symbol, x_i is the position vector and X_i is the position vector of gravity center of the rigid body. From translation acceleration and angular acceleration, the velocity of the rigid body can be obtained.

3.4 High accuracy treatment for surface

In this study, the equivalent viscosity is used to describe the behavior of geomaterials, so that it is necessary to pay much attention to the interface treatment. For this purpose, a tangent transformation method (Yabe and Xiao, 1993) is applied. In the method, density functions are transformed using a tangent function as below,

$$H(\varphi_i) = \tan \left[\pi (\varphi^m - 0.5) \right] \quad (25)$$

where H is the transformed density function. In the calculation, this transformation is applied before advection calculation, and following inverse transformation is applied after advection calculation.

$$\varphi^m = \frac{\arctan [H(\varphi^m)]}{\pi} + 0.5 \quad (26)$$

Using this technique, the interface of different materials can be kept sharply. In this study, the transformation method is applied for the treatment of interface of geomaterials.

4 NUMERICAL SIMULATIONS

In former studies with respect to interaction problem between rigid body and geomaterial we conducted, rigid bodies were constrained as boundary conditions in simulations. Therefore, a numerical method is proposed to simulate the movement of rigid bodies in this study. In order to investigate the validity of proposed numerical method, several interaction problems between geomaterial and rigid body are calculated using numerical framework mentioned in this paper. In this section, two types of numerical simulations are carried out for the interaction problems between geomaterials and rigid body.

4.1 Underground structure in a liquefied ground

Generally, the stiffness of ground will be reduced to a negligible value after liquefaction. If there is a structure which overall density is lighter than the liquefied ground, the structure will be lifted up from the initial position. In this section, the movement of structure in a ground after liquefaction is simulated using proposed method. Two cases of simulations are carried out for a structure in a ground after liquefaction. Figure 4 shows an initial condition and configuration of ground and structure. In this section two types of ground materials are assumed, case 1 for Newtonian fluid and case 2 for cohesive geomaterial. Material parameters for two simulations are listed in Table 1. 10,000 (100 × 100) square mesh (dx = dy = 0.05 m) is used in this simulation in 5 m square field. The density of rigid body is assumed lighter than that of ground materials.

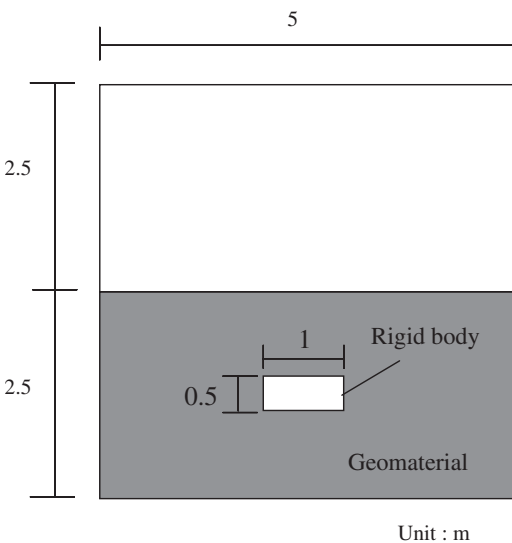


Figure 4. Numerical model.

Figure 5 shows the movement of the structure for both cases at the time of 0.8 s, 1.6 s, 2.8 s and 4.0 s. In case 1, the structure floats up quickly and fluctuates at the ground surface. In the case 2 on the other hand, the structure floats up slowly because of the existing of friction between the structure and cohesive geomaterial. From the results of these simulations, it is

Table 1. Parameters for simulations.

	Structure	Geomaterial	
		Case 1	Case 2
Density (kN/m ³)	5.0	10.0	10.0
Sound speed (m/s)	4000.0	3000.0	3000.0
Cohesion (Pa)	–	0.0	200.0

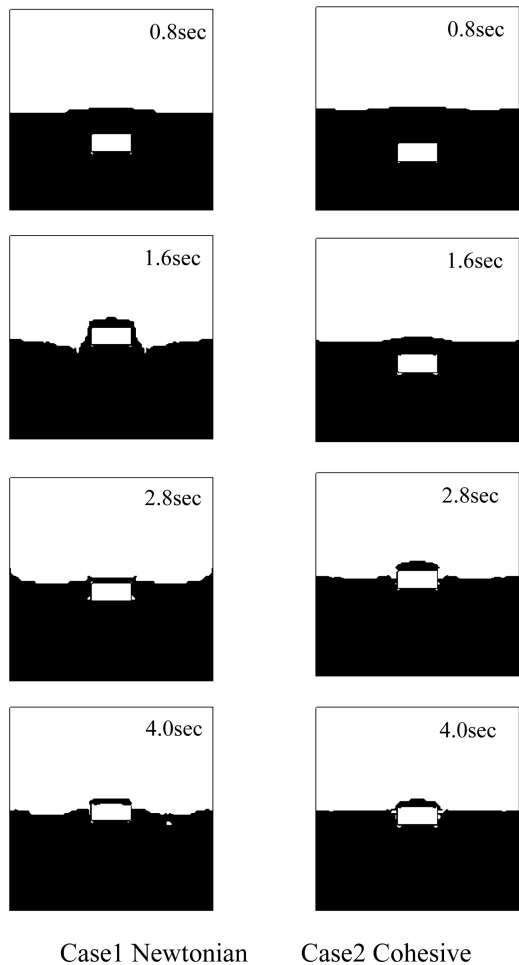


Figure 5. Movement of the structure.

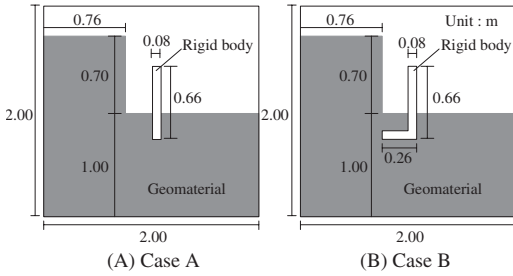


Figure 6. Numerical model.

Table 2. Parameters for simulations of collision.

	Retaining wall	Geomaterial
Density (kN/m ³)	10.00	10.00
Sound speed (m/s)	4000.0	3000.0
Cohesion (Pa)	–	0.0
Internal friction angle (degree)	–	41.0

found that the interaction behavior of the underground structure after liquefaction is simulated appropriately.

4.2 Collision of geomaterial against retaining wall

The collision of geomaterial against retaining wall is simulated in two-dimensional field. Two cases of interaction problems are compared with different shapes of retaining walls. Figure 6 (A) and (B) show numerical models for Case A and Case B respectively. I-shaped retaining wall is used in Case A and L-shaped in Case B. The difference between two cases is only the shape of retaining wall. Parameters used in simulation are shown in Table 2. As shown in Table 2, geomaterial is assumed to be a pure granular material ($\phi = 41$ degree). 10,000 (100 × 100) square mesh ($dx = dy = 0.02$ m) is used in this simulation in 2 m square field. The retaining wall is located close to the collapsed mound.

Figure 7 and 8 show the simulated results for Case A and B respectively. Upper figures show the surface configuration of geomaterial and the retaining wall at different time (0.4 s, 0.8 s and 2.0 s). Contours in lower figures indicate the pressure of the ground. The values of pressure near the retaining wall are influenced

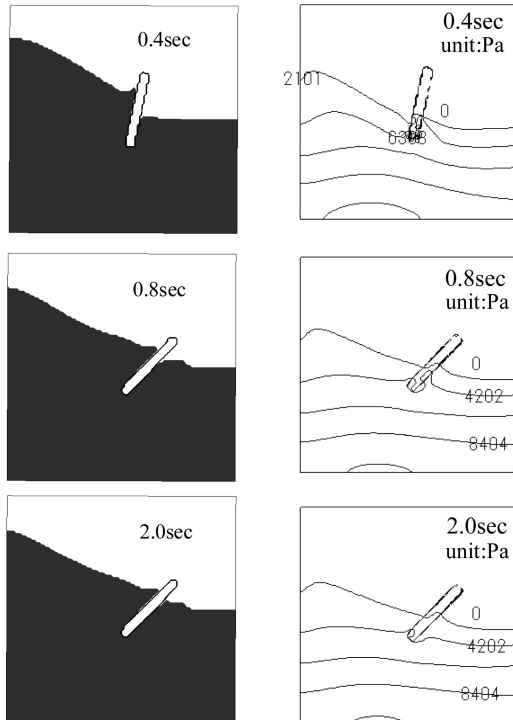


Figure 7. Configuration of geomaterial and retaining wall, and pressure of geomaterial (Case A).

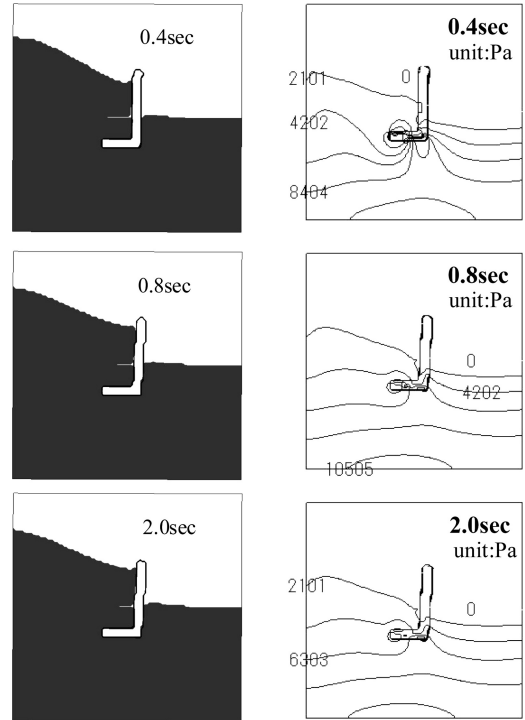


Figure 8. Configuration of geomaterial and retaining wall, and pressure of geomaterial (Case B).

by the motion of retaining wall. From the both figures, retaining wall is affected by the collapse of the mound. In Case A, the retaining wall is falling down due to the collision of the mound (see Figure 7). On the other hand, the retaining wall does not fall down in Case B (see Figure 8). The magnitude of pressure just beneath the horizontal portion in L-shaped retaining wall in figure 8 is larger than other part of geomaterial. The L-shaped retaining wall is found to be very effective to the stability against the collision of mound. Based on these results, it can be concluded that the proposed method can describe the effect of different shape of the retaining wall against slope failure.

5 CONCLUSION

This work presented the numerical framework for the interaction between geomaterial and rigid body. The Bingham fluid model with the Mohr-Coulomb failure criterion was used to describe the behavior of geomaterial, and the CIP-based numerical method was modified to solve the interaction problem. Two types boundary value problems were simulated using the modified method. Simulations related to a structure in a ground after liquefaction and a collision of geomaterial against retaining wall were conducted in this study. The numerical results were investigated based on the change in the configuration of geomaterial and rigid body. In addition, the change in the ground pressure was discussed to investigate the effect of the L-shaped retaining wall. From these numerical results, it is confirmed that the modified numerical method can describe the interaction between geomaterial and rigid body appropriately. However, the method has not been validated based on change in real phenomena. It

is necessary to simulate real phenomena in the near future.

REFERENCES

- Hadush, S., Yashima, A., Uzuoka, R., Moriguchi, S. and Sawada, K., Liquefaction Induced Lateral Spread Analysis Using the CIP Method. *Computers and Geotechnics*, **28**, 549–574, 2001.
- Hughes T.J.R., Liu W.K. and Zimmermann T.K., Lagrangian-Eulerian finite element formulation for incompressible viscous flows, *Comput. Methods Appl. Mech. Engng.*, **29**, 329–349, 1981.
- Moriguchi, S., Yashima, A., Sawada, K., Uzuoka, R. and Ito, M., Numerical simulation of flow failure of Geomaterials based on fluid dynamics, *Soils & Foundations*, **45-2**, 155–166, 2005.
- Sousa J. and Voight B., Continuum simulation of the flow failure, *Geotechnique*, **41**, 4, 515–538, 1991.
- Trunk F.J., Dent D.J. and Lang T.E., Computer modeling of large rockslides, *Journal of the Geotechnical Division*, ASCE, **112** (GE 3), 348–360, 1986.
- Uzuoka R., Yashima A., Kawakami T. and Konrad J-M., Fluid dynamics based prediction of liquefaction induced lateral spreading, *Computers and Geotechnics*, **22** 3/4, 234–282, 1998.
- Xiao, F., A computational model for suspended large rigid body in 3D unsteady viscous flow. *Journal of Computational Physics*, 115, 1999.
- Yabe, T. and Wang, P. Y., Unified Numerical Procedure for Compressible and incompressible fluid, *J. Phys. Soc., Japan*, **60**–7, 2105–2108, 1991.
- Yabe, T. and Xiao, F., Description of Complex and Sharp Interface During Shock Wave Interaction with Liquid Drop. *J. Phys. Soc. Japan* **62**, 2537–2540, 1993.
- Zhang, S.L., NEC Corp. and Fujino, S., *Mathematics in iteration schemes*. Asakura, 1996.

Reservoir, dam and rock mass interaction modeling

D. Divac & D. Vuckovic

Institute for the development of water resources “Jaroslav Cerni”, Belgrade, Serbia and Montenegro

M. Zivkovic & S. Vulovic

Faculty of mechanical engineering, University of Kragujevac, Kragujevac, Serbia and Montenegro

ABSTRACT: The objective of this paper is to show the modeling of filtration and stress-strain processes, during the building of dam and accumulation in naturally loaded structure, using the finite elements method. Analyzed region is modeled by the 3D finite elements mesh, whereas real geometry and disposition of different geological environments are completely respected. Through modeling of filtration, the fields of potential and fluid velocity are obtained for determined boundary conditions and for accepted material properties as well as for field of filtration forces as a measure of interaction between fluid and soil. Achieved filtration forces are used as input for stress-strain analysis. The elasto-plastic material model with critical state is applied for stress-strain analysis. The paper presents developed methodology which gives a very good evaluation of global safety of structure as well as a possibility of the critical zones localization concerning static and filtration stability shown in analysis of FR Macedonian St. Petka dam.

1 INTRODUCTION

High dams as engineering objects have a significant stress value in foundations and supports because of dam dead weight as well as the water pressure on dam and rock mass. The analysis of filtration and stress-strain processes in the interaction of dam and rock mass as well as the analysis of stability of object-rock coupled system represents an important part of engineering studies for projecting of high dams. It also helps to select a certain type of dam for a particular area. Rock mass on dam has to be investigated and modeled by defining certain characteristics of its filtration and stress-strain behavior. These characteristics are quantified by the laboratory tests and investigation *in situ*. According to this the material characteristics for filtration and stress-strain numerical analyses are defined.

By the development of hardware and software technology, numerical methods made great expansion and found application in many fields of technique replacing traditional methods of modeling and offering great possibilities in daily analytical and project work.

By modeling of filtration and stress-strain processes for various conditions, the fields of potential, gradients and fluid velocity are obtained as well as the filtration forces which appear as the result of fluid and soil interaction. By modeling of stress-strain processes, the fields of displacement, stress, elastic and plastic strains of soil are obtained. The fields of all relevant values refer to the complete investigated space: dam, injection

curtain and surrounding rock mass. Based on achieved results critical zones from the aspect of soil stress and strain can be identified as well as the velocity of fluid flow. Also, the cumulative indicators of dam safety (safety factor in relation to appearance of instability, total flow through the dam, etc.) can be determined.

The finite elements method is applied respecting the real behavior of mediums using suitable nonlinear material models. The program PAK (which is developed at Mechanical Faculty in Kragujevac in cooperation with the Institute “Jaroslav Cerni”) is used and adapted for the purpose of solving the problems of fluid flow interaction and deformation of rock mass.

2 MODELING OF FILTRATION PROCESSES

Filtration processes are analyzed according to the differential equation of fluid flow through a porous medium for stationary and non-stationary conditions, which is derived based on Darcy’s law for the case of small velocities

$$\mathbf{q} = -\mathbf{k}\mathbf{i} \quad (1)$$

where \mathbf{q} = the Darcian velocity, \mathbf{k} = hydraulic conductivity. The gradient of potential \mathbf{i} is

$$\mathbf{i} = \nabla\phi \quad (2)$$

where ϕ = total fluid potential or head.

The governing differential equations of incompressible fluid flow through a porous medium of variable permeability have the following form, Desai (1984),

$$\nabla^T (\mathbf{k} \nabla \phi) + Q = S \frac{\partial \phi}{\partial t} \quad (3)$$

where Q = volume source/sink and S = specific storage. For the case of stationary fluid flow right side of Equation (3) is equal to zero.

The finite element equation of balance is

$$(\mathbf{K} + \mathbf{S})^{t+\Delta t} \Phi = {}^{t+\Delta t} \mathbf{f} + \mathbf{S}^t \Phi \quad (4)$$

where \mathbf{S} is the profusion matrix

$$\mathbf{S} = \frac{1}{\Delta t} \int_V S \mathbf{H}^T \mathbf{H} dV \quad (5)$$

\mathbf{K} is the hydraulic conductivity matrix

$$\mathbf{K} = \int_V \mathbf{B}^T \mathbf{k} \mathbf{B} dV \quad (6)$$

and ${}^{t+\Delta t} \mathbf{f}$ is the flux vector

$${}^{t+\Delta t} \mathbf{f} = \int_V {}^{t+\Delta t} Q \mathbf{H}^T dV - \int_A {}^{t+\Delta t} \bar{q} \mathbf{H}^T dA \quad (7)$$

When the procedure converge, we can calculate the gradient of potential (2), Darcy's velocity (3) and flow quantity in each node of the model using the potential,

$${}^{t+\Delta t} \mathbf{f}^p = {}^{t+\Delta t} \mathbf{S}^t \left({}^{t+\Delta t} \Phi^{(i)} - {}^t \Phi \right) + {}^{t+\Delta t} \mathbf{K}^{(i)} {}^{t+\Delta t} \Phi^{(i)} \quad (8)$$

Flow quantity on a contour is equal to the algebraic sum of flows in nodes inside that contour.

3 MODELING OF STRESS-STRAIN PROCESSES

Stress-strain processes are analyzed by elasto-plastic material model with the concept of critical state, Kojic & Bathe (2005). This analysis can give field of displacement, total and plastic strains, stress and other relevant internal variables for given initial and boundary conditions.

The principle of virtual work has the following form:

$$\int_V \boldsymbol{\sigma} \delta \boldsymbol{\epsilon} dV = \int_V \mathbf{F}^v \delta \mathbf{u} dV + \int_{S^\sigma} \mathbf{F}^s \delta \mathbf{u} dS \quad (9)$$

The incremental iterative equilibrium equation of finite element, which can be derived from principle of virtual work (9), has the following form:

$${}^{t+\Delta t} \mathbf{K}^{(i-1)} \Delta \mathbf{U}^{(i)} = {}^{t+\Delta t} \mathbf{F}^s - {}^{t+\Delta t} \mathbf{F}^{v(i-1)} \quad (10)$$

where:

$${}^{t+\Delta t} \mathbf{K}^{(i-1)} = \int_V \mathbf{B}^T {}^{t+\Delta t} \mathbf{C}^{ep(i-1)} \mathbf{B} dV \quad (11)$$

is the stiffness matrix and

$${}^{t+\Delta t} \mathbf{F}^{(i-1)} = \int_V \mathbf{B}^T {}^{t+\Delta t} \boldsymbol{\sigma}^{(i-1)} dV \quad (12)$$

is the vector of internal forces.

${}^{t+\Delta t} \mathbf{F}^s$ is the vector of external forces and $\Delta \mathbf{U}^{(i)}$ is the vector of increment of displacements. The equilibrium iterations continue until the equilibrium Equation (10) is satisfied within a specified tolerance.

To determinate the tangent stiffness matrix, we need to find tangent constitutive matrix

$${}^{t+\Delta t} \mathbf{C}^{ep(i-1)} = \frac{\partial {}^{t+\Delta t} \boldsymbol{\sigma}^{(i-1)}}{\partial {}^{t+\Delta t} \boldsymbol{\epsilon}^{(i-1)}} \quad (13)$$

For the case of small strains, total strains are

$${}^{t+\Delta t} \boldsymbol{\epsilon}^{(i-1)} = {}^{t+\Delta t} \mathbf{B}^{(i-1)} {}^{t+\Delta t} \mathbf{U}^{(i-1)} \quad (14)$$

where ${}^{t+\Delta t} \mathbf{B}^{(i-1)}$ is strain-displacement matrix. The total displacements are

$${}^{t+\Delta t} \mathbf{U}^{(i)} = {}^{t+\Delta t} \mathbf{U}^{(i-1)} + \Delta \mathbf{U}^{(i)} \quad (15)$$

In the implicit numerical procedure for stress calculation we start with the assumption that the stress-strain state is known at a material point and time t . The known quantities are: stress ${}^t \boldsymbol{\sigma}$, strain ${}^t \boldsymbol{\epsilon}$, plastic strain ${}^t \boldsymbol{\epsilon}^p$ at time t , and total strain ${}^{t+\Delta t} \boldsymbol{\epsilon}$ at the end of load step. The task within the stress integration is to determine stress ${}^{t+\Delta t} \boldsymbol{\sigma}$ and plastic strain ${}^{t+\Delta t} \boldsymbol{\epsilon}^p$ at the end of time steps.

The basic steps in concept of the implicit stress integration are as follows:

1. Express all unknown variables in terms of one governing parameter Δe_m^p (increment of the mean plastic strain).
2. Solve the governing equation (yield function) $f(\Delta e_m^p) = 0$
3. Calculate the unknown variables using Δe_m^p the solution of the governing equation.

4 COMPLEX MODEL OF FILTRATION AND STRESS-STRAIN PROCESSES

Unique model for filtration and stress-strain processes at St. Petka dam location (interaction of the reservoir, dam and rock mass) is developed. Modeling is done for terrain within area of dam with basis dimension of 252×250 m, from elevation 230 asl to 400 asl. The 3D elements mesh was developed for all calculations (filtration and stress-strain) with 17099 nodes and 14505 elements (Fig. 1). Model is based on real filtration and stress-strain characteristics of presented mediums. Therefore the mesh was formed to comprise all quasi-homogenous zones by filtration and stress-strain parameters (in total 41 zones). In filtration analysis, boundary conditions with regard to potential are defined as follows: at the part of the contour that corresponds to terrain surface below nominal water level – potential is equal to 364 asl; at the part of the contour that corresponds to terrain surface below river level potential is 318 asl. Contour conditions with regard to discharge (flux) are set according to model limits ($q = 0$).

For stress-strain analysis, displacements for boundary conditions are set up. In these analyses, following loads are used: dead weight, filtration forces and water pressure at dam.

In order to determine the significance of certain elements of technical solution, several versions in regard to prime model were established. Technical solution of injection curtain are varied – dimensions and filtration coefficient. The model without the curtain is used as well as models with injection curtain

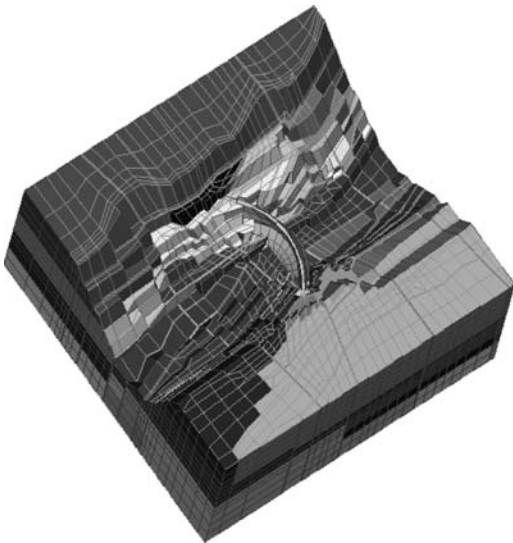


Figure 1. Model of partition place of dam St. Petka.

where its filtration coefficient has been varied within a 0.5–3 Lu range.

5 THE PARAMETRIZATION OF MODEL

The material characteristics for filtration and stress-strain analyses are determined by using experimental and numerical methods with verification on *in situ*. Generally, methods for parameterization are heterogeneous and depend on applied investigation methods as well as on material model. The filtration coefficients for quasi homogenous areas are determined by interpolation and extrapolation of values obtained by experimental investigation of water discharge. The model comprises real position and configuration of defined quasi homogenous zones of natural rock mass and cracking zones as well as injection curtain with possibilities of variation of its dimension and water discharge. An acceptance of filtration coefficient depends on investigation level and results interpretation. Although the rock mass is discontinuous medium, for the dimension problem it can be approximated by the quasi continuum. The constitutive model should describe the most important rock mass features for elasto-plastic behavior comprising strengthening and softening. The model of mechanical behavior for rock mass as a discontinuous and anisotropic medium is developed. The interaction of cracks and monolith is incorporated in the constitutive relations. The concept of constitutive model for cracking rock mass is based on coupling monolith deformation and whole systems respecting their real space location and frequentation. The model for discontinuities which is based on theory of plasticity with appliance of non associative yield is developed. The Desai's one surface yield condition and concept of limit state are used, Desai (1984), Desai & Siriwardane (1984). The methodological procedure and software for data interpretation obtained by investigation is developed in order to obtain parameters of constitutive model of rock mass. This method is based on iterative procedure of simulation by application of finite elements method and errors minimization. The numerical models are formed for simulation of more typical tests. Therefore, the definition of quasi homogenous zones and derived investigation of mechanical properties enable definition of certain values of mechanical characteristics which are used as input data for stress-strain modeling.

6 CRITERIA FOR ANALYSIS

6.1 Criteria for filtration

Criteria for analysis of results of filtration processes model are: allowed accumulation losses and criterion connected to filtration dam stability defined by

allowed gradients. It should be noted that water losses and stability are not independent, because forbidden filtration velocities can also produce progressive increase of water discharge, what would result in progressive increase of water losses, thus endangering dam stability.

Filtration stability at critical locations is investigated, that is, at contacts of various mediums, within a zone where underground water erupt, and at downstream under the dam. With regards to this, filtration stability is defined by a safety factor for maximum output gradients in relation to allowed ones ($F_s = I_{dop}/I_{max}$; where I_{dop} = allowed output gradient, I_{max} = maximum output gradient).

Criteria for allowed gradients are formed, through application of results of numerous and of many years investigations of local filtration deformation appearance and of porous environment filtration collapse. In regards of previous, allowed gradients criterions are spatial variables, because they generally increase when permeability decreases.

6.2 Criteria for stress-strain analysis

Main problem of applied method is criterion of dam collapse. As very important, it has been supposed that a numerical divergence coincide to physical instability. This taken into account, criterion of dam collapse depends on applied numerical method, on control of numerical process and on a selection of tolerance parameters.

Integral stability criterion for the complete structure has been adopted and expressed through one number. Safety factor is defined as the multiplication coefficient for nominal load with which a balance of inner energy can still be achieved. If load is further increased, procedure diverge; Divac et al. (1996), Divac et al. (1998).

With regards to previous, the following procedure of calculations is applied.

Initial stress field within a rock mass (that exists in a nature before dam building) and a field of initial plastic hardening are modeled by stress-strain analysis.

Dam building and accumulation formation, from stress-strain aspect, is equivalent to application of primary load, that is, of water pressure to dam and application of filtration forces due to underground water flow (with its dead weight). Stress and strain fields that correspond to exploitation conditions are then obtained.

After reaching exploitation condition, primary load incrementally increases (dead weight, water pressure and filtration forces) until the appearance of numerical divergence. Integral safety factor of the complete structure is defined here in two ways.

In the first case, safety factor is determined with regards to water pressure on dam and to filtration forces. After determining the initial stress field (from the dead weight load only), pressure and filtration

forces are increased linearly until the dead weight load is constant.

In the second case, safety factor is determined with regards to all loads at the same time (dead weight, hydrostatic water pressure and filtration forces). After determining initial stresses (step 1) and achieving nominal values for pressure and filtration forces (step 2), all loads are increased linearly.

7 THE RESULTS OF FILTRATION

The 3D sections and views are selected to describe filtration analysis around the dam and through surrounding rock mass. They show fields of potential,

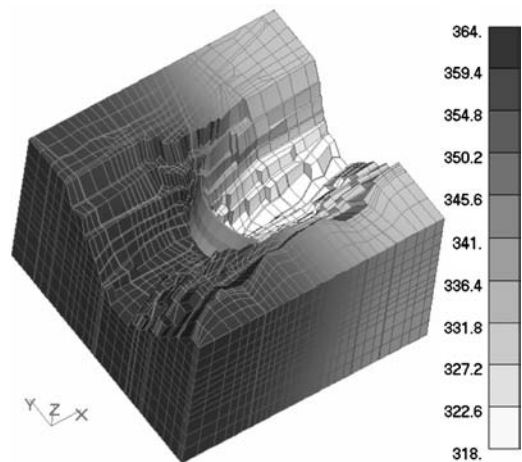


Figure 2. Field of potential ($k_{curtain} = 1 Lu$).

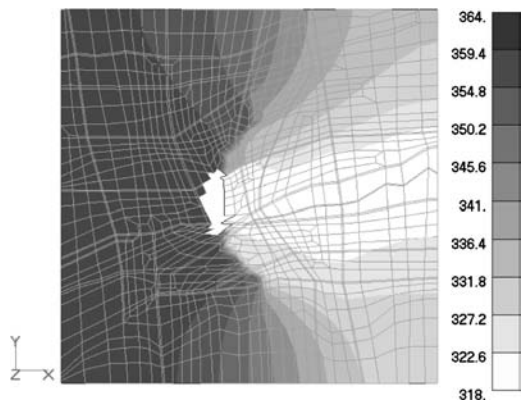


Figure 3. Isolines of potential ($k_{curtain} = 1 Lu$) on 320 m level.

velocity and gradients. Analyses are performed in order to identify the influence of injection curtain water permeability. The total flow dependence of the filtration coefficient for injection curtain is determined.

The results of analyses of filtration for curtain ($k_{curtain} = 1 \text{ Lu}$) are shown on Figures 2–5 (field of potential, velocities and gradients).

The flow dependence of the filtration coefficient around dam and through the surrounding rock mass ranges from 33 l/s (for cases without curtain) to 7.3 l/s (for case with curtain of 1 Lu).

8 THE RESULTS OF STABILITY ANALYSIS

The calculation of the stress field is firstly done, where the load of the dead weigh of soil and dam is used.

Safety factor of the whole structure for the first criterion (Fig. 6) is 4. With further load increase non-stability occurred. Field of stress, in this case, is shown on Figure 6, and field of total displacement on Figure 7.

Safety factor of the whole structure for second criterion (Fig. 8) is 2. With further load increase non-stability occurred. Field of stress, in this case, is shown on Figure 8 and field of displacement in x direction (direction of river flow) on Figure 9.

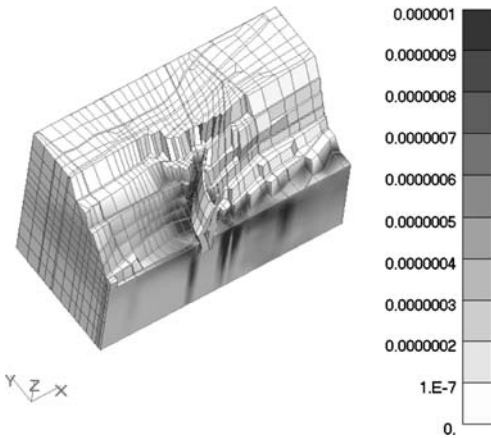


Figure 4. Field of velocity (vertical section, decreased 1.3 times in palette).

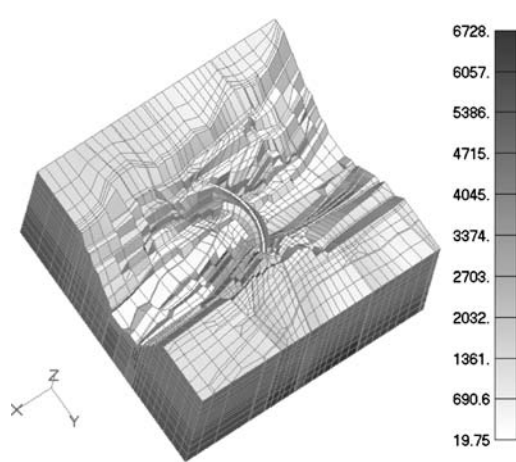


Figure 6. Field of effective stress at the moment of the crash of structure (case 1).

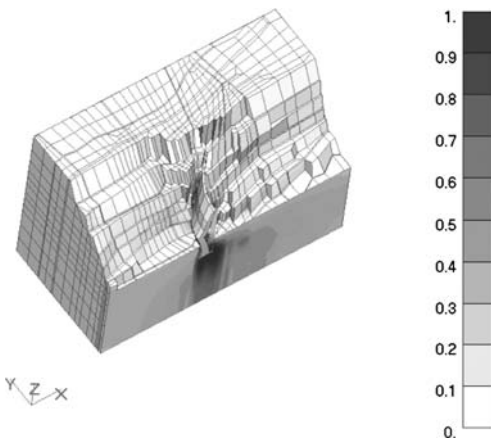


Figure 5. Field of gradient (vertical section, decreased 8 times in palette).

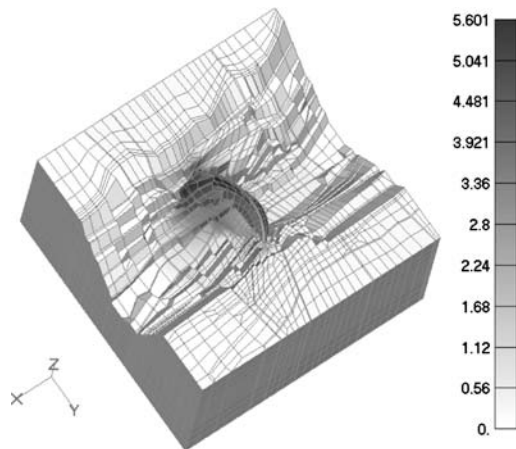


Figure 7. Field of total displacement at the moment of the crash of structure (case 1).

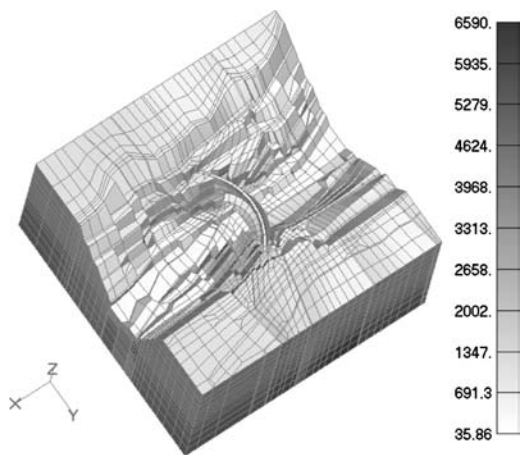


Figure 8. Field of effective stress at the moment of the crash of structure (case 2).

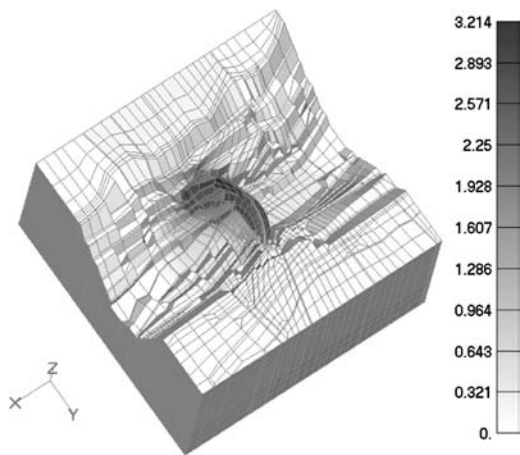


Figure 9. Field of x displacement at the moment of the crash of structure (case 2).

The following fact should be noted. If all loads (dead weight, water pressure and filtration forces) are multiplied, safety factor has less value in comparison to the case with permanent dead weight. Regarding the biggest deformations upstream on the left side of dam, safety of a new structure (dam with rock mass) probably is not less than safety of existing structure (rock mass in natural canyon).

The results show that the global structure stability is satisfied, i.e. building of the dam and forming of the accumulation HEC “St. Petka” do not violate the existing natural balance. A precise inspection is done by using detailed calculations with analysis of potential unstable zones.

9 CONCLUSION

The complex modeling methodology is applied for interaction between underground water flow and stress-strain process that occur due to formulation of dam and accumulation in naturally stressed structure.

More realistic image of structure behavior is gained by creating this model. Rationalization and improved safety can be achieved by application of these modeling results.

Applied methodology gives a very good assessment of global safety of structure, but also make it possible to locate critical zones regarding static and filtration stability.

Based on achieved results it can be concluded that design solutions of dam “St. Petka” have required safety.

Considering significant potential of applied methodology, its generalization and application for different structures is possible. Additionally, more information should be collected through the inspection work and observation.

REFERENCES

- Desai C.S. 1984. Free surface flow through porous media using a residual procedure, in *Finite Elements in Fluids*. Gallagher R.H., Oden J.T., Zienkiewicz O.C., Kawai T., Kawahara M., (eds.), John Wiley & Sons. Vol. 5, Ch. 18, pp. 377–392.
- Desai C.S. & Siriwardane H.J. 1984. *Constitutive laws for engineering materials – with emphases on geologic materials*, Prentice-Hall. Inc., Englewood Cliffs. New Jersey.
- Divac D., Vuckovic D., Masala S. & Denic D. 1996. A new method of modeling subsidence above underground mining excavation. *News Journal, JERM*.
- Divac D., Vuckovic D., Zivkovic M. & Grujovic N. 1998. Numerical modeling of rock mass stress strain changes caused by underground excavation in the Bor copper mine. *4th Eur. conference on numerical methods in geotechnical engineering*, Udine, Italy.
- Kojic M. 1997. *Computational procedures in inelastic analyses of solids and structures*, Center of Scientific Research of Serbian Academy of Sciences and Arts and University of Kragujevac and Faculty of Mechanical Engineering in Kragujevac, Kragujevac.
- Kojic M., Slavkovic R., Zivkovic M. & Grujovic N. **PAK**–Finite element program for static and dynamic nonlinear analysis and heat transfer, Faculty of Mechanical Engineering in Kragujevac, Kragujevac.
- Majewski S. 1997. Elasto-Plastic Model with Isotropic Hardening/Softening Rule for Cohesive-Frictional Materials, *Computational Plasticity, Fundamentals and Applications*, edited by Owen D.R.J., Onate E., Hinton E., CIMNE, Barcelona.
- Kojic M. & Bathe K.J. 2005. *Inelastic of Solid and Structures*, Springer Berlin, Heidelberg New York.

Study on the rheological property of rockfill and its influence on deformation and stress in concrete face rockfill dams

W. Cen & Y. Zhu

Institute of Hydrostructure Engineering, Hohai University, Nanjing, P.R. China

G. Heigerth

Institute of Hydraulic Structures and Water Resources Management, Graz University of Technology, Austria

ABSTRACT: In this paper, the influence of the rheological property of rockfill materials on the stress and deformation behavior within a concrete face rockfill dam (CFRD) is numerically studied using 3-D finite element calculations. Shear rheology and volumetric rheology is taken into account based on the three parameter model given by Shen. The mechanical behavior of the seal strips located between the concrete slabs is modelled with a 3-D connection element by Gu. The results obtained from the numerical calculations show that the rheology of rockfill has a strong influence on the deformation of the rockfill body, the stress state of the concrete slabs and the spatial deformation of the joints. In the present study the rheological component occupies about 20 percent of the total deformation in the dam body.

1 INTRODUCTION

A lot of CFRD's are in operation world wide, as is known. Several dams show relatively high deformations, non-elastic and without any later increase of load. These obviously rheological deformations depend on particle-size and mineralogic type of the rock blocks. They are multiple higher than elastic and creeping deformations of the concrete face and therefore at some dams cause cracks. One typical example observed in detail is Lesu CFRD in Romania (Fu & Feng 1993). At this about 60 m high dam after 2 years of operation the sealing in peripheral joints were destroyed because of large relative deformation between face slab blocks the abutment, with growing leakage; 2 years later some big cracks appeared.

These deformations only could be explained by a statical model including rheological behavior of the rockfill body. This example suggests, that main mechanical properties should include rheological behavior beside of nonlinearity, dilatation and so on.

Although it is difficult to study the rheology of rockfill theoretically, many scientists and engineers were interested in these topics in the past several decades. Wahls (1962) studied the creep of rockfill in the oedometer test. Parkin (1985, 1991) also made rheological tests using oedometers and found the rheological rate in linear relationship with the logarithm

of time. Shen (1991) made rheological test of rockfill in the triaxial apparatus and found that the rheological effect would decrease over time and at last reach a steady value. Based on the test data, he put forward a 3-parameter rheological model, widely used in the numerical calculation. Li (2004) also executed a similar test in a large triaxial apparatus.

First, this paper is orientated to analyze the rheological behavior and rheological theory of rockfill in the aspect of particle components, gradation state, degree of density, particle breaking, rain infiltration and so on. Because of defining the components share, this is a difficult and critical task.

Further on modeling approaches are studied in detail.

Finally, the deformation and stress of a high CFRD is numerically studied using 3-D FEM; the results are discussed.

2 RHEOLOGICAL THEORY OF ROCKFILL AND FACTORS OF INFLUENCE

Rockfill is obviously different from soil in aspect of particle size and particle contacts, with a different theory of rheological behavior. The rheological deformation is caused by shifting, breaking and rearrangement of particles, as rotation and dislocation, under

high contact stress and influenced by rain infiltration causing "wet" deformation and so on.

These effects of high contact stresses decrease during time and gradually tend to a relative steady state.

Physical property of rock, available as natural or broken blocks, has an important effect. The softer the rock, the higher is rheological deformation. It obviously depends on stress level, particle size distribution, degree of density, share of broken particles. Particle breaking under external load results in additional deformation, when broken particles can fill in existing interspaces. Breaking or crushing easier appears at sharp - angled particles.

Experience at many CFRD's shows that settlement velocity increases during heavy rainfall, as monsoon, because of higher lubrication and therefore lower friction. This effect can create macroscopic values.

General there are two main approaches to the macroscopic rheology behavior for geotechnical materials:

One is the direct application of ideal rheological models, consisting of reasonable rheological components.

There are two types of an ideal rheological model, the differential model and the integral model. The differential model is deduced from the comparison of mechanical behavior with some rheological components, with the basic equation in differential form, which can be deduced easily. Some models are often used such as Maxwell, Voigt, Kelvin, Merchant, Schiffman so on. Because of the complexity of rheology and the special applicability, the selection of model should be combined with the macroscopic behavior.

Rheological integral model can consider the construction progress of dam body. According to the Boltzmann superposition principle, the strain of dam body under the load at different time results in

$$\varepsilon = \int_{-\infty}^t \left(\frac{\partial \varepsilon}{\partial t} dt + \frac{\partial \varepsilon}{\partial \sigma} d\sigma \right)$$

It indicates the creep effect and the stress relaxation of rockfill. The integrand can be derived from tests. The rheological properties can be reflected by the integrand which is a function of time and stress state. The rheological integral models are not widely applied at present, because they need complicated mathematical calculation and it is difficult to get the basic parameter values.

The other investigation approach is utilizing the test data in laboratory or in situ. According to tests, the rheological graph can be defined. Then the experimental formula can be deduced by using functions corresponding with reasonable assumptions. Some appropriate existing rheological models can also be used by analogy based on the foregoing rheological graph. These types of model can reflect the true change

character of rheological deformation using reasonable mathematic functions.

3 CONSTITUTIVE MODELING FOR RHEOLOGY OF ROCKFILL MATERIAL

Figure 1 shows creep curves of the dry Xibeikou rockfill material for different stress levels obtained from triaxial laboratory tests carried out by Shen & Zuo (1991). The axial creep strain will attenuate in several hours and it tends towards a steady value called ultra rheological value. Besides, some actual monitoring data of CFRDs also indicate that the rheological deformation will weaken and reach a steady value in several years (Shen & hao 1998).

Shen (1994) assumed that the evolution of creep strain can be described by the following attenuation exponential function, i.e.

$$\varepsilon_t = \varepsilon_f (1 - e^{-ct}) \quad (1)$$

The time derivative of Eq.(1) leads for the strain rate to the relation:

$$\dot{\varepsilon}_t = c\varepsilon_f e^{-ct} = c(\varepsilon_f - \varepsilon_t), \quad (2)$$

where ε_f denotes the ultra rheological value at time $t = \infty$, c is defined as the ratio of the strain rate at $t = 0$ and the ultra rheological value, and ε_t denotes the rheological value at time t , which can be approximated by the summation over the increments, $\dot{\varepsilon}_t \Delta t$, i.e.

$$\varepsilon_t = \sum \dot{\varepsilon}_t \Delta t \quad (3)$$

In order to distinguish between the volumetric rheology and the shear rheology Shen (1994) proposed the following formulas to model the influence of the stress

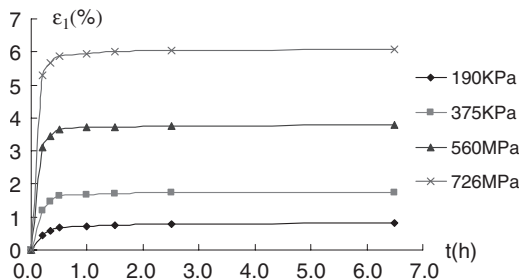


Figure 1. Rheological curves of Xibeikou rockfill (Shen & Zuo, 1991).

state on the ultra shear rheology ε_{vf} and on the ultra volumetric rheology ε_{sf} :

$$\varepsilon_{vf} = b \frac{\sigma_3}{P_a}, \quad (4)$$

$$\varepsilon_{sf} = d \frac{S_t}{1-S_t}. \quad (5)$$

where ε_{vf} denotes the ultra volumetric rheological value, ε_{sf} is the ultra shear rheological value, σ_3 is the confining pressure, P_a the atmospheric pressure, the dimensionless quantity S_t is defined as the ratio of the deviator stress at time t and the deviator stress at the failure, and b and d are dimensionless material constants. In particular b means the ultra volumetric rheological value for $\sigma_3 = P_a$ and d means the ultra shear rheological value when $S_t = 0.5$. The values of parameter b and d can be calibrated based on the data of triaxial creep tests.

It is assumed that volumetric rheology and shear rheology can both be depicted by formula (2). Then the rate of volumetric rheology $\dot{\varepsilon}_v$ and shear rheology $\dot{\varepsilon}_s$ read:

$$\dot{\varepsilon}_v = c\varepsilon_{vf}e^{-ct}, \quad (6)$$

and

$$\dot{\varepsilon}_s = c\varepsilon_{sf}e^{-ct}. \quad (7)$$

With respect of Eq. (4) and Eq. (5) the volumetric strain rate $\dot{\varepsilon}_v$ is higher for a higher confining pressure and the shear strain rate $\dot{\varepsilon}_s$ is higher for a higher deviatoric stress. The magnitude of both quantities decreases with an increase of the time t . According to the Prandtl-Reuss flow rule, the resulting rheological strain tensor $\dot{\varepsilon}$ can be expressed as:

$$\dot{\varepsilon} = \frac{1}{3}\dot{\varepsilon}_v\mathbf{I} + \frac{\dot{\varepsilon}_s}{2q}\mathbf{s} \quad (8)$$

where \mathbf{s} denotes the deviator stress tensor, \mathbf{I} is the unit tensor and q denotes the general shear stress. Based on the model by Shen typical rheological parameter values for different types of rockfill materials are listed in Table 1.

Table 1. Rheological parameters of Shen's model for different rockfill material (Shen & Zhao, 1998).

Parameters	Mud shale (soft)	Limestone (middle)	Granite (hard)	Sand (pebble)
c	0.005	0.007	0.007	0.007
b	0.0012	0.0004	0.0003	0.0002
d	0.008	0.006	0.004	0.003

4 FE MODEL AND MATERIAL PARAMETERS

For the numerical simulation a CFRD with a maximum height of 168 m is considered. The dam body is decomposed of the main rockfill, the minor rockfill, the transition layer, the cushion layer and the concrete slab layer. The conformation of the dam body in the maximum cross section is outlined in Figure 2. The ratio of upstream and downstream slope is for both 1:1.4. The design upstream water level is 285.6 m. There are 23 sections and 22 columns of slab joints in the direction of the dam axis.

Figure 3 shows the FE-mesh of the CFRD. There are 4546 nodes and 3306 elements including 139 elements for slab blocks, 139 contact elements and 152 connection elements for joints. 3-D isoparametric elements each with 8 nodes or 6 nodes are used for the rockfill and concrete material. The nodes at bottom and abutment of the dam are fixed for both rockfill material and concrete toe slabs.

For the instantaneous deformation, the Duncan E - B model is used (Duncan 1980). The two main elastic quantities E_t and B_t of the model are defined as:

$$E_t = KP_a \left(\frac{\sigma_3}{P_a}\right)^n (1-R_f) \cdot \frac{(1-\sin\varphi)(\sigma_1-\sigma_3)}{2c\cos\varphi+2\sigma_3\sin\varphi}^2 \quad (9)$$

$$B_t = K_b P_a \left(\frac{\sigma_3}{P_a}\right)^m \quad (10)$$

Where E_t denotes the tangent modulus, B_t is the bulk modulus, K and K_b are modulus numbers, n and m are modulus exponents, φ is the friction angle, which is calculated according to the formula:

$$\varphi = \varphi_0 - \Delta\varphi \lg(\sigma_3/P_a),$$

where φ_0 denotes the value of φ for $\sigma_3 = P_a$, the value $\Delta\varphi$ reflects the relationship between φ and σ_3 , c is the cohesion, R_f is the failure ratio, P_a is the atmospheric pressure and σ_1 and σ_3 are the maximum and minimum principal stress, respectively.

For constitutive modeling the rheological properties, Shen's 3-parameter rheological model outlined in the forgoing section is used. The relevant values of

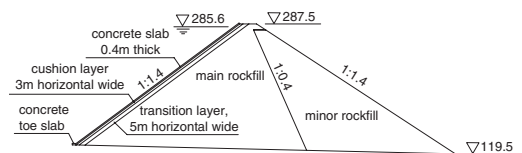


Figure 2. Maximum cross section of the dam.

the constitutive parameters for the Duncan E-B model and Shen's model used in the present calculation are listed in Table 2.

For the concrete slab, a linear elastic material behavior with $\gamma = 24.5 \text{ kN/m}^3$, $E = 2.1 \times 10^7 \text{ kPa}$, and $\mu = 0.167$ is taken into account. So-called Goodman elements (Goodman et al. 1968) are used to simulate the contact property between the concrete slabs and the cushion layer of the rockfill material. The tangent stiffness number K_{st} of the Goodman element is calculated by the following formula.

$$K_{st} = K_I \gamma_w \left(\frac{\sigma_n}{P_a} \right)^n \left(1 - R_f \frac{\tau}{\sigma_n \tan \delta} \right)^2, \quad (11)$$

where K_I denote the modulus number, n is the modulus exponent, δ is the friction angle at interface, γ_w is the bulk weight of water, σ_n is the normal stress at

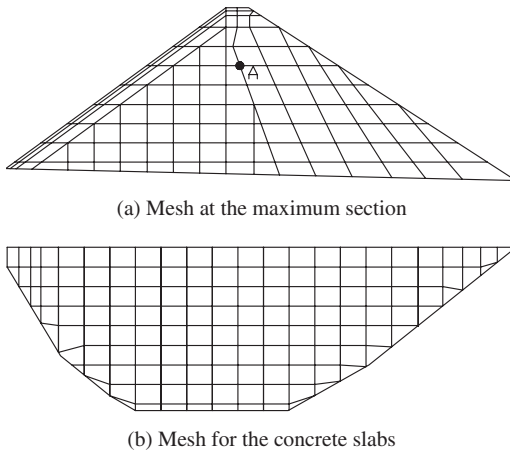


Figure 3. FE-mesh of the CFRD.

interface τ is the shear stress at the interface and R_f denotes the failure ratio. The involved parameters can be calibrated based on the data obtained from direct shear tests. For the present numerical calculations the following values are used: $K_I = 4800$, $n = 0.56$, $R_f = 0.74$ and $\delta = 36.6^\circ$.

In order to model the mechanical behavior of seal strips in joints between the concrete slabs a special connection element is applied. In particular the 3-D connection element by Gu (1989) is used which has 8 nodes and an initially zero thickness as shown in Figure 4. The element can simulate relative displacements of the neighboring concrete blocks in all three directions. It can transmit normal forces and shear forces, but no bending moments. For the design of the present CFRD seal strips made of copper are considered. In the peripheral joints also seal strips made of synthetic material are added. The mechanical property for these two materials and the calibration of the parameters needed for the connection elements is outlined in more details by Cen (2005).

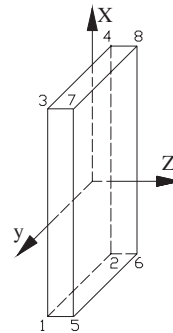


Figure 4. Sketch of the connection element.

Table 2. Values of constitutive parameters for different parts of the rockfill dam body.

Model	Parameters	Cushion layer	Transition layer	Main rockfill	Minor rockfill
Duncan E-B model	$\gamma/\text{KN/m}^3$	23.2	23.0	22.3	22.0
	c	0.0	0.0	0.0	0.0
	$\varphi_0/^\circ$	53	52	51	50
	$\Delta\varphi/^\circ$	9.5	10.0	8.5	9.1
	K	1000	900	800	750
	n	0.48	0.45	0.35	0.38
	R_f	0.82	0.79	0.78	0.76
	K_b	750	600	550	500
	m	0.20	0.15	0.13	0.11
	Shen's model	c	0.005	0.005	0.005
b		0.003	0.002	0.002	0.005
d		0.003	0.004	0.003	0.004

5 NUMERICAL RESULTS

In this paper the results obtained for the numerical simulation of two case studies are compared and discussed: Case 1 considers only instantaneous deformation without rheological effects. Case 2 takes into account not only instantaneous deformation but also rheological deformation during reservoir impounding. Only two loads, gravity of materials and water pressure acting on the concrete face slab, are considered in the present calculation. In Case 2, the water impounding to the design level lasted 8 months. In the numerical calculation, the construction of dam body and impounding process of water are simulated according the construction and operation plans given by the designer.

5.1 Influence of rheology of rockfill on the deformation of rockfill dam body

A comparison of the calculated deformations for Case 1 and Case 2 is shown in Table 3, Figure 5 and Figure 6. In particular Figure 5 represents isoline of the horizontal displacements and Figure 6 represents isoline of the vertical settlements of the dam body at design water level for both cases.

Table 3. The maximum deformation values of dam body at design water level (unit: cm).

Case	Horizontal displacement towards upstream	Horizontal displacement towards downstream	Settlement
Case 1	14.8	40.1	93.8
Case 2	10.9	48.7	108.6

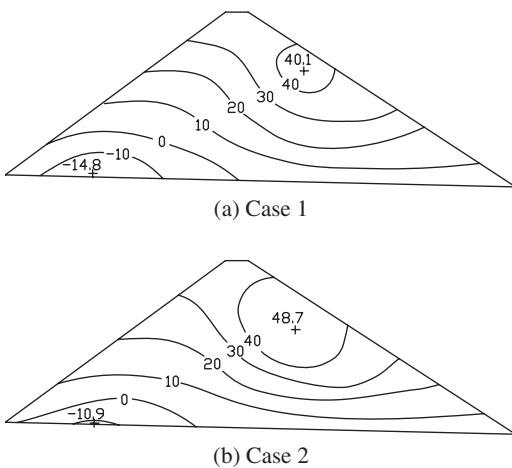


Figure 5. Horizontal displacement distribution of dam body at design water level (unit: cm).

Taking the rheological deformation into account, the deformation of rockfill dam body of Case 2 continues to develop comparing with that of Case 1. Because of rheology, the additional increment of settlement is 15.8 percent of the total settlement of Case 1 and 0.09 percent of the height of dam. The value of rheological deformation in the minor rockfill zone near downstream is bigger than that of other zones because the minor rockfill is softer than the rockfill of the other zones (Figure 6). Figure 7 shows the settlement of point A of the dam body (marked in Figure 3a) during the operation stage of the dam. The velocity of settlements increases within the first two years and then it decreases and dent to zero. In particular the value of the rheological settlement in the first two years of operation stage occupies about 85 percent of the ultra value of rheological settlement in the steady state.

5.2 Influence of rheology of rockfill on the deformation and stress of concrete slabs

Owing to the rheological behavior of rockfill, the dam body shows higher vertical and horizontal deformation towards the center of the valley. The deformation of the rockfill body leads to displacements of concrete slabs towards the center of the dam face both

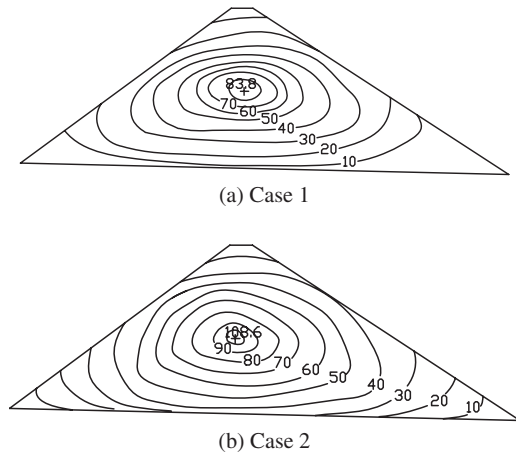


Figure 6. Settlement distribution of dam body at design water level (unit: cm).

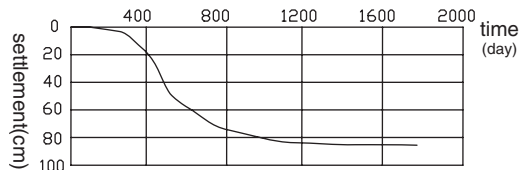
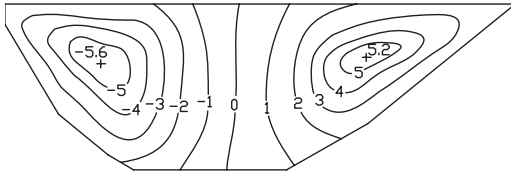
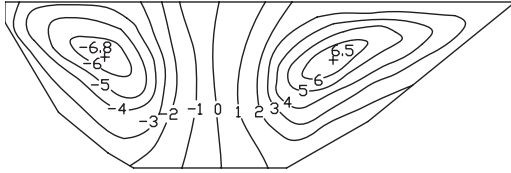


Figure 7. Settlement process of point A (unit: cm).

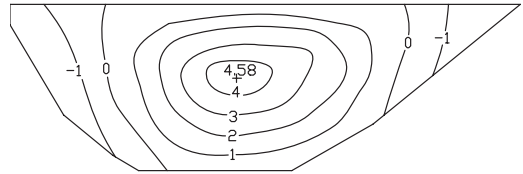


(a) Case 1

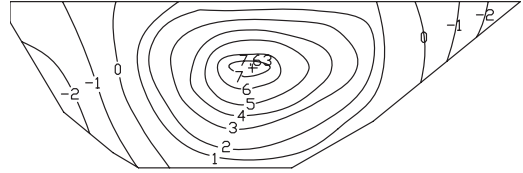


(b) Case 2

Figure 8. Displacement distribution of concrete slabs in the dam axial direction (unit: cm).



(a) Case 1



(b) Case 2

Figure 9. Stress distribution of concrete slabs in the dam axial direction (unit: MPa).

Table 4. The maximum values of stress of concrete slab at design water level (unit: MPa).

Case	In dam slope direction		In dam axial direction	
	Tension stress	Compression stress	Tension stress	Compression stress
Case 1	1.86	5.62	1.95	4.58
Case 2	1.04	8.26	2.48	7.63

in the slope direction and in the axial direction of the dam. Figure 8 presents the displacement isolines of concrete slabs in the axial direction of the dam for two different cases.

A comparison of the maximum values of tension and compress stress in the concrete slab in the slope direction and in the axial direction of the dam at design water level is given in Table 4.

Figure 9 shows the stress isolines of concrete slabs in the axial direction of the dam. Taking rheology of rockfill into account, the maximum value of compression stress of concrete slabs located in the middle area increases from 4.58 MPa to 7.63 MPa and the maximum value of tension stress of concrete slabs located near dam abutment increases from 1.95 MPa to 2.48 MPa.

5.3 Influence of rheology of rockfill on the deformation of joints

The numerical results show that the concrete slabs are mainly in a compression state with the exception of some slab joints near the dam abutment for the above two cases. When the rheology of rockfill is included,

the compression of the central slab joints become bigger and the values of extension of the abutment slab joints turn smaller. The deformation character of slab joints accords with the axial deformation behavior of slab blocks. Besides, the influence of the rheology of the rockfill material makes the shear deformation of peripheral joints larger and also has an effect on the compression or extension deformations of peripheral joints. Taking into account the rheology of rockfill materials, the concrete slabs will move towards the center of the valley in horizontal direction and also move to the lower altitude. Therefore, the interspaces between the upper concrete slabs and the toe slabs will become smaller.

6 CONCLUSIONS

The rheology of rockfill materials can show a strong influence on the long time deformation of the dam body, the stress changes in concrete slabs and the evolution of stress and deformation in individual joints between the concrete slabs. This is demonstrated in the present paper for a CFRD 168 m high using a 3-D finite element calculation. The mechanical behavior of different rockfill materials is modeled based on the Duncan E-B model and Shen's 3-parameter rheological law. The coupling of the individual concrete slabs with seal strips is simulated with a special connection element proposed by Gu. Goodman elements are used to model the interface behavior between the concrete slabs and the cushion layer of the rockfill dam. Two case studies are investigated: the case of instantaneous deformation without rheological effects and the case of instantaneous deformation and rheological

deformation during reservoir impounding. The results obtained from the numerical simulations show that the compression of concrete slabs increases and the stress of slabs under tension decreases in the slope direction when the rheology properties of the rockfill material is taken into account. In the axial direction of the dam, however, the values of the compression stresses and tension stresses in concrete slabs are enlarged in the middle area and in the abutment area. The joint compression increases in the middle area while an extension of joints in the abutment domain is obtained. Shear deformations become large in peripheral joints. These conclusions can be very useful for the design, the construction and the monitoring concept of concrete face rockfill dams.

ACKNOWLEDGMENTS

Support from the Ministry for Science and Technology in China and the Federal Ministry of Education, Science and Culture in Austria for the bilateral scientific technological co-operation between Hohai University in Nanjing and Graz University of Technology in Graz is greatly acknowledged.

REFERENCES

- Cen W., 2005. Hypoplastic modeling for rockfill and numerical analysis of CFRD. *Ph. D. Thesis*, Hohai University, Nanjing, China (in Chinese).
- Duncan J.M., 1980. Strength, stress-strain and bulk modulus parameters for finite element analysis of stresses and movements in soil masses, In *Report NO. UCB.G.T.80-01*, University of California, Berkeley, USA.
- Fu Z. & Feng J., 1993. Concrete face rockfill dam. *Press of Huazhong university of technology* 146.
- Goodman R.E., Taylor R.L. & Brecke T.L., 1968. A model for the mechanics of jointed rock. *Journal of Soil Mechanics And Foundation Division. ASCE* 94(3): 637–659.
- Gu G., 1989. Earthquake engineering of earth-rockfill dam. *Press of Hohai university of technology* 176.
- Li G., Mi Z., Hu H. & Fang W., 2004. Experimental studies on rheological behaviors for rockfills in concrete faced rockfill dam. *Rock and soil mechanics*. 25(11): 1712–1716.
- Parkin A.K., 1985. Settlement rate behavior of some fill dams in Australia. In *Proceedings of 11th ICSMFE*, San Fransisco, USA: 2007–2010.
- Parkin A.K., 1991. Creep of Rockfill. In Maranhadas Neves E. (eds), *Advances in Rockfill Structure*: 221–237. Dordrecht Boston London: Kluwer Academic Publishers.
- Shen Z., 1994. Rheological model of earth and rockfill and its application. *Journal of hydroscience and engineering* 4: 335–342.
- Shen Z. & Zhao K., 1998. Back analysis of rheological deformation of CFRD. *Journal of hydraulic engineering* 6: 1–6.
- Shen Z. & Zuo Y., 1991. Study on the rheological test of rockfill. In *The 6th proceeding of soil mechanics and foundation engineering*. Press of Tongji University.
- Wahls H.E., 1962. Analysis of primary and secondary consolidation. *Journal of Soil Mech. Found. Div.* 88(6): 207–231.
- Wiltshire R.L., 2002. Reclamation's 100 Years of Embankment Dam Design and Construction *Water Resources and Invironmental History 2004, EWRI Annual Meeting 2004*.

Sensitivity analysis to examine tree root effectiveness in soft ground stabilisation

B. Indraratna & B. Fatahi

Civil Engineering, Faculty of Engineering, University of Wollongong, NSW, Australia

ABSTRACT: Native vegetation in Australia is becoming increasingly popular for stabilising railway corridors built over soft soils. A model previously developed to measure the rate of tree root water uptake and a computer model are used to investigate the effect of a wide range of soil, tree, and atmospheric parameters on partially saturated ground. First, sensitivity analysis is used to investigate the affect of different parameters on the maximum initial rate of root water uptake, and then a reference example is simulated using finite element analysis. The influence of parameters such as time, potential transpiration rate and its distribution factor, wilting point suction, the coefficient of permeability, and the distribution of root length density are studied. Soil suction and settlement was found to increase over time, with the effect being more significant in the first stages of transpiration. The most sensitive parameters are wilting point suction, the coefficient of saturation permeability at higher values, the rate of potential transpiration at lower values, and vertical root distribution when the coefficient is high.

1 INTRODUCTION

Throughout the world soil conditions on construction sites have become worse than ever due to the overpopulation in the metropolitan areas. These conditions have compelled engineers to construct earth structures, major highways, and railways over expansive clays and compressive clay deposits. According to Nelson and Miller (1992), expansion and shrinkage are the result of changes in the soil water system that disturb the internal stress equilibrium. If the soil water chemistry alters either by changes to the volume of water or chemical composition, the inter-particle force field will change. If this resulting change in internal forces is not balanced by a corresponding change in the externally applied state of stress, the particle spacing will change to adjust the inter-particle forces until equilibrium is reached. This change in particle spacing manifests itself as shrinkage or swelling. Retarding evaporation, heavy rainfall, and growth of trees and shrubs are the most important factors which result in a noticeable change in the ground moisture. Trees, shrubs, and grasses deplete moisture from the soil through transpiration.

An increase in the cost of common ground modification methods has definitely contributed to new methods of treatment. More recently, native vegetation as a

ground improvement tool has received the attention of many geotechnical engineers. For example, using native vegetation in coastal regions of Australia to stabilise railway corridors built over expansive clays and compressive soft soils has become increasingly popular. New maintenance observations show that where there are trees beside railway tracks, their localised, undrained failure is minimized (Figure 1). Properly selected and implemented vegetation, including native trees and shrubs, can reduce soil moisture by root water



Figure 1. Black Box tree beside rail track, Miram, Australia.

uptake. Moreover, vegetation can increase the shear strength and stiffness of soil by increasing matric suction and control erosion as a secondary effect.

When modelling the vadose zone influenced by vegetation, a detailed consideration of root water uptake is required. Existing models only consider the affect of root reinforcement or a very simplified model for tree root water uptake. For example, Fredlund and Hung (2001) did not consider the realistic root zone and assumed that the root water uptake rate is time independent, which is unrealistic.

As Indraratna et al. (2006) concluded, uncertainties in the assumption of soil parameters, tree root distribution and atmospheric parameters, cause most discrepancies in these predictions. Therefore, the effects of different parameters on the initial rate of root water uptake are investigated in this paper. Then, using finite element analysis, a sensitivity analysis is carried out to study the influence of different model parameters on the ground. The main objective of this study is to identify and evaluate important variables that affect ground under transpiration.

2 CONCEPTUAL DEVELOPMENT

Previous study by Indraratna et al. (2006) attempted to develop a mathematical model for the distribution of water uptake within the root zone. This proposed model combines soil matric suction, root density and potential transpiration. Accordingly, an exceptional mathematical model is developed,

$$S(x, y, z, t) = f(\psi) \cdot G(\beta) \cdot F(T_p) \quad (1)$$

where, $G(\beta)$ is the root density factor, $f(\psi)$ is the soil suction factor, and $F(T_p)$ is the potential transpiration factor. The most appropriate formula for $f(\psi)$ is that suggested by Feddes et al. (1978).

$$\left\{ \begin{array}{ll} f(\psi) = 0 & \psi < \psi_{an} \\ f(\psi) = 1 & \psi_{an} \leq \psi < \psi_d \\ f(\psi) = \frac{\psi_w - \psi}{\psi_w - \psi_d} & \psi_d \leq \psi < \psi_w \\ f(\psi) = 0 & \psi_w \leq \psi \end{array} \right. \quad (2)$$

where, ψ_w is the soil suction at wilting point, the suction limit at which a particular vegetation is unable to draw moisture from the soil, ψ_d is the highest value of ψ and ψ_{an} (soil suction at anaerobiosis point) is the lowest value of ψ at $S = RWU_{max}$, where RWU_{max} is the maximum rate of root water uptake.

The following two equations are suggested by Indraratna et al. (2006) for the root density factor and the potential transpiration factor, respectively,

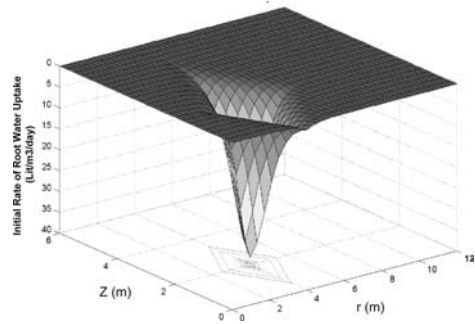


Figure 2. Initial distribution of root water uptake rate.

$$G(\beta) = \frac{\tanh(k_3 \beta_{max} e^{-k_1|z-z_0|-k_2|r-r_0|})}{\int_{V(t)} \tanh(k_3 \beta_{max} e^{-k_1|z-z_0|-k_2|r-r_0|}) dV} \quad (3)$$

$$F(T_p) = \frac{T_p(1 + k_4 z_{max} - k_4 z)}{\int_{V(t)} G(\beta)(1 + k_4 z_{max} - k_4 z) dV} \quad (4)$$

where k_1 and k_2 are two empirical coefficients depending on the tree root system and type, k_3 is an experimental coefficient, z is vertical coordinate (downward is positive), r is radial coordinate, β_{max} is the maximum root length density which is located at the point $(r, z) = (r_0, z_0)$, T_p is the rate of potential transpiration, k_4 is an experimental coefficient to involve the effect of depth on the potential transpiration distribution, and $V(t)$ is the root zone volume at time t .

Figure 2 shows an example of the distribution of initial rate of root water uptake used in the finite element analysis in next section.

The soil water flow differential equation, including the sink term, $S(x, y, z, t)$, can be written as:

$$\frac{\partial \theta}{\partial t} = \nabla \cdot (k \nabla \psi) - \frac{\partial k}{\partial z} - S(x, y, z, t) \quad (5)$$

where, $\theta (= V_w/V)$ is the volumetric moisture content, ($V_w =$ volume of water, $V =$ total volume), ∇ is the divergence vector, Ψ is the soil suction, k is the hydraulic conductivity and z is the vertical coordinate (downward is positive).

3 PARAMETRIC STUDY OF RWU_{MAX}

The sensitivity of RWU_{max} with respect to the various parameters can be investigated using a sensitivity index defined by:

$$(I_S)_i = \frac{\frac{\partial RWU_{max}}{\partial u_i}}{RWU_{max}} \cdot u_i \quad (6)$$

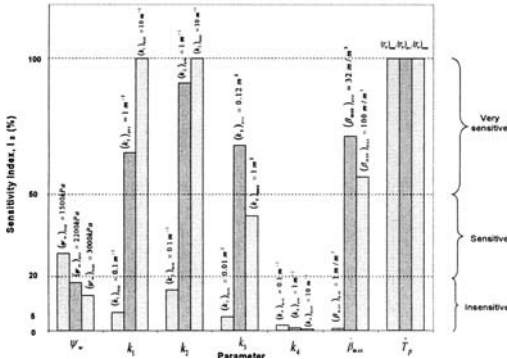


Figure 3. Results of the sensitivity analysis for RWUmax.

where, $(I_s)_i$ is the sensitivity index of i th parameter, RWU_{\max} is the maximum rate of root water uptake, and u_i is the variable which affect the rate of root water uptake.

Based on the sensitivity index, parameters can be categorised as follows:

$$\begin{cases} 0\% < I_S < 20\% & \text{Insensitive} \\ 20\% \leq I_S < 50\% & \text{Sensitive} \\ 50 \leq I_S & \text{Very sensitive} \end{cases} \quad (7)$$

Figure 3 shows the results of the sensitivity analysis. The sensitivity of parameters are examined at the maximum, minimum, and average values of each variable.

It should be noted that they are related to the assumed range and initial values of parameters. Consequently the indices can be influenced by the magnitude and range of the variables.

4 NUMERICAL IMPLEMENTATION

Equation (5) comprises a set of non-linear partial differential equations. As fluid passes through a porous medium, a coupled flow deformation analysis is required to capture the 3-phase interaction between the soil, air, and water. The governing equations for pore fluid diffusion deformation are a combination of Equation (5) and the relevant elasto-plastic deformation equations relevant to the stabilised soil.

The basic theory used to analyse unsaturated soil behaviour is given by Bishop (1959):

$$\sigma'_{ij} = \sigma_{ij} - u_a \delta_{ij} + \chi(u_a - u_w) \delta_{ij} \quad (8)$$

where, σ'_{ij} is the effective stress of a point on a solid skeleton, σ_{ij} is the total stress in the porous medium at the point, u_a is the pore air pressure, u_w is the pore water pressure, δ_{ij} is Kronecker's delta, and χ is the

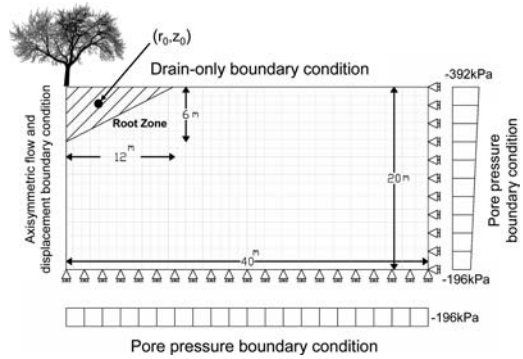


Figure 4. The geometry and boundary conditions of the FE model.

effective stress parameter attaining a value of unity for saturated soils and zero for dry soils.

The finite element method is the most common one for high non-linear flow equations, including the sink term. In this study the non-linear finite element programme ABAQUS has been used to examine the development of soil suction induced by transpiration. The numerical model capturing the authors' root water uptake model is used to describe the parameters representing the soil, tree and atmospheric conditions on ground improvement, with special reference to potential transpiration, root density and permeability.

4.1 Description of reference problem

A two dimensional finite element analysis is used to conduct a sensitivity analysis of the relevant model variables. The finite element mesh and specific boundary conditions are shown in Figure 4. Because of symmetry, a zero flux boundary was applied along the left boundary. Root water uptake was modelled as a moisture flux boundary applied along the top surface of all elements within the root zone. The mesh used in this simulation consists of bi-linear strain quadrilateral element (CPE4P) with 4 displacements, and four pore pressure nodes at the corner of each element. The entire FE mesh consists of 13,041 nodes and 12,800 elements.

The theoretical model representing the rate of root water uptake distribution within the root zone (Eqn. (1)) is used in the FE analysis through a Fortran sub-routine. The coefficient of soil permeability (k) is described using the approach of Brooks and Corey (1964), and the saturated coefficient of permeability is estimated from the well known Kozeny-Carman equation. The soil is assumed to be an over consolidated clay so its consolidation is described by the well known equation:

$$de^{el} = C_s \ln\left(\frac{p_0 + dp}{dp}\right) \quad (9)$$

Table 1. The initial assumed parameter values in the numerical sensitivity analysis.

Parameter	Value	Comments
(r_0, z_0)	(4 m, 2 m)	Corresponding to radial and vertical coordinate of gravity centre of root zone
$\beta_{\max}(t)$	25 m^{-2}	Taken from the general shape suggested by Landsberg (1999)
$k_1 = k_2$	2 m^{-1}	Applied by Knight (1999)
k_3	$8.74 \times 10^{-2} \text{ m}^{-2}$	Taken from the general shape suggested by Landsberg (1999)
k_4	0.014 m^{-1}	Assuming $H_{\text{root}} = -76.5 \text{ m}$ and $R_c = 0.05^*$
(r_{\max}, z_{\max})	(12 m, 6 m)	Root zone boundary
ψ_{an}	4.9 kPa	Feddes et al. (1976), Clay soil and air content of 0.04
ψ_d	40 kPa	Feddes et al. (1976; 1978), $40 < \psi_d < 80 \text{ kPa}$
ψ_w	1500 kPa	Feddes et al. (1976; 1978), $1500 < \psi_w < 2000 \text{ kPa}$
γ_d	18 kN/m^3	Typical earth soil
C_s	0.05	Average value for clay soils in vicinity of building foundations
k_s	$5 \times 10^{-8} \text{ m/s}$	Typical value for clay soils in vicinity of building foundations ($e = 1$)
Passing #200 \times Plasticity Index	20	–
T_p	8 mm/day	Myers and Talsma (1992), Pinus Radiata tree (ACT, Australia)
Initial void ratio (e_0)	1	Typical clay soil

* by comparing Equations (4) and Nimah and Hanks (1973) model, k_4 can be estimated by $k_4 = -(1 + R_c)/H_{\text{root}}$, where H_{root} is the effective water potential in the root at the soil surface where z is considered zero and R_c is the flow coefficient in the plant root system.

where, de^{el} denotes the change of void ratio in the element, C_s is the swelling index, p_0 is the initial mean effective stress, and dp is the mean effective stress change on the soil skeleton. As Figure 2 indicates, the soil water characteristic curve used in this analysis is based on plasticity index as suggested by Zapata et al. (2000).

Only the matric suction component was considered in the numerical model, osmotic suction was not. During the parametric study, one parameter was varied, the others remained at their initial values. The initial values of all parameters are summarised in Table 1. It was assumed that a steady state condition was reached when the rate of change in matric suction ($d\psi/dt$) is less than or equal to 10^{-6} kPa/s .

4.2 Finite element analysis

Considering the initial parameters, the predicted profile of the steady state soil matric suction is presented in Figure 6. The matric suction varies from a maximum of 1081 kPa at point (r_0, z_0) to 196 kPa at 20 m deep. As expected the maximum change in matric suction is at the centre of the root mass (r_0, z_0) gravity, and it decreases away from this point.

Deformation of the soil profile due to root water uptake is predicted through a coupled flow deformation analysis that considers the stress deformation equations. Ground settlement at various depths under steady state conditions is shown in Figure 7.

The radius of the influence zone for which the surface settlement is at least 25 mm (i.e. change of curvature of the settlement plots) is about 14 m. Ground settlement decreases rapidly with horizontal distance from the tree trunk, and beyond 30 m, the predicted settlement is insignificant.

4.3 Effect of time (t)

Because soil suction and consolidation are time dependent, investigating the effect of time on the profile of soil suction and ground settlement are required for design purposes. To study the effect of time the reference case analysis results are compared for 5 different time intervals, from 7 days to steady state, as can be seen in Figure 8.

Figure 8 indicates that ground settlement increases rapidly for 6 months, after which it increases gradually. Maximum ground surface settlement of 7 mm after 7 days increases to 40 mm after six months and then gradually increases to 48 mm after reaching a steady state.

As expected and Figures 9 shows, the generated matric suction induced by tree transpiration increases by the time.

Figure 10 shows the evolution of soil matric suction in different times.

4.4 Sensitivity analysis

When designing foundations, the maximum allowable settlement is an essential criterion. Accordingly,

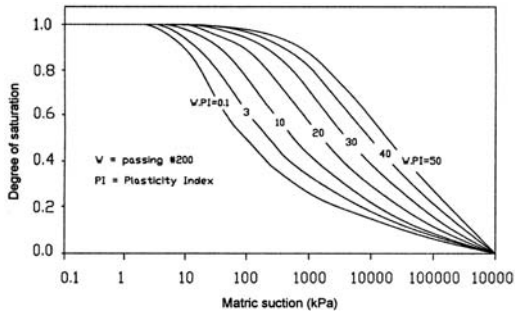


Figure 5. Predicted soil water characteristic curve (modified after Zapata et al. 2000).

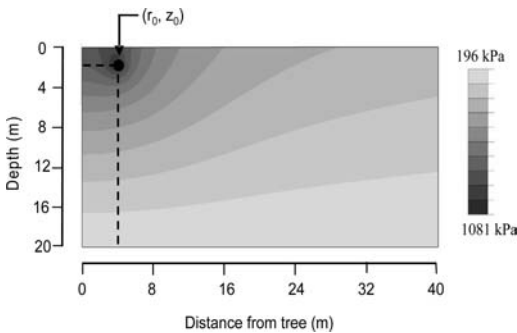


Figure 6. Matric suction profile in steady state condition.

predicting ground settlement induced by transpiration can enhance the approach to designing foundations near tree roots. In this section, the sensitivity of maximum settlement with respect to a number of parameters is investigated using the sensitivity index defined by:

$$(I_S)_i = \frac{\frac{\partial D_{\max}}{\partial u_i}}{\frac{D_{\max}}{u_i}} \quad (10)$$

where, $(I_S)_i$ is the sensitivity index of i th parameter, D_{\max} is the maximum vertical deformation, and u_i is the parameter which influences the ground settlement. Based on the sensitivity index and similar to Equation (7), parameters can be categorised as insensitive, sensitive, and very sensitive. Figure 11 shows the results of the sensitivity indices of various parameters.

The results of the sensitivity analysis shown in Figure 11 are based on assumed initial parameters and an applied range of parameters. Table 2 summarises the sensitivity of maximum ground settlement with respect to variations in the parameters of the model.

The most sensitive parameters are wilting point suction, saturation permeability when the coefficient is

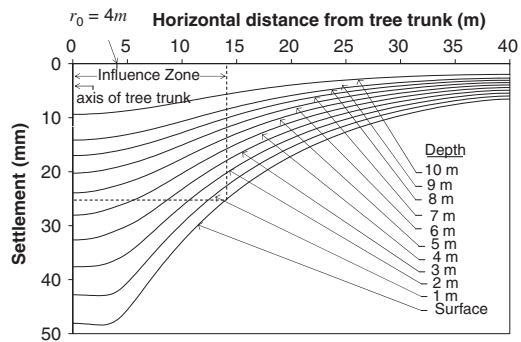


Figure 7. Ground settlement profile at various depths.

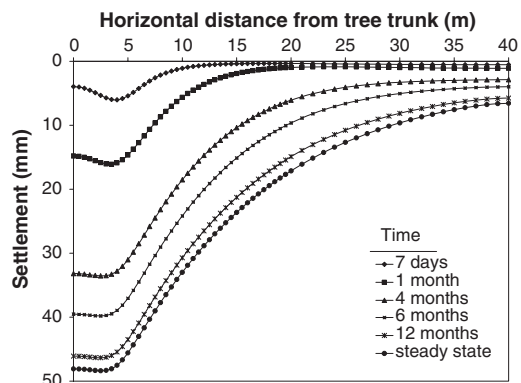


Figure 8. Effect of elapsed time on soil surface settlement.

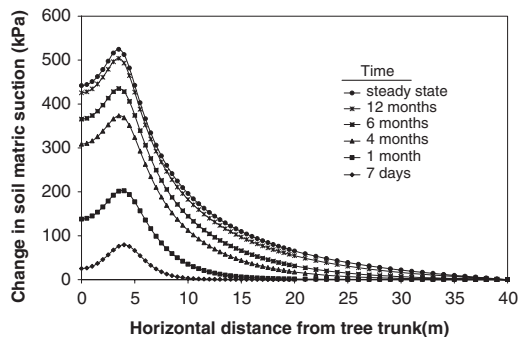


Figure 9. Effect of elapsed time on matric suction change on soil surface.

relatively high ($>3 \times 10^{-8} m/s$), the rate of potential transpiration at lower values (i.e. $T_p < 9 mm/day$), and vertical root distribution coefficient (k_1) when the coefficient is high ($>6 m^{-1}$).

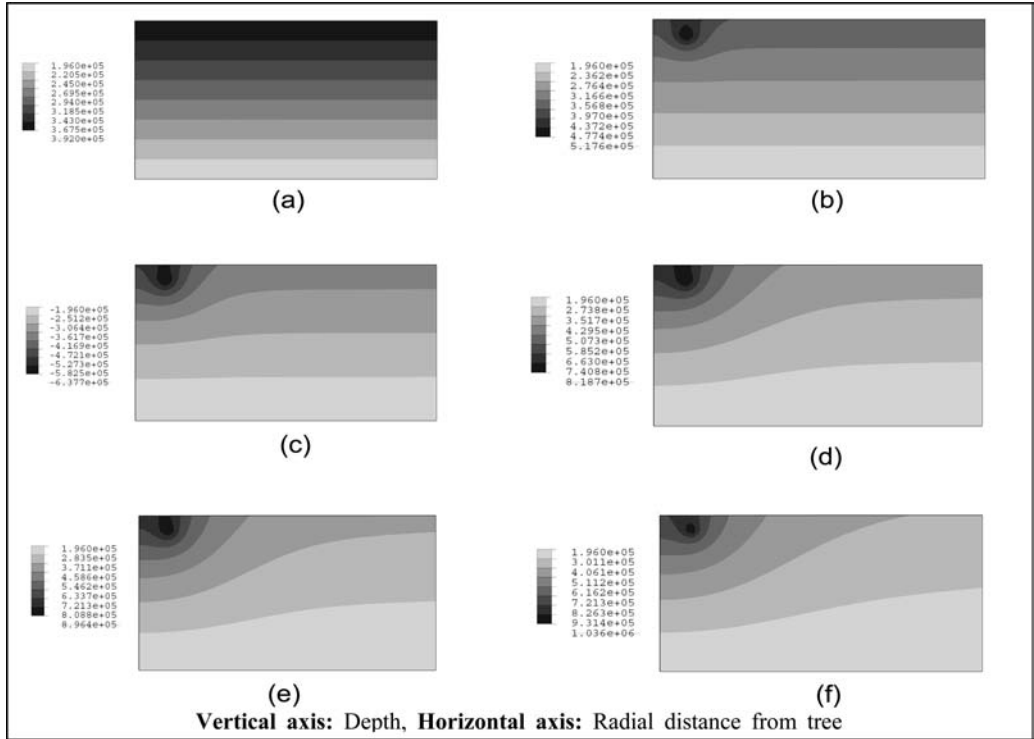


Figure 10. Evolution of soil matric suction (Pa), (a) initial (b) after seven days, (c) one month, (d) four months, (e) six months, and (f) twelve months.

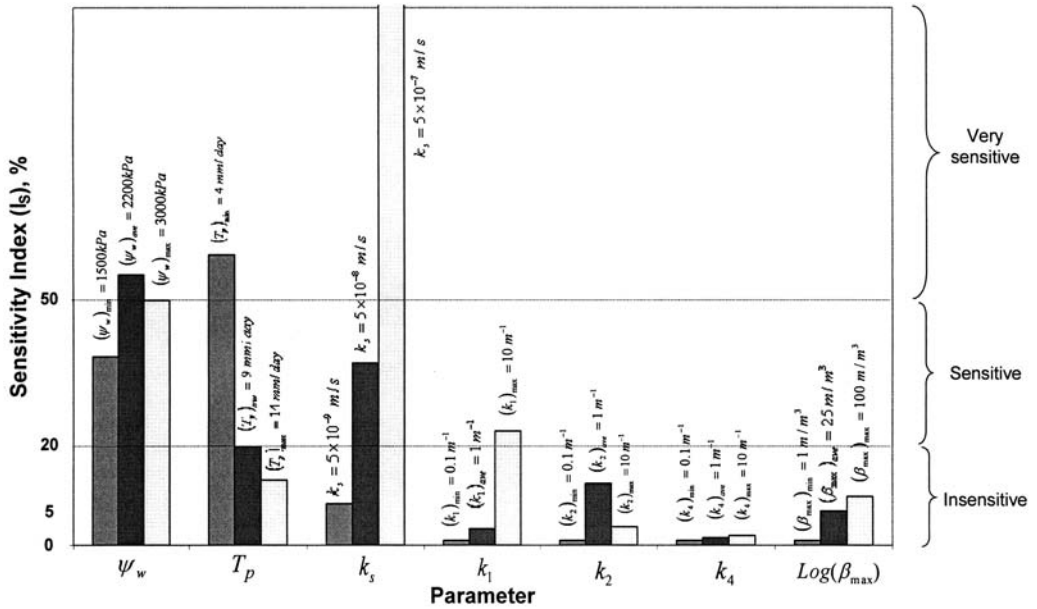


Figure 11. Results of the sensitivity analysis for the maximum ground settlement.

5 CONCLUSIONS

In this paper, a sensitivity analysis and analysis of a reference case are presented to investigate the influence of trees with typical specifications. Tree root suction was considered through the model developed by Indraratna et al. (2006). A sensitivity analysis was conducted to investigate the influence of variables on the initial rate of root water uptake. It was found that the wilting point suction, root density distribution, and potential transpiration are the most important factors influencing the rate of root water uptake.

Based on the theory of water flow in partially saturated soils, and considering the developed model for the root water uptake, an array of numerical analyses were conducted. The root water uptake has been considered as a sink term in the flow equation. An in-depth analysis on the effects of important variables has shown that a complex interaction exists between tree and soil properties. The findings of this study confirm that a number of parameters need to be measured or estimated accurately to design a proper foundation. Soil permeability, wilting point suction, root length density, and the rate of potential transpiration, are significant influences. Other parameters including soil properties (e.g. consolidation and strength parameters, and the soil water characteristic curve) should be measured accurately in the laboratory or field because they are important factors.

This sensitivity analysis shows that some parameters have marginal effects, but these results are related to the initial values and assigned range of parameters used in the reference case. Therefore, in some real cases the results may vary and change the sensitivity indices of the parameters.

ACKNOWLEDGEMENTS

This research has been sponsored by the Australian Cooperative Research Centre for Railway Engineering and Technologies (Rail-CRC). The authors wish to acknowledge the assistance and contributions of Dr. Hadi Khabbz (Former Research Fellow, University of Wollongong) in the numerical analysis. The contributions and feedback from various industry colleagues, particularly Wayne Potter and David Christie, are appreciated. The assistance of Dr. Don Cameron (University of South Australia) is also acknowledged.

REFERENCES

- Bishop, A.W. 1959. The principle of effective stress. *Teknisk Ukeblad*, 106, No. 39, 859–863.
- Brooks, R.H. & Corey, A.T. 1964. *Hydraulic properties of porous media*. Colorado, U.S.A., Colorado State University, Report No. 3.
- Feddes, R.A., Kowalik, P.J., Kolinska-Malinka, K. & Zardny, H. 1976. Simulation of field water uptake by plants using a soil water dependent root extraction function. *Journal of Hydrology*, 31, Issues 1–2, 13–26.
- Feddes, R.A., Kowalik, P.J. & Zardny, H. 1978. *Simulation of field water use and crop yield*, Simulation Monograph. Wageningen, Pudoc.
- Fredlund, D.G. & Hung, V.Q. 2001. (Vipulanandan C. et al. (EDS.)) Prediction of volume change in an expansive soil as a result of vegetation and environmental changes. *Expansive Clay Soils and Vegetative Influence on Shallow Foundations*, Geo Institute, U.S.A., 24–43.
- Indraratna, B., Fatahi, B. & Khabbaz, H. 2006. Numerical analysis of matric suction effects induced by tree roots. *Proceedings of the Institution of Civil Engineers – Geotechnical Engineering*, 159, No. 2, 77–90.
- Knight, J.H. 1999. *Tree Water Use and its Implications in Relation to Agroforestry Systems*. Australia. Rural Industries Research and Development Corporation (RIRDC), Water and Salinity Issues in Agroforestry No. 5, RIRDC Publication No. 99/37, RIRDC Project No. CSM-4A, Kingston, ACT, Australia.
- Landsberg, J.J. 1999. *Tree water use and its implications in relation to agroforestry systems*. Rural Industries Research and Development Corporation (RIRDC), Water and Salinity Issues in Agroforestry No. 5, RIRDC Publication No. 99/37, RIRDC Project No. CSM-4A, Kingston, ACT, Australia.
- Myers, B.J. & Talsma, T. 1992. Site water balance and tree water status in irrigated and fertilized stands of *Pinus radiata*. *Forest Ecology and Management*, 52, 17–42.
- Nelson, J.D. & Miller, D.J. 1992. *Expansive Soils. Problems and practice in foundation and pavement engineering*, John Wiley & Son. pp 259.
- Nimah, M.N. & Hanks, R.J. 1973. Model for estimating soil water, plant and atmospheric interrelations. I: Description and sensitivity. *Proceedings of Soil Science Society of America*, 37, No. 4, 522–527.
- Richards, L.A. 1931. Capillary conduction of liquids through porous medium. *Journal of Physics*, 1, No. 1, 318–333.
- Zapata, C.E., Houston, W.N., Houston, S.L. & Walsh, K.D. 2000. Soil water characteristic curve variability. In *Advances in Unsaturated Geotechnics*, (Shackelford C.D., Houston S.L., Chang N.Y., (eds)). Denver, U.S.A., Geo-Institute.

Parallel three dimensional finite element analysis of dinosaur trackway formation

L. Margetts & J.M. Leng

Manchester Computing, University of Manchester, England

I.M. Smith

School of Mechanical, Aerospace and Civil Engineering, University of Manchester, England

P.L. Manning

Manchester Museum, Manchester, England

ABSTRACT: Fossilised footprints and trackways provide palaeontologists with information regarding dinosaur locomotion such as their gait, posture and speed. Current best practice is to interpret trackways as 2D surface features. Using computational geomechanics, this paper demonstrates that subsurface deformation can lead to transmitted or false footprints at different depths, whose size and shape relates to a distorted 3D pressure bulb. The results of parallel 3D finite element simulations are compared with a set of transmitted tracks owned by Amherst College, USA. At Amherst College, palaeontologists have peeled away each layer of solidified sediment to find a footprint in each one. Each of these footprints has a unique geometry, a different length and angle between digits. If each of these was found in isolation, they would be erroneously interpreted as coming from different species of dinosaur. Significantly, palaeontologists use a simple equation relating the length of the foot and the distance between two footprints (stride) to calculate the dinosaur's speed. As the footprint length changes with depth, so does the apparent stride. The consequence is a different speed for the trackway at each depth: a clear source of misinterpretation. To simulate the transmission of the footprint through the soil layers, an elasto-plastic soil model is used together with a fine resolution 3D mesh. The requirements of such a model have a marked impact on the computational cost and the authors describe how existing parallel libraries were extended to build a scalable footprint simulator.

1 INTRODUCTION

Fossil dinosaur tracks have the potential to reveal information on the size (Thulborn 1990), gait (Day et al 2002) and speed (Alexander 1976) of dinosaurs, their locomotor evolution (Gatesy 1990, 1991 & 1995), as well as providing clues to their behaviour (Lockley 1991). Furthermore, the tracks, together with the surrounding sedimentary rocks, are the record of the global Mesozoic terrestrial environments and ecosystems (Gillette & Lockley 1989). When interpreted correctly, all vertebrate tracks (not just dinosaurs) can potentially unlock past environments, behaviour and ecology, and therefore their study has wide ranging application to themes such as biodiversity and environmental change.

The underlying assumption of many interpretations (through 100 years of literature) is that what is preserved is a surface track. Therefore, data (e.g. track length and width, digit length, number of digits,

interdigital angles) on which these interpretations are based are recorded as 2D features. However, the study of vertebrate tracks and traces, vertebrate palaeoichnology, has concentrated on describing the trace with little or no interpretation of track formation and preservation. The way in which sediments behave before, during and after a track is formed, and the subsequent processes that may further modify a track have been essentially neglected.

Allen (1989, 1997) and Manning (2004) suggest that fossil tracks are not simply 2D surface traces of the maker's foot, but most are complex three-dimensional volumes associated with deformation at the surface and in the shallow (few 10s of cm) subsurface associated with each step. Pilot laboratory experiments (Manning 2004) recovered subsurface track layers yielding, for the first time, detailed information on subsurface track morphology that could be related to 'true' surface trace features. It is clear from this study that many tracks have been misinterpreted as surface

traces when, in fact they are transmitted features that are markedly different in size and morphology to the surface traces.

The Amherst Museum in the USA possesses a sequence of transmitted tracks, in a laminated mudstone. The photographs in Figures 1 and 2 show the top and bottom surface of one of these laminae, where there is a clear variation in track morphology.

The differences described have a major impact on interpretations based on the analysis of tracks. For example, when track length is used in calculations to

determine the speed of a walking dinosaur (e.g. Alexander 1976), estimated speed can be an order of magnitude higher if measurement is taken within the subsurface deformed zone relative to the true surface trace. Caution should also be applied when 'estimating' population dynamics from fossil track assemblages (Lockley 1994). Taxonomic characters, such as track morphology and geometry, that are currently used to define ichnotaxa have been clearly shown to vary with depth within a 3D track volume, substrate type and prevailing environment (Manning 2004), making many ichnotaxa questionable and the animal interpretations derived from them invalid. These simple observations have profound implications for the interpretation of dinosaur tracks, and the broader interpretations that are derived from the analysis of all fossil tracks. What is required is a detailed process-based investigation of the 3D deformation associated with track formation and a reassessment of fossil tracks.

Well established techniques in computational geomechanics are potentially of significant use to the palaeontology community. Numerical analysis using the finite element method and constitutive models for soils can be used to better understand the processes involved. However, this type of study can be quite time consuming. The soil behaviour can only be truly represented using three dimensions. The soil that the dinosaur stepped upon has since turned to rock and a parametric study for a range of soil properties is required to give meaningful results. Reducing solution times to enable detailed scientific studies to be carried out requires parallel computation. This paper presents the results of some preliminary analyses using a parallel finite element program that uses a simple elastoplasticity model.

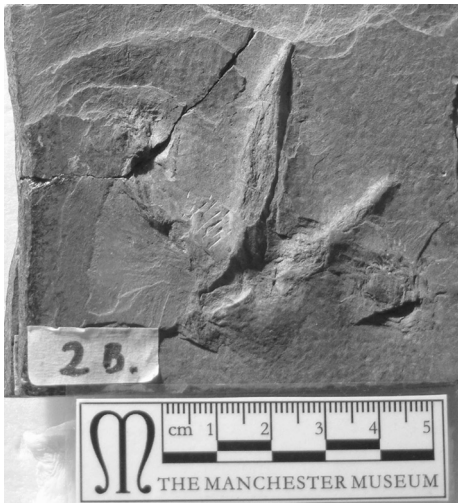


Figure 1. Dinosaur footprint from the Amherst collection.

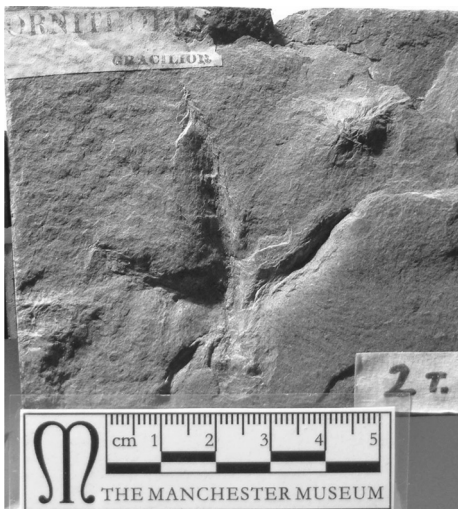


Figure 2. The opposite face of the same layer of rock.

2 SOFTWARE

The software used was a modified version of the parallel program p122.f90 in the Smith and Griffiths text (2004). The program uses the von Mises elastoplasticity model to represent the soil behaviour. An element by element iterative solver is used to solve the system of equations and plasticity is dealt with using a tangent stiffness approach with consistent stress return.

The program proceeds by reading in a pre-processed model and distributing it equally or near equally across the number of processors specified at runtime. Each processor stores its own set of elements, the number of which is determined by dividing the total number of elements by the total number of processors. Each processor computes the stiffness matrices for its own set of elements, an embarrassingly parallel operation. No global stiffness matrix is formed and therefore traditional domain decomposition techniques such as tearing

or substructuring are not part of the process. In fact, the term domain composition is preferred in this case.

The equations are also simply distributed across processors. The vectors of loads and displacements are divided equally or nearly equally between the number of processors used. This, together with simple element distribution, means that the program is scalable in terms of storage: larger problems need to be subdivided over systems with more processors. A side effect of the subdivision of equations is that some equations that are stored on one processor may be needed on one or more other processors.

This is dealt with by passing messages between the processors at the appropriate time, in this case using the message passing library MPI.

Loading is applied using an incremental displacement control technique. Within each load step, a number of plastic iterations are carried out. During each plastic iteration, a system of equilibrium equations is solved using a parallel element by element version of the iterative preconditioned conjugate gradient solver. As a direct solver is not used, no factorisation of a global stiffness matrix is required and it is cost effective to reform the element stiffness matrices during each plastic iteration. This is an embarrassingly parallel operation as stated earlier.

The authors have found that this approach leads to a reduced number of plastic iterations and overall solution times. When a direct solution method is used, reforming and refactorising the element stiffness matrices is more costly than the benefits gained in reduced plastic iterations.

A summary of the program, using quasi-coding is outlined as follows in Figure 3.

```
Read and distribute initial data
Do for local elements
  Calculate stiffness matrices
End do
Do load increments
  Do plastic increments
  Solve equations
  Do for local elements
    Calculate strains/stresses
    Update bodyloads
    Update stiffness matrices
  End do
End do
Update displacements
End do
Collect results and write to disk
```

Figure 3. Outline of program.

The reader should note that there is very little difference between the serial and parallel versions of the programs. All the complicated coding for message passing is hidden away in a series of subroutines. For example, intrinsic FORTRAN functions such as SUM and DOT_PRODUCT are simply replaced by the user functions SUM_P and DOT_PRODUCT_P that function in parallel with distributed data.

Perhaps one of the greatest challenges for the widespread use of parallel computing in research software is the readability of the coding. Here, the serial and parallel codes are almost identical. The parallelisation techniques used can be applied to any general finite element application. The interested reader is encouraged to consult the Smith and Griffiths text where there are a number of example programs, with both serial and parallel versions, covering a wide range of problem types. Source code for the parallel libraries and example programs are provided freely in the ParaFEM library (www.parafem.org.uk).

3 EXAMPLE PROBLEM

Results of the footprint simulation are presented in the following two sections that consider program performance and scientific insight respectively. An image of the mesh is not presented here as it is too fine grained to reproduce graphically in this document.

The model comprises 73,728 8-noded hexahedral elements and 78,449 nodes. There are 224,208 equations to be solved. Two analyses were carried out. In the first, the “simple” case, the foot was displaced vertically downwards into the soil. In the second, loading by the foot was applied in a heel to toe cycle. As the dinosaur walks forwards, its heel makes first contact with the ground and then the weight shifts to the toe before the foot is lifted away. In this paper a von Mises soil has been used, with an undrained shear strength of 150 Nm^2 . This corresponds to the “very stiff” classification for clay, used in the British Standards.

4 PARALLEL PERFORMANCE

The authors do not suggest that the parallel algorithms used here will deliver results in the shortest time compared with other methods. An indepth, objective, comparison has not been made in the literature. Nonetheless, there are many opinions regarding which is the best strategy.

It is of interest to note that parallel direct solvers eventually run out of memory for similar reasons to serial ones. Scalability is generally poor too, with the largest number of processors typically used being

Table 1. Parallel performance.

Processors	1	16	32	64	128
Speed up	1	14	25	40	58
Time (seconds)	26588	1965	1064	675	458

less than 50. Iterative, element by element solvers on the other hand have been shown to scale over many thousands of processors, as long as the problem is large enough (Carey et al 1997).

Another point of note is that at the core of the iterative method used here are repeated matrix-vector and matrix-matrix multiplications that are responsible for more than 90% of the time spent in the solver. These functions make very good use of commodity processors and the authors have seen up to 40% peak machine performance achieved for matrix-vector computations and up to 70% peak for matrix-matrix. In contrast, direct solvers typically achieve 1–2% peak. Whilst it is true that element by element algorithms do more work (judged by counting the floating point operations), they do it very efficiently, especially using parallel computers.

Performance statistics for the dinosaur model are presented in Table 1. The simulations were run using a 512 processor SGI Altix. Access was kindly provided through the UK's national high performance computing service (CSAR).

The Altix has 2 GB memory per processor. Each processor comprises a 1.3 Hz Intel Itanium chip with four floating point operations per clock cycle. From Table 1, it can be seen that solution times can be reduced from around 7.5 hours to 7.5 minutes.

The times given are those that the scientist would wait to receive the results after starting the job. They are for the full analysis, from reading and distributing the input to collecting and writing the results. Considering the speed up figures, the algorithms have been shown to scale over larger numbers of processors elsewhere (Margetts 2002). The decline in performance can be attributed to the size of the problem. Quite simply, when using 128 processors there is insufficient work per processor.

There is a misconception that parallel computing necessitates having access to an expensive machine. The software and generic approach described here can achieve good usage of a cluster of PCs connected together using 10/100 Mb Ethernet.

With hardware prices becoming ever more competitive, it is now possible to purchase an “off the shelf” basic shared memory system with 8 dual core processors for under 20,000€ and a distributed memory system with 16 dual core processors and a super-computer class interconnect (significantly superior to gigabit Ethernet) for under 30,000€.

These systems would provide around 60 and 120 Gflops peak performance respectively.

A Beowulf cluster, with the owner purchasing the components, building and configuring the system, prices would be considerably less.

5 DINOSAUR FOOTPRINT SIMULATION RESULTS

The purpose of this study is to demonstrate whether dinosaur tracks can be transmitted vertically downwards into the soil, changing geometry with depth, as discussed in the introduction. So the obvious procedure is to (a) run the analysis and (b) visualise the results by cutting away the various layers and measuring the dimensions of features belonging to the transmitted footprint.

It turns out that this is not as easy as it first seems. Setting a scaling factor and viewing the deformed geometry is straightforward enough. However, after stripping away layers of elements, identifying an outline of the transmitted footprint is not easy. The principal reason is that identification of the outline depends on both the lighting of the visualisation scene and the subjective judgement of the analyst.

The same problem arises with real fossil footprints. How does one define where the print starts and finishes? Manning, the palaeontologist contributor to this work, has attempted to make the task as objective as possible. Manning defines the edge of the footprint to follow an imaginary line where there is an inflexion in the deformation: between the soil displaced downwards under the foot and the soil displaced upwards nearby. The reader is invited to refer to the photographs of the real footprints in [Figures 1 and 2](#) and consider how one would measure the key features such as length and inter-digital angle (angle between the toes).

Bearing in mind the palaeontologist's technique, a close analogy was to look at the most highly sheared zones in the soil, picked out by selecting values of Mises stress; the technique used to produce the images presented later in the paper ([Figures 8–11](#)).

[Figures 4 to 7](#) show Mises stress using a randomised greyscale colour map. Although this colour map does not encode magnitude information, it does highlight the features of the deformation more clearly than the standard greyed rainbow scheme typical of engineering publications. All the figures use the same maximum and minimum values, with the range shaded using identical intervals.

Comparing [Figures 4 and 5](#), it is interesting to note that the region of soil that has undergone deformation is greater for the analysis in which a heel to toe loading cycle was used.

In [Figure 7](#), there are two prominent shear zones, one to the rear of the heel and the other at the front of the toe. The shear zones run deeper in [Figure 7](#) than in

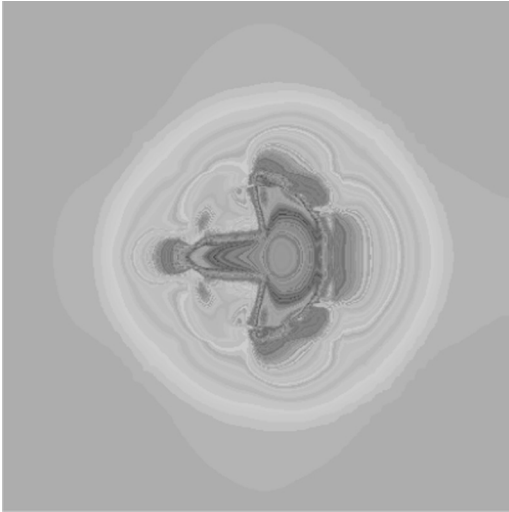


Figure 4. Surface Mises stress plot – simple loading.

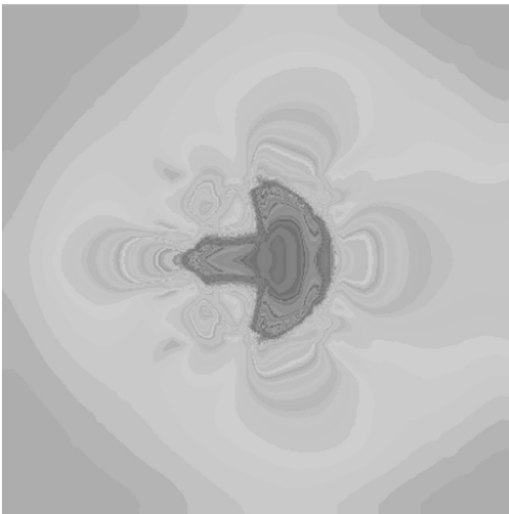


Figure 5. Surface Mises stress plot – heel-toe cycle.

Figure 6, when the loading is applied in the stepping cycle.

In Figures 8 and 9, an isosurface plot shows where the Mises stress has the same value through the soil volume. The value chosen is a representative one that has been taken from the localized region that has undergone yielding. The images show quite clearly how the footprint gets smaller with depth. The isosurface may be thought of representing the pressure bulb that is familiar to geotechnical engineers. Figure 8 shows results from the simple loading and for Figure 9 the heel-toe loading cycle was applied. The toe was more prominent when the heel-toe loading cycle was applied. This

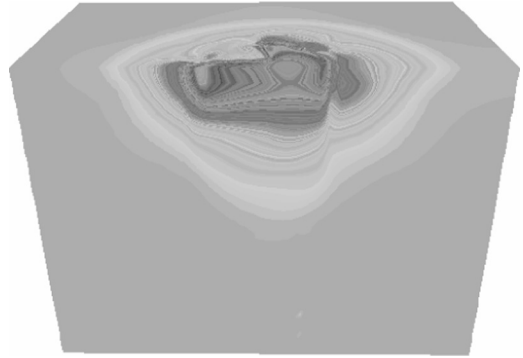


Figure 6. Mises stress cross section – simple loading.

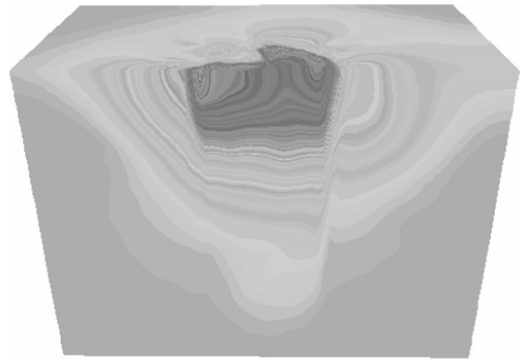


Figure 7. Mises stress cross section – heel toe cycle.

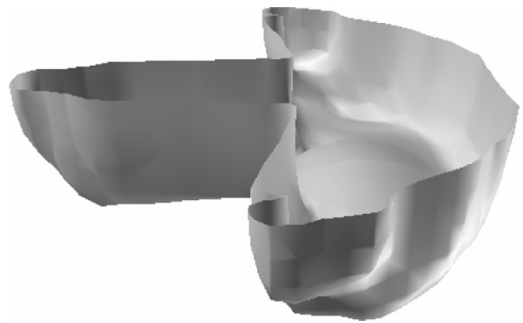


Figure 8. 3D Footprint volume – simple loading.

feature is seen in real tracks and is due to the weight of the dinosaur bearing down on the toe as the foot is lifted from the ground.

If the surface of the soil domain suffered weathering and erosion, as occurs in nature, the isosurfaces of Figures 8 and 9 would be intersected at increasing depths, depending on the length of time taken for the footprint to be buried by more sediments.

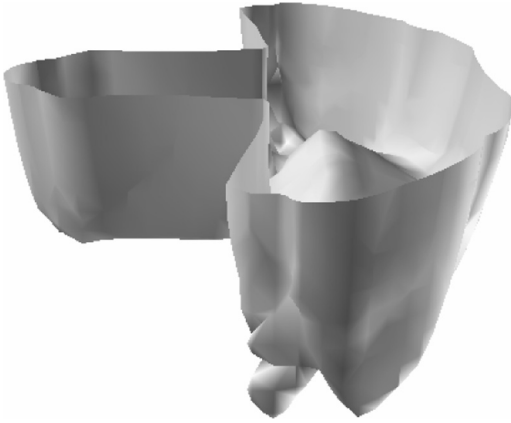


Figure 9. 3D Footprint volume – heel to toe loading cycle.

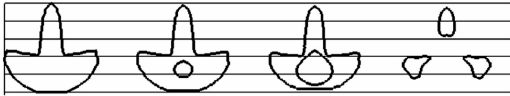


Figure 10. 2D Track, variation with depth – simple loading.



Figure 11. 2D Track, variation with depth – heel toe cycle.

Also, if the later rock is easily split into sheets, as in the Amherst case, each sediment layer would intersect the isosurface at a different depth. The result would be different size footprints on each layer as illustrated by the slices through the isosurface, in Figures 10 and 11.

Figures 10 and 11 show the outline of the footprint that would be seen at different depths in the soil strata. The length of the footprint at the surface is 75 centimetres. In the figures, depth increases from left to right. The depth of the first footprint has been chosen where the initial punching shear ceases. Subsequent footprints are sampled at regularly increasing depths as would be the case if the soil had become a thinly laminated mudstone.

6 CONCLUSIONS

A simple elasto-plastic model has been used to demonstrate (a) that dinosaur footprints may be transmitted

vertically downwards into the soil and (b) that the geometry of the footprint changes with depth. Whilst this may be obvious to those working in geo-mechanics or geotechnical engineering, the results are of importance to the field of palaeontology where there is not a widespread knowledge of either the principles of soil mechanics or of finite element analysis techniques.

Perhaps of more interest to the geomechanics community is the demonstration that practical 3D problems can be solved in a reasonable period of time. With the use of parallel computing, the time to solve the problem presented here was reduced from 7.5 hours to 7.5 minutes using 128 processors. The authors note that these analyses are not particularly large and problems with up to half a billion degrees of freedom have been solved elsewhere (Adams 2004).

REFERENCES

- Adams M.F. et al 2004. Ultrascalable implicit FE analysis in solid mechanics with over half a billion degrees of freedom, Supercomputing, Pheonix, Arizona, 2004.
- Alexander, R. McN. 1976 Estimates of speeds in dinosaurs. *Nature*, 261, 129–130.
- Allen, J.R.L. 1989 Short paper: Fossil vertebrate tracks and indenter mechanics. *J. Geol. Soc. London*, 146, 600–602.
- Allen, J.R.L. 1997 Subfossil mammalian tracks (Flandrian) in the Severn Estuary, S.W. Britain: mechanics of formation, preservation and distribution. *Phil. Trans. R. Soc. London. B.*, 352, 381–518.
- Carey, G.F., Harle, C., Mclay, R. and Swift, S. 1997. MPP solution of Rayleigh Benard Marangoni flows. *Proceedings of Super Computing 97*.
- Day, J.J., Norman, D.B., Upchurch, P. and Powell, P.H. 2002 Biomechanics: Dinosaur locomotion from a new trackway. *Nature*, 415, 494–495.
- Gatesy, S. M. 1990 Caudofemoral musculature and the evolution of theropod locomotion. *Palaeobiology*, 16, 170–86.
- Gatesy, S.M. 1991 Hind limb scaling in birds and other theropods: Implications for terrestrial locomotion. *J. Morphology*, 209, 83–96.
- Gatesy, S.M. 1995 Functional evolution of the hind limb and tail from basal theropods to birds. In Thomason, J. J. (ed.). *Functional vertebrate morphology in vertebrate paleontology*. Cambridge University Press, Cambridge, 277 pp.
- Gatesy, S.M., Middleton, K.M., Jenkins, F.A. Jr., and Shubin, N.H. 1999 Three-dimensional preservation of foot movements in Triassic theropod dinosaurs. *Nature*, 399, 141–144.
- Gillette, D.D. and Lockley, M.G. (eds.). 1989 *Dinosaur tracks and traces*. Cambridge University Press, 454 pp.
- Leakey, M.D. and Hay, R.L. 1979 Pliocene footprints in the Laetoli Beds at Laetoli, northern Tanzania. *Nature*, 278, 317–323.
- Lingen, G.J. and Andrews, P.B. 1969 Hoof-print structures in beach sand. *Journ. Sed. Petrol.*, 39, 350–357.
- Lockley, M.G. 1991 *Tracking Dinosaurs*. Cambridge University Press, 238 pp.

- Lockley, M.G., Hunt, A.P. and Meyer, C.A. 1994 Vertebrate tracks and the ichnofacies concept: Implications for palaeoecology and palichnostratigraphy. 241–268. In Donovan, S. (ed.). *Palaeobiology of trace fossils*. Wiley and Sons. Inc., 268 pp.
- Lockley, M.G. 1994 Dinosaur ontogeny and population structure: Interpretations and speculations based on fossil footprints. In Carpenter, K., Hirsch, K. F. and Horner, J.R. (eds.). *Dinosaur eggs and babies*. Cambridge University Press, Cambridge, 372 pp.
- Manning, P.L. 2004 A new approach to the analysis and interpretation of tracks: examples from the dinosauria. In McIlroy, D. (ed) *The Application of Ichnology to Palaeoenvironmental and stratigraphic analysis*. Geol. Soc. Lond. Spec. Pub., 228, 93–123.
- Margetts, L. 2002. *Parallel Finite Element Analysis*. PhD Thesis. University of Manchester.
- Raikow, R.J. 1985 Locomotor system. In King, A. S. and Mclelland, J. (eds.). *Form and function in birds*. Academic Press, p 57–147.
- Smith, I.M. & Griffiths, D.V. 2004. *Programming the Finite Element Method*. London, Wiley.
- Thulborn, R.A. 1990 *Dinosaur Tracks*. Chapman Hall, London, 410 pp.
- Grove, A.T. 1980. Geomorphic evolution of the Sahara and the Nile. In M.A.J. Williams & H. Faure (eds), *The Sahara and the Nile*: 21–35. Rotterdam: Balkema.

Finite element analysis of buried flexible culverts subjected to rockfall loading

R. Ebeltoft, J. Gloppestad & S. Nordal

Geotechnical Division, Norwegian University of Science and Technology, Trondheim, Norway

ABSTRACT: In general, rockfall shelters are constructed with a concrete structure and a cushion layer of geomaterial. A possibly cheaper and equally safe alternative could in several areas be to use a buried corrugated steel culvert. To avoid significant damage during rockfall these structures, an absorbing cushion layer is added on top with a minimum cover height. In this paper, a simplified finite element analysis is presented simulating the dynamic response of a buried corrugated steel culvert. A 2-D finite element model with an elasto-plastic Mohr-Coulomb constitutive law was used. The simulated numerical results were compared with results gained from an experimental study, where a 4.0 m span arch corrugated steel culvert buried in soil has been instrumented during rockfall loading. Results compared were deceleration history, penetration depth and transmitted accelerations in the buried structure. In spite of the simplifications introduced by using a 2-D model on a truly 3-D problem, many features observed in the field test could be reproduced by the numerical simulation. More field testing followed by 3-D simulations are planned.

1 INTRODUCTION

Natural hazards, like avalanches and rockfalls, will always be a major concern for roads and railways in mountain areas. Several measures are available to protect this infrastructure, but especially in areas with steep slopes and high risks, rockfall- or avalanche shelters are commonly used. Such protection structures are usually made from reinforced/pre-stressed concrete with a cushion layer. A falling rock can produce very high impact energies, these energies are governed by the velocity of the fall and the mass of the rock. The cushion layer, according to Pichler et al. (2005), has the function of being an energy absorber and to distribute the forces on the structure. Thus the forces developed and the corresponding penetration depth are not only dependent on the mass and velocity, but also the properties of the cushion material (Jacquemond 1999).

In general, a rockfall impact on ground surface has two mechanisms; (i) displacement of soil particles in the vicinity of the impact creating an impact crater, and (ii) deformation further out in the soil due to propagation of waves. As the waves propagate deeper into the cushion layer the energy density attenuates, due to both geometric and material damping.

In recent years, experimental studies to investigate rockfall impact on buried structures have been performed by a number of researchers (Labioise et al. 1996, Descocudres 1997, Kishi 1999, Montani Stoffel

1999). These studies were conducted on stiff structures (i.e. concrete) with a cushion layer consisting of either sand or gravel. Another experimental study was performed by Pichler et al. (2005), focusing on the penetration depth and impact forces on the cushion layer (e.g. gravel). Recently Ebeltoft & Larsen (2006) conducted large scale rockfall impact tests on a buried corrugated steel culvert. A number of vertical rockfalls were performed with rock block masses ranging from 200–2650 kg from 5–20 m heights.

The work reported herein describes some initial numerical simulations of rockfall impact on a buried flexible structure, based on the field tests performed by Ebeltoft & Larsen (2006). Although this is a 3-D problem, it was in this preliminary study simplified into a 2D plain strain problem. A 2-D Finite Element model (FE) was developed using the program ABAQUS with their elasto-plastic Mohr-Coulomb constitutive law. The numerical results were compared with results gained from the field study. The deceleration history, penetration depth and transmitted accelerations in the structure were compared.

2 EXPERIMENTAL STUDY

In the experimental study that was conducted, a 15.0 m long structural plate metal arch culvert was installed

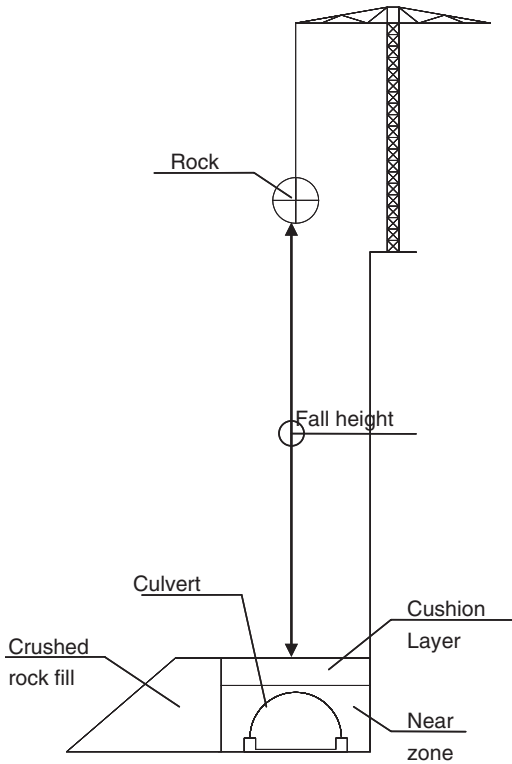


Figure 1. Illustration of experimental set-up for rock fall impact on buried corrugated culvert.

on a reinforced concrete plate foundation, as shown in Fig. 1.

The MP200 Arch type metal culvert (Asset International 2002) was used, which is a galvanized corrugated circular steel arch with a 4.00 m span at the foot and a 1.93 m total rise. The culvert was manufactured from structural plates with 200×55 mm corrugations. The plate thickness was 5.0 mm.

The culvert was backfilled with gravel material. The material in the near zone consisted of 8–16 mm gravel. The cushion layer zone consisted of 23–64 mm size gravel. Confinement of the gravel consisted of rock surface on one side and an 80–200 mm size crushed rock fill on opposite side, Fig. 1.

During the construction sequence the various backfill materials were placed in 300 mm thick layers and compacted. This procedure was commenced until 300 mm above crown. The remaining fill was placed in 600 mm layers without compaction. A closer description of the experimental set-up is given by Ebeltoft & Larsen (2006).

Impact load tests were conducted immediately after the construction was completed. In the present study, natural rock boulders have been used, and the impact

of these rocks were centered above the crown of the culvert. After each impact test the cushion layer was removed and replaced to same level.

3 NUMERICAL SIMULATION

The rockfall impact on a buried structure is dynamic, highly nonlinear and involves wave propagation. As an initial study we have chosen to simplify the analysis by using a 2-D finite element model. Later in this ongoing PhD-project a 3-D simulation will be made. For both cases, acceptable results, with respect to accuracy and stability, is dependent on the mesh discretization, the size of the time step and the damping of the system. These concepts are considered in the following sections.

3.1 Governing equation

The equation that governs the dynamic response of the soil and the structure is:

$$[M]\{\ddot{u}\} + [C]\{\dot{u}\} + [K]\{u\} = \{F\} \quad (1)$$

In matrix terminology; M is mass, C is viscous damping and K is stiffness, while \ddot{u} , \dot{u} and u are vectors of the acceleration, velocity and displacements, respectively. For dynamic problems the external force F is a function of time. In general, soil is a nonlinear material. Thus the stiffness of the soil is composed of an elastic and a plastic part. The stresses in the soil can be computed for a given strain increment using tangent stiffness matrix. To compute this, direct integration with the Newmark β -method is used, where

$$\beta = \frac{1}{4}(1 - \alpha)^2 \text{ and } \gamma = \frac{1}{2} - \alpha \quad (2)$$

A small numerical damping, equal to $\alpha = -0.05$, being the default value in ABAQUS, was used for this study. This provides an unconditionally stable integration method.

3.2 2-D vs. 3-D analysis

Performing an analysis of a rockfall impact on a buried structure, which in general is a typical 3-D problem using a 2-D plain strain model introduces crude simplifications:

- The model can never be very realistic since it actually compares to dropping a long cylindrical object on top of the tunnel.
- One might consider trying to determine some equivalent length of impact loading along the tunnel axis

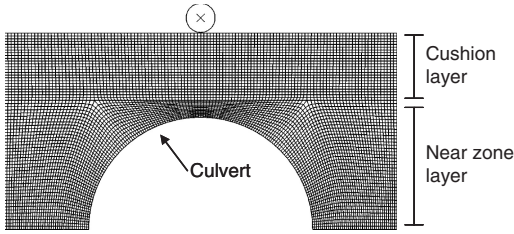


Figure 2. Finite element mesh.

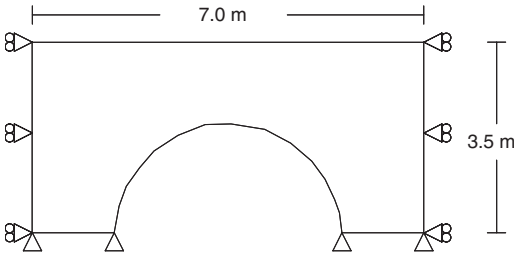


Figure 3. Finite element model boundary conditions.

in order to equalize the 2-D with a 3-D analysis. Due to the dynamics involved, this is considered extremely difficult, and hence a very simple procedure is adopted where the 2-D loading is given by the load of the actual falling stone distributed over a 1 m length normal to the plane strain plane. Thus in reality we are herein simulating the impact of a falling long cylinder with mass per axial meter equal to the mass of the stone.

3.3 Finite element mesh

The dimension of the simplified 2-D model was 7.0 m × 3.5 m, shown in Fig. 2. Elements used in this model were 4 noded elements for the soil and 2 noded linear beam elements for the culvert. Boundary conditions, as shown in Fig. 3, were imposed on the outer edges. Non-reflective boundaries on the sides were not included, as it is assumed that the critical part of the analysis was the first entrance of the propagating impact stresses onto the structure.

Effects of large displacements were not included in the study. Soil plasticity at impact was considered much more significant, and a solution with time stepping, plasticity and geometric non-linearity was not feasible.

3.3.1 Soil and steel parameters

Initial soil parameters assumed in this analysis are as presented in Tables 1 & 2.

These parameters were calculated based on estimated soil values.

Table 1. Mohr Coulomb parameters for the cushion layer material.

E (MPa)	ϕ (°)	ψ (°)	C (kPa)	ν	ρ (kg/m ³)
8	39	8	1.0	0.30	1800

Table 2. Mohr Coulomb parameters for the near zone material.

E (MPa)	ϕ (°)	ψ (°)	C (kPa)	ν	ρ (kg/m ³)
14	39	8	1.0	0.30	1800

Table 3. Parameters for the corrugated steel culvert.

E (GPa)	G (GPa)	ν	σ_y (MPa)
210	80	0.20	229

For the steel the following parameters were used.

The steel parameters, as presented in Table 3, are according to the steel used in the experimental study, and are found from the manufacturers technical specifications (Asset International 2002).

3.3.2 Mesh discretization

In the finite element method, the accuracy of the results depends on the discretization of the mesh in the direction of the wave propagation. Thus an element size must be chosen according to the highest frequency for the lowest velocity of the wave type considered. The element size was determined based on the approximation methods proposed by Zerwer et al. (2002), which states that the element dimension (l_{max}) can be calculated from:

$$l_{max} = \zeta \lambda = \zeta \frac{V_s}{f_{max}} \quad (3)$$

Where λ is the minimum wavelength. The constant ξ is a fraction of the wavelength, and $\xi \leq 0.25$ for linear strain elements and $\xi \leq 0.125$ for constant strain elements.

3.3.3 Size of time step

Implicit methods in general do not have step size limitations due to stability. Accuracy concerns alone determine the step size. According to Ta & Rogers (1986), a suitable time step (Δt) appropriate for the analysis of wave propagation problems is generally selected according to the smallest element size (l_{min}) in the mesh.

$$\Delta t \leq \frac{l_{min}}{v_p} \quad (4)$$

For a two-dimensional plane strain analysis, the compression or body wave velocity, v_p , is defined as

$$v_p = \sqrt{\left(\frac{(1-\nu) E}{(1+\nu)(1-2\nu) \rho} \right)} \quad (5)$$

3.3.4 Damping

Material damping is also an important factor influencing the accuracy of the finite element model. In this study the Rayleigh damping model have been used. Rayleigh damping assumes that the damping matrix, C , are a linear combination of the mass and stiffness matrices:

$$[C] = \alpha[M] + \beta[K] \quad (6)$$

The relationship between damping ratio and the natural frequency, as given by Eq. 5. Where mass damping operates primarily at low frequencies, while the stiffness damping operates more at high frequencies. In our simulation the elasto-plastic model will provide considerable material damping in all yielding material points. The Rayleigh damping is additional damping and a low damping ratio was considered. The damping ratio chosen was $\zeta = 0.5\%$. Assuming no significant mass damping the values $\alpha = 0$ and $\beta = 0.0001$ have been used for this study based on suggestions made by Gu & Lee (2002).

3.3.5 Modeling of impact

The impact from the rockfall is modelled by letting a rigid body with a circular cross section, Fig. 2., hit the surface with an initial speed of 14 m/s determined from the fall height. The contact area between the falling body and the cushion soil increases during impact and is controlled by a contact formulation.

4 COMPARISON AND DISCUSSION OF EXPERIMENTAL AND NUMERICAL RESULTS

The results shown in this section is a comparison of simulations for a 200 kg rock impacting the cushion layer from 10 m. A reasonable agreement was found between the simulated and experimental results even though considerable discrepancy is expected since a 2-D simulation is used.

4.1 Penetration depth

Figure 4 presents the penetration depth found in the experimental and numerical study. The penetration depth from the experimental results was 0.20 m, while

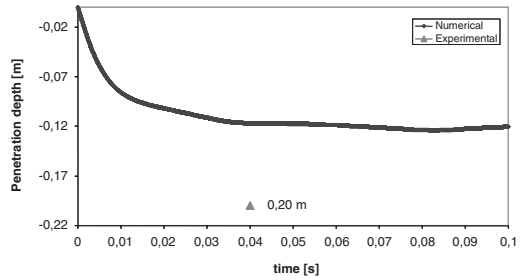


Figure 4. Comparison of penetration depth between numerical and experimental results.

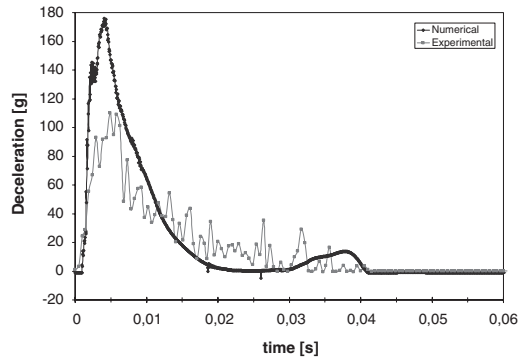


Figure 5. Comparison of deceleration history for a 200 kg rock block impact from 10 m and numerical simulation.

the numerical simulations showed a penetration depth approximately 0.12 m. which is 40% less than what the experimental results show.

4.2 Deceleration history

Deceleration histories found in the numerical simulations and the experimental study are presented in Fig. 5. It can be observed, by comparing the numerical simulations with the experimental results, that the numerical simulations show a higher peak deceleration and a shorter duration than what was experienced in the experimental study. Numerically the impact duration lasts approximately 25 ms, while the experimental results show duration of approximately 40 ms. The rebound is steeper for the numerical results while the experimental result yields a gentler rebound.

4.3 Propagation of waves

Numerical simulations are able to yield results that are not easily achieved in an experimental study. This is in particular the case for the propagation of the waves generated during impact.

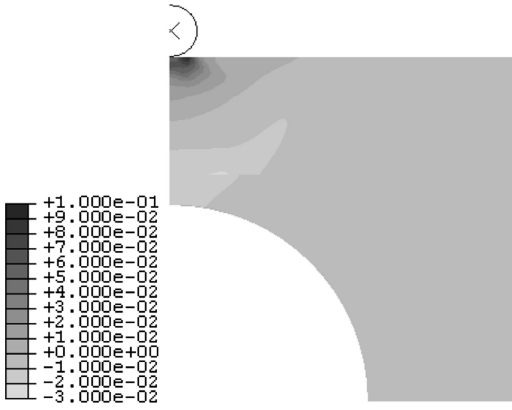


Figure 6. Total volumetric strain at $t = 20$ ms after initial impact.

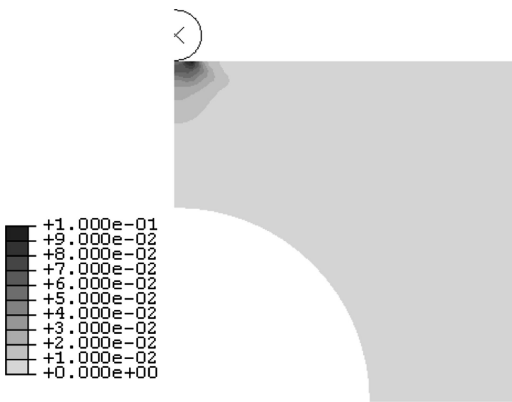


Figure 7. Plastic volumetric strain at $t = 20$ ms after initial impact.

Figures 6 & 7 show the total and plastic volumetric strain at $t = 20$ ms after initial impact. As seen in Fig. 7, the region directly underneath the impact point shows large strains ($\sim 10\%$) which form a crater with 1.5–2 times the radius of the rock. The maximum values of total strain are observed just under the rock at the contact point. The plastic strains create permanent deformations in the cushion layer. The model is not able to reproduce the mounds observed in the field. Outside the influenced zone, approximately 2–3 times the radius of the rock, no irreversible strains are found in the simulations.

The major part of the impact force is taken by compression, while the remaining soil is partly dissipating the energy of the rock fall. No permanent stresses are applied on this remaining soil as far as the plastic zone is bearing the rock. No plastic deformation of the culvert is calculated for this particular simulation

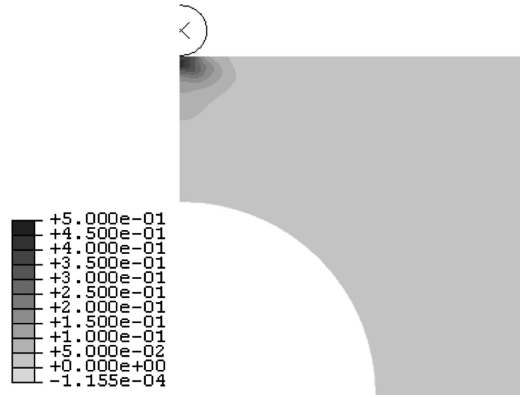


Figure 8. Total Deviatoric strain at $t = 30$ ms after initial impact.

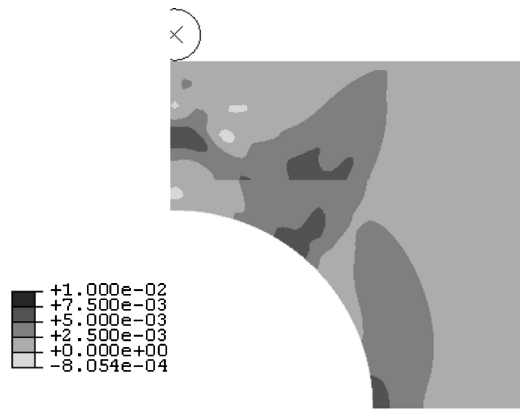


Figure 9. Elastic deviatoric strain at $t = 30$ ms after initial impact.

of a 200 kg rock, dropped from 10 m. This was also observed from the strain gages and deformation measurements in the field test.

Figure 6 show total volumetric strain at $t = 20$ ms after initial impact. Differences seen between Figs 6 & 7 are due to the elastic volumetric strain corresponding to both compression and shear waves. Shear waves also produce some volumetric strain due to dilatancy angle. The shape of the wave into the soil is initially convex corresponding to the shape of the rock. Some reflections and changes in the transmitted waves occur at the interface between the cushion layer and the near zone layer.

Figures 8 & 9 show the total and elastic deviatoric strain at $t = 30$ ms after initial impact.

As seen in Fig. 8 large total deviatoric strain is observed underneath the impacting rock (couple of ten presents). This high localization of strains corresponds

mainly to the influence zone observed in Fig. 6 at $t = 20$ ms. These large deformations occur during pre-peak deceleration, see Fig. 5, while post-peak deceleration (and rebound) does not increase plastic strain. In Fig. 9 we observe that the propagating waves move fast in the culvert and from there radiate back out into the deeper regions of the surrounding soil. We note the concentration of deviatoric strains in the soil at the toe of the wall.

The cushion layer will in reality be transmitting waves in all directions also in the longitudinal direction of the tunnel, a feature which is not reproduced in our 2-D plane strain model.

The cushion layer seems to play the most important role by absorbing energy through plastic strains during the pre-peak phase of the impact, while the remaining energy is transmitted to the soil below and to the side and the culvert. This transfer should be confirmed with a 3-D model with absorbing or non-reflective boundary conditions. However, this elasto-plastic 2-D plane strain model is able to reproduce the main aspects of the behaviour of a buried flexible culvert for rockfall protection.

4.4 Transmitted accelerations

Figure 10 presents the measured and numerically simulated accelerations at the crown of the culvert. It can be observed that the amplitudes for the first cycle, in both simulated and experimental results, are approximately two times gravity, or 2 g. The numerical results show a shorter duration than found by the experimental results.

4.5 Discussion

The results from this preliminary study show that the model can simulate several aspects of the impact and the wave propagation in the soil quite well. The model underestimates the penetration depth compared to the

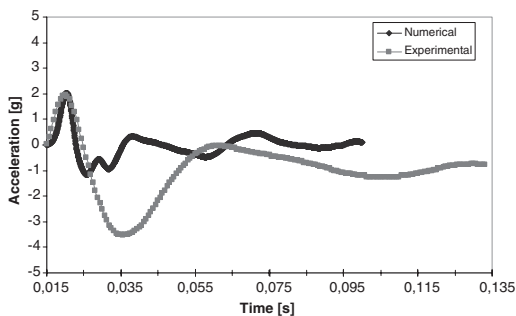


Figure 10. Comparison of transmitted accelerations in culvert for a 200 kg rock block impact from 10 m and numerical simulation.

experimental results. The reason for this is that the finite element model cannot describe the process involved in the displacement of particles in the vicinity of the impact, and the inappropriate use of a 2-D simulation.

The model also seems to overestimates the peak deceleration, but experimental results may be affected by a possibly too low sampling rate for the accelerometer placed on the falling rock.

For the acceleration of the crown of the culvert the simulation was found to give similar amplitude response, but the numerical solution showed oscillations with shorter duration which most likely could be explained by the fact that this is a 2-D simplification of a 3-D problem. Further analyses, comparing a 2-D and 3-D model, and using a more advanced soil model must be performed to investigate this.

5 CONCLUSIONS

In this paper, a simplified numerical model for a buried flexible culvert subjected to rock fall loading has been presented. A very rough 2-D approximation to a real 3-D problem has been considered. Regardless, a reasonable agreement was found between the simulated and experimental results. It has been showed that the 2-D numerical model underestimates the penetration depth. It is believed that a different soil model, which can take into account the process of displacement of particles in the vicinity of the impact, must be considered.

Generally, a protection system against rock fall impacts considering the use of buried flexible culverts require competent backfill material and a backfill procedure that ensures an optimal soil structure interaction. Further emphasis must be placed on:

- That the cushion layer must provides enough cover against penetration, and that it act as a shock absorber against the impact.
- The cushion layer must also be constructed such that it will distribute the load. Numerical simulations may be very useful in identifying the effects of using different designs and alternative cushions and back-fill materials.

6 ONGOING WORK

This preliminary study is part of an ongoing work regarding buried flexible structures subjected to rock-fall impact as a PhD study at NTNU in cooperation with the Norwegian Public Roads Administration.

More field tests may be performed this year and refined numerical analyses will be made. The need for doing a full 3-D analysis is obvious. More elaborate

laboratory tests on the backfill gravel should also be available shortly, which should enable the use of a more advanced soil model. Further the behaviour of the soil in the near impact zone will require some additional considerations.

ACKNOWLEDGEMENTS

Authors are grateful to acknowledge the Norwegian Public Roads Administration for financial support for the experimental studies. The authors also wish to thank the International Centre for Geohazards (ICG) and the Research Council of Norway for supporting this research.

REFERENCES

- Asset International LTD. 2002. Road and Bridges agreement certificate No91/R059. Newport: UK.
- Descoedres, F. 1997. Steinschlag. *Mitteilungen der Schweizerischen Gesellschaft für Boden- und Felsmechanik*. 135.
- Ebeltoft, R. & Larsen, J.O. 2006. Instrumentation of buried flexible structure subjected to rock fall loading. Joint international conference on computing and decision making in civil and building engineering. Montreal: Canada.
- Gu, Q. & Lee, F.H. 2002. Ground response to dynamic compaction of dry sand. *Geotechnique* 52(7): 481–493.
- Jacquemoud, J. 1999. Swiss guideline for the design of rock-fall protection galleries: Background, safety concept and case histories. In H. Masuya & V. Labiouse (eds.), *Impact load by rock falls and design of protection structures; Proc. Joint Japan-Swiss Sci. Seminar.*, Kanazawa, 4–7 October.
- Kishi, N. 1999. Absorbing performance of sand cushion and three-layered absorbing system. In T.S. Lok (ed.) *Shock and impact loads on structures; Proc. 3rd Asia-Pacific Conference.*, Singapore, 24–26 November. Singapore: CI Premier.
- Labiouse, V., Descoedres, F. & Montani, S. 1996. Experimental study of rock sheds impacted by rock blocks. *Structural Engineering International* 3: 171–176.
- Montani Stoffel, S., Labiouse, V. & Descoedres, F. 1999. Vertical and inclined impacts of rock blocks on a rock shed model. In *Rock Mechanics; Proc. 9th Int. Symp.*, Paris, 24–26 August, Rotterdam: Balkema.
- Pichler, B., Hellmich, C. & Mang, H.A. 2005. Impact of rocks onto gravel, design and evaluation of experiments. *International Journal of Impact Engineering* 31(5): 559–578.
- Ta, K.D. & Rogers, R.J. 1985. Control of elastic plane wave dispersion in two-dimensional finite element meshes. *Computers and Structures* 21(6): 1145–1151.
- Zerwer, A., Cascante, G. & Hutchinson, J. 2002. Parameter estimation in finite element simulations of Rayleigh waves. *Journal of Geotechnical and Geoenvironmental Engineering* 128(3): 250–261.

Two and three-dimensional modeling of abutment-backfill system on soft ground

S. Dashdorj, S. Miura & S. Yokohama

Graduate School of Eng, Hokkaido University, Sapporo, Hokkaido, Japan

K. Masumura

Masumura Survey – Design Inc, Abashiri, Hokkaido, Japan

ABSTRACT: In order to reduce a weight of embankment constructed on soft ground air foamed lightweight material has been developed in Japan. The material was applied for bridge abutment backfill and abutment-backfill system behavior is investigated in this research. Reduction of displacement and lateral backfill pressure by placing of elastic plates in FCB backfill is examined by FE analysis. Results from FE analysis revealed that placing of elastic plates in a backfill is effective to reduce the lateral backfill pressure.

1 INTRODUCTION

Application method for embankments of air foamed lightweight material is called Foamed Cement Banking (FCB) as stated in Foamed Cement Banking Method (2000). The material is denoted here as FCB. FCB is made by mixing cement and water and by adding foaming agent that makes material light in its weight. A bridge abutment backfilled with FCB constructed on soft ground in Japan is investigated in detail.

The mechanical behavior and application method of FCB have been investigated by Mishima & Masumura (2000), Dashdorj et al. (2003) and Nagao et al. (1994). However, research on improvement of the application method has not been conducted.

A technique of placing of elastic plates in FCB as one of countermeasures for reduction of lateral pressure and displacement has been developed by Japan Highway Public Cooperation. The technique is examined by 2 and 3D FE analysis in this research.

2 FIELD INVESTIGATION

Bridge backfilled with FCB investigated in this research is constructed in Japan. Abutment No2 is investigated as shown in Figure 1. The abutment is 11.05 m in height and 11.0 m in width was supported by piles on soft ground. The subsoil profile under the abutment-backfill system is consisted of cohesive and sandy layers. In order to investigate deformation behavior of abutment-backfill system settlement at FCB surface and

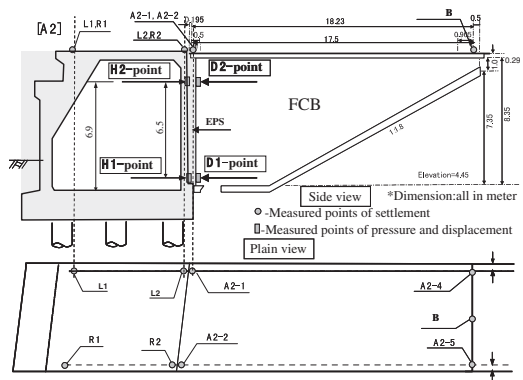
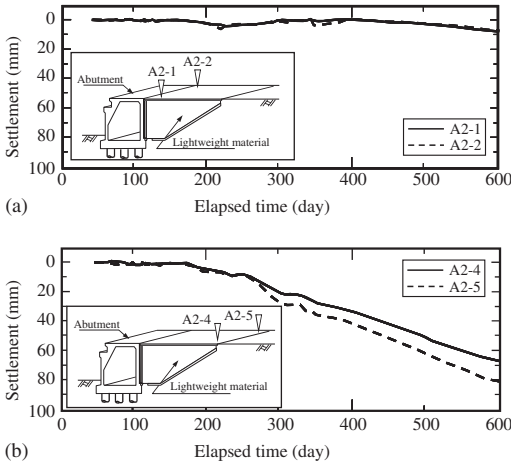


Figure 1. Abutment-backfill system.

horizontal displacement of FCB backfill, and lateral backfill pressure are measured over 600 days after construction of FCB backfill. Measured points of settlement and displacement are shown in Figure 1.

Figure 2a, b show the measured results of settlement accumulated on the surface of FCB backfill. Figure 2a shows that FCB backfill at A2-1 and A2-2 points have been settled slightly over elapsed time. However, settlement of FCB at A2-4 and A2-5 points occurred remarkably with the increase of time as it is illustrated in Figure 2b. Figures 2a, b give an image that as the elapsed time increases FCB backfill is tilting backward at the top of abutment but pushing at the



Figures 2a, b. Settlement of FCB backfill over elapsed time.

bottom of abutment. In the case if the settlement on FCB surface continuously increases the traffic hazard might be occurred. To prevent from such damage the improvement method is essential to apply.

3 NUMERICAL ANALYSIS

3.1 Modeling of abutment-backfill system

FCB-backfill system with its underground soil layers modeled and analyzed by FEM. Mohr-Coulomb elasto-plastic model was applied for embankment and also for subsoil layers laid beneath abutment-backfill system. Concrete for abutment and piles were assumed as linear elastic material in this analysis. Asphalt for pavement laid on FCB and embankment is modeled as linear elastic material.

A mesh for 2D analysis is generated for the analysis even though the deformation of the ground in the direction perpendicular to the bridge axis is completely neglected which is not true in actual case.

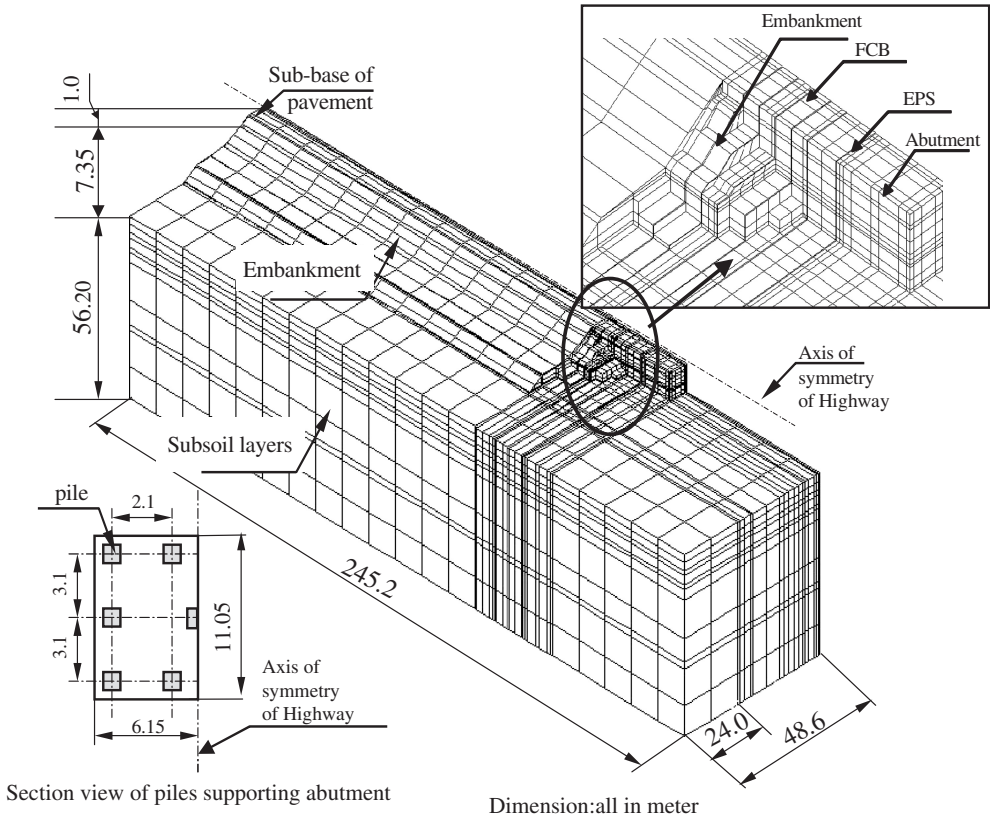


Figure 3. Three-dimensional mesh generation.

Considering the existence of piles and 3D behavior of abutment-backfill system, 3D FE analysis was performed. It was assumed for 3D mesh generation that the alignment of the highway is symmetrical, for simplicity and speedy analysis; a half of the highway was analyzed. A complete view of model simulated by 3D analysis is shown in Figure 3. Boundary condition is fixed as the same as that fixed for 2D mesh. The bottom boundary of the ground layer was fixed as rigid horizontally and vertically. 12590 elements and 14495 nodes were used for 3D mesh, where 8-node hexahedron isoparametric elements were employed.

3.2 Mechanical parameters

Model parameters adopted for concrete abutment, FCB backfill, asphalt pavement and soil layers were specified as shown in Table 1. Parameters for concrete abutment and embankment are taken the same as those were used for typical road and bridges.

Parameters for asphalt for pavement are fixed as the same as that fixed for typical asphalt layer for highway constructed in Japan. For ground layers, internal friction angle, ϕ was determined as specified in the Specifications of highway bridges (2002) and elastic modulus of FCB is set as $8.42 \times 10^5 \text{ N/m}^2$ which is an ordinary rigidity of FCB at 28 days curing condition as specified in Lightweight banking method (2000). Cohesion, c for FCB was determined as half of compressive strength of FCB and Poisson's ratio, ν is taken 0.2 as accepted for case after construction.

In the model, joint element is fixed between EPS and FCB in order to consider an occurrence of sliding between the EPS and FCB backfill.

4 RESULTS AND DISCUSSIONS

4.1 Comparison of 2D and 3D FE analysis results

A series of FE analysis were conducted by inputting measured settlements at the surface of FCB backfill as indicated B point as shown in Figure 2. Figure 4 shows a relationship between lateral backfill pressure at bottom of abutment, H1 and settlement on FCB backfill surface at B point. In this figure measured data at field were compared with data simulated by 2D and 3D FE analysis. From this figure, it can be understood that 3D analysis results were compared well with measured data at the field. However, lateral backfill pressure was overestimated by 2D analysis.

Relationship between horizontal displacement of FCB backfill at bottom of abutment and settlement on FCB backfill surface at B point is given in Figure 5. This figure shows that analysis results simulated in 3D condition are in good agreement with measured data at field. However, analysis results simulated in 2D condition didn't show a good agreement with measured data at field.

From those figures, it can be said that 3D analysis can simulate abutment-backfill system behavior well compare to 2D analysis. This fact indicates that the difference of analysis dimension influences the predicted backfill pressure and deformation of bridge abutment-backfill system. Analysis on lateral displacement of a pile-supported abutment constructed in a soft subsoil profile was performed by Wakai et al. (1997). Their research also approved that abutment with pile foundation is simulated well in 3D simulation than the simulation in 2D condition.

Table 1. Mechanical parameters.

	Elastic modulus E (kN/m ²)	Unit weight γ (kN/m ³)	Poisson's ratio ν	Cohesion c (kN/m ²)	Internal friction angle ϕ (°)
Concrete	2.45×10^7	24.0	0.167	—	—
EPS	1.96×10^3	0.12	0.075	—	—
Asphalt pavement	5.89×10^5	20	0.35	—	—
Upper subbase	1×10^5	20	0.35	—	—
Lower subbase	5×10^4	20	0.35	—	—
FCB	8.42×10^5	6.4	0.2	6.72×10^2	0
Joint element	1.00	—	—	—	—
Embankment	1.96×10^4	19.0	0.35	0	30
Cohesive soil (1)	2.84×10^3	13.0	0.35	18	0
Sandy soil (1)	4.63×10^3	18.0	0.35	0	25
Cohesive soil (2)	4.36×10^3	16.0	0.35	36	0
Cohesive soil (3)	1.74×10^3	18.0	0.35	21	0
Sandy soil (2)	1.32×10^3	18.0	0.35	0	26.9
Sandy soil (3)	3.43×10^3	18.0	0.35	0	29.3
Cohesive soil (4)	3.43×10^3	16.0	0.35	54	0
Sandy soil (4)	8.33×10^3	18.0	0.35	0	31.4
Cohesive soil (5)	9.80×10^3	18.0	0.35	69	0

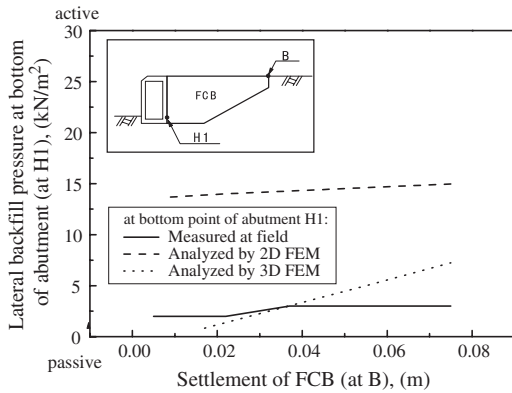


Figure 4. Relationship between lateral backfill pressure and settlement.

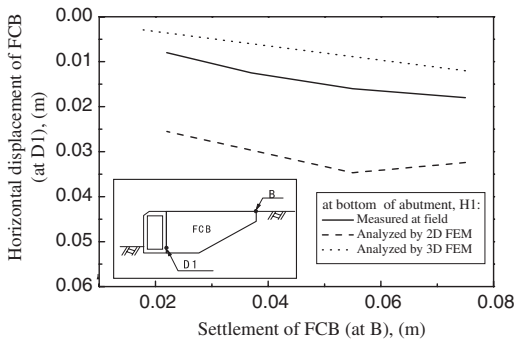


Figure 5. Relationship between horizontal displacement and settlement.

4.2 Placing of elastic plate in FCB backfill and its effect

It is observed at some construction field in Japan that the large deformation such as tilt of FCB backfill has been occurred as stated in Lightweight soil method (2005). Such tilting of FCB backfill may be generated due to consolidation of soft ground. Difference of unit weight between FCB material and ordinary embankment causes forming of the discontinuous surface at the border of FCB and ordinary embankment. Such discontinuous surface might disturb the stability of FCB backfill and be one of the reasons of traffic hazard.

As a technique for reducing of lateral backfill pressure on abutment and settlement on FCB surface, a method of placing of thin elastic plate in FCB backfill is specified in the Specifications of design and construction for FCB method (2005). Fixing of elastic plate in FCB backfill and its effect on placement location of elastic plates to reduce lateral backfill pressure is evaluated by FE analysis in this research. Locations

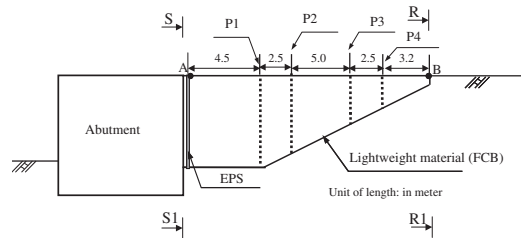


Figure 6. Location of inserting plates.

Table 2. Notation of plates.

Single plate case	Double plates case	Triple plates case
P1: (P1)	P1-2: (P1) and (P2)	P1-2-3: (P1), (P2) and (P3)
P2: (P2)	P1-3: (P1) and (P3)	P1-2-4: (P1), (P2) and (P4)
P3: (P3)	P1-4: (P2) and (P4)	P1-3-4: (P1), (P3) and (P4)
P4: (P4)	P2-3: (P2) and (P3)	P2-3-4: (P2), (P3) and (P4)
	P2-4: (P2) and (P4)	
	P3-4: (P3) and (P4)	

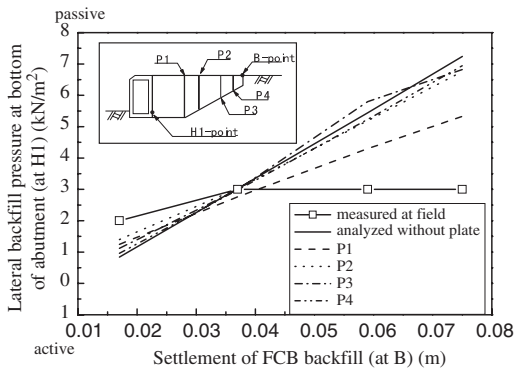
*P: stands for plate.

selected for the placement of elastic plates are shown in Figure 6. Notation of plates is shown in Table 2.

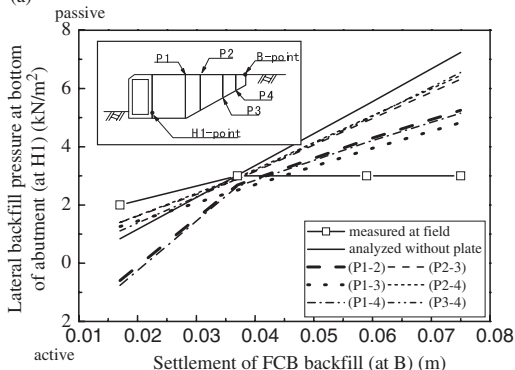
Combination of single, double and triple plate cases are examined through FE analysis to predict an efficient location for placing of elastic plates in FCB backfill in order to reduce lateral backfill pressure. In present analysis thickness of elastic plate is fixed as 100 mm. For parameters of elastic plate, unit weight, γ and Poisson's ratio, ν are assumed to be the same as for EPS, which is the interface element between concrete abutment and FCB backfill. Young's modulus, E for plate is accepted to be as the same as that was assumed for joint element fixed between EPS and FCB backfill.

4.3 Lateral backfill pressure of FCB backfill

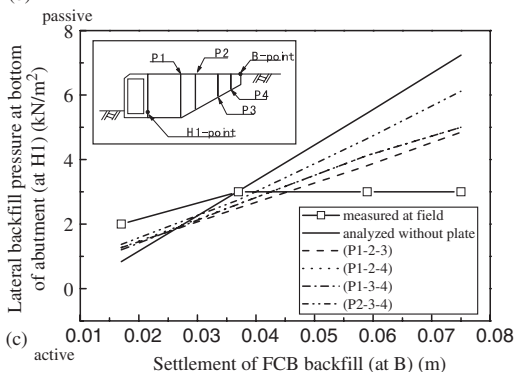
In order to investigate an effect of inserting plates in different locations in FCB backfill, lateral backfill pressure at bottom of abutment at H1 and horizontal displacement of FCB backfill at D1, the bottom of FCB (see Figure 2) were examined based on FE analysis. Figure 7a-c show a relationship between lateral backfill pressure at bottom of abutment at H1 and settlement on FCB backfill surface at B predicted by 3D



(a)



(b)



(c)

Figure 7a–c. Lateral pressure and settlement relation: (a) single plate case, (b) double plate case (c) triple plate case.

analysis. In those figures, cases inserted elastic plates in FCB were compared with normal case of backfill without placement of plate.

When single plates denoted as (P1), (P2), (P3) and (P4) are inserted in FCB backfill, the lateral backfill pressure at bottom of abutment (at H1) had been decreased noticeably than that for without inserting of plate in FCB backfill as shown in Figure 7a. Measured data at field and predicted data simulated by FE

analysis for double and triple plate cases are shown in Figure 7b, c.

From Figure 7a–c, it was found out that for any plate combination cases with P1 plate, the lateral backfill pressure at bottom of abutment (at H1) had decreased remarkably than other plate combination cases. However, reduction in lateral backfill pressure is remarkable for inserting of single plate P1. From Figure 7a–c, it can be concluded that inserting of elastic plate located closer to the abutment wall is most effective for reduction of the lateral backfill pressure on abutment and the horizontal displacement of FCB backfill.

5 CONCLUSION

The following conclusions were derived based on 2D and 3D FE analysis:

1. Numerical analysis result showed that abutment backfill system behavior could be predicted by Mohr-Coulomb model well in 3D condition than 2D condition. 3 dimensional conditions couldn't be neglected in evaluation of abutment-backfill deformation behavior for a bridge abutment with pile foundation backfilled with lightweight material.
2. 3D FE analysis results approved that by placing of elastic plates in FCB backfill, the lateral backfill pressure on abutment and lateral displacement in ground have been decreased. A placement of elastic plate in FCB backfill is recommended as a countermeasure for reducing of FCB backfill pressure on abutment.
3. FE analysis results approved that placing of single plate in FCB backfill is more effective than placing double or triple plates to reduce the lateral backfill pressure. However if elastic plate is fixed closer to the abutment wall, the reduction in backfill pressure would be revealed more significantly.

ACKNOWLEDGEMENT

The authors would like to express their gratitude to Dr. Mishima, N. Mr. Fujioka, K. Prof. of engineering, Kitamura, Y and Kato, Y from Expressway Research Institute, Japan Highway Public Cooperation for their continuous support for the research.

REFERENCES

- Mishima, N. & Masumura, K. *Foamed Cement Banking Method*, 2000. Tokyo: Rikoh-Tosho, Co. Ltd.
- Dashdorj, S., Miura, S. & Yokohama, S. 2004. Effect of lightweight geomaterial on reduction of lateral earth

- pressure and its numerical evaluation. *Proc. of Annual Conference of JGS*, pp. 746–747.
- Nagao, K., Iriyama, T. & Kokubun, K. 1994. Earth pressure reduction method using air-bubble mixing light soil for backfilling. *The Foundation & Equipment*. 22, pp. 71–75.
- Japan Road Association. 2002. *Specifications for highway bridges*. Part 5, Seismic design.
- Wakai, A. et. al. 1997. Analyses of lateral displacement of a pile supported abutment constructed in a soft subsoil profile. *Soil & foundation*. Vol. 37, No 4, pp. 65–76.
- Lightweight soil method*. 2005. No 22, JGS, pp. 149-150, 233–235.
- Specifications on design and construction for FCB method*, 2005. Japan Highway Public Cooperation.

*Special session on numerical modelling
of ground improvement*

Stone columns – group behaviour and influence of footing flexibility

W.C.S. Wehr

Keller Holding GmbH, Offenbach, Germany

ABSTRACT: Recent research on the group action of stone columns points out that the behaviour of an isolated single column is quite different from the one of a stone column in a group of columns under a rigid footing. To highlight the differences, model tests of a rigid footing on a single sand column in clay and model tests of a rigid footing with various numbers of sand columns in clay are compared. Deformations of groups of stone columns depend as well on the rigidity of the footing. In order to demonstrate the different deformation mechanisms, model tests by Hu (1995) with a rigid and a flexible footing are compared.

Additionally a FE-re-calculation of the model tests is performed with an elasto-plastic constitutive model taking into account the mean grain diameter. Beginning with a single isolated column, the deformation mechanism of the column has been reproduced, detecting a wedge shaped shear zone below the footing. The same footing on 20 columns has been analysed to study the group effect. At the end the deformation mechanism of a group of columns below a flexible footing is reproduced. Finally recommendations for practical applications are given.

1 INTRODUCTION

Modelling forces and displacements of stone columns, the width of shear zones has to be considered correctly. This applies for single columns and for groups of columns as well (Wehr 1999a, Wehr 2004). The influences of different parameters like initial density, pressure level and mean grain diameter on the width of the shear zone was studied intensively with model tests (Tejchman '89, Hammad '91, Hassan '95) and could be reproduced with FE-calculations (Tejchman '97, Tejchman et al. '99).

Hu 1995 and Wood/Hu 1997 have observed in model tests with a group of stone columns, that the deformation mechanism depends on the stiffness of the footing.

In this publication model tests on a group of stone columns below a rigid and a flexible footing are compared, before re-calculations of the model tests by means of the finite element method are presented. The aim is to clarify the different deformation mechanisms, but not to curve fit the force displacement curves exactly. The latter is reserved for 3D-calculations.

2 MODEL TESTS

Model tests with groups of sand columns in clay have been executed by Hu ('95) and Wood ('98) to get a closer insight into the deformation mechanisms of a group of stone columns under footings.

The soils of the model tests are Speswhite kaolin clay which was reconstituted from a slurry with a plasticity index of 27 and an average undrained cohesion of $c_u = 13$ kPa, and a poorly graded medium Loch Aline sand ($d_{50} = 0.32$ mm, $e_{max} = 0.80$, $e_{min} = 0.56$, $0.67 < e < 0.74$).

The preparation of the tests, the set-up and all soil and column parameters used were described in detail by Hu (1995). A summary may be found in Wehr (2004).

2.1 Stiff footing

All 16 model tests with columns below a rigid footing were executed using displacement control with a velocity of $v = 0.061$ mm/min. Compared to the tests with single stone columns by Witt (1978) with a velocity of $v = 0.5$ mm/min and a testing time of only 40 min the eight times smaller velocity in the tests by Hu does not play a negligible role. Therefore the stiffness of the clay will most likely increase with testing time. The contribution of the loading velocity on the force and settlement of piles have been shown by Krieg et al. (1998).

The main result in terms of deformation under the footing is that a wedge shaped body is displaced vertically in connection with bulging and buckling of the columns, see Fig. 1. Buckling was observed near the edges of the footing close to the ground surface and bulging occurred under the center of the footing in a deeper region. The columns adjacent to the footing showed only a small amount of bending.

The load bearing mechanism is significantly influenced by the length of the columns as compared to the diameter of the footing D . If the length of the columns l is less than or equal to D ($l \leq D$), the base of the columns will transfer the load to the underlying clay resulting in a significant punching of the columns, Fig. 2. But if the length of the columns is larger than $1.5D$ the penetration of the columns into the clay is insignificant.

This mechanism could be reproduced by FE-calculations by Wehr (2004). Additionally shear zones in

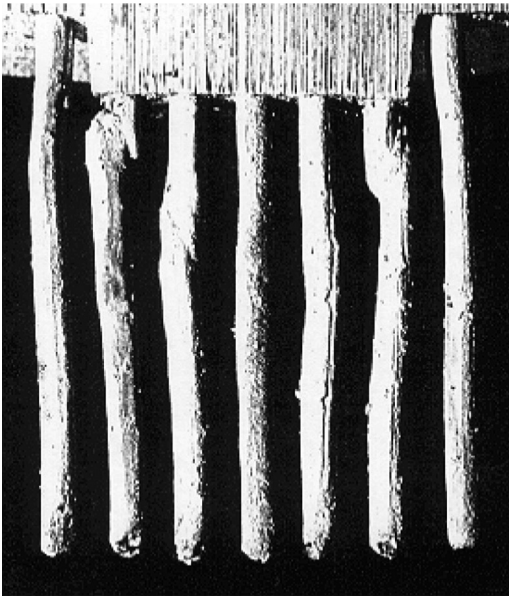


Figure 1. Deformed group of long slender columns, test TS17 (Hu '95).

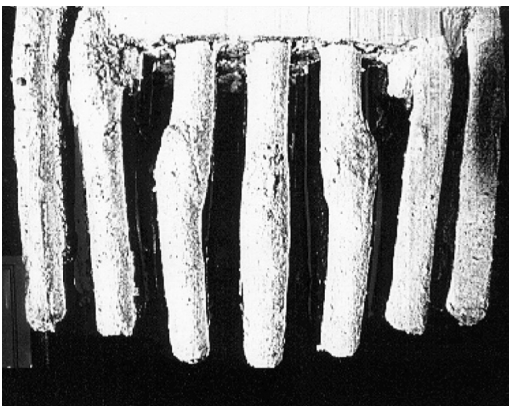


Figure 2. Deformed group of short thick columns, test TS08 (Hu '95).

the clay were detected which were not visible in the model tests due to their small thickness.

2.2 Flexible footing

Furthermore one test with a flexible footing has been executed, Hu (1995). The load was applied by a pressurized cylinder with its bottom part being a rubber membrane. The installation of the columns was not changed with respect to the tests with the stiff footing, however a 4 mm thick sandy load distribution layer was used on top of the columns.

In contrast to the tests with a rigid footing this test was executed with load control. After rising the load from $p = 120$ kPa to $p = 140$ kPa and 8 days loading time the soil displaced rapidly within a few seconds and the test had to be stopped.

Fig. 3 shows the asymmetric deformation of the columns. No distinct wedge-shaped soil body with shear zones could be observed below the footing.

It will be analysed in the following FE-calculations, if this kind of deformations is typical for a flexible footing.

In Fig. 4 the load displacement curves of different tests with rigid and flexible footing are presented.

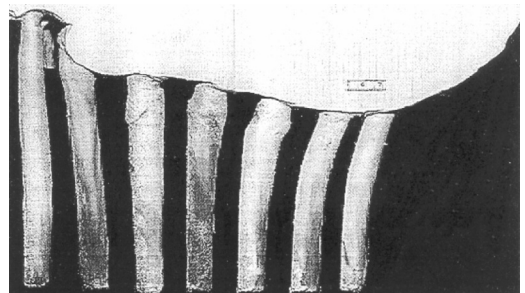


Figure 3. Deformed group of columns below flexible footing (Hu '95).

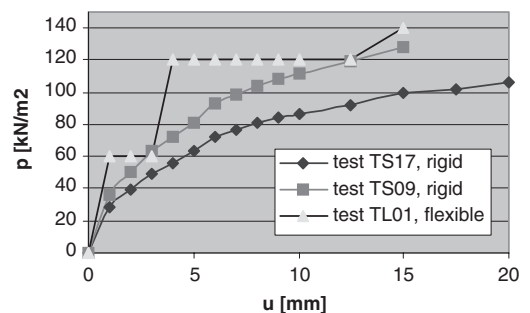


Figure 4. Load-displacement curve below a rigid and flexible footing (after Hu 1995).

Test TS17 of fig.1 and 4 (rigid) with $c_u = 14$ kPa, column diameter $d_s = 11$ mm and column length $l_s = 160$ mm differs from test TS09 (rigid) because of the different column diameter $d_s = 17.5$ mm. In Fig. 4 it may be seen, that slightly higher loads are applicable in test TS09.

Test TL01 (flexible) corresponds to test TS09 (rigid) apart from the slightly higher $c_u = 18$ kPa which results again in a higher applicable load, fig. 4. The extraordinary high load steps in this test were leading to failure which can be guessed nearly optically.

3 ELASTO-PLASTIC CONSTITUTIVE LAW

The Cosserat elasto-plastic constitutive model used here includes isotropic hardening and softening. It has been proposed by Mühlhaus ('87) and is described in detail by Tejchman ('89,'97) and Tejchman/Wu ('93) and Wehr ('99).

Differences from the conventional theory of plasticity are the presence of Cosserat rotations and couple stresses using the mean grain diameter as a characteristic length.

In Table 1, the parameters of the elasto-plastic model for the two materials considered in recalculations of model tests are summarized. The parameters for Karlsruhe sand have been determined by Tejchman ('97) and the parameters for Ahrtal clay has been estimated from the material parameters given by Witt ('78). Modification were necessary due to the loose state only for the peak friction angle and for the E-modulus similar to the parameters by Tejchman (1997). The parameters of Speswhite kaolin clay were estimated from the parameters of test TS17 given by Hu (1995). An important parameter is the cohesion which was determined from vane shear tests. The E-modulus was evaluated using a graph by Ladd et al. (1977) with $E/c_u \sim 100$. The Cosserat-constants were not modified compared to Wehr (2004). Their

Table 1. Material parameters for the elasto-plastic model (Loch Aline Sand, Speswhite clay).

	C [kPa]	φ_p [Grad]	φ_c [Grad]	β_1 [-]
Sand	0	37	35	3
Clay	14	0	0	0
	E [MPa]	ν [-]	γ_p [-]	γ_0 [-]
Sand	15	0.3	0.05	0.03
Clay	1.4	0.45	0.05	0.03
	d_{50} [mm]	a_1 [-]	a_2 [-]	a_3 [-]
Sand	0.32	0.375	0.125	1.00
Clay	0.002	0.375	0.125	0.25

influence have been demonstrated by Tejchman/Wu (1993).

Twelve material parameters are needed to characterise a soil material:

- cohesion c ,
- friction angle at peak φ_p and in the critical state φ_c ,
- angle of dilatancy $\beta = \beta_1 (\sin \varphi_p - \sin \varphi_c)$
- modulus of elasticity E ,
- Poisson's ratio ν ,
- shear strains at the peak γ_p and at the beginning of shearing γ_0
- mean grain diameter d_{50} and
- three Cosserat-constants a_1 to a_3

4 CALCULATIONS

The aim of the next sections is to demonstrate the different deformation mechanisms of a rigid and a flexible footing resting on a soft soil with stone columns. In order to compare both cases the dimensions and soil parameters of the rigid footing has been used for the flexible footing as well.

Utilizing the symmetry of the system only 3.5 of 22 columns have been modelled.

4.1 Stiff footing

Fig. 5 shows the upper part of the deformed group of columns after a displacement $u = 20$ mm. If these results are compared with Fig. 1, a wedge shaped part of the soil below the footing nearly undergoes no deformation. The edge of this wedge consists of a shear zone partly in the sand columns and partly in the clay having the same inclination in the model test and the calculation. Different deformations are observed in the center column which bulges, and in the middle and outer column where a shear zone (buckling) is observed. This corresponds exactly to the observations made during the model tests by Hu '95.

The calculated width of the shear zone around the wedge shaped area in fig. 6 is $d_s = 4$ mm ($10d_{50}$). A shear zone in the clay which could not be observed in the model tests due to the small thickness can be detected in fig. 6 near the column at the edge. It is worth to note that this shear zone extends only to a certain depth depending on the displacement of the column relative to the clay.

Fig. 7 shows the load-displacement curves of test TS17 and the recalculation for a rigid footing. Until a displacement of approximately 6 mm both curves are rather similar. However for larger displacements there seems to be a growing influence of the consolidation of the clay which has not been taken into account in this model.

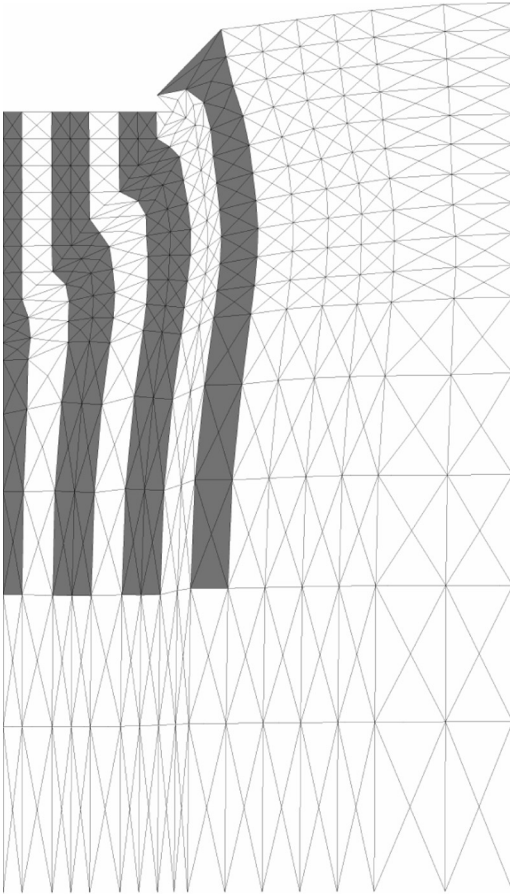


Figure 5. Deformed group of columns below rigid footing, upper part, $u = 20$ mm, clay (white) and column (grey).

4.2 Flexible footing

The displacements for a rigid and a flexible footing are chosen equally in a characteristic point which is $0.74 * D/2$ apart from the center of the plate with D being the diameter of the footing. After a displacement of $u = 10$ mm in the center of the footing the displacements are $S_{flex} = S_{rigid}/0,75$. The initial state for the flexible footing is a horizontal area. With increasing displacement the bending of the footing increases as well.

In fig. 8 the upper part of the deformed group of columns can be seen below a flexible footing after a displacement of $u = 20$ mm. In contrast to fig.5 no wedge shaped zone with shear zones and no buckling of columns is observed, but considerable bulging.

The form of shear zones for a flexible footing in fig. 9 is different from the one of a rigid footing in fig. 6. Starting with a broad vertical shear zone in

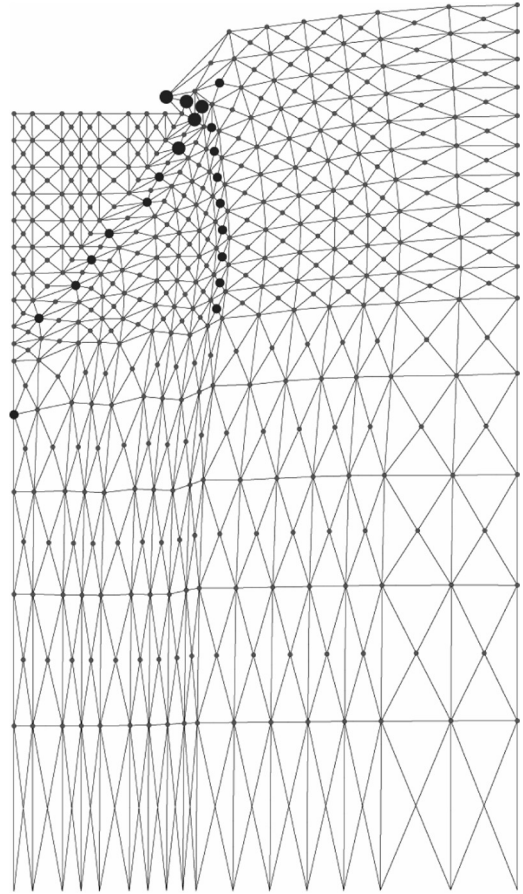


Figure 6. Deformed group of columns below rigid footing, upper part, $u = 20$ mm, Cosserrat rotations: small circle $\omega_c = 0.0$, large circle $\omega_c = 3.4$.

the clay at the edge of the footing, several approximately wedge shaped and parallel shear zones are created.

The first one starts at the edge of the footing in the clay, cuts the first sand column and ends in the clay between the columns.

The second one starts in a certain distance from the footing edge in the direction of the footing center and progresses in the shape of a wedge, similar to the rigid footing.

The third one in fig. 9 just started at this deformation stage. It starts again further apart from the footing edge and runs parallel to the second one only at deformations larger than 20 mm.

Concluding the above a pattern of approximately parallel shear zones is created in the case of a flexible footing. The more shear zones are created, the larger the deflection (bending) of the footing.

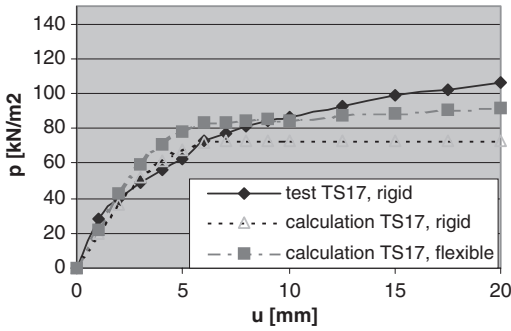


Figure 7. Load-displacement curves of rigid and flexible footing.

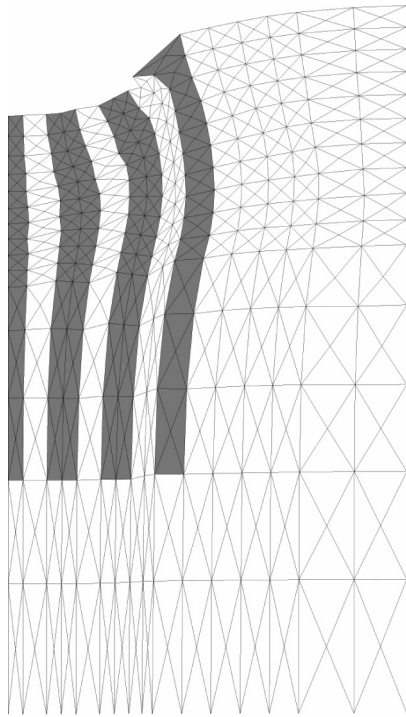


Figure 8. Deformed group of columns below flexible footing, upper part, $u = 20$ mm, clay (white) and column (grey).

Shear zones in the clay which were not observed in the model tests, may be seen in Fig. 9 between all columns and outside the column under the edge of the footing. Note, that these shear zone extends only to a limited depth depending on the movements of the columns relative to the clay. Concerning the widths of the shear zones in clay, they are too large due to too

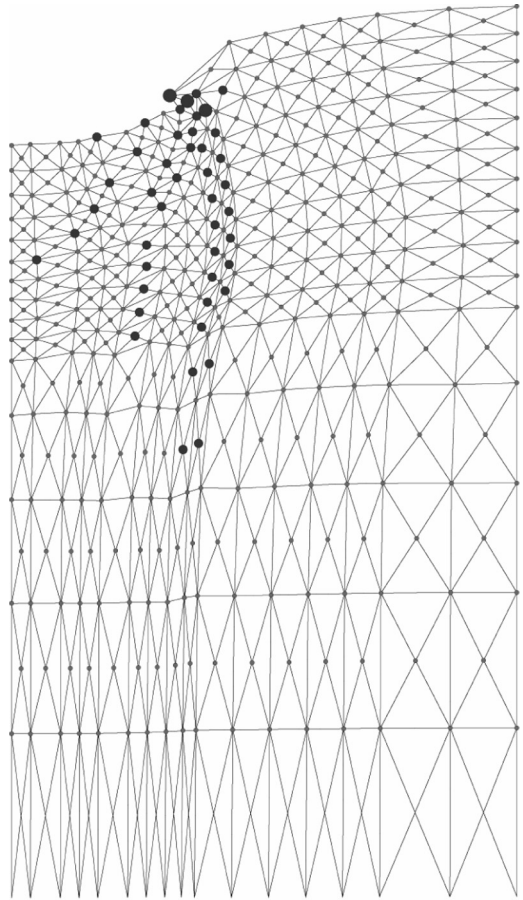


Figure 9. Deformed group of columns below flexible footing, upper part, $u = 20$ mm, Cosserrat rotations: small circle $\omega_c = 0.0$, large circle $\omega_c = 2.6$.

large elements chosen. Between two columns there should exist a shear zone close to each column rather than one shear zone extending from the left column to the right column. The possibility of the unification of two shear zones exists only if two column boundaries are close enough together and the lateral deformation is limited (Wehr '97).

Fig. 7 additionally shows the calculated load-displacement curves of a flexible and a rigid footing. The results may be compared directly, because no other parameter has been changed except of the footing stiffness. The total load which a flexible footing can bear is slightly higher for all deformations than the load of a rigid footing. This is essentially due to the higher forces in the clay which are caused by the wider shear zone below the footing edge and an additional shear zone between the columns.

5 CONCLUSIONS

Model tests of groups of stone columns in clay show a fundamentally different deformation mechanism, if a rigid or a flexible footing is used.

Because of sudden large displacements which occurred during the test with the flexible footing, no general conclusions could be drawn.

Re-calculations of the model tests have been performed by means of the finite element method with an elasto-plastic constitutive law within the Cosserat continuum. In this way, the mean grain diameter which is essential to capture shear zones, is taken into account and the solution is mesh independent.

In the model tests with a rigid footing and in the re-calculation a deformation mechanism was observed with a wedge shaped deformation directly below the footing. Buckling was observed near the edges of the footing close to the ground surface and bulging occurred under the center of the footing in a deeper region.

In case of a flexible footing bulging of all columns in the upper part was observed without any buckling of the columns. Cosserat rotations display multiple parallel shear zones forming a shear zone pattern. The larger the flexibility of the footing, the more shear zones occur.

The applicable load on a flexible footing is always larger than the one on a rigid footing, if the average deformations are equal. It is recommended to construct footings on stone columns only as stiff as necessary making use of the maximum value of the allowable differential settlements.

REFERENCES

- Hammad, W. (1991): Modelisation non lineaire et etude experimentale des bandes de cisaillement dans les sables. PhD. Thesis, Universite de Grenoble,IMG, Labo 3S
- Hassan, A.H. (1995): Etude experimentale et numerique du comportement local et global d'une interface sol granulaire-structure. PhD. Thesis, Universite de Grenoble, IMG, Labo 3S
- Hu, W. (1995): Physical modelling of group behaviour of stone column foundations. PhD thesis, University of Glasgow
- Krieg S., Goldscheider M. (1988): Bodenviskosität und ihr Einfluß auf das Tragverhalten von Pfählen. Bautechnik, Heft 10, 806–820
- Ladd C.C., Foott R., Ishihara K., Schlosser F., Poulos H.G. (1977) Stress-deformation and strength characteristics. State of the art report. Proceedings of the 9th. Int. Conf. on Soil Mech. and Found. Eng., Tokyo, 2, 421–494
- Mühlhaus H.B. (1987): Berücksichtigung der Inhomogenitäten im Gebirge im Rahmen einer Kontinuumstheorie. Publication of the institute for soil and rock mechanics, Karlsruhe university, vol. 106
- Tejchman J. (1989): Scherzonenbildung und Verspannungseffekte in Granulaten unter Berücksichtigung von Korndrehungen. Publication of the institute for soil and rock mechanics, Karlsruhe university, vol. 117
- Tejchman J. (1997): Modelling of shear localisation and autogeneous dynamic effects in granular bodies. Publication of the institute for soil and rock mechanics, Karlsruhe university, vol. 140
- Tejchman J. (1998): Numerical modelling of shear localisation with a polar hypoplastic approach. 4th Int. Workshop on Localisation and Bifurcation Theory for Soils and Rocks, Gifu, Japan, 323–332
- Tejchman J., Wu W. (1993): Numerical study on patterning of shear bands in a Cosserat continuum. Acta Mechanica, Springer Verlag, Vol.99, 61–74
- Tejchman J., Herle I., Wehr W. (1999): FE-studies on the influence of initial void ratio, pressure level and mean grain diameter on shear localisation. Int. Journal for Numerical and Analytical Methods in Geomechanics, Vol. 23, 2045–2074
- Wehr, W. (1999): Granulatummüllte Anker und Nägel – Sandanker – Publication of the institute for soil and rock mechanics, Karlsruhe university, vol. 146
- Wehr, W. (1999a): Schottersäulen; Das Verhalten von einzelnen Säulen und Säulengruppen. Geotechnik, Heft 1/1999, S. 40–47
- Wehr, W. (2004): Stone columns – single columns and group behaviour. 5th Int. Conf. On Ground improvement techniques, Malaysia, 329–340
- Witt, K.J. (1978): Versagensmechanismus einzeln belasteter Schottersäulen im bindigen Untergrund bei plötzlicher Belastung. Thesis of the institute for soil and rock mechanics, Karlsruhe university
- Wood D.M., Hu. W. (1997): Mechanisms of load transfer deduced from failure modes of model stone column foundations. Int. Symposium on Deformation and Progressive Failure in Geomechanics, 5–7.Oct. 1997, Nagoya, Japan, 799–804

Exercise on calculation of stone columns – Priebe method and FEM

J. Wehr

Keller Holding GmbH, Offenbach, Germany

I. Herle

Institute of Geotechnical Engineering, Technische Universität Dresden, Germany

ABSTRACT: The results of an international class-A prediction of an embankment on vibro stone columns are presented. The settlements of the unimproved and the improved case should be calculated with different methods. At first the analytical Priebe method was applied to estimate the final settlements and the Balaam-Booker method was used to calculate the time dependent settlements. Additionally, a finite element model was used with the conventional Mohr-Coulomb soil model. Settlements from calculations are compared, yielding very similar results close to the measured values.

1 INTRODUCTION

Improvement of soft soils with stone columns becomes an everyday practice in the construction industry. The vibro-replacement method is well established and suited for a wide range of soils. It has several positive effects on the treated soil, namely an increase of strength, stiffness and permeability.

The design methods for vibro-replacement are mainly semiempirical. They are based on analytical solutions of simplified geometry and idealized material properties of the column and surrounding soil. The overall trend for the application of numerical methods offers an alternative approach for the design. However, the comparability of numerical simulations with traditional methods should be guaranteed for standard situations. Only such a basis allows for extrapolations towards unknown conditions.

The following paper presents class-A predictions submitted in the framework of an international exercise on calculation of stone columns, organized in Paris, 2004. The settlements below an embankment on both, unimproved and improved soil were calculated with different methods. Moreover, time effects due to consolidation had to be taken into account.

2 PREDICTION EXERCISE

2.1 Input data

For the Symposium ASEP-GI in Paris, 2004, a prediction exercise on the behaviour of an embankment on a soft soil improved by stone columns was organized.

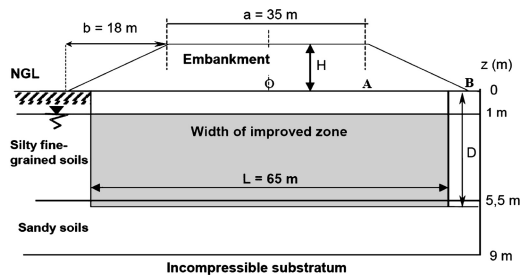


Figure 1. Embankment and subsoil geometry (ASEP-GI, 2004).

The geometry of the embankment and of the improved zone is shown in Fig. 1.

The deformation properties of the subsoil, consisting mainly of silty fine-grained soils, were described by pressuremeter moduli E_M . These were accomplished by a few index properties, compressibility and swelling indices (C_c and C_s) of the fine-grained soil, undrained shear strength c_u and consolidation coefficient c_v , see Fig. 2.

The prescribed geometrical setup of the stone columns and their parameters are summarized in Fig. 3.

The construction procedure included four steps: after the initial state (0), the embankment reached the height of 6 m during 40 days (1), after a rest period of 120 days (2), next 3 m of the embankment were constructed during 40 days (3). The final calculation results were asked for 10 years after the construction beginning (4). Prediction outputs consisted of values

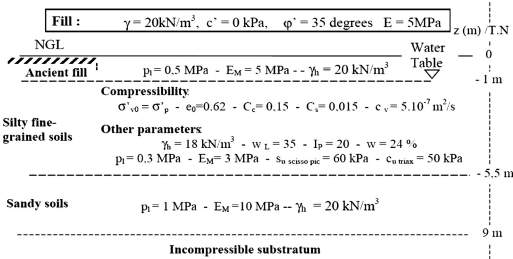


Figure 2. Subsoil properties (ASEP-GI, 2004).

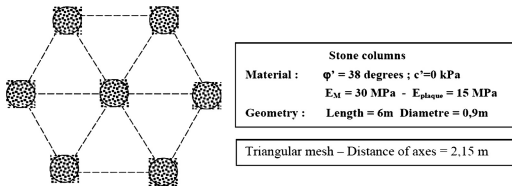


Figure 3. Stone columns parameters (ASEP-GI, 2004).

of the settlements at the points O, A and B (see Fig. 1) for both, unimproved and improved ground.

2.2 Priebe method

A widely used design method for the vibroreplacement was proposed by Priebe, 1976. The basic version combines several simplifying assumptions: stone columns are in the active limit stress state, keeping their volume constant and being supported by the earth pressure at rest of the surrounding soil. Thus, the vertical deformation of the columns corresponds to their radial expansion and the load is distributed between soil and columns according to their area ratio. More details and design charts can be found e.g. in Dhouib et al (2004).

Priebe method was applied for the calculation of final settlements (software GRETA). Pressuremeter moduli were transformed into constrained (oedometric) moduli using the following scheme for the ratios $E_M/E_{oed} = \alpha$: 0.5 for normally consolidated soils, 0.33 for sandy soils, 0.5 for normally consolidated fill and 0.25 for gravel.

The time-dependent behaviour due to consolidation effects is not covered by the Priebe method. One can use solutions for the radial flow to wells published by Barron (1948). His approach originates from the application of the Terzaghi theory for this particular problem case. Several simplifying conditions are assumed: (i) all loads are initially taken by the excess pore water pressure, (ii) all deformations take place only in vertical direction and (iii) water inflow to the drain is radial, (iv) soil and column have the same stiffness. As extension of this theory, effects of a remoulded zone at the column margin and effects of the column permeability can be treated.

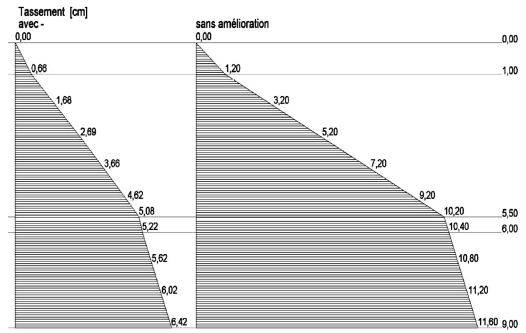


Figure 4. Settlements at the end of the 2nd stage calculated by the Priebe method.

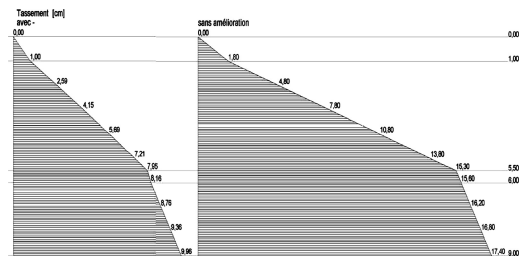


Figure 5. Final settlements calculated by the Priebe method.

For the prediction exercise, time effects were taken into account by the theory of Balaam and Booker (1981). It originates from the Biot's consolidation theory and, contrary to the Barron's solution, different stiffnesses for soil and column are considered. Nevertheless, the mechanical behaviour is described only by elasticity.

The distribution of the calculated settlements at the end of the second construction stage (embankment height of 6 m, rest period) is shown in Fig. 4. The values reached 7 cm with and 12 cm without stone columns. For the final stage, 10 cm with and 18 cm without stone columns were calculated, see Fig. 5.

The results of this standard calculation procedure show that the consolidation is already finished after 16 days. Therefore, the values of settlements of the 6 m high embankment after the first stage (40 days) and after the second stage (160 days) are equal. The same observation applies to stages 3 and 4 in case of the 9 m high embankment. This conclusion coincides well with the experience that the consolidation time with stone columns is usually less than 1–2 months.

2.3 FE calculation

Numerical simulations of the calculation exercise were performed with the finite element code Plaxis,

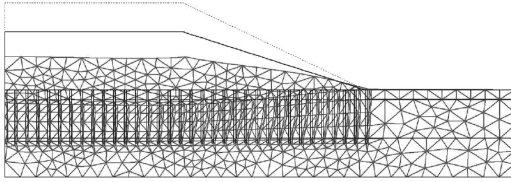


Figure 6. Finite element mesh.

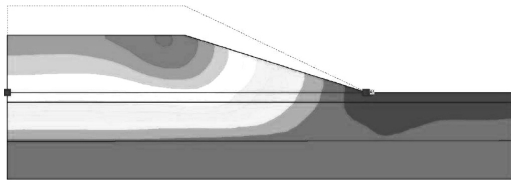


Figure 7. Distribution of vertical displacements at the 2nd stage (unimproved subsoil).

Table 1. FE results – unimproved ground.

Stage	t (days)	H (m)	O (cm)	A (cm)	B (cm)
1	40	6	9.8	11.2	-1.2
2	160	6	10.8	12.4	-1.2
3	200	9	15.6	16.4	-1.0
4	3650	9	16.5	17.5	-1.0

Version 7. Plane-strain 6-node elements were used in the stepwise coupled analysis with closed consolidation boundaries at the mesh edges. In agreement with the prescribed material parameters, linear-elastic perfectly-plastic constitutive model (Mohr-Coulomb) was considered for both, soil and column material (Bazgan, 2004). The finite element mesh is shown in Fig. 6.

Due to plane strain conditions, isolated stone columns were replaced by continuous stone walls. Their width of 0.2 m was obtained from the condition of keeping the volume of the improved soil unchanged.

A typical distribution of vertical displacements in case of the unimproved subsoil is shown in Fig. 7. It may be noticed that the largest deformations are concentrated below the embankment edge and not, as could be expected, in the middle of the fill. This can be related to the stress state in the subsoil which is close to the limit one and extensive plastic zones develop.

Calculated displacements for the unimproved ground are summarized in Table 1.

The behaviour of the embankment on unimproved soil (Fig. 7) can be compared with the case including stone columns. Fig. 8 shows vertical deformations for the embankment height of 9 m in the final stage after

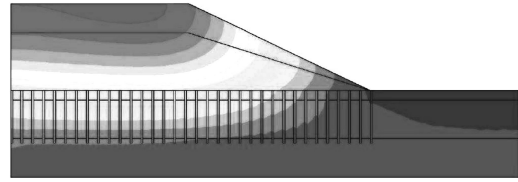


Figure 8. Distribution of vertical displacements at the final stage (improved subsoil).

Table 2. FE results – improved ground.

Stage	t (days)	H (m)	O (cm)	A (cm)	B (cm)
1	40	6	6.8	7.6	-0.2
2	160	6	6.8	7.6	-0.2
3	200	9	10.2	11.0	-0.2
4	3650	9	10.3	11.0	-0.2

Table 3. Comparison of Priebe and FE method for improved soil (Priebe/FEM).

Stage	O (cm)	A (cm)	B (cm)
1	6.4/6.8	6.4/7.6	-/-0.2
2	6.4/6.8	6.4/7.6	-/-0.2
3	10.0/10.2	10.0/11.0	-/-0.2
4	10.0/10.3	10.0/11.0	-/-0.2

10 years consolidation. The distribution of the deformations is more homogeneous in the latter case. Moreover, the maximum settlements are almost 40% smaller, reaching 11 cm.

An overview of the calculated settlements in case of improved ground is given in Table 2.

2.4 Discussion of the results

In case of improved soil, a comparison of the calculation results by the Priebe and the FE method in Table 3 reveals strikingly similar values (the settlements in point B at the end of the embankment cannot be calculated by the Priebe method).

The embankment of the calculation exercise was constructed after the submission of the predictions. The measured settlements reached settlements close to the ones of Tables. 1 and 3 (see the prediction of the authors, No. 8, in Fig. 8 in Mestat et al., 2004). It should be noted that many of the international experts had difficulties already to estimate the settlements in the unimproved case without stone columns. This was a quite surprising result of this class-A prediction.

It seems that the particular task chosen for the calculation exercise fulfils two important assumptions of

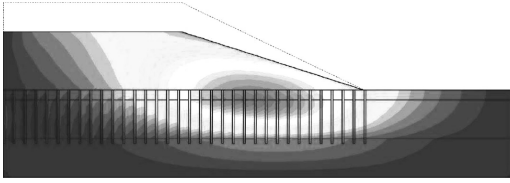


Figure 9. FE calculation, final stage: Horizontal displacements.

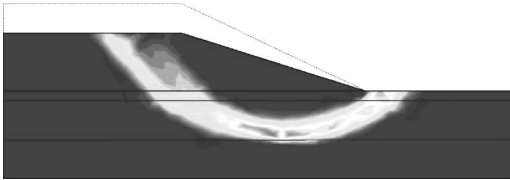


Figure 10. Incremental shear strain in the first calculation step (unimproved subsoil) – standard tolerated error 1%.

the Priebe method which are common with the FE simulations. First, the material behaviour is elastoplastic. The crucial is the choice of an appropriate soil stiffness and column strength. Second, time effects fade away fast, thus having almost no influence on the calculated outputs.

One can consider some additional benefits from the application of a more powerful FE method. E.g. not only an overall distribution of the vertical displacements but also of the horizontal ones can be obtained, see Fig. 9.

However, advantages of FE simulations are counterbalanced by the complexity of the method. Leaving aside many difficulties related to advanced constitutive models, the role of purely numerical parameters is often unclear to many users. They mostly rely on default values of these parameters offered by the program. Changing them can cause unexpected results. For instance, if decreasing the standard tolerated error from 3% to 1%, equilibrium for the first stage in case of unimproved subsoil could not be reached (Plaxis version 8 was used for this investigation). The reason was an embankment failure along a shear surface, see Fig. 10, which however did not occur in reality.

3 CONCLUSIONS

A comparison of the Priebe method and a FE analysis for the calculation of settlements of an embankment on the ground improved with stone columns yielded a close agreement between both methods. If no additional information (e.g. horizontal deformations) is

needed, the Priebe method combined with the Balaam/Booker procedure is more favourable because

- FE method is much more time consuming and
- the risk of input errors in FE calculations is much larger.

In practice, other questions may be even more crucial for the calculated results. The highest uncertainty is usually related with the material parameters:

- The most important parameter for the consolidation time is the c_v -value, see Fig. 2. If “undisturbed” soil samples are used to determine the c_v -value in the laboratory or the parameter is just estimated, this may result in unrealistic consolidation times. It is strongly recommended to use in situ cone penetration tests (CPTU) including dissipation tests in different depths to achieve realistic results.
- Another value which has to be estimated (using a table quite common in France) is the value $\alpha = E_M/E_{oed}$. Users from other countries who are not familiar with pressiometer tests may not know this factor at all or make considerable mistakes.
- In the soil profile of Fig. 1, an incompressible stratum was assumed at 9 m depth. This assumption is only valid if hard rock is present. Otherwise an approach for calculating the limit depth, e.g. according to DIN 4019, should be used.

If the three above parameters are not accurate, a factor of two between measured and calculated results for final settlements and consolidation time may easily be reached.

REFERENCES

- ASEP-GI, 2004. Instructions for the prediction exercise. Paris.
- Balaam, N.P. & Booker, J.R. 1981. Analysis of rigid rafts supported by granular piles. *International Journal of Numerical and Analytical Methods in Geomechanics* 5: 379–403.
- Barron, R.A. 1948. Consolidation of fine-grained soils by drain wells. *ASCE Transactions* 113: 718–742.
- Bazgan, S. 2004. Behaviour of soil-structure interfaces. MSc-Thesis. Technische Universität Dresden/University of Bucharest.
- Dhouib, A., Wehr, J., Soye, B. & Priebe, H. 2004. Méthode de Priebe: Origine, Développement et Applications. In Dhouib, Magnan & Mestat (eds.), *Amélioration des sols en place*: 131–146. Presses de l’ENPC/LCPC, Paris.
- Mestat, P., Dhouib A., Magnan J.-P. & Canepa Y. 2004. Results of the settlement prediction exercise of an embankment founded on soil improvement by stone columns. In Magnan (ed.), *ASEP-GI 2004*, Vol. 2: 1–13. Paris.
- Priebe, H. 1976. Abschätzung des Setzungsverhaltens eines durch Stopfverdichtung verbesserten Baugrundes. *Bautechnik* 53(5): 160–162.

Modelling stone columns in soft clay

P. Andreou & V. Papadopoulos

National Technical University of Athens, Greece

ABSTRACT: The main objective of this study is to examine the influence of important factors on the design and construction of stone columns and to conclude some practical results. The parametric investigation of the behavior of a stone column unit cell with the use of finite elements is presented in this study. More specifically, the effects of these factors, applied load in the ground, area replacement factor, friction angle of the gravel and undrained shear strength of the soil, on the horizontal displacements are analyzed.

1 INTRODUCTION

The vibrated stone column technique is an economical and environmentally friendly process that treats weak ground to enable it to withstand low to moderate loading conditions (Dhouib & Blondeau 2005). Large-sized columns of coarse backfill material are installed in the soil by means of special depth vibrators (Priebe 1976, 1995). Reinforcement of the soil with stone columns provides basically reduction of foundation settlement, improvement of the bearing capacity of the soil, reduction of the risk of liquefaction due to seismic activity and accelerates the consolidation process (Barksdale & Bachus 1983).

The consolidation process in the soil commences right after the moment the load applied (σ_c). Under instant loading, the saturated soft clay behaves incompressible, and the stress in the stone column (σ_c) is small (Han & Ye 2001). Therefore, the soft clay tends to move laterally towards the stone column. The tendency of this lateral movement acts as a relief of excess pore water pressures in the surrounding soil. Since the commencement of the consolidation, the vertical stresses in the soil (σ_s) starts to transfer onto stone columns. In other words, a stress concentration onto the column along with a vertical stress reduction in the soil happens. This stress transfer or concentration induces a reduction of excess pore water pressure in the soil. At the same time the load is transferred onto the column, the lateral stress from the column is increased. The rate of consolidation can be accelerated by increasing the modular ratio and reducing the diameter ratio (influence diameter/column diameter).

The bulging failure of the stone column occurs when the applied load is higher than the lateral resistance of the soil. The lateral resistance increases with depth, so the failure happens in the upper part of the stone

column. The ultimate stress that can be applied to the stone column (Soyez 1985) is:

$$\sigma'_{c,lim} = K_{p,c} \cdot \sigma'_r \quad (1)$$

where (σ'_r) the ultimate lateral stress of the soil and ($K_{p,c}$) the coefficient of passive pressure of the stone column.

The main objective of this study is to examine the influence of different factors and to conclude some practical results on the design of stone columns projects, through finite element analysis. The effects of these factors, applied load in the ground, area replacement factor, friction angle of the gravel and undrained shear strength of the soil, on the horizontal displacements are analyzed.

2 METHOD OF ANALYSIS

The conversion of axisymmetric stone column unit cell model with finite element analysis is used in this study. The stone column and the surrounding soil are assumed to behave as elasto-plastic Mohr-Coulomb materials. After the construction of the improved site it is usually used a rigid foundation system so as to permit a better distribution of the loads. For that reason, the proposed model considers a plate, in the upper part of the model and neglects the effect of its own weight.

The length of the column has been considered 20 m, the diameter 0.8 m, the applied load $\sigma_o = 10, 40, 70, 100, 120$ kPa and the area replacement factor, that represents the percentage of the replacement of the soil by gravel, $a = 0.0704, 0.0959, 0.1253, 0.1958$. Also, the friction angle of the gravel material took values from 38° to 44° and finally the range of the undrained shear strength of the soil (c_u) was from 10

Table 1. Geotechnical parameters used in the parametric study.

	γ kN/m ³	$K_x = K_y$ m/day	E Mpa	ν	γ kN/m ³	ϕ'
Clay	19	0.0001	2	0.33	20	20
Stone	21	10	40	0.25	0.5	40

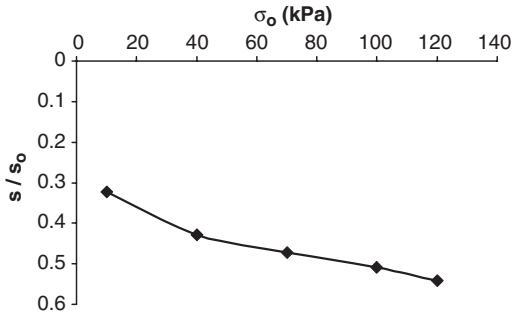


Figure 1. Influence of the applied load (σ_o) on settlements ($a = 0.1253$, $\phi_c = 40$, $c_u = 20$ kPa).

to 60 kPa. The stone and soil material properties that have been used are shown in table 1.

Several factors, such as applied load in the ground and area replacement factor, friction angle of the gravel and undrained shear strength of the soil, influence the prediction of the settlements of foundations supported by end-bearing stone columns. The proposed model determine the influence of each parameter on the horizontal displacements.

2.1 Influence of the applied load

In the first step of this study, Figure 1 indicates the performance of the improved soil by stone columns as the value of the applied load increases. The variation of the (s/s_o) ratio, where (s) is the value of final settlements of the improved soil and (s_o) the settlements of the soil without improvement, as a function of (σ_o) is indicated in Figure 1. It is obvious that this ground improvement technique reduces the total settlements of the soil and moreover as the load increases the settlements increase as well.

Figure 2 demonstrates the variation of the (H_{pl}/l) ratio as a function of (σ_o), where (l), the length of the column and (H_{pl}) the height of its plastic zone. The height of plastic zone of the stone column increases as the applied load increases.

The horizontal displacements at the interface of stone column-soil are shown in Figure 3. The variation of the (r/r_o) ratio, where (r) is the value of final radius of the stone column after the application of the load and (r_o) the initial radius of the column, as a function

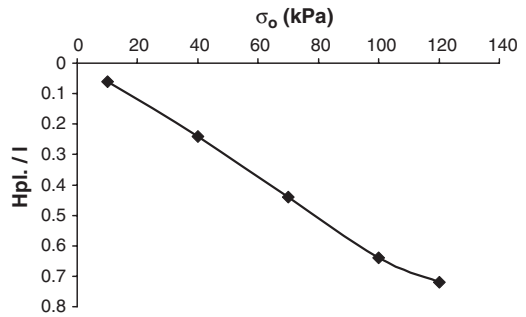


Figure 2. Influence of the applied load (σ_o) on height of the plastic zone ($a = 0.1253$, $\phi_c = 40$, $c_u = 20$ kPa).

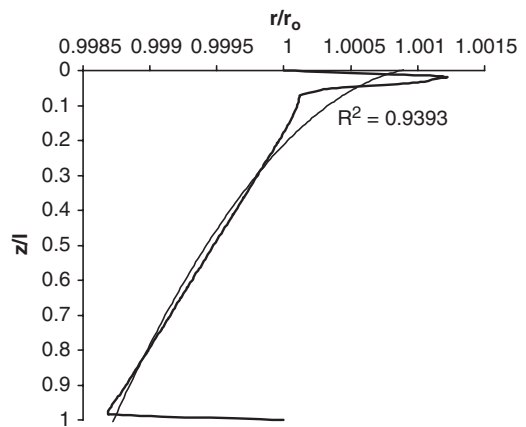


Figure 3. Variation of the (r/r_o) ratio as a function of (z/l) ratio ($a = 0.1253$, $\phi_c = 40$, $c_u = 20$ kPa, $\sigma_o = 10$ kPa).

of (z/l) ratio, where (z) is the increasing depth of the column from the surface is demonstrated in this figure. It is evident from the shape of the curve that the bulging failure tends to occur in the upper part of the stone column and as the lateral resistance of the soil increases with depth it is apparent that the soil tends to move towards the column. Moreover, it is adapted, in the same figure, a polynomial equation for this specific case.

The influence of the applied load, by adopting the polynomial equation of each case, is shown in Figure 4. The higher the load is, the higher the final radius of the stone column is. This remark becomes more obvious in the upper part of the stone column. It is also observed that in deeper levels and at low values of the load, the soil tends to move towards to the column but as the load increases, it is the gravel material that moves towards to the soil.

It is written before that it is more obvious in the upper part of the stone column the higher values of its

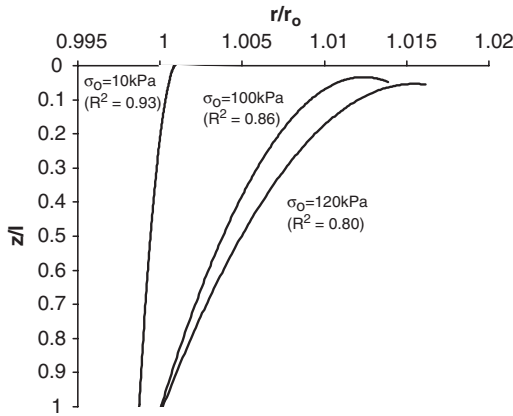


Figure 4. Influence of the applied load on the horizontal displacements ($a = 0.1253$, $\varphi_c = 40$, $c_u = 20$ kPa).

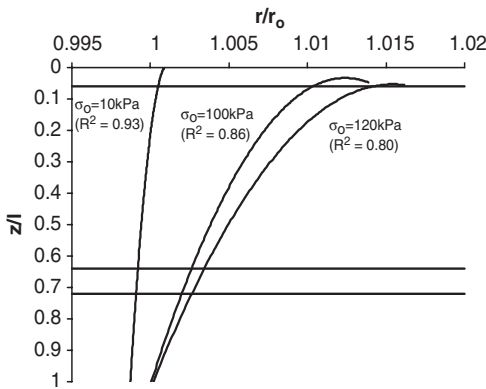


Figure 5. Influence of the applied load on the horizontal displacements and interjection with their plastic zone ($a = 0.1253$, $\varphi_c = 40$, $c_u = 20$ kPa).

final radius. With that in mind and Figure 2, we obtain Figure 5. The horizontal lines separate the plastic from the elastic zone of each case and so, on top of each line the area has been in plastic equilibrium. Furthermore, the point of intersection of the horizontal line and the curve of horizontal displacements in each case, is the point that the inclination of the curve starts to change drastically.

2.2 Influence of the area replacement factor

Figures 6 and 7 indicate the influence of the area replacement factor on the height of the plastic zone and on the horizontal displacements respectively, where the higher the value of (a) is, the lower the plastic zone become. Also, the bulging area is more limited and the soil moves towards to the column.

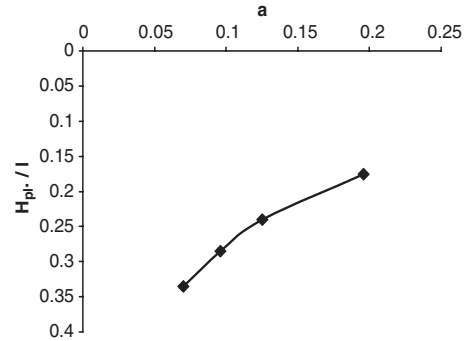


Figure 6. Influence of the area replacement factor (a) on length of the plastic zone ($\sigma_o = 40$ kPa, $\varphi_c = 40$, $c_u = 20$ kPa).

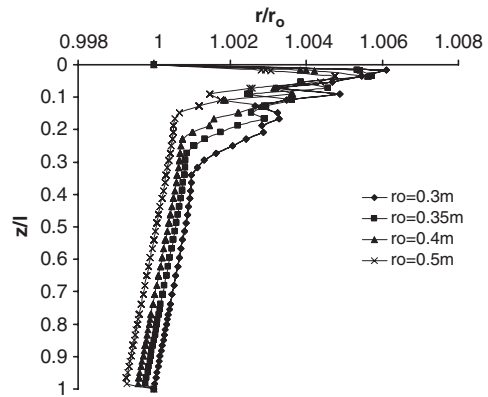


Figure 7. Influence of the area replacement factor (a) on the horizontal displacements ($\sigma_o = 40$ kPa, $\varphi_c = 40$, $c_u = 20$ kPa).

2.3 Influence of the friction angle of the gravel material

It is known that a better compaction of the gravel material decrease the amount of settlements (Andreou & Papadopoulos 2005). From this point of view, Figure 8, demonstrates that indeed, higher values of friction angle of the gravel decrease the height of the plastic zone.

The influence of (φ_c) on the horizontal displacements is indicated in Figure 9, where as before with the influence of (a), the higher this value is, the lower the plastic zone become, the bulging area is more limited and the soil moves towards to the column.

2.4 Influence of the undrained shear strength of the soil

Finally, the influence of the undrained shear strength of the soil on the horizontal displacements seem to be not important (Figure 10).

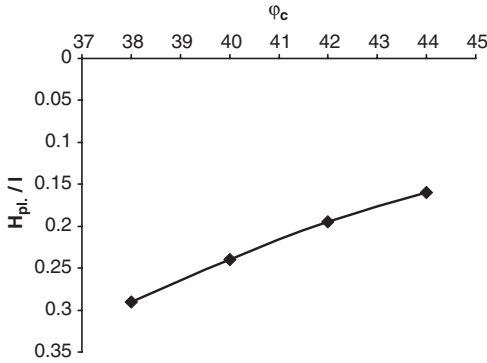


Figure 8. Influence of the friction angle of the gravel material (ϕ_c) on length of the plastic zone ($a = 0.1253$, $\sigma_o = 40$ kPa, $c_u = 20$ kPa).

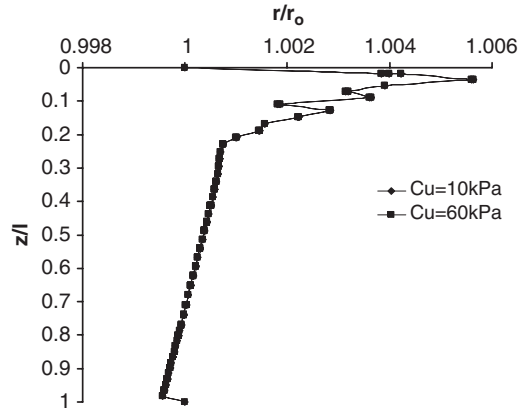


Figure 10. Influence of the (c_u) of the soil on the horizontal displacements ($a = 0.1253$, $\phi_c = 40$, $\sigma_o = 40$ kPa).

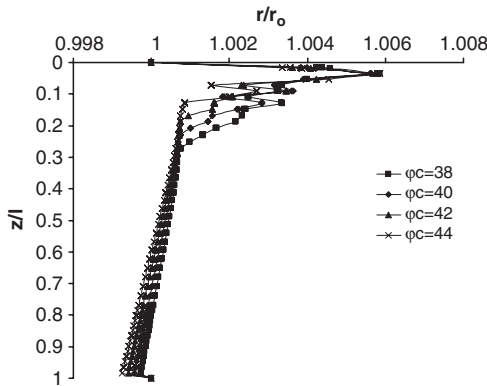


Figure 9. Influence of the friction angle of the gravel material (ϕ_c) on the horizontal displacements ($a = 0.1253$, $\sigma_o = 40$ kPa, $c_u = 20$ kPa).

3 CONCLUSIONS

It is obvious that ground improvement by means of stone columns reduces the total settlements of the soil and moreover as the load increases the settlements and the height of the plastic zone of the stone column increases as well. The bulging failure tends to occur in the upper part of the stone column and as the lateral resistance of the soil increases with depth it is apparent that the soil tends to move towards to the column. The higher the load is, the higher the final radius of the stone column is. This remark becomes more obvious in the upper part of the stone column. It is also observed that in deeper levels and at low values of the

load, the soil tends to move towards to the column but as the load increases, it is the gravel material that moves towards to the soil.

Also, the higher the value of area replacement factor or friction angle of the gravel material is, the lower the plastic zone become, the bulging area is more limited and the soil moves towards to the column.

Finally, the influence of the undrained shear strength of the soil on the horizontal displacements seem to be not important.

REFERENCES

- Barksdale R.D., Bachus R.C. (December 1983). Design and construction of stone columns, Vol. I, FHA, 210p.
- Dhouib A. et Blondeau F. (2005). Colonnes Ballastées, Presses de l'Ecole Nationale des Ponts et Chaussées, Paris, 264p.
- Han J., Ye S.L. (2001). Simplified method for consolidation rate of stone column reinforced foundations, Journal of Geotechnical and Geoenvironmental Engineering, Vol. 127, No. 7, pp 597–603.
- Priebe H.J. (1976). Abschätzung des Setzungsverhaltens eines durch Stopfverdichtung verbesserten Baugrundes, Bautechnik Vol. 53, p.p. 160–162.
- Priebe H. J. (1995). The design of vibro replacement, Keller Grundbau GmbH, Offenbach, Germany, pp. 1–16.
- Soyez B. (1985). Méthodes de dimensionnement des colonnes ballastées, Bulletin de Liaison des Laboratoires des Ponts et Chaussées, no. 135. Paris, pp. 35–51.
- Andreu P. & Papadopoulos V. (2005). Modelling with finite elements Stone Columns in Soft Clay, 2nd International Workshop of Young Doctors in Geomechanics, Paris, pp.79–80.

Bearing capacity of group of stone columns

M. Etezad, A.M. Hanna & T. Ayadat

*Dept. of Building, Civil and Environmental Engineering,
Concordia University, Montreal, Canada*

ABSTRACT: Stone columns method is an effective technique to improve the settlement and bearing capacity characteristics of soft soil. Stone columns may fail individually or as a group. This paper presents a theoretical model to predict the bearing capacity of a group of stone columns. Equivalent unit weight, cohesion and angle of shearing resistance are introduced in this model. The method is based on the actual failure mechanism, which is deduced from the results of numerical modeling on a group and single stone columns as well as the available experimental data in the literature. The interaction between stone columns and the surrounding soil were considered in developing this model. The results produced by the proposed theory were validated.

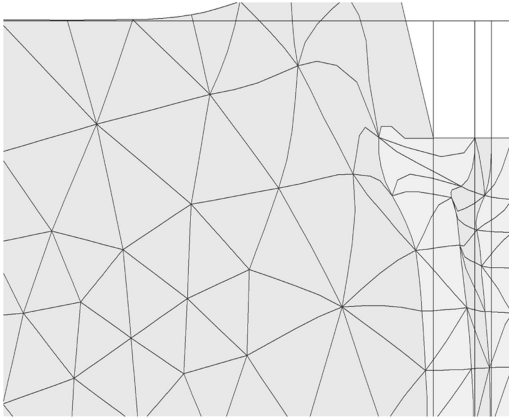
1 INTRODUCTION

Stone columns method is considered as a ground reinforcement technique which is composed of compacted granular material inserted into the soft clay foundation to improve the characteristics of the soil. One of the purposes of using stone columns is to increase the bearing capacity of the soil under the foundation. Unit cell technique was developed for this purpose by Hughes & Withers (1974) and is followed by other researchers over the years. This concept considers that each column in the group of stone columns can act independently from the rest of the columns and no interaction exists between the adjacent columns. Bearing capacity of a single column is calculated and is multiplied by the number of columns in order to estimate the ultimate bearing capacity of the group. In 1995 Hu performed laboratory experimental work for group of stone columns and concluded that group interaction has an important role in the behavior of stone columns and this effect should not be ignored. He observed that failure of group of stone columns is due to shear failure and is different from bulging failure which is considered in the unit cell methods. In 2005 Etezad et al. carried out numerical analysis considering different soil and column materials and ground geometry. Utilizing finite element method, they conducted over 600 tests. They observed group interaction and declared that this effect

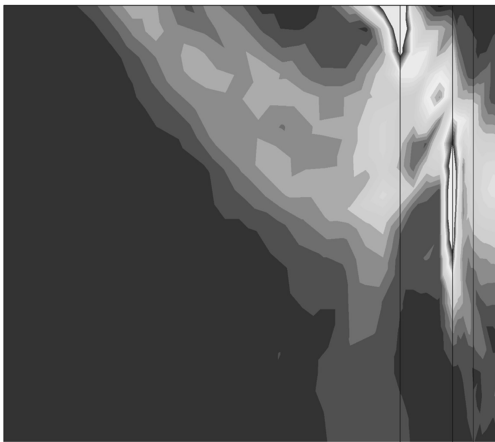
has an important role in predicting the behavior of stone columns. They reported that general, local and punching shear failures modes should be considered as the possible shape of failure for group of stone columns. In the literature, few researches have estimated the bearing capacity of stone columns using general shear failure. In 1978 Madhav & Vitkar developed a theoretical model to calculate the bearing capacity of a granular trench using the upper bound limit analysis. Hamed et al. (1986) declared that this theory yields a higher and unsafe value of bearing capacity comparing to the experimental results. Priebe (1991) developed two methods based on equivalent soil assumption. In the first model, the average cohesion and angle of shearing resistance are considered and accordingly, the ultimate load on the foundation is calculated using the available theoretical methods for unreinforced soil. In the second method the average width of the foundation was assumed and the bearing capacity is then calculated using the material characteristics of the untreated ground. Nevertheless, the equivalent soil properties should fulfill the Mohr-Column failure criteria.

2 THEORETICAL MODEL

Figure 1 illustrates the general shear failure of group of stone columns deduced from the numerical model.



(a)



(b)

Figure 1. (a) Deform behavior (b) Failure shape of stone columns.

Due to symmetry only half of the group is presented. The observed general shear failure is considered as the failure mechanism in this paper. When stone columns are installed in square arrangement, plain strain condition can be considered as a reasonable assumption for large group of columns.

If the A_s is defined as ratio of the area of stone columns over total area of ground under the foundation, the equivalent cohesion and unit weight of the reinforced soil is considered as:

$$c_{equ.} = A_s c_s + (1 - A_s) c_c \quad (1)$$

$$\gamma_{equ.} = A_s \gamma_s + (1 - A_s) \gamma_c \quad (2)$$

Where c_s , c_c , γ_s and γ_c are cohesion and unit weight of the column material and soil respectively.

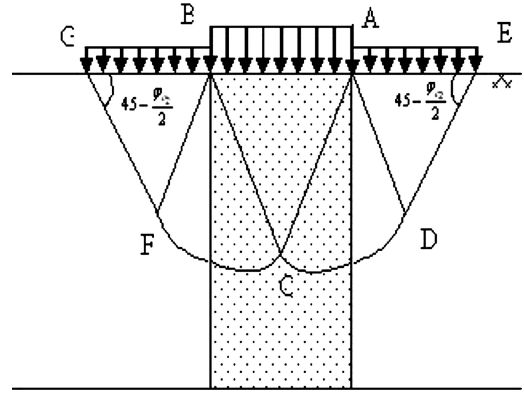


Figure 2. Failure shape in equivalent soil.

The cohesion c_s is taken to be zero for sand. Christoulas et al. (1997) and Mestat & Riou (2004) consider the equivalent angle of friction as:

$$\phi_{equ.} = A_s \phi_s + (1 - A_s) \phi_c \quad (3)$$

However Mohr-Coulomb failure criteria should be valid for the equivalent soil.

$$\tau_{equ.} = A_s \tau_s + (1 - A_s) \tau_c \quad (4)$$

Where $\tau_{equ.}$, τ_s and τ_c are the shear stress of the equivalent soil, stone column and unreinforced ground. ϕ_s and ϕ_c represent the angle of friction of stone column material and soil respectively. Utilizing Mohr-Coulomb failure criteria, friction angle of equivalent soil is calculated as.

$$\phi_{equ.} = \tan^{-1} [A_s \mu_s \tan \phi_s + (1 - A_s) \mu_c \phi_c] \quad (5)$$

Where

$$\mu_s = \frac{n}{1 + (n - 1) A_s} \quad (6)$$

$$\mu_c = \frac{1}{1 + (n - 1) A_s} \quad (7)$$

n , the stress ratio, is considered as the stress in the granular material over the stress in the cohesive soil. Barksdale & Bachus (1983) report that this value ranges from 2 to 5. By conducting experimental work Hu (1995) mentions that n varies in the range of 1 to 5. Using the finite element model (Etezzad et al. 2005a) this value was estimated between 2 to 5 for different ground and soil conditions. However more research should be conducted to investigate the effect of

different soil and stone column material characteristics as well as the ground geometry on this factor.

The soil under the foundation is divided into elastic cone and log spiral and passive Rankine zones. The reinforced soil section is considered as an equivalent soil having c_{equ} , ϕ_{equ} and γ_{equ} . Therefore the ground under failure plan is considered as two sections: the equivalent soil section and clay section which is outside of the reinforced area. The observed failure plan was to have two log spiral surfaces, one in each section, which cross each other at the boundary of the two soils. The centers of the log spirals are not the same. Limit equilibrium technique was used and the method of superposition was implemented where the effect of weight of the foundation is taken separately from cohesion and the surcharge.

2.1 Calculation of q_γ

In order to estimate bearing capacity related to the unit weight of the soil alone, q_γ , Terzaghi (1943) proposed the method of trial and errors to determine the center of log spiral area which gives the lowest value of the passive pressure q_γ . The lowest value of q_γ can be obtained by minimizing the characteristics related to log spiral geometry such as the angle coordinate of the center of log spiral. Kumbhojkar (1993) proposed a numerical technique to evaluate this value. His method is based on minimization of the angle of log spiral section in order to derive the lowest value of q_γ .

As mentioned previously, the failure shape of the ground under the foundation, observed by numerical analysis (Etezd et al., 2005a), consists of two log spiral surfaces one in the equivalent soil part and the other in the surrounding soil section having different centers and different angles θ_1 and θ_2 . (Fig. 3)

Writing equilibrium equation for the equivalent soil section results.

$$\begin{aligned} \Sigma M_{O_1} = 0 \rightarrow & W_1 l_1 + W_2 l_2 + P_\gamma [\cos(\psi - \varphi_{equ.}) \frac{B}{3} + \\ & \sin(\psi - \varphi_{equ.}) (\frac{B}{3} \tan \psi - y_1)] = F \cos \delta (\frac{2}{3} AH - y_1) \end{aligned} \quad (8)$$

Where W_1 , W_2 , l_1 , l_2 , F and y_1 represent weights and lever arms of each soil blocks, pressure on AH and vertical distance of the center of first log spiral to the point A at. The cone angle ψ was derived by Etezd et al. (2005b) as:

$$\psi = A_s \frac{\varphi_s - \varphi_c}{2} + \frac{\pi}{4} + \frac{\varphi_c}{2} \quad (9)$$

The slip line in the Rankin passive pressure zone was assumed to intersect the ground at an angle

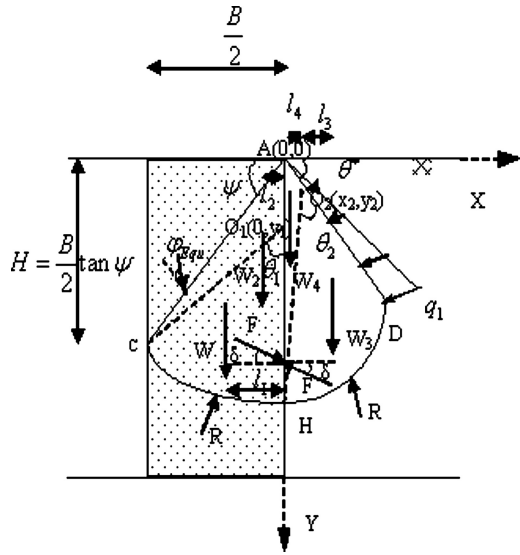


Figure 3. Determination of P_γ ($q = 0$, $c = 0$).

$\theta^* = \pi/4 - \phi_c/2$ with the horizontal. This assumption agrees with the result which is deduced from finite element method developed by Etezd et al. (2005a). By substituting related values into Equation 8 and rearranging the terms following equation is obtained.

$$\begin{aligned} & \gamma_{equ.} \frac{B^3}{24 \sin^3 \theta_1 (9 \tan^2 \varphi_{equ.} + 1)} [e^{3\theta_1 \tan \varphi_{equ.}} - (3 \tan \varphi_{equ.} \sin \theta_1 + \\ & \cos \theta_1)] + \gamma_{equ.} \frac{B^3 (\tan \psi - \cot \theta_1)}{48} + P_\gamma [\cos(\psi - \varphi_{equ.}) \frac{B}{3} \\ & + \sin(\psi - \varphi_{equ.}) (\frac{B}{3} \tan \psi - \frac{B(\tan \psi - \cot \theta_1)}{2})] \\ & = F \cos \delta \frac{B}{3} (\frac{\cot \theta_1 - \tan \psi}{2} + \frac{e^{\theta_1 \tan \varphi_{equ.}}}{\sin \theta_1}) \end{aligned} \quad (10)$$

Similarly, equilibrium equation is written for the unreinforced soil section.

$$\begin{aligned} \Sigma M_{O_2} = 0 \rightarrow & \frac{q_1 \cos^2 \varphi_c}{3} [O_2 D^2 + \frac{A O_2}{2 A D} (O_2 D^2 - A O_2^2)] \\ & + W_3 l_3 = W_4 l_4 + F x_2 \sin \delta + F \cos \delta (\frac{2}{3} AH - y_2) \end{aligned} \quad (11)$$

ϕ_c , x_2 and y_2 presence the angle of friction for the surrounding soil section and horizontal and vertical distances of the second center of log spiral to point A

respectively. Again the quantities in Equation 11 are replaced with their related values and simplification of the equation yields.

$$\frac{\gamma_c B^3}{24 \sin^3 \theta_1} A^3 \cos^2 \varphi_c \sin(45 - \frac{\varphi_c}{2}) \tan(45 + \frac{\varphi_c}{2})$$

$$[\frac{-1}{2}(-\cos \theta^* \cot \theta_2 + \sin \theta^*)^3 + \frac{\cos^2 \theta^* e^{2\theta_2 \tan \varphi_c}}{\sin^3 \theta_2}$$

$$(\frac{-3}{2} \cos \theta^* \cos \theta_2 + \frac{3}{2} \sin \theta^* \sin \theta_2 + \cos \theta^* e^{\theta_2 \tan \varphi_c})]$$

$$+ \frac{\gamma_c B^3 \cos^3 \theta^*}{24 \sin^3 \theta_2 \sin^3 \theta_1 (9 \tan^2 \varphi_c + 1)} A^3$$

$$\cdot [e^{3\theta_2 \tan \varphi_c} (3 \tan \varphi_c \cos \theta^* - \sin \theta^*) + \sin(\theta^* + \theta_2)$$

$$- 3 \tan \varphi_c \cos(\theta^* + \theta_2)] = \frac{\gamma_c B^3}{24 \sin^3 \theta_1} A^3 \cdot D^2$$

$$+ F \frac{B}{\sin \theta_1} A [\frac{\sin \delta}{2} D + \cos \delta (\frac{1}{3} - \frac{1}{2}$$

$$\cdot (-\cos \theta^* \sin \theta^* \cot \theta_2 + \sin^2 \theta^*))]$$
(12)

Where

$$A = \tan \psi \sin \theta_1 - \cos \theta_1 + e^{\theta_1 \tan \varphi_{equ}}$$

$$D = -\cos^2 \theta^* \cot \theta_2 + \sin \theta^* \cos \theta^*$$

Considering the equilibrium of forces for the elastic cone section under the foundation q_γ is calculated as follows.

$$q_\gamma = \frac{2P_\gamma}{B} \cos(\psi - \varphi_{equ}) - \frac{B}{4} \gamma_{equ} \tan \psi \quad (13)$$

In order to calculate q_γ , an arbitrary value of load P_γ is assumed and the equilibrium equation in equivalent soil part is minimized to determine the value of load F which states the critical condition of the failure. First section is minimized respect to θ_1 , the value of θ_1 is evaluated and F is estimated subsequently. Next, the unreinforced soil section is minimized respect to θ_2 and then F for this section is calculated. If the values of F in the first and second sections are equal P_γ is the exact value otherwise the value of P_γ is changed until the force F in both equations becomes equal. A computer program using Visual Basic is written for this purpose. The value of δ is considered equal to ϕ_{equ} . as

F is located in radius of the first log spiral. The values of θ_1 and θ_2 were determined from the results of the numerical model and Newton-Raphson method was used for this purpose.

2.2 Calculation of q_c and q_q

Similar to the previous part two log spirals are considered for the equivalent and unreinforced sections. The bearing capacity of this part is represented as $q' = q_c + q_q$. For unreinforced soil the center of log spiral part is considered at the edge of the foundation in the literature. However, for soil reinforced by stone column due to the interaction effect of two different soils the center of log spirals might not be necessarily in the edge of the foundation. Therefore same procedure as before is used here.

Writing equilibrium equation for equivalent soil section one may have.

$$\Sigma M_{O_1} = 0 \rightarrow P' [\cos(\psi - \varphi_{equ}) \frac{B}{4} + \sin(\psi - \varphi_{equ})$$

$$(\frac{B}{4} \tan \psi - y_1)] + c_{equ} \cdot ACy_1 \cos \psi$$

$$= F \cos \delta (\frac{1}{2} AH - y_1) + \frac{c_{equ}}{2 \tan \varphi_{equ}} (O_1 H^2 - O_1 C)$$
(14)

Substituting with the corresponding values into Equation 14 will produce the following equation.

$$P' [\cos(\psi - \varphi_{equ}) \frac{1}{4} + \frac{1}{2} \sin(\psi - \varphi_{equ}) (\frac{-\tan \psi}{2} + \cot \theta_1)]$$

$$+ c_{equ} \frac{B(\tan \psi - \cot \theta_1)}{4} = \frac{F \cos \delta}{4 \sin \theta_1} (-\tan \psi \sin \theta_1 + \cos \theta_1$$

$$+ e^{\theta_1 \tan \varphi_{equ}}) + \frac{c_{equ} \cdot B}{8 \sin^2 \theta_1 \tan \varphi_{equ}} (e^{2\theta_1 \tan \varphi_{equ}} - 1)$$
(15)

For unreinforced soil section the following equation is obtained.

$$\Sigma M_{O_2} = 0 \rightarrow F \cos \delta (\frac{AH}{2} - y_2) + F \sin \delta \cdot x_2 + c_x AH \cdot x_2$$

$$= \frac{q_2 \cos^2 \varphi_c}{2} (O_2 D^2 - AO_2^2) + \frac{c_c}{2 \tan \varphi_c} (O_2 D^2 - O_2 H^2)$$
(16)

In the above equation $c_x = c_{equ}$. x_2 and y_2 are the distances of the center of log spiral to point A and q is the surcharge.

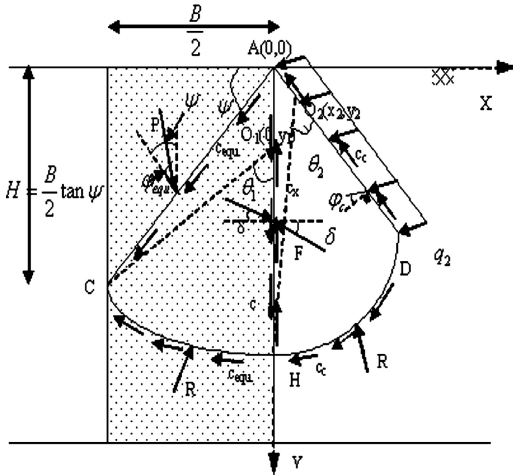


Figure 4. Determination of P_c and P_q ($\gamma = 0$).

The equation for the soil in this section is given as.

$$\frac{q \cdot B^2 \cos^2 \varphi_c \tan(45 + \frac{\varphi_c}{2})}{8 \sin^2 \theta_1 \sin^2 \theta_2} M^2 [\cos^2 \theta^* e^{2\theta_2 \tan \varphi_c} - (-\cos \theta^* \cdot \cos \theta_2 + \sin \theta^* \sin \theta_2)^2] + \frac{c_c}{2 \tan \varphi_c} \cdot M^2 \frac{B^2 \cos^2 \theta^*}{4 \sin^2 \theta_1 \sin^2 \theta_2} \cdot (e^{2\theta_2 \tan \varphi_c} - 1) = F \frac{B}{2 \sin \theta_1} \cdot M \cdot [\sin \delta \cdot N + \cos \delta (\frac{1}{2} + \sin \theta^* \cos \theta^* \cot \theta_2 - \sin^2 \theta^*)] + c_x \frac{B^2}{4 \sin^2 \theta_1} M^2 \cdot N \quad (17)$$

Where

$$M = e^{\theta_1 \tan \varphi_{equ.}} + \tan \psi \sin \theta_1 - \cos \theta_1$$

$$N = (\sin \theta^* \cos \theta^* - \cos^2 \theta^* \cot \theta_2)$$

As before a reasonable value of P' is assumed and calculation is continued until the values of F in Equations 15 and 17 become equal. θ_1 and θ_2 are minimized and their values are solved numerically.

q' can be calculated by considering the equilibrium of forces for the elastic cone section under the foundation.

$$q' = \frac{2P'}{B} \cos(\psi - \varphi_{equ.}) + c_{equ.} \tan \psi \quad (18)$$

3 DISCUSSION AND VERIFICATION

The ultimate bearing capacity of the ground reinforced by stone columns is the sum of the two components of the bearing capacity.

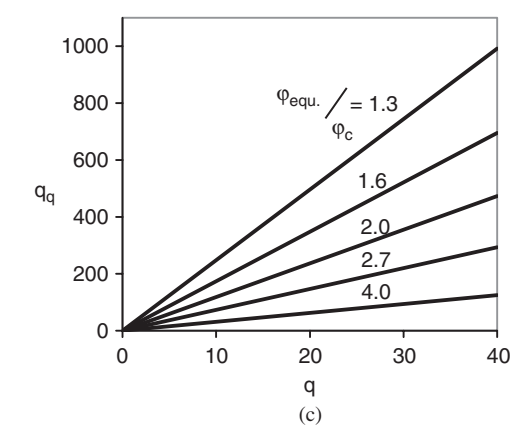
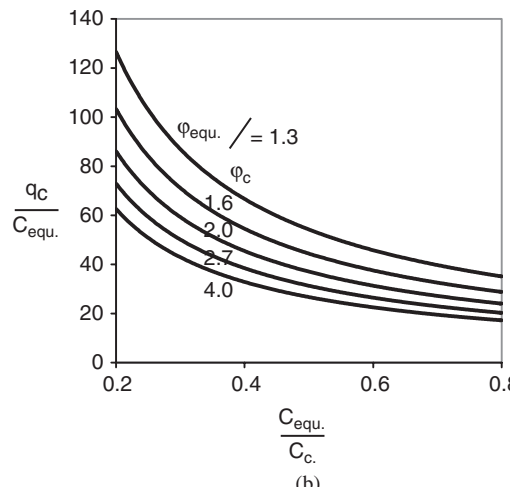
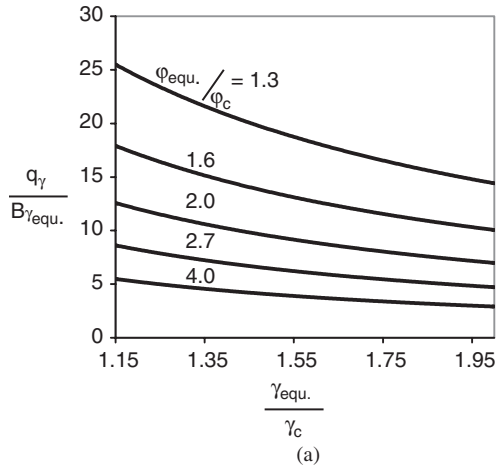


Figure 5. Bearing capacity values (a) q_γ (b) q_c (c) q_q .

Table 1. Comparison between results of the theoretical method with finite element method.

Test	A_s (%)	D (m)	ϕ_s	ϕ_c	c_c	γ_s	γ_c	q (kN/m ²)	n	q_u (kN/m ²)	
										Theory	F.E.M Etezzad et al. (2005)
1	25	1	41	24	10	19	15	0	3	959	845
2	30	1	40	20	7	19	14	11.2	2	625	712

$$q_u = q_\gamma + q' = q_\gamma + q_c + q_q \quad (19)$$

Utilizing the computer program which was written to evaluate q_u , charts are presented that calculate the values of q_γ , q_c , q_q . Charts in Figure 5 are prepared for $\phi_{\text{equ}} = 40$ and charts for other equivalent angle of friction will be presented elsewhere.

Table 1 illustrates the comparison between the results calculated by the theoretical method and finite element technique. In this table q and D represent the surcharge stress and diameter of the stone columns respectively. Good agreement between the results of the two methods is observed.

4 CONCLUSION

Theoretical model was proposed to predict the ultimate bearing capacity of ground reinforced with stone columns. General shear failure has been considered and limit equilibrium has been used. In this analysis, the failure surface of the stone columns and the surrounding soil was made of two log spirals. The ultimate bearing capacity of the system was determined after minimizing the angle of each log spiral. The results deduced by this model have been compared with the finite element technique where good agreement was observed.

REFERENCES

- Barksdale, R.D. and Bachus, R.C. 1983. Design and construction of stone columns, *Report No. FHWA/RD-83/026*, Federal Highway Administration, U. S. A.
- Christoulas, S., Giannaros, C. and Tsiambaos, G. 1997. Stabilization of embankment foundations by using stone columns. *Geotechnical and Geological Engineering*, 15: 247–258.
- Etezzad, M., Hanna, A.M. and Ayadat, T. 2005a. Numerical model for group of stone columns. *73rd Annual Meeting of ICOLD, Tehran, Iran, 1–6 May 2005*.
- Etezzad, M., Hanna, A.M. and Ayadat, T. 2005b. Analytical model of a group of stone columns. *33rd Annual Conference of the Canadian Society for Civil Engineering, Toronto, Ontario, 2–4 June 2005*.
- Hamed, J.T., Das, B.M. and Echelberger, W.F. 1986. Bearing capacity of a strip foundation on granular trench in soft clay. *Civil Engineering for Practicing and Design Engineers*, 5(5):359–376.
- Hu, W. 1995. Physical modeling of group behavior of stone column foundations. *Ph.D. Dissertation*, University of Glasgow.
- Hughes, J.M.O., Withers, N.J. 1974. Reinforcing of soft cohesive soils with stone columns. *Ground Engineering*, 7(3): 42–49.
- Kumbhojkar, A.S. 1993. Numerical evaluation of Terzaghi's N_γ . *Jour. Geotech. Eng. ASCE*, 119(3): 598–607.
- Mestat, P. and Riou, Y. 2004. Validation des modèles numériques de sol amélioré par colonnes. *International symposium on ground improvement, Paris: 229–243*.

Tracking the settlement of sand layers stabilized by stone piles using numerical modeling

M.F. Mishriki

Dept. of Civil and Env. Eng., University of South Florida, Tampa, Florida, U.S.A

J.D. Hussin

Hayward Baker Inc., Tampa, Florida, U.S.A

E.A. Eissa

Dept. of Geology and Geophysical Eng., Suez Canal University, Suez, Egypt

S.I. Shalaby

Dept. of Geol. and Geoph. Eng., Suez Canal University, Suez, Egypt

A.K. Ashmawy

Dept. of Civil and Env. Eng., University of South Florida, Tampa, Florida, U.S.A

ABSTRACT: Several field plate load tests were performed on soft soils stabilized by stone piles installed using the vibro replacement technique in Southeastern United States. In order to simulate field settlement using finite elements, the actual stone pile diameter has been established using different techniques. The study showed that the diameter of the stone pile was tapered from a maximum value at the surface to a minimum value at a certain depth. By dividing the vibro replaced soil into several layers, the diameter of the stone pile was established by assuming that the dry density of the first layer had reached its maximum value. Also the coefficient of earth pressure for both the filling material and surrounding soil were obtained based on the hysteretic model presented by Duncan (1983) and the wall movement theory presented by Fang (1997), respectively. Using these estimated column diameter and coefficient of earth pressure in constructing the numerical model showed a good agreement between the predicted settlement and the measured settlement.

1 INTRODUCTION

The Vibro replacement technique is one of the common methods used to install stone columns (stone piles) which are typically intended to reduce settlement and increase bearing capacity of soft soils. Several attempts have taken place to predict the settlement of vibro-replaced soil using numerical modeling. Some of the predictions were in good agreement with field results Kundu et al. (1994), while others indicated that the numerical modeling overestimate the settlement Mitchell and Huber (1985), Ashmawy et al. (2000). These contradictions are attributed to the assumptions involved in settlement prediction, such as the physical and engineering properties of the filling materials and the surrounding soil, and the inaccurate estimation of the diameter of the stone pile. In addition, in the cases where stress dependent stress-strain paths are used for

both materials, the coefficient of earth pressure has a great influence on the prediction of settlement.

In order to simulate the settlement of vibro replaced soil using numerical models, this paper focused on the estimation of the stone pile diameter by using field results obtained from several projects conducted in Central Florida, and the coefficient of earth pressure of both filling material and surrounding sand using a new application for the hysteretic model and wall movement theory presented by Duncan and Seed (1986) and Fang et al. (1997), respectively.

The physical properties of the filling materials in this study were obtained from laboratory tests. The engineering properties were estimated from widely-accepted values in earlier papers, mainly because of the difficulty of obtaining an undisturbed sample from both the stone filling material and the surrounding sand, as well as the inability to duplicate in the laboratory the high

stresses that are used during the field installation process.

2 STONE PILE DIAMETER

One of the most critical parameters in simulating the stone piles behavior is the diameter of the stone pile. The diameter of the stone pile is typically determined from the amount of the stone around the probe, assuming that the diameter is constant along the whole depth. By observing the installation technique (vibro-replacement) of stone piles, it was noted that the diameter depends solely on the radial resistance from the surrounding soil. The radial resistance from the surrounding soil is governed by two main parameters: the properties of the surrounding soil, and the depth. Since the radial resistance increases with depth, and since the installation pressure is constant, it is reasonable to assume that the diameter of the stone pile tapers from a maximum value at the surface to a minimum value at a certain depth. To examine this conclusion some analyses were performed using the field results from projects conducted in Central Florida.

The first study used the results of SPT borings before and after the installation of stone piles for new condominiums in Jacksonville, Florida. Based on the field boring logs, the soil profile generally consisted of three layers from top to bottom: a fine sand layer with silt and some shell fragments in (SP-SM) with a thickness ranging from (15–18 m); a thin layer of sandy silty clay (CH); and weathered limestone.

The results of the SPT test preceding the stone pile installation were corrected using correlations found in Kulhawy and Mayne (1990), and the relative density of the sand layer was estimated based on Terzaghi and Peck (1967) transformation table. Also, from the results of the corrected SPT that was applied after the installation of the stone piles, relative densities of the surrounding soil were obtained. Based on Hough (1969), the properties for uniform fine sand, e_{max} , e_{min} , and specific gravity were taken equal to 1, 0.4, and 2.64 respectively. From the relative densities before and after the installation of the stone piles, e_{max} , e_{min} , and specific gravity, the dry densities of each layer have been obtained. From the distribution of the stone piles and the distance between them, the volume occupied by sand can be determined, considering that the initial diameter of the borehole is equal to 66 cm, which is 5 cm larger than the diameter of the probe. From this volume and the dry densities of each sand layer before and after installation of the stone piles, the diameter of the pile at various depths was determined. It was concluded that the stone pile diameter increases with depth up to a depth of 2.5 m, then decreases with depth till the end of the stone pile. This can be attributed to the fact that SPT results are not reliable up to a depth range of

Table 1. Properties of gravel that used as a filling material.

Properties	e_{min}	e_{max}	SSD	Max. dry density
Gravel #57	1	0.46	2.32	16.16 KN/m ³
Properties	N	R_f	K	ϕ
Gravel #57	0.333	0.9	1800	45

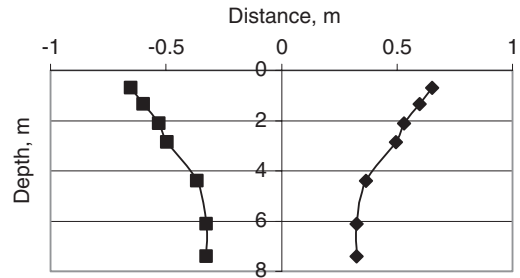


Figure 1. Diameter versus depth estimated from the SPT modified results.

2–3 m Kulhawy and Mayne (1990). It is therefore plausible to say that the diameters of the stone piles estimated from the SPT results above this limit are not accurate. To predict the diameters of the stone pile above this limit, the amount of the stone that was installed in each probe was used. The total amount of stone installed in the pile for a depth equal to 7.5 m was considered to be equal to 1 m³/m³ based on field reports from various projects done by the same company. The properties of the stone filling material were obtained from laboratory tests and are presented in Table 1. The weight of the stone installed in the probe was determined by multiplying the cubic yards per foot of stone by the minimum dry density. Then the weight of the stone installed at depth below 2.5 m was obtained from the multiplication of the volume of the stone below that level by the maximum dry density. Finally, the weight of the stone installed was subtracted from total weight to obtain the remaining weight. The average diameter of the stone pile above 2.5 m was then obtained by dividing the remaining weight by 2.5 m. Assuming that the stone pile in this zone is tapered uniformly, we can then determine the diameter of the stone pile near the surface.

Figure 1 shows the change in diameter versus depth. It can be observed from the figure that the diameter of the stone pile at surface was approximately equal to 1.5 m. In addition, Figure 2 shows the relationship between the increases in diameter due to the installation of the stone pile versus radial stress. It can be noted from the figure that the increase in diameter decreases with depth up to a certain value of radial pressure ranging from 0.3–0.4 times the atmospheric pressure. Beyond this range, there is no change in diameter with

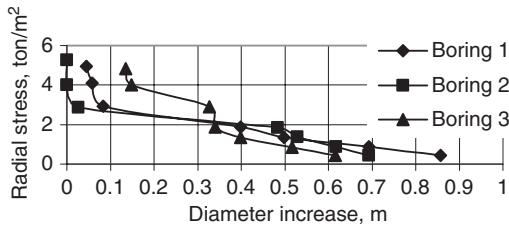


Figure 2. Relationship between diameter increases versus radial stress.

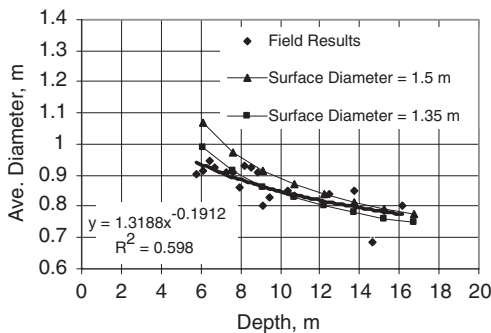


Figure 3. Depth versus diameter estimated from the modified results of the amount of stone.

depth. It should be realized that this radial stress range, shown in Figure 2, depends on the drilling equipment that was used in the installation.

To verify the preceding hypothesis from which we concluded that the diameter of the stone pile was tapered from a maximum value at the surface to a minimum value at a certain depth, another analysis was performed using field reports containing the amount of the stone that was installed in an 850-stone-pile project conducted in Orlando, Florida.

The average amount of stone installed in each pile has been estimated from the field reports then modified based on the relative stiffness of the soil located nearest to each pile, as obtained from the results of the SPT borings. The modified average was then classified according to the depth of each stone pile. It was found that the modified average diameter decreases as the depth increases, as shown in Figure 3, which agrees with the preceding hypothesis. For the purpose of investigating these results, a conic diameter assumption has been made based on the preceding results in which we assumed that the diameter of the stone pile decreased uniformly from the surface to a certain depth, then stays the same until the pile ends. The concept of the conic diameter was established in Figure 3 with the assumption that the diameter at the surface was equal to 1.5 m

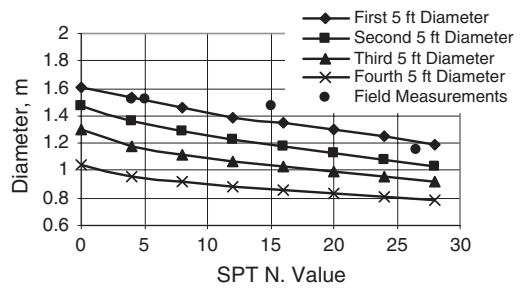


Figure 4. The variation of stone pile diameter versus N-value.

and 1.35 m. The effective depth was equal to 6 m for both surface diameters, where the effective depth is defined as the depth of the tapered zone. There was a reasonable match between the conic shape and the modified field results which supports the preceding hypothesis.

3 SOIL PROPERTIES

In order to estimate the properties of the surrounding soil, the profile was divided into four zones. Each zone had a depth equal to 1.5 m. The diameter of the stone pile was established for each layer by assuming that the density of the surrounding soil in the first 1.5 m after the installation of the stone pile is equal to the maximum dry density. The dry density was uniformly decreased to reach the field density prior to installation at a depth of 6 m. To avoid the overestimation that may occur due to the correlation of the SPT N-value for the first 2.5, the N-value used in that depth was taken as the actual blow count without corrections. Based on that assumption, the diameter of the stone pile was plotted in Figure 4 for the first, second, third, and fourth 1.5-m layers. It should be noted that to use Figure 4 for obtaining the diameter of the stone pile, no SPT blow count correlations are needed because they are built into the figure.

To verify the previous hypothesis, the diameter of the stone pile at the surface was measured in a number of projects that were conducted in Central Florida with similar soil stratigraphy. To measure the diameter of the stone pile, the surface was cleaned and leveled by a loader, and then the stone pile diameter was measured at surface. The results of the measured diameters versus SPT N-value are also shown in Figure 4. It can be concluded that there is a reasonable match between the measured diameters and those obtained from the previous assumption.

According to Kulhawy and Mayne (1990), the constitutive parameters of the surrounding soil were taken as follows: n and R_f were taken to be equal to 0.5, 0.8

respectively, and K and ϕ were calculated from the following equations:

$$K = 300 + 900 D_r \quad (1)$$

$$\phi = 28 + 14 D_r \quad (2)$$

The model parameters n , R_f , and K are the hyperbolic factors according to Duncan and Chang (1970), D_r is the relative density, and ϕ is the angle of internal friction. It should be noted that the relative density of the first layer is always equal to 1. In addition, the properties of the stone filling material were taken as in Table 1.

4 THE COEFFICIENT OF EARTH PRESSURE AT REST, K_0

When hyperbolic stress-strain relationship was adopted in the numerical analysis to simulate the field settlement, the coefficient of the earth pressure at rest, K_0 , proved to be the parameter that most significantly affected the settlement. Many previous studies suggested certain values of K_0 for the soil surrounding the stone piles based on field results. Hafez (2003), indicated that values of K_0 around 1–1.2 yielded the best results in several stone pile projects in Germany. Most references on design of displacement piles recommended a range for the coefficient of earth pressure in the design of driven piles from 1.0 to 1.5. Hafez (2003) concluded that K_0 values may vary from 1.1 to 2.5, with the most likely value being around 1.5. In the following two sections of the paper, the coefficient of earth pressure will be discussed in detail.

4.1 K_0 for the stone filling material

Since the stones in the pile were compacted in layers during the installation procedure, the coefficient of lateral earth pressure can vary significantly. During compaction, the forces exerted by the drilling equipment cause an increase in both vertical and horizontal earth pressures. When the probe is withdrawn, the vertical pressure decreases to its overburden value, whereas the horizontal earth pressure decreases to a lesser extent. Several theories addressed the effect of compaction on the lateral earth pressure either in the free field or on vertical non-deflecting structures. Broms and Ingleson (1971) developed empirical/analytical procedures based on the concept of hysteretic loading and unloading behavior. Mayne and Kulhawy (1982) proposed an empirical equation to estimate the coefficient of earth pressure for pre-compacted soil based on 171 different laboratory-tested soils. Seed and Duncan (1983), and Duncan and Seed (1986) presented models and analytical procedures for the calculation of compaction-induced stresses either in the free field or on vertical non-deflecting structures.

Mayne and Kulhawy's (1982) empirical equation, and Duncan and Seed's (1986) hysteretic model were adopted in this paper to determine the coefficient of earth pressure at rest due to the effect of compaction. To this end, the following parameters were assumed: the weight of the drilling equipment was considered to be equal to 13.5 ton which is 2.5 times the static weight of the driller Duncan and Seed (1986). Based on the field observations the thickness of the compacted layer was taken as 1 m. The vertical stress at the mid point of each compacted layer was estimated according to Boussinesq's solution for normal stresses caused by a point load. The parameters K_{onc} , α , and m_r in Mayne and Kulhawy's equation were taken as $(1 - \sin\phi_c)$, $(\sin\phi_c)$, and $0.75 k_{onc}$, respectively, where ϕ_c is the angle of internal friction of the compacted gravel. Also, the Duncan model parameters (β , and K_0 for virgin loading, $K_{1\phi c}$, and C) were taken as 0.6, $(1 - \sin\phi_c)$, K_p , and 0 respectively. The physical properties of the gravel that were used in this application were obtained from Table 1.

Table 2 shows the results of the coefficient of earth pressure at rest due to compaction for each layer obtained from both Mayne and Kulhawy (1982), and Duncan and Seed (1986) for a project in Orlando, Florida. From the table, it can be observed that there is reasonable agreement between the two methods, except for the first layer.

4.2 K_0 for the surrounding sand

The stone pile installation causes an increase in the diameter; therefore, the surrounding soil is compacted horizontally. None of the earlier research studies evaluated the effect of horizontal compaction in stone piles, although several papers discussed the effect of horizontal movement on lateral earth pressure. In order to predict the change in the coefficient of earth pressure at rest for the surrounding soil due to the increase in stone pile diameter, findings from earlier studies were adopted. Based on experimental results obtained using a centrifuge model wall Schofield (1961), the retaining wall movement required for a loose horizontal backfill to reach a passive state was approximately one fifth of the height. However, the passive wall movement needed for a dense backfill was only 4% of the wall height.

Table 2. K_0 that obtained from Mayne (1982) and Duncan (1986).

Method	Mayne and Kulhawy (1982)	Duncan and Seed (1986)
Layer 1 (Surface-1.5 m)	2.933716	5.828427
Layer 2 (1.5–3 m)	1.020799	0.757168
Layer 3 (3–4.5 m)	0.638215	0.419371
Layer 4 (4.5–6 m)	0.474251	0.342672

Fang et al. (1997) designed a special apparatus to measure the movement needed for the backfill to reach a passive state. The soil used in Fang's study was air-dry Ottawa sand with $G_s = 2.65$, $e_{max} = 0.76$, $e_{min} = 0.5$, $D_{60} = 0.36$ mm, and $D_{10} = 0.23$ mm. The unit weight achieved with the pluviation method was 15.5 kN/m³, with the relative density of 0.19, and the corresponding internal friction angle of 30.9° . Fang concluded that the lateral movement needed to reach a passive state for the horizontal backfill with a translation movement was equal to $0.35 H$.

To be more conservative, the movement causing a passive state was assumed to be equal to $0.35 H$ in all cases, where H is the layer thickness that may be obtained from the following equation.

$$H = S / [\tan(45 + \phi/2)] \quad (3)$$

S is the half distance between the center lines of stone piles.

Equation (3) was constructed based on square shape patterns. It should be noted that H should never exceed 5 ft, the maximum thickness of each lift. For the edge and corner piles, the distance S in equation (3) can be determined from the following relation.

$$S = 5 - K(5 - C) \quad (4)$$

where C is the average half-distance between center lines of stone pile under study and the outer stone piles in feet, and $K = n/\alpha$ where

$$0 \leq K \leq 1$$

n = number of stone piles surrounding the pile under study

$\alpha = \pi$ for edge piles, and 1.5π for corner piles

Table 3 shows the results of the coefficient of earth pressure at rest for the surrounding soil for the same project shown in Table 2.

In Table 3, the term "inner soil" refers to the soil confined in the square pattern whereas the "outer soil" signifies the region outside the pattern for edge piles; H for the outer soil was taken equal to 5 ft. The data in Table 3 were obtained based on the assumption that if the stone moved for a distance equal to $0.35 H$, then K_0 was taken to be equal to K_p , and if there was no movement, K_0 was taken to be equal to K_{onc} , which is equal to $(1 - \sin\phi)$. Linear interpolation was assumed for values between 0 and $0.35H$.

Table 3. K_0 for the surrounding soil

Method	Inner soil	Outer soil
Layer 1 (Surface-1.5 m)	5.044681	3.384899
Layer 2 (1.5-3 m)	4.714335	2.459147
Layer 3 (3-4.5 m)	3.202712	1.570218
Layer 4 (4.5-6 m)	1.783667	1.009927

5 SETTLEMENT PREDICTION USING ANALYTICAL METHODS

The previous results were used to build a finite element model and compare the results with field measurements in three projects conducted in Central Florida. In all cases, the soil profile was sand to silty sand extending to more than 15 m in depth, underlain by sandy to silty clay layer over limestone. For the load tests, 3×3 m rigid plates consisting of steel sheets and beams were used. The pressure was applied using two pistons with total capacity of 600 tons. The reaction was provided through eight ground anchors installed in a 4-m diameter circular pattern to a depth of 15 m. In the top 6 m, the grouting pressures were adjusted to a minimum value to minimize interference with the stone piles and surrounding soil. The settlement was measured using four dial gauges positioned in each corner of the plate.

For the finite element analysis, Plaxis 2D was used in conjunction with a strain hardening soil model which follows a hyperbolic stress-strain relationship for both the filling material and the surrounding soil. The diameter of the stone pile and the properties of the stone and the surrounding soil were obtained from Tables 1, 2 & 3, Figure 4, and Equations 1 & 2. The effect of the ground anchors on the load-settlement behavior was examined using the finite element model. The angle of the interface friction between the anchors and the soil was chosen to range from 10% to 67% of the angle of the internal friction of the surrounding soil. Based on the finite load-settlement results it was found that for the entire range of the interface angle of internal friction the presence of anchors had no significant effect on the load-settlement.

The results of the field load test and finite element simulation in the three projects are presented in Figure 5. It can be observed that there was a good agreement between the load-settlement curve obtained from the field results and that obtained from the finite element program, which further supports the earlier hypotheses.

6 CONCLUSION

A study was conducted to evaluate the effect of variation in stone pile diameter along the stone pile on the load-settlement behavior. An analysis of field data indicated that the stone pile is tapered from a maximum diameter at the surface to a minimum value at the critical depth. The critical depth may differ according to the pressure of the stone pile installation and the type of the surrounding soil. Based on the SPT N-values prior to the installation, the diameter of the stone pile was estimated by assuming that densification of the surrounding soil occurs near the ground surface during installation of the stone pile. The coefficient of lateral

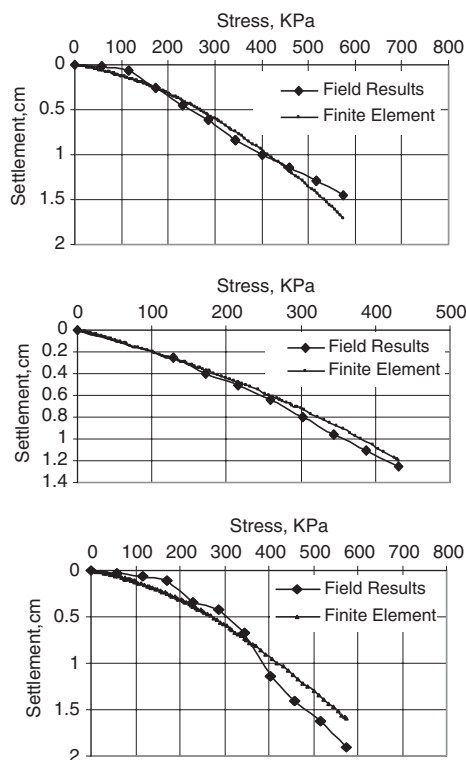


Figure 5. A comparison between field and finite element results.

earth pressure for the stone material was estimated from the hysteretic model presented by Duncan and Seed (1986), while the coefficient of lateral earth pressure for the surrounding soil was obtained from the wall movement theory presented by Fang et al. (1997).

Based on the analyses and field observations, it is not recommended to construct stone piles in a closely spaced pattern because of possible softening of the surrounding soil due to passive failure. To verify the optimum spacing between the stone piles, further studies need to be performed to evaluate the extent of the improvement zone for the sand surrounding the stone pile. A testing program that involves conducting SPT tests after the installation of the stone pile at varying distance from the center of the stone piles would be of benefit in validating such optimum spacing.

ACKNOWLEDGMENTS

The assistance and cooperation of many individuals associated with this study are gratefully acknowledged. The writers are particularly indebted to Mr. John Rubright of Hayward Baker, Inc., who made available company files, records, reports, and data from which

this study was developed. Special thanks are also extended to Hayward Baker, Inc., personnel, especially Michael Smith and Christopher Secrest, who were instrumental in providing the writers with all the necessary data.

REFERENCES

- Ashmawy, A. K., Rokicki, R., and Plaskett, M. E., "Predicted and Actual Settlement of Soils Improved by Vibro Replacement" Advances in Grouting and Ground Modification, Geotechnical Special Publication No. 14, ASCE, August 5-8 2000, pp. 281-295.
- Broms, B., and Ingleson, I., "Earth Pressure against Abutment of Rigid Frame Bridge" *Geotechnique*, Vol. 21 No. 1, 1971, pp. 15-28.
- Duncan, J. M., and Chang, C. Y., "Nonlinear Analysis of Stress Strain in Soils" *Journal of the Soil Mechanics and Foundations Division, ASCE*, Vol. 96, September, 1970, pp. 1629-1653.
- Duncan, J. M., and Seed, R. B., "Compaction-Induced Earth Pressures Under K_0 - Conditions" *Journal of Geotechnical Engineering, ASCE*, Vol. 112, No. 1, January, 1986, pp. 1-21.
- Fang, Y. S., Chen, J. M., and Chen, C. Y., "Earth Pressure with Sloping Backfill" *Journal of Geotechnical and Geoenvironmental Engineering, ASCE*, Vol. 123, No. 3, April 1997, pp. 250-259.
- Hafez, D. H. H., "Finite Element Study of the Behavior of Stone Columns" Thesis Submitted to the Faculty of Engineering at Cairo University in Partial Fulfillment of the Requirements for the Degree of Master of Science, January 2003.
- Hough, B. K., "Basic Soil Engineering" 2nd Ed., Roland Press, New York, 1969, 634 p.
- Kulhawy, F. H., and Mayne, P. W., "Manual on Estimating Soil Properties for Foundation Design" Cornell University, Geotechnical Engineering Group, August 1990.
- Kundu, P. K., Sharma K. G., and Nanda A., "Analysis of Stone Column Foundation for Storage Tank by FEM" Geotechnical Special Publication, ASCE, vol. 1, No. 40, 1994, pp. 701-710.
- Mayne, P. W., and Kulhawy, F. H., " K_0 - OCR Relationships in Soils" *Journal of Geotechnical Engineering, ASCE*, Vol. 108, No. GT6, June 1982, pp. 851-872.
- Mitchell, J. K., and Huber, T. R., "Performance of A Stone Column Foundation" *Journal of Geotechnical Engineering, ASCE*, Vol. 111, No. 2, February, 1985, pp. 205-223.
- Seed, R. B., and Duncan, J. M., "Soil-Structure Interaction Effects of Compaction-Induced Stresses and Deflections" Geotechnical Engineering Research Report No. UCB/GT/83-06, University of California, Berkeley, Ca, 1983.
- Schofield, A. N., "The Development of Lateral Force of Sand Against the Vertical Face of a Rotating Model Foundation" *Proc., 5th International Conference of Soil Mechanics and Foundation Engineering, Paris, Vol.2, 1961, pp. 479-484.*
- Terzaghi, K., and Peck, R. B., "Soil Mechanics in Engineering Practice" 2nd Edition, John Wiley and Sons, New York, 1967, p. 729.

Numerical modelling of deep mixing by volume averaging technique

U. Vogler, M. Karstunen & H. Krenn

Department of Civil Engineering, University of Strathclyde, Glasgow, Scotland

ABSTRACT: Deep mixed columns are commonly used to improve the bearing capacity and reduce settlements of structures on soft soils. The paper describes an enhanced two-dimensional technique, the so-called volume averaging technique to predict the settlements under an embankment load. The simulations of a unit cell of improved Vanntila clay are compared with traditional axisymmetric and fully three-dimensional calculations, using the S-CLAY1S model, a constitutive model that accounts for anisotropy, bonding and destructuration of the in situ soft soil. The differences of the numerical predictions following the three approaches are discussed.

1 INTRODUCTION

Deep mixed columns are extensively used to improve bearing capacity and reduce settlements of structures on soft soils. The mechanical properties of very soft clays, silts and organic soils can be improved with lime, cement or lime/cement columns. Deep mixing is a soil improvement technique in which stabilizing agents are mixed deep into the soil by using auger-type mixing tools either as a slurry or a powder. Deep mixed columns have been used for decades under embankment fills in Scandinavia and Japan, and are increasingly applied in the rest of Europe and the United States.

The existing design methods for structures founded on stabilized soils are still based on simple rigid-plastic solutions to predict ultimate loads and empirical (elastic) techniques to predict settlements. The most recent design guidelines in Sweden (Carlsten & Ekström 1995) and Finland (Korkiala-Tantuu 1997), on which the design guide by EuroSoilStab (2002) is based, rely on the ideas proposed by Broms & Boman (1977). The guidelines assume full interaction between the soft soil and the columns and largely ignore the complex non-linear behaviour of both materials.

An alternative to conventional design methods is to use numerical techniques, such as finite element analysis. With numerical modelling tools the complex stress-strain behaviour of soft soil and stabilized soil can be taken into account by adopting advanced constitutive models.

Natural soft soils are often structured, and as a consequence they exhibit anisotropy in their stress-strain behaviour. Additionally to anisotropy some soft soils exhibit the presence of interparticle bonding. Bonding

increases the strength of natural soft soils in comparison to remoulded soils. Karstunen et al. (2005) demonstrated the relevance of considering anisotropy and bonding on the prediction of vertical and horizontal displacements of Murro test embankment in Finland.

The simulation of circular columns under embankment is a fully three-dimensional problem. As 3D analyses are computationally very expensive an enhanced 2D technique, based on so-called volume averaging technique, is investigated. Basic idea of volume averaging is to map the true three-dimensional problem into two dimensions by describing the column-improved ground as a homogenised composite material. Once the adequate stress-strain response of both composites is defined, the response of column-improved ground subject to arbitrary loading and boundary conditions can be studied in two dimensions.

Firstly, principle of volume averaging is described, followed by a short description of constitutive models used for the soft soil. The performance of the enhanced model is then compared to axisymmetric and true 3D unit cell calculations.

2 VOLUME AVERAGING TECHNIQUE

The idea of volume averaging method is to model a homogenous material in finite element simulations instead of modelling columns and soil individually (Fig. 1). A way to model homogenised material was proposed by Schweiger and Pande (1986). The way they constructed the homogenised stiffness matrix lead to the violation of the equilibrium conditions in radial direction and a pseudo-yield criterion was proposed

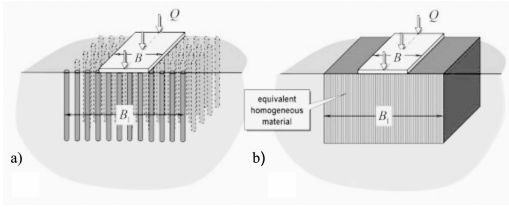


Figure 1. (a) Discrete and (b) homogenized representation of a footing problem (Jellali et al. 2005).

in such a manner that radial equilibrium condition is satisfied. The principles adopted for this study are based on the ideas by Lee & Pande (1989).

It is assumed that the columns are distributed homogeneously within the soft soil. Moreover, perfect bonding is assumed between the deep-mixed columns and the in situ soil. The proposed method allows for adopting elasto-plastic constitutive models for the two materials using a separate constitutive model for each constituent. Equilibrium as well as compatibility conditions are satisfied through stress/strain redistribution in successive iterations.

2.1 Equivalent material stiffness matrix

Homogenisation is carried out using the averaging rule as follows:

$$\bar{\boldsymbol{\sigma}}^{eq} = \mu_s \bar{\boldsymbol{\sigma}}^s + \mu_c \bar{\boldsymbol{\sigma}}^c \quad (1a)$$

$$\dot{\boldsymbol{\epsilon}}^{eq} = \mu_s \dot{\boldsymbol{\epsilon}}^s + \mu_c \dot{\boldsymbol{\epsilon}}^c \quad (1b)$$

where μ is a volume fraction. The superscript *eq, s* and *c* refer to the homogenized material, the soil and the column material, respectively. $\bar{\boldsymbol{\sigma}}$ and $\dot{\boldsymbol{\epsilon}}$ are the (total) stress and strain rate tensors, respectively.

The coordinates are defined with *y* axis in vertical direction. In order to satisfy local equilibrium conditions the following equilibrium conditions are applied to prevent any stress discontinuities on the interface between soil and column:

$$\dot{\sigma}_x^{eq} = \dot{\sigma}_x^s = \dot{\sigma}_x^c \quad (2a)$$

$$\dot{\sigma}_z^{eq} = \dot{\sigma}_z^s = \dot{\sigma}_z^c \quad (2b)$$

$$\dot{\tau}_{xy}^{eq} = \dot{\tau}_{xy}^s = \dot{\tau}_{xy}^c \quad (2c)$$

$$\dot{\tau}_{yz}^{eq} = \dot{\tau}_{yz}^s = \dot{\tau}_{yz}^c \quad (2d)$$

The assumption of perfect bonding between soil and column implies the following kinematic conditions:

$$\dot{\epsilon}_y^{eq} = \dot{\epsilon}_y^s = \dot{\epsilon}_y^c \quad (3a)$$

$$\dot{\gamma}_{zx}^{eq} = \dot{\gamma}_{zx}^s = \dot{\gamma}_{zx}^c \quad (3b)$$

The constitutive equations for the constituents can be described in terms of effective stress increments as:

$$(\bar{\boldsymbol{\sigma}}^s)' = \mathbf{D}^s \dot{\boldsymbol{\epsilon}}^s \quad (4a)$$

$$(\bar{\boldsymbol{\sigma}}^c)' = \mathbf{D}^c \dot{\boldsymbol{\epsilon}}^c \quad (4b)$$

where $\mathbf{D}^{c,s}$ represent the appropriate elastic or elasto-plastic material stiffness matrices for the soil and the column expressed in terms of effective stress. It should be noted here that the stiffness matrixes can be derived based on any elasto-plastic constitutive law. Considering the averaging rules (Eq. 1), the constitutive relations (Eq. 4), the equilibrium and kinematic conditions (Eq. 2, 3), the constitutive relation for the averaged material can be described:

$$(\bar{\boldsymbol{\sigma}}^{eq})' = \mathbf{D}^{eq} \dot{\boldsymbol{\epsilon}}^{eq} \quad (5)$$

With the equivalent stiffness matrix defined as

$$\mathbf{D}^{eq} = \mu_s \mathbf{D}^s \mathbf{S}_1^s + \mu_c \mathbf{D}^c \mathbf{S}_1^c \quad (6)$$

The two material matrixes \mathbf{S}_1^s and \mathbf{S}_1^c are functions of the volume fractions and the constitutive matrices of both constituents (see Lee & Pande 1989 for details).

$$\mathbf{S}_1^{s,c} = f(\mu_s, \mathbf{D}^s, \mathbf{D}^c) \quad (7)$$

2.2 Solution strategy

If one or both constituents are beyond the elastic limit the stresses calculated with the equivalent material stiffness matrix (Eq. 6) would violate the equilibrium conditions due to the return mapping procedure for one or both constituents. Hence, a sub-iteration scheme (Fig. 2) is adopted.

With the help of the equivalent material matrix \mathbf{D}^{eq} , the boundary value problem is solved for a homogeneous medium and the averaged strain increments $\dot{\boldsymbol{\epsilon}}^{eq}$ are obtained. Next the individual strain increments $\dot{\boldsymbol{\epsilon}}^s$ and $\dot{\boldsymbol{\epsilon}}^c$ in soil and columns, respectively, are calculated with the help of the material matrices $\mathbf{S}_1^{s,c}$. From the

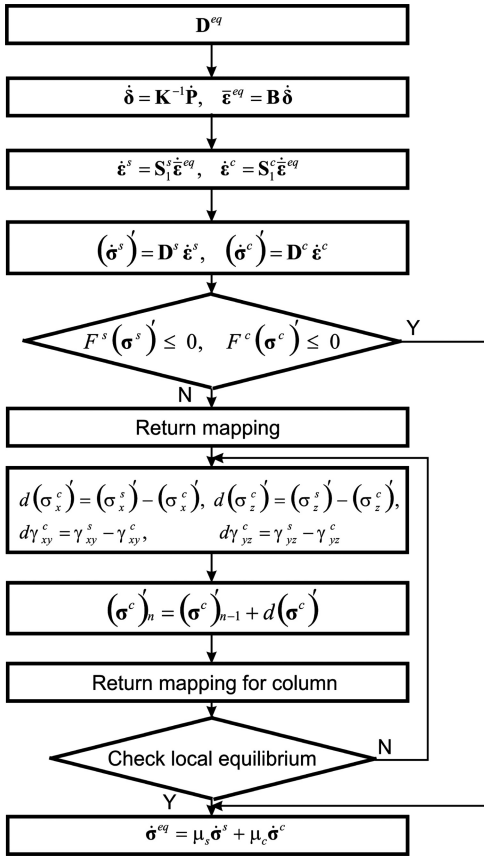


Figure 2. Sub-iteration scheme to correct the equilibrium condition (after Lee & Pande 1989).

constitutive equations the stress increments and the elastic trial stresses for both constituents are determined. If both materials still remain elastic, no further calculations are needed, and the averaged equivalent stress can be determined directly by Equation 1a.

If one or both materials are yielding, return mapping procedures have to be applied. After return mapping the local stresses of soil and columns may violate the equilibrium conditions (Eqs. 2). Possible stress differences (whether positive or negative) are then added to the column stresses.

After adding the stress differences to the column material, the yield condition of the column material has to be checked again. Equilibrium has to be re-checked as it may have become out of balance during the possible return mapping of the column material. If the local equilibrium on the virtual interface between column and in situ soil is satisfied, finally, the stresses on the integration point can be calculated according to the averaging rule (Eq. 1a).

Table 1. Soil constants for column material (Mohr Coulomb).

Layer	G [kPa]	ν'	ϕ' [°]	ψ' [°]	c' [kPa]	γ [kN/m ³]
Dry Crust	1600	0.35	36	0	27	15
Vanttila Clay	2100	0.35	36	0	27	15

3 CONSTITUTIVE MODELLING

3.1 Vanttila clay

The soft clay considered represents Vanttila clay, a soft post-glacial clay from Espoo, in Southern Finland, which is a typical example of sensitive Scandinavian clays. Vanttila clay has a high clay mineral content (48%) with illite as the main clay mineral. The natural water content is very high and exceeds the liquid limit. The stress strain behaviour of Vanttila clay was investigated by performing oedometer and triaxial tests on natural (undisturbed) and reconstituted (remoulded and one-dimensionally consolidated) samples. Vanttila clay in its natural state was found to be highly structured, with a high degree of initial anisotropy (Koskinen & Karstunen 2004).

3.2 Embankment

The embankment is modelled by using a simple Mohr Coulomb model, assuming the following parameter values: Young's modulus $E = 40,000$ kPa, Poisson's ratio $\nu' = 0.3$, friction angle $\phi' = 38^\circ$, dilatancy angle $\psi' = 0^\circ$ and the unit weight of the fill material $\gamma = 20$ kN/m³. For computational reasons a small value of cohesion was assumed ($c' = 1$ kPa).

3.3 Columns

Vanttila clay was one of the test materials for a study on deep stabilization of soft Finnish clays at Helsinki University of Technology. The project investigated the influences of mixing tools and manufacturing process. Laboratory model tests were followed by full-scale field tests as reported by Aalto (2003). The properties of stabilized columns adopted for studies in this paper correspond to cement columns that were produced using 150 kg of cement/m³ of Vanttila clay. The highly non-linear stress strain response of the column material was simplified by the Mohr Coulomb material model. The values for the shear modulus G were based on an appropriate stress level at 0.5 m depth for the dry crust and at 5 m depth for the Vanttila clay.

3.4 S-CLAY1S

The S-CLAY1S model (Karstunen et al. 2005) is a critical state model that is able to account for both initial

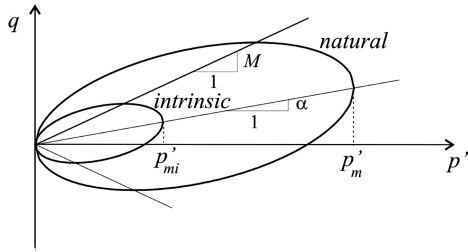


Figure 3. Yield surface of S-CLAY1S (triaxial stress space).

and plastic strain induced anisotropy and degradation of bonding. Anisotropy of the soil is modelled by inclining the yield surface and bonding is described by an “intrinsic yield surface” following the idea of Gens & Nova (1993). The intrinsic yield surface is of the same shape and inclination as the yield surface for the natural soil (Fig. 3), but with a size p'_{mi} that is related to p'_m , the size of the yield surface for the natural clay by

$$p'_m = (1+x)p'_{mi} \quad (8)$$

where x is the amount of bonding. The initial value of x can be estimated based on sensitivity ($x \approx S_t - 1$). Natural and intrinsic yield surfaces are plotted in Figure 3 in triaxial stress space. The yield surface f is described in general stress space by

$$f = \frac{3}{2} \left(\{\boldsymbol{\sigma}'_d - p' \mathbf{a}_d\}^T \{\boldsymbol{\sigma}'_d - p' \mathbf{a}_d\} \right) - \left(M^2 - \frac{3}{2} \{\mathbf{a}_d\}^T \{\mathbf{a}_d\} \right) (p'_m - p') p' = 0 \quad (9)$$

where p' is the mean effective stress, $\boldsymbol{\sigma}'_d$ is the deviatoric stress tensor, M and p'_m are the aspect ratio and the size of the yield curve, respectively and \mathbf{a}_d is the deviatoric fabric tensor, defining the orientation of the yield surface in three-dimensional stress space (see Karstunen et al. 2005 for details). In triaxial stress space for a cross-anisotropic sample \mathbf{a}_d reduces to a scalar value α as can be seen in Figure 3.

The S-CLAY1S model incorporates three hardening laws. The first describes the change of size of the yield surface and is assumed to be related solely to the increments of plastic volumetric strain $d\varepsilon_v^p$ similar to the Modified Cam Clay model.

The second hardening law describes the changes in deviatoric fabric tensor \mathbf{a}_d that relate to the orientation of the yield surface in three-dimensional stress space. The orientation is affected by volumetric and deviatoric $d\varepsilon_{ij}^p$ plastic straining and the current stress path tensor $\boldsymbol{\eta}$ ($=\boldsymbol{\sigma}'_d/p'$) described by:

$$d\mathbf{a}_d = \mu \left[\left(\frac{3}{4} \boldsymbol{\eta} - \mathbf{a}_d \right) \left(d\varepsilon_v^p \right) + \beta \left(\frac{\boldsymbol{\eta}}{3} - \mathbf{a}_d \right) \left(d\varepsilon_d^p \right) \right] \quad (10)$$

Table 2. Initial values for state parameters and K_0 .

Layer	Depth [m]	e	POP [kPa]	K_0	α	x
Dry crust	0–1	1.7	30	1.06	0.63	90
Vanttila clay	1–12	3.2	10	0.571	0.46	20

Table 3. Values for conventional soil constants.

Layer	γ [kN/M ³]	κ	ν'	λ	M
Dry crust	13.8	0.029	0.2	0.25	1.6
Vanttila clay	13.8	0.032	0.2	0.88	1.2

Table 4. Values for additional soil constants.

Layer	β	μ	λ_i	a	b
Dry crust	1.07	15	0.07	11	0.2
Vanttila clay	0.76	40	0.27	11	0.2

with the soil constant μ controlling the rate of yield surface rotation and β controlling the relative effectiveness of plastic shear strains and plastic volumetric strains in the process.

The third hardening law describes the degradation of bonding as a function of plastic volumetric and deviatoric strains:

$$dx = -ax \left[|d\varepsilon_v^p| + b |d\varepsilon_d^p| \right] \quad (11)$$

Similar to the rotation hardening law, a describes the absolute effectiveness of degradation and b the relative effectiveness of plastic volumetric and shear strains. A detailed description of the S-CLAY1S model can be found in Karstunen et al. (2005).

3.5 Model parameters

The values for the parameters describing the soft soil (see Tables 3 and 4) have been chosen to correspond to Vanttila clay (Koskinen & Karstunen 2004). Preconsolidation of the soil is modelled by assuming the vertical pre-overburden pressure POP (Table 2), defined as the difference between the maximum past value and the in situ value of vertical effective stress. The initial values for the void ratio e and the coefficient of earth pressure at rest K_0 are also given in Table 2. The assumed values for the slope of the swelling line κ and the values for M are shown in Table 3. For S-CLAY1S the slope of the intrinsic compression line λ_i is used, rather than the slope of normal compression line λ . Typically for a structured soil the λ_i - values are noticeably smaller than the corresponding λ - values.

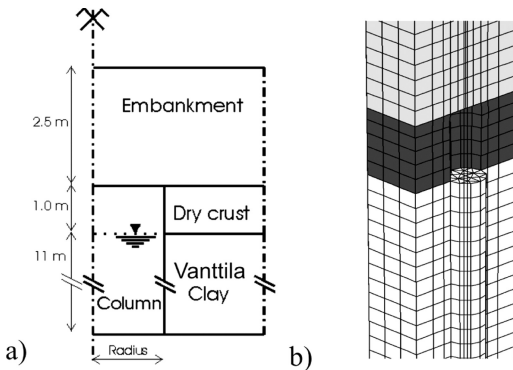


Figure 4. (a) Soil profile and (b) 3D finite element mesh.

4 UNIT CELL CALCULATIONS

The numerical analyses of a unit cell consider an infinitely wide embankment fill founded on Vanttila clay, which has been improved by stabilized cement columns. The geometry of the problem is shown in Figure 4a. The height of the embankment fill is assumed to be 2.5 m based on stability analysis according to the EuroSoilStab (2002) for 1.4 m c/c spacing. Deep stabilized columns are assumed to be installed in a periodic square grid.

The column diameter is taken as 0.6 m, as this is a common diameter used in industry, and for the simulations shown in this paper the c/c spacing is chosen to be 1 m, so that the system is well below the ultimate limit state. Fully drained analyses have been carried out for a unit cell, assuming an infinitely wide embankment load.

The analyses have been performed using the 3D finite element code PLAXIS 3D Foundations for the true unit cell and PLAXIS Version 8.2 for the axisymmetric analyses, in which the problem is modelled both discretely, with the soil and the columns modelled separately, as well as with the volume averaging technique. The lateral boundaries of all models were constraint in horizontal direction and the bottom boundaries in all directions.

4.1 Axisymmetric unit cell

In the axisymmetric analysis the unit cell was discretized using a finite element mesh with about 220 15-noded triangular elements. Separate volume clusters were assigned to Vanttila clay, the dry crust and the embankment fill. After the generation of the initial stress state, the soil at the area of the column was replaced by the column material. In the next step the embankment fill was constructed as volume elements.

4.2 True 3D unit cell

Analogously to the 2D axisymmetric calculations, a true 3D unit cell was created. A section of the finite

Table 5. Vertical displacements at different depths [mm].

Depth [m]	Axisymmetric			3D			VAT
	Avg.	Col.	Soil	Avg.	Col.	Soil	Avg.
0	275	274	275	279	278	279	228
1	258	254	260	261	257	263	211
2	230	230	230	234	234	234	190
5	160	160	160	161	161	161	129

avg. – average, col. – column.

Table 6. Vertical stress increase at different depth [kPa].

Depth [m]	Axisymmetric		3D		VAT	
	Col.	Soil	Col.	Soil	Col.	Soil
0.5	98	34	110	23	82	37
2	143	13	147	12	144	13
5	141	14	145	14	143	13

element mesh used for the 3D calculation can be seen in Figure 4b. The mesh consists of approximately 5000 quadratic 15-noded wedge elements. Boundary conditions were assumed identical to the 2D case.

4.3 Axisymmetric unit cell with volume averaging

The analysis using volume averaging uses the same mesh and boundary conditions as the axisymmetric unit cell. In contrast to the previous analyses, the installation of the columns was modelled by replacing the whole subsoil with materials that are representing the averaged soil/column material behaviour. Like in previous simulations the fill was simulated using volume elements.

4.4 Discussion on the results

The vertical displacements predicted by the different analyses are summarised in Table 5 for certain depths at the symmetry axis (in the column) and the outer boundary (in the soil). VAT stands for volume averaging. The discrete axisymmetric analysis and the 3D calculation of the true unit cell show a very good match. The volume averaging method predicts deformations that are approximately 20% lower than by the other analyses. Based on the results in Table 5, all analyses predict approximately the same amount of deformation in the dry crust.

In Table 6, the predicted increases in the vertical stress are presented. It should be noticed that the values in Table 6 (and 7) are approximate averaged values for a given depth, for the column and the soil, respectively. In this way the inevitable fluctuations have been smoothed. The predicted stresses are approximately in equilibrium with the applied loading. The predicted

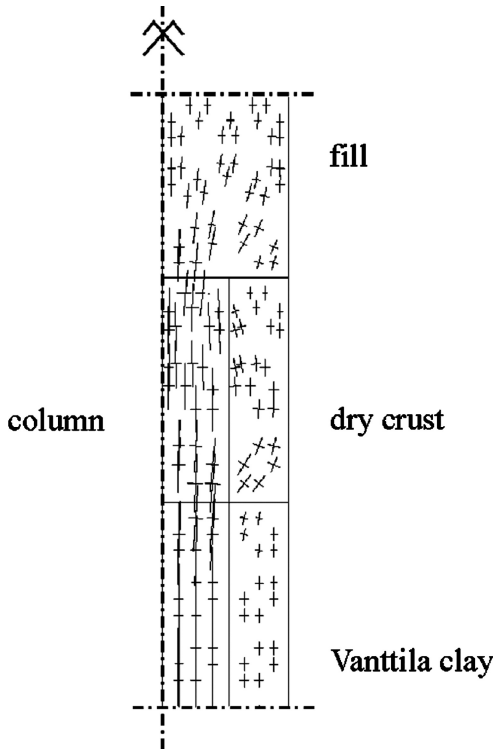


Figure 5. Mean principle stresses in axisymmetric unit cell demonstrate soil arching.

increases in vertical stress within the dry crust differ between the three methods (Table 6). The volume averaging method predicts higher stresses in the soil, and consequently, lower stresses in the column, than the other methods. Below the dry crust in Vanttila clay the predicted load distributions between the soil and the column material are in very good agreement for all three approaches.

For the discrete models of soil and columns, it is possible to investigate the arching mechanisms associated with embankment loading. The mechanisms are rather complex, as demonstrated in Figure 5 for the (discrete) axisymmetric case. The arching is controlled by the relative stiffnesses of the constituents. Because overall the stiffness assumed for the columns is higher than the predicted stiffness of the soil, most of the embankment load has to be transferred to the columns.

Arching is a gradual process and part of the load is transferred to the columns already within the embankment fill, and the remainder of this load transfer occurs in the dry crust. In Figure 5, there is also some indication of some local load transfer from the columns to the soil, due to the fact that in the dry crust, the columns compress more than the soil (see Table 5). This indicates that the top of the columns are yielding. With

Table 7. Horizontal stresses at soil/column interface [kPa].

Depth [m]	Axisymmetric		3D		VAT	
	Prior	After	Prior	After	Prior	After
0.5	8	24	8	25	8	19
2	10	21	9	19	10	16
5	17	30	15	23	17	23

volume averaging, the load is instantly distributed between soil and column according to the respective stiffness ratios, and therefore the vertical stresses in the dry crust are predicted to be much lower than by the other analyses (Table 6).

Comparison of the effective horizontal stresses over the depth has been condensed in Table 7. The results correspond to the situation prior and after the embankment construction. The results are virtually identical prior to construction. Overall, the volume averaging method predicts lower horizontal stresses than the other two methods.

5 CONCLUSIONS AND FUTURE WORK

The paper describes the principle of volume averaging that enables mapping the complex three-dimensional problem involving circular columns in a soft ground to an equivalent two-dimensional analysis. The results of unit cell calculations for a discrete 2D model, a 3D true unit cell and an axisymmetric unit cell with averaged material model are compared.

Overall, the discrete models (2D and 3D) show rather similar response, although there are some local differences in the load distribution. It is also possible to visualise the complex arching mechanics associated to this boundary value problem with the discrete models. The predicted vertical displacements overall seem to be equal in the columns and the soil, which is in agreement with the current design methods.

The preliminary results for the volume averaging method are quite interesting. As the method does not account for arching, the embankment load is instantaneously distributed according to the predicted stiffness ratios at each layer boundary. The vertical displacements predicted by the volume averaging method are smaller throughout than predicted by the discrete models. The reasons for this have to be investigated further before the model is applied to other boundary value problems.

ACKNOWLEDGEMENTS

The work presented was carried out as part of a Marie Curie Research Training Network "Advanced Modelling of Ground Improvement on Soft Soils (AMGISS)" (Contract No MRTN-CT-2004-512120) supported by the EC through the program "Human

Resources and Mobility". The first author is an Early Stage Researcher appointed by the AMGISS network. The third author is sponsored by a Faculty of Engineering Scholarship at the University of Strathclyde.

REFERENCES

- Broms, B. & Boman, P. 1977. Stabilisation of soil with lime columns, *Design Handbook, 2nd Edition*, KHT, Jordoch Bergmekanik, Stockholm.
- Carlsten, P. & Ekström, J. 1995. Lime and lime cement columns, Swedish Geotechnical Society, *SGF Report 4:95E*, Linköping.
- EuroSoilStab 2002. Development of design and construction methods to stabilise soft organic soils. *Design guide soft soil stabilisation. CT97-0351* (Project No. BE-96-3177. European Commission. Industrial & Materials Technologies Programme (Brite-EU-Ram III). Brussels).
- Gens, A. & Nova, R. 1993. Conceptual bases for a constitutive model for bonded soils and weak rocks. *Proc. Int. Symp. Hard Soils-Soft Rocks*, Athens, 485–494.
- Jellali, B., Bouassida, M. & de Buhan, P. 2005. A homogenization method for estimating the bearing capacity of soils reinforced by columns. *Int. J. Numer. Anal. Meth. Geomech.*, 29, 989–1004.
- Karstunen, M., Krenn, H., Wheeler, S.J., Koskinen, M. & Zentar, R. 2005. Effect of anisotropy and destructuration on the behaviour of Murro test embankment. *ASCE International Journal of Geomechanics*, 5, No. 2, 87–97.
- Korkila-Tanttu, L. 1997. Design guide for deep mixed columns (Syvästabiloinnin mitoitusohje), Finnish National Road Administration, *FinnRA report 18/1997*, Helsinki (in Finnish).
- Koskinen, M. & Karstunen, M. 2004. The effect of structure on the compressibility of Finnish clays. In: *Proc. 14th Nordic Geotechnical Meeting, Ystad, Sweden. Swedish Geotechnical Society, Report 3:2004*, pp. A-11–A-22.
- Lee, J.S. & Pande, G.N. 1998. Analysis of stone-column reinforced foundations. *Int. J. for Numer. Anal. Meth. Geomech.*, 22, 1001–1020.
- Schweiger, H.F. & Pande, G.N. 1986. Numerical Analysis of stone column supported foundation. *Computers and Geotechnics*, 2, 347–372.

Equivalent-uniform soil model for the seismic response analysis of sites improved with inclusions

G.D. Bouckovalas & A.G. Papadimitriou
National Technical University of Athens, Greece

A. Kondis
Civil Engineer, Greece

G.J. Bakas
Edrasis – C. Psallidas S.A., Greece

ABSTRACT: This paper studies how 1D equivalent-linear analyses may be accurately used for simulating the seismic response of sites improved with inclusions (e.g. gravel columns). For this purpose, the composite ground is modeled as an equivalent-uniform material, whose dynamic non-linear properties are a function of the respective properties of the natural soil and the inclusion material (e.g. gravel), as well as the replacement ratio of the composite ground. The equivalent-uniform model of the composite ground has a theoretical basis and is verified by comparing parametric results from pertinent 1D and 2D seismic ground response analyses, performed with the equivalent-linear method, for small and high intensity motions. Emphasis is put on replacement and solidification of cohesive soils using a grid of reinforcing columns (inclusions).

1 INTRODUCTION

In cases that the soil is either too soft or too loose, its use as a foundation layer is very often preceded by its improvement with inclusions that are materialized via replacement (e.g. vibro-flotation) or solidification (e.g. soil mixing) methods. The improved site is composite and has more or less different mechanical properties than the natural soil. The amount of differentiation depends on the inclusion material and the replacement ratio of the improvement geometry. For example, a soft clay site improved with gravel piles for the reduction of the anticipated settlements has a different seismic response than the natural soft clay site. Nevertheless, this fact is very often neglected in the seismic design of the superstructure, since taking it into account requires the performance of at least 2D (not to mention 3D) seismic ground response analyses. Moreover, opting for not performing any analyses is often based on the *ad hoc* assumption that the effect of improvement is beneficial for the superstructure, a fact that is not necessarily true

More accurate design could be achieved if the necessary ground response analysis of the improved site could be performed via simpler methodologies, like 1D equivalent-linear analysis (e.g. using SHAKE91,

Idriss and Sun 1992). In an attempt to allow for such analyses, this paper proposes a methodology for modeling the composite (non-uniform) ground as an equivalent-uniform material that if it is subjected to the same base excitation leads to the same overall seismic motion at the ground surface. The methodology calibrates the shear modulus G degradation and damping ξ increase curves with the amplitude of the cyclic shear strain γ of the equivalent-uniform material, as a function of the respective curves of the natural soil and the inclusion material, as well as the replacement ratio a_r of the composite ground. The emphasis is put on grid-like improvement geometries that are usually modeled in 2D plane strain analyses like a series of embedded soldier pile walls.

The methodology has a theoretical basis and is verified by comparing parametric results from 2D and 1D equivalent-linear analyses that assume uniform soft soil and improvement material properties from the ground surface to the base. Despite the simplicity of the analyses, the proposed equivalent-uniform soil model is considered appropriate for use for non-uniform material properties, given the use of the appropriate per depth value of the improvement-to-soil maximum shear stiffness ratio $K_o = G_{ic}/G_{so}$.

Moreover, it is shown to be accurate for sites excited by any earthquake intensity and predominant frequency and approximately accurate for non-uniform improvement geometries (e.g. shallow improvement in deep soft soil deposit or narrow improvement zone in extensive soft soil deposit). Sole exception to this rule is that the use of the proposed equivalent-uniform model is considered appropriate for the improvement of soft soils that do not exhibit excess pore pressure buildup and parallel drainage, a coupled mechanism of fluid flow and deformation that was not addressed in the performed analyses.

2 SEISMIC GROUND SURFACE RESPONSE OF AN IMPROVED SITE

The 2D and 1D analyses in this paper were performed with *QUAD4M* (Hudson et al 1994) and *Shake91* (Idriss and Sun 1992), respectively, two (2) commercial codes that perform an equivalent-linear analysis, the former in the time domain while the latter in the frequency domain. Before proceeding to the analysis of improved sites, it was considered necessary to establish that the two (2) codes produce identical results for the benchmark case of the 1D vertical S wave propagation through a uniform horizontal soil layer over rigid bedrock. This was achieved by disallowing vertical motion of the lateral boundaries of the 2D mesh, whose width was at least 5 times longer than the depth H of the uniform soil column. This type of lateral boundary conditions that are set far enough from the area of interest is the optimal solution for the numerical code at hand, which does not offer the user absorbing or free-field boundaries, as other codes do.

The basic prerequisite for using 1D seismic ground analysis for an improved composite ground is that the actual seismic ground surface response shows negligible spatial variability. If that is the case, then it has the potential to be approximated by an “average” ground surface response, that of an equivalent-uniform material. In order to answer this question, the improvement geometry of Fig.1 was simulated by 2D analyses, with a base excitation that imposes vertically propagating SV waves.

The soft soil and the inclusions are assumed linear visco-elastic materials with $G_{s,0} = 80$ MPa and $G_{i,0} = 800$ MPa having a total depth $H = 10$ m that are imposed to a seismic excitation with peak acceleration at outcropping bedrock equal to 0.15 g.

As shown in this figure, the peak horizontal acceleration a_{max} at various points of the ground surface show small variability (0.22 – 0.23 g). This is also depicted in the time-histories and the elastic response spectra of 2 neighboring nodes at the center of the improvement geometry, one on natural soil and the other on the inclusion that show practically identical

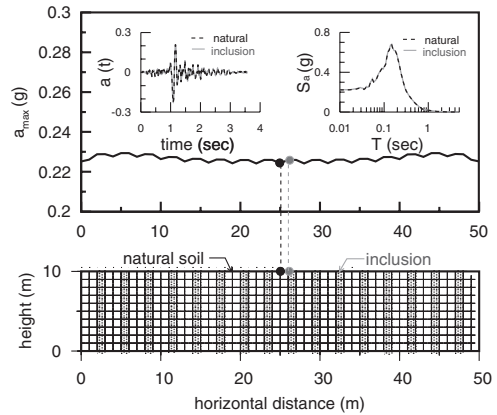


Figure 1. Finite element mesh and results for the variation of seismic acceleration at ground surface from 2D analysis.

results. Hence, the ground surface response can be considered as practically uniform and as such, it can potentially be estimated without the use of a 2D analysis, but via a 1D analysis of the seismic response of an equivalent-uniform soil column of the same depth H .

The question that arises is what are the dynamic properties of this equivalent-uniform material? This is the subject of the following paragraphs.

3 EQUIVALENT-UNIFORM MATERIAL FOR LINEAR ANALYSES

The improvement configuration of any 2D analysis may be identified in terms of two (2) parameters: (a) the improvement-to-soil maximum shear stiffness ratio $K_0 = G_{i,0}/G_{s,0}$ (>1), and (b) the improvement area ratio $a_r = d'/s$ (<1), where d' is the width of the embedded soldier pile walls of the analysis and s their center-to-center interdistance. For the example of Fig.1, $a_r = 1$ m/3 m \cong (33% and $K_0 = 800/80 = 10$. Note that the actual values of d' and s are not important for the seismic ground response, but only the improvement area ratio, i.e. $a_r = d'/s$. This is shown in Fig.2 that compares the elastic response spectra at ground surface from three (3) analyses with the same K_0 ($=10$) value and the same a_r ($=15\%$) value that are excited by the same input motion.

As a first approximation, the maximum shear modulus $G_{eq,0}$ of the equivalent-uniform material can be estimated by assuming that the vertically propagating SV waves impose the same shear strain γ to both the improvement inclusion and the neighboring natural soil (e.g. Baez & Martin 1993).

In such a case, this common value of γ is assigned to the equivalent-uniform material as well. The estimation

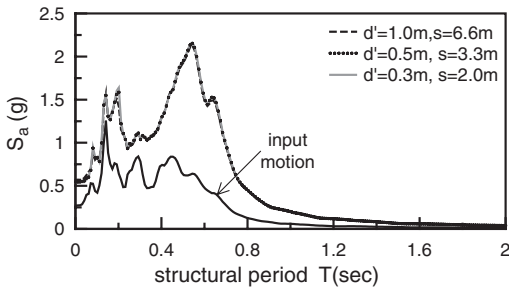


Figure 2. Elastic response spectra (5% damping) at ground surface for 3 different improvement configurations, but the same area replacement ratio a_r .

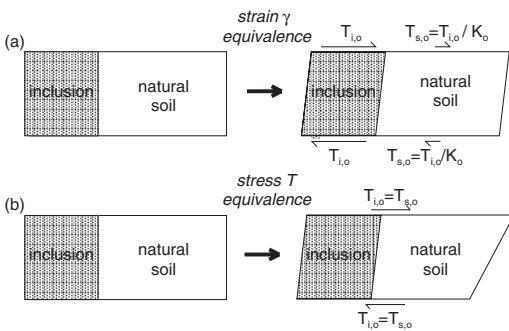


Figure 3. Schematic illustration of deformed soil-inclusion cell based on the assumptions of strain and stress equivalence.

of $G_{eq,0}$ is enabled by estimating the total shear force $F_{eq,0}$ imposed by the SV wave on a unit cell composed by an inclusion and its neighboring soil (see Fig.3a):

$$F_{eq,0} = F_{s,0} + F_{i,0} \Rightarrow \tau_{eq,0} = \tau_{s,0}(1 - a_r) + \tau_{i,0}a_r \quad (1)$$

Given the aforementioned equality of shear strains γ in the inclusion, the soil and the equivalent-uniform material, Eq.(1) leads to:

$$G_{eq,0} = G_{s,0} [(1 - a_r) + K_o a_r] \quad (2)$$

As a second approximation, the $G_{eq,0}$ of the equivalent-uniform material can be estimated indirectly by assuming two (2) materials in sequence, under the same normal stress σ . This 1-D loading leads to deformations d_1 and d_2 in the two materials, two values that are related to their Young's moduli E_1 and E_2 and their initial lengths L_1 and L_2 , respectively. In this case, an equivalent-uniform material would have a total length $L = L_1 + L_2$ and a total deformation $d = d_1 + d_2$, that would be interrelated via the Young's modulus E_{eq} of the equivalent-uniform material. Based on

elasticity theory, the values of E_1 , E_2 and E_{eq} are inter-related as:

$$E_1 = \sigma \frac{L_1}{d_1} \quad ; \quad E_2 = \sigma \frac{L_2}{d_2} \quad ; \quad E_{eq} = \sigma \frac{L_1 + L_2}{d_1 + d_2} \quad (3)$$

Introducing E_1 and E_2 into E_{eq} of Eq.(3), and after some algebra, leads to the following relation for E_{eq} :

$$E_{eq} = E_2 \frac{(E_1/E_2)}{a_r + (1 - a_r)(E_1/E_2)} \quad (4)$$

where $a_r = L_1/(L_1 + L_2)$. By assigning the 1-D physical analogy, to the physical problem of earthquake-induced shearing of the inclusion (material 1) and the natural soil (material 2), the common value of σ is replaced by a common value of τ and the values of E_1 , E_2 and E_{eq} by $G_{i,0}$, $G_{s,0}$ and $G_{eq,0}$. Hence, the $G_{eq,0}$ is given by:

$$G_{eq,0} = G_{s,0} \frac{K_o}{a_r + (1 - a_r)K_o} = G_{s,0} M_o \quad (5)$$

where $M_o \geq 1$, is a dimensionless multiplier of $G_{s,0}$. In such a case, the common value of τ leads to different values of γ for the inclusion and the natural soil, where $\gamma_{i,0} = \gamma_{s,0}/K_o$, as shown schematically in Fig.3b.

Equations (2) and (5) provide two analytical approaches for the value of the equivalent-uniform maximum shear modulus $G_{eq,0}$. In order to ascertain which of the 2 approaches is more appropriate for use in "equivalent" 1D analyses, Fig.4a presents the results from linear 1D analyses that were conducted with $G_{eq,0}$ equal to 320 and 114.3 MPa.

These two (2) values of $G_{eq,0}$ result from using Eqs (2) and (5), respectively, for $G_{s,0} = 80$ MPa, $K_o = 10$ and $a_r = 33\%$. Furthermore, Fig.4a includes the 1D results for the response of the natural soil deposit ($G_{s,0} = 80$ MPa), as well as the results from the 2D analysis of the composite improved ground (the same from Fig.1). It is deduced that a 1D analysis with an equivalent-uniform material whose G value is estimated via Eq.(5) practically duplicates the a_{max} variation at the ground surface of the improved ground, while the use of Eq.(2) leads to erroneous results. The same holds for the amplification of the elastic response spectra S_a , whose typical comparison for case of Fig.1 is given in Fig.4b. Obviously, fine-tuning of the value of $G_{eq,0}$ could lead to an even better match of the 2D results for both the a_{max} variation and the response spectral amplification.

Figure 4 presents an example of how one could back-estimate $G_{eq,0}$ for a specific set of $G_{s,0}$, K_o and a_r . Repeating the same exercise for various values of K_o ($=3.33, 15$) and $a_r = 2.5 - 94\%$ leads to the summary plot of Fig.5 (a total of 67 cases). For comparison with

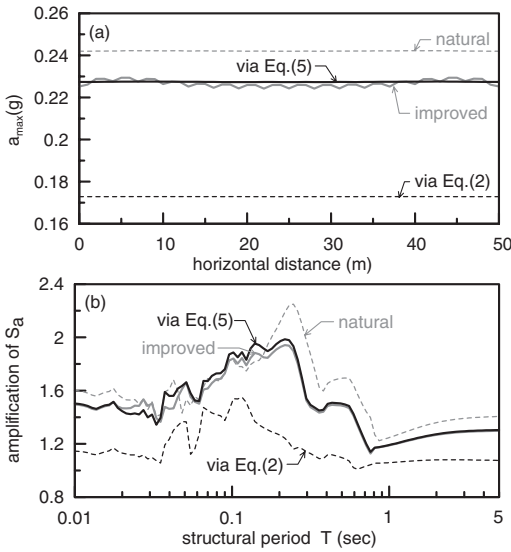


Figure 4. Comparison of results from 1D analyses with equivalent-uniform materials to results from a 2D analysis of composite improved ground, in terms of: (a) a_{max} variation with horizontal distance, (b) S_a amplification for typical surface location.

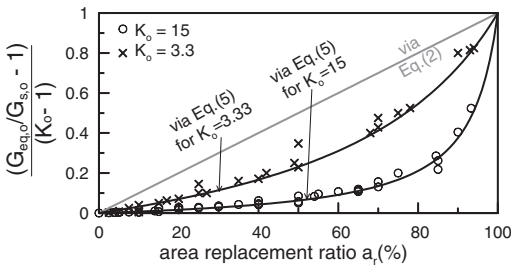


Figure 5. Comparison between numerical estimates of $G_{eq,0}$ and the two (2) analytical approaches.

these numerical estimates of $G_{eq,0}$, the lines procuring from Eqs (2) and (5) are also presented, showing that the accuracy of Eq.(5) is universal, independently of the value of K_0 and a_r . Based on this result, it is deduced that the maximum stiffness $G_{eq,0}$ of the improved site is much less affected by the area replacement ratio a_r , than what Eq.(2) of Baez and Martin (1993) predicts.

It should be underlined that the use of Eq.(5) for the estimation of $G_{eq,0}$ is not restricted to specific ranges of K_0 and a_r , since it has been based on a simplistic theoretical model of the loading of a composite cell of natural soil and a stiffer inclusion and verified from numerical analyses. Yet, it still requires verification from insitu (or centrifuge) measurements from actual cases.

4 EQUIVALENT-UNIFORM MATERIAL FOR NON-LINEAR ANALYSES

The shear stress τ equivalence between the inclusion and the neighboring natural soil holds true for both linear and non-linear analyses. Therefore, Eq. (5) may be re-written as:

$$G_{eq} = G_s \frac{K}{a_r + (1 - a_r)K} = G_s M \quad (6)$$

where G_{eq} , G_s , $K (=G_i/G_s)$ and M are the non-linear (and strain-level dependent) counterparts of $G_{eq,0}$, $G_{s,0}$, $K_0 (=G_{i,0}/G_{s,0})$ and M_0 of Eq.(5). Due to the τ equivalence, the strains γ_i and γ_s that control the values of G_i and G_s , respectively, are not equal. In particular, since $\tau_i = \tau_s$ it holds that $\gamma_s = K\gamma_i$. By defining γ_{eq} as the shear strain of the equivalent-uniform soil, Eq. (6) may be written as:

$$G_{eq}(\gamma_{eq}) = G_s(\gamma_s) \frac{K(\gamma_{eq})}{a_r + (1 - a_r)K(\gamma_{eq})} \quad (7)$$

where:

$$\gamma_{eq} = \gamma_s \left[1 - \left(1 - \frac{1}{K(\gamma_{eq})} \right) a_r \right] \quad (8)$$

Equations (7) and (8) show that the estimation of the $G_{eq}-\gamma_{eq}$ curve to be used in non-linear 1D analysis cannot be performed directly, but requires iterations on the basis of the $G_s-\gamma_s$ and the $G_i-\gamma_i$ curves of the natural soil and the inclusion materials. Given Eq.(5), the foregoing calculations may be performed on the basis of the normalized degradation curves, i.e. the $G_{eq}/G_{eq,0}-\gamma_{eq}$ curve may be estimated on the basis of the $G_s/G_{s,0}-\gamma_s$ and the $G_i/G_{i,0}-\gamma_i$ curves of the natural soil and the inclusion materials.

In more detail, the iterative procedure is performed in steps, i.e. for any given value of γ_s , the following are successively estimated:

- the $G_s/G_{s,0}$ value from the $G_s/G_{s,0}-\gamma_s$ curve,
- the $G_i/G_{i,0}$ value from the $G_i/G_{i,0}-\gamma_i$ curve, on the basis of $\gamma_i = \gamma_s/K_{ini}$ (the first estimate of which can be $K_{ini} = K_0$),
- the $K_{fin} = G_i/G_s = K_0(G_i/G_{i,0})/(G_s/G_{s,0})$ value, which is then used for re-estimating the γ_s value.

This iterative procedure for any given value of γ_s is continued until convergence ($K_{fin} = K_{ini}$). Then, given the converged value of $K (=K_{ini} = K_{fin})$ the values of G_{eq} and γ_{eq} are estimated from Eqs (6) and (8) on the basis of G_s and γ_s . Repeating this iterative procedure for the whole range of γ_s values, constructs the whole $G_{eq}/G_{eq,0}-\gamma_{eq}$ curve.

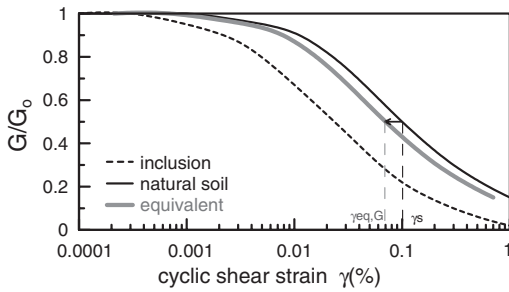


Figure 6. Shear modulus degradation curves for the natural soil, the inclusion and the equivalent-uniform material.

The calculations were performed for the well-established degradation curves of Vucetic & Dobry (1991), i.e. the $G_i/G_{i,0}-\gamma_i$ curve being that for $I_p = 0\%$ and the $G_s/G_{s,0}-\gamma_s$ curve alternatively being that for $I_p = 15\%$ and 30% . Performing such calculations for various values of K_o and a_r showed that the $G_{eq}/G_{eq,0}-\gamma_{eq}$ curve is very little dependent on the $G_i/G_{i,0}-\gamma_i$ curve and practically comes about by a translation of the $G_s/G_{s,0}-\gamma_s$ curve to smaller values of γ . Fig. 6 shows an example of such a translation for $K_o = 15$ and $a_r = 33\%$ for the natural soil curve being that for $I_p = 30\%$.

Detailed analysis of the foregoing calculations showed that this translation can be assumed to be parallel, i.e. $G_{eq}/G_{eq,0}(\gamma_{eq}) = G_s/G_{s,0}(\gamma_s)$, with γ_{eq} being related to γ_s . Since the γ_{eq} in question refers to the G degradation curve, it is hereafter denoted as $\gamma_{eq,G}$ and is interrelated to γ_s according to the following empirical equation:

$$\gamma_{eq,G} = \gamma_s \left[1 - \left(1 - \frac{1}{K_o^{0.85}} \right) a_r \right] \quad (9)$$

Note that Eq.(9) is practically an empirical form of Eq.(8) that came about by best-fitting the iteratively estimated $G_{eq}/G_{eq,0}-\gamma_{eq}$ curve for intermediate strain levels, i.e. around strains where $G_{eq}/G_{eq,0}(\gamma_{eq}) = G_s/G_{s,0}(\gamma_s) = 0.5$ ($\gamma = 0.01 - 0.1\%$) that are of primary concern for this problem in practice.

The damping ratio increase curve of the equivalent-uniform material, $\xi_{eq}-\gamma_{eq}$, is again based on the respective curves for the natural soil, $\xi_s-\gamma_s$ and the inclusion material, $\xi_i-\gamma_i$. Its estimation process is based on the general form of Eq.(6), where the shear modulus values are introduced in terms of their complex forms, i.e. $G_{eq}^* = G_{eq}(1 + 2i\xi_{eq})$, $G_i^* = G_i(1 + 2i\xi_i)$ and $G_s^* = G_s(1 + 2i\xi_s)$. Appropriate algebraic manipulations lead to the following relation between the various ξ values:

$$\xi_{eq} = \xi_s(1 - a_r)M + \xi_i a_r \frac{M}{K} \quad (10)$$

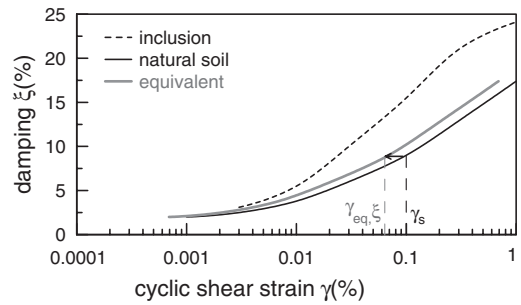


Figure 7. Damping increase curves for the natural soil, the inclusion and the equivalent-uniform material.

where $K (=G_i/G_s)$ and M are the non-linear counterparts of K_o and M_o of Eq.(5).

Following a similar iterative procedure as that for the G degradation curve for various values of a_r and K_o it was deduced that the $\xi_{eq}-\gamma_{eq}$ curve is very little dependent on the $\xi_i-\gamma_i$ curve and practically results from a translation of the $\xi_s-\gamma_s$ curve to smaller values of γ . Fig. 7 shows an example of such a translation for $K_o = 15$ and $a_r = 33\%$ for the natural soil curve being that for $I_p = 30\%$.

Detailed analysis of the foregoing calculations showed that this translation can be assumed to be parallel, i.e. $\xi_{eq}(\gamma_{eq}) = \xi_s(\gamma_s)$, with γ_{eq} being related to γ_s via the following empirical form of Eq.(11):

$$\gamma_{eq,\xi} = \gamma_s \left[1 - \left(1 - \frac{1}{K_o^{0.975}} \right) a_r \right] \quad (11)$$

As for Eq.(9), the empirical estimate of the $\gamma_{eq,\xi}/\gamma_s$ ratio of Eq.(11) came about by best-fitting the iteratively estimated $\xi_{eq}-\gamma_{eq}$ curve for intermediate strain levels, i.e. around strains where $\xi_{eq}(\gamma_{eq}) = \xi_s(\gamma_s) = 8\%$ ($\gamma = 0.01 - 0.1\%$), that are of primary concern for this problem in practice.

5 VERIFICATION OF THE EQUIVALENT-UNIFORM SOIL MODEL

This section presents verification runs for the equivalent-uniform model of improved ground, whose calibration process is described in the foregoing sections. The emphasis here is on non-linear response, since Fig.4 has already presented an example of the accuracy of the proposed methodology for linear analyses.

In particular, the case of an improved site with depth $H = 20$ m, $K_o = 30$ and $a_r = 30\%$ is assumed. The non-linear properties of the natural soil and the inclusions are introduced via the $G/G_0-\gamma$ and $\xi-\gamma$ curves of Vucetic & Dobry (1991) for $I_p = 30\%$ and 0% , respectively. This site subjected to an intense seismic

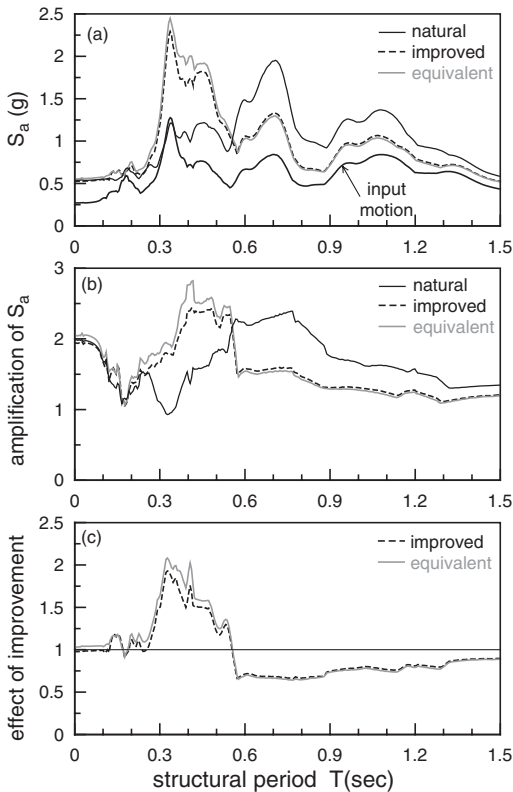


Figure 8. Comparison of seismic response at ground surface for a natural soil site and its improvement analyzed via a composite and an equivalent-uniform model: (a) elastic response spectra S_a , (b) amplification of S_a , (c) effect of improvement on S_a .

excitation with a peak horizontal acceleration of 0.27 g that induces non-linear behavior of the soil. Figs 8a & 8b compare the elastic response spectra and the spectral amplification, respectively, at the ground surface from 3 analyses performed with the foregoing seismic excitation. These 2D analyses refer to: (a) the natural soil site, (b) the improved (composite) site and (c) the equivalent-uniform improved site. It is observed that the analysis for the equivalent-uniform site yields practically the same elastic response spectrum at the ground surface as that for the improved (composite) site. This is an example of the accuracy of the proposed methodology for non-linear analyses.

In addition, this figure provides insight to the effect of the improvement on the ground surface response, which is of primary interest for civil engineering works.

In particular, Fig. 8 shows that the ground response of the natural soil may be very different from that of the improved ground. In particular, Fig. 8b shows that although the peak horizontal acceleration is more or less the same, the spectral values are different. This is

better depicted in Fig. 8c that shows the effect of the improvement on the spectral ordinates. It is observed that the improvement de-amplifies the motion at large structural periods (larger than 0.6s), but amplifies it for intermediate periods (between 0.25 – 0.5s). This is something expected for most cases in practice, where the fundamental period of the natural soil site (here $T_s \cong (0.7s)$) is much larger than the predominant period of the excitation (here $T_e \cong (0.33s)$). The reason is that the improvement introduces stiff inclusions in the soft soil that reduce the fundamental period of the site (here to 0.45s approximately) and bring it closer to the predominant period of the excitation.

Based on the above it is deduced that an amplification of spectral ordinates due to the improvement is expected at periods around the (reduced) fundamental period of the improved site. In addition, Fig. 8 shows that this selective spectral amplification may reach a factor of 2. Although the phenomenon of selective spectral amplification is qualitatively expected in all cases where the predominant period T_e of the excitation is smaller than the fundamental period of the natural soil site T_s , the factor of 2 presented in Fig. 8 must be considered an extremely high value that came about due to resonance phenomena, since the predominant period T_e of the excitation is quite similar to the reduced fundamental period of the improved site.

6 CONCLUSIONS

This paper shows that 2D seismic response analyses of improved sites may be accurately replaced by 1D analyses for an equivalent-uniform material, whose dynamic properties are a function of the respective properties of the natural soil, the inclusion material and the area replacement ratio. The proposed calibration process of an equivalent-uniform material and its use for 1D equivalent-linear analysis (e.g. using *Shake91*, Idriss and Sun 1992) has been shown to effectively duplicate the results of respective 2D analyses for the composite improved site, and this for both linear and non-linear ground response conditions. In addition, it is shown that the improvement itself is not necessarily beneficial for the seismic response at ground surface, since it may lead to selective spectral amplification at periods around the fundamental period of the improved site. These results have been produced by numerical analyses and still require verification from insitu (or centrifuge) measurements from actual cases.

ACKNOWLEDGEMENTS

The authors acknowledge financial support from the General Secretariat of Research and Technology (ITET) of Greece and Edrasis – C. Psallidas S.A.

REFERENCES

- Baez, J.I. & Martin, G.R. 1993, Advances in the design of vibro systems for the improvement of liquefaction resistance. *Symposium of Ground Improvement*, Vancouver
- Hudson, M., Idriss, I.M. & Beikae, M. 1994, *Quad4m: A computer program for conducting equivalent linear seismic response analysis of horizontally layered soil deposits*. User's Guide, Center
- Idriss, I.M. & Sun, J.I. 1992, *Shake91: A computer program for conducting equivalent linear seismic response analysis of horizontally layered soil deposits*. User's Guide, Center for Geotechnical Modeling, Civil Engineering Department, UC Davis
- Vucetic, M. & Dobry, R. 1991, Effect of soil plasticity on cyclic response. *Journal of Geotechnical and Geoenvironmental*, ASCE 117: 1, 89–107.

Equivalence between 2D and 3D numerical simulations of the seismic response of improved sites

A.G. Papadimitriou & G.D. Bouckovalas
National Technical University of Athens, Greece

A.C. Vytiniotis
M.I.T.

G.J. Bakas
Edrasis – C. Psallidas S.A., Greece

ABSTRACT: This paper studies how 2D numerical analyses may be accurately used for simulating the truly 3D problem of the seismic response of improved sites. Specifically, parametric results are compared from pertinent 3D and 2D seismic ground response analyses and a methodology is proposed for replacing the time-consuming (and usually unavailable) 3D analyses with “equivalent” 2D analyses that closely simulate the results of the 3D analyses. Emphasis is put on replacement and solidification methods of soft (cohesive) soils and on three (3) improvement geometries: (a) an embedded soldier pile wall, (b) a grid of columns/piles and (c) a grid of closed square cells.

1 INTRODUCTION

The use of 3D numerical analyses in geotechnical earthquake engineering is very scarce. For practitioners such analyses are considered a luxury, since they are very consuming in terms of time and computational effort. In addition, the commercially available 3D codes for performing numerical analysis of geotechnical earthquake engineering problems are very few and usually these codes have a smaller potential than commercial 2D codes. For example, 2D codes offer the use of advanced constitutive models or element types that are not found in the libraries of 3D codes. Hence, the numerical research in geotechnical earthquake engineering has been historically based on the use of (1-D and) 2D analyses.

In an attempt to bridge this gap, this paper studies how 2D numerical analyses may be accurately used for simulating the truly 3D problem of the seismic response of improved sites. The emphasis is put on three (3) distinct geometries of soil improvement, namely: (a) an embedded soldier pile wall, (b) a grid of columns/piles and (c) a grid of closed square cells. These geometries are usually materialized via replacement (e.g. vibro-replacement) or solidification methods (e.g. Deep Soil Mixing, DSM). In particular, grids of

closed square cells are usually constructed using a solidification method, while the other two (2) geometries are materialized by either improvement method.

This paper compares parametric results from 3D and 2D seismic ground response analyses of improved sites and proposes a methodology for replacing the costly 3D analyses with “equivalent” 2D analyses that closely simulate the results of the 3D analyses. In more detail, this methodology proposes a transformation of the 3D actual improvement geometry to an “equivalent” 2D geometry that if it is subjected to the same base excitation leads to the same seismic motion at the ground surface.

The performed analyses are visco-elastic and assume uniform soft soil and improvement properties from the ground surface to the base. Despite the simplicity of the analyses, the proposed 3D to 2D transformation is considered appropriate for use for non-uniform and non-linear material properties, since it is not affected by non geometric parameters like the improvement-to-soil shear stiffness ratio $K = G_i/G_s$, the predominant period of the base excitation T_e and the Rayleigh damping of the visco-elastic analyses. Sole exception to this rule is that the methodology is considered appropriate for the improvement of soft soils that do not exhibit excess pore pressure buildup and parallel

drainage, a coupled mechanism of fluid flow and deformation that was not addressed in the performed analyses.

2 CALIBRATION OF NUMERICAL CODES

The 3D and 2D analyses in this paper were performed with *FLAC3D* (Itasca Inc 1997) and *FLAC* (Itasca Inc 1993), respectively, two (2) commercial codes that use the finite difference method in performing a time domain analysis. Before proceeding to the analysis of improved sites, it was considered necessary to establish that the two (2) codes produce identical results for the benchmark case of the 1D vertical wave propagation through a uniform horizontal soil layer over rigid bedrock. For this purpose, a mesh of $1 \times 10 \times 1$ cubic elements (in the x , z and y directions respectively) was constructed in *FLAC3D* and free field boundaries were assigned at all lateral faces. Note that in this paper the x and y directions are horizontal and the z is vertical. In comparison, a 2D analysis was performed in *FLAC* and a purely 1D analysis was performed with *Shake91* (Idriss and Sun 1992). In all analyses, the base excitation was applied as an acceleration time history of the base in the x (horizontal) direction. The comparison of results for the seismic response at ground surface (in terms of acceleration time history and elastic response spectrum) showed perfect agreement for all three (3) analyses.

Furthermore, before performing numerical analyses of improved sites with *FLAC3D* it is important to establish its accuracy for another benchmark case that involves purely 2D improvement geometry. For this purpose, the case of a vertical diaphragm wall of thickness $d = 1$ m, height $H = 10$ m and $G_i = 40$ MPa was selected that is embedded in 10 m soft soil with $G_s = 18$ MPa that lies over rigid bedrock. The vertical

wall is aligned along the yz plane. This problem was first analyzed with *FLAC* using a 80×10 mesh of square 1 m wide elements discretizing the xz plane and having free field lateral boundaries. In this analysis, the vertical diaphragm wall is simulated by a centered column of 10 elements with a different value of shear modulus ($K = G_i/G_s = 30$). Using *FLAC3D* for the same physical problem and for comparison purposes entails the use of cubic 1 m wide elements that construct a mesh that is surrounded by free field lateral boundaries. This mesh consists of $80 \times 10 \times Y$ elements, with Y the number of elements necessary for duplicating the results of the 2D analysis. The correct value of Y was estimated by performing parametric 3D analyses for $Y = 1, 6, 10, 20, 80$.

In all 3D and 2D analyses, the seismic excitation was a Chang's signal with $T_e = 0.1$ sec that was applied as an acceleration time history at the nodes of the base of the mesh in the x direction. Of interest for comparison purposes is the amplification of the peak acceleration in the x direction at the ground surface a_{max} due to existence of the diaphragm wall along the yz plane, i.e. the amplification of a_{max} as compared to the free field (soft soil) response. Hence, Fig. 1a presents contours of the amplification of a_{max} from a 3D analysis where $Y = 80$ m. The details of the contours (e.g. the numerical values) are not important here. What is important is that these contours clearly show that the ground response varies only along the x direction and is not a function of the y distance, a fact that underlines the 2D character of the problem.

This is better depicted in Fig. 1b that compares the same results along the x axis, where the 3D results compare perfectly with the 2D results. The question that arises is whether it is actually necessary to perform such a time consuming 3D analysis with 64000 ($=80 \times 10 \times 80$) elements in order to achieve the accuracy of a 2D analysis. The answer is given again in

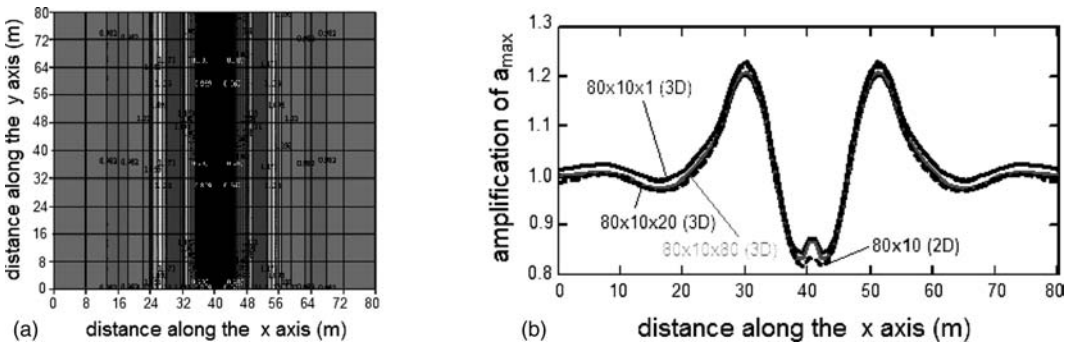


Figure 1. Amplification of peak ground acceleration a_{max} from 3D seismic response analyses of a diaphragm wall ($d = 1$ m), in terms of: (a) contours from an analysis with a $80 \times 10 \times 80$ mesh, (b) variation along the x axis from the reference 2D and all 3D analyses.

Fig. 1b, where the results from two (2) more 3D analyses are presented where $Y = 20$ and $Y = 1$, respectively. Observe that for $Y = 20$ the results are again identical to those for $Y = 80$, and that even for $Y = 1$ the differentiations are marginal. It is concluded that for 2D improvement geometries in the xz plane, a 3D analysis with 1 element in the y direction and free field lateral boundaries suffices.

3 2D ANALYSIS OF SOLDIER PILE WALL

An embedded soldier pile wall in the y direction has a top view as shown in Fig. 2. It consists of a series of improvement piles/columns of diameter d that are equally spaced at a center-to-center distance D along the y direction. Obviously, when $D = d$ the soldier pile wall becomes a diaphragm wall that has a purely 2D geometry, as discussed in the previous section. Nevertheless, in general, a soldier pile wall along the

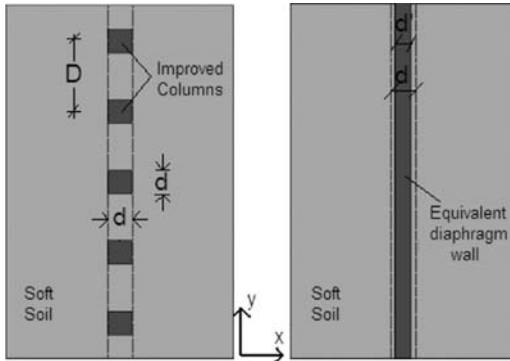
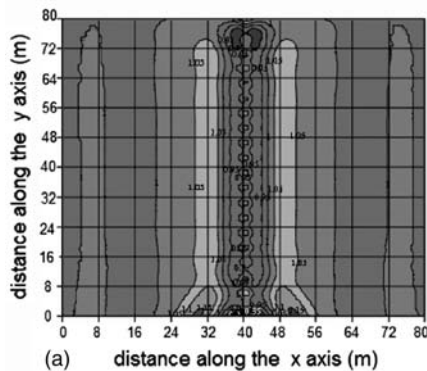


Figure 2. Top views of 3D and equivalent 2D geometries of an embedded soldier pile wall.



y direction with applied base acceleration time history along the x direction is a 3D problem.

This is shown in Fig. 3 that presents the contours of the amplification of a_{max} from a 3D seismic response analysis of an embedded soldier pile wall with $d = 1$ m, $D = 4$ m and $K = 30$ in 10 m of soft soil.

The analysis was performed with a mesh of $80 \times 10 \times 80$ cubic (1 m wide) elements and the soft soil properties and base excitation characteristics described in the calibration section of this paper. As in Fig. 1, the details of the contours in Fig. 3 are not important. What is important is to observe that the amplification of a_{max} along the axis of the wall is not uniform, a fact that underlines the 3D character of the problem. Yet, at small distances perpendicular to the wall axis (e.g. 4–5 m), symmetry of the seismic ground response is established, i.e. the ground response is the same irrespective of the value of the y distance. It is this symmetry that allows for a potential 2D analysis of an “equivalent” diaphragm wall of thickness d' , as shown in Fig. 3b.

The question that arises is whether one could know *a priori* the accurate value of d' for any given set of d and D . The answer to this question is given in this paper using the format of Fig. 3, i.e. by comparing any given 3D analysis (for specific values of d and D) to pertinent 2D analyses with various d' values. In this way, any given set of d and D is related to a unique d' value. By repeating such numerical experiments, the authors constructed a database of (d, D, d') triplets. Yet, a general rule for estimating d' without the need of a 3D analysis had yet to be devised. Such a rule should be based on the form of deformation that the seismic ground excitation applies to an improved ground in its 3D actual geometry and its 2D “equivalent”. In this effort, one could borrow knowledge from beam theory and by doing so three (3) different approaches were

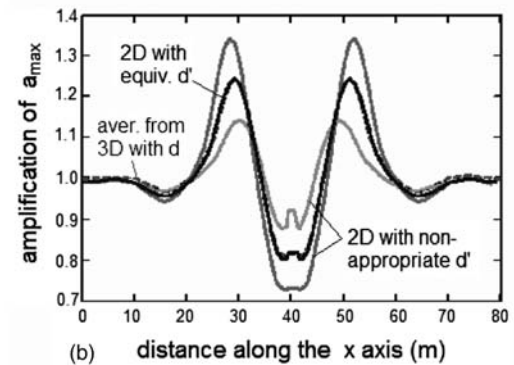


Figure 3. Amplification of peak ground acceleration a_{max} from 3D and 2D seismic response analyses of an embedded soldier pile wall ($d = 1$ m, $D = 4$ m), in terms of: a) contours from the 3D analysis ($80 \times 10 \times 80$ mesh), b) variation along the x axis from the reference 3D analysis (average response) and the various 2D analyses.

examined here, and compared to the database of the numerical experiments. In more detail:

3.1 Area (A) equivalence

This approach assumes equivalence between the cross sectional areas A of the improved ground in the 3D and the “equivalent” 2D geometries, i.e. $A_{3D} = A_{2D}$. Based on Fig. 2, the cross sectional areas of improved ground in a distance D along y are:

$$A_{3D} = d^2 \quad ; \quad A_{2D} = d'D \quad (1)$$

Based on Eq.(1), the d' is given by:

$$d' = d^2/D \quad (2)$$

This A equivalence has been traditionally used for calculations of consolidation rates (e.g. Barron 1948) and settlements (e.g. Priebe 1976) of improved ground. In terms of the latter, it implies an equivalence of the axial (vertical) stiffness between the 3D and 2D geometries.

3.2 Moment of inertia (I) equivalence

This approach assumes equivalence between the moments of inertia I of the cross sections of the improved ground in the 3D and the “equivalent” 2D geometries, i.e. $I_{3D} = I_{2D}$. Based on Fig. 2, the moments of inertia of the cross sections of improved ground in a distance D along y are:

$$I_{3D} = d^4/12 \quad ; \quad I_{2D} = d'^3D/12 \quad (3)$$

Based on Eq.(3), the d' is given by:

$$d' = (d^4/D)^{1/3} \quad (4)$$

This I equivalence is being used in practice for 2D static plane strain analyses of excavations with retaining (soldier pile) walls and implies an equivalence of the bending stiffness between the 3D and 2D geometries.

3.3 Section modulus (W) equivalence

This approach assumes equivalence between the section moduli W of the cross sections of the improved ground in the 3D and the “equivalent” 2D geometries, i.e. $W_{3D} = W_{2D}$. Based on Fig 2, the section moduli of the cross sections of improved ground in a distance D along y are:

$$W_{3D} = d^3/6 \quad ; \quad W_{2D} = d'^2D/6 \quad (5)$$

Based on Eq.(5), the d' is given by:

$$d' = (d^3/D)^{1/2} \quad (6)$$

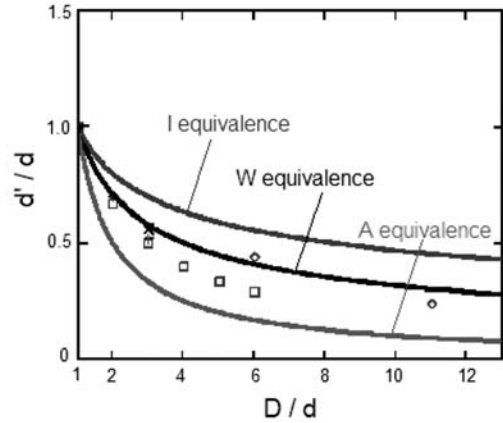


Figure 4. Comparison of analytical predictions of “equivalent” diaphragm wall thickness d' and their estimates from numerical experiments for an embedded soldier pile wall.

As deduced by Eqs (2), (4) and (6), the W equivalence yields values of d' that are intermediate between the values from the I equivalence and the A equivalence. As such, the W equivalence may be viewed empirically as an “overall” stiffness equivalence between the 3D and 2D geometries, that have neither an axial nor a bending stiffness equivalence.

3.4 Back estimation of d'

Figure 4 compares the results of the numerical experiments (symbols) to the pertinent predictions from the 3 analytical approaches. It is concluded, that the W equivalence provides the best fit to the numerical estimates of d' , while the I and A equivalences serve as a upper and lower limits, respectively. This can be attributed to the fact that during shaking, the response of a level ground layer (and its improvement inclusions) reminds that of a shear beam, whose vibration is more confined than that of a bending beam (I equivalence), while it is irrelevant to an axial (vertical) vibration implied by an A equivalence.

Note that the use of Eq. (6) for estimating d' is appropriate, irrespective of the improvement geometry (d and D), the improvement method (K) and the predominant period of the seismic excitation (T_e). This is due to the fact that the numerical experiments summarized in Fig. 4 correspond to 3D analyses with the following characteristics: $d = 1, 2 \text{ m} - D/d = 2, 3, 4, 5, 6, 11 - K = 15, 30 - T_e = 0.1, 0.2 \text{ sec}$.

4 2D ANALYSIS OF GRID OF PILES

Figure 5 presents the contours of the amplification of a_{max} from a 3D seismic response analysis of a grid of

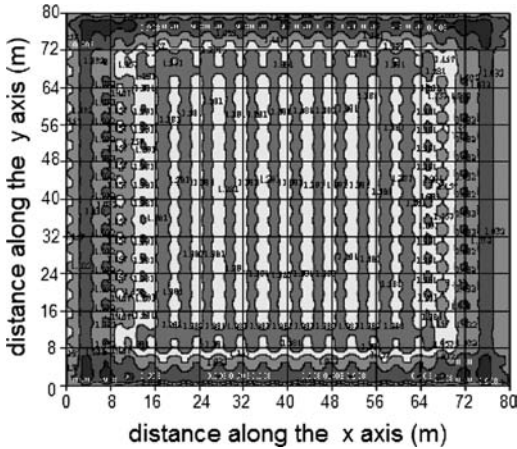


Figure 5. Contours of amplification of peak acceleration a_{max} from a 3D seismic response analysis ($80 \times 10 \times 80$ mesh) of a 19×19 grid of improvement piles ($d = 1, D = 4$ m).

19×19 improvement piles with $d = 1$ m, $D = 4$ m and $K = 30$ embedded in 10 m of soft soil over rigid bedrock. The analysis was performed with a mesh of $80 \times 10 \times 80$ cubic (1 m wide) elements and the soft soil properties and base excitation characteristics described in the calibration section of this paper.

As above, the numerical details of Fig. 5 are unimportant here. Of importance is to observe that the amplification of a_{max} at the ground surface is not uniform, a fact that underlines the 3D character of the seismic response of a grid of columns.

Yet, far from the horizontal mesh boundaries (e.g. for x and y ranging from 20 to 60 m), symmetry of the seismic response is established, i.e. the response is the same irrespective of the value of y .

This symmetry provides the potential for performing “equivalent” 2D analyses, using the methodology devised for a single soldier pile wall in the previous section. In other words, a grid of improvement piles (of diameter d at a spacing D in 3D) may be viewed as a series of “equivalent” diaphragm walls of thickness d' at a centerline-to-centerline distance D that may be analyzed in 2D.

Following the same methodology as in the case of the soldier pile wall, the value of d' for the 2D analyses of a grid of columns was estimated by comparing the ground surface response of reference 3D analyses to trial-and-error 2D analyses. Hence, Fig. 6 compares the results from the foregoing numerical experiments to the three (3) analytical estimates of d' summarized by Eqs (2), (4) and (6). Observe that this comparison shows that the use of Eq. (6), i.e. the W equivalence, gives again the best fit to the 3D response.

Note that the use of Eq (6) for estimating d' for the 2D analyses of a grid of piles is valid, irrespective of the

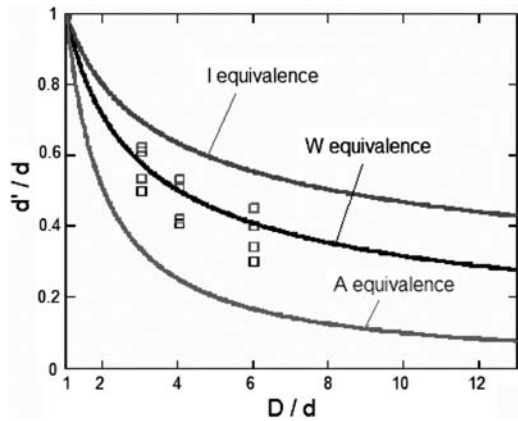


Figure 6. Comparison of analytical predictions for the “equivalent” diaphragm wall thickness d' to their estimates from numerical experiments for a grid of improvement piles.

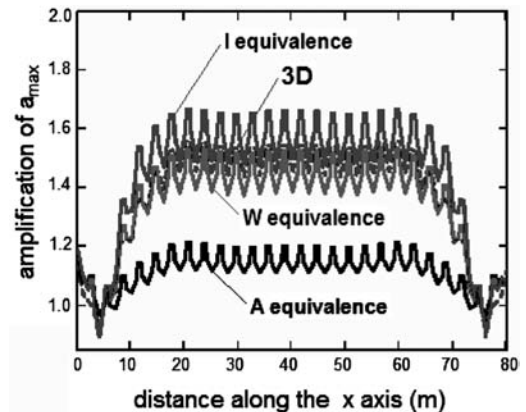


Figure 7. Exemplary estimate of error in the amplification of a_{max} from 2D seismic response analyses of a 27×27 grid of improvement piles.

geometry (d and D) and the method (K) of improvement. This is due to the fact that the numerical experiments summarized in Fig. 6 correspond to 3D analyses with the following characteristics: $d = 1, 2$ m – $D/d = 3, 4, 6$ – $K = 15, 30$.

Both Figs 4 and 6 shows a significant difference between the d' values from Eqs (2), (4) and (6). Yet, of importance for engineering purposes is how much an erroneous estimate of d' may affect the predicted seismic response. As an example, Fig. 7 compares the “average” response of a grid of 27×27 improvement piles with $d = 1$ m, $D/d = 3$ and $K = 30$ as deduced by a 3D analysis (dashed line), to the respective 2D analyses using the three (3) analytical approaches (solid lines). It becomes obvious that the W equivalence

(Eq. 6) gives the best fit to the 3D analysis, while the other two analyses have an error that could surpass 25%.

5 2D ANALYSIS OF GRID OF CLOSED CELLS

An embedded grid of closed square cells has a top view as shown in Fig. 8a and is usually materialized using a solidification method (like the Deep Soil Mixing (DSM) denoted in Fig. 8a). It consists of two (2) series of DSM diaphragm walls (of thickness d) that are perpendicular to one another and which are equally spaced at a centerline-to-centerline distance D along the x and y directions. Obviously, when $D = d$ the grid becomes a DSM block where all the soil has been solidified, a purely 2D geometry.

Nevertheless, in general, the seismic response of a soft soil improved with a DSM grid is a 3D problem. This is shown in Fig. 9a that presents the contours of the amplification of a_{max} from a 3D seismic response

analysis of a DSM grid with $d = 1$ m, $D = 4$ m and $K = 78$ in 10 m of soft soil. The analysis was performed with a mesh of $100 \times 10 \times 80$ cubic (1 m wide) elements and the soft soil properties and base excitation characteristics described in the calibration section of this paper. Observe that the amplification of a_{max} on top of the DSM grid (from $x = 43$ to $x = 56$ m) is not uniform, a fact that underlines the 3D character of the problem. Yet, immediately outside the DSM grid, symmetry of the seismic response is established, i.e. the response is the same irrespective of the value of y .

It is this symmetry that allows for a potential “equivalent” 2D analysis of the longitudinal series of DSM walls (of thickness d at a distance D), as shown in Fig. 8b. But, accurate 2D simulations require that the properties of the material between these DSM walls (denoted as “equivalent” soil-DSM in Fig 8b) are adjusted to account for the existence of the transverse DSM walls. This re-adjustment is performed in terms of the shear modulus G_{eq} , as:

$$G_{eq}/G_s = [1 - (d/D)] + K(d/D) \quad (7)$$

Equation (7) originates from appropriate analytical manipulations of an assumed GI equivalence of the material between the longitudinal DSM walls in the 3D and 2D configurations.

As an example, Fig. 9b compares the ground surface responses from 2 analyses, the “average” from a 3D analysis and that from its “equivalent” 2D analysis, both of which pertain to a DSM grid with three (3) longitudinal walls (with $d = 1$ m, $D/d = 6$ and $K = 78$) that is embedded in 10 m of soft soil. The 3D analysis was performed with a mesh of $100 \times 10 \times 80$ cubic (1 m wide) elements and the soft soil properties and base excitation characteristics described in the calibration section of this paper. The 2D analysis used a

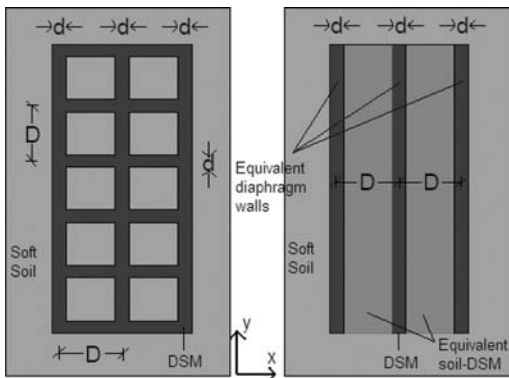


Figure 8. Top views of actual 3D and equivalent 2D geometries of a grid of closed improved cells.

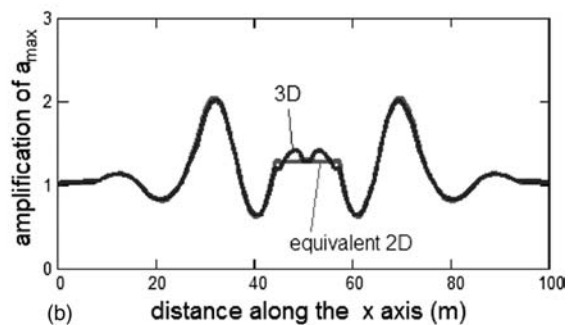
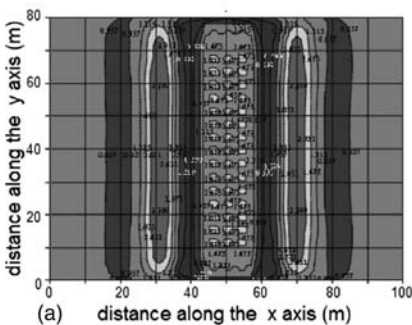


Figure 9. Amplification of peak ground acceleration a_{max} from 3D and 2D seismic response analyses of a grid of closed DSM cells ($d = 1$ m, $D = 4$ m), in terms of: (a) its contours from the 3D analysis ($100 \times 10 \times 80$ mesh), (b) its variation along the x axis from the foregoing 3D and the respective 2D analysis calibrated on the basis of Eq.(7).

mesh of 100×10 square (1 m wide) elements and an “equivalent” soil-DSM material calibrated according to Eq. (7). An excellent agreement is observed between the “average” 3D and the “equivalent” 2D analyses, especially in the area outside the DSM grid. Within the DSM grid, the comparison is merely satisfactory, but the agreement is much enhanced in more realistic DSM grids, where the D/d ratio rarely exceeds 4–5.

6 CONCLUSIONS

This paper shows that 3D seismic response analyses of improved sites may be replaced with “equivalent” 2D analyses. This is achieved by a transformation of the 3D improvement geometry to an “equivalent” 2D, on the basis of equivalence of the section moduli W of the improvement inclusions. The proposed transformation is valid for improvement geometries in the form of a soldier pile wall and a grid of piles, irrespective of improvement method or excitation characteristics. For closed (DSM) cells, “equivalent” 2D analyses are also possible by adjusting the stiffness properties of the soil inside the cells to account for the transverse diaphragm walls. These results hold for improvement of soft soils that do not exhibit excess pore pressure buildup and parallel drainage, a coupled mechanism of fluid flow and deformation that was

not addressed in the performed analyses. In closing, note that these results have been produced by numerical analyses and still require verification from insitu (or centrifuge) measurements from actual cases.

ACKNOWLEDGEMENTS

The authors acknowledge financial support from the General Secretariat of Research and Technology (TTET) of Greece and Edrasis – C. Psallidas S.A.

REFERENCES

- Barron, R.A. 1948, Consolidation of fine-grained soils by drain wells. *Transactions of the American Society of Civil Engineers* 113: 718–742
- Idriss, I.M. & Sun, J.I. 1992, *Shake91: A computer program for conducting equivalent linear seismic response analysis of horizontally layered soil deposits*. User's Guide, Center for Geotechnical Modeling, Civil Engineering Department, UC Davis
- Itasca Consulting Group Inc 1993, *FLAC: Fast Lagrangian Analysis of Continua*. User's Manual
- Itasca Consulting Group Inc 1997, *FLAC3D: Fast Lagrangian Analysis of Continua in 3D*. User's Manual
- Priebe, H.J. 1976, Abschätzung des Setzungsverhaltens eines durch Stopfverdichtung verbesserten Baugrundes. *Die Bautechnik*, 5.

Three-dimensional modelling of an embankment over soft soil improved by rigid piles

O. Jenck, D. Dias & R. Kastner

URGC Géotechnique, INSA de Lyon, Villeurbanne, France

ABSTRACT: A three-dimensional finite-difference numerical modelling of an embankment over a soft ground mass improved by vertical rigid piles is proposed within the framework of the research project ASIRI. The embankment, the piles and the soft ground are explicitly taken into account. A unit cell from the pile grid is modelled. Arching occurs in the embankment granular material, leading to load transfer onto the piles and surface settlement reduction and homogenization. Two soft soil layers and two embankment material are successively simulated. The parametric study focuses on the soft soil and embankment characteristic influence on the settlements and the load transfer mechanism.

1 INTRODUCTION

Rarefaction of good quality soil areas to develop roadway, motorway and railway networks as well as industrial areas necessitates improvement techniques for soft soils. One of these techniques to overcome the problem of surface settlements is the improvement by vertical rigid piles. It consists of a grid of piles driven through the soft layer until a substratum and a granular earth platform or an embankment, as illustrated by Figure 1.

Arching occurs in the granular soil, due to the differential settlements at embankment base, permitting the load transfer onto the piles and the surface settlement reduction and homogenization. The differential

settlements between the rigid pile and the soft ground involve negative friction in the upper part of the piles (Combarieu 1988) and positive friction in the lower part of the piles.

Several design methods exist to determine the load transfer on piles by arching, but they can lead to very different results (Briaçon et al. 2004). The comprehension of the precise mechanisms by which the loads are transferred onto the piles needs to be improved. In France, a national research project has begun (entitled ASIRI, for “Amélioration des Sols par Inclusions Rigides”, which means “Soil Improvement by Rigid Piles”). The aim of this project is to edit guidelines for the design, the construction and the control of soft ground improvement by vertical rigid piles (Briaçon 2002).

Within this framework, a three-dimensional numerical approach of the reinforcement system is proposed, using the finite-difference code Flac3D. The piles, the soft ground and the embankment are simulated. A fictitious case is simulated but with embankment and soft ground materials taken from the literature and a realistic configuration of the reinforced soil mass.

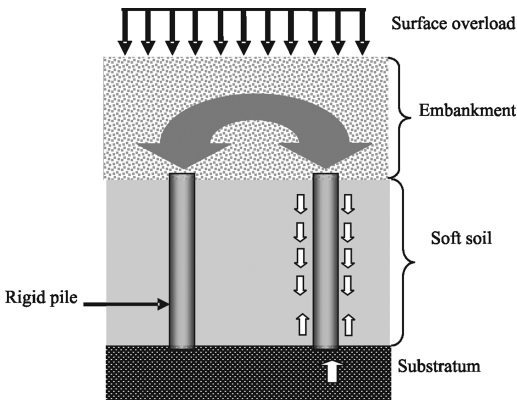


Figure 1. Schematic section of an embankment over pile reinforced soft soil.

2 NUMERICAL MODEL

2.1 Unit cell grid

Figure 2 is a top view of the squared pile grid considered. The piles are 0.35 m diameter concrete piles and the pile spacing is 2 m. The area ratio is the proportion of the total area covered by piles and is here equal to 2.4%. Only a quarter of an elementary part of

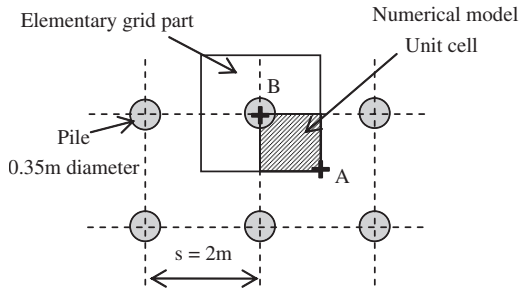


Figure 2. Top view of the pile grid and simulated unit cell.

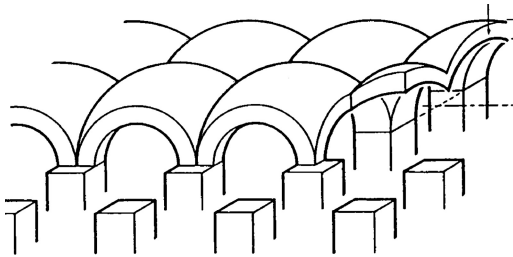


Figure 3. Idealization of the arches by hemispherical domes, as proposed in the Hewlett & Randolph (1988) design method.

the grid needs to be simulated thanks to the symmetry conditions.

The studied problem is typically three-dimensional mainly due to the vault shape in the embankment. As an illustration, Figure 3 is the representation of the vaults assumed by Hewlett & Randolph (1988) in their design method. Kempton et al. (1998) compared plane strain 2D and 3D numerical modelling and showed that a 2D modelling cannot properly simulate the real system behaviour. Moreover, 2D axis-symmetric simulations represent the vaults as “umbrellas” but that does not represent reality neither (Naughton & Kempton 2005). A full three-dimensional approach then appears necessary to reproduce the real system behaviour. 3D simulations of piled embankment representing explicitly the embankment and the improved soft ground remain rare and are recent (Laurent et al. 2003, Stewart & Filz 2005), as the models are large and are computer time consuming.

Figure 4 shows the numerical model which consists of a quarter of a pile, the 5 m-thick soft ground layer and an embankment erected in 10 successive 0.5 m-thick layers until a maximum height of 5 m. Static equilibrium under self weight is reached at each loading stage. Additional overload is then applied on the surface by 10 kPa-stages until 100 kPa. The soft ground layer is made up of a superficial dry crust and a soft soil deposit. It rests on a rigid stratum, simulated by fixing the nodes. The calculation is performed in drained

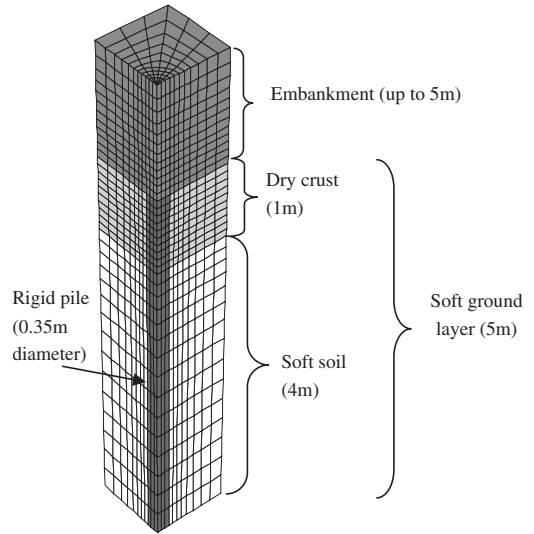


Figure 4. Numerical model of a unit cell.

conditions: the time effect of the consolidation of the soft soil deposit is not taken into account.

Most of the current design methods to assess the load transfer onto the pile do not take the presence of the soft soil layer into account (Hewlett & Randolph 1998, BS 8006 1995, Russell & Pierpoint 1997, Svano et al. 2000) whereas it can contribute to the system behaviour. Nevertheless, Combarieu (1988), Low et al. (1994) and Kempfert et al. (2004) take the soft soil support into account in their design approach. By taking the soft soil layer explicitly into account, the proposed model could be useful to show the importance of this part on the whole system behaviour.

2.2 Materials and constitutive models

The embankment is constituted of granular materials such as gravels or coarse soils. Their behaviour is generally highly non-linear (Paute et al., 1994). The embankment material behaviour is simulated by an elastic perfectly plastic model with a Mohr-Coulomb type failure criterion, as in most of the numerical models of embankment over pile improved soft ground found in the literature (Russell & Pierpoint 1997, Kempton et al. 1998, Rogbeck et al. 1998, Laurent et al. 2003). However, some model use the Duncan & Chang (1970) model to take account for the stress dependent behaviour of the materials (Jones et al. 1990, Han & Gabr 2002).

To take account for the non-linear behaviour of the granular material, the Janbu (1963) formula (Equ. 1) can be used (Varadarajan et al., 1998). It links the Young's modulus E to the minor principal stress σ_3 .

$$\frac{E}{P_a} = k \cdot \left(\frac{\sigma_3}{P_a} \right)^m \quad (1)$$

In our calculation, when using the “Mohr-Coulomb” model for the embankment, the Young’s modulus is recalculated at each embankment loading stage using Equation 1 according to the actual horizontal stress in every soil zone. A hardening elastoplastic model with non linear elasticity can also be implemented (Jenck 2005) to avoid this modulus manipulation and equivalent results were found.

Two embankment materials are successively implemented:

- The Criquebeuf alluvial coarse soil described and tested by Valle (2001), named M1,
- The embankment material described and tested by Fragaszy et al. (1992), named M2.

Triaxial tests at confinement pressure ranging between 50 and 150 kPa were performed by the authors on both materials permitting the determination of the “Mohr-Coulomb” model parameters given on Table 1. The unit weight is 20 kN/m³ and K₀ value is 0.5 for both materials. The shear strength of both material (couple *c* and *ϕ*) is equivalent but material M1 rigidity and dilatancy is larger than for M2.

The reinforced-by-pile soft ground layers are typically clay and/or silt deposits. The Modified Cam Clay model (Roscoe & Burland 1968) is widely used to simulate such deposit behaviour (Mestat et al. 2004): this model is used in the proposed modelling.

Two soft ground deposits are successively simulated:

- The soft deposit of Cubzac-les-Ponts (S1), widely described and implemented in numerical modelling, in particular using the Modified Cam Clay model (Magnan & Belkeziz 1982),
- The marine soft deposit of Muar (S2) in Malaysia notably simulated using the Modified Cam Clay model by Indraratna et al. (1992).

Both deposits present a more rigid or over-consolidated superficial dry crust, above the ground water level, over a saturated soft ground layers. The parameters used in the modelling are given in Table 2. The value of the *λ* parameter indicates that deposit S1 is more compressible than S2.

The piles are reinforced concrete piles and they behave elastically. The elastic parameters are *E* = 10 GPa and *ν* = 0.2.

2.3 The parametric study

The parametric study focuses on the soft soil and embankment characteristic influence on the settlements and the load transfer onto the piles. Table 3 summarizes the four studied cases.

Table 1. “Mohr-Coulomb” material parameters for two embankment materials.

Parameter	Criquebeuf M1	Lake Valley M2
<i>E</i> k	550	163
<i>m</i>	0.65	0.5
<i>ν</i>	0.3	0.4
<i>ϕ</i>	39°	42°
<i>c</i>	27 kPa	0 kPa
<i>ψ</i>	30°	5.4°

Table 2. Modified Cam Clay material parameters for two soft soil deposits.

	Cubzac-les-Ponts S1		Muar S2	
	Soft ground	Dry crust	Soft ground	Dry crust
<i>λ</i>	0.53	0.12	0.11	0.13
<i>κ</i>	0.048	0.017	0.08	0.05
<i>M</i>	1.2	1.2	1.07	1.19
<i>e_λ</i>	4.11	1.47	1.61	3.07
<i>ν</i>	0.35	0.35	0.3	0.3
<i>p_c</i>	p + 10 kPa		p + 10 kPa 110 kPa	
<i>γ'</i> (kN/m ³)	8	18	6	16
<i>K₀</i>	0.7		0.6	

λ: slope of the normal consolidation line

κ: slope of the swelling line

M: frictional constant

e_λ: void ratio at normal consolidation for p = 1 kPa

ν: Poisson’s ratio

p_c: initial preconsolidation pressure

γ': unit weight (*γ'* = *γ* – *γ_w*)

K₀: horizontal earth pressure coefficient at rest.

Table 3. Parametric study on the embankment and soft soil materials.

	Embankment material			
	Cubzac S1		Muar S2	
	M1-S1	M1-S2	M2-S1	M2-S2
Soft soil				

3 NUMERICAL RESULTS

3.1 No improvement by piles

In order to investigate the improvement brought by the piles, the non reinforced case is first simulated.

A soft ground column is loaded by the 5 m-high embankment and then 100 kPa overloads. The final equivalent embankment height is then equal to 10 m.

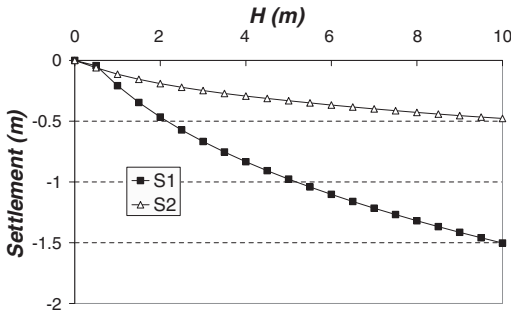


Figure 5. Soft soil deposit surface settlement.

Figure 5 depicts the soft soil surface settlement according to the equivalent embankment height H . The settlement reaches 1.5 m for the soft soil deposit S1 and only 0.5 m for S2.

3.2 Improvement by piles

The numerical model presented in section 2.1, including pile reinforcement, is then implemented.

3.2.1 Settlement reduction

The maximum settlement at embankment base is reached mid-span between piles (point A from Fig. 2). Figure 6 depicts this settlement evolution according to H for the four studied cases. The settlements are reduced compared to the non-reinforced case due to arching that occurs in the embankment, which reduces the load applied on the soft soil layer. The settlements are the same for embankment M1 whatever the soft soil compressibility, whereas the settlements are larger for S1, which is more compressible than S2, when simulating the M2 material.

Table 4 indicates the basal settlement results in terms of settlement reduction compared to the non-reinforced case (Fig. 5). The settlement reduction is very large (80–95%) for soft deposit S1 and embankment M1, whereas the case implementing S2 with M2 lead to a limited settlement reduction (53%).

The results are also investigated in terms of embankment surface settlements. Figure 7 depicts the surface differential settlements due to the application of the next 0.5-thick embankment layer according to the actual embankment height. The differential settlement is the difference of settlement between point A and point B from Figure 2, namely above a pile and amid the piles. Figure 7 shows that the surface differential settlements decrease when the embankment height increases and are negligible from an embankment height of about 2 m for every case. For a smaller height value, the differential settlement is smaller at embankment M1 surface. This material presents effectively

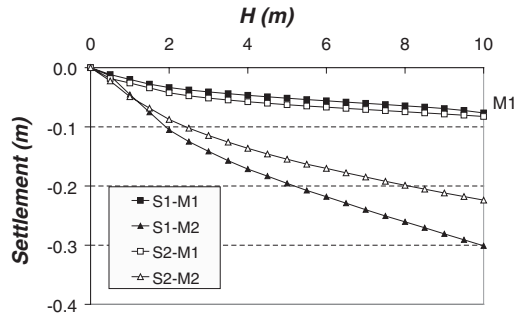


Figure 6. Maximum settlement at embankment base.

Table 4. Embankment base settlement reduction compared to the non reinforced case.

	M1	M2
S1	95%	80%
S2	83%	53%

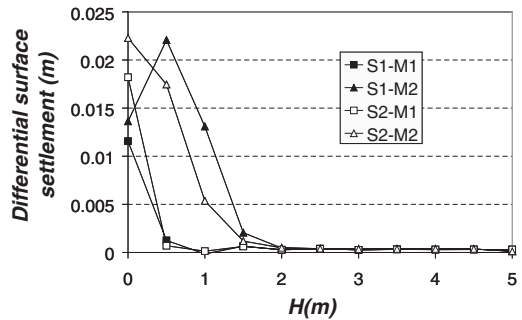


Figure 7. Surface differential settlement due to next 0.5-m-embankment layer.

higher rigidity and dilation values. No significant influence of the soft soil compressibility is recorded (only a small influence on M2 surface differential settlement).

Figure 8 depicts the maximum surface settlement due to the next layer. When differential settlement occurs, the maximum settlement is reached above point A (Fig. 2), amid the piles. Without pile improvement, the surface settlements due to the next layer application range between 0.05 and 0.15 m for S1 and between 0.01 and 0.05 m for S2. The improvement by pile thus permits to considerably reduce the surface settlement. The surface settlements decrease when the embankment height increases. They are smaller at embankment M1 surface, with no influence of the soft soil compressibility. In return, there is a small

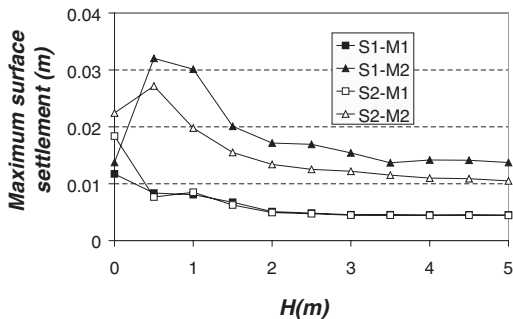


Figure 8. Maximum surface settlement due to next 0.5 m-embankment layer.

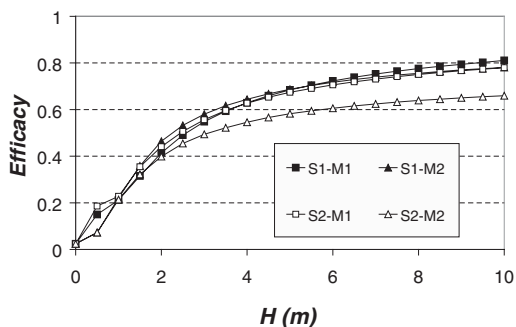


Figure 9. Efficacy according to the equivalent platform height.

soft soil compressibility influence at embankment M2 surface: settlements are larger for the more compressible deposit S1 than for S2.

3.2.2 Load transfer onto the piles

The load transfer onto the piles can be estimated by the “efficacy”, which is the proportion of the total load (embankment + surface overload) transmitted to the piles. When no arching occurs, the efficacy is equal to the area ratio (2.4%).

Figure 9 represents the evolution of the efficacy according to the equivalent embankment height. The efficacy increases with H to reach an almost constant value equal to about 0.8 (except for the case S2-M2), which means that 80% of the total load is transmitted to the piles. The case S2-M2, which corresponds to the weaker embankment material over the less compressible soft deposit, leads to a maximum efficacy equal to 0.65. This is probably because the basal differential settlement is not large enough to lead to full arching occurring in this embankment material.

The proposed numerical model permits to analyze the results in terms of principal stress orientation.

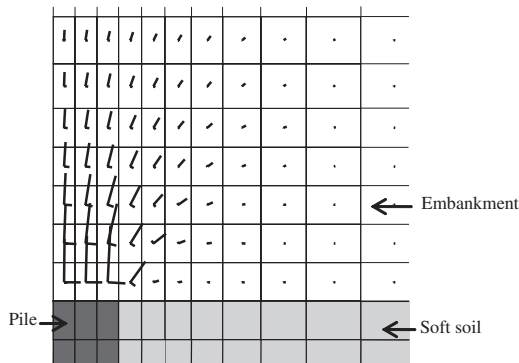


Figure 10. Principal stresses around the pile head.

Figure 10 shows the principal stresses around the pile head at the final state. The stresses are concentrated above the pile and the principal stresses are oriented toward the pile, showing the arching effect in the embankment which transmits the load onto the piles.

4 CONCLUSIONS AND FUTURE WORKS

A three-dimensional finite-difference numerical modelling of a piled embankment is presented. The soft soil, the pile and the embankment are explicitly simulated in a unit cell supported by a rigid stratum. The geometrical and geotechnical parameters are taken from the literature and are realistic values. However, this modelling approach would need a validation on experimental results.

The embankment material behaviour is simulated by an elastic perfectly plastic model with a Mohr-Coulomb failure criterion, incorporating a stress dependant modulus in order to take account for the material non linearity. The soft deposit material is simulated using the Cam Clay model, well adapted to simulate clay and silt.

The parametric study focuses on the geotechnical properties of the soft soil deposit and the embankment material on the piled embankment performance.

It is first showed that the improvement by piles permits to reduce the total and the differential settlements and that arching occurs in the embankment material, leading to load transfer onto the pile. The embankment height influence is also highlighted.

In this study, the soft soil compressibility has no influence neither on the settlements occurring in the embankment nor on the load transfer onto the piles if the embankment material has a high rigidity and/or dilation angle. In return, there is a soft deposit influence on both the settlement and the efficacy for the weaker embankment. In particularly, this embankment material

over the less compressible soft deposit leads to smaller efficacy values.

The coupling between the soft soil and the embankment material properties leads to the conclusion that in the design, not only the embankment material properties must be taken into account, but also the soft soil compressibility.

Future works will be conducted on the proposed numerical model. A precise parametric study will be performed on the embankment and soft soil geotechnical parameters. The aim is to highlight which are the important parameters which should inevitably be taken into account in a simplified but reliable design approach. The influence of the embankment shear strength characteristics will particularly be investigated.

REFERENCES

- Briançon, L. 2002. *Renforcement des sols par inclusions rigides – Etat de l’art*. Paris: IREX. 185p.
- Briançon, L., Kastner, R., Simon, B. & Dias, D. 2004. Etat des connaissances – Amélioration des sols par inclusions rigides. In Dhouib et al. (eds). *Proc. Symp. Int. sur l’Amélioration des Sols en Place (ASEP-GI), Paris, 9–10 Sept. 2004*: 15–44. Paris: Presses de l’ENPC.
- BS8006 (British Standards). 1995. Strengthened/reinforced soils and other fills. Section 8.
- Chai, J.-C., Miura, N. & Shen, S.-L. 2002. Performance of embankments with and without reinforcement on soft subsoil. *Canadian Geotechnical Journal* 39(4): 838–848.
- Combarieu, O. 1988. Amélioration des sols par inclusions rigides verticales. Application à l’édification de remblais sur sols médiocres. *Revue Française de Géotechnique* 44: 57–79.
- Ducan, J. M. & Chang, C. Y. 1970. Non linear analysis of stress and strain in soil. *ASCE, Journal of Soil Mechanics and Foundations* 96: 1629–1653.
- Fragaszy, R. J., Su, J., Siddigi, H. & Ho, C. J. 1992. Modelling strength of sandy gravel. *Journal of Geotechnical and Geoenvironmental Engineering* 118(6): 920–935.
- Han, J. & Gabr, M. A. 2002. Numerical analysis of geosynthetic-reinforced and pile-supported earth platforms over soft soil. *Journal of Geotechnical and Geoenvironmental Engineering* 128: 44–53.
- Hewlett, W. J. & Randolph, M. F. 1988. Analysis of piled embankment. *Ground Engineering* 21(3): 12–18.
- Indraratna, B., Balasubramaniam, A. S. & Balachandran, S. 1992. Performance of test embankment constructed to failure on soft marine clay. *Journal of Geotechnical Engineering* 118(1): 12–33.
- Janbu, N. 1963. Soil compressibility as determined by oedometer and triaxial tests. In *Proc. of the European Conf. on Soil Mechanics and Foundations Engineering, Wiesbaden*. Essen : Deutsche Gesellschaft für Erd-und Grundbau: 19–25.
- Jenck, O. 2005. *Le renforcement des sols compressibles par inclusions rigides verticales. Modélisations physique et numérique*. Thèse de doctorat, INSA de Lyon, Villeurbanne.
- Jones, C. J. F. P., Lawson, C. R. & Ayres, D. J. 1990. Geotextile reinforced piled embankments. In Den Hoedt (ed). *Proc. of the 4th Int. Conf. on Geotextiles Geomembranes and related Products, Den Haag, 28 May-1 June 1990*: 155–160 (vol. 1).
- Kempfert, H. G., Göbel, C., Alexiew, D. & Heitz, C. 2004. German recommendations for reinforced embankments on pile-similar elements. In *Proc. of the 3rd European Geosynthetics Conf., Munich, 1–3 March 2004*: 279–284.
- Kempton, G., Russell, D., Pierpoint, N. D. & Jones, C. J. F. P. 1998. Two- and three-dimensional numerical analysis of the performance of piled embankments. In Rowe (ed). *Proc. of the 6th Int. Conf. on Geosynthetics, Atlanta, 25–29 March 1998*: 767–772.
- Laurent, Y., Dias, D., Simon, B. & Kastner, R. 2003. A 3D finite difference analysis of embankments over pile-reinforced soft soil. In Vermeer et al. (eds). *Proc. of the Int. Workshop on Geotechnics of Soft Soils – Theory and Practice, Noordwijkerhout, 17–19 Sept. 2003*: 271–276. Essen: Verlag Glückauf.
- Low, B. K., Tang, S. K. & Choa, V. 1994. Arching in piled embankments. *Journal of Geotechnical and Geoenvironmental Engineering* 120(11): 1917–1938.
- Magnan, J.-P. & Belkeziz, A. 1982. Consolidation d’un sol élastoplastique. *Revue Française de Géotechnique* 19: 39–49.
- Mestat, P., Bourgeois, E. & Riou, Y. 2004. Numerical modelling of embankments and underground works. *Computers and Geotechnics* 31: 227–236.
- Naughton, P. J. & Kempton, G. T. 2005. Comparison of analytical and numerical analysis design methods for piled embankments. In Anderson et al. (eds). *Proc. of Geo-Frontiers, Austin, 24–26 January 2005*.
- Paute, J.-L., Hornych, P. & Benaben, J.-P. 1994. Comportement mécanique des graves non-traitées. *Bulletin de Liaison des Ponts et Chaussées* 190: 27–38.
- Rogbeck, Y., Gustavsson, S., Soedergren, I. & Lindquist, D. 1998. Reinforced piled embankments in Sweden – Design aspects. In Rowe (ed). *Proc. of the 6th Int. Conf. on Geosynthetics, Atlanta, 25–29 March 1998*: 755–762.
- Roscoe, K. H & Burland, J. B. 1968. On the generalised stress-strain behaviour of “wet” clay. *Engineering Plasticity*: 535–609. Cambridge University Press.
- Russell, D. & Pierpoint, N. 1997. An assessment of design methods for piled embankments. *Ground Engineering* (November 1997): 39–44.
- Stewart, M. E. & Filz, G. M. 2005. Influence of clay compressibility on geosynthetic loads in bridging layers for column-supported embankments. In Anderson et al. (eds). *Proc. of Geo-Frontiers, Austin, 24–26 January 2005*.
- Svanø, G., Ilstad, T., Eiksund, G. & Want, A. 2000. Alternative calculation principle for design of piles embankments with base reinforcement. In *Proc. of the 4th Int. Conf. of Ground Improvement Geosystem, Helsinki, 7–9 June 2000*.
- Valle, N. 2001. *Comportement mécanique d’un sol grossier d’une terrasse alluvionnaire de la Seine*. Thèse de doctorat, Université de Caen/Basse Normandie.
- Varadarajan, A., Sharma, G. & Aly, M. A. A. 1999. Finite element analysis of reinforced embankment foundation. *International Journal for Numerical and Analytical Methods in Geomechanics* 23(2): 103–114.

Influence of the soil nonlinearity and the interface on the seismic response of micropiles

H. Al Saleh & I. Shahrour

University of Sciences and Technologies of Lille, France

ABSTRACT: This paper presents a numerical analysis of the influence of both the non linear behavior of the soil material and the micropile-soil interface on the response of micropiles to seismic loading. Analysis is carried out by means of a three-dimensional numerical model in the time domain using the FLAC3D program. The soil behavior is described by the non associated Mohr-Coulomb criterion. Absorbing boundaries are used to account for the wave radiation at the lateral boundaries of the model. The study shows that the nonlinearities of the soil and the micropile-soil interface have a significant effect on the soil-micropiles-structure interaction.

1 INTRODUCTION

Micropiles present significant advantages for the construction in seismic areas, mainly flexibility, ductility and capacity to withstand extension forces. They can be used as foundation support of new structures as well as for seismic retrofitting of structures which have suffered seismic damage (Forever 2004, Shahrour and Juran 2004).

The seismic behavior of micropiles was investigated using a linear elastic 3D finite element model, which is accepted for moderate seismic loading (Sadek 2003, Sadek & Shahrour 2004, 2006). Observations on devastating earthquakes showed that the soil nonlinearity should be taken into account in the design of pile foundations (Tokimatsu et al. 1996). The response analysis should be performed in the time domain to properly account for the soil nonlinearity and discontinuity conditions at the soil-pile interface.

This paper presents results of analysis on the influence of the non linear behavior of both the soil and the micropile-soil interface on the soil-micropile-structure interaction. Analysis is carried using a full three-dimensional model for the soil-micropile-structure system in the time domain.

2 NUMERICAL MODEL

Analyses were carried using the program FLAC3D (Fast Lagrangian Analysis of Continua in 3 Dimensions). Figure 1 shows the problem under consideration. It concerns the response of a system composed of a soil mass,

a group of 4 micropiles and a super-structure submitted to a seismic loading. Absorbing elements are used at the lateral boundaries in order to reduce the wave reflection at these boundaries.

Micropiles are modeled using 2-node beam elements. They are rigidly connected to a cap which is free of contact with the soil. The thickness of the cap is equal to 1 m and the micropiles spacing (S) is equal to $6D$ (D denotes the micropiles diameter).

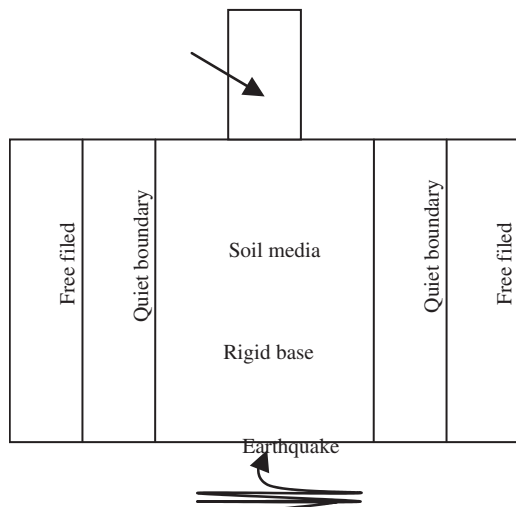


Figure 1. Numerical model used for the soil-micropile-structure system.

The superstructure is modeled as a single degree-of-freedom system (SDOF) composed of a concentrated mass of 40 tons and a column with a height 1 m. The fixed base fundamental frequency of the superstructure is equal to 1.61 Hz. The soil behavior is assumed to be governed by the non associated Mohr-Coulomb criterion. Tables 1a and 1b summarize the properties of the soil and micropiles.

Spring elements are used at the micropile-soil interface to account for the possibility of sliding between the soil and micropiles. The shear stiffness of the interface is assumed to be equal to the shear modulus of the soil. Figure 2 shows the mesh used for the calculation of the soil-micropiles-structure system. It includes 3116 8-node brick elements and 97 beam elements.

The seismic loading is applied as a bedrock motion. The velocity time history of the Earthquake Kocaeli 1999 N-S Component is used as an input loading (Figure 3). The peak ground velocity is equal to 0.40 m/sec. The

frequency spectrum lies mainly between 0.2 and 2 Hz. The peak frequency is equal to 0.9 Hz.

3 INFLUENCE OF THE SOIL PLASTICITY

Figure 4a shows the time history of the horizontal displacement at the top of the superstructure for both elastic (EE) and plastic soils (PE) with a perfect interface between the soil and micropiles. It shows that the soil plasticity induces a decrease in the lateral displacement. Figure 4b shows the spectra of the velocity. It can be observed that plasticity leads to a shift of the frequency of the structure response towards low frequencies. This shift together with the soil damping due to plasticity could explain the influence of the latter on the reduction of the soil displacement.

Figure 4c shows the influence of the plasticity on the axial forces. It can be observed that plasticity results

Table 1a. Properties of the soil material.

Density (kg/m ³)	1700
Young's Modulus (MPa)	8
Poisson's ratio	0.45
Damping ratio	0.05
Friction angle (°)	30
Cohesion (kPa)	17
Dilatation angle (°)	0

Table 1b. Properties of micropiles.

Diameter (m)	0.20
Length (m)	10.0
Density (kg/m ³)	7850
Young's Modulus (GPa)	200
Poisson's ratio	0.20
Damping ratio	0.02

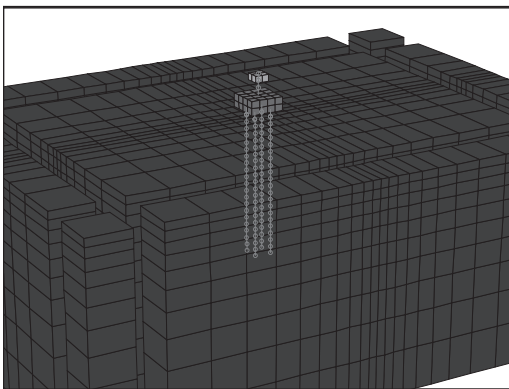


Figure 2. Mesh used for the micropile-soil-structure system (3116 8-node brick elements).

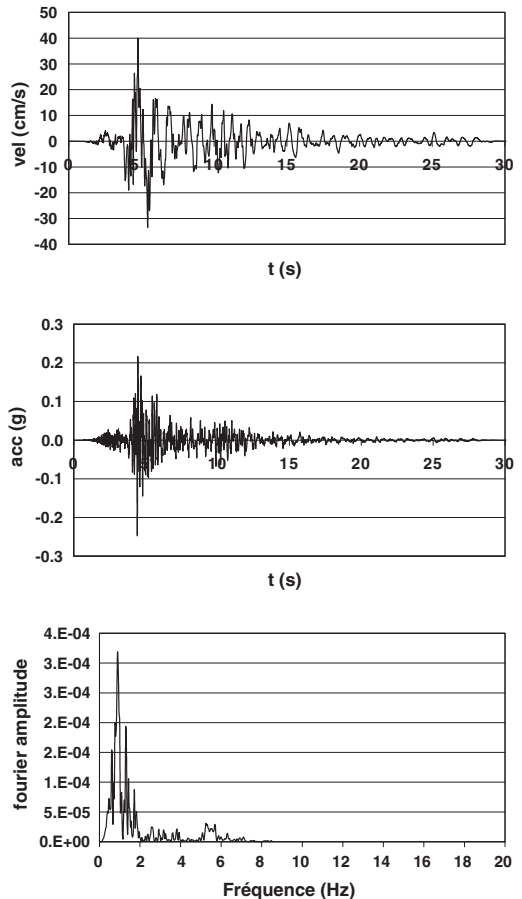


Figure 3. Input seismic loading (Kocaeli Earthquake, 1999).

in a significant decrease in the axial forces which attains approximately 50%.

4 INFLUENCE THE MICROPILE-SOIL INTERFACE

Analyses were carried out with various shearing resistances of the micropile-soil interface: purely cohesive interface with three values of the cohesion ($C_{int} = 150; 100; 50 \text{ kPa}$) and a frictional interface with a resistance which is equal to that of the soil ($C_{int} = 17 \text{ kPa}, \phi_{int} = 30^\circ$). Figures 5a and 5b present the time history of the lateral displacement at the top of the superstructure for different values of the interface resistance. They show a significant decrease in the displacement with the decrease in the interface resistance. Sliding at the interface reduces the transmission of the energy to the superstructure which results in a decrease in the inertial forces.

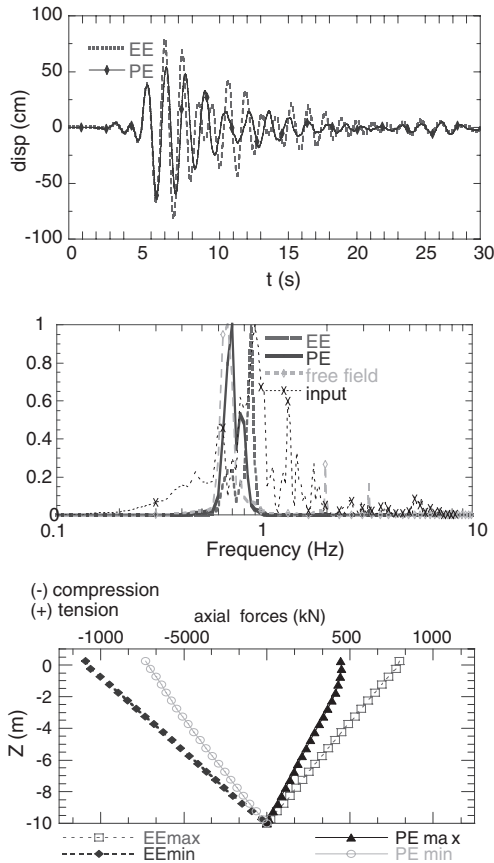


Figure 4. Influence of the soil plasticity on the response of the soil-micropile-structure system.

a) Lateral displacement b) Frequency c) Axial force.

Figures 5c and 5d illustrate the envelopes of the axial force and bending moment. They clearly show that the decrease in the interface resistance results in a decrease in both the axial force and bending moment.

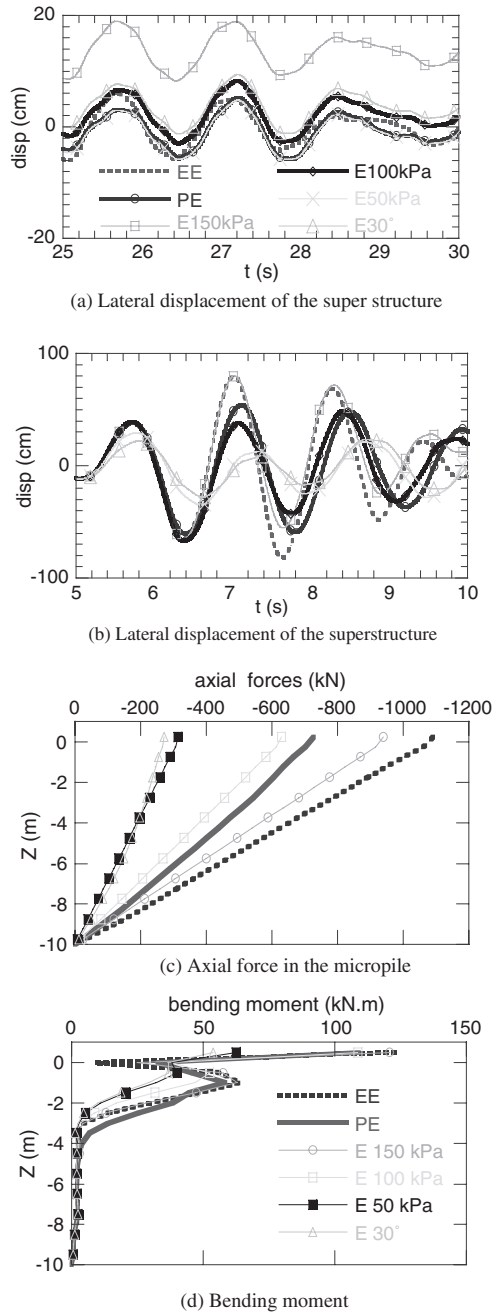


Figure 5. Influence of the interface resistance on the lateral displacement and on the internal forces.

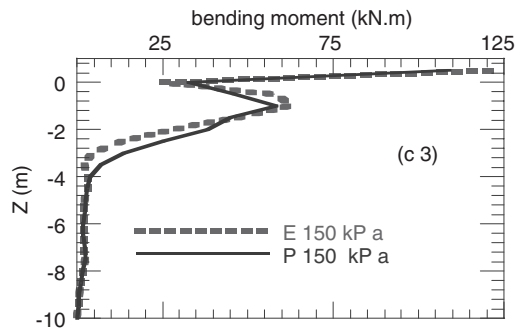
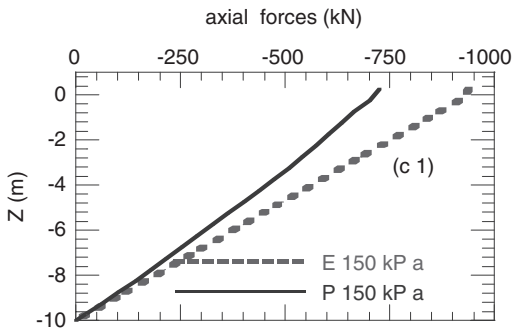
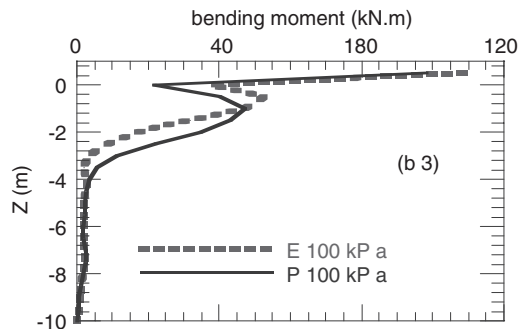
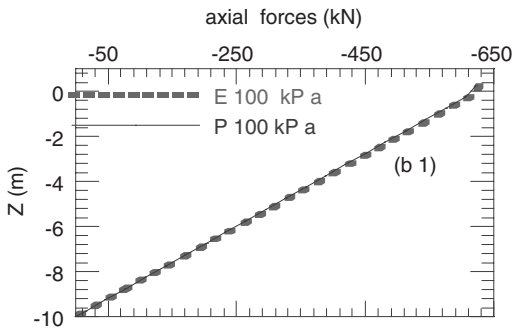
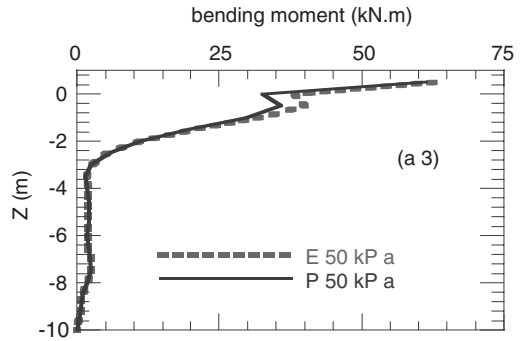
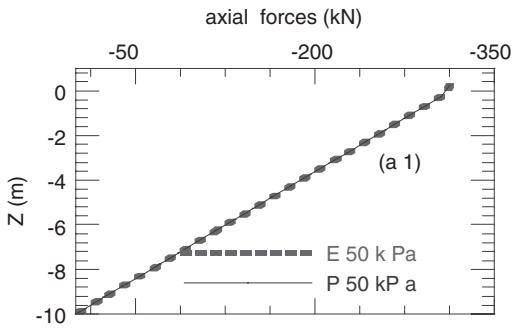


Figure 6a. Influence of the interface resistance on the axial forces in the micropiles.

Figure 6b. Influence of the interface resistance on the bending moment.

5 INFLUENCE OF BOTH THE SOIL PLASTICITY AND THE INTERFACE

The influence of the soil nonlinearity on the response of micropiles group is investigated for different values of the interface resistance.

Figure 6 illustrates the responses of the group of micropiles for three resistances of the interface for both linear (E) and non linear (P) behavior of the soil. It can be observed that for the low interface resistance ($C_{int} = 50 \text{ kPa}$), the soil nonlinearity does not affect the micropiles response. For high values of interface resistance ($C_{int} = 150 \text{ kPa}$), the soil plasticity results

in a decrease in the internal forces. In this case, the high resistance of the interface allows the transmission of stresses to the soil mass, which cause the soil plasticity and affect the micropiles response.

Figure 6c shows the influence of the interface resistance on the extension of the plasticity in the soil mass. It can be observed that the increase in the interface resistance results in an enlargement of the plasticity zone in the soil mass.

Figures 6d shows the influence of the interface resistance on the spectra of the velocity at the superstructure for an elastoplastic soil. It can be observed that the decrease in the interface resistance results in

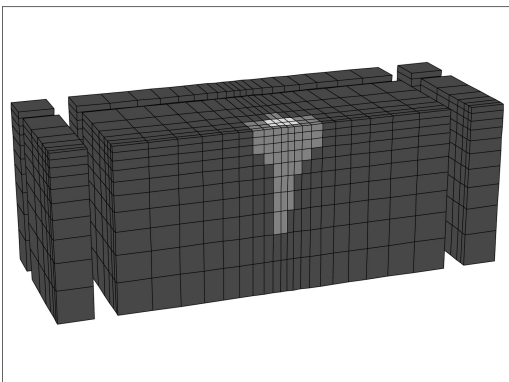
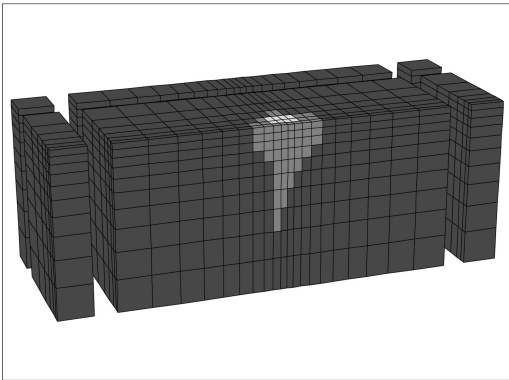
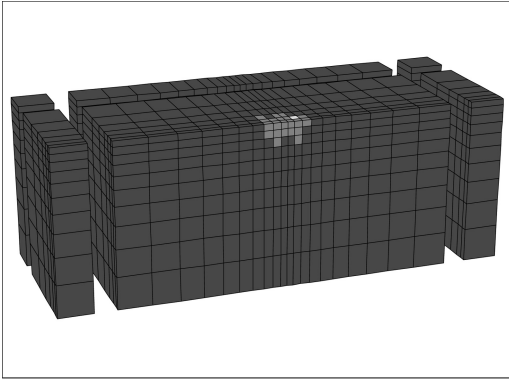


Figure 6c. Influence of the interface resistance on the extension of plasticity in the soil mass.

a shift of the dominate frequencies towards low frequencies. This shift is due to the effect of sliding at the interface in the decrease of the stiffness of the micropiles foundation system, which leads to a reduction of the natural frequencies of the system.

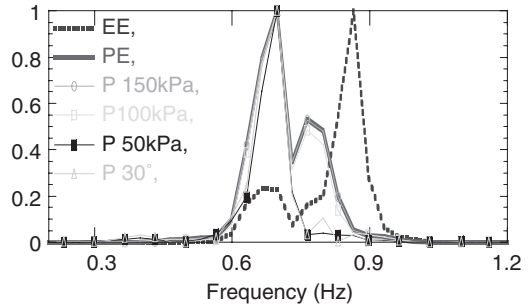


Figure 6d. Influence of the interface resistance on the spectra of the response of the superstructure.

6 CONCLUSIONS

The nonlinear behavior of the both the soil and micropile-soil interface can greatly affect the seismic response of micropiles. The influence of the soil plasticity is moderate for micropiles systems with low interface resistance. In deed, in this case, sliding at the interface limits the transmission of stresses to the soil mass, which results in a reduction of the extension of plasticity in the soil mass.

The influence of the soil plasticity and imperfect interface on the natural frequencies of the soil-micropiles-structure system must be taken into consideration in the design of micropiles in seismic area.

REFERENCES

- FOREVER (2004). "Summary of the results and recommendations of the national Project on the micropiles". Book, presses de l'école nationale des ponts et chaussées, France.
- Sadek M, (2003) "Numerical study of behaviour of micropiles under seismic loading", PhD, University of Sciences and Technologies of Lille 1, Laboratory of Mechanic of Lille.
- Sadek M. & Shahrour I (2004) "Three-dimensional finite element analysis of the seismic behaviour of inclined micropiles" *Soil Dynamics and Earthquake Engineering* 24, 473–485.
- Sadek M. & Shahrour I. (2006) "Influence of the head and tip connection on the seismic performance of micropiles" *Soil Dynamics and Earthquake Engineering* 26, 461–468.
- Shahrour I. & I. Juran (2004) "Seismic behavior of Micropile Systems" *Ground Improvement Journal*, Vol 8, Issue 3, pp. 109–120.
- Tokimatsu, Mizunoh, Kakurai. (1996) "Building damages associated with geotechnical problems". *Soils and Foundations*, Special Issue on Geotechnical Aspects of the January 17 1995 Hyogoken-Nambu Earthquake, Japanese Geotechnical Society, p. 219–234.

Modeling various types of reinforced soil by the finite element method – Application to piled raft foundations

M. Yazdchi, H.C. Yeow & B. Simpson
Ove Arup & Partners, London, UK

ABSTRACT: Reinforcement techniques are increasingly used in different areas of geotechnical engineering (rock bolting for tunnels, soil nailing for retaining structures and ‘micropilling’ techniques, etc) for ground improvement. In such structures, inclusions are periodically introduced along one or two directions. The density of inclusions makes it difficult to treat them separately. From a macromechanical viewpoint, the composite made of soil and inclusions can be replaced by homogeneous material, whose mechanical properties are deduced from those of the constituents. A new approach to model reinforced soil and pile groups is proposed in this paper. The method has the advantage over modeling individual reinforcement/pile in the finite element method in terms of meshing. In this method, the stiffness of nails/piles and the adhesion between reinforcement and soil are smeared over reinforcement area and average behavior of the reinforcement is assessed. Examples are shown of the analyses of a reinforced soil wall and a multi-storey building supported on a large group of piles.

1 INTRODUCTION

Stiff inclusions, such as concrete piles are increasingly used nowadays in the design of reinforcement solutions for foundations on soft soils or slope stabilization systems. Soil nailed embankments; rock-bolted tunnels are some other examples of reinforced soil systems. However, studies on modeling aspects of these systems are few.

Beyond the differences on the installation or construction method of such reinforcements, they undeniably have some common features such as: considerably stronger heterogeneity of the reinforcing material with respect to the surrounding soil, and small volume fraction of the reinforcing material. These two characteristics of reinforced soil, associated with the relatively high number of inclusions, make it very difficult to consider them individually in the finite element analysis in terms of producing very fine mesh to model these small cross section inclusions and hence large size finite element model. Consequently, little literature has been devoted to this kind of approach and researchers have tried to employ the concept of equivalent reinforcement zone for this kind of structures (Randolph, 1994).

2 LITERATURE REVIEW

As regards to piled raft foundation (the problem of concern in this paper), apart from a few attempts to

tackle this problem through FEM (see for example; Small and Zhang, 2002 and Reul, 2004), specific methods have been developed in the last 20 years, such as the ‘hybrid model’ (Clancy and Randolph, 1993 and Chow, 1986) in which piles are modeled by beam elements and the interaction between piles and the soil mass is taken into account by means of springs that allow for describing the shear forces at the pile/soil interface. In addition to time-consuming computational methods used in these methods, they are restricted to the elastic behavior of the reinforced soil constituents, which may be a rather crude approximation as regards to the actual behavior of reinforced foundation systems.

Huang et al (2005) used the 3D finite difference method to model a constructed geosynthetic-reinforced pile supported embankment in Germany. They modeled the piles using pile elements and geogrids were modeled using 2D elements.

Kotake et al (2001) used beam elements to model reinforced soil, without allowing friction between soil and reinforcement. A fairly similar approach was adopted by Guler and Demirkan (2003).

Albert and Kovacs (2003) have adopted a rather simple method by introducing a subgrade model for reinforced soil.

The response of an embankment on soft clay was investigated by finite element method using CRISP program by Kamal et al (2005). As most other researches, they used beam elements to model

reinforcement without simulating the interface between soil and reinforcement.

Recently, a ‘multiphase model’ has been proposed by de Buhan and Sudret (2000) and de Buhan and Sudret (2001) allowing modeling of linear elastic inclusions ignoring their flexural and shear stiffness and considering axial stiffness of reinforcement elements, where perfect bonding between soil and pile was assumed and no allowance was made for the piles to slip through the soil. For many applications such as reinforced earth embankments or soil-nailed slopes this assumption is adequate, but for a piled raft foundation shear and flexural stiffness of the piles could play a decisive role in some situations such as in the case of a foundation subjected to lateral loading; otherwise for vertical loading, assuming only axial stiffness of the piles appears to be adequate.

This paper reports the methodology based on a so-called macromodel to model piled raft foundations. According to this model, a region of soil reinforced by dense and regularly distributed inclusions, such as piles, is described as the superposition of two continuous media, called ‘base material’ and ‘reinforcing medium’, respectively. The base material has the same properties as the soil, while the reinforcing medium is modeled as a homogenized material super-imposed on top of the base material. The aim of the present work is to present a realistic and simplified numerical method for the analysis and design of reinforced soil systems.

The reinforced soil model has been implemented into Oasys finite element SAFE program.

3 PROBLEM STATEMENT

3.1 Description of the model

Figure 1a shows a description of the reinforced soil on the microscopic scale, where inclusions are treated as individual elements embedded in the native soil. On the other hand, according to the macromodel approach, the composite reinforced soil system may be regarded as the superposition of two continuous media, called ‘base material’ and ‘reinforcing material’, respectively. The base material and reinforcing material are geometrically coincident at any node but with different constitutive laws, as shown in Figure 1b. The reinforcement is represented as an averaged (or “smeared”) effect. Slip between the reinforcement and soil is also modeled.

3.2 Numerical implementation of the model

The physics behind the method of analysis directly relates the shear passing between soil and reinforcement to the amount of slip, thus:

The limiting shear stress is set by the adhesion and friction data for the reinforcement, and then the limiting

slip S between the reinforcement and the soil needs to be determined.

The behaviour of the reinforcement is assumed to be *smeared*, and its stiffness can be linear or non-linear. This means that its stiffness is force per unit area of soil (in units of stress), and the adhesion between reinforcement and soil is force/unit area of soil /length of relative movement (or stress/length).

Beside the usual parameters used to model soil, one extra parameter which governs the shear resistance between reinforcement and soil is used.

The program works by storing the displacement of the reinforcement separately from that of the soil. The displacement of the reinforcement is calculated by summing strains from nodes which are bonded to the main mesh (e.g. a pile cap). If necessary, the reinforcement could be bonded to an element which is extremely flexible and so provides no restraint to the end of the reinforcement.

From these relative displacements, the shear stress passing between soil and reinforcement is computed, and this gives the *gradient* of normal stress in the reinforcement. The normal stresses themselves are then computed by working, iteratively, along the reinforcement from a free end at which the stress is zero.

The iterative process operates as follows:

1. At iteration 1, the presence of the reinforcement is considered and displacements of the ground are calculated.
2. The displacement of the reinforcement is then computed, starting from the bonded end (where displacements are the same as those of the corresponding

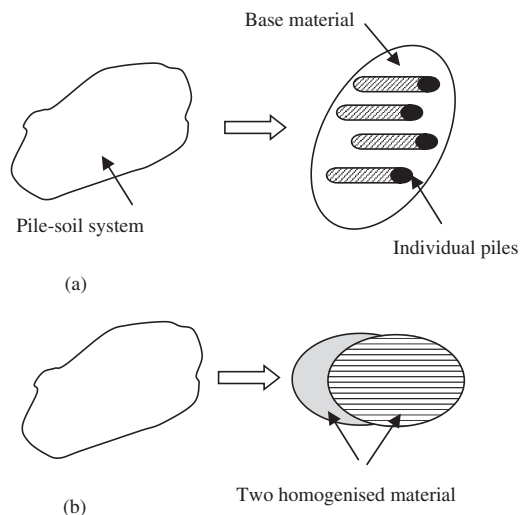


Figure 1. Description of the reinforced material (a) Micromodel, (b) Macromodel.

- elements), and working along the length of the reinforcement. The incremental displacements are computed from the incremental stresses in the reinforcement, using the correct stiffness. The stiffness of reinforcement must not be changed between runs.
- Hence the relative displacement of the soil and reinforcement are known, and the shear passing between them can be computed, from the diagram below (see Figure 2). This shear gives the *gradient* of stress in the reinforcement.
 - Starting from the free end of the reinforcement, and using the gradients, the stress in the reinforcement is computed.
 - This whole process is repeated iteratively.

The program achieves a pseudo-3D solution in a 2D mesh by adding iterative processes to the normal finite element computation.

At the end of each increment, the program outputs displacements of the soil and reinforcement nodes, and the stresses at the nodes joining elements of reinforcement. The finite element process ensures that equilibrium is maintained between the base material and reinforcing medium. The model is validated by checking the gradient of direct stress in the reinforcement in relation to the relative displacements of nodes of the base material and the reinforcing medium. This gradient must be consistent with the shear stress passing between the two materials, as defined by Figure 2.

The program can have two sets of reinforcement overlying each other and this could be extended to more if needed.

Prestressing forces of reinforcement (e.g. into a set of piles) can be applied.

It was assumed that the pile group has significant axial stiffness but very low resistance to bending and this does not cause a problem as long as applied loads are vertical.

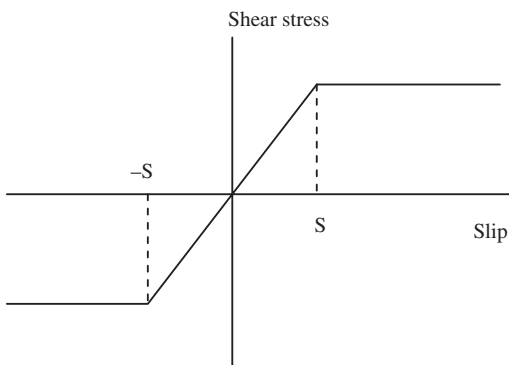


Figure 2. Slip between soil and reinforcement.

4 PROBLEM DESCRIPTION

The piled raft foundation to be analyzed is represented in Figure 3.

This has been used to investigate a settlement problem of a building with original large diameter bored piles, which were overloaded, and additional minipiles provided as underpinning.

The building is modeled as axisymmetric, as shown in Figure 4. The radius of core area is 12 m and that of the whole building is 24 m. The following construction sequence was assumed in the analysis:

- Stage 1: Initialization of the soil
- Stage 2: Construction of the original piles
- Stage 3: Construction of the building
- Stage 4: Construction of the minipiles and jacking – prestressing of these piles
- Stage 5: Application of future loads

Soil stratigraphy is underlain at depth by hard clay which in turn is overlain by soft clay with some made ground.

The region of soil located below the footing has been reinforced by a group of 20 m long piles bored through the soft clay and penetrating into the hard clay to a depth of 5 m.

The meshing shown in Figure 4 was used in the finite element analysis. The ground was discretized into eight-nodded quadrilateral elements. The vicinity of the footing was discretized by finer elements to capture the deformation and failure modes in these critical zones.

As for the boundaries of the ground, vertical rollers were placed along the footing centerline and fixed conditions were used along the bottom and other lateral boundaries of the analysis domain.

The soil is modeled as a Mohr-Coulomb material and the reinforcing elements (piles) are modeled as linear elastic material.

A finite element mesh of the system comprising eight-nodded quadrilateral elements is shown in Figure 3. Quite large elements have been used for this macromodel; individual modeling of each pile would have required a much more refined discretization of

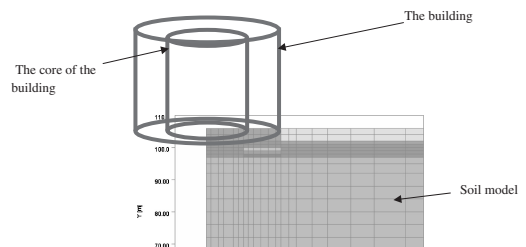
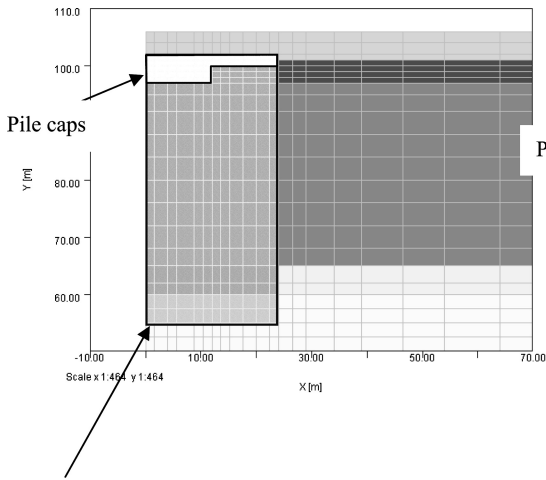
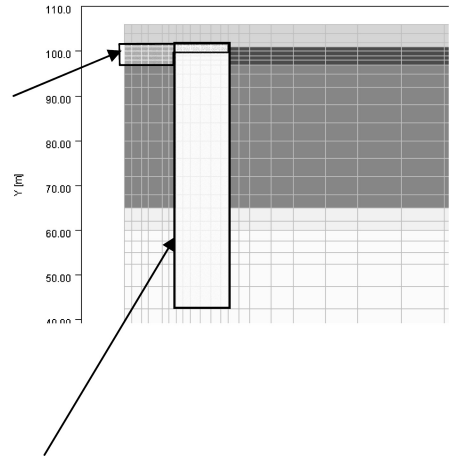


Figure 3. Simplification in the finite element model.



Soil material with overlay reinforcement layer to represent the original piles



Soil material with 2nd overlay layer of reinforcement to model the minipiles

Figure 4. Model piles as reinforcement in SAFE.

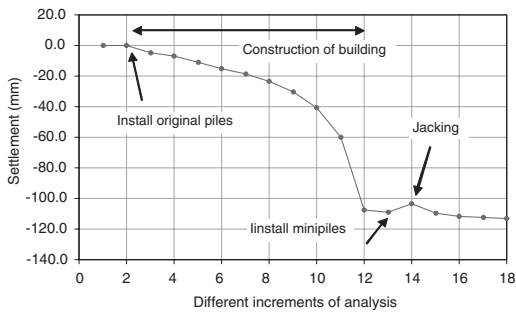


Figure 5. Settlement of building during development.

the model in the piled area, in order to capture the complex interactions prevailing between the soil and the dense network of piles.

Settlement of the building throughout the development of the site could be investigated. Figure 5 shows the settlement of the building at various stages of development. Although continued settlement of the building is computed before installation of the minipiles (as observed), settlement under future loading is computed to be minimal with the minipiles in place. Figure 6 shows the stresses in the soil, the original piles and additional piles at a later stage of the development. At this stage, dissipation of pore water pressure in the soft clay led to negative skin friction, which is seen by forces in the piles increasing with depth.

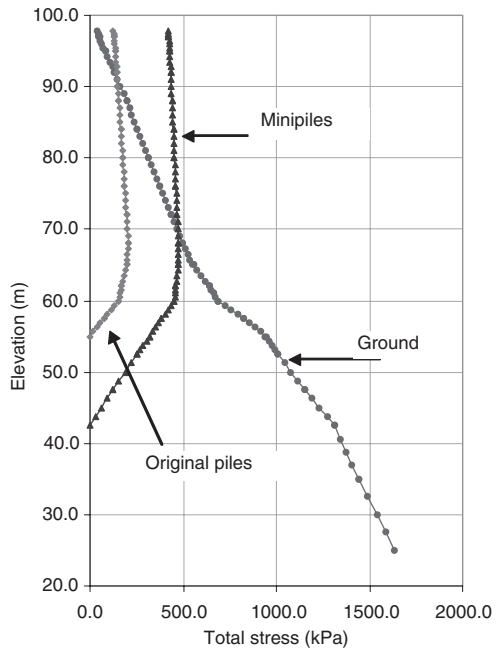


Figure 6. Stresses in the ground and the piles.

Sections of the plot at which the shaft adhesion of the piles is fully mobilised are seen by limiting gradients, as marked on Figure 6.

5 CONCLUSIONS

The macromodel approach presented in this paper to describe behavior of geomaterials reinforced by linear inclusions, allows for simulation and design of any reinforced soil system, leading to a spectacular reduction of the computational time and complexities.

The greater the number of inclusions in the structure, the more accurate the macromodel approach. Whereas the processing time increases with the number of piles in the hybrid or direct methods, it is constant in the macromodel, since only the volume fraction of the reinforcement phase has to be modified and more importantly, finite element meshing for the macromodel is very simplified in compare with the direct methods.

REFERENCES

- Kamal, A.A.A., Lane, P.A. & Heshmati, A.A.R. 2005. Parametric study of reinforced and unreinforced embankment on soft soil. In *13th ACME Conference: University of Sheffield, 21–22 March*, Sheffield, UK.
- Sudret, B. & de Buhan, P. 2001. Multiphase model for inclusion-reinforced geostructures application to rock-bolted tunnels and piled raft foundations. *International Journal for Numerical and Analytical Methods in Geomechanics* 25: 155–182.
- Hassen, G. & de Buhan, P. 2005. Finite element elastoplastic analysis of a piled raft foundation based on the use of a multiphase model. In E. Onate and D.R.J. Owen (ed), *VIII International conference on computational plasticity, COMPLAS VIII, CIMNE*, Barcelona.
- Huang, J., Collin, J.G. & Han, J. 2005. 3D numerical modeling of a constructed geosynthetic-reinforced pile-supported embankment, In A. Adachi (ed), *The 16th international conference on soil mechanics and geotechnical engineering (16ICSMGE), Sep 12–16*, Osaka, Japan.
- Kotake, N., Tatsuoaka, F. & Tanaka, T. 2001, Siddiquee, M.S.A. and Huang, C.C. FEM simulation of the bearing capacity of level reinforced sand ground subjected to footing load, *Geosynthetics International* 8(6): 501–549.
- Albert, P. & Kovacs, M. 2003. Modeling of reinforced soil. *Periodica Polytechnica Ser Civ Eng* 47(2): 169–174.
- Randolph, M.F. 1994. Design methods for pile groups and pile rafts. In *proceedings of XIIIth International conference on Soil mechanics and foundation engineering*, New Delhi, Vol 5: 61–81.
- De Buhan, P. & Sudret, B. 2000. Micropolar multiphase model for materials reinforced by linear inclusions. *European Journal of Mechanics, A/Solids* 19(6): 669–687.
- Clancy, P. & Randolph, M.F. 1993. An approximate analysis procedure for piled raft foundations, *International Journal for Numerical and Analytical Methods in Geomechanics* 17: 849–869.
- Chow, Y.K. 1986. Analysis of vertically loaded pile groups, *International Journal for Numerical and Analytical Methods in Geomechanics* 10(1): 59–72.
- Small, J.C. & Zhang, H.H. 2002. Behaviour of piled raft foundations under lateral and vertical loading, *International Journal of Geomechanics (ASCE)* 2(1): 29–45.
- Reul O. 2004. Numerical study of the bearing behaviour of piled rafts, *International Journal of Geomechanics (ASCE)* 4(2): 59–68.
- Guler, E. & Demirkan, M.M. 2003. A Numerical analysis of the geosynthetic reinforced soil walls with cohesive backfill under seismic loads, in *International conference ICNSMGE – ZM 2003 – New developments in soil mechanics and geotechnical engineering*, Lefkosa, TRNC.

Numerical modelling of vertical drains with advanced constitutive models

A. Yildiz

Department of Civil Engineering, Çukurova University, Adana, Turkey

M. Karstunen & H. Krenn

Department of Civil Engineering, University of Strathclyde, Glasgow, UK

ABSTRACT: When modelling vertical drains in a real boundary value problem the radial flow around a drain needs to be mapped into equivalent plane strain conditions. This can be done by using either permeability, geometry or combined mapping. Whilst the procedure is very simple and straight-forward, the paper suggests that for advanced constitutive models the mapping procedures may need to be done separately for each constitutive model. Three constitutive models are used in the finite element analyses. The S-CLAY1 accounts for initial and plastic strain induced anisotropy and the S-CLAY1S model accounts, additionally, for inter-particle bonding and degradation of bonds. For comparison, the simulations are also performed by the isotropic Modified Cam Clay model.

1 INTRODUCTION

Natural soft clays tend to have significant anisotropy of fabric, developed during deposition and one-dimensional consolidation. During subsequent plastic straining, the fabric anisotropy can change. Anisotropy can influence both elastic behaviour and plastic behaviour. For normally consolidated or lightly overconsolidated soft clays, plastic deformations are likely to dominate for many problems, such as the embankment loading considered in this paper. In addition to anisotropy, natural clays exhibit the effect of inter-particle bonding. When plastic straining occurs, the bonding degrades, referred to as destructuration. These effects can be accounted for with S-CLAY1 and S-CLAY1S models. S-CLAY1 is an extension of conventional critical state models, with anisotropy of plastic behaviour represented through an inclined yield surface and a rotational component of hardening (Wheeler et al. 2003). The S-CLAY1S additionally accounts for bonding between clay particles and destructuration (Koskinen et al. 2002) by using the concept of intrinsic yield surface proposed by Gens and Nova (1993).

Vertical drains are often used under embankments on soft soil to speed up consolidation. Three-dimensional finite element modelling of vertical drains is often not practical and consequently a two-dimensional plane strain model is usually adopted. However, the problem of water flow into a vertical drain is axisymmetric and therefore, the vertical drain system must be converted

into equivalent plane strain model. Hird et al. (1992, 1995) proposed a mapping procedure by which an axisymmetric unit cell can be converted to an equivalent plane strain unit cell. This can be achieved by manipulating either the drain spacing and/or soil permeability. Certain simplifying assumptions are made: each single drain is assumed to work independently, soil has a constant permeability and the consolidation takes place in a uniform soil column with linear compressibility characteristics in the absence of lateral movement. Such restrictive conditions are not likely to be achieved in normally or lightly overconsolidated soils under embankment loading. Furthermore, soft soils tend to be structured and their behaviour is highly non-linear. The question is how well the mapping procedures apply when complex elasto-plastic models are used. This paper studies the performance of the mapping procedures proposed by Hird et al. (1992, 1995) in a 2-D plane strain analysis of Haarajoki test embankment, considering the section that was improved with vertical drains. Simulations are performed with S-CLAY1 and S-CLAY1S models as well as the isotropic Modified Cam Clay model.

2 HAARAJOKI TEST EMBANKMENT

Haarajoki Test Embankment was built as a noise barrier in 1997. The embankment is 3.0 m high and 100 m long. The crest of the embankment is 8 m wide and

the slopes have a gradient of 1:2. Haarajoki deposits can be characterized as sensitive anisotropic soft clays/clayey silts. The organic content is between 1.4 and 2.2% in the depth of 3–13 meters. The water content (67–112%) is often higher than the liquid limit. On the top there is a 2 m thick layer of dry crust and under that a 20 m thick layer of clay. Half of the embankment is constructed on area improved with vertical drains and the other half on natural deposits without any additional ground improvement. The embankment itself was constructed as 0.5 m layers with each of the layers applied within 2 days. In the improved area, the vertical drains were installed in square pattern with 1 m c/c spacing.

3 INPUT DATA

The embankment was modelled with Mohr Coulomb model using the following values: Young's modulus $E = 40000 \text{ kN/m}^2$, Poisson's ratio $\nu' = 0.35$, friction angle $\phi' = 40^\circ$, dilatancy angle $\psi = 0^\circ$, cohesion $c' = 2 \text{ kN/m}^2$, and unit weight $\gamma = 21 \text{ kN/m}^3$. Based on previous analyses (see e.g. Aalto et al. 1998), the increase in stress is negligible below the depth of 15 m and therefore, the deepest clay and silt layers have been ignored in the unit cell analyses.

The values for model and state parameters for the S-CLAY1 and S-CLAY1S models were estimated for each layer based on laboratory results (Tables 1-3). The initial values for the state parameters are shown in Table 1. Pre-overburden pressure (POP) defines the difference between the vertical preconsolidation stress (σ'_{vp}) and the in situ vertical effective stress (σ'_{vo}). The in-situ K_0 values (coefficient of earth pressure at rest) are estimated with the equation proposed by Mayne and Kulhawy (1982). The initial inclination α_0 of yield surface (Table 1) was determined using the procedure by Wheeler et al. (2003). The bonding parameter x_0 is related to the sensitivity (S_t) of the soil, and $S_t - 1$ can be considered as a lower bound of x_0 (Koskinen et al. 2002). The values for the standard soil constants in Table 2 (unit weight γ , ν' , slope of the swelling/recompression line κ , slope of the normal compression line λ , and stress ratio at critical state M) were determined in a conventional manner from triaxial and oedometer tests on natural samples. The values of permeability used for calculations were derived by Näättäen et al. (1998) based on vertical and horizontal oedometer tests.

The values for the additional model parameters required for the S-CLAY1 and S-CLAY1S models are listed in Table 3. The values of λ_i (the slope of the intrinsic compression line) need to be measured from oedometer tests on reconstituted samples. In the absence of these tests, the values were estimated assuming similar λ/λ_i ratios with the other Finnish clays.

Table 1. The initial values for the state variables.

Layer	Depth	e_0	POP	K_0	α_0	x_0
1	0.0–1.0	1.4	76.5	0.40	0.58	4
2	1.0–2.0	1.4	60.0	0.40	0.58	4
3a	2.0–3.0	2.9	38.0	0.52	0.44	22
3b	3.0–4.0	2.9	34.0	0.52	0.44	22
3c	4.0–5.0	2.9	30.0	0.52	0.44	22
4	5.0–7.0	2.8	24.0	0.54	0.42	30
5	7.0–10.0	2.3	21.0	0.55	0.41	45
6	10.0–12.0	2.2	28.5	0.55	0.41	45
7	12.0–15.0	2.2	33.5	0.52	0.44	45

Table 2. Values for MCC soil parameters.

Layer	γ	ν	κ	λ	M
1	17.0	0.35	0.006	0.12	1.50
2	17.0	0.35	0.009	0.21	1.50
3a	14.0	0.18	0.033	1.33	1.15
3b	14.0	0.18	0.033	1.33	1.15
3c	14.0	0.18	0.033	1.33	1.15
4	14.0	0.10	0.037	0.96	1.10
5	15.0	0.10	0.026	0.65	1.07
6	15.0	0.28	0.031	1.16	1.07
7	15.0	0.28	0.033	1.06	1.15

Table 3. Values for the additional soil parameters for S-CLAY1 and S-CLAY1S.

Layer	β	μ	λ_i	a	b
1	1.00	50	0.04	8	0.2
2	1.00	50	0.06	8	0.2
3a	0.70	20	0.38	8	0.2
3b	0.70	20	0.38	8	0.2
3c	0.70	20	0.38	8	0.2
4	0.64	20	0.27	8	0.2
5	0.60	20	0.19	8	0.2
6	0.60	20	0.33	8	0.2
7	0.70	20	0.30	8	0.2

The values of soil parameter β relating to rotational hardening were calculated as outlined in Wheeler et al. (2003) using estimated normally consolidated K_0 values. The values of μ , which control the rate of yield surface rotation, were estimated based on apparent values of λ , as suggested by Zentar et al. (2002). For the parameters a and b that control rate of degradation of bonding typical default values were assumed based on experience with other Finnish clays.

4 UNIT CELL ANALYSIS

The analyses of Haarajoki test embankment by utilizing a unit cell were done with the 2D finite element code PLAXIS V8.2 (Brinkgreve, 2002). The S-CLAY1

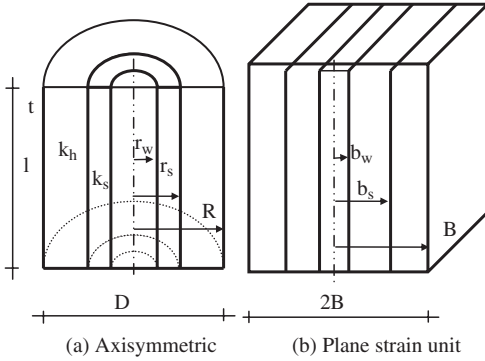


Figure 1. Axisymmetric and plane strain unit cell.

and S-CLAY1S models have been implemented as user-defined soil models. The problem was discretized by using a finite element mesh with about 77 six-noded triangular elements. The groundwater table is at the ground surface. The lateral boundaries are restrained horizontally and the bottom boundary is restrained in both directions. Drainage boundaries are assumed to be at the level of ground surface and at the bottom of the mesh. The excess pore pressures were set to zero along the drain boundary to simulate complete dissipation. The construction of embankment was done in 0.5 m layers, each taking 2 days accounting for the real construction schedule. The construction of embankment was completed in 35 days. After the construction of each layer a consolidation phase is introduced to allow the excess pore pressures to dissipate.

Figure 1 shows an axisymmetric unit cell with the total radius, R and its equivalent plane strain unit cell with half width, B. The length of the vertical drains (l) is 15 m and only a single drain is modelled in the analyses. The equivalent drain radius (r_w) and unit cell radius (R) were calculated as 0.034 m and 0.565 m, respectively.

The installation of vertical drains by means of mandrel causes significant disturbance in the soil surrounding the drain. Thus, a zone of smear with reduced permeability develops. The size of the smear zone depends on the method of drain installation, the size and shape of mandrel and the soil structure. The horizontal permeability of the soil k_h was reduced to a lower value of k_s within the radius of smear zone (r_s) in the analyses. Well resistance was neglected in the analyses. The axisymmetric unit cell was converted into equivalent plane strain unit cell by following the mapping procedures proposed by Hird et al. (1995). The geometric mapping was done according to equation:

$$\frac{B}{R} = \left\{ \left[\frac{3}{2} \ln \left(\frac{R}{r_s} \right) + \left(\frac{k_h}{k_s} \right) \ln \left(\frac{r_s}{r_w} \right) - \left(\frac{3}{4} \right) \right] \right\}^{\frac{1}{2}} \quad (1)$$

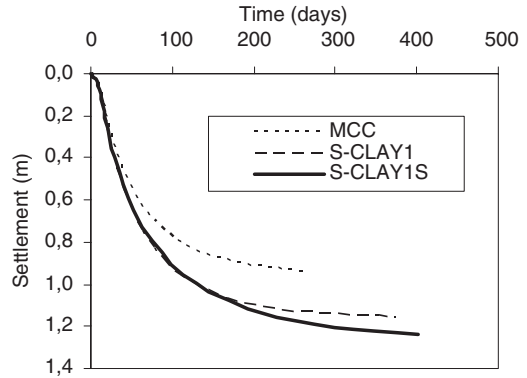


Figure 2. Time-settlement curves predicted by the axisymmetric unit cell.

The permeability mapping can be done by using

$$\frac{k_{pl}}{k_{ax}} = \frac{2}{3 \left[\ln \left(\frac{R}{r_s} \right) + \left(\frac{k_{ax}}{k_s} \right) \ln \left(\frac{r_s}{r_w} \right) - \left(\frac{3}{4} \right) \right]} \quad (2)$$

where k_{ax} and k_{pl} are the values of horizontal permeability of axisymmetric and plane strain conditions, respectively. It is also possible that a value of B is pre-selected and then k_{pl} is calculated by using combined mapping procedure as:

$$\frac{k_{pl}}{k_{ax}} = \frac{2B^2}{3R^2 \left[\ln \left(\frac{R}{r_s} \right) + \left(\frac{k_{ax}}{k_s} \right) \ln \left(\frac{r_s}{r_w} \right) - \left(\frac{3}{4} \right) \right]} \quad (3)$$

5 RESULTS OF NUMERICAL ANALYSES

The first set of finite element analyses was conducted using an axisymmetric unit cell. The problem was modelled using large strain analyses. Figure 2 shows the predicted settlements versus time for all models (MCC, S-CLAY1 and S-CLAY1S). Smear effect is neglected in the analysis of vertical drained area. The smear effect can be neglected by using $k_h/k_s = 1$ or $r_s = r_w$ in the analysis. Differences between the three models become significant during consolidation. The isotropic MCC model predicts smaller settlements than the two anisotropic models and the highest values were predicted by S-CLAY1S.

For the plane strain analyses the axisymmetric unit cell is converted into equivalent plane strain unit cell according to Eqs 1–3 (Table 4). The predicted vertical displacements by the axisymmetric and equivalent

Table 4. The equivalent plane strain model for perfect drain.

k_h/k_s	r_s/r_w	Geometry mapping	Permeability mapping	Combined mapping
1	1	$B = 1 \text{ m}$	$k_{pl}/k_{ax} = 0.32$	$k_{pl}/k_{ax} = 1.014$ ($B = 1 \text{ m}$)

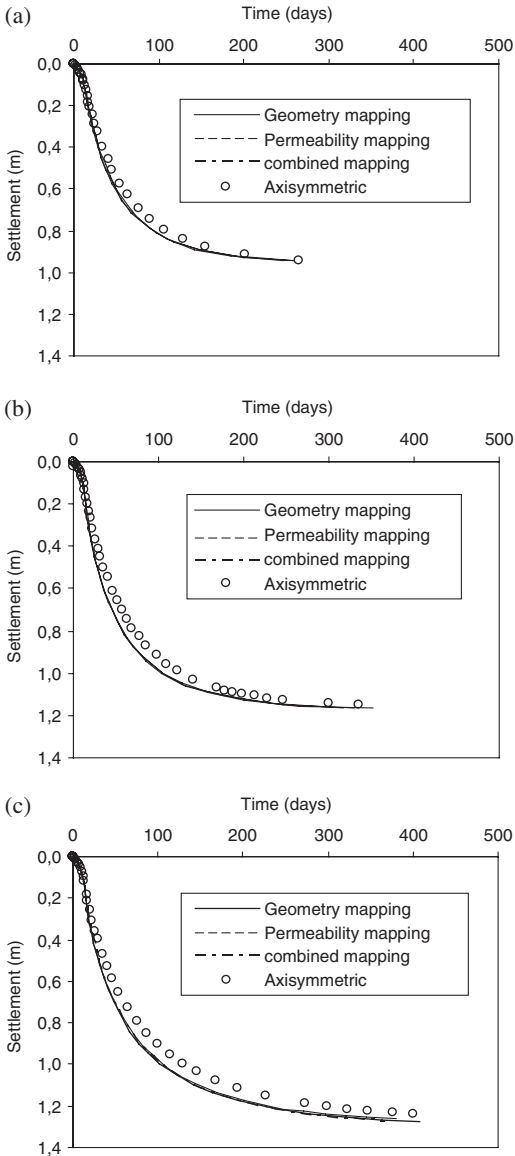


Figure 3. The results of axisymmetric and plane strain analyses for perfect drain: (a) MCC; (b) S-CLAY1 and (c) S-CLAY1S.

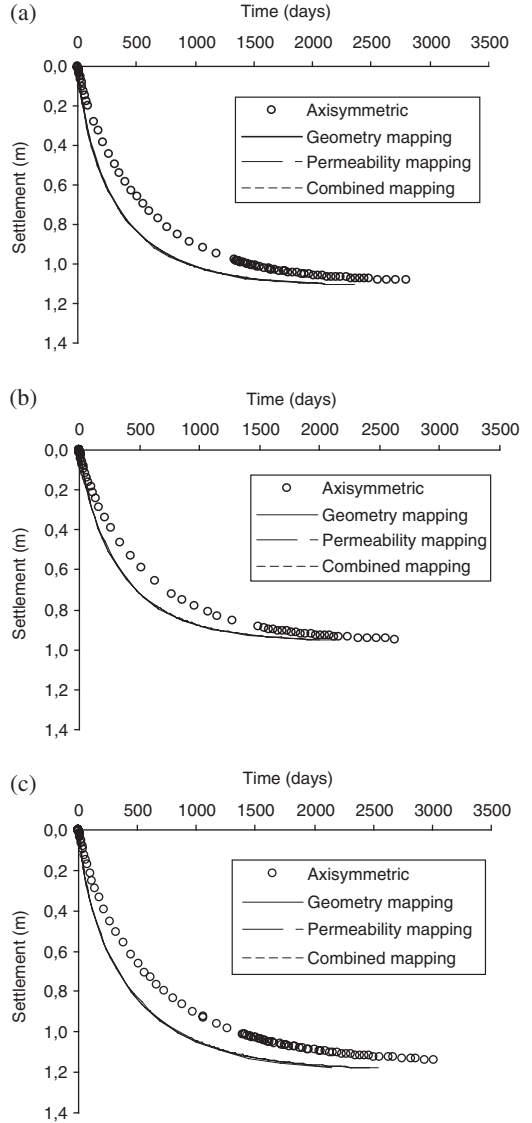


Figure 4. The results of axisymmetric and plane strain analyses with smear effect ($k_h/k_s = 10$ and $d_s/d_m = 5$): (a) MCC; (b) S-CLAY1 and (c) S-CLAY1S.

plane strain analyses are compared in Figure 3. It can be seen that all three mapping procedures produce virtually identical results. Consolidation rate in the equivalent plane strain analyses is predicted to be faster than that in the axisymmetric analysis. During consolidation, the maximum error in the predicted settlements between the axisymmetric and equivalent plane strain analyses is about 6% with MCC, whilst errors of about 9% and 8% results with S-CLAY1 and S-CLAY1S, respectively.

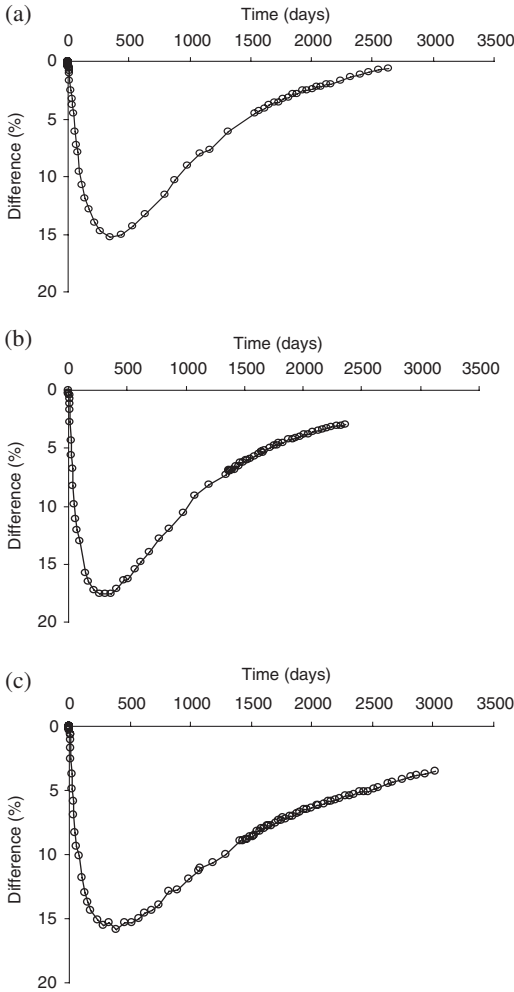


Figure 5. Differences between axisymmetric and plane strain results ($k_h/k_s = 10$ and $d_v/d_m = 5$): (a) MCC; (b) S-CLAY1 and (c) S-CLAY1S.

The match is therefore reasonable, but not perfect. Given the error is different from model to model, it might be necessary to consider each model separately in order to improve the match. The predicted maximum value of excess pore pressures at the end of construction is predicted to be the same for all models in the axisymmetric analyses, but rate of dissipation excess pore pressures is higher with S-CLAY1S model than the other models. Because either geometry or soil permeability are changed in mapping, the excess pore pressures in the equivalent plane strain model are not comparable with those by the axisymmetric model.

Installation of vertical drains by means of a mandrel causes significant remoulding of the subsoil, especially

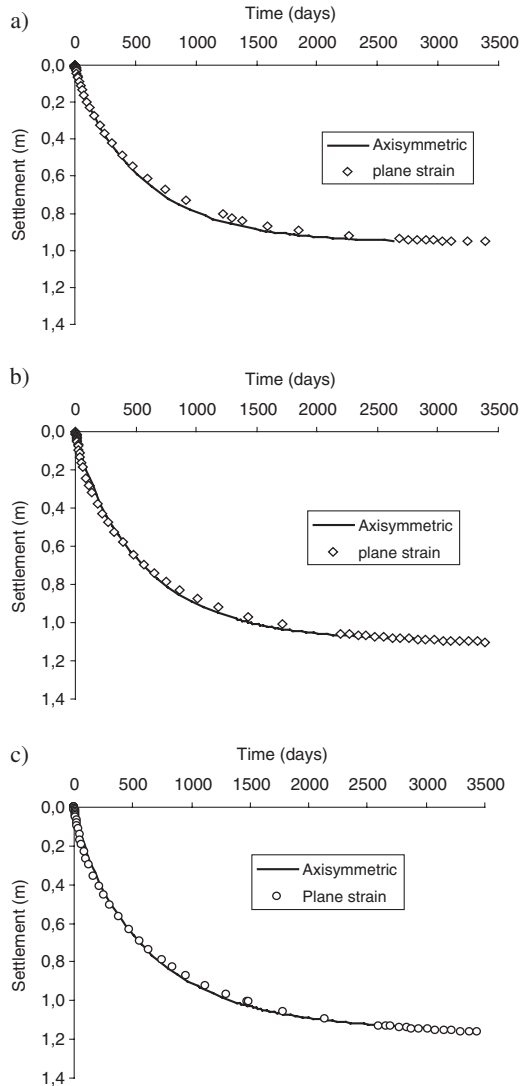


Figure 6. k_h/k_s ratio is increased from 10 to 20 in the plane strain analyses to improve the match: (a) MCC; (b) S-CLAY1 and (c) S-CLAY1S.

in the immediate vicinity of the mandrel. Haarajoki deposits are very sensitive. Thus, considerable disturbance is expected in the subsoil during the installation of vertical drains. In order to investigate the influence of soil disturbance due to mandrel insertion, a parametric study was performed by changing the radius of smear zone and the horizontal permeability within smear zone. It was obvious that the smear effect has major influence on the settlement behaviour. The difficulty is to estimate the extent of the smear zone and the influence of the smear on soil properties. According

to Indraratna and Redana (1998) the smear zone radius is typically of 4–5 times the radius of the mandrel (r_m). Bergado et al. (1993) proposed the ratio of k_h/k_s between 5 and 20 based on full-scale field test.

Figure 4 shows the vertical displacements by the axisymmetric and equivalent plane strain analyses accounting for smear effect assuming $k_h/k_s = 10$ and $r_s/r_m = 5$. Again, all mapping procedures produce effectively identical settlement response. However, the agreement between axisymmetric and equivalent plane strain analyses is far from perfect. The rate of consolidation in the plane strain analysis is notably faster than that in axisymmetric analysis. Figure 5 illustrates the calculated errors in the plane strain analyses with smear effect compared to the axisymmetric unit cell. The results of combined mapping procedure are taken as reference for the error calculation. The maximum errors are about 15%, 18% and 16% for MCC, S-CLAY1 and S-CLAY1S, respectively. At the end of consolidation, the errors are about 0.6%, 3.5% and 3% for MCC, S-CLAY1 and S-CLAY1S, respectively. In order to improve the match, the ratio of k_h/k_s is increased from 10 to 20 in the equivalent plane strain analysis while the ratio of k_h/k_s is kept constant in the axisymmetric analysis. The results of axisymmetric and mapped plane strain analyses are compared in Figure 6. The quality has improved, although for a perfect match, each model would need to be considered separately.

6 CONCLUSIONS

This paper studied the mapping procedures developed for 2D plane strain analysis of a vertical drain under an embankment load. The actual axisymmetric condition of a vertical drain was converted into equivalent plane strain model, considering both ideal drain and the smear effect due to the installation of vertical drains. The soft clay was chosen correspond to Haarajoki test embankment in Finland. Two anisotropic constitutive models, S-CLAY1 and S-CLAY1S, were used in the analyses. The simulations were also done with the isotropic MCC model. Based on results of numerical analyses the following main conclusions can be drawn:

- Ignoring fabric anisotropy and micro-structure would lead to underprediction of settlements.
- The three alternative mapping procedures proposed by Hird et al. (1995) produce identical results. Combined mapping procedure is the most convenient as it enables controlling mesh geometry in the finite element analysis.
- The rate of consolidation in the equivalent plane strain analyses tended to be faster than that in the axisymmetric analyses.
- Smear effect increases the errors between the axisymmetric and equivalent plane strain results.

Based on these results, the matching procedures proposed by Hird et al. (1995) can only be used as a crude estimate when advanced models are used. In order to improve the match, the permeabilities for the equivalent plane strain model need to be adjusted further. As the predicted coefficients of consolidation differ from model to model, in some cases this further adjustment may need to be done model by model basis. If the mapping procedures are applied to a real embankment geometry, it would be unwise just to rely solely on the equation proposed by Hird et al. (1995), and studies such as presented here would need to be conducted before choosing the permeability values for the plane strain analyses.

ACKNOWLEDGEMENTS

The work presented was carried out as part of a Marie Curie Research Training Network “Advanced Modelling of Ground Improvement on Soft Soils (AMGISS)” (MRTN-CT-2004-512120) supported the European Community through the programme “Human Resources and Mobility”. In addition, the first author was supported by the Scientific and Technological Research Council of Turkey (TUBITAK). The third author is sponsored through a scholarship by the Faculty of Engineering, University of Strathclyde, UK.

REFERENCES

- Aalto, A. 1998. The calculations on Haarajoki test embankment with the finite element program Plaxis 6.1. *Proc 4th European Conference on Numerical Methods in Geotechnical Engineering (NUMGE)*, Udine, Italy, 14–16 October, 1998.
- Bergado, D.T., Mukherjee, K., Alfaro, M.C., Balasubramaniam, A.S. 1993. Prediction of vertical-band-drain performance by the finite-element method, *Geotextiles and Geomembranes*, 12, 567–586.
- Brinkgreve, R.B.J. 2002. PLAXIS, Finite element code for soil and rock analyses, 2D-Version 8, Rotterdam: Balkema.
- Gens, A. & Nova, R. 1993. Conceptual bases for a constitutive model for bonded soils and weak rocks. *Proc. Int. Symp. On Hard Soils – Soft Rocks*, Athens: 485–494.
- Hird, C.C., Pyrah, I.C., Russell, D. 1992. Finite element modeling of vertical drains beneath embankments on soft ground. *Géotechnique*, 42, 499–511.
- Hird, C.C., Pyrah, I.C., Russell, D., Cincicoglu, F. 1995. Modelling the effect of vertical drains in two-dimensional finite element analyses of embankments on soft ground. *Canadian Geotechnical Journal*, 32, 795–807.
- Indraratna, B. & Redana, I.W. 1998. Laboratory determination of smear zone due to vertical drain installation. *J. Geotech. and Geoenvironmental Engineering*, 124, 180–184.
- Koskinen, M., Karstunen, M. & Wheeler, S.J. 2002. Modelling destructuration and anisotropy of a natural soft clay. *Proc. 5th European Conference on Numerical Methods in*

- Geotechnical Engineering (NUMGE)*, Paris 2002; Presses de l'ENPC/LCPC: 11–20.
- Mayne, P.W. & Kulhawy, F.H. 1982. K_0 – OCR relationship in soil. *J. of Geotechnical Engineering.*, 18(6), 851–872.
- Näätänen A., Vepsäläinen, P., Lojander, M. 1998. Finite element calculations on Haarajoki test embankment. *Proc 4th European Conference on Numerical Methods in Geotechnical Engineering (NUMGE)*, Udine, Italy, 14–16 October, 1998.
- Näätänen, A., Wheeler, S., Karstunen, M. & Lojander, M. 1999. Experimental investigation of an anisotropic hardening model. *Proc 2nd Int. Symp. on Prefailure Deformation Characteristics of Geomaterials*, Turin, Balkema, 541–548.
- Wheeler, S.J., Näätänen, A., Karstunen, M. & Lojander, M. (2003). An anisotropic elasto plastic model for soft clays. *Canadian Geotechnical Journal*, 40, 403–418.
- Zentar, R., Karstunen, M., Wheeler, S.J. 2002. Influence of anisotropy and destructuration on undrained shearing of natural clays. *Proc. 5th European Conference on Numerical Methods in Geotechnical Engineering (NUMGE)*, Paris 2002; Presses de l'ENPC/LCPC: 21–26.

Coupling finite elements and discrete elements methods, application to reinforced embankment by piles and geosynthetics

B. Le Hello & P. Villard

Lirigm, Université Joseph Fourier, Grenoble, France

A. Nancey & Ph. Delmas

Bidim Geosynthetics SAS, Bezons, France

ABSTRACT: The design of geotechnical earth structures is, due to the use of new technologies and new materials, more and more sophisticated. This needs the development and the adaptation of the existing numerical models to take into account the specificity and the particularity of the behaviour of each component of the structure. A coupling between Finite Elements Method and Discrete Elements Method was done in order to clarify the mechanical behaviour of embankments soil reinforced by piles and geosynthetics. The coupling of the two numerical models allows us to keep the main advantages of each method: use of a continuous model defined by the macroscopic parameters to describe the fibrous structure of the geosynthetic sheet and its interaction with the soil, and use of a discrete model to describe the mechanisms of arching effect and transfer of load in the soil. Applications to embankments built on compressible soil and reinforced by piles and geosynthetic sheets are presented. Results given are the displacements and the deformations of the structure, the tensile forces acting in the armed directions of the geosynthetic and the efficiencies of piles, geosynthetic and supporting soil.

1 INTRODUCTION

The upgrading of very soft soil areas (recent deposits and mud) requires innovating processes. Reinforcement with vertical piles is a 'traditional' process used to improve the bearing pressure of the very soft soil. A recent approach of this concept is the addition of a geosynthetic like reinforcement at the base of the embankment (Fig. 1). The geosynthetic has to allow the transfer of the vertical load, due to the weight of the embankment, to the piles in order to minimise the applied load on the soft soil.

The vertical load due to the weight of the embankment can be directly transferred to the piles by an arching effect or indirectly via the membrane effect of the geosynthetic. Loads transmitted to the piles are reported primarily to the bedrock or partially to the soft soil by friction.

The main numerical difficulties correlated to the modelling of this type of structure result from:

- The significant deformability of the structure needed to develop tensile force into the flexible reinforcement sheet,
- The complex interaction between the soil, geosynthetic and piles at the interfaces,
- The specific behaviour of materials constitutive of these reinforced earth structures (membrane

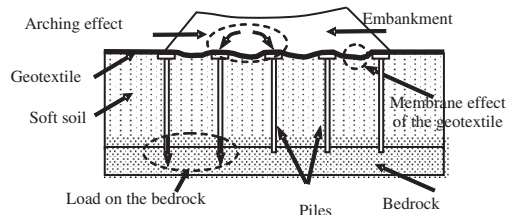


Figure 1. Reinforced embankment by piles and geosynthetics.

behaviour of the geosynthetic, arching effect and transfer of load in the soil).

The coupling between finite element and discrete element models is motivated by:

- The need to use finite elements to describe the fibrous structure of the geosynthetic sheet (modelling by discrete elements does not allow to take into account particular directions of reinforcement and the non linear tensile behaviour of each fibre direction),
- The need to use discrete elements to fit well the particular behaviour of granular soils: influence of the variation of porosity on the mechanical behaviour of the soil during the collapse of the embankment on the geosynthetic sheet, expansion, dilatancy, arching

effect and representative transfer of load in the granular soil (shape and granular distribution of the particles of soil have experimentally and numerically a great influence on the mechanism of arching effect),

- The need to take into account the interface behaviour. The major disadvantage of modelling both the soil and the geosynthetic by discrete elements lies in the restitution of the macroscopic behaviour of the interface which is tributary, at the same time, of the relative roughness of the particles of soil with the sheet (relative roughness being able to evolve during simulation if the geosynthetic sheets are very weak), and of the inter granular microscopic friction (the fitting between micro and macro properties being difficult to obtain in this case). The advantage to model the soil by discrete element and the sheet by finite element is that it is possible to define directly the interface behaviour by specific contact laws using the macroscopic friction angle (no fitting between micro and macro properties).

2 THE NUMERICAL APPROACH

The numerical approach selected to allow the coupling between the discrete and finite elements, consist to insert in an existing discrete element code SDEC (Donzé & Magnier, 1997) the specific finite elements characteristic of the geosynthetic sheet behaviour. The behaviour of these finite elements is governed, like the discrete elements, by the Newton's law of motion. The interaction behaviour between these two kinds of elements is given by specific contact law defined at each contact point. The assumptions which manage the behaviour of each element and the numerical specificities linked to the coupling of the two methods are presented below.

2.1 *The finite elements used to describe the membrane behaviour of the geosynthetic sheet*

The finite elements included in the three dimensional discrete elements software are three nodes elements developed previously in a finite element procedure (Villard & Giraud, 1998) to simulate the behaviour of earth reinforced structures. These elements allow to take into account the fibrous structure of any type of geosynthetic (woven, non woven geosynthetic reinforced in specific directions or knitted geosynthetic) and to well describe the tensile and membrane behaviour of the sheet (due to their constitution, geosynthetic sheet has no rigidity in flexion).

These numerical developments were validated by comparison with analytical solutions of the membrane effect obtained in simple cases (Villard et al., 2000) and with experimental results of laboratory tests or full-scale experiments (Gourc & Villard, 2000).

The fundamental assumptions which lead to the establishment of the behaviour of a three nodes element are:

- Each element consists of a set of fibres with various orientations, initially forming a plane,
- The intersection and the tangle of wire are such as it does not have to slip between the wire (presence of connection points between wire). It results that the behaviour of a fibre network is obtained by superposition of behaviours obtained in each fibre direction,
- The tensile efforts in each direction of fibres are directed in the direction of fibres after deformation (great displacements),
- The tensile stress supported by a set of fibres with the same direction is defined by the relation $\sigma = E(\epsilon) * \epsilon$. $E(\epsilon)$ is the secant module of fibres (function of the density of fibres) and ϵ is the deformation of fibres in the direction considered. ϵ is defined by the relation $\epsilon = (l' - l)/l$ with respectively l the initial length and l' the length after deformation of considered fibres. The modulus of elasticity in compression is very weak compared to the elastic modulus in traction (no compression in fibres),
- There is no bending stress,
- The deformations in each fibre directions are constant on an element, due to the use of linear interpolations functions for the definition of the three nodes elements.

The fundamental equation characteristic of the behaviour of a three nodes finite element can be written as:

$$\{F\} = [K_u]\{u\} + \{F_u\} \quad (1)$$

where $\{F\}$ are the forces acting on the nodes of an element, $\{u\}$ the nodal displacements of the element, $[K_u]$ the elementary matrix of rigidity depending on the final position of the three nodes, and $\{F_u\}$ a corrective vector force resulting from the large displacements formulation.

2.2 *The discrete element model*

The discrete element model used is a three dimensional software (SDEC) based on a Newtonian approach which uses rigid bodies (Donzé & Magnier, 1997). The basis elements employed are spherical particles of various sizes which can interact together (two elements may be considered as interacting while not touching). The algorithm of calculation used consists in successively alternating the application of the Newton's second law of motion to the particles and a force-displacement law to the contacts. The equations

of motion are integrated using an explicit centred finite difference algorithm involving a time step Δt .

Recent numerical developments allow jointing together several spherical particles to make clusters. These developments are necessary to obtain more realistic mechanical behaviour of soil.

Interaction laws, locally defined, make it possible to restore a global macroscopic behaviour of the particles assembly. The granular distribution, initial porosity, shape of clusters and the methodology of setting up the particles have a great influence on the numerical material behaviour.

The identification of the micro mechanical parameters of contact needed to reproduce the macro mechanical behaviour of the material is complex and need a fitting of the model. Generally, numerical simulations of triaxial tests are enough to identify the main mechanical parameters (elastic modulus, Poisson coefficient, cohesion, dilatancy and friction angles).

The curves presented on figures 2 and 3 give, for a set of micro mechanical parameters, the macro mechanical answers of the discrete elements model. The numerical samples tested are constituted by approximately 6000 spherical particles of several sizes; each diameter of particles is randomly chosen between a range of d and $2d$. The spherical particles are setting to an initial porosity by progressive enlargement. Numerical triaxial tests at several initial

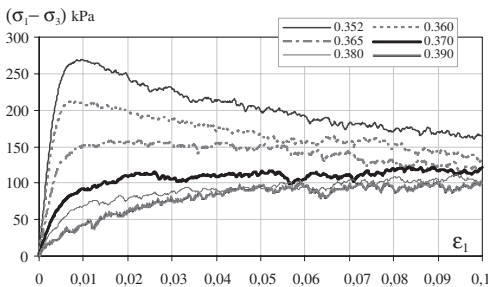


Figure 2. Numerical results of triaxial tests: deviatoric stress versus axial strain for several porosities ($\sigma_3 = 110$ kPa).

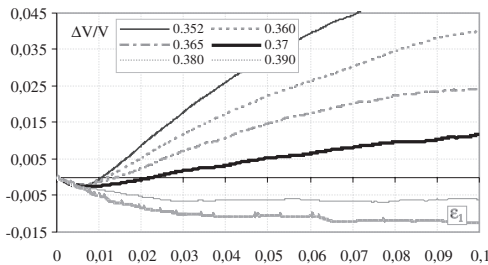


Figure 3. Numerical results of triaxial tests: volumetric strain versus axial strain for several porosities ($\sigma_3 = 110$ kPa).

porosities are simulated (the minimal porosity obtained is 0.352). We can note (Fig. 2 and Fig. 3) that the discrete model allows to describe in a very satisfactory way, the mechanical behaviour of granular material (contractancy, dilatancy, characteristic state).

2.3 Coupling finite elements/discrete elements

The finite elements included in the discrete element code are similar to those previously described. A thickness e has been given to them to prevent the interpenetration of the soil particles in contact with the two faces of one element. The geosynthetic sheets are defined by three nodes elements jointed together. To guarantee the regularity and the continuity of the contact surface between the triangular elements and the soil particles during the deformation of the sheet, cylinders and spheres of diameter e are placed respectively at the side and on the nodes of each triangle (Fig. 4).

So and thanks to the continuous surface of contact, the frictional forces are preserved when a soil element moves from a sheet element to another (what is not the case when a soil element loses the contact and comes into contact with another soil element).

Specific interaction laws are used to characterize the interface behaviour between the soil particles and the sheet elements. The main contact parameters are the normal rigidity, the tangential rigidity and the friction angle. Taking into account the absence of relative roughness between the sheet elements and the soil particles, the microscopic friction angle of contact correspond exactly to the macroscopic friction angle given by the model.

The three nodes sheets elements are treated like deformable discrete elements. For this reason, the behaviour of each sheet element is governed by the Newton's second law of motion applied to each node. For each cycle of calculation, the relative position between the sheet elements and the particles of the soil (sphere or assembly of spheres) are considered. The interpenetration of the elements the ones between the others allows the determination of the contact forces supported by each element, and by the way, for the three nodes of the sheet elements via the interpolation functions defined by the finite element model. The behav-

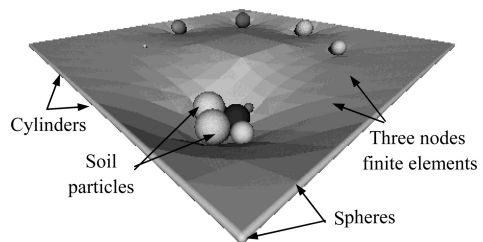


Figure 4. Interaction between soil and sheet elements.

four law of each element (defined by equation 1) allows, knowing nodal displacements of the element, the determination of the nodal forces resulting from the sheet deformation. Knowing the forces applied to each soil elements or each node of the sheet elements, it is possible thanks to the Newton's second law of motion to calculate its acceleration, its speed and the nodal displacement between two steps of successive times. Displacements of the elements the ones compared to the others initiate a new sequence of calculation.

Simple applications, carried out to validate the new numerical developments, show the efficiency of the new formulation for static or dynamic applications. We can note that the results of applications using sheet elements are rigorously the same to those obtained with the initial finite element software.

3 APPLICATIONS TO REINFORCED EMBANKMENTS

3.1 Description of the structure modeled

The geometry of the applications treated is given in figure 5 ($H = 1\text{ m}$, $s = 1.5\text{ m}$ and $a = 0.6\text{ m}$). For reasons of symmetry and to prevent long time of calculation, only one square mesh of the embankment will be modelled. The embankment is reinforced by a geosynthetic sheet armed in two orthogonal directions. The tensile rigidity J of the reinforcement, defined for a meter width ($T = J\varepsilon$), is in each direction 1000 kN/m . T , defined for a meter wide, is the tensile force acting in the armed direction and ε the corresponding strain.

The soil embankment is assumed to be a granular material issue from 7055 spherical discrete elements (diameter ranging between 0.04 m and 0.08 m) positioned in space with a random distribution at porosity of 0.36 . The macro mechanical behaviours of the assembly of particles are those given in figures 2 and 3.

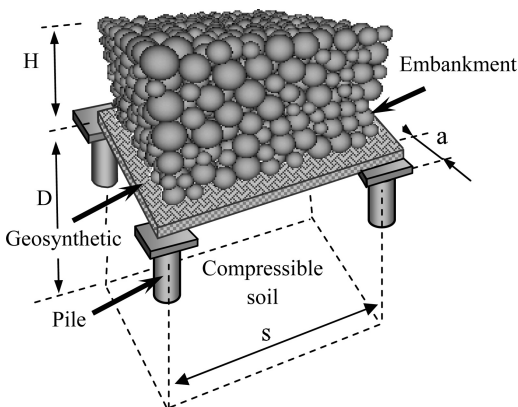


Figure 5. Geometry of the reinforced embankment.

The corresponding friction angle of the granular material simulated is in this case 30° and the young modulus is around 60 MPa . The particle density is 29.5 kN/m^3 , so the apparent density of the granular soil embankment is 18.88 kN/m^3 .

The geosynthetic sheet is modelled with 200 triangular finite elements. The angle of friction between the geosynthetic sheet and the soil particles is 25° .

The compressible subsoil under the geosynthetic sheet is assume to be very soft and is modelled by the Winkler's Spring Model (1867). The rigidity of the spring is given by $K = ES/D$ with E the oedometric modulus of the soft soil (depending of the simulation carried out, $E = 0\text{ MPa}$ or 0.5 MPa), D the thickness of the layer of the compressible soil ($D = 10\text{ m}$) and S the surface of influence of each spring.

The boundaries conditions are no vertical displacements of the nodes of the sheet over the pile caps and no horizontal displacements of the particles of soil at the edges of the model.

The mechanism studied is the deformation of the geosynthetic sheet and the movement in the soil embankment due to the weight of the soil particles.

3.2 Numerical results

The discrete elements approach coupling with the finite element model allows to determinate the interacting forces between each element, the displacements of the soil particles, the displacements of the nodes of the geosynthetic sheet and the tensile forces acting in each three nodes element in the two directions of reinforcement. The numerical simulations were carried out for comparison with $E = 0\text{ MPa}$ (Case A) and $E = 0.5\text{ MPa}$ (Case B).

The deformations of the geosynthetic sheet and the displacements of any particles of soil, resulting from

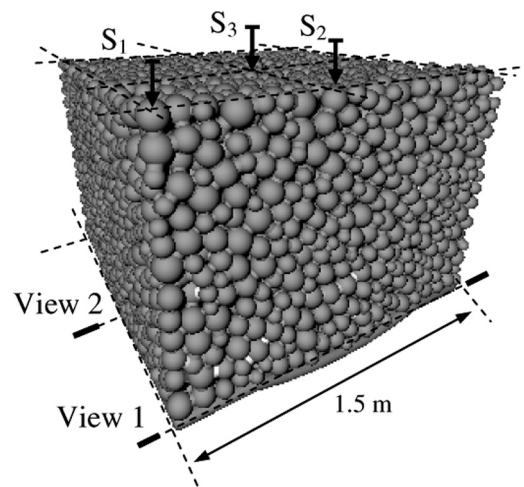


Figure 6. Global view of the modelled embankment.

the application of the weight embankment, are given in figure 6.

The numerical surface settlements obtained on the top of the embankment are reported in table 1 for points S_1 , S_2 and S_3 (Fig. 6). We can note that the surface settlements are not uniform; the great values being obtained at the centre of the square mesh (point S_3).

The curves shown in figure 7 give the vertical displacements of the geosynthetic sheet for two cross sections: between the piles (View 1) and at the axis of the square mesh of piles (View 2). The results are given with or without the action of the sub grade soil (Case A and Case B). Due to the membrane effect, the vertical displacements at the centre of the square mesh are bigger than those between the piles. The action of the sub grade soil is important especially in the great displacement areas. By comparison (Tab. 1 and Fig. 7) we can note that the vertical displacements at the centre of the square mesh are more important than those obtained at the surface level. This is due to the disorganization of the soil particles during the collapse of the embankment on the sheet (expansion and dilatancy).

In order to evaluate the mechanism of dilatancy, an expansion coefficient C_e was estimated and reported in table 2. C_e is defined as the ratio between the thickness of the soil embankment after the simulation and its initial thickness before simulation ($H = 1$ m). The

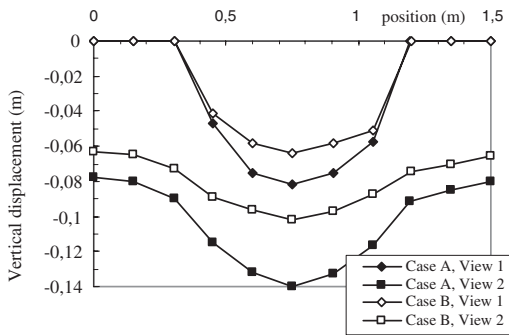


Figure 7. Vertical displacements of the geosynthetic sheet.

Table 1. Surface settlements at point S_1 , S_2 and S_3 .

	Point S_1 (m)	Point S_2 (m)	Point S_3 (m)
Case A	0.014	0.023	0.040
Case B	0.011	0.019	0.034

Table 2. Expansion coefficient of the soil embankment.

	Point S_2 (m)	Point S_3 (m)
Case A	1.059	1.1
Case B	1.045	1.068

expansion of the soil is correlated to the porosity of the soil. The differences of porosity obtained in different areas of the embankment justify the use of a discrete element model to characterize the behaviour of the soil embankment (the macroscopic behaviour of the discrete elements assembly depends directly of the porosity, Fig. 2 and Fig. 3).

The tensile forces acting in the armed directions of the geosynthetic in the two cross sections (View 1 and View 2) are given figure 8. We can note that the presence of the sub grade soil induce a decrease of the tensile forces in the geosynthetic.

In order to estimate the influence of each component on the behaviour of the embankment we have reported in table 3 the following ratios:

- The efficacy of the pile E_p : ratio between the vertical loads transmitted to the piles (by membrane and arching effects) and the weight of the soil embankment,
- The efficacy of the geosynthetic E_g : ratio between the vertical loads transmitted to the geosynthetic by membrane effect and the weight of the soil embankment,
- The efficacy of the supporting soil E_s : ratio between the vertical loads transmitted to the supporting soil and the weight of the soil embankment,
- The efficacy of the arching effect E_a : ($E_a = E_p - E_g$).

We can note (Tab. 3) that the parts of load transmitted by arching effect are in the two cases (Case A and Case B) very important (67%). We can conclude that for the simulated soil (assembly of great particles and for the chosen geometry) there is an important

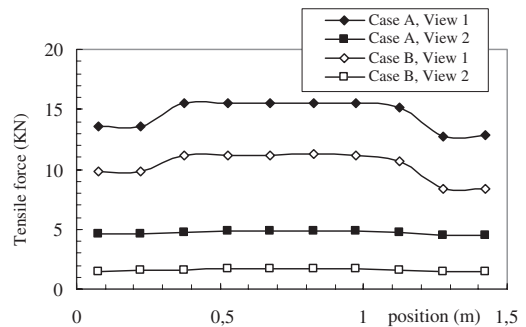


Figure 8. Tensile forces supported by the geosynthetic sheet.

Table 3. Efficacy of each component of the reinforced structure.

	E_p	E_a	E_g	E_s
Case A	100%	66%	34%	0%
Case B	88%	67%	21%	12%

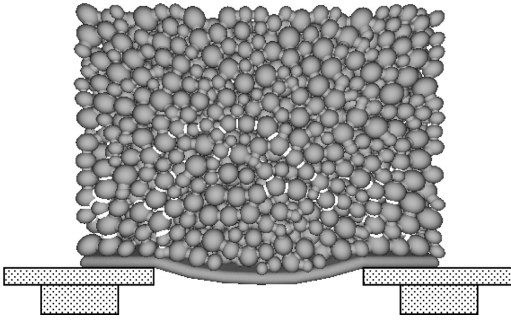


Figure 9. Arching effect in the soil embankment.

mechanism of transfer of load and probably formation of an arch in the soil embankment. In order to visualize this mechanism, we have drawn (Fig. 9) the network of contact forces acting between the particles of soil (the contact forces exceeding a limit value are drawn in white). As one can see on figure 9, we obtain an arch supported by the piles and acting in the soil embankment.

4 CONCLUSION

This model, coupling finite element method and discrete element method, let us think that it is a good way to simulate the behaviour of an embankment reinforced by piles and geosynthetics. The coupling finite elements/discrete elements makes it possible, in this case, to use the advantages of each method: a continuous model to describe the fibrous structure of the geosynthetic sheet and its interaction with the soil, and a discrete model to describe the behaviour of the granular soil. As shown, the main interest of the coupling MEF/MED is to take into account the membrane behaviour of the sheet and the mechanism of transfer of load into the soil embankment. However, a particular attention must be paid to the determination of the micro-mechanical parameters of contact to insert into the model. Moreover, a specific procedure of calculation must be carried out to place the particles of soil at a given initial porosity.

For a better understanding of the mechanisms involved in embankments built on soft soil and

reinforced by piles and geosynthetic, additional modelling works need to be carried out.

In particular, complementary studies are needed to confirm the first results obtained, using clusters (rigid assembly of particles), various granular distributions of particles, a great number of particles for modelling the soil, several geometries of networks of piles and various types of reinforcement. This work, performed for frictional granular soil, can be extending to cohesive material.

The results of the numerical model will be confronted with experimental results obtained on full-scale instrumented experiments (Villard et al., 2004; Chew et al., 2004). These works can be concluding by the realization of design abacus or by the establishment of analytical design methods.

REFERENCES

- Chew, S.H., Phonn, H.L., Loke, K.H., Lim, L.K., Le Hello, B. & Villard, P. 2004. Geotextile reinforced piled embankment – full scale model tests. *3rd Asian Regional Conference on geosynthetics*, GeoAsia 2004 (Now and Future of Geosynthetics in Civil Engineering), Seoul, Korea, Editors: J.B. Shim, C. Yoo and H.-Y. Jeon, June 21–23 2004, pp. 661–668.
- Donzé, F.V. & Magnier, S.-A. 1997. Spherical Discrete Element Code. In: *Discrete Element Project Report no. 2. GEOTOP*, Université du Québec à Montréal.
- Gourc, J.P. & Villard, P. 2000. Reinforcement by Membrane Effect: Application to Embankments on Soil Liable to Subsidence. Keynote lecture, Geosynthetics ASIA 2000, *Proceedings of the 2nd Asian Geosynthetics Conference*, Kuala Lumpur, Malaysia, 29–31 May 2000, Vol. 1, pp. 55–72.
- Villard, P. & Giraud, H. 1998. Three-Dimensional modelling of the behaviour of geotextile sheets as membrane. *Textile Research Journal*, Vol. 68, N° 11, November 1998, pp. 797–806.
- Villard, P., Gourc, J.P. & Giraud, H. 2000. A geosynthetic reinforcement solution to prevent the formation of localized sinkholes. *Canadian Geotechnical Journal*, Vol. 37, N° 5, October 2000, pp. 987–999.
- Villard, P., Le Hello, B., Nancey, A., Chew, S.H. & Loke, K.H. 2004. Use of high strength geotextiles over piles – results from a full scale test. *Proceedings of the 3rd European Geosynthetics Conference*, Munich, Germany, 01–04 March 2004, Vol. 1, pp. 295–298.

D.E.M. modeling in impact condition of geocomposite cells dedicated to rockfall protection barriers

D. Bertrand

Cemagref & Lirigm-UJF Laboratories, Grenoble, France

Ph. Gotteland

Lirigm-UJF, Grenoble, France

S. Lambert & F. Nicot

Cemagref Laboratory, Grenoble, France

ABSTRACT: The study is related to rockfall protection barriers built with assembly of cells. These kind of structures is model by a multi-scales approach where one distinguishes the cell scale and the global barrier scale. This paper is dedicated to the numerical modeling of cells filled with granular matter surrounded by a wire mesh. The medium is described by the distinct element method (D.E.M.) well suited to simulate granular matter. The calibration and the validation of the model are done by comparing numerical simulation results to experimental data coming from mechanical tests carried out on cubic like cells. These tests were performed in quasi-static condition and dynamic condition of impact. Numerical results are in good agreement with experiments.

1 INTRODUCTION

In geotechnics, geocomposite cells filled with natural materials are often used to build cellular structure coming from civil engineering. A cell is generally a wire netting cage filled with site materials (e.g. gravel, stones, sand or adapted material such as a composite material, including or not an appropriate geosynthetic sack). Cells are commonly called gabions and this technique is used for the construction of retaining walls, noise protection structures, or hydraulic erosion protection. Another use of this kind of structures is to protect people against rockfalls. The paper is dedicated to the numerical modeling of cells filled with stones (Fig. 1).

In order to explore the mechanical response of this mechanical system under quasi static and dynamics loadings, D.E.M. numerical modeling of the cell is presented and results coming from quasi-static compression tests and impact tests are exhibited. Different kinds of loading paths are considered and compared to several experiments performed in the same loading conditions.

2 NUMERICAL MODELING OF A CELL

A cell is composed of two mechanical systems. The first one is the filling material, which is composed of angular limestone blocks, and the second one is a double

twisted hexagonal mesh surrounding the granular material. In order to simulate the mechanical behavior of a cell, the model has to take into account both the two systems. Moreover, considering the granular nature of



Figure 1. Geocomposite cell filled with natural stones used for civil engineering structures.

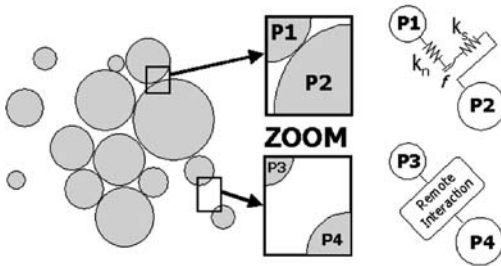


Figure 2. Assembly of distinct elements. Contact model are used to simulate the interactions between blocks of the cell and remote interactions are used to model the wire mesh.

the filling material, the distinct element method had been adopted for the modeling.

2.1 Distinct element method (D.E.M.)

The distinct element method is a numerical model to describe the mechanical behavior of discontinuous bodies (Cundall, 1979). The method is based on the use of an explicit scheme (see for instance Pöschel, 2005) that monitors the particle interaction through contacts and remote interactions (Fig. 2). It calculates the particle motion through Newton's second law. Calculations alternate between the application of Newton's law to the particle motions and a force-displacement law coming from contact and remote interactions model where local parameters (microparameters) of the model appear. With a D.E.M. approach, the medium is described at a microscopic scale, which means the element scale.

In our case, on the one hand, the interactions between blocks included in the cell are computed by a specific contact model which account for the fragmentation of the elements (Bertrand, 2005b) and on the other hand remote interactions are used to model the wire mesh of the metallic cage surrounding the stones.

Thanks to this numerical method, large displacements between elements are easy to simulate. This method is very well suited to model a geocomposite cell where important strains may occur during a loading test. All the simulations have been performed in three dimensions with the software Particle Flow Code (Itasca, 2003).

2.2 Wire mesh modeling

The wire netting box is described by a set of spherical particles. The particles are located at the physical nodes of the mesh, i.e. at the wire intersection (Fig. 3a). Forces accounting for the mechanical behavior of the wires are applied to the wires netting particles. The mechanical behavior of the wires is modeled by an elasto-plastic with failure relation. Experimental tensile tests on single wires were carried out to calibrate the parameters of the elasto-plastic relation (Bertrand,

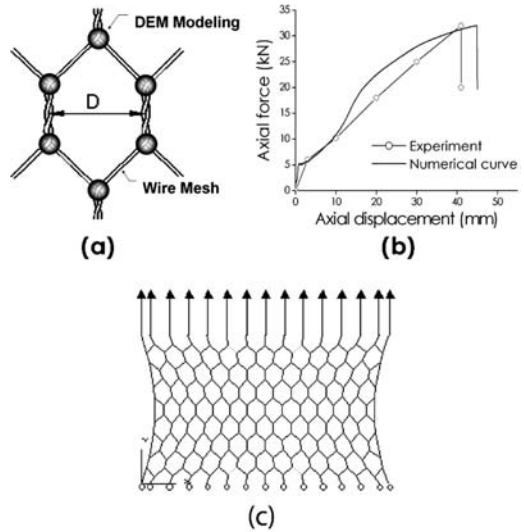


Figure 3. (a) D.E.M. modeling of the wire mesh. (b) Validation of the numerical model from macroscopic test. (c) Macro tensile test of the wire mesh (1000 mm by 500 mm).

2005b). In order to validate the model, a set of numerical simulations were performed and compared to experimental tensile tests (Bertrand, 2006a). These ones were carried out on a wire mesh sheet of 1000 mm by 500 mm and a good agreement with numerical results and experimental data was found (Fig. 3b).

For the generation of a wire mesh, the positioning of the particles in space is carried out one particle at a time. Each case of study, implying a different geometry of wire mesh, requires a suitable algorithm.

In the case of a two-dimensional wire mesh sheet, the positioning of the particles remains not too difficult. The repetitive hexagonal shape of the mesh led to the development of algorithms not too long and easy to use.

For a wire netting cage, the process is more complicated. It takes as a starting point the real process of construction. The particles are initially positioned in two dimensions in a single plan, for instance (xOy). Thus, each faces of the wire netting cage is defined. Then, the rotation and the translation of each panel are carried out (Fig. 4) in order to build the 3D cage. Afterward, adjoining particles are detected and the cage is ready to be loaded.

2.3 Filling material modeling

Cells are filled with crushed blocks coming from limestone quarry. The forms of the elements are irregular and angular. Preliminary studies showed that the shape of the element has a significant influence on the macroscopic behavior of the cell (Bertrand, 2005a). In order to simulate the mechanical phenomena

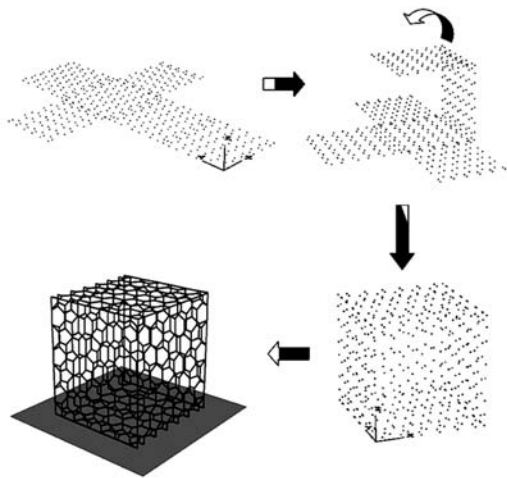


Figure 4. Wire mesh particle positioning in three dimensions.

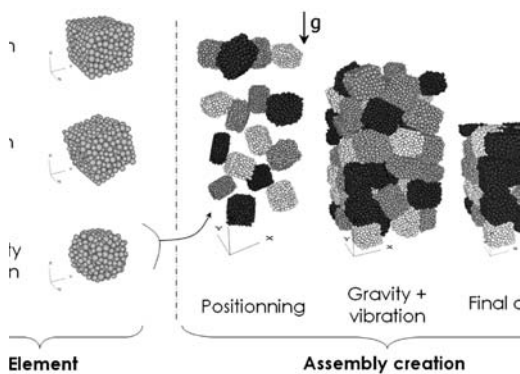


Figure 5. Creation of an element and after elements positioning into the cell.

developing during the cell loading, it is necessary to take into account the shape of the element. The technique used to model the non spherical shape of particle consists in bonding several spherical particles each others (see for instance Sallam, 2004).

The description of the angular shapes of the elements requires two stages to create the assembly of grains (Bertrand, 2006a): the generation of the element and thereafter their association (Fig. 5).

When a cubic-like element has been created, two rotations along two different axes are applied on it and the spherical particles lying on the edges are removed in the aim to reduce the element angularity.

All the numerical blocks are placed on the upper part of the cell and the application of the gravity allows to put them into the cell. As soon as a mechanical state of balance is reached, a vibration of the elements is carried

out in order to decrease the initial porosity. Finally, all the particles lying over the cell height are deleted.

Thanks to this approach, it is possible to accurately reproduce the gradation curve and the porosity of the experimental cells (Bertrand, 2004). After their generation, the filling material and the wire mesh are added together. At this stage, the cell is ready to undergo loading.

Due to the granular nature of the filling material, the variability of the mechanical response of the cells is significant. In order to describe the mechanical behavior from an average point of view, ten different cells were numerically created and tested systematically.

3 EXPERIMENTS

The lack of information concerning the mechanical behavior of cells under quasi-static and dynamic loadings led to develop experimental tests. Two types of tests were carried out in confined and unconfined conditions. In the first case, the lateral strains of the vertical faces of the cell were not allowed during the loading. In the second case, the vertical faces could move freely. The cubic-like cells were 500 mm in height.

During quasi-static compression tests, the axial force applied to the upper side of the cell was recorded in terms of axial displacement. The compression velocity was constant. Four tests were performed in unconfined condition and two in confined condition (Lambert, 2004).

Impact tests were also carried out. The experimental device was composed of a spherical projectile and a concrete slab where the cell was placed before the impact (Fig. 6). The diameter of the spherical block was 530 mm and its weight was 250 kg. In the center of the sphere a triaxial accelerometer recorded the three components of the acceleration. Thus, it was possible to deduce the force applied to the block during the shock (Lambert, 2006) by multiplying the acceleration signal per the block mass.

4 NUMERICAL RESULTS

All these experimental tests were simulated numerically. The fragmentation of the elements was taken into account by a specific contact model in the normal direction (Bertrand, 2005b) which assumes an elasto-plastic behavior at the contact points in the normal direction of the contact plan.

The results of simulation are expressed as average out of ten numerical tests carried out under the same loading conditions, but considering each time a granular medium (cell) without the same fabric.

Only the tests of unconfined compression were not averaged. Because of the high variability of the results,

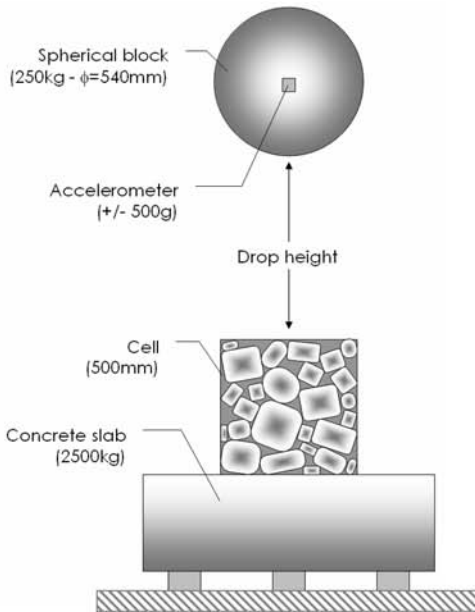


Figure 6. Experimental device used for impact on cells in confined and unconfined conditions.

it was impossible to identify an average tendency of mechanical behavior.

The calibration of the numerical microparameters was performed with the confined compression tests (Fig. 7). Then, the model was validated by unconfined

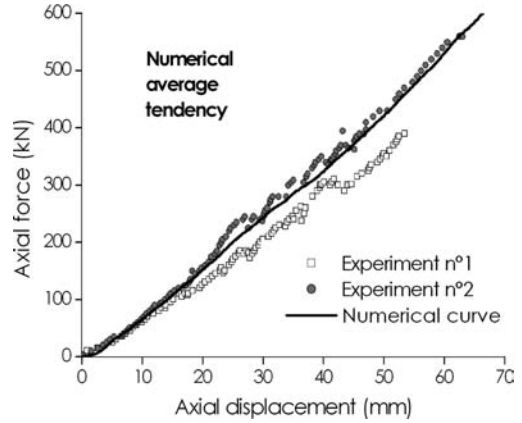


Figure 7. Confined compression tests. Comparison between the average tendency of ten numerical simulations (continuous curve) and experimental data.

compression tests and impact tests (confined and unconfined).

In the case of unconfined compressions, the general trends of evolution of the axial force in terms of axial displacement are correctly reproduced by the numerical model (Fig. 8). For axial displacement under 20–30 mm, a regular increase of the axial force is observed. Afterward, the axial force falls suddenly after having reached a maximum. Then the axial force shows several peaks followed by abrupt decreases.

One can explain this mechanism by the collapse of chains of force within the granular skeleton. A succession of grains in contact, which carry high contact forces, suddenly collapse by motion or failure of elements. This phenomenon generates a reorganization of the elements which causes dynamics crisis and a brutal drop of the axial force applied to the loading plate.

For each cell, the orders of magnitude are the same ones but each cell has its own mechanical response. The mechanical behavior of a cell is strongly related to the initial arrangement of the elements. This is all the more marked when the elements have the possibility to move easily (unconfined condition). The dispersion of the experimental data is also observed in simulations. As it is observed for the real cells, the global strain of numerical cells is strongly influenced by the initial fabric of the assembly (Fig. 9).

Thereafter, the ability of the numerical model to reproduce the mechanical behavior of a cell under dynamic conditions was explored (Fig 10). The same parameters determined in the quasi-static condition were used during dynamics simulations of impact.

The physical characteristics of the impacting block (diameter and mass) and its initial impact velocity were numerically reproduced. The impact velocity was 8 m/s which correspond to a kinetic energy of 8 kJ.

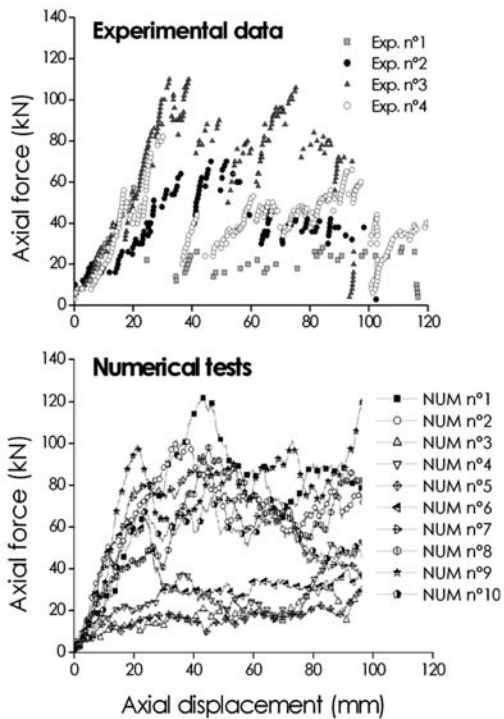


Figure 8. Unconfined compression tests. Comparison between experimental data (Exp. n°1 to n°4) and ten simulations (NUM n°1 to n°10).

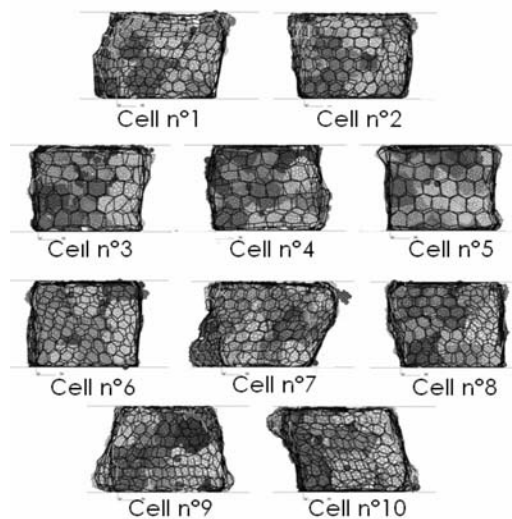


Figure 9. Unconfined compression tests. Shapes of ten numerical cells for 16% of axial strain.

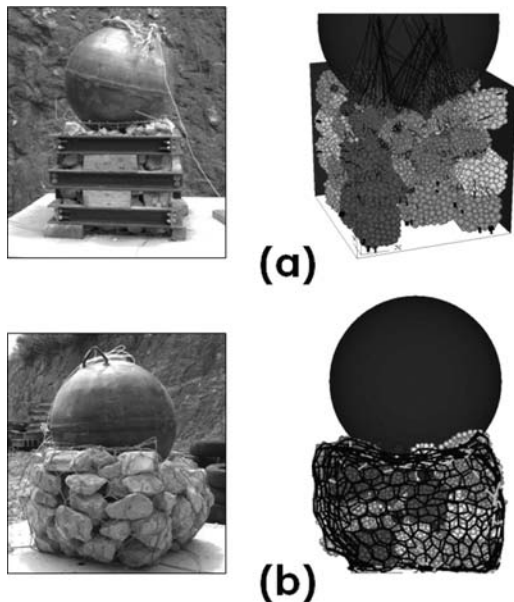


Figure 10. Visual comparison between simulations and experiments. (a) Confined impact and (b) Unconfined impact.

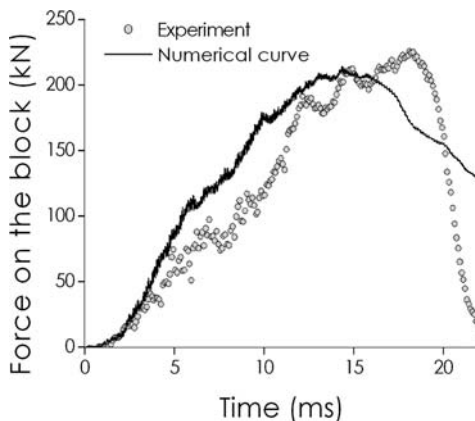


Figure 11. Impact loading in confined condition. Comparison between numerical results (averaged tendency) with an experiment curve.

Figures 11 and 12 show a comparison between experiments and simulations. The numerical curves were averaged out of ten impact tests.

The comparison between experimental and numerical curves shows that a satisfying fit was obtained. The model correctly reproduces the experimental tests of impact even if the boundary conditions are changed from confined to unconfined. The characteristic time of the phenomena is well reproduced. The force magnitude

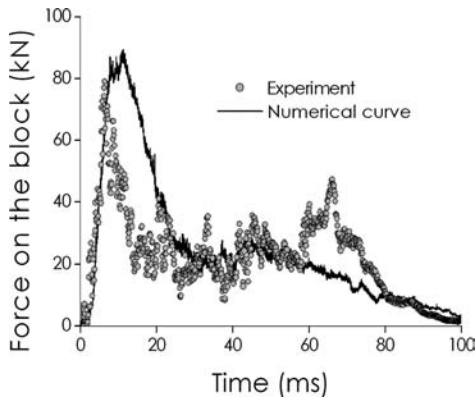


Figure 12. Impact loading in unconfined condition. Comparison between numerical results (averaged tendency) with an experiment curve.

upon the block, i.e. the peak strength and post peak oscillations (in unconfined condition), is also in good agreement with experimental data.

Although the mechanical behavior of stones is strain rate dependant (see for instance Lajtai, 1991), one note that the set of parameters calibrated under quasi-static loading makes it possible to accurately describe the macroscopic behavior of the cell in dynamic condition.

The mechanical response of the system is likely not caused by a material effect associated to the stones mechanical properties. Thus, at the cell scale, the strain rate effect is mainly due to the inertia of the elements, naturally taken into account by the model.

5 CONCLUSION

This study take part of a project dedicated to develop an innovative technology for rockfall protection structures. The structures considered are built with cells assembly. The cells which composed the cellular structure are often filled with a granular material which could undergo large deformations.

This article focuses on the numerical modeling of a cell and the validation of the cell model proposed by comparison with experimental data. Throughout this paper, cells were composed of a wire mesh box wrapping an assembly of limestone blocks, along confined or unconfined loading paths.

First of all, the numerical model of the double twisted hexagonal wire mesh was undertaken. The physical geometry of the cell cage provides the necessary data to determine all the positions of the particles. Elasto-plastic interaction models with strain hardening were developed in order to take into account the mechanical features of the wire netting metal. The calibration and the validation of the model were carried

out by comparing experimental and numerical results coming from tensile tests.

Thereafter, the cell modeling was exposed. The physical characteristics of the filling material were reproduced in terms of gradation curve and porosity. Due to the variability of the experimental data, ten cells were numerically created in order to obtain an average mechanical response of the cell. The calibration of the contact parameters was difficult because of the variability of the results from one cell to another, inherent to granular medium. The contact parameters were chosen to fit experimental data coming from the confined compression tests.

The validation of the cell model was confirmed by simulating the other experimental tests. The numerical results obtained showed a good agreement with the experimental data in confined or unconfined condition and for quasi-static and dynamics loadings. The proposed cell model could accurately reproduce the mechanical behavior of a geocomposite cell even if boundary conditions and loading condition are changed.

In the near future, the simulation of other types of mechanical tests, difficult to carried out form an experimental point of view, is plan. For instance, triaxial compression tests would allow studying the effect of an eventual containment on the cell response. It makes it possible to better understand the mechanical behavior of a cell within a cellular structure.

Finally, results will be used to improve the numerical model of the structure (Bertrand, 2006b).

ACKNOWLEDGMENTS

This research was completed within the framework of the research network RNVO: Natural Hazards and Vulnerability of Structures. This network is funded by the French Ministry of Research and combines different laboratories in Rhône-Alpes region and offers a wide spectrum of multidisciplinary competencies on natural and technological hazards. This project was financed by France Maccaferri SA, part of the Maccaferri group and had the financial support of the PGRN (Pôle Grenoblois des Risques Naturels). We extend special thanks to all the members of the research group for the interest they have shown in this work.

REFERENCES

- Bertrand, D., Gotteland, P., Lambert, S., Nicot F., Derache, F. 2004. A multiscale mechanical modeling of unusual geocomposite material for rockfall impact. *Proc. 9th Int. Congr. on NUMerical MOdel in Geomechanics Rock Mech*, Ottawa (Canada), p. 709–716.
- Bertrand, D., Gotteland, P., Nicot F. 2005a. D.E.M. modeling of natural stones assembly confined in wire mesh, *Powders & Grains 2005*, Stuttgart (Germany), p. 681–685.

- Bertrand, D., Nicot, F., Gotteland, P., Lambert, S. 2005b. Modeling a geo-composite cell using discrete analysis, *Computer and Geotechnics* 32(8): 564–577.
- Bertrand, D. 2006a. *Modélisation du comportement mécanique d'une structure cellulaire de protection soumise à une sollicitation dynamique localisée – Application aux structures de protection contre les éboulements rocheux (in french)*. Thèse de doctorat, Université Joseph Fourier.
- Bertrand, D., Gotteland, Ph., Lambert, S., Nicot, F., Derache, F. 2006b. Multi-scale modeling of cellular geo-composite structure under localized impact. *Revue Européenne de génie civil*, in press.
- Cundall, P.A., and Strack, O.D.L. 1979. A discrete numerical modeling method for granular assemblies, *Geotechnique*, 29: 47–65.
- Lajtai, E., Duncan, E., Carter, B. 1991. The effect of strain rate on rock strength. *Rock mechanics and rock engineering*. 24: 99–109.
- Lambert, S., Gotteland, P., Ple, O., Bertrand, D., Nicot, F. 2004 Modélisation du comportement mécanique de cellules de matériaux confinés, *Journée Nationale de Géotechnique et de Géologie*, Lille (France), p.219–226.
- Lambert, S., Gotteland, P., Bertrand, D., Nicot, F. 2006. Modélisation du comportement mécanique de cellules de matériaux confinés. *Journée Nationale de Géotechnique et de Géologie*, Lyon (France).
- Nicot, F. 1999. Etude du comportement mécanique des ouvrages souples de protection contre les éboulements rocheux. Thèse de doctorat, Ecole Centrale de Lyon.
- Itasca consulting group, Inc. 2003. Particles Flow Code in three dimensions – version 3.0, “User’s guide”, “FISH in PFC” and “Theory and Background”, Minneapolis : Itasca.
- Pöschel, T., Schwager T. 2005. Computational granular dynamics – Models and algorithms. City: Berlin. Springer Eds.
- Sallam, A., Ashmawy, A., Runkles, B. 2004. Experimental validation of modeling irregular particle shapes using dem. *Proc. of the second Inter. PFC Symposium : Numerical modeling in Micromechanics via particle methods*, Kyoto (Japan), p. 363–372.

Experimental observations and theoretical interpretation of the mechanical behaviour of a grouted pyroclastic silty sand

A. Flora & S. Lirer

University of Napoli 'FedericoII', Italy

A. Amorosi & G. Elia

Technical University of Bari, Italy

ABSTRACT: This paper deals with the mechanical characterisation of an artificially structured material, obtained by grouting a low permeability pyroclastic silty sand (pozzolana) with a sodium silicate solution. Notwithstanding the low permeability of pozzolana ($k_{sat} = 10^{-6} \div 10^{-7}$ m/sec), a preliminary set of laboratory tests has shown that the very diluted silicate grouts adopted are effective in enhancing its mechanical behaviour. The paper refers on a detailed experimental programme carried out to investigate the stress-strain behaviour of the grouted soil in order to outline its peculiar mechanical properties. With this aim, oedometer, CID and CIU triaxial tests were carried out. The whole set of results shows the typical behaviour of a structured material, with a brittle behaviour at low stress levels, and structural degradation at higher stresses. A first attempt to explain the experimental observations is proposed in the light of the classical *Critical State Soil Mechanics* theory and some preliminary conclusions are discussed.

1 INTRODUCTION

In engineering practice it is often necessary to find remedial measures to geotechnical problems which may cause some hazard into urban areas. In such cases, ground improvement techniques like grouting may be much more convenient and with a lower impact than more traditional approaches. The different grouting techniques (permeation grouting, compaction grouting, jet-grouting, ...) are classified according to the type of grout and the injection method adopted, being the increase in soil strength the first goal of all of them.

In permeation grouting, for instance, the grout (solution, suspension or emulsion) is usually injected into the voids among soil particles with a pressure low enough to prevent soil displacement or hydro fracturing. For such a reason, groutability of a soil is strictly connected to its permeability, being the soil shear strength also important to set a proper injection pressure. Grouts are rather complex fluids and can have a wide range of rheological properties, initial viscosity, setting time, final strength, stability and durability. All the above properties have to be taken into account to plan the injection process, which must be long enough to allow permeation, but cannot exceed the time needed to start hardening (gel time).

There has been an extensive use of permeation grouting in time, and many successful applications

are shown in literature with different kinds of grouts, especially in sands and gravels which, because of their high or very high permeability, exhibit minor problems during the permeation process. Due to the continuous technological progress, applications to lower permeability soils have been attempted in the last two decades by using chemical solutions with lower and lower viscosities.

One of these unusual applications has been successfully tested at the University of Napoli Federico II, injecting very diluted sodium silicate based solutions into a fine grained, low permeability pyroclastic silty sand (*pozzolana*), which constitutes a relevant part of Napoli subsoil. Pozzolana is a well graded cohesionless silty sand whose mechanical properties strongly depend on the degree of saturation (usually lower than one on site). Its behaviour has been carefully investigated in situ and in laboratory in the past, and the main features of its mechanical behaviour are nowadays fairly well known (Pellegrino, 1967; Scotto di Santolo, 2000). The range of typical values of physical and mechanical properties of unsaturated pozzolana are summarized in Table 1. The research has been carried out to verify the capability of permeation grouting to give some cohesion to pozzolana, thus mitigating the hazard caused by the well known volumetric collapse and loss of shear strength that such material shows upon wetting.

Table 1. Ranges of typical values of the main physical and mechanical properties of pozzolana.

G_s	e	w (%)	S	k (m/sec)	φ (°)
2.2–25	1.2–1.5	15–30	0.2–0.6	10^{-6} – 10^{-7}	35–38

The grouts based on sodium silicate solutions are widely used in practice, and both in situ and laboratory investigations on their effectiveness are reported in literature (Littlejohn, 1992, Jefferies, 2003). However, the typical viscosity of these grouts would make them unsuited for low permeability soils like pozzolana. This limitation could be overcome by using a very low sodium silicate content and keeping the initial viscosity as low as that of water (≈ 1 cps) (Lirer *et al.*, 2004). Grouting of pozzolana has proved to be successful because of the chemical activity of pozzolana particles, and could be assessed by a number of laboratory tests.

In particular, carrying out a large number of simple unconfined compression tests it has been possible to highlight the influence of curing time, moisture condition and amount of retained grout. A detailed description of the procedures adopted to analyse grouting effectiveness from a mechanical and chemical point of view can be found elsewhere (Lirer *et al.*, 2004). The laboratory investigation has then been focused on a more detailed analysis of the stress-strain behaviour of the material treated with the best suited grout. To this aim, a large testing programme was planned: this paper refers on the experimental results obtained and on the indications gained for an accurate mechanical characterization of the grouted pozzolana.

The results obtained from oedometric and isotropic compression tests as well as from triaxial tests, clearly indicate that grouted pozzolana specimens show a complex mechanical behaviour due to the new artificial structure induced by grouting.

For natural soil, structure depends on the physical and chemical conditions applied during deposition, consolidation, ageing and unloading (Mitchell, 1976). Many works in literature have given a contribution to the understanding of the role of structure (term used to combine fabric and bonding) on the overall mechanical soil behaviour.

Following this approach, in this paper the influence of such artificial structure on the behaviour of grouted pozzolana has been carefully analysed, using as a reference state the behaviour of the untreated natural pozzolana.

2 THE USE OF SODIUM SILICATE SOLUTIONS AS CHEMICAL GROUTS

Sodium silicates are highly alkaline viscous solution $[(\text{SiO}_2)_n\text{n}(\text{H}_2\text{O})]$. They are able to improve soil

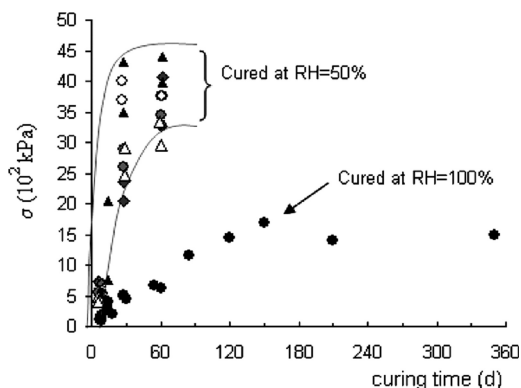


Figure 1. Unconfined compression tests on grouted pozzolana specimens (Lirer *et al.*, 2004).

mechanical properties by becoming a solid glassy reticulated material $[(\text{SiO}_2)_n]$. The network of glassy material fills part of the intergranular voids (*physical improvement*). The behaviour of sodium silicates is basically well understood, and there is a large number of paper concentrating on the influence of the main factors affecting it (e.g. Sheikh *et al.*, 1992): silicate/soda relative percentage, kind of additives, their relative and absolute percentages, as well as curing time and temperature. Published data indicate that the effectiveness of grouting depends essentially on retained grout content, usually agreeing on the fact that grouting increases only the cohesive component of the shear strength (Littlejohn, 1992).

The sodium silicate solution used in this study (PROCHIN ITALIA) has a high silica to soda weight ratio ($\text{SiO}_2/\text{Na}_2\text{O} = 3.5$) and a density of 1.36 g/ml. An inorganic additive (sodium bicarbonate water solution) has been used to trigger the condensation reaction; this choice allows to have the best possible performance in terms of durability of the grouted soil. Several grout solutions with different setting times have been analyzed, keeping in all cases the initial viscosity less than 1.8 cps, before finding the best possible combination of ingredients (Lirer *et al.*, 2004). In pozzolana, these solutions are also able to trigger chemical reactions among grains, thus adding a further positive effect (*chemical improvement*).

3 MECHANICAL BEHAVIOUR OF SILICATE GROUTED POZZOLANA

As previously mentioned, the basic features of the rheological and mechanical properties of grouted pozzolana have been initially analysed by means of unconfined compression tests. Details on these tests and on their interpretation are given in Lirer *et al.* (2004). As expected, these results (Fig. 1) indicate that the very

Table 2. Experimental testing programme.

Test	Specimen	n°	e_0	S
OED	natural	4	0.98–1.11	<1
	grouted	4	1.09–1.17	<1
ISO	natural	3	0.88–1.04	1
	grouted	5	1.09–1.14	1
CID	natural	—	—	—
	grouted	3	1.09–1.14	1
CIU	natural	3	0.88–1.04	1
	grouted	2	1.09–1.14	1

diluted silicate grouts adopted are effective in this case, improving the mechanical properties of pozzolana. The uniaxial strength of grouted pozzolana increases with increasing curing time and grout content. Furthermore, the measured uniaxial strength is larger for specimens cured at lower surrounding moisture conditions (relative humidity RH = 50%).

Testing programme. Once the general information on the overall behaviour of grouted pozzolana was known, a complementary testing programme has been carried out on natural (untreated) and grouted pozzolana specimens (Table 2) by means of oedometer tests and high pressure triaxial tests. All natural and grouted specimens have been reconstituted in laboratory. Grouted specimens have been obtained by stirring together grout and pozzolana: the resulting slurry has been poured to cure into plastic moulds. With this procedure, specimens fully saturated by the grout (best possible effect) have been prepared. All specimens have been cured at controlled moisture condition (relative humidity RH ≈ 100%) for about three months: from the results shown in Figure 1 it is evident that such curing time is long enough to allow the complete development of the grout hardening process.

In Table 2 the experimental programme is summarised, highlighting the kind of test (OED = oedometer, ISO = isotropic and CID/CIU = triaxial test) and the main specimens properties.

On site, pozzolana is usually unsaturated and it is nowadays well known that this partial saturation plays a major role on its mechanical behaviour (Nicotera, 1988; Scotto di Santolo, 2000). However, the testing programme is composed by tests performed on both saturated and unsaturated soil. In particular, the oedometric tests have been carried out on unsaturated specimens while for the other tests in which volume change measurements are needed, the specimens have been saturated prior to testing. Due to the very low permeability of the grouted specimens, they have been saturated using a mixed procedure, first boiling and then filtrating them (Maccarini, 1987).

One-dimensional and isotropic compression testing. Oedometer tests have been carried out up to a maximum vertical effective stress of about 20 MPa.

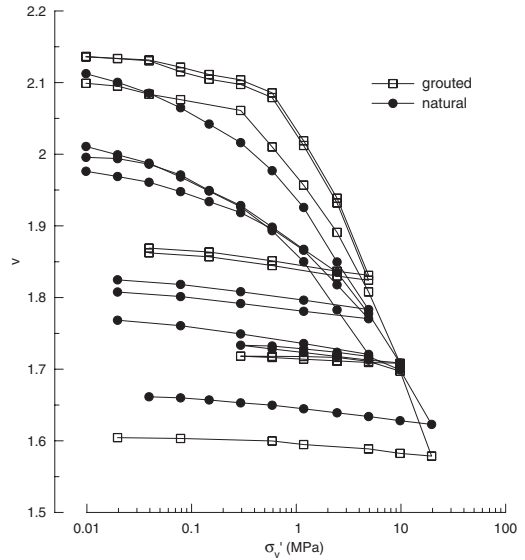


Figure 2. One-dimensional compression behaviour of natural and grouted pozzolana specimens ($S < 1$).

It is well known that for granular materials (e.g. Liu & Carter, 1998), it is not possible to detect a unique virgin compression curve: different void ratios are possible at any given stress state for a normally consolidated material. The reason for this is that the compressibility of these materials generally depends on micro-structural features and different initial structures are possible in relation to different depositional processes. Natural pozzolana fully behaves like a granular material and, as a consequence, a large influence of the initial void index must be expected on its mechanical behaviour. Furthermore, in the case of partial saturation, structure also depends on soil suction s ($s = u_a - u_w$, where u_a and u_w are air and water pressures, respectively), being s a function of the initial water content w ($s = s(w)$).

In Figure 2 the oedometer test results on natural and grouted pozzolana specimens are shown in the v – $\log(\sigma'_v)$ plane. Natural pozzolana specimens show gently curving slopes, which tend to converge but do not identify a unique normal compression line (NCL). On the contrary, the results of all tests carried out on grouted pozzolana show a much stiffer response up to the yield stress (about 0.3 MPa); beyond this point, the compressibility of the grouted material becomes very large. Differently from the natural pozzolana, in this case a unique curve can be identified both before and after the yield stress has been reached.

Such features are typical of soft rocks (Aversa, 1991) and structured clays (Kavvas et al., 1998). In the case of grouted pozzolana, the structure is artificially induced by grouting, but its role is similarly relevant.

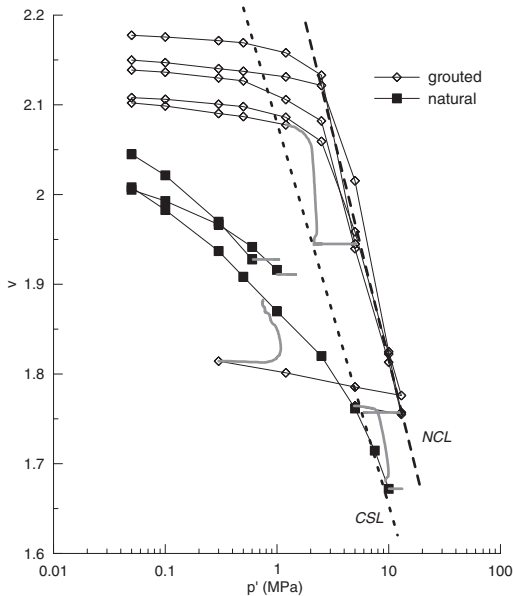


Figure 3. Isotropic compression and triaxial behaviour of natural and grouted pozzolana specimens ($S = 1$).

After the yield stress is reached, structure is progressively damaged and, ideally, the soil behaviour should tend towards the one exhibited by the natural specimens. Test results are in good agreement with this hypothesis.

During oedometer tests both deviatoric and isotropic effective stress components change, inducing the accumulation of the corresponding deviatoric and volumetric plastic strain. It is very likely that both these components play a role in the overall mechanical behaviour of the material. In order to highlight this aspect and carefully study the mechanics of the grouted material, isotropic compression tests followed by subsequent shearing stages have been performed.

In order to explore the material behaviour in a wide range of stresses, the response of both grouted and natural soil has been observed compressing the specimens up to relatively high level of stresses (maximum value of about 13 MPa) prior to shearing. In such tests all the specimens have been saturated before testing, in order to allow the measure of volume changes by means of standard volume gauges.

In Figure 3 the results of the isotropic compression tests are plotted in the v - $\log(p')$ plane. The figure also shows the volumetric response as observed in the subsequent triaxial shearing stages, discussed in detail in the next section. The differences between natural and grouted specimens are even more striking than in the oedometric tests: the curves pertaining to the grouted specimens, which are all characterised by

Table 3. Triaxial testing programme.

Test	Spec.	v_0	p' (MPa)	OCR	q/p'_{peak}
1 – CID	grouted	1.81	0.3	43	2.16
2 – CID	grouted	2.07	1.2	2.1	1.4
3 – CID	grouted	1.76	5	2.6	1.5
4 – CIU	grouted	2.17	5	1	1.65
5 – CIU	grouted	1.76	13	1	1.5
6 – CIU	natural	1.93	0.6	1	1.5
7 – CIU	natural	1.91	1.1	1	1.64
8 – CIU	natural	1.67	10	1	1.02

a similar initial void ratio, almost completely overlap the ones relative to the natural soil. A yield stress of 2.5 MPa can clearly be identified in this case. Beyond this value, a sharp change in compressibility is observed, which indicates the ongoing of isotropic destructuration. The three isotropic compression curves of the natural pozzolana start from different void ratios but show similar trends. No unique normal compression line can be identified for them up to the highest stress level applied, consistently with standard behaviour of granular materials. From a constitutive point of view, this peculiarity adds a difficulty in identifying a reference de-structured behaviour for the artificially bonded pozzolana.

Triaxial testing. Eight triaxial tests have been carried out: five on grouted specimens (three CID and two CIU), and three CIU tests on natural specimens (Table 3). The wide range of confining pressures applied prior to shearing ($0.05 \text{ MPa} < p' < 13 \text{ MPa}$) allows to test specimens which have experienced different degrees of structural degradation induced by isotropic compression. In particular, one test has been carried out applying a confining stress lower than the yield value, while in all the other tests a confining stress well above yield has been imposed.

The CID tests results are reported in Figure 4a in terms of deviatoric stress (q) and volumetric strains (ϵ_v) against axial strains (ϵ_a). Large dilation and a brittle stress-strain behaviour is only observed in the case of the very overconsolidated specimen (test with a confining pressure of 0.3 MPa), while the other two tests show a contractant response.

A similar behaviour can be observed for the CIU test results reported in Figure 4b: in this case pore pressure (u) is plotted against axial strains. Both tests show an increase in excess pore water pressure with axial strain, consistently with the contractant behaviour exhibited in the corresponding drained tests.

Three CIU tests have been carried out on natural specimens (Fig. 4c). Two tests have been performed applying a confining pressure lower or equal to 1 MPa, while the third one has been subjected to a cell pressure of 10 MPa prior to shearing. The tests at low cell pressures show a similar value of the deviatoric stress

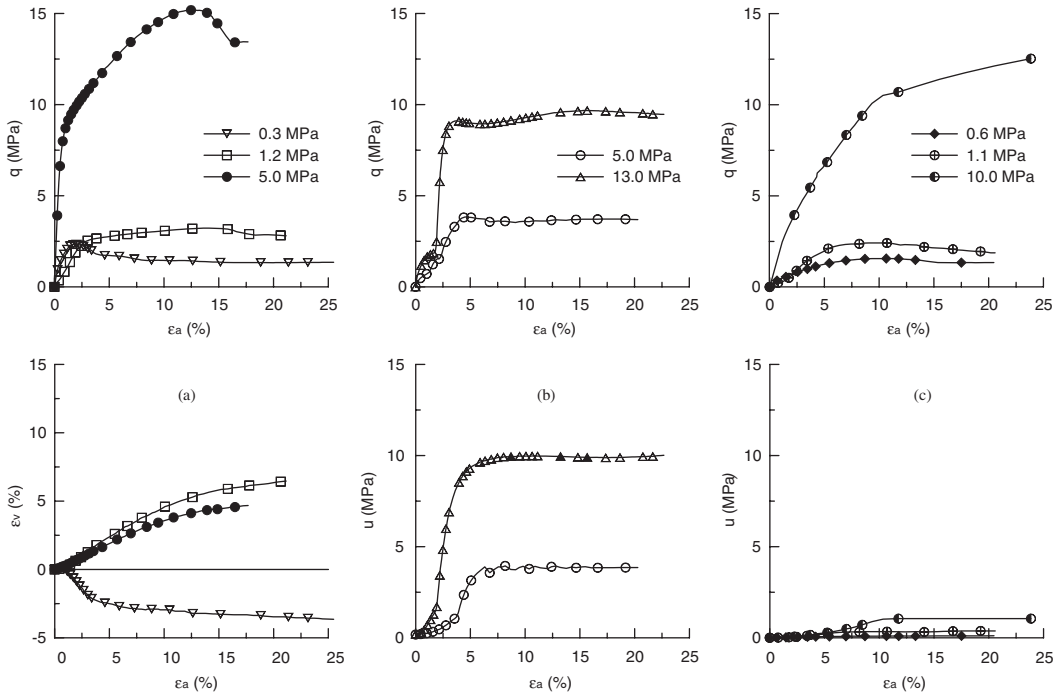


Figure 4. Results of triaxial tests: (a) CID tests on grouted specimens, (b) CIU tests on grouted specimens, (c) CIU tests on natural specimens.

at peak (about 2 MPa) and a contractant volumetric behaviour, with correspondingly low pore pressure increments ($0.1 \text{ MPa} < \Delta u < 0.4 \text{ MPa}$). In the test carried out applying a confining pressure of 10 MPa, a much larger value of the peak deviatoric stress has been observed.

With the exception of the highly overconsolidated specimen, all the triaxial tests performed on grouted material show similar values of the maximum mobilised stress ratio q/p'_{peak} as indicated in Table 3.

4 ANALYSIS OF EXPERIMENTAL RESULTS AND CONCLUSIONS

A first attempt to interpret the experimental observations discussed in the previous sections is here proposed in the framework of Critical State Soil Mechanics (CSSM) (Roscoe & Burland, 1968).

The volumetric response observed during the triaxial tests performed on both natural and artificially cemented pozzolana sand is reported in Figure 3 in the $v\text{-}\log(p')$ plot. In this plane it is possible to define a unique normal compression line for the grouted specimens, as already mentioned above.

Moreover, the final states observed during the triaxial tests performed on the cemented material lie along

a straight line that can be identified as the Critical State Line (CSL) projection on the compressibility plane. This line is almost parallel to the normal compression line of the same grouted soil. This result is consistent with the observation of a unique critical state value of the stress ratio q/p' mobilised during both drained and undrained triaxial tests on grouted pozzolana specimens. A unique Critical State can thus be defined for the grouted material. Natural samples of pozzolana exhibit a less clear volumetric response during shearing. Nonetheless, a careful inspection of the results of the undrained triaxial tests performed on natural specimens indicates that they tend towards the same CSL deduced for the bonded material in the $v\text{-}\log(p')$ plane.

Figure 5 shows in the $q\text{-}p'$ plane the stress paths observed on natural and grouted pozzolana sand during the triaxial tests: a unique critical state line of slope M equal to 1.5 is also shown in the figure. A detailed examination of the stress-strain behaviour summarized in Figure 4 has allowed the yield point to be identified for each triaxial test. Those points are reported in Figure 5 along the corresponding stress paths.

In CSSM, the existence of a unique State Boundary Surface (SBS) in the $p'\text{-}q\text{-}v$ space is postulated. It is possible to represent this surface in a normalised plane by means of the equivalent pressure p'_{es} , defined as the

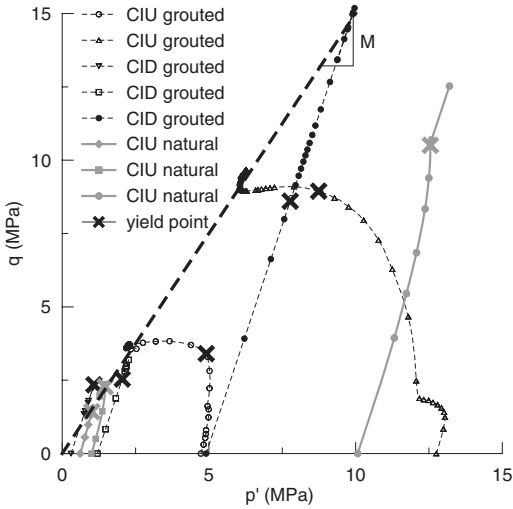


Figure 5. Stress paths of both natural and grouted specimens.

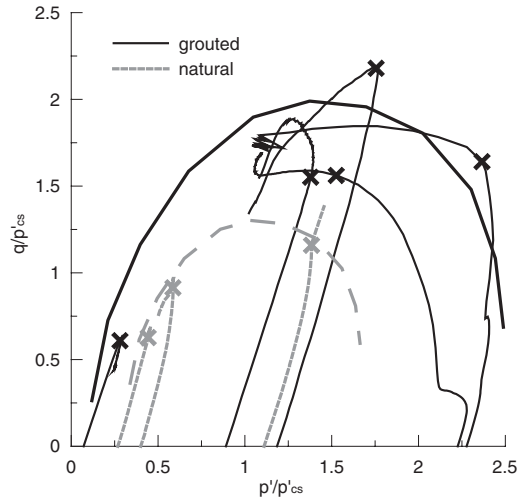


Figure 7. Grouted material, stress paths normalized with respect to p'_{cs} .

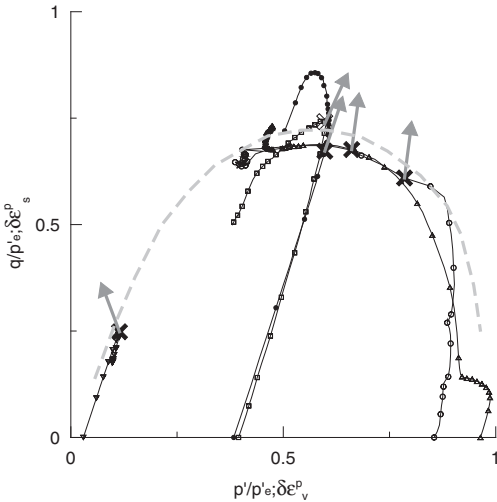


Figure 6. Grouted material, stress paths normalized with respect to p'_c .

mean effective pressure read on the isotropic compression line for the current specific volume. Figure 6 shows the stress paths relative to the grouted soil normalised with respect to p'_c . A unique SBS can be inferred for this set of results, as indicated in the figure. The same figure also shows the vectors representing the direction of the increment of plastic strain as evaluated at yield. These have been calculated based on the total strain components measured during the tests and

the corresponding elastic portion, evaluated assuming an elastic constitutive model for the soil.

To perform a comparison of the normalised paths observed on the grouted and natural soil, an alternative normalising approach has been adopted. In fact, the stress paths have been normalised with respect to the critical state mean effective pressure p'_{cs} , defined as the pressure on the CSL corresponding to the current specific volume. This was necessary as for the natural material no unique isotropic compression line has been observed, making impossible to adopt the equivalent pressure as normalising factor. On the contrary, a unique Critical State Line has been detected, allowing to adopt it as a unique reference state for both the natural and grouted samples. This normalisation is reported in Figure 7, where the two resulting SBS for the grouted and natural material are sketched. As expected, the grouted material is characterised by a larger SBS as compared to the one obtained by the natural soil, the differences being in terms of dimension but not in shape. This last finding can be interpreted as an indication of the isotropic character of the structuring and de-structuring process induced on the grouted material.

Finally, no conclusive indications emerge from the data concerning the character of the flow rule (associative or not) of this artificially bonded material. At this scope, further experimental investigation is required.

REFERENCES

Aversa S. 1991. Mechanical behaviour of soft rocks: some remarks. *Proc. of the Workshop on "Experimental*

- characterization and modelling of soils and soft rocks*", Napoli, Italy, p. 191–223.
- Jefferies S.A. 2003. Long term performance of grouts and the effects of grout by-products. *Proc. III Int. Conf. on Grouting and Ground Treatment*, ASCE, p. 1141–1152.
- Kavvas M. & Anagnostopoulos A. 1998. A framework for the mechanical behaviour of structured soils, *Proc. II Int. Symp. on the Geotechnics of Hard Soil-Soft Rocks*, Napoli: Balkema.
- Lirer S., Flora A., Borrelli M., Evangelista A. 2004. Modelling low pressure grouting of unsaturated silty sands. *Proc. V Int. Conf. on Ground Improvement Techniques*, Kuala Lumpur, Malaysia, p. 211–218.
- Lirer S., Flora A., Evangelista A., Verdolotti L., Lavorgna M., Iannace S. 2004. Laboratory investigation on the mechanical effectiveness of low pressure grouting of pyroclastic silty sands. *Proc. V Int. Conf. on Ground Improvement Techniques*, Kuala Lumpur, Malaysia, p. 203–210.
- Littlejohn G.S. 2003. The development of practice in permeation and compensation grouting: a historical review (1802–2002). Part 1: permeation grouting. Keynote Lecture, *Proc. III Int. Conf. on Grouting and Ground Treatment*, ASCE, p.50–144.
- Littlejohn G.S. & Haji-Bakar 1992. Engineering properties and behaviour of silicate grouted sand. *Proc. of the Conference "Grouting in the ground"*, London, p. 25–35.
- Liu M.D. & Carter J.P. (1998). On the volumetric deformation of reconstituted soils. Research Report n° R765, The University of Sidney NSW 2006, Australia.
- Maccarini M. 1987. Laboratory studies of a weakly bonded artificial soil. Ph.D. Thesis, University of London.
- Mitchell J.K. 1976. *Fundamentals of Soil Behaviour*. New York: John Wiley.
- Nicotera M.V. 1988. The effects of the degree of saturation on the mechanical behaviour of a neapolitan pozzolana. Ph.D. Thesis, University of Napoli Federico II (in Italian).
- Pellegrino A. 1967. Physical and mechanical properties of the neapolitan volcanic soils. *Proc. VIII Italian Geotechnical Conference*, Cagliari, Italy, p. 113–145 (in Italian).
- Roscoe K.H. & Burland J.B. 1968. On the generalised stress-strain behaviour of "wet" clay. *Engineering Plasticity*, Cambridge University Press, Cambridge, p. 535–609.
- Scotto Di Santolo A. 2000. Analysis of a steep slope in unsaturated pyroclastic soils. *Proc. of the Asian Conf. on Unsaturated Soils*, Singapore, p. 569–574.
- Sheikh B.A. & Jefferies S.A. 1992. Prediction of the strength of chemically grouted sand. *Proc. of the Conference "Grouting in the ground"*, London, p. 53–70.

Numerical method for sheet pile quay walls with sea-side ground improvement

M.R.A. Khan, K. Hayano & M. Kitazume

Soil Stabilization Division, Port and Airport Research Institute, Yokosuka, Japan

ABSTRACT: The stability of sheet pile quay walls on a thick clay deposit against horizontal load was investigated through a series of centrifuge model tests. An area at the sea-side adjacent to the quay wall was improved with cement-treated Kawasaki clay. Under 50g centrifugal acceleration, cyclic horizontal load was applied to the quay wall. A numerical method for estimating the mechanical behavior of the sheet pile quay walls subjected to horizontal load is presented. The method is a theoretical solution obtained by assuming that the portion above the ground level consists of sheet piles with applied horizontal load and below the ground level sheet piles subjected to horizontal resistance from the ground and the layer of improved deep mixing clay. The calculation results show good agreement with the centrifuge test results. The method can be used for predicting the deflection, bending moment and shear force of the quay wall.

1 INTRODUCTION

Due to large deformation of quay wall anticipated to be caused by dynamic loading, surrounded port-infrastructures are exposed to structural instability. During many earthquakes a number of sheet pile quay walls failed with different degrees of rotation and horizontal displacement. The seismic stability of a sheet pile quay wall can generally be increased by: (i) increasing the effective angle of internal friction or cohesion of backfill soil, (ii) driving the sheet pile into a dense layer of sand, (iii) increasing the thickness of sheet pile, and (iv) supporting the wall by ties and anchorages. Most of the techniques require large efforts and execution period, especially in the case of an existing quay wall. For an existing quay wall it would be preferable not to close the port for a long period. Sea-side ground improvement is one of the techniques which will not hamper the port-side activities during its execution, so that the service of the port is uninterrupted. Almost all of the researches related to the stability of the quay walls are involved the above mentioned techniques. Among recent researches, Hosseini et al. 2004 showed a numerical interpretation of the interaction of sheet pile quay walls and liquefied backfill soils. It is considered necessary to conduct a comprehensive study on the effects of sea-side ground improvement on the stability of existing sheet pile quay walls.

The sea-side ground improved with cement deep mixing (CDM) (CDIT 2002) is studied through a series of centrifuge model tests. The stability of the improved

sheet pile quay wall subjected to a number of cycles of horizontal load is investigated. The sheet pile quay wall studied here is without anchorage and tie. A numerical method for estimating the mechanical behavior of the improved sheet pile quay wall subjected to a horizontal load is introduced. Comparison between the results of numerical calculations and centrifuge model tests is presented to validate the numerical model. Basic equation of deflection of sheet pile is introduced and solved for the boundary conditions. The numerical model can be effectively used in predicting the deflection, bending moment and shear force acting on the sheet pile quay wall. These are the important design elements.

The relationship between the seismic active earth pressure and horizontal seismic coefficient obtained by the Okabe 1924 method is shown in Figures. 1(i) & (ii). In the centrifuge model (Fig. 1(iii)), seismic active earth pressure can be produced by applying an incremental horizontal load, F_h from the port-side. Here F_h will act

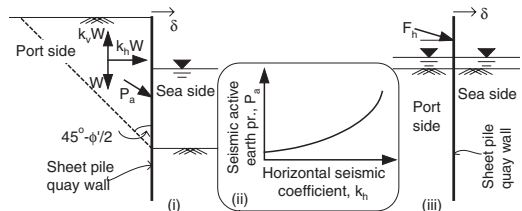


Figure 1. Conditions of field and model quay walls.

as an equivalent resultant thrust from the backfill ground, so that the load-deflection and other characteristics in the field (Fig. 1(i)) and in the experiments (Fig. 1(iii)) become similar.

2 CENTRIFUGE MODEL TESTS

Geotechnical centrifuge, Mark-II in the Port and Airport Research Institute (PARI) was used to perform the model tests. Figure 2 shows the schematic illustration of the model set-up. In a rectangular container a layer of kaolin clay (160 mm) was placed over a layer of dense Toyoura sand (60 mm) whose relative density was about 90%. A 2 mm thick instrumented steel plate was used as model quay wall. Prototype section of this plate becomes the Japanese standard sheet pile of type *SP-II*. It was inserted until the bottom of the sand layer. The clay layer was prepared with overconsolidated stress history where OCR varies from 33 to 2 and maximum past vertical pressure is 150 kPa. A specified area in the sea-side adjacent to the quay wall was improved with cement treated Kawasaki clay which is called as CDM. The Portland cement used was 40% of dry weight of Kawasaki clay. Seven days curing was allowed to gain standard strength (unconfined compression strength,

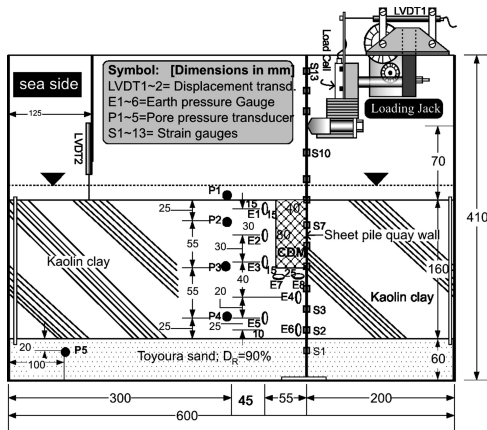


Figure 2. Model set-up of Case 4 (in model scale).

Table 1. Test conditions in prototype scale.

Test Cases	1	2	3	4	5	6	7
Clay depth (m)	8	8	8	8	8	8	8
CDM zone(m ²)	0 × 0	10 × 8	10 × 4	2 × 4	4 × 4	8 × 2	4 × 2
No. of load cycle	4	4	5	5	5	5	5
q_u of CDM (kPa)	–	920	617	1173	1536	1333	1020

$q_u = 920\text{--}1536\text{ kPa}$, Table 1) by the CDM. Under 50g centrifugal acceleration, the clay deposit was consolidated and at 70 mm above the ground level cyclic horizontal line-load was applied to the quay wall until large strain on the quay wall was observed. As shown in Figure 3 loading cycles were increased from 16 kN/m to 70 kN/m. Each cycle comprises 6 turns of loading and unloading with the jack speed of 3 mm/min. Width and depth of the improved area were varied and performance was compared with the quay wall on unimproved ground. Details of the centrifuge model tests and results are reported in Khan et al. 2006.

In this paper seven centrifuge tests are presented to validate the proposed numerical model. Test condition in prototype scale is shown in Table 1. All of the test cases are identical except for the size of the CDM block. Stability of unimproved and improved sea-side ground has been examined from the unimproved case (Case 1) and the improved cases.

3 FORCE EQUILIBRIUM

Forces applied to the sheet pile quay walls due to seismic motion are shown in Figure 4. Unimproved case is considered with the same backfill sand as used in the bottom sand layer. Horizontal cyclic load, F_h of 70 kN/m is equivalent to a dynamic active earth pressure from

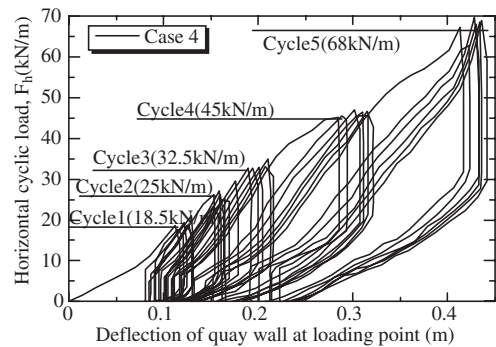


Figure 3. Cyclic load applied to the quay wall in Case 4.

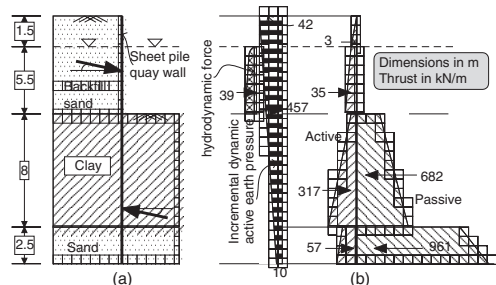


Figure 4. Pseudo-static force equilibrium (Case 1) at $k_h=0.2$.

a 7 m backfill which experiencing a seismic motion with horizontal seismic coefficient, k_h is 0.2. Various parameters of the backfill, sand layer, clay, sheet pile wall and the CDM block are listed in Table 2. The pseudo-static analysis presented here is based on the Okabe 1924 method and assumed $k_h = 0.2$. Dynamic active earth pressure which is the summation of static and incremental active earth pressure, dynamic passive earth pressure, hydrodynamic pressure are shown in the figure. Larger passive force is developed due to long embedment depth of the quay wall. Although in force equilibrium point of view quay wall is safe, i.e. resisting force, 1643 kN > the driving force, 908 kN, it is unsafe in rotation about the toe. Resisting moment (M_r) obtained about the toe is 5218 kN-m and driving moment (M_d) is 7540 kN-m. These values give a rotational factor of safety, $FS (=M_r/M_d)$ equal to 0.69. Figure 5a shows the variation of active earth thrust with the k_h and Fig. 5b shows the variation of FS with k_h for both unimproved and improved cases. In the calculation, forces in improved case (Case 3, CDM = $10 \times 4\text{m}^2$) a CDM layer of 4 m depth is assumed on top of the clay layer which produced passive pressure like clay ground. Since the CDM in Case 3 has the maximum width, it showed the highest factor of safety which is about 6 times larger than that of unimproved case (Case 1). All other cases will fall in between these two lines. The interaction among the CDM, the surrounding clay and the sheet pile should be taken into account in calculating the cases with intermediate sizes CDM.

Table 2. Parameters used in numerical analysis.

Backfill & bottom sand		Clay foundation	
γ_{sat} (kN/m ³)	15.9	γ_{sat} (kN/m ³)	18.8
γ_{wet} (kN/m ³)	13.9	γ' (kN/m ³)	8.8
γ' (kN/m ³)	6.1	c_u (kN/m ²)	25
ϕ'	42°		

Steel sheet pile wall		CDM zone	
I (m ⁴ /m)	8333×10^{-8}	γ_{sat} (kN/m ³)	15
E (kN/m ²)	2.1×10^8	γ' (kN/m ³)	5.2
EI (kN · m ²)	17170	c_u (kN/m ²)	460

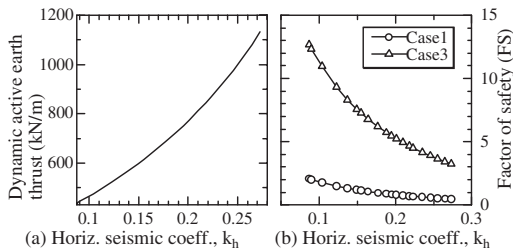


Figure 5. Dynamic force and factor of safety versus k_h .

4 TEST RESULTS AND DISCUSSIONS

4.1 Deflection of sheet pile quay wall

Deflection of the quay wall is the main index in describing stability. Figure 6 shows the relationship between horizontal load, F_h and deflection of quay wall at loading point. Deflection at $F_h = 45$ kN/m, δ_{45} , is chosen to compare with the data of all cases and is tabulated in the figure. Deflection δ_{45} of unimproved Case 1 is 0.47 m whereas full-depth CDM improved ground of Case 2 is 0.12 m. Improved stiffness becomes almost four times larger than that of the unimproved sea-side ground. Here stiffness is indicated as horizontal load per unit deflection. Cases 4, 5 and 3 with the same depth of CDM (=4 m) but different width (respective widths: 2 m, 4 m & 10 m) have δ_{45} of 0.29 m, 0.13 m and 0.12 m respectively. Even though the width in Case 3 was more than double that of the width of Case 5, the deflection was not decreased proportionally as decreased in Cases 4 and 5. The results imply that in increasing the width or size of the CDM to the full depth of the clay, a small amount of deflection of the quay wall will take place. This is defined here the limit of least deflection. Cases 7 and 6 with the same depth of CDM (=2 m) but different width (respective widths: 4 m & 8 m) have δ_{45} of 0.24 m, and 0.14 m respectively. The stiffness offered by the quay wall in these cases is almost proportional with the width of the CDM. The effect of depth of the CDM is investigated from Cases 5 and 7 with the same width but different depth (depths of CDM: 4 m & 2 m) have δ_{45} of 0.13 and 0.24. However, the interaction between the quay wall and the CDM, and between the CDM and surrounding clay are not yet thoroughly investigated. These interaction processes can affect the deflection of the quay wall significantly. Cases 2 and 3 having floating or half-depth and full-depth CDM have a δ_{45} value of 0.12 m in each case. Increasing the depth

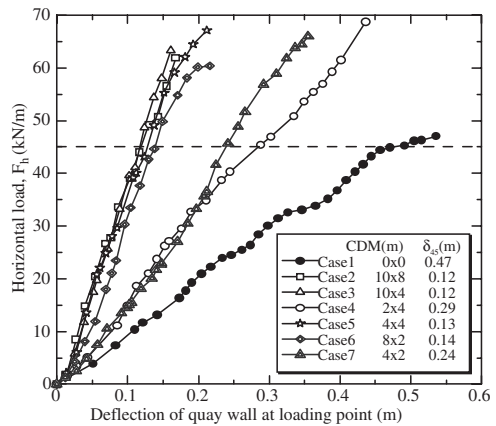


Figure 6. Load deflection curve of sheet pile quay wall.

of CDM may have stiffened the ground and reduced the wall deflection towards the limit of least deflection. Area wise performance of the CDM can be also compared from Cases 4 & 7 and Cases 5 & 6.

4.2 Bending moment and deflection distribution

Bending moments were derived from the responses of strain gauges along the wall. Figures 7a and b show the bending moment and deflection distribution of the sheet pile quay wall. Unimproved Case 1 shows the maximum bending moment of 215 kN-m below the ground level whereas the cases with improved sea-side ground show nearly half of this value. Maximum bending moments in the improved cases take place at the ground surface. Although the maximum bending moments in the cases with same CDM depth ranges from 120 to 130 kN-m trend of Cases 4 and 7 with smallest CDM shows curvature like the unimproved case. CDM is relatively much stiffer than the surrounded clay. The top part of the CDM adjacent to the sheet pile quay wall resists F_h primarily and distributes it to the surrounding clay.

Quantic spline functions were used to fit the bending moment distribution. The marks in the bending moment curve (Fig. 7a) are test data and the curve itself from spline equations. Two successive integrations of this curve give the lateral displacements along the wall which is shown in Figure 7b. From the displacement distribution of the sheet pile quay wall firm fixity at the bottom part, gradual bending near the ground surface and maximum displacement at the top can be visualized.

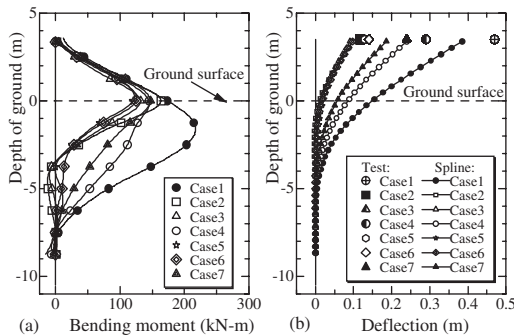


Figure 7. Moment and deflection of quay wall at 45 kN/m.

Test data of deflection at 45 kN/m load also agree well with the plot of displacement distribution of Figure 7b.

4.3 Horizontal subgrade reaction

Two successive differentiations of spline-curve of the bending moment give the horizontal soil reaction on the wall below the ground level which is shown in Figure 8a. Figure 8b shows the plot of horizontal soil reaction versus displacement at the ground surface. Average trend line is shown in each case with an equation. The slope of the trend line is the coefficient of horizontal subgrade reaction, k_s , at the ground surface and is determined likewise along the depth. Figure 8c shows the variation of k_s with depth. The resistance from the CDM can be visualized from the figure up to about 4 m of depth for Cases 3, 4, 5 and 2 m of depth for Cases 6, 7 except for Case 2 with up to about full depth. The value of k_s at ground surface in the improved cases ranges from 625 to 11,000 kN/m³ whereas k_s of

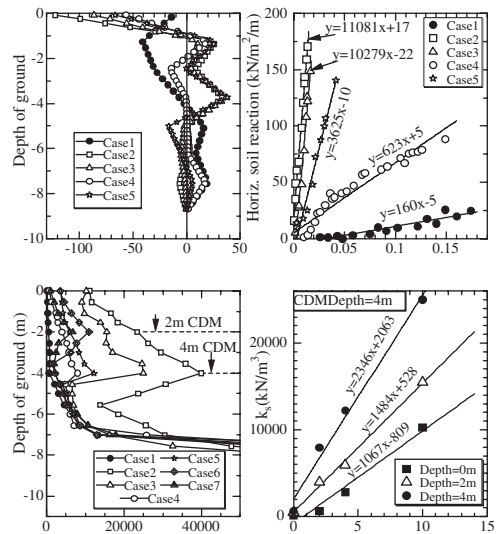


Figure 8. Determination of coefficient of horizontal subgrade reaction, k_s at 45 kN/m: (a) horizontal soil reaction along depth, (b) soil reaction vs. displacement at ground surface, (c) k_s along depth, and (d) k_s vs. width of CDM block of 4 m depth.

Table 3. Average k_s values (in kN/m³) used in calculation.

Depth (m)	Case1	Case2	Case3	Case4	Case5	Case6	Case7
0	160	11080	10280	625	3625	3510	1010
0-2	300	16200	11700	2300	4500	6700	3400
2-4	700	32800	20500	6300	9500	4400	2400
4-6	3900	12400	7000	5500	5400	5100	5300
6-8	61000	48000	31100	55900	53800	45700	53500
≥8	136900	88400	65200	113600	123600	103600	125300

unimproved case is 160 kN/m³. It is found that k_s until the depth of improved zone increases almost proportionally. The effect of width of the CDM on k_s is shown in Figure 8d at 0 m, 2 m and 4 m depth. The k_s increases almost proportionally with increases in width of the CDM. The relationship of k_s versus CDM width can be produced for any other depths also. The k_s corresponding to any other widths are determined from these relationships and used in the numerical method. The k_s can also be obtained from the relationships of various parameters like shear modulus, Poisson's ratio, shear strength, friction angle along the depth of the ground. Average k_s values used in the calculations along the depth is tabulated in Table 3.

5 NUMERICAL METHOD

5.1 Formation of equations

Elastic equilibrium of forces acting on the horizontal slice of sub-divided layers below the ground level is considered. Portion of the sheet pile quay wall above the ground level is treated simply as a cantilever beam where lateral distributed pressure, P acting on it. In simulation of the centrifuge model condition, it is assumed that the value of P is zero and a concentrated force F_h acts at 3.5 m above the ground level. Figure 9 shows the position of F_h and sub-divided layers in the clay stratum. As stated before the F_h is the equivalent dynamic active earth thrust. In actual field condition, P can be a polygonal pressure distribution. According to the theory of elastic beam, equation of deflection, y , of the sheet pile quay wall above the ground level,

$$EI \frac{d^4 y}{dx^4} = P \quad (1)$$

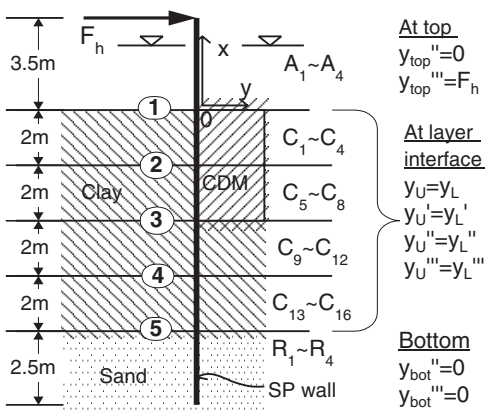


Figure 9. Numerical model of the sheet pile quay wall.

where EI is the flexural rigidity of the sheet pile, x is the vertical coordinate of elevation as shown in Figure 9. General solution of Eq. (1) is obtained as:

$$y = A_1 x^3 + A_2 x^2 + A_3 x + A_4 + Zx^4 \quad (2)$$

where $A_1 \sim A_4$ are integral constants obtained from boundary conditions and $Z = P/(24EI)$. Behavior of sheet pile quay wall below the ground level is calculated by the method of horizontal subgrade reaction (Chang 1937). Underground deflection of the sheet pile quay wall can be expressed as:

$$EI \frac{d^4 y}{dx^4} = -k_s y \quad (3)$$

where k_s is the coefficient of horizontal subgrade reaction on the sheet pile. General solution of Eq. (3) is obtained as:

$$y = C_1 e^{\beta x} \cos \beta x + C_2 e^{\beta x} \sin \beta x + C_3 e^{-\beta x} \cos \beta x + C_4 e^{-\beta x} \sin \beta x \quad (4)$$

where $\beta = \sqrt[4]{k_s/(4EI)}$, $C_1 \sim C_4$ are integral constants obtained from the boundary conditions in each layer of the clay ground ($\approx C_1 \sim C_{16}$ are used in application). Similar general solution can be written as Eq. (5) for the sand layer with the integral constants R_1 to R_4 .

$$y = R_1 e^{\beta x} \cos \beta x + R_2 e^{\beta x} \sin \beta x + R_3 e^{-\beta x} \cos \beta x + R_4 e^{-\beta x} \sin \beta x \quad (5)$$

5.2 Boundary conditions and solutions

To put the appropriate value of k_s to the equations the clay ground has been divided into four layers. Number of layers can be varied according to field conditions and required degree of accuracy of the prediction. Properties of the ground, sheet pile, CDM and average k_s values for each layer are shown in Tables 2 and 3. As shown in the figure, integral constants used in this method are $A_1 \sim A_4$, $C_1 \sim C_{16}$ and $R_1 \sim R_4$. y, y', y'', y''', y'''' will represent zero, 1st, 2nd, 3rd and 4th degree of derivative whose physical meanings are deflection, angle of deflection, bending moment, shear force and distributed load on the quay walls respectively. At top of the wall: $y_{top}'' = 0$, $y_{top}''' = F_h$, $P = 0$ and 2 equations are formed with constants $A_1 \sim A_4$. Left hand side of these 2 equations is the 2nd and 3rd derivative of Eq. (2). At each of the five layer-interfaces 4 equations are formed with the following boundary conditions: $y_U = y_L$, $y_U' = y_L'$, $y_U'' = y_L''$, $y_U''' = y_L'''$, where 'U' stands for upper layer and 'L' stands for lower layer of a particular layer-interface. In layer-interface 1 (ground level), different degrees of derivative of Eqs. (2) and (4)

are set on both sides of the boundary equations. $A_1 \sim A_4$, and $C_1 \sim C_4$ appears in the interface 1. Likewise $C_1 \sim C_{16}$ and $R_1 \sim R_4$ are used in the equations of remaining interfaces. In the five layer-interfaces total of 20 equations are formed. At bottom of the wall: $y_{bot}'' = 0, y_{bot}''' = 0$ and 2 equations are formed with constants $R_1 \sim R_4$. Left hand side of these boundary conditions is the 2nd and 3rd derivative of Eq. (5). 24 unknowns are then derived from the set of 24 equations. Particular solutions are obtained by using these constants in each layer. Successive differentiations of deflection equations (particular solutions) give corresponding bending moment, shear force and load distribution on the quay wall.

6 NUMERICAL RESULTS AND DISCUSSIONS

6.1 Deflection and bending moment

By using the particular solutions bending moment, deflection distribution, shear force and distributed horizontal load on the quay wall are determined for each test condition and presented in Figure 10. All of the results shown in the figures are derived while the quay wall was experiencing 45 kN/m horizontal load. Since k_s represents the reaction of the ground to the wall and was considered the appropriate value for each layer of the ground, the prediction of bending moment and deflection becomes reasonable. Test data

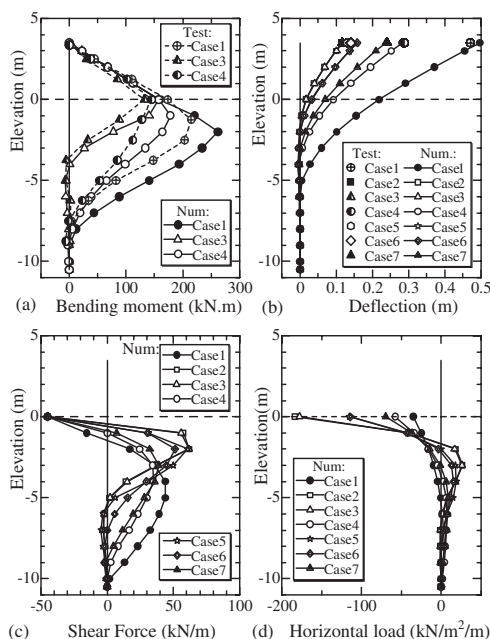


Figure 10. Bending moment, deflection, shear force and load distribution derived by the numerical method.

of bending moments are shown as dashed line in Fig. 10a. Deflection at loading point which is 3.5 m above the ground level was recorded at 45 kN/m loading and is plotted in Figure 10b as the test data. Though the magnitude of bending moment shows some differences from the test results, the shape and overall profile agree well with the centrifuge test data. Likewise deflection distribution of the sheet pile quay wall shows good agreement with the test points. Unimproved case (Case 1) shows large deflection as well as bending moment in the clay zone. Maximum bending moment in the improved cases is found at or near the ground level. Shear force distribution is shown in Figure 10c. Shear force at the ground level is -45 kN/m and below the ground level it reaches to about $+60$ kN/m. Horizontal distributed load on the quay wall as shown in Figure 10d is a kind of horizontal subgrade reaction which was stated in Fig. 8a. It is larger at the ground surface and the maximum value is about -184 kN/m²/m.

6.2 Effect of CDM size

As stated in the previous section interaction in terms of friction, adhesion and shearing during loading becomes larger with increasing width of the CDM block. Thus the deflection of the quay wall is reduced accordingly. Deflection is obtained numerically for various width and depth of the CDM by using the suitable k_s value. Figure 11 shows the relationship between deflection at loading point at the 45 kN/m loading stage and the width of the CDM block. Test data and numerical prediction are plotted in the figure. The lower line indicates the trend for CDM of depth equal to 4 m and the upper line for CDM of depth equal to 2 m. In the lower line, increasing the width of CDM block up to about 3 m proportionally reduces the deflection of the quay wall, which then reduces to the lowest deflection quickly. Deflection presented by the upper line decreases proportionally up to about 4 m of CDM width and then reduces to the

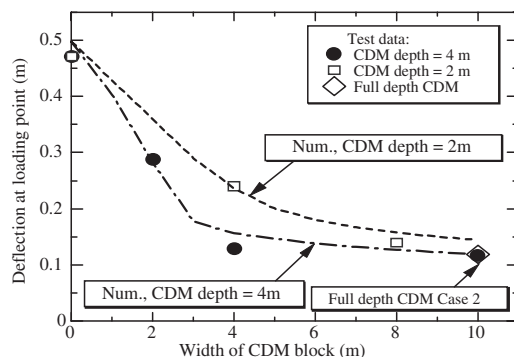


Figure 11. Effect of width of CDM block at 45 kN/m loading.

lowest deflection. Full-depth CDM (Case 2) also falls in the zone of lowest deflection. This figure implied that beyond 4 m width, CDM of 2 m depth is more efficient than that of 4 m depth or full-depth in reducing the deflection of the sheet pile quay wall. Since Cases 2 and 3, which have the same width but different depths (full- and half-depth), show the same deflection, from an economical feasibility point of view half-depth or the floating type CDM is more efficient for the field situation. Numerical prediction agrees well with the test data.

7 CONCLUSIONS

The conclusions of the study are as follows:

1. Numerical model of a sheet pile quay wall with sea-side ground improvement was established.
2. Prediction by the numerical model agrees fairly well with the results of centrifuge model tests.
3. Compared with the case of a quay wall embedded in unimproved ground, significant resistance against cyclic horizontal load was observed to

develop in the CDM improved cases, i.e. the horizontal deflection was effectively reduced.

4. The horizontal deflection of the model quay wall decreased proportionally with increase in width of the CDM area until it reaches a certain limit.

REFERENCES

- Chang, Y.L. 1937. Discussion of 'Lateral pile loading tests by L.B. Feagin', *Transactions of ASCE*, No. 102, pp. 272–278.
- Coastal Development Institute of Technology (CDIT), Japan (ed.). 2002. *The deep mixing method – principal, design & construction*. Rotterdam: Balkema.
- Hosseini, S.M.M. & Mosalmanzadeh, A. 2004. Interaction of sheet pile quay walls and the liquefied backfill soils. *Electronic J. of Geotech. Engg. (EJGE)*, Vol. 9/D: 1–13.
- Khan, M.R.A., Hayano, K. & Kitazume, M. 2006. Effects of sea-side ground improvement on the stability of existing sheet pile quay walls, *Proc. Conf. Physical Modelling in Geotechnics*, August 2006, Hong Kong (to be published).
- Okabe, S. 1924. General theory on earth pressure and seismic stability of retaining wall and dam. *Journal of Japan Society of Civil Engineers*, Vol. 10 (6): 1277–1323.